MICROBEAM ANALYSIS
1982

K. F. J. Heinrich, *Editor*

PUBLISHER'S NOTICE

The Microbeam Analysis Society (MAS) and its publisher since 1979, San Francisco Press, Inc., are not responsible for the information and views presented in this volume by the several contributors.

Back issues are available for 1979 through 1981 at $25 each; for 1981, there is also a separate volume of papers from the Analytical Electron Microscopy workshop at $25. Spiral-bound copies for 1974, 1975, 1976, and 1978 are also available from San Francisco Press at $20 each. The 1977 issue is out of print, but most of the papers from that meeting (held in conjunction with the 8th International Conference on X-ray Optics) have been published in full length and are available as a separate publication at $90.

Table of Contents*

*An Author Index appears on p. 529.

Officers of the Microbeam Analysis Society (1982)

MAS Executive Council

President:	Robert L. Myklebust, National Bureau of Standards
Past President:	James R. Coleman, University of Rochester
President Elect:	Roger Bolon, General Electric R & D Center
Treasurer:	Mary C. Finn, Lincoln Laboratory
Secretary:	Charles E. Fiori, Bldg. 13, Rm. 3W13, NIH, Bethesda, MD 20205 (301) 496-2599

Members at Large

David C. Joy, Bell Laboratories, Murray Hill, N.J.

Phillip B. DeNee, Mesa, Ariz.

Constance K. Barsky, Owens-Corning, Granville, Ohio

Fred Schamber, Tracor Northern Inc., Middleton, Wis.

Roy H. Geiss, IBM Research Laboratory, San Jose, Calif.

Thomas R. McKee, Southern Clay Products, Gonzales, Tex.

Honorary Members

L. S. Birks, Naval Research Laboratory, USA

I. B. Borovskii, Academy of Sciences, Moscow, USSR

Raymond Castaing, University of Paris (Orsay), France

V. E. Cosslett, University of Cambridge, England

Peter Duncumb, Tube Investments Research Laboratories, England

Gunji Shinoda, Osaka University, Japan

Sustaining Members' Information

AMRAY Inc.

160 Middlesex Turnpike
Bedford, MA 01730

Contact: James Furlong, (617) 275-1400

Product Line: Largest manufacturer of scanning electron microscopes and accessories in the
  USA.

Sales Offices:
  Tom Levesque, Dallas, Tex., (214) 247-3542
  Warren Johnson, Cleveland, Ohio, (216) 579-0035
  George Bruno, New York State, (617) 275-8310
  Don Pollock, Lico, New England, (617) 275-8310
  Ken Benoit, N.J., (609) 662-3922
  Gene Werbick, Los Angeles, Calif., (714) 848-1940
  Dr. Bart Yatchmenoff, San Francisco, Calif., (415) 964-5900

BABCOCK AND WILCOX RESEARCH CENTER

Alliance Research Center
Box 835
Alliance, OH 44601

Contact: Alex S. Miller, (216) 821-9110, Ext. 360

BAUSCH & LOMB/ISD

9545 Wentworth Street
Sunland, CA 91040

Contact: (213) 352-6011

Product Line: Nanolab scanning electron microscopes, SEMQ scanning electron microprobe
  x-ray analyzer, Omnicon image analysis system.

Sales Offices:
  9545 Wentworth St., Sunland, CA 91040, (213) 352-6011
  820 Linden Ave., Box 9189, Rochester, NY 14625, (716) 338-8209
  340 Melvin Dr., Northbrook, IL 60662, (312) 498-0400
  2131 Kingston Court SE, Marietta, GA 30067, (404) 952-9061
  2930 Baseline Rd., Nepean, Ont., Canada K2H 8T5, (613) 820-9437

CAMBRIDGE INSTRUMENTS INC.

40 Robert Pitt Drive
Monsey, NY 10952

Product Line: Research scanning electron microscopes and accessories, research production
  beam microfabrication systems, image analysis equipment.

Contact: Peter W. Boutell, (914) 356-3331

Sales Offices:
  Dick Harniman, Monsey, N.Y., (914) 356-3331
  Don Nelson, Pittsburgh, (412) 561-0313
  Mike Webber, Atlanta, (404) 926-9636
  John Pong, Calif., (714) 893-1609
  Jack Oltheten, Montreal, (514) 337-4343

CAMECA INSTRUMENTS, INC.

2001 West Main Street
Stamford, CT 06902

Contact: Barbara Alton, (203) 348-5252

Product Line: CAMBAX/MICRO x-ray microanalysis system with up to four WDS and one EDS spectrometers, fully automated by MICROBEAM for instrument control, data acquisition, and data processing. IMS-3F ion microanalyzer.

Sales Offices:
  Thomas Fisher, West Springfield, Mass., (413) 734-0617
  Robert D. Boies, Fresno, Calif., (209) 266-6372
  Harry Rundall, Dallas, Tex., (214) 423-4361

EDAX INTERNATIONAL, INC.

Box 135
Prairie View, IL 60069

Contact: R. W. Lichtinger, (312) 634-0600

Product Line: Manufactures energy-dispersive x-ray analysis systems for x-ray microanalysis in SEMs, TEMs, and electron probes as well as energy-dispersive x-ray fluorescence spectrometers. System configurations from basic qualitative to fully automated quantitative (with computer control and data processing) are available, including an automated WD/ED system with stage and spectrometer controls.

Sales Offices:
  V. Balmer, 637 Sunnyside Rd., Vermilion, OH 44089
  E. Martin, Box 547, New Rochelle, NY 10802
  J. Moore, Box 2253, Boulder, CO 80306

EG&G ORTEC

100 Midland Road
Oak Ridge, TN 37830

Contact: Charles Thomas, (615) 482-4411, Ext. 501

Product Line: Energy-dispersive systems for electron optical microscopes of all types. Wavelength-dispersive system electronics. Backscattered electron detection systems.

Sales Offices:
  Joe Redmond, Box 6041, Boston, MA 02209
  Peeter Kark, 9401 Comprint Court, Suite 101, Gaithersburg, MD 20760
  Robert G. Bardorf, Box 3355, Oak Ridge, TN 37930
  Dick Tischler, 21360 Center Ridge Rd., Rm. 304, Cleveland, OH 44116
  Earl Klugman, 310 Melvin Dr., Northbrook, IL 60062
  Richard Meiman, 21718 Rotherham Dr., Spring, TX 77379
  Val Johnson, Box 1678, Boulder, CO 80306
  Dave Butterfield, 29 Lumni Key, Bellevue, WA 89006

CHARLES EVANS & ASSOCIATES

1670 S. Amphlett Boulevard, Suite 120
San Mateo, CA 94402

Contact: Charles Evans or Vaughn Deline, (415) 572-1601.

Product Line: A materials characterization laboratory specializing in surface analysis. Our equipment includes Cameca IMF-3f secondary ion mass spectrometers (O^- and Cs^+), JEOL-JAMP-10 Auger, and General Ionex Rutherford backscatter spectrometer. We also offer spark source mass spectrometry, ESCA, and profilometry.

GATAN, INC.

780 Commonwealth Drive
Warrendale, PA 15086

Contact: Terry Donovan, (412) 776-5260

Product Line: Specializes in equipment for electron microscopy; products are: electron energy loss spectrometer (EELS), ion beam milling equipment, image intensifier system, analytical stages of beryllium construction, general EM specimen preparation equipment.

HITACHI SCIENTIFIC INSTRUMENTS
NISSEI SANGYO AMERICA, LTD.

460 E. Middlefield Road
Mountain View, CA 94043

Contact: Rod Norville, (415) 961-0411

Product Line: Transmission and scanning electron microscopes, atomic absorption UV-Vis spectrophotometers and amino acid analyzers.

Sales Offices:
  TEM/SEM: 1300 Quince Orchard Blvd., Gaithersburg, MD 20878, (301) 840-1650
  AAA/AA: 825 Third Avenue, Suite 2620, New York, NY 10022, (212) 755-2900

INTERNATIONAL SCIENTIFIC INSTRUMENTS, INC.

3255-6C Scott Boulevard
Santa Clara, CA 95051

Contact: Wayne Rogers, (408) 727-9840

Product Line: Scanning electron microscopes with a full complement of accessories including WDX spectrometers. The ISI SEM line includes: Alpha-9, Super IIIA, ISI-40, ISI S-100B, and ISI DS-130. Also in the product line is our new light/transmission electron microscope, the ISI LEM-2000. A complete line of scanning electron microscopes suited for any application and budget.

Sales Offices:
  Bill Maguire, Avon Park South, 20 Tower Lane, Bldg.2, Avon, CT 06001, (203) 677-0016
  Bud Bowen, c/o Santa Clara address, (312) 437-7790
  John Fitzpatrick, c/o Santa Clara address, (713) 777-0321

JEOL U.S.A., INC.

11 Dearborn Road
Peabody, MA 01960

Contact: Robert Santorelli, (617) 535-5900

Product Line: Manufacturers and dealers of scanning electron microscopes, transmission electron microscopes, scanning transmission electron microscopes, electron probe microanalyzers, scanning Auger microprobes, and energy loss analyzers.

Sales Offices:
  John Bonnici, American Office Mall, 275 Route #18, East Brunswick, NJ 08816, (201) 254-5600 or 5603
  Thayer Brickman, 1633 Bayshore Highway, Suite 245, Burlingame, CA 94010, (415) 697-9220
  Jack Francis, 1402 Rambling Hills Dr., Cincinnati, OH 45230, (513) 232-7350
  Thomas V. Gildea, 11 Dearborn Rd., Peabody, MA 01960, (617) 535-5900
  Ray Gundersdorff, 6236 Gilston Park Rd., Catonsville, MD 21228, (301) 953-2959
  Mike Hassel Shearer, 7586 Parkview Mountain, Littleton, CO 80123, (303) 979-0169
  Richard Lois, One Kingwood Place, Suite 122B, 600 Rockmead Dr., Kingwood, TX 77339, (713) 358-2121
  Lewis McDonald, 3223 G Post Woods Dr., Atlanta, GA 30339, (404) 434-9724
  Jean-Pierre Slakmon, Soquelec Ltd., 5757 Cavendish Blvd., Suite 101, Montreal, Quebec, Canada H4W 2W8, (514) 482-6427
  Robert Steiner, 640 Pearson St., Suite 102, Des Plaines, IL 60016, (312) 825-7164

KEVEX CORPORATION

1101 Chess Drive
Foster City, CA 94404

Contact: Robert P. Johnson, (415) 573-5866

Product Line: Analytical systems for x-ray energy spectrometry, wavelength-dispersive x-ray spectrometry, Auger, and electron energy spectrometry. Detector/cryostats and analytical spectrometer systems are compatible with all electron microprobe, SEMs, and TEMs in current production. Systems are available for both qualitative and quantitative analysis.

Sales Offices:
  Blaise Fleischmann, 6436 Barnaby St. NW, Washington, DC 20015
  Dana Kelley, 1101 Chess Dr., Foster City, CA 94404
  Frank Mannino, 627 Harvest Glen Dr., Richardson, TX 75081
  Ken Matz, 702 Main St., Collegeville, PA 19426
  Steve Miller, 602 S. Fairview, Park Ridge, IL 60068

KRISEL CONTROL, INC.

16 Farsta Court
Rockville, MD 20850

Contact: Christos Hadidiacos, (301) 762-1790

Product Line: Automation equipment for electron microprobe/microscope, featuring on-line data acquisition and reduction using Alpha and ZAF correction schemes. Single-crystal automation system for on-line data collection, centering, calculation of orientation matrix, and refinement of cell parameters for an x-ray diffractometer.

LINK SYSTEMS (USA), INC.

11735 Bowman Green Drive
Reston, VA 22090

Contact: William D. Stewart, (703) 471-1905

Product Line: Energy-dispersive x-ray microanalysis systems including interface with software support for electron energy loss (EELS), Auger, ESCA, and cathodoluminescence acquisition and processing. Simultaneous data acquisition and processing from energy-dispersive and wavelength-dispersive spectrometers including control of the microscope stage and spectrometers for fully automated analysis.

Sales Offices:
  Int'l. Instrument Corp., 64 E. Main St., Marlton, NJ 08053, (609) 983-6550
  Pulcir, Inc., Box 357, Oak Ridge, TN 37830, (615) 483-6358
  Tom Baum, RR 2, Box 109A, Kaufman, TX 75142, (214) 452-3116
  The Buhrke Co., 1500 Old County Rd., Belmont, CA 94002, (415) 592-2904

WALTER C. McCRONE ASSOCIATES, INC.

2820 South Michigan Avenue
Chicago, IL 60616

Contact: John Gavrilovic, (312) 842-7100

Product Line: Ultramicroanalytical services in chemistry and physics.

MICRON, Inc.

Box 3536
Wilmington, DE 19807

Contact: James F. Ficca Jr., (302) 998-1184

Product Line: Scanning electron microscopy, electron spectroscopy, electron probe x-ray analysis, transmission electron microscopy, quantitative image analysis, x-ray diffraction, x-ray fluorescence, optical microscopy and metallography, micro hardness, optical emission spectroscopy, differential scanning calorimetry, ultra microtomy, sample preparation.

MICROSPEC CORPORATION

265-G Sobrante Way
Sunnyvale, CA 94086

Contact: Richard C. Wolf, (408) 733-3540

Product Line: WDX-2A wavelength-dispersive x-ray spectrometer systems. X-ray microanalysis systems for use as accessories on scanning electron microscopes and other electron beam instruments. Capable of x-ray analysis of all elements down to beryllium, atomic number 4. Unique design permits attachment to most SEM electron columns.

PHILIPS ELECTRONIC INSTRUMENTS, INC.

85 McKee Drive
Mahwah, NJ 07430

Contact: Don Rodgers, (201) 529-3800

Product Line: The latest and most advanced scanning electron microscopes and transmission electron microscopes available.

Sales Offices:
  Bruce Roberts, 1104 U.S. Highway 130, Suite A, Cinnaminson, NJ 08077, (609) 829-4454
  Dennis Ahr, Clark Bldg., Suite 503, 5565 Sterrett Ave., Columbia, MD 21044, (301) 930-2100
  Larry Williams, 7094 Peachtree Indust. Blvd., Suite 220, Norcross, GA 30071, (404) 449-7206
  Ron Powley, 7525 Long Ave., Skokie, IL 60077, (312) 676-1714
  Harold Oemke or Harry Ittner, 2000 Scott Blvd. (S. 113), Santa Clara, CA 95050, (408) 727-5333

PHYSICAL ELECTRONICS
DIVISION OF PERKIN-ELMER CORP.

6509 Flying Cloud Drive
Eden Prairie, MN 55344

Contact: John Green, (612)828-6315

Product Line: Surface analysis instrumentation including Auger, ESCA, SIMS; also MBE.

Sales Offices:
  John Callaghan, 415 W. Golf, Arlington Heights, Ill., (312) 228-0130
  Edward Graney, 5 Progress St., Edison, N.J., (201) 561-6530
  Leslie Holmes, 1011 S. Sherman St., Richardson, Tex., (214) 669-4400
  Dan Jean, 2 Taunton St., Plainville, Mass., (617) 695-7181
  Jude Koenig and Dixie Sinkovits, 151 Bernal Rd., San Jose, Calif., (408) 629-4343
  Guy Messenger, 7310 Ritchie Hwy., Glen Burnie, Md. (301) 761-3053
  Pete Seamans, 655 Deap Valley Dr., Rolling Hills, Calif., (213) 377-7750
  Jerry Rosenthal, 1382 Old Freeport Rd., Pittsburgh, (412) 963-6717
  Elm Sturkol, 6509 Flying Cloud Dr., Eden Prairie, Minn., (612) 828-6332

PRINCETON GAMMA-TECH

1200 State Road
Princeton, NJ 08540

Contact: Chellie Goldberg, (609) 924-8980

Product Line: Energy-dispersive x-ray microanalysis and x-ray fluorescence systems, providing a full range of qualitative and quantitative capabilities. Wide variety of detector interfaces optimized for use with all current electron column instruments. Display scan generators for analyzer control of electron beam.

Sales Offices:
  Ray Prevost, 1009 Ridgefield Dr., Plano, TX 75075, (214) 423-3214

556 Weddell Dr., Suite 3, Sunnyvale, CA 94086, (408) 734-8124
Joe Piersante, Rt. 2, Box 50-A16, Gainesville, GA 30501, (404) 887-9100
Denny Cannon, P. O. Box 36157, Denver, CO 80236, (303) 978-0786
Tom Griffin, 701 Morewood Parkway, Rocky River, OH 44116, (216) 333-1931
Jay Sylvester, Rt. 2, Box 46A3, Gainesville, GA 30501, (404) 889-9573
Scientific System Sales Corp.:
  333 Jericho Turnpike, Jericho, NY 11753, (516) 882-4880
  203 Middlesex Turnpike, Burlington, MA 01803, (617) 273-1660
  14300 Gallant Fox Lane, Suite 212, Bowie, MD 20715, (301) 262-4104

C. M. TAYLOR CORPORATION

289 Leota Avenue
Sunnyvale, CA 94086

Contact: Dr. Charles M. Taylor, (408) 245-4229

Product Line: Various types of multi-element standards for microbeam analysis by SEM, micro-
  probe, and ion probe using energy, wavelength, and mass spectrometers. The standards
  available exceed 175 different metals, alloys, glasses, compounds, or minerals. Bence-
  Albee standards are available. Also manufacture many types of sample holders, polishing
  jigs, and other types of equipment for sample preparation. Also offers analytical ser-
  vices to customers desiring electron beam microprobe analysis using MAC-5 instrument.
  Have full ZAF correction capability for microprobe data, using FRAME B or BENCE-ALBEE
  procedures.

M. E. TAYLOR ENGINEERING INC.

11506 Highview Avenue
Wheaton, MD 20902

Contact: M. E. (Gene) Taylor, (301) 942-3418

Product Line: Scintillators for SEMs and microprobes, backscatter and secondary electron
  detectors of the quartz light pipe/scintillator design. Other products include Brimrose
  image intensifiers, ISI filaments and apertures, specimen mounts, and adhesive tabs.

Sales Offices:
  Agar Aids, 66A Cambridge Rd., Stansted, Essex, England, OM24 8DA
  Science Services, Badstrasse 13, 8000 München 70, Federal Republic of Germany

TRACOR NORTHERN

2551 West Beltline Highway
Middleton, WI 53562

Contact: Jim Aeschbach, (608) 831-6511

Product Line: Wide range of data-processing instrumentation for qualitative and quantita-
  tive x-ray analysis. Products include data acquisition, reduction, and automation for
  electron microprobe, SEM, TEM, and STEM. Featuring simultaneous EDS/WDS acquisition/
  reduction, digital beam control allowing for digital mapping, line scans, and other
  digital image processing. And now particle location, sizing, and elemental characteriza-
  tion. Flexible packaging allows instrument to be also used for ELS, Auger, ESCA, SIMS,
  etc. Other products are used in nuclear, optical, signal-averaging, and medical
  applications.

Sales Offices:
  345 E. Middlefield Rd., Mountain View, CA 94043, (415) 967-0350
  4215 Beltwood Parkway, Dallas, TX 75234, (214) 387-0606
  Miamisburg Centerville Rd., Dayton, OH 45459, (513) 439-3990
  Box 448, Lebanon, NJ 08833, (201) 534-4081
  3040 Holcomb Bridge Rd., Norcross, GA 30071, (404) 449-4165

TRACOR XRAY

Box 117
1400 A Stierlin Road
Mountain View, CA 94043

Contact: William D. Stewart, (415) 967-0350

Product Line: Automated energy dispersive x-ray fluorescence systems. Energy dispersive
  x-ray detectors for use on SEM, TEM, and electron microprobes.

Sales Offices:
  Buhrke Company, 1500 Old Country Road, Belmont, CA 94002, (415) 592-2904
  International Instrument Corp., 64 E. Main St., Marlton, NJ 08055, (609) 983-6550
  Instruments and Technology, 220 E. 14th St., Naperville, IL 60540, (312) 355-7748
  Buhrke Company, 508 Washington Ave. #4, Golden, CO 80401, (303) 278-0340
  Technical Instrument Co., 4215 Beltwood Pkwy., Suite 106, Dallas, TX 75234,
    (214) 387-0606
  Pulcir, Inc., Box 357, Oak Ridge, TN 37830, (615) 483-6358

CONFIDENCE IN MICROANALYSIS: LIES, DAMNED LIES, OR STATISTICS?

P. J. Statham

There are treatments of statistics in the literature[1],[2] that give a good idea of attainable levels of accuracy and detection limits in microanalysis. However, the influence of peak overlap is rarely considered and background subtraction is usually given only superficial treatment. Because of the wide variety of spectrum processing techniques that are employed, general formulas are not always suitable and often underestimate the statistical error. When elements are not detected that should be present or results fall outside the expected range of concentrations it is all too easy to blame the equipment. Conversely, when the equipment is given a clean bill of health, any unexplained inaccuracies can always be written off as statistical in nature. With a better understanding of methods of calculation, the analyst can usually decide what is the true situation. This paper therefore attempts to establish a few statistical concepts and to demonstrate calculation methods which, although not always mathematically rigorous, are sufficiently accurate for most practical applications.

Statistical Fluctuations

Imagine an experiment in which the count in a particular channel of an x-ray spectrum is recorded and the experiment is repeated a thousand times under identical conditions. If the results were plotted as a function of spectrum number we would obtain a graph similar to Fig. 1, where it is clear that the counts fluctuate despite the control of experimental conditions. A histogram showing the frequency of occurrence of different count values would take the appearance of a peak centered around $\bar{N}$, the mean value of the channel count over all spectra. If the count in a channel is a true indication of the number of quanta (photons) collected, then statistical theory tells us that this histogram should approximate a Gaussian function with full width at half maximum fwhm = 2.355σ, where $\sigma = \bar{N}^{\frac{1}{2}}$. (The distinction between "Poisson" and "normal" distributions is unimportant for the current purpose.) Another way to characterize the scatter in results is to calculate the root-mean-square (rms) fluctuation from the formula

$$\text{rms fluctuation} = \frac{1}{n} \sum_{i=1}^{n} (N_i - \bar{N})^2 \qquad (1)$$

where N_i is the channel count for the i'th spectrum. For a large number of measurements, the rms fluctuation is very close to σ, the "standard deviation" of the distribution. Of course it would be impossible to run such a sequence of experiments in practice and with only a single channel count N_i at our disposal, the estimate $\sigma = N_i^{\frac{1}{2}}$ can be used to predict the likely fluctuation. For a single measurement, there is a 99.73% chance that the value will be within 3σ of the true mean so the results tend to fall in a band of width 6σ centered around the mean (Fig. 1).

The $\sigma = N^{\frac{1}{2}}$ relationship is independent of channel width in the x-ray spectrum, so identical arguments apply to results obtained by integration over fixed energy windows. In spectrum processing, peak intensities are often calculated by combining results N_i from more than one window in a formula such as $N = f(N_i, i = 1 \text{ to } m)$; to calculate the expected statistical variation we make use of the following relationship:

$$\sigma_N^2 = \sum_{i=1}^{m} \left(\frac{\partial f}{\partial N_i}\right)^2 \sigma_{N_i}^2 \qquad (2)$$

The author is with Link Systems Limited, Halifax Road, High Wycombe, Bucks HP12 3SE, England.

which holds provided the individual results N_i are "statistically independent." Integrals from energy regions that do not overlap are statistically independent because if by chance an extra count fell in one region it would have no effect on the integrals for the others. If ranges do overlap, the chance addition of a count could affect the integrals for more than one region and in this case, Eq. (2) has to be expanded to include cross-correlation terms.[3] Equation (2) implies that if a result N is multiplied by a factor k then statistical variations are scaled by the same factor (i.e., $\sigma_{kN} = k\sigma_N$). Furthermore, if a result N is obtained by either addition or subtraction of the results A and B (i.e., $N = A + B$ or $N = A - B$) then $\sigma_N = (\sigma_A^2 + \sigma_B^2)^{\frac{1}{2}}$, the quadrature sum of the individual standard deviations.
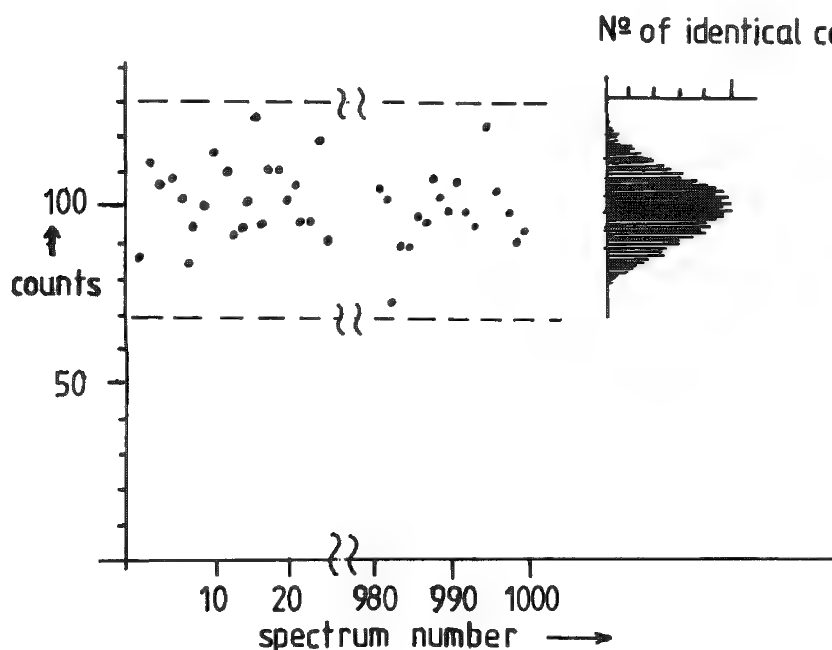
FIG. 1.--Results of hypothetical experiment where counts in a spectrum channel are recorded for 1000 spectra taken under identical experimental conditions; histogram shows mean count $\bar{N} = 100$, dashed lines show calculated limits of $\pm 3\sigma$ ($\sigma = \bar{N}^{\frac{1}{2}} = 10$).
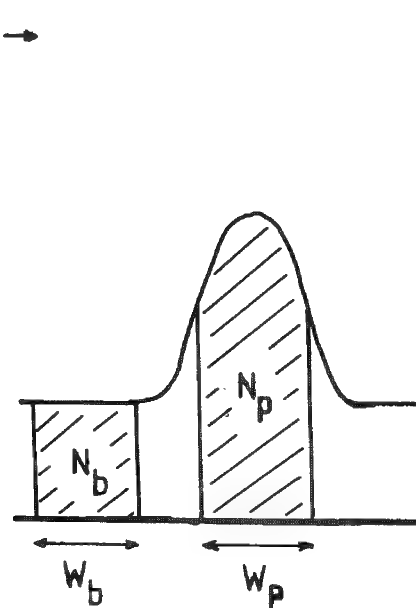
FIG. 2.--Integration ranges for single peak on uniform background.

Detection Limits

Consider the case of a single peak superimposed on a uniform background with integration ranges as shown in Fig. 2. (If the background is tilted, the background window can be split into two halves, one on either side of the peak.) The quantity

$$I = N_p - (W_p/W_b)N_b \tag{3}$$

derived from window integrals N_p and N_b is proportional to the net peak area. From Eq. (2),

$$\sigma_I = [N_p + (W_p/W_b)^2 N_b]^{\frac{1}{2}} \tag{4}$$

Usually it is quite easy to calculate an approximate conversion factor γ between counts and concentration, either from measurements on a known sample or indirectly from a peak for a different element in the same sample via the "k-factor" for thin-foil analysis,[1] so the standard deviation in estimated concentration is $\gamma\sigma_I$. For very small concentrations, $I \rightarrow 0$, so that $N_p = (W_p/W_b)N_b$ and by substitution in Eq. (4) we obtain

$$\sigma_0 = \{N_b(W_p/W_b)[1 + (W_p/W_b)]\}^{\frac{1}{2}} \tag{5}$$

From the earlier discussion it should be clear that even for a true concentration of zero, statistical fluctuations could produce concentration results as high as $3\sigma_0$. However, if the result were greater than $3\sigma_0$, we could be 99.86% certain that there was a nonzero concentration of the element concerned; this limit of significance is commonly referred to as

2

the "detection limit" or "minimum detectable mass fraction" (MMF). But if the true element concentration was equal to MMF, this would only guarantee that a *positive* result was obtained for I; the minimum concentration that would insure (to 99.86% confidence) that the measured concentration would exceed MMF is in fact 2MMF or $6\gamma\sigma_0$.

For a fixed number of counts in the peak window, $N_b W_p/W_b$,

$$MMF \propto [1 + (W_p/W_b)]^{\frac{1}{2}} \tag{6}$$

which shows the advantage of a large background window. However, even with an infinite W_b, MMF is only about 30% below the value it takes for $W_b = W_p$. If the peak window is adjusted to include a constant fraction of the total peak counts, then the width W_p is proportional to the fwhm of the peak, so for a fixed ratio (W_p/W_b), the counts N_b in the background are also proportional to fwhm. Furthermore, if the total count rate from the detector is n Hz then $\gamma \propto 1/n$ and $N_b \propto n$, so

$$MMF \propto (fwhm/n)^{\frac{1}{2}} \tag{7}$$

Thus we see that a two-fold improvement in count rate only reduces MMF by a factor of 0.7 and a 10% improvement in detector resolution produces a reduction in MMF of only 5%.

Effect of Peak Overlap

The above analysis considers a rather simple situation. When peak overlaps occur, not only is it often difficult to find a convenient region for background measurement but also the net peak area has to be corrected by subtraction of contributions due to overlapping peaks. Since the correct formula for σ includes terms for all the overlapping peaks and perhaps enhancement of the background term because of a restricted range of integration, the MMF may be considerably worse than the textbook value. Ryder[4] has analyzed the case of two overlapping peaks superimposed on a uniform (known) background where the "least-squares" technique is used to resolve the overlap. Working from Ryder's equations, we obtain for the MMF for an element with a peak in the wing of a large overlapping peak with area I_2

$$MMF \simeq 3\ \gamma\ \frac{fwhm}{d}\ (0.54B + 0.28I_2)^{\frac{1}{2}} \tag{8}$$

where B is the background integral over a range equal to fwhm and d is the peak separation; the formula is valid provided d >> fwhm. As is clear from this equation, the MMF may be unfortunately large if overlap is severe, and indeed it may even be impossible to assay an element with any realistic accuracy. As we would expect, good resolution is even more important when overlaps have to be resolved. If we consider the worst case, with both a high background (B >> I_2) and severe overlap, and note that B $\propto$ (fwhm/n), then

$$MMF \propto (fwhm)^{3/2}/n^{\frac{1}{2}} \tag{9}$$

In this case, a 10% improvement in detector resolution gives a 15% reduction in MMF.

Before we leave the subject of peak overlap, it is worth pointing out that if we are attempting to deconvolve a series of overlapping peaks, then the more peaks are included in the fit, the worse is the statistical error for each result. Thus, although it may be tempting to include as many elements as possible and leave a computer to "unscramble" the spectrum, higher precision is obtained if the operator can specify exactly which elements are likely to be present. For example, a spectrum of iron sulfide was analyzed by the filtered least-squares (FLS) approach[5]. When only the sulfur K peaks were present in the fit the estimated error in sulfur concentration was 0.24%, whereas when Pb M and Mo L peaks were included, the estimated error rose to 0.81%.

Concentration Differences

If we analyze two different samples and obtain different results, C_1 and C_2, for concentration of a particular element with associated estimates of statistical error σ_1 and σ_2, then we can determine whether the difference is significant by considering the statistical error in $(C_1 - C_2)$. From Eq. (2) we can say that $\sigma_{diff} = (\sigma_1^2 + \sigma_2^2)^{\frac{1}{2}}$. If the two samples have identical concentrations of the element then statistical fluctuations cause $(C_1 - C_2)$ to take values distributed about zero but with a 99.73% probability of being within $\pm 3\sigma_{diff}$. Thus, if

$$|C_1 - C_2| > 3\sigma_{diff} \tag{10}$$

we can be 99.73% confident that the two samples differ in composition. If σ_1 and σ_2 are roughly the same, then the criterion reduces to $|C_1 - C_2| > 4.2\sigma_1$.

If we have several measurements at our disposal, the confidence level can be more precisely defined and the degree of homogeneity for example can be determined using Student's t distribution.[2]

EELS Spectra

Electron energy loss spectra are commonly recorded by serial data collection. Although the original signal is produced by the arrival of discrete quanta (electrons), one can produce a spectrum--by analog-to-digital conversion (ADC), use of a voltage-to-frequency converter (VFC), or "pre-scaling" of counts from a threshold discriminator--in which channel-to-channel fluctuations are smaller than would be predicted by the $\sigma = N^{\frac{1}{2}}$ relationship. However, if channel counts are converted to equivalent numbers of detected electrons by application of a suitable scale factor, statistical errors can be calculated. (If an ADC or VFC is the only method of detection available, the scale factor may have to be estimated by observation of the residuals from a least-squares fit to a region of background.)
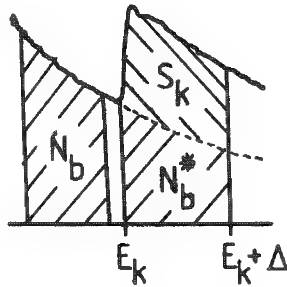
FIG. 3.--Regions of interest in EELS quantitation; fitted background curve is shown extrapolated beneath K-loss edge.

In the common method for K-edge quantitation, a curved background of the form AE^{-r} is extrapolated beneath the edge and subtracted to give the net integrated signal S_k (Fig. 3). We convert it to concentration in atoms/unit area by multiplying by the factor $1/[S_0\sigma_k(\Delta,\beta)]$, where S_0 is the counts obtained by integration of a window of width Δ over the zero-loss peak and $\sigma_k(\Delta,\beta)$ is the partial cross section for energy range Δ and collection angle β.[6] If the functional form of the background is known, the integral N_b of counts in the background region preceding the edge can be used to calculate the background $N_b{}^*$ beneath the edge by application of a factor derived from values for the energy limits and the exponent r. The standard deviation in $N_b{}^*$ is then simply $N_b{}^*/N_b{}^{\frac{1}{2}}$. If the total integral in the edge region is N_k, then $S_k = N_k - N_b{}^*$ with standard deviation $(N_k + (N_b{}^*/N_b) N_b{}^*)^{\frac{1}{2}}$. If we ignore errors in S_0, the 3σ-detection limit is therefore

$$3\{[1 + (N_b{}^*/N_b)]N_b{}^*\}^{\frac{1}{2}}/[S_0\sigma_k(\Delta,\beta)] \text{ atoms/cm}^2 \tag{11}$$

Although this formula seems reasonable, it does assume that r is fixed so the background can be obtained by scaling. If r is unknown and has to be determined from the data either by least-squares fitting or by application of a special formula,[6] the uncertainty in the extrapolation is increased. Since a detailed analysis of error propagation through either technique does not appear to yield any simple analytical formula, a simple approach has been used to estimate the added uncertainty. The background region is assumed to be split into two halves centered at E_1 and E_2 with integrals N_1 and N_2 which are used to calculate the equation of a straight line. The error in the background integral when this line is extrapolated is

$$\sigma_{N_b{}^*} = N_b{}^*[(1 - f)^2 N_1 + f^2 N_2]^{\frac{1}{2}}/[(1 - f)N_1 + fN_2] \tag{12}$$

where $f = (E_k + 0.5\Delta - E_1)/(E_2 - E_1)$. In the simple case where $N_1 = N_2 = N_b/2$, and for a typical value of $f = 3$, $\sigma_{N_b{}^*} = 5.1 N_b{}^*/N_b{}^{\frac{1}{2}}$. This result is somewhat alarming since it implies that the error is considerably worse (by a factor of 5.1) than if r were known.

This analysis is rather artificial; in an alternate approach, a background of the form $\exp(27.55)E^{-3.54}$ was combined with simulated Gaussian statistical noise and a log-log least-squares approach was used to fit the background to a curve of the form $\exp(a)E^{-r}$ over a fitting range from E = 213 to 273 eV at 1 eV per channel. The integral in the range E = 284 eV to E = 364 eV was compared with the extrapolated background integral for 100 simulations and the differences were used to calculate the standard deviation from Eq. (1). Typical values for N_b and $N_b{}^*$ were 210 000 and 100 000 counts, respectively, and the resulting detection limit was a factor of 3.1 greater than that predicted by Eq. (11). Although no overriding conclusions can be drawn from these results, they do suggest that cal-

4

culations which do not take into account the uncertainty introduced by fitting of the exponent r lead to unduly optimistic estimates of minimum detectable concentration.

Imaging

If an image is considered to be segmented into a fine grid of picture elements or "pixels," then the integrated intensity in a pixel can usually be related to the number of quanta Q detected and we can apply simple statistical calculations to see whether a given feature will be visible. If the feature covers an area including N_A pixels, by adjusting the eye-image distance we can arrange for the eye to average the intensity over the area and compare it with a region of similar size in the surrounding picture. For the feature to be visible, the intensity difference must exceed the level of statistical fluctuations, so

$$N_A Q_f - N_A Q_s > 5(N_A Q_s)^{\frac{1}{2}} \tag{13}$$

where the factor 5 implies the "Rose criterion" for visibility[7] and the subscripts f and s refer to feature and surrounds respectively. Figure 4 shows x-ray maps that were collected by use of a digital mapping facility described elsewhere.[8] In Fig. 4(b) a dwell time of 32 ms per pixel was used on a 64×64 grid and some small blobs are just visible running down the center of the image. Each blob occupies an area of about 4 pixels with a count per pixel Q_f of about 26, and is surrounded by an area of pixels with a count Q_s around 14; application of Eq. (13) gives $48 > 37$, which confirms that the blobs should be visible. In Fig. 4(a) the dwell time is only 8 ms per pixel and since $Q_f \simeq 7$ and $Q_s \simeq 4$, Eq. (13) suggests that the blobs are just below the limit of visibility.

Smoothing

The average of several measurements of the same parameter is subject to a smaller statistical standard deviation than the result of a single measurement. Spectrum smoothing relies on this principle and in the simplest application involves replacing a channel count N_i by the average over 3 adjacent channels, $(N_{i-1} + N_i + N_{i+1})/3$. This would be called a "3-point smooth"; 5-, 7-, and 9-point routines can similarly be defined. Although this procedure does reduce the magnitude of statistical fluctuations, it also degrades spectrum resolution, so that there have been many attempts to generate a smoothing technique that reduces the apparent noise while preserving resolution. The "Savitzky/Golay" procedure,[9] which replaces a channel count by a weighted sum over neighboring channels, is popular but techniques based on the Fourier transform can be even more effective.[10] Although these techniques produce results with more esthetic appeal than the raw data, it is important to consider quantitative effects on spectrum interpretation. The standard deviation at a particular channel can be calculated from Eq. (2) and is generally smaller than $N_i^{\frac{1}{2}}$, but any smoothing procedure introduces a correlation between fluctuations for nearby channels. In a noise excursion in a single channel, smoothing reduces the amplitude but spreads it over several channels in a form that matches the shape of the weighting function; for a polynomial smooth, this result normally means that spiky statistical noise is transformed into a series of wavy artifacts distributed throughout the spectrum. If we are using smoothing to aid peak detection, these wavy artifacts only complicate the issue and there is little justification for using a complicated smoothing technique when a simple one will be just as ineffective! A common misconception is that smoothing removes statistical noise, whereas in fact it is only "transmuted" into a form that is visually less apparent. If smoothing is performed prior to a series of processing algorithms, this procedure will make the expected error in the result even more difficult to calculate than it is already.

Chi-square Test

When a series of peaks, or a mathematical function, is fitted to a set of n data points y_i, i = 1 to n, the "goodness of fit" is normally assessed by observing the sum

$$\chi^2 = \sum_{i=1}^{n} [(y_i - s_i)/\sigma_i]^2 \tag{14}$$

5
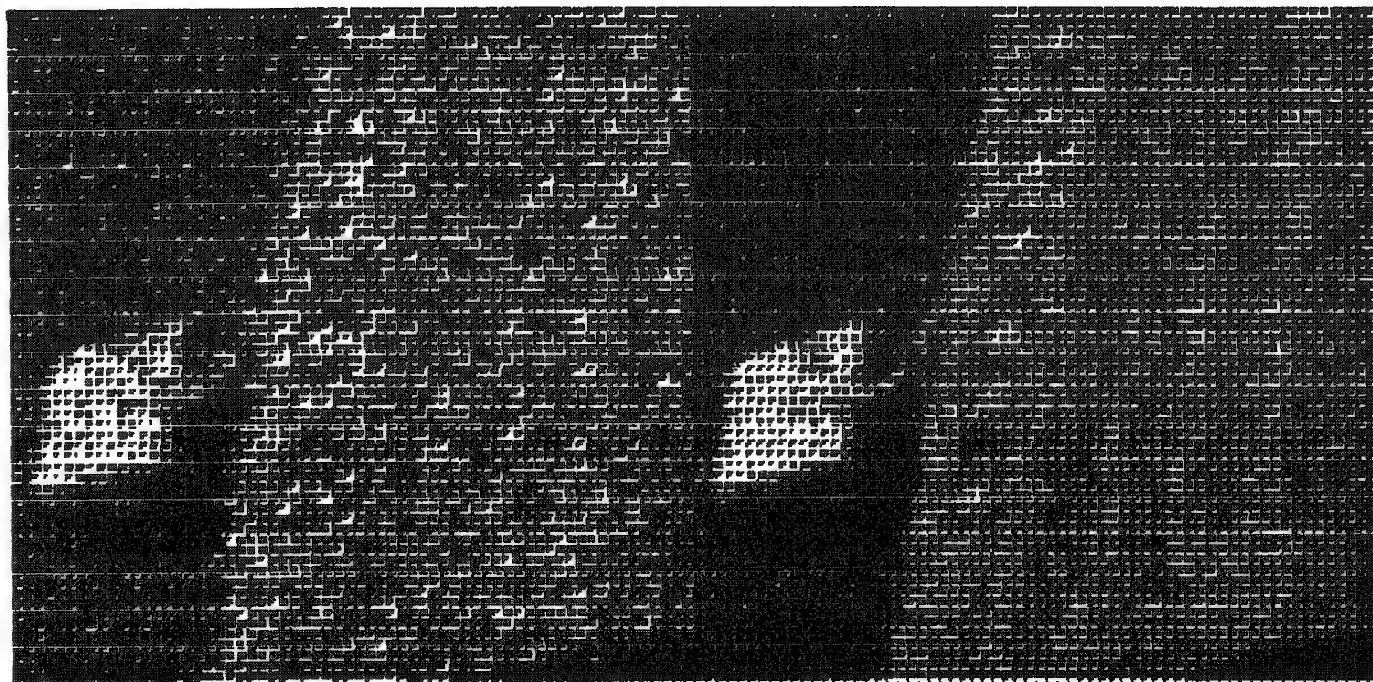
FIG. 4.--Digitized x-ray maps reproduced by dot-matrix printer, each with a 64 × 64 grid of pixels; frame times: (a) 33 s, (b) 131 s.

where s_i is the fitted result and σ_i is the statistical standard deviation at point i. If the individual data points y_i are statistically independent, then for large n, χ^2 is distributed according to a chi-square distribution with (n - m) degrees of freedom, where m is the number of fitted parameters. If s_i were the true mean at each point, then we might expect χ^2/n to be fairly close to 1; so if χ^2/n is much greater than 1 the fit is "bad." Although statistical theory can be used to apply tests to examine the validity of the fit, in practice it is usually sufficient to consider χ^2/n merely as an index that describes how great the observed differences are relative to random statistical errors. Since the relative statistical error is high in a spectrum with few counts, χ^2 is usually smaller than for a spectrum with good counting statistics. Of course that does not imply that results are better at short counting times and it is important to realize that χ^2 does not give a direct indication of accuracy.

Conclusions

Since the signal strength is severely limited in the microanalysis of thin films, statistical considerations have a much greater bearing than for microprobe analysis of bulk specimens. Even with a simple approach to error calculation it is possible to assess whether an experiment has any chance of success. It seems that closer attention to detail in statistical calculations is warranted when elements are close to the limit of detection.

References

1. J. I. Goldstein, in J. J. Hren, J. I. Goldstein, and D. C. Joy, Eds., *Introduction to Analytical Electron Microscopy*, New York: Plenum, 1979, 109-116.

2. J. I. Goldstein et al., Eds., *Scanning Electron Microscopy and X-Ray Microanalysis*, New York: Plenum, 1981, ch. 8.

3. P. R. Bevington, *Data Reduction and Error Analysis for the Physical Sciences*, New York: McGraw-Hill, 1969, ch. 4.

4. P. L. Ryder, *SEM/1977*, I, 273-280.

5. P. J. Statham, *Anal. Chem.* 49: 2149, 1977.

6. R. F. Egerton, *SEM/1978*, I, 133-142.

7. A. Rose, in L. Marton, Ed., *Advances in Electronics*, New York: Academic Press, 1948, vol. 1, p. 131.

8. P. J. Statham and M. Jones, *Scanning* 3: 168, 1980.

9. A. Savitzky and M. J. E. Golay, *Anal. Chem.* 36: 1627, 1964.

10. P. J. Statham, "Resolution enhancement of x-ray spectra," in D. R. Beaman et al., Eds., *Proc. 8th Int. Conf. X-Ray Optics and Microanalysis*, Midland, Mich.: Pendell Pub., 1980.

THE PRACTICE OF MODIFYING AN ANALYTICAL ELECTRON MICROSCOPE TO PRODUCE CLEAN X-RAY SPECTRA

L. F. Allard and D. F. Blake

In recent years, both conventional scanning transmission electron microscopes (TEM-STEM) and dedicated scanning transmission electron microscopes (D-STEM) instruments have come into widespread use as quantitative microanalytical tools. A number of articles have been published which address the need for modifying as-manufactured instruments to permit the collection of x-ray data suitable for quantitation. (References 1-4 are excellent tutorial articles which contain reviews of the literature concerning modifications for specific instruments.) Much effort has been concentrated on the elimination of peaks which appear in EDS spectra as a result of the excitation of x rays, by various processes, from areas away from the point of analysis on the specimen. Such peaks, generally called "systems peaks," may preclude accurate quantitative energy dispersive (EDS) analyses, reduce the sensitivity for detection of minor or trace elements, or impair the spatial resolution of analysis.

Systems peaks have been shown to originate from two general sources of exciting radiation. The first source, the "upper column", includes all components of the electron optical column above the specimen. Upper column sources produce a shower of x rays and high-energy electrons that can bathe the specimen and surrounding materials, creating a detectable spectrum even when the primary beam is allowed to pass directly through a hole in the specimen. A spectrum acquired in this fashion is usually called an "in-hole" or "hole count" spectrum. The second general source of exciting radiation is the sample itself, which produces not only the desired characteristic x-ray spectrum from the point of analysis, but also continuum x rays and backscattered electrons (BSEs) having energies up to the energy of the primary beam. This specimen-generated radiation can interact in a number of complex ways with adjacent volumes of the sample and surrounding materials to produce an x-ray spectrum that is not representative of the area analyzed.

This paper presents an example of a systematic procedure for modifying a typical analytical electron microscope (AEM) to identify sources of spectral contamination and minimize their effect on the sample spectra. The results of the modifications are described in a step-by-step fashion, with the physical processes that produce changes in the resulting spectra (peak ratios, background, etc.) analyzed and explained. A number of benchmark tests, using easily prepared specimens, are described that may be useful in establishing procedures for quantifying the performance of an AEM-EDS system.

Scope of the Paper

We describe a procedure for modifying a 100kV TEM-STEM (JEOL JEM-100CX), fitted with a horizontally mounted EDS detector. The modification procedure described follows, in general, the steps outlined by Bentley et al.[2] First, radiation generated from upper column components is identified and eliminated. Next, systems peaks generated by sources around the specimen, including the specimen itself, are identified and minimized. We do not address problems associated with microscopes operated in excess of 100 kV, or problems specific to dedicated STEM instruments. It is likely, however, that many of the specific tests suggested here would be useful for characterizing systems peaks in such instruments as well.

After a description of the modifications required to produce clean spectra for a stan-

dard set of conditions, some useful instrument calibrations are outlined to illustrate the effect of various operating parameters on the production of systems peaks in the EDS spectrum. Such calibrations are necessary so that the analyst can determine the range of operating conditions that give acceptable results. Tests are described which are designed to evaluate proper detector collimation, the presence and extent of electron tails, the effects of bremsstrahlung and characteristic radiation on sample self-excitation, and the like.

Upper Column Modifications

The flux of radiation from the upper column can be completely characterized by use of hole-count spectra from appropriate samples. An ideal specimen for this part of the procedure is a gold washer, prepared by drilling of a small hole (#80 drill) in a 3-5mil-thick gold foil. This sample is easily constructed and provides a large bulk of readily fluoresced material close to the beam path. In addition, gold has high-energy (9.7keV Lα) and low-energy (2.15keV Mα) lines useful for determining whether the peaks are generated by x-rays or electrons. The Au Mα intensity increases relative to the Au Lα intensity when there is appreciable excitation by electrons.[1,2] Gold is also useful for this and later tests because the Au Lα line efficiently fluoresces both copper and iron present in various components of the specimen chamber and thus gives an indication of the extent to which these components produce systems peaks by x-ray fluorescence mechanisms.

Experimental Conditions. For characterization of hole-count spectra, the gold washer was placed in a standard copper alloy specimen holder, to provide additional bulk around the specimen so that the lateral extent of x-ray fluorescence away from the specimen could be determined. The detector was inserted to a position which permitted the closest approach possible to the specimen when an appropriately designed detector collimator was in place. However, to determine the lateral extent of radiation from the upper column most effectively, the detector collimator was removed for all hole count tests. This procedure permitted x rays from any source within the specimen chamber to be detected.

Standard instrument operating conditions were chosen and used for all spectra acquired, unless otherwise specified. The standard conditions were: an accelerating voltage of 100 kV, with the emission current adjusted to produce an incident current of 0.5 nA, as measured by a simple Faraday cup inserted just above the sample. (This incident current is sufficient to give a count rate of about 500 cps on a 50nm-thick gold film). All spectra were acquired for 200 s, with a standard 35.° sample tilt used.

Modifications. Figure 1(a) shows the hole count spectrum obtained with the microscope in its pristine condition, with the beam positioned through the hole in the gold foil washer. The washer was held in the copper specimen holder in the single-tilt copper rod. The hole-count spectrum indicates that there is a large flux of radiation from the upper column which is incident over the entire sample area as well as the specimen holder. This spectrum gives initial evidence that the major problem in the JEM-100CX is x-ray fluorescence from the upper column rather than scattered electrons, since the low-energy Au Mα lines are substantially less intense than the high-energy Au Lα lines. In fact, the geometry of the CL system clearly precludes any substantial flux of scattered electrons from exiting the CL system, except for those electrons scattered in the forward direction and constrained by lens fields to remain near the beam.

The major sources of characteristic and continuum x rays in the upper column are the Mo thin-foil apertures of the CL system. To reduce the hard x-ray flux substantially, the thin fixed apertures were augmented by installation of thick Pt apertures with a slightly larger hole diameter directly beneath the thin apertures.[2] For example, if 625μm Pt apertures 250 μm thick are placed beneath the 600μm thin Mo apertures of the JEM-100CX, the transmission of hard x rays is reduced to less than 1% of the original intensity. The thickness of the Pt apertures should not be excessive, to minimize the potential for scattering of electrons from the bore. Figure 1(b) shows the reduction in the hole-count spectrum obtained with the "composite" fixed apertures described above. (Note the change in vertical scale.)

The flux of x rays resulting from the 200μm molybdenum thin-foil adjustable CL aperture can be reduced if this aperture is replaced by a 250μm-thick platinum aperture. One can fit this aperture to the aperture blade in the first aperture position by cutting away the seldom-used 400μm aperture from the aperture strip and leaving the remaining thin apertures intact. It is desirable to retain the thin-foil apertures for normal TEM

imaging since they do not contaminate as quickly as the thick apertures and provide routine capability for high-resolution imaging. Figure 1(c) shows the further reduction in the hole counts obtained using the thick aperture in the adjustable aperture blade. (Note change in vertical scale.)
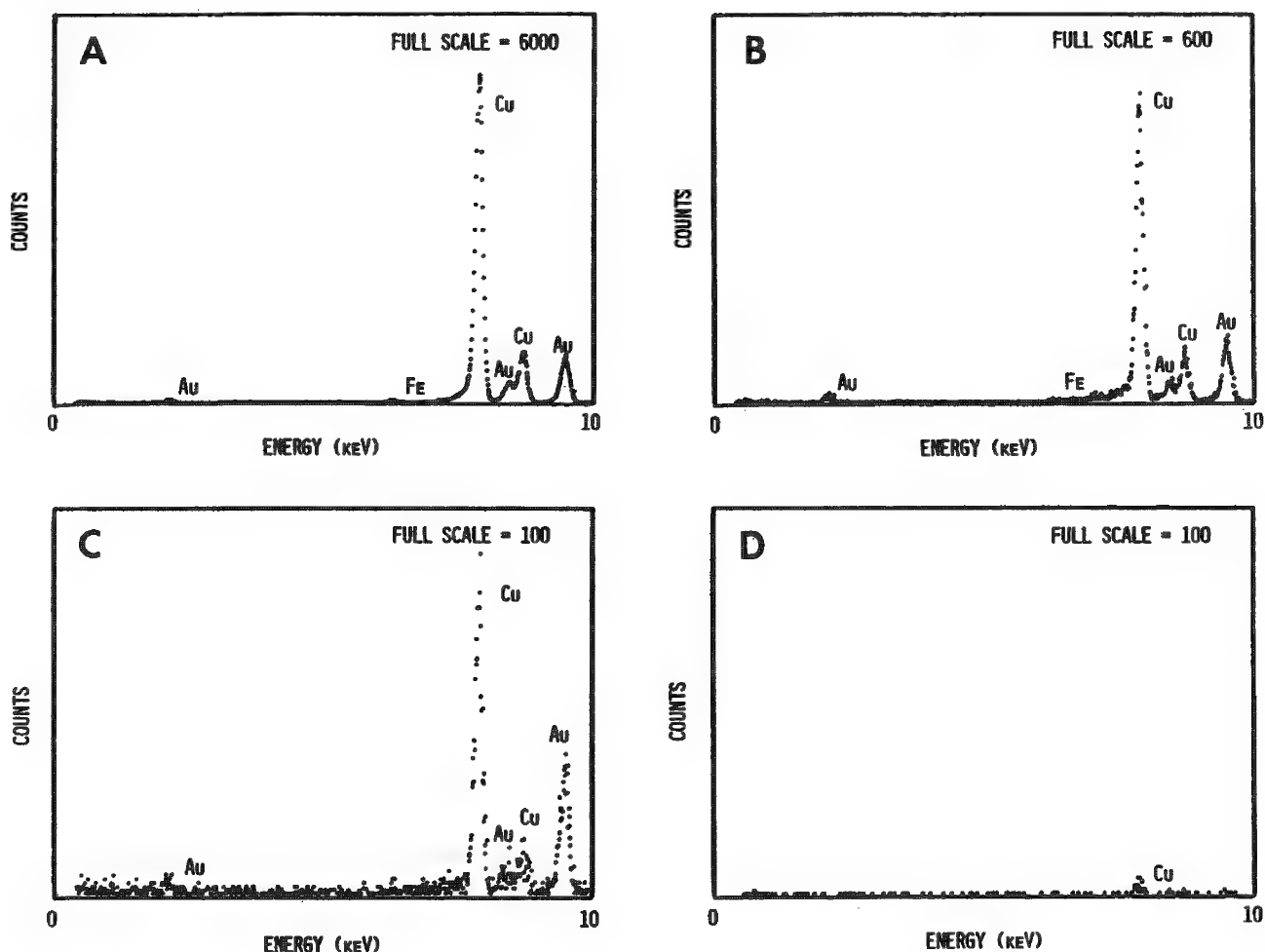
FIG. 1.--Hole count spectra from thick gold-foil test specimen (detector collimator removed): (a) unmodified upper column; (b) fixed CL thin foil apertures replaced by thick "composite" apertures; (c) same as (b) above, but with thin foil CL2 adjustable aperture replaced by 200μm-thick platinum aperture; (d) same as (c) but with 200μm-diameter "hard x-ray" aperture installed and properly centered.

The remaining x-ray flux from the upper column can be removed by a "non-beam-defining" aperture above the specimen. Various geometries of this aperture have been described in the literature.[1,5,6] Desirable features of such a "hard x-ray" aperture (HXA) are as follows: (1) the aperture should be removable so that it does not impair normal operating modes of the microscope; (2) it should effectively fill the bore of the column to the extent that no stray x-ray or electron scattering can result from its insertion around the beam path; and (3) it should block the x-ray flux as effectively as possible without intersecting the primary electron beam.

The hard x-ray aperture device available from JEOL for the JEM-100CX has the desirable features listed above. The HXA blade is installed above the OL polepiece through a slot in the magnetic shield tube, about 5 cm above the specimen. The advantage of this location is that it can be imaged by secondary electrons so that it can be roughly centered. In addition, it is sufficiently far above the specimen so that the flux of scattered radiation from the specimen does not interact extensively with the aperture to generate spectral artifacts. The aperture blade holds a platinum aperture 500 μm thick with a 200μm

cylindrical hole.

The alignment of the hard x-ray aperture with respect to the primary beam is critical. Fortunately, the aperture can be simply aligned by observation of the secondary-electron image (SEI) signal on a waveform monitor when the electron beam is in STEM "point" mode. The signal should appear as a point whose vertical position above the zero-signal baseline depends upon the SEI signal collected by the detector. The height of the signal above the baseline can then be minimized by adjustment of the aperture controls.

The diameter of the HXA should be only slightly larger than the beam diameter at the plane of the aperture, to minimize the total flux of hard x rays passing through the bore of the aperture. Unfortunately, the beam diameter at the plane of the aperture changes significantly with operating mode. The operator must be careful to insure that for different CL currents the HXA does not become beam-defining. For example, in the JEM-100CX, a 200μm HXA acts as a non-beam-defining aperture in "LO MAG" mode, but intercepts the electron beam substantially in "STD" mode.

The spectrum of Fig. 1(d) was collected under conditions identical to those of Fig. 1(c), but with the HXA inserted and properly centered. This spectrum shows only a few counts in the copper peak, even with no detector collimator in place and no special materials used in the sample chamber. With the use of a properly constructed detector collimator, or with low-atomic-number materials around the specimen, this hole count can be eliminated.

Sample Chamber Considerations

Effects of Sample-generated Spectral Contamination. Before discussing specific procedures for "cleaning up" the specimen environment, we shall find it instructive to outline the possible interactions between "sample-generated" fluorescing radiation and the specimen environment. If we assume that the hole count is effectively zero, then the point of analysis on the sample can be considered as the sole source of radiation that creates systems peaks when sample counts are acquired.[7] Figure 2 shows schematically the several important interactions which cause an x-ray or electron flux to enter the detector. The only useful signal is, of course, that of the electron-fluoresced x-ray signal from the analysis point (Fig. 2a). All other signals that enter the detector contribute to systems peaks or to background in the spectrum. A wide variety of materials near the specimen can be fluoresced by either x rays or backscattered electrons from the point of analysis on the sample. Figure 2(b) shows schematically how these x rays can enter the detector and produce systems peaks. It is also possible for electrons to backscatter from materials near the specimen and enter the detector, but this effect is probably negligible. A second mechanism for the production of systems peaks is illustrated in Fig. 2(c). X rays and/or backscattered electrons from materials near the specimen can fluoresce bulk regions of the specimen, producing incorrect relative peak heights in the spectrum.[8] Perhaps the most important source of x-ray spectral contamination, however, is self-excitation of the sample by x rays and backscattered electrons from the point of analysis (Fig. 2d). This effect is particularly nefarious since sample self-excitation results in changes in relative peak heights in the spectrum that are not as obvious as other types of spectral contamination. This is a major problem with thin-foil analysis in an AEM, dependent to some extent on sample type. There is at present no way to prevent this sample self-fluorescence, and no way to prevent it from contributing to the acquired spectrum. Even a well-designed collimator permits x rays from an entire 3mm sample to enter the detector.

This brief overview is intended to put the problem in perspective before the necessary modifications are described. It is important for the analyst to be fully aware of the possible sources of systems peaks within the sample chamber before a clean-up procedure is devised for a particular instrument.

Detector Collimation. Before the sample chamber is modified, it is necessary to install a detector collimator to prevent x rays from large distances away from the specimen from entering the detector. If a collimator is not used, it is difficult to isolate and eliminate sources of x rays in a systematic fashion. Once systems peaks are adequately removed with a collimator in place, subsequent removal of the collimator can provide information on the residual x-ray or BSE sources within the chamber.

In a typical collimator design (Fig. 3), the graphite liner of the collimator has a hole tapering from 1.5 mm at the tip to 2.5 mm at the base over a 5mm length, with the

front surface tapered at 45° to permit the detector to be positioned as close as possible to the sample. Such a collimator effectively absorbs off-axis copper and iron x rays and reduces the intensity of these major spectral contaminants to only a few percent of their incident intensity. The tapered bore permits the largest possible solid angle to be subtended by the detector[9] but limits the penumbra of solid angle to a reasonable size.
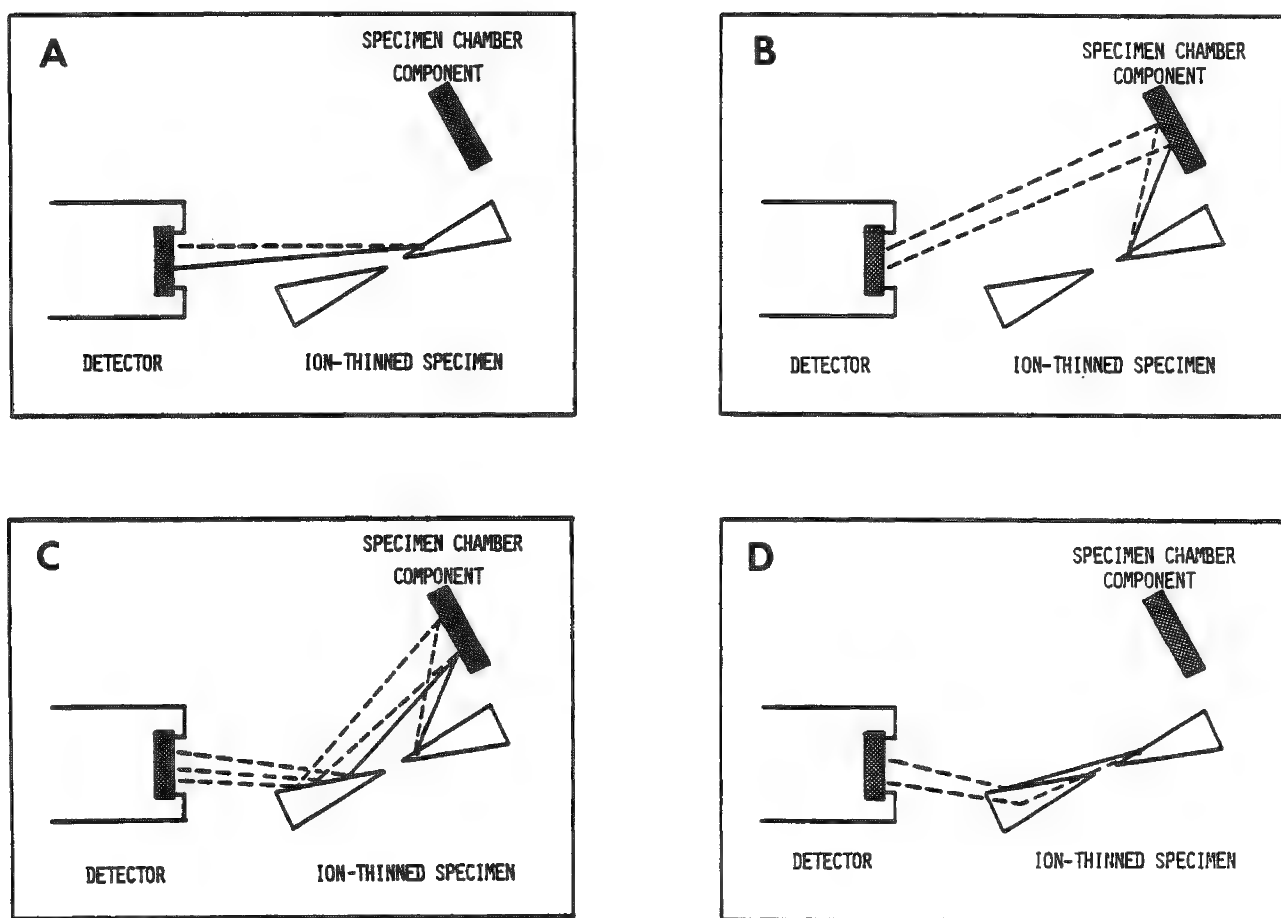
FIG. 2.--Possible sources of spectral contamination generated in specimen chamber by x rays (dashes) and electrons (solid lines) from specimen: (a) characteristic and continuum x rays from the point of analysis, as well as backscattered electrons; (b) sample-generated radiation fluoresces x rays from chamber components; (c) sample-generated x rays and electrons interact with chamber components to produce x rays and electrons, which in turn fluoresce bulk areas of the specimen away from the point of analysis; (d) sample-generated x rays and electrons fluoresce bulk areas of specimen away from the point of analysis.
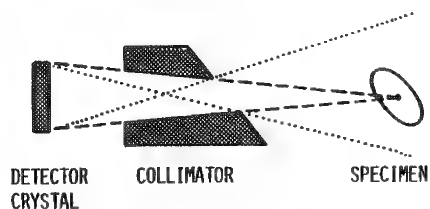
FIG. 3.--Design of graphite collimator to maximize cone of acceptance or umbra (dashes) of x rays from point of analysis while minimizing the cone of acceptance or penumbra (dots) of x rays from surrounding volume.

A detector collimator cannot prevent high-energy BSEs or high-energy x rays from entering the detector along with the normal spectrum. The extent to which these signals produce spectral artifacts has been discussed recently and will not be reviewed here.[10] An advantage of a horizontal detector over a high-angle detector is that BSEs are effectively swept out of the detected cone of radiation by the lens field. High-angle detectors require special collimation to minimize the BSE signal that enters the detector.[11]

One potential problem with the installation of a collimator is proper alignment of the axis of the

detector with the analysis point. It is possible that an as-received detector will not be correctly aligned with the analysis point, so that when a collimator with a small entrance hole is installed it will intercept a portion of the incident cone of x rays. If that happens, low-energy x rays are preferentially absorbed over higher-energy x rays, and improper ratios between high- and low-energy lines results. Figure 4(a) shows the effects of an improperly aligned detector. A spectrum of bulk tungsten was acquired, which shows strong peaks from the W Lα, Lβ lines, but virtually no intensity in the W Mα line. With a properly aligned detector and collimator, the spectrum showed a reversal in the ratio of W Lα and W Lβ peaks, as well as an intense W Mα peak (Fig. 4b). In addition, the background was decreased substantially.
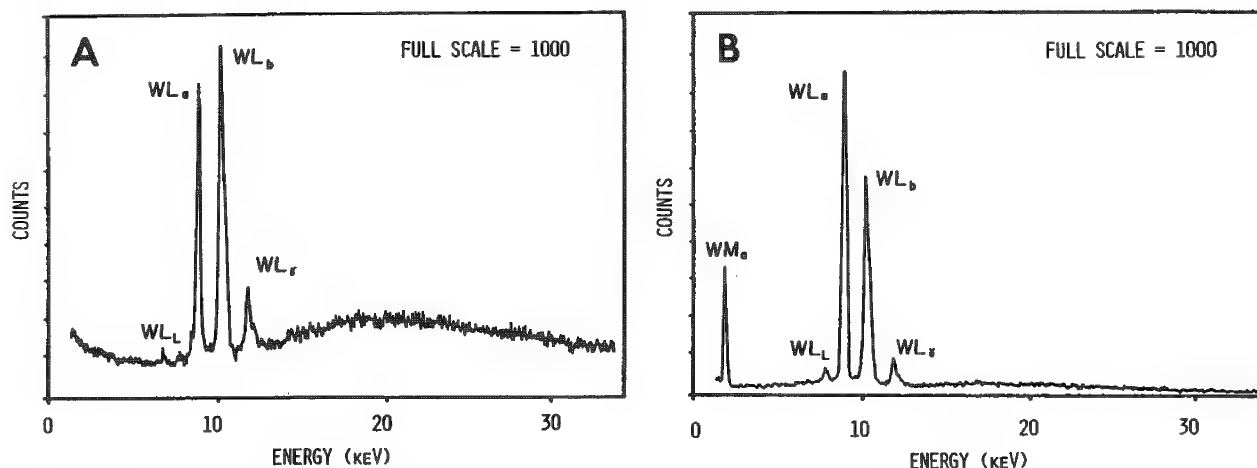
FIG. 4.--Demonstration of (a) poor and (b) good detector-collimator-sample alignment. Sample: bulk tungsten. Note relative changes in peak heights.

Sample Chamber Modifications

Sample Types. As with the upper-column modification procedure, gold is considered to be an ideal material to serve as a worst-case sample for sample chamber tests. Two types of specimens were prepared, a 50nm gold film sputtered onto a carbon film supported on a beryllium grid, and a composite sample that results when this thin film is placed over the thick gold washer used previously for hole-count spectra.

Sample counts were acquired with the same beam conditions used for hole count spectra, and with the sample tilted at 35°. The OL aperture was retracted to the zero position, and an anticontamination device was in place.

An initial sample count was acquired from the thin Au film, with the specimen retained in the single-tilt copper specimen rod (Fig. 5a). The primary spectral contaminant is copper, clearly from the large bulk of copper surrounding the specimen. The copper appears to be primarily x-ray excited, since there is no evidence of a Cu Mα peak at 0.93 keV. This result illustrates the importance of using the appropriate test specimen; if a low-atomic-number material had been used as a test specimen, the copper peak would have been much reduced, which would indicate less severe sample chamber spectral contamination. Figure 5(b) shows a similar spectrum with the specimen held in a graphite specimen holder but still in the copper specimen rod.[12] The reduction in copper indicates that much of the copper in the original spectrum originated directly in the copper specimen holder. However, simple replacement of the original sample holder with one made of graphite is not sufficient to remove copper as a spectral contaminant.

A simple test was used to determine the extent to which the remaining sources of copper were located above or below the plane of the specimen. When the thick gold washer was inserted below the thin gold film, the spectrum of Fig. 5(c) resulted. This further reduction of copper indicated that there was a significant source of copper x rays below the specimen, as the washer effectively collimates any flux of radiation from below the specimen plane. The nearest copper sources below the specimen were the floor of the cold cup and the top of the copper guard tube in the OL bore. By fitting a piece of beryllium sheet 150 μm thick to the floor of the cold cup, and replacing the top of the copper guard tube with an identical part made from Al,[5] we obtain the spectrum of Fig. 5(d). This spectrum
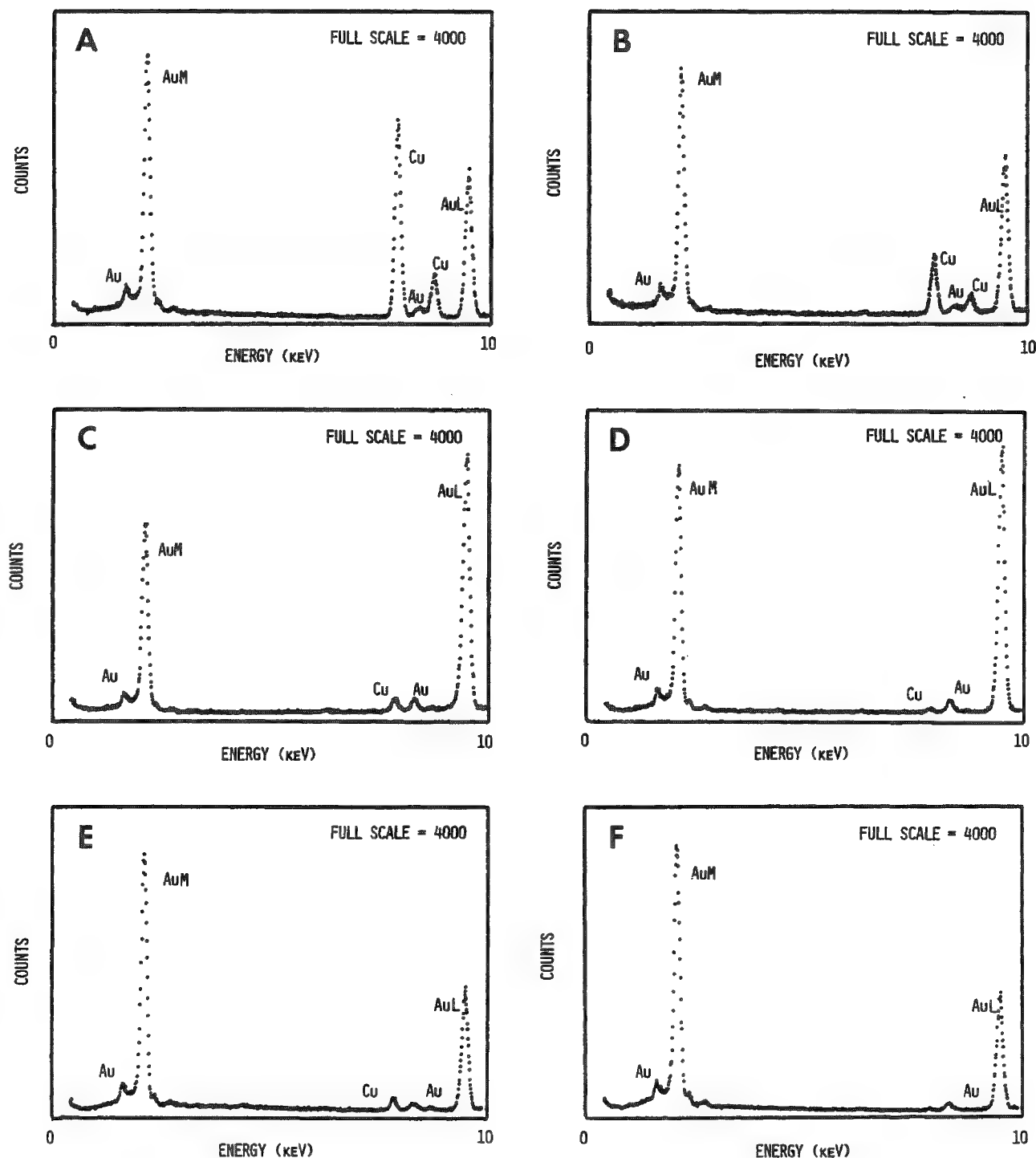
FIG. 5.--Spectra of gold-foil sample resulting from sample chamber modifications: (a) gold thin foil, copper specimen rod, copper specimen holder, no modifications; (b) copper holder replaced by graphite holder; (c) same conditions as (b) but with thick gold washer under thin gold film (reduction of copper peak suggests that source is below sample); (d) same conditions as (c) but with beryllium foil covering floor of cold cup and copper guard tube replaced by aluminum tube; (e) same conditions as (d) but with gold washer removed from below specimen (increase in copper peak suggests additional copper source below specimen); (f) same conditions as (e) but with copper specimen rod replaced by one made from aluminum.

shows copper reduced to a level barely above background, which indicates that most of the copper x-ray sources below the specimen plane were eliminated. It is informative to compare the relative heights of the Au La and Au Ma peaks between Figs. 5(b) and (c). The change in relative peak heights from the thin-foil spectrum of Fig. 5(b) to the thin-foil spectrum of Fig. 5(d) resulted from the presence of the thick gold washer. This effect is shown schematically in Fig. 2(d). X rays from the point of analysis on the thin foil fluoresce the bulk gold of the washer, which results in an increase in the Au La peak relative to the Au Ma peak. A further change in the peak ratios shown between Figs. 5(c) and (d) suggests that some of the gold x-ray fluorescence was generated by continuum x rays from the cold cup and the copper guard tube. When this source was removed by installation of beryllium foil and the Al guard tube, the Au La was reduced in intensity relative to the Au Ma.

The spectrum of Fig. 5(e) was acquired under conditions identical to those of Figs. 5(d), but with only the thin gold film in place. The re-appearance of copper in the spectrum indicated that there was an additional source of copper x rays below the specimen plane. Calculations indicated that the graphite specimen holder was not thick enough in the vicinity of the specimen to absorb the copper x rays that were produced in the specimen rod by both characteristic and continuum x rays from the gold sample. To eliminate this source of copper x rays from the spectrum, a facsimile single-tilt rod was constructed from aluminum, since only about 30 μm of graphite is required to attenuate 99% of the Al Ka x rays. Figure 5(f) shows the resulting thin-film spectrum, which demonstrates that the copper peak was effectively eliminated by this final sample chamber modification, and that the aluminum rod did not contribute a systems peak.
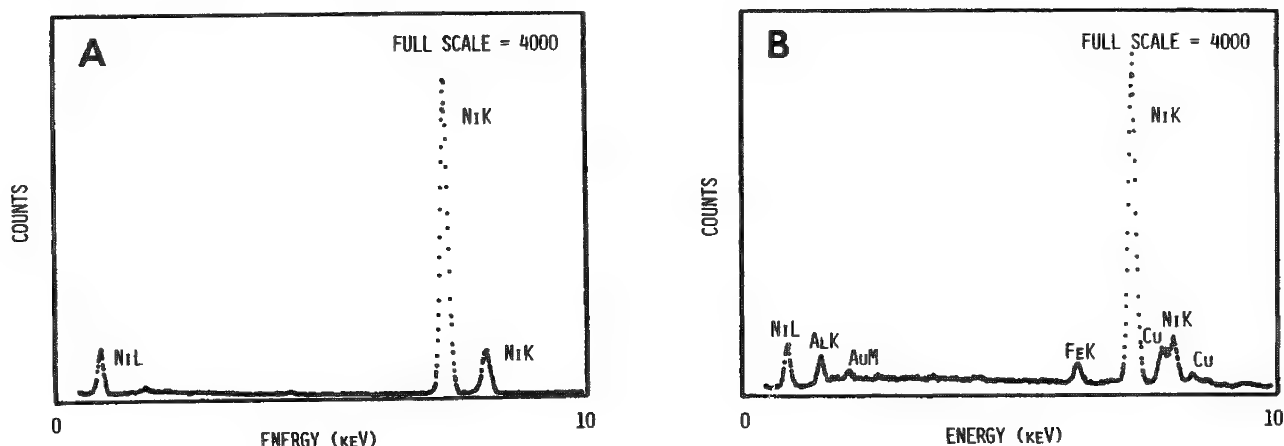
FIG. 6.--Spectra from nickel foil, showing effect of collimator in removing systems peaks: (a) collimator in place; (b) collimator removed.

Collimator. One can demonstrate the collimator's effectivenes in eliminating systems peaks that originate at large radial distances from the specimen simply by acquiring a sample spectrum with no collimator in place. Figure 6 shows such a test. A spectrum acquired from a thin nickel film supported by a beryllium grid is shown with the collimator in place (Fig. 6a) and with the collimator removed (Fig. 6b). Although the collimated spectrum is apparently free of contamination, the uncollimated spectrum indicates that there are additional sources of x rays which have not been removed. The sources of copper and gold are most likely remote areas of the cold cup not protected by beryllium. The minor gold signal seems to be electron excited and probably originates in the thin Au coating on the gold cup. The iron peak doubtless originates from the polepiece.

It is reassuring to know that the collimator is capable of effectively keeping this spectral contamination from entering the detector. However, the extent to which x rays and high-energy electrons are fluorescing bulk areas of the sample is unknown. The analyst should not be lulled into the false sense of security provided by a well-designed collimator. Such collimators are highly effective in removing systems peaks of the type shown in Fig. 2(b), but are only marginally effective in removing other sources such as those shown in Fig. 2(c).

System Characterizations

Changes in Operating Conditions. Once acceptably clean EDS spectra can be acquired for some standard mode of operation, it is useful to determine how operating conditions can be varied without re-introduction of systems peaks. For example, when very thin edges of a specimen are being analyzed, it is advantageous to increase the incident-beam intensity to improve counting statistics. This goal is commonly achieved by reduction of the CL1 current. It was determined that the beam intensity could be increased 20-fold with a negligible increase in hole counts. The hole counts for this test were acquired 0.1 μm from the edge of a 70nm-thick gold film so that increases in the flux of electron tails might also be detected. The resulting spectra showed noticeable Au Mα peaks at the highest beam intensities (lowest CL1 settings), but the effects were negligible. It appears that the upper column modifications described here are relatively insensitive to increases in beam current. However, large changes in CL1 current affect the beam diameter at the plane of the HXA. It was found for the JEM-100CX that the 200μm HXA would accommodate large current increases without intersecting the beam, although at the lowest CL1 setting aperture centering was extremely critical.

The Extent of Electron Tails. The term "electron tails" has generally been used to describe those electrons which fall outside of some nominal primary beam diameter. Electrons scattered at large angles with respect to the primary beam are easily removed by suitable plugs in the CL bore.[2] Electrons scattered at small angles and which remain in the near vicinity of the beam are more difficult to remove. These electrons can be generated by scattering within the bore of thick apertures, or by scattering by contamination within the bore of any aperture above the specimen.[2] In order to characterize this effect, a dirty thick platinum aperture was installed in the adjustable CL2 aperture blade. Hole count spectra were acquired from the thick gold washer specimen, at decreasing distances from the edge of the washer. The thick aperture was then removed and cleaned by flaming, and a second set or hole counts under identical conditions was acquired with the clean CL2 aperture. The integrated counts at FWHM under the Au Lα peak from both sets of measurements are plotted in Fig. 7. This figure graphically indicates that contaminated apertures can have a large effect on the extent of electron tails, which can severely degrade x-ray spatial resolution.

Experimental Considerations and Examples

Tests for Sample Self-flourescence. Sample self-fluorescence is a problem which, dependent upon the nature of the sample and the type of information desired, can seriously affect the results of a thin-film EDS analysis. As described earlier, the sample can be fluoresced by a number of sources. If we consider that fluorescence from x rays and BSEs from nearby objects has been minimized, there remains the possibility that both x rays and BSEs from the analysis point can excite other areas on the sample. This problem is most severe for ion-thinned or electropolished foils, which have a large bulk of material near the point of analysis. Very thin evaporated films or crushed grain specimens supported on carbon films on low-atomic-number support grids do not present the necessary bulk to produce a significant flux of x rays from areas other than the point of analysis.

FIG. 7.--Effect of contaminated aperture in CL system on the extent of electron tails; count totals represent FWHM integrated area for Au Lα peak with thick gold washer used for specimen.

A simple test specimen was devised to characterize the effects of sample self-fluorescence by characteristic and bremsstrahlung x rays. The specimen consists of crushed grains of silicon deposited on a carbon film on a beryllium grid, supported on a copper single-hole grid with a 1.0mm-diameter central hole. The copper grid was dipped in colloidal graphite to produce a thick coating of carbon on its surface sufficient to

prevent any excitation by BSEs. Spectra were acquired with the beam on a thin edge of a silicon grain, with the sample tilted first at 20° and then at 35°. Counting times were used that yielded identical integrated intensities in the Si Kα peak. Results are shown in Figs. 8(a) (20° tilt) and 8(b)(35° tilt). Both spectra clearly show the presence of a Cu Kα peak with no evidence of the Cu Lα peak, which indicates that the copper is x-ray fluoresced. In addition, the higher tilt angle of Fig. 8(b) produced a more intense copper peak. As shown in Fig. 8(d), the bremsstrahlung intensity is peaked in the forward scattering direction. Higher tilt angles cause the bulk copper of the grid to intersect a higher flux of bremsstrahlung intensity.[3,4] This test, therefore, shows that there is a significant effect of bremsstrahlung radiation at large distances (500 μm in this case) from the analysis point, since silicon characteristic x rays do not excite copper.
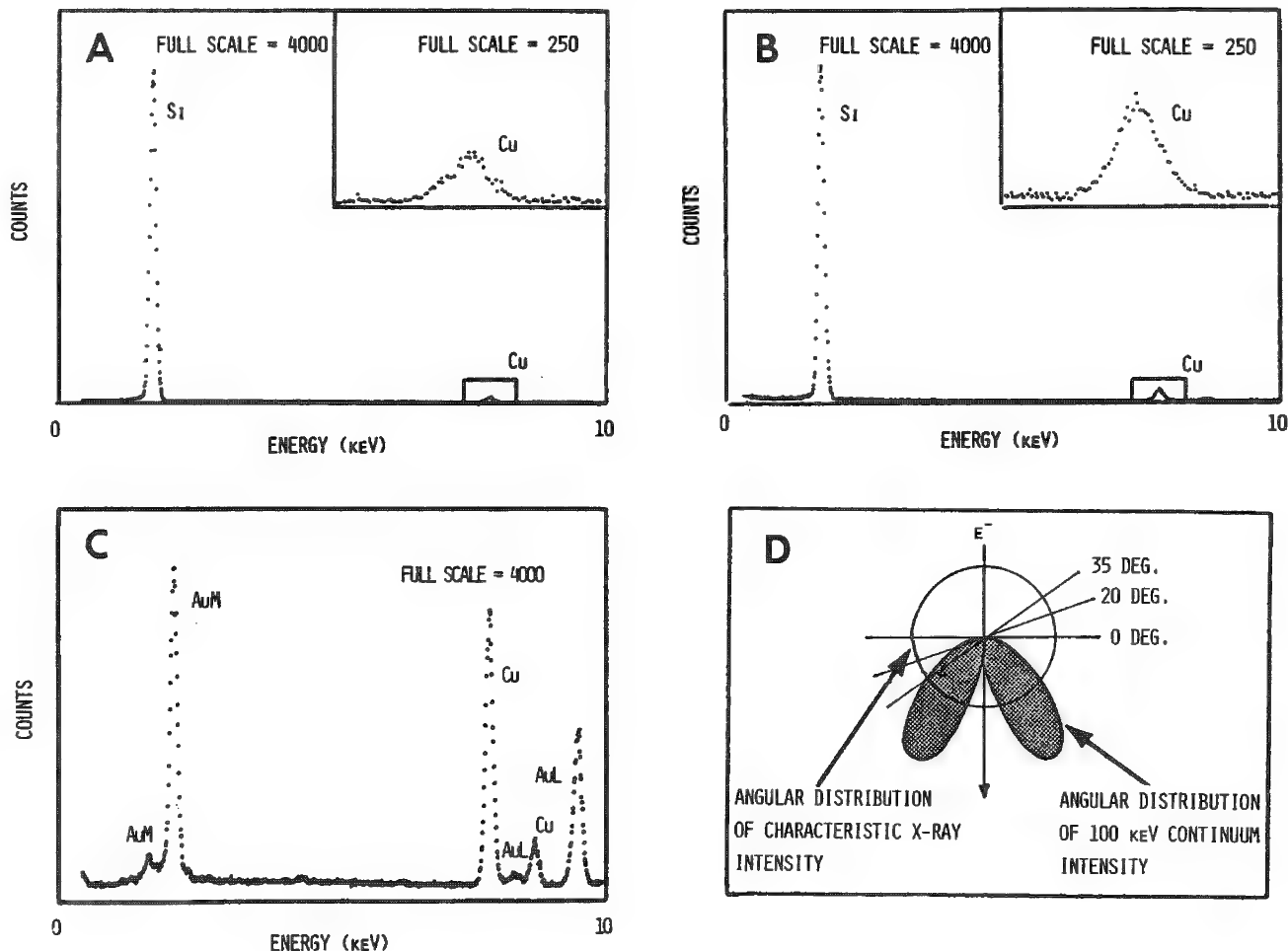
FIG. 8.--Effect of sample-generated fluorescence in model specimens: (a) crushed grain of silicon on carbon film over beryllium grid, 10μm-thick copper slot grid with 1000μm central hole placed below specimen, sample tilted to 20°; (b) same sample as (a) but tilted to 35°, with increase in copper peak relative to (a) due to interception of higher intensity bremsstrahlung by specimen at higher tilt angle; (c) thin gold film on beryllium grid replacing silicon crushed grain specimen in (a), with increase in copper by Au Lα. (Copper slot grid in above tests coated with graphite to preclude fluorescence by electrons). (d) Schematic of distribution of bremsstrahlung and characteristic x-ray intensity at 100 kV (after Goldstein and Williams[4]).

A similar sample was prepared by replacing the silicon crushed grain specimen with a 50nm-thick film of gold. Figure 8(c) shows the resulting spectrum. The much greater Cu Kα signal here was due both to excitation of the copper grid by bremsstrahlung radiation and by the Au Lα characteristic x rays, which efficiently excite Cu Kα x rays.

This example serves to point out that specimen self-fluorescence by x rays can be a severe problem in ion-thinned or electropolished specimens. Bremsstrahlung fluorescence of bulk regions of the sample can be minimized by use of the lowest tilt angles possible, a condition that favors intermediate and, especially, high-angle detector configurations. However, since characteristic x rays are emitted isotropically, fluoresence of bulk sample areas by these x rays cannot be prevented. Both effects clearly depend greatly on the nature of the sample being analyzed. For example, it would be difficult, if not impossible, to analyze small particles or grains in an ion-thinned foil for elements that are present in large amounts in the bulk matrix.[7] Such analyses would require that the particles of interest be extracted from the matrix so that the bulk of the specimen is removed and the self-fluorescence effects are minimized.

Example of a Typical Particle Analysis. An example of the deleterious effect of sample self-fluorescence is illustrated in Fig. 9. An ion-thinned, low alloy steel containing equiaxed MnS inclusions was prepared.[13] The MnS inclusions typically thinned faster than the steel matrix, and several electron-transparent inclusions that clearly penetrated the entire foil thickness could be found. The MnS inclusions usually exhibited a central core particle which showed microstructural differences from the bulk of the inclusion. Figure 9(a) is a secondary-electron image of a MnS inclusion, with the central core particle clearly visible.
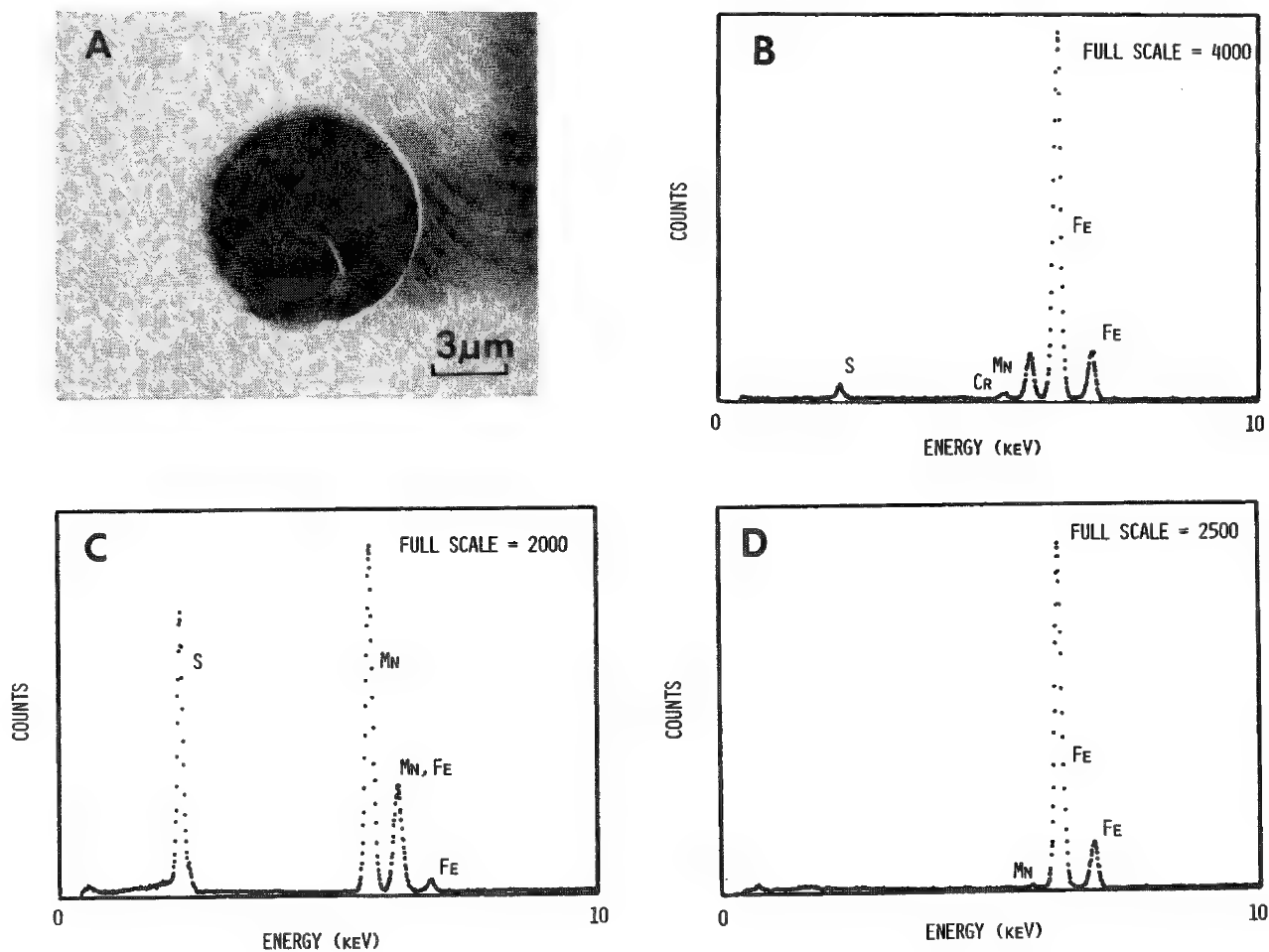
FIG. 9.--Example of continuum fluorescence of ion-thinned sample, MnS inclusions in steel: (a) SEI micrograph of ion-thinned MnS inclusion in steel matrix; (b) spectrum from central core of inclusion (point 1); (c) spectrum from bulk of inclusion (point 2); (d) spectrum from thin edge of steel matrix.

A spectrum from the core particle of the MnS inclusion, acquired at point 1 of Fig. 9(a), is shown in Fig. 9(b). This spectrum shows that the core is rich in iron, but manganese and sulfur are also present. Figure 9(c), the spectrum from the MnS inclusion away from the core particle (point 2), shows high manganese and sulfur, but a significant iron peak is also present. For comparison, Fig. 9(d) is a spectrum obtained from an electron-transparent edge of the steel matrix.

The only spectrum in this example not markedly affected by specimen-induced fluorescence is that of the steel matrix (Fig. 9d). Since there is little bulk of manganese in the specimen, there is probably little contribution to the small manganese peak due to fluorescence of manganese by Fe Kα or bremsstrahlung x rays. However, the manganese and sulfur peaks seen in Fig. 9(b) could easily have resulted from the strong fluorescence effect of Fe Kα x rays from the core particle on the surrounding manganese and sulfur in the inclusion. Similarly, the iron present in the spectrum from the MnS inclusion away from the core particle could have resulted from bremsstrahlung excitation of the large bulk of iron in the foil itself, since characteristic x rays from manganese and sulfur will not excite Fe Kα. Some contribution to these spectra from backscattered electrons is also possible, but the primary mechanism appears to be x-ray fluorescence.

This example illustrates the difficulty encountered in determining the composition of small particles in a bulk matrix. Such analyses always give ambiguous results, unless the particles can be extracted from the matrix.

Conclusions

We conclude that:

1. The in-hole spectrum of a properly modified AEM can be effectively reduced to nil, even for a worst case specimen, which eliminates the necessity for subtracting hole counts from sample spectra.

2. Systems peaks generated by radiation originating from the specimen can be minimized, chiefly by replacing or shielding of sample chamber components with low-atomic-number materials. In general, it is probably not necessary to utilize expensive materials such as beryllium for many of the sample-chamber modifications. An aluminum specimen rod, for example, equipped with a graphite specimen holder will not produce an Al Kα systems peak. This should be true for both single-tilt and double-tilt specimen rods, although only a single-tilt rod has thus far been tested.

3. Sample self-fluorescence is a major problem that complicates both quantitative and qualitative analyses in specimens with a large bulk of material near the point of analysis. It is simply not possible to avoid the generation of x rays from bulk specimen areas by characteristic x rays, bremsstrahlung, or backscattered electrons. The effects of sample self-fluorescence can only be avoided by analyses of crushed grains, extracted particles, or thin films.

References

1. D. B. Williams and J. I. Goldstein, "Minimization of systems-produced x-ray counts in a Phillips EM300 TEM/STEM," *Analytical Electron Microscopy*, 1978.

2. J. Bentley et al., "Optimization of an analytical electron microscope for x-ray microanalysis: Instrumental problems," *SEM/1977* II, 581-594.

3. N. J. Zaluzec, "Quantitative x-ray microanalysis: Instrumental considerations and applications to Materials Science," in J. J. Hren et al., Eds., *Introduction to Analytical Electron Microscopy*, New York: Plenum Press, 1979.

4. J. I. Goldstein and D. B. Williams, "X-ray analysis in the TEM/STEM," *SEM/1977* I, 651-662.

5. W. A. P. Nicholson et al., "The characterization of x-ray spectra from thin specimens in the transmission electron microscope," Inst. Phys. Conf. Ser. No. 36, 1979, ch. 9, 373-376.

6. T. J. Headley and J. J. Hren, "Sources of background x-radiation in analytical electron microscopy," *Ninth Intern. Cong. E.M.* I, Toronto, 1978, 504-505.

7. J. Bentley, "Systems background in x-ray microanalysis," *Analytical Electron Microscopy--1981*, 54-57.

8. E. A. Kenik and J. Bentley, "Influence of x-ray induced fluorescence on energy dispersive x-ray analysis of thin foils," in G. W. Bailey, Ed., *Proceedings EMSA/1977*, 328-329.

9. E. F. Sturcken, "SEM and XES in high beta-gamma radiation fields," *SEM/1976* I, 247-256.

10. C. E. Fiori and D. E. Newbury, "Artifacts observed in energy dispersive x-ray spectrometry in the scanning electron microscope," *SEM/1977* I, 401-422.

11. C. E. Fiori and D. E. Newbury, "Operation of energy-dispersive spectrometers in the analytical electron microscope," *Analytical Electron Microscopy--1981*, 17-24.

12. B. Liljesvan and G. M. Roomans, "Use of pure carbon specimen holders for analytical electron microscopy of thin specimens," *Ultramicroscopy* 2: 105-107, 1976.

13. A. J. Mardinly, "TEM/STEM analysis of non-metallic inclusions in steel," *Microbeam Analysis--1980*, 176-177.

QUANTIFICATION OF ENERGY-DISPERSIVE SPECTRA FROM THIN-FOIL SPECIMENS

D. B. Williams, J. I. Goldstein, and J. R. Michael

A major driving force for the development of the analytical electron microscope (AEM) was that the quantification procedure for the x-ray energy-dispersive spectrometer (EDS) output obtained from thin specimens should be simple in comparison with the process for bulk specimens, because in many cases, the absorption and fluorescence corrections that are required when bulk specimens are analyzed can be ignored. The degree to which this assumption is justified, the methods used for quantification, and current limits to the quantification process are discussed in this article. The article is tutorial in nature, but in the rapidly changing AEM field, opinions on the best method to perform certain operations vary substantially, as reflected in the amount of discussion in the sections below. Current extraneous problems that still exist concerning x-ray analysis in the AEM, such as spurious x-ray signals entering the detector and artifacts introduced during specimen preparation, are discussed elsewhere in this volume by Allard[1] and Fraser,[2] respectively.

Selection of Experimental Parameters

Prior to quantitative x-ray analysis in the AEM, there are a number of instrumental variables that can be optimized to insure that, for example, quantification is accurate, or that the best conditions exist for detecting trace element segregation. As described by Statham in this volume,[3] x-ray counting statistics may be the limiting factor in quantification. Therefore, it is essential to maximize the count rate of the characteristic x rays of interest. However, the time to acquire the x-ray counts must also be short enough to insure that specimen drift or contamination does not degrade the desired spatial resolution. Spatial resolution is optimized by small probes and thin specimens, conditions that are exactly the opposite of those required to generate high count rates. In general, therefore, a compromise experimental set-up is often required by which reasonably accurate quantification (about ±5% relative accuracy) can be achieved at a reasonable spatial resolution (about 10-30 nm).

The quantification process, as we shall see, requires acquisition of the maximum characteristic x-ray intensity above the continuum background. Therefore, the peak-to-background ratio (P/B) should be maximized along with the absolute count rate. As a rule of thumb, the total x-ray count rate over the *whole* of the energy spectrum (up to E_0, the accelerating voltage) should not exceed about 3000 counts per second, since the x-ray detector resolution may be impaired. Even in thin foil specimens using small probes, this count rate can often be achieved in modern AEMs, so caution is required. Under these circumstances the count rate in a small peak may be so low that long times (300-500 s) may be required to accumulate sufficient counts for quantification. Then spatial resolution may be lost, and it is more than ever essential to insure that the AEM is optimized for x-ray analysis. The relevant instrumental variables over which the operator has control will now be discussed.

Choice of Accelerating Voltage. Several theoretical treatments (e.g., Joy and Maher[4]) predict that P/B increases with voltage but there is a lack of conclusive experimental evidence for it. However, there is no evidence that P/B decreases with increasing voltage, and given that the gun brightness (A m^{-2}sr^{-1}) is a linear function of E_0, there is good reason to operate at the highest voltage available, particularly if the number of

generated x-ray counts is a limiting factor. The fact that spatial resolution also improves with voltage is an added advantage.

Choice of Electron Gun. The choice for the average user is between a conventional W hairpin filament and a LaB_6 gun. The latter is brighter by a factor of about 10 at 100 kV, but substantially more expensive. However, if properly operated and maintained, a single LaB_6 source will operate for many months compared with the several days commonly obtained from a W hairpin. The relatively poor brightness of the W gun can be offset partially by the fact that operation at emission currents of 100 µA or more is not unreasonable for short periods of time, if a reduced filament life is acceptable. However, operating a LaB_6 gun much above 10µA emission may result in premature breakdown. (This difference in emission current does not totally offset the inherent brightness difference, since the probe diameter formed by a LaB_6 source is at least half that from a W source.) In a multi-user laboratory/teaching institution such as ours we still find it more practical to operate with a W filament, and have rarely encountered x-ray statistical limitations in our microanalyses. However, few of the problems we address require working at the lowest sensitivity, levels where the W gun would be a limiting factor. The field-emission gun as an alternative source is expensive, requires ultrahigh-vacuum conditions, and is available in very few laboratories. But in situations where the highest spatial resolution in both images and microanalysis is demanded, and minimum detectability problems are encountered, it is the best electron source to use.

Choice of Probe Parameters. Besides emission current, which is a function of the gun, the operator has a choice of the probe size (C_1 lens strength) and the probe convergence angle $2\alpha_s$ (C_1 aperture size). The current in the probe at the specimen can be varied over two orders of magnitude depending on the probe size (Fig. 1). If spatial resolution is a secondary consideration then a large probe size will minimize any x-ray count problems. Similarly, an increase in the value of $2\alpha_s$ increases the probe current (Fig. 2) for a fixed probe size. In theory probe size is independent of $2\alpha_s$, but in practice spherical aberration at very high $2\alpha_s$ values may result in loss of resolution. In routine operations we use a C_2 aperture about 70 µm in diameter, which gives a probe current of about 10^{-10} A at a probe diameter of 10 nm. This configuration gives both adequate image resolution and good x-ray statistics.

EDS Variables. The EDS detector itself has a fixed geometry with respect to active area (about 30 mm^2) and take-off angle (0°, 20° or about 70°, depending on the specific instrument). The solid angle is usually maximized, again to maximize the number of detected x-ray photons, by being placed as close (within about 15 mm) to the specimen as possible. The detector can be backed off mechanically if the count rate is too high, or if it is considered that extraneous radiation (e.g., backscattered electrons or hard x rays from the illumination system) is penetrating the collimator.[5] Attention should be given to the choice of spectral display variables, in particular the energy range of the display on the multichannel analyzer (MCA) and the experimental counting time. The former should always be as large as possible (at least 40 keV) in the case of an unknown specimen, where the existence of K and L lines above 10 keV may be essential in initial qualitative analysis (e.g., as shown in Fig. 3, it is possible to distinguish between Mo and S L/K overlap at 2.3 keV by observation of the Mo Kα line at 17.5 keV). Selection of the desired energy range for analysis should then maximize the resolution of the display to about 5-10 eV/channel if all the peaks of interest can still be displayed in the 1024 available channels. If the specimen is known, the appropriate energy range can of course be selected immediately.

Counting time is important insofar as it should be minimized to reduce the effects of contamination, specimen drift, and elemental volatilization (in the case of Na and other mobile species). This limitation must be counterbalanced by the need to acquire enough counts for acceptable errors.

Measurement of X-ray Peak and Background Intensities

The only experimental information that is required for quantification of the EDS spectrum are the characteristic peak intensities I_A, I_B, etc., of the elements of interest. As discussed in the following section these values can then be converted directly into values of the wt.% of each element C_A, C_B, etc., or corrected for absorp-
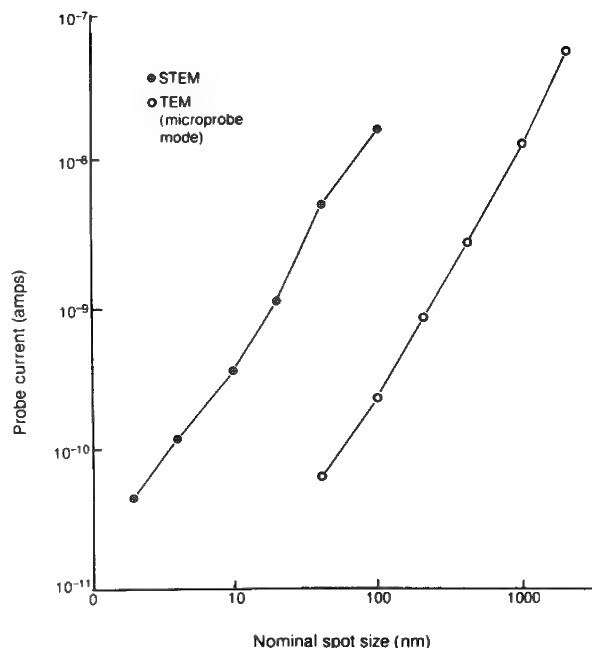
FIG. 1.--Variation of probe current in
Philips EM400T TEM/STEM as function of
nominal probe size (courtesy Norelco
Reporter).
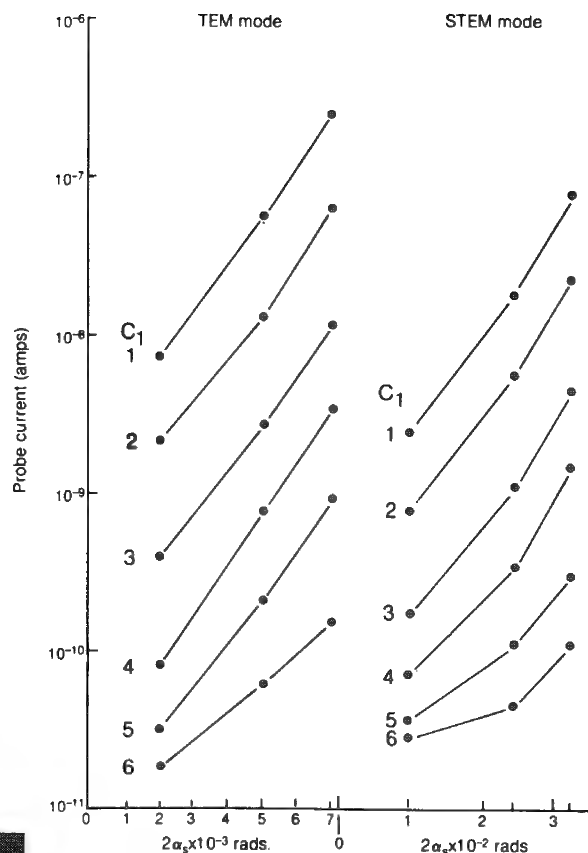
FIG. 2.--Variation of probe current in
Philips EM400T TEM/STEM as function of C_2
aperture size $(2\alpha_s)$ and probe size
(C_1 setting) (courtesy Norelco Reporter).
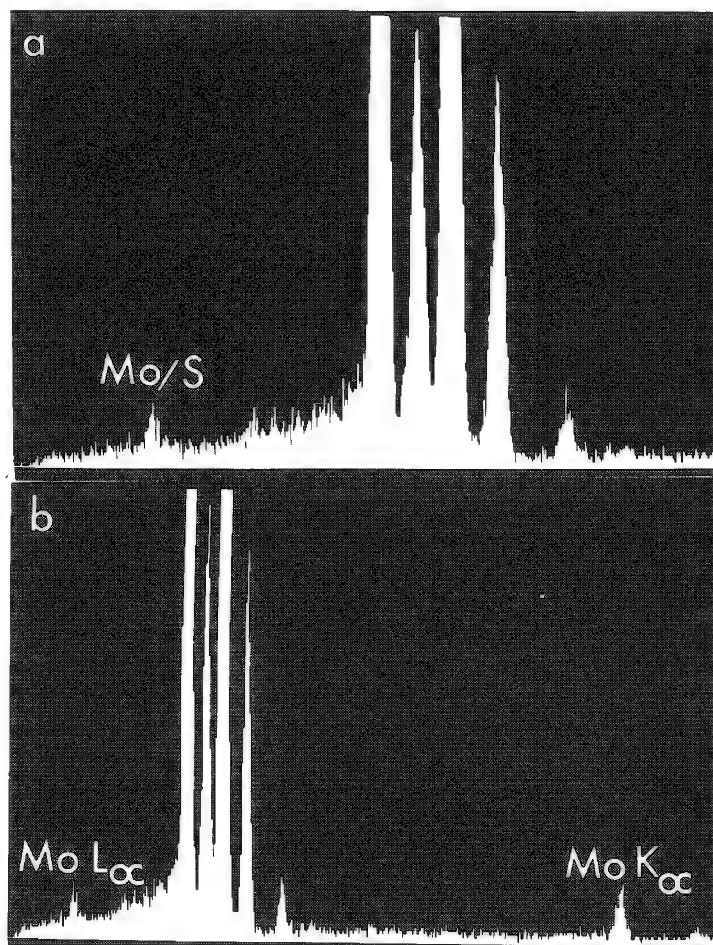
FIG. 3.--EDS spectrum from inclusion in
$2\frac{3}{4}$ Cr-1 Mo pressure vessel steel. The poor
resolution of EDS cannot distinguish between
S and Mo at 2.3 keV (a). However, observa-
tion of spectrum out to 20 keV (b) de-
monstrates that Mo is present.

tion, etc., where necessary. The determination of the characteristic intensity requires first that the continuuum background (bremsstrahlung) radiation contribution to the peak be removed. This procedure can be carried out by one of several methods, depending on the degree of sophistication of the available computer hardware. A full description of the methods of determining the peak and background intensities has been given elsewhere.[6] In this section we shall deal only with three representative methods of varying sophistication; two require computer curve-fitting and the other uses windows on the MCA display to select specific regions of peaks and equivalent regions of the background.

In current EDS/MCA systems the background intensity variation is usually accounted for in one of two ways. In the first, the detected intensity variation is described mathematically as originally proposed by Kramer[7] and then modified by taking into account absorption in the detector. The second method assumes that the background intensity variation is a "smooth" function compared with the rapidly changing intensity in the characteristic peak. The application of a digital filter to the spectrum then removes any background without substantially affecting the superimposed characteristic peaks.[8] Once the background is removed by either method, the characteristic peak intensity is obtained, again by one of two methods. The first method involves generation of Gaussian peaks and fitting them to the experimental peaks. In the second method, the experimental peaks are compared with library peaks obtained from reference standards. Both these methods can handle complex multielement spectra, and are essential when peak overlap occurs. Figure 4 shows the MCA display when x-ray peaks and the background intensity are determined in this manner. More advanced methods for handling peak overlap, and minimizing the resultant errors, are still evolving; progress will continue as mini-computer capabilities increase.[9]

If the x-ray spectrum obtained is relatively simple (i.e., peak overlaps do not occur) and the continuum background is not changing rapidly (> 2 kV) then quantification can be achieved with an acceptable degree of accuracy (about ±5% relative) by the method of defining the characteristic peak area with a "window" in the spectrum. The windows available on a MCA display should select equivalent (i.e., same number of channels) regions of both the characteristic peaks, including background and a "typical" region of background, as shown in Fig. 5. (This approach is clearly not possible if peak overlap occurs.) When counts are integrated in this manner the optimal window width to maximize the peak counts and minimize background counts is about 1.2 FWHM.[10] This arrangement gives the best sensitivity. If the selected peak contains sufficient counts and the background intensity is not varying rapidly with energy, then this process is more than adequate for obtaining I_A and I_B for subsequent quantification. In our experience, data obtained by both curve-fitting and spectral-window techniques are identical, within the experimental error, in many routine analysis situations. The advantages of the more sophisticated curve-fitting procedures are that data processing is more rapid, multielement spectra can be easily handled, and peak overlaps present no barrier to quantification.

Quantification of X-ray Data

i. *Ratio Method.* Once x-ray spectra are obtained from the desired regions of the specimen, the values of I_A and I_B can be converted to values of C_A and C_B by either a ratio method or thin film standards. The former method is more widespread and will be discussed in detail, along with the necessary corrections when absorption and fluorescence are significant.

In electron-transparent thin films, electrons lose only a small fraction of their energy in the film. In addition, few electrons are backscattered and the trajectory of the electrons can be assumed to be the same as the thickness t of the specimen film. Under these circumstances the generated characteristic x-ray intensity I_A^* for element A can be given by a simplified formula:

$$I_A^* = \text{const. } C_A \omega_A Q_A a_A t / A_A \tag{1}$$

where C_A is the weight fraction of element A; ω_A is the fluorescence yield for the K. L, or M characteristic x-ray line of interest; Q_A is the ionization cross section (the

FIG. 5.--Cu Kα peak showing window selecting about 1.2 FWHM of gross peak (P). Windows selecting equivalent portions of background (B) on either side of peak are selected, averaged, and subtracted from P to give net integrated intensity in peak.

FIG. 4.--EDS spectrum from precipitate in Al-4% Cu showing Cu Lα, Kα, Kβ, and Al K peaks on slowly changing continuum background (a). Use of digital filter and library standard peaks permits removal and full integration of any combination of peaks, e.g., (b) Cu Lα, Al K, (c) Al K, Cu Kα Kβ, and (d) Cu Lα Kα Kβ.

probability per unit path length of an electron of a given energy causing ionization of a particular K, L, or M shell of an atom A in the specimen); a_A is the fraction of the total K, L, or M line intensity that is measured; and A_A is the atomic weight of A. In Eq. (1) only Q_A varies with E_0.

If we assume that the analyzed film is "infinitely" thin, the effects of x-ray absorption and fluorescence can be neglected, and the generated x-ray intensity and the x-ray intensity leaving the film are identical. (This assumption is known as the thin-film criterion; we shall discuss its validity in later sections.) However, the measured intensity I_A from the EDS spectrum may be different from the generated intensity I_A^* because as mentioned the generated x rays may be absorbed as they enter the EDS detector in the Be window, gold surface layer, and silicon dead layer. Therefore the measured intensity is related to the generated intensity by

$$I_A = I_A^* \varepsilon_A \qquad (2a)$$

where

$$\varepsilon_A = \exp\,[-\mu/\rho|_{Be}^A \rho_{Be} X_{Be}] \,\cdot\, \exp\,[-\mu\,\rho|_{Au}^A {}_{Au} X_{Au}] \,\cdot\, \exp\,[-\mu/\rho|_{Si}^A \rho_{Si} X_{Si}] \qquad (2b)$$

and μ/ρ, ρ, and X are respectively the appropriate mass absorption coefficients of element A in Be, Au, and Si; the densities of Be, Au, and Si; and the thicknesses of the Be window, the gold surface layer, and the silicon dead layer.

From Eqs. (1) and (2), it appears that the composition of element A in an analyzed region can be obtained simply by measurement of the x-ray intensity I_A and by calculation of the constant and other terms. In practice, however, that is not easy because many of the geometric factors and constants cannot be obtained exactly. In addition, the specimen thickness varies from point to point, which makes continual measurement of t inconvenient.

If the x-ray intensity I_A, I_B of two elements A and B can be measured simultaneously, the procedure for obtaining the concentrations of element A and B can be greatly simplified. If one combines Eqs. (1) and (2) to calculate the intensity ratio I_A/I_B the following relationship for the concentration ratio C_A/C_B is obtained:

$$\frac{C_A}{C_B} = \left[\frac{(Q\omega a/A)_B \cdot \varepsilon_B}{(Q\omega a/A \cdot \varepsilon_A} \right] \cdot \frac{I_A}{I_B} \tag{3}$$

In this case the constants and the film thickness t drop out of the equation and the mass concentration ratio is directly related to the intensity ratio. The term in the brackets of Eq. (3) is a constant at a given operating voltage and is referred to as the k_{AB} factor or Cliff-Lorimer factor. Equation (3) is usually given in a simplified form as:

$$C_A/C_B = k_{AB} \cdot I_A/I_B \tag{4}$$

This relationship was developed and applied initially by Cliff and Lorimer[11] using an EDS detector. The Cliff-Lorimer ratio method has gained great popularity due to its simplicity. (It must be borne in mind however that the technique is based on the assumption of the thin-film criterion.)

In a binary system, using Eq. (4) we can determine C_A and C_B independently since:

$$C_A + C_B = 1 \tag{5}$$

In ternary and higher order systems the intensities of all the elements whose mass concentrations are unknown must be measured. A series of intensity ratio equations (like Eq. 4) are used in combination with an equation which sums all the mass concentrations to unity (like Eq. 5) to determine the mass concentration of each element.

The ratio method is often referred to as a standardless technique. However this description is strictly true only when k_{AB} is determined by calculation of the Q, w, etc., factors given in Eq. (3). More often the k_{AB} factor is determined using standards where the concentrations C_A, C_B, etc., are known. In this case the characteristic x-ray intensities are measured and the Cliff-Lorimer k_{AB} factors are determined directly from Eq. (4). The standards approach is often more accurate, particularly because ε_A and ε_B vary from one instrument to another and as we have observed may vary even in a single instrument over a period of time.

By convention k_{AB} factors are compared to Si, i.e., tabulation usually occurs as k_{ASi}, k_{BSi}, etc., and the values are called k factors. The relationship between k factors and k_{AB} factors is given by

$$k_{AB} = \frac{k_{ASi}}{k_{BSi}} = \frac{k_A}{k_B} \tag{6}$$

Until recently the only comprehensive range of measured k factors for Kα lines of a number of elements were reported by Cliff and Lorimer[11] and Lorimer et al.[12]   These results were obtained with an EMMA-4 analytical instrument which has a relatively large probe size (about 10^2 nm). Limited work has been carried out on modern analytical instruments[13] but most reported results refer to a single k_{AB} determination for a system of interest to the investigator.

Recently two sets of k factors have been measured.[14,15] Figure 6 shows a selection of k factor measurements of Wood et al.[14] plotted as a function of Kα characteristic x-ray energy. The measurements of k were made with a Philips EM400T AEM operated at 120 kV. The values of k_{ASi} are all close to 1.0 except for Mg and Na. Figure 7 shows experimental
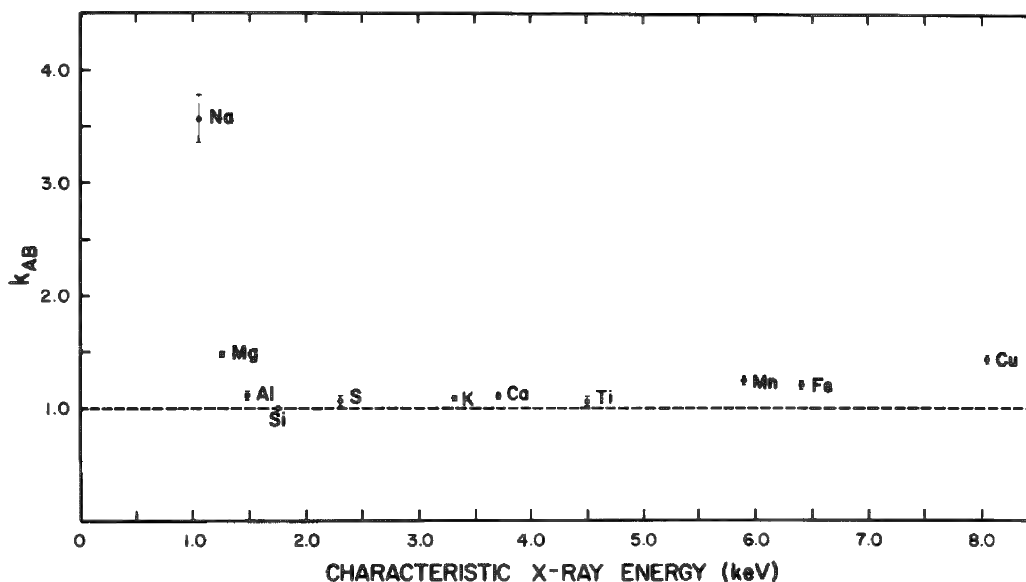
FIG. 6.--Variation of experimentally determined k factors with characteristic x-ray energy for selection of elements studied. Operating voltage 120 kV; k factors are relative to Si. Error bars represent 95% confidence limits.

k_{AB} factors where element B is iron.[16] We consider it more useful for the metallurgist to display the k factors in this manner because of the large number of common metals that can be alloyed in a convenient, homogeneous manner with the transition metals. Direct determination of k_{AFe} is then possible and few interpolations are required. By contrast many interpolations are required to obtain k_{ASi} because convenient metallurgical standards often cannot be fabricated. The measurement errors approach ±1% relative in a few selected cases. More typically, measurement errors are in the range ± 1 to ± 4%. Since the measurement of the concentration C_A is directly related to the k_{AB} factor (see Eq. 4), the accuracy of the ratio method is limited to the error in the measurement of k_{AB}.

For most analyses it is not possible to use these measured and tabulated k factors, since the characteristics of EDS detectors vary from one instrument to another. Also many k factors, particularly for L and M lines, have not been measured and operating voltages other than 100 or 120 kV are used. Therefore it is often advisable for the analyst to measure the ncessary k_{AB} factors directly. In many cases well-characterized alloys or stoichiometric oxides containing the elements of interest are available. When direct k_{AB} factor measurement is not possible the analyst must resort to using the standardless ratio method and calculate k_{AB} factors directly.

To calculate k_{AB} directly, the various terms in the brackets of Eq. (3) must be obtained. Figure 8 shows a comparison between measured and calculated k factors for K lines at a 120 kV operating potential.[14] In this case the Green-Cosslett ionization cross section[17] Q_K was chosen. Values of ω_K were taken from the fitted ω_K values of Bambynek et al.[18] with use of the Burhop equation.[19] The values of a and μ/ρ were obtained from Heinrich et al.[20] and Heinrch,[21] respectively. The EDS detector parameters as suggested

by Zaluzec[22] were X_{Be} = 7.6 µm (0.3 mil), Y_{Au} = 0.02 µm and X_{Si} = 0.1 µm.

From Fig. 8 it is clear that above Si the calculated and experimental values follow the same trend, increasing with increasing Kα energy. It is not possible to explain the differences between the calculated and measured values shown in Figure 8 with certainty but it appears that errors in the calculation of the ionization cross section may be largely responsible.

Other expressions for Q_K are available. In general the formula for K shell cross section Q can be written in the form:[23]

$$Q = const \ (1/E_0 E_K) \ ln(C_K E_0/E_K) \tag{7}$$
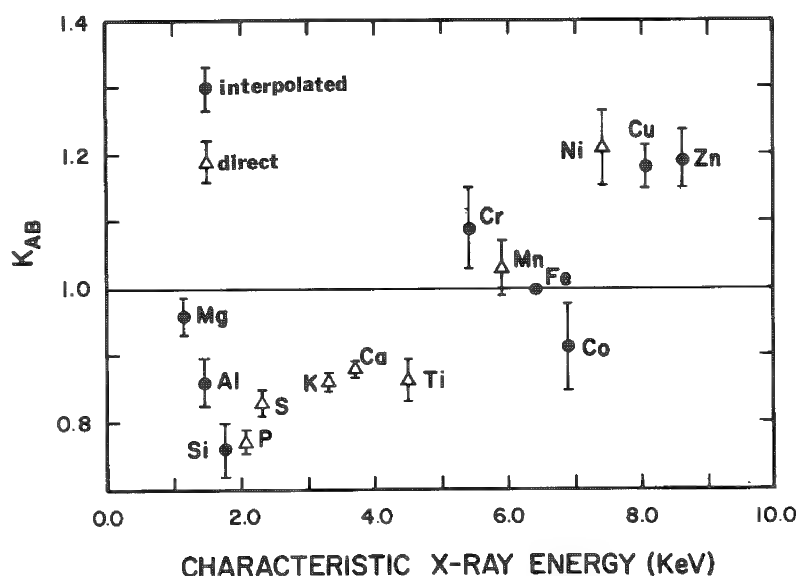
FIG. 7.--Variation of experimentally determined k factors with characteristic x-ray energy for selection of elements studied. Operating voltage 120 kV; k factors are relative to Fe. Error bars represent 95% confidence limits.
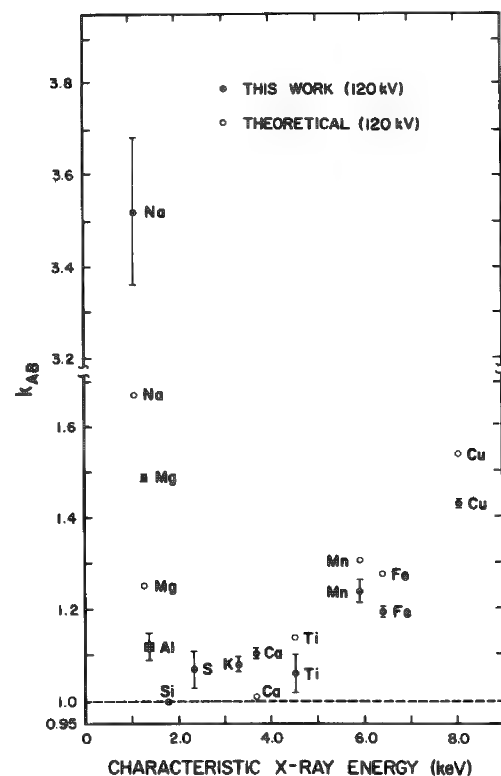
FIG. 8.--Comparison of experimental results in Fig. 6 with calculated k factors at 120 kV. Error bars represent 95% confidence limits.

where E_K is the binding energy of electrons in the K shell. The parameter C_K is different for different models of the ionization cross section. The values of C_K in Eq. (7) are 2.42, 1.0, and 0.65 for Q Mott-Massey,[24] Q Green-Cosslett[17] and Q Bethe-Powell.[23] Zaluzec[22] uses a form of Q in which C_K varies with E_K. Schreiber and Wims[15] used measured k_{AB} values to back-calculate a best-fit ionization cross section. Maher et al.[25] show that the uncertainties in using the Mott-Massey vs the Zaluzec modified Q equations lead to an error in the calculated k_{AB} of less than about 15%. Goldstein et al.[26] report a similar uncertainty when comparing calculated k_{AB} values using the cross sections of Mott-Massey, Green-Cosslett, and Bethe-Powell.

Until more accurate measurements of Q_K in the 100-200 kV range are made, inaccuracies in k_{AB} for Kα lines will remain in the range of 10 to 15%. These errors are much larger than those currently obtained for measured k_{AB} factors. The differences in the values of

ionization cross sections for L and M lines are much larger than those for Q_K. Therefore, calculated compositions using L and M lines have correspondingly larger errors.

ii. Effects of Absorption. The thin-film criterion states that the effects of x-ray absorption and luorescence can be neglected. Both Tixier and Philibert[27] and Goldstein et al.[26] have given criteria by which it can be determined whether the thin-film approximation has broken down and an absorption correction must be made. Both thin-film criteria give the film thickness at which the intensity ratio I_A/I_B is altered by more than 10% from the ratio obtained from an infinitely thin film (Eq. 3).

The arbitrary assumption that absorption is only significant if I_A/I_B is changed by more than $\pm$ 10% was justified originally, because that was the level of accuracy with which k_{AB} factors and the values of I_A and I_B could be experimentally determined. With recent improvements in STEM electron optics and the development of clean specimen environments, measurements of k_{AB} factors and of I_A and I_B can be made more accurately. As we have already discussed k_{AB} factors can be routinely determined with an error of between $\pm$1-4%. Given this accuracy, the arbitrary definition of significant absorption should be lowered accordingly to $<\pm$5%, and perhaps as low as $\pm$1%. Such a new definition of significant absorption will reduce the thickness of specimens required to avoid absorption corrections, in many cases to small values (e.g., < 10 nm in NiAl), difficult to obtain in practice. Thus the accuracy of the absorption correction process becomes more critical.

In order to correct for absorption, the k_{AB} factor can be modified by a correction factor (CF) due to preferential absorption of one of the measured x-ray lines from element A or B.

Based on the original work of Tixier and Philibert[27] and of Konig,[28] Goldstein et al.[26] have derived an equation to correct the k_{AB} factor:

$$ CF = \frac{\int_0^t \phi_B(\rho t) \exp[-\mu/\rho|_{SPEC}^{B} \csc \alpha(\rho t)] \, dt}{\int_0^t \phi_A(\rho t) \exp[-\mu/\rho|_{SPEC}^{A} \csc \alpha(\rho t)] \, dt} \tag{8} $$

where $\phi_{A,B}(\rho t)$ is the depth distribution of x-ray production from element A or B as a function of specimen density ρ and measured film thickness t, and α is the x-ray take-off angle. The terms $\mu/\rho|_{SPEC}^{A}$ and $\mu/\rho|_{SPEC}^{B}$ are the mass absorption coefficients of characteristic x rays of element A and B in the specimen.

On the assumption that $\phi_A(\rho t) = Q_B(t) = 1$ (i.e., x-ray production is uniform throughout the specimen), the integrals in Eq. (8) can be evaluated to give:

$$ CF = \frac{\mu/\rho|_{SPEC}^{A}}{\mu/\rho|_{SPEC}^{B}} \frac{1 - \exp[-\mu/\rho|_{SPEC}^{B} \csc \alpha(\rho t)]}{1 - \exp[-\mu/\rho|_{SPEC}^{A} \csc \alpha(\rho t)]} \tag{9} $$

To apply the correction factor CF for absorption to k_{AB} the values of μ/ρ, α, ρ, and t must be accurately known. The following sections discuss the limitations in the application of Eq. (9) and make some suggestions for minimizing the correction.

Mass Absorption Coefficient. Values of the mass absorption coefficient are accurately known from earlier studies of x-ray absorption, and may be obtained from any one of several sets of tables available in the literature.[21,19] It is worth noting here that when

29

$\mu/\rho\big|_{SPEC}^A = \sum_i C (\mu/\rho)_i^A$ is computed for any given system, *every* component i in that system has to be included even if the x rays from certain elements are not detected by conventional EDS. Significant absorption of x rays from elements Na through Si can occur if oxygen, nitrogen, or carbon are present in substantial amounts. Clearly when thin window or windowless EDS systems are available, consideration of absorption by (and absorption of x rays from) elements $Z = 6$ and above will be more important.

$\phi(\rho t)$. The depth distribution of x-ray production $\phi(\rho t)$ is usually assumed to be constant throughout the thin film, but it is by no means certain that this is a valid assumption in all materials. For example, Kyser[30] has calculated that in 400 nm of Cu and Au, $\phi(\rho t)$ should increase by 5% and 20%, respectively, thus indicating that Eq. (8) (and therefore Eq. 9) are not valid descriptions of any absorption correction involving these elements, in foils of this thickness. Recently, Stenton et al.[31] have experimentally determined $\phi(\rho t)$ for up to 380 nm of Ni and found that at 120 kV the assumption of a constant value of $\phi(\rho t)$ is only valid up to about 80 nm. Above this value $\phi(\rho t)$ increases up to about 30% at 380 nm. These experimental data were greater than the 10% increase predicted up to 400 nm in Monte Carlo techniques at 120 kV.[32] Both these data are shown in Fig. 9. However, until more $\phi(\rho t)$ data are available, Eq. (9) should be used, but with the understanding that, particularly for $Z \gtrsim 25$, the assumption of a constant $\phi(\rho t)$ may be incorrect at most reasonable specimen thicknesses, which significantly affects the value of any absorption-corrected k_{AB} FACTOR. If an increase in $\phi(\rho t)$ is not taken into account then Eq. (9) will overcompensate for absorption.
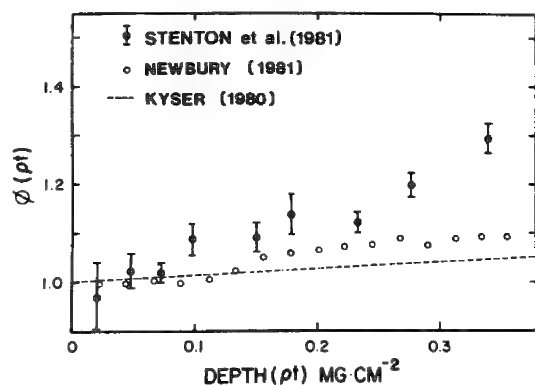
FIG. 9.--The increase in Ni Kα x-ray production as a function of mass thickness at 120 kV determined experimentally by Stenton et al.[31] and calculated by Monte Carlo techniques by Newbury.[32] Also shown are data reported by Kyser[30] for Cu at 100 kV.
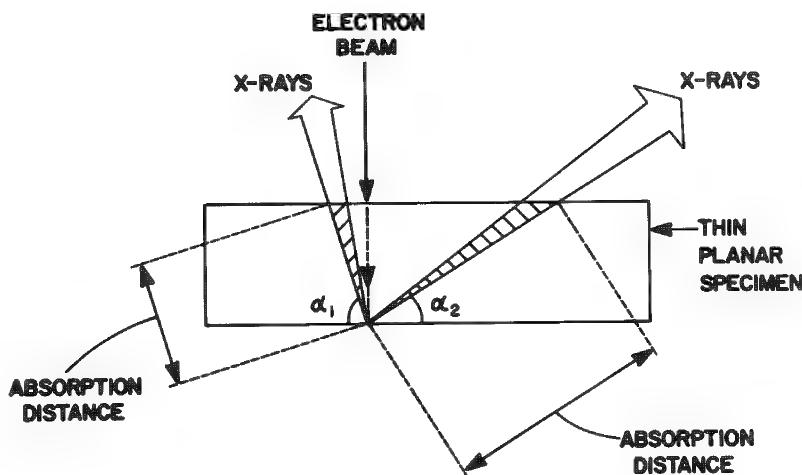
FIG. 10.--Ideal specimen configuration assumed in absorption calculations showing effect of differing take-off angle α on absorption path length.

The X-ray Path Length--t cosec α. If one assumes a parallel-sided thin foil of thickness t, with the primary beam at normal incidence, the x-ray path length through the specimen is t cosec α, where α is the x-ray detector take-off angle (Fig. 10). Clearly the higher the α the shorter the path length and the less the absorption correction for a given thickness. Since the variation in correction factor as a function of α changes rapidly around 20° and below,[33] the value of α should be known accurately for any data taken in this configuration.

Measurement of t is a major problem in correcting for absorption. Several ways are reported in the literature, none universally applicable and accurate. The contamination spot separation method first used by Lorimer et al.[34] is applicable if contamination can be generated. However, the accuracy of this technique has been called into question on

several occasions.[31,35,36] Stenton et al.[31] carried out contamination spot separation measurements on evaporated thin films and compared the data with interfermotery measurements. Errors of 50-200% were reported, with the contamination spots invariably overestimating the thickness and thus causing an overcorrection in any absorption calculation. Rae et al.[36] have reported the presence of relatively broad contamination deposits beneath the sharp cones that are usually apparent on the specimen, and describe the overall configuration as that of a "witch's hat" (Fig. 11a). By comparison with Fig. 11(b), which is the generally assumed morphology from which measurements are made, it is easy to see the reason for overestimation. This effect is clearly demonstrated in Fig. 11(c), which shows contamination spots deposited above and below a grain boundary.[31] The faintly visible boundary fringe contrast does not intercept the top and bottom contamination deposits. Errors associated with this measurement technqiue may also contribute to any overcorrection observed in data that have been adjusted for absorption.
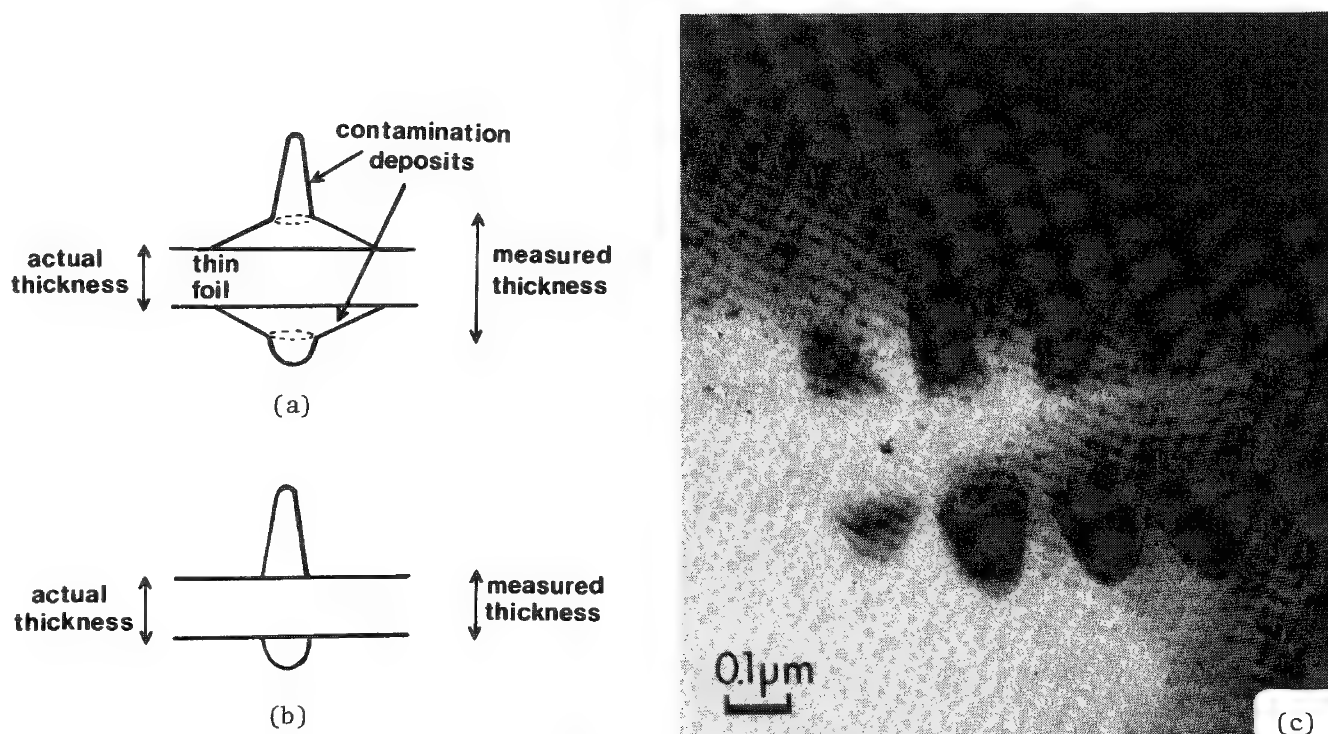
FIG. 11.--Schematic diagram of (a) proposed morphology of the contamination deposits[3] that would account for overestimation of thickness often observed in the use of technique, (b) morphology of contamination deposits apparently observed in AEM and used to measure thickness, (c) TEM image of contamination deposits placed along grain boundary in Cu showing discrepancy between boundary fringe position and apparent base of contamination deposits.

The second most generally applied method is that of measuring the spacing of the Kossel-Möllenstedt fringes in convergent-beam diffraction patterns.[37] This method often requires a double-tilt holder to set up the correct diffraction conditions with a symmetrical fringe pattern inside the hkl disk. Also, a minimum of three dark fringes on each side of the central bright fringe must be present, since a straight-line interpolation is used to measure t, unless the extinction distance ξ_g is known. This procedure results in a lower limit for thickness determination; the range of applicabilty of the technique has been examined in detail by Allen.[38] The required conditions are not always easy to obtain in practice at precisely the region of interest; to make the technique practical, a low-background double-tilt holder and contamination-free instrument are required such that data acquisition and thickness determination can be carried out concurrently.

Alternative methods of thickness determiantion are invariably less universal. For example, under two beam conditions, the extinction distance ξg can be calculated[39] and then thickness can be determined by counting observed thickness fringes. However, these fringes are not always discernible since they depend on the foil geometry. Also micro-analysis should not be performed under two-beam conditions because of possible anomalous x-ray generation.[40] The relative transmission of electrons is useful for amorphous specimen studies and Joy and Maher[41] have also reported its use for crystalline materials. This use requires careful calibration of transmitted currents with a Faraday cage, and is clearly a function of diffracting conditions. Other techniques such as the latex ball method[42] or projected width of planar defects[43] are limited in the their general applicability. The measurement of the relative heights of the zero loss and first plasmon loss peaks in an electron energy loss spectrum[44] requires that the plasmon mean free path be known; information that may not be available for many multicomponent practial materials.

In summary, the determination of the thickness t of a parallel-sided specimen is a most uncertain factor in the application of the absorption correction in thin film micro-analysis.

Specimen Geometry. The assumption, implied in all the preceding discussion, that the specimen is a parallel-sided thin film (Fig. 10) is rarely if ever achieved in practical x-ray microanalysis because of the way in which materials specimens are characteristically produced. Twin-jet electropolishing or ion-beam thinning both give rise to a wedge shaped specimen (Fig. 12), which complicates the situation considerably. As first pointed out by Glitz et al.[45] it is essential to know (a) the configuration of the EDS detector with respect to the specimen, and (b) the exact specimen dimensions in the plane parallel to the axis of the detector. If the specimen is of a simple geometry (constant wedge angle) then the correction is relatively trivial, but that is rarely the case and more generally, the situation can be quite complex (Fig. 12). Clearly under these circumstances the specimen must be homogeneous, not only through thickness (as is invariably assumed in all analytical electron micro-scopy), but also along the path length for absorption. In a multiphase specimen, any inter-faces should be aligned parallel to the EDS detector axis, a requirement that is facilitated by a tilt rotation holder (pre-ferably a low-background one, if available). The specimen geometry problem may be minimized by use of thin flake specimens prepared by

FIG. 12.--Wedge sample cross section showing how absorption path length may vary as a function of specimen geometry and detector position with respect to specimen.

window polishing and sandwiched between Be grids. The specimen wedge angle is usually smaller than for a self-supporting disk. (These specimens have an added advantage in that they minimize spurious effects due to stray radiation.) High take-off angle detectors (beyond $20°$) are essential, as has long been recognized in the microprobe field, where absorption is invariably present.

Specimen Density ρ. The specimen density is a function of composition and any absorp-tion correction procedure is an iterative process in which an approximate density and μ/ρ value are assumed prior to the determination of C_A and C_B. When these values are de-termined, the corrected values should be used in a second iteration, and so on until a self-consistent result is obtained. The density of a particular phase is not always a linear function of composition and in such cases the variation must be known accurately.

In summary, most of the factors currently employed in the standard absorption correc-tion equation are not accurately known and can contribute to significant errors in

quantification. Specifically, thickness determination and specimen geometry are critical factors; they probably cause the largest error at present. As these factors are determined more accurately, any variation in $\phi(\rho t)$ will become more significant and will have to be accounted for. Perhaps the most useful approach to minimizing the absorption correction will be to develop better methods for thinning specimens so that the specimen thickness and the effect of absorption will be decreased and the thin specimen region will be fairly uniform in thickness.

iii. Effects of Fluorescence. When element A can be excited by continuum x radiation or by characteristic x-ray lines of element B in the foil, a fluorescence correction may be necessary. Philibert and Tixier[46] have found that continuum fluorescence is negligible and that characteristic fluorescence will be negligible if $\mu/\rho|_{SPEC}^{B} \cdot \rho t \ll 1.0$. Tixier[47] has stated that the characteristic fluorescence correction is small if $\mu/\rho|_{SPEC}^{B} \cdot \rho t < 0.1$.

A correction for characteristic fluorescence of element A by element B in thin films has been developed by Philibert and Tixier:[46]

$$\frac{I_f^A}{I_A} = 2\omega_B C_B \frac{r_A - 1}{r_A} (A_A/A_B) \, \mu/\rho|_A^B \cdot \mu/\rho|_{SPEC}^B \cdot \frac{E_{KA}}{E_{KB}} (\rho t)^2 \tag{10}$$

where I_f^A is the fluorescence intensity which is added to the primary intensity I_A, r_A is is the absorption jump ratio for element A, A_A and A_B are the atomic weights of elements A and B, and E_{KA} and E_{KB} are the critical excitation energies for the characteristic K lines of elements A and B.

Another formulation for the characteristic fluorescence correction has been developed by Nockolds et al.[48] using the K shell ionization cross sections of Green and Cosslett:[17]

$$\frac{I_f^A}{I_A} = \omega_B C_B \frac{r_A - 1}{r_A} (A_A/A_B) \, \mu/\rho|_A^B \, \frac{E_{KA}}{E_{KB}} \frac{\ln(E_0/E_{KB})}{\ln(E_0/E_{KA})} \cdot \frac{t}{2} [0.923 - \ln(\mu/\rho|_{SPEC}^B \cdot t)] \tag{11}$$

It is important to note that the model of Tixier[47] predicts a t^2 variation, whereas the model of Nockolds et al.[48] predicts a t log t enhancement due to fluorescence. The behavior of the two models is very different for thin (< 200 nm-thick) specimens and the Nockolds et al. expression indicates a much larger effect of fluorescence for thin specimens. It is difficult to determine which of these models is more correct experimentally because accurate measurements of t must be made (which as we have already seen is a problem), fluorescence effects coming from extraneous x rays generated in the column must be removed, and well-characterized, appropriate samples must be available. To date suitable experimental data are not available to detail the effects of fluorescence.

iv. Thin-film Standards. An alternative to the ratio method employs thin-film standards. As discussed by Zaluzec,[49] in the thin-film approximation the absolute intensity of element A, measured in an unknown specimen I_A^U, relative to the absolute intensity of the same x-ray line in a thin-film standard I_A^S is given by an equation of the form:

$$\frac{I_A^U}{I_A^S} = \frac{(\eta \, \rho t \, C_A)^U}{(\eta \, \rho t \, C_A)^S} \tag{12}$$

where η, ρ, t, and C_A are respectively the absolute electron flux, specimen density, thickness, and concentration in the standard S or the unknown U. In this case neither k_{AB} or ϵ_A values need be calculated. Unfortunately one must know η, ρ, and t for both standard and unknown and have a standard for each element measured in the unknown. As discussed previously, accurate measurements of t are difficult to make. In this case t must be measured for both the unknown and for all the standards. These disadvantages are so serious that this technique has seen little practical use. Recently Brown et al.[50] have used pure-element Al, Mo, and Ni standards to determine the composition of β-NiAl and δ-NiMo alloys. Besides difficulties in preparing pure-metal standards, changes in beam current lead to instabilities in the absolute electron flux. Unless standards preparation become easier and thickness measurements become more accurate the thin film standards technique will not be employed widely. The ratio method will continue to be employed by the vast majority of AEM users.

Limits of Microanalysis

It is pertinent to ask what the limits of EDS microanalysis are; specifically, with what accuracy can the average composition be determined and what is the minimum mass fraction (wt.%) that may be determined?

If x-ray counting statistics obey Gaussian behavior, at the 2σ confidence level, the relative error in the number of counts I is $2(I)^{-\frac{1}{2}} \times 100\%$. Since the Cliff-Lorimer relation (Eq. 4) uses the x-ray ratio I_A/I_B, the relative error for this ratio is the sum of the relative errors for I_A and I_B, and the total relative error in C_A/C_B for any one measurement is the sum of the errors for I_A, I_B, and k_{AB}. As we have seen k_{AB} may be determined experimentally with an accuracy between 1% and 4%. For a minimum of 10^4 counts in each characteristic peak I_A I_B, the total error is 5-8%, which is still high in comparison with bulk x-ray microanalysis errors. Still more accurate k_{AB} factors and as many accumulated counts as possible (concomitant with maintaining resolution) are required if accuracy in C_A/C_B is to be better than 5%.

The only theoretical approach to determination of the minimum mass fraction (MMF) was described by Joy and Maher[4] who predicted values of $0.2 \rightarrow \sim 3$ wt.% for species of $Z \simeq 15 - 40$ in a Si matrix depending on the microscope conditions.

Assuming Gaussian statistics (which is debatable at small peak intensities) MMF of element A in a matrix of B may be given by[13]

$$\text{MMF} = \frac{3(2I_b^A)^{\frac{1}{2}}}{I_B} k_{AB} C_B \tag{13}$$

where I_b^A is the continuum background for element A. This equation shows that the MMF decreases as the characteristic counts or peak-to-background increase. To increase the counts one can use larger probe sizes, brighter electron sources, and moderately thick foils if high spatial resolution is not required. Optimization of the AEM is therefore essential if the MMF limit is to be approached; the considerations outlined in the first section of this article should be followed. Recent work in our laboratory by Michael[51] using a Philips EM400T AEM, where count times are not limited by carbon contamination, has demonstrated that about 0.3 wt.% Mn can be detected in Cu by counting for about 300 s with a 10nm probe to accumulate over 10^3 counts. Extrapolation of these data by using Eq. (13) indicates that given sufficient counts, the MMF can approach about 0.1 wt.% with a tungsten filament. High-brightness guns should improve the detectability limits accordingly.

Conclusions

Quantitative x-ray microanalysis in the AEM can be routinely performed by the ratio method with an accuracy of about ±5%. True standardless microanalysis based on calculated k_{AB} factors is significantly less accurate, and severe practical difficulties exist for

microanalysis based on thin-film standards. Correction for absorption is possible but complicated by several factors of which the most prominent is the difficulty of accurate thickness determination. The fluorescence correction need rarely be applied and there is still uncertainty concerning the best correction to use. The MMF is significantly less than 1%, but depends on instrumental parameters over which the operator has control.

References

1. L. F. Allard, these proceedings, p. 25.
2. H. L. Fraser, these proceedings, p. 37.
3. P. J. Statham, these proceedings, p. 54.
4. D. C. Joy and D. M. Maher, "Sensitivity limits for thin specimen x-ray analysis," *SEM/1977* I, 325.
5. C. E. Fiori and D. E. Newbury, "Operation of energy-dispersive x-ray spectrometers in the analytical electron microscope," *Microbeam Analysis--1981*, 17.
6. J. I. Goldstein et al., *Scanning Electron Microscopy and X-ray Microanalysis*, New York: Plenum Press, 1981.
7. H. A. Kramers, "On the theory of x-ray absorption and of the continuous x-ray spectrum," *Phil. Mag.* 46: 836, 1923.
8. J. J. McCarthy and F. H. Schamber, "Least squares fit with digital filter: A status report," in K. F. J. Heinrich et al., Eds., *Energy Dispersive X-ray Spectrometry*, Washington, E.C.: NBS Special Publication 604, 1981, 273.
9. C. E. Fiori et al., "Sequential simplex: A procedure for resolving spectral interference in energy dispersive x-ray spectrometry," *ibid.*, p. 233.
10. L. V. Sutfin and R. E. Ogilvie, in J. C. Russ, Ed., *Energy Dispersion X-ray Analysis: X-ray and Electorn Probe Analysis*, Philadelphia: ASTM, 1971, 197.
11. G. Cliff and G. W. Lorimer, "The quantitative analysis of thin specimens," *J. Microsc.* 103: 203, 1975.
12. G. W. Lorimer et al., "The quantitative analysis of thin specimens: Effects of absorption, fluorescence and beam spreading," in D. L. Misell, Ed., *Developments in Electron Microscopy and Analysis*, Briston and London: The Institute of Physics, 1977, 369.
13. A. D. Romig and J. I. Goldstein, "Detectability limit and spatial resolution in STEM x-ray analysis: Application to Fe-Ni alloys," *Microbeam Analysis--1979*, 124.
14. J. Wood et al., "Determination of Cliff-Lorimer k-factors for a Philips EM400T," in G. W. Lorimer et al., Eds., *Quantitative Microanalysis with High Spatial Resolution*, Book 277, London: The Metals Society, 1981, 35.
15. T. P. Schreiber and A. M. Wims, "A quantitative x-ray microanalysis thin film method using K-, L-, and M Lines," *Ultramicroscopy* 6: 323, 1981.
16. J. Wood et al., "Determination of Cliff-Lorimer k factors," to be submitted *J. Microsc.*, 1982.
17. M. Green and V. E. Cosslett, "The efficiency of production of characteristic x-radiation in thick targets of a pure element," *Proc. Phys. Soc.* 78: 1206, 1961.
18. W. Bambynek et al., "X-ray fluorescence yields, Auger and Coster-Kronig transition probabilities," *Rev. Mod. Phys.* 44: 716, 1972.
19. E. H. S. Burhop, "Fluorescence yields," *J. Phys. Radium* 16: 625, 1955.
20. K. F. J. Heinrich et al., "Relative transition probabilities for x-ray lines from the k level," *J. Appl. Phys.* 50: 5589, 1979.
21. K. F. J. Heinrich, "Mass absorption coefficient tables for microprobe analysis," in T. D. McKinley et al., Eds., *The Electron Microprobe*, New York: Wiley, 1966, 351.
22. N. J. Zaluzec, "Quantitative x-ray microanalysis: Instrumental considerations and applications to materials Science," in J. J. Hren et al., Eds., *Introduction to Analytical Electron Microscopy* New York: Plenum Press, 1979, 121.
23. C. J. Powell, "Evaluation of formulas for inner-shell ionization cross sections," in K. F. J. Heinrich et al., Eds., NBS Special Publication 460, 1976, 97.
24. N. F. Mott and H. S. W. Massey, *The Theory of Atomic Collisions*, London: Oxford University Press, 2d ed., 1949, 243.
25. D. M. Maher et al., "Relative accuracy of k-Factor calculations for thin-film x-ray analysis," in R. H. Geiss, Ed., *Analytical Electron Microscopy--1981*, 33.
26. J. I. Goldstein et al., "Quantitative x-ray analysis in the electron microscope," *SEM/1977* I, 315.

27. R. Tixier and J. Philibert, "Analysis quantitative d'échantillons minces," in G. Möllenstedt and K. H. Gaukler, Eds., *Proc. 5th Intern. Cong. on X-ray Optics and Microanalysis*, Berlin: Springer-Verlag, 1969, 180.

28. R. König, "Quantitative x-ray microanalysis of thin foils," in H. R. Wenk, Ed., *Electron Microscopy in Mineralogy*, Berlin: Springer-Verlag, 1976, 526.

29. B. L. Henke and E. S. Ebisu, in *Advances in X-ray Analysis*, New York: Plenum Press, 1974, 17: 150.

30. D. F. Kyser, "Monte Carlo simulation in analytical elecron microscopy," in J. J. Hren et al., Eds., *Introduction to Analytical Electron Microscopy*, New York: Plenum Press, 1979, 199.

31. N. Stenton et al., "Determination of $\phi(\rho t)$ curves for thin foil microanalysis," in G. W. Lorimer et al., Eds., *Quantitative Microanalysis with High Spatial Resolution*, Book 277, London: The Metals Society, 1981, 35.

32. D. E. Newbury, private communication.

33. D. B. Williams and J. I. Goldstein, "Absorption effects in quantitative thin film x-ray microanalysis," in R. H. Geiss, Ed., *Analytical Electron Microscopy--1981*, 39.

34. G. W. Lorimer et al., "Determination of the thickness and spatial resolution for the quantitative analysis of thin foils," in J. A. Venables, Ed., *Developments in Electron Microscopy and Analysis*, London: Academic Press, 1976, 153.

35. G. Love et al., "Foil thickness measurments in transmission electron microscopy," in D. L. Misell, Ed., *Development in Electron Microscopy and Analysis*, Bristol and London: The Institute of Physics, 1977, 347.

36. D. A. Rae et al., "Problems in measuring foil thickness in the TEM," in G. W. Lorimer et al., Eds., *Quantitative Microanalysis with High Spatial Resolution*, Book 277, London: The Metals Society, 1981, 57.

37. P. M. Kelly et al., "The determination of foil thickness by scanning transmission electron microscopy," *Phys. Stat. Sol.* A31: 771, 1975.

38. S. M. Allen, "Foil thickness measurements from convergent beam diffraction patterns," *Phil. Mag.* A43: 325, 1981.

39. J. W. Edington, *Practical Electron Microscopy in Materials Science*, New York: Van Nostrand Reinhold, 1976, 329.

40. D. Cherns et al., "Characteristic x-ray production in thin crystals," *Z. Naturforschung* 28A: 565, 1973.

41. D. C. Joy and D. M. Maher, "Determination of crystal thickness from relative transmission measurements," in G. W. Bailey, Ed., *Proc. 33rd Ann. EMSA Meeting*, 1975, 242.

42. M. von Heimendahl and V. Willig, "A general method for determining specimen thickness," *Norelco Reporter*, 27: 22, 1980.

43. E. L. Hall and J. B. Vander Sande, "On projected widths of stacking faults used for foil thickness determinations," *Phil. Mag.* 32: 1289, 1975.

44. D. C. Joy, "The basic principles of electron energy loss spectroscopy," J. J. Hren et al., Eds., *Introduction to Analytical Electron Microscopy*, New York: Plenum Press, 1979, 223.

45. R. W. Glitz et al., "Considerations of x-ray absorption for STEM x-ray analysis of Ni-Al foils," *Microbeam Analysis--1981*, 309.

46. J. Philibert and R. Tixier, "Electron probe microanalysis of transmission electron microscope specimens," in B. M. Siegel and D. R. Beaman, Eds., *Physical Aspects of Electron Microscopy and Microbeam Analysis*, New York: Wiley, 1975, 333.

47. R. Tixier, "Electron probe microanalysis of thin samples," in C. Lechene and R. Warner, Eds., *Microbeam Analysis in Biology*, New York: Academic Press, 1979, 209.

48. C. Nockolds et al., "X-ray fluorescence correction in thin foil analysis and direct methods for foil thickness measurement," in T. Mulvey, Ed., *Developments in Electron Microscopy and Analysis*, Bristol and London: Institute of Physics, 1979, 417.

49. N. J. Zaluzec, "Limitations of AEM-based x-ray microanalysis," in *Analytical Electron Microscopy--1981*, 47.

50. J. M. Brown et al., "Quantitative energy dispersive x-ray analysis of thin foils with pure elemental standards," *ibid.*, p. 61.

51. J. R. Michael, "Application of Analytical Electron Microscopy to Grain Boundary Segregation in Copper Alloys," M. S. Thesis, Lehigh University, 1981, 74.

A COMPARISON OF TWO MODELS FOR THE CHARACTERISTIC X-RAY FLUORESCENCE CORRECTION IN THIN-FOIL ANALYSIS

M. E. Twigg and H. L. Fraser

It has recently become apparent that there are two alternative formulations for the contribution of characteristic x-ray fluorescence in thin foils.[1] The formula of Philibert and Tixier[2,3] predicts considerably less characteristic fluoresence than that of Nockolds et al.[4] The source of discrepancy between these two results lies in mathematical execution rather than in any differences due to assumptions inherent in either model. Whereas the computations of Nockholds et al. appear to be carried out correctly, those of Philibert and Tixier do not. Errors in computation account for a difference of approximately three orders of magnitude; dissimilarities in formulation cause these two results to differ by less than a factor of two. Though it also appears from these considerations that Philibert and Tixier's equation for continuum fluorescence is incorrect, we shall confine our attention in this paper to characteristic fluorescence.

The Model of Philibert and Tixier

Let us first consider the model proposed by Philibert and Tixier. They considered a thin foil of mass thickness t that is composed of elements A and B. The critical energy E_A of element A is less than the energy of the K^α line of element B. As a result, the K_B^α x-ray line is capable of fluorescing the K_A^α line; furthermore the K_B^β line can also fluoresce the K_A^α line. It is assumed that the x rays generated by B can be regarded as originating from a point source in the middle of a foil of thickness t, as shown in Fig. 1. The total intensity of K_B x rays (both K_B^α and K_B^β lines as well as other K_B lines) are assigned an intensity I_B. There are 4π steradians to a sphere; hence the x-ray intensity per steradian is $I_B/4\pi$. Assuming the geometry expressed in Fig. 1, the intensity of x rays not yet absorbed by the sample and directed at an angle θ and a distance $z \sec \theta$ from the origin of the radiation source is

$$dI_B^0 = \frac{I_B}{4\pi} 2\pi \sin \theta \; d\theta \; e^{-\mu_B z \sec \theta} \qquad (1)$$

where μ_B is the coefficient for the absorption of K_B^α by the sample. One hopes K_B^β is close enough to the K_B^α so that μ_B adequately approximates the absorption of K_B^β as well.

From the weight fraction C_A of element A within the foil and the coefficient μ_B^A for mass-absorption of K_B^α radiation by element A, we know that the probability for a given K_B^α x ray ionizing an atom of atomic species A in a volume of mass thickness dz is $C_A \mu_B^A \sec \theta$ dz. For a K_A absorption edge characterized by a jump ratio r_A, the probability that a given ionization is that of the K_A shell is $(r_A - 1)/r_A$. Therefore, assuming a fluorescent yield ω_A, and a partition coefficient a_A for the relative intensity of the K_A^α line within the K_A series, the probability that a given
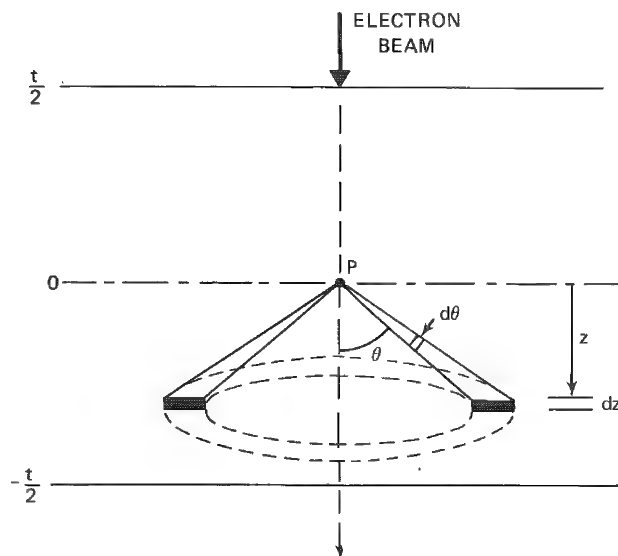
FIG. 1.--Geometry for characteristic x-ray fluorescence model of Philibert and Tixier;[3] point P indicates the position of x-ray source.

The authors are with the Department of Metallurgy and Mining and the Materials Research Laboratory, University of Illinois, Urbana, IL 61801.

K_B^α photon is absorbed by a differential volume of mass thickness dz and subsequently gives rise to K_A^α photon is

$$P_B^A = a_A \omega_A \frac{r_A - 1}{r_A} C_A \mu_B^A \sec \theta \ dz \tag{2}$$

If μ_B^A does not vary significantly from the mass absorption coefficient for absorption of K_B^A or the other lines of the K_B series by element A, Eq. (2) is valid for all K_B radiation. The differential intensity of the contribution of the characteristic fluorescence of the K_A^α line is then

$$
\begin{aligned}
dI_A^f &= dI_B^o \ P_A^B \\
&= \frac{I_B}{2} a_A \omega_A \frac{r_A - 1}{r_A} C_A \mu_B^A \ e^{-\mu_B z \sec \theta} \tan \theta \ d\theta \ dz
\end{aligned} \tag{3}
$$

We are, of course, interested in how the intensity of the contribution of characteristic fluoresence to the K_A^α line compares with the intensity of this line due to electron irradiation of the sample. We know from Eq. (3) how the fluorescent contribution to the K_A^α line compares with the K_B intensity; we only need to establish the relationship between the K_A^α and K_B intensities, which we can do via the Cliff-Lorimer[5] relationship. That is,

$$\frac{I_B}{I_A^\alpha} = \frac{C_B \omega_B Q_B / A_B}{C_A a_A \omega_A Q_A / A_A} \tag{4}$$

where Q_A and Q_B are the cross sections for K-shell ionization, and A_A and A_B are the atomic weights. Therefore, from Eqs. (3) and (4), we can deduce that

$$\frac{dI_A^f}{I_A} = \frac{C_B}{2} \omega_B \frac{Q_B}{Q_A} \frac{A_A}{A_B} \frac{r_A - 1}{r_A} \mu_B^A \ e^{-\mu_B z \sec \theta} \tan \theta \ d\theta \ dz \tag{5}$$

If we were interested in a more exact calculation, we would employ a more recent version of the x-ray cross section, such as that of Zaluzec.[6] For our purposes, however, let us regard Q_A as proportional to $U_A \ln U_A$, where U_A is the overvoltage for element A. That is,

$$U_A = E/E_A \tag{6}$$

where E is the energy of the incident electron beam and E_A is the critical voltage for ionization of A's K shell. For such values of this cross section, we find that Eq. (5) can assume the form

$$\frac{dI_A^f}{I_A} = \frac{C_B}{2} \omega_B \frac{A_A U_B \ln U_B}{A_B U_A \ln U_A} \frac{r_A - 1}{r_A} \mu_B^A \ e^{-\mu_B z \sec \theta} \tan \theta \ d\theta \ dz \tag{7}$$

In order to obtain the ratio I_A^f/I_A from the differential element described in Eq. (7), we must integrate over the volume illustrated in Fig. 1. Obviously, we can regard the foil in two sections, one on top of the K_B source ($0 \le z \le t/2$) and one underneath the K_B source ($0 \ge z \ge -t/2$). The fluorescent radiation generated in the top section is of the same intensity as that generated in the bottom, so that the total intensity of the fluorescent contribution to K_A^α is

$$
\begin{aligned}
\frac{I_A^f}{I_A} &= 2 \frac{C_B}{2} \omega_B \frac{A_A U_B \ln U_B}{A_B U_A \ln U_A} \frac{r_A - 1}{r_A} \mu_B^A \int_0^{t/2} dz \int_0^{\pi/2} d\theta \ e^{-\mu_B z \sec \theta} \tan \theta \\
&= 2\eta \int_0^{t/2} dz \int_0^{\pi/2} d\theta \ e^{-\mu_B z \sec \theta} \tan \theta
\end{aligned} \tag{8}
$$

where

$$\eta = \frac{C_B}{2} \, \omega_B \, \frac{A_A U_B \, \ln U_B}{A_B U_A \, \ln U_A} \, \mu_B^A \, \frac{r_A - 1}{r_A} \tag{9}$$

Through the substitution $u = \sec \theta$, Eq. (8) can be recast in the form,

$$\frac{I_A^f}{I_A} = 2\eta \int_0^{t/2} dz \int_1^\infty du \, \frac{e^{-\mu_B z u}}{u} \tag{10}$$

The nth exponential integral is defined as[7]

$$E_n(a) = \int_1^\infty dt \, \frac{e^{-at}}{t^n} \tag{11}$$

so that Eq. (10) can also be expressed as

$$\frac{I_A^f}{I_A} = 2\eta \int_0^{t/2} dz \, E_1(\mu_B z) \tag{12}$$

Because of the following algorithm, the integral in Eq. (12) is easy to evaluate:

$$\frac{d}{dx} E_n(x) = -E_{n-1}(x) \tag{13}$$

The value of the nth exponential integral with zero as an argument is also simply calculated. That is (for $n > 1$),

$$E_n(0) = \frac{1}{n - 1} \tag{14}$$

From Eqs. (13) and (14), Eq. (12) can be reduced to

$$\frac{I_A^f}{I_A} = \frac{-2\eta}{\mu_B} E_2(\mu_B z) \Big|_0^{t/2} = \frac{2\eta}{\mu_B} [1 - E_2(\mu_B t/2)] \tag{15}$$

The nth exponential integral can also be expressed as an infinite series. That is,

$$E_n(z) = \frac{(-z)^{n-1}}{(n-1)!} [-\ln z + \Psi(n)] - \sum_{\substack{m=0 \\ m \neq n-1}}^\infty \frac{(-z)^m}{(m - n + 1)m!} \tag{16}$$

where $\Psi(n) = -\gamma + \sum_{m=1}^{n-1} \frac{1}{m}$ and $\gamma = 0.5772$. If we use the algorithm in Eq. (16) for small values of z (i.e., small thicknesses), we find that

$$E_2(z) = 1 - z [0.4228 + (z/2) - \ln z] \tag{17}$$

so that Eq. (15) can take the form

$$\frac{I_A^f}{I_A} = \frac{2\eta}{\mu_B} \frac{\mu_B t}{2} [1.12 + \mu_B(t/4) - \ln(\mu_B t)] = \eta t [1.12 + \mu_B(t/4) - \ln(\mu_B t)] \tag{18}$$

By evaluating η via Eq. (9) and substituting this expression in Eq. (18), we find that the fraction of the fluorescent contribution to the K_A^α intensity is

$$\frac{I_A^f}{I_A} = C_B \omega_B \, \frac{A_A U_B \, \ln U_B}{A_B U_A \, \ln U_A} \, \frac{r_A - 1}{r_A} \, \frac{\mu_B^A t}{2} [1.12 + \mu_B(t/4) - \ln(\mu_B t)] \tag{19}$$

39

Philibert and Tixier's version of this equation is, however,

$$\frac{I_A^f}{I_A} = 2\omega_B C_B \frac{r_A - 1}{r_A} \frac{A_A}{A_B} \mu_B^A \mu_B \frac{\nu_A}{\nu_B} t^2 \tag{20}$$

where ν_A and ν_B are the frequencies of the K_A^α and K_B^α radiation. If we were to assume, as did Philibert and Tixier, that $\ln U_A$ does not differ significantly from $\ln U_B$, and observe that $U_B/U_A = \nu_A/\nu_B$, we would cast Eq. (19) in the form

$$\frac{I_A^f}{I_A} = C_B \omega_B \frac{r_A - 1}{r_A} \frac{A_A}{A_B} \frac{\nu_A}{\nu_B} \frac{\mu_B^A t}{2} [1.12 + \mu_B(t/4) - \ln(\mu_B t)] \tag{21}$$

Even with these assumptions, Eq. (21) differs significantly from Eq. (19). This difference is primarily due to Philibert and Tixier's integration of Eq. (5). Their integration of Eq. (5) was of the form,

$$\frac{I_A^f}{I_A} = 4\eta \int_{-t/2}^{t/2} dz \int_0^\pi d\theta \, e^{-\mu_B z \sec \theta} \tan \theta \tag{22}$$

In comparing Eq. (22) with Eq. (8), we see that Philibert and Tixier's formula is incorrect. If it were Philibert and Tixier's intent to choose limits of integration that would include the entire specimen, we would expect the constant coefficient in front of the integral to be η rather than 4η. The limits of integration employed in Eq. (22) are, however, also incorrect. This choice of limits allows the absorption factor $e^{-\mu_B z \sec \theta}$ to be greater than one when $z > 0$ and $\pi/2 < \theta < \pi$, or when $z < 0$ and $0 < \theta < \pi/2$. This outcome is, of course, impossible, since a positive value of this factor would call for generation of K_B radiation where there should be absorption. Furthermore, within the range $\pi/2 < \theta < \pi$, the integrand is negative, which would imply that for certain directions, the x-ray intensity due to characteristic fluorescence is negative, which is certainly unphysical.

In order to illustrate the discrepancy between Philibert and Tixier's formulation (Eq. 20) and our correction (Eq. 21), let us calculate the characteristic fluorescence ratio for a case considered by Philibert and Tixier.[2,3] They considered a 500Å foil composed of 95 wt.% nickel and 5 wt.% iron. Because the critical excitation energy of Fe is less than the K_{Ni}^α energy, Fe atoms would be fluoresced by K_{Ni} radiation; hence we would be interested in the characteristic fluorescence of Fe. Philibert and TIxier employed the following parameters in their calculation: $\omega_{Ni} = 0.385$, $r_{Fe} = 8.13$, $A_{Fe} = 55.847$ g/mole, $A_{Ni} = 58.71$ g/mole, $\mu_{Ni}^{Fe} = 384$ cm^2/g, $\mu_{Ni} = 74.3$ cm^2/g, $E_{Fe} = 7.110$ kV, $E_{Ni} = 8.330$ kV, and $t = 4.42 \times 10^{-5}$ g/cm^2. For this system, Philibert and Tixier then found that Eq. (20) yielded the value

$$\frac{I_{Fe}^f}{I_{Fe}} = 2.90 \times 10^{-5} \tag{23}$$

which is certainly insignificant. Our version of Philibert and Tixier's formula, which employs Eq. (21), yields the value,

$$\frac{I_{Fe}^f}{I_{Fe}} = 1.51 \times 10^{-2} \tag{24}$$

Though still small, our version is different from that obtained by Philibert and Tixier by about three orders of magnitude. For thicker samples, we might expect that the characteristic fluorescence would make a significant contribution to the K_{Fe}^α peak. For a 500Å foil of the composition described, about 10% of the K_{Fe}^α intensity would be due to the characteristic fluorescence according to one formulation. Even for a sample of such thickness, Philibert and Tixier's formula would predict a contribution of only 0.2%.
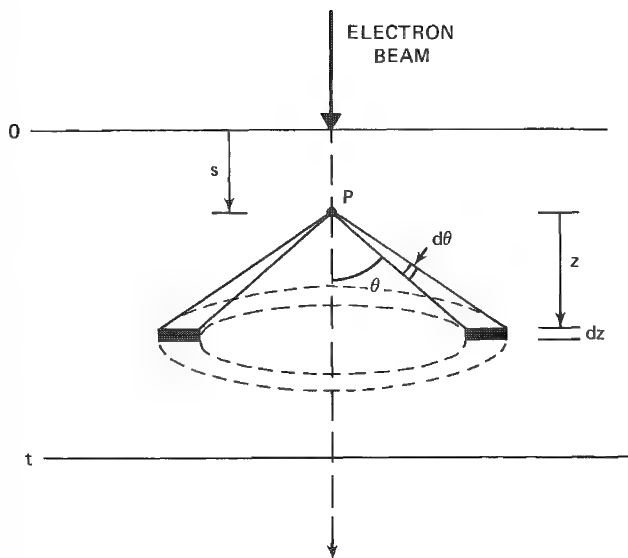
FIG. 2.--Geometry for characteristic x-ray fluorescence model of Nockolds et al.[4]

The Model of Nockolds et al.

A recent paper of Nockolds et al.[4] successfully corrected for characteristic fluorescence in thin film x-ray microanalysis. They recognized that for thin foils, the x-ray generation due to direct electron radiation could occur with equal likelihood at any point along a straight line defined by the electron beam within the sample. With the geometry illustrated in Fig. 2, Eq. (7) can be integrated as

$$\frac{I_A^f}{I_A} = \frac{\eta}{t} \int_0^t ds \; [\int_0^s dz \int_0^{\pi/2} d\theta \; e^{-\mu_B z \sec \theta} \tan \theta$$

$$+ \int_0^{t-s} dz \int_0^{\pi/2} d\theta \; e^{-\mu_B z \sec \theta} \tan \theta] \qquad (25)$$

where s is the position of the K_B x-ray source that is uniformly distributed from zero to t along the z-axis. Again we make the substitution $u = \sec \theta$ and find that Eq. (25) can be expressed in terms of the exponential integral defined in Eq. (11). That is,

$$\frac{I_A^f}{I_A} = \frac{\eta}{t} \int_0^t ds \; [\int_0^s dz \; E_1(\mu_B z) + \int_0^{t-s} dz \; E_1(\mu_B z)] \qquad (26)$$

From Eqs. (13) and (14) we see that

$$\frac{I_A^f}{I_A} = \frac{\eta}{\mu_B t} \int_0^t ds \; [2 - E_2(\mu_B s) - E_2 \mu_B(t - s)] = \frac{2\eta}{\mu_B t} \{1 + (1/\mu_B t)[E_3(\mu_B t) - 1/2]\} \qquad (27)$$

From Eq. (16), we find that for small z, $E_3(z)$ can be expressed as,

$$E_3(z) = \frac{1}{2} - z + \frac{z^2}{2} [0.923 - \ln z] \qquad (28)$$

Therefore,

$$\frac{I_A^f}{I_A} = \eta t \; [0.923 - \ln(\mu_B t)] \qquad (29)$$

Employing the definition of η from Eq. (9), we find that

$$\frac{I_A^f}{I_A} = C_B \omega_B \frac{A_A}{A_B} \frac{U_B}{U_A} \frac{\ln U_B}{\ln U_A} \frac{r_A - 1}{r_A} \frac{\mu_B^A t}{2} [0.923 - \ln(\mu_B t)] \qquad (30)$$

Conclusion

For the Ni-5 wt.% Fe foil of 500 Å thickness discussed by Philibert and Tixier, the formula of Nockolds et al. (Eq. 30) calculates I_A^f/I_A as 1.38×10^{-2}. Though this result does not differ significantly from our evaluation of Philibert and Tixier's geometry via Eq. (21), it is much greater than the value predicted by Philibert and Tixier's calculation as expressed by Eq. (20). Nockolds et al. have shown that their formula is supported by x-ray microanalysis of Fe-10.5 wt.% Cr foils for thicknesses ranging from 200 to 7000 Å. These data do not, however, support Philibert and Tixier's equation. On the other hand, the results of a similar experiment, conducted by Tixier et al., on Fe-17.3 wt.% Cr foils, tend to support the negligible contribution of characteristic fluorescence predicted by Philibert

and Tixier's equation. From these conflicting results, no definitive judgment can be drawn on the validity of the formula of Nockolds et al. As for the equation of Philibert and Tixier, it clearly suffers from weaknesses in the mathematical execution of a fairly well-formulated model. At least these weaknesses are not apparent in the derivation followed by Nockolds et al.

References

1. R. Tixier, B. Thomas, and J. Bourgeot, "Principles, limits and statistical evaluation of x-ray analysis," *Quantitative Microanalysis With High Spatial Resolution*, Manchester, England: Metals Society, 1981, 15-23.

2. R. Tixier, *Microanalyse par sonde électronique des echantillons mince*, Ph.D. Thesis, University of Paris, Orsay A 196 (CNRS No. A.0.8.833), 1973.

3. J. Philibert and R. Tixier, "Electron probe microanalysis of transmission electron microscope specimens," in B. Siegel and D. R. Beaman, Eds., *Physical Aspects of Electron Microscopy and Microbeam Analysis*, New York: Wiley, 1975, 38-54.

4. C. Nockolds, G. Cliff, and G. W. Lorimer, "Characteristic x-ray fluorescence correction in thin foil analysis," *Micron* 11: 325-326, 1980.

5. G. Cliff and G. W. Lorimer, "The quantitative analysis of thin specimens," *J. Microsc.* 203: 203-207, 1975.

6. N. J. Zaluzec, "Quantitative x-ray microanalysis," in J. J. Hren, J. I. Goldstein, and D. C. Joy, Eds., *Introduction to Analytical Electron Microscopy*, New York: Plenum, 1975, 121-167.

7. M. Abramowitz and I. A. Segun, *Handbook of Mathematical Functions*, New York: Dover, 1965, 228-235.

PRINCIPLES AND PRACTICE OF QUANTITATIVE ELECTRON ENERGY-LOSS SPECTROSCOPY

R. F. Egerton

Now that electron spectrometers are commercially available for attachment to a transmission electron microscope, electron energy-loss spectroscopy (EELS) is beginning to take its place among the arsenal of techniques for microanalysis with high spatial resolution. The aim of this tutorial paper is to discuss how the spectrometer can be used most efficiently, and to review some problems in interpretation of energy-loss spectra and methods for obtaining quantitative information on elemental concentrations.

Three important parameters in EELS microanalysis are: the energy resolution ΔE in the energy-loss spectrum, the diameter d of the region being analyzed, and the angular range α (measured relative to the optic axis, directly after transmission through the specimen) of electrons allowed into the spectrometer (Fig. 1). In fact, these three quantities are each interrelated; nevertheless, we shall consider them in turn, to the extent possible.
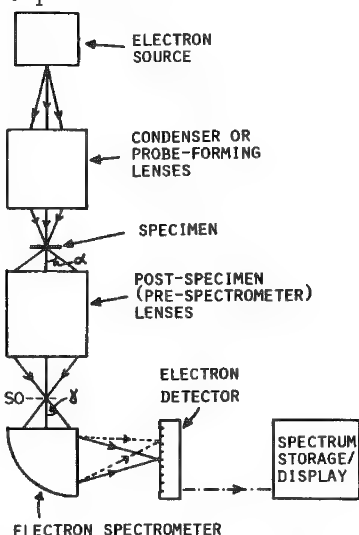
FIG. 1.--Typical EELS system; lens column can be either conventional or scanning transmission microscope.

1. Achieving Good Energy Resolution

ΔE itself depends on several factors that are at least partly under the control of the experimenter: optics of the spectrometer and of pre-spectrometer lenses, the geometry of the electron detector, and the type of electron source.

a. Focusing the Energy-loss Spectrum. The first requirement for good energy resolution is that the electron spectrometer be "focused"; i.e., that to first order, its image plane coincides with the detector slit (for serial data collection) or with the detector itself (in the case of parallel-recording devices). One could accomplish such focusing by physically moving the detector assembly toward or away from the spectrometer, but fine adjustments are more easily done electrically. Spectrometers that are attached to a CTEM column but operate with the projector lens turned off are fine-focused by variations in the intermediate-lens current (and therefore in the height of the spectrometer object plane SO; see Fig. 1). On the other hand, spectrometers that operate with the projector lens on (and with the projector crossover as their object plane) must be provided with their own means of focusing, for example a weak lens built into the entrance region of the spectrometer. It may be necessary to readjust spectrometer focus if the projector-lens current is varied (e.g., to achieve very low magnifications on the viewing screen).

Spectrometer focusing is normally done (with or without a specimen in place) by rapid scanning through the zero-loss peak and adjustment of the latter for maximum height and minimum width (Fig. 2b). The resulting energy width at one-half of the peak height (the so-called FWHM) is usually quoted as the energy resolution ΔE. In practice, ΔE is not constant throughout the spectrum but increases with energy loss owing to the increasing

angular width of the inelastic scattering.
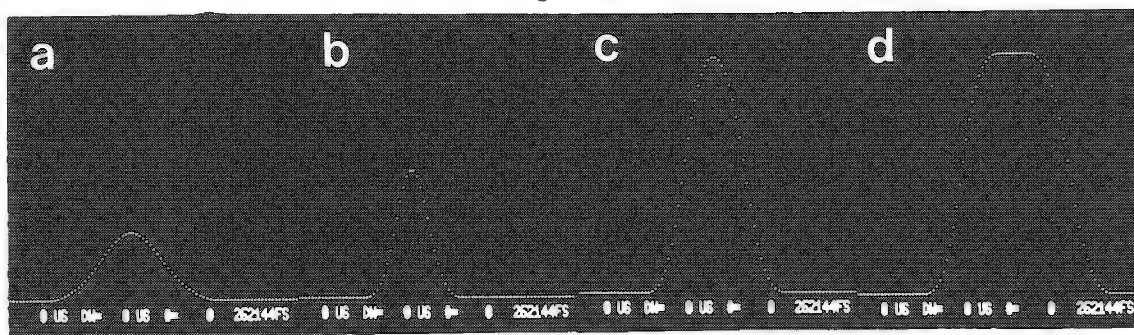
FIG. 2.--Change in shape of zero-loss peak as spectrum is focused (a and b) and as detector slit is widened (b through d).

b. *Spectrometer Alignment.* Occasionally, a spectrometer may need to be re-aligned--for example, if the alignment of the microscope itself has altered. Re-alignment is done mechanically or by deflection coils built into the spectrometer. One can optimize this alignment by observing the width of the zero-loss peak or the shape of the small aberration figure produced at the image plane of the spectrometer. In a more convenient approach, one rocks the entrance beam at the spectrometer object plane SO (e.g., by energizing the STEM scanning coils of the microscope), and displays the detector signal as a function of rocking angle on a cathode-ray tube (e.g., the STEM-image display screen). The resulting "alignment figure" is brought to the center of the screen and made as symmetrical as possible. In aberration-corrected spectrometers, the alignment figure is expanded in area as much as possible by adjustment of the aberration-correction fine controls. An angle-limiting aperture (objective aperture or spectrometer entrance aperture) can then be inserted and aligned for minimum ΔE (and maximum signal) by centering of its outline around the center of the alignment figure.[1]

Many spectrometers are now fitted with stray-field compensation controls which inject a mains-frequency current (of variable phase and amplitude) into the spectrometer excitation coils. Such controls can also be set by use of the alignment figure (by insuring that its edges are smooth rather than sinusoidally modulated), or else by observation of a low-loss portion of the energy-loss spectrum and adjusting for minimum "ripple" (Fig. 3).

c. *Setting the Slit Width (for Serial Recording).* In most current EELS systems, the spectrum is acquired sequentially into some form of electronic memory by scanning of the spectrometer exit beam across a stationary slit. If the slit is too wide, energy resolution is sacrificed (i.e., ΔE is undesirably large); if too narrow, the detected signal (and hence signal/noise ratio) becomes unacceptably low. A useful compromise is achieved by decrease of the slit width until the height of the zero-loss peak is reduced by a factor of about two (Fig. 2b).

d. *Choice of Lens Conditions.* The energy resolution attainable from an electron spectrometer also depends on the excitation of any electron lenses that follow the specimen. These postspecimen lenses may be used to present a magnified or demagnified image of the specimen at the spectrometer object plane SO; or alternatively to present a diffraction pattern of the specimen (or, at least, the central spot) at the spectrometer object plane. The two possibilities have previously been termed "image (or spot) mode" and "diffraction mode," respectively.[2,3] However, these terms can lead to misunderstanding in the case of spectrometers mounted beneath a CTEM column and which use the projector-lens crossover as their object plane; the spectrometer is then working in "diffraction mode" when the CTEM column itself is in "image mode" (i.e., produces an image of the specimen at the CTEM screen), and vice versa! So to avoid confusion, we shall refer to the lenses as providing either *image coupling* or *diffraction coupling* to the spectrometer.

Diffraction coupling is the condition normally employed in the Technics model-5 spectrometer and in some earlier JEOL designs. With the projector lens turned off, a diffraction pattern of camera length equal to a few millimeters is provided by SO, which lies approximately at the level of the viewing screen. Acceptable energy

resolution is obtained if the collection semi-angle α (determined by an objective aperture) is kept below about 10 mrad, in order to avoid an unduly large object size at SO.

Diffraction coupling exists also for spectrometers that use a projector-lens crossover as the object point (e.g., Gatan model 607 or the spectrometer supplied with a JEM-1200), *provided* an image of the specimen is present at the level of the CTEM screen. Utilization of both the objective and projector lenses results in a much smaller camera length, given by $L \simeq w/M_{VS}$ where w is the height of the projector polepiece above the viewing screen and M_{VS} is the image magnification at the screen. A large collection angle (limited by the angular acceptance of the objective lens, typically 100-200 mrad) is therefore possible, without the spectrometer object size (and therefore ΔE) becoming excessive. A penalty with this arrangement is that the diameter d of the analyzed area must be kept reasonably small (e.g., below 10 μm), otherwise ΔE may become excessive due to spectrometer aberrations; however, this is not really a restriction in most microanalysis situations.

Image coupling occurs for those spectrometers mentioned in the previous paragraph, when a diffraction pattern is placed at screen level or if the objective excitation is increased so as to operate the column in STEM mode. The value of α is then limited by the spectrometer entrance aperture (at or just below the level of the CTEM screen); the maximum value is about 10 mrad for a 1mm-diameter aperture and camera length L_{VS} = 5 cm at the viewing screen.

e. Energy spread of the electron source. Even with an ideal spectrometer and other parameters optimized, energy resolution is ultimately limited by the energy spread of electrons coming from the source, about 1.5 eV for a tungsten filament, about 1 eV for LaB_6, and 0.5 eV or less for a cold field-emission source. The energy spread of a thermal source can be reduced somewhat by operation at a lower temperature, but at the expense of considerably reduced beam current. Of course LaB_6 and (particularly) field-emission sources have higher electron-optical brightness, which helps in the attainment of high spatial resolution.
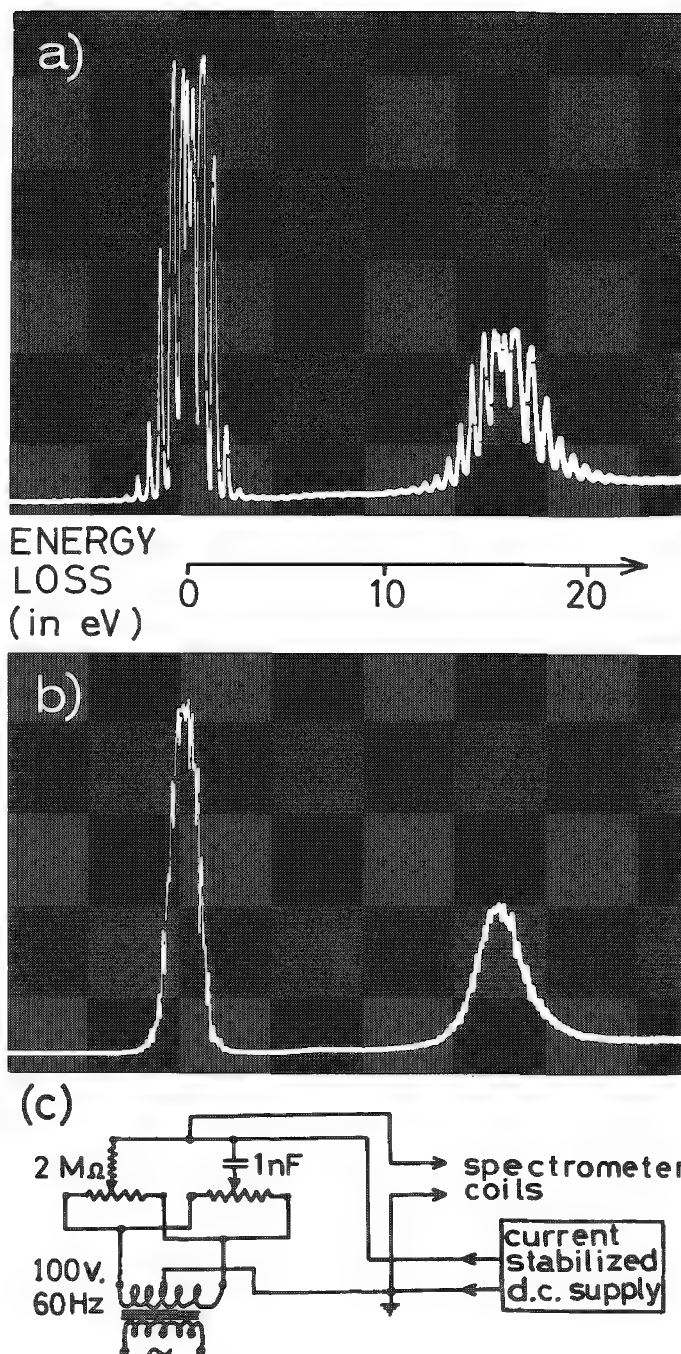
FIG. 3.--(a) Zero-loss and first-plasmon peaks of aluminum recorded with scan time of about 1 s, in presence of considerable mains-frequency interference; (b) same spectrum recorded with ac compensation circuit adjusted for minimum ripple (FWHM of zero-loss peak = 1.8 eV); (c) details of stray-field compensation circuit.

2. *Choice of Spatial Resolution*

Chemical information is often required on as fine a scale as possible, which implies a small value for the diameter d of the analyzed area. In addition, since most specimens are not uniformly thin, a small value of d makes it easier to find suitable regions that have sufficiently small thickness for successful EELS analysis. (For low background to the characteristic edges, the thickness should be less than the total inelastic mean free path, which for 100keV incident electrons and a typical sample is in the range 50-100 nm.)

However, choice of too small a value of d may introduce problems. If the area being analyzed is defined by the incident beam itself (as in STEM mode), the high current density associated with a very small incident probe increases the risk of hydrocarbon contamination and (in beam-sensitive materials) of radiation damage. Contamination is more serious in EELS than in x-ray microanalysis, since it increases the background throughout the spectrum and introduces a carbon K-edge at 285 eV, which may interfere with nearby edges being analyzed.

If, on the other hand, the area of analysis is defined by means of an area-selecting aperture, too small an aperture reduces the available signal and makes the spectrum noisy. A further complication with selected-area methods arises as a result of chromatic aberration. If CTEM selected-area apertures are used in the standard way (the objective lens focused such that both specimen and aperture are in focus on the viewing screen), electrons that have undergone a substantial energy loss E brought to focus at a plane which is higher by an amount $C_c E/E_0$, where C_c is the chromatic-aberration constant of the objective lens and E_0 the incident energy. This shift limits the possible spatial resolution to a value of about $\alpha C_c E/E_0$, which is 200 nm in a typical case ($\alpha \simeq 10$ mrad, $C_c \simeq 2$ mm, $E = 1000$ eV, $E_0 = 100$ keV). Fortunately, this problem is avoidable; the objective-lens current is simply reduced by a fraction $C_c E/2E_0 f$ (i.e., by 0.05% for each 100 eV of energy loss, if $f \simeq C_c \simeq 2$mm, $E_0 = 100$ keV) in order to restore the image to the correct plane. If the spectrum is acquired serially, this restoration could be achieved by the application of a suitable fraction of the spectrometer ramp voltage to the lens power supply. (Similar considerations apply to the use of a spectrometer entrance aperture as the area-selecting device; the chromatic effect of lenses which follow the objective should be negligible in comparison.) Correction for objective-lens chromatic aberration also improves the energy resolution ΔE.[3]

The *ultimate* spatial resolution for energy-loss analysis (obtainable only with a very small incident probe or via energy-filtered CTEM imaging) is limited by spherical aberration of the probe-forming or objective lens, by angular spreading of the beam,[5,6] and by localization effects[7] (or, for higher energy losses, by diffraction "at" the objective aperture). A resolution below 1 nm has been claimed experimentally.[8]

3. *Choice of Collection Angle*

As previously mentioned, it is necessary with some spectrometer systems to restrict the collection angle in order to achieve satisfactory energy resolution. In fact, one gains some inherent advantage in using a small value of α: it tends to minimize the intensity of the background in the energy-loss spectrum, relative to that of the characteristic edges.[6,9,10] Furthermore, if very high spatial resolution is desired, a restricted value of α may be necessary to avoid the effects of beam spreading.[5,6]

But there are some compensating advantages to choosing a *large* value of α: one may avoid possible complications in quantitation (see below) and improve the signal/noise ratio in the recorded spectrum, as a result of the higher collected signal.

The "best" value of α therefore depends on the specimen, the instrumentation, and the experimental aims and conditions. For quantitative microanalysis, it is useful to record spectra with at least two values of α; comparison of the results then provides a valuable means of checking the quantitation method and the experimental procedure.

4. *Spectrum Acquisition*

For spectrum storage in some form of multichannel analyzer, parameters under the control of the operator are: total acquisition time, number of scans of the spectrometer (for serial collection) or of the detector (in the case of diode-array systems), and the number of storage channels employed.

With a low-noise electron detector (e.g., a suitably chosen scintillator and photomultiplier tube), the main noise component in the spectrum is shot noise (due to Poisson statistics of the arriving electrons), which is proportional to $s^{\frac{1}{2}}$, where s represents the accumulated signal per channel. Thus, the signal-to-noise ratio is proportional to $s/s^{\frac{1}{2}} = s^{\frac{1}{2}}$, which in turn is proportional to (incident-beam current × acquisition time)$^{\frac{1}{2}}$. Lower noise level is therefore achieved by increasing the incident current or the acquisition time. Incident current is limited by the capabilities of the electron source and by specimen heating; exposure time is limited by the stability of the microscope and spectrometer power supplies and by the patience of the operator. The product (current × time) may also be limited by hydrocarbon contamination of the specimen or (in beam-sensitive samples) by radiation damage. In practice, exposure times within the range 20-200 s are typical for serial-collection systems.

With serial acquisition, there is normally no difference in signal/noise ratio between a spectrum obtained by scanning of the spectrometer once and an accumulated spectrum obtained from several faster scans, provided the total detection time is the same. But for diode-array detectors, where readout noise can be significant, there *is* some advantage in the use of only a single exposure and readout.

Spectra are commonly acquired into 1024 channels; each channel represents an energy increment of about 1 eV, which gives a useful range of about 1000 eV in energy loss. If the energy resolution amounts to several eV (e.g., as a result of using a wide detector slit to increase the signal), the resulting spectrum has been "oversampled," which results in a higher noise content and no better energy resolution than if, say, half the number of channels had been used. In extreme cases, this additional noise may cause difficulties with background fitting,[3] though it could be removed by digital smoothing.[11]

In order to compress the dynamic range of the stored data, a detector-gain change is often introduced during serial acquisition. In a photomultiplier detector, one can achieve this compression by increasing the voltage applied to the tube at some suitable point during the scan, possibly accompanied by a change to pulse counting rather than digitization by a voltage-to-frequency or analog-to-digital converter.

5. *Spectrum Processing*

a. Energy Calibration. Due to drift of the high voltage or spectrometer power supplies, the position of the zero-loss peak in the recorded spectrum may vary. But the E-axis sensitivity (i.e., eV/channel) usually remains constant and can be found by recording of the spectrum of a standard specimen with known edge energies.[12]

Therefore routine calibration need only involve locating the zero-loss peak and instructing the microprocessor which controls the spectrum display to label the energy axis accordingly. Location of the zero-loss channel can either be done by eye or by a small segment of software which locates the first maximum in the data, ignoring background noise.[3]

b. E-axis Linearity. The simplest way of scanning the energy-loss spectrum is to vary the induction B within a magnetic spectrometer by means of a linear current ramp. Since the detector slit remains stationary, the selected electron orbit (within the magnetic field) has a constant radius R given by:

$$\frac{mv^2}{R} = Bev \tag{1}$$

where v is the electron velocity, e is the electronic charge, and m is the relativistic electron mass. This equation can be rewritten in terms of the electron rest energy E_r and the kinetic energy ($E_0 - E$) of electrons which enter the detector:

$$B = \frac{E_r}{eRc} \left[\left(\frac{E_r + E_0 - E}{E_r} \right)^2 - 1 \right]^{\frac{1}{2}} \tag{2}$$

where c is the velocity of light in vacuum. Because this relationship between B and E is not a linear one, there must be some nonlinearity in the energy-loss axis, even if changes in B are strictly proportional to the scan current. Differentiation of Eq. (2) shows that:

$$\left|\frac{dE}{dB}\right|_R \quad \propto \quad \left[\ 1\ -\ \left(\frac{E_r\ +\ E_0\ -\ E}{E_r}\right)^{-2}\right]^{\frac{1}{2}} \qquad (3)$$

(Fig. 4a) and allows the E-axis nonlinearity to be estimated (Fig. 4b). For $E_0 \simeq 100$ keV, the predicted change in eV/channel is less than 0.4% per 1000 eV of energy loss. All the same, this change can amount to several eV, which may be significant for the measurement of chemical shift of an ionization edge; a solution is to calibrate the axis using a standard whose known ionization edge is similar in energy to the edge under investigation.

We have assumed that the change in magnetic field is proportional to scan current, i.e., that hysteresis and eddy-current effects are negligible. For spectrometer magnets constructed from high-permeability materials, this appears to be a good approximation within the middle of a scan, but some nonlinearity can be expected at the beginning; therefore it is advisable to keep the zero-loss peak away from the first few channels (or to start the spectrometer scan before that of the multichannel analyzer). Likewise, some loss of linearity can be anticipated from the use of a "segmented" scan, where only parts of the spectrum are sampled or where the dwell time per channel is changed during acquisition.

We can avoid the nonlinearities we have been discussing by using a fixed spectrometer excitation and scanning the potential of the electron source by an amount proportional to the channel advance of the multi-channel analyzer. However, this method is inconvenient, since it involves high-voltage engineering and tends to defocus the incident beam. Scanning via an electrically isolated drift tube is possible[13] but a change in spectrometer focus has been observed[14] in cases where the electron beam enters the spectrometer through a small entrance aperture; this observation suggests an appreciable electrostatic lens effect at the entrance to the drift tube, which could also make the energy scale nonlinear.

In the case of parallel detection, the energy scale is again slightly nonlinear, this time owing to a variation of the dispersive power D with energy loss. This effect is caused by second-order aberrations, but of a different type from those which cause loss of energy resolution; therefore, spectrometers which are "aberration corrected" to allow a larger range of entrance angles still suffer from this nonlinearity. Calculations suggest that for a typical design D will decrease by about 1% per 1000 eV of energy loss.

FIG. 4.--(a) Range of energy loss scanned for given scan current (normalized to value E = 100 keV) plotted as function of incident energy E_0; (b) percentage change in E-axis sensitivity over 1000eV range of energy loss, plotted as function of incident energy.

c. *Background Subtraction.* The background intensity underlying an ionization edge is usually assumed to be of the form AE^{-r}, with values of the constants A and r determined by measurements within a "fitting region" just before the edge. Current software uses one of several methods to compute A and r.

(1) The least-squares method uses standard statistical formulas to obtain the best straight-line fit for the *logarithm* of background intensity plotted as a function of the *logarithm* of energy loss.[15] The formulas assume that the noise level is constant over

the fitting region, although this approximation could be removed by use of a weighted least-squares fit.[16] Systematic errors can occur (owing to the effect on the noise distribution of taking the logarithm of intensity) but are only noticeable in the case of very noisy data.[3,16] In certain cases, the fitting accuracy has been improved by including nonlinear (polynomial) terms into the fitting procedure.[17] The computation time is typically 1-20 s, depending on the instrumentation and the width of the fitting region.

(2) An alternative method divides the fitting region into two halves, with A and r obtained from the two areas under the data by means of empirical formulas (Fig. 5). These formulas[3] are exact only for r = 2, but work surprisingly well up to r = 6 (the maximum value expected). Less computation is necessary compared to the least-squares
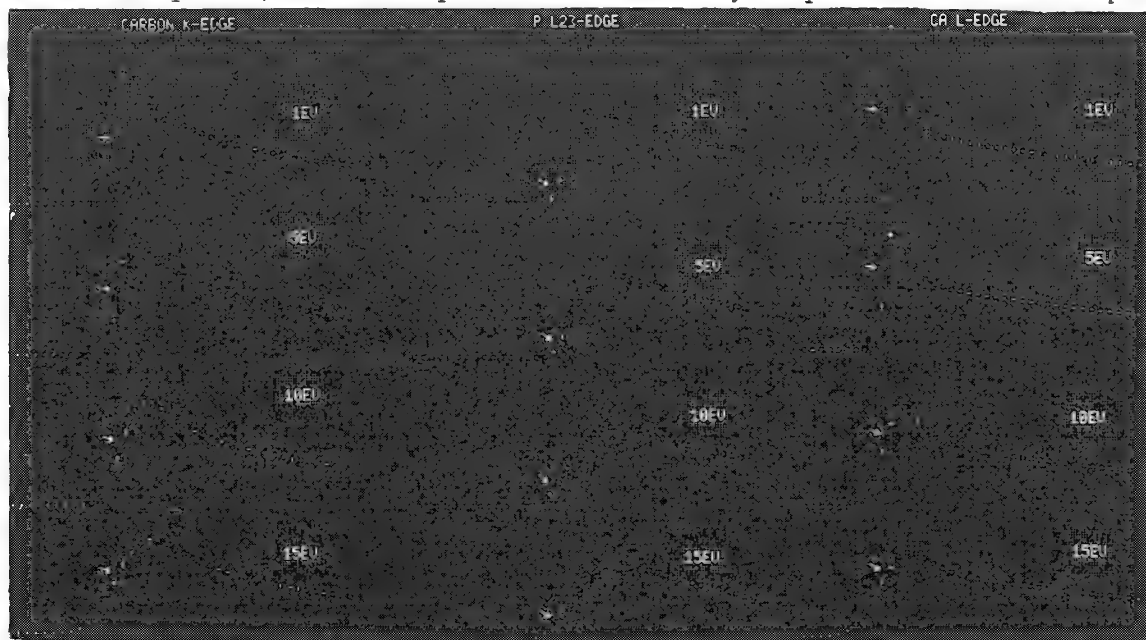
FIG. 5.--Change in shape of (from left to right) carbon K-edge, phosphorus L_{23}-edge, and calcium L_{23}-edge with (from top to bottom) increasingly degraded energy resolution ΔE (shown in eV). Arrow marks position of edge in each case; E-axis sensitivity is 2.5 eV/ channel. Edge shapes were taken from Leapman et al.[27] and convoluted with Gaussian function of FWHM = ΔE.

method, so the algorithm will run in less than 1 s even when programmed in a relatively slow language such as BASIC.

(3) With values of A and r given by the previous method taken as a first approximation, a ravine-search technique has been used to calculate an optimized fit.[18] Although the computation time is relatively long (about 5 min with FLEXTRAN on a PDP-1105), this method could be valuable for situations (e.g., low elemental concentrations) where the characteristic edge is only barely discernible above background noise.

d. Deconvolution Techniques. Plural inelastic scattering increases the background level and may introduce extra peaks, particularly with thicker specimens. Its effect can be removed from the energy-loss spectrum by appropriate deconvolution, by one of the following:

(1) If one takes the logarithm of the Fourier coefficients of the spectral data (followed by an inverse Fourier transform), plural scattering is removed from the entire spectrum.[19,20] Before computing the Fourier coefficients, one must remove any gain changes between different energy regions, thereby increasing the dynamic range of the data. So unless extended-precision arithmetic is employed, the method is more feasible for energy losses below about 300 eV, where the range of intensity is more restricted. Although the plural-scattering contribution to the background is removed, its associated

noise component is left behind. Neverthless, Leapman and Swyt have found that in thicker specimens deconvolution can alleviate problems of background fitting for low-lying edges and may improve the accuracy of quantitative analysis.[21]

(2) "Mixed" scattering (i.e., plural scattering involving inner-shell + valence-electron excitation) can be removed from a *core-loss* region if the experimental background is first subtracted and the result deconvoluted (e.g., by division of Fourier coefficients), with the low-loss region used as a "deconvolution function."[22] As in the previous method, noise amplification is avoided by use of a reconvolution function[19] or by replacing of the zero-loss peak by a delta function of equal area.[21] (The reconvolution-function technique involves a bit more computing but offers the possibility of correcting the spectral data for distortion caused by a nonsymmetric resolution function.) The two energy regions are normally of equal width, and the electron intensity should (if necessary) be extrapolated to zero at both ends of each region (Fig. 6). The dynamic range and the total energy range are usually less than with the previous method; the computing time is typically a few seconds with an efficient fast-Fourier-transform algorithm.

(3) Iterative methods can also be used for deconvolution.[23,24] The procedure can be informative but has the disadvantage of being rather slow.
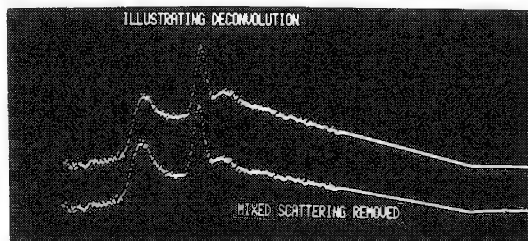
FIG. 6.--Carbon K-edge followed by calcium L-edge, before (upper trace) and after (lower trace) deconvolution with low-loss region. Before deconvolution, valence-loss background is subtracted and core-loss intensity extrapolated to zero at upper end of range.

Generally speaking, deconvolution is more worthwhile in the case of thicker specimens ($t > 0.5 \lambda_i$, where λ_i is the total inelastic mean free path), in which plural scattering is more severe, or in the case of EXELFS analysis[10,25] where spurious peaks due to mixed scattering must be removed. For thin specimens, the effect of deconvolution is relatively small (see Fig. 6).

e. Measurement of Areas in the Energy-loss Spectrum. Quantitative microanalysis involves measuring an "area" (i.e., sum of channel counts) over an well-defined energy range Δ above each ionization-edge energy E_k (Fig. 7). First of all, the value of E_k must be determined; because of possible chemical shifts and E-axis nonlinearity, that is best done from the recorded spectrum rather than from a table of atomic binding energies. However, the experimental determination of E_k also involves some uncertainty, dependent on the instrumental energy resolution ΔE and on the inherent "shape" of the edge. K-edges, which are "abrupt" (if recorded on an ideal instrument with $\Delta E = 0$), present little difficulty; provided the resolution function (i.e., the shape of the zero-loss peak) is roughly symmetrical, the observed edge profile becomes progressively less sharp with increasing ΔE and the edge energy corresponds approximately to the channel at which the core-less intensity has risen half way toward its maximum value (Fig. 5). But for "rounded" edges (e.g., L_{23}-edges of the elements Mg through Cl), E_k always corresponds to a point *below* the halfway mark, whereas for edges that are abrupt *and sharply peaked* just above E_k (e.g., L_{23} edges of K, Ca, and Ti), the experimental edge energy lies somewhat *above* the half way point (Fig. 5).

So in practice the determination of

$$I_k(\alpha,\Delta) = \int_{E_2}^{E_k+\Delta} J(E)dE - \frac{A}{1-r}\left[(E_k+\Delta)^{1+r}-E_2^{1+r}\right]$$

$$r \doteq 2\log(I_1/I_2)/\log(E_2/E_1)$$

$$A = (I_1+I_2)(1-r)/(E_2^{1+r}-E_1^{1+r})$$

FIG. 7.--Schematic energy-loss spectrum, illustrating measurement of areas for use in quantitation formulas and one method of background fitting.

E_k involves some guesswork, which will be more accurate if the shape of the edge is known (from calculations[27] or experimental data[12]) *and* if the energy resolution is kept as good as possible.

The edge energy E_k is required only for setting the *upper* limit of integration (to an energy $E_k + \Delta$). The lower limit E_ℓ is set somewhat *below* E_k in order to allow for the instrumental resolution (Fig. 7). The exact value of E_ℓ is not critical, since, after subtraction of the background contribution, the resulting inner-shell intensity tends rapidly to zero below E_k. For convenience, E_ℓ may be set equal to the *upper* limit E of the background-fitting region (Fig. 7).

   f. Quantitation Formulas. If the area $I_k(\alpha,\Delta)$ is measured "directly" from core-loss data (i.e., with the background contribution subtracted but without deconvolution; see Fig. 7), the following equation can be used to obtain the "concentration" N of a given element:

$$N \div \frac{1}{G} \cdot \left[\frac{I_k(\alpha,\Delta)}{I_\ell(\alpha,\Delta)} \right] \cdot \frac{1}{\sigma_k(\alpha,\Delta)} \tag{4}$$

$I_\ell(\alpha,\Delta)$ is an area measured from the low-loss region of the spectrum (see Fig. 7) and $\sigma_k(\alpha,\Delta)$ is a "partial" ionization cross section for the appropriate shell k (k = K, L, etc.) of the element, which can be calculated (see next section). If σ_k is in m^2 per atom, the formula gives N in atoms per square meter of specimen. The factor G allows for any difference in detector gain between the low- and high-energy regions of the spectrum (Fig. 7).

Equation (4) has been found to be reasonably accurate ($\pm 10\%$) provided the integration range Δ is at least 50 eV and the local thickness of the sample is less than the total inelastic mean free path (typically 50-100 nm for 100keV primary electrons).[26,15] Bigger errors are possible with strongly diffracting crystalline specimens, but are avoided if the collection semi-angle α is large.[6] A correction to Eq. (4) is necessary for small incident probes of large convergence semi-angle[15], but that is also avoidable if α can be made sufficiently large (> 30 mrad).

If the core-loss region has been deconvoluted to remove mixed scattering, the following equation may be used:

$$N = \frac{1}{G} \cdot \left[\frac{I_k'(\alpha,\Delta)}{I_0} \right] \cdot \frac{1}{\sigma_k(\alpha,\Delta)} \tag{5}$$

$I_k'(\alpha,\Delta)$ is the area under the deconvoluted core-loss data and I_0 is the area beneath the zero-loss peak.

Where absolute quantitation is not required, elemental ratios can be obtained from either Eq. (4) or Eq. (5). With Eq. (4) used with the *same* integration range Δ for each edge, $I_\ell(\alpha,\Delta)$ cancels; therefore the low-energy region of the spectrum need not be recorded. If Eq. (5) is used, I_0 cancels (even if different values of Δ are used for the various edges) but the low-loss region is still needed in order to carry out the deconvolution.

   g. Calculation of Cross Sections. The partial cross sections required in Eqs. (4) and (5) are not found in standard tables but can be calculated (for each element) for the particular values of α, Δ, and E_0 used experimentally. Computer programs have been written to do this calculation, based either on Hartree-Slater wavefunctions[27] or on a hydrogenic approximation.[28] The Hartree-Slater method is more exact and can be applied to M-, N-, and O-shells of the heavier elements, but the computations are somewhat lengthy. The hydrogenic method is probably limited to K- and L-shells, but uses analytic formulas; a 100-line Fortran version runs in a few seconds even on a mini-computer. Both approaches assume an *atomic* model (i.e., solid-state effects are ignored), so the resulting cross sections are probably not accurate to getter than 10%.

h. Overlapping Edges. As in x-ray microanalysis, situations sometimes occur in which the characteristic features to be analyzed are sufficiently close in energy so that their intensities overlap appreciably. In the energy-loss case, fitting a background to the edge of higher energy becomes difficult since the intensity due to the "background" (actually the tail of the previous edge) may not follow a smooth AE^{-r} dependence, even if plural scattering has been removed by deconvolution. One way around this is to fit a background to the first (lower-energy) edge, use a small energy window Δ_1 ($< E_k^B - E_k^A$) to estimate the concentration N^A of the corresponding element (using Eq. 4 or 5); then a larger integration range Δ_2 (including both edges) to measure the concentration N^B of the second element, after the cross sections $\sigma_k^A(\alpha, \Delta_2)$ and $\sigma_k^B(\alpha, \Delta_2 + E_k^A - E_k^B)$ have been computed (see Fig. 8a). This procedure has been applied successfully to the analysis of TiO_2 dielectric films (Fig. 8b); its main limitation arises from the fact that the background extrapolation must extend over 100 eV or more, which increases the possibility of systematic error in subtraction of the background.

References

1. R. F. Egerton, "Alignment and characterization of an electron spectrometer," *Ultramicroscopy* 6: 93, 1981.

(a)

$$I_k^1(\alpha, \Delta_1) = N^A \cdot \sigma_k^A(\alpha, \Delta_1) \cdot I_\ell(\alpha, \Delta_1)$$

$$I_k^2(\alpha, \Delta_2) = N^A \cdot \sigma_k^A(\alpha, \Delta_2) \cdot I_\ell(\alpha, \Delta_2)$$
$$+ N^B \cdot \sigma_k^B(\alpha, \Delta_2 + E_k^A - E_k^B) \cdot I_\ell(\alpha, \Delta_2 + E_k^A - E_k^B)$$
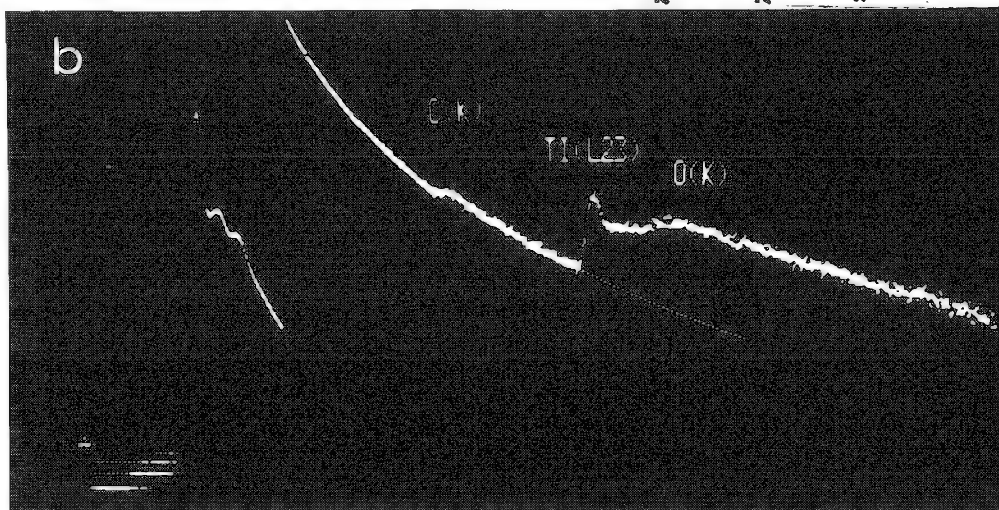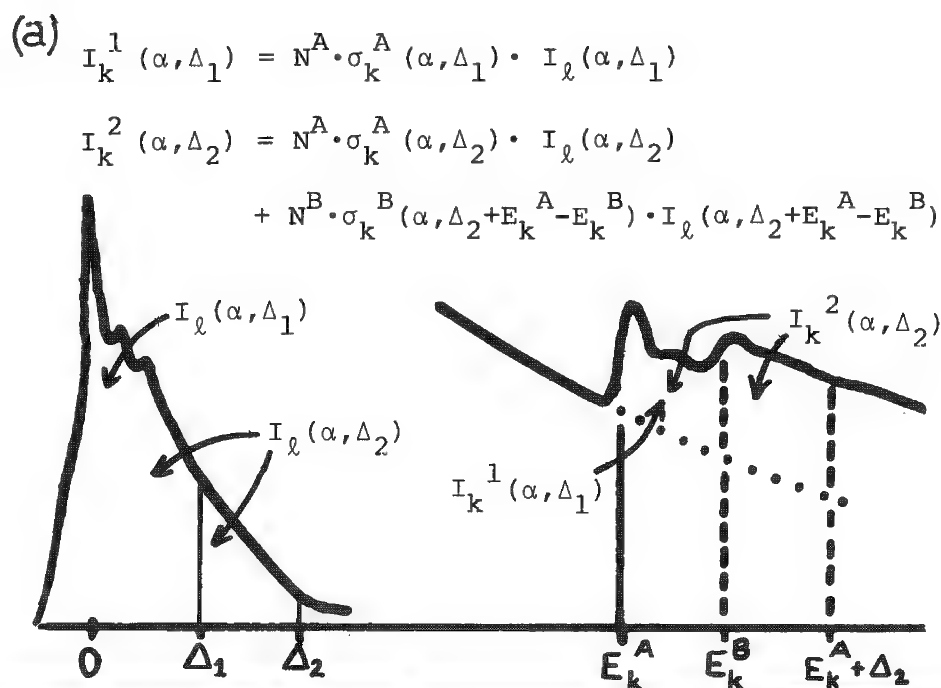
FIG. 8.--(a) One technique for analyzing ionization edges which are close in energy; (b) energy-loss spectrum (with logarithmic vertical scale) of TiO_2 sputtered onto carbon support film. Dotted curve shows background fit for titanium-L and oxygen-K edges.

2. D. E. Johnson, "Basic aspects of energy-loss spectrometer systems," *Ultramicroscopy* 3: 361, 1979.

3. R. F. Egerton, "Instrumentation and software for energy-loss microanalysis," *SEM/1980* I, 41-52.

4. R. Vincent and J. Silcox, "Dispersion of radiative surface plasmons in aluminum films by electron scattering," *Phys. Rev. Letters* 31: 1487, 1973.

5. J. I. Goldstein, J. L. Costley, G. W. Lorimer, and S. J. B. Reed, "Quantitative x-ray analysis in the electron microscope," *SEM/1977* I, 315-324.

6. R. F. Egerton, "Energy-loss spectrometry with a large collection angle," *Ultramicroscopy* 7: 207, 1981.

7. A. J. Bourdillon, P. G. Self, and W. M. Stobbs, "Crystallographic orientation effects in x-ray analysis," *Phil. Mag.* 44: 1401, 1981.

8. K. M. Adamson-Sharpe and F. P. Ottensmeyer, "Spatial resolution and detection sensitivity in microanalysis by electron energy loss selected imaging," *Journal of Microscopy* 122: 309, 1981.

9. D. C. Joy and D. M. Maher, "The choice of operating parameters for micronalaysis by electron-loss spectroscopy," *Ultramicroscopy* 3: 69, 1978.

10. C. Colliex, V. E. Cosslett, R. D. Leapman, and P. Trebbia, "Contribution of electron energy loss spectroscopy to the development of analytical electron microscopy," *Ultramicroscopy* 1: 301, 1976.

11. M. U. A. Bromba and H. Ziegler, "Application hints for Savitsky-Golay digital smoothing filters," *Anal. Chem.* 53: 1583, 1981.

12. N. J. Zaluzec, "A reference library of electron energy loss spectra," *Analytical Electron Microscopy--1981*, 193-194.

13. P. E. Batson, S. J. Pennycook and L. G. P. Jones, "A new technique for the scanning and absolute calibration of electron energy loss spectra," *Ultramicroscopy* 6: 287, 1981.

14. O. L. Krivanek, personal communication.

15. D. C. Joy and D. M. Maher, "The quantitation of electron energy loss spectra," *Journal of Microscopy* 124: 37, 1981.

16. W. C. Bigelow, personal communication.

17. J. Bentley, G. L. Lehman, and P. S. Sklad, "Background fitting for electron energy loss spectra," *Analytical Electron Microscopy--1981*, 161-163.

18. C. Colliex, C. Jeanguillaume, and P. Trebbia, "Quantitative local microanalysis with EELS," in T. E. Hutchinson and A. P. Somlyo, Eds., *Microprobe Analysis of Biological Systems*, New York: Academic Press, 1981, 251-271.

19. D. W. Johnson and J. C. H. Spence, "Determination of the single-scattering probability distribution from plural-scattering data," *J. Phys. D* 7: 771, 1974.

20. J. C. H. Spence, "Uniqueness and the inversion problem of incoherent multiple scattering," *Ultramicroscopy* 4: 9, 1979.

21. R. D. Leapman and C. R. Swyt, "Electron energy loss pectroscopy under conditions of plural scattering," *Analytical Electron Microscopy--1981*, 164-172.

22. R. F. Egerton and M. J. Whelan, "The electron energy loss spectrum and band structure of diamond," *Phil. Mag.* 30: 739, 1974.

23. G. K. Wertheim, "Deconvolution and smoothing: applications in ESCA," *J. Electron Spectrosc. and Related Phenomena* 6: 239, 1975.

24. P. Trebbia, "Contribution au développement de la microscopie électronique analytique par utilisation quantitative de la spectroscopie des pertes d'énergie," *Thèse (Docteur ès Sciences)*, Université Paris-Sud, pp. 39-43.

25. D. E. Johnson, S. Csillag, and E. A. Stern, "Analytical electron microscopy using EXELFS," *SEM/1981* I.

26. R. F. Egerton, "The range of validity of EELS microanalysis formulae," *Ultramicroscopy* 6: 297, 1981.

27. R. D. Leapman, P. Rez, and D. F. Mayers, "K, L and M shell generalized oscillator strengths and ionization cross sections for fast electron collisions," *J. Chem. Phys.* 72: 1232, 1980.

28. R. F. Egerton, "K-shell ionization cross sections for use in microanalysis," *Ultramicroscopy* 4: 169, 1979.

29. R. F. Egerton, "SIGMAL: a program for calculating L-shell ionization cross sections," *39th Proc. EMSA*, 1981, 198-199.

A DETERMINATION OF SYMMETRY CHANGES IN ORDERED ALLOYS BY CONVERGENT BEAM ELECTRON DIFFRACTION

H. L. Fraser

A recent paper has described the application of convergent beam electron diffraction to the detection of symmetry changes in a recrystallized Ni-base superalloy (Udimet 720).[1] Specifically, tetragonal distortions of the γ' phase (usually considered to possess the $L1_2$ structure and based on Ni_3Al) were noted. These authors proposed that this distortion is due to ordering of alloying elements on the Ni sublattice, and that the tetragonal form of γ' may well represent the lowest energy configuration for this phase. One complicating factor in their experiments concerns the influence of the coherency strains that are present in γ/γ' alloys (γ is the Ni based solid solution). Thus, the sublattice ordering or tetragonality may be a result of these strains, and not necessarily an intrinsically stable form of the $L1_2$ structure. In the present study, attempts have been made to separate out the effect of strain by making observations on the one hand on a single crystal of γ' alloyed with 7at.% Ta, and on the other hand a γ' in a euctectic alloy where the phase is subjected to very large stresses during thermal processing. Preliminary results are described below.

Small changes in symmetry are sensitively detected by the form of the higher-order laue zone (holz) line patterns that are visible in the bright field (000) diffraction disk.[2] A computer program has been developed that simulates these patterns for the cases of first- and second-order Laue zone (folz and solz, respectively) lines for cubic, tetragonal, or orthorhombic crystals. The calculation is based on the kinematical approximation, which does not permit absolute values of lattice parameters to be derived, but does allow relative changes to be determined rather accurately.[3] In the present work, the dynamical origin of the holz lines was accounted for in a crude way. Thus, the "pure" Ni_3Al was used as a standard where the lattice parameter was assumed to be known (3.56 Å) and the effective electron energy determined by matching holz lines between experiment and theory with computer simulation. This electron energy was then used for the other alloyed γ' phases, on the assumption that the projected potential differences caused by alloying are small.

In the first experiment, the symmetry of large-grained single-phase Ni_3Al has been compared to that of single crystal Ni_3Al alloyed with 7at.% Ta. Convergent-beam electron diffraction patterns from both materials are shown in Fig. 1. In the case of the unalloyed γ' (Fig. 1a), the pattern of folz lines yields a symmetry of 3m, whereas for the Ta alloyed γ' (Fig. 1b) this pattern symmetry is reduced to m. The computed pattern simulations are shown in Figs. 1(c) and (d), and the best fit to the experimental pattern of Fig. 1(b) is given by a tetragonality described by $c/a = 1.002$. The dynamic splitting of some of the lines in Fig. 1(b) is not predicted by the kinematical calculations that leads to Fig. 1(d). It is reasonable to propose that sublattice ordering of the Ta is responsible for this tetragonal distortion. A comparison between the intensities of the $1\bar{1}0$ superlattice reflections of the unalloyed and Ta alloyed γ' phases is shown in Fig. 2. It can be seen that in the case of the alloyed γ', the intensity of the superlattice reflections is considerably reduced, and so the difference in scattering factors between the sublattice is diminished. This result strongly suggests that the Ta is ordering on the Al sublattice, although a study has not been made of other intensity maxima that may result from such ordering.

(a)   (b)   (c)

FIG. 1.--Experimental and simulated [111] zone axis convergent beam electron diffraction patterns: (a) γ'; (b) γ' alloyed with 7at.% Ta; (c) simulated pattern corresponding to (a); (d) simulated pattern corresponding to (b). Accelerating voltage 120 kV; adjusted wavelength for simulations, λ = 0.03364 Å.

(d)

FIG. 2.--[111] zone axis convergent beam electron diffraction patterns from γ' (left) and γ' alloyed with 7at.% Ta (right). Note the intensities of the 110 superlattice reflections.
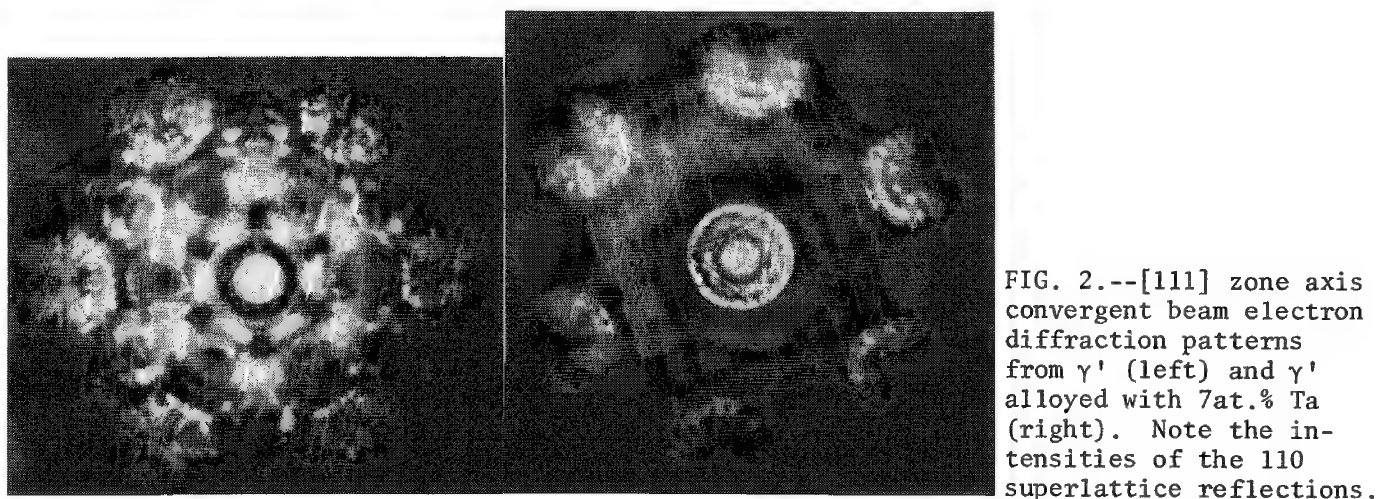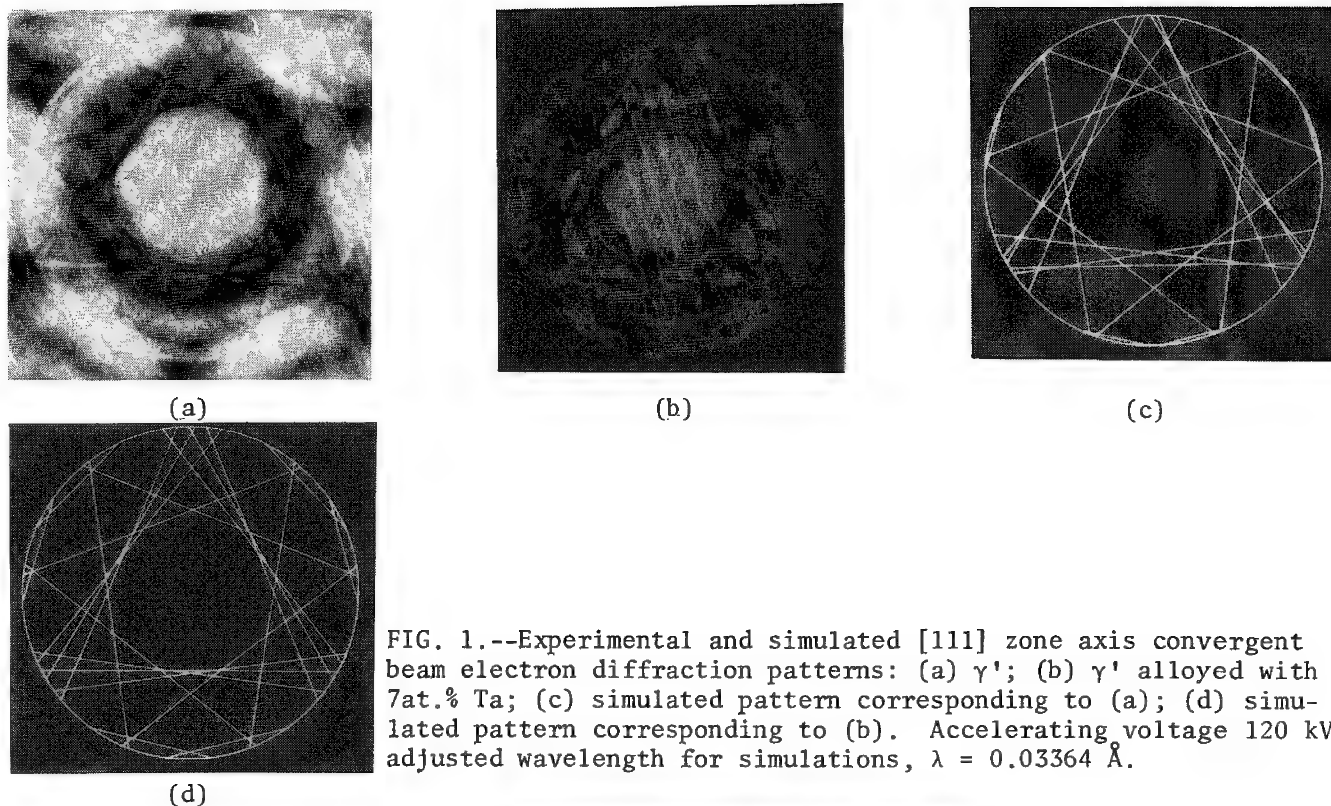
     The second experiment involves observations of γ' in a Ni-Al-Mo eutectic alloy where, as a result of directional solidification, rods of α-Mo surrounded by coarse γ' are produced. The matrix consists of a conventianal γ/γ' dispersion. During slow cooling from elevated temperatures, extremely high stresses are established in both the coarse γ' and the α-Mo rods because of differences in thermal contraction. The fine γ' in the matrix is not significantly subjected to such stresses. A comparison of the holz line patterns with the electron beam parallel to [114] for the matrix (unstressed) γ' and coarse (stressed) γ' is shown in Fig. 3. Computer simulated patterns are given in Figs. 3 (c) and (d), and a reasonable fit is achieved for an orthorhombic distortion given by $c/a = 1.002$ and $c/b = 0.9953$. This distortion may be caused by stress-induced sublattice ordering or simply be a result of the elastic stresses caused by differential thermal contraction. It is thought more likely to be the former since in thin foils the proximity of the surfaces are likely to permit a relaxation of stresses. Further work is in progress aimed at resolving this issue.

(a)

(b)

(c)

(d)
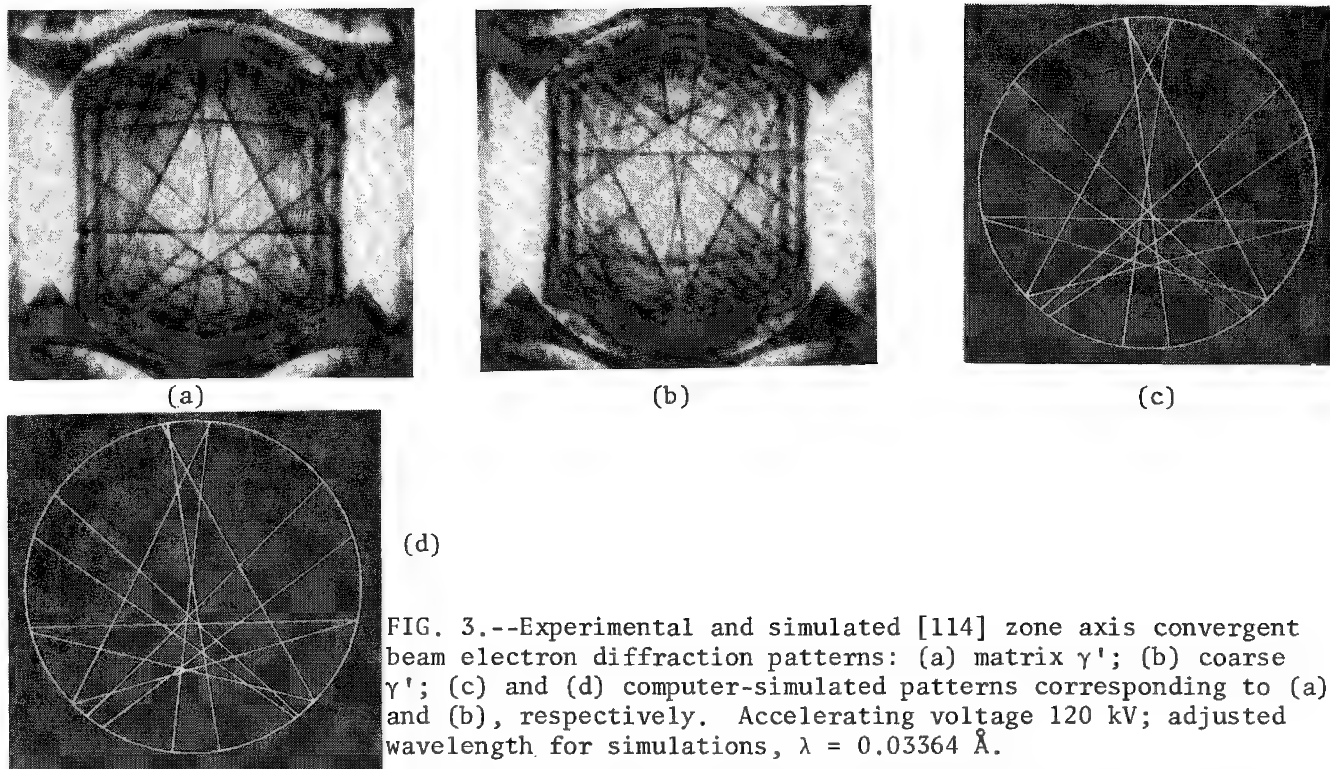
FIG. 3.--Experimental and simulated [114] zone axis convergent beam electron diffraction patterns: (a) matrix γ'; (b) coarse γ'; (c) and (d) computer-simulated patterns corresponding to (a) and (b), respectively. Accelerating voltage 120 kV; adjusted wavelength for simulations, λ = 0.03364 Å.

These results clearly demonstrate that tetragonal distortions of γ' may occur in un-stressed alloyed γ' as well as in crystals that are subject to an imposed stress.

References

1. A. J. Porter, M. P. Shaw, R. C. Econ, and B. Ralph, "The application of convergent-beam electron diffraction to the detection of small symmetry changes accompanying phase transformations: II. Recrystallization of superalloys," *Phil. Mag.* 44: 1135-1148, 1981.

2. P. M. Jones, G. M. Rackham, and J. W. Steeds, "Higher order Laue zone effects in electron diffraction and their use in lattice parameter determination," *Proc. Roy. Soc. Lond.* A354: 197-222, 1977.

3. J. W. Steeds, "Converged beam electron diffraction," in J. J. Hren, J. I. Goldstein, and D. C. Joy, Eds., *Introduction to Analytical Electron Microscopy*, New York: Plenum Press, 1979, 387-422.

THE THEORETICAL CHARACTERISTIC TO CONTINUUM RATIO IN ENERGY DISPERSIVE ANALYSIS IN THE ANALYTICAL ELECTRON MICROSCOPE

C. E. Fiori, C. R. Swyt, and J. R. Ellis

X rays observed by the energy-dispersive detector in the analytical electron microscope (AEM) arise from two types of inelastic interactions between fast beam electrons and speicmen atoms. In one case a beam electron interacts strongly with a core electron and imparts sufficient energy to remove it from the atom. The ejected core electron can have any energy up to the beam energy minus the characteristic shell energy. The beam electron is depreciated in energy by whatever kinetic energy the ejected electron has acquired plus the characteristic energy required to remove it. A "characteristic" x ray is occasionally emitted when the ionized atom relaxes to fill the core vacancy. It is called characteristic because its energy equals the difference in energy between the two levels involved in the transition and this difference is characteristic of the element. Since these levels are well defined the photon energy distribution which results from a statistically meaningful quantity of x rays, from the same transition and from an ensemble of atoms of the same atomic number, generally suffices to identify the atom species. This x-ray "line" is characterized by a "natural width" and is normally specified by the full width at half the peak maximum (FWHM). There is usually instrumental broadening when an x-ray line is measured and we must make the distinction between the measured distribution and the line. Consequently, we shall call the measured distribution a "peak" and specify its width, also, as FWHM. The difference between these distributions is very large when a solid-state energy-dispersive detector is used. For example, the natural width of the Mn $K\alpha_1$ line is 1.48 eV.[1] This line is broadened to a peak of typically 155 eV by a $30mm^2$ lithium-drifted silicon detector and its associated electronics.

The second type of inelastic interaction we must consider occurs between a fast beam electron and the nucleus of a specimen atom. A beam electron can decelerate in the Coulomb field of an atom, which consists of the net field due to the nucleus and core electrons. Depending on the deceleration a photon is emitted which can have an energy ranging from near zero up to the energy of the beam electron. The interaction of a large number of beam electrons with a thin foil of a given element produces an emitted spectrum with a distribution approximately proportional to 1/E, where E is the photon energy. The magnitude of this distribution is approximately proportional to the square of the average atomic number of the atoms comprising the foil. Other factors, such as beam current, measurement time, and specimen mass thickness, scale the vertical axes linearly. The beam energy E_0 and observation angle θ affect the overall shape of the distribution in a complex manner that will be discussed below. X rays which emanate due to this interaction process are referred to here as continuum x rays. Alternative names are "background," "white," or "bremsstrahlung" x rays.

By counting characteristic x rays we obtain a measure of the number of analyte atoms present in the volume of specimen excited by the electron beam. By counting continuum x rays we obtain a measure proportional to the product of the square of the average atomic number and the mass thickness of the excited volume If the average atomic number of the specimen is known, the continuum signal gives a measure of specimen mass thickness. This is generally true in biological microanalysis. In the ratio of a characteristic signal to a continuum signal, factors that affect both signals equally cancel. Since, in the

---

The authors are at the Division of Research Services, Biomedical Engineering and Instrumentation Branch, National Institutes of Health, Bethesda, MD 20205.

usual energy-dispersive system, the two signals are recorded simultaneously, the effects of recording time and incident probe current cancel. Similarly, for sufficiently thin specimens such that specimen self absorption and multiple electron scattering are not a problem, the effects of mass thickness cancel in the ratio. Marshall and Hall developed a highly successful analytical procedure, based on the above, which is widely used in biological applications in the scanning electron microscope and microprobe.[2] The purpose of this paper is to comment on certain difficulties one encounters in forming a meaningful characteristic-to-continuum ratio in the analytical electron microscope operating between 70 and 200 kV, and certain properties of the ratio itself. We restrict our discussion to K radiation from elements of atomic number 11 to 37.

The Characteristic Signal

We can predict the number of characteristic x rays generated into 4π steradians from the following relation:

$$I_{ch} = (N_0 \rho C_a / A) Q_a \omega_a F_a N_e \, dz \tag{1}$$

where N_0 is Avogadro's number, ρ is the density of the specimen in the analyzed volume, C_a is the weight fraction of the analyte in the volume, and A is the atom weight (the quantity in parentheses is the number of atoms of analyte in the analyzed volume); Q_a is the ionization cross section for the shell of interest and has dimensions of area; ω_a, the fluorescent yield, is the probability that an x ray will be emitted due to the ionization of a given shell; F_a is the probability of emission of the x-ray line of interest relative to all the lines which can be emitted due to ionization of the same shell; N_e is the number of electrons which have irradiated the specimen during the measurement time; and dz is the specimen thickness in the same units of length as used in Q. Terms in Eq. (1) other than the cross section which are subject to uncertainty are ω_a and F_a. Values for both these quantities have been obtained primarily by measurement. Consequently, the use of mathematical fits to the various experimental determinations serves to mask the underlying uncertainty due to measurement. To demonstrate this point in this paper we use some of the primitive data on which the fits have been made.[3-5] Plots of the theoretical characteristic-to-continuum ratio as a function of atomic number Z, to be shown later in the paper, manifest this experimental scatter. For analytical procedures the use of fits is perfectly reasonable and probably desirable. Some recent results are given in Ref. 6.

The basic functional form of the characteristic cross section is due to Bethe:[7]

$$Q = 6.51 \times 10^{-20} (n_s b_s / U E_c^2) \ln(C_s U) \tag{2}$$

where the constant is the product πe^4 (in keV^2-cm^2; e is the charge of an electron), n_s is the number of electrons which populate the s'th shell or subshell of interest ($n_k = 2$), E_c (in keV) is the energy required to remove an electron from a given shell or subshell, U is the over-voltage ratio E_0/E_c (where E_0 is the energy of the impinging beam electron), and b_s and C_s are constants for the s'th shell or subshell. Powell reviewed a number of semi-empirical cross sections for the beam energy range commonly found in the electron microprobe (<40keV).[8,9] He recommends for the K shell that $b_k = 0.9$ and $C_k = 0.65$ when the energies are expressed in keV. Powell favorably notes a modification to the Bethe formula by Fabre, which we include here only for the purpose of comparison:

$$Q_F = 6.51 \times 10^{-20} (n_s \ln U) / [E_c^2 a(U + b)] \tag{3}$$

where a = 1.18 and b = 1.32 are constants for the K shell. The range of the overvoltage ratio is recommended to be $1.5 < U < 25$ and the subscript F on Q denotes "Fabre." The other terms are as above. It was not intended that these cross sections should be applied above about 40 keV; it is not surprising that they cause anomalous results in the

range of beam energies found in the AEM. There are several ionization cross sections which have been suggested for the incident energy range 70-200 keV. This is an energy region where the effects of relativity should not be ignored and a generally useful cross section should accommodate the effects explicitly, or at least provide empirical adjustment.

Zaluzec[10,11] has recommended the formulation, given in Mott and Massey,[12] of the relativistic cross section derived by Bethe and Fermi[13] and Williams:[14]

$$Q_Z = (\pi e^4 n_s a_k / E_c E_0) \ln[b_k U - \ln(1 - \beta^2) - \beta^2] \tag{4}$$

where all energies are given in keV, a = 0.35 (K shell),

$$b_k = 0.8U/[(1 - e^{-\gamma})(1 - e^{-\delta})], \quad \gamma = 1250/(E_c U^2), \quad \delta = 1/(2E_c),$$
$$\text{and } \beta = v/c = \sqrt{1 - [1 + (E_0/511)]^{-2}}$$

is the relativistic correction factor. The coefficients were determined by Zaluzec. In references [10, 11] b_k is given incorrectly [Zaluzec, personal communication].

Recently, Schreiber and Wims[15,16] proposed a highly empirical variant of the Bethe equation with coefficients determined indirectly from their relative measurements of characteristic lines at two beam energies, 100 and 200 keV, using an uncalibrated x-ray detector and specimens of unknown mass-thickness. Their formulation is unique in that the coefficients are functions of atomic number. They give the cross section as:

$$Q_{s-w} = \pi e^4 n_s b \ln U/(E_c^2 U^d) \tag{5}$$

where b = 8.874 - 8.158 ln Z + 2.9055 (ln Z)^2 - 0.35778 (ln Z)^3 for Z ≤ 30 and b = 0.661 for Z > 30; and d = 1.0667 - 0.00476Z.

These authors include in their paper coefficient expressions for the L and M shells, again determined indirectly. The cross section coefficients proposed by these authors are machine and procedure dependent and should be taken out of context with care.

Kolbenstvedt has given a relatively simple approximate formula for K ionization by relativistic electrons much higher in energy than the ionization energy.[17] He has obtained good agreement with experimental data for the elements silver and tin for energies from under 100 keV to 2 MeV. His equation is written as:

$$\sigma_k = \frac{0.275}{I} \frac{(E_0' + 1)^2}{E_0'(E_0' + 2)} \left[\ln \frac{1.19(E_0' + 2)}{I} - \frac{E_0'(E_0' + 2)}{(E_0' + 1)^2} \right]$$

$$+ \frac{0.99}{I} \frac{(E_0' + 1)^2}{E_0'(E_0' + 2)} \left[1 - \frac{I}{E_0'} \left\{ 1 - \frac{E_0'^2}{2(E_0' + 1)^2} + \frac{2E_0' + 1}{(E_0' + 1)^2} \ln \frac{E_0'}{I} \right\} \right] \text{ (barns)} \tag{6}$$

where E_0 is the kinetic energy of the incident electron and I is the ionization energy, both in units of the electron rest energy. For our purposes we require the following conversions:

$$Q_k = 10^{-24} \sigma_k \text{ (cm}^2); \quad I = E_c/511; \quad E_0' = E_0/511$$

where E_c and E_0 are the critical excitation energy and beam energy, respectively, in keV.

We have presented these cross sections not to make a critical evaluation but merely to demonstrate their functional form and numeric variation. They are plotted as a function of Z for the range $11 \leq Z \leq 37$ in Figs. 1 and 2 for the beam energies of 100 and 200 keV, respectively. It is apparent from the plots that our first difficulty in formulating a theoretical characteristic-to-continuum ratio is a choice of cross section to appear in Eq. (1), the numerator.
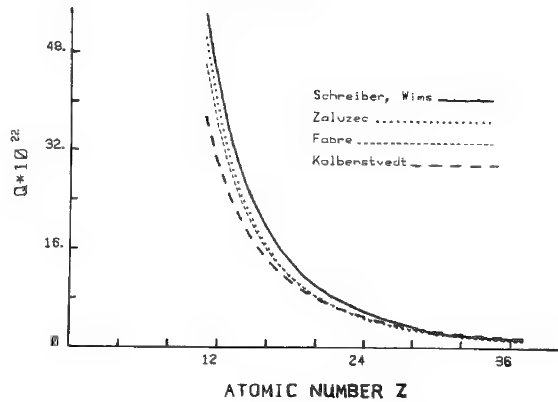
FIG. 1.--Plot of characteristic cross sections as function of Z for beam energy of 100 keV.
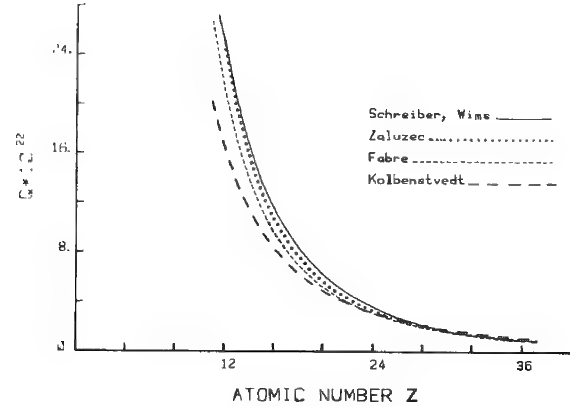
FIG. 2.--Same as Fig. 1 but 200 keV. (Note change in vertical scale.)

The Continuum Signal

We can predict the number of continuum x rays generated into a unit steradian from the following relation:

$$I_{CO} = \frac{N_0 \rho}{A} \; QN_e \; dz \tag{7}$$

where N_0 is Avogadro's number, ρ is the density of the specimen in the analyzed volume, A is the average atomic weight (the quantity in parentheses is the total number of atoms in the analyzed volume), Q is the continuum cross section and has dimensions of area, N is the number of electrons which have irradiated the specimen during the measurement time, and dz is the specimen thickness in the same units of length as used in Q. We note the following differences between the generation of characteristic and of continuum radiation. For our purposes, the ionization of an atom by a fast electron and subsequent emission (in some cases) of a characteristic photon are independent events. A characteristic photon has equal probability of being emitted in any direction after the ionization (isotropy). Relativistic considerations apply only to the probability of ionization. The probability of continuum emission, on the other hand, is intimately related to the probability that a fast-beam electron will decelerate in the Coulomb field of an atom. Indeed, the emission is a direct consequence of the deceleration. Furthermore, the probability of continuum emission is directionally dependent and peaked in the forward direction as defined by the direction of travel of the beam electrons (Fig. 3). We define the observation angle to be the angle between the incident beam direction and the x-ray detector. The "angle" and magnitude of the maximum of each of the lobes shown in the figure are affected by the photon energy being observed, the beam energy, and the average atomic number of the specimen. Specimen tilt has no effect (other than to change the apparent thickness of the specimen). Because of this anisotropy, continuum radiation is usually expressed as emission into a unit steradian at a specified angle, not as uniform emission into 4π steradians, as is the characteristic cross section. Dyson[18] has observed that the angle of maximum intensity, for photons having an energy near the beam energy, approximately satisfies the equation

$$\beta(1 + \sin^2\theta) = \cos\theta \tag{8}$$

where β is defined above and θ is the observation angle.

We begin our discussion of particular continuum cross sections by deriving the expression used in the Marshall-Hall procedure for biological microanalysis. For the discussion of this particular cross section we use the symbol E to denote photon energy and the symbol V_0 to denote incident electron kinetic energy. We first note several properties of continuum radiation.

1. The maximum energy that can be given up by an incident beam electron is its kinetic energy, which is numerically equal to the beam voltage V_0. Consequently, there is a highest energy E_0 that can appear in a continuum spectrum due to beam electrons of energy V_0. This highest energy is the so-called high-energy limit, or the Duane-Hunt limit.

2. If the specimen is sufficiently thin, both theory and experiment indicate that the amount of emitted energy in an energy interval dE is approximately uniformly distributed from near zero up to the high energy limit (Fig. 4).[19]
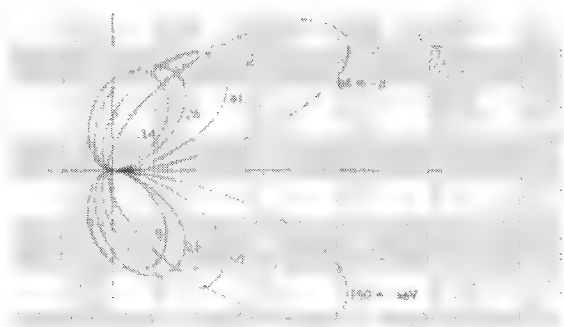
FIG. 3.--Plot of continuum distribution demonstrating anisotropic property. Beam direction is left to right.
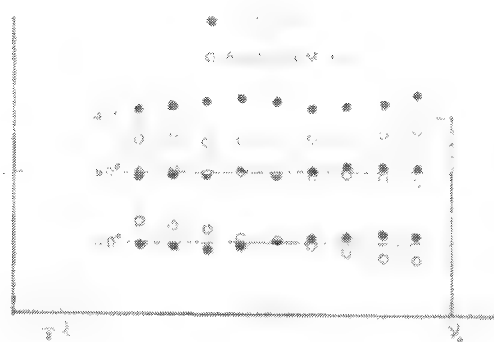
FIG. 4.--Plot of emitted continuum energy as function of photon energy for two elements and three observation angles. Note essentially uniform distribution up to beam energy V_0. (From Compton and Allison.[19])

From (2), we can define the fraction of the total emitted continuum energy E_t, in the interval from E to E + dE, as $dE/(E_0 - 0)$. The efficiency of the generation of continuum in a thin film is defined as the total continuum energy (from near zero to E_0) generated by electrons which lose an amount dV of their energy divided by the energy lost. Kirkpatrick and Wiedmann[20] have determined from the theory of Sommerfeld that this efficiency is $2.8 \times 10^{-9} ZV_0$, where V_0 is the beam voltage in kV and Z is the atomic number. We can thus express the total radiated continuum energy as:

$$E_t = 2.8 \times 10^{-9} ZV_0 \, dV \tag{9}$$

The fraction of this quantity in an energy interval dE provides us with the number of photons $I_{c\theta}$ of energy E. The number of photons in the vanishingly small interval dE is obtained by dividing the amount of energy in that interval by the photon energy E. Consequently, the number of photons in the energy interval dE is given by the quantity $E_t \cdot dE/(EE_0)$ or:

$$I_{c\theta} = 2.8 \times 10^{-9} (Z/E) \, dE \, dV \tag{10}$$

61

The energy loss dV of electrons traversing a thin film of matter of thickness dz can be given by the Bethe equation for the slowing down of electrons in matter:[21]

$$- dV = \frac{2\pi e^4 N_0 Z}{V_0 A} \ln \left[\frac{1.166 V_0}{J} \right] \rho \, dz \tag{11}$$

where J is the mean loss of energy suffered by an electron while interacting with an atomic core electron,[22,23] 1.166 is the square root of half the base of the natural logarithms, dz is the specimen thickness in cm (if ρ is given in g/cm , and the other terms are as defined earlier. For a discussion of the assumptions used in the Bethe equation see Ref. 22, pp. 226-232.

Combining the previous two equations gives the number of continuum photons generated in a photon energy interval dE from a thin film of thickness dz due to one beam electron of energy V_0 :

$$I_{co} = \frac{220 Z^2}{A \, V_0 \, E} \ln \left[\frac{1.166 V_0}{J} \right] \rho \, dz \, dE \tag{12}$$

where the energy terms are in eV.

We can express Eq. (12) in units of a cross section, differential in energy, by multiplying by the quantity $A/(N_0 \, \rho \, dz)$, which gives

$$Q_{iu} = \frac{3.65 \times 10^{-22} \, Z^2}{V_0 E} \ln \left[\frac{1.166 \, V_0}{J} \right] dE \tag{13}$$

The subscripts iu on Q distinguish this cross section by its principal characteristics: isotropy and uniformity in energy distribution from property 2 above. The resulting cross section now has the required dimensions of area in cm^2 per beam electron. For the purposes of comparing this cross section with others, we use in Eq. (11) the well-known Sternheimer formulation of the J factor (given in Ref. 22):

$$J = Z(9.76 + 58.82 Z^{-1.19}) \quad (eV) \tag{14}$$

Equation (13) is an apparently simple expression of the continuum cross section. The simplicity is, however, a result of the use of approximations and assumptions in the derivation. We next consider two continuum cross sections which take more exact account of the physical processes involved in continuum generation. However, these more "exact" cross sections also result from certain simplifications since the formulation of the cross section from which they are derived cannot be solved in closed form. There are two fundamentally different types of approximations of particular relevance to applications in the AEM. We shall discuss a representative cross section, utilizing each approximation.

The Coulomb Approximation: Sommerfeld's Theory

Sommerfeld[24] developed a theory of continuum generation that neglects the presence of atomic electrons (screening) and assumes a pure Coulomb field about a point nucleus. Relativity, electron spin, and retardation of potential are neglected and the incoming electron and the scattered electron are represented by plane waves which occupy all space. Other assumptions that affect the spectral distribution at both the extreme high and low energy limits have been made but have little effect on the distribution in the range of interest to us.[25]

The Sommerfeld theory is troublesome to evaluate due to its mathematical form. Numerical estimates for selected atomic numbers and values of photon and electron energies have been made by Kirkpatrick and Wiedmann,[20] following the method of Weinstock.[26] These estimates are accurate to within 2% of the fully calculated theory. The Sommerfeld theory is only valid for incident-beam energies smaller than several keV. However, it is possible to apply a relativistic correction factor and extend the range of utility to encompass the AEM range. The neglect of screening effects of core electrons, especially in heavy atoms, can be expected to cause some error.

The algebraic fit Q_{k-w} of Kirkpatrick and Wiedmann to the Sommerfeld theory is given by

$$Q_{k-w} = I_x(1 - \cos^2\theta) + I_y(1 + \cos^2\theta) \tag{15}$$

where

$$I_x = (300Z^2/E_0)\{0.252 + a[(E/E_0) - 0.135] - b[(E/E_0) - 0.135]^2\} \, 1.51 \times 10^{-28}$$

$$I_y = (300Z^2/E_0) \, \{-j + k/[(E/E_0) + h]\} \, 1.51 \times 10^{-28}$$

$a = 1.47B - 0.507A - 0.833$ 　　　　　$A = \exp(-0.223E_0/300Z^2) - \exp(-57E_0/300Z^2)$

$b = 1.70B - 1.09A - 0.627$ 　　　　　$B = \exp(-0.0828E_0/300Z^2) - \exp(-84.9E_0/300Z^2)$

$h = \dfrac{-0.214y_1 + 1.21y_2 - y_3}{1.43y_1 - 2.43y_2 + y_3}$ 　　　　　$j = (1 + 2h)y_2 - 2(1 + h)y_3$

$k = (1 + h)(y_3 + j)$ 　　　　　$y_1 = 0.22[1 - 0.39\exp(-26.9E_0/300Z^2)]$

$y_2 = 0.067 + 0.023/[(E_0/300Z^2) + 0.75]$ 　　　$y_3 = -0.00259 + 0.00776/[(E_0/300Z^2) + 0.116]$

E and E_0 are expressed in eV.

Q_{k-w} can be made differential in energy and angle by multiplication by $d\Omega$ and dE, the differential of solid angle subtended by the detector at the angle θ and the differential of energy, respectively.

Zaluzec has recommend the relativistically corrected form,[10,11]

$$Q_{k-w} = I_x\left[\frac{1 - \cos^2\theta}{(1 - \beta \cos \theta)^4}\right] + I_y\left[1 + \frac{\cos^2\theta}{(1 - \beta \cos \theta)^4}\right] \tag{16}$$

where β, the relativistic correction factor, is as defined for Eq. (4.)*

Motz and Placious have recommended another formulation of relativistic correction which is markedly different in form and results:[27]

$$Q_{k-w} = I_x\left[\frac{1 - \cos^2\theta}{(1 - \beta \cos \theta)^2}\right] + I_y\left[\frac{1 + \cos^2\theta}{(1 - \beta \cos \theta)^2}\right] \tag{17}$$

---

*In a private communication, Zaluzec gives the following source for this correction: M. Scheer and E. Zeitter, Z. *Phys.* 140: 642, 1955.

(Note that the relativistic correction made to the continuum radiation is zero for a 90° observation angle.) They derived this formulation by comparing the relativistic and nonrelativistic cross sections given in Heitler (Ref. 28, p. 242, Eqs. 13 and 17). As pointed out by Motz and Placious, Heitler's cross sections are derived with free-particle wave functions. Consequently, the corrected cross section can be considered only a rough estimate of the exact cross section that would be obtained with relativistic Coulomb wave functions. The Motz-Placious correction has been used by Statham[29] for a lower beam energy (20 keV) Monte Carlo study in bulk specimens (photon energies 1-10 keV) in which continuum anisotropy is examined.

The Born Approximation

The Born theory also assumes free-particle wave functions. An extensive review and bibliography of continuum cross sections obtained by a number of workers using the Born approximation is given in Koch and Motz.[30] As pointed out by these authors, such cross sections are available in a relatively simple analytical form for relativistic energies, with or without screening correction. For the Born approximation to be valid, the initial and final electron kinetic energies in an electron-nuclear interaction must be large enough to satisfy the two conditions:

$$(2\pi Z/137\beta_0), \quad (2\pi Z/137\beta) \quad << 1$$

where β is as defined in Eq. (4). Despite the fact that the beam and photon energies in the AEM often do not satisfy these conditions, the theory is useful in predicting the shape of the continuum distribution. Koch and Motz report that the absolute error for total emission is within a factor of two in the worst case and can be considerably less for lower atomic number specimens, 90° observation angle, and higher AEM beam energies (> 150 keV).

A representative Born cross section, differential in photon energy and angle, is given by:

$$Q_{E,\theta} = \frac{dk}{k} \frac{p}{p_0} sZ^2 \, d\Omega \left\{ \frac{8 \sin^2\theta (2E_i^2 + 1)}{p_0^2 \Delta^4} - \frac{2(5E_i^2 + 2E_f E_i + 3)}{p_0^2 \Delta^2} - \frac{2(p_0^2 - k^2)}{G^2 \Delta^2} + \frac{4E_f}{p_0^2 \Delta} \right.$$

$$+ \frac{L}{pp_0} \left[\frac{4E_i \sin^2\theta (3k - p_0^2 E_f)}{p_0^2 \Delta^4} + \frac{4(E_i^2 + E_f^2)}{p_0^2 \Delta^2} + \frac{2 - 2(7E_i^2 - 3E_f E_i + E_f^2)}{p_0^2 \Delta^2} \right.$$

$$\left. + \frac{2k(E_i^2 + E_f E_i - 1)}{p_0^2 \Delta} \right] - \left(\frac{4\varepsilon}{p\Delta} \right) + \left(\frac{\varepsilon^G}{pG} \right) \left[\frac{4}{\Delta^2} - \frac{6k}{\Delta} - \frac{2k(p_0^2 - k^2)}{G^2 \Delta} \right] \right\} \qquad (18)$$

where $k = E/511$, $dk = dE/511$, $E_i = (E_0/511) + 1$, $E_f = E_i - k$,

$$p_0 = (E_i^2 - 1)^{\frac{1}{2}}, \quad p = (E_f^2 - 1)^{\frac{1}{2}}, \quad S = 2.31 \times 10^{-29}, \quad G^2 = p_0^2 + k^2 - 2p_0 k \, \cos\theta$$

$$L = \ln\left(\frac{E_f E_i - 1 + pp_0}{E_f E_i - 1 - pp_0} \right), \quad \Delta = E_i - p_0 \cos\theta, \quad \varepsilon = \ln\left(\frac{E_f + p}{E_f - p} \right), \quad \varepsilon^G = \ln\left(\frac{G+P}{G-P} \right)$$

and $d\Omega$ is the solid angle subtended by the detector at an angle θ, θ is the observation angle of the detector relative to the electron beam axis as described above, E is the photon energy (keV), and E_0 is the energy of the beam electrons (keV). This equation is essentially Eq. 2BN of Ref. 30, which is given in units of $m_0 c^2$. We have included the conversions to beam and photon energies in keV. Again, we have presented these cross sections not to make a critical evaluation but merely to demonstrate the functional form and numeric variation for the energy range of interest to us. For the purposes of plotting the various cross sections we can utilize the nominal Z^2 and 1/E dependence of continuum emission to normalize the plots. If we divide each cross section by Z^2 and multiply by the photon energy, the plots will reveal only deviations from these expected continuum properties. Figures 5, 6, and 7 show the forms of the three cross sections discussed in this paper plotted for one observation angle (158°), one atomic number (11), and three beam energies: 50, 100, and 200 keV. The two relativistically corrected forms of the Kirkpatrick-Wiedmann equation are plotted. The notation M-P denotes the Motz-Placious form and the notation Z denotes the Zaluzec form. The notation M-H denotes the cross section used in the Marshall-Hall method and B denotes the Born approximation cross section. We observe the strong deviation from the 1/E form and the change in spectral distribution as a function of beam energy for all the cross sections except the Marshall-Hall. (Note the change in vertical scale among the figures.)

Figures 8 and 9 plot M-P, M-H, and B against photon energy for a fixed beam energy (100 keV), two observation angles (90° and 158°), and three atomic numbers (11, 19, and 26). To simplify the figures we use only the Motz-Placious form of the Kirkpatrick-Wiedmann equation. The purpose of these plots is to demonstrate (1) the deviation of the M-H and M-P cross sections from the nominal Z^2 dependence of the continuum emission, and (2) the change in the cross section distribution with change in observation angle generated from the Sommerfeld and Born theories. The Born cross section does not exhibit a deviation from the Z^2 dependence, since this is one of the assumptions made in the approximation. The plot of the Born cross section is most useful here for an examination of the dependence on photon and beam energy. A discussion of the significance of the above distributions is the purpose of the next section.

The Nominal Z^2 and 1/E Dependence of the Continuum Emission

The accuracy of the Marshall-Hall method, when a standard of average atomic number different from that of the specimen is used, relies, among other things, on the ability of the continuum cross section to accomodate the change. The major dependence of the continuum emission on average atomic number is predicted by the square of Z factor but there is a nontrivial residual Z^2 dependence. The Marshall-Hall cross section approximately accounts for the residual effect by the J factor in the logarithmic term in Eq. (13). The dependence, however, is uniform with photon energy; as can be seen from Figs. 8 and 9. The Sommerfeld theory, on the other hand, predicts a residual which is not uniform with photon energy and indeed reverses its prediction as photon energy increases above about 14 keV for a 100keV beam. As can be seen from Figs. 8 and 9, the two predictions of the residual Z^2 dependence most closely agree for photon energies below about 4 keV. There has been considerable debate as to the best energy at which to measure the continuum signal for the Marshall-Hall procedure. The question is not easy to answer and must involve a consideration of statistics (there is more continuum signal at lower photon energies); instrumental effects (where in the continuous spectrum will there be a minimum of spectral artifacts, overlaps, effects of scattered electrons, etc.?); and physical considerations (how accurate are the physical and mathematical models?). However, in consideration of only the physics involved and assuming that the Sommerfeld prediction of the residual Z^2 dependence is correct, it would seem that the optimal region to measure the continuum for the Marshall-Hall procedure would be in the energy region below about 4-5 keV. It should be noted that there are implementations of the Marshall-Hall procedure which neglect the logarithmic term of Eq. (13). For those implementations Figs. 8 and 9 indicate that the optimal region would be near a photon energy of 14 keV for a 100keV beam.

In principle, it is possible to extend the idea of the Marshall-Hall procedure to the "one-standard" concept, advocated by Russ,[31] at least over a restricted range of photon energy. In the "one-standard" method, the ratio of Eqs. (1) and (7), multiplied by a coefficient, is set equal to a measured characteristic-to-continuum ratio obtained from a standard and the coefficient is determined. By appropriate substitution of the quantities in the equations for another, nearby element, it is possible
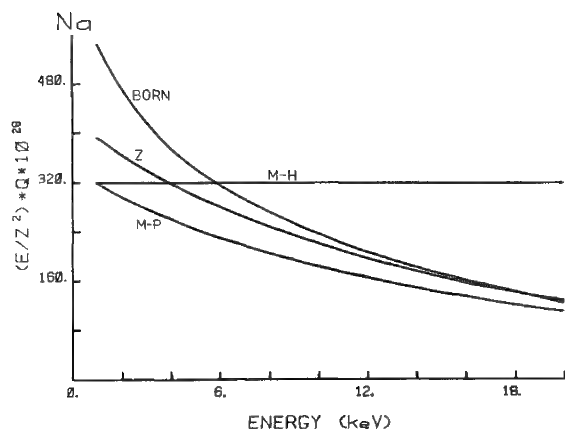
FIG. 5.--Plot of normalized continuum cross sections against photon energy for 158° observation angle, one atomic number (11), and 50 keV beam.
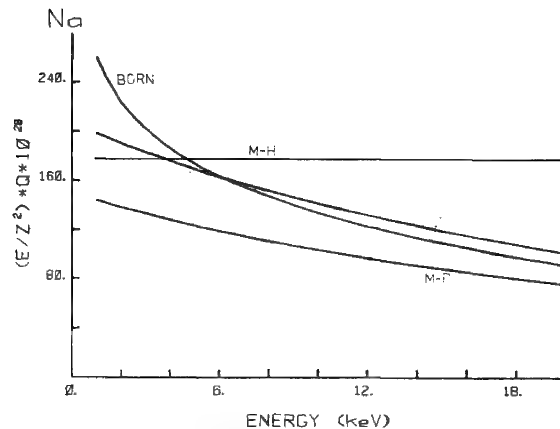
FIG. 6.--Same as Fig. 5 but 100keV beam. (Note change in vertical scale.)
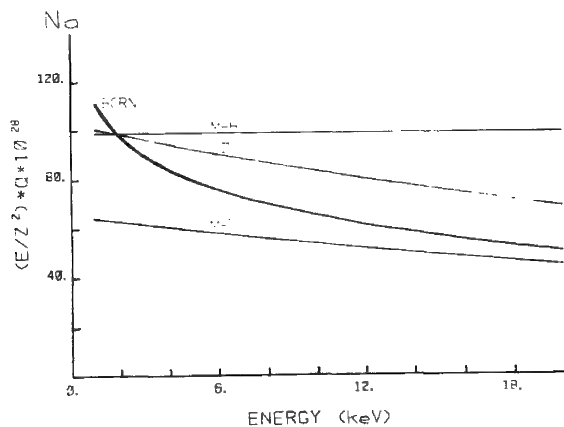
FIG. 7.--Same as Fig. 5 but 200keV beam. (Note change in vertical scale.)
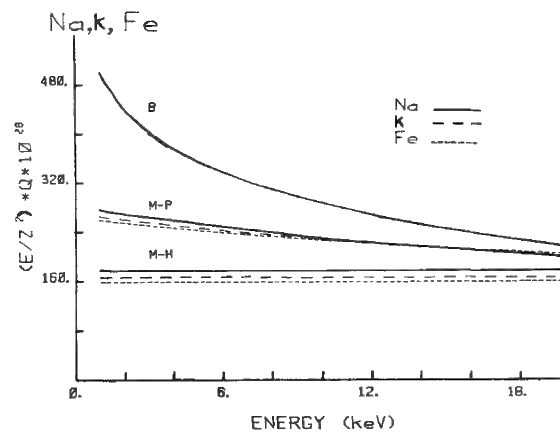
FIG. 8.--Plot of normalized continuum cross sections against photon energy for fixed beam energy (100 keV), three atomic numbers (11,19,26) and 90° observation angle.
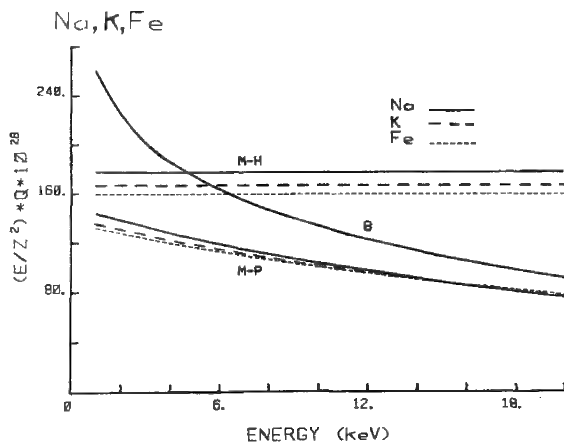
FIG. 9.--Same as Fig. 8 but 158° observation angle. (Note change in vertical scale and change in distribution shape.)
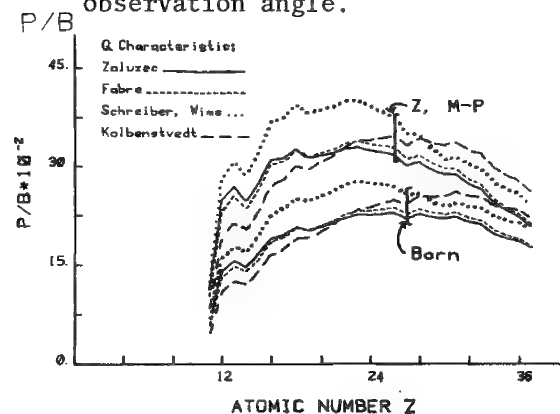
FIG. 10.--Plot of characteristic (K shell) to local continuum ratio according to various cross sections against atomic number form 11 to 37 for 100keV beam and 90° observation angle.

to predict the ratio of intensities which would be emitted by a standard containing the new element. To do so, however, one should not use the cross sections in the procedure as it was originally formulated for lower beam energy applications. In addition to the Z dependence of the continuum radiation, the assumption of a 1/E form is greatly in error, as evidenced by an examination of Figs. 5 through 9. Unless the continuum cross section can accommodate a change in measured photon energy, the measured interval must then remain fixed at some energy during the course of an analysis. This is an unncessary restriction which will be discussed below. Note, again, that the shape of the generated continuum distribution, as predicted by both the Born and the Sommerfeld theories, changes with observation angle. This is an important point to consider if one is to formulate a method generally useful for instruments of different manufacture and different observation angles. The Kirkpatrick-Wiedmann equation could be used to replace the original cross section of Marshall and Hall; and for instruments with a 90° observation angle, a relativistic correction would not be required.

The exact choice of characteristic cross section for a "one-standard" extension of the Marshall-Hall procedure as applied to the AEM is not so important since the various options have the same form, even though they differ significantly in absolute value, at least for the restricted energy range over which they would be utilized.

The Characteristic to Local Continuum Ratio: A Definition

It is useful to define the ratio of a characteristic intensity to an intensity of continuum radiation in an energy interval dE centered at the energy of the characteristic line. This ratio, when determined experimentally, is extremely useful as an indicator of analytical suitability for a particular electron column x-ray detector interface.[10,11,32] Any effects due to scattered electrons, beam-induced contamination, stray x rays, etc. are made readily apparent by comparison of the measured ratios to a theoretical prediction. Furthermore, such a ratio is useful as an analytical signal. For example, in the Marshall-Hall procedure "thicker" specimens may be analyzed, since the distribution in depth of the characteristic and the continuum radiation tends to be the same and specimen self absorption effects will cancel in the ratio. A standardized method of forming the ratio independent of spectrometer resolving power would permit the comparison of data obtained from different analytical microscopes. To make the ratio independent of the spectrometer resolution, an observed x-ray peak must be integrated over its full width, so as to provide a measure of the intensity of the originating x-ray line. There are two ways to specify the denominator. One method is to use a continuum energy interval which would be as wide as the "natural" x-ray line. However, the width of the natural lines varies with the energy of the line; and the reported widths are not in complete agreement, especially for the L and M x-ray lines. A second way is to settle on a fixed energy interval such as 10 eV. This particular interval has two advantages: most multichannel analyzers used with x-ray detectors on an AEM are calibrated for 10 eV per channel; and 10 eV is a value not much larger than the natural x-ray line widths. Consequently, a ratio formed with this value is of the same order as the ratio obtained if the natural line width had been used. For the remaining discussion we shall utilize an energy interval of 10 eV.

The Theoretical Characteristic to Local Continuum Ratio

It is obvious from our examination of both the characteristic and continuous x-ray cross sections that the value of the ratio we obtain by dividing Eq. (1) by Eq. (7) depends significantly on the choice of cross section used. Figure 10 displays plots of the ratios obtained from each of the four characteristic cross sections discussed to both the Born and the Sommerfeld continuum cross sections. The plot is a function of atomic number from 11 to 37. The characteristic cross sections used in the plot are designated by the length of the dash and the continuum cross sections used are denoted by a vertical brace. The beam energy used is 100 keV and a 90° observation angle is assumed. As mentioned earlier, the use of measured values for the fluorescent yields and relative x-ray transition probabilities in the numerator cause the plots to exhibit irregularity. This plot is useful for comparison against measured characteristic-to-continuum ratios obtained from pure-element foils for the stated conditions.

Statistical Properties of Characteristic-to-continuum Ratios

For this discussion we assume that the characteristic and continuum signals can be obtained from a measured spectrum by one of the standard procedures used for this purpose. The various ratios that can be made from the separated signals have attractive natural normalization properties. The functions P/B, $[P(C) - B(C)]/[P(1) - B(1)]$, and $[P(C)/B(C)]/[P(1)/B(1)]$, where C denotes specimen quantity and 1 denotes standard quantity, are slightly different algebraic forms that all represent estimates of characteristic intensity with continuum correction.

If these functions are to be used with confidence, limits on their possible errors need to be established. It is accepted practice to represent an estimate as a mean value plus or minus a standard deviation. Other specifications, such as the confidence level of a given hypothesis, can be given by somewhat different treatment of the same data. The statistical principles and framework are not changed.

Although statistical properties of the components and composite are known with confidence, estimates of the statistical properties of the ratio, are desirable. Let us assume that estimates of the mean, variance, and other moments of the variables composing these ratio functions are known. Estimates of the statistical properties of the functions can be derived from the following framework.

Suppose that we consider a general function of variables x, y, ... to avoid inferences that this framework is restricted to quotients of characteristic and continuum. Let $f = f(x,y,...)$, and let subscript 0 indicate evaluation of a variable or a function at the mean estimate. Then the total differential of this function is

$$\Delta F = \left(\frac{\partial f}{\partial x}\right)_0 \Delta x + \left(\frac{\partial f}{\partial y}\right)_0 \Delta y + \left(\frac{\partial^2 f}{\partial x^2}\right)_0 (\Delta x)^2 + \left(\frac{\partial^2 f}{\partial y^2}\right)_0 (\Delta y)^2 + \left(\frac{\partial^2 f}{\partial x \partial y}\right)_0 \Delta x \; \Delta y + \ldots$$

where $\Delta x = x - x_0$, $\Delta y = y - y_0$, etc. In most cases of interest here, second and higher-order terms should be negligible. They are, of course, well defined and easily calculated.

The variance of this function over an ensemble is derivable in a strightforward manner.

$$\text{var}[f(x,y,...)] = \overline{(f - f_0)^2}$$

$$= \overline{\left[\left(\frac{\partial f}{\partial x}\right)_0 \Delta x + \left(\frac{\partial f}{\partial y}\right)_0 \Delta y + \ldots\right]^2}$$

$$= \left(\frac{\partial f}{\partial x}\right)_0^2 (\Delta x)^2 + \left(\frac{\partial f}{\partial y}\right)_0^2 (\Delta y)^2 + \left(\frac{\partial f}{\partial x}\right)_0 \left(\frac{\partial f}{\partial y}\right)_0 \Delta x \; \Delta y + \ldots$$

$$= \left(\frac{\partial f}{\partial x}\right)_0^2 \text{var}(x) + \left(\frac{\partial f}{\partial y}\right)_0^2 \text{var}(y) + \left(\frac{\partial f}{\partial x}\right)_0 \left(\frac{\partial f}{\partial y}\right)_0 \text{cov}(x,y) + \ldots$$

The overbar indicates an appropriate ensemble average of a variable or function.

A normalized variance is often more meaningful than a raw one. By appropriate manipulation, we obtain

$$\frac{\text{var}(f)}{f_0^2} = \frac{\left[\frac{\partial f}{\partial x}\right]_0^2}{\left(\frac{f_0}{x_0}\right)^2} \frac{\text{var}(x)}{x_0^2} + \frac{\left[\frac{\partial f}{\partial y}\right]_0^2}{\left(\frac{f_0}{y_0}\right)^2} \frac{\text{var}(y)}{y_0^2} + \frac{2\left[\frac{\partial f}{\partial x}\right]_0 \left[\frac{\partial f}{\partial y}\right]_0}{\left(\frac{f_0}{x_0}\right)\left(\frac{f_0}{y_0}\right)} \frac{\text{cov}(x,y)}{x_0 y_0} + \ldots$$

For example, when $f(x,y) = x/y$, then

$$\text{var}(x/y) = (1/y_0)^2 \text{var}(x) + (-x/y^2)_0^2 \text{var}(y) + 2(1/y)_0 (-x/y^2)_0 \text{cov}(x,y) + \ldots$$

This may be written in the symmetric form

$$\frac{\text{var}(x/y)}{(x/y)_0^2} = \frac{\text{var}(x)}{x_0^2} + \frac{\text{var}(y)}{y_0^2} - 2\frac{\text{cov}(x,y)}{x_0 y_0} + \ldots$$

Note that, to first order, the normalized variances add, whereas the normalized co-variances subtract. (Covariances exist, for example, if the average effects of either the characteristic or continuous signals are incorrectly subtracted.) So, if the factors of a quotient are statistically independent, the variation of a quotient is the sum of the variations of its components. If the factors are completely dependent, e.g., y is a multiple of x, then the variation of the quotient is zero.

Letting $x = P$ and $y = B$, we obtain

$$\frac{\text{var}(P/B)}{(P/B)_0^2} = \frac{\text{var}(P)}{P_0^2} + \frac{\text{var}(B)}{B_0^2} - 2\frac{\text{cov}(P,B)}{P_0 B_0}$$

For a pure Poisson process, which is a good approximation for both characteristic and continuum count generation in electron beam microanalysis,

$$\text{var}(P) = P_0 \quad \text{and} \quad \text{var}(B) = B_0$$

If the samples are independent, then

$$\text{cov}(P,B) = 0$$

This is also a good approximation for correctly estimated characteristic and continuum, since each is the sum of variables that are mutually independent. However, nonzero co-variance are introduced into this formulation by misestimation of either component. Thus,

$$\frac{\text{var}(P/B)}{(P/B)_0^2} \simeq \frac{P_0}{P_0^2} + \frac{B_0}{B_0^2} = \frac{1}{P_0} + \frac{1}{B_0}$$

69

From this normalized form, the variances can be written very compactly.

$$\frac{\text{var}(P/B)}{(P/B)_0^2} \simeq \frac{\text{var}(P)}{P_0^2} + \frac{\text{var}(B)}{B_0^2} - 2\frac{\text{cov}(P,B)}{P_0 B_0} \quad ;$$

$$\frac{\text{var}\{[P(c) - B(c)]/[P(1) - B(1)]\}}{\{[P(c) - B(c)]/[P(1) - B(1)]\}_0^2} \simeq \frac{\text{var}[P(c) - B(c)]}{[P(c) - B(c)]_0^2}$$

$$+ \frac{\text{var}[P(1) - B(1)]}{[P(1) - B(1)]_0^2} - \frac{2\,\text{cov}\{[P(c) - B(c)], [P(1) - B(1)]\}}{[P(c) - B(c)]_0\,[P(1) - B(1)]_0} \quad ;$$

$$\frac{\text{var}\{[P(c)/B(c)]/[P(1)/B(1)]\}}{\{[P(c)/B(c)]/[P(1)/B(1)]\}_0^2} \simeq \frac{\text{var}[P(c)]}{P(c)_0^2} + \frac{\text{var}[B(c)]}{B(c)_0^2}$$

$$+ \frac{\text{var}[P(1)]}{P(1)_0^2} + \frac{\text{var}[B(1)]}{B(1)_0^2} - \frac{2\,\text{cov}[P(c), B(c)]}{P(c)_0\,B(c)_0} - \frac{2\,\text{cov}[P(1), B(1)]}{P(1)_0\,B(1)_0}$$

$$- \frac{2\,\text{cov}[P(c), P(1)]}{P(c)_0\,P(1)_0} - \frac{2\,\text{cov}[B(c), B(1)]}{B(c)_0\,B(1)_0}$$

$$+ \frac{2\,\text{cov}[P(c), B(1)]}{P(c)_0\,B(1)_0} + \frac{2\,\text{cov}[P(1), B(c)]}{P(1)_0\,B(c)_0}$$

The portion of this result containing variances obtained by propagation of errors is shown by Heinrich.[22] A different approach, oriented toward determining counting times necessary for appropriate levels of confidence, is reported by Ancey, Bastenaire, and Tixier.[33]

Conclusions

The characteristic-to-continuum ratio has several desirable qualities for biological applications of electron-beam microanalysis. Meaningful usage of this ratio requires understanding of its properties, capabilities, and uncertainties. Discussion of the characteristic-to-continuum ratio leads naturally to separate consideration of each component.

Each component depends critically on the appropriate cross section. Several models for cross sections have been proposed for the range of energies used in the AEM. In general, they have substantially different functional forms. Regions of validity of the models and extrapolation beyond these regions have been discussed.

Major sources of error for each cross-section model and variable region were examined. A general, usable statistical framework for determining the estimation uncertainty of the ratio from the data was presented.

References

1. M. O. Krause and J. H. Oliver, *J. Phys. Chem. Ref. Data* 8 (No. 2): 329-328, 1979.
2. D. J. Marshall and T. Hall, in Castaing, Descamps, and Philibert, Eds., *X-ray Optics and Microanalysis* Paris: Hermann, 1966, 374.
3. W. Bambynek, et. al., *Rev. Mod. Phys.* 44: 716, 1972.
4. K. F. J. Heinrich, C. E. Fiori and R. L. Myklebust, *J. Appl. Phys.* 50: 5589, 1979.
5. V. W. Slivinsky and P. J. Ebert, *Phys. Rev.* A5: 1581, 1972.
6. M. D. Krause, *J. Phys. Chem. Ref. Data* 8 (No. 2), 1979.
7. H. Bethe, *Ann. Phys.* 5: 325, 1930
8. C. J. Powell, *Rev. Mod. Phys.* 48: 33, 1976.
9. C. J. Powell, in Heinrich, Newbury, and Yakowitz, Eds., *Use of Monte Carlo Calculations in Electron Probe Microanalysis and Scanning Electron Microscopy*, NBS Special Publication 460, 1976, 97-104.
10. N. J. Zaluzec, "Quantitative x-ray microanalysis: Instrumental considerations and applications to materials science," in Hren, Goldstein and Joy, Eds., *Introduction to Analytical Electron Microscopy*, New York: Plenum, 1979, 121.
11. N. J. Zaluzec, *An Analytical Electron Microscope Study of the Omega Phase Transformation in a Zirconium-Niobium Alloy*, PhD. Thesis, University of Illinois, 1978.
12. N. F. Mott and H. S. W. Massey, *The Theory of Atomic Collisions*, London: Oxford University Press, 1965, 3d ed.
13. H. Bethe and E. Fermi, *Z. Physik* 77: 296, 1932.
14. E. J. Williams, *Proc. Roy. Soc.* 139: 163, 1933.
15. T. P. Schreiber and A. M. Wims, *Ultramicrosc.* 6: 323-334, 1981.
16. T. P. Schreiber and A. M. Wims, *Microbeam Analysis--1981*, 313-319.
17. H. Kolbenstvedt, *J. Appl. Phys.* 38: 4785-4787, 1967.
18. N. A. Dyson, *Proc. Phys. Soc.* 72: 924-936, 1959.
19. A. H. Compton and S. K. Allison, *X-rays in Theory and Experiment*, New York: Van Nostrand, 1935, 2d ed.
20. P. Kirkpatrick and L. Wiedmann, *Phys. Rev.* 67: 321-339, 1945.
21. H. A. Bethe in *Handbook of Physics*, vol. 24, Berlin: Springer, 1933, 273.
22. K. F. J. Heinrich, *Electron Beam X-ray Microanalysis*, New York: Van Nostrand Reinhold, 1981.
23. J. I. Goldstein et al., Eds. *Scanning Electron Microscopy and X-ray Microanalysis*, New York: Plenum Press, 1981.
24. A. Sommerfeld, *Wellenmechanik*, New York: Ungar, 1950, Chap. 7; and *Ann. Physik* 11: 257, 1931.
25. S. T. Stephenson in *Encyclopedia of Physics*, vol 30, Springer-Verlag, 1967, 337-369.
26. R. Weinstock, *Phys. Rev.* 61: 585, 1942; 65:1, 1944.
27. J. W. Motz and R. C. Palacious, *Phys. Rev.* 109: 235-242, 1958.
28. W. Heitler, *The Quantum Theory of Radiation*, New York: Oxford University Press, 1954, 3rd ed.
29. P. J. Statham, *X-ray Spect.* 5: 154-168, 1976.
30. H. W. Koch and J. W. Motz, *Rev. Mod. Phys.* 31: 920-955, 1959.
31. J. C. Russ, *Proc. 9th MAS Conf.*, 1974, paper 22.
32. W. A. P. Nicholson et. al., *J. Microsc.* 125(Pt 1): 25-40, 1982.
33. M. Ancey, F. Bastenaire and R. Tixier, "Application of statistical methods to electron probe microanalysis," *8th International Congress on X-Ray Optics and Microanalysis*, Boston, 1977, 49-56.

THE EVALUATION OF SOLUTE DISTRIBUTIONS MEASURED BY STEM-EDS MICROANALYSIS

Peter Doig and P. E. J. Flewitt

There have been a number of recent advances in the application of electron optical techniques for characterizing the microstructure of materials. Perhaps of most significance has been the development of high-resolution chemical microanalysis for determining local composition. In particular, the introduction of scanning transmission electron microscopy (STEM) with high-intensity electron probes has, when interfaced with energy-dispersive x-ray spectrometers (EDS), offered the possibility of x-ray microanalysis on thin foil samples to a spatial resolution approaching that achieved when imaging in the conventional transmission mode.[1-3]

Characteristic x-ray emissions generated by fine, high-energy electron probes have been used for the last twenty years in electron microprobe analyzers (EPMA) for the chemical analysis of small volumes at the surface of bulk samples. In such cases the electron probe is scattered elastically and inelastically as it penetrates the sample and x rays are excited from within a volume that is defined by the boundary where the inelastic scattering has reduced the electron energy to less than that necessary for the excitation of the characteristic x rays. This volume is determined by the atomic number of the material and accelerating voltage of the electron probe and, in general, tends to a pear shape up to a maximum diameter of several micrometers.[4] Thus the spatial resolution of x-ray microanalysis is determined by the scattering of the electron beam. In thin foils examined in STEM, however, higher energy incident electron probes are involved and very few electrons are sufficiently reduced in energy for the spatial resolution of any microanalysis to be defined by consideration of the boundary at which the beam energy has been reduced to below that required for x-ray excitation. In this case most electrons suffer only a small number of inelastic collisions such that the volume of sample from which x rays are excited by the incident electron probe is determined primarily by the elastic scattering.[5-14] This volume, or some part of it, is then taken to represent the spatial resolution of any microanalysis. Thus, microstructural features larger than this limit may be directly sampled, and therefore analyzed, by the incident electron probe. The limit lies typically in the range 20-100 nm for conventionally prepared metal foils, which is an order of magnitude better than that attainable from bulk samples in EPMA. However, such a spatial resolution limit is not sufficient for investigation of many metallurgical phenomena in which chemical information to a distance scale of better than 1 nm is desirable, i.e., to a scale that is even finer than most currently available incident electron probe diameters.

This paper describes and discusses a method for obtaining quantitative chemical information by STEM-EDS microanalysis over distances smaller than the measured spatial resolution defined by the electron scattering within foil samples.

Analysis of the Spatial Resolution for X-ray Microanalysis

The spatial resolution of x-ray microanalysis within thin foils by STEM-EDS is controlled by elastic scattering of the electron probe. The measured characteristic x-ray intensity I' is a convolution of the distributions of electron flux intensity I(v) and the solute composition C(v) within the total sampled region of the foil:

$$I' = K \int_V I(v) \cdot C(v) \ dv \tag{1}$$

where K is a constant that describes the efficiency of x-ray generation, emission, and detection for the particular element of interest.
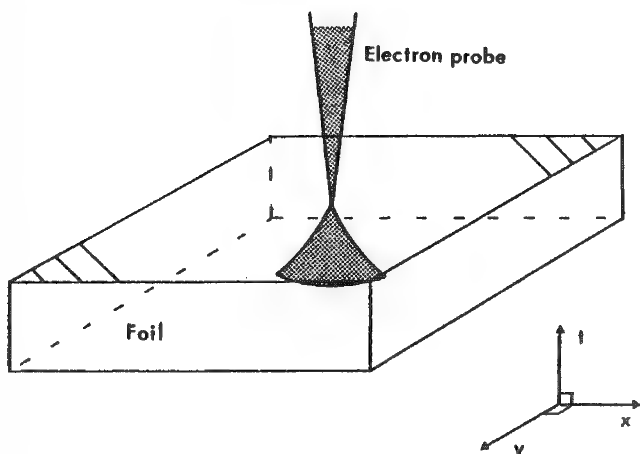
FIG. 1.--Schematic diagram showing coordinate directions used in present analysis.
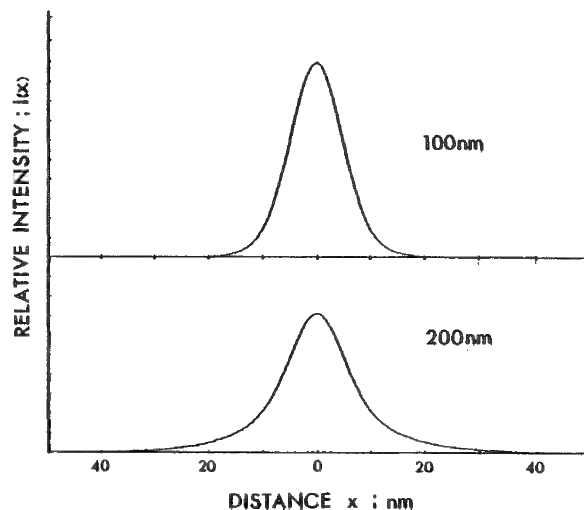
FIG. 2.--Normalized effective intensity distributions projected on x-y plane for iron base foils of thickness 100 and 200 nm.

For a thin foil of geometry shown in Fig. 1, it is possible to map the measured x-ray intensities and thus chemical compositions in the x-y plane where the direction t is parallel to the incident electron beam. Experimental conditions are often established such that compositional variations are functions of x and y only; i.e., for measurement of solute profiles up to interfaces the foil is tilted to orient the interface parallel to the incident electron probe. The measured x-ray intensity is then a function of x and y given by

$$I'(x_1,y_1) = K \int_{-\infty}^{+\infty} \int_{-\infty}^{+\infty} I(x,y) \cdot C(x_1 - x, y_1 - y)\, dx dy \tag{2}$$

where x_1 and y_1 are coordinate positions in the x-y plane. For clarity we shall consider the case of a composition profile up to planar interfaces where the solute distribution is a function of x only and Eq. (2) reduces to:

$$I'(x_1) = K \int_{-\infty}^{+\infty} I(x) \cdot C(x_1 - x)\, dx \tag{3}$$

Here, the measured x-ray intensity profile $I'(x_1)$ is a function of x and is usually measured at discrete distances x_1 across the interface until the measured x-ray intensity approaches a constant value.

From the measured value of $I'(x_1)$ we require to obtain the true composition distribution $C(x)$, which in turn needs a description of the term $I(x)$, the effective distribution of electron intensity within the sampling electron probe as a function of distance x from the probe center in the direction of the interface normal. A previous analysis of the electron intensity distribution $I(x,y,t)$ within an analyzing STEM probe has given:[11]

$$I(x,y,t) = \{I/\pi(2\sigma^2 + \beta t^3)\} \cdot \exp\{-(x^2 + y^2)/(2\sigma^2 + \beta t^3)\} \tag{4}$$

where $\beta = (4Z/E)^2 (\rho/A) \cdot 500$, I is the total electron flux, σ (nm) is a measure of the incident electron probe size, Z and A are the mean atomic number and weight of the foil material with density ρ, and E is the electron accelerating voltage in volts. We thus have

$$I(x) = \int_0^T \{I/(\pi(2\sigma^2 + \beta t^3))^{\frac{1}{2}}\} \cdot \exp\{-x^2/(2\sigma^2 + \beta t^3)\} dt \tag{5}$$

which is evaluated in Fig. 2 for an iron-base foil of thickness T = 100 and 200 nm.

The true composition profile $C(x)$ may then be determined in various ways[15] that can be categorized into two basic approaches. First,[16-18] a physically realistic functional form for $C(x)$ may be assumed and inserted into Eq. (3) and the values of $C(x_1)$ calculated and compared with the experimental values. The defining coefficients of $C(x)$ are then adjusted until the calculated values of $C(x_1)$ provide the best fit to the experimental values.[3,15] This approach requires some physical interpretation of the basic phenomena that give rise to the composition profile. Unfortunately, in most cases, such information is not available or is poorly defined. Indeed, it is usually in an attempt to elucidate such processes and mechanisms that the measurements are made. Thus, it is necessary to deconvolute the terms $I(x)$ and $C(x_1 - x)$ directly from the measured $I'(x_1)$ (Eq. 3), which may be conveniently accomplished by Fourier analysis techniques,[19] since the transform of a convolution of two functions is proportional to the product of the individual transforms:

$$FT^-[I(x)].FT^-[C(x)] = FT^-[I'(x)] \qquad (6)$$

such that

$$C(x) = FT^+\{FT^-[I'(x)]/FT^-[I(x)]\} \qquad (7)$$

where FT^- represents the forward and FT^+ the inverse Fourier transform. Such an approach has been considered previously for electron probe microanalysis measurements[20-22] on bulk samples, with the use of experimentally derived descriptions for $I(x)$. For the present case of thin foils, however, the function $I(x)$ is given by Eq. (5) for a given material β, incident beam size σ and foil thickness t_1.

Experimental measurement of the function $I'(x)$ at fixed intervals Δx confines us to define the Fourier transform of I' at a finite number of points. This procedure limits the maximum frequency contribution to the Fourier transform of the evaluated $C(x)$ to $2/\Delta x$ (Nyquist criterion), which thus limits the accuracy of its evaluation. In practice, for an experimental x-ray intensity profile $I'(x)$ measured at intervals of Δx, the electron intensity profile $I(x)$ may be evaluated at the same intervals and the Fourier deconvolution and reconstruction (Eqs. 6 and 7) carried out numerically on a digital computer.[22]

An example of such a procedure is illustrated schematically in Fig. 3 for a measurement interval of $\Delta x = 10$ nm in an iron-based foil of thickness 200 nm. Clearly, the precision with which the peak value of composition may be derived depends on the maximum frequency (or Nyquist frequency) contribution to the Fourier transform of the $I'(x)$ profile; i.e., the spacing Δx. In general, increasing the interval Δx results in a smoothing of the resulting evaluated $C(x)$ profile with an underestimate of peak values and a corresponding overestimate of profile spatial extent.

The accuracy of the deconvolution process is limited by the frequency information included in the Fourier transform descriptions of the measured x-ray profile $I'(x)$, and the calculated electron intensity profile $I(x)$. Since the deconvolution process involves division of Fourier coefficients at the same frequency, the Fourier transform of $I(x)$ can only include frequencies up to that
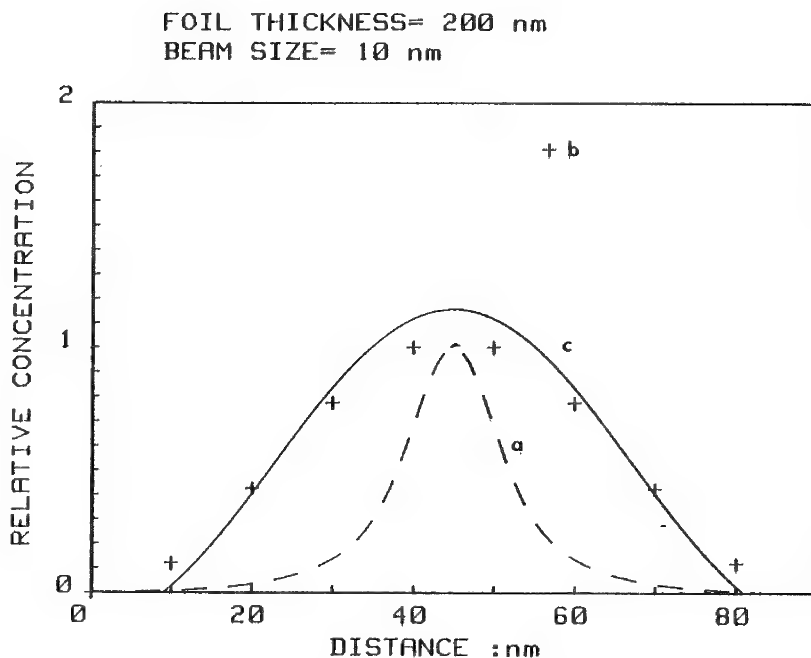

FOIL THICKNESS= 200 nm
BEAM SIZE= 10 nm

FIG. 3.--Schematic illustration of deconvolution of (a) electron intensity distribution $I(x)$, from (b) measured x-ray data $I'(x)$, to give (c) calculated true composition profile $C(x)$.

describing the measured profile $I'(x)$, i.e., $2/\Delta x$. The effective sampling electron intensity profile $I(x)$ is a function of the incident electron probe size σ, foil material β, and foil thickness T_1 in Eq. (5), and the precision with which it can be represented by its Fourier transform, truncated at the Nyquist frequency $2/\Delta x$, changes with each of these parameters. Thus the accuracy of any deconvolution to evaluate composition profiles also depends on these parameters.

Results

The relative effects of each parameter on the accuracy of the deconvolution procedure will be considered with reference to a composition profile of the type shown in Fig. 4 with

$$C(x) = C_0 \exp[-(|x|/A)] \tag{8}$$

where A is a constant that defines the spatial extent of the profile and the true peak concentration at the interface $x = 0$ is C_0. Since in many applications it is this peak value C_0 that is required, we shall consider how accurately the deconvolution predicts this concentration $C_0{}^*$.

The influence of the measurement interval Δx on the accuracy of peak evaluation $C_0{}^*/C_0$, is most simply examined with a point-source electron intensity ($\sigma = T_1 = 0$ in Eq. 4), which thus isolates contributions from the electron intensity profile $I(x)$. The evaluated $C_0{}^*/C_0$ ratio is shown in Fig. 5 as a function of sampling interval Δx/HWHH (*h*alf *w*idth at *h*alf *h*eight) of the true concentration profile $C(x)$, (HWHH = A ln 2). Clearly the accuracy of estimating C_0 decreases with increasing sampling interval Δx. However, it is noteworthy that sampling at an interval Δx = HWHH of the profile yields a predicted peak concentration $C_0{}^*$ within 5% of the true value C_0.

The effect of the introduction of a real electron intensity distribution $I(x)$ is an increase in the error in evaluating the composition profile $C(x)$. This effect is illustrated in Fig. 6, where $C_0{}^*/C_0$ is evaluated as a function of sampling interval Δx for a true composition profile with HWHH = 10 nm in iron-based foils of thickness = 0, 100, 200, and 300 nm, and an incident beam size of 2 nm at 100 kV. These results show that for the range of sampling intervals up to about 60 nm, an increase in the foil thickness decreases the accuracy of estimating the peak concentration C_0. At a sampling interval of 10 nm, which represents a realistic experimental lower limit, the value of $C_0{}^*$ decreases from $0.88C_0$ at 100nm to $0.75C_0$ at 300nm foil thickness.

The accuracy with which we can determine the peak concentration C_0 clearly depends on the spatial extent of the profile, i.e., the value A. This is shown in Fig. 7 for the range of profile widths (HWHH) 5, 10, 20, and 50 nm for an iron-base foil of thickness 200 nm and an incident electron probe size of 2 nm at 100 kV. If we consider a lower limit to practical measurement intervals as 10 nm, the accuracy of estimating C_0 may be plotted as a function of true composition profile width (HWHH) for foil thicknesses of 100 and 200 nm (Fig. 8). Here we observe the significant benefit of using thinner foils for estimating C_0, particularly as the width of the composition profiles decreases below 50 nm. This result is of significance since many metallurgical phenomena of technological importance involve the development of composition profiles that fall into this category.[2,23,24]

All the above results have been derived on the assumption of no error in the measured x-ray intensity profile $I'(x)$. Clearly this assumption is never achieved in practice and some statistical error in the recorded x-ray counts always occurs. For reasonable counting statistics this error is approximated by $\sqrt{N}$, where N is the number of counts and the percentage accuracy is $100/\sqrt{N}$. Implicitly this random error in $I'(x)$ must be carried into the derived composition profile $C(x)$ and peak value $C_0{}^*$. For the present true composition profile shape (Eq. 8) this error is about 2.5 times that in the individual $I'(x)$ data. Thus for x-ray data with about 100 counts in the recorded peak, the estimated value of $C_0{}^*$ will be in error by up to about 25% in addition to that predicted by the present analysis. However, experimental procedures may be adopted to reduce this measurement error, such as increasing the number of x-ray counts by recording for longer times, using higher brightness electron sources, increasing the incident electron probe size, and increasing the foil thickness. As shown in Figs. 5-7, however, these latter procedures serve to increase the effective sampling electron distribution $I(x)$ and so increase the error in determining C_0. Clearly, a compromise between increasing foil thickness and decreasing x-ray counting sta-

tistics will optimize the accuracy of C_0* depending on the particular absolute number of x-ray counts obtained.
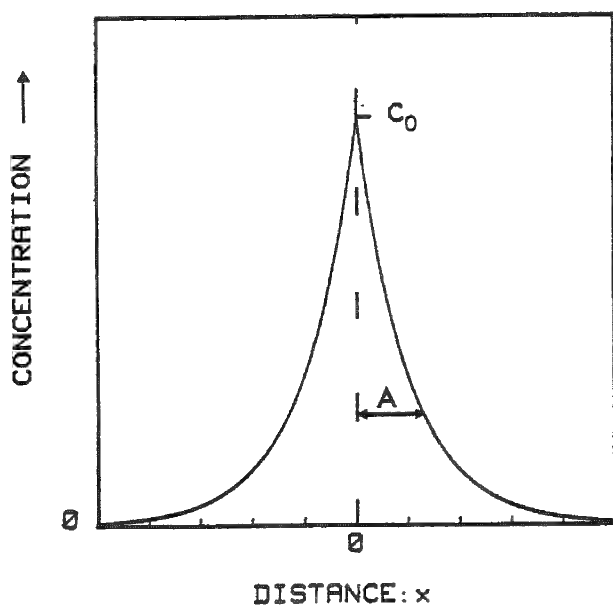
FIG. 4.--Schematic diagram showing composition profile assumed in present analysis.
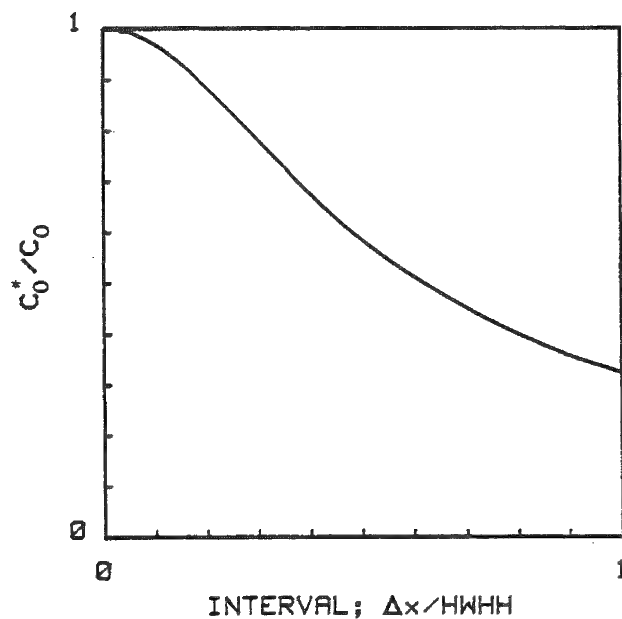
FIG. 5.--Evaluated peak composition/real peak composition $(C_0$*$/C_0)$ as function of measurement interval Δx/profile HWHH. Values calculated for point source of sampling electron intensity.
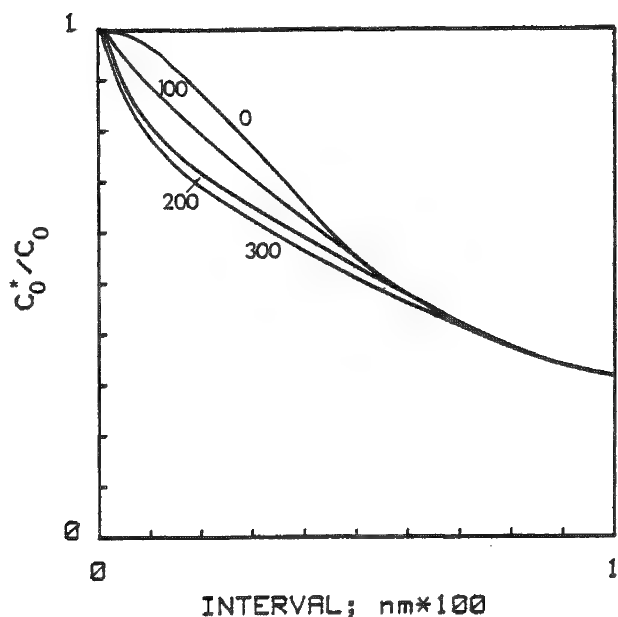
FIG. 6.--Evaluated ratio C_0*$/C_0$ for profile HWHH = 10 nm as function of measurement interval Δx for range of foil thicknesses 0, 100, 200, and 300 nm. Iron-base foil, incident electron probe size = 2 nm, 100 kV.
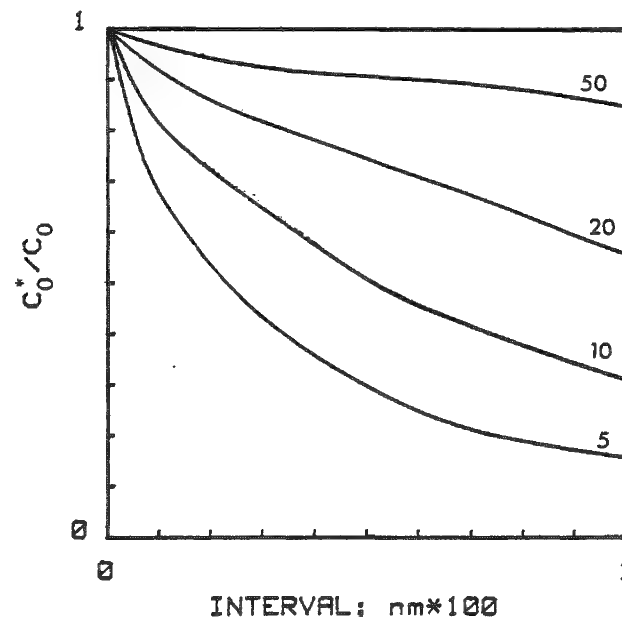
FIG. 7.--Evaluated ratio C_0*$/C_0$ as a function of measurement interval Δx for range of profile widths (HWHH) = 5, 10, 20 and 50 nm. Fixed iron-base foil thickness = 200 nm. Incident electron probe size = 2 nm, 100 kV.

Discussion

The present analysis illustrates a procedure for evaluating true composition distributions from experimental STEM-EDS x-ray intensity data. The concept of a limiting spatial resolution for microanalysis, determined by some arbitrary description of the electron scattering, is not of direct value in defining the smallest composition fluctuation that may be detected and quantified with this technique. This limit is more directly controlled by the statistical accuracy and sampling interval of the recorded data.

The work described in this paper has been based on a specific composition profile shape (Eq. 8) chosen to approximate concentration fluctuations associated with either equilibrium or nonequilibrium (diffusion-limited) segregation phenomena. The precise numerical values quoted in the present text vary with the particular profile shape but the trends of the results are of general applicability. In general, narrower electron intensity distributions $I(x)$ can provide a more accurate evaluation of the true composition profile $C(x)$. However, such narrower intensity profiles, associated with smaller incident probe sizes and foil thicknesses, result in a lower confidence in the measured x-ray data $I'(x)$ and thereby reduce the overall accuracy of the evaluated composition profile $C(x)$.

The approximate analytical description for the electron intensity distribution within the scattered electron probe (Eq. 4)[3,11] provides a convenient form to establish $I(x)$ for use in the present analysis. Other procedures such as Monte Carlo or refined single-scattering models may be used for this evaluation and subsequent deconvolution of the measured data $I'(x)$. Regardless of the particular description for $I(x)$, the approach and conclusions of the present analysis will remain unchanged.
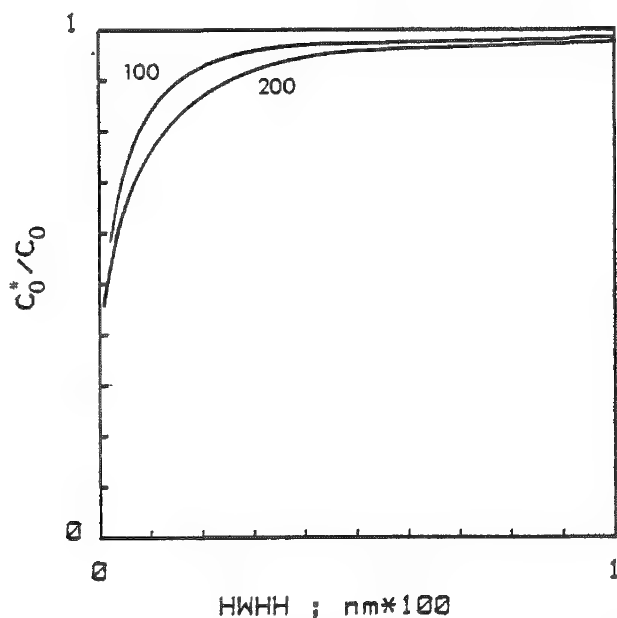
FIG. 8.--Evaluated ratio $C_0{}^*/C_0$ as function of composition profile width (HWHH) for fixed measurement interval Δx = 10 nm, in iron-base foil[5] of thickness = 100 and 200 nm. Incident electron probe size = 2 nm, 100 kV.

The parameters that are of overriding importance in establishing the true composition profile $C(x)$ from the measured x-ray intensity profile $I'(x)$ are shown by the present analysis to be the measurement interval Δx, and the statistical confidence in the recorded data. At present, the limit on Δx is determined by the mechanical and electrical stability of the microscope and for recording times of about 100 s is in the region 10-50 nm for the current generation of commercial instruments. For iron foils of reasonable thickness, 100-200 nm, when one is using a recording interval of 10 nm and ignoring noise in the recorded data, the accuracy of evaluating the peak value of a composition fluctuation with HWHH = 10 nm is limited to 10-20% of its true value (Fig. 8). Similarly, for such a measurement interval, composition profiles with HWHH less than 1 nm may be detected and the peak value $C_0{}^*$ estimated to within a factor of two of its true value C_0 (Fig. 8).

Conclusions

The present analysis has shown that the concept of a fixed spatial resolution in STEM x-ray microanalysis is of little value in defining the limits of detection and evaluation of composition fluctuations in thin foils. The deconvolution procedure described provides a means of obtaining quantitative microanalysis of composition fluctuations whose spatial extent is very much smaller than the size of the sampling electron intensity distribution. The major limitations to the ultimate accuracy of the microanalysis are the minimum sampling interval and the statistical accuracy of the recorded data rather than the finite volume of the foil excited by the incident electron probe.

References

1. K. E. Easterling, *Int. Met. Rev.* 213: 1, 1977.
2. P. Doig et al., *Micron* 10: 277, 1979.
3. P. Doig et al., *Met. Trans.* 12A: 1277, 1981.
4. P. Duncumb and P. K. Shields, *Brit. J. Appl. Phys.* 14: 617, 1963.
5. J. I. Goldstein et al., "Quantitative x-ray analysis in the electron microscope," *SEM/1977* I, 315.
6. R. G. Faulkner et al., *X-ray Spectrom.* 6: 73, 1977.
7. R. G. Faulkner and K. Nörrgard, *X-ray Spectrom.* 7: 184, 1978.
8. E. L. Hall et al., *Phil. Mag.* A43: 1569, 1981.
9. R. H. Geiss and D. F. Kyser, *Ultramicroscopy* 3: 397, 1979.
10. R. Hutchings et al., *Ultramicroscopy* 3: 401, 1979.
11. D. E. Newbury and R. L. Myklebust, *Ultramicroscopy* 3: 391, 1979.
12. P. Doig et al., *Phil. Mag.* A41: 761, 1980.
13. P. Doig et al., "Electron intensity distributions in STEM-EDS microanalysis of thin foils," in *Quantitative Microanalysis with High Spatial Resolution,* Metals Society, UMIST, Manchester, 1981.
14. D. F. Kyser, in J. J. Hren, J. I. Goldstein, and D. C. Joy, Eds., *Introduction to Analytical Electron Microscopy,* New York: Plenum, 1979.
15. J. A. Irvin et al., *Rev. Sci. Instrum.* 52: 191, 1981.
16. A. E. McKinnon et al., *J. Phys. Chem.* 81: 1564, 1977.
17. A. E. W. Knight and B. K. Sellinger, *Spectrochim. Acta* 27A: 1223, 1971.
18. A Papoulis, *The Fourier Integral and Its Application,* New York: McGraw-Hill, 1962.
19. A. R. Stokes, Proc. Phys. Soc. (London) A61: 382, 1948.
20. E. J. Rapperport, in A. J. Tousimis and L. Marton, Eds., *Electron Probe Microanalysis: Supplement 6,* New York: Academic Press, 1969.
21. J. B. Cohen, *Diffraction Methods in Materials Science,* New York: Macmillan, 1966, 80-105.
22. J. W. Cooley and J. W. Tukey, *Mathematics of Computation* 19: 297, 1965.
23. P. Doig et al., *Met. Trans. A.* 1982, in press.
24. P. Doig and P. E. J. Flewitt, *Acta Met.* 29: 1831, 1981.

BEAM BROADENING IN THE ANALYTICAL ELECTRON MICROSCOPE

D. E. Newbury

X-ray microanalysis in the analytical electron microscope (AEM) is characterized by much better spatial resolution than that obtainable in the conventional analysis of bulk specimens in the electron probe microanalyzer.[1,2] This improvement in spatial resolution is a result of three major factors: (1) High brightness sources and strong condenser lens systems provide beams of the order of 10 nm in diameter which carry sufficient current for x-ray microanalysis with the energy-dispersive x-ray spectrometer; (2) high beam energies, typically in the range 80-200 keV, decrease the cross section for elastic scattering, which is principally responsible for causing beam electrons to deviate from their initial trajectories; and (3) sample thicknesses of the order of 100 nm reduce the number of possible scattering events, so that most electrons traverse the foil with only slight energy loss. However, the improvement in spatial resolution over that of conventional analysis is not without limit. Elastic scattering results in significant beam broadening, as illustrated in Fig. 1. The volume of excitation in the absence of scattering would be the cylinder whose cross section is defined by the incident beam area. The excitation would not be constant within this cylinder; the incident beam typically has a Gaussian distribution of intensity across its diameter. Beam spreading or broadening degrades this cylinder to a complex three-dimensional form with a cross-sectional area that increases continually with depth. The intensity distribution across this area is also modified by the scattering process. Rare large-angle scattering events can cause electrons to backscatter out of this volume and further degrade the spatial resolution.

Beam broadening affects both the compositional accuracy and the spatial resolution of x-ray microanalysis. When a structure of interest is smaller than the volume defined by beam broadening, atoms in the surrounding matrix are excited as well as those in the structure, which can lead to possible errors in both the qualitative and the quantitative analyses of the structure. In the usual method of quantitative analysis, relative elemental sensitivity factors, $k_{AB} = (C_A/C_B) \cdot (I_B/I_A)$, where C is the concentration and I is the measured intensity for elements A and B, are used to analyze the unknown.[3] Errors occur in the quantitative analysis of the structure due to beam broadening if either species A or B is contained in the matrix excited around the structure. Finally, the ability to define the position of a compositional interface from analytical data alone is degraded. The measured apparent compositional profile is a complex convolution of the true compositional profile and the intensity profile of the beam. The intensity profile of the beam may change abruptly at an interface if the scattering powers of the two phases differ markedly.

The scattering conditions for a foil can be estimated from the total elastic scattering cross section σ_e:

$$\sigma_e = 5.21 \times 10^{-21} \frac{Z^2}{E^2} \frac{4\pi}{\alpha(1 + \alpha)} \left(\frac{E + m_0 c^2}{E + 2m_0 c^2} \right)^2 \tag{1}$$

where σ_e is in terms of events/e^-/(atom/cm^2), E is in keV, $m_0 c^2 = 511$ keV, Z is the atomic number, and $\alpha = 3.4 \times 10^{-3} Z^{0.67}/E$.[4,5] The mean free path λ_e can be calculated from the cross section by means of the equation:

$$\lambda_e = A/\sigma_e N_0 \rho \qquad \text{(cm)} \tag{2}$$

where A is the atomic weight, N_0 is Avogardro's number, and ρ is the density. Values of the mean free path for aluminum, copper, and gold are given in Table 1. Finally, the dis-

---

The author is with the National Bureau of Standards, Center for Analytical Chemistry, 222/A121, Washington, DC 20234.

tribution of probabilities of various scattering angles $P(\theta)$ is given by:

$$P(\theta) = (1 + \alpha)[1 - 2\alpha/(1 - \cos \theta + 2\alpha)] \qquad (3)$$

where θ is the scattering angle measured from the incident electron direction. Probabilities of various scattering angles are presented in Table 2. The data in Table 1 indicate that for a typical foil thickness of 100 nm and a beam energy of 100 keV, a condition of single scattering (i.e., the average electron undergoes only one scattering event while passing through the foil) exists for light element targets, whereas for intermediate and high atomic number targets, plural scattering takes place. Even for targets as heavy as uranium, fewer than 25 scattering events (the condition for multiple scattering) are experienced by the average electron in traversing the foil, and thus a condition of multiple scattering is not achieved. Operation at higher beam energies such as 200 keV further reduces the elastic scattering cross section, which results in fewer scattering events. For single scattering, the angular distribution is sharply peaked in the forward direction, and the most probable scattering angle is of the order of a few degrees, as shown in Table 2. Plural scattering gradually broadens this distribution.

Beam broadening has now been investigated by a variety of techniques. A catalog of these methods follows, with comments on their strengths and weaknesses.

Analytic Models

Analytic models have been developed by use of an equation to describe the angular distribution of the scattered electrons. From an assumed conical beam-spreading geometry, the angular distribution is converted into a spatial distribution. Beam broadening is quantified by a distance parameter which describes this cone, generally the diameter of the base. To constrain the cone dimensions, beam broadening is arbitrarily defined as the volume
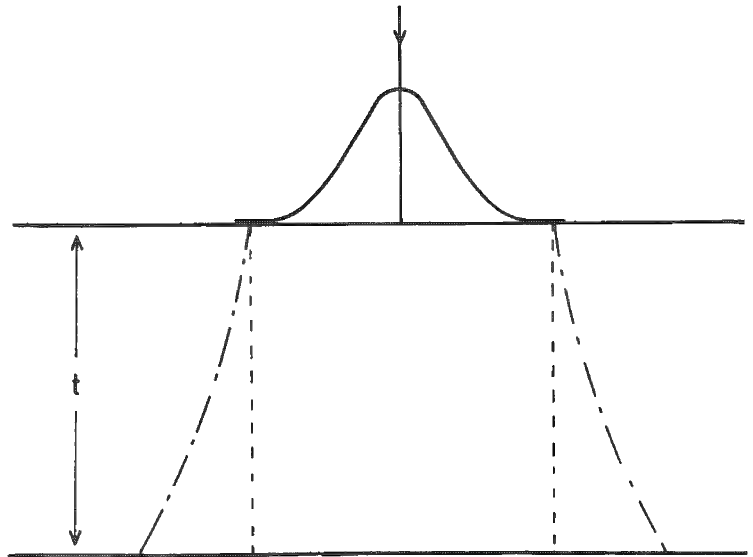
FIG. 1.--Schematic illustration of beam spreading in AEM showing the Gaussian profile of incident beam, volume sampled in absence of scattering (dashed), and with scattering (broken).

TABLE 1.--Elastic mean free path

Element	100 keV	200 keV
Al	96 nm	168 nm
Cu	24	41
Au	8.9	15

TABLE 2.--Elastic scattering angle probabilities (copper target, E = 100 keV).

θ, degrees	$P(\Delta\theta)$*
1°	.190
2°	.294
3°	.195
4°	.111
5°	.065
6°	.039
7°	.026
8°	.018
9°	.012
10°	.009
20°**	.030
30°	.0065
40°	.0022
50°	.0010
90°**	.0011
180°	.0002

*Probability for scattering into an angle interval $\Delta\theta$.

**Note change in the angle interval.

containing 90% of the beam electrons. Analytic models have the general advantage of yielding a single equation which gives a closed-form solution relating the spreading parameter to the specimen and beam properties. The following analytic models have been developed.

Single Scattering. Goldstein et al. derived a beam broadening equation from the cross section for single scattering:[6]

$$b = 6.25 \times 10^2 (\rho/A)^{0.5} (Z/E) t^{1.5} \qquad (4)$$

where b is the broadening (cm) as defined in Fig. 2 experienced by a point beam of energy E (keV). From Table 1, the single-scattering model should be

FIG. 2.--Scattering geometries assumed by (a) single scattering model of Goldstein et al.[6] and (b) plural scattering model of Cliff and Lorimer.[10]

applicable to light element foils, but targets of intermediate and high atomic number should show deviation due to plural scattering. The value of b from Eq. (4) should be regarded as a simple estimate of the beam broadening. By using this estimate, the analyst becomes aware of the minimum size of a structure that can be analyzed with expected matrix sampling errors less than 10% of the measured composition. However, b from this model gives no information on the distribution of electron trajectories within the scattering cone. Direct comparisons of this model with experimental intensity profiles can be misleading. In one case, the apparent discrepancy was erroneously taken as evidence of diminished importance of beam broadening.[7]

The single-scattering model has been refined in two ways to improve its applicability to real measurements. Newbury and Myklebust described a numerical integration technique based upon a planar intersection with the scattering cone which gives a more accurate view of the geometric relationship between the broadening parameter and a simple boundary.[8] Hall et al. incorporated the broadening parameter of Eq. (4) in an intensity distribution equation which convolved the Gaussian distribution of the incident beam with the scattering distribution, on the assumption that it remained Gaussian during its passage through the foil.[9] For a light element foil, this is a reasonable assumption.

Plural Scattering. Cliff and Lorimer have described a beam broadening model based on a description of plural scattering:[10]

$$b = \frac{\theta_0^{1-(2/n)}}{P(\theta)^{\frac{1}{2}}} \left(\frac{6.51 \times 10^{-20} Z^2 N_0 \pi \rho}{E^2 A} \right)^{1/n} t^{1+(1/n)} \qquad (5)$$

where θ_0 is the screening parameter ($\theta_0 = 3.69 \times 10^{-3} Z^{0.33} E^{-\frac{1}{2}}$), $P(\theta)$ is the probability for single scattering through an angle θ, and n is a parameter which describes the condition of plural scattering such that n = 2 when 25 scattering events have occured (the multiple-scattering transition) and n = ∞ when one event has occurred (single-scattering transition). $P(\theta)$ is taken as 0.1 to describe the cone of semi-angle θ which contains 90% of the scattering. The b parameter in Eq. (5) is defined at the midpoint of the foil, and so values from Eq. (5) should be doubled to obtain the cone dimensions at the bottom of the foil. From the data in Table 1, Eq. (5) should provide a better description of broadening for targets of intermediate and high atomic number. A disturbing feature of Eq. (5) is the fact that, as demonstrated by Cliff and Lorimer, substitution of n = 2 (i.e., the multiple scattering condition) in Eq. (5) results in an equation which is nearly identical to Eq. (4) for single scattering. This anomaly remains to be resolved.

Multiple Scattering. Doig et al. have described a model for beam broadening based on a multiple-scattering description of the angular distribution of the scattered electrons.[11] In this case, the angular distribution is Gaussian, and these authors give the following equation for the intensity as a function of radial position r and depth t:

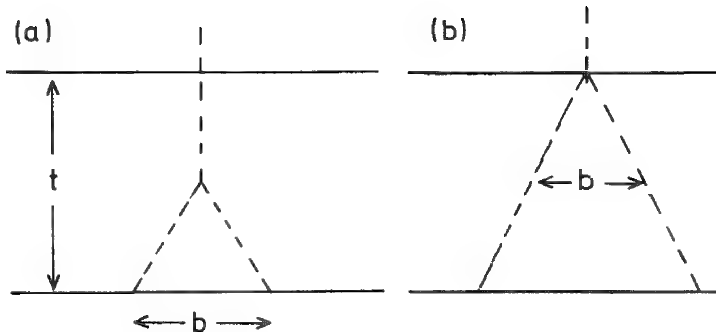$$I(r,t) = I_e [\pi(2\sigma^2 + \beta t^3)]^{-1} \exp[-r^2/(2\sigma^2 + \beta t^3)] \qquad (6)$$

where I_e is the total incident beam current, σ is the standard deviation of the Gaussian beam distribution, and β is given by

$$\beta = \frac{4Z^2}{E} \frac{500}{A} \tag{7}$$

From Table 1, it is expected that this model should only apply to thick foils of high atomic number elements at lower beam energies.

Other Analytic Models. Doig et al. in an earlier paper described a beam broadening model based on an analogy to a radial diffusion equation:[12]

$$I(r,t) = I_e(4\pi D)(t_0 + t)\exp\{-r^2/[4D(t_0 + t)]\} \tag{8}$$

where D is a dispersion coefficient obtained from Monte Carlo calculations and t_0 is the initial beam width parameter. This diffusion model has come under severe criticism for several reasons, including the lack of a physical basis for establishing any analogy with thermal diffusion.[13] Equation (8) predicts a t^2 dependence on thickness as compared to the $t^{3/2}$ of the single scattering equation. We shall not consider the diffusion model further.

Monte Carlo Electron Trajectory Simulation

In the Monte Carlo electron trajectory simulation, the discrete electron paths through the foil are calculated in a stepwise fashion. The scattering is based on appropriate equations for the mean free path and the scattering angle is derived from the differential elastic scattering cross section. Details of adapting the Monte Carlo simulation to the case of a thin foil appropriate to the AEM have been described by Newbury and Myklebust[14,15] and by Kyser.[16] The use of Monte Carlo simulations has been very popular and useful for the study of beam broadening.[13-19] In considering this work, it is worth noting that the term "Monte Carlo simulation" denotes a general technique and not a specific procedure. Thus, different authors have employed different details within their Monte Carlo simulations, such as Mott versus Rutherford cross sections,[19] discrete inelastic scattering versus continuous energy loss (Bethe formula), various screening parameters, and others. Most of these differences can be determined from the description of the simulation provided by the authors. However, there are many fine details that bear on the ways in which the step-by-step trajectory simulation is carried out. These details are rarely reported though they can significantly affect the results. For example, the exact way in which a boundary is introduced into the calculation can have an effect on the final outcome and make comparison of results among different similations difficult. The great strength of the Monte Carlo simulation is the capability of introducing into the calculation any sample/beam geometry desired. The weakness is the necessity of making extensive calculations, since each new situation, e.g., each beam position along a profile, must be recalculated. Often, 25 000 trajectories per point must be calculated, with the consequent computer costs.

Discussion

A comprehensive comparison of this diverse collection of models for beam broadening has not yet been carried out. However, it is possible to make a first-order comparison since all the authors have conveniently reported calculations for beam broadening in foils of aluminum, copper, and gold of approximately 100 nm thickness. These results have been collected in Table 3 and have been reduced to a common basis, namely the diameter of the base of the scattering cone that contains 90% of the electrons. The results are quite surprising. Despite the wide range of physical bases, the models produce similar values of the broadening parameter. Thus, for the relatively strong scattering situation of 100 nm of gold, the values produced by the analytic models and Monte Carlo simulations span a range of only 30%. The largest variation occurs for the relatively weak scattering situation of 100 nm of aluminum, where a factor of three in range is found, with multiple scattering yielding the smallest value. Clearly, the constraints that have been placed on the models serve to minimize the differences in the physical bases of the models, which would not be expected to correspond so closely. In reality, all these models are modifications of single scattering and are strongly influenced by this characteristic. The choice of a "right" model is somewhat ambiguous and will require construction of carefully designed experiments

to sort out differences in the models.

TABLE 3.--Beam spreading from a point beam in thin
foils: Broadening parameter* (nm).

Model	Al	Cu	Au
Single[6]	8.1	21.4	48.9
Plural[10]**	17.4	24.8	36.6
Multiple[11]	6.0	17.0	38.0
Monte Carlo[14]	7.6	17.5	52.2
Monte Carlo[16]	9.0	16.0	38.0

Conditions: 100nm foil, 100keV point beam.
 *Broadening parameter defined as diameter
of scattering cone base containing 90% of
electrons.
 **Results scaled to 100nm thickness.

References

1. J. J. Hren, J. I. Goldstein, and D. C. Joy, Eds., *Introduction to Analytical Electron Microscopy,* New York: Plenum, 1979.

2. J. I. Goldstein, D. E. Newbury, P. Echlin, D. C. Joy, C. E. Fiori, and E. Lifshin, *Scanning Electron Microscopy and X-ray Microanalysis* New York: Plenum, 1981.

3. G. Cliff and G. W. Lorimer, "The quantitative analysis of thin specimens," *J. Microscopy* 103: 203-207, 1975.

4. L. Reimer and E. R. Krefting, "The effect of scattering models on the results of Monte Carlo calculations," in K. F. J. Heinrich, D. E. Newbury, and H. Yakowitz, Eds., *Use of Monte Carlo Calculations in Electron Probe Microanalysis and Scanning Electron Microscopy,* National Bureau of Standards Special Publication 460, Washington, D.C., 1976, 45-60.

5. H. E. Bishop, *The History and Development of Monte Carlo Methods for Use in x-ray Microanalysis,* NBS Special Publication 460, Washington, D.C., 5-13.

6. J. I. Goldstein, J. L. Costley, G. W. Lorimer, and S. J. B. Reed, "Quantitative x-ray analysis in the electron microscope," *SEM/1977* I, 315-324.

7. E. L. Hall and J. B. Vander Sande, "The effect of sample thickness on high spatial resolution composition profiles," *Proc. EMSA* 37: 474-475, 1979.

8. D. E. Newbury and R. L. Myklebust, "Calculations of electron beam spreading in composite thin foil targets," *Microbeam Analysis--1980,* 173-175.

9. E. L. Hall, D. Iveson, and J. B. Vander Sande, "On producing high spatial resolution composition profiles via scanning transmission electron microscopy" *Phil. Mag.* A43: 1569-1585, 1981.

10. G. Cliff and G. W. Lorimer, "Influence of plural electron scattering on x-ray spatial resolution in TEM thin foil microanalysis," in *Quantitative Microanalysis with High Spatial Resolution,* Book 277, Metals Society (London), 1981, 47-52.

11. P. Doig, D. Lonsdale, and P. E. J. Flewitt, "Electron intensity distributions in STEM-EDS x-ray microanalysis of thin foils," *ibid.,* 41-46.

12. P. Doig, D. Lonsdale, and P. E. J. Flewitt, "The spatial resolution of x-ray microanalysis in the scanning transmission electron microscope," *Phil. Mag.* A41: 761-775, 1980.

13. I. P. Jones, "Comment on 'The spatial resolution of x-ray microanalysis in the scanning transmission electron microscope,'" *Phil. Mag.* A44: 1401-1405, 1981.

14. D. E. Newbury and R. L. Myklebust, "Monte Carlo electron trajectory simulation of beam spreading in thin foil targets," *Ultramicroscopy* 3: 391-395, 1979.

15. D. E. Newbury and R. L. Myklebust, "A Monte Carlo electron trajectory simulation for analytical electron microscopy," *Analytical Electron Microscopy--1981,* 91-98.

16. D. F. Kyser, "Monte Carlo simulation in analytical electron microscopy," in Ref. 1, 199-221.

17. R. G. Faulkner, T. C. Hopkins, and K. Norrgard, "Improved spatial resolution microanalysis in a scanning transmission electron microscope," *X-ray Spectrometry* 6: 73-79, 1977.

18. I. P. Jones and M. H. Loretto, "Some aspects of quantitative STEM x-ray microanalysis," *J. Microscopy* 124: 3-13, 1981.

19. T. A. Stephenson, M. H. Loretto, and I. P. Jones, "Beam spreading in thin foils," in Ref. 10, 53-56.

LOCALIZATION IN THE ORIENTATION DEPENDENCE OF X-RAY AND ENERGY LOSS SPECTRA

A. J. Bourdillon

The Borrman[1] effect, first observed in x-ray scattering, occurs also in electron scattering and is due to channeling of elastically scattered particles in the atomic planes of a crystalline lattice. Such channeling belongs to the mainstream of studies involving electron imaging in a transmission electron microscope. The effect can cause serious errors in microanalysis by energy-dispersive spectroscopy (EDS);[2,3] though it can also be positively used, for example, to identify interstitial positions of atomic species,[4-6] or, as a fundamental feature of transmission electron microscopy, to gain understanding of quantitative electron energy-loss spectroscopy[7] (EELS) and of localization in electron scattering.

When a crystalline foil in an electron microscope is rocked about the Laue condition for a low-index diffraction plane there is generally found to be an increase in absorption as it is tilted from beyond the Bragg condition to the symmetric Laue condition. In monatomic systems, such as nickel and germanium, Hall[8] has correlated his observations with calculations based on an independent Block-wave approach, and Cherns, Howie, Jacobs[9] were able to give a better description of the thickness dependence of similar results by taking into account Block-wave summations. In compound systems and ordered alloys, although the absorption tends again to increase when the foil is rotated towards the Laue condition, the different potentials at the sites of the different atomic species tend to cause different local current intensities that result in one species absorbing more strongly than another. Bourdillon, Self, and Stobbs[2] measured the change of ratio of Cu to Pt x-ray emission intensities as an ordered alloy was rotated about 111, 11$\bar{3}$ and 33$\bar{1}$ Bragg conditions, and correlated their results convincingly with Block-wave calculations using a systematic row of thirteen summed beams. They found ratios of count rates varying by 45% depending on the crystal orientation adopted (Figure 1), whereas calculations showed that much larger variations are to be expected in foils thinner than those actually studied.

In routine microanalysis one can reduce these variations by insuring that measurements are taken away from low-index Bragg conditions and also, where probe size can be sacrificed, by using probes of high convergence (i.e., larger than the Bragg angle), which will tend to average out the fluctuations. The convergence used in the measurements of Figure 1 was 1/5 of the Bragg angle, which is less than that of a typical STEM probe. These procedures are important since corrections are difficult to make. Nonsystematics have an effect on the absorption that is extremely difficult to calculate, and the absorption ratios are sensitive to foil thickness, the absorption rate (computed using a complex potential), the atomic potentials, crystal structure and defects, and the temperature of the foil. (Extraction replicas can rise several hundred degrees under an electron beam.) On the other hand, the ratio of emission rates of foils containing solid solutions should be unaffected by the Borrman effect, but behave as shown by the dotted line in Fig. 1. There has also been some doubt[10] about the localization of the electron interaction which, if it is larger than the crystal lattice spacing, tends to reduce the orientation effects. The following calculations are an attempt to give an improved description of the impact parameter, first independently of scattering angle effects, and second by comparison with Rutherford scattering.

Localized Effects

    a. From time-dependent perturbation theory. In conventional scattering experiments

---

The author is at the Department of Metallurgy and Materials Science, University of Cambridge, England.
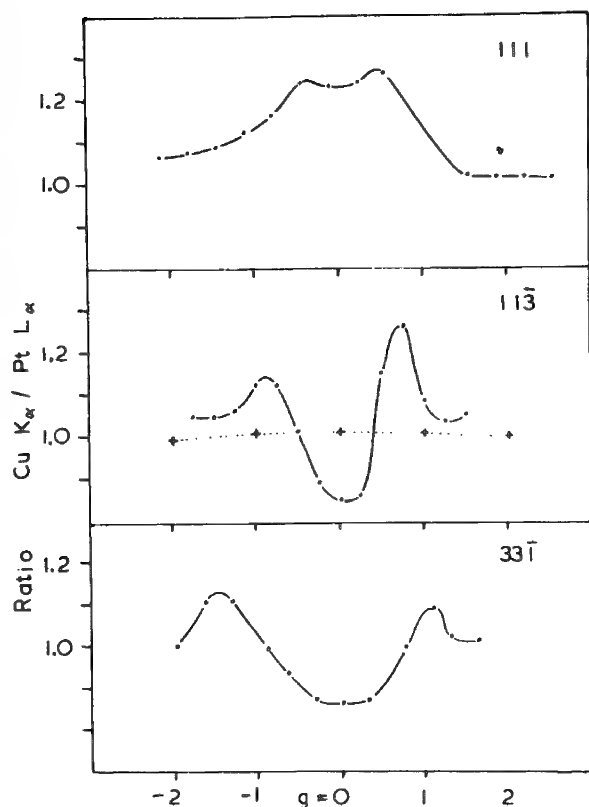
FIG 1.--Measured ratios of Cu Kα to Pt Lα peak intensities at tilts around Bragg 111, 11$\bar{3}$ and 33$\bar{1}$ conditions for films of thickness $6\xi_{111}$, $3\xi_{111}$, and $4\xi_{111}$, respectively. Dotted line shows ratio at 113 condition when superlattice is not evident. Orientation is expressed in multiples of basic reciprocal lattice (not superlattice) vector. A value of 1 corresponds to Bragg condition being satisfied for this lattice vector. (Courtesy *Phil. Mag.*)

FIG. 2.--Calculated values of f (see text), derived from $P(K_0^2 + K_1^2)$, as function of cutoff radius. Dotted line shows effect of ignoring term in K_1^2, arrows show cutoff radii for shells measured in Ref. 7.

the impact parameter is not observed since the detector is placed far away from the scatterer and what happens in its immediate vicinity is not measured. From semiclassical time-dependent perturbation theory,[11,12] the probability for exciting an atomic electron state i to an optically allowed state j, by a passing fast electron in an approximately nonrelativistic rectilinear orbit, with velocity v and impact parameter b, may be written

$$P_{ji}(b) = \frac{e^4}{(4\pi\varepsilon_0 \hbar)^2} \frac{R_{ji}}{3\rho_i} \frac{4}{(bv)^2} \beta^2 [K_0^2(\beta) + K_1^2(\beta)] \qquad (1)$$

where $\quad R_{ji} = \Sigma | \int \psi_j(\underline{r}) \cdot \underline{r} \cdot \psi_i(\underline{r}) \ d^3r |^2$

summing over the degenerate states of the initial and final levels, $\beta = b\Delta E/\hbar v$, and ΔE is the energy loss suffered by the incident electron; K_0 and K_1 are modified Bessel functions and ρ_i is the statistical weight of level i.

The distribution of Eq. (1) can be used to obtain an expectation value for the impact parameter of the form

$$\langle b \rangle = \frac{\hbar v}{2\Delta E} \cdot f$$

where f is a factor that may be numerically calculated provided a cut-off plateau is substituted for $P(K_0^2 + K_1^2)$, where $\beta < \beta_c$ and β_c represents the finite size of ψ_i. Calculated values of f as a function of β_c are shown in Fig. 2, including values for some ground state shells whose size is taken from calculated Slater orbitals,[13] and also a more elementary value previously described, where the change in $|k|$ vector of the scattering particle was ignored.

These results imply that in EDS measurements that typically involve energy losses of more than 1 kV, orientation effects are normally to be expected. However, measurements have been conducted at lower energies by EELS in order to check this theory.
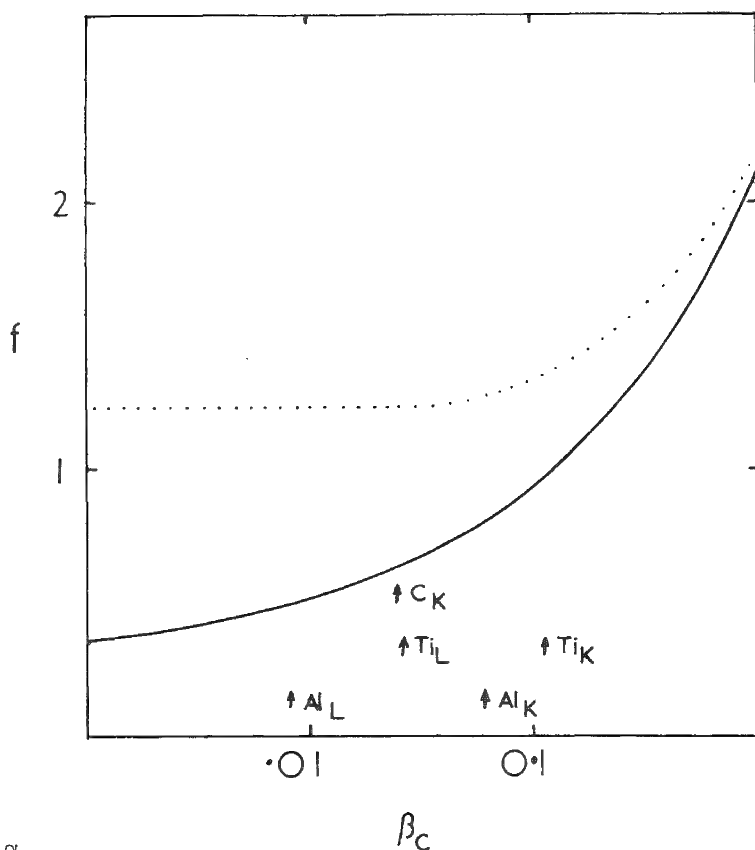
The impact parameter applicable to EELS differs from that in EDS in three important respects. In the former, energy losses tend to be smaller, collection angles are defined, and energy windows are defined. These factors have been previously discussed,[2] and the energy dependence was found to be generally consistent with experiment.[7] The importance of the second factor is consistent with the classical result that small impact parameters imply large scattering angles. Thus a defined collection angle imposes a lower limit on b whose dependence on the scattering angle θ may be calculated from classical Rutherford scattering formulas.

b. *From Rutherford Scattering.* Here,

$$b = \frac{e^2}{4\pi\varepsilon_0 m' v^2} \cot \theta/2$$

where m' is the reduced electronic mass and ε_0 the permittivity of free space.

For a given axial collection angle θ_c, the expectation value $\langle\theta\rangle$, can be calculated from the well known probability distribution proportional to $\theta/(\theta^2 + \theta_{\Delta E}^2)$,[14,15] where $\theta_{\Delta E} = \Delta E/mv^2$. Thus

$$\langle\theta\rangle = [\theta_c - \theta_{\Delta E} \arctan(\theta_c/\theta_{\Delta E})]/\ln[(\theta_c^2 + \theta_{\Delta E}^2)/\theta_{\Delta E}^2)$$

whence $\langle b \rangle$ may be derived (Fig. 3) for the specific case of an energy loss of 500 eV, less than less detailed previous estimates.[2] These calculations are consistent with our experimental findings, in which EELS orientation effects showed little change when the collection semi-angle was varied between 25 and 5 mrad for the TiL(456 eV) edge.

In conclusion, although results available at present are reasonably consistent with theoretical considerations, continued effort should make it possible to measure the impact parameter more precisely by means of EELS in spite of the difficulties involved in disentangling elastic from inelastic effects. A knowledge of this parameter is of importance not only to microanalysis and EELS, but also to a variety of related studies including fine structure studies and Compton scattering.[16]
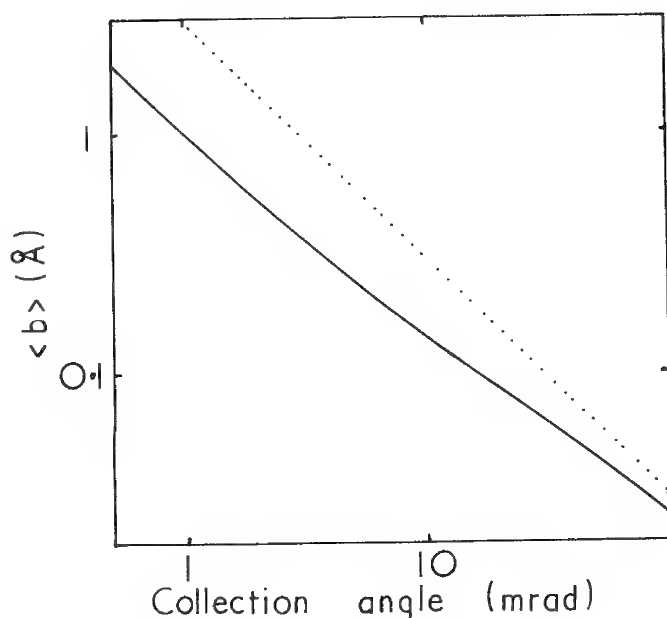
FIG. 3.--Calculated expectation value for ⟨b⟩ vs collection semi-angle, θ_c (solid line) compared with limiting values derived from uncertainty principle (dotted line) for incident energy of 100 kV and energy loss of 500 eV.

References

1. G. Borrman, *Phys. Z.* 42: 157, 1941.
2. A. J. Bourdillon, P. G. Self, and W. M. Stobbs, "Crystallographic orientation effects in energy dispersive x-ray analysis," *Phil. Mag.* A44: 1335, 1981.
3. J. Taftø, "Channelling effects in electron-induced x-ray emission from diatomic crystals," *Z. Naturf.* 34a: 452, 1979.
4. J. A. Golovchenko, B. W. Batterman, and W. L. Brown, "Observation of internal x-ray wave fields during Bragg diffraction with an application to impurity lattice location," *Phys. Rev.* B10: 4239, 1974.
5. S. K. Anderson, J. A. Golovchenko, and G. Mair, "New applications of x-ray standing wave fields to solid-state physics," *Phys. Rev. Lett.* 37: 1141, 1976.
6. J. Taftø, J. C. H. Spence, and O. L. Krivanek, "Channelling and blocking effects in characteristic energy losses of 100 keV electrons" (to be published).
7. A. J. Bourdillon and W. M. Stobbs, "Current applications of electron energy loss spectroscopy," High-resolution Workshop, Arizona, January 1982 (to be published in *Ultramicroscopy*).
8. C. R. Hall, "On the production of characteristic x-rays in thin metal crystals," *Proc. Roy. Soc.* A295: 140, 1966.
9. D. Cherns, A. Howie and M. H. Jacobs, "Characteristic x-ray production in thin crystals," *Z. Naturf.* 28a:565, 1973.
10. A. Howie, "The theory of high energy electron diffraction," *J. Microsc.* 117: 1, 1979.
11. M. J. Seaton, "The impact parameter method for electron excitation of optically allowed atomic transitions," *Proc. Phys. Soc.* 79: 1105, 1962.
12. U. Fano, "The formulation of track structure theory," G. E. Adams, D. K. Bewley, and J. W. Boag, Eds., *Proc 2nd L. H. Gray Conf.*, Cambridge, 1970, 1.
13. E. Clementi, "Simple basis set for molecular wavefunctions containing first- and second-row atoms," *J. Chem. Phys.* 40: 1944, 1964.
14. J. Hubbard, "The dielectric theory of electronic interactions in solids," *Proc. Phys. Soc.* A68: 976, 1955.
15. R. A. Ferrel, "Angular dependence of the characteristic energy loss of electrons passing through matter," *Phys. Rev.* 101: 554, 1956.
16. B. G. Williams and A. J. Bourdillon, "Measurement of electron momentum densities using an electron microscope: A new approach to Compton scattering," *Proc. EMAG*, Cambridge, 1981, Institute of Physics (to be published).

BEAM BROADENING IN A STRONGLY SCATTERING TARGET IN THE ANALYTICAL ELECTRON MICROSCOPE

A. D. Romig Jr., D. E. Newbury, and R. L. Myklebust

Beam broadening has been studied in alloys of uranium-niobium and uranium-molybdenum. Profiles have been measured across interphase boundaries for which the solute element is located exclusively in one phase. Experimental measurements have been compared with calculated profiles obtained with a Monte Carlo electron trajectory simulation. Good agreement is obtained in the immediate region of the boundary. A long low intensity tail is indicated by the calculations but this tail is not observed experimentally. Studies of the effect of varying specimen and beam parameters indicate the difficulty in obtaining accurate experimental profiles. Uncertainties of the order of ±10% in these parameters produce measurable effects.

The problem of evaluating beam broadening in thin foils analyzed in the analytical electron microscope (AEM) has been studied by mean of both theoretical and experimental approaches.[1,2] The experiments reported to date have been carried out on materials of low to intermediate atomic number, including TiC,[3] Fe-15% Ni,[4] various steels,[5-7] MgO with an Fe grain boundary enrichment,[8,9] and silicon with a gold tracer.[10] Beam broadening is a direct result of elastic scattering, and the elastic scattering cross section increases with the square of the atomic number ($\sigma_e \propto Z^2$). It should therefore be interesting to examine beam broadening in a situation of strong scattering in a high-atomic-number matrix. For this purpose, we have chosen to examine interphase boundaries in uranium-niobium and uranium molybdenum alloys. The properties of these alloys are summarized in Table 1. Both alloys contain two phases which consist of a matrix of essentially pure uranium and a second phase in which all the solute resides, and forms an intermetallic compound in the U-Mo system (U_2Mo) and a solid solution in the U-Nb system. The densities of all three phases are high and the solute is present at a level of approximately 15 wt.% in the second phase. The electron scattering powers are thus similar on both sides of the interface. Since the solute element is located exclusively in one phase, it provides a sharp change in signal at the boundary which is useful in evaluating the tail of the scattering distribution.

Experimental Procedure

Alloys were prepared by induction melting of the pure elements (99.9% purity), vacuum arc remelting, upset forging, and cross rolling. Heat treatments are listed in Table 1. The lamellar structure which is obtained in both alloys is shown for U-2 wt.% Mo in the scanning electron micrograph of Fig. 1. The techniques employed for sample preparation for the AEM included electropolishing and have been described previously.[11]

The configuration of the AEM included an energy-dispersive x-ray spectrometer at 90° to the beam, which necessitated tilting the specimen to 45° to obtain a satisfactory x-ray take-of angle (45°). The interphase boundary was carefully oriented parallel to the beam and facing the detector. A beam 18 nm in diameter (calculated from manufacturer's data) was traversed in 10nm steps from -100 nm to +100 nm across the boundary. Approximately 10 000 counts were accumulated in the Kα x-ray peak of the solute element when the beam was located within the second phase. With replicate determinations, this count level yields a statistical uncertainty of σ = 1% in this intensity (I solute-2nd phase). The intensity ratios across the profile were calculated as ratio = ^{I}solute/^{I}solute-2nd phase. When the normalized intensity ratio fell to 0.1, the uncertainty increased to approxi-

Author Romig is a member of the technical staff of Sandia National Laboratory, Box 5800, Albuquerque, NM 87185; authors Newbury and Myklebust are with the Center for Analytical Chemistry, National Bureau of Standards, Washington, DC 20234.

TABLE 1.--Alloy phase data.

Uranium - Niobium (alloy composition U - 6 weight % Nb)

    α - pure U (density 19.05 g/cc)

    γ - U - 12 weight % NB (density 16.60 g/cc) solid solution

        Heat treatment: 850 °C for 1 hour; furnace cool to
                      600 °C, hold 2 hours at 600 °C;
                      water quench.

Uranium - Molybdenum (alloy composition U - 2 weight % Mo)

    α - pure U (density 19.05 g/cc)

    δ - U_2Mo (density 16.63 g/cc) intermetallic compound;
        U = 83.2 weight %; Mo = 16.8 weight %

        Heat treatment: 850 °C for 1 hour; furnace cool to
                      450 °C; hold 2 hours at 450 °C;
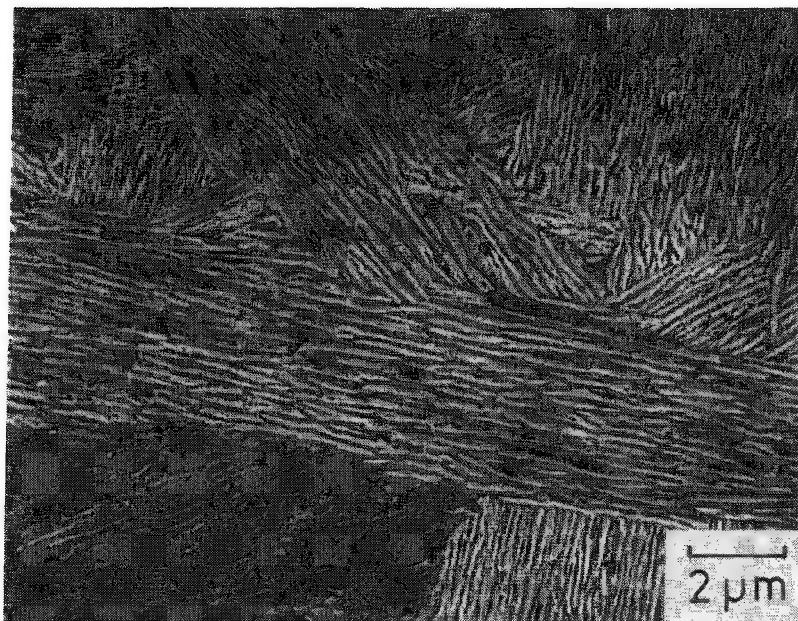   water quench

FIG. 1.--Structure of U-Mo alloy produced by heat treatment described in Table 1.

mately σ = 4%, and at a ratio of 0.01, the uncertainty increased to σ = 10%. Peak intensity values were separated from spectral background by means of a digital filter. Interfering minor uranium L peaks were stripped from the Nb Kα peak by an empirical technique described previously.[11] The thickness of the foil was determined by means of two independent techniques: (1) the contamination spot method and (2) an x-ray absorption method.[12] The absorption technique is based on a solution of the equation:[13]

$$\frac{I_A}{I_B} = \frac{(C_A/C_B)}{k_{AB}} \left[\frac{\mu/\rho \Big|_{spec}^{A}}{\mu/\rho \Big|_{spec}^{B}} \right] \left[\frac{1 - \exp\left(-\mu/\rho \Big|_{spec}^{B} \csc \psi\rho \ t\right)}{1 - \exp\left(-\mu/\rho \Big|_{spec}^{A} \csc \psi\rho \ t\right)} \right] \tag{1}$$

where I is the measured intensity, k_{AB} is the Cliff-Lorimer sensitivity factor determined on a known standard, μ/ρ is the mass absorption coefficient for the constituent in the specified phase, ψ is the take-off angle, C is the concentration, A and B denote two elements, and t is the thickness. For a measured I_A/I_B value Eq. (1) is solved iteratively for t until $(I_A/I_B)^{calc} = (I_A/I_B)^{meas}$. Thicknesses calculated with Eq. (1) were found to agree with thicknesses determined by the contamination spot method within 10%. The phases were found to polish nearly identically, so that virtually no change in thickness occurred across the interface.

Monte Carlo Electron Trajectory Calculations

A comprehensive Monte Carlo electron trajectory simulation adapted specifically to the case of planar boundaries in thin foils was used to calculate intensity profiles across interphase boundaries.[14,15] The details of this Monte Carlo procedure, which employs a screened Rutherford cross section for elastic scattering, have been previously described.[14,15] A Gaussian intensity profile across the beam was assumed, aand the beam diameter was calculated to be 18 nm from the instrument manufacturer's data. On the assumption that this beam contained 80% of the total flux, a standard deviation σ could be calculated for the Gaussian beam. The extent of the calculated beam was taken to ±4σ of this distribution. The intensity calculated for the solute element at each location was normalized with the intensity calculated in the pure second phase, e.g., U_2Mo or U-12%Nb.

At each point in the profile, 25 000 electron trajectories were calculated. The reproducibility of the calculation was estimated by replication of calculations for identical conditions of beam position and sample parameters but with different random number sequences. When the beam position was located such that the calculated intensity ratio was 0.1, the standard deviation of six calculations was 2.3%.

Discussion

The experimental and calculated profiles are compared for the two alloy systems at two different thicknesses in Tables 2A, 2B (U-Nb) and 3A, 3B (U-Mo). In general, the agreement between the calculated and measured profiles is satisfactory. For thin samples more scatter is noted; this scatter may result from differences in sample thickness. The calculation follows the measured value in the immediate region of the boundary. The calculated profiles show a long tail in the low-intensity region that is not observed experimentally. Considering the difficulty in measuring relative intensities at a level of 1-2%, it is perhaps not surprising that this tail is not observed. We believe this calculated tail is a real effect that might be detected with longer accumulation times.

Monte Carlo calculations can also be used to study the effect of deviations in the values of beam and foil parameters. Table 4 contains the results for conditions of one foil composition and thickness and one beam location as the following parameters are varied: beam size (±3 nm); beam position (±2.5 nm); sample thickness (±10 nm); and differences in the sample thickness (±10 nm) between the reference location in the pure phase used for profile normalization and the beam location along the profile. Substantial deviations from the nominal value of the ratio are observed as beam and specimen parameters are varied. Variations in beam position and sample thickness produce especially large deviations. It is thus not surprising that occasional deviations between experimental and calculated values are noted. Table 4 reveals the need for careful experimental work

TABLE 2.--Intensity profile across an α/γ interface in U-Nb; E = 100 kV, beam = 18 nm; ratios are of $I_{solute}/I_{solute-2nd\ phase}$.

(A) t = 60 nm			(B) t = 110 nm		
Position (nm)	Measured ratio	Calculated ratio	Position (nm)	Measured ratio	Calculated ratio
-100	.99	1.0	-100	1.0	.98
-90	1.02	1.0	-90	1.0	.98
-80	.99	1.0	-80	.98	.97
-70	1.0	1.0	-70	.99	.98
-60	.99	1.0	-60	.99	.96
-50	.99	.99	-50	.98	.96
-40	.98	.99	-40	.95	.96
-30	1.0	.98	-30	.93	.94
-20	.95	.97	-20	.91	.91
-10	.89	.92	-10	.84	.83
0	.49	.51	0	.51	.51
10	.11	.095	10	.20	.19
20	.056	.034	20	.13	.10
30	.011	.021	30	.091	.070
40	.023	.016	40	.066	.054
50	0.0	.017	50	.052	.044
60	.005	.013	60	.041	.037
70	0.0	.013	70	.018	.028
80	0.0	.009	80	.006	.029
90	0.0	.009	90	0.0	.026
100	0.0	.007	100	0.0	.023

TABLE 3.--Intensity profile across an α/δ interface in U-Mo; E= 100 kV, beam = 18 nm; ratios are of $I_{solute}/I_{solute-2nd\ phase}$.

(A) t = 55 nm			(B) t = 115 nm		
Position (nm)	Measured ratio	Calculated ratio	Position (nm)	Measured ratio	Calculated ratio
-100	1.0	1.0	-100	1.0	1.0
-90	1.0	.99	-90	1.0	1.0
-80	1.0	.99	-80	1.0	1.0
-70	1.0	.99	-70	1.0	1.0
-60	1.0	.99	-60	.99	.99
-50	1.0	.99	-50	.97	.97
-40	.99	.99	-40	.96	.96
-30	.99	.98	-30	.94	.94
-20	.97	.98	-20	.91	.92
-10	.93	.92	-10	.83	.83
0	.51	.51	0	.50	.51
10	.10	.090	10	.19	.19
20	.048	.032	20	.11	.10
30	.020	.020	30	.072	.066
40	.019	.017	40	.061	.051
50	.010	.012	50	.037	.043
60	.009	.011	60	.020	.041
70	0.0	.0085	70	.013	.036
80	0.0	.0083	80	.005	.033
90	0.0	.0082	90	0.0	.027
100	0.0	.0080	100	0.0	.021

if accurate profiles are to be obtained.

Conclusions

Beam spreading in strongly scattering foils can be modeled with reasonable accuracy with the Monte Carlo electron trajectory simulation. Parameter variation studies suggest that errors of the order of ±10% in critical parameters, such as thickness, beam size, and beam position, will substantially affect measured profiles.

References

1. D. E. Newbury, "Beam spreading in the analytical electron microscope," *Microbeam Analysis-1982,*
2. I. P. Jones and M. H. Loretto, "Some aspects of quantitative STEM x-ray microanalysis," *J. Microscopy* 124: 3-13, 1981.
3. R. G. Faulkner, T. C. Hopkins, and K. Norrgard, "Improved spatial resolution microanalysis in a scanning transmission electron microscope," *X-ray Spectrometry* 6: 73-79, 1977.
4. A. D. Romig Jr., Thesis, Lehigh University, 1979.
5. P. Rao and E. Lifshin, "Microchemical analysis in sensitized stainless steels," *Proc. 12th Conf. Microbeam Analysis Society,* 1977, 118A-F.
6. D. B. Williams and J. I. Goldstein, "STEM/x-ray microanalysis across alpha/gamma interfaces in Fe-Ni meteorites, *Proc. 9th Int. Congress E.M. (Toronto)* 1: 416-417, 1978.
7. C. E. Lyman, P. E. Manning, D. J. Duquette, and E. Hall, "STEM microanalysis of duplex stainless steel weld metal," *SEM/1978-1,* 213-220.
8. T. Mitamura, E. L. Hall, W. D. Kingery, and J. B. Vander Sande, "Grain boundary segregation of iron in polycrystalline magnesium oxide observed by STEM," *Ceramurgica Int.* 5: 131, 1979.
9. E. L. Hall, D. Imeson, and J. B. Vander Sande, "On producing high-spatial-resolution composition profiles via scanning transmission electron microscopy," *Phil. Mag.* A43: 1569-1585, 1981.
10. R. Hutchings, M. H. Loretto, I. P. Jones, and R. E. Smallman, "Spatial resolution in x-ray microanalysis of thin foils in STEM," *Ultramicroscopy* 3: 401, 1979.
11. A. D. Romig Jr., "Quantitative x-ray microanalysis of U-Nb alloys with the scanning transmission electron microscope," *Microbeam Analysis--1981,* 249-257.
12. A. D. Romig Jr., "Calculation of foil thicknesses by an X-ray absorption technique," submitted to *J. Microscopy,* 1982.
13. J. I. Goldstein, J. L. Costley, G. W. Lorimer, and S. J. B. Reed, "Quantitative x-ray analysis in the electron microscope," *SEM/1977,* 315-324.
14. D. E. Newbury and R. L. Myklebust, "Monte Carlo electron trajectory simulation of beam spreading in thin foil targets," *Ultramicroscopy* 3: 391-395, 1979.
15. D. E. Newbury and R. L. Myklebust, "A Monte Carlo electron trajectory simulation for analytical electron microscopy," *Analytical Electron Microscopy--1981,* 91-98.

TABLE 4.--Effect of variation in sample and beam parameters on calculated intensity ratios.

Nominal Conditions

Composition, U/U-12 Nb; thickness, 110 nm; beam location, -10 nm (in U-NB phase); beam diameter, 18 nm; calculated $I_{Nb}/I_{Nb(pure-2nd phase)}$ = 0.826.

Variations in Beam Size

15 nm, ratio = 0.833; 25 nm, ratio = 0.818.

Variations in Beam Position

-7.5 nm, ratio = 0.779; -12.5 nm, ratio 0.856.

Variations in Sample Thickness

Thickness identical at beam position and at reference point:
100 nm, ratio = 0.863; 120 nm, ratio = 0.810.

Reference thickness = 110 nm:
100 nm, ratio = 0.779; 120 nm, ratio = 0.887.

SPECIMEN PREPARATION LIMITATIONS IN QUANTITATIVE THIN FOIL MICROANALYSIS

H. L. Fraser and J. P. McCarthy

The limitations of specimen preparation techniques in quantitative microchemical analysis of thin foils is considered. An example of such limitations is given for the case of electropolished Ni-base alloys. In particular, the surface layers that form as a result of this prepration technique have been studied. It is shown that the presence of these films causes serious errors in quantitation of x-ray microanalytical data since their compositions are usually somewhat different from that of the specimen itself. Attempts have been made to remove the films by Ar ion sputtering; although these experiments are not yet complete, it appears that this technique may indeed reduce the errors involved in analysis arising from this phenomenon.

In general, thin foils of bulk metallic specimens are prepared by either electropolishing, chemical, or ion-milling techniques. Although foils suitable for imaging in transmission are produced in this way, it appears that the surfaces of prepared specimens are not typical of the bulk material of interest.[1,2] The presence of surface layers having compositions different from that of the underlying specimen may cause large errors during quantification of intensity data. Thus, it is generally accepted that microchemical determinations by scanning transmission electron microscopy (STEM) coupled with either energy dispersive x-ray spectroscopy (EDS) and/or electron energy loss spectroscopy (ELS) should be effected in as thin a foil as possible. The reasons include maximizing the x-ray spatial resolution of EDS, which is degraded by beam spreading in thick sections, and reducing the extent of plural scattering in ELS. The nature of these surface films differ according to the preparation technique used and the materials being studied. In the interest of brevity, this paper considers the problems associated with electropolishing by giving an example taken from a recent study of quantitation of thin foils of β-NiAl, an ordered intermetallic compound, and a multiphase Ni-base superalloy.

Surface Layers on β-NiAl

Thin disks were cut from well-characterized single crystal of β-NiAl of composition 50.4 at.%Al, and were electropolished in a 10% perchloric acid/methanol solution at 0°C with an applied voltage of about 30 V. Measurements were made of the ratio of intensities of the Ni Kα to Al Kα peaks in foil less than 900 Å thick, i.e., sufficiently thin so that x-ray absorption effects may be ignored. At an accelerating voltage of 120 kV, the average value of the measured intensity ratio was

$$I_{Ni}/I_{Al}\Big|_{experimental} = 1.87 \pm 0.05$$

A recent contribution concerning the use of pure elemental standards has shown that reliable standards exist for the case of Ni and Al (electropolished Ni, and rapidly solidified Al powers).[1] Since intensity/thickness values were obtained on the same electron microscope used in the present study, they may be applied directly in the analysis of the intensity data derived for β-NiAl. Thus, if the composition of the β-NiAl compound is known, the intensity ratio, determined experimentally above, may be deduced from the standards. The value obtained is given by

$$\left. I_{Ni}/I_{Al}\right|_{standards} = 2.18 \pm 0.07$$

The difference between the two sets of results may be accounted for in the following manner. Suppose there are thin surface layers of Al_2O_3 on the foil of β-NiAl; the data from the standards may then be used to calculate the expected intensity ratio. For example, on a foil 900 Å thick, the difference in the intensity ratios given above imply an oxide layer of about 57 Å. To verify this deduction independently, Auger electron spectroscopy (AES) was used coupled with Ar ion sputtering to permit a depth profile of the surface of electropolished β-NiAl to be determined. The results are given in Fig. 1, where it is clear that there is indeed a significant surface layer rich in Al. On the basis of sputtering yields for Al_2O_3, this surface layer is found to be 60-100 Å thick. The agreement between the results of these two independent determinations should be noted. It is concluded, then, that a thin Al-rich oxide layer exists on the surfaces of electropolished β-NiAl, the presence of which causes an error of approximately 13% to be introduced into the quantitative analysis procedures.

Surface Layers on Ni-base Superalloys

A large number of electropolished Ni-base superalloys, of widely differing compositions, has been examined regarding the possibility of surface films. The results of experiments aimed at determining the presence and effect of such films were essentially identical in all alloys studied, so that the following discussion will be limited to the case of one alloy, Ni-13Al-9Mo-2Ta, whose behavior is considered typical.
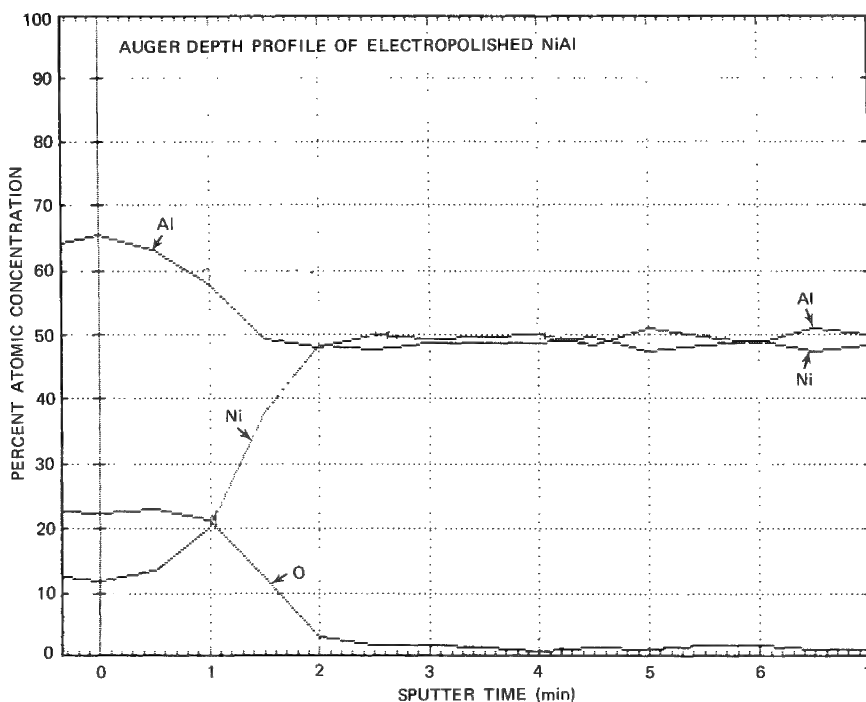
FIG. 1.--Depth profile for the surface of electropolished β-NiAl produced using Auger electron spectroscopy and Ar ion sputtering.

Figure 1 shows the two phase (γ/γ') structure of an as-electropolished sample. The crystal has been oriented such that the electron beam is close to the <001> direction, and the corresponding diffraction pattern is shown in Fig. 3. Clearly visible are both the fundamental and $L1_2$ superlattice reflections. After approximately 20 min exposure to the electron beam (current density of about 20 A/cm^2), a large number of very small ($\leq$100 Å) precipitates have formed on the surfaces of the foil (Fig. 4). The corresponding diffraction pattern (Fig. 5) reveals the presence of a number of rings, which are consistent with a polycrystalline assembly of the compound Al_3Ni_2. The origin of these small phases of Al_3Ni_2 is not known, but it is reasonable to assume that beam heating has permitted the compound to precipitate from the surface film that results from electropolishing. The Al_3Ni_2 appears to be rather stable even in the presence of the oxide.

The effect that such a surface layer might have concerning quantification of x-ray data may be estimated by a simple calculation for the phase Ni_3Al. Thus, for a 900Å-thick foil of Ni_3Al with Al_3Ni_2 surface layers about 60 Å thick with the data from the pure elemental standards discussed above, the following intensity ratios may be calculated.
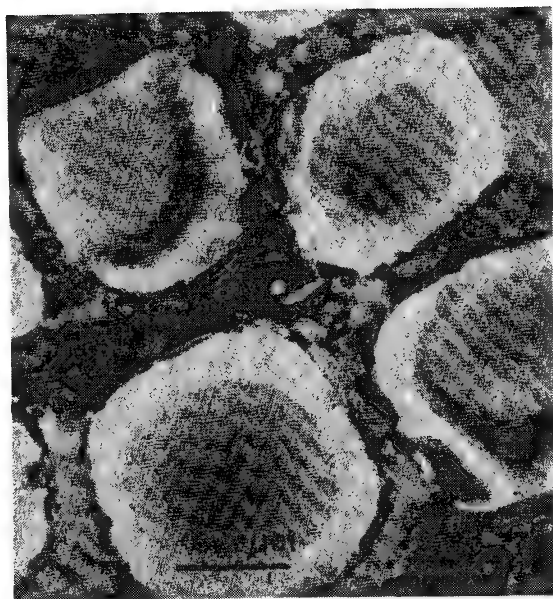
FIG. 2.--γ/γ' distribution in an as-electropolished Ni-base superalloy. Accelerating voltage 120 kV.
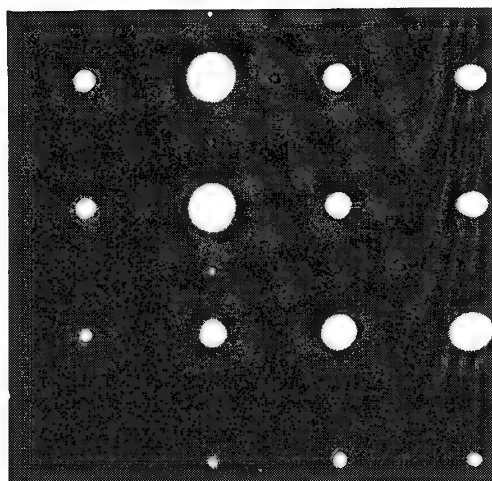
FIG. 3.--Diffraction pattern corresponding to the micrograph shown in Fig. 2. Beam direction near <001>.
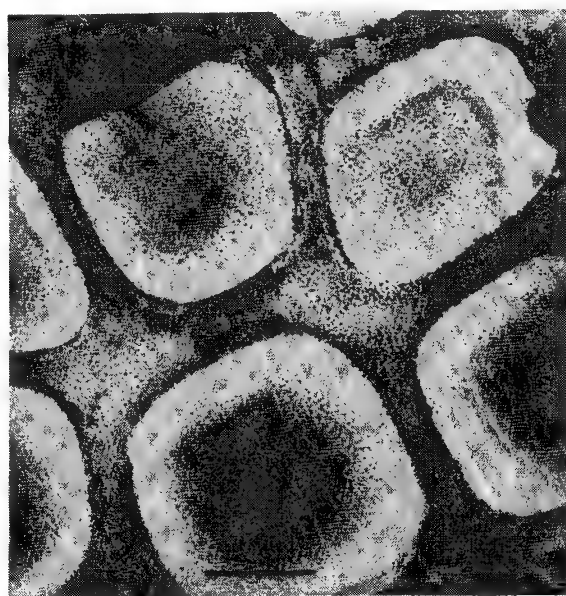
FIG. 4.--Same area as shown in Fig. 2 after 20 mins exposure to the electron beam (accelerating voltage 120 kV, kV, current density ~ 20 amps/cm^2).
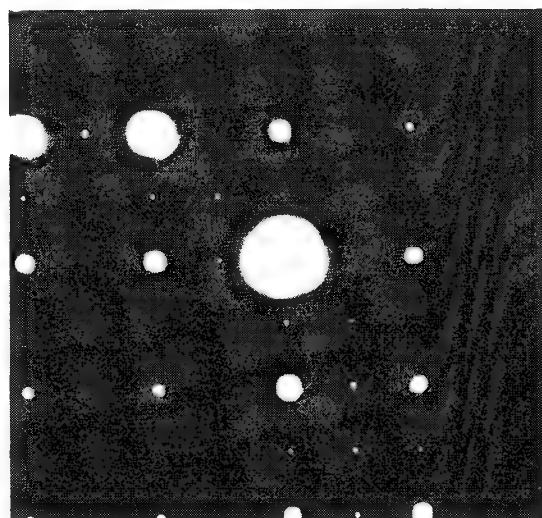
FIG. 5.--Diffraction pattern corresponding to the micrograph shown in Fig. 4.

$$I_{Ni}/I_{Al}\Big|_{\text{including film}} = 5.52$$

$$I_{Ni}/I_{Al}\Big|_{\text{without film}} = 6.55$$

This is an approximately 16% change in apparent chemistry, which is clearly unacceptable.

Removal of Surface Layers

Two methods of reducing the extent of surface films are being investigated at present. First, various polishing solutions are being used as an alternative to the highly oxidizing perchloric acid-based solutions; and second, AES coupled with Ar ion sputtering is being used in an attempt to remove the films following preparation. Regarding the former, there has been little or no significant reduction in the surface films that result when using alternative solutions. Consequently, emphasis has been placed on the removal of these films by sputtering. Thin foils which had been exposed to the electron beam so that the Al_3Ni_2 precipitates had developed were placed in an AES instrument (Physical Electronics 595) and each of the surfaces were sputtered for about 10 min. From the sputtering yields for Al_2O_3, this length of sputtering would correspond to about 500 Å, so that it was expected that the surface films would have been removed. Moreover, the chemistries deduced for the Ni and Al appeared to be typical of the bulk material. However, when introduced into the electron microscopy once again, though their number and extent had been reduced, the small precipitates of Al_3Ni_2 were still visible; the rings in the diffraction pattern were very much reduced in intensity and were also somewhat diffuse. Apparently, the sputtering treatment was not sufficient to remove the surface layers completely, and further work in this direction is being performed.

Conclusions

The present study has shown that significant surface films exist on electropolished alloys whose composition includes Ni and Al. These films introduce large errors in quantification of microchemical data. It is important that methods of reducing the possibility of surface layer formation or removal of surface layers after thin foil preparation be established. It has been shown that Ar ion sputtering may partially remove these layers; further work is in progress aimed at assessing whether this technique may indeed be used to remove this artifact successfully.

References

1. J. M. Brown, M. H. Loretto, and H. L. Fraser, "Quantitative energy-dispersive x-ray analysis of thin foils with pure elemental standards," *Analytical Electron Microscopy--1981*, 61-64.

2. D. G. Howitt, "Ion milling of bulk specimens for electron microscopy," *ibid.*, pp. 252-256.

LIGHT-ELEMENT ANALYSIS BY XEDS AND EELS

N. J. Zaluzec

The coupling of computer-based data acquisition and processing systems with modern x-ray energy-dispersive and electron energy loss spectrometers (XEDS, EELS) on an analytical electron microscope gives today's experimentalist an extremely powerful tool for micro-characterization. In order fully to appreciate and make use of all the potentials of this instrumentation it is essential that one understand the limitations of XEDS and EELS with respect to microanalysis. This presentation considered thin film quantification, absorption and multiple scattering corrections, spectral resolution, detectability limits, and heterogeneous specimen microanalysis, as they relate to light-element analysis.

The author is with Argonne National Laboratory, Materials Science Division, Argonne, IL 60439.

PROCESSING ELECTRON ENERGY LOSS SPECTRA

D. C. Joy

Electron energy loss spectra are now conventionally stored by being read into a multi-channel analyzer (MCA) operated in sequential mode, as such a scheme is both convenient and efficient. However, although modern MCAs are well equipped to perform the manipulations (e.g., smoothing, background fitting, peak stripping, etc.) necessary to obtain both qualitative and quantitative data from energy-dispersive x-ray (EDS) spectra, few commercial machines offer any facilities specifically provided for electron energy loss (ELS) operation. The purpose of this paper is to describe some spectral processing techniques suitable for use with ELS spectra.

EDS and ELS Spectra

Figure 1 compares the EDS (a) and the ELS (b) spectra obtained simultaneously from the same area of sample, in this case a biological thin section. The spectra were recorded for an acquisition time of 100 s and both contain 1024 channels. The differences between the two spectra are very evident. The EDS trace is dominated by peaks (Iron, K_a and K_b and smaller peaks from Al and Si, together with an escape peak from the iron) which are superimposed on the slowly varying bremsstrahlung background. Since the peaks are Gaussian in shape they are readily distinguished from random counting noise of the background. The ELS spectrum, on the other hand, is dominated by the zero-loss peak at the left hand edge of the spectrum, beyond which the spectral intensity falls rapidly with increasing energy loss; the total change in signal intensity between the zero-loss and 700 eV loss is in excess of 5000 times. Apart from the very strong carbon K-edge at 284 eV, the other inner shell ionization edges (N at 400 eV, 0 at 532 eV, and Fe L23 at 700 eV) are barely distinguishable from the background, since they are much lower in magnitude than the local background intensity, and have a shape similar in form to the variation of the background signal with energy loss. Unlike EDS, therefore, where the background can be ignored for most qualitative purposes and modeled approximately for many quantitative purposes, an essential first step in almost any ELS analysis is the removal of the background. Once the background has been accounted for, the other operations necessary for the recognition or quanitation of the edge become possible.

Background Fitting

Modeling the background in the EDS spectrum is made easier by the facts that both sides of the peak are accessible and that the peak-to-background ratio is relatively large. Except in cases where the highest accuracy is required, simple linear interpolations underneath the peak are thus possible. In the ELS spectrum only the low energy loss side of the edge is accessible, and past the onset of the edge the intensity is always higher than it would have been in the absence of the edge. Consequently no interpolation is possible, and the calculated background must be extrapolated beneath the edge. Second, because the jump ratio (maximum to minimum height) of the edge is typically close to unity, the result of the stripping of the background is a small difference between two large numbers, and its statistics much poorer than that of the original spectrum. Under most experimental conditions the background intensity I(E) varies with the energy loss E such that:

$$I(E) = AE^{-r} \tag{1}$$

Author D. C. Joy is with Bell Laboratories, Murray Hill, NJ 07974.
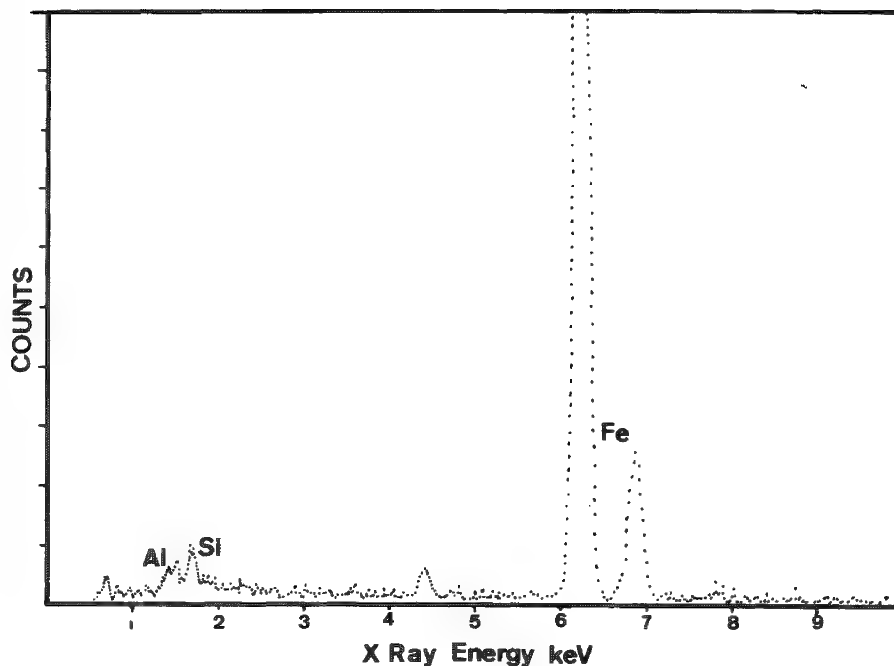
(a)
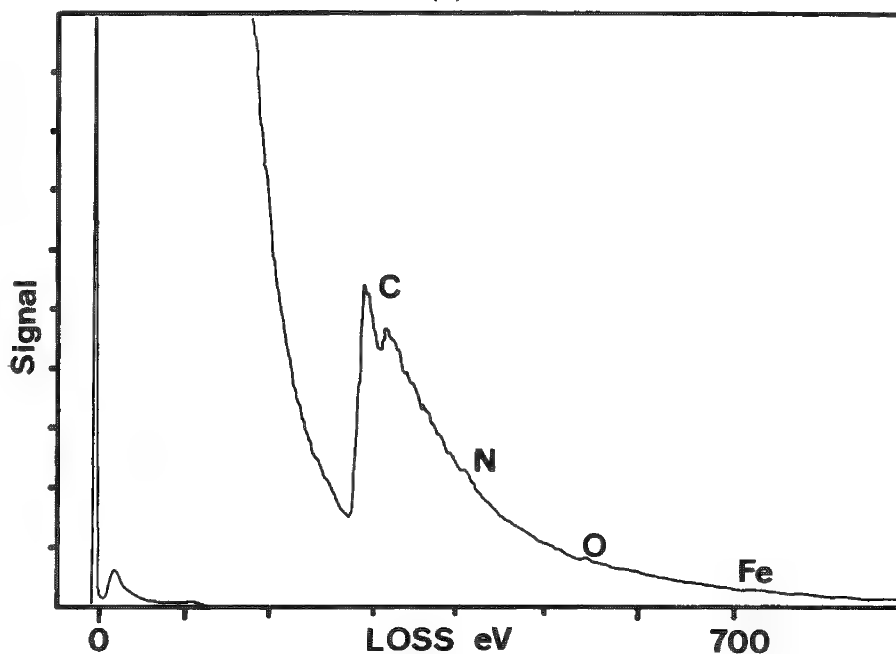
(b)

FIG. 1.--(a) EDS spectrum and (b) corresponding
ELS spectrum acquired simultaneously from
same area of thin biological section; spectra
were recorded at 100 keV in 100 s; each con-
tains 1024 channels.

where A and r are constants
across a limited region of
the spectrum.[1] The appro-
priate values for A and r
can be found in several
ways. If we take the lo-
garithms of Eq. (1) we
obtain a linear log-log
relation from which the
values of A and r may be
found by the standard for-
mulas for linear regression,
a process that can be
carried out in a few se-
conds on a minicomputer.[2]
Alternatively, in a method
due to Egerton,[3] the region
of the background to be
fitted is divided into two
equal areas and a simple
pair of algebraic relations
then gives the desired va-
lues of A and r. In either
case one can judge the
accuracy of the fit visually
by superimposing the com-
puted fit over the original
data. Through the fitted
region any divergence be-
tween the fitted and the
original data is easily
detected even though the er-
ror is usually comparable
with the channel-to-channel
noise. Beyond the edge
onset, however, one can
examine the accuracy of the
extrapolation only by
checking that the background
does not intersect the
measured data but rather
asymptotically approaches
it. Both methods give good
results even in the pre-
sence of noisy data, but the
best results will always be
obtained for the best spec-
trum statistics and the
widest fitting region. Al-
though the form of Eq. (1)
is applicable over most of
the inner shell loss energy
range, there are conditions
when the approximation is
unsatisfactory, as for
example in the presence of
instrumental scattering

artifacts, plural scattering, or when edges are overlapped. In such cases the options
are: try to account analytically for the deviations from the form of Eq. (1) by adding
polynomial or other functional terms to the equation,[4] minimize the deviations by a prior

processing of the spectrum such as deconvolution (to remove the effects of plural scattering), or try to eliminate the problem by some quite different approach such as the use of direct spectrum modeling (for overlapped edges).

Smoothing

Smoothing a spectrum is a cosmetic operation which, though it does not enhance the information content of the spectrum, does make it more visually pleasing and acceptable. Figure 2 shows a nitrogen edge, part of the spectrum of Fig. 1, after the background has been stripped. When presented in this expanded form the noise of the original data is magnified because of the removal of the large background component. Although this noise need not affect the accuracy of such operations as finding the integral beneath the edge, one often wants to reduce the scatter in the edge, for example for publication or comparison with other data, and so some form of smoothing is required. The signal processing conventionally fitted to EDS type MCAs smooths data by simple firmware or software algorithms, the most common of which is the "running n-point" smooth, sometimes called a Savitsky-Golay digital filter. In this method, the smoothed intensity of channel m in the spectrum is represented as the weighted average of the channels from $m - (n/2)$ to $m + (n/2)$. With an optimized choice of weighting coefficients such a smooth can be shown to be optimal in terms of its recovery of data from a noisy original.[5] However, the performance of such filters is less than satisfactory when the spectrum is noisy, or when large changes of intensity occur over a few channels (as at the onset of a major edge). In particular, the effect of such a filter on a noisy spectrum is to introduce an instability in the data with a periodicity related to the number of points sampled in the smoothing algorithm. Figure 3 shows this effect in the seven-point running smooth of the spectrum of Fig. 2. The strong oscillations now visible past the edge are solely due to the smoothing operation. Although the integrated area under the edge is well preserved by this approach, clearly its distortion of the edge shape is unacceptable. An alternative approach is to operate on the spectrum in frequency space using a "Fourier" filter. Figure 4 shows the power spectrum (intensity vs frequency) of the data in Fig. 2. The intensity initially falls with increasing frequency but then reaches a plateau and begins to oscillate. The Fourier components beyond the frequency at which the power spectrum levels out contain mostly the noise counts of the spectrum (i.e., high-frequency terms); the details of the shape of the edge are carried in the low-frequency terms. One can reduce the noise by eliminating or reducing the amplitude of these high-frequency components. Figure 5 shows the edge of Fig. 2 after smoothing in this way. The routine used here first computes the Fourier components of the region to be smoothed, by use of a standard library transform program (FORIT). Fourier coefficients coming from events with wavelengths of two channels or less are then modified by being multiplied by a function chosen so that each successive coefficient is smaller than the one that preceded it, with the highest frequency Fourier coefficient (representing single channel "noise" events) set to zero. The modified Fourier coefficients are then transformed back to give the desired spectrum. This type of smooth gives both a good edge profile and freedom from the oscillations induced previously. Because the "wavelength" of edges in the ELS spectrum is long (i.e., low in frequency) compared with the usual noise signal, this kind of approach is generally very successful in cleaning up the data. Its main drawback is that it requires fairly large computing times. The smooth shown in Fig. 5, which contained 229 channels of data, required 1.2 min on a PDP 11-03 minicomputer, and the time used increases about as the square of the number of channels included. With the advent of array processors, however, it should eventually be possible to perform this type of smoothing in times competitive with those now used for simple digital smooths.

Edge Identification

It has already been seen that the visibility of an edge in the ELS spectrum is relatively low. When the spectrum is also noisy then the task of positively distinguishing an edge from noise, and subsequently using the edge for microanalysis, is very difficult. In the case of the EDS spectrum this job is simpler because the peaks have a known (constant) shape and the data can be quickly tested for the "goodness of fit" to a test Gaussian. In the ELS case the shape of an edge is neither constant nor

FIG. 3.--Edge of Fig. 2 after a running 7-point smooth. (Note periodic oscillation generated in profile.)

FIG. 5.--Edge of Fig. 2 after smoothing operation in which Fourier coefficients for wavelengths of less than two channels are progressively reduced to zero.

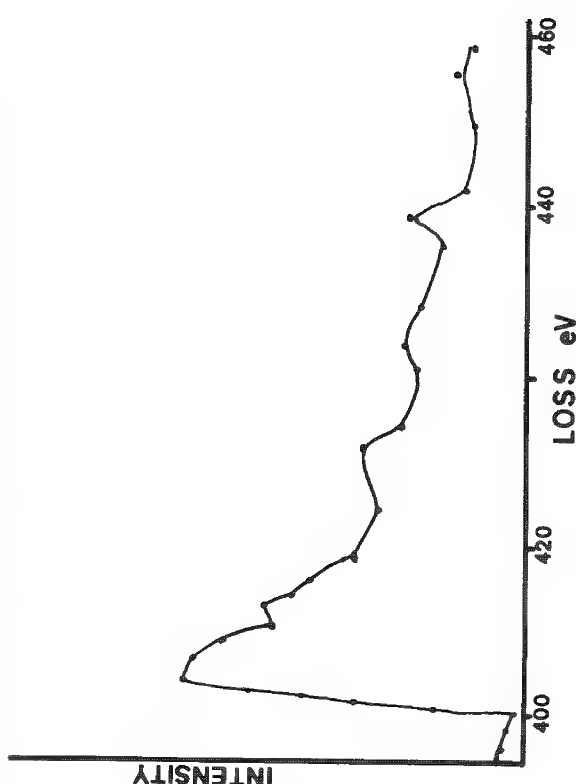FIG. 2.--Nitrogen edge from ELS spectrum of Fig. 1(b) after background stripping.

FIG. 4.--Power spectrum (intensity vs frequency) of the edge of Fig. 2 for a window of 229 channels.

expressible in a simple analytical form. One solution to this problem is to calculate the approximate shape of the edge of interest, under the appropriate experimental parameters, by use of the hydrogenic models SIGMAK and SIGMAL due to Egerton.[6,7] These models allow the form of the edge to be computed in a relatively short time (typically 15 to 20 s) and then displayed on the MCA at the correct energy loss and eV/channel. Although the constants used in these hydrogenic models were chosen to give the best agreement with the measured cross-section data rather than with the shape of the edge, the actual quality of the fit away from the onset region is surprisingly good.[8] Figures 6 and 7 show examples of some K- and $L_{2,3}$-edges as calculated and displayed on the MCA. Figure 8 shows how such calculated profiles are then used for edge verification and identification. The figure shows what was believed to be an oxygen edge in the spectrum of Fig. 1, although after background stripping the edge is so noisy that neither its onset nor shape are sufficiently well defined to allow an unambiguous identification to be made. The spectrum was recorded at 100 keV with a 23 millirad acceptance angle, and stored at 0.46 eV/channel. With these experimental parameters the oxygen K-edge profile predicted by the hydrogenic SIGMAK model was calculated and displayed on the MCA screen starting at the correct channel for the theoretical onset energy (532 eV). A window 119 eV wide was then chosen, starting at 532 eV, and the area under the theoretical edge was scaled so as to be equal to the area under the experimental spectrum, with the result shown. Visually it can be seen that the apparent agreement is good, with the SIGMAK profile following the noisy data well over the entire window; but a more sensitive measure of the fit is the "chi-squared" test. If there are N channels of data, and if I_{ϵ} is the experimental point and I_{σ} the intensity calculated for the same channel from the SIGMAK/SIGMAL model when normalized to give the same integral, then

$$\chi^2 = \Sigma(I_{\epsilon} - I_{\sigma})^2/(I_{\sigma}) \qquad (2)$$

The goodness of fit between the two profiles can then be judged by evaluation of this quantity and use of standard tables for the chi-squared distribution. Here χ^2 was 22.86 for the 229 channels. The tables show that such a low value of χ^2 would only be obtained on a random chance basis with a 1 in 6 probability, so that there is indication with good certainty that this is indeed an oxygen K-edge. As a comparison a 119eV portion of the same spectral data can be checked against the next nearest common edge, the V $L_{2,3}$ edge at 513 eV. Application of an identical procedure to the one discussed above gives a χ^2 value of 45.3, which indicates a 90% probability that random data would give as good a fit. Thus the test can both verify the existence of an edge and aid in its probable identification. The limit to the application of this approach is the quality of the edge profile model with which the experimental data are compared, and the quality of the experimental data. Although the computed profiles have the advantage of being available for any arbitrary set of experimental conditions, they are usually unable to predict the profile near to the edge onset region. A more desirable
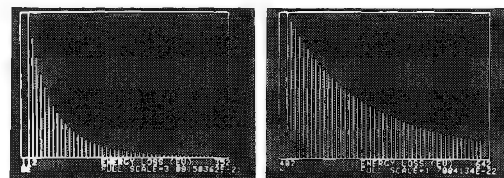
FIG. 6.--The K-edge profiles of Be and N calculated by SIGMAK for 100keV accelerating voltage and 15 milliradians acceptance angle; bars represent 5eV increments.
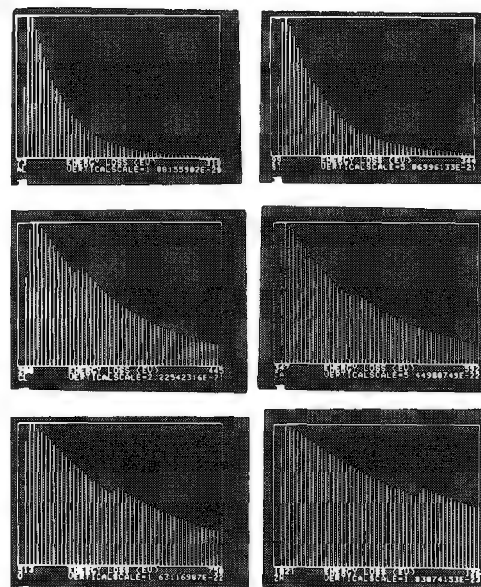
HYDROGENIC L - EDGES

FIG. 7.--$L_{2,3}$-edge profiles of Al,Sl,Cl, Ca,V, and Zn computed by SIGMAL for same conditions as those of Fig. 6.
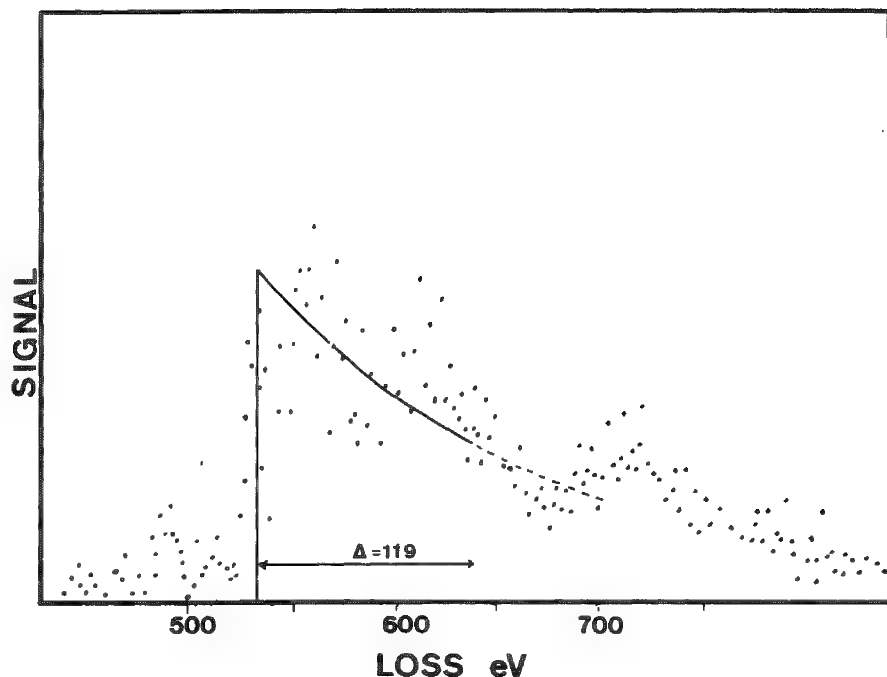
FIG. 8.--Oxygen edge from data of Fig. 1 after
background stripping, and SIGMAK profile computed
for appropriate experimental conditions (100 keV,
23 milli-radians acceptance, and 0.46 eV/channel)
and normalized to the same integral for a window
of 119 eV.

approach would be to have access to a library of standard edges, acquired under a variety of conditions, which could be used for the same purpose; several laboratories are now producing such libraries for distribution. In either case the result is influenced by plural scatering in the spectrum since that makes the experimental edge profile dependent on the thickness of the sample and makes the correspondence with the test profile less exact.

Edge Overlaps

Because electron energy loss edges have substantial intensity above background for several hundred electron volts past their onset, it is clear that overlaps between edges will often be a problem. A typical example is shown in Fig. 9, where the spectrum from CaCO has severe overlap between the C K-edge and the Ca L_{23} edge. Even though in this case the two edges are separately identifiable, there would be no possibility of performing a quantitative

analysis in this case because it would be impossible analytically to fit a background to the tail of the carbon edge. An approximate solution is to use a procedure of the type described above and find the optimum fit between the SIGMAK hydrogenic profile and the

FIG. 9.--Part of energy loss spectrum for
CaCO$_3$ after background is stripped ahead
of carbon edge and showsing C, Ca, and
O edges.
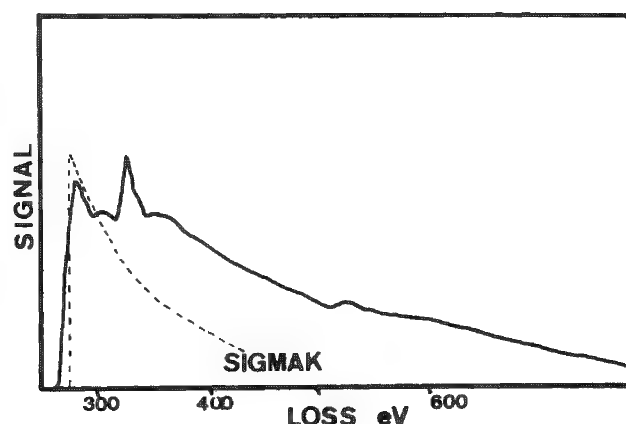
FIG. 10.--Spectrum of Fig. 9 together with
optimized carbon K-edge profile calculated
from SIGMAK to allow for stripping edge
overlap.

experimental carbon edge. This profile can then be extrapolated under the calcium edge. The result of this operation is shown in Fig. 10; although the fit is not perfect, because the goodness of fit can only be tested in a region of the carbon edge where plural scattering and fine structure effects are evident, it is sufficiently good to allow a quantitation to be obtained. The time taken for this operation is determined by the time taken to compute the SIGMAK/SIGMAL profile and optimize the "chi-squared" fitting parameter. The example shown here required about 3 min of computing time. An alternative is again to use experimental library edges as t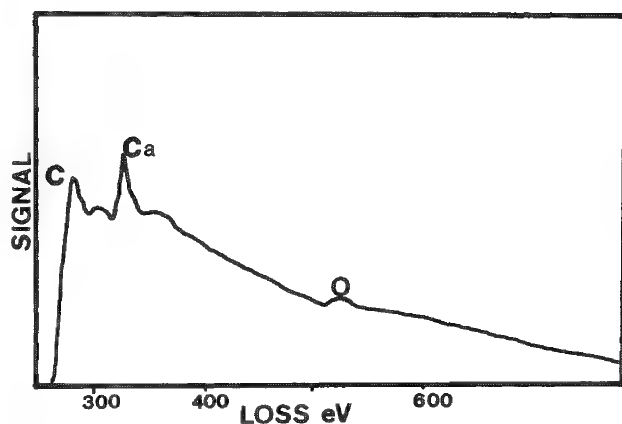he appropriate background. In many cases this procedure is advantageous because the library edge correctly accounts for the detailed edge shape features and the effects of plural scattering (which the computed profile omits); however, implementation of this option requires a comprehensive library and suitable sotftware to allow display at the correct screen scaling (eV/channel and total counts). Both techniques therefore have their uses, depending on the application in hand.

Deconvolution

The energy loss spectrum is assumed to be the result of allowing each transmitted electron to be scattered once, and only once, before it leaves the sample. While such a single-scattering profile can be experimentally obtained from specimens whose thickness is a small fraction of the inelastic mean free path, in general in samples a few hundred angstroms thick and operating at 100 keV, a substantial fraction of the exiting electrons have been scattered more than once. The probability of any sequence of plural scattering events depends on the product of the cross sections for each kind of event. The most likely sequence is a multiple plasmon loss, since the plasmon has the highest cross section; the next most likely is a mixed scattering event, an inner shell loss followed by a plasmon loss or a plasmon loss followed by an inner shell excitation. Since each of these events has a different angular scattering distribution the effect of plural scattering is to convolute the spectrum with itself in both energy and angle. For small amounts of plural scattering the effect is not too severe (an increase in background level and the replication of plasmon peaks on top of the core loss structure), but for higher levels of scattering the shape of an edge can be drastically modified and backgrounds can become so distorted as to make a sensible fit impossible to obtain. Since several of the techniques described above depend for their operation on an accurate (and consistent) knowledge of the edge profile, it is clearly desirable to be able to account for the effects of plural scattering. In addition, multiple scattering reduces the sensitivity of microanalysis by lowering the visibility of edges, and degrades the accuracy of any quantitation that is performed.

A complete deconvolution involves operations in both energy and angular space, and is far too lengthy for practical purposes. However, if a sufficiently large collection angle into the spectrometer is used then a deconvolution in energy alone is of high enough accuracy. One can then recover the true single-scattering spectrum from the experimental spectrum by taking the logarithm of the Fourier components and performing the inverse transform.[9] This spectrum obtained in this way is ideally suited for microanalytical purposes because it is independent of the sample thickness and has an enhanced edge-to-background ratio.[10] But from a practical point of view there are several difficulties. First, the whole spectrum must be treated at one time, which typically involves 1024 channels of data. On computers not equipped with an array processor the time required for a Fourier transform varies as about the square of the number of points involved, so on a small system of the type fitted to an MCA (e.g., a PDP-1103) computation times of 30 min or more are required. Second, in order to obtain adequate accuracy across the whole spectrum, which may have a dynamic range of 1000 to 1 or more, double precision arithmetic operations are required that result in a further increase in computational time.

A simpler process can be used for the removal of the efects of mixed scattering (i.e., an inner shell loss preceded or followed by a plasmon loss) from the core loss profile. The inner shell edge A, after background stripping, is assumed to be the convolution of the single scattering edge profile B with the low loss spectrum C.[11] Thus

$$A = B \# C \hspace{8cm} (3)$$

where the "#" symbol represents the convolution operation. In Fourier space Eq. (3) then becomes

$$\tilde{A} = \tilde{B} \cdot \tilde{C} \tag{4}$$

where "~" represents the Fourier transform. The desired single scattering profile can now be obtained by inversion of this equation to give

$$\tilde{B} = \tilde{A}/\tilde{C} \tag{5}$$

and performing the inverse transform. This method has the advantages that only a limited number of data channels need to be transformed, and that the dynamic range of the data is limited so that single-precision arithmetic can be used. Direct application of Eq. 5 produces an unacceptably noisy result because of chance zeroes in the Fourier components of the low-loss spectrum.[10] One way to eliminate this problem is to replace the zero-loss peak with a delta function of equal area, but this procedure has the drawback that distortion in the spectrum arising from a nonsymmetric instrument response function are then not removed by the deconvolution. Here the data are instead reconvoluted with a suitable function S which reduces or eliminates the effects of noise amplification. Thus:

$$\tilde{B} = (\tilde{A}/\tilde{C}) \cdot \tilde{S} \tag{6}$$

where S is a symmetric function we obtain by reflecting the high side of the zero loss peak about its center, which generates an idealized instrument response function with a resolution equal to that of the experimental data. Equal numbers of channels from low-loss spectrum and the stripped edge are Fourier transformed by standard library routines. The instrument response function S is then generated from the spectrum and Eq. (6) is used to form the Fourier coefficients for the deconvoluted spectrum. Before inversion a Fourier filter similar to that described above is used to minimize noise and random dropouts in the data. Figures 11 and 12 show a carbon K-edge, recorded at 100 keV from a foil 450 Å thick, before and after deconvolution. For comparison the computed SIGMAK edge profile for these experimental conditions is also shown. The effect of the deconvolution is to reduce the intensity beyond the edge onset (which indicates that much of it is due to plural scattering) and to increase the edge slope. The correspondance between the deconvoluted edge and the SIGMAK model is also much better than that between the original edge and the model. Thus, operations
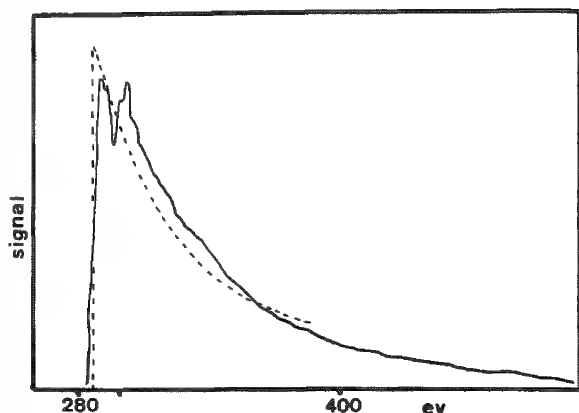

FIG. 11.--Carbon K-edge, after background stripping, recorded from sample 450 Å thick; 100 keV, acceptance angle 23 mrad. Corresponding SIGMAK profile is shown for comparison.
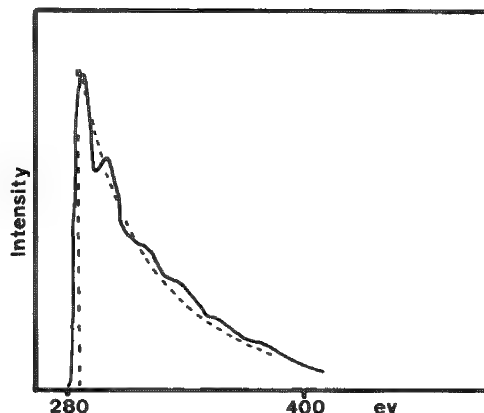
FIG. 12.--Edge of Fig. 11 after deconvolution against low-loss portion of spectrum; improved fit to corresponding SIGMAK profile is also shown.

such as edge identification or peak overlap removal that rely on the use of computed, or library, edge profiles are improved if the spectrum is first deconvoluted. In addition the stability of a quantitation result is improved after deconvolution because of the improved match to the SIGMAK/SIGMAL profiles.

A program of the type outlined here requires about 3 min of computing time on a small (PDP-1103) computer using standard library routines. A faster machine and more efficient algorithms would reduce this time still further and make deconvolution a practical part of a routine microanalysis and quanitation.

References

1. D. M. Maher et al., "Energy differential ionization cross-sections for carbon," *J. Appl. Phys.* 50: 5105, 1979.
2. D. C. Joy et al., "Progress in the quanitation of energy loss spectra," *SEM/1979* II, 817-825.
3. R. F. Egerton, "Automated System for Energy Loss Microanalysis" Proceedings 38th Annual Meeting EMSA ed. G. W. Bailey, 130-1, 1980.
4. J. Bentley et al., "Background fitting for energy loss spectra," *Analytical Electron Microscopy 1981*, 161-163.
5. M. Bromba and H. Ziegler, "Application of a Savitsky-Golay digital smoothing fitter," *Anal. Chem.* 53: 1583, 1981.
6. R. F. Egerton, "K-shell ionization cross sections," *Ultramicroscopy* 4: 169-174, 1979.
7. R. F. Egerton, "L-shell ionization cross sections," *Proc. 39th Annual Meeting EMSA*, 1981, 198-199.
8. R. F. Egerton, private communication.
9. D. W. Johnson and J. C. H. Spence, "Determination of single scattering probability distribution from plural scattering data," *J. Phys.* D-7: 771, 1974.
10. R. D. Leapman and C. R. Swyt, "Electron energy loss spectroscopy under conditions of plural scattering," *Analytical Electron Microscopy--1981*, 164-172.
11. R. F. Egerton and M. J. Whelan, "The electron energy loss spectrum and the band structure of diamond," *Phil. Mag.* 739, 1974.

THE EFFECTS OF SPHERICAL ABERRATION IN PROBE-FORMING LENSES ON PROBE SIZE, IMAGE RESOLUTION, AND X-RAY SPATIAL RESOLUTION IN SCANNING TRANSMISSION ELECTRON MICROSCOPY

Graham Cliff and P. B. Kenway

It is accepted that image resolution and x-ray spatial resolution in bulk specimens examined in the scanning electron microscope (SEM) are different. This paper presents evidence that a difference in the two resolutions can also apply to thin specimens examined in a scanning transmission electron microscope (STEM) and that this difference is a result of spherical aberration in the probe forming lens.

In 1966 Reed introduced the need to distinguish between image resolution as determined from image detail ($\ll 1$ μm) on the surface of a bulk specimen and x-ray spatial resolution which is determined by the spatial extent (> 1 μm) of the volume within the specimen producing the x rays.[1] The x-ray spatial resolution Q_B in bulk specimens is much greater than the scanning image resolution q when examined in the SEM because electrons scattering in the bulk of the specimen generate x rays in a large volume beneath the surface (Fig. 1a). Image resolution is usually judged to depend on the probe size at the specimen surface: the smaller the probe, the better the image resolution.

If the bulk of the specimen is removed and a thin foil examined in the STEM it is assumed that the x-ray spatial resolution and image resolution are comparable (Fig. 1b).

(a)   (b)
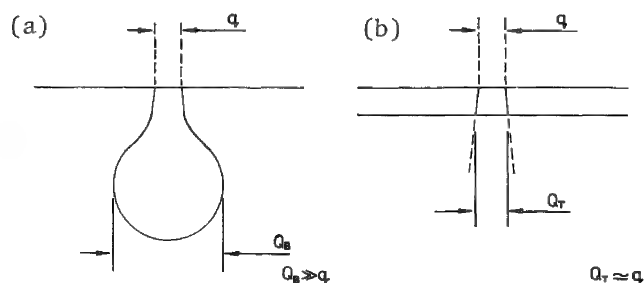
FIG. 1.--Electron scattering and x-ray generating volumes in bulk and thin-foil specimens: (a) bulk specimen, electron scattering diameter Q_B much greater than beam diameter q, x-ray spatial resolution inferior to scanning image resolutions; (b) thin-foil specimen, electron scattering diameter Q_T approximately equal to beam diameter q, x-ray resolution equal to scanning image resolution.
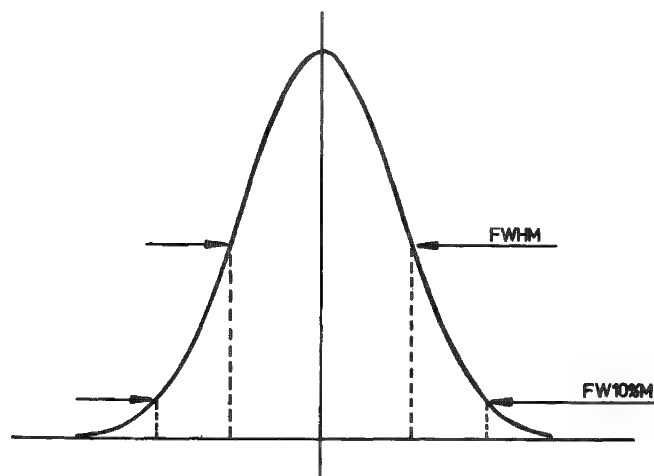
FIG. 2.--Gaussian distribution, (volume normalized).

It is usually assumed that the electron intensity profile across the electron probe in both SEM and STEM has a Gaussian distribution (Fig. 2), and since a Gaussian distribution extends to infinity the probe size is defined as the full width at half maximum (FWHM). Normalizing the volume under this Gaussian distribution and equating this to the total electron probe current one finds that 50% of the electrons in the probe are

contained within the probe diameter (FWHM). X-ray spatial resolution may be defined as that diameter from which 90% of the x rays emanate. Assuming that the x-ray generation depends linearly on the electron density then 90% of the x rays are generated within a diameter of full width at 10% maximum (FW 10% M) for the normalized Gaussian probe. Since FW 10%M = 1.82 × FWHM, the x-ray spatial resolution is 1.81 × probe size for a Gaussian probe.

Based on the criterion that two scanning image points are resolved when they are separated by a distance equal to the probe size, image resolution is often used as a measure of probe size. However, Venables and Janssen note that in an F.E.G. SEM if the zero suppression (black level) is used to enhance the contrast then the spot size could be increased without loss of image resolution on closely spaced gold islands.[2] "The resolution thus obtained was essentially independent of probe size until the contrast disappeared completely."

Investigations by the authors indicate that many of the above statements have to be re-assessed when very small, highly convergent probes are used for imaging and x-ray analysis.

Experimental

Figure 3 shows two scanning electron micrographs of a thin gold coated carbon film. With a split-screen facility, the bright field STEM image on the left may be compared with the SEM image on the right. The magnification of both images is 100 000× and inspection reveals detail at 10nm resolution. If this image resolution is used as a measure of probe size then it is concluded that the probe size is 10 nm and that the x-ray spatial resolution of such a probe would be 19 nm.

The micrographs were taken on a Philips EM400T-STEM with the high-resolution STEM facility and a 70µm top hat condenser aperture.

The EM400T-STEM has the facility to observe and focus the specimen and probe simultaneously in any of its operational modes. Figure 4 is a micrograph of the probe taken at the longest diffraction camera length with the STEM unit operating in the spot mode under the conditions of image focus required to produce the scanning micrographs of Figure 3. The probe has an intense center surrounded by a clearly observable halo.
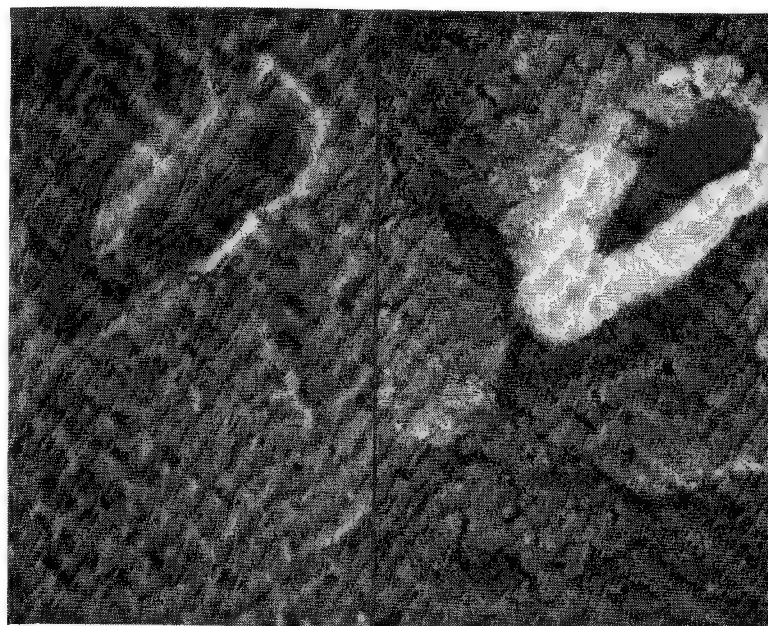

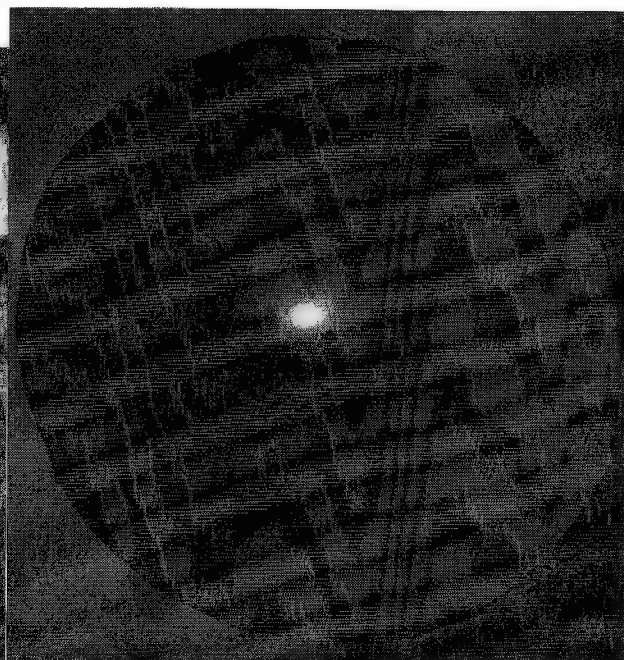FIG. 3.--Electron scanning images of gold on a thin carbon film. Left: STEM image. Right: SEM image.

FIG. 4.--Micrograph of an electron probe exhibiting spherical aberration.

The shape of the probe in Fig. 4 can be explained by Fig. 5, which illustrates a ray diagram for a lens exhibiting spherical aberration. The paraxial image of the gun crossover is focused by the objective pre-field into the specimen plane producing a reduced Gaussian image, the intense center of Fig. 4. The spherically aberrated nonaxial rays are focused into a plane before the specimen and produce a halo of illumination at the specimen

FIG. 5.--Ray diagram: Probe-forming lens with spherical aberration.

with a diameter that depends on the convergence angle, i.e., the C_2 aperture diameter.

Spherical aberration in the probe-forming lens can affect the electron intensity distribution of the probe in other operational modes. The micrographs of Fig. 6 were all taken with a 70μm condenser aperture. Figure 6(a) shows the microprobe or CTEM probe where the pre-field lens is effectively cancelled; the convergence angles are low, and hence the probe is not aberrated and is essentially Gaussian. Figure 6(b) shows the nano probe where the pre-field is used; convergence angles are high and spherical aberration is evident. Figute 6(c) shows the STEM probe; the convergence angles are equivalent to the nano probe and the sperically aberrated halo diameter is equivalent. Figure 6(d) shows the H.R. STEM probe from Fig. 3 for comparison; the convergence angles are larger and give rise to the increased halo diameter.

Densitometer traces across micrographs of such aberrated probes show that the intense center of the probe is Gaussian, with a measured FWHM corresponding to probe sizes quoted by the manufacturer. Following the definition of resolution in scanning electron images it is this FWHM which determines the image resolution; the signal generated by the halo is eliminated by zero suppression (black level). The intense center of the probe in Fig. 4 used to obtain the images of Fig. 3 measured 10 nm FWHM from the micrograph, in agreement with the image resolution.

Measurements of the electron density in the probe from densitometer traces indicate that the halo contains a significant proportion of the total probe current, 80% for a nano probe of 4 nm with a 70μm diameter aperture and an estimated 95% for a small STEM probe with a 70μm aperture. If the definition of x-ray spatial resolution (diameter containing 90% of the probe current) is applied to these spherically aberrated probes, it is found that the x-ray spatial resolution can be 40× probe size for a STEM probe such as shown in Fig. 4 compared with 1.82× probe size for a Gaussian probe.

It is possible to reduce the diameter of the spherically aberrated halo and eliminate it by use of smaller C_1 apertures, but this reduction would be at the expense of probe current.

The effects reported above are not unique to the EM400T/STEM but occur in any electron optical system in which a highly convergent probe is formed at the specimen. The postspecimen lenses of the EM400T/STEM, however, allow the spherical aberration and the effects on x-ray spatial resolution to be observed and assessed.

Conclusion

It is essential that the spherical aberration of the probe-forming lens and its effects are known and allowed for if high spatial resolution in x-ray microanalysis is to be achieved.

FIG. 6.--Micrographs and schematic electron density distributions of the probes in the EM400T STEM.
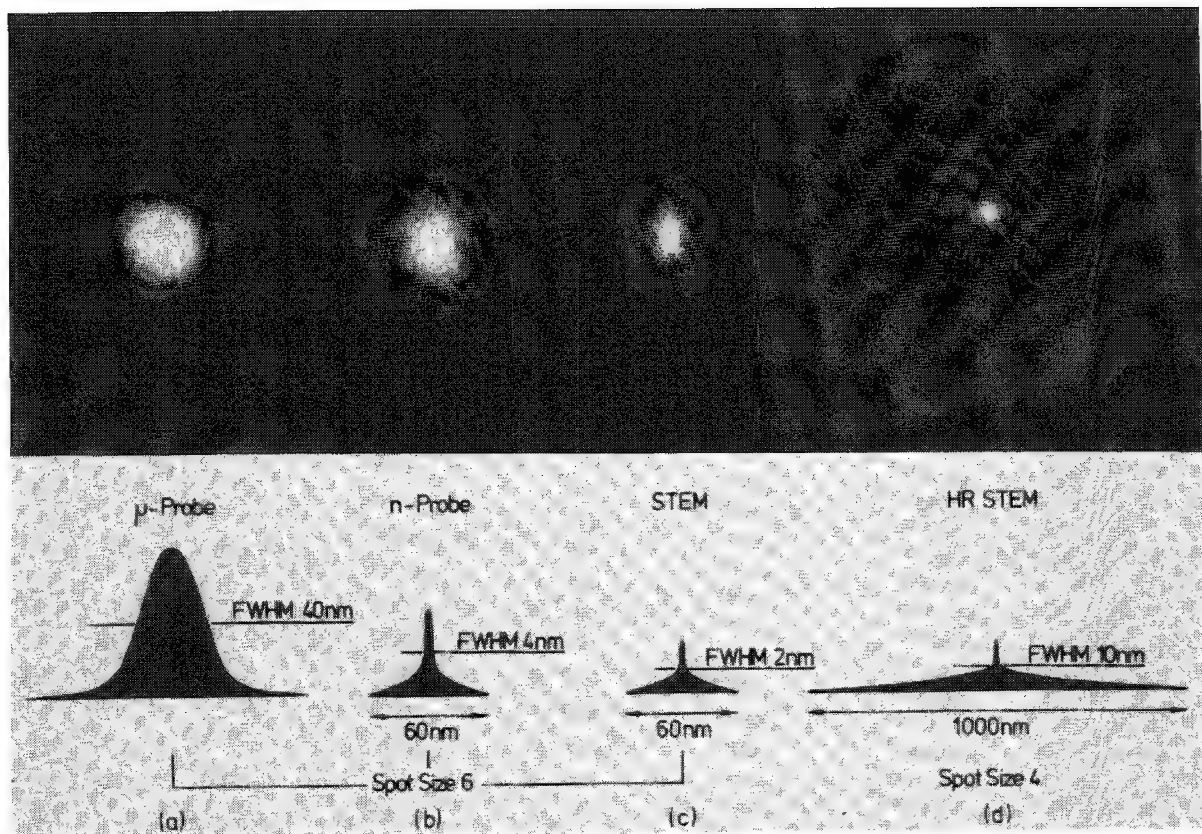
References

1. S. J. B. Reed, "X-ray optics and microanalysis," in R. Castaing, P. Deschamps, and J. Philibert, Eds., *4th Int. Congress*, Orsay, 1965, Paris: Hermann, 1966, 339.
2. J. A. Venables and A. P. Janssen, *Ultramicroscopy* 5: 297-315, 1980.

EXELFS SPECTROSCOPY OF AMORPHOUS MATERIALS

R. D. Leapman

Extended energy loss fine structure (EXELFS), which occurs above the core edges in electron energy loss spectra, gives information about the local atomic environment in a solid. EXELFS can be analyzed in the same way as extended x-ray absorption fine structure (EXAFS) by use of the formulation of Sayers, Stern and Lytle.[1-3] There has been particular interest in applying both techniques to the study of amorphous materials since they are potentially capable of determining radial interatomic distances around each individual atomic species.[4-6] The standard EXAFS technique has encountered a number of experimental difficulties in the soft x-ray range.[7] Although a new related x-ray method, which relies on measuring the secondary electron yield, has been successfully applied to light elements it is nevertheless a surface technique,[8] whereas EXAFS requires bulk samples several microns thick. EXELFS measurements can be made with an electron microscope combined with an electron spectrometer, so that this technique may be applied to a third type of sample--thin films containing microscopic regions of low atomic number elements.[9-13] Thus, a material may be characterized by microdiffraction and high resolution imaging at the same time.[6] The latter techniques are sometimes capable of identifying structures in crystalline materials but not necessarily in amorphous ones. Electron diffraction, for example, does not separate information about interatomic distances around the different atomic species.

In this paper we present some EXELFS measurements on two materials, amorphous silicon nitride and a complex glass containing several elements. We demonstrate some refinements to the data analysis and discuss limitations of the technique in terms of the minimum concentration of an element. Since the fine-structure modulations are so weak, especially the contribution from non-nearest neighbors, it is extremely important to obtain as high a signal/noise ratio as possible. It is clear that in order to obtain data of sufficient quality, the instrumentation must be fully optimized.

Data Analysis

The oscillatory part of the energy loss spectrum above a core edge is given by the standard EXAFS formula,[1-3] which describes the interference between the outgoing ejected electron and backscattered parts of the final state.

$$\chi(k) = \frac{1}{k} \sum_j (N_j/R_j^2) \, f_j \, \exp\{-2\sigma_j^2 k^2 - 2R_j/\lambda(k)\}\sin[2kR_j + \phi_j(k)] \tag{1}$$

This equation is written in terms of the wavevector k of the ejected electron which is simply related to its kinetic energy, i.e., the difference between the energy loss E and the edge threshold E_x,

$$\hbar k = [2m(E - E_x)]^{\frac{1}{2}} \tag{2}$$

where $\hbar$ is Planck's constant and m is the mass of the electron.

Summation in Eq. (1) is over the j different coordination shells at radius R_j each containing N_j atoms surrounding the excited atom. The backscattering amplitude function $f_j(k)$ depends on the type of atom. The term $\exp(-2\sigma_j^2 k^2)$ is a temperature factor that takes into account thermal vibrations; $\lambda(k)$ is the range of the ejected electron, which depends on its kinetic energy. The phase shift $\phi_j(k)$ has two parts, one due to the potential of the ex-

cited central atom and the other due to the backscattering atom. In order to obtain the radial distribution function from Eq. (1) we have analyzed our data as follows:

1. Effects due to plural inelastic scattering are removed from the spectrum above the core edges.[14,15] Plural scattering tends to distort and smear out the EXELFS modulations, especially near threshold where the peak spacing is similar to the plasmon energy ($\sim$25 eV). The plasmon typically has a comparable intensity to the zero loss peak, i.e., its mean free path is of the same order as the sample thickness, a few hundred Å at 100 keV of beam energy. The same thickness t can be estimated in terms of the inelastic mean free path λ by measurement of the ratio of the total area under the spectrum A_T to that under the zero loss peak A_0.

$$E = \lambda \ \ell n \ (A_T/A_0) \tag{3}$$

Derivation of the single-scattering intensity distribution involves measuring the low-loss spectrum up to 100 or 200 eV, which includes the zero-loss peak, plasmons, and single electron excitations. The background intensity preceding the core edge is subtracted by means of the extrapolation of the form E^{-r} ($r \simeq 3$ or 4)[16] and the result is deconvoluted by the low-loss spectrum. The measured core-edge intensity $I_M(E)$ is related to the single-scattering intensity $I_S(E)$ and the low-loss spectrum $I_L(E)$ by

$$I_M(E) = I_S(E)*I_L(E) \tag{4}$$

The single-scattering distribution is found by dividing Fourier transforms of I_M and I_L. It is important to truncate the high-frequency Fourier coefficients which produce noise, which can be achieved by reconvoluting with the instrumental resolution function $I_0(E)$.[17] We have also shown that this procedure is equivalent to replacing the zero loss peak in $I_L(E)$ by a δ-function of equivalent area.[15] Denoting the Fourier transform by lower case we have

$$I_S(E) = F^{-1} \frac{i_M(e)i_0(e)}{i_L(e)} \tag{5}$$

where F^{-1} is the inverse Fourier transform. Although plural scattering can in principle be removed from a spectrum for any thickness, practical considerations of the deterioration of signal/noise limit the thickness to less than about 1.5λ in EXELFS analysis.

2. The deconvoluted core-edge intensity is then changed from a function of ejected electron kinetic energy to a function of wavevector by Eq. (2). A total of 1024 data points are chosen up to k_{max}, which is defined below. Uncertainty in the choice of the threshold energy E_x ($k = 0$) gives rise to an effective k-dependent phase shift as discussed by Csillag et al.[18] We choose E_x as the inflexion point at the edge.

3. $\chi(k)$ is obtained by careful fitting of a third-order polynomial in k to the core edge intensity and subtracting it.

4. The resulting modulations are multiplied by k^n (where n = 2 or 3) to take account of the attenuation by the backscattering amplitude function $f_j(k)$. The most appropriate choice of n depends on the atomic number of the backscattering atom. A value of 3 has been suggested for low-Z elements.

5. The oscillations are now truncated below k_{min} and above k_{max}. The lower limit is chosen as about 3Å^{-1} (35 eV above the edge) to exclude near-edge effects and a strong dependence on the band structure of the solid. The upper limit is determined by the energy at which noise begins to dominate or another edge occurs. To obtain a reasonably accurate result k_{max} should be typically at least 10 or 12 Å^{-1}. It is very difficult to obtain meaningful results when k_{max} is below 8 Å^{-1}.

6. In order to decrease the step size in the radial distribution function, the 1024 data points are reduced to 256; the remaining points are set to zero. The magnitude of the 1024 point fast Fourier transform (FFT) is then computed. The step size in the resulting radial distribution function is $\Delta R = (\pi/4)k_{max}$.

7. The phase shift ϕ is estimated from the data of Teo and Lee[19] and is applied to each pair of central and backscattering atoms. Equation (1) shows that the shift in the radial distance is approximately half the linear part of ϕ and we therefore use the average value of $\frac{1}{2} d\phi/dk$ from k_{min} to k_{max}.

Our determinations of nearest-neighbor distances are probably accurate to within about ± 0.07 Å, if we allow for errors in the phase shift and choice of k = 0. Errors in second-nearest-neighbor distances are greater because of noise in the spectrum and truncation effects in the FFT. We have not attempted to obtain any information about the number or type of atoms in a given coordination shell, which would require a more sophisticated analysis than is described here.

Experimental

Spectra were recorded at 200keV incident beam energy by means of a Hitachi H700H electron microscope coupled with a magnetic sector spectrometer and Kevex 7000 multichannel analyzer. This relatively high accelerating voltage has the advantage of allowing us to analyze EXELFS in thicker samples than would be possible at 100 keV. Total mean free paths for inelastic scattering at 200 keV are about 1000 Å in silicon nitride and silica, so a sample thickness of this order can be used.

Energy loss spectra were obtained in the STEM mode with a current of about 10 nA into a 1000Å diameter probe. The intermediate lens was excited so as to demagnify the scattering angles into the spectrometer. The acceptance semi-angle at the specimen of about 10 mrads was greater than the characteristic scattering angle $\theta_E = E/2E_0$ (where E_0 is the accelerating voltage), which took a value of 1 mrad for the nitrogen K edge (400 eV) and 4.5 mrad for the silicon K edge (1838 eV). The collection efficiency was therefore high even at energy losses above 1000 eV. Multiple sweeps of the spectrum were added together to give a total dwell time of about 0.5-2 s per 2eV channel. Spectra were processed by means of interactive programs running on a DEC PDP 11/60 computer interfaced to the Kevex 7000 to display intermediate steps of the analysis.

Results

Amorphous Silicon Nitride. We have recorded EXELFS data from a sample of chemical-vapor-deposited amorphous silicon nitride prepared on a silicon substrate which was then etched away. This experiment extends some preliminary results[15] on the silicon K edge described earlier. The structure of this material has already been quite well established from x-ray diffraction.[20] Further data have been obtained from the surface EXAFS technique,[8] so that we can also compare our electron energy loss measurements with these results.

Figure 1 shows the background-subtracted N and Si K edges as well as the low-loss spectrum that is necessary to remove plural scattering effects from the core edges. The sample thickness was estimated as 1.1λ or about 1000 to 1500 Å. The deconvoluted edges are also shown in Fig. 1 and are scaled to the measured intensities at threshold for convenience. Measured intensities at both the N and Si edges were in excess of 10^5 counts/channel. Figure 2 shows $k^3\chi(k)$ plotted as a function of wavevector. For the N edge k_{min} and k_{max} were chosen as 2.0 and 8.0 Å^{-1}, respectively. For the Si edge k_{min} and k_{max} were chosen as 3.0 and 9.8 Å^{-1}. A lower k-range was selected for the nitrogen edge because the intensity decreases faster with energy above threshold and the EXELFS modulations were correspondingly weaker. Consequently a rather higher accuracy is expected in the silicon K edge data. We note the presence of a very weak sharp peak at 535 eV in Fig. 1 which is also evident at k = 5.9 Å^{-1} in Fig. 2. A similar peak was observed by Stöhr[8] in surface EXAFS data from Si_3N_4 and can probably be attributed to a small amount of oxygen impurity in the sample (O K edge is at 534 eV). This result points to a possible difficulty in trying to carry out elemental microanalysis for low concentrations (≤ 1 at.%): the confusion of weak edges with extended fine structure.

The Fourier transform of $k^3\chi(k)$ is shown in Fig. 3 for the nitrogen and silicon edges. Nearest-neighbor peaks occur at the same distance for both edges (1.38 ± 0.05 Å). A second weak peak rising above the noise is visible in the Si data at 2.70 Å. This peak is also evident in the nitrogen data but we are less able to attribute the peak to a second-nearest neighbor correlation because of the smaller k range and the possible contamination of oxygen mentioned above. Computed data of Teo and Lee[19] give an average linear part of the phase shift of 0.40 ± 0.05 Å for Si—N and Si—Si, and 0.35 ± 0.05 Å for N—Si and N—N. Nearest and second nearest neighbor distances are therefore 1.78 ± 0.07 Å (Si—N) and 3.1 ± 0.1 Å (Si—Si). The nitrogen edge does not give a significantly different distance for the Si—N bond length (1.73 ± 0.07 Å). This result is in agreement with existing x-ray data[20] where the Si—N bond

length was determined as 1.75 Å and the second nearest correlation distance for Si–Si and N–N as 3.0 Å. Silicon is tetrahedrally coordinated with four nitrogen atoms and nitrogen is coordinated with three silicon atoms as shown in Fig. 3. The local structure is probably close to the crystalline β phase of Si_3N_4, in which the difference between Si–Si and N–N distances is about 0.2 Å.[20] Although we are unable to resolve this difference in our data, it seems that it should be possible to do so with improved statistics and more accurate analysis.
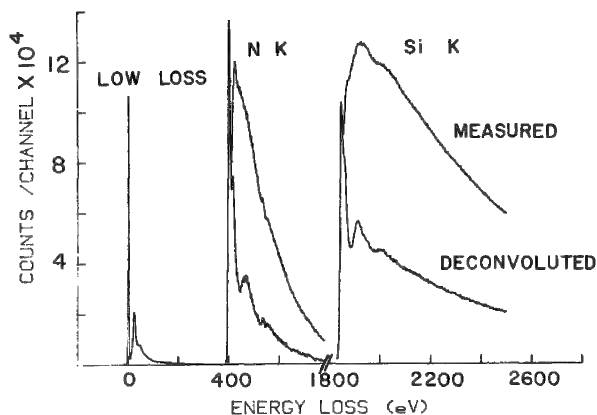
FIG. 1.--Low-loss and core-edge spectra from amorphous silicon nitride. Measured and deconvoluted K edges for nitrogen (400 eV) and silicon (1838 eV) are shown.
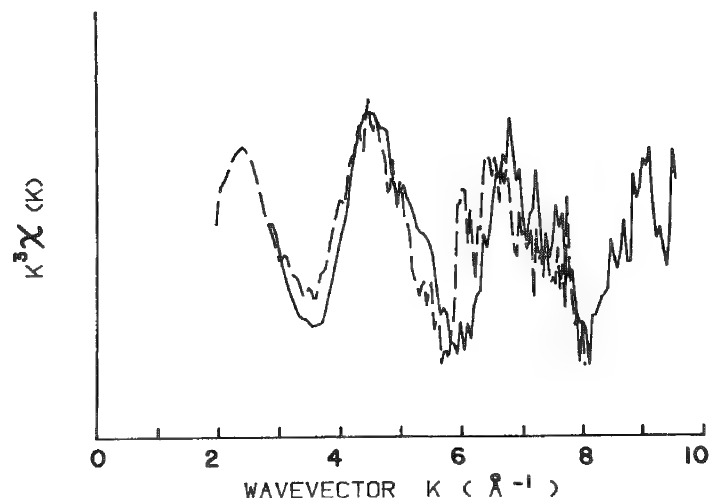
FIG. 2.--Subtracted EXELFS for silicon nitride as a function of wavevector for both Si K edge (solid line) and N K edge (dashed line).
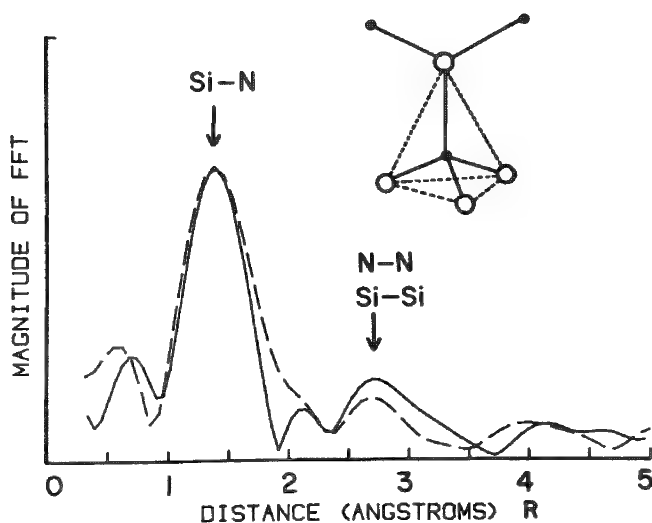
FIG. 3.--Radial distribution function (solid line) and nitrogen (dashed line) showing peaks at 1.38 Å and 2.7 Å (no phase shift added). Coordination of nitrogen (open circles) around silicon (closed circles) is indicated.
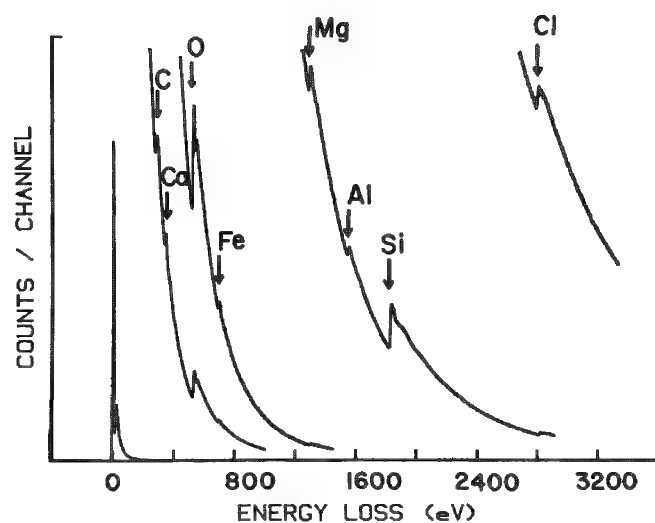
FIG. 4.--Energy loss spectrum from zero to 3200 eV from an NBS K412 silica glass. Following edges are visible: C K (285 eV), Ca L_{23} (346 eV), O K (534 eV), Fe L_{23} (708 eV), Mg K (1303 eV), Al K (1560 eV), Si K (1838 eV) and Cl K (2820 eV). Energy resolution about 6 eV.
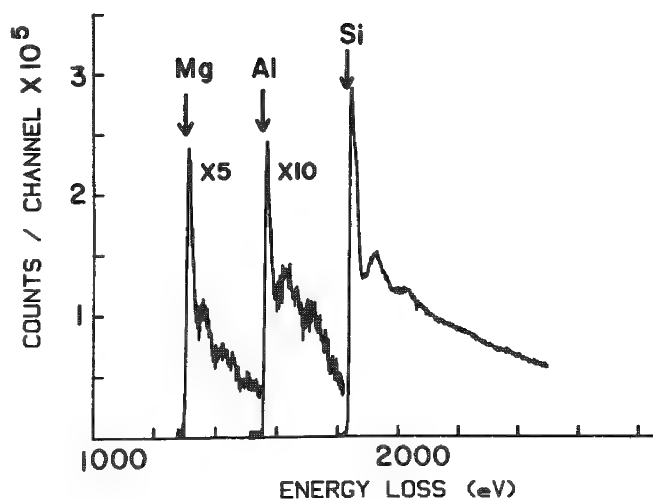
FIG. 5.--Deconvoluted Mg, Al, and Si K edges from glass sample. General similarity between edge shapes is observed.
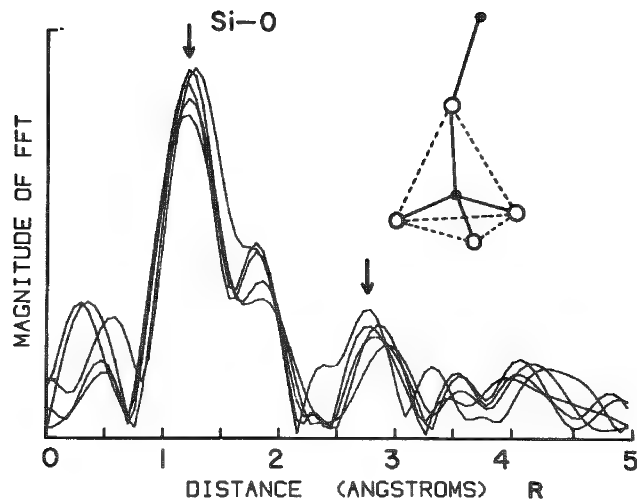
(a)
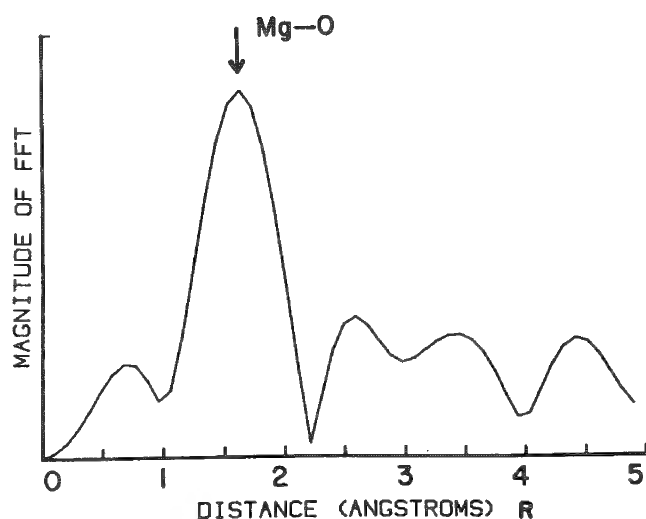
(b)
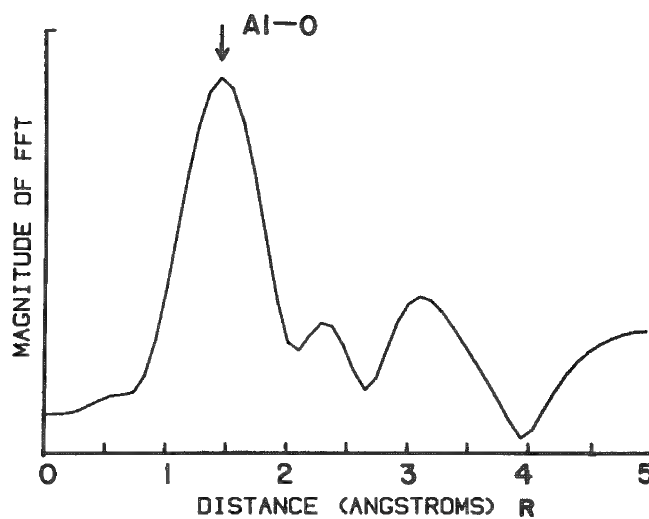
(c)

FIG. 6.--(a) Radial distribution function for silicon in the glass sample: five curves correspond to different k ranges for Fourier transform; k_{min} was the same in each (4 Å^{-1}) and k_{max} was 9, 10, 10.5, 11, and 11.5 Å^{-1}. Peaks are observed at 1.26 Å and 2.8 Å. Tetrahedral coordination of oxygen atoms (open circles) around silicon (closed circles), and coordination of two silicon (or silicon and metal) atoms with each oxygen is indicated. (b) Radial distribution function for Mg showing nearest neighbor peak at 1.62 Å; k range was from 3.0 to 8.1Å^{-1}. (c) Radial distribution function for Al showing nearest neighbor peak at 1.45 Å; k range was from 3.0 to 8.5 Å^{-1}.

A *Silica Glass*. In order to investigate the information that can be obtained from a more complicated amorphous material we have recorded EXELFS data from a silica glass containing several oxides: MgO, CaO, Al_2O_3, and FeO. The glass was a standard NBS glass research material (K412) and a thin film was prepared by ion beam sputtering onto a carbon substrate, as described previously.[21] Its composition in atomic percent was: 16.5% Si, 11.0% Mg, 5.9% Ca, 4.3% Al, 3.1% Fe, and 59.2% O. The energy loss spectrum from zero to 3200 eV is shown in Fig. 4, where edges are visible for all the elements in the glass. A chlorine K edge is also seen at 2820 eV, which can be attributed to contamination in the sputtering system. Measurement of the low-loss spectrum indicates that the sample is 0.5λ thick (about 500 Å). We were not able to obtain useful data above the oxygen K edge nor

115

the calcium and iron L_{23} edges. For Ca and O another edge occurred less than 200 eV above threshold, which limited k_{max} to 7 Å^{-1} or less. The signal/background ratio was insufficient to obtain reasonable statistics for Fe.

We have been able to analyze the Mg, Al, and Si K edges, however. Figure 5 shows the deconvoluted K edges obtained from the background-subtracted intensities and the low-loss spectrum. For the silicon K edge three spectra were added together to yield a signal/noise greater than 100. The Fourier transform of $k^3\chi(k)$ is shown in Fig. 6(a), where five different curves obtained from different ranges of k are superimposed. A value of 4 Å^{-1} was chosen for k_{min} and k_{max} was varied between 9 and 11.5 Å^{-1}. The nearest-neighbor peak is almost independent of k-range; we estimate its position as 1.26 ± 0.05 Å. A second peak is also observed in all five curves at ~2.8 Å as well as a shoulder at ~1.8 Å.

Using an estimated phase shift for Si–O of 0.40 ± 0.05 Å, we find a nearest neighbor distance of 1.66 ± 0.07 Å which agrees with the Si–O bond length in SiO_2, given as 1.61 Å.[22] Tetrahedral coordination of oxygen around silicon and the coordination of two atoms of silicon (or one silicon and one metal atom) around oxygen is shown in Fig. 6(a). The second nearest neighbor peak at 3.2 Å after phase-shift correction is greater than the Si–Si distance in pure silica and may represent a combination of distances from silicon to various metal atoms. The metal–oxygen bonds are longer than the silicon-oxygen one (Al–O = 1.9 Å, Mg–O = 2.1 Å, Fe–O = 2.2 Å, Ca–O = 2.4 Å). The explanation for the weak shoulder at a distance of about 2.2 Å after phase-shift correction is not clear. It may be an artifact but could perhaps be due to the chlorine impurity that is present.

Since the EXELFS for the Mg and Al K edges were much noiser than the Si data, we were only able to obtain nearest-neighbor distances for these elements. Radial distribution functions are shown in Figs. 6(b) and 6(c). Peaks are observed at 1.62 ± 0.05 Å for Mg and 1.45 ± 0.05 Å for Al. After the phase shifts are applied the Mg–O distance of 2.0 ± 0.1 Å and the Al–O distance of 1.85 ± 0.1Å agree with the expected values of 2.1 Å and 1.9 Å, respectively.[22]

Detection Limits and Conclusions

We have demonstrated that it is possible to obtain nearest-neighbor distances in amorphous materials at least to an accuracy of 0.1 Å by means of EXELFS spectroscopy. An accuracy of 0.05 Å should be possible if the phase shifts were treated more fully. In amorphous solids the nearest neighbors give by far the strongest peak in the radial distribution function. However weak second-nearest-neighbor correlations also seem to be observed in the materials we have investigated.

FIG. 7.--Plot of total number of counts (S + B) as function of signal/background for various values of signal/noise. Observed signal/background ratios are indicated for edges analyzed in Si_3N_4 and glass samples.
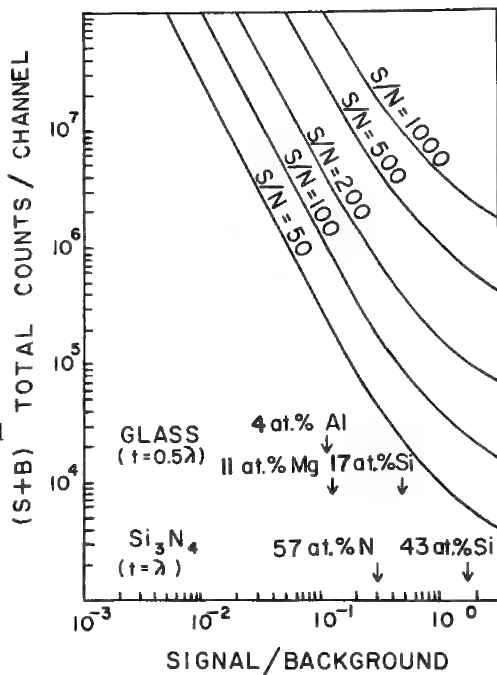
Often the elements of interest are present in relatively small concentrations, e.g., Al and Fe in the glass sample. In such cases signal/noise limits the determination of the radial distribution function. Thus, we were able to analyze the aluminum K edge data but not the iron L_{23} edge. In general the atomic fraction of an element is proportional to the signal/background ratio (S/B) at the core edge. EXELFS analysis requires a signal/noise $(S/\sqrt{S + B})$ of about 100 and for very accurate results a signal/noise of 500 would be desirable to increase the k-range available for transforming the data. This S/B is achievable with EXAFS analysis of heavier elements by use of synchrotron radiation. We have plotted (Fig. 7) the total count rate (signal + background) required to produce a given signal/background ratio for various values of signal/noise (S/N). Also indicated are our observed (S/B) ratios for the elements in the silicon nitride and glass samples. For S/N = 100 and S/B = 2 (Si K edge in Si_3N_4) only 2 × 10^4 counts per channel are needed; for S/B = 0.3 (N K edge in Si_3N_4), 2 × 10^5 counts are required. The relatively small S/B ratio for the N K edge is caused by

116

plural scattering and clearly it is advantageous to use thinner samples especially for edges at lower energy losses. In order to obtain S/N = 100 for Mg and Al edges in the glass sample, where S/B is only about 0.1, 10^6 counts per channel are necessary.

With a parallel detection system to increase the collection efficiency[23] and a probe current of about 5 nA we estimate that it would be possible to record core edge spectra in the energy range of a few hundred eV with 10^7 counts per channel in a reasonable counting period of, say, 1 min. EXELFS analysis might then be successfully carried out for an element present at a concentration of only 1 at.% in the analytical volume. Although this value seems to represent the lower limit, the possibility still exists for establishing the local environment around a minor atomic species.

References

1. E. A. Stern, D. E. Sayers and F. W. Lytle, "Extended x-ray absorption fine structure technique: determination of physical parameters," *Phys. Rev.* B11: 4836, 1975.
2. E. A. Stern, "Theory of the extended x-ray absorption fine structure," *Phys. Rev.* B10: 3027, 1974.
3. F. W. Lytle, D. E. Sayers and E. A. Stern, "Extended x-ray absorption fine structure: Experimental practice and selected results," *Phys. Rev.* B11: 4825, 1975.
4. S. H. Hunter, "EXAFS of amorphous materials," in B. K. Teo and D. C. Joy, Eds., *EXAFS Spectroscopy: Techniques and Applications*, New York: Plenum Press, 1981, 163.
5. P. E. Batson and A. J. Craven, "Extended fine structure on the carbon core ionization edge," *Phys. Rev. Lett.* 42: 893, 1979.
6. P. E. Batson, J. M. Gibson, and R. P. Ferrier, "Structural studies on small areas using STEM," *IBM Research Report* 33831, 1979.
7. J. Stöhr, D. Denley and P. Perfetti, "Surface extended x-ray absorption fine structure in the soft x-ray region: Study of an oxidized Al surface," *Phys. Rev.* B18: 4132, 1978.
8. J. Stöhr, "EXAFS and surface EXAFS studies in the soft x-ray region using electron yield spectroscopy," *J. Vac. Sci. Technol.* 16: 37, 1979.
9. C. Colliex et al., "Contribution of electron energy loss spectroscopy to the development of analytical electron microscopy," *Ultramicroscopy* 1: 301, 1976.
10. M. Isaacson and M. Utlaut, "A comparison of electron and photon beams for determination of micro-chemical environment," *Optik* 50: 213, 1978.
11. R. D. Leapman, L. A. Grunes, P. L. Fejes, and J. Silcox, "Extended core edge fine structure in electron energy loss spectra," in B. K. Teo and D. C. Joy, Eds., *EXAFS Spectroscopy: Techniques and Applications*, New York: Plenum Press 1981, 217.
12. S. Csillag, D. E. Johnson, and E. A. Stern, "Extended energy loss fine structure studies in an electron microscope," *ibid;* p. 241.
13. M. M. Disko, "An EXELFS analysis system and the preliminary orientation dependence of EXELFS in graphite," *Analytical Electron Microscopy--1981*, 214.
14. A. B. Ray, "Deconvolution of multiple scattering effects from core level EELS," *Proc. 37th Annual EMSA Meeting*, 1979, 522.
15. R. D. Leapman and C. R. Swyt, "Electron energy loss spectroscopy under conditions of plural scattering," *Analytical Electron Microscopy--1981*, 164.
16. R. F. Egerton, "Inelastic scattering of 80 keV electrons in amorphous carbon," *Phil. Mag.* 31: 99, 1975.
17. D. W. Johnson and J. C. Spence, "Determination of the single scattering distribution from plural scattering data," *J. Phys.* D7: 771, 1974.
18. S. Csillag, D. E. Johnson, and E. A. Stern, "EXELFS analysis: The useful data range," *Analytical Electron Microscopy--1981*, 221.
19. B. K. Teo and P. A. Lee, "Ab initio calculations of amplitudes and phase functions for EXAFS spectroscopy," *J. Am. Chem. Soc.* 101: 2815, 1979.
20. T. Aiyama et al., "An x-ray diffraction study of the amorphous structure of chemical vapor deposited silicon nitride," *J. Non-Cryst. Solids* 33: 131, 1979.
21. E. Steel, D. E. Newbury, and P. Pella, "Preparation of thin-film glass standards for analytical electron microscopy," *Analytical Electron Microscopy--1981*, 65.
22. R. W. G. Wyckoff, *Crystal Structures*, New York: Wiley, 1964.
23. H. Shuman, "Parallel recording of electron energy loss spectra," *Ultramicroscopy* 6: 163. 1981.

ON-LINE PROCESSING OF DIGITAL SEM IMAGES

J. J. McCarthy and P. R. Ferrara

The use of an on-line computer control system to acquire, process, and display digital images (collected from the SEM) is a powerful technique. On-line processing provides the capability to improve image quality and form new types of images using a variety of processing techniques. These operations range from fairly simple manipulations such as color coding of the image, or thresholding the image for display purposes, to more complex operations such as smoothing, contrast enhancements by manipulation of gray level histograms, two-dimensional derivatives, and fast Fourier transforms.

This paper describes an on-line computer system capable of image processing and illustrates the power of this technique with examples of processed digital SEM images.

Instrumentation

The hardware and software of this system (Tracor Northern VIP 2000) have been described in detail in earlier publications and will only be reviewed here.[1,2] The key hardware components are: (1) a PDP-11/23 or LSI-11/23 with 64K words of memory and mass storage devices, (2) a high-resolution (512 × 256 pixels) color video monitor integrated with a standard EDS multichannel analyzer, and (3) a digital scan generator which controls the SEM scan with a resolution of up to 4096 by 4096 pixels. The software for the system is a combination of programs written in a high-speed interpreter (FLEXTRAN) and support functions written in assembly language. Software support for image display includes routines for point and area painting, color-to-intensity look-up tables, and generation of vectors and complex figures. A number of utility programs provide computer control of beam positioning, video signal acquisition and storage, and output of graphics, spectral data, and image data to the microscope CRTs. Image acquisition is normally collected over a 256 × 256-point raster with 8-bit resolution per pixel and stored in memory. Larger images may be collected and stored to disk in segments during the acquisition. Typical dwell times on the order of 1 ms allow the image to be collected and stored in approximately one minute.

Display of digital images in pseudo-color can enhance the perception of features provided the color code is properly chosen. Initially, the range of intensities in the image is equally divided into 16 bins to which a unique color is assigned. These color assignments can be changed by the operator. Pre-programmed sets of color codes are provided including a "chromatic" code with cool colors (low intensity) to hot colors (high intensity), and a "photography" code which produces a normal gray-scale image in a black-and-white photograph.

Image Processing

Jones and Smith have published a comprehensive review of image processing as applied to scanning electron microscopy.[3] For example, contrast and brightness changes can be effected by subtraction or multiplication of the entire image by a constant. The observed noise in an image can be reduced by employing smoothing operations such as filtering or nearest-neighbor averaging. The image may be further enhanced by changing the pseudo-color coding (with the aid of the gray-level histogram) to accent various features, or to expand the contrast over a selected gray-scale range.

In addition to the operations referred to above, the image processing software implemented on this system includes a continuous readout of intensity at the location of a

Authors McCarthy and Ferrara are with Tracor Northern, Inc., Middletown, WI 53562.
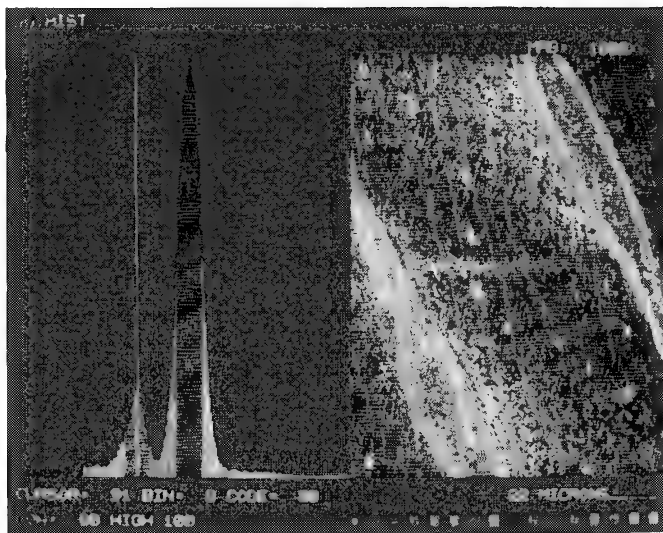
FIG. 1.--Unprocessed backscattered electron
(BSE) image of MnS inclusions in steel.
Normal color-coded gray level histogram is
shown on left.
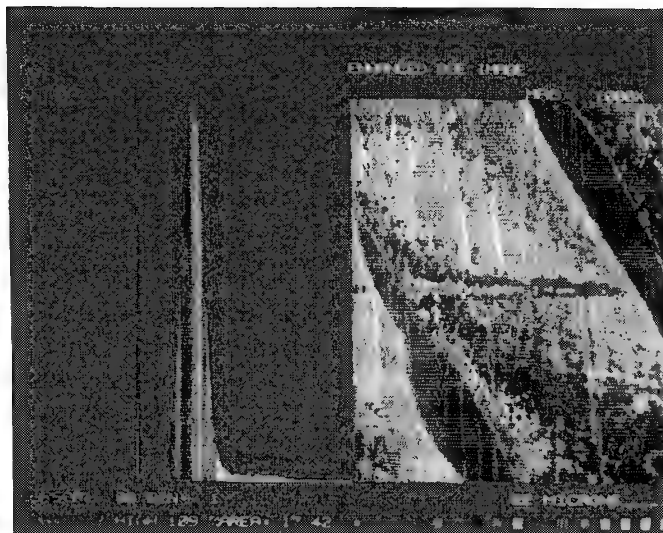
FIG. 2.--Nearest-neighbor-averaged, con-
trast-enhanced BSE image of the steel of
Fig. 1 and modified gray-level histo-
gram. Area fraction of MnS inclusions
has been computed and displayed.

FIG. 3.--Nearest-neighbor-averaged, con-
trast-enhanced BSE image of the MnS inclu-
sions of Fig 1 and modified gray-level
histogram. Area fraction of steel has
been computed and displayed.
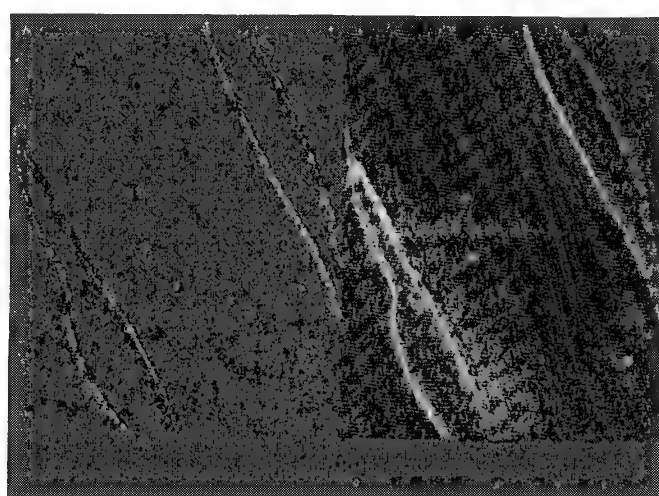
FIG. 4.--Unprocessed BSE image (right)
and two-dimensional derivative of that
image (left). Features with sharp
contrast changes are highlighted in
derivative image.

cursor in the image, line profiles across the image, and computation of the percent of the image in each histogram bin. Some examples of image processing are illustrated in Figs. 1 through 4.

Figure 1 presents the backscattered electron (BSE) image of several inclusions of MnS in a stainless steel matrix, and the color-coded gray-level histogram for this image. This histogram is coded for black-and-white photography and with 16 equal width color bins. This image will serve as a reference point to compare the effects of the image processing illustrated in Figs. 2, 3, and 4.

In Fig. 2, the BSE image has been processed by nearest-neighbor averaging, and enhanced by expansion of the contrast of the steel matrix. This enhancement was accomplished by changing the color-coding of the gray level histogram as shown on the left-hand side of Fig. 2. The original histogram was partitioned in 16 bins of equal width; the modified histogram has 2 large bins above and below the peak corresponding to the steel, and 14 smaller bins in this peak. The effect of these enhancement operations is clarified by comparison with the BSE image in Fig. 1. The MnS inclusions have been isolated and appear with uniform contrast, and the more subtle detail in the steel matrix has been emphasized. Much of the smaller detail has been made more prominent. Several features, such as the contamination spot in the lower-right corner and the line across the center of the image (due to contamination from a previous linescan) have become much more pronounced. The area fraction represented by the MnS inclusions can be readily obtained from the modified histogram. This result is computed as the contents of the red bin and displayed with the histogram information. Alternatively, rather than expanding the contrast of the matrix one may choose to expand the contrast of the MnS inclusions, as illustrated in Fig. 3. The steel matrix has been totally suppressed by being coded as black. The smaller inclusions are quite clearly visible, as is much more detail in the large inclusions. The area fraction of the steel matrix has been calculated and displayed.

Figure 4 presents the MnS BSE image on the right-hand side, and the two-dimensional derivative of the image on the left-hand side. As expected, regions in the image that contain large contrast changes have been highlighted in the derivative image. The advantages of the digital derivative versus the normal analog techniques is that it retains information perpendicular to the scan directions which is normally lost by analog processing. By proper scaling of both images and their addition, the areas of changing contrast would appear enhanced in the new image. Although the result is not particularly dramatic with the image used here, Smith has shown several examples where this technique is quite useful.[4] In addition, Smith has shown that a polar plot of the magnitude and direction of the gradient may be useful in studies of surface roughness and texture.

Summary

Digital image processing has been used for some time in areas such as medical imagery and remote sensing. The application of these techniques to electron microscopy is a recent development with great potential.

We have described an on-line computer system capable of collecting and processing digital images. Several examples of enhanced images obtained by processing have been discussed as illustrations of the power of this technique.

References

1. J. J. McCarthy, G. S. Fritz, and R. J. Lee, "Acquisition, storage, and display of video and x-ray images," *Microbeam Analysis--1981*, 50-56.

2. J. J. McCarthy, R. M. Fisher, and R. J. Lee, "Application of computers in electron microscopy," *Ultramicroscopy* (to be published).

3. A. V. Jones and K. C. A. Smith, "Image processing for scanning microscopists," *SEM/1978* 1, 13-26.

4. K. C. A. Smith et al., "Gradient image processing using an on-line digital computer," *SEM/1977* 1, 49-56.

MINERALIZED BIOLOGICAL TISSUES STUDIED BY AUGER ELECTRON AND X-RAY PHOTOELECTRON SPECTROSCOPY

W. J. Landis, M. D. Grynpas, R. M. Latanision, and J. R. Martin

Vertebrate calcification is the deposition of a calcium phosphate solid mineral phase in living tissues and is regulated by highly specific physical, chemical, and biological interactions between the mineral ions and organic tissue components. Although such interactions have been studied in situ with the use of electron optical instrumentation, such as transmission and scanning electron microscopy and electron probe microanalysis to correlate ultrastructural and chemical characteristics of many different mineralizing systems,[1-3] these approaches have been limited to the identification and localization of elements of $Z \geq 10$. Consequently, the low-Z elements (including carbon, nitrogen, and oxygen, which comprise the bulk of the organic matrices in mineralizing and other biological tissues) have been largely overlooked in previous work. This report describes the current application of Auger electron spectroscopy (AES) and x-ray photoelectron spectroscopy (XPS), techniques sensitive to both light and heavy elements, to investigations of a variety of normal mineralized biological tissues and synthetic mineral standards. Initial studies by AES or XPS have (a) identified the chemical elements and determined the inorganic and organic compositional characteristics in thick (1-2μm) biological tissue sections and synthetic standards, (b) revealed the distribution of such elements with respect to histological and ultrastructural features of the tissues, and (c) followed changes in the physical-chemical nature of the inorganic and organic tissue constituents as a function of increasing mineralization and age. For convenience, AES and XPS studies will be described separately.

AES: Materials and Experimental Techniques

In the relative absence of any literature describing biological tissue preparation or analysis with AES, the following method was developed to obtain thick sections for studies in situ. Specimens were fresh, unerupted mandibular or maxillary incisors and molars, and epiphyseal growth plate cartilage from proximal tibiae of normal newborn (3-6 day old) Wistar-Lewis rats. These specimens were prepared by aqueous fixation in 2.5% glutaraldehyde-paraformaldehyde[4] or by anhydrous treatment in organic solvents to minimize artifacts in the mineral phase introduced by aqueous solvents.[5] Tissues were embedded in Spurr medium and sectioned at 1-2 μm thickness on a Porter-Blum MT-2 microtome. Sections were cut either dry or on 100% ethylene glycol with glass knives, and some were stained with toluidine blue and examined by light microscopy. Alternate dry serial sections to be used for AES analysis were picked up from the microtome knife with fine forceps and placed in a small drop of absolute ethanol on 1 cm² sheets of clean aluminum foil. Sections cut on ethylene glycol were transferred to foil in a small wire loop containing glycol or ethanol. The liquid droplets were subsequently evaporated to dryness over low heat on a hotplate, which left the thick sections firmly mounted on the foil. Foils with sections were then placed and held with set screws on a stainless-steel holder for Auger analysis.

Uncoated and unstained specimens were examined in a Physical Electronics Model 590 scanning Auger microprobe with maximum 0.2μm lateral spatial resolution. Applicable fundamental principles of AES have been detailed elsewhere.[6] An electron beam of 3-5 kV potential and variable current (microampere range) was used to excite the sample introduced into instrument high vacuum (10^{-9} to 10^{-10} Torr) and was initially rastered over the section surface to generate a secondary electron image of structural features, recorded on Polaroid film. Auger electrons also escaping to vacuum from the sample surface following ionization were collected by a cylindrical mirror analyzer and signals increased by a standard cascade photoelectron multiplier of the multiple dynode type. Static spot Auger spectra were recorded on a graphic plotter and single-element line profiles and maps were photographed on Polaroid film. In certain instances, sputtering of the sample surface was accomplished with the use of a differentially pumped ion gun to generate an inert ion beam, usually argon, of variable potential (2-5 kV as required).
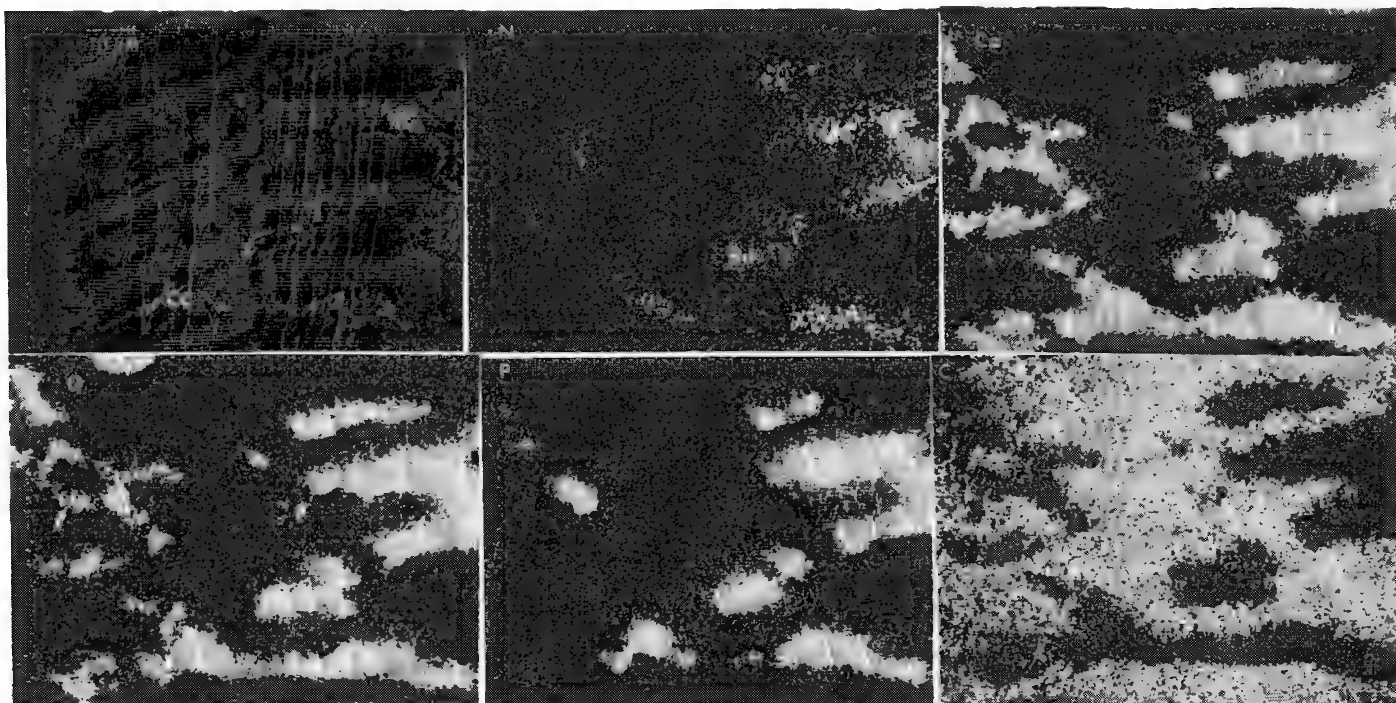
FIG. 1.--Auger elemental maps from tibial epiphyseal growth plate cartilage of normal 5-day-old rat. The sample was prepared by anhydrous ethylene glycol technique[5] and mounted on aluminum. Secondary-electron image (top left) shows calcified cartilage (CC) and circle indicates region of stationary spot analysis (Fig. 2).

AES: Results

Figure 1 shows the secondary-electron image and single Auger element maps obtained from a 2μm-thick uncoated and unstained longitudinal section of the hypertrophic region from rat epiphyseal growth plate cartilage. From Fig. 1(a) relatively little structural detail is present in a typical secondary-electron image, but identification of calcified cartilage areas and comparison of like regions with light microscopic features provide appropriate orientation. In addition to those illustrated, other Auger maps of biological specimens have been generated for Na, Mg, S, Cl, and K, although attendant noise levels are high for Na and Mg. The spectrum of elements within local surface areas can be determined by stationary spot probing, such as shown in Figure 2, and elemental line profiles can be obtained as well, in this case from a 1μm transverse section of a rat incisor shown in Figure 3.
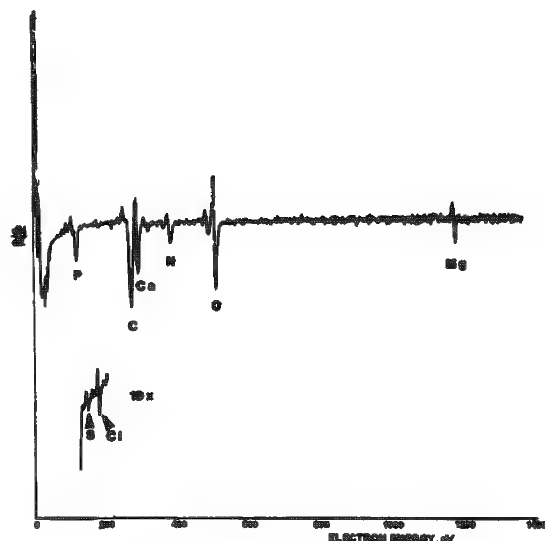
FIG. 2.--Auger spectrum from growth plate cartilage shown in Fig. 1(a). Stationary electron beam (5 kV potential) was centered over calcified cartilage and adjacent tissue viewed at 1000× (circle in Fig. 1a).

AES: Discussion

The structural detail and spatial resolution of the samples examined are not as great as those observed in the electron probe and other electron optical instruments, yet it is clear from these first results that Auger elemental spectroscopy is sufficient to provide correlation in situ of structural and chemical information from thick sections of mineralized tissues. Of particular importance, the identification in biological specimens of C, N, and O can be made by this technique, unlike electron probe microanalysis. Further, the localization and distribution of these and other elements appear to follow the known tissue composition determined from other studies. For example, the detection of O, P, and Ca principally within calcified cartilage, dentin, and enamel regions corresponds to the presence of hydroxyapatite $[Ca_{10}(PO_4)_6(OH)_2]$, the mature form of the mineral phase in these tissues. Mg is also found in the same areas, where it would be an expected substituent of the mineral phase as well. Carbon, on the other hand, is observed in regions of sections outside the mineral and forms an Auger image complementary to that of Ca (Fig. 1). Although actual cellular definition is missing in these first sections examined and will have to be enhanced by other means, possibly by the use of alternative specific elemental or heavy metal stains, the distribution of C is consistent in part with the known location of cells and extracellular matrix adjacent to mineralized portions of the calcified cartilage and dental tissues. Cells should be predominantly marked by C, N, and O (nucleic acids, proteins, carbohydrates, lipids) and by certain levels of P (membrane phospholipids, for example) and Na and K (ions of intracellular salts). The extracellular organic tissue matrices should also contain C, N, and O (carbohydrates and proteins, as collagen for instance) and relatively high levels of S (sulfated proteoglycans) as observed. The source of Cl may originate in either organic matrices (salt ion) or the Spurr embedment itself with C and O in addition.

XPS: Materials and Experimental Techniques

The few previous biological studies with XPS have examined dental enamel slabs several microns thick.[7-12] Our initial purpose with XPS was not the investigation of tissue samples but the preparation of dry powders of synthetic mineral standards to be used for spectrometer calibration. These standards, each pressed under 6000 psi into thin, small disks 13 mm in diameter, included refluxed and poorly crystalline hydroxyapatite $[Ca_{10}(PO_4)_6(OH)_2]$, fluorapatite $[Ca_{10}(PO_4)_6F_2]$, calcium carbonate $[CaCO_3]$, octacalcium phosphate $[Ca_8H_2(PO_4)_6 \cdot 5H_2O]$, monetite $[CaHPO_4]$, brushite $[CaHPO_4 \cdot 2H_2O]$, calcium pyrophosphate $[Ca_2(P_2O_7)]$, and an amorphous calcium phosphate prepared at neutral pH $[Ca/P = 1.47]$. Pressed disks were held with clamps on stainless-steel holders for XPS analysis.

Biological tissue samples included bone obtained from tibial mid-diaphyses of normal 16-day-old embryonic chicks and 1-year-old chickens, and enamel obtained from fresh, unerupted mandibular and maxillary incisors and molars of embryonic calves (30-150 days in utero). Whole bone and enamel were lyophilized, then ground under liquid nitrogen in a hammer-percussion mill to a powder consisting of particles of 5 μm average size (range 1-10 μm).[13] Enamel powder was treated further by differential gradient centrifugation in organic solvents of increasing density,[13] a method that partitions the bulk enamel mineral scraped from single teeth into individual fractions homogeneous with respect to the age of their constituent mineral phase particles. Studies of such fractions therefore correlate structural and chemical changes with progressive mineral phase maturation. Bovine enamel fractions (isolated in $0.1g/cm^3$ steps) spanned a range of $1.6 < \rho < 2.3$ g/cm^3 and contained hydroxyapatite and carbonate detected by x-ray powder diffraction and infrared spectroscopy, respectively.[14]

FIG. 3.--Auger elemental line profiles from an uncoated and unstained section of incisor prepared anhydrously[5] from a normal 5-day-old rat. Regions identified are predentin (PD), dentin (D), and enamel (E).

Uncoated pressed disks of mineral standards, whole bone powder, and fractionated enamel powder were examined in a Physical Electronics Model 548 XPS, Auger, and LEED (low energy electron diffraction) spectrometer maintained at high vacuum (10^{-8} to 10^{-9} Torr). A primary beam of Mg $K\alpha$ x-rays (10kV source potential, 40mA current) was used. Photoelectrons excited from sample surfaces[6] were collected by a cylindrical mirror analyzer of the double-pass retarding-field type to limit the lateral spatial resolution of analysis (minimum 1.5 mm) and to maintain constant energy resolution. Signals were amplified by a spiral type photoelectron multiplier. Binding-energy band width routinely sampled was approximately 1000 eV to 0 eV with energy resolution 0.6 eV at 100 eV pass energy and 0.15 eV at 25 eV pass energy. Survey and high resolution binding-energy spectra were printed on a graphic plotter.

XPS: Results

Figure 4 shows composite survey spectra of selected standards and mineralized tissues and Table 1 the comparative binding energies from high resolution spectra of principal chemical species of mineralized tissues. Notable features of the spectra are (a) detectable differences among the mineral species and biological tissues in the binding energies of O_{1s}, Ca_{2p}, and P_{2p}; (b) presence of N_{1s} in biological tissues; (c) increasing O, Ca, and P, and relatively constant N with increasing chick bone age; (d) comparable elemental content in 1-year-old chicken bone and highest density embryonic calf enamel fractions; (e) an apparent double peak of O_{1s} (binding energy difference of 1.4 eV) for brushite, but for no other sample; and (f) presence of adventitious C_{1s} in all samples with a double peak (binding energy difference 5.4 eV) for calcium carbonate.

Repeated XPS analyses performed at various times over the same sample (either minerals or biological tissues) indicate that some inconsistencies arise in binding energy peak positions (on the order of a few tenths of an electron volt). Binding energy differences between peaks relative to C_{1s} are reproducible, however. The data indicate
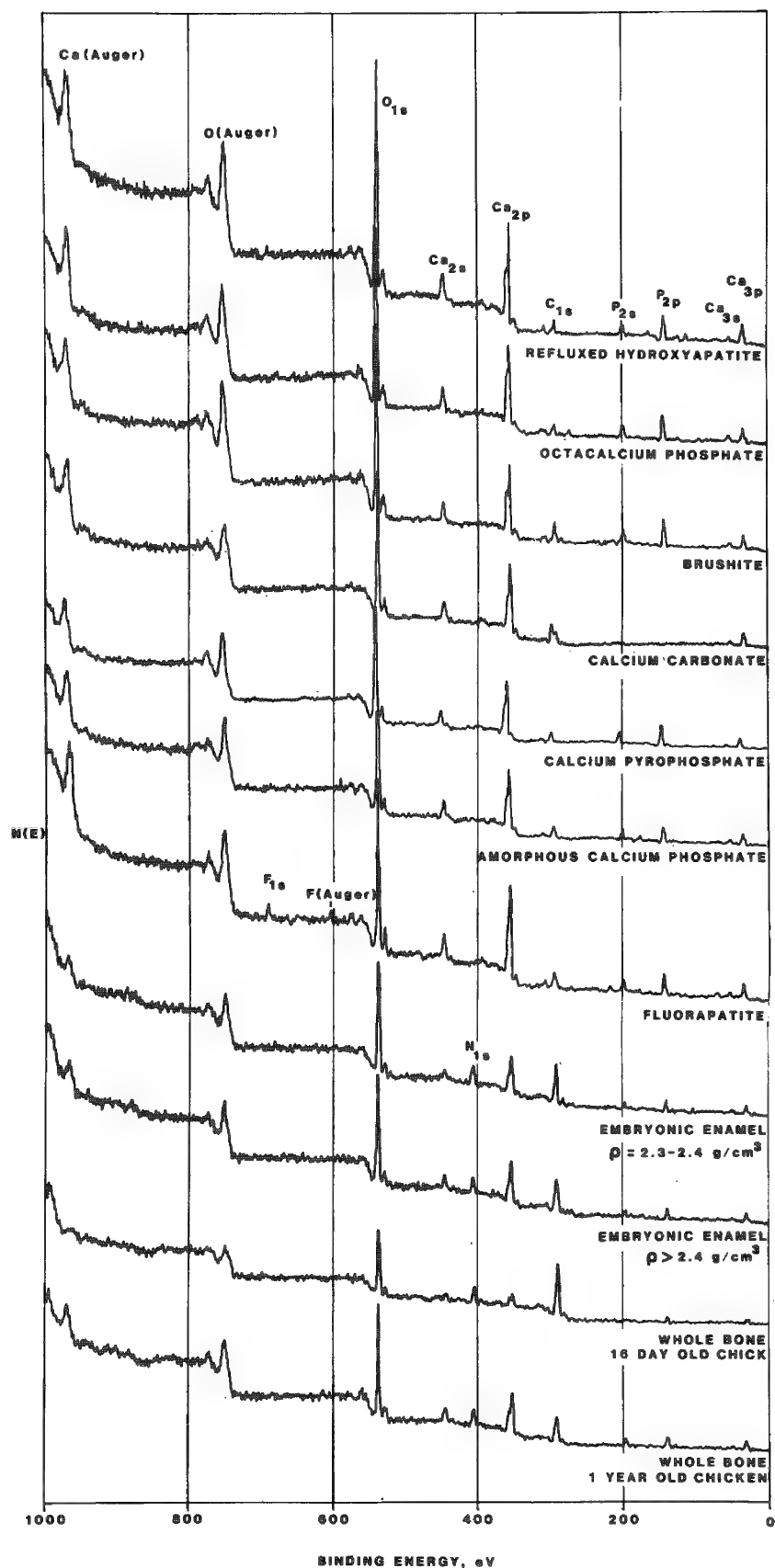
FIG. 4.--XPS survey spectra of selected mineral species and biological tissues.

125

that space-charge effects occur with these samples and consequently preclude precise assignment of binding energies. For this reason, high-resolution XPS spectra are not presented here and binding energies for mineral standards cannot yet be given; the values shown in Table 1, though obtained from spectra generated consecutively, must also be considered approximate.

TABLE 1.--Comparative binding energies of selected mineralized tissues.

Sample	Binding Energy, eV					
	O_{1s}	N_{1s}	$Ca_{2p_{1/2}}$	$Ca_{2p_{3/2}}$	C_{1s}	P_{2p}
Embryonic enamel, ρ = 1.8-1.9 g/cm^3	535.8	404.1	355.3	351.7	289.5	137.8
Embryonic enamel, ρ = 2.3-2.4 g/cm^3	536.3	404.7	355.5	352.1	290.2	138.3
Embryonic enamel, ρ > 2.4 g/cm^3	536.4	405.1	355.8	352.4	290.3	138.3
Unfractionated 16-day-old chick bone	536.2	404.4	355.4	351.8	289.6	137.7
Unfractionated 1-year-old chicken bone	536.4	405.3	356.0	352.4	290.7	138.5

Binding energies given are subject to variation and must be considered approximate values (see text).

XPS: Discussion

On the basis of initial measurements, XPS of pressed dry powder of inorganic mineral standards and biological material is suitable for the detection of C, N, O, F, Ca, and P in such samples and binding energy differences in these chemical species may be detected. The observations that binding energies are not reproducible with some of the specimens as a result of space-charge effects mean that standardization techniques for determining absolute binding energies for mineral and biological samples must be developed. One approach is the use of the adventitious C_{1s} line.[15] This line presumably originates from a thin surface layer of hydrocarbon contamination, and in CaCO$_3$ its binding energy (290.3 eV) is distinct from that of intrinsic carbon (295.7 eV), giving rise to the double peak noted in high resolution spectra. In other samples in addition to CaCO$_3$, carbon referencing for charge correction yields consistent data.

The N in both bone and enamel is attributable to organic matrices. The apparent double peak for O_{1s} in brushite may be useful in determining the presence of this acidic calcium phosphate phase in certain biological samples, such as low-density fractions of embryonic chick bone and rat dentin, where brushite has sometimes been seen by x-ray diffraction methods.[13,16] Poorly crystalline apatite, brushite, and octacalcium phosphate all contain acidic phosphate, which is known to be present in young mineralized tissues.[17-19]

It is intended that further work will extend these preliminary data identifying chemical species in standards as well as mineralized biological tissues at various developmental stages. In addition, though it is recognized that XPS provides only an imprecise means for positioning the primary x-ray beam over a sample, correlation in situ of chemical composition with morphology may also be possible by use of depth profiling methods and tissue sections prepared to facilitate analysis at progressively more mature sites.

Summary

This paper has detailed initial studies by AES and XPS of a number of normally mineralizing biological tissues and synthetic mineral standards. The methods can be used successfully to obtain qualitative compositional data of biological interest, particularly with regard to C, N, and O, in both thick tissue sections and pressed, dry powders of material prepared in vitro. Quantitative studies utilizing these surface analysis methods will follow to help identify and characterize the inorganic mineral phase of calcifying tissues; elaborate physiochemical and age changes in the specimens; and localize elements, ions, and chemical compounds of biological importance in intracellular and extracellular tissue matrices.

References

1. W. J. Landis and M. J. Glimcher, "Electron diffraction and electron probe micro-analysis of the mineral phase of bone tissue prepared by anhydrous techniques," *J. Ultra-struct. Res.* 63: 188-223, 1978.

2. W. J. Landis, "Application of electron probe x-ray microanalysis to calcification studies of bone and cartilage," *SEM/1979* II, 555-570.

3. W. J. Landis and M. J. Glimcher, "Electron optical and analytical observations of rat growth plate cartilage prepared by ultracryomicrotomy," *J. Ultrastruct. Res.*, in press.

4. M. J. Karnovsky, "A formaldehyde-glutaraldehyde fixative of high osmolality for use in electron microscopy," *J. Cell Biol.* 27: A137, 1965.

5. W. J. Landis, M. C. Paine, and M. J. Glimcher, "Electron microscopic observations of bone tissue prepared anhydrously in organic solvents," *J. Ultrastruct. Res.* 59: 1-30, 1977.

6. W. Katz, "Applied surface analysis," *Microbeam Analysis--1981*, 287-295.

7. N. L. Craig and D. M. Hercules, "Composition profiles of dental enamel studied by x-ray photoelectron spectroscopy (ESCA)," *Analytical Letters* 8: 831-838, 1975.

8. D. M. Hercules and N. L. Craig, "Composition of fluoridated dental enamel studied by x-ray photoelectron spectroscopy (ESCA)," *J. Dent. Res.* 55: 829-835, 1976.

9. D. M. Hercules and N. L. Craig, "Fluorine and tin uptake by enamel studied by x-ray photoelectron spectroscopy (ESCA)," *J. Dent. Res.* 57: 296-305, 1978.

10. R. L. Bowen, "Adhesive bonding of various materials to hard tooth tissues: XIV. Enamel mordant selection assisted by ESCA (XPS)," *J. Dent. Res.* 57: 551-556, 1978.

11. H. Duschner, H. Uchtmann, and G. Ahrens, "Elektronenspektroskopische Bestimmung der Ca-, P-, O- und F-Verhältnisse in ultradünnen Schichten der Schmelzoberfläche," *Dtsch. zahnärztl. Z.* 35: 306-309, 1980.

12. K.-J. Reinhardt and J. Vahl, "Zur Reaktion von Natriummonofluorophosphat mit Zahnschmelz," *Dtsch. zahnärztl. Z.* 35: 415-417, 1980.

13. A. H. Roufosse, W. J. Landis, W. K. Sabine, and M. J. Glimcher, "Identification of brushite in newly deposited bone mineral from embryonic chicks," *J. Ultrastruct. Res.* 68: 235-255, 1979.

14. W. J. Landis and M. Navarro, "Correlated physicochemical and age changes in em-bryonic bovine enamel," *Calcif. Tissue Int'l.*, submitted.

15. C. D. Wagner, "Energy calibration of electron spectrometers," in T. L. Barr and L. E. Davis, Eds., *Applied Surface Analysis, ASTM STP 699*, Philadelphia: Am. Soc. Testing and Materials, 1980, 137-147.

16. P. L. Glick, "Identification of mineral fractions in developing rat incisors," in Arthur Veis, Ed., *The Chemistry and Biology of Mineralized Connective Tissues*, New York: Elsevier/North Holland, 1981, 309-311.

17. M. D. Francis and N. C. Webb, "Hydroxyapatite formation from a hydrated calcium monohydrogen phosphate precursor," *Calcif. Tissue Res.* 6: 335-342, 1971.

18. W. F. Neuman and M. W. Neuman, "The nature of the mineral phase in bone," *Chem. Rev.* 53: 1-45, 1953.

19. W. E. Brown and L. C. Chow, "Chemical properties of bone mineral," *Ann. Rev. Mat. Sci.* 6: 213-236, 1976.

COMPARISON OF MICROANALYSES ON CALCULI BY X-RAY FLUORESCENCE AND PROTON-INDUCED X-RAY EMISSION SPECTROSCOPY

B. E. Taylor

The techniques of x-ray fluorescence (XRF) and proton-induced characteristic x-ray emission spectroscopy (PIXE) have been used in the analyses of urinary and biliary calculi. All the stones analyzed were then subjected to a rigorous ultrastructural analysis in the scanning electron microscope (SEM) with simultaneous x-ray microanalysis. The results of the analyses are compared and the significance of the findings is discussed with particular reference to the application for trace element determination.

With the advent of new and progressively better analytical techniques, the limits of detection for elements and chemical compounds have become progressively lower.[1] Hence, ever more sophisticated measurements on biological systems have revealed ever more subtle processes involving the so called "trace elements" which originally defied detection.

All trace elements have come under scrutiny in recent years, but special interest has centered on the trace metals, which exert an influence (direct or indirect) out of all proportion to their concentration, often due to their association with enzyme systems, which in turn maintain delicate balances in our metabolic processes.

The essential trace elements Cr, Mn, Fe, Co, Ni, Cu, Zn, Se, Mo, I, and Sn are all required for the natural and proper working of the body, and all have their own homeostatic systems to insure their optimum levels in the body. However, when a deficit or surfeit of these trace elements exists, certain diseases result; among them is urinary and biliary tract infection leading to the formation of stones.[2]

It is therefore of particular significance to determine the trace elements present in urinary and biliary calculi to give a clearer understanding of the pathogenesis of the disease.

Experimental

Interior and exterior calculi sections have been examined by PIXE by the Dynamitron accelerator at Birmingham Radiation Centre. A beam of 2.5MeV protons with a beam current of 10-20 nA was employed and a counting period of the order of 20 min with a charge of 10 μC was used for each section.

Further sections were examined by XRF with a commercial Philips 1410 spectrometer in conjunction with a LiF (200) analyzing crystal. There is a provision on the spectrometer for filtering the primary beam, to remove the characteristic Cr radiation with an aluminum filter, and it was used for the measurements. Fixed-time counting was employed for all measurements and the background was taken as the mean of the two background levels on either side of the peak (linear interpolation). The parameter chosen for comparison among samples was the corrected peak-to-background ratio.

The scanning electron microscope used was an International Scientific Instrument (100 A) equipped with a Link Systems Analyzer for x-ray microanalysis.

Results

The results of the analyses using the complementary techniques on sections of the same stones were compared with particular reference to their application for trace-element determination. For example, a urinary calculus supplied by Dudley Road Hospital in Birmingham showed the presence of spherical aggregates of minute crystallites in the SEM (Fig. 1). The energy dispersive x-ray microanalysis of this stone revealed the presence of calcium and phosphorus only.

The author is in the Department of Physics of the University of Birmingham, England B15 2TT.
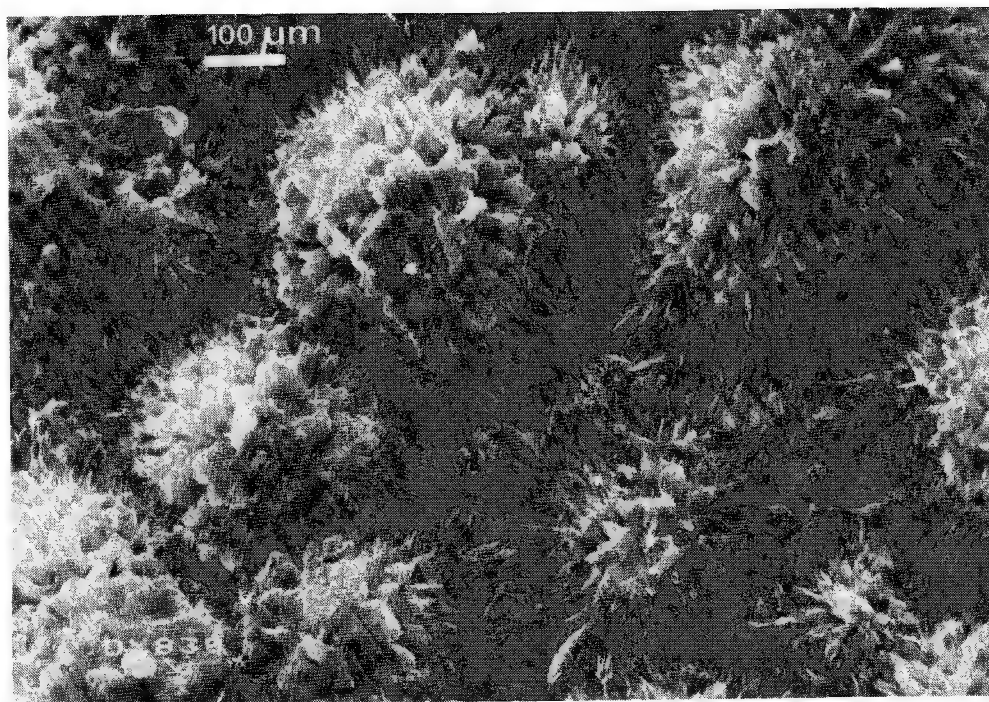
FIG. 1.--Electron micrograph of urinary calculus.
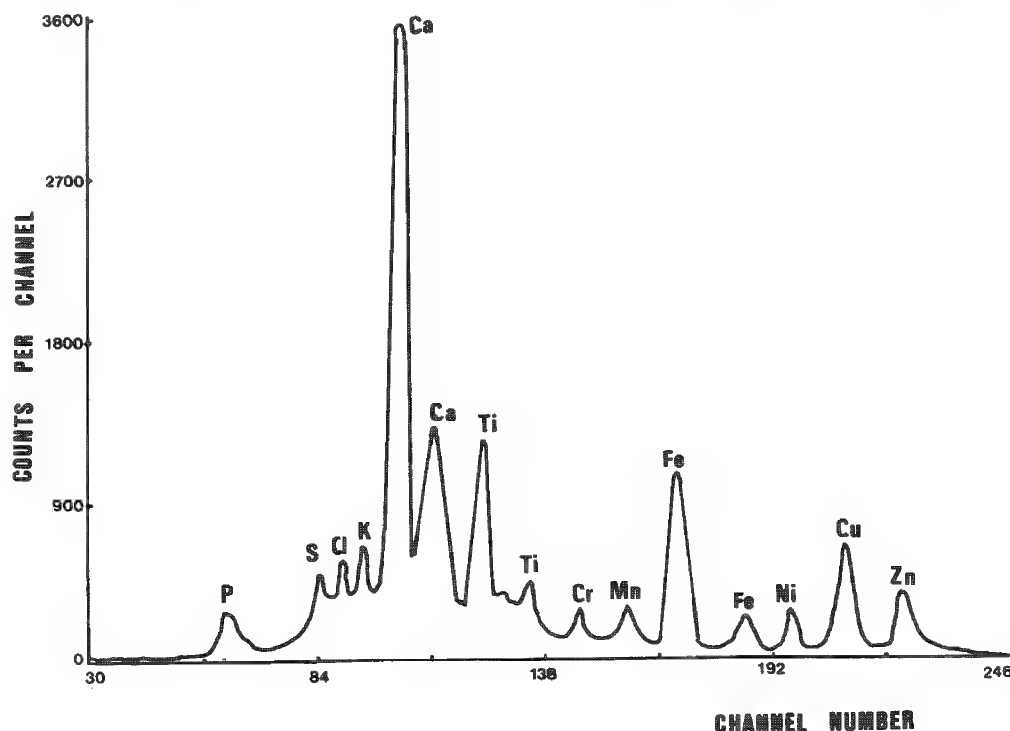
FIG. 2.--Proton-induced x-ray spectra of urinary calculus.

The XRF analysis of this stone revealed the trace elements Zn, Ni, Fe, Cu, and Cr, whereas the PIXE spectra of this region (Fig. 2) showed the presence of P, S, Cl, K, Ca, Ti, Cr, Mn, Fe, Ni, Cu, and Zn.

Conclusions

The impracticability of using the x-ray microanalysis technique in the determination of trace elements is clearly seen in the results where the limits of detection are only of the order of 0.5%. Even though the lower limits of detection of the XRF system here are of the order of tens of parts per million, the presence of the further elements as found in the PIXE analysis have not been detected.

Although there is no absolute detection limit for XRF, as in principle any desired limit may be reached provided the measurement is continued for a sufficiently long time, figures for detection limits are generally based on a statistical limit of 3σ for peak intensity within a reasonable and practicable counting time.

In XRF, matrix effects due to significant changes in the absorption properties of the matrix under certain conditions mean that critical concentrations are considerably lower than their counterparts experienced in PIXE; the fluorescent x-ray path lengths inside the specimen are considerably greater in XRF due to the greater penetration of x rays compared with protons, which tends to amplify any absorption effects.

In conclusion, it must be said that the facility for simultaneous multi-element analysis with good sensitivity by the combined use of (p,X) excitation and an energy-dispersive detection system with multichannel analysis (i.e., PIXE) is of great significance for trace element determination.

References

    1. B. E. Taylor and S. Saied, "Trace element analysis of urinary calculi using proton induced x-ray emission (PIXE)," *Brit. J. of Urol.* 1982 (in press).

    2. J. L. Meyer and L. H. Smith, *Invest. Urol.* 13: 36, 1975.

ENERGY-DISPERSIVE X-RAY MICROANALYSIS BY THE PEAK-TO-BACKGROUND METHOD: EMPIRICAL CORRECTIONS FOR DETECTOR-DEGRADED COUNTS

M. C. Foster and W. A. Hagins

For microprobe analysis of rough samples with complex topography, the ratio of characteristic to bremsstrahlung intensities in the same energy range gives a measure of element concentration.[1-4] Correction factors are less sensitive to geometry in this peak-to-background method than in the conventional ZAF procedure based on intensities per unit electron beam current of characteristic peaks alone. When an energy-dispersive x-ray detector is used, however, the peak-to-background method encounters a special problem: detector-degraded counts in the x-ray spectrum produced by physical events occuring in the Si(Li) detector during the detection process. These "spurious" counts appear at energies lower, often much lower, than that expected for incoming photons of known energy. Spurious counts contribute to the apparent x-ray continuum and thus cause errors in the analysis, especially for light elements such as Na and Mg, whose soft x rays are strongly attenuated in the sample or in the beryllium window of the detector. The spurious counts, being generated in the detector itself, are not attenuated, and thus the apparent peak-to-background ratio is too low.

A low-energy shelf of spurious counts appears in all x-ray spectra detected with energy-dispersive analyzers. This phenomenon is illustrated in Fig. 1, which shows spurious counts at low energy that are not significantly attenuated when mylar filters 2.5 and 5 μm thick are placed in front of the detector to absorb incoming x rays. In principle, spurious counts can be caused by noisy electronics, by backscattered electrons that penetrate the Be window of the detector, or by interactions of higher energy x-ray photons in the detector. In the spectra of Fig. 1, they are not caused by noisy electronics, for they are absent when the beam is turned off. They are not caused by backscattered electrons, for a 5μm filter of mylar in front of the detector would strongly attenuate backscattered electrons from a 20keV beam.[1] In this paper we show that the spurious counts arise primarily from interactions of higher energy x rays in the detector, producing current pulses that are degraded or shifted to lower energy from their expected positon in the pulse height spectrum of a Si(Li) detector. We demonstrate a method for measuring correction coefficients for a Si(Li) detector that can be used to correct spectra for detector-degraded counts.

Rationale

We want to determine the probability that a photon of given parent energy E_p will produce a spurious count in the spectrum at a given (lower) shelf energy. For a monochromatic source of x rays, this probability or correction factor $k(j,1)$ is the ratio of the number of counts $N_s(j)$ in the shelf in channel j to the number of counts $N_p(1)$ at parent energy E_p in channel 1:

$$k(j,1) = N_s(j)/N_p(1)$$

Correction factors must be measured for each detector. (Monochromatic sources of x rays are not required, however, and correction factors can be measured with the detector in the electron-beam instrument in which it is used.) For any spectrum taken with a given detector, the total number of spurious counts at a given shelf energy can then be calculated as the sum of contributions from higher energy x rays:

$$N_s(j) = \sum_{1>j} k(j,1)N_p(1)$$

and the detector-degraded counts can be subtracted from the spectrum. If correction factors have been correctly determined, calculated corrections should account for detector-degraded counts observed in all spectra taken with a given detector.
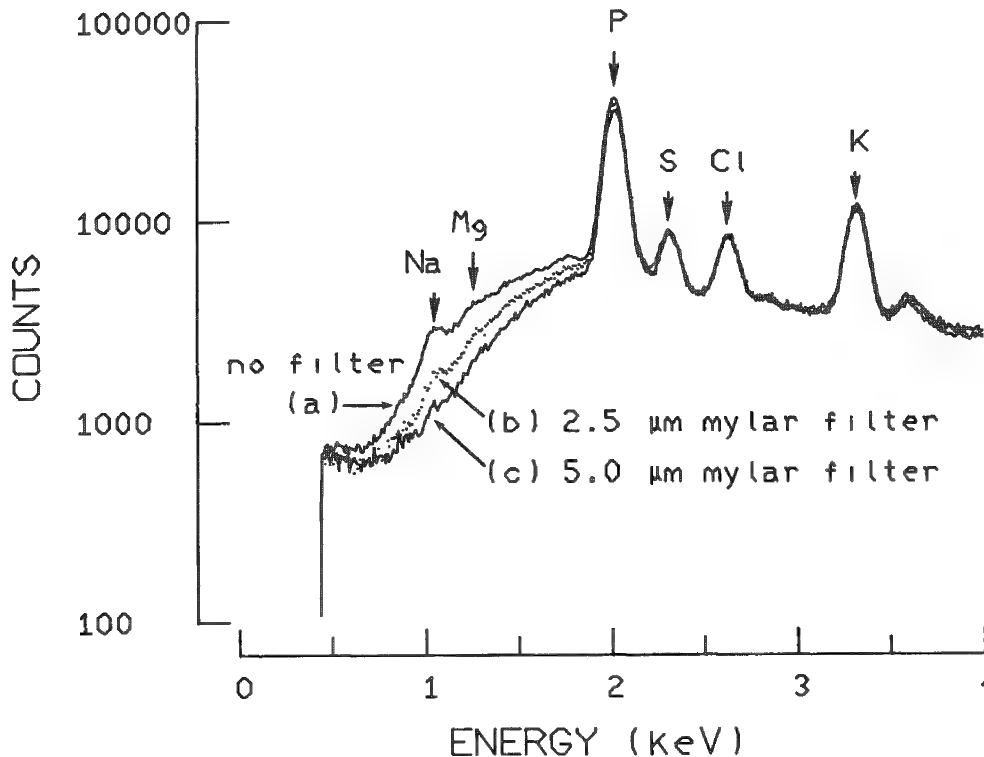
FIG. 1.--X-ray spectra detected with a Si(Li) energy-dispersive analyzer. Shelf of detector-degraded counts is evident at low energy where incoming x rays are attenuated by Be window of detector and by mylar in front of detector: (a) no mylar, (b) 2.5 μm mylar, and (c) 5 μm mylar placed between sample and detector. Electron beam energy, 19.2 keV. Sample: polished glass standard (K1635, described in Ref. 5). Detector Be window, 12.3 μm thick.

In order to determine correction coefficients, it is necessary for ratios of counts at low and high energy regions of the spectrum to be independent of count rate or dead time, for a given source of x rays. That may not necessarily be the case, for pulse pileup rejection may affect low and high energy regions differently. A quick way to test this is to measure the relative peak heights of the Cu Kα and Lα lines for different count rates. When the fast discriminator threshhold for pulse-pileup rejection on the amplifier (NSI 513A) in our analyzing system was set too high, the Cu Lα (0.93 keV) to Cu Kα (8.05 keV) peak ratio was as much as 25% lower at 40% dead time than at 8% dead time, and the variation in pulse pileup rejection over the energy range 1 to 2 keV made accurate corrections for detector-degraded counts impossible. When the threshhold was lowered, a ratio of counts in the Cu Kα and Lα peaks was obtained that was independent of count rate to within about 3%, which was considered adequate. With the discriminator threshhold thus reduced, the amplifying system showed about 5% dead time even with no incoming source of x rays.

Measurements of Detector-degraded Counts

A scanning electron microscope (ETEC autoscan) fitted with a TN2000 energy dispersive analyzing system uspplied by Tracor Northern was used in the measurements to be described. The x-ray detector (Model 106-41 SP) is a top-hat Si(Li) disk, 10 mm^2 in area, in an evacuated housing with a 12μm beryllium entrance window. A carbon-lined aluminum collimator protected the window and shielded the detector from stray electrons and x rays. It also provided a support for the mylar filter holder used for these measurements.

In order to evaluate the correction factors k(j,1), pairs of x-ray spectra were recorded from targets with strong isolated characteristic lines: LiCl or PVC for Cl, KNO_3 for K, $LiSO_4$ for S, Li_3PO_4 for P, CaCO3 for Ca, and the elements Al, Si, Cr, Fe, and Cu. The two spectra of each pair were recorded with different thicknesses of mylar placed in front of the detector to absorb about ¼ and ½ of the peak intensities of the characteristic x rays.

The difference spectrum of each pair suppresses the high-energy continuum and isolates the shelf contribution of the characteristic x rays. Figure 2 shows the spectra pairs and the difference spectrum used to isolate the shelf contribution primarily from Cl Kα x rays. A series of 10 pairs of measurements similar to these were made to isolate the contribution from 10 different parent energies.

For parent energies above the Cu Kα peak it became impractical to use mylar filter pairs to isolate shelf contributions. Measurements were made instead on carbon at different beam energies, with a 3mm thickness of mylar placed in front of the detector to absorb incident x rays of less than about 5 keV. Spectra pairs were normalized so as to coincide over the energy range 7 to 9 keV and subtracted to produce a difference spectrum. Figure 3 shows spectra used to isolate the shelf contribution from parent x rays in the energy range 14 to 18 keV. Similar spectra were taken at 7 different beam energies to give 6 pairs of spectra.

For x rays below 30 keV there are 3 distinct contributions to the shelf: the escape peak, incomplete charge collection, and Compton scattering. The observed shelf is, to a first approximation, a linear combination of these contributions.

Escape

The Cl escape peak at about 0.88 keV is evident in the spectra of Fig. 2. It results from the escape of a Si Kα X ray from the detector and the consequent loss of 1.74 keV from the parent Cl Kα x-ray energy of 2.62 keV. The escape probability k_{es} was measured as the ratio of the net counts in the parent peak to that in the daughter peak within ± 1 FWHM of their peak energies. Results from measurements at a number of energies are shown in Fig. 4, curve a, which resembles other published curves.[6-9] The solid line in Fig. 4 is a fit to the function $k_{es} = (a_{es}/E_p) + b_{es}$, which was used to generate a channel-by-channel subtraction for the escape correction. A nonlinearity in the energy scale of our multichannel analyzer at energies less than about 2 keV caused escape peaks in this region to appear 10 to 20 eV lower than expected. Since the low energy escape peaks are most prominent, the number of counts subtracted from a given shelf channel was taken to be the product of the escape coefficient and the number of counts in the parent channel located 1.75 (and not 1.74 keV) higher. For Cl parent x rays, our measurements show an escape peak which is 1.1% of the parent peak. This value is within about 5% of those obtained by Reed[6] (p. 148) from other measurements and theoretical calculations. (See also Reed and Ware[8] and Statham.[9])

Incomplete Charge Collection

Counts remaining in difference spectra such as that in Fig. 2(a) were attributed to a linear combination of degraded counts:

$$N_s(j) = \sum_{1>j} k_{ic}(j,1)N_p(1)$$

where 1 is summed over 10 different parent energy regions. For each shelf energy j there are 10 equations in 10 unknowns, which were solved for the values of $k_{ic}(j,1)$. The values obtained for the shelf energy in the region of Na Kα are plotted in Fig. 4, curve b, as a function of parent energy. The correction coefficient for incomplete charge collection k_{ic} is only a weak function of shelf energy; values just above and just below Na Kα are equal to those at Na Kα within experimental error. It is a strong function of parent energy, however, generally decreasing with increasing parent energy. There is an abrupt change at the Si absorption edge, and the data are well fit by a curve proportional to the Si absorption coefficient (solid line in Fig. 3, curve b). This result suggests that x rays that are absorbed in the detector near the partially dead layer at its front surface are most likely to be detected as lower energy x rays and that we are measuring the effect of incomplete charge collection. (See Reed,[6] p. 41.)

Compton Scattering

X rays at 10 keV make a negligible contribution to spurious counts at low energy, but at higher energies another process produces spurious counts, as shown by the difference spectrum of Fig. 3(b). Compton scattering of x rays in the detector is probably responsible for these spurious counts (see discussions on Compton scattering in Woldseth[7]), although we have no direct evidence that this is the case. From difference spectra such as that of
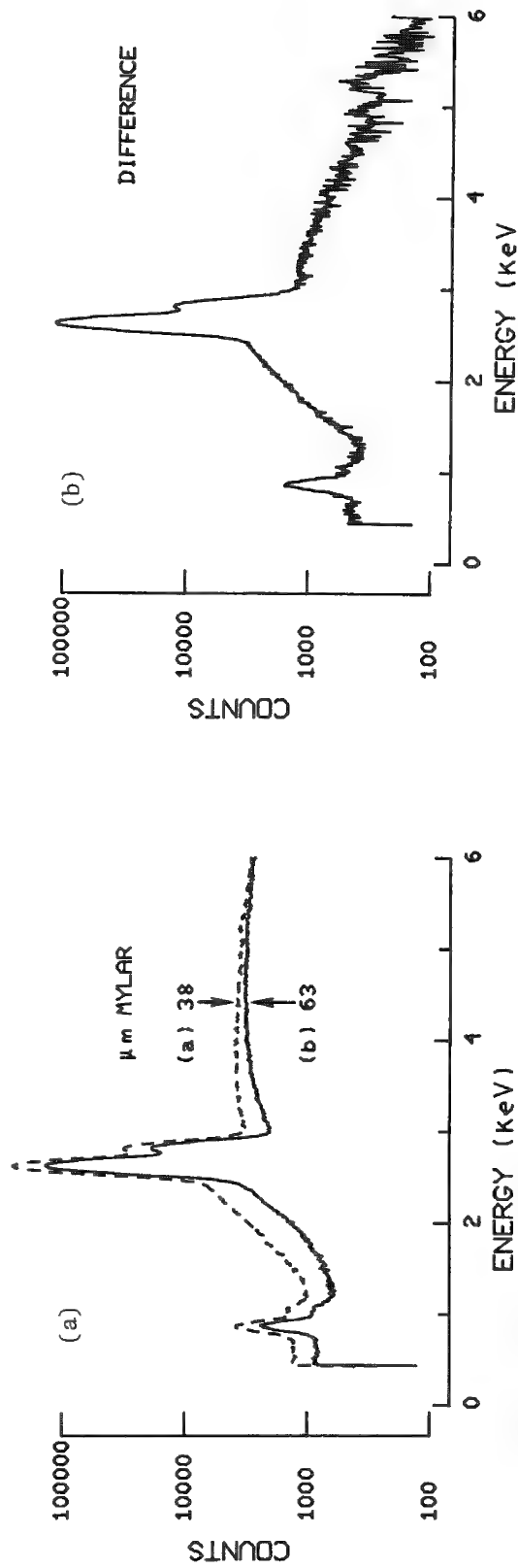
FIG. 2.--Measurement of detector-degraded counts originating from x rays at Cl characteristic energy of 2.62 keV. x rays were generated from 19.2keV electrons incident on sample of polyvinylchloride. Different thicknesses of mylar film in front of the detector attenuate low-energy x rays from the sample. (a) spectra obtained with mylar (a) 38 and (b) 63 μm thick in front of detector; (b) difference between spectra (a) and (b) in Fig. 2(a): Cl escape peak is evident at 0.88 keV, superimposed on shelf caused mainly by incomplete charge collection in Si(Li) detector.
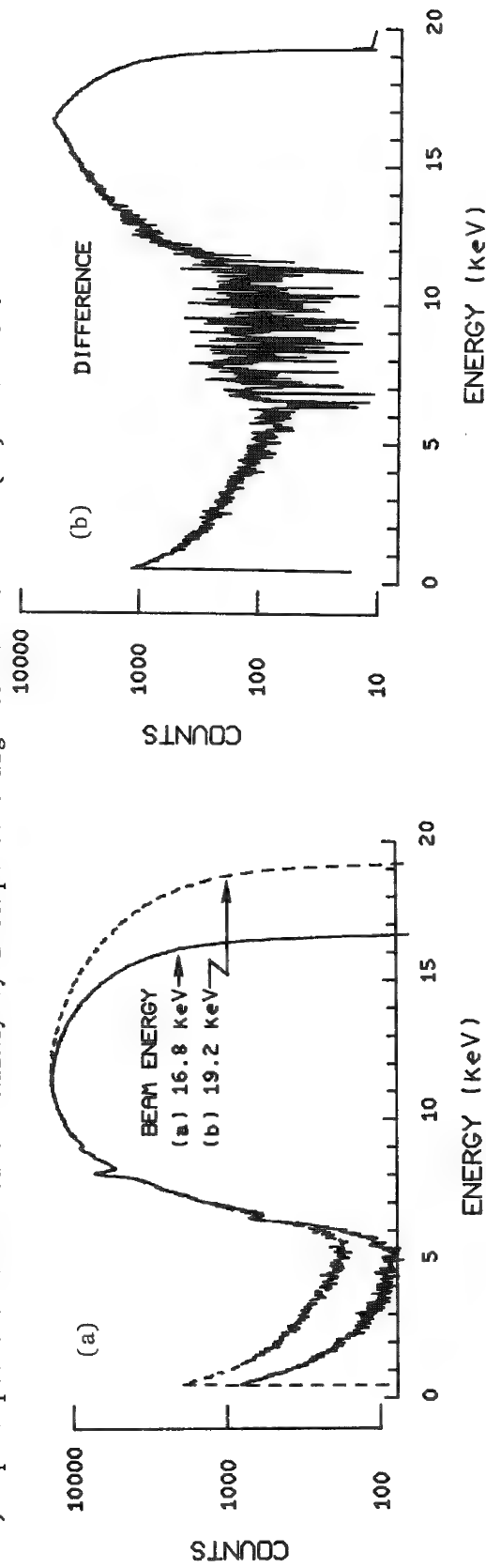
FIG. 3.--Measurement of detector-degraded counts originating from x rays in 14-18keV range. Low energy x rays from sample were attenuated by mylar 0.120 in. thick placed in front of sample. (a) Spectra generated from (a) 16.8 and (b) 19.2 keV electrons incident on carbon; (b) difference between spectra a and b in Fig. 3(a): spurious counts below about 5 keV are caused by Compton scattering of high-energy x rays in detector.

134

FIG. 4

CORRECTION COEFFICIENT k

.01

(a) ESCAPE

.001

(b) INCOMPLETE CHARGE COLLECTION

(c) COMPTON

.0001

.00001

1   2   4   6   8   10   20

PARENT ENERGY (keV)
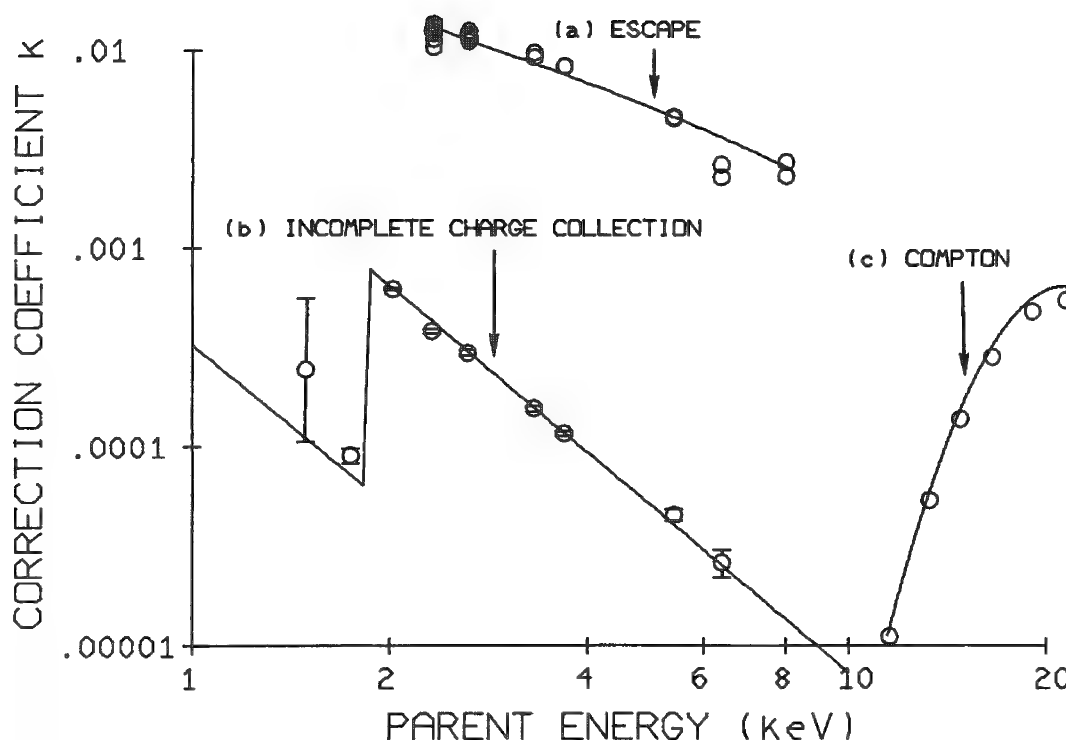
FIG. 4.--Correction coefficients measured for our Si(Li) detector as a function of energy of parent x ray. Correction coefficient k is the ratio of detector-degraded counts appearing in shelf region of spectra to counts in parent region. Data points for curves (a), (b), and (c) were determined from measurements such as those illustrated in Figs. 2 and 3, respectively. (a) Escape correction: fraction of x rays which are degraded by 1.74 keV in Si(Li) detector as a function of energy of parent x ray; energy lost is characteristic energy of Si Kα x ray, which escapes from the detector; solid line (a) is a fit to function $k_{es} = a_{es}/E_p + b_{es}$. (For parent energies in GeV, $a_{es} = 0.0333$, $b_{es} = -0.00158$.) (b) and (c) Incomplete charge collection and Compton scattering corrections: fraction of incident x rays that interact in detector to give spurious counts near 1.04 keV; solid line (b) is a fit for energies between 1.84 and 10 keV of log of correction coefficient to log of Si mass absorption coefficient plus a constant; solid line (c) is a fit for energies above 10 keV of function $\log_{10} k_c = a_c(\log_{10} E_p)^2 + b_c\log_{10}E_p + c_c$. (For parent x-ray energies in GeV, $a_c = -23.3$, $b_c = 62.2$, $c_c = -44.7$.)

FIG. 5

COUNTS

10000

(a) UNCORRECTED

(b) CORRECTED

1000

(c) CORRECTION

(d) INCOMPLETE CHARGE COLLECTION

100

(e) ESCAPE

(f) COMPTON

10

0   1   2   3

ENERGY (keV)
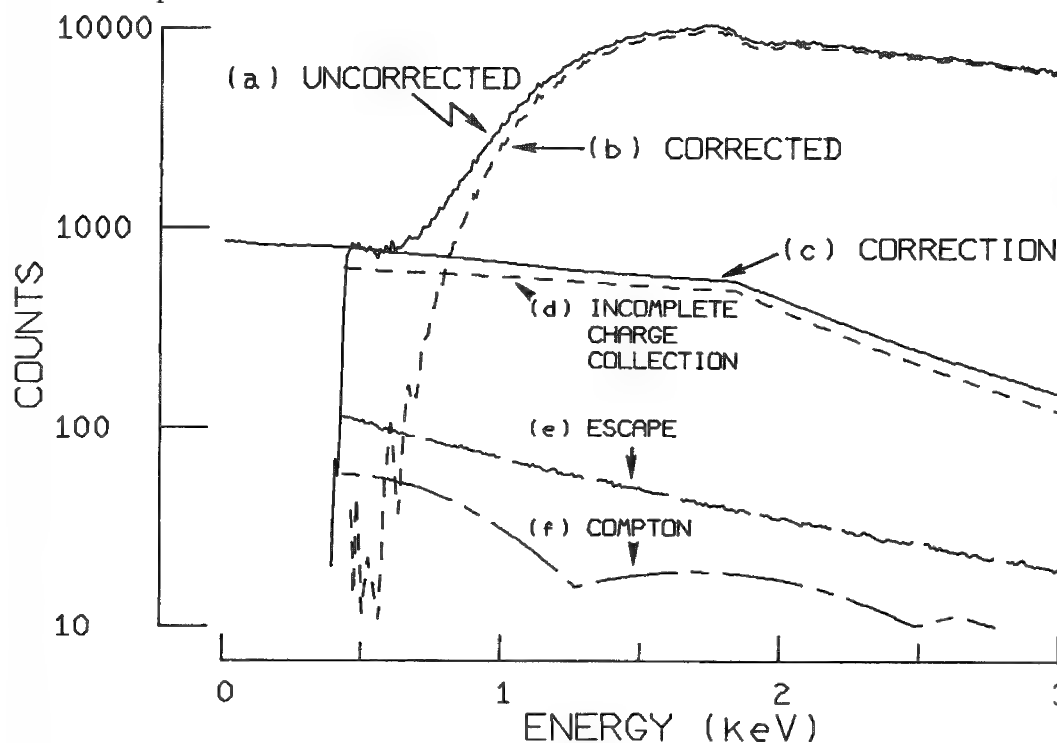
FIG. 5.--X-ray spectrum generated from 19.2keV electrons incident on carbon and detected with Si(li) detector (a) before and (b) after correction for detector-degraded counts. Correction (c), which was calculated from correction coefficients measured for our detector, is sum of (d) incomplete charge collection, (e) escape, and (f) Compton corrections. Bumps in calculated Compton correction are artifacts that arise from approximations for energy-dependence of correction coefficient.

Corrections are product, or sum of products, of counts in spectrum with correction coefficients illustrated in Fig. 4.

Fig. 3(b), the shelf was assumed to originate from parent x rays at an energy $<E_p>$ which was an average weighted with the correction coefficient:

$$<E_p(j)> = [\sum_{l>j} k_c(j,l)E_p(l)N_p(l)]/[\sum_{l>j} k_c(j,l)N_p(l)]$$

Two iterations were judged sufficient to determine values for k_c and $<E_p>$. The coefficients k_c determined for the shelf region at Na $K\alpha$ are plotted in Fig. 4, curve c, as a function of parent energy E_p. The solid curve c is a fit to the function

$$Log[k_c(j)] = a_c(j)x^2 + b_c(j)x + c_c(j)$$

where $x = log<E_p(j)>$. The correction coefficients k_c for Compton scattering increase rapidly with increasing parent energies and with decreasing shelf energies. For ease in calculating the Compton correction for the carbon spectrum in Fig. 5, the coefficients $a_c(j)$, $b_c(j)$, and $c_c(j)$ were fit empirically as a second degree polynomial function of shelf energy. Since spectra were collected only for energies up to 10 keV, the bremsstrahlung was extrapolated to higher energies for the Compton correction. The high energy continuum was described by the function

$$[K_1 (E_0 - E) + K_2 (E_0 - E)^2]/E$$

where E_0 is the beam energy and E is the x-ray energy.[10] The parameters K_1 and K_2 were fit to the smooth part of the spectrum below 10 keV.

Results

Escape, incomplete charge collection, and Compton correction coefficients determined for our detector are plotted in Fig. 4. When these correction coefficients are applied to a carbon spectrum excited by a 19.2keV electron beam, the calculated correction accounts for the low-energy shelf in the region where the Be window strongly attenuates incident x rays, as shown in Fig. 5. In the energy region around 1 keV, the calculated correction is about 20% of the total counts.

In this spectrum, approximately 85 to 90% of the spurious counts below 2 keV is caused by incomplete charge collection, 10% by escape, and 2 to 3% by Compton scattering. The escape coefficient is the largest correction coefficient, but not the largest correction; at a given parent energy, escape affects only one shelf energy, that occuring 1.74 keV lower, and incomplete charge collection and Compton scattering affect all lower energies. The escape correction is important, however, because escape introduces spurious peaks in a spectrum which can bias fits from the analysis program that measures peak areas. The Cl escape peak, for example, falls just to the lower energy side of the Na peak and, if not subtracted from the spectrum, would cause the Na peak to be underestimated. For routine analysis of our spectra, corrections for incomplete charge collection and for Compton scattering are made only for energies below 1.5 keV, and escape corrections are made for the entire spectrum.

We have tested the shelf correction by measuring Na and Mg concentrations by the peak-to-background method in a standard with various amounts of shielding of the emitted radiation.[5] Calculated concentrations should be independent of shielding for spectra properly corrected for detector-degraded counts. Fitted values for peak and bremsstrahlung counts were input to the analysis program ZAFPB,[11] which compared peak-to-background ratios of samples and standards and computed corrections for differences in mean atomic number, backscattering, etc., by use of equations given by Statham.[1] For spectra without shelf corrections, increasing shielding caused a steady decrease in the calculated concentrations, since shielding reduced the intensity of characteristic peaks and bremsstrahlung without affecting the shelf. In a range of moderate shielding where analyses of uncorrected spectra gave a systematic bias and a variation of 40%, analyses of corrected spectra gave concentrations for Na and Mg accurate to within about 15% (relative).

Since heavier shielding, which attenuated more than 60% of the emitted x rays in the Na region, caused Na concentrations to be underestimated, even for corrected spectra, we defined a shielding ratio that allowed spectra with moderate shielding to be selected objectively. Such a shielding ratio could be defined for any element: a ratio of bremsstrahlung counts near the low-energy region of interest to bremsstrahlung counts at high energy. For reliable analysis of Na in our spectra, for example, we found that the ratio of counts at

1.25 keV to counts at 3.05 keV should be greater than 0.5.

With the shelf correction and with moderate shielding, the peak-to-background method gave results for these elements with soft x rays which begin to approach the accuracy of results for elements with harder x rays. These peak-to-background analyses were done with samples and standards with approximately the same mean atomic numbers. This procedure minimized the correction in ZAFPB and doubtless contributed to the accuracy of the results.

A suggested simplified procedure for calibrating a Si(Li) detector for spurious counts is as follows,

1. Adjust discriminator threshold so that the Cu Lα to Cu Kα peak ratio is independent of count rate.

2. Measure difference spectra for Si (25 and 50 μm mylar), P (25 and 50 μm mylar), Cl (138 and 63 μm mylar), and K (63 and 125 μm mylar), as illustrated in Fig. 2.

3. Calculate correction coefficients for escape from the Cl and K spectra and for incomplete charge collection from all four spectra. Decide whether correction coefficients for your detector and those for the detector in this work can be described by the same functions or whether more data are needed for your detector. Look, for example, for an abrupt change in the incomplete charge correction coefficient at the silicon absorption edge. You will see this abrupt change only if samples give characteristic peaks on either side of the edge. Difference spectra from a sample such as carbon without appropriate characteristic peaks give averages over energy regions too wide to demonstrate abrupt changes in the correction coefficient.

4. For beam energies greater than 20 keV, or for light elements measurable with a windowless detector, Compton scattering is likely to be important. In this case, take spectra at beam energies of about 17, 20, and 25 keV with a thick mylar filter in front of the detector. Obtain difference spectra, as shown in Fig. 3, and calculate Compton correction coefficients. Decide whether Compton correction coefficients for your detector and those for the detector in this work can be described by the same function or whether more data are needed for your detector.

5. Correct your spectra for detector-shifted counts. For the escape correction, use a channel-by-channel correction of the entire spectrum. Check first the linearity of the energy scale of the multichannel analyzer; see if the escape peaks for both Cl and K are shifted by 1.74 keV from their parent peaks. For incomplete charge and Compton corrections, calculate an average correction to be applied only to the Na and Mg regions (or to the lowest energy regions of interest).

References

1. P. J. Statham, "A ZAF procedure for microprobe analysis based on measurement of peak-to-background ratios," *Microbeam Analysis--1979*, 247-253.

2. J. A. Small, D. E. Newbury, and R. L. Myklebust, "Analysis of particles and rough samples by FRAME P: A ZAF method incorporating peak-to-background measurements," *Microbeam Analysis--1979*, 243-246.

3. P. J. Statham and J. B. Pawley, "A new method for particle X-ray micro-analysis based on peak to background measurements," *SEM/1978* I, 469-478.

4. J. A. Small, K. F. J. Heinrich, C. E. Fiori, R. L. Myklebust, D. E. Newbury, and M. F. Dilmore, "The production and characterization of glass fibers and spheres for microanalysis," *SEM/1978* I, 445-454.

5. M. C. Foster, W. A. Hagins, and D. H. Blackburn, manuscript in preparation.

6. S. J. B. Reed, *Electron Microprobe Analysis*, New York: Cambridge University Press, 1975.

7. R. Woldseth, *X-ray Energy Spectrometry*, Burlingame, Calif.: Kevex Corp., 1973.

8. S. J. B. Reed and N. G. Ware, "Escape peaks and internal fluorescence in X ray spectra recorded with lithium drifted silicon detectors," *J. Physics* E5: 582-584, 1972.

9. P. J. Statham, "Escape peaks and internal fluorescence for a Si(Li) detector and general geometry," *J. Phys.* E9: 1023, 1976.

10. C. E. Fiori, R. L. Myklebust, K. F. J. Heinrich, and M. Yakowitz, "Prediction of continuum intensity in energy-dispersive X-ray microanalysis," *Anal. Chem.* 48: 172-176, 1976.

11. Jon McCarthy, personal communication.

SECONDARY ION MASS SPECTROMETRIC (SIMS) ANALYSIS OF ION EXCHANGE IN BIOLOGICAL TISSUE BY USE OF STABLE ISOTOPES

M. S. Burns

Since SIMS uses a mass spectrometric detection system, it should be possible to analyze and quantitate ion exchange processes in localized areas by use of stable isotope substitution for the isotope of greatest natural abundance.[1,2] The feasibility of such an analysis was examined with ion exchange in toad lens used as a paradigm.

Experimental

The intraocular lens depends on ion exchange from the surrounding fluid (aqueous humor) for maintaining transparency. The lens can be maintained in vitro for prolonged periods (24 hr) in a solution approximating the composition of aqueous humor.[3] Substitution of lithium for sodium, rubidium for potassium, and 42-calcium or 44-calcium for 40-calcium was made in the incubating solution. Following freezing (at -130°C) and freeze-drying (at -30°C) the specimens were directly embedded in epoxy resin, sectioned, and supported on a silicon wafer overlaid with 99.999% Au for charge conductance.

Analyses were performed on a Cameca IMS-3f, with O_2^+ bombardment at a current density of 10^{-4} A/cm^2 and collection of positive secondary ions. Ion images, quantitation routines, high mass resolution, and ion energy distributions were used for data analysis.

Results

Mass interferences pose a potential problem for quantitative analysis. High mass resolution showed that masses 7^+, 23^+, 39^+ and 85^+ were free of significant interferences.[4] However, the calcium isotopes exhibited interferences which were significant when the calcium concentration was low. In particular, ^{44}-Ca had a high background due to hydrocarbon interferences, most probably arising from CO_2^+ generated above the specimen surface.

The possibility of charging effects giving rise to artifactual ion localization was investigated by the use of ion energy distributions. No significant charging or matrix-induced effect was found.

Reproducibility of quantitation is less good in the IMS-3f than previously reported in the IMS-300.[1] Nevertheless quantitation was approached by normalization to a matrix ion, 12^+.

Lithium exchanges for sodium quickly, but not completely, and exhibits a decreasing cortical to nuclear gradient. Rubidium substitution for potassium is much slower and is evenly distributed throughout the lens at incubation times as long as 5 hr. By the use of quantitative data in addition to ion images, a preferential location of calcium was found in the apical epithelial space. Extracellular capsule and calcium isotope exchange within the lens is much slower than reported in studies using radioactive isotopes.[3] Images indicate that large amounts of unincorporated calcium are bound to the external tissue surface, which may be responsible for the discrepant results.

SIMS can be used to perform "pulse-chase" studies in biological specimens using stable isotopes.

References

1. M. S. Burns-Bellhorn, "Secondary ion mass spectrometry (SIMS) of standards for analyses of soft biological tissue," *Anal. Biochem.* 92: 213-221, 1979.

2. M. S. Burns and D. M. File, "Localization and quantitation of sodium, potassium and calcium in galactose induced cataracts in rats by SIMS," *Invest. Ophthal. Vis. Sci. Suppl.* 54, 1980.

3. G. F. Baldwin and P. J. Bentley, "The calcium metabolism of the amphibian lens," *Exp. Eye Res* 30: 379-389, 1980.

4. M. S. Burns, "Polyatomic interferences in high-resolution secondary ion mass spectra of biological tissues," *Analyt. Chem.* 53: 2149-2152, 1981.

COMBINED X-RAY MICROANALYSIS AND RADIOAUTOGRAPHY OF DIFFUSIBLE ELEMENTS IN AQUEOUS SUSPENSIONS OF CELLS AND CELL FRAGMENTS

W. A. Hagins, M. C. Foster, J. G. George, and Benes Trus

Identification and analysis of small particles by electron beam excited x-ray microanalysis is a commonplace procedure for particles extracted from air or other gases by filtration.[1] When mixtures of fragile particles in aqueous suspensions must be studied, however, special problems arise. The suspension must be spread thinly enough so that the particles do not overlap and can be recognized in the dried residue of solutes; the solvent must be removed by means that do not destroy or distort the particles or selectively remove any of them; and the substrate on which the particles are distributed must not interfere with particle identification or x-ray microanalysis. This paper describes a method for harvesting and studying suspended cells and cell fragments that meets these three requirements and that also permits radioautographic measurement of beta-emitting radioisotopes in the dried residue of the suspension even when water-soluble elements or compounds must remain undisturbed. The isolated outer segments of vertebrate retinal rod cells are used to illustrate the procedure to study the distribution of K, Os + P, and ^{45}Ca in unusually unstable objects.

Procedure

Suspensions of rod outer segments (ROS) were harvested from live frog retinas by a method described previously.[2] The suspending medium contained 20 mM NaCl, 80 mM K isethionate, 10 mM N-2-hydroxyethyl piperazine-N'-2-ethane sulfonate (buffer), 20 mM phosphocreatine, 5 mM of guanosine and adenosine triphosphates, and 15 mM $MgSO_4$. A trace of $^{45}Ca^{++}$ was added to provide a suitable radioisotope for the particles to accumulate. The suspension contained about 1000 ROS per microliter, and about the same concentration of 4µm glass microspheres was added for reasons to be explained. The suspending medium thus contained deci- or millimolar levels of Na, P, S, Cl, and K.

Polyester films about 2 µm thick (mylar, obtained from Polysciences, Inc.) were stretched tightly over "embroidery rings" and cemented across thin 35mm diameter acrylic rings with α-cyanoacrylate adhesive. A 1-ml drop of particle suspension was spread by capillarity between two films, frozen by dropping into liquid N_2, warmed to -80°C and stripped of its topmost film as shown in Fig. 1. The stripping was made easier if the top film had previously been exposed to dichlorodimethyl silane vapor for 2 hr to make it hydrophobic. The stripped layers were about 4-5 µm thick, because the glass microspheres prevented the two mylar films from approaching more closely. After freeze-drying the layers at -76°C for 8-36 hr the films were exposed to OsO_4 vapor for 5 min and the particle-free *trans* sides coated with Ilford K5 radioautographic emulsion in a photographic darkroom. After 2-4 days to allow the emulsion to be exposed to the ^{45}Ca radiation in a dry chamber at 4°C, the emulsion was developed, fixed, and dried by standard methods.[3] The film was coated on both sides with 10-30 nm of carbon by vacuum evaporation.

The particle-bearing *cis* side of a typical film is shown in Fig. 2(a). ROS and glass microspheres (S) are seen, along with crystals (C) formed from solutes during the drying stage of freeze-drying. In addition to their function as spacers, the microspheres serve as position markers and as microanalysis standards that (in this case) contained known amounts of Si, K, and Ca. Si area maps of particular regions (not shown) showed patterns of distributions of spheres that could be recognized from either the *cis* or *trans* side of the film.

The first three authors are with the Laboratory of Chemical Physics, NIADDK; author Trus is with the Computer Systems Laboratory, DCRT, National Institutes of Health, Bethesda, MD 20205.

The thickness of the polyester film was great enough to arrest 10keV electrons, but more energetic electrons excited elements on both *cis* and *trans* sides. The patterns of spheres were used to key maps of elements made from the *cis* sides of the films (on which the particles could be seen by SEM) with maps of Ag made from the *trans* sides (from which the particles could not be seen by SEM). The polyester film could be punched through mechanically or with the electron beam to form a Faraday cup useful for measuring beam current. Three holes were punched into each film to provide fiducial marks that could be recognized from both *cis* and *trans* sides at low magnification. The positions of regions on the trans side could then be computed from settings of the stage coordinates when the films were mounted with either the *cis* or *trans* sides facing up.

Results

Element maps from the area shown in Fig. 2(a) were made with a 10keV electron beam at 2.5 nA by means of an energy-dispersive spectrometer (Tracor-Northern TN2000). Mapping regions centered on the Kα emission lines of P (Fig. 2b, c), K(Fig. 2e) and the L lines of Ag (Fig. 2d). The P map also contained counts from the unresolved Os M emission lines, thus enhancing the x-ray contrast of the ROS, whose highly unsaturated lipids react with at least 2 moles of Os per fatty acid residue.[4,5] The Ag map was made from the *trans* side of the film; the others, from the *cis* side of the same region. The counts above continuum were grouped in an array of 50×50 pixels and interpolated to an array 99×99. The Ag map was reversed so as to match those of the other elements. To make an even closer comparison between the distribution of Ag and that of the elements on the *cis* side, the *cis* maps of P + Os (Fig. 2b) and of K (not shown) were convolved with the radial diffusion function for the radioautographic process.[6] The resulting maps (Figs. 2c and e) thus appear as if they had been observed with the same spatial resolution as that of the β radiation sources (Fig. 2d).

If a point source of radiation is located at a height h above a radioautographic emulsion and the emerging β particles penetrate through both the emulsion and the polyester film with negligible attenuation (a good approximation for the 255keV β particles of ^{45}Ca), then the density D(r) of developed silver grains will be of the form

$$D(r) = A/(r^2 + h^2) \tag{1}$$

where r is radial distance along the emulsion from a point just below the source. This relation applies out to radial distances at which the obliquity of the β particle tracks is so great that they are totally absorbed in the emulsion, at which point D(r) becomes[6]

$$D(r) = B/(r^2 + h^2)^{3/2} \tag{2}$$

For the energetic radiation of ^{45}Ca Eq. (1) holds out to distances of about 100 μm, virtually the dimensions of the areas shown. Empirical measurements of the radial distribution of Ag grains about point sources of ^{45}Ca radiation in mitochondrial suspensions freeze-dried on films similar to that of Fig. 2 yielded a value for h of 6.1 ± 1.0 μm. This is slightly greater than that to be expected from the known 2.5μm thickness of the polyester film and the 3μm thickness of the undeveloped Ilford K5 emulsion, but the difference is not great. The empirical value for h was used to transform the *cis* maps. The effect of the transformation on map resolution can be seen by comparing Figs. 2(b) and (c). Fig. 2(d) shows accumulation of ^{45}Ca in the ROS and to a lesser extent in the glass microspheres, where it presumably substitutes for Ca in the silica matrix. The distribution of K is quite unlike that of P + Os, which is especially intense over the ROS.

Although the distribution of Ag could have been measured by light microscopy, use of x ray mapping is much more convenient despite its limited dynamic range in assessing image density in a developed emulsion.[7]

Conclusions

From study of many preparations like that of Fig. 2 we conclude: (1) Although the fluid layers froze quickly (in less than 0.2 s) with no obvious inhomogeneities, major relocation of diffusible elements such as K took place during the drying process. Apparently small molecules and ions have considerable lateral mobility in the interface between a vacuum and a receding ice surface. The 2-4μm separation between K-rich crystals visible in Fig. 2 suggests that diffusible elements cannot be located accurately by freeze-drying unless some

stable framework of indiffusible material can be provided to immobilize them during the drying step. The distributions of K and S varied in texture in different preparations, but once formed, they were stable as long as the film was kept strictly dry. The low water permeability of mylar made that possible even during processing of the radioautographic emulsions. (2) The distribution of β-emitting radioisotopes in freeze-dried suspensions can be measured quantitatively if the sensitivity and thickness of the radiosensitive emulsion can be determined accurately. Although relations like those of Eqs. (1) and (2) are useful, their unknown parameters A, B, and h must be computed from measurements on calibrated sources of radiation of known intensity and spatial distribution. Although such calibrations are tedious, the high amplification of the radioautographic process makes possible the application of the present method to a much wider variety of problems than are accessible to x-ray microanalysis alone.

References

1. K. F. J. Heinrich, Ed., *Characterization of Particles*, N.B.S. Special Publication 533, 1980.
2. W. E. Robinson and W. A. Hagins, "GTP Hydrolysis in intact rod outer segments and the transmitter cycle in visual excitation," *Nature* 280: 398-400, 1979.
3. A. W. Rogers, *Techniques of Autoradiography*, Amsterdam: Elsevier, 1973, ch. 2.
4. J. Eichberg and H. H. Hess, "The lipid composition of frog retinal rod outer segments," *Experientia* 23: 993-994, 1967.
5. R. E. Anderson and M. B. Maude, "Phospholipids of bovine rod outer segments," *Biochemistry* 9: 3624-3628, 1970.
6. M. M. Saltpeter, L. Bachmann, and E. E. Saltpeter, "Resolution in electron microscope radioautography," *J. Cell Biol.* 41: 1-21, 1969.
7. D. L. Fry, A. J. Tousimis, T. L. Talbot, and S. J. Lewis, "Methods to quantify silver in radioautographs," *Am. J. Physiol.* 238: H414-422, 1980.
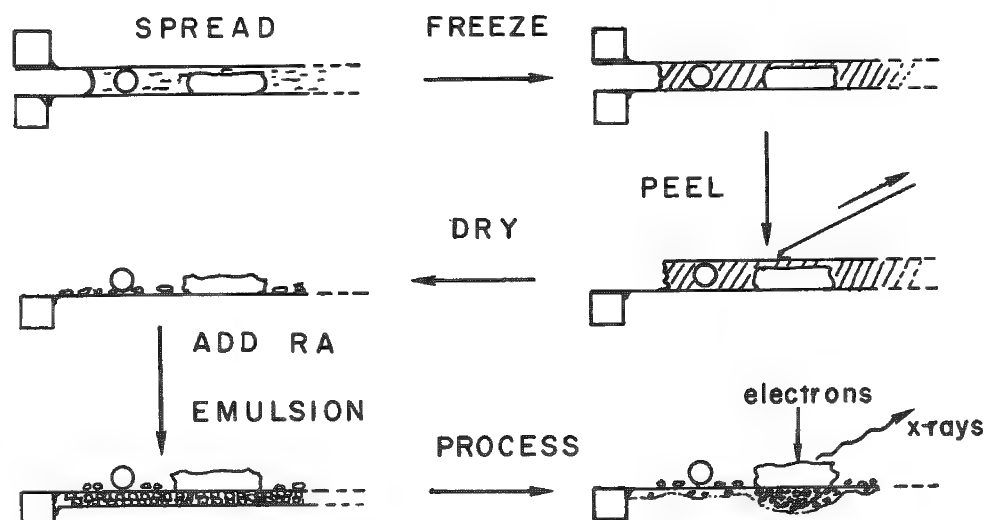
FIG. 1.--Procedure for forming and radioautographing thin aqueous films of suspended particles.
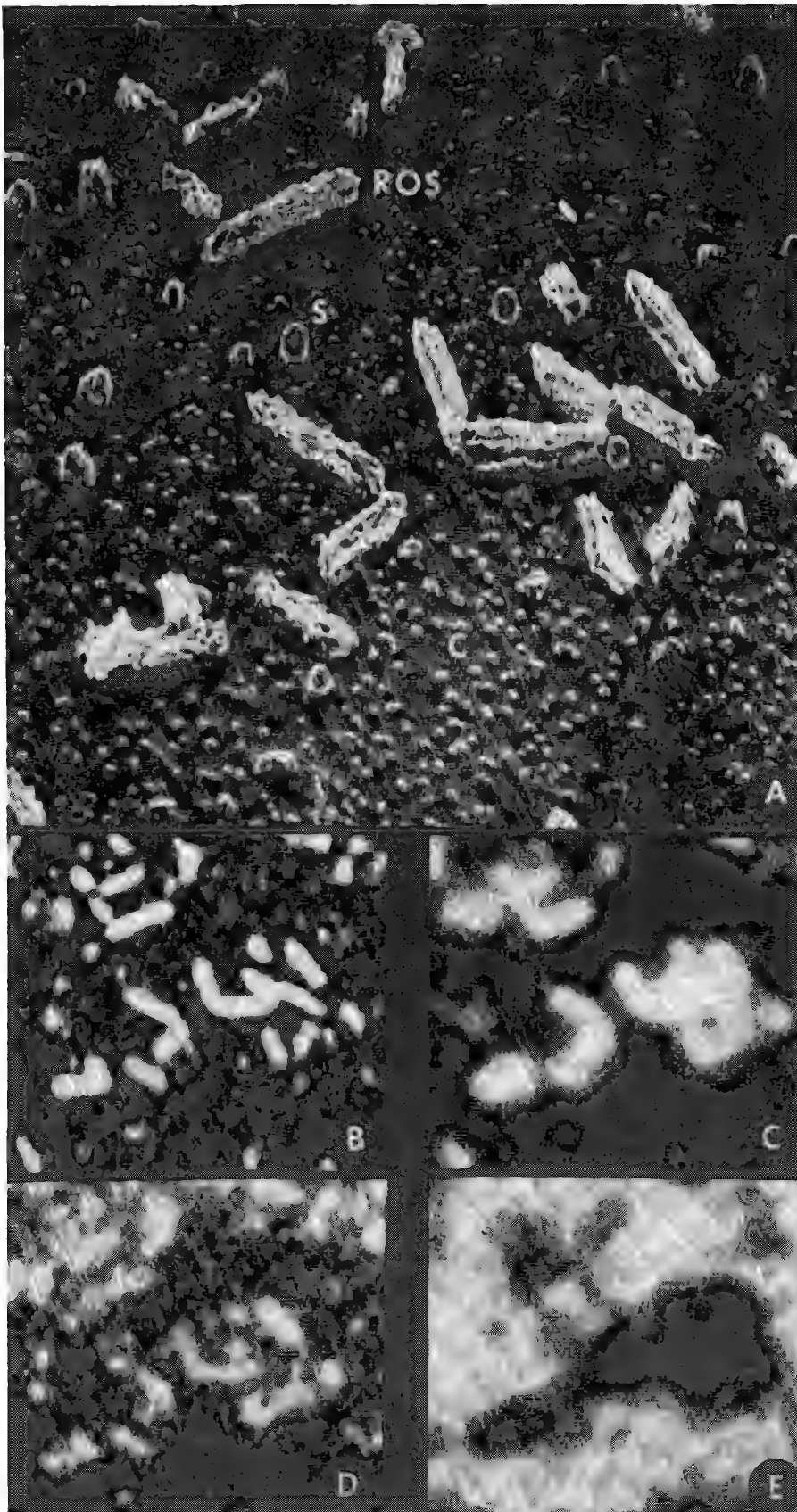
FIG. 2.--Images of area of freeze-dried suspension of frog rod outer segments (ROS) containing 4μm glass microspheres (S); 10keV excitation. A. SEM image at a beam current of 50 pA. Many small crystals containing K and S are visible between the ROS. Picture width, 250 μm. B. Phosphorus K + Osmium M x-ray map of same area as (A). Beam current, 2.5 nA. Scanning period, 1 hr. Scans collected counts between 1.9 and 2.1 keV and were grouped in computer memory to form map 50×50 pixels. X-ray continuum counts were digitally subtracted from map and pixels were interpolated onto grid of 100×100 pixels. Light areas represent regions of high elemental abundance. No ZAF corrections were applied. C. P + Os map of (B) convolved in two dimensions with radial diffusion function of radiographic process (Eq. 1) with h = 6.1 μm. Resolution of map obtained is to be compared with radioautographic images of Ag on *trans* side of film cover-in same region. D. Elemental map of *trans* side of same region with Ag L emission. Beam current, 2.5 nA. Scanning period, 30 min. Distribution of Ag is concentrated over ROS, which indicates they have accumulated ^{45}Ca after 1hr incubation; 10μM ruthenium red was added to incubation medium to inhibit Ca accumulation by mitochondria. Ag counts in unexposed area of emulsion were subtracted and empirically determined Ag counts:β exposure relation for Ilford K5 emulsion was used to convert Ag counts to equivalent β particle exposure. Resulting map is approximate representation of radiation source density in particle layer. E. Elemental map of potassium: K emission made from *cis* side of area shown in (A). Continuum counts subracted and image convolved with diffusion function (Eq. 2). Interpolated to 100×100 pixels. K occurs mainly in small crystals C visible in (A) and not in ROS. Beam current, 2.5 nA. Scanning period, 1 hr.

PIXE AND XRF ELEMENTAL ANALYSIS OF HUMAN OCULAR TISSUE

B. J. Panessa, H. W. Kraner, J. B. Warren and K. W. Jones

In humans, as in other vertebrates, vision depends on the ability to respond appropriately to photon excitation. When the rhodopsin in the photoreceptors of the retina absorbs photons, Ca^{2+} is released intracellularly which decreases the movement of Na ions at the plasmalemma and thus alters the membrane potential at the synapse.[1] Therefore the maintenance of vision depends not only on the function of the various ocular cells, but also on the presence and availability of adequate amounts of specific elements. Recent investigations on the damaging effects of free radicals produced by light damage and oxygen toxicity have also revealed that a group of metallo-enzymes are essential for the preservation and optimal function of the retina. Peroxidase and superoxide dismutase have been found in the retina pigment epithelium (RPE), which suggests that a complex system of free radical production and disposal may be continually operating here.[2] Superoxide dismutase has also been found in the retina with highest activity in the rod outer segments (ROS).[3] These detoxifying enzymes, along with such essential enzymes as retinol dehydrogenase, carbonic anhydrase, and tryosinase, require the presence of Cu, Zn, or Se. Therefore it can be assumed that optimal retinal function depends on the presence of these trace metals as well as the routine electrolytes. Previous studies have shown that the melanin pigment in the eye may act as a cation reservoir, especially in the RPE.[4,5] For this reason the pigmented cells of the iris, choroid, and RPE are especially interesting.

This paper describes the elemental composition of normal and pathological human ocular tissues from subjects ranging from 28 weeks gestation to eighty years of age.

Methods

Recent studies have shown that human RPE cells removed within 6-96 hr after death are still viable and can be successfully cultured in vitro.[6,7] To reduce the possibility of elemental alterations the tissue used in this study was obtained between 12 and 60 hr post mortem. Initially the eyes were placed in 3% glutaraldehyde in 0.1 m cacodylate or PIPES buffer (pH 7.35) immediately after enucleation. Preliminary analyses demonstrated elemental loss following fixation for more than 12 hr. Separation and dissection of unfixed tissue produced torn and contaminated layers of retinal and RPE tissue. To facilitate peeling away the retina and underlying RPE, the eyes were briefly fixed at room temperature for 20 min to 4 hr. This procedure hardened the tissues sufficiently to permit the neurological retina to be lifted away from the RPE and removed. The RPE was removed as a sheet with the underlying choriocapillaris and pigmented choroid (labelled RPE-C) attached. Portions of nonpigmented choroid and the pupillary margin of the iris were also prepared for analysis. The isolated tissue was trimmed into small rectangular pieces (1.5 × 2 mm to 2 × 3 mm) and prepared for x-ray fluorescence spectrometry (XRF) and proton induced x-ray emission spectroscopy (PIXE). The tissue segments along with 2μl samples of fixative and buffer were mounted between two layers of formvar (70-90 mm thick) suspended on a lexan frame. The remaining tissue was either immediately dehydrated in acetone, dried by the critical point method, and prepared for SEM analysis (samples for electron beam x-ray microanalysis were attached to carbon stubs with colloidal graphite and coated with 50-70 nm carbon); or
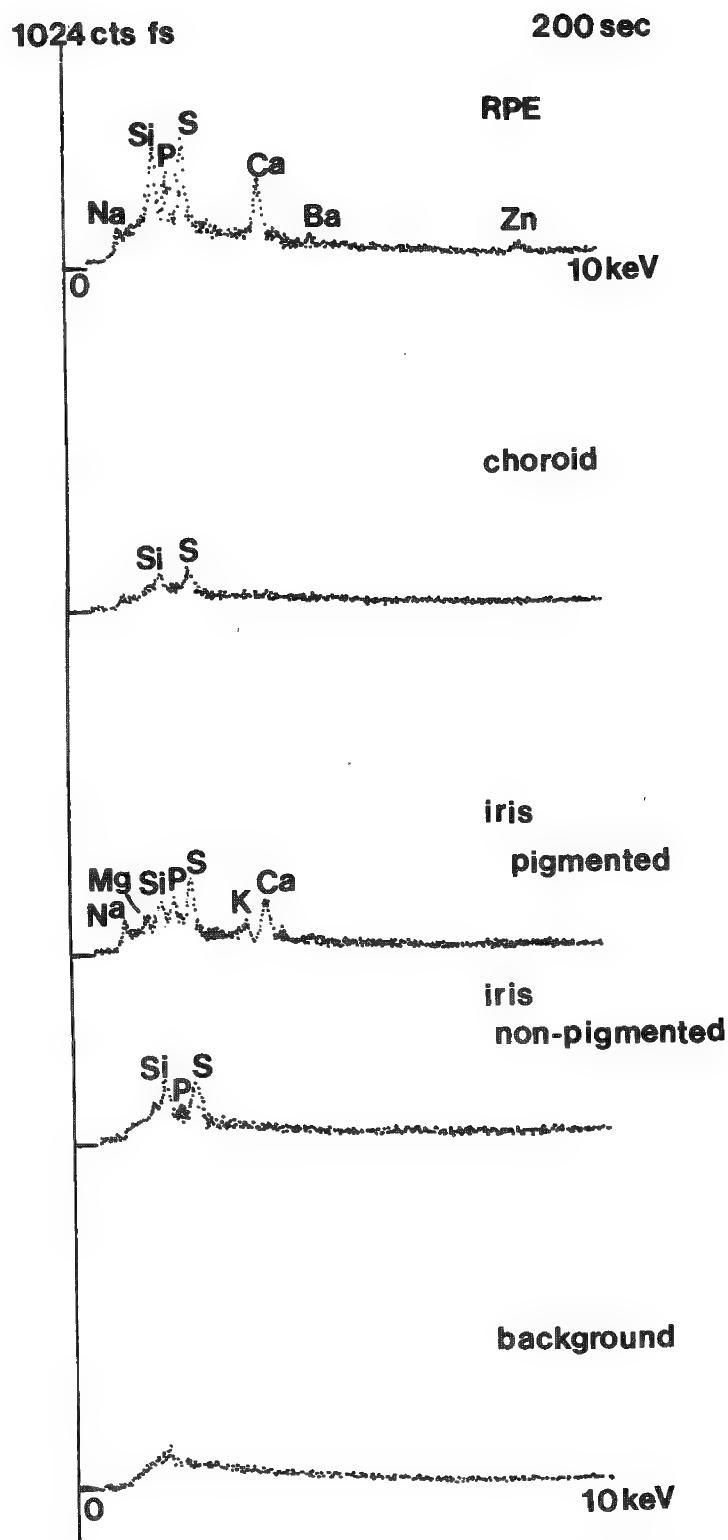
FIG. 1.--Occular tissue from 28-week fetus (death due to cord accident). Electron beam x-ray microanalysis reveals that pigmented tissues exhibit far more cations than nonpigmented adjacent tissues, 20 keV, 100 μA, 10° tilt, 200 s, spot diameter 50 nm.

the tissue was postfixed in 1% OsO_4 at room temperature for 1 hour, dehydrated in acetone, infiltrated with plastic, and examined by light and transmission electron microscopy.

After elemental analysis the PIXE and XRF samples were removed from the formvar and weighed on a Cahn electrobalance for future quantitative analysis.

The XRF analyses were done with a tube-excited hardened, filtered (0.006in. molybdenum) x-ray beam, Si(Li) detector system. PIXE analyses were done with a 2.5MeV proton beam (~ 4 mm in diam.) with a high-resolution Si(Li) spectrometer placed ~4 cm from the specimen. PIXE analysis complements XRF for lighter elements. Commercially available trace element standards in a representative matrix were used for energy and concentration calibrations.

Results

Electron beam induced x-ray microanalysis of human ocular tissue produced spectra suggesting that the majority of cations are associated with the pigmented tissues of the eye. Analyses of fixed isolated RPE-pigmented choroid show Na, P, S, Ca, Ba, and Zn signal (Fig. 1). The nonpigmented choroidal tissue and nonpigmented portion of the iris from a 28-week fetus do not exhibit significant Ca x-ray signal. The pigmented portion of the iris however produces prominent Na, S, P, K and Ca x-ray events (Fig. 1).

Although the fixed, critical point dried preparations produced clear spectra, charging was a considerable problem and necessitated the recoating of the specimens with additional carbon. That in turn made the detection of trace amounts of Ba, Cu, Se, etc. difficult. XRF and PIXE spectrometry permit analysis at higher sensitivity with minimal tissue preparation, and so eliminated sample charging. Figure 2 shows an XRF spectrum of an unfixed RPE-C preparation from the same neonatal ocular tissue as in Fig. 1. Unlike the electron beam induced spectrum, the background is noticeably less and the softer x-ray lines, as well as the Ba L lines, are clearly evident.

Glutaraldehyde-fixed tissue analyzed by XRF and PIXE exhibited a loss of K and Ca from retinal and iris tissue. This loss increased with the length of time that the tissue remained in fixative.
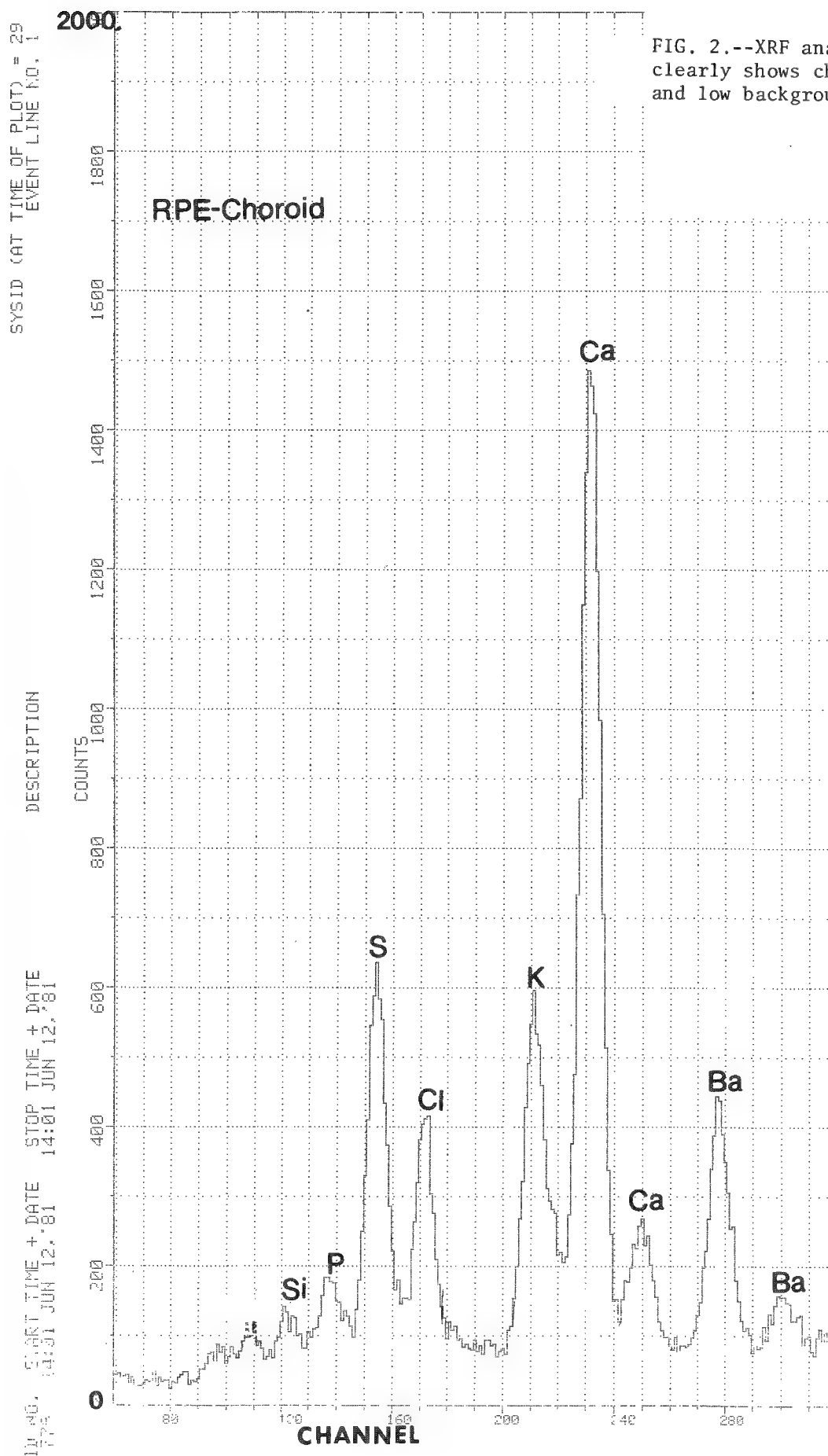
FIG. 2.--XRF analysis of human RPE-C clearly shows characteristic peaks and low background; 30 kV.

Table 1 shows the quantitative results from ocular tissue that had been prepared immediately following fixation and after 5 months in fixative. The RPE and retina were found to rapidly lose K and Ca. K was progressively lost with time; Ca was initially lost but then stabilized at a fixed amount, after which no further loss occured. After fixation the iris appeared to accumulate more Ca than would normally be found in the natural state. Because of these findings, tissue was not left in fixative after enucleation. Prior to mounting the samples the tissue was briefly fixed for less than 4 hr and immediately prepared for analysis.

TABLE 1.--Elemental content after fixation

		Element (μg/mg dry wt.)		
		K	Ca	Zn
7/81	RPE A_1	1.40	1.64	0.14
	RPE A_2	2.29	0.80	0.06
	Retina A_3	1.06	2.47	0.10
11/81	RPE B_1	0.79	0.40	0.15
	RPE B_2	0.36	0.34	0.17
	Retina B_3	None	0.74	0.10

XRF and PIXE analyses of RPE-C preparations always showed significant amounts of P, S, Cl, K, Ca, Fe, Zn, Cu, and (to a lesser extent) Se.

Human fetal and neonatal RPE-C samples yielded more Ca and usually more Cu and Zn x-ray signal than normal adult tissue (the normal adults were 52, 79, 79, and 80 years of age). Although Ba has been routinely observed in the retinas of toads,[8] frogs,[5] and some lower mammals,[9] normal human adult RPE-C preparations did not reveal any Ba x-ray events. Barium was also not found in the retina or iris of normal eyes. However, barium was observed in the RPE and iris of babies who suffered from oxygen toxicity, and in the RPE from a patient with advanced diabetic retinopathy. Both the neonatal oxygen toxicity tissue and the diabetic ocular tissue also showed elevated Ca levels. Although Cu is not usually seen to any extent above background, small Gaussian Cu Kα peaks could be clearly seen for both RPE and iris analyses from the oxygen toxicity and advanced diabetic patients. There is also a slight increase in Zn content in these samples.

No significant increase in Ca or Cu content was observed in darkly versus lightly pigmented eyes.

Ocular tissue from babies suffering from anencephaly and hydrocephaly yield spectra with less Ca and Zn. Too few samples have been studied to date to determine if these elemental differences are related to abnormal neurological development or to nutrition and care following delivery.

In summary, PIXE and XRF have provided a quick analysis of the elemental composition of specific isolated ocular tissues, and reveal that the composition of human tissue is very similar to that of other vertebrates. An exception is the absence of detectable amounts of Ba in normal adult fetal and newborn RPE, iris, and retina. Unlike frogs, toads, cats, and cows, humans lack significant amounts of ocular Ba. Significant amounts of Ba were found in iris and RPE tissue from a patient with advanced diabetic retinopathy and in three neonates suffering from anoxia and/or oxygen toxicity. The Ca content in the iris and RPE tissues from these subjects was also about twice that of normal individuals. Perhaps such an increase in total tissue Ca deposition is also accompanied by the deposition of Ba. RPE samples from a patient with mild retinopathy also showed a 1.1-2 fold increase in Ca content, but no detectable Ba.

The slight elevation in Cu and Zn x-ray signal in the aforementioned pathological specimens may be due to increased superoxide dismutase or other free radical detoxifying enzymes. Further analyses are necessary to determine whether the altered Zn and Cu levels are characteristic of severe retinopathy.

References

1. W. Hagins, *Physiology of the Eye*, St. Louis, Mo.: Mosby, 1981.
2. L. Feeney and E. Berman, "Oxygen, toxicity, membrane damage by free radicals," *Investigative Opthal.* 15: 789-792, 1976.
3. M. Hall and D. Hall, "Superoxide dismutase of bovine and frog outer segments," *Biochem. Biophys. Res. Commun.* 67: 1199, 1975.
4. M. Hess, "The high calcium content of retinal pigmented epithelium," *Exp. Eye Res.* 21: 471-479, 1975.
5. B. Panessa and J. Zadunaisky, "Pigment granules: A calcium reservoir in the vertebrate eye," *Exp. Eye Res.* 32: 593-604, 1981.

6. M. Del Monte and I. Maumenee, "*In vitro* culture of human retinal pigment epithelium for biochemical and metabolic study," *Vision Research* 21: 137-142, 1981.

7. M. Flood and P. Gouras, "The organization of human retinal pigment epithelium in vitro," *ibid.*, pp. 119-126.

8. K. Brown and D. Flaming, "Opposing effects of calcium and barium in vertebrate rod photoreceptors," *Proc. Nat. Acad. Sci.* 75: 1587-1590, 1978.

9. M. Bellhorn and R. Lewis, "Location of ions in retina by secondary ion mass spectrometry," *Exp. Eye Res.* 22: 505-518, 1976.

FLUORINE ELECTRON MICROPROBE ANALYSIS: VARIATIONS OF X-RAY PEAK SHAPE

T. N. Solberg

Fluorine microprobe analysis of various minerals at our laboratory with the use of a 16-element analytical scheme[1] has agreed with wet chemical analysis with the exception of topazes; our topaz analysis for fluorine is about 20% too low. A study of the fluorine Kα peak shape was done to help resolve why topaz should be analytically aberrant.

We used our ARL SEMQ long-wavelength x-ray scanning spectrometer which was initially equipped with a TAP crystal. Although TAP does give higher count rates than RAP, the poor resolution of TAP obscures peak shapes and it was therefore replaced with a RAP crystal. A 15kV beam potential was used for this study since we use this potential for most microprobe analysis. Figure 1 shows the superimposed F Kα scans from norbergite and a topaz. The original trace was produced on a x-y analog plotter whose x-axis was controlled by a potentiometer coupled to the motion of the x-ray spectrometer. A count rate meter controlled the y-axis. Although topaz contains more fluorine than the norbergite, the peak heights are nearly identical. However, when one measures the areas of the two peaks, one finds that the topaz has 20% more area than the norbergite. This is somewhat encouraging in that an area measurement rather than peak measurement would bring microprobe fluorine analysis into agreement with wet chemical analysis for topaz. But this would probably not be a practical procedure given the low count rates of less than 1 cps for most minerals. We want to increase neither count times nor beam currents. The difference in shape of the F Kα peaks for these two minerals was unexpected. Other light elements such as aluminum have been studied[2] and spectra variations were expected since coordinations do indeed vary. Study of the fluorine Kα spectra from various compounds should help determine appropriate standards for mineral analysis. Also, empirical factors might be determined to correct analysis for spectra shape differences.
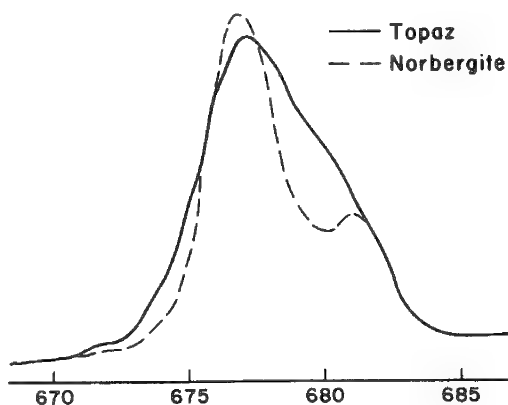
FIG. 1.--Fluorine Kα x-ray emission vs electron volts (15kV RAP crystal) from norbergite (13.5 wt.% F) and topaz (17.6 wt.%). Topaz peak area is 20% larger than that of the norbergite.

However, when we try to measure the peaks from many minerals of interest by the method used for Fig. 1, we find that the spectrometer potentiometer is neither linear nor accurate enough for careful peak studies. Also, the count rates are so low that statistical noise is equal to the peak intensity.

Since we have a computer-automated microprobe we wrote a program for signal-averaging 110 1s counts, corrected for beam current drift, through the F Kα peak. These 110 stored counts were then averaged with subsequent scans. The number of passes varied from 8 to 300; the longest took 10 hr. When the material being studied was large enough, the stage was also stepped 4 μm after each pass. The beam was rastered over a 10 × 8μm area. Data were stored on a disk file for later smoothing and calculations.

The disk-stored, signal-averaged F Kα spectra data were later plotted by a terminal 132 characters wide. There still was too much scatter for the less intense peaks. An attempt to smooth the data by a moving weighted average did reduce noise but distorted peak shapes too much. However, a least-squares method for smoothing data has been published[3] that preserves peak shape. We used a five-point method in which the new data point value is calculated from the equation

The author is at the Department of Geological Sciences of the Virginia Polytechnic Institute and State University, Blacksburg, VA 24061-0796.

$C'(I) = (1/35)[17C(I) + 12C(I + 1) - 3C(I + 2)]$ and normalized.

This method of least-squares smoothing exceeded our expectations and the final results of smoothing and subtracting background for the F Kα spectra were plotted on the terminal with peak height and sums of counts above background also printed out.
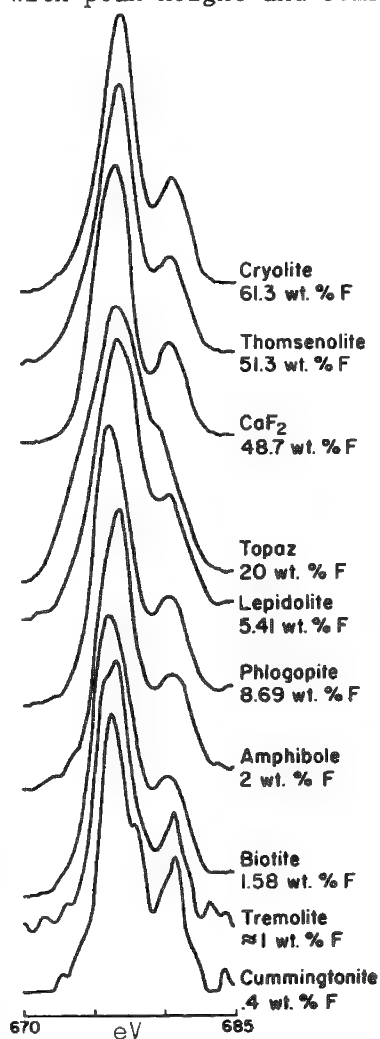
FIG. 2.--Normalized Kα x-ray spectra from various minerals. $K\alpha_1$ and $K\alpha_2$ peak not resolved for topaz.
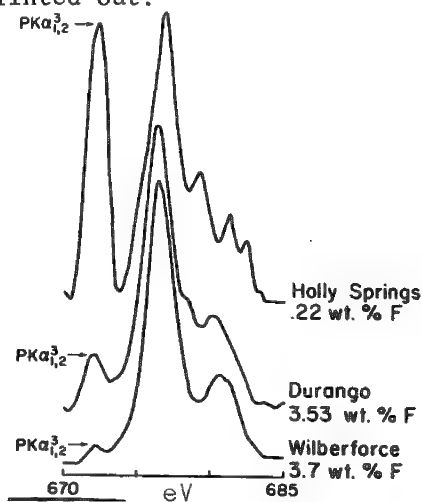
FIG. 3.--Apatite Kα x-ray spectra. Note interference by $PK\alpha^3_{1,2}$ x-ray line.
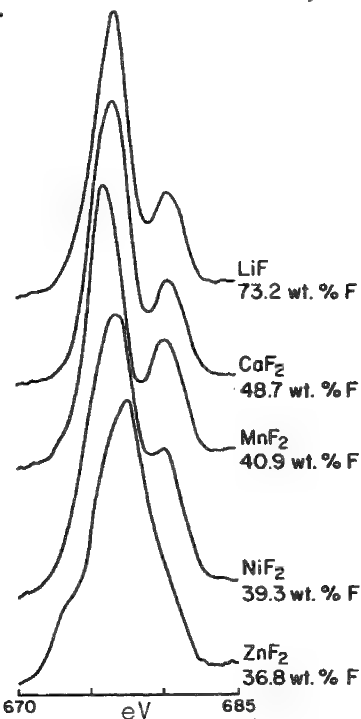
FIG. 4.--Comparison of fluorine Kα spectra from simple fluorides.

Figure 2 shows the F Kα spectra of several minerals in which we are interested. Note that all have a resolved $K\alpha_1$ and $K\alpha_2$ peak, with topaz the exception. Not shown is a comparison of the F Kα peak from a fluorine-rich topaz (Thomas Range, Utah) with a OH rich topaz (Brewer, S.C.), since the spectra are identical.

Table 1 compares peak counts and our summed counts, which approximate an area measurement. Note that the topazes have a ratio of sum to peak around 25 and most minerals have a ratio of 20.

Figure 3 shows the fluorine peak for some apatites of wide fluorine values. Note the interfering $P K\alpha^3$ peak. Pulse height settings and crystal resolution require special care in apatite analysis.

TABLE 1

MINERAL TYPE	NUMBER OF SAMPLES/RUNS	SUM (CPS) / PEAK (CPS)	ONE σ
TOPAZES	6	26.15	1.20
AMPHIBOLES	5	19.29	0.92
MICAS	7	20.52	1.21
CRYOLITE	1	19.24	-
FLUORITE	1	18.69	-
THOMSENOLITE	1	20.21	-
HUMITES	3	19.82	0.20

Some fluoride compound Kα spectra are shown in Fig. 4. The ZnF_2 fluoride would seem inadequate as a standard for most minerals.

We now have confidence that we can use an empirical correction for topaz fluorine analysis with our normal 16-element mineral analysis scheme.[1] We hope to do more work at different voltages and on other materials to understand the fluorine bonding and chemistry.

The averaging and least squares method we implemented would help us in other microprobe studies, such as trace element analysis and X-ray spectra studies of the L lines of transition elements.

References

1. T. N. Solberg and J. A. Speer, "QALL, a 16-element analytical scheme for efficient petrologic work on an automated ARL-SEMQ: Application to mica reference samples," *Microbeam Analysis--1982*, 422.

2. D. W. Fisher and W. L. Baun, "The effects of electronic structure and interatomic bonding on the soft x-ray Al K emission spectrum from aluminum binary systems," *Advances in X-ray Analysis* 10: 374-388, 1966.

3. Abraham Sauitzky and M. J. E. Golay, "Smoothing and differentiation of data by simplified least-squares procedures," *Analytical Chemistry* 36: 1627-1642, 1964.

QUANTITATIVE ELECTRON PROBE MICROANALYSIS: A REVIEW

J. D. Brown

The idea of analysis of materials by x rays generated by an electron beam had its origin in the work of Mosley[1] about 70 years ago; the first true electron-probe microanalyzer was built by R. Castaing[2] about 30 years ago. He is also responsible for the ideas of quantitative microanalysis based on pure element standards, recognizing that the use of standards close in composition to the unknown, as generally used in x-ray spectrometry, is just not practical in electron probe microanalysis. If the standard and unknown are very different in composition, then corrections must be applied to measured x-ray intensities to obtain the composition. The major corrections have now been identified; absorption of the characteristic x rays as they leave the specimen at some angle ψ, fluorescence of a second element due to excitation by absorption of the characteristic x rays of the first element or by absorption of continuum radiation, and an effect of average atomic number of the specimen that alters the number of x rays produced per electron per unit concentration. The first of these corrections is the absorption correction, the second the fluorescence correction , and the third the atomic number correction.

R. Castaing[2] in his thesis clearly showed the need for an absorption and fluorescence correction and within ten years of the publication of his thesis identified the two factors that lead to an atomic number correction.[3] Since the beginnings of quantitative analysis, correction methods have tended to proceed along one of three or four pathways. The first and most prominent method has involved the isolation and calculation of atomic number, absorption, and fluorescence effects separately--the so-called ZAF method. In the second, analytic expressions are used to describe the relationship between intensity and concentration, similar to the influence coefficient methods of x-ray spectrometry. The third important group of methods model the interaction of an individual electron with the solid specimen by use of Monte Carlo methods or energy transport equations. Finally, attempts have been made to model the depth distribution of x-ray production from which all the corrections may be derived. Because the first experimental measurements were made by Castaing and Descamps,[4] who termed the x-ray production curves $\phi(\rho z)$ curves, these methods have become known as $\phi(\rho z)$ methods. The purpose of this paper is to review these approaches, underlining their strengths and limitations and to suggest areas in which further work is warranted.

ZAF Corrections

When energetic electrons strike the surface of a solid target, x rays are generated not only at the surface but also within the volume of the target [$\phi(\rho z)$ curves]. When they leave the specimen, absorption takes place. This is the origin of the absorption correction, illustrated in Fig. 1, in which the upper curve shows the origin of the x rays as a function of depth in the specimen, whereas the lower curve shows the intensity that escapes from the specimen. In general, the absorption is different in the specimen and the pure element standard both because the mass absorption coefficients are different and because the shape of the $\phi(\rho z)$ curves is different. The absorption correction requires that this fraction of x rays $f(\chi)$ escaping from the sample be known so that the intensity of the characteristic x-ray line of element A from the specimen,

compared with the intensity of the same line under identical electron bombardment conditions from the pure element, K_A, is given by

$$K_A = W_A \frac{f_A(\chi_A)}{f_S(\chi_S)}$$

where W_A is the weight fraction, χ is the absorption parameter $\mu \csc \psi$, μ is the mass absorption coefficient, ψ is the x-ray take-off angle, and A and S refer to the unknown and pure element standard, respectively. This relation holds provided only an absorption correction is necessary. Values of $f(\chi)$ as a function of χ (absorption correction curves) were first produced by Castaing from measurements of $\phi(\rho z)$ curves. Very soon thereafter a number of authors, notably Green,[5] measured x-ray intensity as a function of take-off angle to obtain $f(\chi)$ curves. Philibert then derived an expression for $f(\chi)$ which has become the most widely used absorption expression. In its simplified form, which Philibert warned was not applicable in high-absorption conditions,

$$f(\chi) = \frac{1 + h}{[1 + (\chi/\sigma)]\{1 + h[1 + (\chi/\sigma)]\}}$$

where $h = 1.2A/Z^2$, A is the atomic weight, Z is the atomic number, and σ is an electron absorption parameter. The absorption correction in this form implies a $\phi(\rho z)$ distribution which is zero at the surface and decays exponentially past the region of highest intensity.[7] Both these assumptions are incorrect. Philibert originally proposed using Lenard's coefficient for σ, which depends only on the incident electron energy, but it was quickly realized by Duncumb and Shields[8] and by Heinrich[9] that σ should also depend on the absorption edge energy to yield better agreement with absorption correction curves, particularly at low electron energies; and so similar expressions for σ were proposed by those two authors.

More recently, particularly with reference to analysis of low atomic number elements,[10,11] investigators have reverted to the more complete Philibert expression

$$f(\chi) = \frac{\dfrac{1}{1 + (\chi/\sigma)} + h \dfrac{R_0}{R_\infty}}{\left[1 - \left(1 - \dfrac{R_0}{R_\infty}\right)\dfrac{1}{1 + h}\right]\left[1 + h\left(1 + \dfrac{\chi}{\sigma}\right)\right]}$$

in which the major problem is the values to be introduced for R_0 and R_∞, the values for the mean electron path length at the surface and at the depth where complete randomization has occurred. Philibert proposed using $R_\infty = 4$ and Duncumb and Melford[12] have shown that R_0 is equivalent to $\phi(0)$. Although this complete expression has a finite value for $\phi(0)$, the expression is still based on an exponentially decaying $\phi(\rho z)$, which still overestimates the x-ray intensity at large depths in the specimen.

The opposite trend toward simplified expressions for the absorption have also occurred. Duncumb and Melford,[12] for low atomic number elements and high absorption situations, proposed their thin film model, in which the escaping x-ray intensity decays exponentially from the surface value. Bishop[13] has proposed a model in which the $\phi(\rho z)$ curve is approximated by a constant intensity. Heinrich and Yakowitz[14] have proposed a

CARBON Kα IN AND FROM TiC
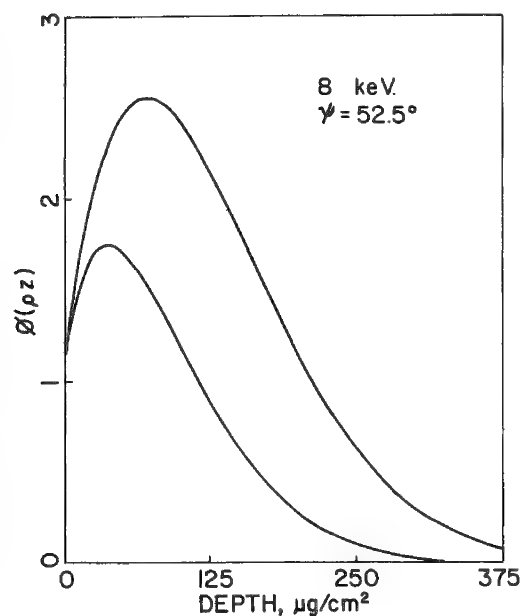
FIG. 1.--X-ray generation curves $\phi(\rho z)$ for C K line in TiC (upper curve) and origin of x rays emitted from sample at an x-ray take-off angle of 52.5% (lower curve).
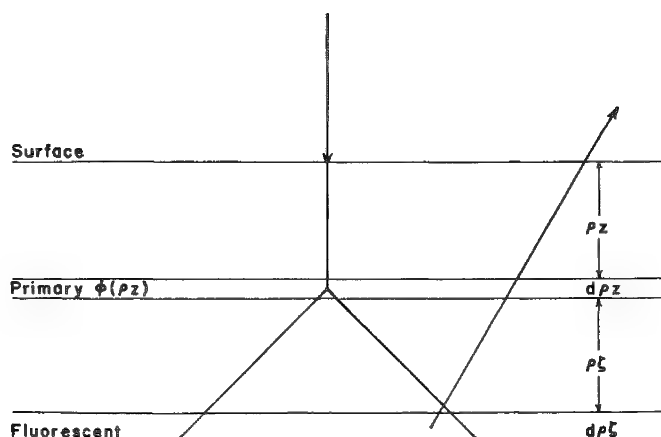
FIG. 2.--Geometry used in calculation of fluorescene effect.

quadratic expression in χ for $f(\chi)$, implying an independence of $f(\chi)$ on Z and A of the target. In all cases, these expressions can be used with reasonable accuracy in limited circumstances and they do possess the advantage of being simple mathematically. However, with the easy access to quite sophisticated and inexpensive computers, the need for such simplifications is rapidly disappearing.

The Fluorescence Correction

If an element is present in a specimen that strongly absorbs the characteristic radiation of a second element in the specimen, the inevitable consequence is that the absorbing element will be excited by ionization in one or more of its inner shells. This effect in turn leads to emission of characteristic x rays which add to that emitted as a consequence of direct electron excitation. A number of authors[15-17] beginning with Castaing[2] have derived expressions to calculate this fluorescent contribution. The geometry used is shown in Fg. 2. Primary x rays of element B from a layer dρz at depth ρz in a specimen are absorbed by A atoms in a thin layer d$\rho\zeta$ at a depth deeper into the specimen leading to emission of characteristic x rays of A which can escape from the specimen diminished by absorption on the path leaving the specimen. By appropriate integration over all depths for the secondary radiation, and then for all depths for the primary radiation, the contribution of fluorescent radiation can be calculated. The sole remaining task is to relate x-ray intensities of two different elements.

In the derivations, because of difficulties in integrating the expressions, simplified expressions for the $\phi(\rho z)$ curves are used which are either a point source of primary x rays at the surface[16] or an exponential decrease in intensity from the surface.[2,17] Expressions such as those of Rosseland[18] or Webster[19] have been used to relate the intensities of two characteristic lines into which empirical factors were introduced by Duncumb and Reed depending on which lines from different electron shells are involved. The accuracy of the fluorescence correction is also limited by the large

number of physical constants required such as the fluorescent yields and the absorption jump ratios. Since the largest correction is the order of 20% of the primary intensity and frequently is negligible or only a few per cent, it has been argued that the fluorescence correction is known well enough.

In the same way that fluorescence can occur as a result of absorption of characteristic radiation, the absorption of continuum can have the same effect. Henoc[20] derived an expression for continuum fluorescence in which the additional integration over the wavelengths of the continuum was performed assuming Kramers's formula[21] for the continuum. The result is a very complex expression indeed, which has subsequently been analyzed and simplified by Springer.[22] This correction has largely been neglected in quantitative corrections, although both Duncumb et al.[23] and Springer and Rosner[24] have evaluated the effect and found it to be greater than 1% for less than 20% of analyses.

The Atomic Number Effect

The atomic number effect is the consequence of a difference in the number of x rays generated per electron per unit concentration in matrices of different average atomic number Z. The higher the Z, the greater the number of x rays emitted per electron. The atomic number effect increases as the electron energy decreases towards the absorption edge energy. The two important effects that contribute to the atomic number effect are the stopping power for electrons and the backscatter factor R. The differences in stopping power lead to greater x-ray generation as Z increases; and because the backscatter coefficient increases with Z carrying off more energy, x-ray generation decreases with increasing Z.

The intensity ratio K_A', after correction for absorption, can be written as the ratio of the intensity gnerated inside the sample:

$$K_A' = W_A \frac{R_A}{R_S} \frac{\int_{E_0}^{E_A} \frac{Q_A(E)dE}{dE/d\ell}}{\int_{E_0}^{E_A} \frac{Q_S(E)dE}{dE_S/d\ell}}$$

where Q represents the ionization cross section for the element A in unknown and standard and $dE/d\ell$ is the energy loss per unit path length (stopping power). The first atomic number correction was published by P. M. Thomas,[25] who assumed that an average stopping power S could be used for the integral of $dE/d\ell$ and that the ionization cross section was identical in form for both unknown and standard. The backscatter factor R was obtained by a simplistic integration of the backscatter data of Brand[26] and the stopping power from Nelm's data.[27]

Duncumb and Reed[28] improved on the backscatter factor using Bishop's data[29] and used Bethe's expression[30] to generate a better stopping-power expression. Philibert and Tixier[31] introduced a variation of Q with energy into their atomic number expression. Recently, Love et al.[11] have also proposed changes to this same basic formulism by using a different stopping power expression and a different expression for R based on Monte Carlo calculations.

Many of the proposed atomic number corrections have been justified on the basis of error histograms, as first suggested by Poole.[32] The difficulty with this kind of evaluation, particularly if the simplified expression of Philibert is used for the absorption correction, is that any errors in the absorption correction then become part of the correction for the atomic number effect. Consequently, although in practical terms the correction procedures lead to acceptable accuracy for quantitative analysis, the model

and the reasons for using particular equations may be quite inaccurate. Note that even if mass absorption coefficients for two elements in a binary specimen are identical, a significant absorption correction can still be present because the shape of the $\phi(\rho z)$ varies significantly as a function of Z. This point will be discussed further later.

Analytic Expressions

Rather than trying to model the electron interactions, several authors beginning with Ziebold and Ogilvie[34] attempted to model the relationship between intensity and concentration. These equations have had the formulism of the second approximation of Castaing.[2]

$$K_A = \frac{\alpha W_A}{\sum\limits_i \alpha_i W_i}$$

The α values were approximated from the Philibert formula, empirical measurements, or simplified quantitative models. This approach has received much wider acceptance in x-ray spectrometry than in electron probe microanalysis, probably as a consequence of the easier application of theoretical calculation methods to the problem of the inter-action of monoenergic electrons with matter. In mineral analysis, Bence and Albee[35] have proposed such a relationship for silicates and oxides in terms of oxide weight percentages, in which each oxide is assigned an α coefficient and treated as if it were an element. This approach has received some acceptance. This formulism is identical in form to the influence coefficient equations.

Monte Carlo and Transport Equations

In the Monte Carlo method, the trajectories of individual electrons are followed with the key interaction events being predicted on the basis of random numbers. To obtain reasonable statistics, a large number (1000 to 10 000) of electrons must be followed, from the moment of impact on the surface, through hundreds or thousands of interactions, until the electron either loses enough of its energy so that it can no longer excite x rays or leaves the specimen surface as a backscattered electron. In the calculations, models for electron energy loss, electron scattering, x-ray cross section, and mean ionization potential are required. These interactions must be known in quite great detail for the proper modeling. Some of the strengths of the Monte Carlo method are the ability to predict a large number of experimentally measurable quantities such as electron backscatter coefficients, energy and angular distribution, x-ray production with depth, Auger electron yields, and energy deposition contours. An additional strength of the method lies in the relatively simple way thin layers, small particles, interfaces, and layered structures can be modelled. With many of the programs excellent agreement is being obtained among these experimentally measured parameters, and workers in Japan have succeeded in accurately predicting $\phi(\rho z)$ curves at low electron energies as well as the yield of Auger electrons. Models of electron interactions are being modified to give better agreement with these various experimentally measured properties.

D. B. Brown[36] was the first to advocate the use of an energy transport equation for modeling electron interactions of importance to electron probe micronalysis. This formulism has the advantage of being much less demanding of computer time but is more complicated in that the equations model collective behavior of electrons rather than single interactions. These equations have received much less attention than Monte Carlo calculations.

$\phi(\rho z)$ *Equations*

Castaing[3] pointed out that the measured intensity ratio can be written in terms of the depth distribution of x-ray production, as

$$K_A = \frac{W_A \int_0^\infty \phi_A(\rho z) \, e^{-\mu_A \rho z \, \csc \psi} \, d\rho z}{\int_0^\infty \phi_S(\rho z) \, e^{-\mu_S \rho z \, \csc \psi} \, d\rho z}$$

He also showed in a paper with Descamps[4] that by use of a sandwich sample, the $\phi(\rho z)$ curves could be measured. If the $\phi(\rho z)$ curves are known, then both the absorption and atomic number corrections can be calculated. For absorption,

$$f_A(\chi_A) = \frac{\int_0^\infty \phi_A(\rho z) \, e^{-\mu_A \rho z \, \csc \psi} \, d\rho z}{\int_0^\infty \phi_A(\rho z) d\rho z}$$

Note that the $f(\chi)$ value depends not only on χ, but also the detailed shape of the $\phi(\rho z)$ curve which changes as a function of Z. The h in the Philibert expression is the only factor which accounts for this variation, and it is not completely satisfactory. As a consequence, some of the Z dependence of the absorption correction spills over the atomic number correction in the conventional ZAF approach. The atomic number correction

$$K_A' = W_A \frac{\int_0^\infty \phi_A(\rho z) d\rho z}{\int_0^\infty \phi_S(\rho z) d\rho z}$$

is just the area under the curves, i.e., the total intensity for x-ray generation per unit concentration. If the primary x-ray distribution is known, it is a rather straightforward task to calculate any characteristic fluorescence effects that might occur in a specimen.

The first attempts to model $\phi(\rho z)$ curves analytically were by authors who were developing fluorescence corrections.[2,16] As a consequence, simple expressions that could be integrated were proposed without great concern for accuracy. As has been already pointed out, the Philibert adsorption correction in its simplified form implies a $\phi(\rho z)$ curve which is zero at the surface, rises rapidly to a maximum, and then decays exponentially at greater depths. Heinrich[37] proposed overcoming these obvious limitations by offsetting both axes of that expression, which would give curves more in agreement with the shape of the measured curves. Wittry[16] proposed a Gaussian form to the $\phi(\rho z)$ curve with the maximum centred at the maximum in the $\phi(\rho z)$ curve. More recently, Parobek and Brown[38] and then Robinson and Brown[39] looked at an empirical fit to a large body of experimentally measured $\phi(\rho z)$ curves and modelled the curves by the equation

$$\phi(\rho z) = DKn[K(\rho z - \rho z_0)]^{n-1} \exp[-K(\rho z - \rho z_0)^n]$$

156

with the four parameters D, K, n, and z_0 being established by the fits to experimental data and appropriate plotting to find the functional dependence.

This equation could be used to calculate $\phi(\rho z)$ curves to perform quantitative analysis but suffers from the limitation of empirical equations, that is extrapolating to conditions of measurement away from those of the measured $\phi(\rho z)$ curves is subject to large error.

Packwood and Brown[40] have shown that the $\phi(\rho z)$ curves are indeed Gaussian but with the Gaussian centered at the surface of the specimen. Further, they were able to relate the parameters of the Gaussian

$$\phi(\rho z) = \gamma_0 \left[1 - \frac{\gamma_0 - \phi(0)}{\gamma_0} e^{-\beta \rho z} \right] e^{-\alpha^2 (\rho z)^2}$$

which are α, β, and γ_0, to the laws of electron scattering and energy loss. With the Gaussian equation, error histograms have been obtained that are comparable to the best obtained by the conventional ZAF approach. These error histograms change quite quickly and distinctly with rather small changes in the three parameters, which suggests that the accuracy of quantitative analysis is more sensitive to the shape of the $\phi(\rho z)$ curve than previously thought. A significant advantage to the use of the Gaussian expression for $\phi(\rho z)$ curves for quantitative analysis is that it can be tested and improved at several levels. First, since the parameters of the equation can be derived from electron scattering laws, improvements in theory should lead to improved parameters. Second, as more $\phi(\rho z)$ curves are either experimentally measured or generated from Monte Carlo calculations, the Gaussian expression can be improved. Finally, quantitative calculations leading to error histograms can be used as a guide to adjusting the parameters.

A major outstanding problem in electron probe microanalysis is the effect of electron incidence angle on quantitative analysis. Progress in using the Gaussian equation in this situation is the subject of another paper at this conference.

References

1. H. Mosley, *Phil. Mag.* 26: 1024, 1913.
2. R. Castaing, Ph.D. Thesis, University of Paris, 1951.
3. R. Castaing, *Adv. Electron. Electron Phys.* 13:317, 1960.
4. R. Castaing and J. Descamps, *Comp. rend. Acad. Sci.* 238:1506, 1954.
5. M. Green, in H. H. Pattee, V. E. Cosslett, and A. Engström, Eds., *Proc. 3rd Intern. Conf. on X-ray Optics and Microanalysis*, New York, Academic Press, 1963, 361.
6. J. Philibert, *ibid.*, p. 379.
7. J. Criss, in K. F. J. Heinrich, Ed., *Quantitative Electron Probe Microanalysis*, NBS Special Publication 298, Washington, D. C.: National Bureau of Standards, 1968, 53.
8. P. Duncumb and P. K. Shields, in T. D. McKinley, K. F. J. Heinrich, and D. B. Wittry, Eds. *The Electron Microprobe*, New York: Wiley, 1966, 284.
9. K. F. J. Heinrich, NBS Technical Note 521, Washington, D. C.: National Bureau of Standards, 1970.
10. J. Ruste and C. Zeller, *Comp. red. Acad. Sci.* 284B: 507, 1977.
11. G. Love, M. G. C. Cox, and V. D. Scott, *J. Phys.* D-11:7, 1978.
12. P. Duncumb and D. Melford in R. Castaing, P. Deschamps, J. Philibert, Eds., *Proc. 4th Intern. Conf. on X-ray Optics and Microanalysis*, Paris: Hermann, 1966, p. 240.
13. H. E. Bishop, *J. Phys.* D-7:2009, 1974.
14. K. F. J. Heinrich and H. Yakowitz, *Anal. Chem.* 47:2408, 1975.
15. L. S. Birks, *J. Appl. Phys.* 32:387, 1961.
16. D. B. Wittry, Ph.D. Thesis, California Institute of Technology, 1957.
17. S. J. B. Reed, *Brit. J. Appl. Phys.* 16:913, 1965.
18. S. Rosseland, *Phil. Mag.* 48:65, 1923.
19. D. L. Webster, W. W. Hansen, and F. B. Duveneck, *Phys. Rev.* 43:893, 1933.

20. J. Henoc, in K. F. J. Heinrich, Ed., *Quantitative Electron Probe Microanalysis* NBS Special Publication 298, Washington, D. C.: National Bureau of Standards, 1968, 197.

21. H. A. Kramers, *Phil. Mag.* 46:836, 1923.

22. G. Springer in G. Shinoda, K. Kohra, and T. Ichinokawa, Eds., *Proc. 6th Intern. Conf. on X-ray Optics and Microanalysis*, University of Tokyo Press, 1972, 141.

23. P. Duncumb, P. K. Shields-Mason, and C. DaCasa, in G. Möllenstedt and K. H. Gaukler, Eds., *5th Intern. Cong. on X-ray Optics and Microanalysis*, Berlin: Springer, 1969, 146.

24. G. Springer and B. Rosner, *ibid.*, p. 170.

25. P. M. Thomas, *Brit. J. Appl. Phys.* 14:387, 1963.

26. J. O. Brand, *Ann. Phys.* 26:609, 1936.

27. A. T. Nelms, NBS Circular 577 (1956), Supplement, 1958.

28. P. Duncumb and S. J. B. Reed in K. F. J. Heinrich, Ed., *Quantitative Electron Probe Microanalysis*, NBS Special Publication 298, Washington, D. C.: National Bureau of Standards, 1968.

29. H. E. Bishop, Ph.D. Thesis, University of Cambridge, 1966.

30. H. A. Bethe, *Ann. Phys.* 5:325, 1930.

31. J. Philibert and R. Tixier, *J. Phys.* D-1:685, 1968.

32. D. M. Poole, in K. F. J. Heinrich, Ed., *Quantitative Electron Probe Microanalysis*, NBS Special Publication 298, Washington, D. C.: National Bureau of Standards, 1968.

33. D. M. Poole, *ibid.*, p. 93.

34. T. O. Ziebold and R. E. Ogilvie, *Anal. Chem.* 36:322, 1964.

35. A. E. Bence and A. L. Albee, *J. Geol.* 76:382, 1968.

36. D. B. Brown and R. E. Ogilvie, *J. Appl. Phys.* 37:4429, 1966.

37. K. F. J. Heinrich, *Electron Beam X-ray Microanalysis*, New York: Van Nostrand Reinhold, 1981, 292-296.

38. L. Parobek and J. D. Brown, *X-ray Spectr.* 7:26, 1978.

39. J. D. Brown and W. H. Robinson, *Microbream Analysis--1979*, 238.

40. R. H. Packwood and J. D. Brown, *X-ray Spectr.* 10:138, 1981.

CORRECTION FOR ELECTRON INCIDENCE ANGLE IN QUANTITATIVE ANALYSIS

W. H. Robinson and J. D. Brown

A quantitative electron probe microanalysis method for non-normal electron incidence is desirable because of the variety of geometries that can exist in electron probe microanalyzers or in scanning electron microscopes equipped with energy-dispersive x-ray spectrometers. One method of studying the effect of electron incidence angle (the angle between the surface and the electron beam) in quantitative analysis is to examine how the depth distribution of primary x-ray production $\phi(\rho z)$ is altered with changing Φ. A Gaussian expression for $\phi(\rho z)$ can be used to model this effect.

Quantitative analysis based on $\phi(\rho z)$ was first proposed by Castaing[1] for a measured x-ray intensity ratio K,

$$K = W_A \frac{\int_0^\infty \phi_A(\rho z) \exp[-(\mu_A^A \rho z \csc \psi)] \, d(\rho z)}{\int_0^\infty \phi_S(\rho z) \exp[-(\mu_A^S \rho z \csc \psi)] \, d(\rho z)}$$

where subscript A refers to the unknown specimen and subscript S refers to the pure element standard, W_A is the weight fraction of A, μ_A^A and μ_A^S are the mass absorption coefficients, and ψ is the x-ray take-off angle. Measurements of $\phi(\rho z)$ may be performed by the sandwich sample technique.[2] A modified Gaussian expression has been proposed to model $\phi(\rho z)$ curves, which has been shown to be a very accurate correction procedure.[3] The $\phi(\rho z)$ curve is described by

$$\phi(\rho z) = \gamma_0 e^{-\alpha^2 (\rho z)^2} (1 - q e^{-\beta \rho z}) \quad \text{and} \quad q = \frac{\gamma_0 - \phi(0)}{\gamma_0}$$

The term α describes the x-ray production for depths greater than the maximum of the $\phi(\rho z)$ distribution, β describes the process of randomization from zero depth to the maximum of $\phi(\rho z)$, γ_0 describes the amplitude of the Gaussian at zero depth, and $\phi(0)$ describes the actual x-ray production at zero depth. The equations for these terms are given elsewhere.[3]

The $\phi(\rho z)$ curve shown in Fig. 1 was measured[4] for electron incidence angles of 75° and 60° as well as for $\Phi = 90°$ (normal incidence),[5] the sandwich sample is composed of a zinc tracer in a copper matrix, and the electron accelerating voltage was 25 kV. The $\phi(0)$ value used for normal incidence was determined from the equation proposed by Reuter.[6]

$$\phi(0) = 1.0 + 2.8(1.0 - 0.9 E_c / E_0) \eta$$

where E_c is the absorption edge energy, E_0 is the electron energy, and η is the backscatter coefficient. Values of η are from Heinrich.[7] Values $\phi(0)$ at non-normal incidence were estimated by multiplying $\phi(0)$ at normal incidence by the ratio of the x-ray intensity from the tracer layer on the matrix at angle Φ to the x-ray

---

The authors are at the Faculty of Engineering Science and Centre for Interdisciplinary Studies in Chemical Physics of the University of Western Ontario, London, Ont., Canada.
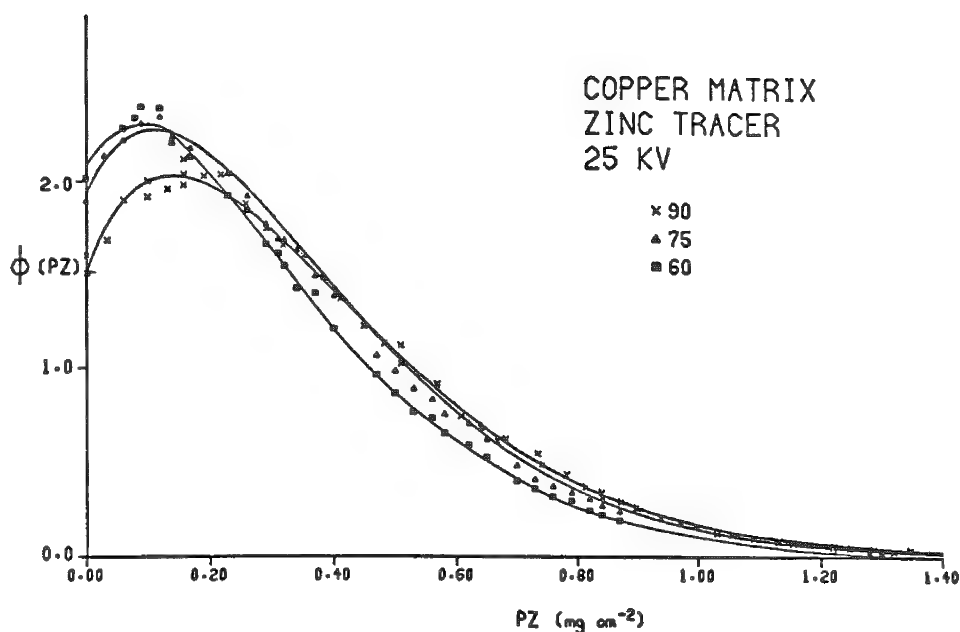
FIG. 1.--Measured $\phi(\rho z)$ curves for zinc tracer in copper at 25 kV.

intensity from the tracer on the matrix at normal incidence. Since the path length of the tracer layer at the surface increases as the incidence angle decreases, a $\sin \Phi$ correction is included. The depth of maximum x-ray production tends to shift to smaller depths as the incidence angle decreases and indicates a decrease in the absorption correction.

The Gaussian expression should be modified to include the effect of the incidence angle Φ. The values of α and β are derived starting from a screened Rutherford scattering cross section and are not influenced Φ. However, the depth over which these parameters act is altered by a simple geometric factor $\sin^{-1}\Phi$. The amplitude of the Gaussian is modified by $\sin^{-1}\Phi$ to account for oblique trajectories (relative to the surface normal) that produce more x rays per layer of sample. An increase in $\phi(0)$ with decreasing angle may be accounted for by an increase in the backscatter coefficient with decreasing angle. Values of η have been measured as a function of Φ and can be described[8]

$$\eta_{\overline{\Phi}} = 0.891 \left(\frac{\eta}{0.891} \right)^{\sin\Phi}$$

The backscatter coefficient at normal incidence is η and at angle Φ is η_{Φ}. The modified form of Gaussian expression to include incidence angle and comparisons to measured x-ray intensities will be discussed.

References

1. R. Castaing, in L. L. Marton and C. Marton, Eds., *Advances in Electronics and Electron Physics*, New York: Academic Press, 13: 317, 1960.
2. R. Castaing and J. Descamps, *J. Phys. Radium* 16: 304, 1955.
3. J. D. Brown and R. H. Packwood, submitted to *X-ray Spectrometry*.
4. W. H. Robinson, M.E.Sc. Thesis, University of Western Ontario, 1979.
5. J. D. Brown and L. Parobek, in Shinoda et al., Eds., *Proc. Sixth Intern. Conf. X-ray Optics and Microanalysis*, Tokyo: University of Tokyo Press, 1972, 163.
6. W. Reuter, IBM Research Report RC 3590, 1971.
7. K. F. J. Heinrich, *X-ray Optics and Microanalysis*, Paris: Hermann, 1966, 379.
8. E. H. Darlington, *J. Phys.* D-8: 85-93, 1975.

RELATIVE INTENSITIES OF K- AND L-SHELL X-RAY LINES

T. P. Schreiber and A. M. Wims

Because of the limited data in the literature, we measured and calculated relative intensities for K- and L-shell x-ray lines of interest in energy dispersive spectrometry (EDS). The results we have obtained will be useful in EDS micronalysis with high-voltage scanning transmission electron microscopes (STEM) and adaptable to lower-voltage scanning electron microscopes (SEM) with proper corrections for bulk sample effects.

To make satisfactory analyses with energy dispersive x-ray spectrometers (EDS), the measured x-ray spectra must be fully evaluated. This evaluation requires a detailed knowledge of the relative intensities of x-ray lines, so that elements can be properly identified and overlaps corrected. The L-shell relative intensities in current use in analytical electron microscopy[1-3] are not satisfactory and can be misleading when element identification is attempted.

Because the three L-subshells have different ionization potentials, the ionization cross sections change at different rates as the energy of the ionizing electrons is reduced. This effect is not significant for thin specimens excited at high voltages (100 to 200 kV) in a STEM because very little energy is lost in traversing the specimen and the overvoltages (ratio of beam voltage E_0 to critical ionization voltage E_c) are high. For bulk specimens and the lower voltages (30 kV) used in an SEM, the situation is much different. When an electron beam strikes a bulk specimen the electrons lose energy through successive collisions and ionizations and cause the total ionization for each subshell to be due to electrons from the energy range E_0 to E_c. In addition, the lower-energy ionizations occur deeper in the specimen and suffer greater absorption in exiting. These complications result in L-shell relative intensities which are sensitive to beam voltage. The data in this report are not directly applicable to bulk specimens, but a possible correction procedure will be suggested.

This report describes the K- and L-shell relative intensity data for specific x-ray lines obtained during our work on relative intensity factors for thin film analysis[4] where only the intensity data on combinations of lines were needed. Some of the data presented here were obtained experimentally by us and by others[5]; some were calculated from experimental and theoretical data in the literature. The report shows how theoretical data from the literature[6] can be used to develop functions for calculating improved relative intensities.

Experimental

Measurements. Relative intensity values were obtained for L-shell x-rays with two instruments: a Japan Electron Optics Laboratory Model JEM 200 C scanning transmission electron microscope (STEM) equipped with a Kevex energy-dispersive x-ray spectrometer (EDS); and an Applied Research Laboratories Model EMX electron probe microanalyzer equipped with crystal spectrometers. The STEM (at 200 kV) was used to obtain L-shell intensity data for the heavier elements, barium and above, where the EDS adequately resolves sufficient x-ray lines so that relative intensities can be evaluated. The electron probe (at 20 kV) was used for the lighter elements because its crystal spectrometers are capable of much higher resolution than the EDS.

The EDS data were corrected for background using the Kevex computer program,[3] and data are presented only for elements for which satisfactory resolution was obtained. We applied no voltage corrections because the overvoltages were very high owing to the 200 kV beam voltage, and the thin specimens we used caused practically no energy loss.

The electron probe data were corrected for background and no corrections were made for variations in spectrometer efficiency because errors from this source are small due to the proximity of the most intense lines. The voltage correction described by Myklebust et al.[7] was applied to the probe data for atomic numbers 50 and below.

Samples. Samples for the STEM were finely divided powders of either metals or compounds which were dispersed onto carbon coated carbon grids. For the electron probe, bulk specimens of metals and compounds were used.

Results and Discussion

L-Shell Relative Intensities. The emission of L-shell x rays is complicated by the subshell structure where Coster-Kronig[8] transitions, which occur between the subshells, change the vacancy location within the shell. Since the distribution of the vacancies is reflected in the relative line intensities, the Coster-Kronig transitions are important in determining relative intensities.

Burhop and Asaad[9] have shown that the Coster-Kronig transitions alter the initial vacancy distribution N_i to an effective distribution V_i (where "i" refers to the subshell), as follows: $V_1 = N_1$; $V_2 = N_2 + f_{12}N_1$; $V_3 = N_3 + f_{23}N_2 + (f_{13} + f_{12}f_{23})N_1$; where f_{12}, f_{13}, f_{23} are the probabilities of the Coster-Kronig transitions $L_1 \rightarrow L_2$, $L_1 \rightarrow L_3$, and $L_2 \rightarrow L_3$, respectively.

The primary vacancy distrition N_i is a function of the mode of excitation, but for electron impact where the electron beam voltage is greater than three times the ionization voltage of the particular atomic level, the value of N_i is very nearly equal to the statistical weight of the level. Since the electron distribution for the L-shells is $L_1 = 2$, $L_2 = 2$, $L_3 = 4$, the values of N_i are $N_1 = 0.25$, $N_2 = 0.25$, and $N_3 = 0.5$.

To calculate relative intensities, we developed equations that utilize the data from the literature. The intensity per L-vacancy, $I(L_iY_i)$, of an x-ray line is

$$I(L_iY_i) = V_i \ \frac{\Gamma_R(L_iY_i)}{\Gamma_t(L_i)} \tag{1}$$

where L_i is the vacant atomic level, Y_i is the atomic level donating the electron, Γ_R is the x-ray emission rate, and Γ_t is the total decay rate which is the sum of the x-ray, Auger, and Coster-Kronig rates. By definition, the fluorescence yield ω_i is

$$\omega_i = \frac{\Gamma_R(L_i)}{\Gamma_t(L_i)} \tag{2}$$

which on rearrangement and substitution into Eq. (1) gives

$$I(L_iY_i) = \omega_i V_i \ \frac{\Gamma_R(L_iY_i)}{\Gamma_R(L_i)} \tag{3}$$

For the $L\alpha_1$ x-ray line, $L_i = L_3$ and $Y_i = M_5$, and Eq. (3) becomes

$$I(L\alpha_1) = \omega_3 V_3 \frac{\Gamma_R(L_3M_5)}{\Gamma_R(L_3)} \tag{4}$$

We have calculated the intensity for a line originating from an L_iY_i transition, relative to the $L\alpha_1$ line, by dividing Eq. (3) by Eq. (4) and using theoretical data from the literature.[10-13]   Some of the data from these calculations and the associated experimental data are shown in Figs. 1-3.

FIG. 1.--Plots of intensity of L_1-shell lines, (a) β_3 and (b) $\gamma_{2,3}$, relative to $L\alpha_1$ line. Points have following origin: O - calculated from data of Scofield[13] and Bambynek[14]; ◇ - data of Allison[5]; Δ - electron probe with no voltage correction; □ - electron probe data with voltage correction of Myklebust et al.[7] Curves are subjective fits to data and were used to develop equations in Table 1(a).

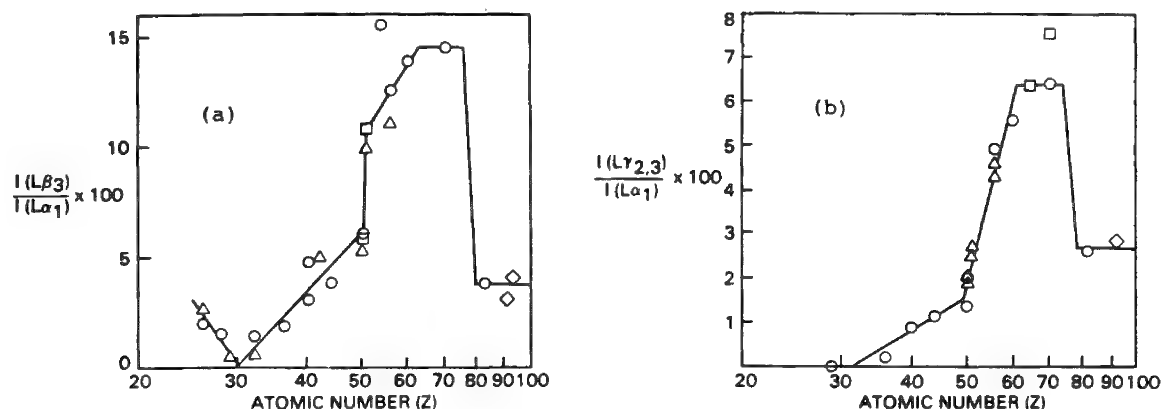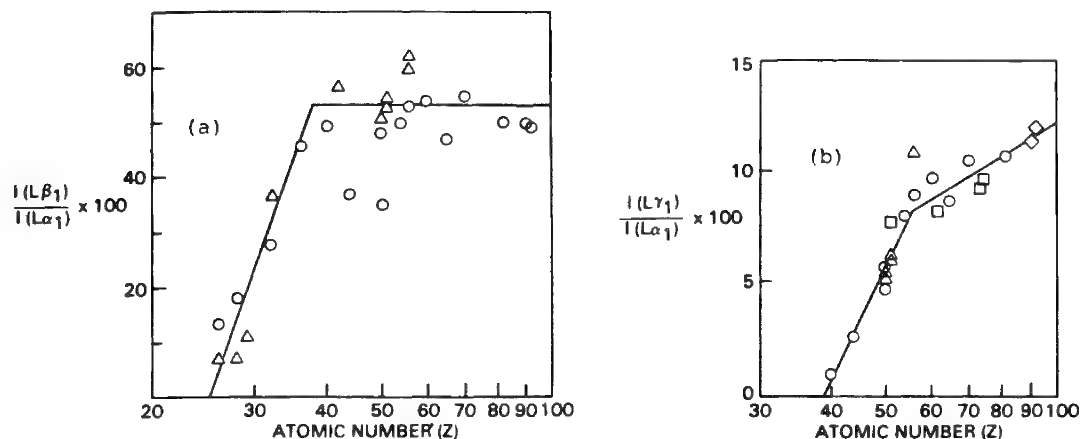

FIG. 2.--Plots of intensity of L_2-shell lines, (a) β_1 and (b) γ_1, relative to $L\alpha_1$ line. Points have same origins as in Fig. 1 except that squares are for EDS data.
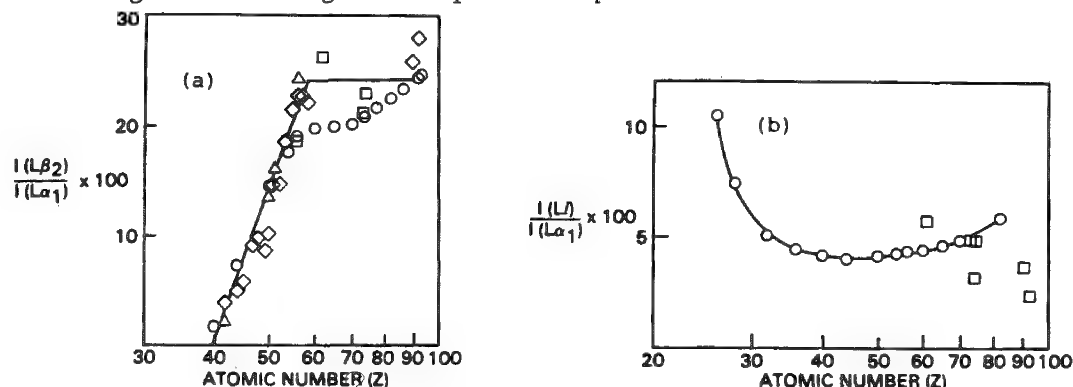

FIG. 3.--Plots of intensity of L_3-shell lines (a) β_2 and (b) ℓ relative to $L\alpha_1$ line. Points have same origins as in Fig. 2 and curves were used to develop equations in Table 1(a).

For convenience, we shall discuss these results for groups of lines originating from a given L-shell vacancy.

L_1-*Shell Vacancy:* Figure 1 shows $I(L\beta_3)$ and $I(L\gamma_{2,3})$ relative to $I(L\alpha_1)$ plotted against log atomic number Z. The curves are our attempts to fit the data and to obtain usable functions. Both plots show a peak in the 55 to 75 Z range which corresponds to the minimum in the f_{13} Coster-Kronig probability indicated by Bambynek.[14] The other L_1-lines have the following relative intensities based upon Scofield's data:[13] $I(\beta_4) = 0.625I(\beta_3)$; $I(\gamma_4) < 1$ for $Z < 51$ and $I(\gamma_4) \simeq 1$ for $Z > 50$; and $I(\beta_9)$ and $I(\beta_{10}) < 1$.

L_2-*Shell Vacancy:* Figure 2 shows data similar to Fig. 1 but for the β_1 and γ_1 lines. In this case the intensity variations with Z are simpler than those for L_1-lines. For the other L_1-lines, Scofield's data[13] indicate that $I(\eta) \simeq 1$ and all other lines are less than 1.

L_3-*Shell Vacancy:* Figure 3 shows data for β_2 and ℓ lines. Here Scofield's[13] data indicate $I(\alpha_2) = 11.3$, $I(\beta_6) \simeq 1$, and all others are less than 1.

Although there is scatter in the data, they do show that the L-shell spectrum changes considerably with atomic number. The curves have been fitted with functions for computer evaluation of spectra (Table 1). These results can be used directly for thin foil-STEM analyses where the overvoltage is high and there is essentially no electron-beam energy loss in the specimen. For bulk specimens in an SEM, the overvoltage changes as the electron beam penetrates into the specimen. This effect causes the L-shell vacancy distribution to vary from the values assumed in our calculations and results in a reduced intensity for the L_1- and L_2- lines. A voltage correction of the type used by Myklebust et al.[7] may be used for bulk specimens.

K-Shell Relative Intensities. The theoretical calculations of Scofield[6] have been found by Heinrich[15] to be in good agreement with experimental data for $I\beta/I\alpha$. This result supports the value of Scofield's calculations for the relative intensities of individual K-lines. Figure 4 is a plot of Scofield's data for the intensities of the α_2 $\beta_{1,3}$, and β_2 relative to the α_1 line. These plots show considerable variability of intensity with atomic number. The solid curve segments indicate the type of functions that can be used to calculate relative intensities and to which we have the least-square fits shown in Table 2.

References

1. J. I. Goldstein, J. L. Costley, G. W. Lorimer, and S. J. B. Reed, "Quantitative x-ray analysis in the electron microscope," *SEM/1977*-I, 315.

2. N. J. Zaluzec, *An Analytical Electron Microscopy Study of the Omega Transformation in a Zirconium-Niobium Alloy Phase*, Ph.D. Thesis, University of Illinois, 1978; also Oak Ridge National Laboratory Report ORNL/TM6705.

3. J. W. Colby, Kevex Quantex Program, Version 3.1W, October 1979.

4. T. P. Schreiber and A. M. Wims "Relative intensity factors for K-, L-, and·M-shell x-ray lines," *Microbeam Analysis--1981,* 317-319; *X-ray Spectrometry* 11: 42, 1982.

5. S. K. Allison, "An experimental study of the relative intensities of x-ray lines in the L-spectrum of thorium," *Phys. Rev.* 30: 245, 1927.

6. J. H. Scofield, "Exchange correction of K x-ray emissions rates," *Phys. Rev.* A: 1041, 1971.

7. R. L. Myklebust, C. E. Fiori, and K. F. J. Heinrich, *Frame C: A Compact Procedure for Quantitative Energy-Dispersive Electron Probe X-Ray Analysis*, National Bureau of Standards Technical Note 1106, 1979.

8. D. Coster and R. de L. Kronig, "A new type of Auger effect and its influence on the x-ray spectrum," *Physica* 2: 13, 1935.

9. E. H. S. Burhop and W. N. Asaad, "The Auger effect," in D. R. Bates and I. Esterman, Eds., *Adv. Atomic Mol. Phys.* 8: 62, 1972.

10. E. J. McGuire, "Atomic L-shell Coster-Kronig, Auger, and radiative rates and fluorescence yields for Na-Th," *Phys. Rev.* A-3: 587, 1971.

11. M. H. Chen, B. Craseman, and V. O. Kastroun, "Theoretical L_2- and L_3-subshell fluorescence yields and L_2 - L_3 x Coster-Kronig transition probabilities, *Phys. Rev.*

TABLE 1.--Equations for calculating L-shell relative intensities with $I(\alpha_1) = 100$, based on curves of Figs. 1-3.

Line	Z Range	Equation
$L\beta_3$	26 to 30	$-16.5 \ln Z + 56$
	31 to 50	$11.7 \ln Z - 40$
	51 to 62	$17.5 \ln Z - 58$
	63 to 75	14.5
	76 to 79	$-161 \ln Z + 709.9$
	80 to 92	3.5
$L\beta_4$	26 to 92	$0.625\ I(\beta_3)$
$L\beta_{9,10}$	26 to 92	0.5
$L\gamma_{2,3}$	26 to 31	0
	32 to 49	$3.52 \ln Z - 12.2$
	50 to 60	$21.6 \ln Z - 82.6$
	61 to 74	6.3
	75 to 77	$-55 \ln Z + 243.3$
	78 to 92	2.7
$L\gamma_4$	26 to 49	0.5
	50 to 92	1
$L\beta_1$	26 to 37	$126.6 \ln Z - 407.4$
	38 to 92	53
$L\gamma_1$	26 to 38	0
	39 to 59	$23.2 \ln Z - 85$
	60 to 92	10
$L\gamma_{5,6,8}$, $L\nu$	26 to 90	0
$L\eta$	26 to 90	1
$L\alpha_2$	10 to 90	11.3
$L\beta_2$	26 to 39	0
	40 to 59	$61.75 \ln Z - 227.8$
	60 to 92	24
$L\beta_6$	26 to 92	1
$L\beta_{5,7,15}$	26 to 92	0
$L\ell$	26 to 92	$36503 - 45570.5 \ln Z$ $+ 22716.2\ (\ln Z)^2 - 5650.22\ (\ln Z)^3$ $+ 701.11\ (\ln Z)^4 - 34.71\ (\ln Z)^5$
$L_{s,t,u}$	26 to 92	0

TABLE 2.--Equations for calculating K-shell relative intensities with $I(\alpha_1) = 100$, based on curves of Fig. 4.

Line	Z Range	Equation
$K\beta_{1,3}$	12 to 20	$-25904.2 + 38935.1 \ln Z - 21916.9\ (\ln Z)^2$ $+ 5471.9\ (\ln Z)^3 - 510.76\ (\ln Z)^4$
	21 to 29	$1.86 \ln Z + 14.74$
	30 to 90	$13.15 \ln Z - 23.13$
$K\beta_2$	31 to 39	$15.68 \ln Z - 53.85$
	40 to 47	$6.2 \ln Z - 19.1$
	48 to 56	$16.87 \ln Z - 60.3$
	57 to 70	$3.41 \ln Z - 5.98$
	71 to 90	$11.23 \ln Z - 39.22$
$K\alpha_2$	10 to 90	$49.72 + 0.04127\ Z + 0.000175\ Z^2$ $+ 0.000009512\ Z^3$

A-4: 1, 1971.

12.   B. Craseman, M. H. Chen, and V. O. Kostroun, "Auger and Coster-Kronig transition probabilities to the atomic 2s state and theoretical L_1 fluorescence yields," *Phys. Rev.* A-4: 2161, 1971.

13.   J. H. Scofield, "Hartree-Fock values of L x-ray emission rates," *Phys. Rev.* A-10: 1507, 1974.

14.   W. Bambynek, B. Crasemann, R. W. Fink, H. U. Freund, H. Mark, C. D. Swift, R. E. Price, and P. V. Rao, "X-Ray fluorescence yields, Auger and Coster-Kronig transition probabilities," *Rev. Mod. Phys.* 44: 716, 1972.

15.   K. F. J. Heinrich, C. E. Fiori, and R. L. Myklebust, "Relative transition probabilities for x-ray lines from the K level," *J. Appl. Phys.* 50: 5589, 1979.
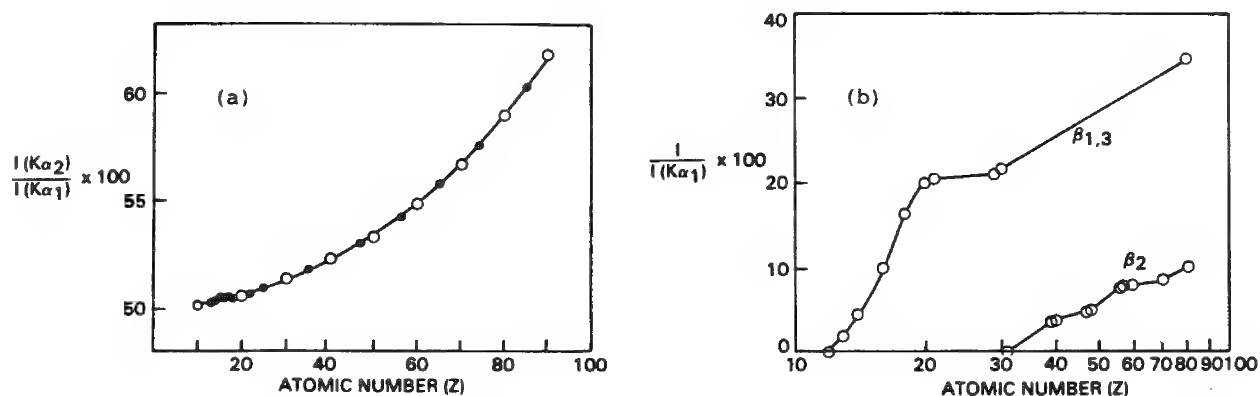
FIG. 4.--Plots of data from Scofield[6] for K-shell (a) α_2 and (b) β lines relative to $K\alpha_1$ line.   Curves are least-square fits to open circled points and are given by equations in Table 2.

CHARACTERIZATION OF STRATOSPHERIC AEROSOLS

E. J. Mroz

The stratospheric aerosol layer primarily consists of submicron droplets of concentrated sulfuric acid. This aerosol layer interacts with solar and terrestial radiation in ways that can affect the climate. Understanding the potential for climatic change requires a detailed physical and chemical characterization of the aerosol layer and its constituents. This paper describes an instrument which, when used in conjunction with particle microanalysis techniques, provides information about the mass concentration and size distribution of the aerosol as well as particle morphology and chemistry. Although the application described is specific for stratospheric aerosol the technique is applicable to any aerosol measurement problem.

Aerosol Collection Techniques

In general, aerosols are characterized by collection of particles by filtration or inertial impaction techniques or by *in situ* optical methods. In the stratosphere the particle concentration is so low (generally $< 1.0 \ \mu g/m^3$) that no single technique provides an adequate measure of all the physical, chemical, and optical properties of the aerosol and its constituent particles. Single-stage inertial impaction on passive collection surfaces has provided limited data on the number concentration, size distribution, and (in conjunction with microprobe techniques) chemical composition. But the accuracy of this technique is limited by (1) a pile up of the particles on the impaction area, (2) uncertainties about how to relate the apparent diameter of the impacted flattened droplet to its aerodynamic diameter, and (3) uncertainties about the density of the particles. Also, the threat of contamination of the sample is an ever-present problem. For example, it is now known that the collected droplets of sulfuric acid aerosol are rapidly ammoniated (and hence physically modified) by exposure to tropospheric air.

Filtration of large volumes of stratospheric air followed by aqueous extraction of the filters and chemical analysis of the extracts has shown the aerosol to be predominately sulfuric acid. But these techniques do not yield particle size or total mass concentration data. Here, too, contamination of the filters is an ever-present threat.

Optical techniques have successfully counted particle number concentration as a function of size. These methods yield no information on chemical composition; to arrive at a mass concentration one must make an assumption about the density of the particles.

All these methods have been used in concert to arrive at our current picture of the stratospheric aerosol. But even for instruments carried on the same aircraft the inlet geometry of each instrument is different and the agreement among instruments is not always good.

A Hybrid Approach

The quartz crystal microbalance (QCM) cascade impactor measures, in real time, both the mass concentration and size distribution of aerosols. This capability results from the combined utilization of a ten-stage cascade impactor that separates particles down to an aerodynamic diameter of 0.05 μm with collection surfaces of piezoelectric quartz crystals and a microprocessor-based data acquisition system. The particles collected and weighed on the quartz crystals are retained for analysis by single-particle microanalysis techniques.

The author is at the Los Alamos National Laboratory, Los Alamos, NM 87545.

Figure 1 schematically depicts the operation of one stage of a QCM. The aerosol stream is accelerated through a nozzle by a pump and some of the particles impinge on the quartz crystal. As particles are collected on the crystal surface the oscillation frequency of the crystal decreases. Immediately behind the sensing crystal (and shielded from the air flow by it) is the reference cyrstal. The output frequency signals of the two crystals are mixed such that changes in the beat frequency are directly
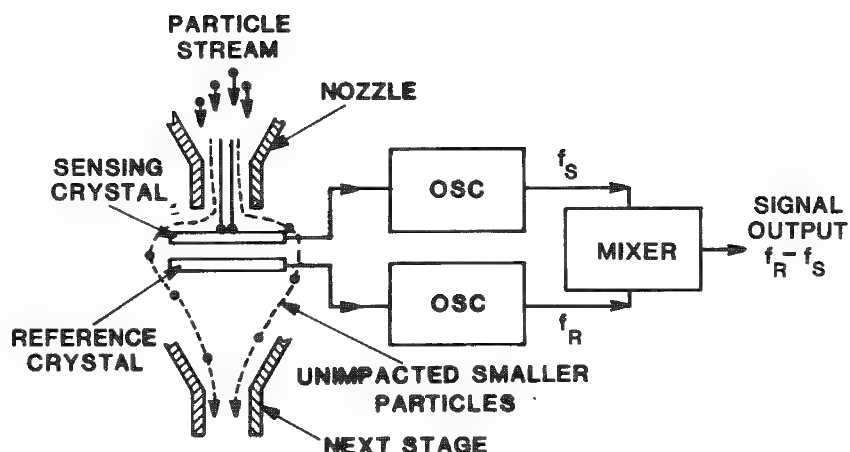

FIG. 1.--Schematic diagram of a single QCM impactor stage.

proportional to the mass loading on the sensing cyrstal. A 1Hz frequency shift corresponds to a mass loading of 6 ng on the first stage and 0.6 ng on the tenth stage. The variation in sensitivity comes about because the response of the crystals to increasing mass is a function of the fraction of the area of the crystal surface that is covered by the particles. Since stratospheric aerosols consist overwhelmingly of sulfuric acid droplets there is little or no problem with particle bounce-off or blow-off. However, it is possible to coat the crystal with a thin layer of grease to provide a sticky substrate and still get a useful signal from the crystals.

Since the impactor consists of ten stages there are ten frequency signals which are handles by a microprocessor that computes the mass collected on each stage. The data can then be sent directly to a thermal printer or stored in memory for later playback through the printer. A valve on the inlet of the impactor allows the operator to select a purge mode that allows dry, particle-free air to pass through the impactor.

Installation of QCM in a WB-57F Aircraft

For measuring stratospheric aerosols we have installed a QCM in a WB-57F high-altitude aircraft. This aircraft is dedicated to sampling gases and aerosols that comprise the upper troposphere and lower stratosphere as part of the Department of Energy's High Altitude Sampling Program (HASP).

Ram air enters an inlet that extends a meter forward of the nose of the aircraft. The air is decelerated by increasing the cross-sectional area of the inlet in a stepwise fashion until the velocity at the exit end of the deceleration tube approximates the inlet velocity of the QCM. The aircraft typically cruises at 400 ± 20 knots so that departures from isokinetic conditions are small. Air flowing through the QCM is measured by a mass flowmeter. Frequency data from each of the ten stages along with data from the flowmeter are collected by the microprocessor at a selectable time interval. The data stored in memory during the flight and are transmitted to a printer when the flight is completed.

SEM Examination of Crystals

Figure 2 shows two stages from the cascade impactor with sensing cyrstals. The crystal is a thin quartz disk about the size of a dime with an electrode plated onto each surface. Particles are collected on the electrode, which is made up of successive layers of nickel, silver, and chromium. Since this is a conductive surface it usually provides adequate electrical contact with the particles to provide suitable imaging. But if charging is a problem the sample can be coated with silver.

The presence of Si, Ni, Ag and Cr x rays can sometimes hinder particle indentification. This problem can be alleviated by counting the particle under constant conditions and then displacing the beam from the particle of interest. Attempts to remove particles from the surface can be successful if the particles are large enough.
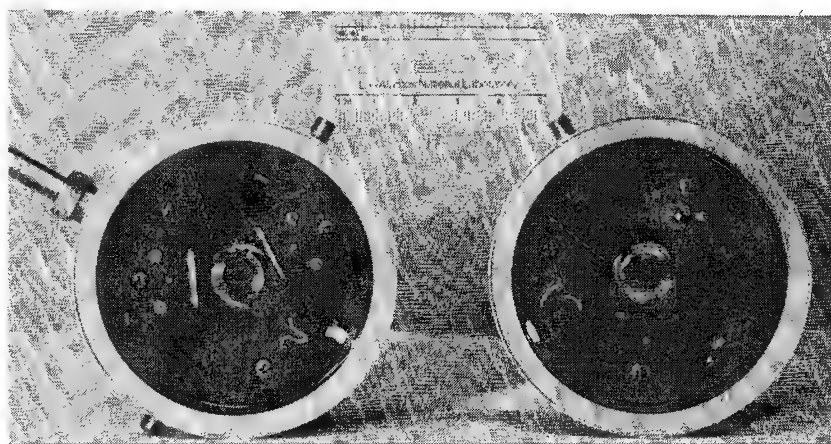
FIG. 2.--Two QCM stages: left stage is shown with both reference and sensing crystals in place, right stage is shown with only sensing crystal in place. A circuit board for signal processing is integrated into each stage.
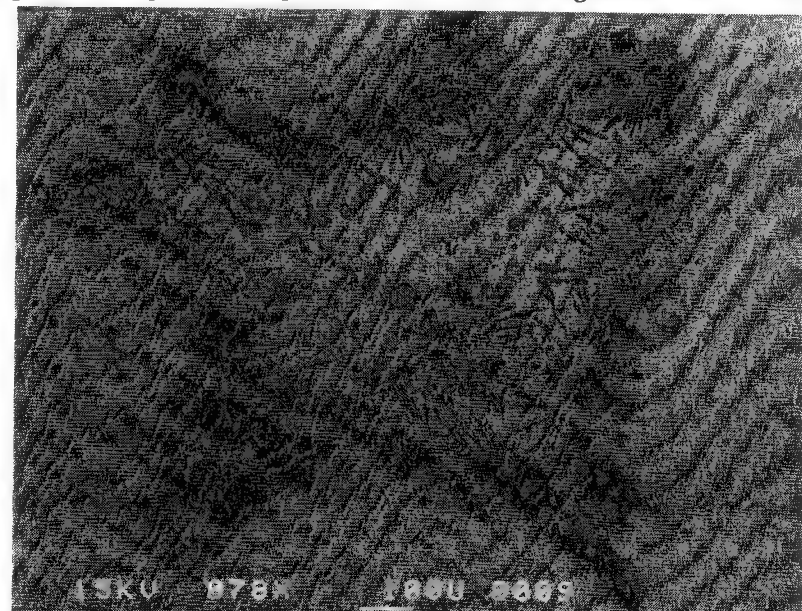
Figure 3(a) is a backscatter image of the impaction area of a crystal exposed to debris from the eruption of the Alaid volcano in May 1981. The dark areas are coalesced droplets of sulfuric acid. Figure 3(b) is a secondary-electron image of the same region at a higher magnification that shows the individual droplets. Almost no volcanic ash was observed in our samples--probably because most of the ash had already been depleted from the plume by the time it crossed the United States.

Summary

The QCM is a valuable tool for acquiring particle size, mass, and composition of many single-particle microanalytical techniques. Current efforts include development of techniques to examine the collected particles by means of a laser microprobe mass analyzer (LAMMA).

(a)

(b)

FIG. 3.--(a) Backscatter image of impaction zone: dark areas are coalesced droplets of sulfuric acid; (b) secondary-electron image of impaction zone at somewhat higher magnification. Individual droplets can be discerned among coalesced ribbons of sulfuric acid.

169

XPS STUDIES OF SIZE-RESOLVED ATMOSPHERIC PARTICLES

X. B. Cox and R. W. Linton

Ambient aerosols have been shown to influence acid rainfall, to reduce visibility via light scattering, and to affect the long range atmospheric transport of heavy metals and adsorbed gaseous pollutants. For a better understanding of the environmental sources and sinks of airborne particles, bulk elemental concentrations (µg/g) have been examined as a function of particle size and resultant fluctuations have been attributed to variable source contributions to aerosol size distributions.[1] However, bulk analysis results may not reflect the unique chemistry and possible secondary origins of aerosol surfaces. Surface layers are significant in part because they may contain high concentrations of acidic sulfur and nitrogen compounds that are directly available to the environment via leaching by atmospheric moisture, by surface waters following dry deposition, or by body fluids following particle inhalation. Although Novakov and co-workers have demonstrated the utility of x-ray photoelectron spectroscopy (XPS) for surface studies of atmospheric particles,[2] little research has been devoted to the XPS characterization of size-resolved ambient aerosols, which is the focus of this investigation.

Experimental

Particles were collected in a Battelle-type, circular orifice, five-stage cascade impactor that separated particles according to aerodynamic diameter into the following size fractions: > 4 µm, 4-2 µm, 2-1 µm, 1-0.5 µm, and 0.5-0.25 µm. The collection substrate was In foil pressed onto an Al foil backing. Samples were collected at the top of a 10-story building on the UNC-CH campus, and at ground level in a residential area of Chapel Hill. Collection periods ranged from 18 to 55 hr, so as to yield suitable coverages of the substrates.

The sensitivity of XPS was evaluated from four preliminary samples that consistently gave detectable signals for C, N, S, O, Si, and Cl. For each foil a survey scan was taken covering the binding energy range of 1000 eV to 0 eV. A high resolution "window" was acquired, with signal averaging, for each element of interest, to be used for quantitation and speciation studies. Quantitative analysis was performed by use of empirical elemental sensitivity factors. All binding energies were charge-referenced by assigning organic carbon to 284.6 eV. The XPS studies employed a Perkin-Elmer Physical Electronics Industries Model 548 AES/XPS spectrometer containing a double-pass cylindrical-mirror analyzer operated in a retarding mode. Main chamber pressure during analysis was typically 5×10^{-9} Torr. Data acquisition and handling, quantitation, and curve-fitting routines were carried out by an Intel 8080-based 64K RAM microcomputer.[3]

Results and Discussion

The XPS results for size-resolved urban aerosols are summarized in Table 1. Surface compositions are remarkably constant as a function of particle size with a relative standard deviation (RSD) about the mean for all elements in all size fraction of less than 34%. One exception is Cl in the rooftop sample, which has a larger RSD (64%) owing to an enhanced Cl concentration in the > 4 µm fraction. The above results are in marked contrast to conventional measurements involving size-dependent bulk (µg/g) concentrations of these elements.

TABLE 1.--XPS-derived surface atomic percents in urban aerosols according to size fraction (sum of detectable elements normalized to 100% atomic).

Element	Size Fractions (μm)				
	> 4	4-2	2-1	1-0.5	0.5-0.25
C	58.5	46.4	63.1	61.3	52.9
N	5.1	5.7	3.9	3.2	2.9
Si	8.5	14.5	9.1	11.3	14.5
S	1.2	1.9	1.0	0.89	1.0
Cl	0.39	1.0	0.46	0.85	0.72
O	26.2	30.3	22.5	22.5	27.9
	GROUND LEVEL SAMPLE				
C	53.4	51.3	56.2	58.1	57.6
N	4.3	2.8	3.9	3.9	3.9
Si	14.9	17.5	13.4	14.1	14.3
S	0.94	1.6	1.6	1.5	1.4
Cl	2.5	0.76	0.63	0.62	0.82
O	23.9	26.0	24.2	21.7	21.9
	ROOF TOP SAMPLE				

Coarse particle fractions (> 2 μm) generally consist largely of windblown dust and soil which show elevated bulk Si concentrations owing to the siliceous nature of many natural minerals.[4] The lack of increased Si surface concentrations in the large fractions (Table 1) at least partially reflects the surface deposition of species containing C, N, or S, which diminish the Si signal from the silicate substrates as the result of the small sampling depth (< 100 Å) of the XPS experiment.

The fine particle fractions (< 2 μm) are formed primarily from the accretion of atmosphere pollutant gases including the acidic oxides of nitrogen and sulfur.[5] Hence, small particles are normally enriched in bulk nitrogen and sulfur content as the consequence of gas-to-particle conversion, nucleation, or coagulation processes in the atmosphere. Indeed, Raman spectra of fine aerosols indicate $(NH_4)_2SO_4$ as a principal species.[6] Mass loadings of particulate sulfate are confined largely to the submicrometer range, although significant nitrate loadings may extend up to particles as large as 3 μm.[5] Carbonaceous particles or graphitic soot of very small crystallite size also predominate in the submicrometer fractions and originate from both primary combustion sources and secondary gas-to-particle conversions in the atmosphere.

The lack of surface concentration enrichments of C, S, and N in small particles (Table 1) can be attribured to adsorption, condensation, or nucleation processes involving vapor-particle surface interactions in fractions of all sizes and to the heterogeneous agglomeration of smaller particles on larger particle surface.

It is not known to what extent cascade impaction collection influences the above processes as the result of the exposure of impacted particles to an air stream contaning gaseous pollutants and fine particles. However, it is not unreasonable to conclude that the surface compositions of particles in coarse fractions may closely approximate the bulk compositions of fine particle fractions formed by more homogeneous nucleation mechanisms. The surface components of a large particle may thus have diverse secondary sources, including sorbed pollutant gases produced by remote combustion processes. However, the subsurface or substrate composition of such a particle may reflect a single primary source, including noncombustion origins such as entrained dust or soil.

It is also of interest to examine changes in surface speciation, particularly of C, N, or S, as a function of particle size. Typical photoelectron lineshapes are shown in Fig. 1. A problem in lineshape evaluation is the possibility of differential
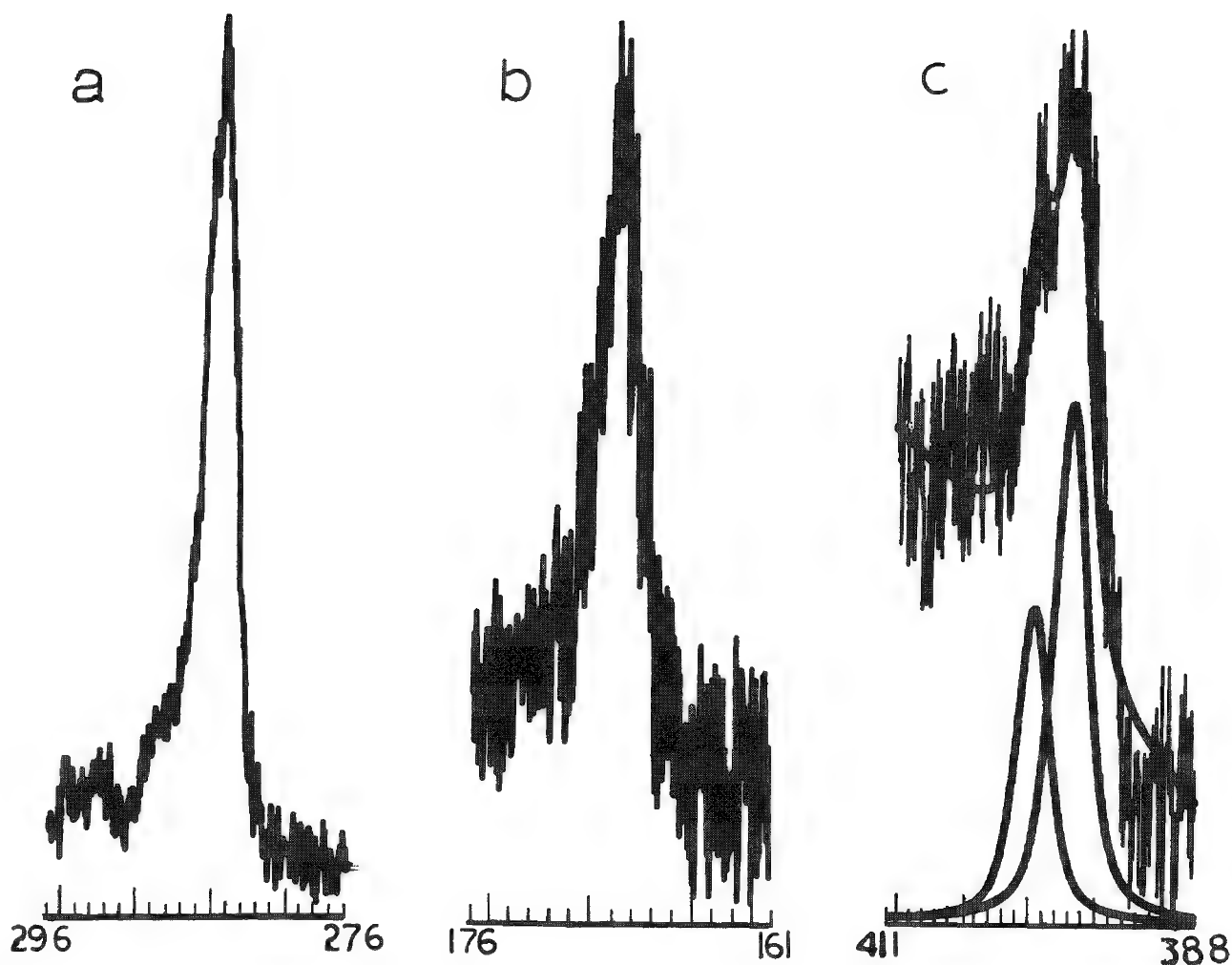
FIG. 1.--Typical XPS lineshapes observed for atmospheric particles (ground level sample, 4-2μm size range): (a) carbon (1s), (b) sulfur (2p), (c) nitrogen (1s), including two-component curve fit.

charging effects from particle to particle which reflect variable conductivity, e.g., insulating minerals containing silicon oxides versus highly conducting graphitic soot substrates. At best, differential charging is likely to broaden lineshapes and hinder the utility of curve-fitting procedures used to identify specific chemical states.

Carbon 1s lines show minimal variation with particle size. Surface C on larger particles is largely adsorbed aliphatic or aromatic organic species that differ little in binding energy (B.E.) from C in graphitic soot, which probably predominates in smaller particles. Only very minor C contributions from CO_3^- (B.E. $\simeq$ 293 eV) are observed in all size fractions.

Sulfur 2p lines indicate that S^{+6} species are major components in all fractions; $SO_4^=$ at a charge-corrected B.E. of approximately 169 eV is a predominant form. This result is in agreement with prior studies of aerosols by Novakov et al.[2,6] Low signal-to-noise ratios hinder S curve-fitting results. However, there is evidence of sorbed SO_2 (B.E. $\simeq$ 168 eV) in many fractions, and minor amounts of $SO_3^=$ (B.E. $\simeq$ 166 eV), particularly in the largest size fractions (Fig. 2). In general, there is a minor but systematic shift to higher binding energy as a function of decreasing particle size, which suggests that S is slightly more oxidized in the smaller fractions.

(a)

(b)

(c)

(d)

(e)

176   156
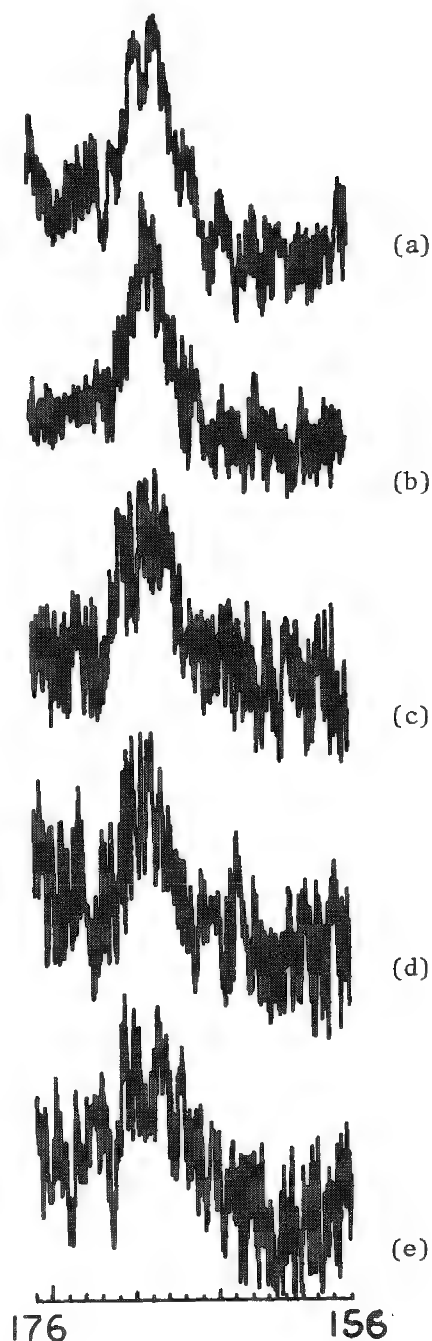
FIG. 2.--Changes in sulfur
lineshape as a function of
particle size: (a) > 4 μm;
(b) 4-2 μm, (c) 2-1 μm,
(d) 1-0.5 μm, (e) 0.5-0.25 μm.

Results for curve fitting of the nitrogen 1s lines
are summarized in Table 2. In agreement with prior XPS
studies of aerosols,[2,7] the N photopeak is decomposed
into an NH_4^+ component and a reduced N component (N_x)
thought to consist of species including amines, amides,
and nitriles. With the exception of the 1-0.5μm
fraction, the NH_4^+/N_x ratios are smaller than unity,
as observed previously for other aerosols.[2,7] Many of
the size fractions have NH_4^+/total S ratios very close
to 2 (Table 2) suggesting $(NH_4)_2SO_4$ as a predominant
form. Two fractions (4-2 μm, 0.5-0.25 μm), however,
have ratios very close to unity, which suggests
$(NH_4)HSO_4$ or a combination of the sulfate, bisulfate,
sulfuric acid, and sorbed SO_2. There is little evi-
dence of significant NO_3^-. However, volatile NH_4NO_3
is suspected to desorb during ultrahigh vacuum surface
analysis. All samples were therefore subjected to
nearly identical treatment during XPS characterization
to minimize differences in desorption of volatiles for
different size fractions. Only one fraction (Rooftop:
4-2 μm) had a substantial NO_3^- component (B.E. $\simeq$ 407 eV)
in the XPS study. The NO_3^- did decrease with sample
residence time in the vacuum in conjunction with a
decrease in NH_4^+ relative to N_x indicating a loss of
NH_4NO_3 (Fig. 3). Use of a liquid nitrogen cooled sample
stage is planned to minimize possible desorption effects.

Conclusions

The utility of a single orifice cascade impactor to
obtain size-resolved aerosols for XPS surface studies has
been demonstrated. In contrast to typical bulk analysis
results, XPS data usually indicate only small changes in
surface elemental composition or speciation as a function
of particle size. Surface layers on larger particles
appear similar to the bulk compositions of smaller
particles generated primarily by atmospheric nucleation
processes. Particle surface composition may be therefore
largely independent of the primary sources of particle
substrates.

References

1. E. S. Macias and P. K. Hopke, Eds., *Atmospheric
Aerosol: Source/Air Quality Relationships*, ACS Symposium
Series 167, 1981.
2. T. Novakov, R. L. Dod, and S. G. Chang, "Study
of air pollution particulates by x-ray photoelectron
spectroscopy," *Z. Anal. Chem.* 282: 287-290, 1976.
3. D. P. Griffis, W. S. Woodward, and R. W. Linton,
"Microcomputer approach to elemental depth profiling
with Auger electron spectrometry," *Anal. Chem.* 53: 2377-
2379, 1981.
4. J. P. Berry, P. Henoc, and P. Galle, "Chemical and cyrstallographic micro-
analysis of fine particles in the urban atmosphere," *Envir. Res.* 21: 150-164, 1980.
5. Y. Mamane and R. F. Pueschel, "A method for detection of individual nitrate
particles," *Atmos. Environ.* 14: 629-639, 1980.
6. H. Rosen and T. Novakov, *Identification of Primary Particulate Carbon and
Sulfate Species by Raman Spectroscopy*, Lawrence Berkeley National Laboratory Publication
5912, December 1976.

7.   R. L. Dod and T. Novakov, *Application of Thermal Analysis and Photoelectron Spectroscopy for the Characterization of Particulate Matter*, ACS Symposium Series--Industrial Application of Surface Analysis, in press.

TABLE 2.--XPS-derived results for nitrogen in size-resolved urban aerosols (ground level sample).

Size Fraction (μm)	NH_4^+ B.E.(eV)	N_x B.E.(eV)	$\dfrac{NH_4^+}{N_x}$	$\dfrac{NH_4^+}{total\ N}$	$\dfrac{NH_4^+}{total\ S}$
> 4	399.5	396.9	0.81	0.45	1.9
4-2	400.2	397.4	0.61	0.38	1.1
2-1	400.5	397.1	0.91	0.48	2.0
1-0.5	399.7	396.9	1.37	0.58	2.1
0.5-0.25	400.1	397.0	0.71	0.42	1.2
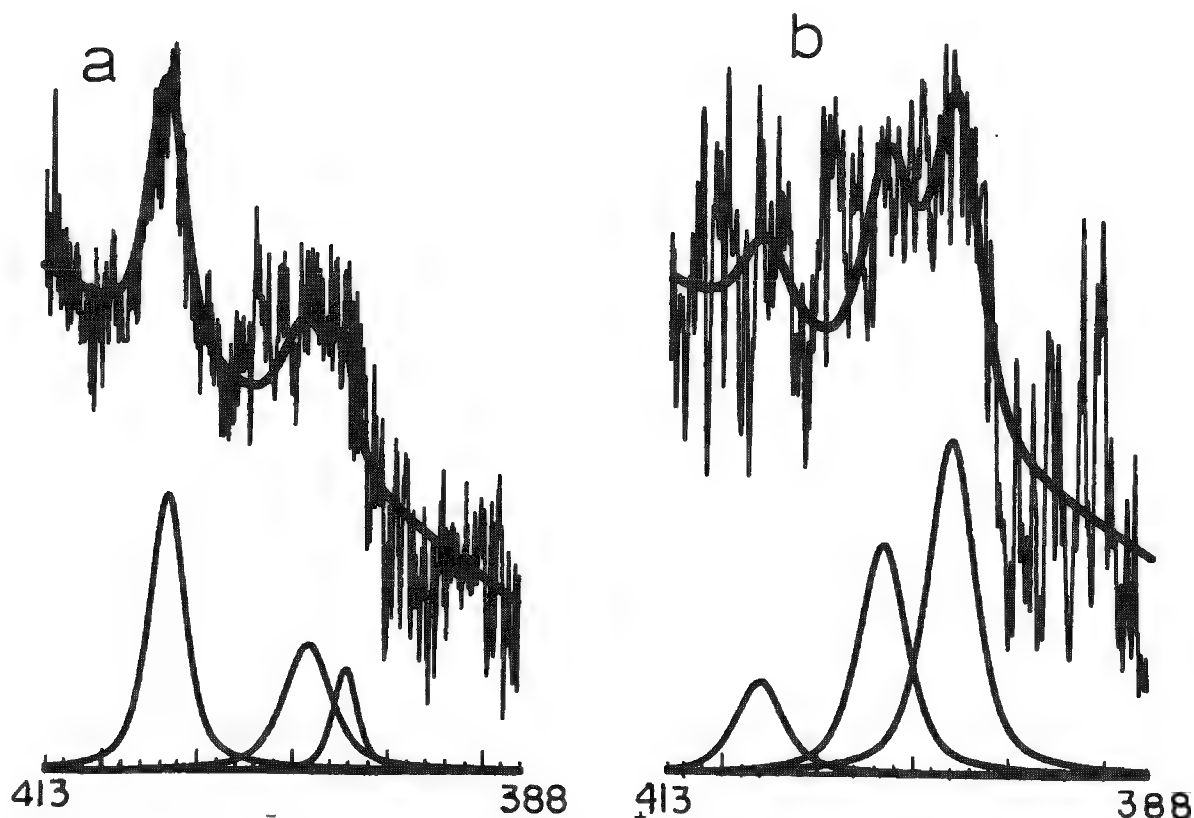
FIG. 3.--Decrease of NO_3^- (B.E. $\simeq$ 407 eV) and NH_4^+ (B.E. $\simeq$ 400 eV) components relative to N_x(B.E. $\simeq$ 397 eV) with residence time in vacuum: (a) 2 hr in vacuum (4000 counts full scale), (b) 5 hr in vacuum (2000 counts full scale).

NEW ZAF AND α-FACTOR CORRECTION PROCEDURES FOR THE QUANTITATIVE ANALYSIS OF INDIVIDUAL MICROPARTICLES

J. T. Armstrong

A modification of the Armstrong-Buseck ZAF correction procedure for individual unpolished microparticles has been developed that includes a modified version of the Brown x-ray depth distribution function. This new expression provides a better extrapolation of relative x-ray intensities produced in small particles to those in thick polished specimens, and requires substantially less computer time for calculation. Matrices of particle α-factors have been generated with the new ZAF expressions. Tests of the new correction procedures on analyzed particle standards indicate that the new ZAF and α-factor corrections are of comparable accuracy, both somewhat better than the previous ZAF approach.

Particle ZAF Correction

Theoretical equations have been developed that correct for absorption, atomic number, and fluorescence effects in unpolished microparticles of given size and shape.[1] The Armstrong-Buseck ZAF corrections enable the accurate quantitative x-ray analysis of individual microparticles.[2,3] They can be employed with either wavelength-dispersive or energy-dispersive x-ray analysis in an electron microprobe or SEM, are applicable for a wide range of particle sizes, and do not require assumptions regarding the nature of the background radiation.

An important factor in particle ZAF correction procedures is the expression for the relative primary x-ray production as function of depth in the sample, $\phi(\rho z)$. Armstrong and Buseck, in their original correction, employed a modified version of the $\phi(\rho z)$ expression of Reuter.[4] This expression, initially derived for the analysis of thin metal films on thick substrates, requires considerable computer time to evaluate for thick polished specimens and, in certain cases, appears to produce small but systematic errors in the extrapolation of relative intensities of elements in thin specimens to those in thick specimens. More recently, Brown and his co-workers have derived simpler expressions for $\phi(\rho z)$ which best fit experimentally determined $\phi(\rho z)$ curves.[5,6] Their expressions for $\phi(\rho z)$ are of the form

$$\phi(\rho z) = \gamma_0 \exp[-\alpha^2(\rho z)^2][1 - q \exp(-\beta\rho z)] \qquad (1)$$

where

$$q = [\gamma_0 - \phi(0)]/\gamma_0 \qquad (2)$$

$$\gamma_0 = \frac{5\pi U_0}{(U_0 - 1) \, \ell n(U_0)} \ [\ell n(U_0) - 5 + 5U_0^{-0.2}] \qquad (3)$$

$$\beta = \frac{8.5 \times 10^5 Z^2}{AE_0^2(\gamma_0 - 1)} \qquad (4)$$

and α has been expressed variously as

$$\alpha = 2 \times 10^5 \ \frac{Z^{1.16}}{A} \ \left[\frac{\ell n(1.166\overline{E}/J)}{E_0(E_0^2 - E_c^2)} \right]^{0.5} \tag{5}$$

(Brown/XRS)[5] and

$$\alpha = 4 \times 10^5 \ \frac{Z^{0.95}}{A} \ \left[\frac{\ell n(1.166\overline{E}/J)}{E_0(E_0^2 - E_c^2)} \right]^{0.5} \tag{6}$$

(Brown/MAS).[6] (See Ref. 5 for the definitions of terms in these equations.)

I have processed a series of electron microprobe analyses of well-characterized, thick polished silicate standards, performed by Shaw and Albee,[7] with the two alternate Brown expressions for $\phi(\rho z)$ and compared the results with those obtained by conventional Bence-Albee[7,8] and ZAF (NBS-Frame[9] and Love/Scott[10]) corrections as well as those obtained by use of the Reuter $\phi(\rho z)$ expression. The results of these data processings are given in Table 1. The errors produced by use of the Brown $\phi(\rho z)$ expression are similar to those produced by the conventional Bence-Albee and ZAF corrections and smaller than those produced by use of the Reuter expression. The errors produced by the Brown $\phi(\rho z)$ expression are minimized if an alternate expression for α is used which is intermediate to the Brown/XRS and Brown/MAS expressions:

$$\alpha = 2.97 \times 10^5 \ \frac{Z^{1.05}}{A} \ \left[\frac{\ell n(1.166\overline{E}/J)}{E_0(E_0^2 - E_c^2)} \right]^{0.5} \tag{7}$$

(Brown/JTA in Table 1). The errors produced with this expression are equivalent to those using the Bence-Albee corrections and slightly superior to those employing the conventional ZAF expressions. Similar results were found in the processing of other silicate data and the binary alloy data of Poole.[11] The modified Brown $\phi(\rho z)$ expression thus has the potential of being a superior basis for the particle ZAF corrections. A particle ZAF correction program based on the Armstrong-Buseck method but employing this new modified Brown $\phi(\rho z)$ expression has been written in BASIC and is available (see below).

Particle a-Factor Correction

It has been demonstrated that particle ZAF correction procedures can be employed to generate matrices of particle a-factors,[12] to be used in a rapid correction procedure similar to that employed by Bence and Albee for thick polished silicate and oxide specimens.[8] The details, equations, and initial results of the particle a-factor method have been published previously.[12]

Programs have been written to generate particle a-factor matrices by means of the Armstrong-Buseck particle ZAF corrections with the modified Brown $\phi(\rho z)$ expression and store the matrices on disk. A series of multielement particle a-factor matrices have been generated and stored and are available. Matrices have been generated for an accelerating potential of 15 keV and spectrometer take-off angles of 38.5° and 40°. Mass diameters used in the a-factor generation are 0.1, 0.2, 0.5, 1, 1.5, 2, 2.5, 3, 4, 5, 6, and 8 mg/cm^2 Geometric models used in the simulations include the rectangular prism, the tetragonal prism, the triangular prism, and the square pyramid. (See Armstrong and Buseck[1] for a description of these models.) Several a-factor matrices covering a range of sizes and

TABLE 1.--Mean percent relative errors for analyses of minerals and glasses when processed by various correction procedures.

Correction Procedure	Mean % relative error $\pm 2\sigma$[1]			
	MgO	Al$_2$O$_3$	SiO$_2$	CaO
Bence-Albee (CIT-Ultimate/ Shaw)	-0.2±2.1	0.2±3.2	-0.1±1.4	-0.1±1.8
ZAF-Frame	0.4±2.4	0.4±3.2	1.1±1.4	0.3±2.1
ZAF-Love/Scott	-0.2±2.2	-0.4±3.2	0.4±1.6	0.6±2.3
Reuter $\phi(\rho z)$	-1.9±3.9	-0.3±3.9	1.8±3.5	-1.3±2.3
Brown/XRS $\phi(\rho z)$	0.3±2.2	0.0±3.2	0.9±1.7	0.3±2.1
Brown/MAS $\phi(\rho z)$	-0.5±2.2	-1.1±3.6	-0.6±0.9	-0.3±2.0
Brown/JTA $\phi(\rho z)$	-0.1±2.2	-0.6±3.4	0.1±1.2	0.0±2.0

[1]Mean and standard deviations of the percent relative errors obtained for the multiple analyses of 23 synthetic and natural minerals and glasses. Raw analytical data is taken from the work of Shaw and Albee (1979).[7]

TABLE 2.--α-factor matrices and k_A values for tetragonal prism (model 3) and square pyramid (model 5) particles of various diameters at E_0 = 15 keV and ψ = 40°.

--- A-FACTORS AND k-ptc/tps FOR MODEL 3 WITH DIAMETER = 0.10 mg/cm^2 ---

	Na2O	MgO	Al2O3	SiO2	K2O	CaO	TiO2	V2O3	Cr2O3	MnO	FeO	NiO
Na	1.000	.979	1.008	1.022	.990	1.015	1.067	1.078	1.092	1.110	1.131	1.185
Mg	1.133	1.000	.971	.988	.952	.971	1.011	1.011	1.016	1.028	1.028	1.054
Al	1.080	1.084	1.000	.957	.926	.944	.978	.972	.972	.965	.967	.977
Si	1.056	1.056	1.064	1.000	.909	.928	.961	.950	.947	.934	.932	.933
K	1.101	1.097	1.098	1.096	1.000	.840	.961	.963	.971	.962	.963	.962
Ca	1.086	1.082	1.083	1.080	1.021	1.000	.907	.919	.937	.933	.940	.945
Ti	1.064	1.061	1.061	1.058	.991	1.001	1.000	.983	.821	.842	.869	.903
V	1.082	1.079	1.078	1.076	1.006	1.016	1.018	1.000	.983	.797	.839	.896
Cr	1.088	1.085	1.084	1.082	1.010	1.021	1.036	1.000	1.000	.979	.786	.869
Mn	1.109	1.107	1.106	1.104	1.030	1.041	1.055	1.039	1.021	1.000	.994	.838
Fe	1.113	1.111	1.110	1.108	1.035	1.045	1.058	1.042	1.037	1.005	1.000	.779
Ni	1.120	1.119	1.117	1.116	1.043	1.054	1.064	1.047	1.042	1.023	1.019	1.000
k	.380	.376	.354	.349	.362	.376	.375	.383	.402	.412	.435	.483

--- A-FACTORS AND k-ptc/tps FOR MODEL 3 WITH DIAMETER = 1.00 mg/cm^2 ---

	Na2O	MgO	Al2O3	SiO2	K2O	CaO	TiO2	V2O3	Cr2O3	MnO	FeO	NiO
Na	1.000	1.089	1.165	1.250	1.404	1.534	1.684	1.816	1.972	2.185	2.397	2.869
Mg	1.697	1.000	.992	1.056	1.139	1.223	1.294	1.361	1.453	1.564	1.688	1.959
Al	1.411	1.495	1.000	.993	1.047	1.112	1.214	1.270	1.238	1.297	1.378	1.548
Si	1.225	1.286	1.321	1.000	.987	1.025	1.039	1.050	1.091	1.116	1.170	1.278
K	1.066	1.097	1.092	1.117	1.000	.857	.931	.930	.960	.952	.979	1.016
Ca	1.027	1.055	1.048	1.070	1.138	1.000	.861	.867	.903	.899	.928	.965
Ti	1.057	1.085	1.075	1.096	1.103	1.133	1.000	.975	.831	.847	.895	.956
V	1.084	1.112	1.101	1.121	1.110	1.140	1.026	1.000	1.012	.807	.868	.951
Cr	1.072	1.099	1.087	1.107	1.081	1.111	1.075	.989	1.000	.972	.796	.903
Mn	1.106	1.133	1.121	1.141	1.102	1.133	1.095	1.078	1.030	1.000	1.014	.876
Fe	1.092	1.119	1.107	1.126	1.080	1.110	1.071	1.051	1.067	.986	1.000	.797
Ni	1.086	1.112	1.099	1.118	1.059	1.089	1.049	1.025	1.039	1.014	1.031	1.000
k	1.123	1.096	1.071	1.049	1.011	1.008	1.006	1.005	1.004	1.004	1.003	1.002

--- A-FACTORS AND k-ptc/tps FOR MODEL 3 WITH DIAMETER = 5.00 mg/cm^2 ---

	Na2O	MgO	Al2O3	SiO2	K2O	CaO	TiO2	V2O3	Cr2O3	MnO	FeO	NiO
Na	1.000	1.117	1.218	1.320	1.549	1.712	1.961	2.172	2.386	2.723	3.018	3.701
Mg	1.976	1.000	1.005	1.078	1.201	1.300	1.422	1.529	1.650	1.825	1.990	2.368
Al	1.562	1.663	1.000	.998	1.078	1.151	1.214	1.270	1.347	1.442	1.545	1.775
Si	1.312	1.382	1.436	1.000	.987	1.047	1.078	1.103	1.154	1.201	1.268	1.409
K	1.076	1.108	1.105	1.131	1.000	.858	.934	.935	.967	.962	.991	1.032
Ca	1.033	1.062	1.056	1.080	1.186	1.000	.862	.871	.908	.905	.936	.976
Ti	1.059	1.087	1.078	1.100	1.128	1.157	1.000	.976	.832	.850	.898	.961
V	1.085	1.113	1.103	1.124	1.127	1.157	1.026	1.000	1.012	.808	.870	.954
Cr	1.072	1.100	1.088	1.109	1.094	1.123	1.090	.988	1.000	.972	.797	.905
Mn	1.105	1.133	1.121	1.141	1.111	1.142	1.105	1.092	1.030	1.000	1.014	.877
Fe	1.092	1.119	1.106	1.126	1.086	1.116	1.078	1.061	1.079	.986	1.000	.797
Ni	1.085	1.112	1.099	1.118	1.062	1.092	1.053	1.031	1.045	1.022	1.039	1.000
k	1.027	1.021	1.016	1.011	1.002	1.002	1.001	1.001	1.001	1.001	1.001	1.000

--- A-FACTORS AND k-ptc/tps FOR MODEL 5 WITH DIAMETER = 0.10 mg/cm^2 ---

	Na2O	MgO	Al2O3	SiO2	K2O	CaO	TiO2	V2O3	Cr2O3	MnO	FeO	NiO
Na	1.000	.971	.995	1.004	.965	.980	1.015	1.017	1.022	1.028	1.038	1.067
Mg	1.089	1.000	.967	.982	.940	.952	.980	.975	.974	.969	.971	.981
Al	1.056	1.055	1.000	.955	.919	.933	.958	.947	.944	.931	.929	.928
Si	1.043	1.040	1.043	1.000	.904	.920	.946	.932	.926	.909	.903	.896
K	1.112	1.106	1.106	1.101	1.000	.839	.959	.958	.965	.951	.950	.944
Ca	1.100	1.095	1.094	1.089	1.011	1.000	.907	.917	.932	.925	.929	.929
Ti	1.079	1.073	1.072	1.068	.984	.993	1.000	.980	.815	.834	.859	.887
V	1.100	1.095	1.094	1.089	1.002	1.012	1.021	1.000	.991	.792	.831	.882
Cr	1.110	1.104	1.102	1.098	1.010	1.019	1.038	1.000	1.000	.975	.780	.858
Mn	1.136	1.130	1.129	1.125	1.034	1.044	1.062	1.042	1.025	1.000	.991	.831
Fe	1.143	1.138	1.137	1.133	1.042	1.052	1.070	1.050	1.041	1.009	1.000	.774
Ni	1.156	1.151	1.149	1.146	1.055	1.065	1.082	1.062	1.054	1.030	1.021	1.000
k	.088	.087	.082	.081	.087	.091	.091	.094	.099	.103	.110	.124

--- A-FACTORS AND k-ptc/tps FOR MODEL 5 WITH DIAMETER = 1.00 mg/cm^2 ---

	Na2O	MgO	Al2O3	SiO2	K2O	CaO	TiO2	V2O3	Cr2O3	MnO	FeO	NiO
Na	1.000	1.066	1.137	1.206	1.333	1.440	1.594	1.717	1.849	2.047	2.226	2.636
Mg	1.621	1.000	.991	1.044	1.109	1.178	1.257	1.318	1.393	1.494	1.597	1.827
Al	1.361	1.425	1.000	.983	1.025	1.077	1.122	1.151	1.198	1.250	1.314	1.454
Si	1.206	1.251	1.284	1.000	.962	1.007	1.033	1.044	1.074	1.097	1.138	1.224
K	1.079	1.099	1.097	1.114	1.000	.851	.942	.944	.968	.963	.982	1.009
Ca	1.048	1.066	1.062	1.077	1.130	1.000	.877	.888	.918	.917	.940	.968
Ti	1.059	1.076	1.070	1.083	1.083	1.105	1.000	.977	.829	.849	.890	.943
V	1.081	1.098	1.091	1.104	1.087	1.109	1.022	1.000	.979	.805	.860	.935
Cr	1.075	1.092	1.084	1.097	1.067	1.090	1.073	1.000	1.000	.976	.794	.894
Mn	1.103	1.120	1.112	1.124	1.085	1.107	1.089	1.076	1.026	1.000	.976	.863
Fe	1.096	1.113	1.104	1.117	1.070	1.093	1.073	1.058	1.068	.993	1.007	.791
Ni	1.095	1.112	1.103	1.115	1.058	1.081	1.059	1.039	1.048	1.028	1.038	1.000
k	.613	.605	.588	.580	.577	.585	.584	.588	.598	.603	.615	.638

--- A-FACTORS AND k-ptc/tps FOR MODEL 5 WITH DIAMETER = 5.00 mg/cm^2 ---

	Na2O	MgO	Al2O3	SiO2	K2O	CaO	TiO2	V2O3	Cr2O3	MnO	FeO	NiO
Na	1.000	1.116	1.206	1.296	1.457	1.581	1.740	1.869	2.011	2.216	2.405	2.836
Mg	1.795	1.000	1.011	1.087	1.203	1.294	1.383	1.457	1.548	1.661	1.778	2.030
Al	1.562	1.650	1.000	1.007	1.109	1.188	1.250	1.299	1.369	1.442	1.528	1.704
Si	1.392	1.466	1.515	1.000	1.020	1.092	1.137	1.170	1.227	1.275	1.342	1.474
K	1.128	1.168	1.177	1.213	1.000	.862	.953	.966	1.005	1.015	1.054	1.119
Ca	1.071	1.106	1.110	1.141	1.408	1.000	.875	.892	.935	.945	.983	1.042
Ti	1.074	1.105	1.103	1.128	1.283	1.313	1.000	.976	.840	.867	.920	.995
V	1.090	1.120	1.116	1.139	1.252	1.282	1.019	1.000	.983	.816	.881	.975
Cr	1.075	1.102	1.097	1.119	1.194	1.224	1.201	1.000	1.000	.979	.804	.919
Mn	1.100	1.127	1.120	1.141	1.189	1.220	1.193	1.205	1.023	1.000	1.016	.883
Fe	1.086	1.113	1.104	1.125	1.149	1.178	1.150	1.154	1.184	.985	1.000	.800
Ni	1.079	1.104	1.094	1.113	1.103	1.132	1.101	1.094	1.116	1.113	1.149	1.000
k	.715	.715	.726	.743	.827	.838	.850	.853	.861	.864	.871	.884

shapes for an accelerating potential of 15 keV and a take-off angle of 40° are given in Table 2.

Analytical Results

To test the accuracy of the new particle ZAF and *a*-factor corrections, analyses were performed on randomly chosen particles of known composition with a range of sizes and shapes. A fragment of a standard glass of known composition and homogeneity (Table 3) was crushed in a boron-carbide mortar and pestle, dispersed in liquid freon by ultra-sonication, and pipetted onto a vitreous graphite planchette. The dispersed particles on the planchette were then carbon-coated and 30 randomly chosen particles were analyzed with an automated MAC-5-SA3 electron microprobe. Conventional thick polished specimens of simple oxides and silicates were used as standards. Particle sizes and shapes were estimated by optical microscopy. (Much better estimates of particle size and shape can be made by SEM examination; but to make the test more severe, no SEM examination was employed before data processing.)

The particle analysis data were processed by (a) conventional ZAF thick polished specimen correction procedures with normalization, (b) the Armstrong-Buseck ZAF method with the Reuter $\phi(\rho z)$ expression, (c) the Armstrong-Buseck ZAF method with the modified Brown $\phi(\rho z)$ expression, and (d) the particle *a*-factor method with the factors calculated by the Armstrong-Buseck/Brown ZAF expression. The results are given in Table 3. As can be seen, the Armstrong-Buseck/Brown ZAF correction and the particle *a*-factor correction give the best results, having considerably smaller systematic (mean) errors and a somewhat smaller scatter of errors (σ). No significant difference between these two expressions is observed, which thus demonstrates the validity of the *a*-factor approach for particles. The results using the Armstrong-Buseck/Reuter ZAF correction are considerably better than those using the conventional thick polished specimen corrections, but not quite as good as those with the Brown $\phi(\rho z)$. [Closer examination of the data showed that whereas both the Brown and Reuter $\phi(\rho z)$ expressions give the same estimates of the relative absorption and X-ray production in the particles, the Reuter $\phi(\rho z)$ gives a somewhat poorer estimate of the amount of absorption in the simple oxide thick polished standards.] Thus the Brown $\phi(\rho z)$ modification of the Armstrong-Buseck ZAF method appears to provide a correction procedure of improved accuracy.

Discussion

Computer programs have been written in BASIC for use on HP9845 series minicomputers which incorporate all the corrections discussed in this paper and are available from the author upon request. (It is anticipated that these programs and *a*-factor matrices will be available soon in a format compatible for use in DEC computers.) Each of the programs requires less than 64 Kbytes of memory for execution, and most require less than 48 Kbytes. A typical analysis (6 elements and 4 iterations until convergence) employing the Armstrong-Buseck ZAF correction with the modified Brown $\phi(\rho z)$ expression requires about 120 s for processing, less than half the time required with the Reuter $\phi(\rho z)$ expression. The same analysis based on the *a*-factor correction procedure takes less than 1 s for data processing. (Approximately 30 s is required initially to calculate an *a*-factor; or 72 hr of minicomputer time to generate *a*-factor matrices for a 12 × 12 element array with 5 particle geometric models at each of 12 particle diameters. These *a*-factor matrices, however, need to be generated and stored only once for a given accelerating potential and take-off angle.)

With the ability to perform rapid, on-line analyses employing particle *a*-factor correction procedures, there is no longer any excuse not to attempt to account for the effects of particle size and shape on emitted x-ray intensities in the microanalysis of individual particles.

References

1. J. T. Armstrong and P. R. Buseck, "Quantitative chemical analysis of individual microparticles using the electron microprobe: Theoretical," *Anal. Chem.* 47: 2178-2192, 1975.
2. J. T. Armstrong, "Methods of quantitative analysis of individual microparticles with electron beam instruments," *SEM/1978* I, 455-467.

3. J. T. Armstrong, *Quantitative Electron Microprobe Analysis of Airborne Particulate Material*, Ph.D. Thesis, Arizona State University, Ann Arbor, Mich.: Microfilms International, 1978.

4. W. Reuter, "The ionization function and its application to the electron probe analysis of thin films" in G. Shinoda, K. Kohra, and T. Ichinokawa, Eds., *Proc. Sixth Intern. Conf. X-ray Optics and Microanalysis*, Tokyo: University of Tokyo Press, 1972, 121-130.

5. R. H. Packwood and J. D. Brown, "A Gaussian expression to describe $\phi(\rho z)$ curves for quantitative electron probe microanalysis," *X-ray Spectrometry* 10: 138-146, 1981.

6. J. D. Brown, R. H. Packwood, and K. Milliken, "Quantitative electron probe microanalysis with Gaussian expression for $\phi(\rho z)$ curves," *Microbeam Analysis--1981*, 174.

7. H. F. Shaw and A. L. Albee, "An empirical investigation into possible nonlinearities of the microprobe correction factors in the system $MgO-CaO-Al_2O_3-SiO_2$," *Microbeam Analysis--1979*, 227-230.

8. A. E. Bence and A. L. Albee, "Empirical correction factors for the electron microanalysis of silicates and oxides," *J. Geol.* 76: 382-403, 1968.

9. H. Yakowitz, R. L. Myklebust, and K. F. J. Heinrich, *FRAME: An On-Line Correction Procedure for Quantitative Electron Probe Microanalysis*, NBS Technical Note 796, 1973.

10. G. Love and V. D. Scott, "Evaluation of a new correction procedure for quantitative electron probe microanalysis," *J. Phys.* D11: 1369-1376, 1978.

11. D. M. Poole, "Progress in the correction for the atomic number effect," in K. F. J. Heinrich, Ed., *Quantitative Electron Probe Microanalysis*, NBS Special Publication 298, 1968, 93-131.

12. J. T. Armstrong, "Rapid quantitative analysis of individual microparticles using the a-factor approach," *Microbeam Analysis--1980*, 193-198.

TABLE 3.--Results of analyses of particles of a standard glass fassaite composition when processed by various correction procedures.

A. TPS-ZAF (normalized)[1,2,3]				B. PTC-ZAF [Reuter $\phi(\rho z)$]			
EL.Wt.%±2σ	%2σ	%2σ$_m$	Δ%	EL.Wt.%±2σ	%2σ	%2σ$_m$	Δ%
Mg 6.36±0.77	12.1	2.2	-2.8	Mg 6.27±0.70	11.1	2.1	-4.2
Al 10.48±0.92	8.8	1.6	-1.5	Al 10.58±0.89	8.4	1.6	+0.6
Si 18.29±1.44	7.9	1.5	-2.8	Si 18.88±1.30	6.9	1.3	+0.3
Ca 17.91±2.15	12.0	2.2	+5.7	Ca 17.16±1.66	9.7	1.8	+1.2
Ti 3.27±0.48	14.7	2.7	+7.7	Ti 3.13±0.39	12.6	2.3	+2.9
O 43.69				O 44.15			

C. PTC-ZAF [Brown $\phi(\rho z)$]				D. PTC-a-Factor [Brown $\phi(\rho z)$]			
EL.Wt.%±2σ	%2σ	%2σ$_m$	Δ%	EL.Wt.%±2σ	%2σ	%2σ$_m$	Δ%
Mg 6.49±0.71	11.0	2.0	-0.8	Mg 6.50±0.70	10.7	2.0	-0.6
Al 10.74±0.87	8.1	1.5	+0.9	Al 10.72±0.86	8.0	1.5	+0.8
Si 18.78±1.15	6.1	1.1	-0.2	Si 18.79±1.22	6.5	1.2	-0.2
Ca 16.92±1.25	7.4	1.4	-0.2	Ca 16.92±1.32	7.8	1.4	-0.2
Ti 3.07±0.33	10.8	2.0	+1.0	Ti 3.07±0.34	11.0	2.0	+1.0
O 44.00				O 44.00			

[1]Actual composition: Mg = 6.54, Al = 10.64, Si = 18.82, Ca = 16.95, Ti = 3.04.

[2]A = conventional thick polished specimen ZAF correction with normalization; B = particle ZAF correction, Reuter $\phi(\rho z)$ expression; C = particle ZAF correction, modified Brown $\phi(\rho z)$ expression; D = particle a-factor correction based on particle ZAF/Brown calculations.

[3]σ_m = standard deviation of the mean, Δ% = 100 × (mean-actual)/actual.

MEASUREMENT OF THE THICKNESS OF AMPHIBOLE ASBESTOS FIBERS WITH THE SCANNING ELECTRON MICROSCOPE AND TRANSMISSION ELECTRON MICROSCOPE

A. G. Wylie, K. B. Shedd, and M. E. Taylor

Knowledge of the cross-sectional shape of mineral fibers is important for their accurate dimensional characterization. Two techniques for the measurement of width and thickness of fibers are described and compared: one for the scanning electron microscope (SEM), and one for the transmission electron microscope (TEM). The frequency distributions of log thickness and log width determined by these techniques are considerably more accurate when the TEM is used. However, the use of either technique results in essentially the identical quantitative descriptions of the relationship between thickness and width for amosite and crocidolite. A general relationship between thickness and width for amphibole asbestos is log thickness = 0.692 log width - 0.493; a rectangle is a reasonable approximation of its cross-sectional shape.

The Particulate Mineralogy Unit of the Bureau of Mines, Department of the Interior, concerned with the accurate characterization of minerals. Recent studies include the characterization of mineral fiber populations for health-related studies and mineral particles found in both the occupational and nonoccupational environment. The dose of mineral fibers for biological experimentation and the human exposure to mineral fibers from air or water are usually expressed in some unit of mass such as fibers pers microgram,[1-3] or nanograms per cubic meter.[4-6] In order to establish these values of concentration, either the thickness of the mineral fibers must be derived or measured, or some reasonable model for the cross-sectional shape of the fiber must be assumed so that volume can be calculated from the measurements of length and width alone. The purposes of this study were (1) to compare and evaluate two methods of measuring the thickness of mineral fibers by electron microscopy, and (2) to propose a reasonable model for the cross-sectional shape of amphibole asbestos.

Sample Preparation

Two samples of asbestos, one of amosite and the other of crocidolite, were examined. Both have been extensively characterized.[7-8] Microgram quantities of each sample were briefly sonicated in filtered distilled water. Drops of the suspensions were placed on highly polished brass SEM stubs and on 200-mesh Formvar and carbon-coated copper TEM grids. Over 99% of the fibers settle out of suspension with their smallest dimension normal to the surface of the substrate. A drop of filtered distilled water containing tiny glass spheres was added to the brass stubs; grids containing only glass spheres were also prepared. The brass stubs were coated with AuPd to a maximum thickness of approximately 200 Å. The TEM grids were placed in rows on a glass slide about 7 cm from a source of AuPd and at an angle to it of about 30° from the horizontal. They were then coated to a maximum thickness of 175 Å .

Experimental Technique

Scanning Electron Microscope. All SEM measurements were made on an ISI Model 60 operated in a backscatter mode with a Taylor Engineering Combination Electron Detector. (Reference to specific trade names or equipment does not imply Bureau of Mines endorsement.) The technique used to measure thickness was first suggested to us by Daniel Baxter, Science Applications Laboratory, La Jolla, Calif. The detector is employed in a low angle position in the plane of sample tilt (Fig. 1). The working distance is set at 14 mm, and the sample is tilted through angle ϕ (in this study $\phi = 45°$). The instrument is operated at 20 kV and maximum spot size. In this configuration, "shadows" are formed along the edges of particles because the particles prevent the directional backscattered electrons from reaching the detector (Fig. 2).

According to the geometric arrangement shown in Fig. 1, the length Sm of the shadow as measured on the cathode ray tube (CRT) is related to the thickness of the particle by

$$h = \frac{Sm \sin \theta}{\cos(\phi - \theta)} \tag{1}$$

where θ is established from the measurement of the radius r and shadow length S_c of the small glass spheres (Fig. 3) by the relationship

$$\tan \frac{\theta}{2} = \frac{r \cos \phi}{S_c + r(1 - \sin \phi)} \tag{2}$$

In this study $\theta \simeq 15°$. The shadow must always be measured in the plane perpendicular to the axis of tilt. This plane contains the beam and the axis of the detector. On the ISI 60, the trace of the plane on the CRT is vertical. The direction of the trace of this plane on other instruments can be established from the direction of shadow elongation of the glass spheres. As long as the fibers are aligned parallel to this direction on the CRT, the measured width W_m is a direct measurement of true width W. However, if the fibers are horizontal, W_m is related to W by

$$W = \frac{W_m}{\cos \phi} \tag{3}$$

If the particle makes an angle γ with the vertical, then the relationship becomes

$$W = W_m \sqrt{\cos^2\gamma + (\sin^2\gamma/\cos^2\phi)} \tag{4}$$

Equation (4) is derived from the equation for an ellipse, where the long axis is the true width W, the short axis is the measured width with maximum foreshortening (W cos ϕ), and γ is the angle a radius makes with the long axis of the ellipse. This elliptical relationship is discussed by Boyde.[9]

All measurements were made at 10 000×. It was found that at higher magnification, it became increasingly difficult to determine the shadow boundaries, and no increase in precision was gained by an increase in magnification. Consequently, there is a lower limit on width and shadow length measurements of 0.10 μm, and the smallest thickness that could be calculated is approximately 0.05 μm. In fact, there did not appear to be any shadows at all from most fibers less than 0.15 μm wide.

The widths and thicknesses were calculated from W_m, γ, θ, and S_m for 160 amosite fibers and 128 crocidolite fibers. The data were collected by measurments on all nontouching fibers in randomly selected fields of view.
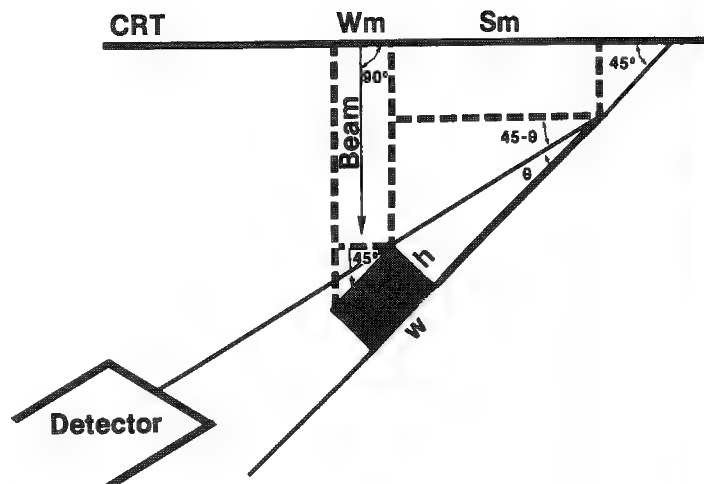
182

FIG. 1.--Sample, detector and beam positions for SEM technique. S_m is shadow length measured on cathode ray tube (CRT), W_m is measured width, angle of sample tilt $\phi = 45°$, W is true width, h is thickness, and θ is angle between axis of detector and surface of specimen stub.
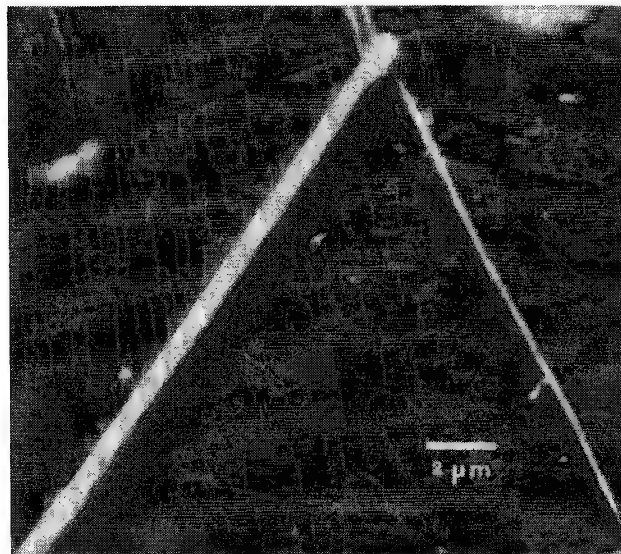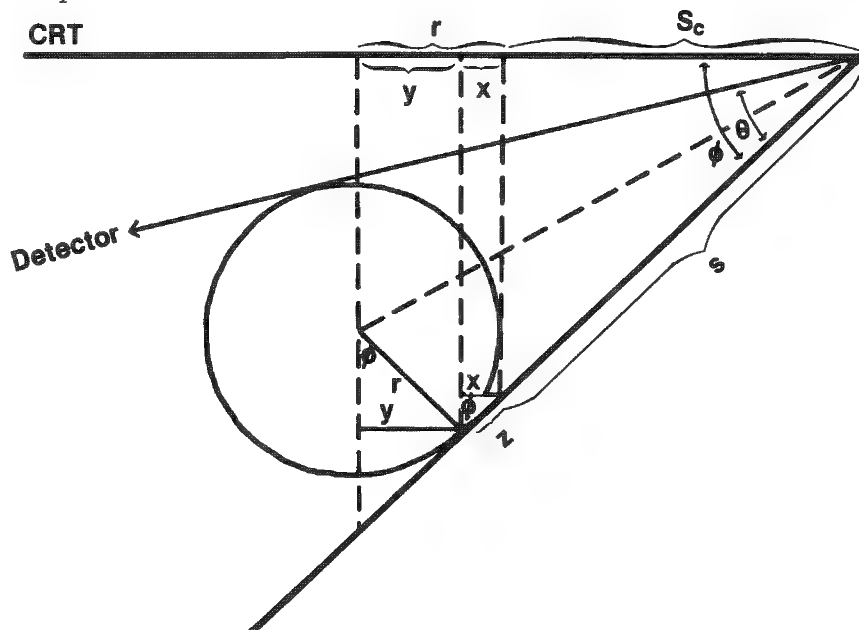

FIG. 2.--Shadows formed on crocidolite fibers on SEM.

FIG. 3.--Geometric relationships for the calculation of θ: r = radius of sphere, ϕ = angle of sample tilt (in this study $\phi = 45°$); θ = angle between the detector axis and the surface of the specimen stub (in this study, $\theta \simeq 15°$); S_c = projection of the shadow S on the cathode ray tube (CRT).

Transmission Electron Microscope. The technique we used to measure thickness on the TEM is well established.[10] The low-angle coating of the grids by AuPd produces a clearly visible "shadow" whose length S1 is related to the thickness of the particles t and the coating angle α by the relationship

$$t = S1 \tan \alpha \tag{5}$$

In this case the "shadow" is formed because the particles block the AuPd during the coating process. The value of α is established from the radii r and from the shadow lengths measured from the center of the glass spheres S1 by the relationship

$$\tan \frac{\alpha}{2} = \frac{r}{S1} \tag{6}$$
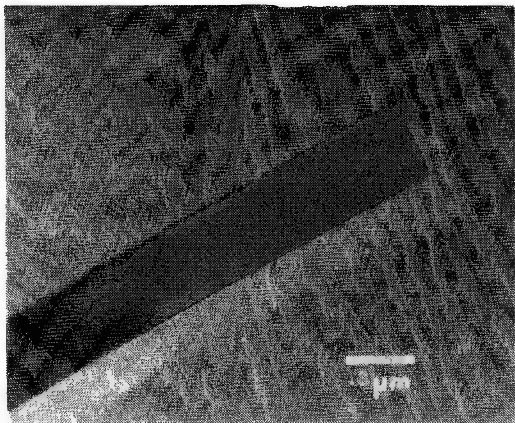
FIG. 4.--Amosite fiber and shadow formed by absence of AuPd coating.

S1 must be measured in the direction of the AuPd source. This direction is easily established from the shadow pattern at the end of the fibers (Fig. 4).

The width and shadow lengths of 143 crocidolite fibers and 150 amosite fibers were measured and thicknesses calculated. All measurements were made at 37 000× directly from the CRT on a Hitachi Model H600 scanning transmission electron microscope.

Results

A statistical description of the populations of width and thickness is given in Table 1. Frequency distributions of log width and log thickness are plotted in Fig. 5. A least-squares linear regression analysis of the form log thickness (μm) = F log width (μm) + b was conducted. The regression coefficients F and b, the standard error of the estimate, and the correlation coefficient r are also given in Table 1. Figure 6 is a plot of these least-squares linear regressions.

Discussion

From Table 1 and Fig. 5, it is evident that larger particles were measured by means of the SEM technique. Not only are the mean widths and thicknesses greater, but the frequency distributions are skewed, which reflects the omission of smaller particles in the measurements. This bias is a result of the inherently lower resolution of the SEM compared to the TEM and to the specific operating conditions of the SEM for this technique. Spot size, backscatter mode, working distance, operating voltage, and collection efficiency of the detector affect the resolution. These parameters were optimized for shadow visibility rather than resolution. Also, fibers less than about 0.15 μm wide were not measured on the SEM because shadows were not visible on these thin fibers.

Figure 6 and Table 1 present the results of the least-squares linear regression analyses. There is a remarkable similarity in the regression coefficients from the four analyses. Wylie and Schweitzer[11] discuss the variability of the values of F and b relating log width to log lenght for the mineral wollastonite. They conclude that values of F derived from populations of 250 particles whose ranges and standard errors are comparable to our data are statistically indistinguishable if they differ by no more than 0.22. Considering that the sample sizes of our populations are much smaller than 250 and that the maximum difference in F is 0.18, there are probably no significant differences among the four analyses. This result implies that for all practical purposes, either technique can be used to obtain the regression relationship relating thickness to width--even though the regression equations are derived from different segments of the fiber populations. Therefore, all data can be combined to give a general regression relationship for amphibole fibers of the form

log thickness = 0.692 log width - 0.493 (7)

Although both techniques used in this study resulted in the same regression relationship between thickness and width, there are strong arguments to be made in favor of the TEM technique for the characterization of asbestos. First, the range of widths measured was greater when this technique was used. In general, the larger the range in the measurements, the more "well fixed" the regression line.[11] Second, the regression analysis is based on the assumption of normal distributions of log width and log thickness. The skewness of the distributions derived from the SEM technique could affect the usefulness of the regression coefficients as descriptive parameters. Third, the measurements of width and thickness on the TEM are more precise and are more likely to reflect the true
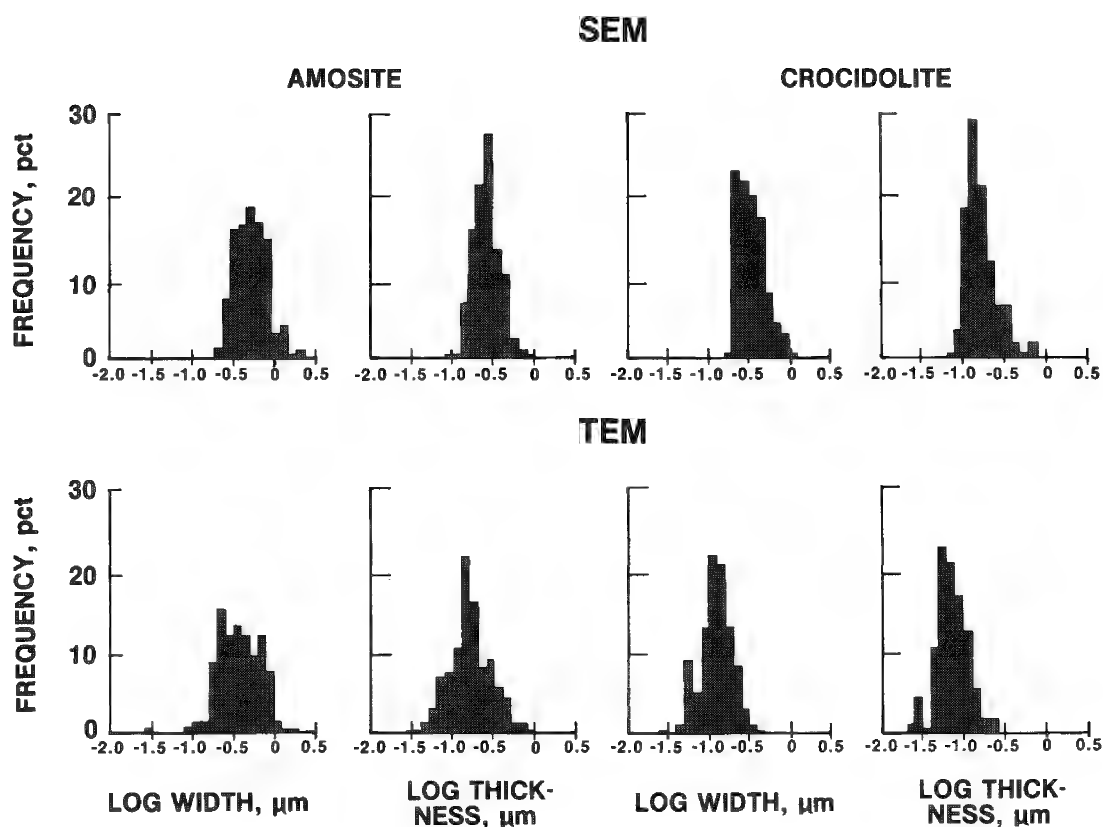
FIG. 5.--Frequencies of log width and log thickness obtained by SEM and TEM techniques.

TABLE 1

	Amosite (SEM)	Amosite (TEM)	Crocidolite (SEM)	Crocidolite (TEM)
Mean width (μm)[a]	0.55	0.35	0.35	0.12
Log width (μm)				
mean	−0.262	−0.453	−0.456	−0.922
standard deviation	0.186	0.270	0.174	0.208
minimum	−0.673	−1.355	−0.775	−1.569
maximum	0.230	0.205	0.048	−0.304
Mean thickness (μm)[a]	0.22	0.16	0.14	0.08
log thickness				
mean	−0.665	−0.802	−0.848	−1.112
standard deviation	0.165	0.266	0.199	0.198
minimum	−1.085	−1.784	−1.270	−1.592
maximum	−0.181	−0.022	−0.177	−0.564
Number of particles	160	150	128	143
Regression analysis				
$\log t = F \log w + b$				
F	0.607	0.792	0.729	0.724
b	−0.506	−0.443	−0.515	−0.445
standard error[b]	0.121	0.160	0.154	0.129
r[c]	0.686	0.802	0.638	0.760

[a]Geometric mean.
[b]Standard error of the estimate = $\sqrt{variance}$.
[c]Correlation coefficient.

FIG. 6.--Plot of linear least-squares regression relationships between log thickness and log width. Mean log width for each is designated by appropriate symbol. Solid lines are drawn to represent ± 2 standard deviations of log width. Dashed lines extend relationships through complete range of measured log widths.
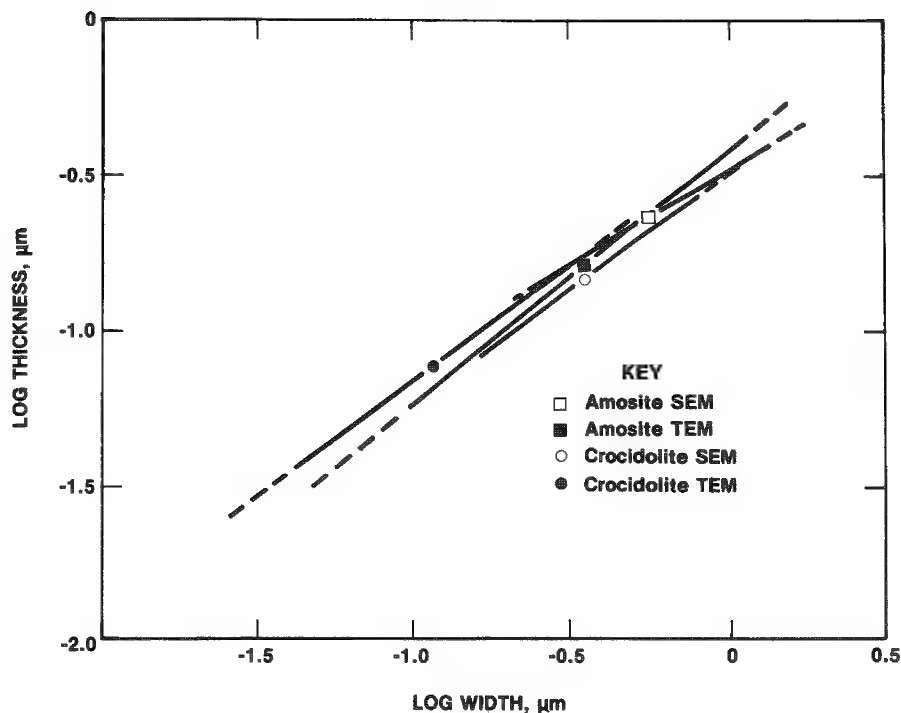
distributions in the population.

Neither of these techniques gives an exact picture of the cross-sectional shape of the fibers. From structural considerations, it is unlikely that they are bounded by curved surfaces. The shape of the shadow formed by the amosite fiber shown in Fig. 4 suggests that the fiber is rectangular. Shadows similar to this one were observed on many fibers of both amosite and crocidolite. The most common prismatic forms that develop on monoclinic amphiboles are {100}, {010}, and {110}. Electron diffraction indicates that the {100} surface frequently occurs perpendicular to the electron beam.[12] If only {100} and {010} bound the fibers, their cross-sectional shape would be rectangular. If other faces such as {100} are also present, the shape would be somewhat different. Although our data do not provide a conclusive picture of cross-sectional shape, they support the rectangular model as a reasonable approximation.

Within the range of all widths measured, the width to thickness ratio w/t predicted from Eq. (7) varies from approximately 1.0 particles with widths of 0.03 μm to 3.7 for particles width of 1.7 μm. If a rectangular cross section is assumed, calculated fiber volumes are smaller than when circular cross sections are assumed. Therefore, the use of a cylindrical model for fiber geometry[1-3] results in an underestimation in any calculation of the numbers of fibers that occur in a microgram of amphibole asbestos. Similarly, calculations of the concentration of asbestos in air or water expressed in units of nanograms per cubic meter[3-6] overestimate amphibole asbestos if they are based on a cylindrical model.

References

1. M. F. Stanton and M. Layard, "The carcinogenicity of fibrous minerals," in C. C. Gravatt et al., Eds., *Workshop on Asbestos: Definitions and Measurement Methods*, NBS Special Publication 506, 1978, 143-152.

2. M. F. Stanton and C. Wrench, "Mechanisms of mesothelioma induction with Asbestos and Fibrous Glass," *J. Nat. Cancer Inst.* 48: 797-821, 1972.

3. Freidrich Pott, "Some aspects of the dosimetry of the carcinogenic potency of asbestos and other fibrous dusts," *Staub-Reinhalt Luft* 38: 486-490, 1978.

4. E. J. Chatfield et al., *Preparation of Water Samples for Asbestos Fiber Counting by Electron Microscopy*, EPA-600/4-78-OM, 1978.

5. A. V. Samudra et al., *Electron Microscope Measurements of Airborne Asbestos Concentrations*, EPA-600/2-77-178, 1977 (revised 1978).

6. P. Sebastien et al., *Measurement of Asbestos Air Pollution Inside Buildings Sprayed with Asbestos*, EPA-560/13-80-026, 1980.

7. W. J. Campbell et al., *Chemical and Physical Characterization of Amosite, Chrysotile, Crocidolite, and Nonfibrous Tremolite for Oral Ingestion Studies by the National Institute of Environmental Health Sciences*, Bureau of Mines Report of Investigations 8452, 1980.

8. H. G. Siegrist and A. G. Wylie, "Characterizing and discriminating the shape of asbestos fibers," *Environmental Research* 23: 348-361, 1980.

9. Alan Boyde, "Three-dimensional aspects of SEM images," in O. C. Wells, Ed., *Scanning Electron Microscopy*, New York: McGraw-Hill, 1974, 304.

10. C. E. Hall, *Introduction to Electron Microscopy*, New York: McGraw-Hill, 1953, 329-338.

11. A. G. Wylie and P. Schweitzer, "The effects of sample preparation and measuring techniques on the shape and shape characterization of mineral particles: The case of wollastonite," *Environmental Research* 25: 52-73, 1982.

12. Richard Lee, U. S. Steel, personal communication.

187

VIBRATIONAL MICROSPECTROSCOPY OF INTERPLANETARY DUST IN THE LABORATORY

P. Fraundorf, R. I. Patel, P. Swan, R. M. Walker, F. Adar, and J. J. Freeman

Thanks to the remarkable ability of the earth's upper atmosphere to decelerate micrometeorites "gently" in the 2-50μm size range, stratospheric collectors on NASA aircraft are capable of obtaining relatively pristine samples of solar system dust.[1,2] In particular, the extraterrestrial origin of stratospheric aggregate particles with compositions similar to those of "chondritic" meteorites has been confirmed by trace element[3] and noble gas isotopic[4] studies. Although similar to meteorites in composition, collected micrometeorites often appear to differ drastically from known meteoritic materials in texture and mineralogy.[5] Because of the probable cometary, and perhaps primitive, origins for at least some fraction of the particles, they have become the subject of intense study in spite of their rarity and small size. In fact, a cosmic dust curation program at Johnson Space Center has recently been established to make individual particles available to the general scientific community.[6]

Although collected particles are proving to be challenging subjects for many microbeam analysis techniques, only optical spectroscopic methods allow direct comparison of collected particles with dust in astrophysical settings (e.g., in comets, in circumstellar nebulae, etc.). In addition, vibrational spectroscopy can provide important clues to the molecular makeup of the poorly crystallized and low-Z materials which frequently constitute the bulk of individual particles. We describe here infrared transmission spectra and micro-Raman results obtained from individual nanogram-sized specimens. Because of the uniqueness of individual particles, we have integrated these spectroscopic techniques into a handling sequence which also allows weighing, volume estimation, analytical electron microscopy (AEM), and annealing studies of the same specimen.[7,8] These corollary techniques are not discussed in detail here.

Specimen Preparation

Particles are transferred from stratospheric impaction collectors to a Nuclepore mount where they are individually examined optically and with a scanning electron microscope/ energy-dispersive x-ray (SEM/EDX) system. The particle of interest is then transferred to a clean quartz plate, where it is dispersed to micron or submicron thicknesses over a 70μm area with a second quartz plate and the aid of a crushing jig (Fig. 1). The jig allows fine xyz control of the top crushing plate so that aggregate particles can be gradually "coaxed" into a dispersed configuration even if the initial tendency is simply to flatten. For particles larger than 15 μm, one can often repeat this process with additional quartz plates to create numerous aliquots of dispersed material from the same particle.

The dispersed specimens are then embedded into a freshly cleaved flat of KBr (typically around 2 × 2 × 0.2 mm) by gentle pressing. It is an empirical fact that the KBr usually removes dispersed material from the quartz very efficiently. The KBr is transparent in the visible and IR, which facilitates transmission spectroscopy in those spectral regions, and by virtue of its intimate contact with the particle also acts as a moderately good heat sink to minimize heating of opaque specimens during micro-Raman analysis. Moreover, because of its solubility in water, a film evaporated onto the dispersed specimen can easily be floated off of the KBr with specimen intact. This procedure allows subsequent
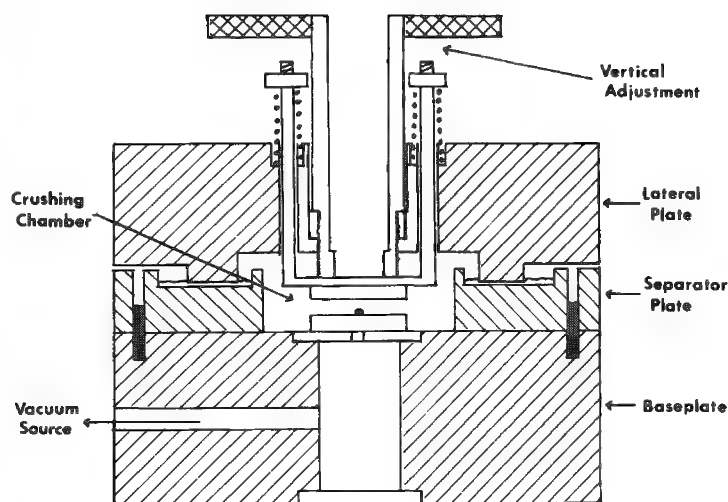
FIG. 1.--Particle crushing jig with vacuum chuck to hold bottom crushing plate. Fine control of top crusing plate is facilitated by threaded vertical adjustment, and damping of lateral motion with a viscous oil. Particle can be observed in transmitted and reflected light throughout process.
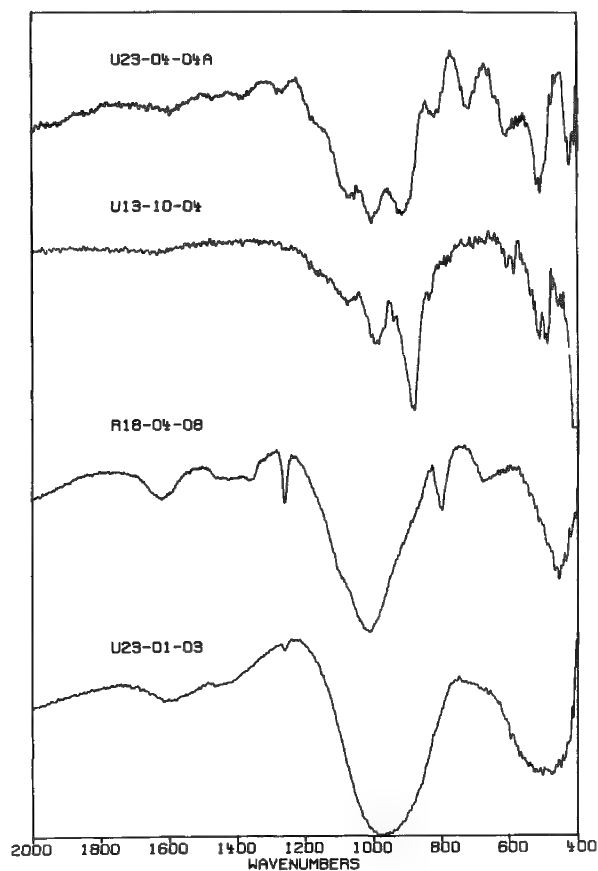

FIG. 2.--Infrared transmission spectra of several compositionally similar micrometeorites.

remounting of the specimen onto transmission electron microscope (TEM) grids for AEM, annealing studies, and possibly further spectroscopic studies. One caution: dessicator storage is necessary to prevent aqueous degradation of the mount during long term storage of specimens on KBr.

IR Transmission Spectroscopy

Infrared (IR) transmission spectra between 6000 and 400 wavenumbers were obtained by use of a Nicolet 7199 Fourier Transform spectrometer equipped with a globar source, a KBr beam splitter, a mercury-cadmium-telluride detector, and a dry nitrogen purge. Samples were centered in a 70μm aperture and illuminated using a 4× beam condenser with reflecting optics. Spectra taken with 4-wavenumber resolution were obtained by spectral averaging of around 100 blocks of 1000 scans each, followed by ratioing to a comparable background spectrum. Data accumulation times for spectra were on the order of 10 hr each.

Figure 2 illustrates the range of IR spectral types identified so far. The major features near 1000 and 500 wavenumbers are due to SiO_4 vibrational modes. Even though the particles had typical morphologies and compositions, the IR spectra indicate significant differences in bulk silicate mineralogy. The top spectrum looks like that of a pyroxene, and is similar to an IR spectrum reported previously for a mount of three interplanetary dust particles.[9] The second appears to be dominated by olivine. The third suggests the presence of hydrated silicates,[9] and the last shows broad, structureless 10 and 20μm features[10] that may indicate the presence of amorphous silicate and are suggestive of features observed in cometary emission.[11] There is a caution here: The IR absorption bands exhibited by these specimens may show some flattening and loss of structure as a result of saturation effects if the particle was not sufficiently well dispersed. Nevertheless, the results show infrared spectroscopy to be useful for bulk characterization of individual particles, and promise to shed light on the relationship between collected particles and observed comet dust.

Micro-Raman Spectroscopy

Figure 3 shows Raman spectra from several 5-10µm regions on a KBr mount which contained fragments from three micrometeorites.[12] The spectra were obtained with a Ramanor U-100 laser Raman microprobe. An IR spectrum of the specimen mount suggested the presence of pyroxenes,[9] an identification that was corroborated by the Raman spectrum from region 2 which indicates an orthorhombic Mg-rich pyroxene.[13] Region 2 was one of several optically transparent portions of the mount, all of which were subsequently shown by EDX analysis to have compositions consistent with the IR/Raman spectral identifications. Regions 1 and 4 were by contrast optically opaque. The Raman spectrum of the first suggests the presence of iron oxide, probably hematite or perhaps maghemite. Subsequent EDX analysis confirms the iron-rich nature of this region. Moreover, meteorite fusion crusts commonly contain diamond face-centered iron oxides (magnetite or maghemite), and preliminary electron diffraction data from Region 1 supports the presence of such oxides. Finally, the region 4 spectrum suggests the presence of disordered graphite, a phase of considerable interest in the study of meteorites. Thus micro-Raman spectroscopy promises to be a powerful tool, especially in combination with IR and AEM studies, for characterization of the solar system dust cloud.
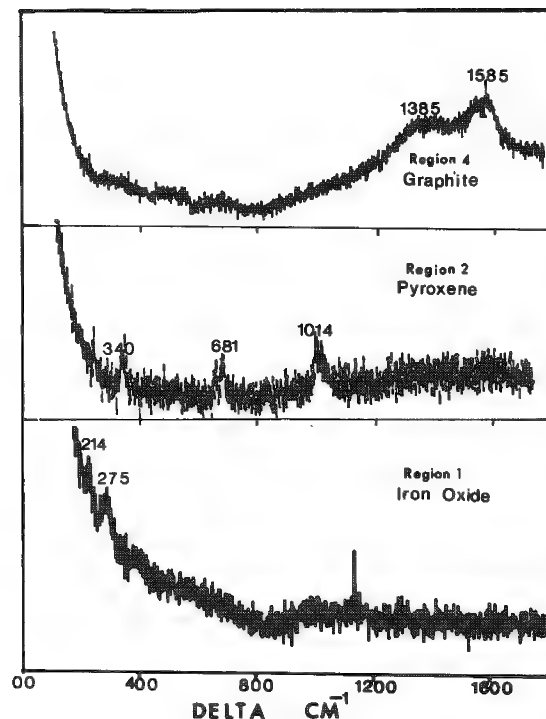

FIG. 3.--Raman microprobe spectra of different regions on mount composed of fragments from three micrometeorites. Analyses: Region 1 (opaque) 100 min defocused (3-5 µm) spot; Region 2 (transparent) 15 min focused spot; Region 4 (opaque) 12 hr defocused spot.

References

1. D. E. Brownlee, "Microparticle studies by sampling techniques," in A. M. McDonnell, Ed., *Cosmic Dust,* New York: Wiley, 1978, 295-335.

2. P. Fraundorf et al., "Laboratory studies of interplanetary dust," in L. Wilkening, Ed., *Comets,* Tucson: University of Arizona Press, 1981 (in press).

3. Ganapathy and D. E. Brownlee, "Interplanetary dust: Trace element analysis of individual particles by neutron activation," *Science* 206: 1075-1076, 1979.

4. B. Hudson et al., "Noble gases in stratospheric dust particles: proof of extraterrestrial origin," *Science* 211: 383-386, 1980.

5. P. Fraundorf, "Interplanetary dust in the transmission electron microscope: Diverse materials from the early solar system," *Geochim. et Cosmochim. Acta* 45: 915-943, 1981.

6. U. S. Clanton et al., "Possible comet samples: The NASA cosmic dust program," in *Lunar and Planet. Sci.* XIII, Houston: Lunar and Planetary Institute, 1982, 109-110.

7. P. Fraundorf et al., "Determination of the mass, surface density, and volume density, and volume density of individual interplanetary dust particles," *ibid.,* 225-226.

8. P. Fraundorf et al., "Deceleration heating of interplanetary dust in the earth's atmosphere, and its simulation using analog materials," *ibid.,* 227-228.

9. P. Fraundorf et al., "Infrared spectroscopy of interplanetary dust in the laboratory," *Icarus* 47: 1981, 368-380.

10. P. Fraundorf et al., "Multidisciplinary studies of individual stratospheric micrometeorites," in Ref. 6, 229-230.

11. M. S. Hanner, "Physical characteristics of cometary dust from optical studies," in I. Halliday and B. A. McIntosh, Eds., *Solid Particles in the Solar System,* Dordrecht: Reidel, 1980, 223-236.

12. P. Fraundorf et al., "Raman spectroscopy of graphite and other phases in meteorites and interplanetary dust," in Ref. 6, 231-232.

13. W. B. White, "Structural interpretation of lunar and terrestrial minerals by Raman spectroscopy," in C. Karr, Ed., *Infrared and Raman Spectroscopy of Lunar and Terrestrial Minerals,* New York: Academic Press, 1975, 325-358.

LASER MICROPROBE MASS ANALYSIS OF COAL AND OIL FLY ASH PARTICLES

Eric Denoyer, Thad Mauney, David F. S. Natusch, and Fred Adams

Assessment of the potential environmental and toxicological effects of particulae matter emitted to the atmosphere, together with design of emission control strategies, requires detailed physical and chemical characterization of the particles. Information on an individual particle basis can be obtained with a number of microanalytical techniques, in an effort to gain insight into the distribution of various chemical entities on specific particle types present within a heterogeneous population.[1,2]

We have investigated the utility of laser microprobe mass analysis (LAMMA) for studying environmental particles, and have applied the technique to fly ash derived from coal and oil-fired power plants. These ashes have previously been extensively characterized and a large body of information is available against which to judge the extent to which either existing or new physical and chemical information is provided by LAMMA.

Experimental

Coal fly ash was collected in bulk from electrostatic precipitation in the stack of the Corette Power Plant in Billings, Montana, USA. Oil fly ash was obtained from the French Petroleum Institute.

Laser microprobe mass analysis was performed using a LAMMA-500 instrument (Leybold-Heraeus, Köln, Germany). All particles were mounted on conventional electron microscopy grids (200 mesh) coated with a Formvar film (thickness ~0.1 μm) by touching the coated grid to the bulk particle sample. Analysis was carried out at using the 32× objective.

Results and Discussion

Oil Fly Ash. All the oil fly ash particles were jet black and exhibited morphologies which varied from that of near rounded spheres to lacey or spongey lumps, which indicates a long exposure history to heat and oxidants.[3]

Typical positive and negative ion spectra of the oil fly ash are given in Fig. 1. The elements detected by LAMMA include C, O, S, Na, Mg, Al, K, Ca, V, Fe, Ni, Zn, Sr, Mo, and Ba. All the elements detected by LAMMA, except Sr, Ba, and Mo, which were detected by x-ray fluorescence (XRF); and Pb was only detected by XRF (at trace levels) and not by LAMMA. Mo, Ba, and Sr exhibited strong signals in some particles and were undetectable in others, which reflects their heterogeneous distribution among the individual fly ash particles. However, this effect may results in a low total bulk concentration, which might explain their lack of detection by XRF. Why one cannot detect Pb by LAMMA, however, is not clear at this point.

The carbonaceous nature of the particles is suggested in both the positive and negative ion spectra by the presence of the homologous series of $C_n H_m^{+/-}$ cluster ions, which are predominant LAMMA spectral features of carbonaceous materials such as graphite and carbon blacks. Although V (and Ni) are thought to be present in crude petroleum as metal porphyrins,[4] the LAMMA spectra (Fig. 1) indicate the presence of oxides of V in the fly ash combustion product, by the series of $V_x O^{+/-}$ cluster ions. These clusters are observed in the LAMMA spectra of pure vanadium oxides (V_2O_3, V_2O_5). Finally, the presence of oxides of sulfur are suggested by the characteristic $S_x O_y^-$ cluster ions observed in LAMMA spectra of both sulfates and sulfites. However, no chemical-state
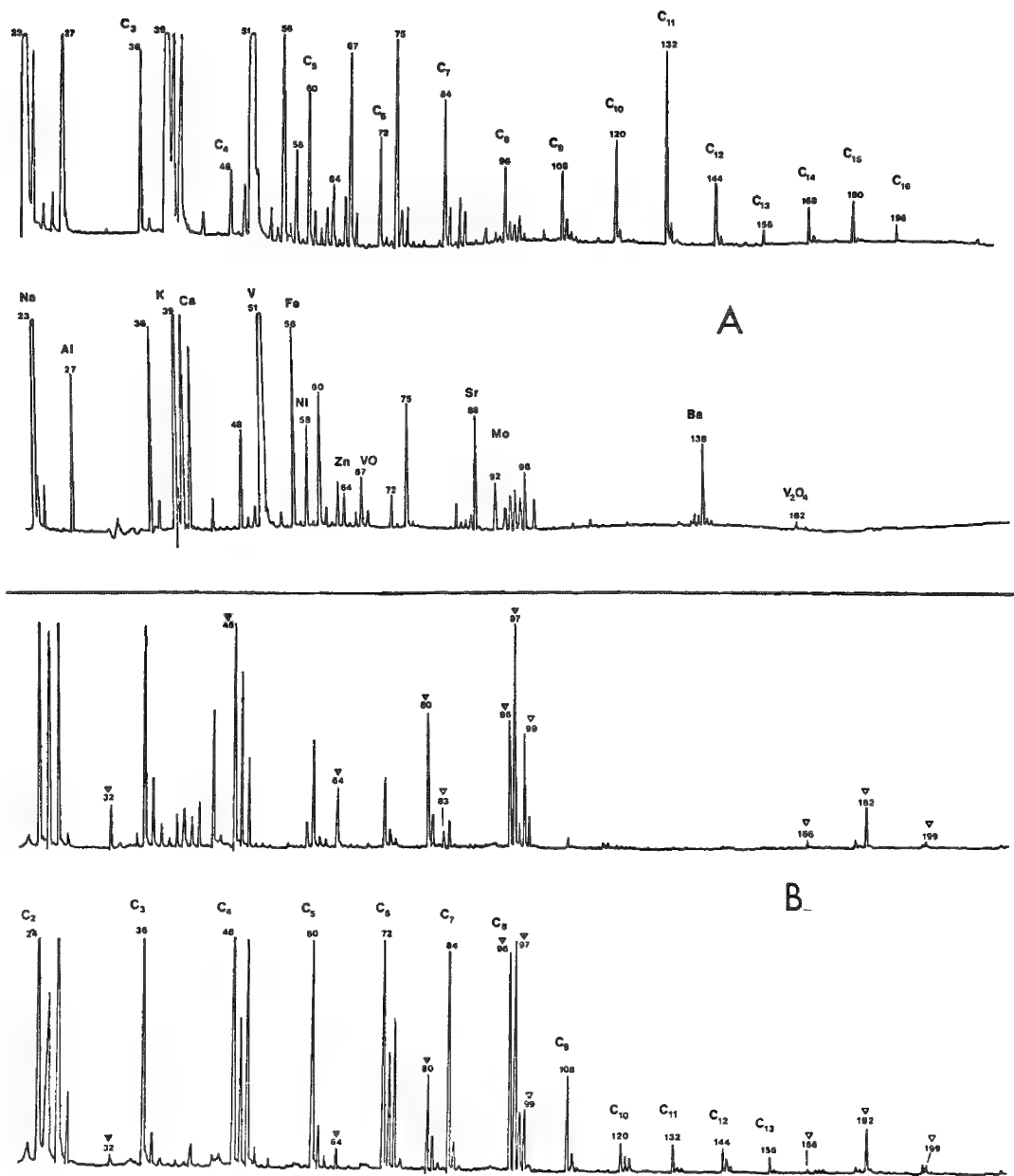
FIG. 1.--Typical positive and negative LAMMA spectra of individual oil fly ash particles
(A) positive ion spectra; (B) negative ion spectra. (∇ = peaks associated with oxides
of vanadium; ▼ = peaks associated with oxides of sulfur.)

information could be extracted about the sulfur and vanadium oxides from the LAMMA
spectra.

    Coal Fly Ash. All morphological forms previously reported for coal fly ash[5] could be
observed and identified microscopically (400× and 1250×). For the purpose of this
investigation, however, only three morphological classifications were employed: clear
or glassy white particles whose morphology varied from regular spheres to rounded lumps,
dark black (often glassy spheres), and irregularly shaped jet black particles.
    Typical spectra of the three classes are presented in Figs. 2 and 3, and the
elements detected are given in Table. 1. The positive ion spectra of the clear glassy
and black spherical particles are very similar; however, a higher iron signal was
observed in a large number of the black spheres. In a statistical analysis of the
Fe/Ca ration for about 50 particles of these two types, a discontinuity in the frequency
distributions of the measured Fe/Ca ratios for the black spherical particles is observed

POSITIVE ION SPECTRA

A

B

NEGATIVE ION SPECTRA

A

B

FIG. 2.--Positive and negative ion spectra of (A) individual clear glassy and (B) black spherical coal fly ash particles.
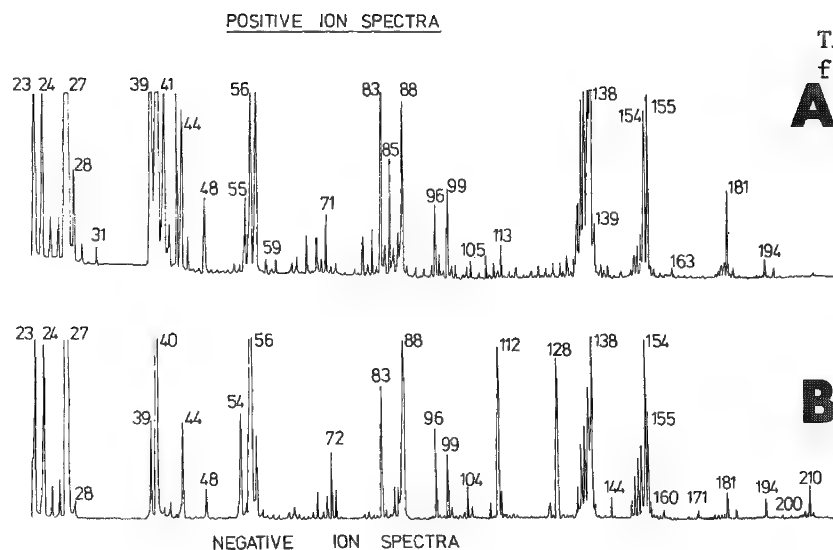
TABLE 1.--Elements detected in coal fly ash with LAMMA.
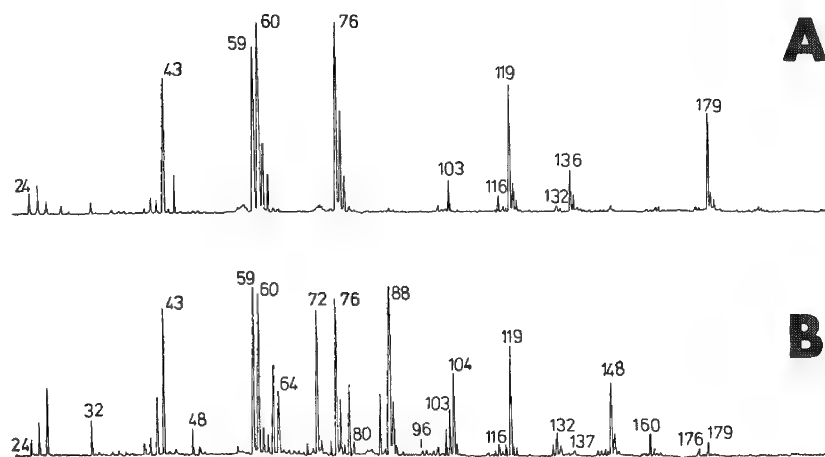
	Spherical (clear and black)		Irregular (jet black)	
Positive Ion Spectra:				
	Na	Mn	Na	K
	Mg	Fe	Mg	Ca
	Al	Co	Al	Fe
	Si	Rb	Si	Sr
	P	Sr		
	Ca	La		
	K	Cs		
	Ti	Ba		
Negative Ion Spectra:				
	Cl		Cl	

at a value of 1.4, which divides the sampled population into two distinct subclasses. Thus, 76% of the black spherical particles analyzed have a composition for which the Fe/Ca ratio is >1.4; and 24% <1.4. The black spherical particles for which the ratio Fe/Ca is <1.4 are statistically indistinguishable from the clear glassy particles on this basis.

These findings are, in fact, unique to LAMMA and illustrate that the technique can be used to indicate quite small compositional differences in an ensemble of particles. The reasons for the distinct compositional differences among the black spherical particles are not clear. One possible explanation, which derives some support from x-ray diffraction studies of coal fly ask,[6] is that the low-iron subfraction of the black spherical particles contains nonmagnetic Fe_2O_3, whereas the high-iron subfraction contain ferromagnetic Fe_3O_4. That would account for the similarity in Fe/Ca ratios between clear glassy spheres and the low-iron subfraction of the black spherical particles, since clear particles have been shown to contain a nonmagnetic form of Fe_2O_3.[6,7]

Consistent with the above discussion, the spectra of the black spherical particles suggest that the iron is present in an oxide form (peaks at m/e = 72, 112, 128, 144 in positive spectra; peaks at m/e = 72, 88, 104, 160, 176 in negative spectra; see Fig. 2). The aluminosilicate nature of both the clear glassy black spherical particles is indicated by the negative spectra where $Al_xSi_yO_z^-$ cluster ions, characteristic of a wide variety of
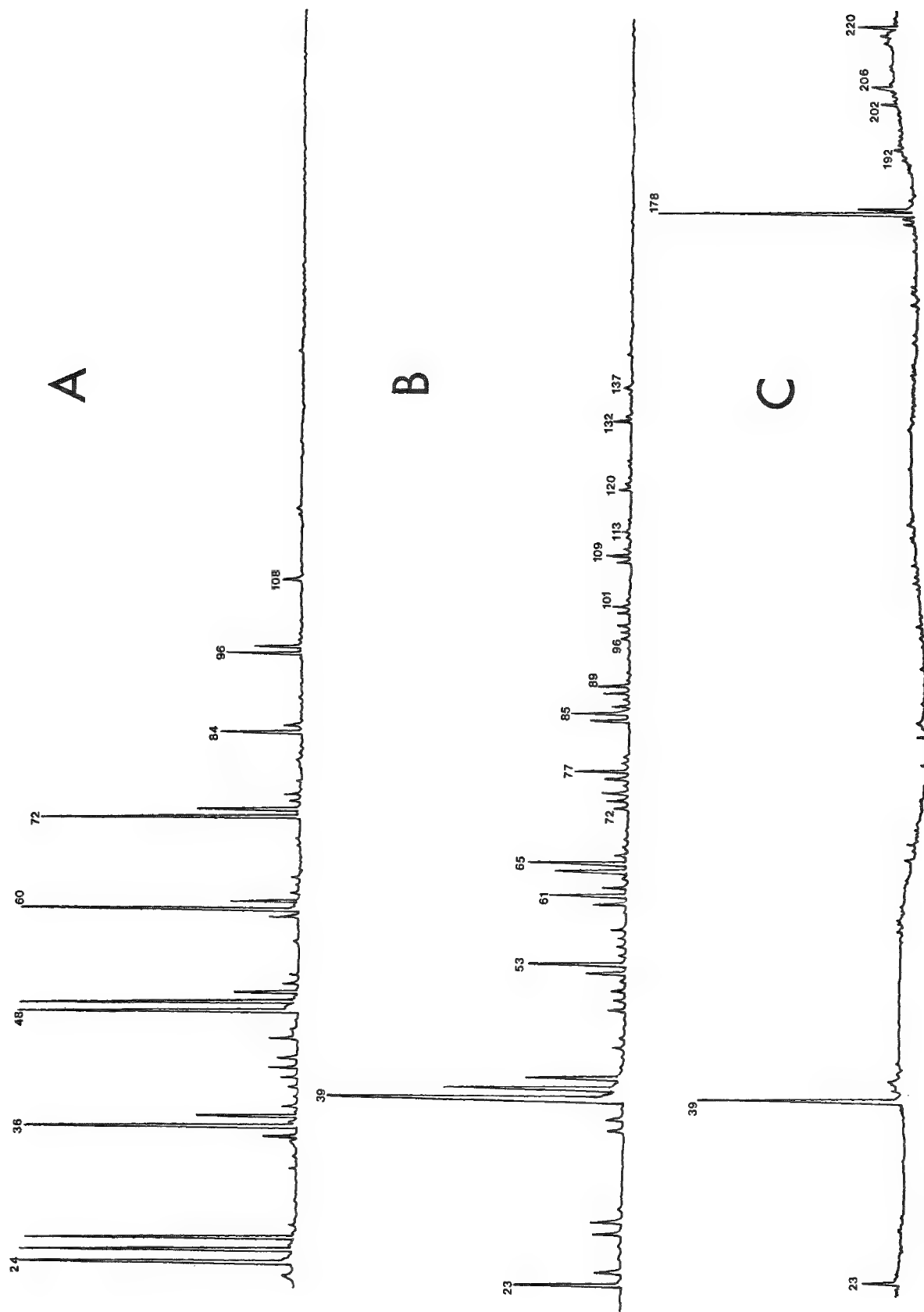
FIG. 3.--LAMMA spectra of individual irregular jet black coal fly ash particles. (A) negative ion spectrum; (B) positive ion spectrum; high laser irradiance; (C) positive ion spectrum; low laser irradiance.

194

aluminosilicate materials, are observed at m/e = 179, 137, 119, 103, 76, 60, 59, 43. Finally, peaks associated with sulfur oxides, m/e = 32, 48, 64, 80, 96, 97, can be observed in the negative spectra.

The negative LAMMA spectra of irregular black particles (Fig. 3a) indicate that these particles are carbonaceous, since the predominant feature is the characteristic series of $C_nH_m^-$ cluster ions. The positive ion spectra (Fig. 3b), however, are not suggestive of a carbon derived from a reducing environment (e.g., C black); rather, the fragmentation pattern resembles that of an activated carbon (peaks at m/3 = 53, 65, 77, 89, 101, 113). This is consistent with the highly absorbing nature of this fraction of coal fly ash.[8]

Organic Constituents. Figure 3(c) shows the LAMMA spectrum of a black irregular particle at low laser irradiance (0.18 µJ) conditions, below the ion appearance threshold of the $C_nH_m^+$ cluster ions. Under these low energy conditions, peaks at mass 178 and above become predominant, and correspond to polynuclear aromatic hydrocarbons (PAH) which are known to be present in coal fly ash.[9] The masses observed are listed in Table 2, along with tentative assignments. Again, due to inhomogeneous distribution among individual particles, not all compounds are observed on each particle, but peaks at mass 178, 192, 202, 206, and 220 appear most frequently (see example in Fig. 3b).

TABLE 2.--Peaks typically appearing at low laser irradiance in LAMMA spectra of individual jet black irregularly shaped coal fly ash particles (e.g., see Fig. 3).

m/e	Possible Assignment
178*	Phenanthrene, Anthracene
192	Methylphenanthrene, Methyl anthracene
202*	Fluoranthene, Pyrene
206*	Dimethylphenanthrene, Dimethylanthracene
216*	Benzofluorene, Methylpyrene
220	Trimethylphenanthrene, Trimethylanthracene
228*	Chrysene, Benzo-a-Anthracene, Napthacene, Triphenylene

* Known to be present in coal fly ash; see (9)

Besides the correlations of peak masses with PAH compounds known to be present in this fly ash sample, further support for the identification of these peaks as PAHs comes from studying model systems. Although it is known that parent molecular ions of pure PAH compounds can be obtained via laser ionization, and are favored at lower laser powers,[10] we have established that PAH compounds can also be detected when adsorbed onto a matrix. For example, phenanthrene, 9,10-diphenylanthracene, and coronene were adsorbed onto coal fly ash, alumina, and activated carbon, respectively (the first by vapor adsorption, the other two by solution doping). All showed the same dependence of parent molecular ion intensity with laser power and exhibited a maximum intensity at approximately 0.15 µJ. The molecular ions observed were almost exclusively the parent ions of the PAH; however, cationization by Al^+ was observed for 9,10-diphenylanthracene on Al_2O_3 at m/e = 357, $(P + 27)^+$, in one case out of approximately fifty. Further investigation is needed to determine the specific conditions conducive to cationization of PAHs from different surfaces.

Conclusion

In conclusion, it can be stated that LAMMA consitutes a fast and effective tool for conducting qualitative characterization of coal and oil fly ash particulate material. Both elemental as well as molecular information can be extracted, and in the case of PAHs, it is apparent that LAMMA provides the unique capability of detecting these species on a micrometer scale. These preliminary results exploiting LAMMA in an organic microprobe capacity are indeed encouraging, and warrant further methodological development.

References

1. K. F. J. Heinrich, Ed., *Characterization of Particles,* NBS Special Publication 533, April 1980.

2. H. Malissa, Ed., *Analysis of Particulates by Physical Methods,* CRC Press, 1978.

3. W. C. McCrone and J. G. Delly, Eds., *The Particle Atlas,* Ann Arbor Sci., 1973, 2d ed., vol. 2, p. 543.

4. R. A. Hofstader et al., Eds., *Analysis of Petroleum for Trace Metals,* Advances in Chemistry Series, No. 156, American Chemical Society. 1976.

5. G. L. Fisher et al., *Environ. Sci. Technol.* 12: 447, 1978.

6. A. H. Miguel, "Studies of Gas Solid Reaction of Environmental Significance: I. Pyrine Adsorption onto fly ash; II. Thiol oxidation and adsorption by activated charcoal," Ph.D. thesis, University of Illinois, Urbana, 1967.

7. R. L. Davison et al., *Environ. Sci. Technol.* 8: 1107, 1974.

8. P. A. Soltys, "The Extraction Behavior of PAH from Coal Fly Ash," M.S. Thesis, Colorado State University, Fort Collins, 1980.

9. R. P. Hangebrauck, D. J. von Lehmden, and J. E. Meeker, *Sources of Polynuclear Hydrocarbons in the Atmosphere,* U.S. National Pollution Control Administration, Durham, N. C., 1967.

10. H. J. Heinen, *Intern. J. Mass Spectrom. Ion Phys.* 38: 309, 1981.

IDENTIFICATION OF PIGMENTS OF ARTISTIC, FORENSIC, AND INDUSTRIAL IMPORTANCE BY THE RAMAN MICROPROBE (MOLE) AND SCANNING ELECTRON MICROSCOPY WITH ENERGY-DISPERSIVE X-RAY ANALYSIS

M. E. Andersen

Raman microprobes have been applied to a wide variety of both organic and inorganic samples for chemical identification of regions or particles as small as 1 μm.[1] These unique capabilities are ideal for the examination of art objects because the small sample size requirements make the Raman microprobe a nearly nondestructive analytical technique. forensic examination of evidence may also require such nondestructive analysis for legal reasons. Because pigments are used in both artists' and industrial paints and in plastics and polymer fibers, their chemical analysis on a microscale may be important both in determining their identity and in relating their presence or distribution to other properties of the products. As with all other analytical tools, a complete understanding of the makeup of a sample frequently requires the use of more than one technique. In the study of pigments, the morphological and elemental information derived from scanning electron microscopy (SEM) with an energy-dispersive x-ray system (EDS) is often helpful in identifying which reference compounds should be compared spectrally with that of the unknown. This paper demonstrates how the Raman microprobe can be integrated with other analytical tools in the analysis of pigments.

Applications of Pigment Analysis

The identification of pigments used by artists is of interest for several reasons. In the past particular pigments have been favored by artists and have then fallen from favor for reasons such as availability, economics, health hazards, and color stability. A knowledge of trade patterns and manufacturing advances may allow art historians to determine the temporal and geographic provenances of paintings. Such information is critically important in art authentication.[2] Art conservators must also identify painting materials to determine how best to preserve or restore objects exposed to the environment. The modern artist frequently purchases a pigment whose name represents a particular chemical compound. Although the hue of such a pigment is similar to that of the compound, sometimes the pigment is composed of entirely different compounds. The chemical differences may dramatically alter a painting's appearance or stability.

The physical characteristics of paints, plastics, and polymer fibers are altered by the amount, type, and distribution of pigments. Pigment identification often becomes important in trouble shooting production or field-failure problems or in keeping pace with competitors. The variations in types of pigments used by various manufacturers over time is very useful from a forensic standpoint, since the variations serve as fingerprints of a particular manufacturer for a particular time period. Success in matching a paint sample or a polymer fiber found on a suspect to the scene of a crime may provide evidence that makes the difference between conviction and acquittal.

Pigment Identification Schemes

Pigments are often complex mixtures of components blended together to yield a particular color. Different phases of the same compound (such as TiO_2, PbO, or phthalocyanine)

display different chemical and physical properties. The detailed analysis of all the microscopic components present in a pigment serves to fingerprint it, so that microanalytical techniques must usually be employed.

The most widely employed tool is the optical microscope, which provides information on refractive index, birefringence, color, morphology, and particle size of major, minor, and trace components in a pigment.[2] Together these data are often sufficient to characterize the pigment. In cases where particle sizes are small (<2 or 3 μm) and/or refractive indexes are high (>1.8), elemental information is often necessary and is obtained through microchemical testing[3] or electron microprobe analysis. Where the sample is composed of only one or two crystalline components, x-ray diffraction (XRD) or infrared (IR) spectroscopy[4-6] can yield precise identification data. In more complex mixtures or where particle morphology is important, transmission electron microscopy (TEM) with selected area electron diffraction (SAED) may be employed.[7]

The Raman microprobe fills a unique niche in the analysis of both organic and inorganic pigments since it yields chemical information, including phase identification, of particles as small as 1 μm. Thus, it improves upon the capabilities of IR analysis of organic samples, which is limited to particles greater than about 25 μm.[8] The practical lower limit for XRD is about 10 μm,[9] so here too micro-Raman analysis expands phase identification capabilities. The Raman microprobe, MOLE (Molecular Optics Laser Examiner), is designed around a research quality microscope that can be easily set up for polarized light microscopical studies.[10] Raman spectra from optically characterized particles can be recorded without remounting.

Instrumentation and Sampling Techniques

The pigment samples were spread onto a polished beryllium SEM stub on which a grid had been scribed. Beryllium was chosen because it has no interfering spectrum for either Raman or EDS analysis. Unshadowed particles were first analyzed at 20 kV with a Cambridge Mark 2A SEM and then with the MOLE Raman microprobe. In some cases particles were first examined by MOLE on a glass slide before being transferred to a beryllium stub. A Leitz 100× (0.90 N.A.) infinite-tube-length-corrected objective was used in all Raman analyses.

Examples of Pigment Analysis

Naples yellow[11,12] is a pigment whose history is not well known. It is thought to be lead antimonate $Pb_3(SbO_4)_2$, but through the years numerous materials have been substituted to produce similar hues without a change in name. The pigment is usually made by roasting of the mixed oxides. The hue can be controlled to some extent by the Pb/Sb ratio and by limiting the extent of the reaction since the lead oxides are yellow and the antimony oxides are white. Traces of the unreacted oxides often remain.

A Naples yellow from Weber was composed almost entirely of equant isotropic submicrometer yellow particles. The Raman spectrum of a 3μm agglomerate (Fig. 1) was readily obtained (Fig. 2), but it matched no available reference spectrum. The EDS spectrum (Fig. 3) indicated the particle contained primarily lead and antimony with a trace of zinc. (The iron peak is an instrumental artifact.) Zinc is frequently added to lead pigments to inhibit discoloration from atmospheric sulfide, since zinc sulfide is white. Two cubic forms of lead antimony oxide exist; monimolite, $Pb_3[SbO_4]_2$; and bindheimite, $Pb_2Sb_2O_6(O,OH)$. X-ray diffraction data confirmed that the isotropic phase in this Naples yellow is bindheimite.

Another Naples yellow (Roberson) also contained bindheimite, as confirmed by Raman microprobe. A minor phase displayed a needle-like morphology and yielded the Raman spectrum shown in Fig. 4. The crystal was identified as valentinite,[13] the orthorhombic form of Sb_2O_3. EDS analysis of the crystal confirmed this identification (Fig. 5).

A third Naples yellow (Roberson--pale) was composed primarily of equant submicrometer, white, lead-bearing particles and deeply colored yellow needles (Fig. 6) containing lead and chromium. Raman microprobe identified these components as cerussite ($PbCO_3$, Fig. 7) and crocoite ($PbCrO_4$, Fig. 8).

Some organic pigments tend to be sensitive to laser-beam damage and natural-product organic pigments may also fluoresce. Nonetheless, many organic pigments yield strong characteristic Raman spectra (Fig. 9).

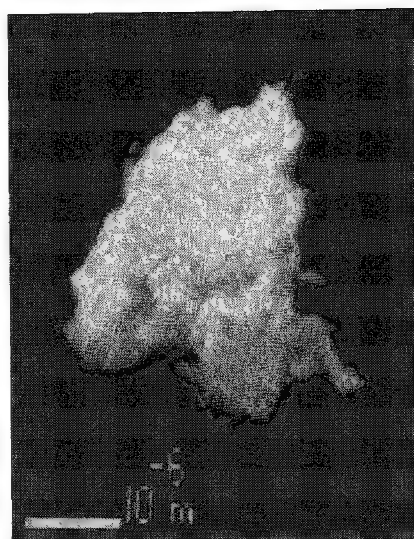An example of both industrial and forensic interest is the examination of pigmented

FIG. 1.--SEM micrograph of Weber Naples yellow pigment particle; no conductive coating on beryllium substrate.
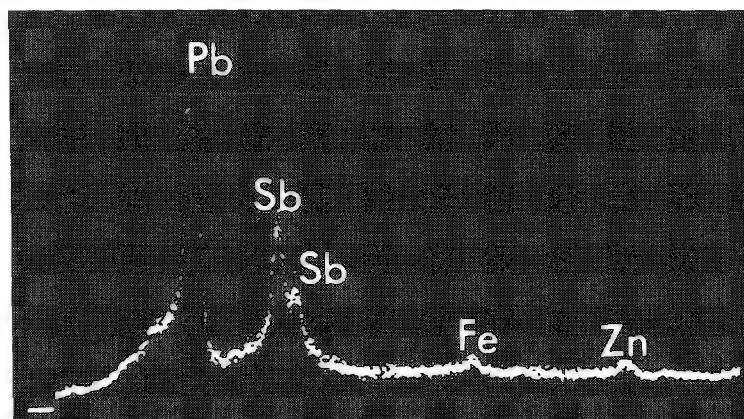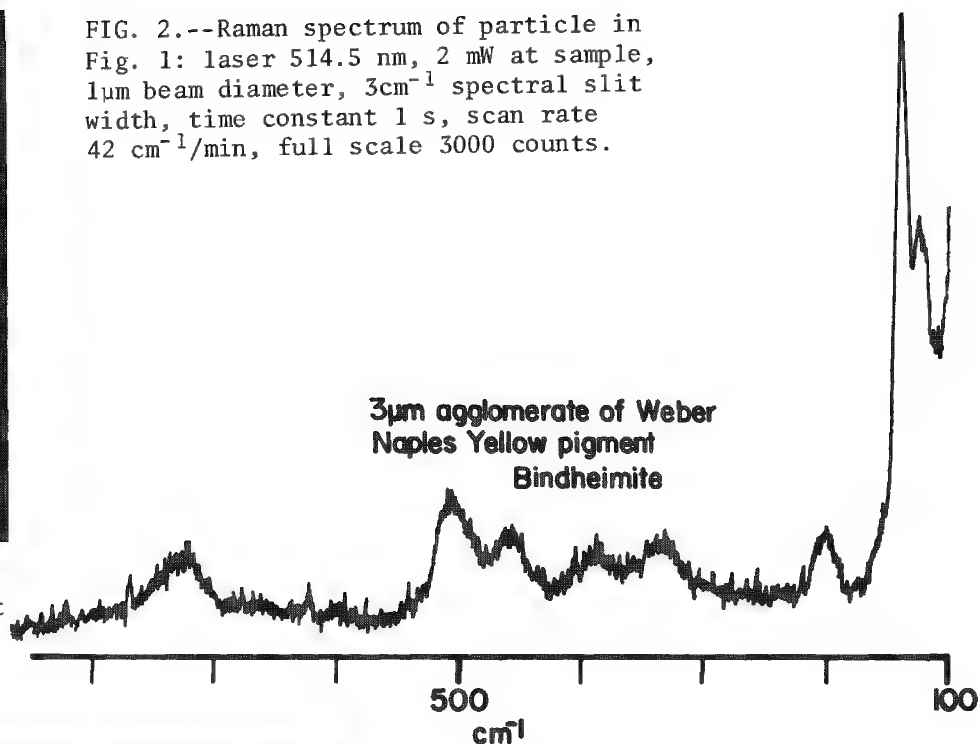

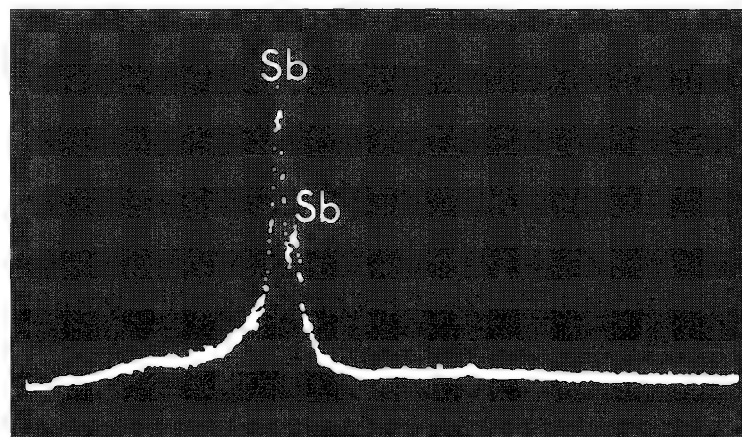FIG. 2.--Raman spectrum of particle in Fig. 1: laser 514.5 nm, 2 mW at sample, 1μm beam diameter, 3cm^{-1} spectral slit width, time constant 1 s, scan rate 42 cm^{-1}/min, full scale 3000 counts.

3μm agglomerate of Weber Naples Yellow pigment Bindheimite

500 cm^{-1} 100

FIG. 3.--EDS spectrum of particle in Fig. 1.

15x4μm crystal of valentinite in Roberson Naples Yellow pigment

500 cm^{-1} 100

FIG. 4.--Raman spectrum of colorless needle-like crystal of valentinite in Roberson Naples yellow pigment. Laser 514.5 nm, 5 mW at sample, 1μm beam diameter, 4cm^{-1} spectral slit width, time constant 3 s, scan rate 17 cm^{-1}/min, full scale 1000 counts.
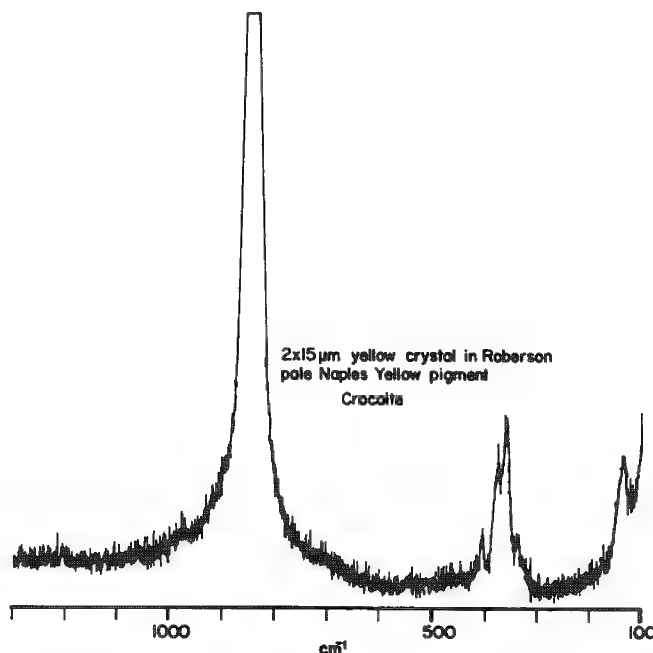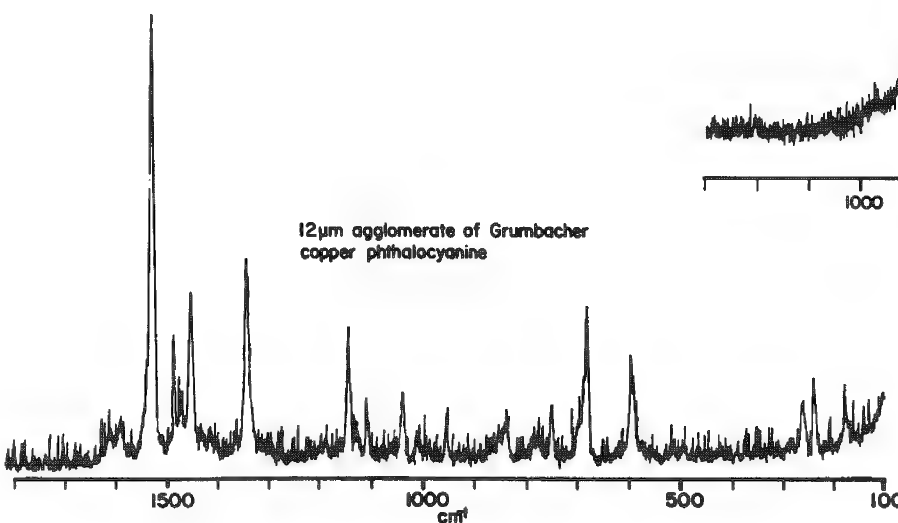

FIG. 5.--EDS spectrum of valentinite crystal.
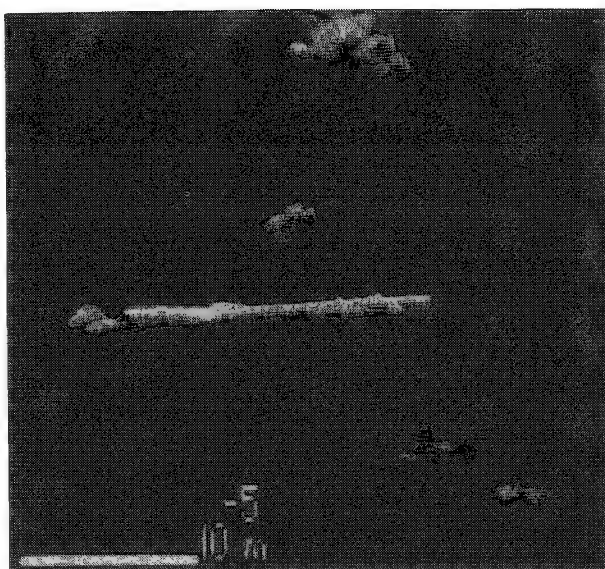
FIG. 6.--SEM micrograph of yellow lead-chromium bearing needle-like crystals and white lead-bearing equant particles. Roberson pale Naples yellow pigment. No conductive coating on beryllium substrate.

8μm agglomerate of white particles in Roberson pale Naples Yellow pigment

Cerussite
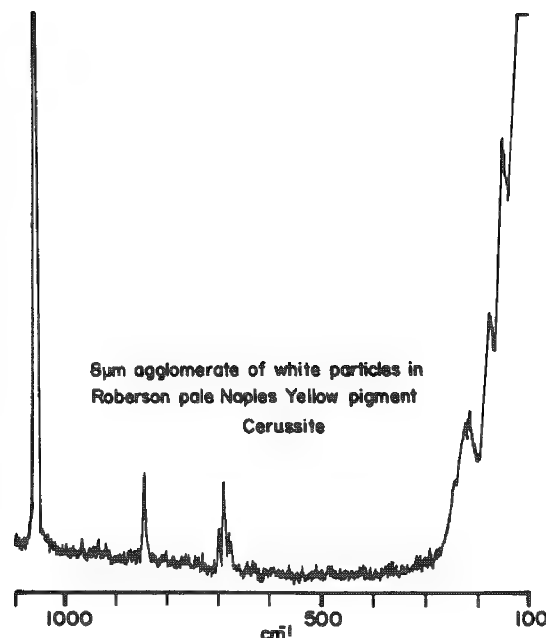
FIG. 7.--Raman spectrum of white equant particles such as pictured in Fig. 6; laser 514.5 nm, 5 mW at sample, 1μm beam diameter, 4 cm^{-1} spectral slit width, time constant 1 s, scan rate 42 cm^{-1}/min, full scale 3000 counts.

FIG. 8.--Raman spectrum of yellow needle-like crystal in Fig. 6; laser 514.5 nm, 2 mW at sample, 1μm beam diameter, 3 cm^{-1} spectral slit width, time constant 0.3 s, scan rate 42 cm^{-1}/min, full scale 3000 counts.

2x15μm yellow crystal in Roberson pale Naples Yellow pigment

Crocoite

12μm agglomerate of Grumbacher copper phthalocyanine

FIG. 9.--Raman spectrum of "Thalo" blue pigment; laser 514.5 nm, 1 mW at sample, 12μm beam diamter, 3 cm^{-1} spectral slit width, time constant 1 s, scan rate 42 cm^{-1}/ min, full scale 1000 counts.

polymers and delustered fibers. Filled polymers must usually be pyrolyzed before analysis by IR, and the filler material must be analyzed separately by, for instance, the electron microprobe. With the Raman microprobe one can identify both the inorganic and organic components simultaneously. The spectrum of a spandex fiber (Fig. 10) reveals both the rutile (TiO_2) pigment (peaks below 700 cm^{-1}) and the polyurethane spectra. The presence of rutile pigment distinguishes this fiber from most spandex fibers that use anatase as a pigment because anatase is less abrasive.
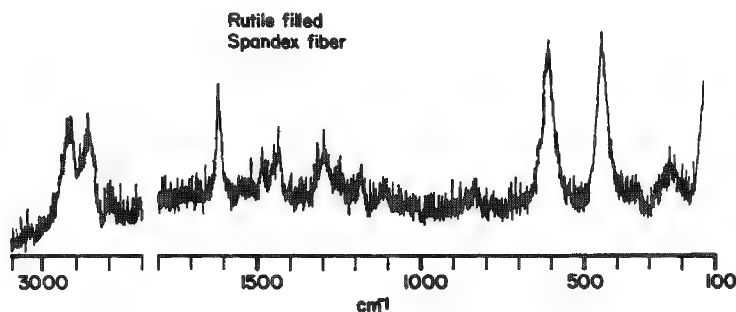
FIG. 10.--Raman spectrum of delustered spandex fiber; laser 514.5 nm, 15 mW at sample, 10μm beam diameter, 5cm^{-1} spectral slit width, time constant 1 s, scan rate 42 cm^{-1}/min, full scale 1000 counts.

Conclusions

The Raman microprobe is a useful tool for analyzing organic and inorganic pigments, especially where sample size constraints are a problem. While fluorescence and photo-induced sample degradation are occasionally problems, most pigments yield strong Raman spectra. A major drawback is the lack of a suitable reference library of spectra. The creation of such a library for a particular inorganic pigment is facilitated by a knowledge of the elemental content of the pigment particle, readily obtained by SEM with EDS.

References

1. A number of such recent applications can be found in the *Microbeam Analysis--1979*, 148-196.
2. W. C. McCrone, "Application of particle study in art and archaeology conservation and authentication," in W. C. McCrone, J. G. Delly, and S. J. Palenik, *The Particle Atlas*, Ann Arbor, Mich.: Ann Arbor Sciences Publishers, 1979, 2d ed., vol. 5, pp. 1402-1413.
3. S. J. Palenik, "Microchemical reactions in particle identification," *ibid.*, pp., 1175-1184.
4. L. C. Afremow and J. T. Vandeber, "High resolution spectra of inorganic pigments and extenders in the mid-infrared region from 1500 cm^{-1} to 200 cm^{-1}," *J. Paint Technol*. 38: 169-202, 1966.
5. M. J. D. Law and N. S. Baer, "Application of infrared Fourier transform spectroscopy to problems in conservation," *St. in Cons*. 22: 116-128, 1977.
6. R. Newman, "Some applications of infrared spectroscopy in the examination of painting materials," *JAIC* 19: 42-62, 1980.
7. W. C. McCrone, "Authenticity of a medieval document tested by small particle analysis," *Anal. Chem*. 48: 676A-679A, 1976.
8. Howard Humecki, personal communication, 1982.
9. W. C. McCrone and J. G. Delly, *The Particle Atlas*, Ann Arbor, Mich.: Ann Arbor Science Publishers, 1973, 2d ed., vol. 1, pp. 119-129.
10. M. E. Andersen and R. Z. Muggli, "Microscopical techniques with the Molecular Optics Laser Examiner Raman microprobe," *Anal. Chem*. 53: 1772-1777, 1981.
11. R. J. Gettens and G. L. Stout, *Painting Materials: A Short Encyclopaedia*, New York: Dover Publications, 1966, 133.
12. R. Mayer, *The Artist's Handbook of Materials and Techniques*, New York: Viking Press, 1970, 94.
13. C. A. Cody, L. DiCarlo, and R. K. Darlington, "Vibrational and thermal study of antimony oxides," *Inorg. Chem*. 18: 1572-1576, 1979.

PRECISION AND ACCURACY OF HIGH RESOLUTION ISOTOPIC MEASUREMENTS WITH THE ION MICROPROBE AND SYSTEMATICS OF ION FORMATION

J. T. Armstrong, J. C. Huneke, and G. J. Wasserburg

The ion microprobe has been demonstrated to be a valuable tool in determining isotopic and chemical variations in microvolumes of lunar, meteoritic, and terrestrial samples.[1-3] Yet applications of the ion microprobe to the study of terrestrial and extraterrestrial materials have been limited by the severity of the isobaric interferences in the mass spectrum and the lack of sufficient instrument control to obtain high precision measurements at the high resolving powers needed to eliminate these interferences. We report the development of analytical techniques and instrumental modifications to PANURGE, the Caltech-modified CAMECA IMS3F ion microprobe, to enable the accurate and routine measurement of isotopic and chemical ratios at high resolving powers in an automated peak jumping mode, to increase the useful ion yield, and to acquire data on a time scale short compared to variations in analytical conditions.

Magnet Field Control

High-precision isotopic measurements at high mass resolving power require (1) a high level of electrostatic and magnetic field stability during measurements, (2) an ability to compensate for minor field instabilities and drift and repeatedly and precisely set the magnet field for preselected mass values, and (3) procedures that compensate for significant magnet hysteresis. The addition of high-stability power supplies for the mass spectrometer electrostatic analyzer and improved temperature control of the Hall probe magnetic field sensor have significantly improved field stabilities. New computer control software has been developed for data acquisition by sequential stepping of the magnet field to precisely determined values. The shapes of the various major mass peaks and magnet field values corresponding to centroids and half heights are initially determined in the order of data acquisition. During data acquisition, intensities are measured at each cycle on the nominal half height positions as well as the top of each peak which contains sufficient intensity. For use in the next cycle, the stored field values are then corrected for the change in the field calculated from the relative half height intensity measurements. The magnet field values of low-intensity peaks are given by fixed dispersion factors relative to reference peaks determined in previous experiments. The constancy of the dispersion factors between major peaks are determined as a check on the accuracy of the fixed dispersion factors for the minor intensity peaks. The typical measured short term (10min) stability of the magnetic field with this control program is approximately ± 1 ppm (2σ) corresponding to shifts of ± 0.05 mamu, which is equivalent to one-tenth of one of the digital magnet field control steps. The long-term measured field variations during data acquisition (1 hr) are typically approximately ± 5 ppm (2σ) corresponding to ± 0.2 mamu or ± 0.5 digital steps. Dispersion values appear to be constant over the course of a series of data acquisitions (1 day) to ± 0.5 mamu or ± 1 digital control step. The ability to relocate mass peaks by programmable magnet field control has been found to be sufficient to obtain high precision isotopic ratio data at mass resolving powers ($M/\Delta M$) of 8000 and routinely at $M/\Delta M < 6500$.

Counting Linearity

In order to obtain interpretable high-precision isotopic measurements, the ion pulse counting system must operate at relatively high gain, but with very low background. It must also be close to linear over a very wide dynamic range (0 to 10^6 cps) and the small degree of nonlinearity must be constant and correctable. Substantial changes have been made to the electron multiplier counting system to meet these requirements. The electron multiplier typically operates at a gain of the order of 10^8. The measured background is typically <0.1 cps. Direct measurements of pulse pair resolution and precise measurements of isotopic ratio variations obtained at different counting rates both indicate that the pulse counting system has a linearity consistent with a simple deadtime of 17 ns (requiring a correction of <2% at 10^6 cps).

Measurement Precision

Typical measured standard deviations of isotope ratios, both for high-intensity and low-intensity peaks, approximately equal the precisions predicted by counting statistics. The measured standard deviations of the averages of blocks of isotope ratio data also typically approximate the precisions predicted from counting statistics indicating a convergence of the mean. For typical (1 hr) experiments, the relative precisions (2 standard errors of the mean, $2\sigma_m$) obtained for about 50 measurements of major isotope ratios (e.g., 46/48, 47/48, 49/48, 50/48 in Ti metal) are approximately $1^\circ/_{\circ\circ}$. Typical relative precisions of Ti, Si, and Mg isotopic ratio determinations ($2\sigma_m$) in a glass of Al-, Ti-rich pyroxene (fassaite) composition are $1-2^\circ/_{\circ\circ}$. Typical relative precisions obtained for Mg isotopes in plagioclase crystals from Ca-, Al-rich inclusions in the Allende meteorite (approximately 500 ppm Mg) are $2-4^\circ/_{\circ\circ}$. For trace Mg in an anorthite glass (approximately 20 ppm), typical relative precisions of $5-10^\circ/_{\circ\circ}$ have been obtained in 1 hr experiments (about 50 ratio measurements).

Fractionation

Instrumental mass discrimination or fractionation must be known and kept relatively constant between experiments in order to make accurate determination of isotopic fractionation anomalies possible. In samples with normal isotopic composition, the isotopic ratios typically fall within counting statistics of a linear mass fractionation line. Instrumental parameters can significantly change the amount of instrumental mass discrimination. When conditions are kept relatively constant, however, the degree of mass fractionation can be stable. A series of experiments determining Ti isotopic composition in normal Ti metal showed a fractionation of -1.50% ± 0.16%/amu (2σ). (Negative values indicate fractionation favoring light isotopes.) Si instrumental isotopic fractionation in fassaite glass was found to be -3.63% ± 0.74%/amu (2σ). Although the degree of fractionation varies considerably from element to element, it does not appear to be especially sensitive to matrix composition. The fractionation for Ti isotopes was found to be -1.46%/amu in fassaite glass and -1.50%/amu in Ti metal. Si instrumental isotopic fractionation was found to be -3.64%/amu in fassaite glass, -3.72%/amu in Allende WA plagioclase, and -3.69%/amu in Allende 3529Z plagioclase. Mg isotopic fractionation was found to be -1.09%/amu in fassaite glass, -1.04%/amu in Lake County plagioclase, and -1.18%/amu for the trace Mg (20 ppm) in synthetic anorthite glass G1.

Elemental Abundance Determination

The relative efficiency of secondary-ion production is a complex and poorly understood function of a number of matrix-dependent parameters (e.g., Ref. 3), which limits the accuracy of element abundance determinations with the ion microprobe. However, in matrices of similar composition, the relative ionization efficiency can be relatively constant and reasonably accurate factors for the calculation of atomic ratios from measured sputtered ion currents can be determined. Such relations were determined for the major element pairs in the various plagioclase crystals and anorthite glasses studied in this experiment. The ratio of the measured Ca^{++}/Al^+ to the relative atomic abundance was determined to be 0.051 ± 0.006 (2σ) in anorthite glass G1, 0.053 ± 0.004 in Allende 3529Z plagioclase, 0.054 ± 0.002 in Allende WA-IPPL9 plagioclase, and 0.056 ± 0.001 in Allende WA-IPPL10 plagioclase. Measured Mg^+/Al^+ in anorthite glass, pyroxene glass, and Allende

plagioclases differed from known atomic abundance ratios by only 15%, $Mg^+/Al^+ = 1.15 \pm 0.10Mg/Al$.

References

1. C. Meyer Jr., D. H. Anderson, and J. G. Bradley, "Ion microprobe mass analysis of plagioclase from 'non-mare' lunar samples," *Geochim. Cosmochim. Acta* (Suppl. 5) 1: 685-706, 1974.

2. J. G. Bradley, J. C. Huneke, and G. J. Wasserburg, "Ion microprobe evidence for the presence of excess ^{26}Mg in an Allende anorthite crystal," *J. Geophys. Res.* 83: 244-254, 1978.

3. I. M. Steele, R. L. Hervig, I. D. Hutcheon, and J. V. Smith, "Ion microprobe techniques and analyses of olivine and low-Ca pyroxene," *Am. Mineral.* 66: 526-546, 1981.

STANDARD CaAl$_2$Si$_2$O$_8$ GLASSES WITH VARIOUS Mg ISOTOPIC COMPOSITIONS FOR ION MICROPROBE CHARACTERIZATION

J. T. Armstrong, J. C. Huneke, H. F. Shaw, T. A. Finnerty, and G. J. Wasserburg

The ion microprobe has the capability of measuring the isotopic composition of a large variety of elements in solid specimens. The accurate determination of isotopic variations in microvolumes of material has important applications in diverse fields including cosmochemistry, geochemistry, materials science, and biochemistry. Accurate measurement is often hindered by the multitude of isobaric interferences of molecular ion species and by large isotopic fractionations that often result from the combination of the sputtered ion formation process and the ion extraction and measurement methods. Thus, the accurate quantitative analysis of isotopic compositions in complex materials with the ion microprobe requires measurement at high mass resolving powers and precise determinations of mass fractionation and detector nonlinearity effects. The confirmation of the reproducibility and accuracy of such measurements requires testing of the instrument with the use of well-characterized standards, which are not naturally available. This paper describes (a) the synthesis of a series of standard glasses, nominally CaAl$_2$Si$_2$O$_8$ (anorthite), with added trace amounts of Mg (about 300 and 1000 ppm) of various known isotopic compositions (^{25}Mg excesses of about 0, 1, 3, 10, and 30%), and (b) the results of ion microprobe analyses of these glasses to test the precision and accuracy obtainable.

Preparation of Standards

Starting materials for the standard glasses were prepared by the method of Finnerty et al.,[1] in which organic acid solutions of the cations of interest are mixed with a stabilized colloidal suspension of silica to make a homogeneous aqueous mixture of the desired composition. This mixture is rapidly frozen and the water removed by sublimation under vacuum. The dry residue is then heated in air at about 1000°C to oxidize the organic anions. The result is an intimate mixture of oxides which can then be melted to a homogeneous glass. In order to prepare the enriched Mg standards, one batch of an aqueous mixture approximately the composition of anorthite (CaAl$_2$Si$_2$O$_8$) was prepared from stock cation solutions. (Exact anorthite stoichiometry was not obtained due to inaccurate calibration of the concentration of one or more of the stock solutions.) This solution was then split into two equal volumes. Mg of normal isotopic composition was added to each volume to bring the Mg concentrations in the final anorthite glasses to approximately 300 and 1000 ppm. The two mixtures were then each split into four parts. A solution of ^{25}Mg (99.2% ^{25}Mg, 0.4% ^{26}Mg, 0.4% ^{26}Mg) was added to these mixtures in order to create enrichments (relative to terrestrial normal Mg) of approximately 0, 1, 3, and 10% ^{25}Mg in the 1000ppm materials and approximately 0, 3, 10, and 30% ^{25}Mg in the 300ppm materials. (The nominal compositions of the various glasses are given in Table 1.) After freeze drying and heating as described above, the oxide powders were brought to about 1500°C over 1 hr and held at that temperature for 1 hr at 1 at. in covered Pt crucibles. The melts were then quenched in air to form the glasses.

After cooling, the glasses were crushed in individual, specially prepared stainless-steel mortars and pestles, and fragments were selected for analysis. Each mortar and pestle was used once and then discarded to eliminate contamination. Single 0.5mm-sized chips were mounted in epoxy in millimeter-sized cavities in stainless-steel cylinders and polished with diamond polishing materials. Separate laps were used for polishing each sample to avoid

TABLE 1.--Elemental composition of anorthite (An-Mg) glasses (in oxide wt.%).

	Nominal Glasses 1-4	Glasses 5-8	Electron probe results (9 analyses/glass) An-Mg-6±$2\sigma_m$	An-Mg-7±$2\sigma_m$	An-Mg-8±$2\sigma_m$
CaO	20.15	20.12	21.67±0.13	21.73±0.15	21.59±0.10
Al_2O_3	36.64	36.60	37.47±0.28	37.80±0.32	37.37±0.34
SiO_2	43.17	43.12	40.64±0.40	40.60±0.50	40.61±0.22
MgO	0.048	0.166	0.18±0.05	0.15±0.03	0.15±0.02
Σ	100.01	100.01	99.96	100.28	99.72
ppm Mg	292	1000			

TABLE 2.--Mg isotopic composition of anorthite (An-Mg) glasses.[1]

Glass	Nominal ppm Mg	$^{25}Mg/^{24}Mg$	$\delta^{25}(Mg/^{24}Mg)$	$^{26}Mg/^{24}Mg$
An-Mg-1	292	0.12663	0	0.139805
An-Mg-2	292	0.13033	29.2°/°°	0.13982
An-Mg-3	292	0.13951	101.7°/°°	0.13985
An-Mg-4	292	0.16690	318.0°/°°	0.14123
An-Mg-5	1000	0.12663	0	0.139805
An-Mg-6	1000	0.12782	9.4°/°°	0.13981
An-Mg-7	1000	0.13029	28.9°/°°	0.13982
An-Mg-8	1000	0.13903	97.9°/°°	0.13985

[1]Calculated relative to "normal" Mg isotopic composition: $^{25}Mg/^{24}Mg$ = 0.12663 and $^{26}Mg/^{24}Mg$ = 0.139805.

TABLE 3.--Results of ion microprobe isotopic measurements of anorthite (An-Mg) glasses.

Analytical conditions	Glass	$\delta(^{25}Mg/^{24}Mg)$ Grav.	Ion probe ±$2\sigma_m$	$F(°/°°/amu)±2\sigma_m$ F_{Mg}	F_{Si}
A	An-Mg-2	29.2	31.4±5.4	-10.7±2.3	-36.3±2.8
	An-Mg-4	318.0	310.0±3.7	-5.8±1.5	-35.6±3.6
	An-Mg-5	0	2.2±2.9	-10.0±1.2	-35.8±2.5
	An-Mg-6	9.4	9.1±2.3	-10.3±1.0	-37.0±1.8
	An-Mg-8	97.9	96.7±2.1	-10.1±0.8	-37.2±1.8
B	An-Mg-1	0	3.3±3.4	-15.1±0.8	-41.6±1.7
	An-Mg-3	101.7	101.2±4.7	-14.8±2.0	-40.4±3.6
	An-Mg-4	318.0	312.2±4.9	-16.0±1.9	-38.8±1.6
	An-Mg-5	0	0.1±3.3	-14.2±1.4	-43.7±3.7
	An-Mg-7	28.9	29.6±4.8	-17.6±1.7	-45.9±2.7

cross contamination. The polished specimens were carbon coated, analyzed with the electron microprobe, repolished to remove the carbon, then gold coated and put into the ion microprobe for analysis. Separate fragments of the glasses were selected for chemical and isotopic analysis by normal thermal emission mass spectrometric techniques. The bulk of the glass standards has been stored for future investigation and later may be made available to other laboratories.

Analytical Results

The major element composition of the glass standards were determined by electron microprobe analysis with an automated MAC-5-SA3. The correction procedures of Bence and Albee[2] were employed. An anorthite standard was analyzed at the same time as the glasses to determine that no systematic errors occurred. The results of the analyses of representative glasses are given in Table 1. The glasses appeared to be homogeneous on a micron scale to the precision determined by the counting statistics. No statistically significant differences in the major element composition were found among the various glasses. The Mg composition was nominally the same as that predicted by gravimetry, although the uncertainty due to counting statistics at such low Mg concentrations is quite large.

Ion microprobe analyses were performed on the various glasses using PANURGE, a Caltech-modified Cameca IMS-3F ion microprobe. The samples were bombarded by a negatively charged oxygen beam of about 5 nA current. A $50 \times 50\mu m$ area was rastered to remove the gold coat and surface contamination before analysis. The analyses were performed with a $10\mu m$ focused beam or $15 \times 15\mu m$ rastered area in the center of the $50 \times 50\mu m$ rastered field. A $150\mu m$ imaged field was focused through the secondary optics. Minimal energy filtering was employed, sufficient to enable analysis at a mass resolution of $M/\Delta M = 3000$.

Mg^+ and Si^+ isotopic ratios and Ca^{++}/Mg^+ and Al^+/Mg^+ were measured at a mass resolving power of $M/\Delta M \simeq 3000$ to avoid isobaric interferences by hydride and multiply charged ion species (e.g., $^{24}MgH^+$, $^{48}Ca^{++}$). Detailed peak shapes and magnetic field strengths corresponding to each mass peak were first established, and ion currents measured by repetitive stepping of the field to peak sides to determine precise peak location and then to peak maxima to acquire data. The field was stepped to the peak location determined in the preceding cycles. By these means, the reproducibility of the programmed magnetic field position over the course of the experiment was typically ±8 ppm (2σ) or about ±0.35 mamu.

Mg and Si isotopic results are summarized in Table 3. Errors are $2\sigma_{mean}$. In all the isotopic experiments, the scatter of intensity ratios was approximately that predicted by counting statistics and the means converged. Standard deviations were found to exceed the counting statistics by a factor of 1.5 or more only when the sample was charging or the primary beam was unstable. The experimental mass fractionations for Mg and Si were calculated by the expressions:

$$F_{Mg} = 1000 \times \frac{(26/24)_{meas} - (26/24)_{grav}}{2 \times (26/24)\ grav} \tag{1}$$

$$F_{Si} = 1000 \times \frac{(30/29)_{meas} - (30/29)_{norm}}{(30/29)_{norm}} \tag{2}$$

in $^o/_{oo}$ per amu, where meas = the mean ratio of measured ion beams corrected for instrumental drift by time interpolation of the reference isotope, grav = determined by gravimetry, norm = normal terrestrial isotopic ratio.

The deviations from normal compositions of ^{25}Mg, due to added excess ^{25}Mg, and of ^{28}Si, due to nonlinearities or deadtime of the counting system at the high count rates of about 10^6 cps at which this isotope was measured, were determined by the approximations

$$\delta(^{25}Mg/^{24}Mg) = 1000 \times \frac{(25/24)_{meas} - (25/24)_{norm}}{(25/24)_{norm}} - F_{Mg} \tag{3}$$

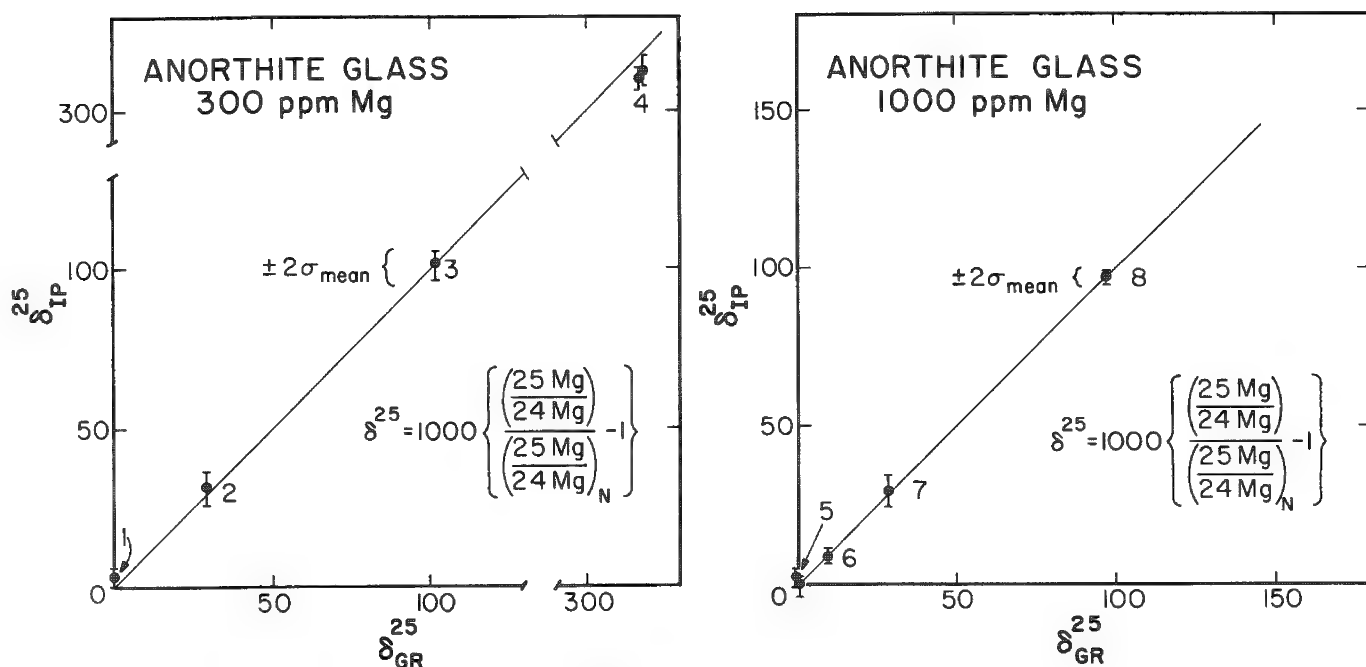$$\delta(^{29}Si/^{28}Si) = 1000 \times \frac{(29/28)_{meas} - (29/28)_{norm}}{(29/28)_{norm}} - F_{Si} \tag{4}$$

FIG. 1.--^{25}Mg/^{24}Mg in isotopically enriched anorthite glass standards with (a) 300 ppm Mg and (b) 1000 ppm Mg, with enrichment in ^{25}Mg measured by ion microprobe at $M/\Delta M \simeq 3000$ plotted vs gravimetrically calculated enrichments.
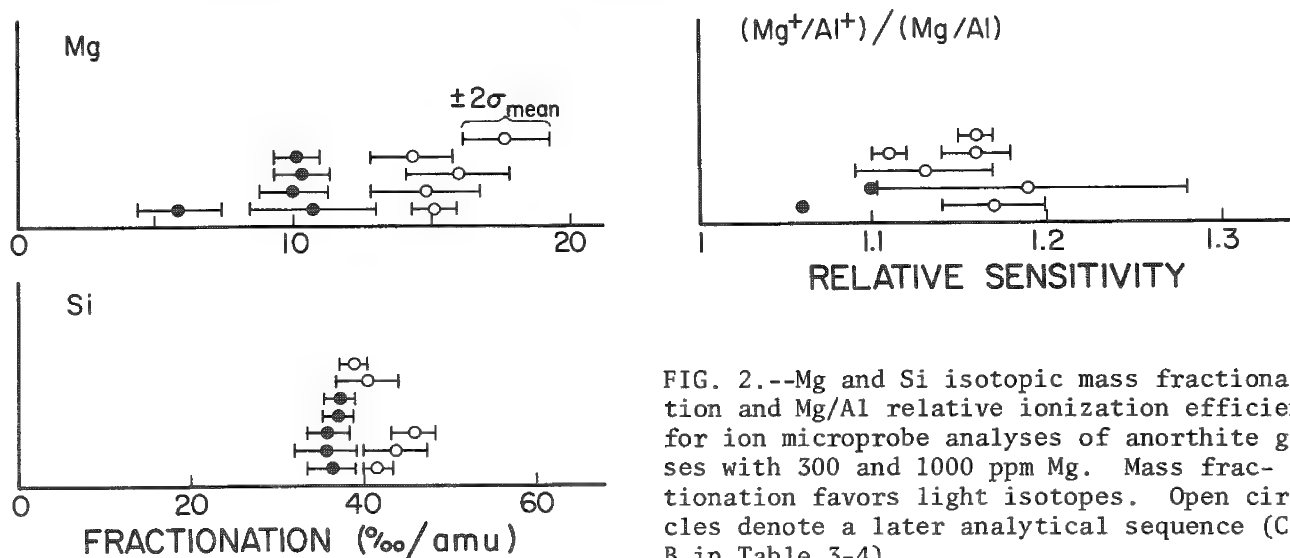

FIG. 2.--Mg and Si isotopic mass fractionation and Mg/Al relative ionization efficiency for ion microprobe analyses of anorthite glasses with 300 and 1000 ppm Mg. Mass fractionation favors light isotopes. Open circles denote a later analytical sequence (Case B in Table 3-4).

The $\delta(^{29}$Si/^{28}Si) values were consistent with a counting system deadtime of 18 ± 2 ns, which is in excellent agreement with the independently measured pulse pair resolution for the counting system of 17 ns. The maximum countrate of ^{24}Mg was about 30 000 cps, and no dead-time correction was required for the Mg isotopic results.

The comparisons between the measured $\delta(^{25}$Mg/^{24}Mg) values and those predicted by gravimetry are shown in Fig. 1. As can be seen in the figure, the agreement between measured and predicted values is excellent. In all cases except An-Mg-4, the measured value lies within $2\sigma_{mean}$ of the value calculated by gravimetry. An-Mg-4 is the glass with greatest added excess ^{25}Mg. The measured and calculated $\delta(^{25}$Mg/^{24}Mg) for An-Mg-4, and the relatively small difference, may be due to uncertainty in the exact composition of the ^{25}Mg spike. Determination of whether the deviation between measured and actual $\delta(^{25}$Mg/^{24}Mg) for An-Mg-4

is real will require the results of the independent mass spectrometric analyses. These measurements show one can routinely collect precise isotopic data with the ion microprobe, operating in a programmable peak jumping mode and at high mass resolving powers; accurately correct for mass fractionation; and quantitatively resolve Mg isotopic differences as small as $10^{\circ}/_{\circ\circ}$ with a precision of $\pm 3^{\circ}/_{\circ\circ}$ ($2\sigma_m$) in silicate samples with Mg elemental concentrations as low as 300 ppm.

The analyses of the standard glasses occurred over a period of two months and under two slightly differing sets of analytical conditions (A and B in Table 3). The two sets of analytical conditions had no effect on the measured $\delta(^{25}Mg/^{24}Mg)$, as can be seen from the replicate analyses of glasses An-Mg-4 and An-Mg-5. However, they did affect the magnitude of the measured fractionation for Mg and Si. Within each set of analytical conditions, the measured fractionation was constant within $\pm 5^{\circ}/_{\circ\circ}$ (equivalent to the measurement precision), as is shown in Fig. 2. Mg^+ fractionation, relative to normal Mg, varied from -6 to $-16^{\circ}/_{\circ\circ}$ per amu; Si^+ is more heavily fractionated at -36 to $-46^{\circ}/_{\circ\circ}$ per amu.

The measured Ca^{++}/Si^+, Mg^+/Ca^{++}, Mg^+/Si^+, Al^+/Si^+, Al^+/Ca^{++}, and Mg^+/Al^+ varied considerably during the course of the individual experiments and yielded standard deviations as much as 10 times greater than predicted by counting statistics (Table 4). Such variations are routinely observed during the sputtering of homogeneous specimens. For given sets of analytical conditions, the relative sensitivities (measured ion ratio/atomic ratio) for Ca^{++}/Si^+, Mg^+/Ca^{++}, Mg^+/Si^+, Al^+/Si^+, Al^+/Ca^{++}, and Mg^+/Al^+ did not appear to vary over measurement precision (about 10% relative 2σ) from sample to sample. The relative sensitivities determined for the glasses did not appear to differ from those measured for terrestrial and meteoritic anorthites.

Summary

A series of glasses of nominal anorthite composition, doped with trace amounts of Mg of variable isotopic compositions, have been prepared. The excellent agreement between Mg isotopic compositions measured by the ion microprobe and calculated by gravimetry demonstrates the ability to measure, under high mass resolution conditions, Mg isotopic enrichments of only $10^{\circ}/_{\circ\circ}$ with a precision and accuracy of $\pm 3^{\circ}/_{\circ\circ}$ ($2\sigma_m$) for Mg at the 300 ppm level in silicate material.

References

1. T. A. Finnerty, G. A. Waychunas, and W. M. Thomas, "The preparation of starting mixes for mineral syntheses by a freeze-dry technique," *Am. Mineral.* 63: 415-418, 1978.

2. A. E. Bence and A. L. Albee, "Empirical correction factors for the electron microanalysis of silicates and oxides," *J. Geol.* 76: 382-403, 1968.

TABLE 4.--Results of ion microprobe elemental sensitivity factor measurements of anorthite (An-Mg) glasses ($\pm 2\sigma$).

Analytical conditions	Glass	$\dfrac{(Ca^{++}/Si^+)}{(Ca/Si)}$	$\dfrac{(Mg^+/Ca^{++})}{(Mg/Ca)}$	$\dfrac{(Mg^+/Si^+)}{(Mg/Si)}$	$\dfrac{(Al^+/Si^+)}{Al/Si}$	$\dfrac{(Al^+/Ca^{++})}{Al/Ca}$	$\dfrac{(Mg^+/Al^+)}{(Mg/Al)}$
A	An-Mg-2	0.21±0.04	25.1±2.8	5.1±0.4	–	–	–
	An-Mg-4	0.22±0.02	24.3±0.7	5.1±0.5	–	–	–
	An-Mg-5	0.22±0.03	23.6±2.6	5.0±0.5	–	22.1	1.06
	An-Mg-6	0.22±0.03	23.4±2.6	5.1±0.7	4.6±0.6	19.6±0.1	1.10±0.01
	An-Mg-8	0.22±0.03	24.4±1.5	5.2±0.5	–	–	–
B	An-Mg-1	0.28±0.04	18.7±1.0	5.1±0.7	4.8±0.1	16.1±0.5	1.13±0.04
	An-Mg-3	0.28±0.06	21.5±1.4	5.4±0.6	4.9±0.3	18.2±0.7	1.11±0.01
	An-Mg-4	0.30±0.03	19.0±0.7	5.5±0.6	4.8±0.2	16.0±0.7	1.16±0.02
	An-Mg-5	0.28±0.02	20.0±1.4	5.6±0.5	4.8±0.3	17.2±1.1	1.17±0.03
	An-Mg-7	0.30±0.02	18.4±1.0	5.4±0.4	4.7±0.4	15.8±0.4	1.16±0.01

SIMS ANALYSIS OF NMOS VLSI DEVICES

D. S. Koellen

A central support group at MOSTEK, the Analytical Beam Laboratory, provides surface analysis for all groups. The groups supported include Failure Analysis, Research and Development, product groups, assembly and manufacturing groups. Submitted samples vary greatly, from incoming raw silicon wafers to finished packaged devices. Typical analyses range from identifying unknown contaminants and corrosion agents, dopant analysis, and process parameter measurement to flame retardant identification and plastic packaging material analysis.

The CAMECA IMS-3f ion microanalyzer is one instrument used in this laboratory. Its excellent sensitivity and depth profile capabilities are used to provide analysis on the device level as well as with specially produced monitor wafers. Both oxygen and cesium primary ions are used; positive oxygen, with electron flooding, is moste widely used because of the great number of oxides analyzed. In most analyses no gold layer is needed even when very thick insulators are analyzed.

Contending with charging, layer mixing, and imaging problems is very difficult, especially at the device level. Discussion of such problems and examples of analyses on devices as well as on other samples are presented in this paper.

Procedure

Many of the samples submitted for analysis are VLSI devices with very complex configurations, often as small as 3-5 μm. These devices are multilayered with various oxide, polysilicon, metal, and dopant layers. The surface tends to be rough with widely varying topology. All these factors make analysis difficult. The oxide layers encountered are thick; typical thicknesses range from 4 kÅ to 12 kÅ. Total oxide thicknesses as great as 28 kÅ have been profiled successfully.

Choosing the area of analysis is important. Several factors must be taken into consideration. The area of analysis must be easily located with the instrument. Also, the area of analysis should be as flat as possible to reduce layer mixing, and be located as far from the edge of the die as possible.

Capacitors, large transistors, and bond pads are excellent choices. Obtaining the distribution of contaminants or dopants through various device layers is a frequent request that is easily done in one of the abovementioned areas. An empty bond pad is favored because it is flat and easily imaged, since the metal is exposed through an opening in the top passivation. Other areas of the die are covered with a passivating layer of SiO_2 which makes imaging and area location difficult.

Calculating or measuring depth of analysis can be difficult on rough samples. Standard techniques that use a mechanical stylus or SEM are almost impossible on a device. Measurement of certain elements provides "flags" that make it possible to determine the analysis depth. A typical cross section of a device is shown in Fig. 1. Phosphorous, aluminum, and silicon provide depth information here. The phosphorous signal indicates location of the top passivation layer and the phosphorous stabilization layer (PSL); aluminum provides the location of the metal layer. The silicon signal intensity is much higher in the oxide layers than in the aluminum or polysilicon layers (silicon intensity is also reduced at the substrate) and thus provides a "flag" for the polysilicon and gate oxide location. Chlorine may also be used to locate the dichlorosilane glass (hotwall SiO_2); and substrate

dopants also provide junction information. Figure 2 is an example of the use of "flags"; the area profiled is a 50 × 50μm transistor. The structure consist of 6 kÅ of hotwall SiO_2 on 4 kÅ of polysilicon; immediately below the polysilicon is a 600Å gate oxide. The chlorine signal clearly indicates the top oxide layer. Reduction of silicon ($Si_2{}^{60}$) intensity and disappearance of the chlorine signal happens at the polysilicon layer. The second rise in silicon intensity is the gate oxide. Silicon intensity reduces as the substrate is entered. Notice the chlorine reduction before the silicon reduction at the hotwall SiO_2-polysilicon interface; a thin layer of thermal oxide on the polysilicon causes this chlorine reduction.
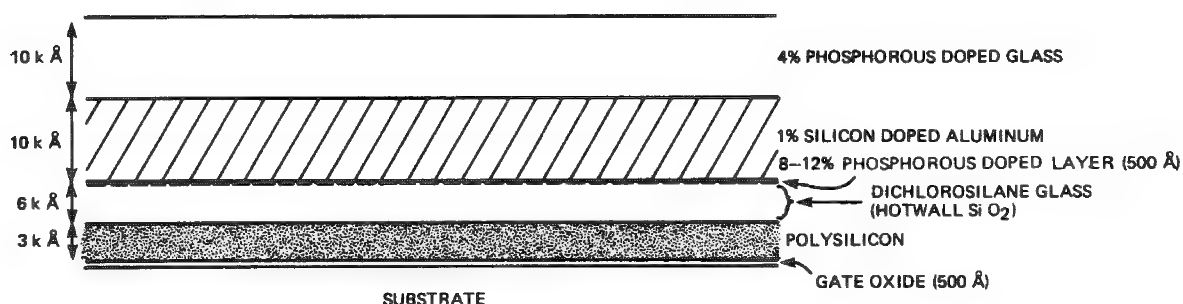
FIG. 1.--Typical device cross section.

Analyses

Ionic Contamination. Identification of contaminants, especially positive mobile ions, and their distribution is a frequent request. Positive ionic contamination affects the turn-on voltage V_T of transistors on a device. A mobile contaminant causes the turn-on voltage to change with temperature and time, a most undesirable feature. Sodium is the most common ionic contaminant, as is well known in the MOS industry. A sample with low turn-on voltages was submitted for analysis; the turn-on voltage was found to shift with temperature. Sodium and potassium were prime suspects but depth profiles showed that the levels were normal. Mass spectra indicated abnormal lithium levels, which was confirmed by a depth profile performed through a bond pad with silicon, phosphorus, and aluminum used as "flags." Figures 3 and 4 are the normal and low-V_T sample profiles; the lithium level is much higher in the low-V_T sample. Lithium-based grease in the ion implanters used in the fabrication areas is a possible source of this contamination.

Impurities from Gold Evaporation. Standard procedure for analysis of insulating materials was to evaporate a thick (about 500Å) film of gold onto the sample to reduce charging. This layer of gold also adds significant amounts of potassium, sodium, and calcium to the sample surface, as demonstrated in comparative depth profiles of aluminum with a thick layer of gold on the surface (Fig. 5) and aluminum without gold (Fig. 6). Potassium, sodium, and calcium are present at the surface of the gold-coated sample at much higher concentrations than in the sample without gold. Gold is now rarely used. Reduction of charging effects now depends largely on sample mounting and electron flooding.

Plastic Package Contaminants. Modern integrated circuits are variously packaged. Plastic injection-molded packages are popular and economical. However, the plastic is porous and is often blamed as a source of contamination. The surfaces of three samples were analyzed to identify the source of ionic contaminants such as potassium and sodium. Obviously, from the prior example, no gold could be used on these samples. Depth profiles were obtained for three samples: a plastic-packaged device with large V_T shifts (Fig. 7), a good plastic packaged device (Fig. 8), and a device originally packaged in a hermetic ceramic package (Fig. 9). The plastic-packaged device with V_T shifts had the greatest levels of potassium and sodium at the surface of the die. The normal plastic device had less sodium and potassium than the V_T shift sample but more than the ceramic packaged device. The high contaminant concentrations detected at the surface of the plastic devices supports the claim that the plastic package is a source of contaminants.
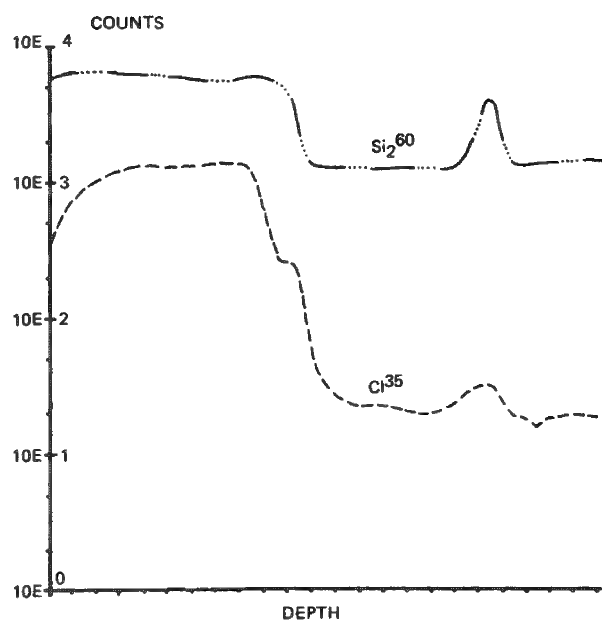
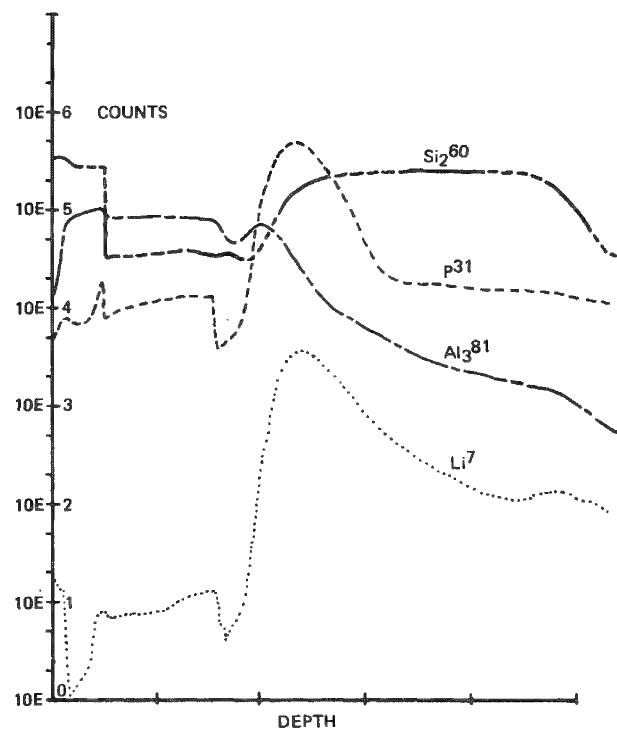FIG. 2.--Element "flag" showing analysis depth.

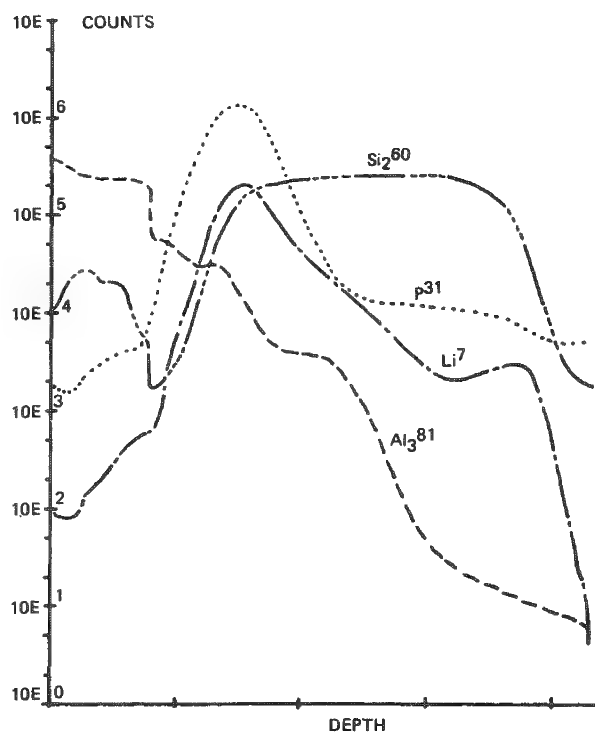Fig. 3.--Depth profile: Normal V_T sample.
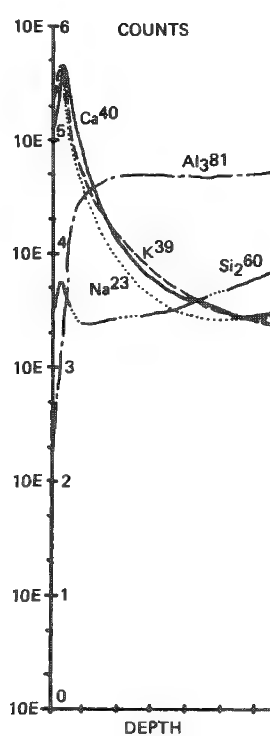

FIG. 4.--Depth profile: Low V_T sample.
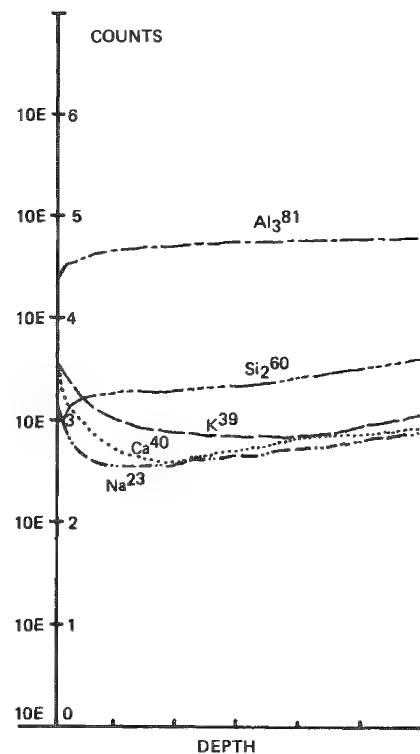

FIG. 5.--Depth profile: Aluminum with gold coat.

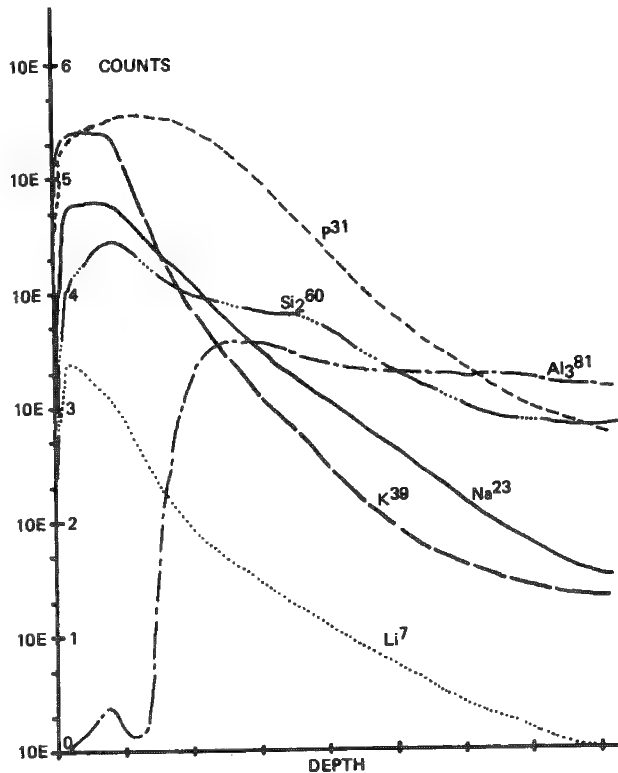FIG. 6.--Depth profile: Aluminum without gold coat.

212

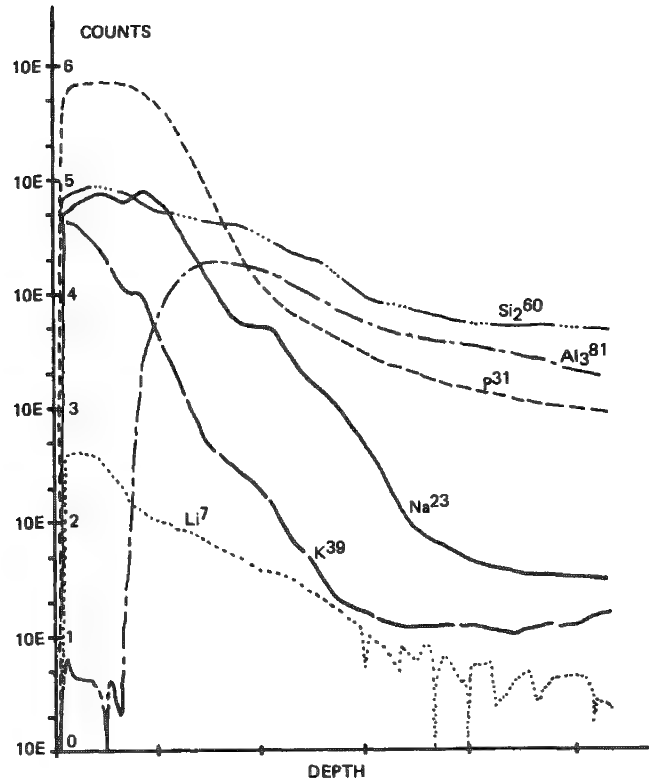FIG. 7.--Depth profile: Plastic package, shifted V_T.

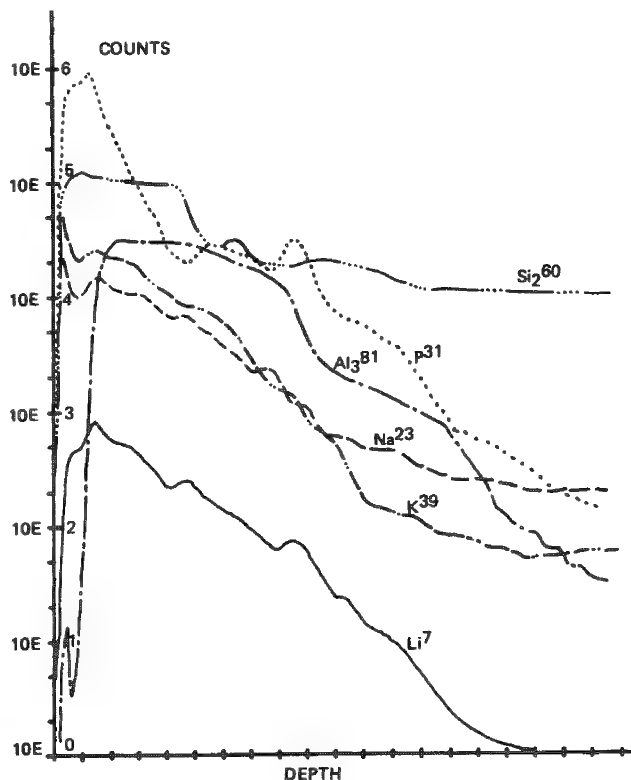FIG. 8.--Depth profile: Plastic package, normal V_T.

FIG. 9.--Depth profile: Ceramic package.

Sealing Glass. Sealing glass is used to bond two halves of a ceramic package together. The glass flows at a low temperature and has very low conductivity. Sealing glasses from two vendors were analyzed to find differences between the samples. Both vendors claimed the glasses were identical even though one is dark and the other is light. The glass, on ceramic material, was analyzed for constituents. The glass is 0.4 mm thick. Only the electron flood gun was used to reduce charging. Figures 10 and 11 are the 120-240 AMU portions of the mass spectra acquired from the light and dark sample, respectively. The samples are not the same; the light sample has barium in addition to the other constituents found in both samples.

Summary

The CAMECA IMS-3f ion microanalyzer can be successfully used for analysis of VLSI devices and related materials. For a successful analysis a number of factors must be considered: analysis area location and selection, device charging, layer mixing, and depth location "flags."

Examples of analyses performed demonstrate the importance of these factors. Identifying ionic contamination used depth location "flags" and careful area of analysis selec-

213

tion, and also demonstrated the importance of using a control device. Examination of gold on aluminum demonstrated why one should use electron flooding and sample mounting without gold coats for charge reduction during insulator analysis. The utility of this technique was shown in the study of surface contaminants from plastic packages and the elemental makeup of thick sealing glass on ceramic substrates.
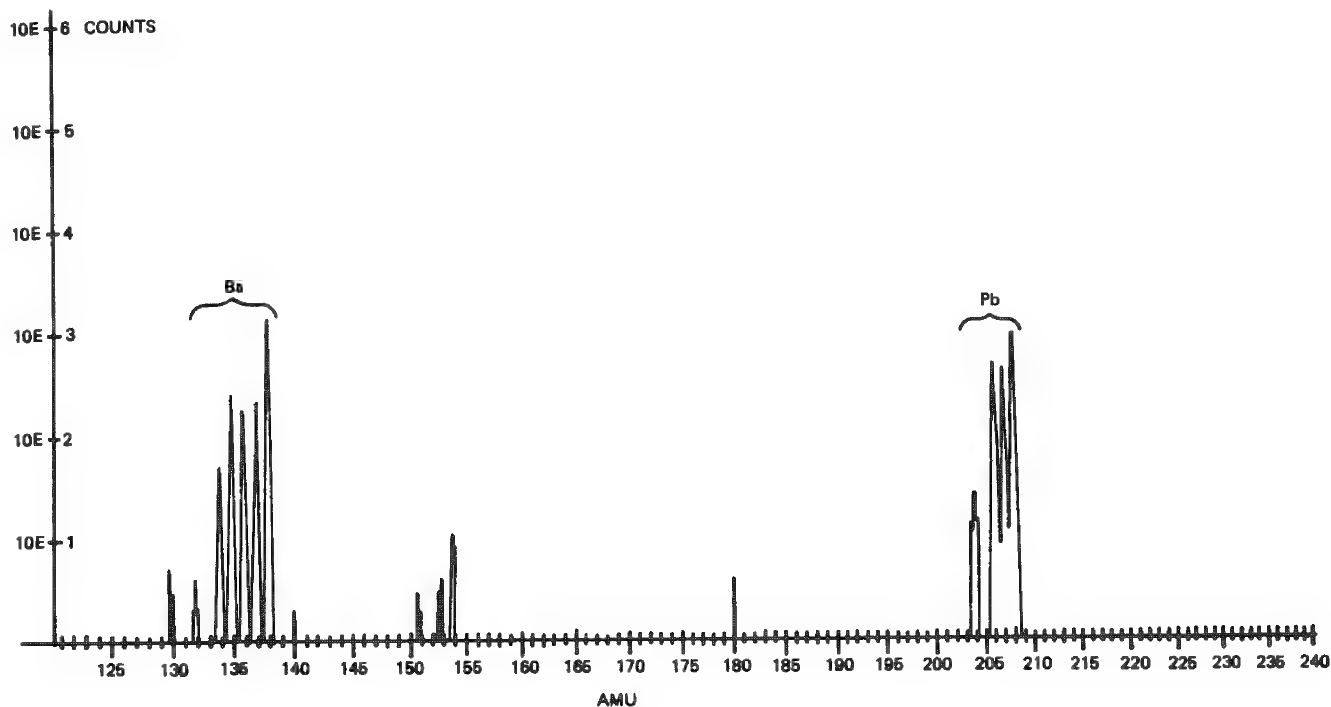

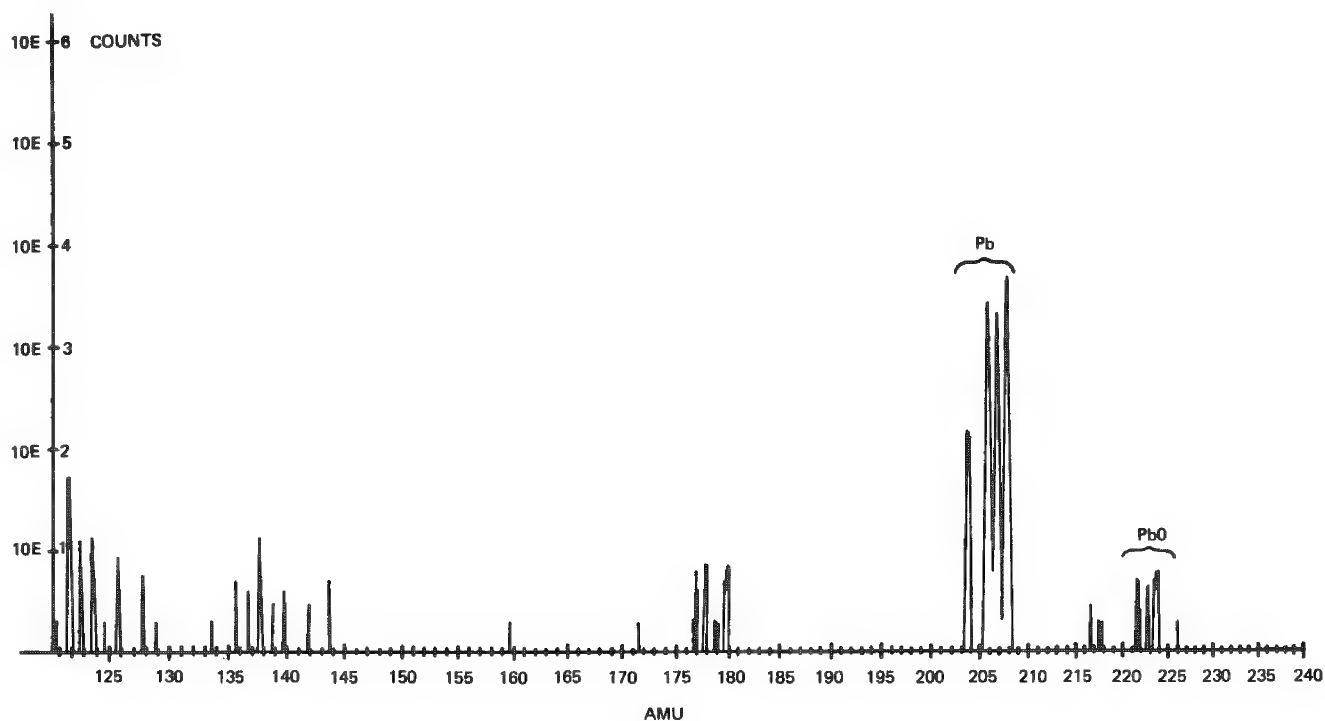FIG. 10.--Mass spectrum (120-240 AMU): Light glass.

FIG. 11.--Mass spectrum (120-240 AMU): Dark glass.

SECONDARY ION MICROSCOPY OF HYDROGEN IN IRON AND NICKEL BASED ALLOYS

William Katz, C. L. Briant, and G. A. Smith

Hydrogen had long been known to cause deleterious effects in alloy steels. If iron or nickel based alloys are mechanically tested in a hydrogen bearing environment, one often finds that the mechanical properties of the material are degraded. Secondary ion microscopy (SIM) has been used to determine the lateral distributions of hydrogen in both iron and nickel based alloy systems. The data indicate two different fracture mechanisms. In inconel and low-alloy steel the hydrogen appeared relatively uniformly distributed and showed no detectable preference for the grain boundary. In the case of 304 L stainless steel, the hydrogen did, however, show clear evidence of segregation to the martensite laths.

The effects of segregation of impurity elements to grain boundaries are known to result in intergranular fracture. Elements from groups IV, V, and VI of the periodic table are known to be embrittling elements. Other elements such as Ti and Mo, however, are known to act as segregation inhibitors whereas others, such as Ni and Mn, act to enhance segregation. For example, the addition of Mo to a Ni-Cr steel doped with P is noted to retard embrittlement[1] and the addition of Mn enhances it.[2] It can be seen that the segregation of impurities in steels often containing many elements is an extremely complex process.

Apart from the abovementioned elements known to embrittle alloy steels, one element recognized as a species that can lead to brittleness in steels is hydrogen. If a fracture occurs as a result of the presence of hydrogen, the process is often known as hydrogen embrittlement or hydrogen-assisted cracking (HAC). If a material susceptible to HAC is stressed in a hydrogen-bearing environment or is charged with hydrogen prior to the stress application, the results are often a reduction in the ultimate tensile strength and in the total elongation at fracture as well as a loss in percentage reduction in area of fracture and the occurrence of subcritical crack growth.[3]

The opportunity for a steel to pick up hydrogen during either processing or application are prevalent. In order to simulate hydrogen pick-up by steels in the laboratory, the material is either thermally or cathodically charged with hydrogen and tested mechanically, or the mechanical test is performed in either an aqueous or gaseous hydrogen ambient.

If iron or nickel base alloys are mechanically tested in a hydrogen bearing environment, one often finds that the mechanical properties of the material are degraded-hydrogen embrittlement. Although the specific response of the material depends on alloy composition, hydrogen pressure, sample configuration, and test mode, several observations hold true in all cases. One is that in nickel base alloys and low alloy steels, the fracture mode in hydrogen is often intergranular. For austenitic stainless steels it often occurs within the martensite laths that form upon deformation.

As a result of these observations, the question has arisen as to whether or not hydrogen preferentially segregates to any regions of the material. In particular, one would like to know if hydrogen is segregated to the grain boundaries of nickel-base alloys and low-alloy steels or the martensite laths of stainless steel.

Experimental

The ability to analyze for hydrogen is an extremely difficult analytical problem. Not many analytical methods can detect hydrogen. Moreover, the methods that can analyze for hydrogen must, in this situation, also be able to localize the species, that is to say,

---

The authors are at General Electric Corporate Research and Development Laboratory, Schenectady, NY 12301.

determine the lateral distribution of the hydrogen in the matrix.

Perhaps the ideal experiment would be to fracture the sample in a vacuum and analyze the fracture surface. This type of in situ fracture of metallurgical specimens is often performed with scanning Auger microscopy (SAM). However, since the Auger process involves three electrons, this type of analysis is not capable of detecting hydrogen. We therefore decided to use the imaging capabilities of our secondary ion mass spectrometer (SIMS). SIMS offers the advantages of being able to analyze (both laterally and in depth) for hydrogen directly with relatively high sensitivity. Unfortunately, an in situ fracture was not possible with the instrument used. However, a carefully controlled SIMS experiment on a polished surface should yield the desired information.

To perform these experiments samples of inconel 600, a low-alloy steel, and a deformed piece of 304 L stainless steel were electropolished to provide a smooth, flat surface. The samples were cathodically charged with hydrogen for times varying from zero (control) up to 30 min. The samples were stored at liquid-nitrogen temperatures prior to analysis to minimize hydrogen diffusion.

The analysis was performed with a CAMECA IMS 3-f ion microscope. The samples were analyzed with a mass filtered primary beam of $8.0\text{kV}^{133}\text{Cs}^+$ and monitoring of the negative secondary ions.
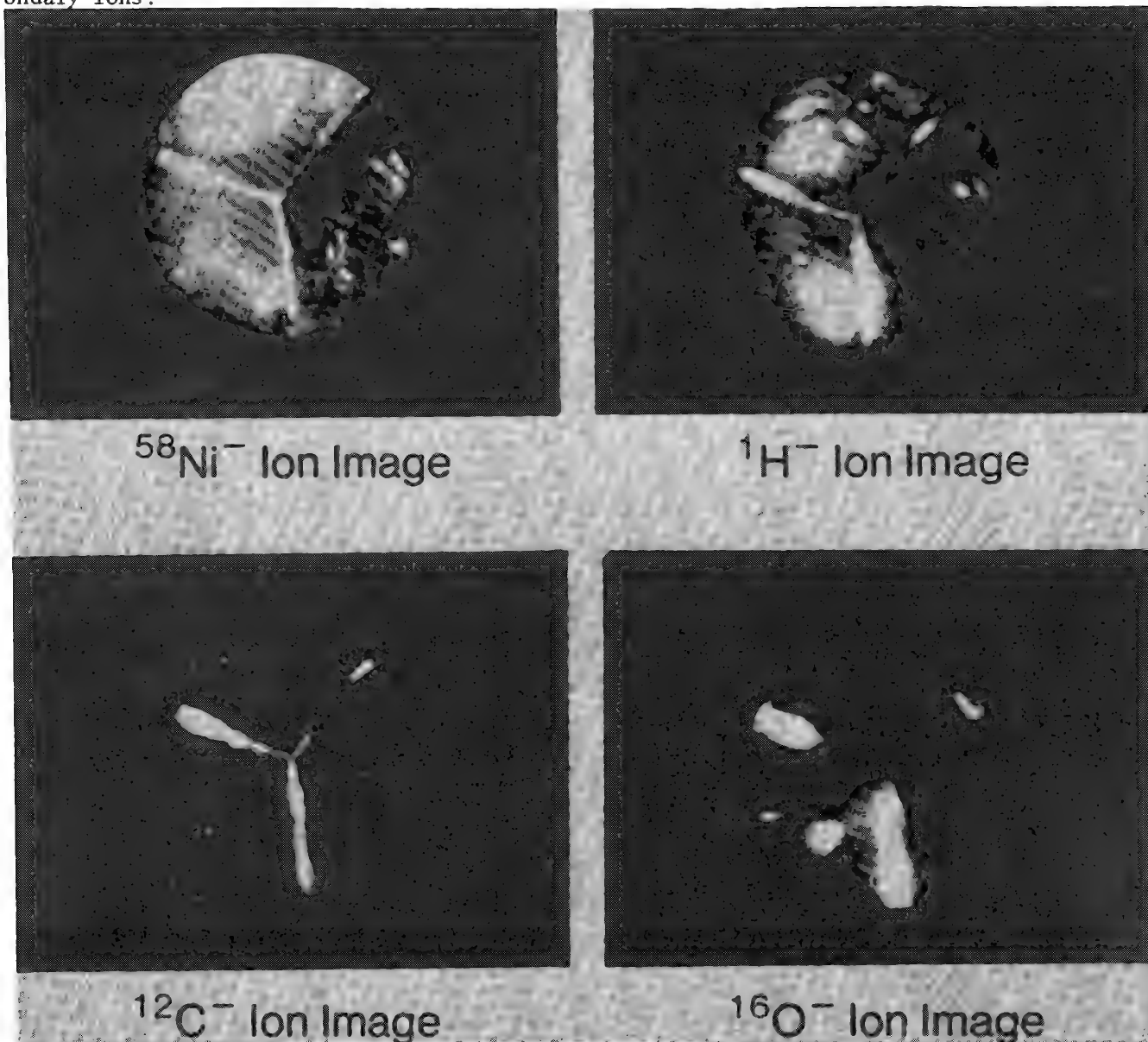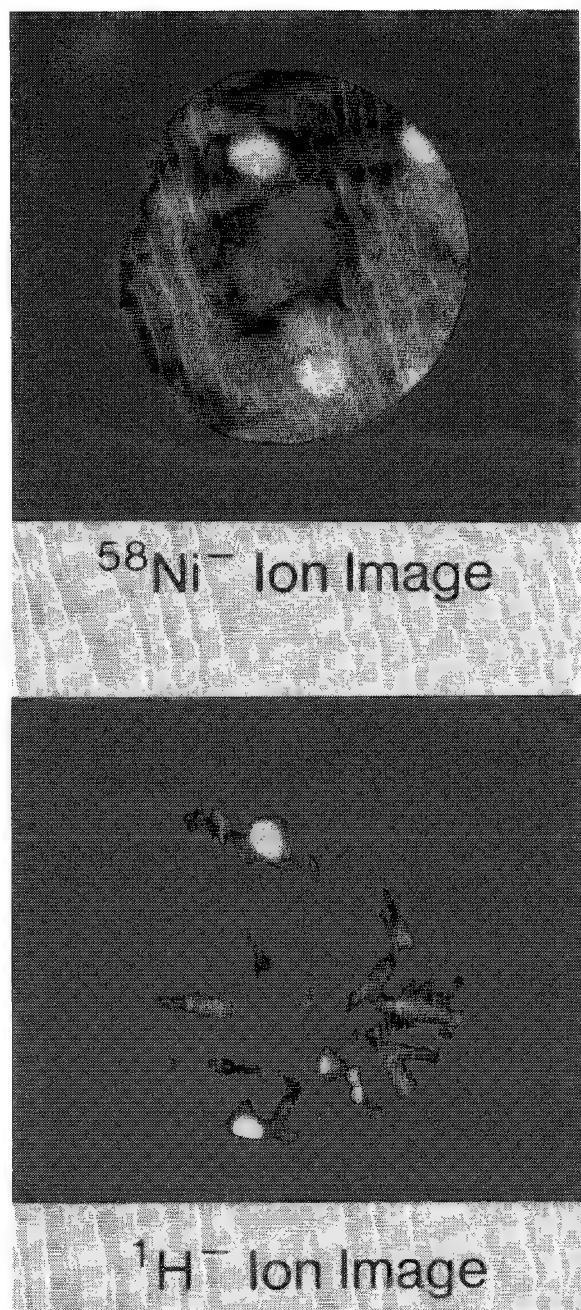

FIG. 1.--Secondary ion microscopy of inconel 600.

216

58Ni⁻ Ion Image

¹H⁻ Ion Image

FIG. 2.--Secondary ion microscopy of 304 L stainless steel.

Secondary ion microscopy (SIM) was performed on the samples under identical analytical conditions. Figure 1 shows four such ion images of $^{58}Ni^-$, $^1H^-$, $^{12}C^-$, and $^{16}O^-$ from the same area of an inconel 600 sample. The field of view in all cases was 150 μm. In order to avoid the effects of any surface contamination, images were recorded only after approximately five minutes of sputtering. In order to minimize the amount of residual vacuum contaminants being deposited on the sample surface during analysis, and thus maximize detection limits, sputtering rates in excess of approximately 100 Å/s were used.

The $^{58}Ni^-$ ion image clearly depicts a triple point or an area in the alloy where three grains come together. The pits in the material are probably due to the electropolishing process. In the corresponding $^1H^-$ ion image, it is clear that the hydrogen is relatively uniformly distributed across the grains. Samples cathodically charged for shorter times did not show detectable amounts of hydrogen under the analytical conditions used. This result establishes a real level of hydrogen actually in the sample rather than residual vacuum contaminants during analysis. Ion images of $^{12}C^-$ and $^{16}O^-$ are seen to decorate the grain boundaries.

Figure 2 shows a similar analysis of 304 L stainless steel. The $^{58}Ni^-$ image in this sample shows no marked grain structure. The bright round spots in the image were determined to be due to oxygen and are useful reference points. The corresponding $^1H^-$ ion image shows dramatic segregation to the martensite laths in the sample.

Conclusions

This work has clearly demonstrated two different mechanisms of hydrogen embrittlement. In the inconel 600 and low-alloy steel, the hydrogen was relatively uniformly distributed with no detectable preference for the grain boundaries. The reason for the preferred grain boundary fracture in these alloys probably results from the fact that dislocations pile up at the boundary and cause very high local stress intensities. These localized areas of high stress in the presence of hydrogen may cause decohesion. It may also be possible that segregated impurities plus hydrogen may especially weaken the boundaries. These data contrast the embrittling mechanism in the 304 L stainless steel where clear evidence of hydrogen segregation to the martensite laths was indicated.

Secondary ion microscopy is a powerful analytical tool for metallurgical systems. In spite of the disadvantage of not being able to perform in situ fractures, it has been demonstrated that the approach can provide valuable results with a controlled set of samples. In fact, SIMS ion imaging may actually be the preferred method when the lateral distributions of low-level impurities are required.

References

1. C. J. McMahon Jr., A. K. Cianelli, and H. C. Feng, "The influence of Mo on P-induced temper embrittlement in Ni-Cr steel," *Metall. Trans.* 8A: 1055, 1977.

2. B. J. Schulz and C. J. McMahon Jr., *Temper Embrittlement in Alloy Steels*, Philadelphia: American Society for Testing and Materials, STP 499, 1972, 104.

3. C. L. Briant and S. K. Banerji, "Intergranular failure in steel: The role of grain-boundary composition," *Intern. Metal. Rev.* 1978 (No. 4), 164.

# NEUTRON-INDUCED REACTIONS AND SECONDARY ION MASS SPECTROMETRY: COMPLEMENTARY TOOLS FOR DEPTH PROFILING

R. G. Downing, R. F. Fleming, D. S. Simons, and D. E. Newbury

The determination of the distribution in depth of the constituents of a sample provides important information for the characterization of materials. Many problems in the physical and biological sciences as well as in technology require information on the depth distribution for correct interpretation of structure and/or properties. A variety of techniques for depth profiling has been developed, including secondary ion mass spectrometry (SIMS), Rutherford backscattering, ion sputtering/Auger electron spectroscopy, and high-energy ion bombardment for inducing nuclear reactions.[1] Each of these techniques has its characteristic strengths and weaknesses. All cause substantial structural damage to the sample during the measurement of the depth profile. In the techniques based on sputtering, the region analyzed is completely destroyed; in the high-energy ion techniques substantial lattice damage from atom "knock-on" effects occurs.

Currently we are developing a facility similar to that at Grenoble for depth profiling by means of nuclear reactions induced by a beam of low-energy neutrons.[2] This technique offers the attractive possibility of causing minimal direct damage to the sample in those situations where it can be applied, since the primary beam only interacts significantly with the atoms of interest. Neutron depth profiling is based on the principle of nuclear capture of thermal neutrons to create an unstable nucleus with subsequent emission of high-energy monoenergetic alpha particles or protons. A typical reaction is:

$$^{10}B + {}_0n^1 \rightarrow {}^4He + {}^7Li \tag{1}$$

Other useful high cross section reactions occur with lithium-6, helium-3, nitrogen-14, and sodium-22. In all of these reactions the unstable nucleus decays immediately after neutron capture. In addition, a unique delayed emission reaction is available for bismuth:

$$^{209}Bi + {}_0n^1 \rightarrow {}^{210}Bi \xrightarrow[5.01\ d.]{\beta\ \gamma} {}^{210}Po \xrightarrow[138.4\ d.]{\alpha} {}^{206}Pb \tag{2}$$
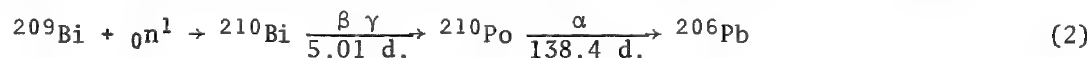
The energy spectrum of the particles emitted from the specimen is measured, and from a knowledge of stopping power of the sample, the energy spectrum can be transformed into a distribution in depth for the species of interest.

For all of the reactions except that involving bismuth, the measurement is performed in a scattering chamber on a reactor beam line. The delayed emission in bismuth allows the sample to be activated in the reactor and conveniently moved to a remote spectrometer site for measurement.

As an example of the synergistic possibilities of combining neutron depth profiling (NDP) studies with depth profiling by means of other techniques, we have conducted parallel measurements on bismuth distributions by means of NDP and SIMS. Figure 1 shows the bismuth distribution in a 30keV ^{209}Bi implant in silicon (dose $4.4 \pm 0.1 \times 10^{15}$ atom/cm^2)[3] determined by SIMS and the corresponding energy spectrum as measured by NDP. In this particular case, the implant is so shallow that essentially no energy loss occurs for the alpha particle traveling in the silicon, so that the width of the energy distribution by NDP is determined by the spectrometer response function. From the independent determination of the total bismuth implanted in the silicon from the RBS round robin, the integrated counts in the NDP spectrum can be used to obtain a calibration factor for the NDP system.

The authors are with the Center for Analytical Chemistry, National Bureau of Standards, Washington, DC 20234.
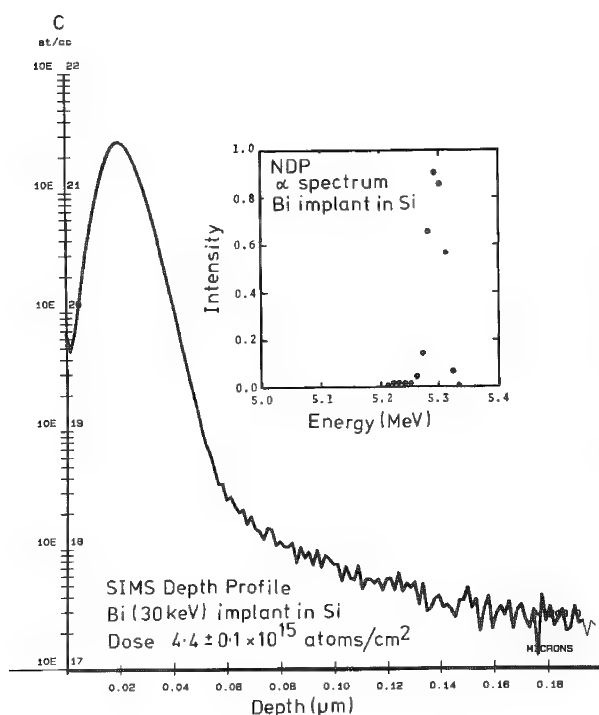
FIG. 1.--Depth distribution of bismuth implanted at 30 keV into silicon, as determined by SIMS (oxygen ion bombardment at 14.5 keV). Inset: corresponding profile as measured by NDP.

A second bismuth-containing sample was then analyzed. This sample consisted of an approximately 2.5μm-thick bismuth layer evaporated on a tin substrate, heated in air at 150°C and rapidly cooled. A SIMS depth profile (Fig. 2) of the resulting layer revealed mixing of the bismuth and tin, with an apparent surface peak in both bismuth and tin overlying a layer of bismuth-tin alloy of homogeneous composition. Obviously both tin and bismuth cannot increase at the surface. The apparent enhancement is at least partially due to matrix effects on the secondary-ion intensities. An NDP profile of the same layer (Fig. 3) confirms the existence of a real surface bismuth peak as well as the homogeneous subsurface layer. The bismuth calibration factor obtained from the bismuth-silicon implant can be used to derive the number of bismuth atoms per unit volume in the homogeneous layer. Assuming the density of this layer to be approximately that of tin, the major component, and determining the number of tin atoms per unit volume by difference, yielded a Bi/Sn atom of 0.14 in the homogeneous layer. This ratio corresponds very well with the solubility of bismuth in tin at the temperature of heat treatment. A SIMS sensitivity factor $S_{Bi/Sn} = (I_{Bi}/C_{Bi})/(I_{Sn}/C_{Sn})$ can thus be calculated from this NDP atom ratio and the SIMS intensities measured in the homogeneous layer, and we find $S_{Bi/Sn} = 2.9 \times 10^{-2}$ from these calculations. Finally, by using this SIMS sensitivity factor, the initial portion of the SIMS depth profile can be corrected to yield an apparent concentration ratio axis, as shown in figure 4.

This example demonstrates some of the potential for synergistic interaction of neutron profiling with the more commonly available methods of depth profiling. Although at least initially the NDP technique is limited in application to the five elements of adequate sensitivity, refinement of the charged particle spectrometry to include coincidence counting may extend the method to additional systems.

References

1. C. A. Evans Jr., "Surface and thin film compositional analysis: Description and comparison of techniques," *Anal. Chem.* 47: 818A, 1975.

2. J. P. Biersack, D. Fink, R. A. Henkelmann, and K. Muller, "The use of neutron induced reactions for light element profiling and lattice localization," *Nucl. Inst. Meth.* 149: 93, 1978.

3. The Bi-Si sample was kindly supplied by Dr. John Baglin of IBM (Yorktown Heights); the dose was derived from a round-robin study by Rutherford backscattering (Baglin, unpublished results).
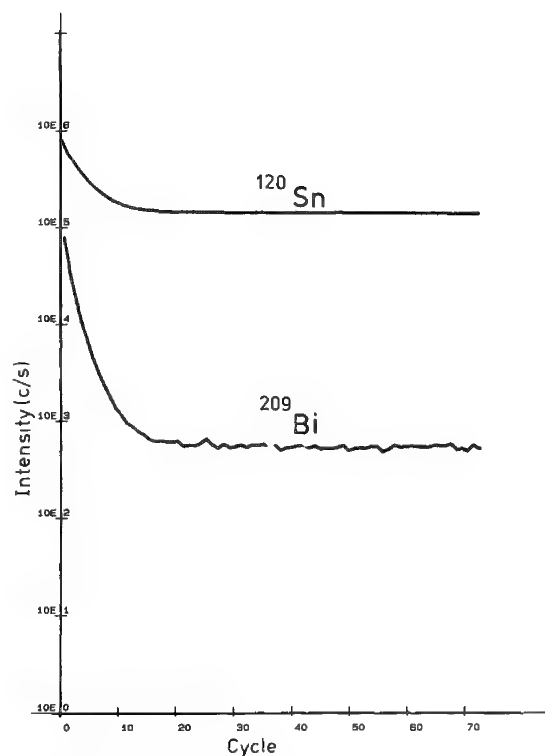
FIG. 2.--Intensity profiles of bismuth
and tin in heat-treated (150°C, 16 hr)
sample as measured by SIMS (oxygen ion
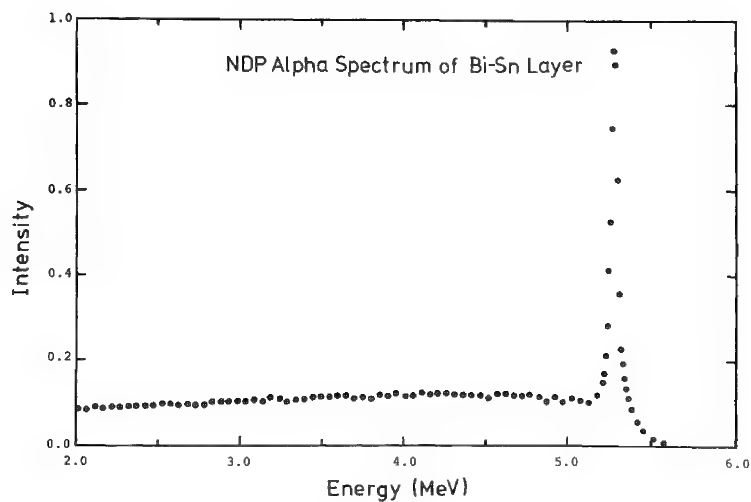bombardment at 14.5 keV).

FIG. 3.--NDP profile of heat treated bismuth-tin
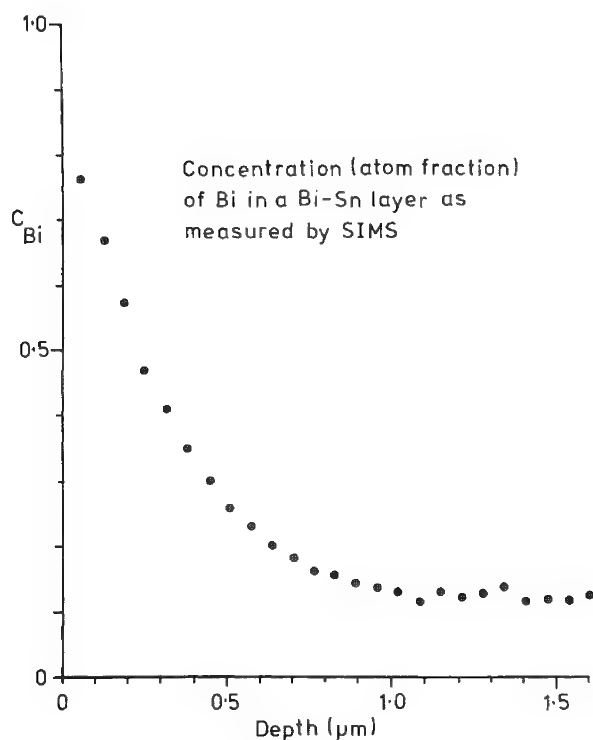layer as shown in Fig. 2.

FIG. 4.--SIMS depth profile of bismuth in the bismuth-tin alloy layer with sensitivity
factor correction applied to derive a concentration axis.

APPLICATIONS OF A COMBINED DIRECT IMAGING LASER IONIZATION-SECONDARY IONIZATION MASS SPECTROMETER TO MATERIALS ANALYSIS

B. K. Furman and C. A. Evans, Jr.

Two mass spectrometric techniques are at present employed for trace analysis and the microscopic analysis of materials. The now classical technique of secondary ion mass spectrometry (SIMS), as exemplified by the ion microprobe[1] or ion microscope,[2] is capable of producing trace element characterization with depth profiling resolutions of a few tens to a few hundreds of Ångstroms over several microns in depth, and of producing lateral elemental distributions with either probe or microscope imaging techniques. Details of the SIMS technique have been described elsewhere.[3]

The other mass spectrometric technique, which is currently being developed for trace element analysis, is the laser microprobe,[4] commercially available as the so-called LAMMA by Leybold-Heraeus or the LIMA from Cambridge Mass Spectrometers. In this technique, the sample is irradiated by photons from a Q-switched Nd-YAG laser. Once the area to be analyzed is found, typically in a biological material or individual particulates on a surface, the laser pulse is struck and causes instantaneous vaporization and ionization of the bombarded micrometer-sized area. Since the ions are produced within 10-20 ns, they can be efficiently collected and analyzed with a time-of-flight (TOF) mass spectrometer. The ions are accelerated to a constant kinetic energy by the imposed electrostatic voltage. Since $E_{final} = mv^2/2$, the ions separate in time according to their mass, as the velocity of the lighter ions is greater than that of the heavier ions. After time dispersion in the time-of-flight mass spectrometer, the ions are detected by specialized ion detection which records ion intensity as a function of time and so produces the time-of-flight mass spectrum. The LAMMA instrument operates only in the transmission mode of excitation; applications include three specific sample types: (1) dispersion of particles on a transparent substrate, such as a copper grid; (2) thin sections of biological materials; and (3) thin sections of geological materials. The recently introduced laser ionization mass analyzer (LIMA) from Cambridge Consultants[5] has been operated in a front-side illumination or reflection mode and has been shown to produce and analyze ions from the front surface of the material.

The two techniques discussed above, high-performance secondary ion mass spectrometry and laser ionization mass spectrometry, have advantages and limitations. The advantage of the SIMS techniques are numerous and include the ability to provide high-quality depth profiles, as well as rapid lateral imaging with a good quantitative capability if standards are available. However, it is limited in its ability to detect organic species as distributed on the surface of the material, and is unsuited to the performance of a survey analysis of a microvolume of material.

The authors have demonstrated[6] that combination of a laser source for ion formation with a CAMECA IMS-3f Ion Microanalyzer for ion microscopy can provide a direct-imaging laser mass analysis (DILMA) and have successfully produced the first ion images resulting from photon irradiation of various materials. This paper presents data obtained by simultaneous use of ion and photon bombardment for selected application of material analysis. In addition, results obtained with the cw laser source for in situ laser processing are also presented.

Figure 1 shows a diagram of the instrumentation used for these experiments. A CAMECA IMS-3f Ion Microanalyzer was the "ion optical bench" for the instrumentation. Two very different lasers were utilized as laser sources: a Nd-YAG pulsed laser and an Ar+ cw laser (Table 1).
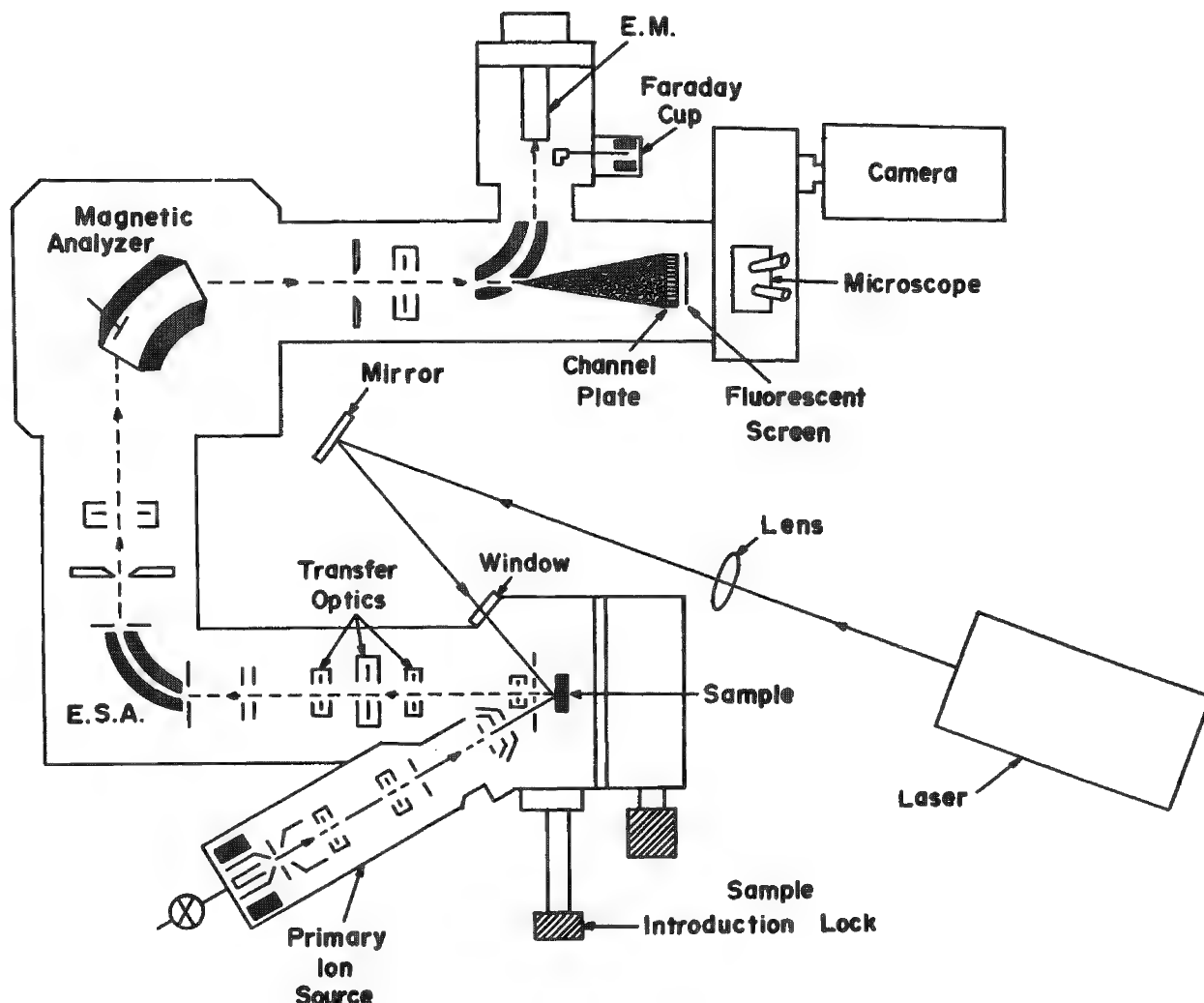

FIG. 1.--Schematic drawing of CAMECA IMS-3f Ion Microanalyzer with laser.

TABLE 1.--Laser sources.

Type	ND-YAG	Ar+
Manufacturer	Quanta-Ray	Lexel
Model	DCR-1A	95
Mode	Pulsed ~100-200 ns non-Q-switched	CW
Beam	Focused toroid	Focused spot
Energy	<60 mJoules/pulse	<4 Watts
Power Density (W/CM^2)	<10^8	<10^6
λ (NM)	530	514 (multiline)

The appropriate laser beam was focused by a lens with a focal length of about 1 m to a spot size about 1 mm in diameter. The beam was introduced into the CAMECA IMS-3f through a high-purity quartz window and irradiated the sample surface at about 45° incidence. This configuration allowed the laser beam to strike the sample surface in the same area as the conventional ion beam. A CAMECA IMS-3f Ion Microanalyzer[7] equipped with a General Ionex

Model 133 Cesium Ion Source was used for all analyses. Directly below the sample in the chamber is a recirculating He refrigerator with dual cryogenic panels. Sample chamber pressure was 1×10^{-8} Torr. Although the chamber is bakeable to 120°C, no bake was performed prior to analysis.

Mounted directly adjacent to the chamber, a Molytek quadrupole-type (SM800A) residual gas analyzer (RGA) was used to monitor and identify vacuum contaminants prior to analysis. Samples were prepared from <100> Si ion implanted with hydrogen, carbon, nitrogen, and oxygen.[1] Implantation conditions were: (1) ^{1}H, 35 keV, 1.0×10^{16} atoms-cm^{-2}; (2) ^{12}C, 65 keV, 1.0×10^{15} atoms-cm^{-2}; (3) ^{16}O, 85 keV, 1.0×10^{15} atoms-cm^{-2}; (4) ^{14}N, 75 keV, 2.0×10^{15} atoms-cm^{-2}.

Another sample of silicon was ion implanted with boron, phosphorus and arsenic. Implantation conditions were: (1) ^{11}B, 80 keV, 3.0×10^{14} atoms-cm^{-2}; (2) ^{31}P, 80 keV, 3.0×10^{14} atoms-cm^{-2}; (3) ^{75}As, 270 keV, 3.0×10^{14} atoms-cm^{-2}.

Samples were profiled by use of Cs+ ion bombardment, with simultaneous monitoring of the negatively charged ions of ^{1}H$^-$, ^{12}C$^-$ and ^{42}SiN$^-$ or ^{11}B$^-$, ^{31}P$^-$, and ^{75}As$^-$. Nitrogen was monitored as ^{28}Si^{14}N molecular ion at 42 amu due to the absence of ^{14}N$^-$.[2] Typical sputtering rates were 15 Å-sec^{-1}.

Laser heating was accomplished by 514nm irradiation from the multiline output of a Lexel Ar$^+$ ion laser (Model 95) operating at 2 W as recorded on the laser.

Results and Discussion

The intent of this study was to employ the ion imaging and mass spectrometric capabilities of the CAMECA IMS-3f Ion Microanalyzer with laser heating and excitation for materials analysis. Laser irradiation was used both for ionization of surface contamination and for in situ laser annealing.

When the Nd-YAG pulsed laser was used, it was operated in the non-Q-switch mode so as to maintain a low power density to prevent damage to the optical window into the vacuum system. Therefore, most of the species acquired from the surface of the material were those that could be obtained in the desorption rather than the explosive detonation mode. These species included Li, Na, K, Ca, Rb, and Cs in the positive spectroscopy mode and H, C, O, and the molecular species CO in the negative spectrum. Halogens such as F and Cl were also observed when present. Ion images were obtained from the particles as surface contamination present on the surface of an Si wafer and from the surface of bulk NBS standard glasses which were highly insulating. These last results were the most astounding since we found that no charging problems were associated with the production of ions from the surface of these bulk glass material. The species found to be emitted were thought to be surface contamination either in the form of adsorbed layers or particulates rather than actual consumption of the bulk glass material. Similar results were obtained with the cw argon laser, in which laser irradiation only produced ion images of surface contamination (Na, K) on silicon devices. In addition to the unique analytical applications of laser excitation combined with direct imaging mass spectrometry, we found that the laser provided an unique capability for actual processing of the material in the sample chamber of the ion microanalyzer.

The effects of the gaseous (inactive) impurities (hydrogen, carbon, nitrogen, and oxygen) on the physical and electrical properties of silicon have long been a topic of active research. Perhaps the most widely studies of these impurities is oxygen.[8] Oxygen and carbon are perhaps the most abundant impurities unintentionally incorporated in Czochralski (Cz) grown silicon. To obtain true three-dimensional impurity distributions, secondary ion mass spectrometry is the superior method of analysis.[9] Negative secondary ion yields of hydrogen, carbon, and oxygen in silicon are extremely high when Cs$^+$ ion bombardment is used, and the ultimate detection limits should be 10^{15} atoms-cm^{-3} with Cs/SIMS. Unfortunately, high background intensities greatly increase these detection limits. Elements such as hydrogen, carbon, nitrogen, and oxygen are present as vacuum contaminants even at high vacuum. Adsorption on the surface of the silicon produces a high background count rate that can overwhelm intrinsic levels present in the silicon matrix. Previously the use of Cs/SIMS with extremely fast sputtering rates (about 100 Å/s) has been shown to reduce background levels of carbon and oxygen.

In many analyses one cannot sputter at these rapid rates due to the loss in depth resolution, especially for shallow ion-implanted samples or multi-element profiles. To alle-
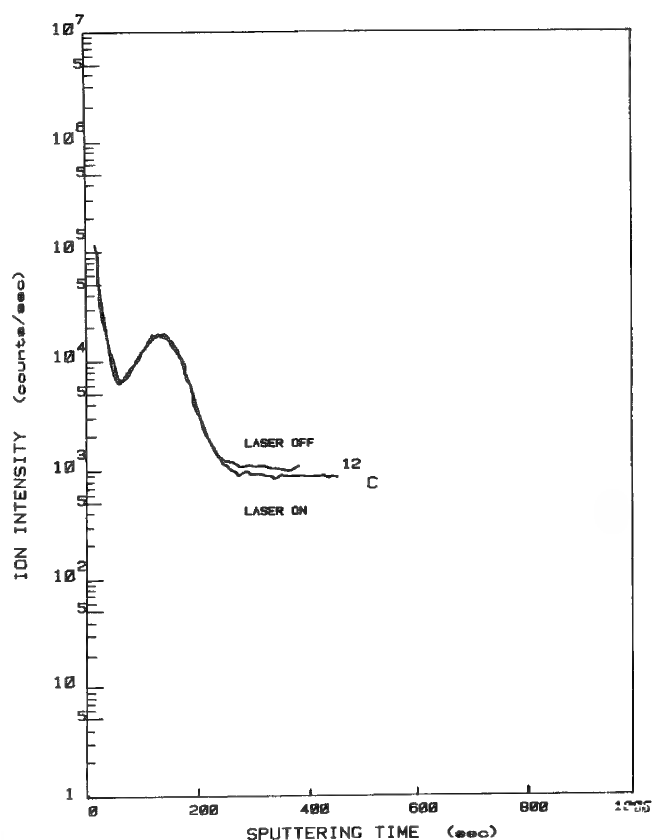
FIG. 2.--In-depth distribution of oxygen ion
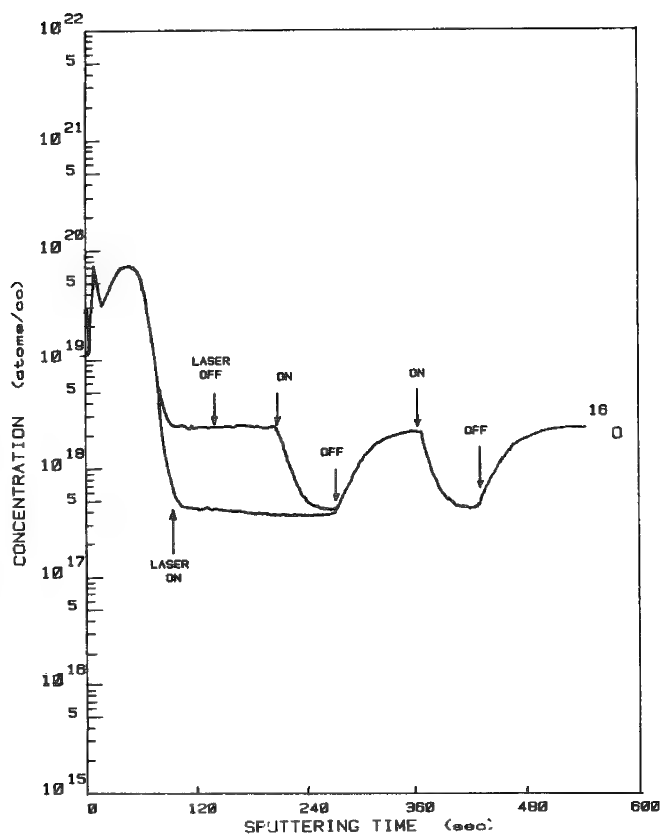implanted into FZ silicon with and without
laser heating.

FIG. 3.--In-depth distribution of carbon ion
implanted into Cz silicon with and without
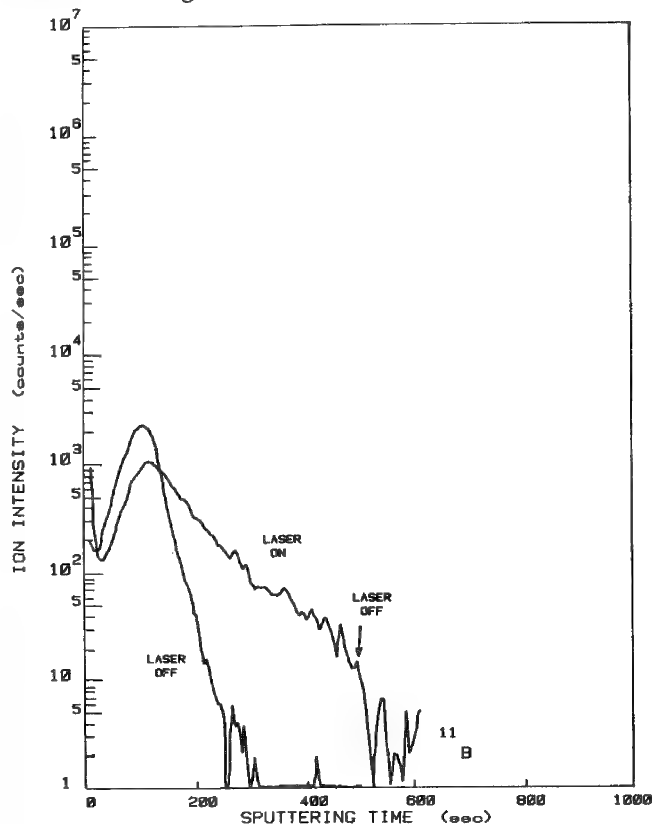laser heating.

FIG. 4.--In-depth distribution of boron ion
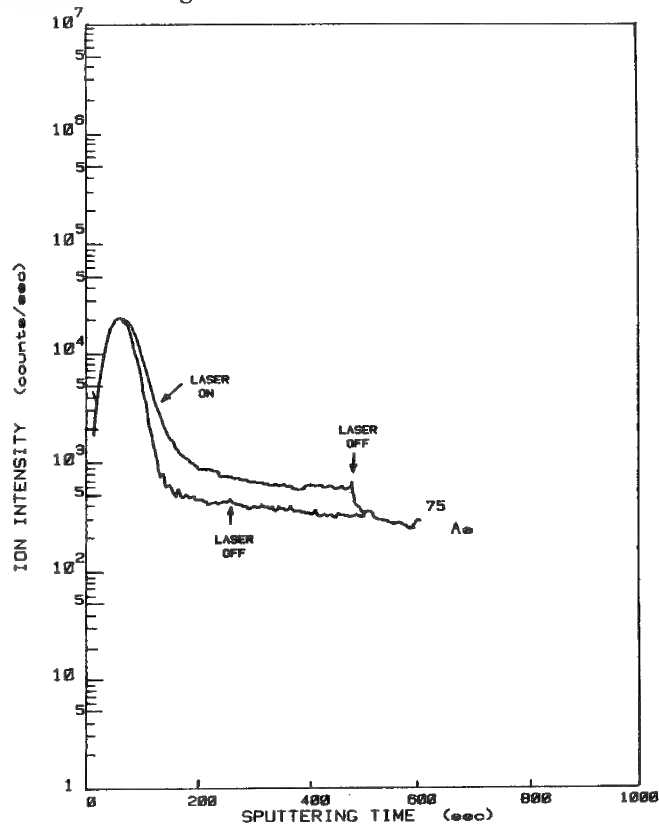implanted into Cz silicon with and without
laser heating.

FIG. 5.--In-depth distribution of arsenic
with and without laser heating.

225

viate this problem the authors have investigated sample heating by laser irradiation to reduce the sticking coefficient of residual vacuum contamination, especially H_2O at elevated temperatures.

Figure 2 shows a depth profile for a 70keV, 1×10^{15} atom-cm^{-2} oxygen implant into float-zone Si. The first part of the profile represents the oxygen distribution without laser heating. After a background level of 2×10^{18} atoms-cm^{-3} was established at this particular sputtering rate, the Ar ion laser was turned on. Almost immediately the background level decreases and stabilizes after 60 s at 4×10^{17} atoms-cm^{-3}. If the laser is then turned off, the background level slowly returns to its original level. The cooling process takes about twice as long as heating. This result can be explained by the thermal isolation of the sample in a 10^{-8} Torr vacuum. In the second profile the laser was turned on 60 s prior to the analysis and remained on during profiling. No redistribution of oxygen is observed; background levels are an order of magnitude lower than without the laser. In this mode, a much slower sputtering rate can yield background levels previously obtainable only with rapid sputtering.

Figure 3 shows a depth profile of the carbon distribution in the multi-element implant sample with and without laser heating. Very little difference in the background carbon level is observed, as expected from the residual gas analysis results. Since very little carbon contamination is present in the residual vacuum, laser heating plays a minor role in background reduction. In vacuum systems with conventional diffusion pumps, carbon levels would probably show a greater reduction with laser heating.

Hydrogen also showed reduction from desorption of H_2O as well as very fast redistribution in the silicon. Results of this finding are reported elsewhere.[10]

Using laser heating the authors also observed in situ laser annealing of dopants in silicon. In the past SIMS has been used to study redistribution of dopants after laser annealing. Figure 4 illustrates the effect of laser annealing on the boron distribution in silicon. It appears that the boron is driven deeper into the material with simultaneous SIMS laser annealing. When the laser is turned off, the boron ceases to diffuse and the level drops. A similar effect is observed in Fig. 5 for arsenic.

Summary

The combination of laser irradiation with the specialized ion optics necessary to provide high-performance secondary ion mass spectrometry provides a new, unique analytical capability and allows for rapid study of materials-related phenomena. As reported previously, we were able to provide a new analytical capability in performing ion microscopy using laser desorption for ion formation; and this study demonstrated thermal processing of materials with laser irradiation prior to or simultaneous with the SIMS analysis providing the heat input.

References

1. H. Liebl, *J. Appl. Phys.* 38: 5277, 1967.
2. G. H. Morrison and G. Slodzian, *Anal. Chem.* 47: 932A, 1975.
3. C. A. Evans, Jr., *Anal. Chem.* 44: 67A, 1972.
4. F. Hillenkamp et al., *Appl. Phys.* 8: 341, 1975.
5. Cambridge Mass Spectrometry Limited.
6. B. K. Furman and C. A. Evans, Jr., *Microbeam Analysis--1981*, 336.
7. M. Lepareur, *Rev. Tech. Thomson-CSF* 12: 225, 1980.
8. H. F. Huff, Ed., *Semiconductor Silicon 1981*, Pennington, N.J.: Electrochemical Society, 1981, chap. 3.
9. H. Koyama, *J. Appl. Phys.* 51: 3202, 1980.
10. B. K. Furman and C. A. Evans, Jr., *Appl. Phys. Lett.* 1982 (submitted).

QUANTITATIVE ION MICROSCOPY OF SOFT BIOLOGICAL TISSUES

W. C. Harris Jr. and G. H. Morrison

Since secondary ion mass spectrometry (SIMS) was first applied to biological samples by Galle, Blaise, and Slodzian,[1] the technique has been used to determine elemental distributions in a variety of tissue types.[2,3] These analyses have utilized both the depth profiling mode of SIMS, to determine distributions with depth; and the imaging mode, to provide information on the lateral distribution of elements within the field of view. Methods for quantitative depth profile analysis of hard tissue samples have been successfully developed and applied, yet quantitative SIMS analysis of soft tissue samples is still far from routine, particularly in the imaging mode, which is the most frequently used mode of analysis of soft biological tissue by SIMS.

Quantitative analysis of ion images is accomplished by application of a quantitative correction procedure to each point of the image. The most popular approach to this problem has been to use the local thermodynamic equilibrium (LTE) model to correct ion image to concentration. This model has been shown to be capable of providing concentrations accurate to within a factor of two in most cases. Owing to the degree of uncertainty in the calculated concentrations, we decided to employ a relative sensitivity factor approach based on empirical standards made from gelatin or agar. The empirical standard approach to quantitation has been demonstrated to be superior to the use of semitheoretical models provided the standard matrix closely matches that of the unknown.

Gelatin was proposed as a calibration standard for SIMS analysis of biological tissue by Bellhorn[4] and subsequently a good deal of work has been done to validate and optimize these standards.[5,6] To apply this procedure to the ion image requires an internal standard at each pixel to which the ion intensity of the element to be determined can be referenced, so that one can correct for any local variations in ion yield (such as topographic effects). Soft biological tissue is commonly embedded in plastic and cut into thin sections for SIMS analysis to provide a planar surface with good conductivity. Carbon was chosen as an internal standard element since carbon from the plastic embedding material is present throughout the tissue at approximately the same concentration. Calibration lines were then generated with carbon as the internal standard to provide the relative sensitivity factors used to convert the ion image to concentration.

Quantitation of the ion image is made possible by computerized image processing. Images are acquired and digitized directly from the fluorescent screen of the ion microscope (CAMECA IMS-3f) by use of the MIDAS system developed in our laboratory.[7] This system uses a variable-gain, low-light-level TV camera interfaced to a 12 bit/pixel, 256 × 256 frame buffer to acquire digitized images. The useful field of view of an image can be varied in diameter from 400 to 50 μm with the ion optics of the 3f. A zoom lens on the low-light-level TV camera allows further magnification of the image while preserving the 1μm spatial resolution of the 3f image. Single-frame image acquisition time is 1/30 s; however, the image can be integrated over any time interval, up to saturation of the frame buffer, for increased sensitivity. The use of this system allows images of the elements to be determined and of a suitable internal standard element to be rapidly acquired and stored from the area of interest before significant destruction of the sample by the primary beam occurs.

The first step in obtaining a quantitative concentration map is to convert the raw image intensities into ion intensities at every pixel. This step is rapidly performed with the use of a calibration equation obtained by the recording of a series of images of

homogeneous standards at various intensities and the recording of the ion intensity of the image by the electron multiplier detector. Doing this over a range of TV camera and channelplate gain settings results in an equation that relates ion intensity to the image intensity at each pixel as a function of the gain settings.

The ion intensity images of the element to be determined and the internal standard element are then registered relative to each other. Once this step is accomplished, the image of the element of interest is divided by that of the internal standard to produce an intensity ratio at each pixel. As mentioned previously, this procedure compensates for any local variations that affect all elemental ion yields equally, such as topographic effects. It also helps correct for preferential sputtering of different features within the field of view, on the assumption that ion yield ratios are independent of sputter rate--which may not necessarily be true, but is a first approximation.

The intensity ratio at each pixel is then finally converted to concentration by application of the relative sensitivity factors derived from the calibration lines. The final concentration map can then be displayed in several ways: contour plots, 3-D plots where the z axis is concentration, a reconstructed black and white image with intensity proportional to concentration, or in pseudocolor (in which each concentration is assigned a color on a continuous color scale).

These concentration maps of elemental distribution within the tissue provide an extra dimension that qualitative assessment of ion images does not, as well as correcting for SIMS artifacts that can distort the ion intensity image so that it does not reflect elemental concentration accurately. SIMS ppm detection limits allow determination of trace elements in the biological matrix as well as major components, and labeling of organic compounds present in the tissue with metal atoms can also be employed for quantitative study of their distributions. Combined with other data such as light micrographs or electron-probe x-ray images, detailed information on the sample can be obtained.

References

1. P. Galle and G. Slodzian, *Fourth Nat. Conf. Electron Microprobe Analysis* (Caltech), 1969, I-36.

2. P. Galle in T. Hall, P. Echlin, and R. Kaufmann, Eds., *Microprobe Analysis as Applied to Cells and Tissues,* New York: Academic Press, 1974, 89-105.

3. P. Galle in A. Benninghoven et al., Eds., *Secondary Ion Mass Spectrometry SIMS II,* New York: Springer, 1979, 238-243.

4. M. Burns-Bellhorn and D. M. File, "Empirical standards for quantitative analysis of biological tissues by secondary ion mass spectrometry," *Proc. 12th MAS Conf.,* 1977, 137.

5. M. Burns-Bellhorn and D. M. File, *Anal. Biochem.* 92: 213-221, 1979.

6. D. Zhu, W. C. Harris, and G. H. Morrison, *Anal. Chem.* 54: 419-422, 1982.

7. B. K. Furman and G. H. Morrison, *Anal. Chem.* 51: 2305-2310, 1980.

THEORETICAL MATRIX SENSITIVITY FACTORS FOR SPUTTERED IONS FROM LOW-ALLOY STEELS

Z. Jurela

Theoretical matrix sensitivity factors of constituent elements in low-alloy steels have been determined by means of the nonequilibrium surface ionization (NESI) for positive and negative sputtered ions. It is the ratio of the degree of ionization of the examined constituent atoms to that of the matrix element atoms.

SIMS technique has become more inviting for the quantitative chemical analysis of various alloys, minerals, and organic and inorganic compounds. Until recently the model of plasma in local thermal equilibrium (LTE) on the surface was used exclusively.[1-5] In recent years the thermodynamic model of the nonequilibrium surface ionization (NESI) has been developed and applied.[6,7] It offers a good agreement between theoretical and experimental results for ALCAN aluminum, ferro-niobium and basalt rock.[7] Basic principles for the application of the nonequilibrium surface ionization model to all kinds of samples, and particularly to low-alloy steels, have been presented previously.[8] The greatest problem for the application of the SIMS technique is in changeability of the matrix sensitivity factors of various constituents, depending on experimental conditions.

The aim of this study is the determination of the theoretical matrix sensitivity factors of various constituents in alloys and compounds, and the analysis of the influence of experimental conditions on the change of TMSF values.

Application of the Nonequilibrium Surface Ionization Model

Starting from general equations for the degree of ionization of α_+ and α_- sputtered atom of the NESI model in previous papers, we obtain the equations for the degree of ionization of alloy or compound i-constituent:

$$\alpha_i^+ = (Q^p_i/Q^a_i) \exp\{5040[\phi_{exp} + (2/r_i) - I_i]/T_{sc}\} \tag{1}$$

for positive ions and

$$\alpha_i^- = (Q^n_i/Q^a_i) \exp\{5040(A_i - \phi_{exp})/T_{sc}\} \tag{2}$$

for negative ions,[7,8] where Q^p_i, Q^n_i, and Q^a_i are the partition functions of sputtered positive and negative ions and neutral atoms, respectively; ϕ_{exp} is the work function of bombarded surface obtained experimentally for the corresponding experimental conditions; $2/r_i$ is the correction of the ionization potential in electron volts for r_i, the radius of the i-constituent atom, in Ångstroms; I_i is the ionization potential of the i-constituent in electron volts; A_i is the electron affinity of the i-constituent; and $T_{sc}|K|$ is the mean temperature of sputtering centers during ejection of sputtered particles from the bombarded surface.

In this TMSF calculations, the Corliss values[9] have been used for the partition functions Q^p_i and Q^a_i; for Q^n_i, as before, $Q^n_Z = Q^a_{Z+1}$, where Z is the atomic number of the element.[6] The work function ϕ_{exp} of the bombarded surface should be determined during the experiment. In a number of cases the tabular values of the work function for a clean surface can be used. These are the cases in which the samples are bombarded by inert gas ions and the residual pressure of the reactive gases (carbon, nitrogen, oxygen, etc.) is low enough to prevent formation of carbides, nitrides, oxides, or other compounds of impurities on the spot. We know that bombarding the targets by inert gas ions forms solid solutions, and implanted atoms of inert gases do not change the work function of the bombarded surface, the same as in the case of self-sputtering.

The author is at the Boris Kidrič Institute of Nuclear Sciences, P.O.B. 522, Belgrade; his permanent address is VTŠ "R. Končar," Konavljanska 2, Zagreb, Yugoslavia.

If the sample is bombarded by ions of reactive elements, the compounds of some constituents are formed on the spot. Different constituents have different affinities toward the composition of such compounds; some elements (noble metals) form no compounds. Therefore, bombarding samples by ions of reactive elements changes the structure and chemical composition at the spot. It also causes other changes in physico-chemical and thermal properties of the spot. The essential changes which occur on the spot, and which crucially influence the emission of sputtered ions of some constituents, are: (i) change in the work function, (ii) nonuniform sputtering of some constituents and their compounds, and (iii) increase of the T_{sc} temperature owing to the increased specific energy disipation of the incident ions and lower thermal conductivity of the generated compounds. These three reasons cause the greatest changes in the emission of sputtered ions. The worst thing is that these changes cannot be brought under control, so that the results differ each time the experiment is repeated. Even slight changes in the degree of coverage on the spot cause considerable changes in the emission of sputtered ions. Consequently, it is all the same whether the target is bombarded by ions of reactive elements, or whether the reactive elements are in the chamber as gases and the sample is bombarded by ions of inert gases.

The correction of the ionization potential $\Delta I = -2/r_i$ has been calculated by means of the Slater radii;[10] for the electron affinity the Lineberger[11] and Zollweg[12] values have been used. The temperature T_{sc} of the sputtering centers has been determined from experimental measurements of the secondary ion yields made by Storms, Brown, and Stein.[13] For steel and low-alloy steels $T_{sc} = 2500°K$.[8]

As all the values in Eqs. (1) and (2) have been determined, it is possible to calculate α^+_i and α^-_i for every constituent. The obtained values are presented in Tables 1 and 2. Consider first the values for positive ions presented in Table 1, in which α^+_i values are presented in column 6. It is evident that α^+_i values cover a wide range, from 0.12 for aluminum to 8.95×10^{-15} for nitrogen. The values for the transition elements range from 10^{-2} to 10^{-5}; the lowest are for the nonmetallic elements (S, P, C, O, and N), from 10^{-9} to 10^{-15}. For the matrix element, $\alpha^+_{Fe} = 7.70 \times 10^{-5}$ $|ion/atom|$. If we divide α^+_i values by α^+_{Fe}, we obtain the theoretical matrix sensitivity factor (TMSF) values for constituents in the observed low-alloy steels. As TMSF for the matrix element is 1.00, TMSF values for other constituents range from 1.16×10^{-10} for N to 1560 for Al. Constituents with TMSF > 1 have the increased yield of secondary ions; for constituents with TMSF < 1 the yield of secondary ions in relation to its concentration c_i in atoms $|\%|$ is decreased in inverse proportion to the TMSF value of that constituent. That is the reason some constituents can be easily detected even when their concentration in the examined sample is low, and some can be detected only with difficulty (or not at all) even when their concentration is relatively high.

The α^-_i and TMSF values for negative ions are shown in Table 2. It is characteristic that α^-_i values for negative ions are much lower than for positive ions; they range from 9.94×10^{-11} for Mn to 2.10×10^{-5} for S. For the matrix element, $\alpha^-_{Fe} = 4.55 \times 10^{-9}$. In addition, for all other constituents except Mn, V, and N $\alpha^-_i > \alpha^-_{Fe}$, which means that the ratio $\alpha^-_i/\alpha^-_{Fe} = TMSF > 1$. Nonmetals and amphoteric elements have the highest TMSF values in the cases examined (4615 for S). For transition elements these values are lower; Mn is the lowest, for its atoms have negative electron affinity (A = -0.97). The values in Tables 1 and 2 show that it is obviously easier to detect nonmetalic elements as negative than as positive ions, by as much as 10^4-10^6 Times.

Conclusions

From the above it follows that:

a. For quantitative chemical analysis by SIMS it would be best if the examined samples would be bombarded by a primary ion beam of the sample matrix element. Then the original chemical composition of the samples under consideration would not be disturbed by ion bombardment, or such effects would be negligible. Second, physico-chemical and thermal properties of the spot would be changed only slightly during bombardment.

b. If condition (a) is not attainable, the next best approach would be bombardment of samples by an ion beam of inert gases. These gases are implanted in a lattice of the sample as solid solutions without changing the physico-chemical properties of the spot (work function, etc.).

c. In order to obtain higher yields of secondary ions at energies of 5-100 keV, it is more convenient to use ions of heavy inert gases: argon, krypton, and particularly xenon.

TABLE 1.--Degree of ionization and matrix sensitivity factor constituent elements in low-alloy steels NBS no. 461-468 (positive ions).

Element	Atomic number	I, eV	-ΔI, eV	I+ΔI-φ, eV	α_+ ions/atom	Theoretical matrix sensitivity factor (TMSF)
1	2	3	4	5	6	7
B	5	8.296	2.353	1.633	8.51×10^{-5}	1.10
C	6	11.256	2.857	4.089	3.68×10^{-9}	4.78×10^{-5}
N	7	14.53	3.077	7.143	8.95×10^{-15}	1.16×10^{-10}
O	8	13.614	3.333	5.971	4.08×10^{-13}	5.29×10^{-9}
Al	13	5.984	1.600	0.074	1.20×10^{-1}	1560
Si	14	8.149	1.818	2.021	5.06×10^{-5}	0.657
P	15	10.484	2.000	4.174	7.01×10^{-9}	9.10×10^{-5}
S	16	10.357	2.000	4.047	3.08×10^{-9}	4.00×10^{-5}
Ti	22	6.82	1.428	1.082	1.21×10^{-2}	157
V	23	6.74	1.481	0.949	1.08×10^{-2}	140
Cr	24	6.764	1.428	1.026	5.88×10^{-3}	76.4
Mn	25	7.432	1.428	1.694	4.61×10^{-4}	5.99
Fe	26	7.87	1.428	2.132	7.70×10^{-5}	1.00
Co	27	7.86	1.481	2.069	6.11×10^{-5}	0.794
Ni	28	7.633	1.481	1.842	6.95×10^{-5}	0.903
Cu	29	7.724	1.481	1.933	5.28×10^{-5}	0.686
Ge	32	7.88	1.600	1.970	6.10×10^{-5}	0.792
As	33	9.81	1.739	3.761	3.41×10^{-8}	4.43×10^{-4}
Zr	40	6.84	1.290	1.24	4.18×10^{-3}	54.3
Nb	41	6.88	1.379	1.191	3.63×10^{-3}	47.1
Mo	42	7.10	1.379	1.411	1.23×10^{-3}	16.0
Ag	47	7.574	1.250	2.014	4.35×10^{-5}	0.565
Sn	50	7.342	1.379	1.653	2.81×10^{-4}	3.63
Ta	73	7.88	1.379	2.191	5.16×10^{-5}	0.669
W	74	7.98	1.481	2.189	4.15×10^{-5}	0.539
Pb	82	7.415	1.111	1.994	1.25×10^{-4}	1.62

TABLE 2.--Degree of ionization and matrix sensitivity factor constituent elements in low-alloy steels NBS no. 461-468 (negative ions).

Element	Atomic number	A, eV	φ+A, eV	α_- ions/atom	Theoretical matrix sensitivity factor (TMSF)
1	2	3	4	5	6
B	5	0.28	4.03	1.16×10^{-8}	2.55
C	6	1.268	3.042	3.17×10^{-7}	69.67
N	7	-0.21	4.52	1.74×10^{-9}	0.382
O	8	1.462	2.848	1.21×10^{-6}	265.9
Al	13	0.46	3.85	2.79×10^{-8}	6.13
Si	14	1.385	2.925	6.01×10^{-7}	132.1
P	15	0.7464	3.5636	1.31×10^{-7}	28.79
S	16	2.0772	2.2328	2.10×10^{-5}	4615
Ti	22	0.2	4.11	8.31×10^{-9}	1.83
V	23	0.5	3.81	4.53×10^{-9}	0.996
Cr	24	0.66	3.65	2.69×10^{-8}	5.91
Mn	25	-0.97	5.28	9.94×10^{-11}	2.18×10^{-2}
Fe	26	0.14	4.17	4.55×10^{-9}	1.00
Co	27	0.7	3.61	4.88×10^{-8}	10.72
Ni	28	1.15	3.16	3.34×10^{-8}	7.34
Cu	29	1.226	3.084	2.53×10^{-7}	55.60
Ge	32	1.2	3.11	3.21×10^{-7}	70.55
As	33	0.8	3.51	1.37×10^{-7}	30.11
Zr	40	0.5	3.81	1.50×10^{-8}	3.30
Nb	41	1.0	3.31	7.27×10^{-8}	15.98
Mo	42	1.0	3.31	8.54×10^{-7}	187.7
Ag	47	1.303	3.007	4.33×10^{-7}	95.16
Sn	50	1.25	3.06	6.06×10^{-7}	133.2
Ta	73	0.6	3.71	2.41×10^{-8}	5.30
W	74	0.6	3.71	1.87×10^{-8}	4.11
Pb	82	1.1	3.21	9.08×10^{-7}	199.6

d. The smaller the incident angle of the primary ion beam to the bombarded surface, the more uniform the sputtering of the successive layers of the sample. To avoid the formation of grooves on the spot, the sample must be rotated during bombardment rotates around an axis through the center of the spot.

e. The emission of secondary ions is not a stationary process. It is a thermodynamic nonequilibrium process. Stable emision of secondary ions is reached only after prolonged bombardment, beginning when, owing to radiation damage, the sample becomes amorphous along the whole depth of penetration of the primary ion beam. Only then does the rate of expansion of the amorphous structure in the spot depth equal the rate of sputtering of surface layers. Until this state is reached there is intense migration toward the surface of the atoms of the constituents whose melting temperature is low. At the beginning of bombardment they leave the surface as an avalanche (especially the atoms of alkaline elements). In contrast, atoms of hard-melting constituents are sputtered slower than atoms of the matrix element, which results in the increase of their concentration in surface layers. Consequently, after prolonged bombardment the chemical composition of surface layers on the spot is changed.

f. We may conclude that experimental values of MSF will vary less from experiment to experiment if the conditions at the spot during bombardment are cleaner. If there are large discrepancies between the experimental values of MSF and TMSF, it means that the experimental conditions are not good enough.

References

1. C. A. Andersen and J. R. Hinthorne, *Anal. Chem.* 45: 1421, 1973.
2. A. E. Morgan and H. W. Werner, *Anal. Chem.* 48: 699, 1976.
3. J. M. Schroeer, *J. Vac. Sci. Technol.* 14: 343, 1977.
4. D. H. Smith and W. H. Christie, *Intern. J. Mass Spectrom. Ion Phys.* 26: 61, 1978.

5. H. W. Werner, *Surf. Interface Anal.* 2: 56, 1980.
6. Z. Jurela, *Intern. J. Mass Spectrom. Ion Phys.* 12: 33, 1973.
7. Z. Jurela, *Intern. J. Mass Spectrom. Ion Phys.* 37: 67, 1981.
8. Z. Jurela, 3rd Intern. Conf. Secondary Ion Mass Spectrometry, Budapest, 1981, 101.
9. C. H. Corliss, *J. Rez. Phys. Chem.* 66A: 169, 1962.
10. J. C. Slater, *J. Chem. Phys.* 41: 3199, 1964.
11. W. C. Lineberger, *IEEE Trans.* NS-23: 934, 1976.
12. R. J. Zollweg, *J. Chem. Phys.* 50: 4251, 1969.
13. H. A. Storms, K. F. Brown, and J. D. Stein, *Anal. Chem.* 49: 2023, 1977.

MICROSPECTROPHOTOMETERS FOR SMALL-SAMPLE ANALYSIS

H. H. Hausdorff and V. J. Coates

Computerized microspectrophotometers for obtaining spectra in seconds or minutes of small samples or spots down to 1-20 μm in size in the ultraviolet, visible, and infrared spectral regions are discussed. Typical applications including microsample identification and improved sampling techniques that increase sensistivity and reduce scattering are shown.

Introduction

As in forensic investigations, the production of research laboratory in industry is often called upon to identify or match small particles to solve major production problems. In many cases these objects or sample areas are too small to be subjected to conventional absorption spectrophotometric analysis. Standard microsampling attachments are only operative down to 0.5-1 mm sample size. A series of computerized microspectrophotometers developed by Nanometrics, Inc., have limitations in sample size dictated by wavelength only and offer the additional advantage that the particle or sample area can be viewed for precise positioning of target area from which the spectrum is to be obtained.

UV-VIS-NIR Microspectrophotometers

In historical order, the first of the systems developed was a microspectrophotometer for the spectral region from 220 to 900 nm. (ultraviolet and visible).[2] The spectrophotometer head or holographic grating monochromator can be fitted on to the camera port of any trinocular microscope. Spectral measurements are possible in transmission (absorption), reflectance, polarization, and fluorescence modes.[1] Particles as small as 1 μm can be analyzed. The complete system (NanoSpec[TM]/10S) with microprocessor-computer and X-Y recorder is shown in Fig. 1.

This microspectrophotometer has been widely used in the forensic laboratory for fiber, paint-chip, and ink matching,[6] but also in other laboratories of industries such as microelectronics, fiber manufacturing, printing, photographic film, television tubes (phosphors), medical research, metallurgy,[7] and others.

Figure 2 shows spectral differences obtained with red, blue, yellow, and black fibers in the absorbance mode. Figure 3 relates to a recent rape-murder case in Long Island where the only piece of evidence was a 1in. red fiber 25 μm in diameter, found on one of the suspect's socks that could be linked to the carpet on the scene of the crime. The spectrum of the suspect's fiber is the lower curve with the most absorption peaks. This spectrum was completely different from those of other red fibers found in the apartment, which the suspect claimed he might have picked up in the closet, since he had visited the victim previously. The carpet fiber match was also confirmed by infrared microspectrophotometry which indicated that the polyester base was also the same. A thin-layer chromatography separation showed that more than one dye was used on this fiber that resulted in more than a usual number of peaks in the visible spectrum.

A software option has recently been added to the NanoSpec[TM]/10-S microspectrophotometer for direct printout of tristimulus values and chromacity coordinates, which simplifies cataloging of data and search from spectral libraries.

There is a sister version of this instrument in which the microprocessor computer is the same but its monochromator has a wavelength range from 400 to 2700 nm and therefore covers the visible and near-infrared spectral regions. This instrument (NanoSpec[TM]/10-NIR) provides small-particle information for organic constituents such as films on metals. It is also used for crystal studies and special applications for measuring near-infrared transmittance of small objects such as light transmitting fibers, etc.

The authors are with Nanometrics, Inc., 239 Danbury Road, Wilton, CT 06897.
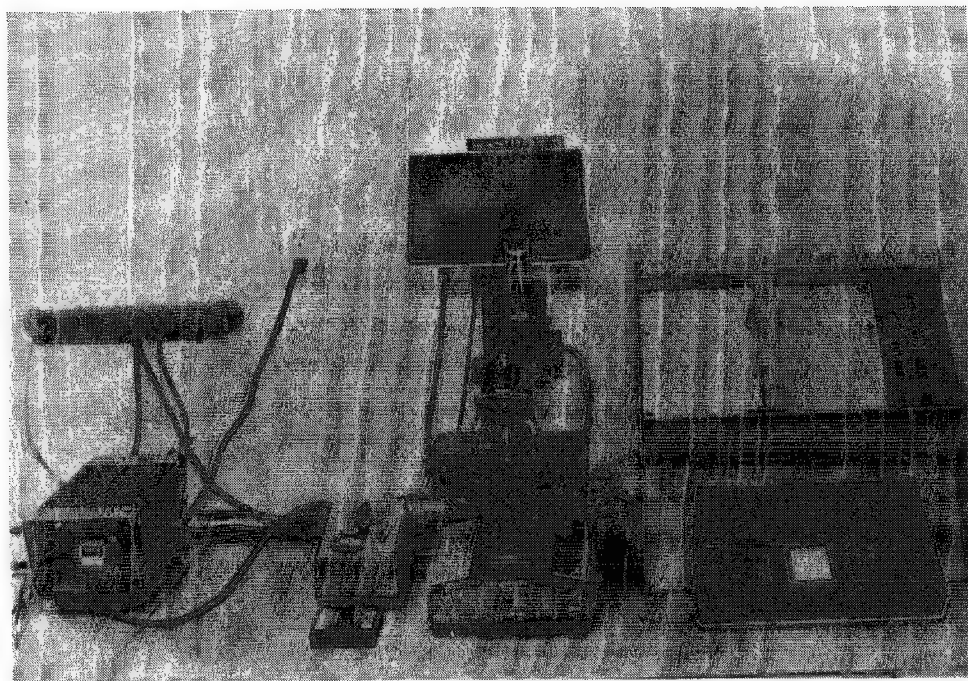
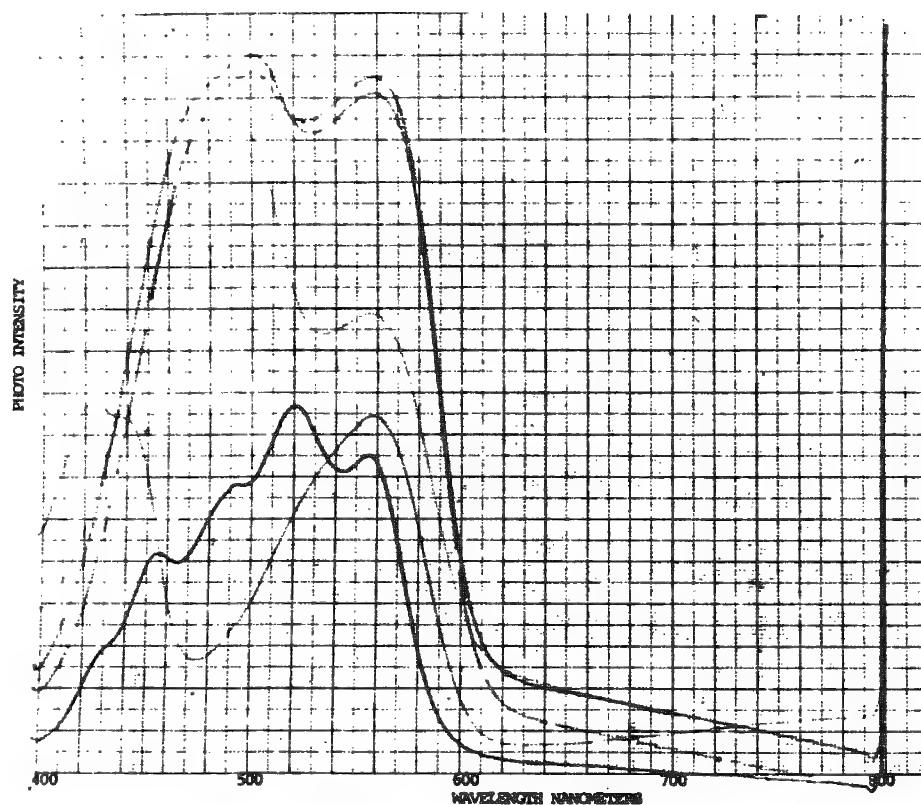FIG. 1.--NanoSpec^{TM}/10 UV-VIS-NIR Microspectrophotometer system.

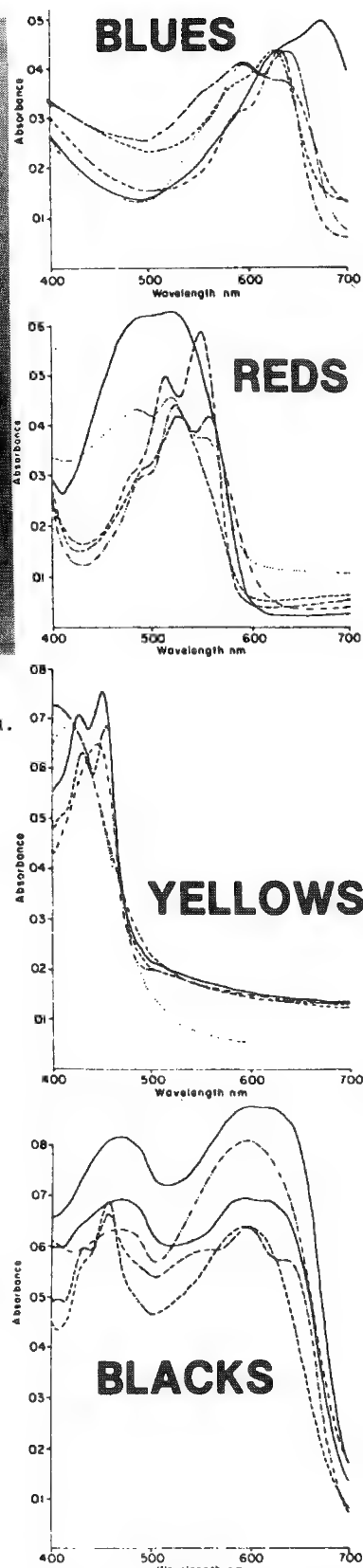FIG. 3.--Forensic matching of fiber in case work (visible spectral region).

FIG. 2.--Absorbance spectra of fibers. (*Courtesy Pierre Lachambre Laboratoire de Police Scientifique, Montreal, Canada.*)

The Infrared Microspectrophotometer

One of the most recent developments with very significant impact on the field of micro-analysis is the NanoSpec[TM]/20-IR, which operates in the standard infrared range from 2.5 to 14.5 μm (4000-690 cm^{-1}). Figure 4 shows this system with its more elaborate computer, X-Y recorder on top, and the combined microscope-spectrophotometer unit to the left. Ordinary microscopes cannot be used in this case because of transmission limitations of microscope optics in the infrared. The combination of a sophisticated optical design, high-speed high-sensitivity Hg Cd Te detector, and a transmission-efficient circular variable filter have made it possible to obtain spectra of good quality of small samples down to 20 μm in minutes. (Details have been described previously.[3])

The major applications for this instrument have been in a variety of industries such as microelectronics,[3-5] connectors, photovoltaic systems, plastics, rubber, textiles, paper, coal research, pharmaceuticals, pollution, medical, etc., but also in special fields such as gemstone analysis for the grading of precious stones and the differentiation between naturals and synthetics.

Forensic applications[6] for this instrument are again very obvious; the example shown in Fig. 5 also relates to the criminal case mentioned earlier for the analysis of the fiber dye by means of the visible microspectrophotometer. In the infrared region none of the other fibers matched the carpet fiber either. The latter was identified as polyethylene terephthalate and was identical to the spectrum of the suspect's fiber.

The most common application of the infrared microspectrophotometer is the analysis of spots, blemishes, or particles down to 20 μm in size that are problem contaminants for which the source or origin has to be traced by identification or spectrum matching. Another significant application is very small area measurement in larger samples for homogeneity analysis qualitatively and quantitatively. The quantitative set-up and quantitative measurement modes of the NanoSpec/20-IR are particularly useful in this case since they allow the operator to set up his own quantitative analysis with his own parameter selection and standards using either a single or dual wavelength (ratio) mode. A baseline method is used by the computer for which the operator selects two reference wavelengths for each measurement wavelength. This procedure makes it possible to measure thicknesses of films or concentration of components on or in a substrate.

Accessories

Figure 6 shows a standard sample holder in the microposition of the NanoSpec/20-IR. These anodized metal plates of microscope slide format are provided with 1, 6, or 13mm holes for holding the sample directly or when placed on an infrared transmitting window.

A heatable window holder with controller power supply has been developed (Fig. 7) which is probably the most useful accessory for difficult powders or samples that have poor transmission characteristics because of light scattering resulting from nonhomogeneous agglomerates. With this accessory the operator can melt the sample by dialing into the controller the melting point of the substance or if the latter is unknown, by bringing up the temperature gradually. The spectroscopist then has the option of running the sample in liquid form (droplet) or to let the sample recrystallize, in which case usually clear single crystal zones can be found as suitable target areas. Figure 8 shows the transmission of a 40μm agglomerate of O-phenyl-phenol (lower curve) which transmits only about 10%. The upper curve with an average transmittance of over 90% was obtained after the substance was melted on the heated window and run as a clear liquid.

A similar gain in transmittance can be noticed for the same sample after it had cooled and crystallized to offer a choice of several clear areas. As expected, there are some minor differences between the spectra of the sample in liquid and crystal form. That could be useful for orientation studies by means of an infrared polarizer.

Conclusion

Microspectrophotometers with which one can obtain good spectra from samples or areas much smaller than can be examined by conventional spectrophotometers with microsampling attachments considerably enlarge the applications horizon in microanalysis. The sample-handling aspects are greatly simplified, low noise level and fast spectra can be obtained without time-consuming accumulation. Quantitative measurements can be made in very small
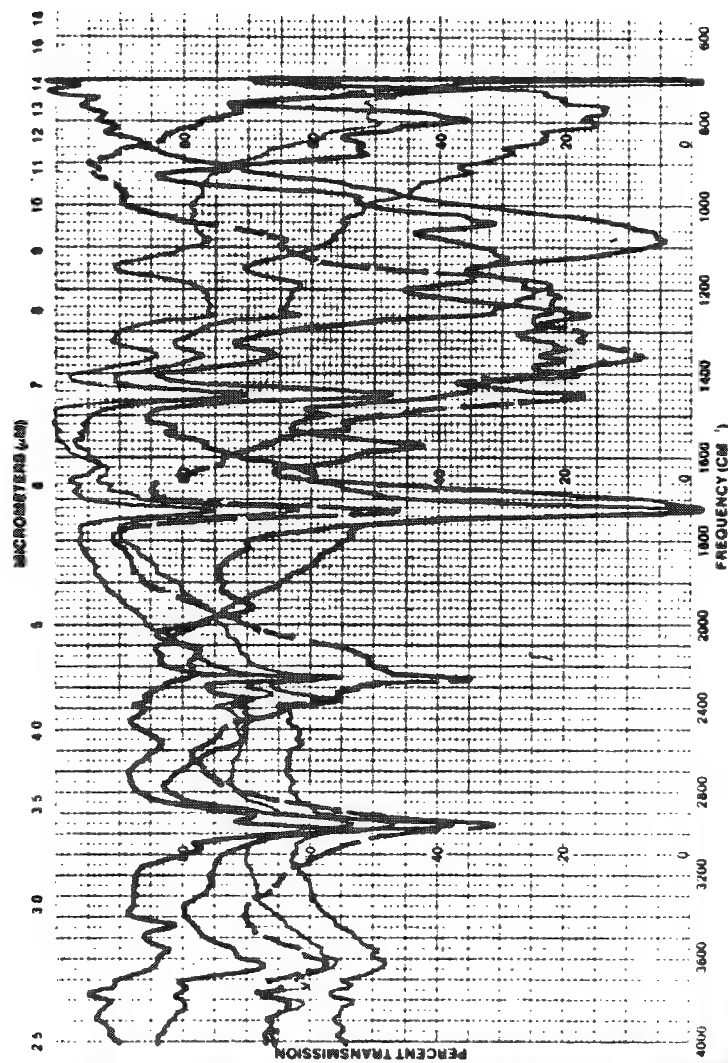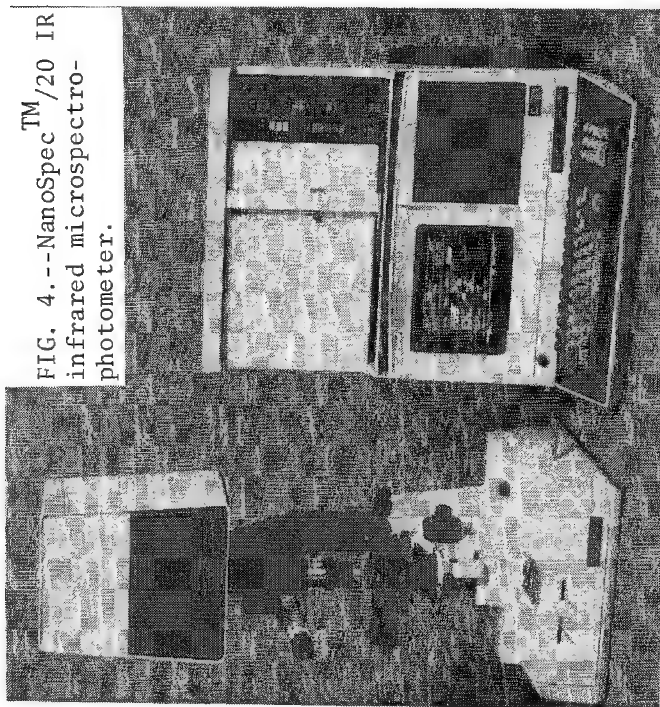
FIG. 5.--Forensic matching of fiber in casework
(infrared spectral region).
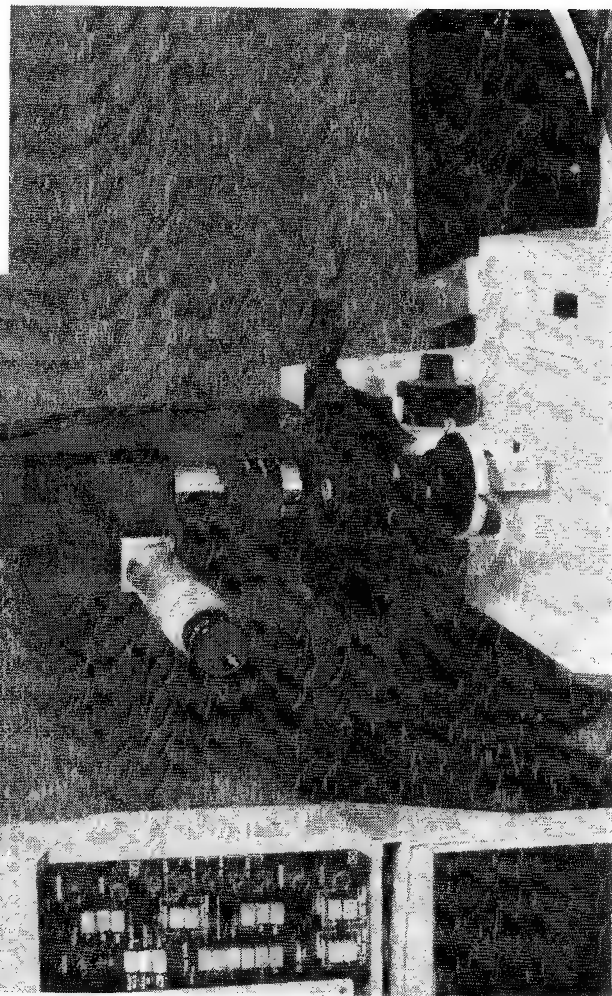
FIG. 6.--Microsampling area with window holder
plate.

FIG. 4.--NanoSpec^{TM}/20 IR
infrared microspectro-
photometer.

adjacent sample areas for homogeneity analysis. Forensic applications for microspectro-photometers are obvious. Similarily, production control laboratories in all major indus-trial fields stand to benefit from these new investigative tools for identifying very small samples and tracing them to their origin for corrective action.

References

1. M. W. Berns and V. J. Coates, "A new and simple approach to quantitative micro-spectrofluorimetry," *J. Cell Biol.* 70: 179a, 1976.

2. V. J. Coates, "Advances in microspectrophotometry," *Pittsburgh Conference on Analytical Chemistry and Spectroscopy*, 1978.

3. J. N. Ramsey and H. H. Hausdorff, "Applications of small-area infrared analysis to semiconductor processing problems," *Microbeam Analysis--1981*, 91-95.

4. D. J. Zaring and V. J. Coates, "Small area measurement of multiple film thickness, dopant concentrations and impurity levels using a new infrared microspectrophotometer," *Optical Characterization Techniques for Semiconductor Technology*, SPIE vol. 276, 1981, 257.

5. R. M. Scott and J. N. Ramsey, "Applications of microinfrared to se-miconductor processing problems," *Pittsburgh Conf. Anal. Chem. and Spectroscopy*, 1982.

6. H. H. Hausdorff and V. J. Coates, "Computerized microspectro-photometers for forensic applications, *ibid.*

7. P. N. Quested and K. W. Raine, "Phase identification by interference film microscopy," *Metals & Materials*, October 1981.

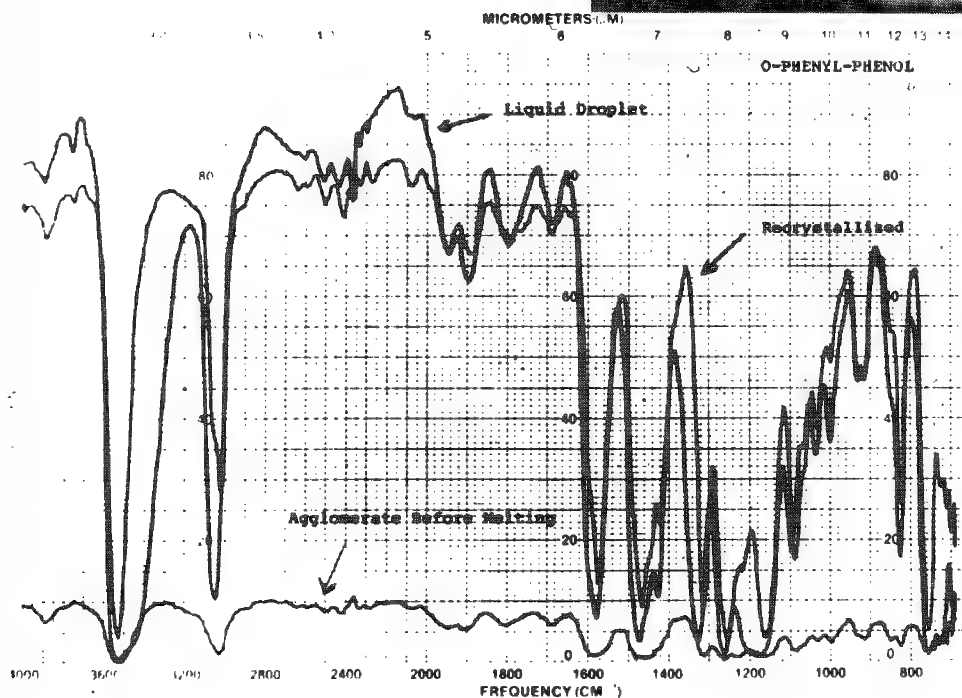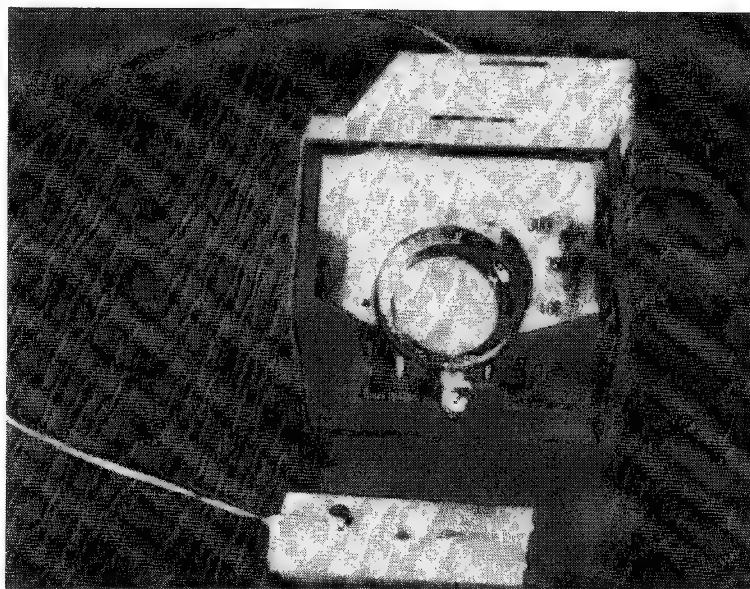FIG. 7.--Heated sample stage for poor light transmitting samples.

FIG. 8.--Transmittance improvement after sample melting for O-phenyl-phenol agglomerate.

237

DEVELOPMENT AND USE OF A COMBINED BEAM CONDENSER MICROSCOPE FOR FT-IR SPECTROSCOPY

J. W. Brasch, R. J. Jakobsen, and C. J. Riggle

It is imperative in our spectroscopic studies of materials under high pressures to corre-
late spectral changes with any physical changes in the samples. Visual observation of the
sample is therefore a most important consideration. We are also interested in spectral ef-
fects immediately before phase transitions and of metastable sample conditions, which re-
quires obtaining spectral data and making visual observations without moving the high pres-
sure cell. For these reasons, considerable effort has gone into the design and construction
of a combined visual microscope/beam condenser accessory compatible with our Digilab Fourier
transform infrared spectrometer systems.

The resultant accessory is very convenient to use, meets all the requirements, and pro-
vides exceptional data, even though it was constructed with available components and at
minimal expense, and is optically very poorly matched to the spectrometer optics. It has
proved to be generally useful in obtaining infrared spectra of small samples, and the abil-
ity to observe the exact area examined is highly desirable.

The system design is based on the principles of the Perkin-Elmer infrared microscope of
the early 1950s and has similarities to the present Nanospec design. Beck 15× reflecting
lenses are used for condenser and collector; the latter also serve as the microscope objec-
tive. Mirror flip directs light from the sample plane to a conventional microscope or to
the spectrometer detector. An iris diaphram serves as a limiting aperture and permits iso-
lation of areas as small as 100 µm. Figure 1 shows photomicrographs of a calibrated scale,
in focus at the sample position, with the aperture set at about 500 µm and set at about 120
µm. Figure 2 is a photomicrograph of three fibers from a textile sample said to be 100%
acrylic. The aperture was used to isolate one fiber at a time; spectra showed that two of
the fibers were acrylic polymers and the third was a polyester. These techniques have been
used advantageously in environmental sample analysis, corrosion studies, and in studying
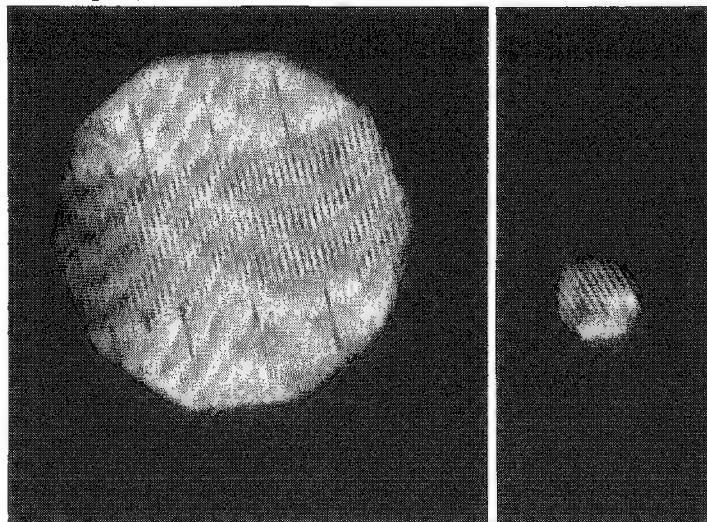blood-polymer surface interactions.

FIG. 1.--Photomicrographs of calibrated
scale at sample position with aperture set
at 500 and at 120 µm.

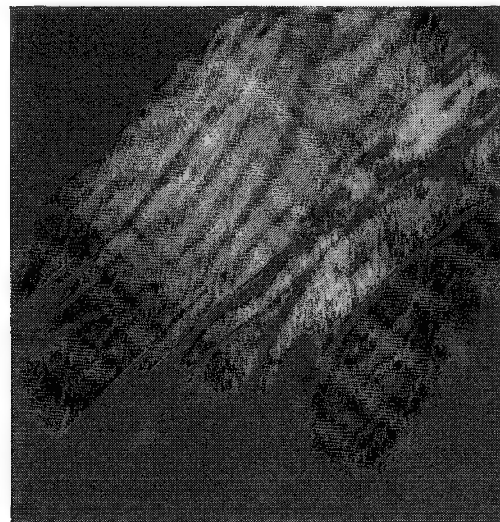FIG. 2.--Photomicrograph of
three fibers from textile sam-
ple. Separate infrared spectra
were obtained of these fibers.

APPLICATIONS OF MICROINFRARED TO SEMICONDUCTOR PROCESSING PROBLEMS

R. M. Scott and J. N. Ramsey

In the semiconductor industry, with its numerous physical/chemical process steps, which ultimately result in a highly dense electronic package, small-area contamination is an important concern. The presence of trace process residues, the reaction or incompatibility of materials, and the contamination from handling and transferring on a microscale can affect the cleanliness and yield of the processed parts. Small-area analytical techniques such as microprobe, SEM, Auger, electron diffraction in TEM, x-ray diffraction, SIMS, and MOLE have been successfully applied to inorganic analysis. Mass spectroscopy, plasma chromatography/mass spectroscopy, ESCA, NMR, MOLE, conventional infrared, and FTIR have been successfully applied to organic analysis. However, small amorphous or organic particles and some thin films are generally difficult to analyze. The NanoSpec[TM]/20-IR has been discussed previously.[1] This instrument provides a molecular analysis in regions as small as 20×20 μm, and is therefore complementary to all the above techniques. This paper reviews the instrument and includes several examples of solutions to practical problems in microelectronics as practiced today.

The NanoSpec[TM]/20IR, a computerized infrared microspectrophotometer, is a combination of an all reflecting microscope and infrared spectrophotometer which allows one to locate, view, and analyze areas near 20×20 μm (150×). The optical system (Fig. 1) consists of a Nernst glower focused by a lens through a cell compartment to a beam chopper. The frequency scanning is achieved by computer-controlled rotation of a circular variable filter. The adjustment of the objective (above) and condenser (below) the rotatable X-Y microscope stage optimizes the transmission through a sample. A variable aperture and a monocular with graduated reticule defines the sample area of interest. The infrared radiation then passes through the aperture to a highly sensitive liquid-nitrogen-cooled mercury cadmium telluride photodetector. The electronic gain is set automatically by the microprocessor computer. An A/D converter averages and digitizes the detector signal each 2 cm^{-1} over the range of 4000-690 cm^{-1} (2.5-14.5 μm). The microprocessor computer with CRT, X-Y plotter, tape printer, and optional dual floppy disk allows a large variety of operating modes and manipulation of the data. The microscope is a transmission system and so the particle or film of interest must be IR transparent, as must also be the supporting material (as it is with silicon wafers). Particles or films on non-IR transparent supporting material must be removed and placed on a proper material, such as BaF_2 crystals.

OPTICAL DIAGRAM

FIG. 1

There are two basic building blocks in microelectronics: the silicon integrated circuit and the package through which this circuitry communicates to the outside world. Each has its own set of critical dimensions that can be altered by a contamination particle or by a thin residual layer.
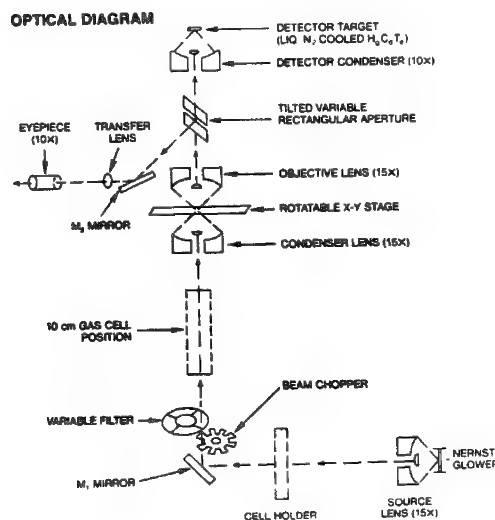
The authors are with IBM Corp., East Fishkill Facility, Hopewell Junction, NY 12533.

Silicon Chip and Chip Joining

IBM uses a flip-chip mode of joining to a substrate, with Pb/Sn solder pads (the controlled collapse chip connector, or C-4). At present all 121 C-4 pads on a chip are bounded simultaneously with use of a flux containing abietic acid, among other things. It is desirable to clean off the residual flux after joining. The in-situ analysis of small areas/thin films of flux is not an easy task. UV fluorescence gives a broad, fairly nondescript spectrum; Raman (MOLE) is unsuccessful because of fluorescence; and SEM/EMP gives only carbon. Figure 2 shows the IR spectrum of a residue in which the C-H and C=O are typical of an organic acid. In this particular case, the thin film (visible only with UV light source) was washed to the edge of the substrate with methylene chloride and then removed with a diamond tip probe.

Another example consisted of a deposit (shown in top left corner of Fig. 3). This was thought to be a residue from the double-sided tape used when dicing the wafer into chips. However, the residue was found to be a natural polyol rather than the suspected poly isobutylene-styrene copolymer.

SiO, used for insulating thin films, has been discussed previously,[2] at which time the question "Does SiO really exist?" was addressed. At that time, ESCA and Raman users said "SiO is unique," and cathodoluminescence and wavelength-dispersive x-ray analysts said, "SiO is a mixture of SiO_2 and Si." The discussion at the time revolved around the number of repeating molecular patterns of amorphous material required to be interpretable by various analytical techniques. Figure 4 shows IR spectra from 50 × 50 μm regions of 550nm SiO_2 film and two SiO films, 200 nm and 500 nm thick. (The 200 nm etched faster than normal SiO films.) Because Raman and IR are analyzing the same vibrational levels, one would expect IR also to "see" SiO as being different than SiO_2, and that is borne out. In addition, there are differences in the shapes of the curves for the two SiO films. Work is continuing in the use of this small-area characterization technique to relate it to property differences.

The right-hand side of Fig. 4 shows the individual absorption locations for silicon nitride, silicon dioxide, and phosphosilicate glass,[1] and for SiO. Thus, all the insulating layers commonly used on silicon devices an be unequivocally analyzed in areas of 50 × 50 μm. This will be a powerful complementary technique in failure analysis.

Si Epi Thickness

The layer of silicon grown epitaxially on the wafer is of vital importance to the industry, because, in general, all the circuitry is built in/on it. Characterization of uniformity and thickness are done by rather large area techniques, by MAS standards, e.g., usually around 1/4 in. in diameter.[3] Thus, we are always looking for analytical techniques applicable to smaller areas, comparable to the sizes of our regions of interest. Figure 5 shows both transmission and reflection interference patterns obtained from the analysis of the epitaxial layer, which is on a heavily doped arsenic subcollector, which is in turn on P⁻ silicon. The unfocused reflection spectrum, which was obtained with a single-reflection attachment, is shown as an inverted comparison to the focused beam (50 × 50μm) transmission spectrum. The results from the transmission spectra (1.56 μm) agreed favorably with the larger area conventional infrared (1.60μm) analysis.[3]

The Package

Masks are used as a means of delineating a pattern of metallic paste being squeezed through the mask. Cleanliness is important to provide the high level of uniformity required in the process. Figure 6 shows a white mouse-shaped contamination. The material is a natural product such as cotton, which is thought to have come from the twill-jean cloth used to wipe the masks. The spectrum was obtained in situ through the 125μm circular hole.

A long uniform filament was found near a chip site which had to be removed and put on a BaF_2 disk. Figure 7 shows the IR spectrum, with CO stretch at 1270 and 1100 cm^{-1} (with sharp aromatic absorption and para substitution at 730 cm^{-1}) to be polyethylene terphthlate polymer (Dacron) from laboratory gloves.

Black, partially melted, particles were found on modules in plastic boxes after transport/storage from a brazing operation. Figure 8 shows the spectrum of the particle

FIG. 2

FIG. 3

FIG. 4

FIG. 5

FIG. 6

FIG. 7

FIG. 8

FIG. 8

241
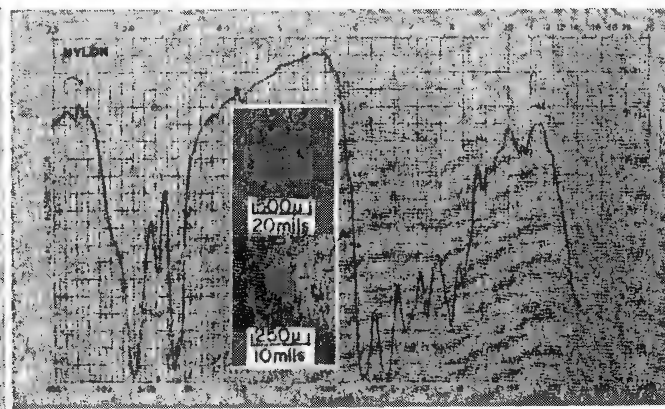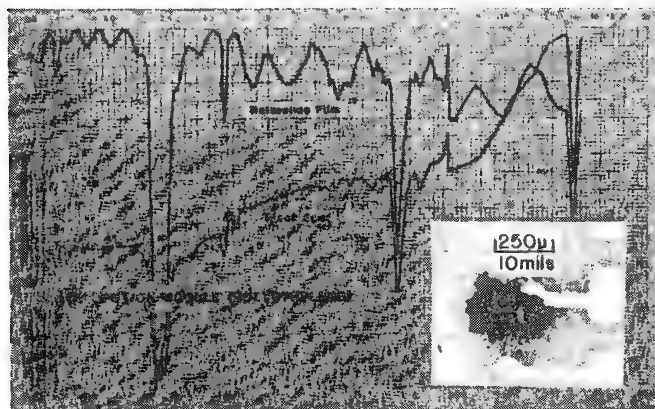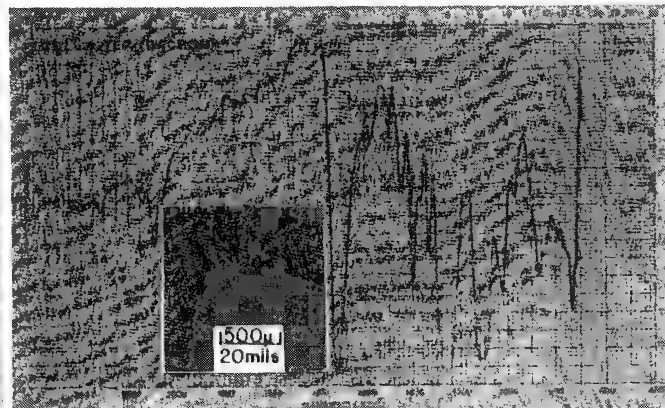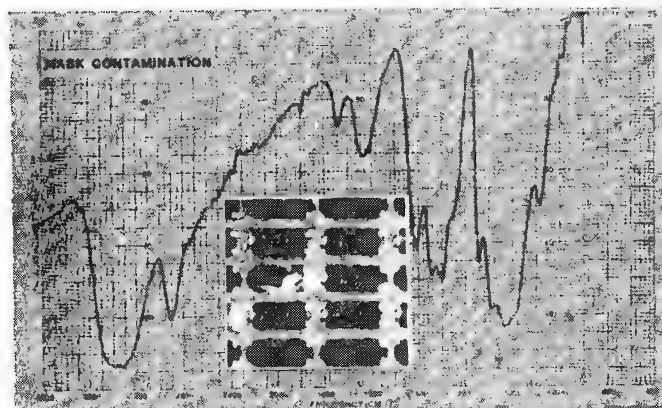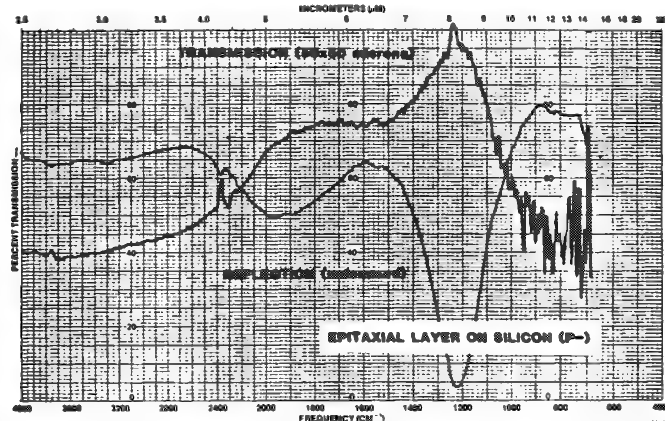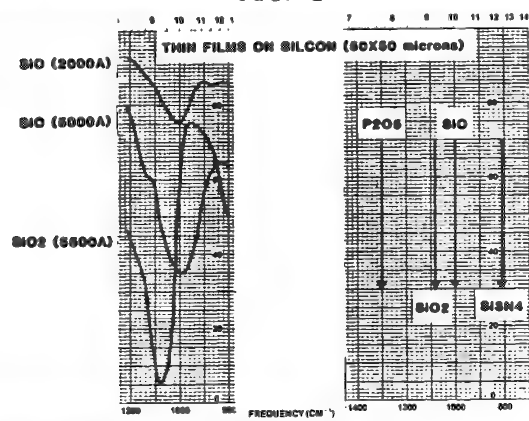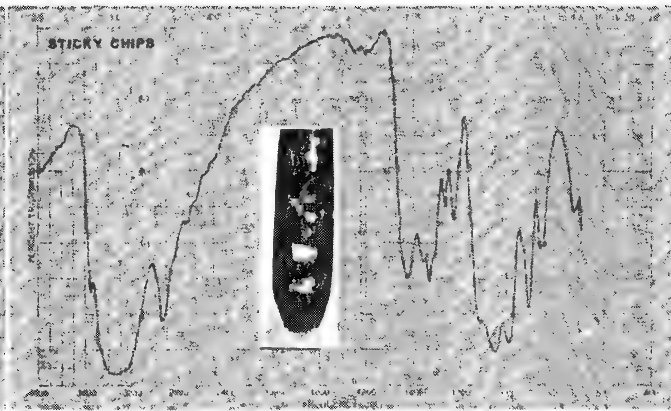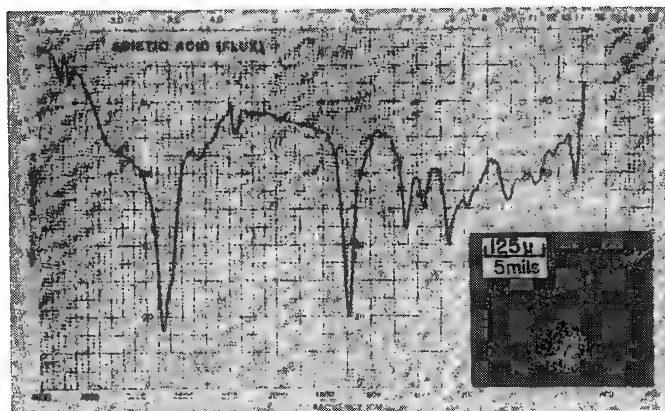
(polyethylene) and a confirming spectrum polyethylene sheet.

The next example is fluorescent hemispherical particles, which had partially melted and rounded after having been deposited. Figure 9 shows the particles to be a polyamide (nylon): Amide I (1640 cm^{-1}) and Amide II (1540 cm^{-1}) are shown. (Natural polyamides such as skin flakes show broader bands for C—N and C—H absorptions through 300 to 2850 cm^{-1}.) The melting point of 265°C allows isolation of the point in the process at which the contamination occurred. The source of the nylon was difficult to assess because the shape was altered by melting; however, it is either shreds from clothing or from nylon gears in an adjacent stirrer.

Conclusion

The NanoSpec^{TM}/20-IR allows analysis of a wide range of organic and inorganic films and particles, both in situ (if transparency is possible) and with removal to BaF_2 disks for IR transmission; complementary techniques are also possible with one form factor or the other.

The coordination of the microinfrared analysis with manufacturing engineering staff made elimination of these contaminations during the device and substrate processes possible. This is a good example of the increased process control possible with small area analysis capability.

References

1. J. N. Ramsey and H. H. Hausdorff, "Applications of small-area infrared analysis to semiconductor processing problems," *Microbeam Analysis--1981*, 91-94.

2. Fran Adar, M. J. Mitchell, and J. N. Ramsey, "Raman analysis of SiO source materials by means of the MOLE," *Microbeam Analysis--1979*, 165-168.

3. ASTM Test Method E 95-73.

MICRO SAMPLE IDENTIFICATION WITH FTIR SPECTROSCOPY

H. J. Humecki and R. Z. Muggli

The need to characterize very small solid and liquid organic samples has always existed. Techniques such as electron microprobe analysis or x-ray diffraction are useful for the analysis of inorganic compounds because of the variety of elements present in various samples and the good database. Raman analysis is very useful for small amounts of both organic and inorganic materials, but the limited database is a distinct disadvantage.[1] However, with organic compounds, elemental analysis is of limited value and the x-ray diffraction database for solid organic compounds is very small. These techniques are of very limited analytical use with liquid samples.

Recent computer advances have led to the fourier transform infrared (FTIR) instruments now in common use. In addition to being more rapid than dispersing instruments, they have detection limits that are markedly reduced. With many samples, contaminants present at low levels can be separated and concentrated for microanalysis, especially with special particle handling techniques.[2] Contaminants in samples such as injectables, inclusions in polymers, or organic pigments and dyes on works of art are often too small for analysis with standard infrared techniques. Small samples of filled plastics are often impossible to analyze directly because the filler restricts the transmission of the infrared energy.

With the development of sophisticated FTIR instruments with more sensitive detectors, a new plateau has been reached, but special handling techniques are needed to take full advantage of the new technology.

Instrumentation

A Digilab FTS-20C equipped with a mercury-cadmium-telluride detector was used to produce most of the spectra. The beam condenser used was a refractive Beckman 6X model with NaCl lenses. The sample and aperture holder are described below and shown in Fig. 1. A capillary brush utilized for the pyrolysis techniques is also described below and can be seen in Fig. 2. The sample handling tools, microscopes, etc. are described in *The Particle Atlas*.[2]

Sample-handling Techniques

When only a minute sample exists, one must attempt to get as much of the sample in the analyzing beam as possible. Small transparent chips or flakes can be transferred to a salt plate directly. Using a stereomicroscope with both reflected and transmitted light capability and tungsten needles sharpened to points of 5 μm or less, one can pick up samples less than 200 μm in size and deposit them at a small, prescribed location. Normally, electrostatic forces are sufficient to hold the particle in position even if the salt window is inverted. If there is concern that the particle may move, it can be glued to the surface by the application of a small drop of very dilute collodion solution.[2] The resulting layer of collodion is so thin that its spectrum will not be registered with that of the sample.

The sample should fill as much of the analytical aperture as possible to maximize the signal-to-noise ratio. This goal can be accomplished if several apertures of different diameters are available and the largest one consistent with the sample size is selected. We have designed and built a holder for the sample and aperture. It consists of a disk with a 1mm hole in the center to which a salt window or chip is taped or glued. After the
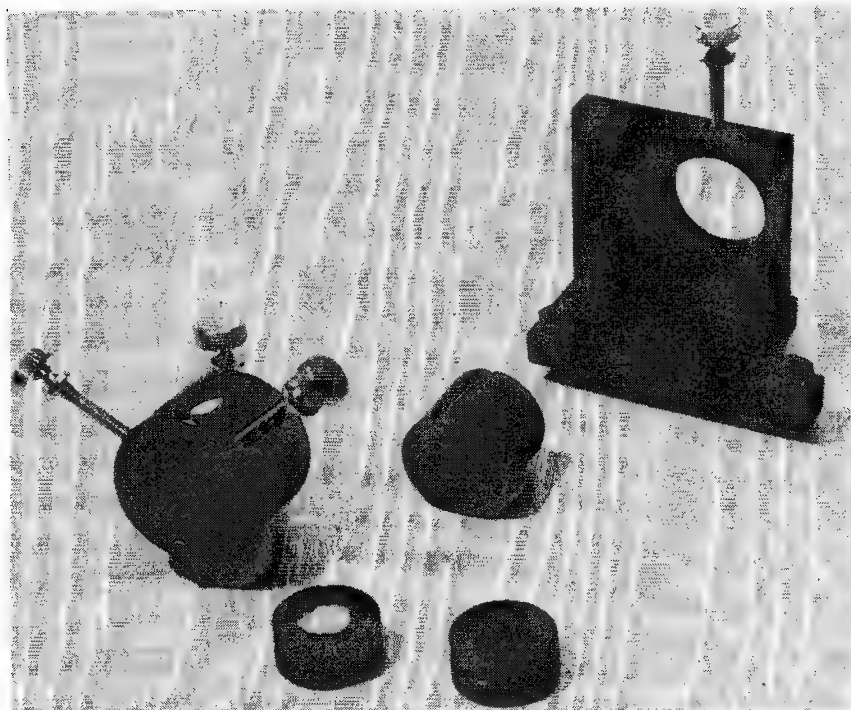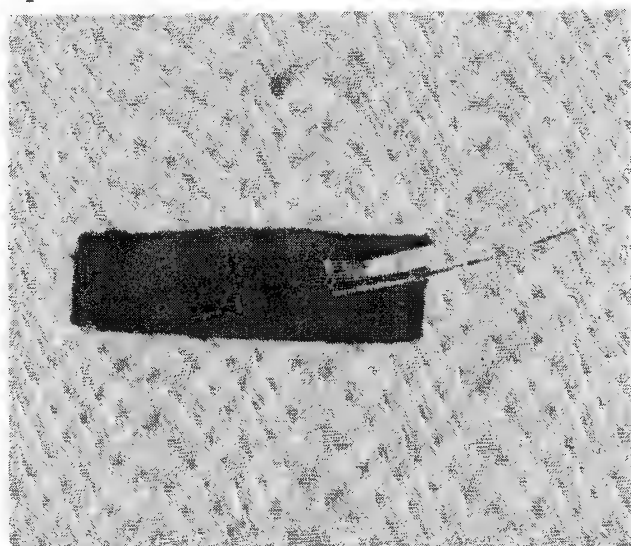
FIG. 1.--Sample holder and mounted apertures.

FIG. 2.--"Brush" and salt window.
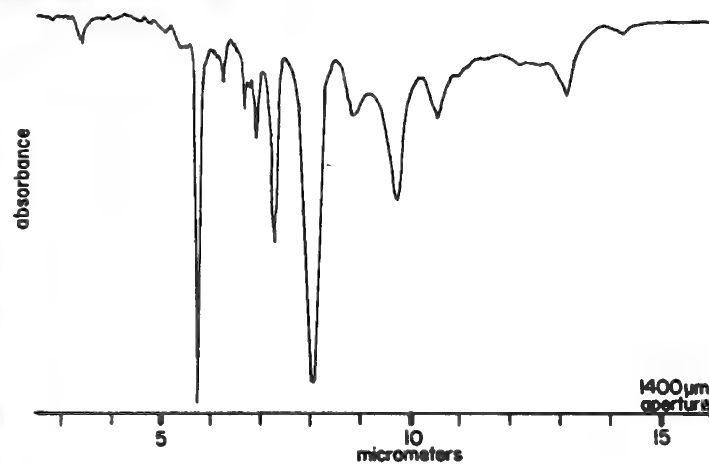

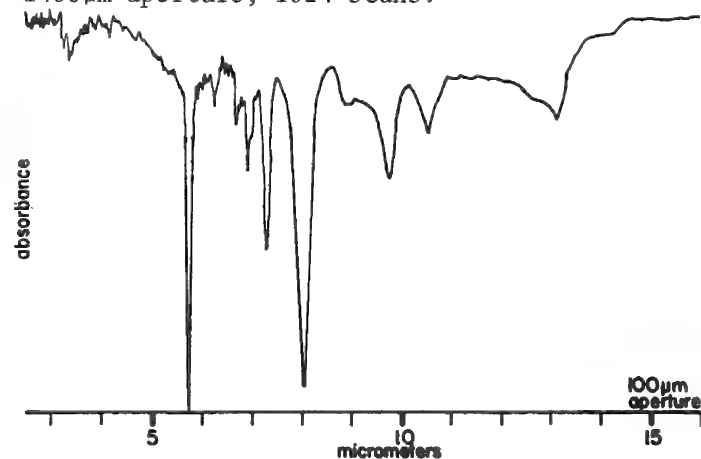FIG. 3.--Infrared spectrum of polymer mixture; 1400μm aperture, 1024 scans.

FIG. 4.--Infrared spectrum of polymer mixture; 100μm aperture, 1024 scans.

sample is in place, a preselected aperture, mounted on a ring, is lowered over the particle. It is positioned by means of three set screws, all at 12 to 50× magnification with a stereoscope using transmitted light. The mounted sample is placed in the beam condenser, which focuses the beam to a spot size of about 3 mm. Spectra of samples down to 25 µm can be obtained with this technique.

Polymer samples containing pigments and fillers can be pyrolyzed in a capillary tube to separate the organic species from the inorganic fillers. Borosilicate capillaries of 0.2 to 0.5 mm ID and 3 to 6 cm long are used. A short length of borosilicate glass wool is twisted and inserted into the tube while it is observed under a microscope. The glass wool is fused to the inside by gentle playing of the flame of a hobbyist minitorch near, but not at, the end of the tube. The glass wool is trimmed to form a brush (Fig. 2). A drop of ethylene dichloride is applied to the opposite end of the tube and the brush end is touched to an absorbent surface to draw out the solvent. This cleaning operation reduces background contamination.

A few sample particles are pushed into the open end of the capillary tube with a tungsten needle or wire to a depth of 2 to 4 mm. The tube end is sealed with a torch and the flame is played gently over the area containing the sample until sample pyrolysis is complete. When the heated end has cooled, it is broken off and a drop of solvent is applied while the capillary is held in a horizontal position. The capillary is brought into position over the salt plate and tipped so that the liquid washes over the pyrolysis condensate and flows into the brush. The brush is touched lightly to the salt plate. As the solvent evaporates, the brush confines the liquid to an area less than 200 µm in diameter by capillary action.

The capillary-brush technique can be used for depositing any liquid in a restricted area. To restrict spreading of the liquid or to minimize the production of interference fringes in the spectra, a pinhole well is sometimes made in a salt plate. The well is made by gently twisting a tungsten needle into a salt window. The needle must have a stout point, not the fine delicate point used for small particle handling. Typically a hole with a depth of up to 50 µm is produced. The powdered salt from the piercing operation is pushed back into the hole and tapped down, and the liquid sample or solution is then deposited from the brush in the powder filled well. Scattering of the energy by the powdered salt is not a problem because the powder is wetted by the liquid to produce a transparent or almost transparent sample site.

Results and Discussion

Transparent or translucent samples as small as 25 µm have been analyzed in 5 to 6 min (instrument time) with good spectral integrity. The three spectra of a polymer, a polystyrene-polyester mixture (Figs. 3, 4, and 5), illustrate this point. Some of the weaker bands are not very well differentiated from the background in the spectrum produced with the 25µm aperture. However, additional signal averaging further enhances this spectrum. These data show a reduction in sample area requirements by a factor of four over that reported by Cournoyer et al.[3] Also, the sample and aperture holder described here facilitate the handling of the diminutive samples. The minimum sample size has yet to be determined. It varies to some extent, because of sample absorption characteristics and spectral requirements in each specific case. For most samples it is not more than 25 µm and often less.

Filled polymer samples are best analyzed by the pyrolysis technique proposed by Harms,[4] but as reported "sample may vary from 2 grams to a few hundred milligrams." With more sensitive spectrometers and careful techniques the usual pyrolysis still requires a few hundreds or tens of milligrams of sample. The brush technique was used to produce the spectrum shown in Fig. 6 from a few micrograms of a carbon black filled polymer with the FTS-20C spectrometer, a TGS detector, and only 128 scans. The utility of the technique is apparent in the quality of the spectrum.

Conclusion

We have outlined two techniques that yield analytically usable spectra from samples with infrared spectroscopy. Use of the tools described eases the difficulty of manipulating minute samples. It has been shown that samples as small as and probably smaller

than 25 μm in diameter are of adequate size for analysis.

References

1. M. E. Andersen and R. Z. Muggli, "Microscoptical techniques with the Molecular Optics Laser Examiner Raman microprobe," *Anal. Chem.* 53: 1772-1777, 1981.

2. W. C. McCrone and J. G. Delly, *The Particle Atlas*, Ann Arbor, Mich.: Ann Arbor Science, 1973, 2d ed., vol. 1.

3. R. Cournoyer, J. C. Shearer, and D. H. Anderson," Fourier transform infrared analysis below the one-nonogram level," *Anal. Chem.* 49: 2275-2277, 1977.

4. D. L. Harms, "Identification of complex organic materials by infrared spectra of their pyrolysis products," *Anal. Chem.* 25: 1140-1155, 1953.
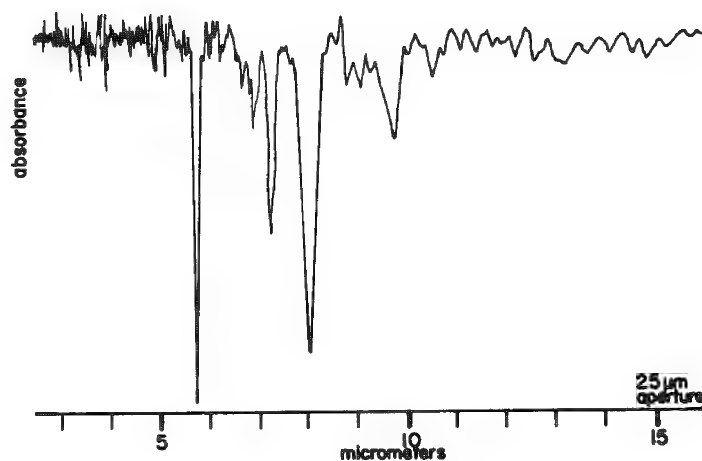

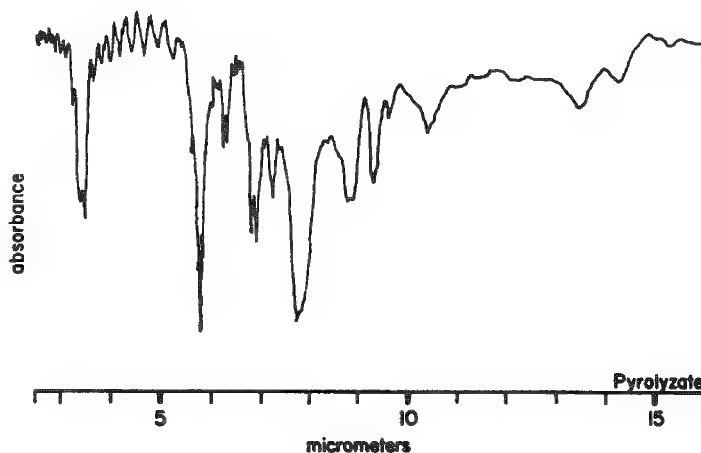FIG. 5.--Infrared spectrum of polymer mixture; 25μm aperture, 1024 scans.

FIG. 6.-Infrared spectrum of pyrozate, TGS detector, 128 scans ("brush" technique).

MICROSPECTROSCOPY

Tomas Hirschfeld

The boom in electron and ion microbeam methods, with its overwhelming proliferation of new methods (and acronyms) and eager exploitation of every available technological advance, has tended to obscure the very wide usage of the corresponding optical methods. The present review of optical microprobe techniques includes UV-VIS absorption techniques, fluorescence microspectroscopy, Raman measurements, and other microprobes such as the infrared ones, scatter, and the various partially optical methods. Also discussed are technological advances that may have an impact on these fields. The natural place of microspectroscopy is shown to be as a higher-discrimination, lower-resolution companion of electron and ion beam microprobes.

Microspectroscopy from the Electron/Ion Beam Probe Viewpoint

How would you like to have your microprobe run with 0.003kV beam voltage, 1A beam current, 3500Å resolution, and energy discrimination of 0.0001 eV? These are the normal capabilities of microprobes based on optical beams. A more detailed examination of this technology is clearly in order.

The unique attributes of optical microspectroscopy can be briefly described as follows (Table 1):

TABLE 1.--Optical microbeam methods.

	UV-VIS Absorption	Fluorescence	Raman	IR Absorption	Scattering
Resolution	$\sim$3500Å	$\sim$3500Å	$\sim$3500Å	$\sim$10µm	$\sim$3500Å
Detection Limits					
Size	$\sim$2500Å	$\sim$100Å	$\sim$500A	5µm	$\sim$100Å
Concentration	10-100ppm	1ppb	>1000ppm	>1000ppm	1ppm
Quantity	10^{-17}g	10^{-21}g	10^{-13}g	10^{-12}g	10^{-19}g
Universality	with reagents	no	almost	yes	no
Qualitation					
Recognition	with reagents	often	yes	yes	rarely
Identification	no	often	yes	yes	no
Quantitation	1%	1%	2%	1%	2%

The author is with the Chemistry Department of the Lawrence Livermore National Laboratory (L-325), Livermore, CA 94550.

1. *Low energy*. The energies involved in optical photon beams range from 0.1 to 6 eV/photon and involve the lowest-energy radiation whose with a large enough wavelength to allow reasonable microscopic resolution. At these energies, sample alteration has low probabilities even if the beam is strongly absorbed by the material.

2. *High source brightness*. Photons are neutral and thus have no space charge. Moreover, they can be amplified coherently, which leads to the enormous brightness of the laser (10^{14} W/cm^2, routine for small commercial lasers, is equivalent to about a 10^{14} A/cm^2 source). This feature permits us to exploit the low-damage efficiency of photons to bring illumination intensities right up to the sample's thermal limit.

3. *Better defined interaction mechanisms*. Since the energy in the photons is deliberately made comparable to the energy involved in the transitions to be observed, the behavior of the beam's energy during interaction is quite simple, with a very restricted number of well-separable mechanisms operating at any one time. This orderliness is made more valuable by the quite detailed understanding of these mechanisms available in optical spectroscopy. As a result, very detailed interpretation of the data provided by each of these separate interaction mechanisms can be made. The high energy resolution of all forms of optical spectroscopy ($\Delta E/E = 10^{-4}$ or better, even at these low energies) is quite helpful here.

4. *Multiplicity of observable parameters*. A beam of light is characterized not only by its intensity and energy, but also by polarization, phase, even ellipticity, all of which can be separately determined. Furthermore, the low energy of the transitions allows some longer-lived phenomena to occur, so that much useful characterization can be done in the time domain as well. Beyond that, the intensities attainable in optical technology are large enough so that many nonlinear phenomena occur that add to the discrimination power provided by the normal absorption, scatter, refraction, diffraction, reemission, etc.

5. *Highly developed technology*. As befits their long history, optical techniques are quite mature. Among normal accomplishments are detection of radiation at over 50% photon counting efficiency over more than 10^3 parallel channels simultaneously, $\Delta E/E$ discrimination to below 10^{-4}, time discrimination to 10^{-12} s, and measurement of a given radiated energy in the presence of another 10^{14} times stronger at the same location and direction. Even the main drawback of optical microbeams, their 10^4 or more times longer wavelength, is partially mitigated by the superiority of "optical optics" over their electron/ion beam counterparts, so that resolutions better than 1 μm can be nevertheless reached. And it can all be done in air, under water, or at selected points deep *inside* transparent samples!

Altogether, if optics were now being discovered by electron/ion beam microprobes users, they would be hailed as a godsend. And they are, despite having been around for a long time.

Classical UV-VIS Absorption Microspectroscopy

The technique of defining a single spot in the field of view of a microscope by means of a diaphragm and using that as a spectrometer source to obtain the spectrum of a microscopic object goes back to the 19th century. It is no different from a beam microprobe, since it is not the beam itself that is used but the spot at the end of the beam. Whether a spot on the sample is defined by the incoming illumination beam or by the fact that only one spot is being observed is a somewhat artificial distinction, one that was further weakened as microscopists realized the photometric accuracy advantages of using equivalent diaphragms on the illumination--a process that becomes intrinsic if laser illumination is used.

The technique was coupled in the 1930s with photoelectric readouts and soon extended into the UV spectral range down to 200 nm. It was used not only to measure the detailed spectrum of a point but also (at a specific wavelength) as a routine tool of quantitative microscopy. As data processing technology advanced, integration of specific sample areas was eventually supplemented by contour measurements, shape descriptor calculation, texture measurements, and statistical analysis of the reconstructed image.

The great strength of all these methods derives precisely from what one might think is their weakness: most substances do not strongly absorb visible light (indeed, that is why it is visible). To yield strong signals, most samples must have chemical dyes added to them. And the selectivity of this dye binding process, carefully enhanced by centuries of selection of ever more discrimination dyes, is a cornerstone of optical microscopy. The

sensitivity of this process to minute structural, environmental, accessivity, or steric hindrance effects at all kinds of binding sites is not the whole story. Many dyes can be used in combinations and differentiated in parallel by their respective colors, either to enhance contrast or to furnish even finer discrimination by the comparison of their relative strength. In some cases, the dye itself shows color changes that further describe the sample. The selectivity of such processes has been pushed to their ultimate limits by the use of enzymatic or immunochemical reactions, either to generate the dyes at a specific target or to bind them at it.

Since these dyes are individual small molecules and can be detected at quite low levels, they can often penetrate complex structures without disturbance and require no complex chemical amplification or marking techniques for detectability. The number of commercially available reagents for these purposes is in the thousands.

Absorption methods, particularly when intensively absorbing reagents are available, are reasonably sensitive. As little as 0.3% absorption at a given location is detectable with contrast enhancement software, which may correspond to as little as 10^{-4} M concentration of sample (100 ppm), or about 10^{-17} g in a sample spot whose minimum diameter is 2500-5000 Å and whose depth is about 1000 Å.

Fluorescence Microspectroscopy

From a spectroscopist's point of view fluorescence has much to recommend it over absorption and has grown more popular. If we measure not the absorbed radiation, but the fraction of it that the sample reemits, the absence of a signal gives us a dark background rather than a lighted one. The lower shot noise of a dark background benefits the detection limit, which can be as much as 1000 times lower in fluorescence. To be sure, the average signal levels are lower, but with modern detectors (and especially when laser sources are used) they are nearly always high enough so as not to become limiting. Also, although fluorescence is even rarer than absorption, the additional effort of finding a suitable dye is usually offset by lower background and scattering interference and the much higher contrast. But the main benefit of fluorescence is the complexity of the phenomena, which involve a number of interactions large enough to provide abundant data without becoming so complex that they cannot all be separated at will.

In common with absorption, fluorescence is characterized by a specific wavelength and intensity, as well as a polarization sensitivity. Beyond that it can be characterized by an emission lifetime, an emission wavelength and polarization (both of which may vary along the lifetime), and an emission efficiency. All of them can in turn depend on the illumination wavelength and polarization.

This characterization is above and beyond the discrimination ability already provided by the use of dyes and can be used to enhance it further by observation of the detailed interactions of the dye with the various features of the sample. It can also be used for distinguishing features of the samples that coexist in a single spatial-resolution element, or to enhance the distinguishability of dye from background or of several simultaneously used dyes from each other.

The above potential is compounded by the parallel phenomenon of phosphorescence, in which a part of the reemission is long delayed by an intramolecular quantum-mechanical rearrangement. All the additional variables observable in fluorescence are again repeated as further data points in phosphorescence, with the additional feature that one may observe the cross correlation of all these magnitudes between fluorescence and phosphorescence.

The richness of fluorescence microspectroscopy is even greater with powerful sources such as lasers, capable of saturating the fluorescence phenomenon in either the exposure or the intensity domains. Measurements of a single fluorescent species (natural or dye reagent) furnish up to 32 independent parameters (each of them quantitatively measurable) to describe the sample.

Fluorescent microspectroscopy is capable of detecting ppb concentrations in volumes of less than 1 μm^3, samples down to a few thousand molecules are observed routinely. With laser illumination and special reagents, single-molecule detection has been demonstrated.

"Quasi-microbeam" Methods

The choice between microbeam methods and imaging is somewhat different in the optical domain from what it is in electron/ion beam techniques. Low damage rates in samples, ample

available power, high-efficiency imaging detectors and low lens aberrations combine to make whole-image processing an effective competitor. Moreover, the technology often blurs the boundary between microbeam methods and imaging. For example, in flow photometric techniques, a continuous stream of suspended sample particulates (or a thin sample layer affixed to a moving support) is scanned past a beam focus to provide a histogram of the photometric characteristics of individual sample points. This technique, which uses a line instead of a point beam focus, can also provide a shape in one dimension, or in two or three if two detector arrays at right angles to each other and to the illumination are used in fluorescence. The ability of the beam to propagate in a gas or liquid medium is also useful.

Devices that use stationary beams and a scanning sample give considerably less information about structured samples than imaging methods do, but they accumulate information incomparably faster. With several laser beams intersecting the sample stream in succession, and with a multiplicity of dyes giving off signals to an array of detectors sensitive to different polarizations and wavelengths at different angles, many channels of accurate quantitative information can be obtained for an individual particle or sample spot in a few microseconds.

Flow photometers have been used to measure samples at rates of 3 to 10^5 discrete particles a second, with quantitative accuracies exceeding 1% and sensitivities down to a few tens of molecules in up to eight channels simultaneously. They are an ideal solution for describing distributions and statistics or detecting rare events, when the average information on the bulk sample is insufficient and extremely detailed information on each particle or spot is not required.

Raman Microprobes

The exquisite selectivity of absorption and fluorescent spectroscopy is bought at a cost: the use of reagents. For absorption, these reagents provide needed added selectivity; for fluorescence, they provide the needed generality. In both cases, they must be developed in the first place, the sample must be permeable to them, and a specific reagent must be selected to provide detection, quantitation, and sometimes additional characterization of a given target.

This technique thus does not address the qualitative analysis problem except through yes/no answers on specific questions; one must have a good idea of what one is looking for. Since the number of reagents usable in parallel is limited, so is the number of questions; one is led to guessing and incomplete answers if the sample is too complex.

What is clearly needed is a universal spectroscopic technique that would be capable of blind identification of an unknown, require no reagents or sample modification, and allow direct quantitation of the sample as well. For elemental analysis of compounds simple enough to be totally defined by their elemental composition, such a technique is available for electron/ion beam probes via characteristic x-ray emission, or in optical spectroscopy by laser vaporization of a spot followed by optical emission spectroscopy (sometimes too drastic a procedure).

For detailed molecular composition and structure, this approach is not enough. Being told that a sample contains C, O, and N (and we can suspect H) hardly tells us which organic we are looking at. Here the existence of the Raman phenomenon comes in handy. Raman scattering of light is an extraordinarily inefficient process in which a fraction of the scattered light undergoes wavelength changes whose spectrum is characteristic of the vibrations of the molecule. This process generates a complex pattern whose recognition (often left to a computer) against a library of reference spectra uniquely identifies the compound. If the compound is not in the database, the particular features of the spectrum are indicative of selected molecular subgroups, so that a good deal of the structure involved can be inferred.

Near ideal as that sounds, Raman signals are extraordinarily weak and are difficult to detect not only against instrumentation noise but against even very weak fluorescences in the sample. The existing Raman microprobe devices are thus compelled to work at the very edge of the state of the art. In fact, it is the application of such a superior Raman technology to fluorescent observation that made single-molecule detection possible.

Nevertheless, the sample illumination, sample survival, signal detection, and background rejection problems of Raman microprobes have been solved, and the technique is

250

rapidly maturing into a general microprobe procedure whose use is essential if molecular structure or complex composition must be determined. Depending on the specific instrumentation, the resolution of the instrument can be from 0.5 to 3 µm, with measurement times per point ranging from 1 s to 10 min. Concentration lower limits of 0.1-1% must be combined with a low quantity threshold of 10^{-13} g.

Other Techniques

Infrared (IR) spectroscopy, which operates at much longer wavelengths, provides a spectrum of the molecular vibrations in much the same way as does Raman. However, it is a far more efficient process, and the amount of energy that must reach the sample to give an observable spectrum is much lower--just as well, since IR sources (including lasers, not employed so far) are less bright. On the other hand, less light makes the job harder on the detector, which in the IR version is less sensitive, anyway.

Until recently, a further drawback was the unavailability of multiple IR detector arrays, so that scans were required for a single-point measurement. The use of Fourier transform methods has allowed much more rapid measurements (partially wasted in optical design mismatches). Forthcoming IR detector arrays may make fast measurements of entire images possible in ombination with Fourier methods, but that will prove to be a definite strain on the computers and data-handling (and output) procedures used at present.

At lower resolutions (about 10-20 µm) with similar concentration sensitivities of 0.1-1%, 10^{-12}g sensitivities, and measurement times of a few seconds per spot, IR methods give the same benefits as Raman ones. When the lowered resolution is tolerable, their higher speed, less sample damage, and indifference to sample fluorescence makes IR techniques preferable.

Scattering spectroscopy is another type of optical microspectroscopy, which can give us information about sample features far smaller than the beam's resolving power. From measurements of the angular and polarization distribution of scattered light, the mean and even the distribution of scattering center size and symmetry can be calculated. For micro-particulate samples capable of Brownian motion in the surrounding medium, the resulting signal fluctuations can provide information on the hydrodynamic radius, symmetry, and absolute scattering power of the particulates. The technique can detect single particles down to 60 Å in size, about 10^{-19} g, even against the background of molecular scatter by the solvent. The method can measure symmetry and size to a few percent relative accuracy, although it degrades for nonresolvable polydisperse samples.

Some hybrid techniques cannot be described as specifically optical microbeam methods, e.g., cathodoluminescence, in which an SEM beam excites optical fluorescence in a sample. Here the full benefit of using selective fluorescent reagent awaits the development of beam-resistant fluorescent reagents. Another pair of rather drastic techniques vaporizes a sample spot a few micrometers in size to provide a sample for either an ICP emission spectrometer or a mass spectrometer. The collateral effects of scanning a laser beam over the sample in order to excite photoelectron emission, photoacoustic effects, or variously detected thermal waves within the sample have also been used as a microbeam spectroscopic technique. The comparative evaluation of these techniques is not very far advanced.

Whither the State of the Art?

In general microspectroscopic methods that use optics have a considerable edge in molecular composition and structural analysis, and a substantially lower resolution. They have fairly similar sensitivity for UV-VIS absorption, a very superior performance for fluorescence, and a lower one for Raman spectroscopy. Except for very low resolution requirements (where IR will do), the last is the technique of choice for general qualitation and structural analysis.

Except for Raman spectroscopy (but there very significantly), the sensitivity and light gathering power of current instrumentation is ample. Improved array detectors, with still lower noise and higher dynamic range, can be expected to provide modest gains here. In the borderline between microbeam and imaging techniques, where imaging speed needs increasing, longer arrays are desirable. More powerful sources would be useful here, in IR work, and in flow cytometry. Improvements in optics, although coming up against the law of diminishing returns in principle, still will be significant to make "real world" performance approach the "lucky days" one. The use of parallel rather than scanning imaging

and of flow techniques whenever possible is clearly dominant and will disturb the legitimacy of microspectroscopy as a "microbeam" technique (for those who care about such things).

The crucial area in which further development is required is clearly resolution. At first, the prospect of resolutions better than a light wavelength does not seem encouraging. However, examples of optical discrimination of 1-10Å distances exist. Two fluorescent dyes, one of which emits at the wavelength that the other absorbs, are used in combination. At normal concentrations, the two-step excitation of the second dye by illumination of the absorption band of the first, via two successive absorption-emission states, is negligible. But if the two dyes get within about 60 Å of one another, a very efficient quantum-mechanical tunneling process takes over and allows emission of one dye by excitation of the other. The effect varies as a high power of the distance and thus measures the mean distance between the two dyes.

A more "conventional" form of increasing resolution is to slow down the speed of light to reduce the wavelength at a given frequency, either by an increase in the refractive index of the medium, or more extensively (by factors of 10 and more) by substitution of the evanescent wave of total reflection for the normal propagating light wave. The sample is held against a high-index window within which the illuminating beam is totally reflected. The surface layer of the sample is then illuminated to a 300Å depth by a special wave in which lateral resolutions of 600 Å have already been demonstrated.

As the state of the art in microspectroscopy progresses, the amount of data it produces will increase with both discrimination and resolution improvements. Substantial improvements in computer I/O rates, data storage capacity, processing rate, and display capability are urgently required. Yet even with the possibilities in this area from large disks and perhaps video storage, array processors, and high-power terminals, we shall still be in trouble. Unless we come up with some innovative data-processing schemes, we shall end by saturating the computer we were born with.

References

1. G. L. Wied, Ed., *Introduction to Quantitative Cytochemistry*, New York: Academic Press, 1966.

2. A. A. Thaer and M. Jerrety, Fluorescence Techniques in Cell Biology, Heidelberg: Springer, 1973.

3. M. R. Melamed, P. F. Mullaney, and M. L. Mendelsohn, *Flow Cytometry and Sorting*, New York: Wiley, 1979.

4. F. P. Milanovich, T. Hirschfeld, and D. C. Johnson, "The Lawrence Livermore National Laboratory Raman microprobe," *Microbeam Analysis--1982*, 270.

5. T. Hirschfeld, M. J. Block, and W. Mueller, *J. Histochem. Cytochem.* 25: 719, 1977.

6. T. Hirschfeld, "Optical microscopic observation of single small molecules," *Appl. Opt.* 15: 2965, 1976.

INELASTIC SCATTERING BY MOLECULES EMBEDDED IN OR AT THE SURFACE OF SMALL PARTICLES

Milton Kerker

The spectacular optical effects of microparticles such as the brilliant colors of sunsets or of "stained" glass can be ascribed to so-called elastic scattering in which there is no wavelength shift. For inelastic scattering, of which fluorescence and the Raman effect are examples, there is excitation of electronic vibrational and rotational transitions at the incident wavelength and emission of light at some shifted wavelength.

In several important areas of investigation inelastically scattering molecules are embedded within small particles; the most active are flow fluorimetry of biological cells, Raman microprobe analysis of colloidal particles, and Lidar detection of fluorescent aerosols. More recently, the interest in surface-enhanced Raman scattering has led to studies of this phenomenon when the Raman scattering molecules are attached to the surface of collodial particles.

Some years ago we raised the following query regarding such experiments: How are inelastic signals affected by embedment of active molecules within small particles? We have been able to show in such cases that, in addition to depending on the polarizability tensor, the signals also depend on the particle size, shape, and orientation; on the refractive index of the particle; and on the spatial distribution of the active molecules within the particle.

We have formulated a theoretical model in which the active molecules at each site within the particle are stimulated by the local electrical fields at that site and in turn the emitted radiation at the shifted frequency must propagate to the observation point from each particular site in the microparticle. This theory has been formulated for spheres,[1] concentric spheres,[2] cylinders,[3] and spheroids,[4] and numerous computed results have been obtained.[3-7] Many of the predicted features have been verified by experiments with fluorescently tagged polystyrene latex particles.[8-11]

Anomalously intense Raman scattering was first observed for pyride adsorbed at a silver electrode that had been roughened by successive oxidation reduction cycles. The subsequent discovery that molecules adsorbed at the surface of silver colloids led us to extend the theory for inelastic scattering by molecules embedded within microparticles to the case where the molecules are outside the particles. This theory has been applied to spheres,[12,13] spheroids,[14] and spherical shells.[15]

Early experiments with silver hydrosols coated with a monolayer of citrate[16] demonstrated that enhanced Raman signals of the order of 10^5 to 10^6 were obtained in agreement with the predictions of the theory. However, the wavelength dependence of SERS on the excitation wavelength differed from the theoretical predictions. More recent experiments have resolved this discrepancy and delineate the dependence of the SERS signals on particle size and morphology.

References

1. H. Chew, P. J. McNulty, and M. Kerker, "Model for Raman and fluorescent scattering by molecules embedded in small particles," *Phys. Rev.* A13: 396-404, 1976.

2. H. Chew, M. Kerker, and P. J. McNulty, "Raman and fluorescent scattering by molecules embedded in concentric spheres," *J. Opt. Soc. Am.* 66: 440-444, 1976.

3. H. Chew, D. D. Cooke, and M. Kerker, "Raman and fluorescent scattering by molecules embedded in dielectric cylinders," *Appl. Opt.* 19: 44-52, 1980.

4. D.-S. Wang, M. Kerker, and H. W. Chew, "Raman and fluorescent scattering by molecules embedded in dielectric spheroids," *ibid.*, pp. 2315-2328.

The author is at the Clarkson College of Technology, Potsdam, NY 13676.

5. M. Kerker, P. J. McNulty, M. Sculley, H. Chew, and D. D. Cooke, "Raman and fluorescent scattering by molecules embedded in small particles: Numerical results for incoherent optical processes," *J. Opt. Soc. Am.* 68: 1676-1686, 1978.

6. H. Chew, M. Sculley, M. Kerker, P. J. McNulty, and D. D. Cooke, "Raman and fluorescent scattering by molecules embedded in small particles: Results for coherent optical processes," *ibid.*, pp. 1686-1689.

7. M. Kerker and S. D. Druger, "Raman and fluorescent scattering by molecules embedded in spheres with radii up to several multiples of the wavelength," *Appl. Opt.* 18: 1172-1179, 1979.

8. J. P. Kratohvil, M.-P. Lee, and M. Kerker, "Angular distribution of fluorescence from small particles," *Appl. Opt.* 17: 1978-1980, 1978.

9. E.-H. Lee, R. E. Benner, J. B. Fenn, and R. K. Chang, "Angular distribution of fluorescence from monodispersed particles," *ibid.*, pp. 1980-1982.

10. P. J. McNulty, S. D. Druger, M. Kerker, and H. W. Chew, "Fluorescent scattering by anisotropic molecules embedded in small particles," *Appl. Opt.* 18: 1484-1486, 1979.

11. M. Kerker, M. A. Van Dilla, A. Brunsting, J. P. Kratohvil, P. Hsu, D.-S. Wang, J. W. Gray, R. G. Langlois, "Is the central dogma of the flow cytometry (fluorescence intensity is proportional to cellular dye content) true?" *Cytometry* (in press).

12. D.-S. Wang, H. Chew, and M. Kerker, "Enhanced Raman scattering at the surface (SERS) of a spherical particle," *Appl. Opt.* 19: 2256-2257, 1980.

13. M. Kerker, D.-S. Wang, and H. Chew, "Surface enhanced Raman scattering (SERS) by molecules adsorbed at spherical particles: Errata," *ibid.*, 4159-4174.

14. D.-S. Wang and M. Kerker, "Enhanced Raman scattering by molecules adsorbed at the surface of colloidal spheroids," *Phys. Rev.* B24: 1777-1790, 1981.

15. M. Kerker and C. G. Blatchford, "Elastic scattering, absorption and surface-enhanced Raman scattering by concentric spheres comprised of a metallic and a dielectric region," *Phys. Rev.* (submitted).

16. M. Kerker, O. Siiman, L. A. Bumm, and D.-S. Wang, "Surface-enhanced Raman scattering (SERS) of citrate ion adsorbed on colloidal silver," *Appl. Opt.* 19: 3253-3255, 1980.

MORPHOLOGY-DEPENDENT RAMAN SPECTRA FROM MICROPARTICLES

J. F. Owen, P. W. Barber, and R. K. Chang

In Raman spectroscopy of bulk samples, the energy shift of each peak in a Raman spectrum can be uniquely ascribed to a specific molecular vibration and the intensity of each peak is linearly proportional to the concentration of the specific molecule and the Raman scattering cross section of the particular vibrational mode. However, for an ensemble of microparticles, the use of Raman scattering as a diagnostic probe becomes significantly more complicated. Experiments indicate that the effective Raman scattering cross sections for molecules embedded in powder[1] and aerosols[2] can be increased by as much as a factor of ten from that in bulk. Theoretical formalism has been developed for a variety of microparticle shapes.[3,4] The purpose of this paper is to demonstrate that even more severe complications can arise in the analysis of Raman scattering from single or highly monodispersed microparticles as a result of morphology-dependent resonances which occur in particles with well defined geometries, e.g., in spheres, cylinders, and spheroids. Such resonances can actually give rise to sharp peaks in a Raman spectrum that are not present for a bulk sample of the same composition. Peaks can result from resonance-induced enhancement of the Raman emission or enhancement of a fluorescence background. The physical nature of these resonances will be illustrated in a calculation of the electric field distribution within an infinite dielectric cylinder when illuminated by a plane wave at a resonance wavelength. Effects of such resonances on inelastic emission will be illustrated in fluorescence emission spectra from a 10μm-diameter silicate glass fiber coated with a thin layer of fluorescent dye and Raman scattering spectra from a homogeneous 10μm-diameter silicate glass fiber. Sharp peaks, not present in the fluorescence spectrum of the dye in bulk or in the normally broad and featureless Raman spectrum of silicate glass, appear in the fluorescence emission and Raman scattering spectra from the two fibers. Although our investigations have been restricted mainly to cylindrical geometry, similar effects are expected in other shapes (e.g., spheres[5] and spheroids[6]). If misinterpreted, resonance-induced peaks could lead to considerable confusion in the analysis of Raman spectra.

Internal Fields

Morphology-dependent resonances in microparticles were first observed experimentally in the optical levitation of liquid droplets.[7] Since optical levitation is related to elastic scattering, calculations based on the Lorenz-Mie formalism showed that the sharp decreases observed in the laser power which was necessary to levitate the droplets for certain values of size parameter x ($x = 2\pi a/\lambda$, where a is the radius) resulted from resonances in elastic scattering.[8] Similar resonances were predicted theoretically for inelastic scattering[9] and first observed experimentally in fluorescence emission from 10μm-diameter dye-embedded polystyrene spheres suspended in water.[5]

Insight into the physical nature of the morphology-dependent resonances in microparticles can be gained by study of calculations of the electric-field distribution within a microparticle. Figure 1(a) shows a calculation[10] of the internal field intensity $[\vec{E}(r,\phi)\cdot\vec{E}^*(r,\phi)]$ in a plane perpendicular to the axis of an infinite, lossless dielectric cylinder which is illuminated by a plane wave polarized perpendicular to the fiber axis (TE polarization) and propagating in the direction shown. The relative index of the cylin-

FIELD INTENSITY, TE

OFF RESONANCE

X = 45.6

m = 1.530

0°(Forward)

7.0

(a)
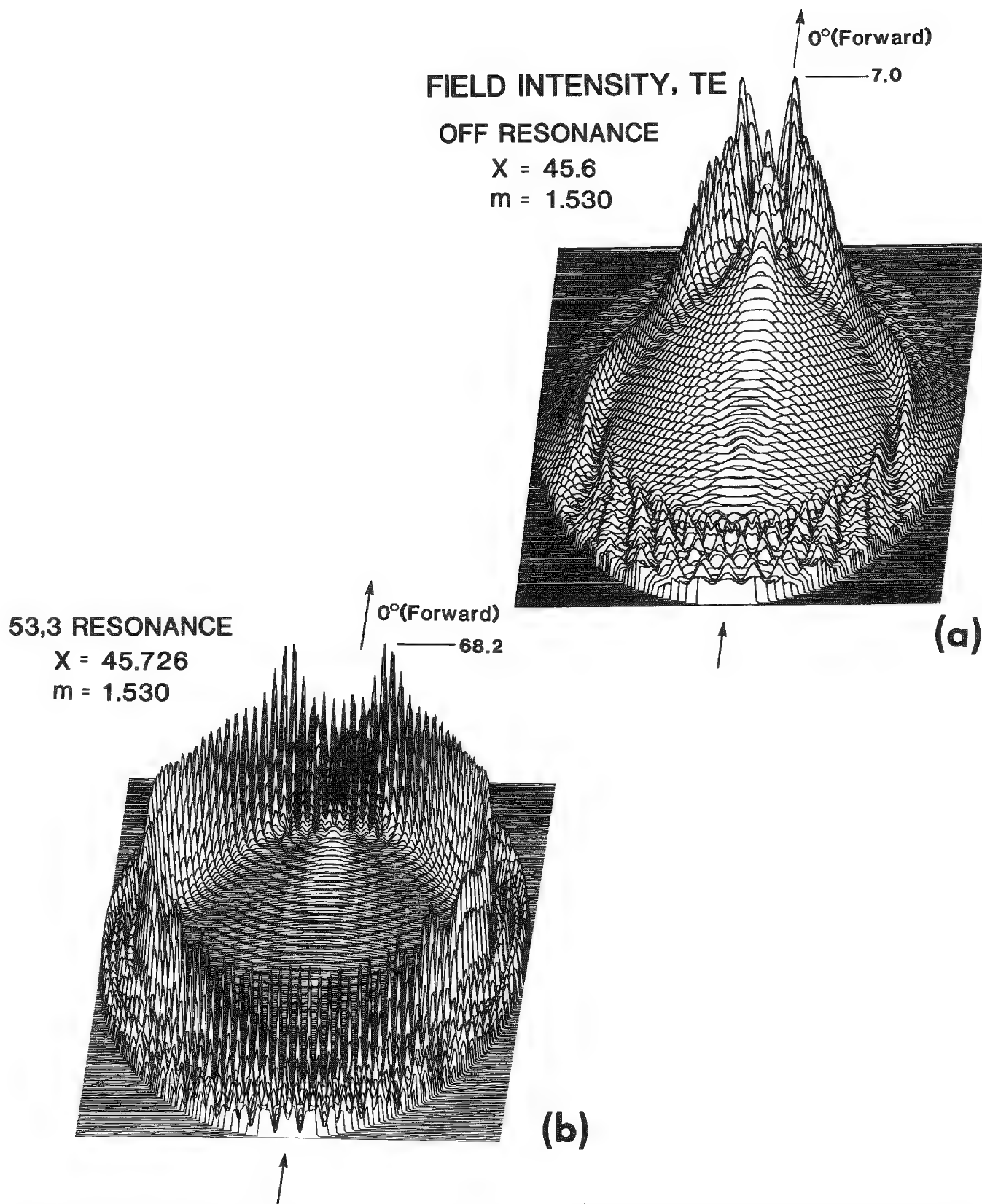
53,3 RESONANCE

X = 45.726

m = 1.530

0°(Forward)

68.2

(b)

FIG. 1.--(a) Internal TE electric field intensity ($\vec{E}\cdot\vec{E}^*$) for an infinitely long dielectric cylinder with a relative index (m = 1.530) and size parameter (x = 45.6) which do not satisfy resonance condition. (b) Same as (a) but for x = 45.726, which satisfies mode 53,3 resonance condition.

der, m = 1.530 ($m = n_p/n_m$, where n_p and n_m are the indices of the particle and surrounding medium, respectively), and the size parameter, $x = 45.6$, corresponding to a diameter of approximately 8.7 µm at $\lambda = 600$ nm, do not satisfy a resonance condition. The increase in intensity toward the forward portion of the cylinder results from focusing of the incident plane wave by the curved surface and the smaller series of ridges throughout the plane result primarily from interference between the forward-traveling and backward-traveling waves reflected from the surface. When the radius or wavelength are changed slightly to satisfy a resonance condition, the field distribution changes dramatically. Figure 1(b) shows the case for $x = 45.726$. The central area is virtually unchanged, but three concentric rings of 106 large peaks now appear near the circumference. This resonance corresponds to mode number $n = 53$ (half the number of peaks around the circumference) and mode order $\ell = 3$ (the number of ridges in the radial direction), which we designate as mode 53,3. Physically, such resonances result from waves that travel close to the surface, internally reflected at the interface. Resonances occur at wavelengths for which a wave is in phase with itself upon circumnavigating the cylinder.

The average field intensity in the outer 20% of the cylinder is approximately an order of magnitude larger for the on-resonance condition in Fig. 1(b) than for the off-resonance condition shown in Fig. 1(a). The spatial distribution and intensity of fluorescence or Raman scattering generated within a particle is directly related to the internal field distribution. For example, a molecule located in the outer 20% of this cylinder and re-emitting either fluorescence or Raman radiation would experience a factor of ten increase in the exciting electric field for an incident wavelength corresponding to $x = 45.726$, the resonance condition, compared with a wavelength corresponding to an off-resonance size parameter, assuming the same incident intensity for both wavelengths. Thus, peaks can occur in the excitation spectrum of a particle at wavelengths that satisfy resonance conditions. From reciprocity arguments, the efficiency with which re-radiation from a molecule within a particle can couple to the far field (i.e., the intensity at the detector) is also related to the internal field distribution, but at the re-radiating wavelength. Consequently, enhancement of fluorescence or Raman emission is expected at emission wavelengths corresponding to resonance conditions.

Fluorescence Emission

Figure 2(a) shows two fluorescence emission spectra[11] from a thin layer (~5 nm) of oxazine dye coated on a 9.8µm-diameter glass fiber. For excitation of the dye, the fiber was illuminated normal to its axis with a beam from a Rhodamine 6G dye laser polarized normal to the fiber axis. Fluorescence radiation was collected normal to the fiber axis at 90° from the incident beam with an f/5.6 lens and imaged onto the entrance slit of a double monochromator equipped with a photomultiplier and photon counting electronics. An analyzer in the collection optics passed radiation polarized normal to the fiber axis, allowing only TE resonances to be detected. Although the emission spectrum of oxazine in bulk is completely featureless in this region, sharp peaks occur in the two spectra at emission wavelengths which satisfy resonance conditions of the fiber. The excitation wavelength for the less intense spectrum of Fig. 2(a) was 615 nm, which does not correspond to a fiber resonance. However, for a pump wavelength of 616.95 nm, which corresponds to an $\ell = 3$ resonance, the intensity of the entire spectrum is increased by almost a factor of 3. Thus, as expected from the internal field calculations, enhancement of fluorescence occurs for either emission or excitation wavelengths which satisfy resonance conditions of the fiber. Note that the internal field calculations in Fig. 1 indicate that an increase in intensity of an order of magnitude should occur for re-radiation of molecules on the surface of a cylinder for an incident wavelength corresponding to an $\ell = 3$ resonance. The fact that the intensity of the on-resonance spectrum is only three times that for the off-resonance case indicates that the fiber cannot support $\ell = 3$ resonances to the extent predicted for the "perfect" cylinder assumed in the calculation.

Elastic Scattering

Morphology-dependent resonances also give rise to peaks in elastic scattering spectra from microparticles.[12] Since elastic scattering calculations for spheres and cylinders are relatively straightforward and since experimental elastic scattering spectra can be obtained with the same apparatus used to obtain fluorescence or Raman spectra simply by

illuminating the microparticle with a broad-band source, it is useful to study resonances in elastic scattering for comparison with inelastic results. Figure 2(b) shows an elastic scattering spectrum obtained by blocking the laser used to excite fluorescence in the dye layer (Fig. 2a), illuminating the same portion of the fiber with broadband radiation from an incandescent lamp, and scanning the spectrometer over the same wavelength range. A calculated elastic scattering spectrum, where m and the fiber diameter d have been adjusted to obtain the best fit to the experimental results, is shown in Fig. 2(c). Each resonance peak is labeled by n, ℓ. Note that the ℓ = 3 resonances are barely visible in the experimental elastic scattering spectrum, since the fiber cannot support these resonances completely; yet these resonances give rise to relatively large peaks in the fluorescence spectra. Elastic scattering is indicative of the far-field intensity, calculated from far-field scattering coefficients that never exceed unity.[13] The far-field intensities never become particularly large even for resonance wavelengths. Inelastic emission is a function of the internal electric field, calculated from the internal-field coefficients which can be much larger than unity. The internal electric field intensities can become extremely large under resonance conditions. The lower the order ℓ of a resonance, the narrower the linewidth and the larger the internal fields associated with the resonance, i.e., the higher the Q of the resonance. Because of the high Q, the low-order resonances tend to be dampened by imperfections of the microparticle (e.g., surface irregularity, irregularity in cross section, and absorbing species within the bulk or on the surface). The relatively small enhancement of fluorescence by ℓ = 4 resonances in Fig. 2(a) is consistent with internal field calculations which show an increase in the local field intensity of only 50% for ℓ = 4 resonances.[11]

FIG. 2.--(a) Fluorescence emission from dye-coated 9.8μm-diameter glass fiber. Excitation wavelength was resonant with mode 59,3 for upper curve and off resonance for lower curve. (b) Experimental elastic scattering spectrum from the same fiber. (c) Calculated elastic scattering spectrum for infinite cylinder with relative index m = 1.530 and diameter d = 9.833 μm.

Raman Scattering

Figure 3(a) shows the Raman spectrum from a 10.1μm-diameter silicate glass fiber (solid curve), the Raman spectrum from a similar, although not identical, bulk glass sample (long dashed curve), and the Raman spectrum from a bulk sample of fused silica (short dashed curve).[14] Pump radiation was coupled into the end of the fiber and Raman emission was collected normal to the fiber axis and imaged onto the entrance slit of a three-stage spectrograph (Spex Tiplemate). Detection was accomplished with a linear photodiode array (PAR Model 1420) at the spectrograph focal plane. An analyzer in the collection optics passed only TE polarized radiation. The excitation wavelength in Fig. 3(a) is 488.0 nm. Although the broad features of the Raman spectra from the fiber and from the bulk glass are similar, additional sharp peaks occur in the fiber spectrum. When the incident wavelength is changed to 514.5 nm, the broad features of the Raman spectra remain unchanged in energy shift while the relative positions of the sharp structure are quite different, as shown in Fig. 4(a). This result could lead an experimentalist to believe that the sharp structure is associated with fluorescence superimposed on the Raman spectrum, since the sharp peaks are a function of the wavelength, whereas Raman features are constant in energy shift from
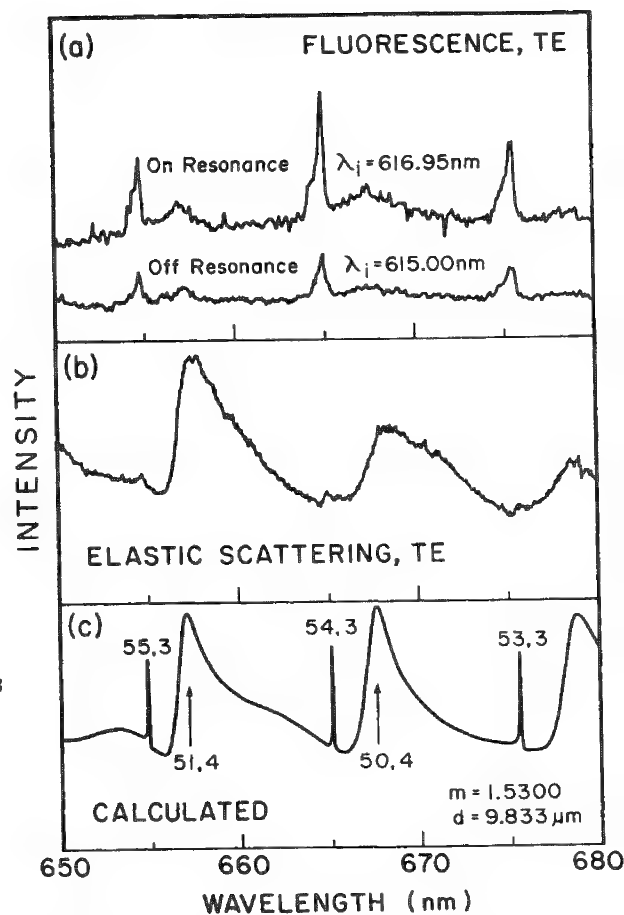
the excitation line. However, comparison with experimental and calculated elastic scattering spectra over the same wavelength ranges, obtained in the manner described in the previous section and shown in Figs. 3(b), 3(c), 4(b), and 4(c), confirms the fact that these peaks are associated with resonances in the fiber. The resonances remain fixed in wavelength; the peaks which appear in the Raman spectra excited by 488.0 and 514.5nm laser radiation actually correspond to different sets of resonances. As was the case for resonances in fluorescence emission, a larger Raman enhancement occurs for lower ℓ resonances.
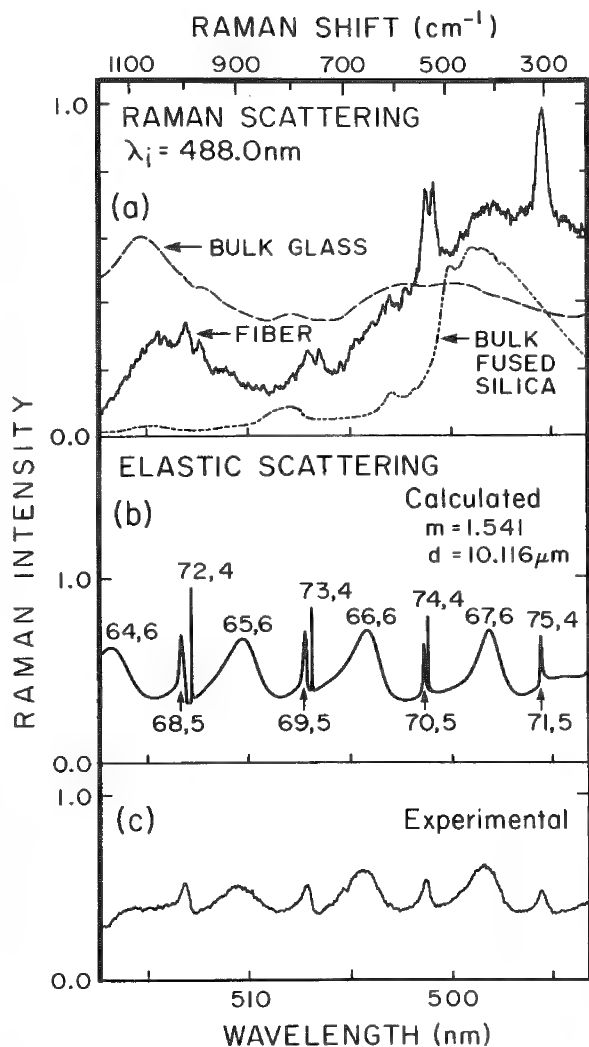
FIG. 3.—(a) Raman emission from a 10.1μm-diameter glass fiber (solid), a bulk glass sample of similar although not identical composition (long dashed), and a bulk fused silica sample (short dashed), with 488.0nm excitation. (b) Corresponding calculated elastic scattering spectrum. (c) Experimental elastic scattering spectrum from fiber.

FIG. 4.—Same as in Fig. 3 but with 514.5nm excitation of Raman emission.

Conclusions

Morphology-dependent resonances manifest themselves in elastic scattering, fluorescence emission, and Raman scattering from microparticles. For an incident wavelength that satisfies a resonance condition, the microparticle acts as a "receiving antenna," i.e., the intensity of the fields within the microparticle increase and the overall intensity of fluo-
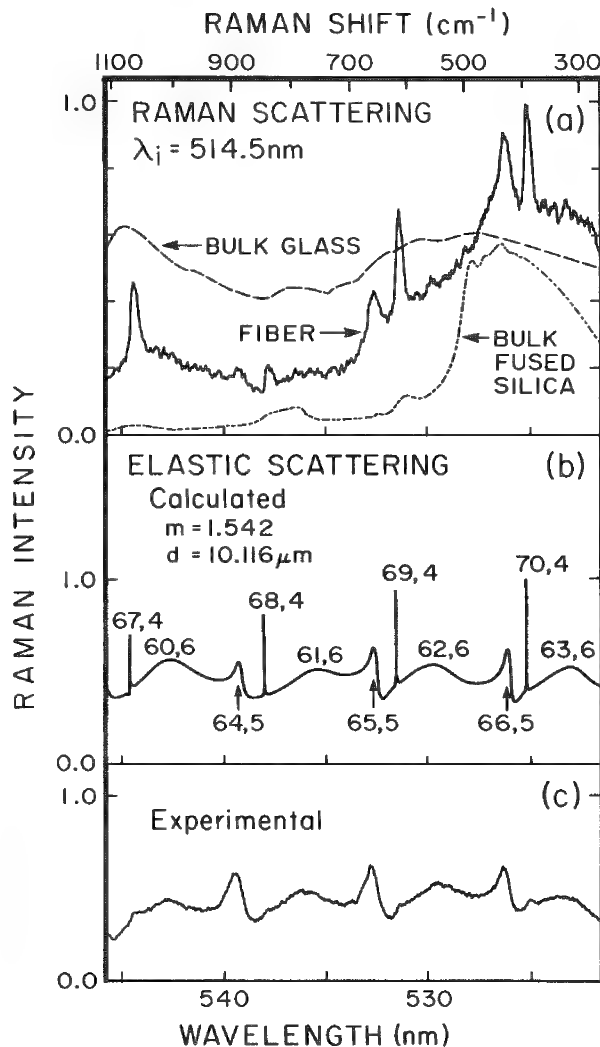
rescence or Raman emission is enhanced. Furthermore, a microparticle can act as a "transmitting antenna" for inelastic re-radiation at wavelengths that satisfy resonance conditions, and thus greatly increase the intensity of inelastic emission at the specific wavelengths. Such morphology-dependent resonances can greatly distort the lineshapes of Raman peaks with linewidths similar to the widths of the resonances or can add sharp structure to normally broad, featureless Raman lines.

In Raman spectroscopy of single microparticles, care must be taken not to identify erroneously peaks that result from resonance enhancements of a Raman line as fluorescence peaks superimposed on the Raman signal, since they remain fixed in wavelength, or to attribute sharp peaks which result from resonance enhancements of a fluorescence background to Raman scattering from discrete molecular vibrational modes. One relatively simple technique for determining whether or not a particle under investigation can support such resonances is to illuminate the particle with broadband radiation and analyze the elastically scattered radiation over the same wavelength range. Although the narrow, low-order resonances which cause the largest enhancement of inelastic emission are difficult to detect in elastic scattering, the presence of higher-order resonances in the elastic spectra should cause a spectroscopist to suspect that the inelastic spectra may also be influenced by resonances in the particle.

References

1. M. L. Wright and K. S. Krishnan, *Feasibility Study of in Situ Source Monitoring of Particulate Composition by Raman or Fluorescence Scatter*, Report EPA-R2-73-219, Washington, D.C.: Environmental Protection Administration, 1973.

2. R. G. Stafford, R. K. Chang, and P. J. Kindlmann, "Laser Raman monitoring of ambient sulfate aerosols," in *Methods and Standards for Environmental Measurement, Proc. 8th IMR Symposium*, Special Publication 464, Washington, D.C.: National Bureau of Standards, 1977, 659-667.

3. H. Chew, P. J. McNulty, and M. Kerker, "Model for Raman and fluorescent scattering by molecules embedded in small particles," *Phys. Rev.* A 13: 396-404, 1976.

4. D.-S. Wang, M. Kerker, and H. W. Chew, "Raman and fluorescent scattering by molecules embedded in dielectric spheroids," *Appl. Opt.* 14: 2315-2328, 1980; and references therein.

5. R. E. Benner, P. W. Barber, J. F. Owen, and R. K. Chang, "Observation of structure resonances in the fluorescence spectra from microspheres," *Phys. Rev. Lett.* 44: 475-478, 1980.

6. P. W. Barber, J. F. Owen, and R. K. Chang, "Resonant scattering for characterization of axisymmetric dielectric objects," *IEEE Trans.* AP-30: 168-172, 1982.

7. A. Ashkin and J. M. Dziedzic, "Observation of resonances in the radiation pressure on dielectric spheres," *Phys. Rev. Lett.* 38: 1351-1354, 1977.

8. P. Chýlek, J. T. Kiehl, and M. K. W. Ko, "Optical levitation and partial-wave resonances," *Phys. Rev.* A 18: 2229-2233, 1978.

9. G. J. Rosasco and H. S. Bennett, "Internal field resonance structure: Implications for optical absorption and scattering by microscopic particles," *J. Opt. Soc.* 68: 1242-1250, 1978.

10. J. F. Owen, R. K. Chang, and P. W. Barber, "Internal electric field distributions of a dielectric cylinder at resonance wavelengths," *Opt. Lett.* 6: 540-542, 1981.

11. J. F. Owen, P. W. Barber, P. B. Dorain, and R. K. Chang, "Enhancement of fluorescence induced by microstructure resonances of a dielectric fiber," *Phys. Rev. Lett.* 47: 1075-1078, 1981.

12. J. F. Owen, P. W. Barber, B. J. Messinger, and R. K. Chang, "Determination of optical fiber diameter from resonances in the elastic scattering spectrum," *Opt. Lett.* 6: 272-274, 1981.

13. M. Kerker, *The Scattering of Light and Other Electromagnetic Radiation*, New York: Academic Press, 1969.

14. J. F. Owen, R. K. Chang, and P. W. Barber, "Morphology-dependent resonances in Raman scattering, fluorescence emission, and elastic scattering from microparticles," submitted to *Aerosol Sci. Tech. J.*

INSTRUMENTATION AND RECENT APPLICATIONS IN MICRO RAMAN SPECTROSCOPY

P. Dhamelincourt

Over the past five years, there has been a growing interest in laboratories involved in spectrochemical analysis in regard to Raman measurements in the microscopic domain. So, in this paper, before presenting a limited number of recent applications, I shall present a brief review of instrumentation for micro-Raman spectroscopy and give some indication pertaining to the design of coupling optics between microscope and spectrometers that could be useful to workers who want to add micro-Raman capabilities to their conventional Raman spectrometers.

Review of Instrumentation for Micro-Raman Spectroscopy

Most of the laboratories throughout the world involved in micro-Raman spectroscopy use two types of specially designed instruments, which have been extensively reviewed in the literature.[1-5] One is the Raman microprobe developed at NBS for the analysis of micro-size particles, and the other is the Raman microprobe/microscope (MOLE) developed several years ago in our CNRS laboratory at the University of Lille. The MOLE instrument has been until recently commercialized by Instruments S.A., Inc., J.Y. Optical Systems Division. It is now superseded by a modular system, the Ramanor U-1000, in which a conventional macro-Raman spectrometer may be fitted with an optical microscope for micro-Raman measurements. A new generation of computerized instruments is at present being developed in close collaboration between our laboratory and a French company (DILOR, 244 ter rue des Bois Blancs, Lille) employing spectrographic dispersion with a very sensitive multichannel detector (intensified diode array) and an original system of sample exploration by the laser beam.[6] This instrument, commercially available under the name of MICROMARS (Microscope Optical Multichannel Raman Spectrometer), will be described in detail in another paper of this meeting.[7] A Raman microprobe prototype with multichannel optical detection has recently been built at NBS as well.[8]

Besides these specific instruments in which all parts have been chosen to obtain the very best in performance, a few attempts have been made in some laboratories to convert macro-Raman spectrometers (or spectrographs) into micro-Raman instruments by the addition of an optical microscope.[9-10] The idea may be excellent because it is the cheapest way for modest laboratories to perform micro-Raman experiments with their available Raman systems. But achieving this goal implies the design of a proper coupling optic between a microscope and the spectrometer (spectrograph).

Fundamentals and Practical Design of Coupling Optics Between Microscopes and Raman Spectrometers (Spectrographs)

The optimum use of Raman light flux collected from the sample implies that the "étendue" (throughput) of the scattered light beam should be maintained along the entire optical path from sample to detector. This can be done by an optic matching the apertures of the microscope optic and the spectrometer. In general, microscope optics are flat field and monochromators in spectrometers have a sufficiently low aperture for the Abbe sine condition (which is equivalent to the conservation of the "étendue" of the light beam) to be valid. The Abbe sine condition (Fig. 1) is expressed as

$$n \sin \mu_0 h = \sin \mu_0' h'$$

where n is the refractive index of the source-space medium, μ_0 is the half angle of collection for the objective, h is the size of the source, μ_0' is the half angle subtended by marginal rays entering the pupil of the monochromator, and h' is the size of the source image. Assuming that the monochromator aperture is low, one may write

$$\sin \mu_0' \simeq \mu_0' \simeq \frac{P}{2D}$$

where P is the effective size of the entrance pupil of the monochromator and D is the distance between pupil and slit. The Abbe condition may be then rewritten as

$$\frac{N.A.}{\gamma_0} < \tfrac{1}{2}\, \gamma \frac{P}{D}$$

where N.A. and γ_0 are the numerical aperture and the magnification factor of the microscope

FIG. 1.--Illustration of the parameters for calculation of coupling optics.

objective, respectively; γ is the magnification factor of the coupling optic. In this formula the inequality expresses that the pupil of the monochromator must not be overfilled by the light coming from the source. The P/D ratio, which is the monochromator aperture, is the instrumental constant; so it is clear that the magnification factor of the coupling optic is directly linked to the optical characteristics of the microscope objectives. Then there are several possibilities for matching microscopes and spectrometers which may be summarized as follows:

Design a variable-magnification optic adjustable for any particular objective mounted on the microscope turret.

Design as many interchangeable fixed-magnification optics as objectives mounted on the microscope turret.

Design a unique optic whose magnification will be adapted to a particular objective suitable for insuring both good spatial resolution and large Raman light collection. Generally this is a high-magnification high-N.A. objective. In this case other objectives mounted on the microscope turret will be chosen according to the N.A./γ restriction given above. (A choice of several N.A. is always proposed by objective manufacturers for any particular magnification.) The first possibility, which seems ideal, has a serious drawback because variable magnification optics are very complex and costly, and have generally a poor transmission factor (T $\simeq$ 0.6). Above all, they cannot be designed by nonopticians. The other two possibilities are far more useful. Fixed-magnification optics are easy to design (even by nonopticians) and have an excellent transmission factor (T > 0.9) when build with coated lenses. Several solutions of lens combinations are possible. The calculation of a simple three-lens coupling optic is given as an example. Parameters used for calculations are illustrated Fig. 1 and defined as follows: h is the size of the source (laser spot on the sample); P_0 is the size of the pupil of the objective (diameter of the pupil stop inside the objective); d is the optical distance between the stop and the magnified image of the sample given by the objective; P_1 is the size of an intermediate image of the pupil stop formed on L_2; h_0 and h' are the size of the source images, first given by the objective and second formed on the entrance slit by $L_1 - L_2$; F_1, F_2, F_3 are the focal lenghts of lenses L_1, L_2, and L_3, respectively; X is the distance between the pupil stop and L_1; X' and Y are the distances between $L_1 - L_2$ and $L_1 - L_3$, respectively; and Z is the distance between L_1 and a virtual image of the source formed by this lens.
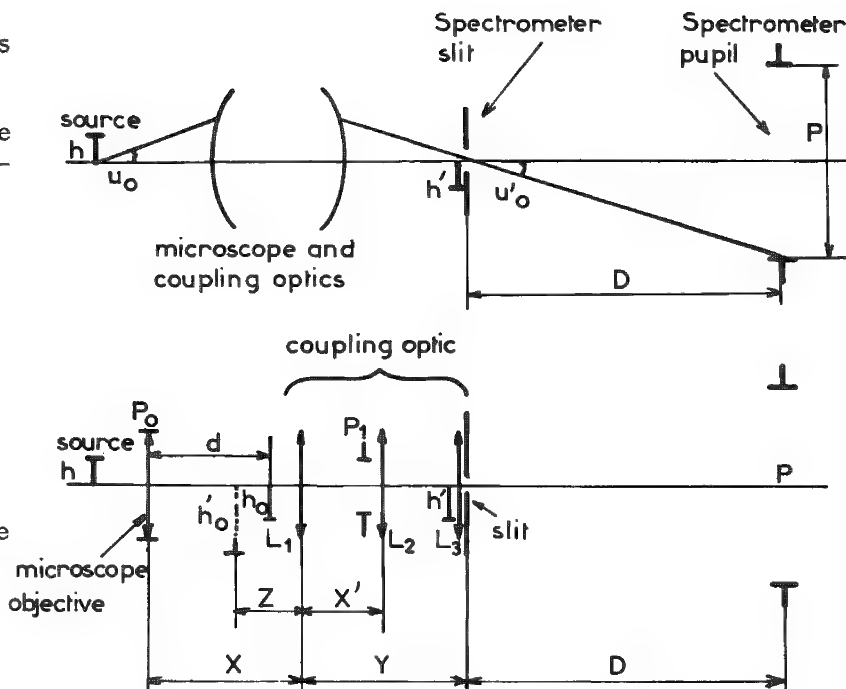
By use of coaxial lenses, equations that are valid in the image-space of the microscope objective can be written:

Lens L_1: $\dfrac{1}{X - d} - \dfrac{1}{Z} = \dfrac{1}{X} + \dfrac{1}{X'} = \dfrac{1}{F_1}$ and $P_1 = P_0 \dfrac{X'}{X}$

Lens L_2: $\dfrac{1}{Z + X'} + \dfrac{1}{Y - X'} = \dfrac{1}{F_2}$ and $\dfrac{Z}{X - d} \dfrac{Y - X'}{Z' + X'} = \dfrac{h'}{h_0}$

Lens L_3: $\dfrac{1}{Z + X'} + \dfrac{1}{D} = \dfrac{1}{F_3}$ and $\dfrac{D}{Y - X'} = \dfrac{P}{P_1}$

Combining all these formulas yields:

$$F_1 = \frac{XY}{(X + Y) + [P_0/(P/D)]}$$

$$F_2 = \frac{P_0{}^2 Y}{[X(P/D) + P_0]^2} \frac{P}{D} \frac{X}{P_0} + \frac{\alpha F_1}{F_1(\alpha + Y) - \alpha Y}$$

$$X' = \frac{(P/D)XY}{(P/D)X + P_0} \text{ and } \gamma = \frac{F_1 . Y}{(P/D)(X/P_0)[F_1(\alpha + Y) - \alpha Y] + \alpha F_1}$$

$$F_3 = \frac{Y}{(Y/D) + [(P/D)(X/P_0) + 1]}$$

where $\alpha = X - d$ represents the distance between the image of the source given by the objective and the field lens L_1. The distance α must not be equal to zero in order to avoid the focusing of fluorescence that may be emitted by the glass of the lens on the monochromator slit. A good value for α would be of the order of 10 to 20 mm (i.e., output of an ocular tube). The values of X and P_0 (which are generally not given in microscope specifications) may be easily determined by measurement of the size and position of the image of the objective pupil stop formed on a screen by a lens (whose focal length must be smaller than the microscope tube length) set up in place of L_1. The object must be a uniformly illuminated diffusing object (i.e., a piece of fine ground glass).

If we recall that X, P_0, d, P, and D are instrumental constants, we see that this coupling optic is entirely defined when the parameter Y (which is roughly the distance between the microscope output and the entrance slit of the monochromator) has been chosen.

With this optic, which rigourously couples objective and monochromator pupils, a large number of points may be simultaneously focused on the slit of the monochromator and analyzed without any loss of light. One may thus take advantage of a multichannel detector for obtaining rapidly Raman intensity profiles along a straight line across the sample and Raman image mapping by a "frame" scanning movement of the sample.

Applications of Micro-Raman and Microfluorescence Spectroscopy

We present here a few selected examples of investigations conducted with the MOLE microprobe in several areas of microanalysis.

Geology. Microthermometry--micro-Raman spectroscopy combination for analysis of fluid inclusions in minerals.

When a mineral forms it may trap in its defects small portions of the fluid phase from which it is growing. These fluid inclusions are real witnesses of the genesis of minerals because they have memorized composition and density of the original mixture. The knowledge of these two characteristics permits the geologist to retrace the chemistry and thermobarometric conditions of rock formation. In natural minerals, fluid inclusions are generally of the order of 1-100 μm. Hitherto, microthermometry was mainly the sole technique used by geochemists for fluid inclusion studies. It is based on the observation, under a microscope equipped with a cooling-heating stage, of the melting temperatures of solid phases and the equilibration temperatures of volatile fluids along with an estimation of their volume ratio. By use of the P, T, X (pressure, temperature, composition) thermodynamic curves corresponding to the entrapped system, microthermometry measurements permit the identification of fluids and the estimation of their chemical composition and thermo-

barometric conditions with respect to their formation. Yet these measurements are sometimes altered and the resulting misinterpretation of fluid-phase equilibria leads to incorrect conclusions about past rock formation events. Microthermometric measurements are generally altered by the presence of other unknown volatile fluids and the formation of gas hydrates in the course of cooling or heating samples. A great improvement has been provided by micro-Raman "in situ" measurements.[11-12] Such measurements in most cases permit the confirmation of microthermometric results, detection and estimate of the proportion of all fluids, and the identification of hydrates. Table 1 is a good example of the contribution of the micro-Raman technique in the study of the CO_2-CH_4-$NaCl$-H_2O system entrapped in metamorphic schists of the French Massif Central.[13] Microthermometry and micro-Raman measurements are perfectly consistent for inclusion 1 but inconsistent for inclusion 2, 3, and 4. Differing microthermometry results have been found to come from the uncertainty in the estimation of CO_2-CH_4 volume ratio for inclusion 2, from the presence of fluids other than CO_2, CH_4, H_2O for inclusion 3, and from the formation of a CO_2, CH_4 gas hydrate (evidenced by Raman) for inclusion 4. Sometimes unique information may be drawn only from Raman probe analysis, as illustrated by the following examples.

Both quantitative evaluation of free sulfate ion concentration in brine and direct identification of solid phases inside salt inclusions of the saliferous basin of French Lorraine have permitted a more precise definition, from thermodynamic calculations, of the geochemistry of ancient evaporating waters.[14]

TABLE 1.--Comparison of results obtained by microthermometry and micro-Raman spectroscopy for four complex carbonic inclusions (X: mole fraction of constituents).

CO_2-CH_4-$NaCl$-H_2O system	Microthermometry	Micro Raman Spectroscopy
INCLUSION N°1	$X_{CH_4} = 0.02$ $X_{CO_2} = 0.98$	$X_{CH_4} = 0.02$ $X_{CO_2} = 0.98$
INCLUSION N°2	$0.25 < X_{CH_4} < 0.5$ $0.5 < X_{CO_2} < 0.75$	$X_{CH_4} = 0.42$ $X_{CO_2} = 0.58$
INCLUSION N°3	$X_{CH_4} = 0.40$ $X_{CO_2} = 0.60$	$X_{CH_4} = 0.12$ $X_{CO_2} = 0.82$ $X_{C_2H_6} = 0.03$ $X_{N_2} = 0.03$
INCLUSION N°4	$X_{CH_4} = 0.50$ $X_{CO_2} = 0.50$	$X_{CH_4} = 0.05$ $X_{CO_2} = 0.95$

Free hydrogen, undetectable by microthermometry (Fig. 2), and free oxygen have been discovered inside fluid inclusions in quartzes from two precambrian uranium deposits (Rabbit Lake in Canada and Oklo in Gabon). This finding can be explained only by radiolysis of water. A close relationship has been found in Oklo uranium deposit between H_2-rich inclusions and natural nuclear reaction zones.[15]

So, although no panacea by itself, the micro-Raman technique is here and is now one of the most powerful tools available for fluid inclusion studies.

FIG. 2.--Raman microprobe spectrum of free H_2 inside one fluid inclusion within quartz host mineral from precambrian uranium deposits (Oklo, Gabon).

Studies of reactions at surfaces and interfaces by use of controlled atmosphere and temperature cells.[16] Controlled atmosphere and temperature cells are indispensable for the study of solid reactivity. With conventional Raman spectrometers such cells are often difficult to operate and become sources of trouble. When micro-Raman instruments incorporating a microscope are used, studies at different temperatures and under controlled (even corrosive) atmospheres become far easier when one employs commercially available or laboratory-made heating cells that fit directly onto the microscope stage. Moreover, these studies benefit from the high spatial resolution high sensitivity of micro-Raman instruments, as illustrated by the following examples.

Solid-phase reaction between MoO_3 and NiO (Fig. 3). The experiment has been performed under air in a commercial cell (Leitz 1350) with a grain of NiO (70 µm in linear dimension) included below the surface of a MoO_3 disk and heated to 550°C. The α $NiMoO_4$ phase was observed to form at the interface between NiO and MoO_3. When the system is cooled, the α-β $NiMoO_4$ phase transition has been observed.

Sulfidation by H_2S of an industrial Co-Mo-γAl_2O_3 hydrodesulfurization (HDS) catalyst (Fig. 4). The HDS catalysts generally have to be sulfided before they can be used in reactors, so that investigation of sulfidation is of great interest. Sulfidation was performed with a H_2-H_2S (10%) mixture at 320°C in a laboratory-made cell over only a few minutes. Then in situ Raman spectra were recorded at the same temperature. After the sulfiding treatment, the initial Raman characteristics of the sample in the oxide form[17] had completely disappeared and only two lines were evidenced. These lines are those of MoS_2 (Mo-S stretching modes) with a slight shift in wavenumber that is thought to be related to Ni or Co intercalation between MoS_2 layers. Another interesting thing is the time-dependent phenomenon, observed as a broad band around 570 cm^{-1} at the begining of sulfidation (Fig. 4a), which could be related to a deposited molybdenum oxysulfide or to polysulfide species.

Thiophene interaction with HDS catalysts (Fig. 5). Some experiments have been performed on various molybdenum-based HDS catalysts in various chemical states (precursor oxide, prereduced or presulfieded oxide). The main results are the following. When thio-
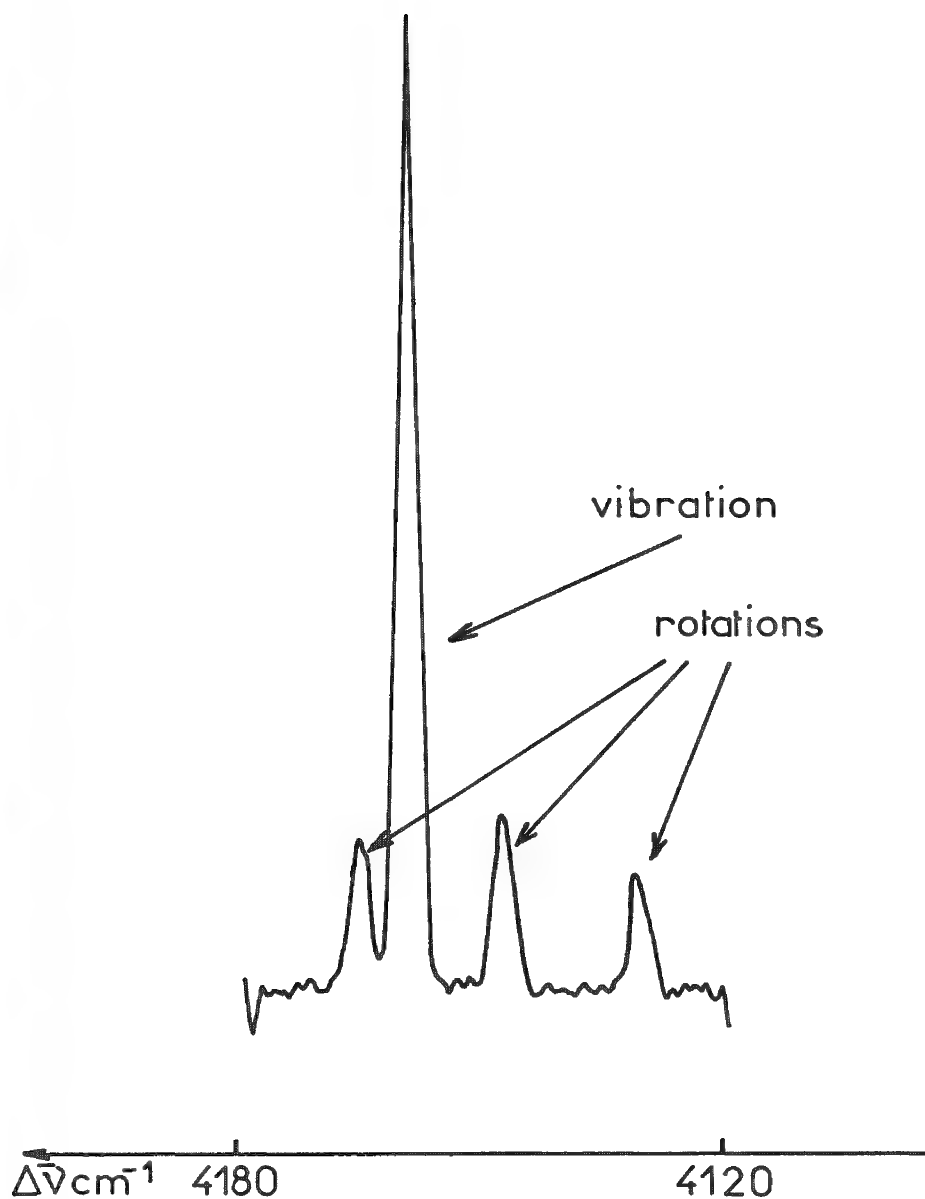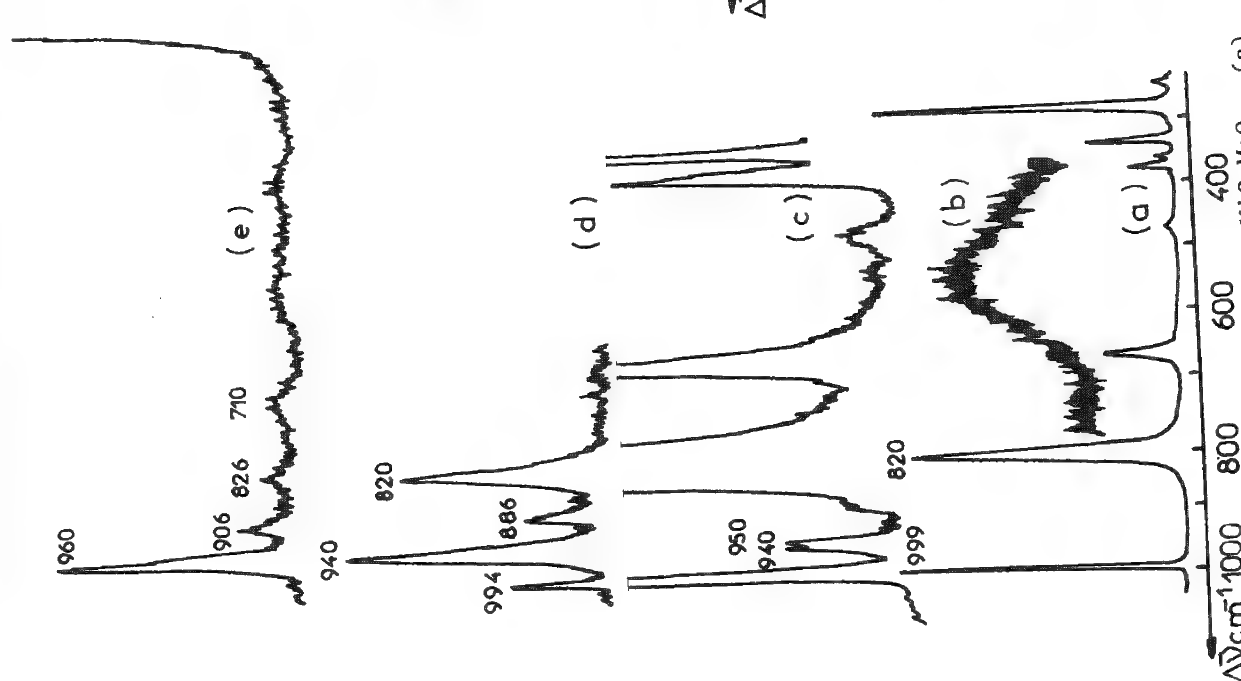
266

FIG. 3.--Solid phase reaction: NiO-MoO₃. (a) Pure MoO₃ at room temperature; (b) pure NiO at room temperature; (c) after reaction at 550°C (823°K) during a few minutes; (d) after reaction at 550°C during 1 hr: Raman spectrum corresponds to mixture of MoO₃ with αNiMoO₄; (e) after cooling at room temperature: Raman

FIG. 4.--Sulfidation of industrial HDS Co-Mo-γAl₂O₃ catalyst. (a) Spectrum recorded just after H₂-H₂S mixture admission; (b) subsequent recording.
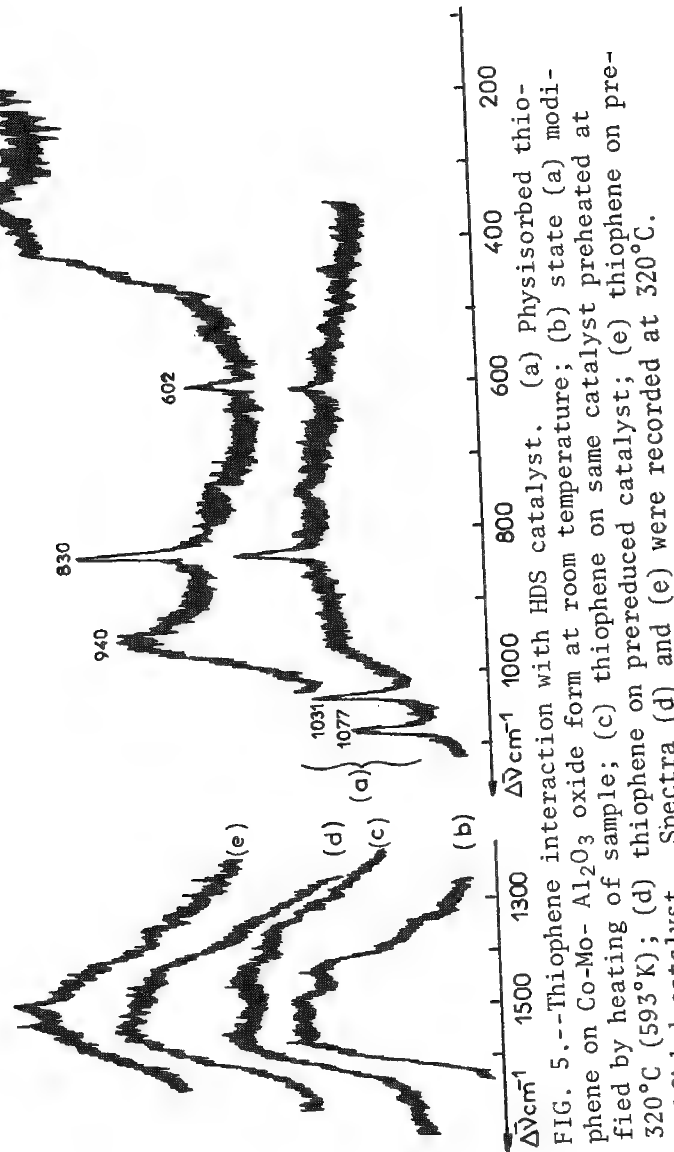
FIG. 5.--Thiophene interaction with HDS catalyst. (a) Physisorbed thiophene on Co-Mo- Al₂O₃ oxide form at room temperature; (b) state (a) modified by heating of sample; (c) thiophene on same catalyst preheated at 320°C (593°K); (d) thiophene on prereduced catalyst; (e) thiophene on prereduced catalyst. Spectra (d) and (e) were recorded at 320°C.

phene interacts with the oxide form at room temperature, Raman spectra are characteristic of physisorbed thiophene. Then the physisorbed state is strongly modified by heating as evident from the appearance of a broad band in the 1300-1600cm^{-1} range, which proves that physisorbed thiophene decomposes by heating into carbonaceous species strongly chemisorbed on the oxide form of the catalyst. When thiophene is introduced on catalysts that have been previously prereduced in the cell by H_2 at high temperature or on presulfided catalysts, evidences of physisorption are absent in Raman spectra recorded at room temperature, but when heated at 320°C these catalysts exhibit a Raman spectrum characteristic of carbonaceous species resulting from a nondetected, sorbed species. These results are consistent with XPS measurements carried out on the same samples where the S_{2p} signal is interpreted as originating from both chemisorbed thiophene and sulfidic species.

To conclude this part, this experimental approach (which couples a micro-Raman instrument with commercial or specially designed cells) has wide applicability in many domains such as corrosion problems, solid-gas, or solid-solid reaction studies.
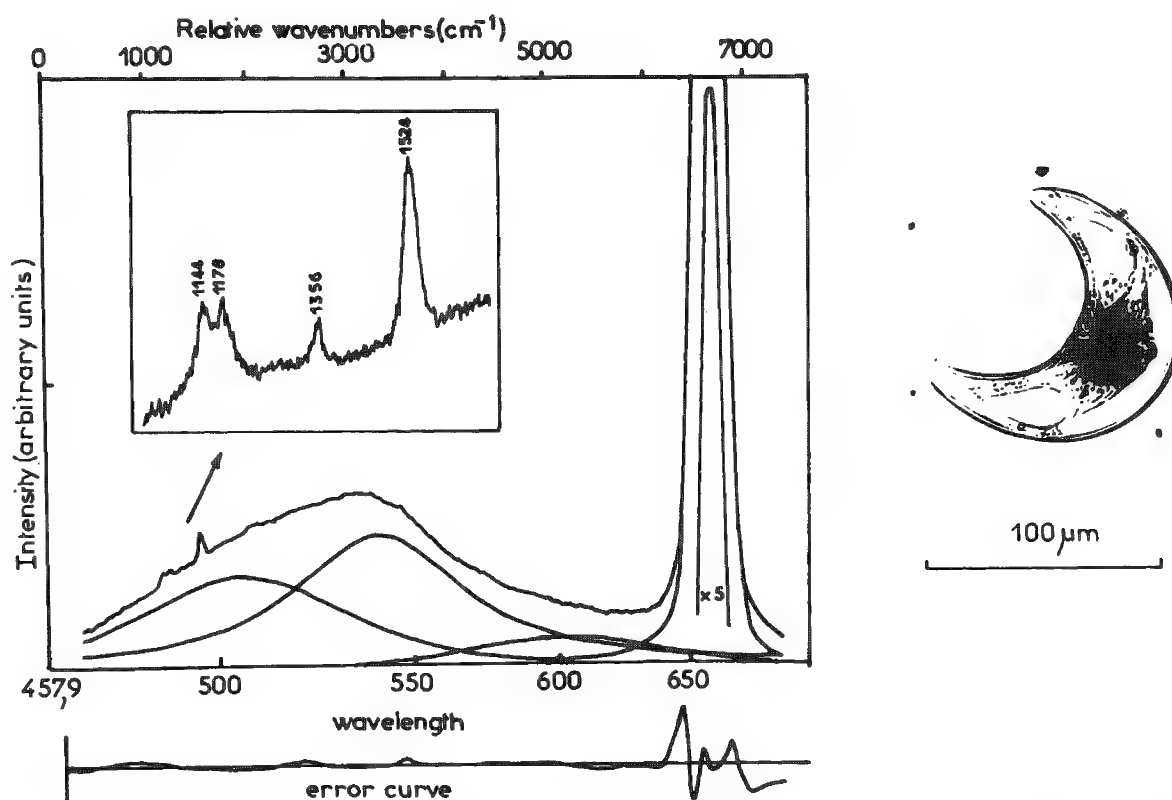

FIG. 6.--Left: In vivo fluorescence and resonance Raman spectra (frame insert) of single *Pyrocystis lunula* cell; excitation, 458 nm. Right: *Pyrocystis lunula*.

Biology. Past studies of biological samples with the MOLE have demonstrated in situ identification of purines in standard histological fixed thin sections of tissues from organs of various animals[18] and of particulates of pesticides in ciliated protozoa.[19] Another area of successful applications of the MOLE has been the study of fluorescence from living cells. A first example (Fig. 6) is the "in vivo" fluorescence spectrum obtained from the cytoplasm of a single microscopic bioluminescent algae, *Pyrocystis lunula*.[20] The spectrum exhibits three main bands which have been assigned to the chlorophyll (674 nm) and luciferin (518-542nm) fluorescence emissions. The resonance Raman spectrum of the peridinin carotenoid has been recorded, too. It gives information on the peridinin-chlorophyll-protein complex of the algae. By use of the image mode of the MOLE, fluorescence images corresponding to the chlorophyll and luciferin emissions have been compared to images of induced bioluminescence. They indicate that the photosynthetic apparatus and bioluminescence sources are located in the same region of the cell (central part of the cytoplasm). A second example is the study of intracellular fluorescence of a chemotherapeutic agent

267

(Adriamycin) from single leukemia cells. Whereas laser-flow cyto-metry has contributed to the intracellular detection, and quantitation of anthracyclines in whole-cell populations, very few attempts have been made at the single-cell level. The MOLE has been successfully employed to record nuclear and cytoplasmic fluorescence spectra in single cells isolated from the human erythroleukemia cell line K 562 and treated with Adriamycin (ADM).[21] Comparison between spectra of free and intracellular ADM (Fig. 7) clearly shows frequency and intensity modification (bathochromic effect and fluorescence quenching)--particularly in the nucleus--which are characteristic of the ADM interaction with DNA. This new spectroscopic approach may be extended to other anthracyclines or fluorochromes. The results could be useful in the scheduling of chemotherapy and would permit reduction or minimization of the toxicity to normal tissues.
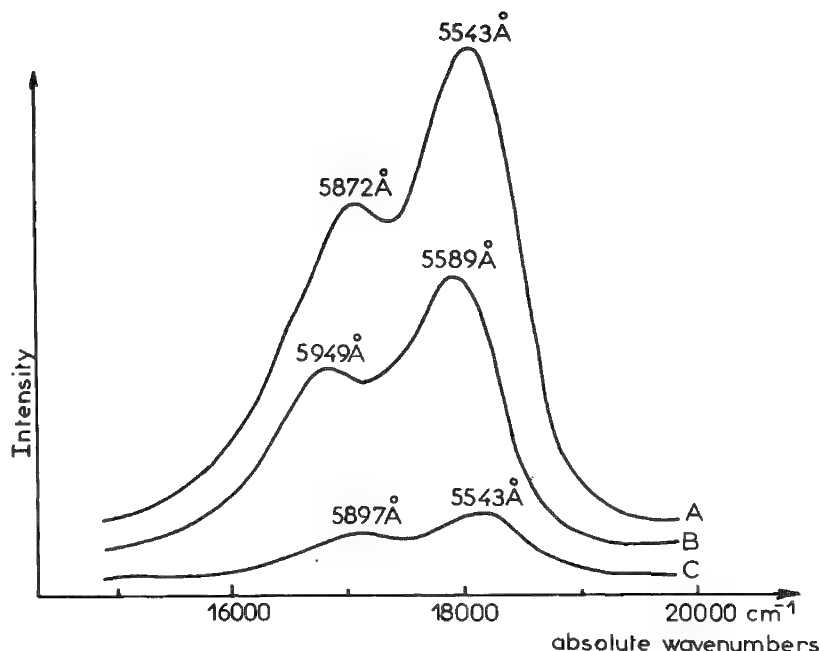

FIG. 7.--Fluorescence spectra of Adryamycin (ADM). (a) Free ADM; (b) in nucleus; (c) in cytoplasm of single leukemia cell. Excitation, 458 nm.

References

1. P. Dhamelincourt, "Developments and applications of the MOLE laser microprobe," *Microbeam Analysis--1979*, 155-164.

2. P. Dhamelincourt et al., "Raman molecular microprobe (MOLE)," *Anal. Chem.* 51: 414A-421A, 1979.

3. G. J. Rosasco, "Raman microprobe spectroscopy," in R. J. H. Clark and R. E. Hester, Eds., *Advances in Infrared and Raman Spectroscopy*, London: Heyden, 1980, vol. 7 (Chap. 4), 223-282.

4. E. S. Etz and J. J. Blaha, "Scope and limitations of single particle analysis by Raman microprobe spectroscopy," in K. F. J. Heinrich, Ed., *Characterization of Particles*, Proc. 13th Annual Conference of Microbeam Analysis, NBS Special Publication 533, Washington, D.C., 1980, 153-197.

5. F. Adar, "Developments in Raman microanalysis," *Microbeam Analysis--1981*, 67-73.

6. M. Delhaye et al., "Dispositif optimisant le couplage de deux systèmes optiques pour l'observation et l'analyse d'objets," *French Patent* application 812 332, 1981.

7. M. Delhaye et al., "A new generation of laser micro-Raman Spectrometers: MICROMARS," *Microbeam Analysis--1982*, 275.

8. E. S. Etz, "New Raman microprobe with multichannel optical detector," *Dimensions/ NBS* 64: 16-17 1982.

9. B. W. Cook and J. D. Louden, "A 180° microscope sampling and viewing attachment for a laser Raman spectrometer," *J. Raman Spectrosc.* 8: 249-250, 1979.

10. R. E. Hester, "Raman microprobe lab well established," *European Spectroscopy News* 38: 8, 1981.

11. P. Dhamelincourt et al., "Analyse d'inclusions fluides à la microsonde MOLE à effet Raman," *Bull. Mineral.* 102: 600-610, 1979.

12. N. Guilhaumou et al., "Etude des inclusions fluides du système N_2-CO_2 de dolomites et de quartz de Tunisie septentrionale: Données de la microcryoscopie et de l'analyse à la microsonde à effet Raman," *Geochim. Cosmochim. Acta.* 45: 657-673, 1981.

13. C. C. Ramboz and J. M. Beny, "Quantitative analysis of complex carbonic fluid inclusion by laser Raman microprobe and microthermometry: Geological implications," submitted

to *Contrib. Mineral. Petrol*, 1982.

14. J. Dubessy et al., "The determination of sulphate in fluid inclusions with the Raman microprobe MOLE: Applications to a keuper halite and geochemical consequences," submitted to *Geochim. Cosmochim. Acta.*, 1981.

15. J. Dubessy et al., "Evidence by Raman spectroscopy of free hydrogen and free oxygen in fluid inclusions from two uranium deposits," *Abstracts of the 12th Meeting of International Mineralogical Association*, Orléans, France, 1980.

16. E. Payen et al., "Study of Co (or Ni)-Mo oxide phase transformation and hydrodesulfurization catalysts by Raman microprobe equipped with new cells," *Appl. Spectrosc.* 36: 30-37, 1982.

17. P. Dufresne et al., "Study of Ni-Mo-γAl_2O_3 catalysts by x-ray photoelectron and Raman spectroscopy: Comparison with Co-Mo-γAl_2O_3 catalysts," *J. Phys. Chem.* 85: 2344-2351, 1981.

18. C. Ballan-Dufrancais et al., "Interest of Raman laser microprobe (MOLE) for the identification of purinic concretions in histological sections," *Biol. Cell.* 36: 51-58, 1979.

19. M. Delhaye et al., "Analysis of particulates by Raman microprobe," *Toxicol. Environ. Chem. Rev.* 3: 73-87, 1979.

20. A. Dupaix et al., "Intracellular spectroscopic studies of a bioluminescent cell: *Pyrocystis lunula,*" *Biol. of the Cell*, in press, 1982.

21. P. Jeannesson et al., "Intracellular fluorescence spectra of Adriamycin (ADM) at the single cell level," *Abstracts of the UICC Conference on Clinical Oncology.*, Lausanne, Switzerland, 1981.

THE LAWRENCE LIVERMORE NATIONAL LABORATORY RAMAN MICROPROBE

F. P. Milanovich, Tomas Hirschfeld, and D. C. Johnson

The current applications of Raman microtechniques are the outgrowth of pioneering feasibility studies by Delhaye[1] and Hirschfeld.[2] These studies have resulted in several independently developed Raman microprobes such as those at the National Bureau of Standards (NBS)[3] and the University of Lille in France,[4] as well as commercially available Raman microprobes.[5,6] Hirschfeld recently reviewed the technologies related to optical microtechniques and presented a design for an optimally sensitive Raman microprobe.[7] With this design and mindful of specific Lawrence Livermore National Laboratory (LLNL) research needs in biomedical and environmental research, laser fusion, and weapons development, we have designed and constructed a Raman microprobe. Here we describe this LLNL microprobe and present examples of its capabilities.

Instrumentation

Microprobe. The LLNL Raman microprobe is shown in Fig. 1. The dedicated illumination sources are a Spectra-Physics Model 165 Ar-ion laser and a Spectra-Physics Model 171 Kr-ion laser. These sources were chosen for their ease of operation, stability, reliability, and multiplicity of laser wavelengths. Several other lasers, pulsed-dye and UV, are available on an intermittent basis.

The laser output is guided by a series of beam-directing mirrors to a spatial-filter beam-expander. The expanded beam is then turned at right angles by a Pellin-Broca prism and focused by a 400mm achromatic lens to a 100 µm pinhole. This pinhole and the spatial-filter serve as excellent fiducial marks for day-to-day reproducibility of laser beam location. After passing through the final pinhole, the expanding beam is tightly focused onto the sample stage by a reflecting objective (illuminator).

The collected Raman signal is passed from the illuminator at f/8 to an Instrument SA model DL-203 spectrograph. The prefilter stage of the DL-203, which is designed for high stray-light rejection, can be replaced by a high-throughput notch-filter assembly for applications where stray light is not a problem. The wavelength-dispersed Raman signal is then focused onto the photocathode of a PAR model 1254 intensified vidicon camera. The camera is housed in a PAR 1212 dry-ice-cooled housing. The prefilter, spectrograph, and camera with housing are mounted on an X-Y-Z adjustable platform. The platform is supported at three positions by air-cushioned legs that allow microadjustment of the light detecting assembly relative to the illuminator.

Illuminator. A cross section of the LLNL Raman microprobe illuminator is shown in Fig. 2. The expanding light from the 400mm achromatic lens (1) and pinhole assembly (2)
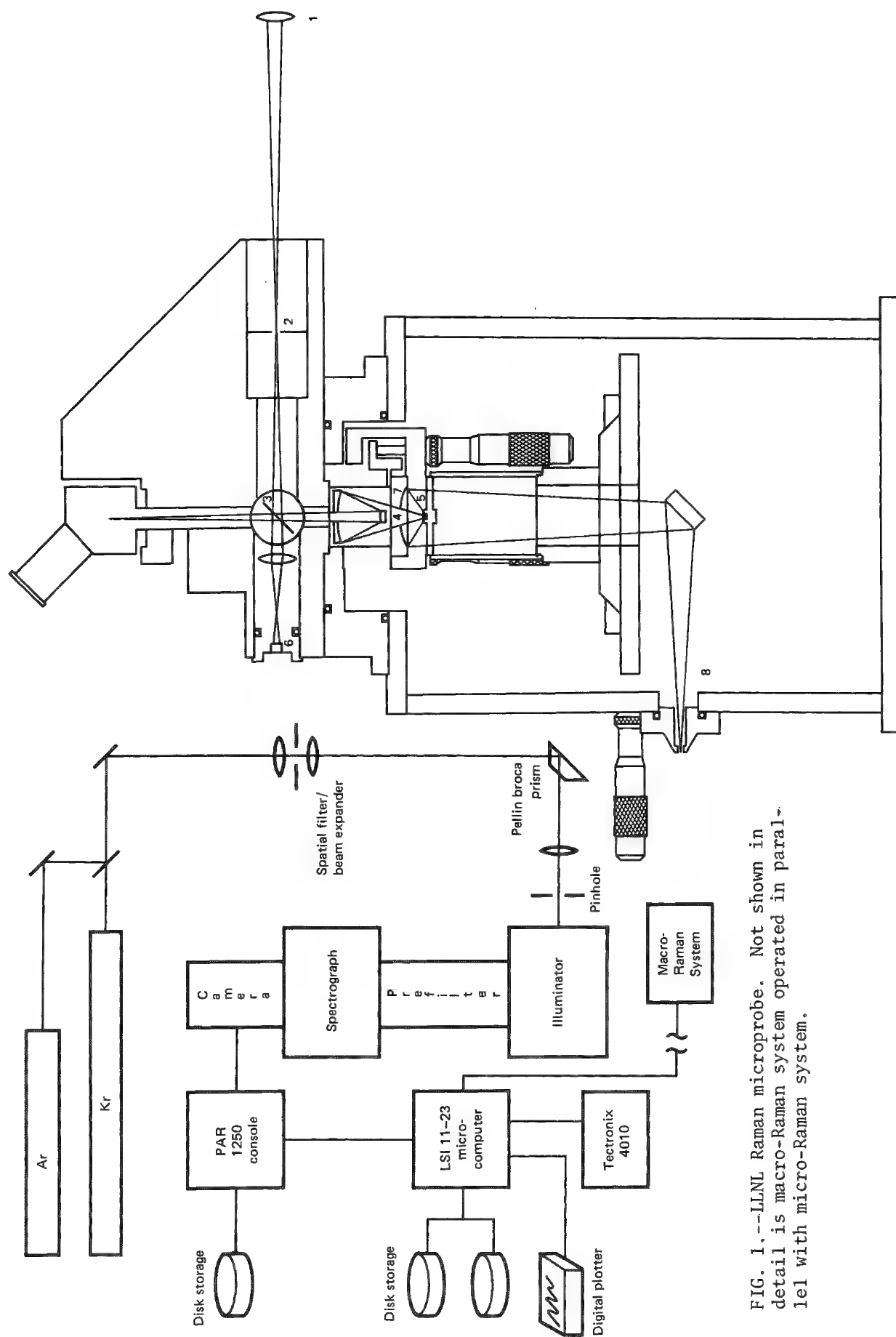
FIG. 1.--LLNL Raman microprobe. Not shown in detail is macro-Raman system operated in parallel with micro-Raman system.

FIG. 2.--Schematic of illuminator. Numbered components are disussed in text.

271

is directed via a beam splitter (3) to a Beck Model X-15 reflecting objective with a numerical aperture of 0.28. The objective directs the light through a hole in an ellipsoidal collecting mirror (4) where it is then tightly focused on the sample stage (5). The stage is of a conventional spider-like design with three course and three fine X-Y-Z adjustments. The light passing through the beam splitter is directed onto a photodiode (6) to monitor the input beam power.

The principal component of the illuminator is the ellipsoidal collection mirror (7). The ellipsoid has a primary focus of 18 mm, secondary focus of 332 mm, and a 2.94 teradian collection area. This configuration yields a convergence angle at the non-polarizing magic angle of 60.9°.[8]

A swing-away beam splitter and penlight assembly (8) provides sample-stage illumination by back illuminating the sample in the collecting ellipsoid. In addition, light from the beam splitter is directed into the DL-203 for intensity calibration. The penlight is operated under-voltage for extended lifetime and has been calibrated against an NBS intensity standard.

The illuminator has been designed for vacuum operation.

Operation

The light-detecting element of the LLNL Raman microprobe is the silicon-intensified target (SIT) of a PAR Model 1254 detector head, which is controlled by a PAR OMA 2 Model 1250 console. The operating principle of these multichannel detectors has been described,[9] and recent comparison of OMA sensitivity with photon counting has been performed.[10]

The detection system gives the experimenter a day-to-day, if not run-to-run, maintenance problem--that of intensity and wavelength calibration. To enhance our ability to perform these calibrations, we have added computer capabilities in parallel with the PAR OMA 1250 console (see Fig. 1). The computer is an LSI 11-23 controlled from a Tektronix 4010 keyboard. The computer is driven by LLNL-developed software that gives an expanded format for data storage over the PAR 1250 and an increased capacity to perform mathematical operations with the data. In addition, the LSI 11-23 operating in series with a Tektronix 4051 microcomputer also provides data basing and manipulation for a separate macro-Raman system. This configuration gives the added benefit of being able to handle data from both a macro- and micro-Raman system with the same software.

In a typical operation, a spectrum is first acquired by the PAR 1250 console. If necessary, wavelength and/or intensity calibrations are then performed and this information, including the original spectrum, is transferred to the LSI 11-23. The data are consequently stored in two locations, which provides a convenient backup.

The wavelength calibration is routinely performed by obtaining the spectrum of a macroscopic particle of naphthalene (~100 μm), shown in Figure 3(a). Naphthalene is chosen for its ready availability; ease of handling; and well-spaced, narrow Raman lines. The known location of the Raman shifts are then utilized in the PAR 1250 software to calibrate the 500-channel wavelength axis of the SIT.

Figures 3(a) and (b) give excellent examples of the instrument's capability. The spectrum of Fig. 3(a), which is of a 70μm naphthalene particle, was taken with 12s illumination at 2 mW and 514.5 nm. Figure 3(b) is a spectrum of a micro-naphthalene particle (~10 μm) acquired under ambient conditions. The particle sublimed in a very short time.[11] However, the light-gathering capabilities of the illuminator and multichannel nature of the detector yielded a discernible naphathalene spectrum.

Application

The first application of the LLNL Raman microprobe was a weapons program problem concerning the explosive pentaerythritol tetranitrate (PETN), which has long been a widely used secondary explosive. Its popularity is in part attributable to its high chemical stability, which allows manufacturing and handling with comparative safety.

Recently, a significant reliability decrease was noted in PETN-filled detonators that were exposed to high temperatures. In an attempt to gain an understanding of this decrease, various analytical determinations were performed on the heated PETN. Elemental analysis indicated no major impurities or compositional variations outside the interbatch fluctuations typical of PETN preparations. This fact indicated the possibility of subtle
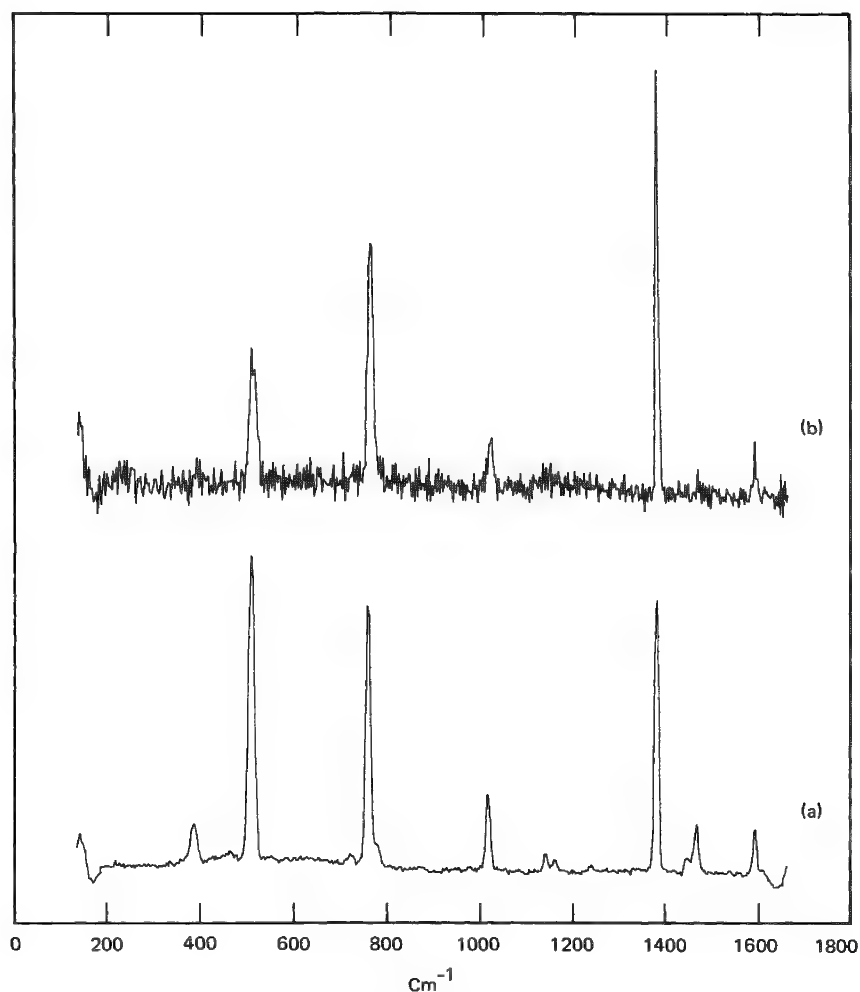
FIG. 3.--Raman spectra of micro- and macro-naphthalene particles taken with LLNL Raman microprobe. Measurement parameters: (a) particle size, 70 μm; laser power, 2 mW; laser wavelength, 514.5 nm; prefilter bandpass, 40 nm; slit width, 167 μm; (b) particle size, 10 μm; laser power, 500 μW; other parameters idential to (a).

structural differences, since it is known that crystal-strain reductions reduce sensitivity in the explosive.

The PETN is presumed stable below 140°C as a non-hygroscopic, crystalline solid (alpha-PETN). The crystals are uniaxial with a tretragonal unit cell of nominal dimensions $\alpha = 9.3$ Å and $c = 6.7$ Å. Qualitative information is available on the existence of polymorphs of this structure. The principal one, beta-PETN, is observed on heating to 130 to 140°C. It is presumed to revert completely to alpha-PETN on cooling.

Initially, two spectroscopic techniques were applied in structural studies of the heated PETN--x-ray diffraction and Fourier transform IR (FTIR). The x-ray diffraction studies showed a barely detectable line narrowing. The FTIR was more successful.[12] Comparisons of spectra of heated and unheated PETN showed no changes in peak location; however, several peaks were shown to have significant intensity differences (heated versus unheated). The similarity of spectral peak locations indicated no difference in composition, whereas the variation in their intensities indicated local symmetry changes such as crystallinity, crystal defect levels, stress, strain, etc.

The FTIR data were obtained on the bulk material. A better understanding of the nature of these postulated structural differences could be obtained by complementary microanalysis of PETN crystals. This analysis was performed with the Raman microprobe. Figure 4(a) shows the Raman spectrum of the heated PETN taken with a macro-Raman system and Fig. 4(b) shows the Raman spectrum of an individual crystallite taken with the Raman microprobe. A particle-by-particle analysis showed one recurring major spectral difference (Fig. 4c). The 594 cm^{-1} is strongly enhanced along with the fluorescence background. Attempts to produce this spectral change by methodical increases in laser intensity on native particles were unsuccessful.

This difference is well in excess of reproducibility differences for a given particle, yet reflect no major compositional change because no peaks disappear nor are any of them missing. Analogous to the FTIR data, changes in crystalline structure are suggested, but they are now shown to be microscopically heterogeneous. This finding indicates that the degradation mechanism cannot be a simple bulk one, but must reflect either a macroscale stochastic mechanism or be influenced by a much smaller initial sample heterogeneity on a crystal-by-crystal basis.

References

1. M. Delhaye and M. Migeon, "Intérêt de la concentration d'un faisceau laser pour l'excitation de l'effet Raman," *C. r. Acad. Sci. Paris* 262(B): 1513-1516, 1966.

2. T. Hirschfeld, "Raman microprobe: Vibrational spectroscopy in the femtogram range," *J. Opt. Soc. Am.* 63: 476-477, 1973.

3. G. J. Rosasco and E. S. Etz, "The Raman microprobe: a new analytical tool," *Res. Dev.* 28: 20-35, 1977.

4. M. Delhaye and P. Chamelincourt, "Raman microprobe and microscope with excitation," *J. Raman Spectrosc.* 3: 33-43, 1975.

5. P. Dhamelincourt et al., "Laser Raman molecular microprobe (MOLE)," *Anal. Chem.* 51: 414A-421A, 1979.

6. SPEX Industries, Inc. "Macro Info from Micro Samples," *SPEX Speaker* 26(2): 1-5, 1981.

7. T. Hirschfeld, "Design considerations in a micro-Raman spectrometer," *Microbeam Analysis--1979*, 196.

8. T. Hirschfeld, Lawrence Livermore National Laboratory, Livermore, Calif., private communication, 1973.

9. Y. Talmi, "TV-type multi-channel detectros," *Anal. Chem.* 47: 697A-709A, 1975.

10. J. J. Freeman et al., "Raman spectroscopy with high sensitivity," *Appl. Spectrosc.* 35: 196-202, 1981.

11. M. E. Anderson and R. Z. Muggli, "Microscopical techniques with the molecular optics laser examiner Raman microprobe," *Anal. Chem.* 53: 1772-1777, 1981.

12. T. Hirschfeld, Lawrence Livermore National Laboratory, Livermore, Calif., private communication, 1981.
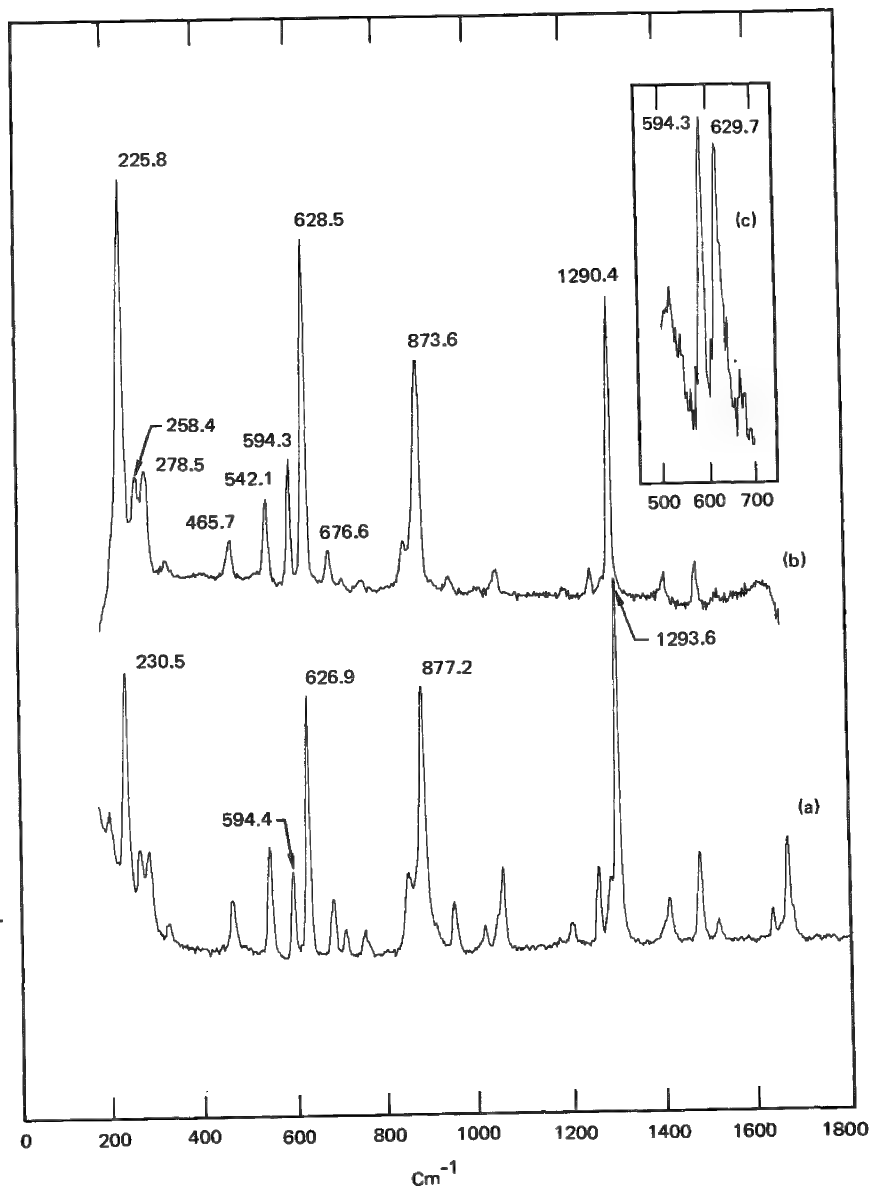
FIG. 4.--(a) Macro; (b),(c) micro Raman spectra of PETN. Measurement parameters: (a) laser power, 200 mW; laser wavelength, 514.5 nm; resolution, 6 cm^{-1}; scan time, 16 min; time constant, 3s; (b) and (c) particle size, 8-μm nominal; later power, 4 mW; slit width, 167 μm; prefilter bandpass, 40 nm; integration time, 24 s.

A NEW GENERATION OF LASER RAMAN MICROSPECTROMETERS: MICROMARS

M. Delhaye, M. Bridoux, P. Dhamelincourt, J. Barbillat,
E. Da Silva, and B. Roussel.

Various applications of Raman microspectrophotometry and microprobing have been developed during the past decade. The experimental setups used in the first generation of Raman microprobes essentially benefit from the advantage of focusing of the laser beam to a small area of the observed sample and collecting the scattered light by a large-aperture optic. Most spectra have been recorded by means of conventional optical monochromator/photomultiplier instrumentation. The Raman lines are thus recorded sequentially by scanning of the spectrum.

A second generation of micro-Raman instruments has been recently proposed, which profits from the advantages of the so called "multichannel" photodetectors to measure simultaneously a large number of spectral elements.

Since the early stage of "multichannel" Raman detection, pioneered by some of us twenty years ago, we have been able to use and to compare a variety of image intensifiers, low level television cameras, phototubes, and solid-state photodetectors. After having evaluated the capabilities of such detectors for time-resolved and space-resolved Raman spectrometry, we decided to work in close collaboration to create a new instrument, now commercially available and called MICROMARS.

The study and realization of this new instrument has been based on the following principles.

● The available photodiode arrays offer the best compromise for sensitivity, wide dynamic range, geometrical stability, signal handling, and treatment.
● The whole optical system has to be designed to fit the multichannel photodetector.
● Attention must be paid to the optimization of the coupling optics, from the sample to the detector, so that the full benefit from the "multichannel" advantage is derived, both for spatial resolution and spectral requirements.
● All mechanical motions, spectral parameters, and signal treatments must be computerized or computer controlled.

Multichannel Detector

Two detectors are used (1) a linear photodiode array (Reticon 1024 elements) with a quartz window, covering the spectral range 200 to 1000 nm; and (2) an intensified detector made by coupling-- by means of optic fibers-- an image intensifier (LEP proximity-focused microchannel plate intensifier) to a Reticon 512-element photodiode array). The spectral range is limited to 400-850 nm but the overall gain enables single-photon detection.

The whole detector head, filled with argon and sealed, is cooled to -28°C by Peltier elements. A part of the electronic circuit, comprising the FET low-noise preamplifiers and control, is included in the head. To avoid extra noise, this unit is powered by CdNi batteries.

The rest of the electronics is rack-mounted in a console: Gauss filter, sampling, multiplexing A/D converter (12 bits, 5 µs), and control logic.

The signal output (TTL, 12 bits coded) is compatible with a fast HP-1000L computer.

A built-in data-treatment arithmetic unit with two 1K memories can store signal and background and perform background substraction, with either a TTL output at slow rate (100 µs to 10 ms per step) or an analog output to the strip chart recorder.

The first four authors are at the Laboratoire de Spectrochimie Infrarouge et Raman CNRS, Université de Lille, C.5, 59655 Villeneuve d'Ascq Cedex, France; the last two, at DILOR, 244 ter rue des Bois Blancs, 59000 Lille, France.

FIG. 1.--Optical diagram of MICROMARS spectrometer:

Rm₁ Rm₂ Rm₃ Rm₄ = rotating arms
PM - photomultiplier for single-channel detection
G₁ G₂ G₃ G₄ - plane holographic gratings
S₁ S₂ S'₂ S₃ - spectrometer slits.

T = 1500 s

Single channel (photomultiplier)

ASPIRIN
λ = 488NM, 100MW

T = 10 s

Multichannel detection

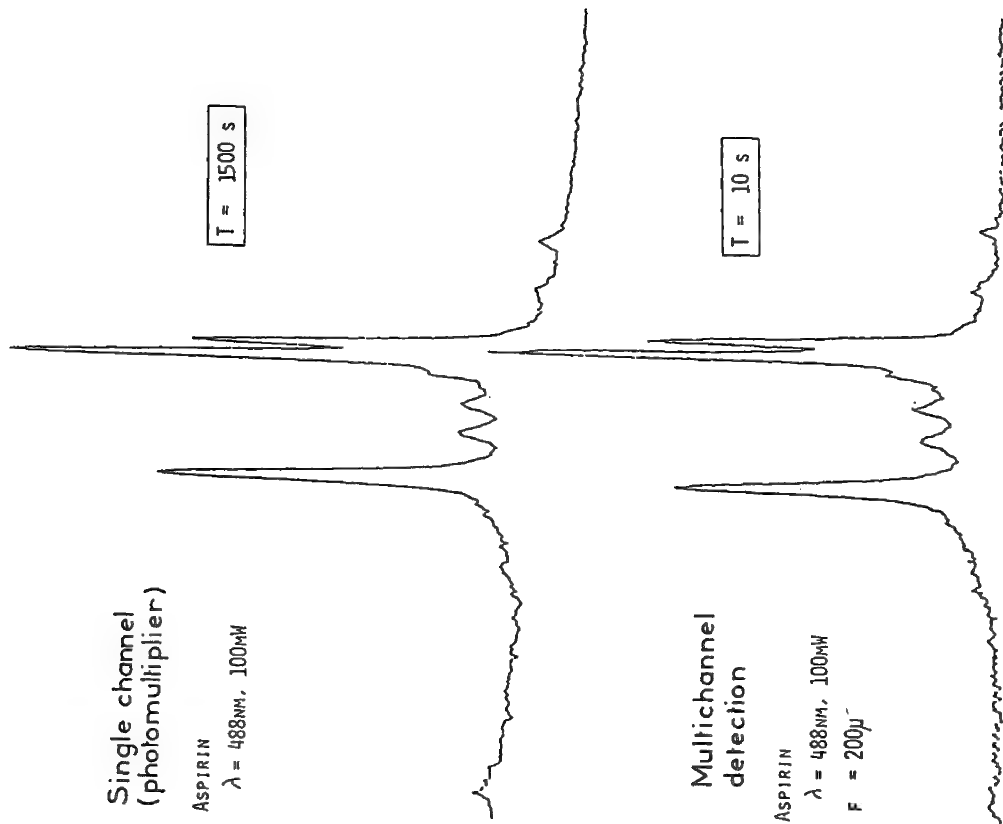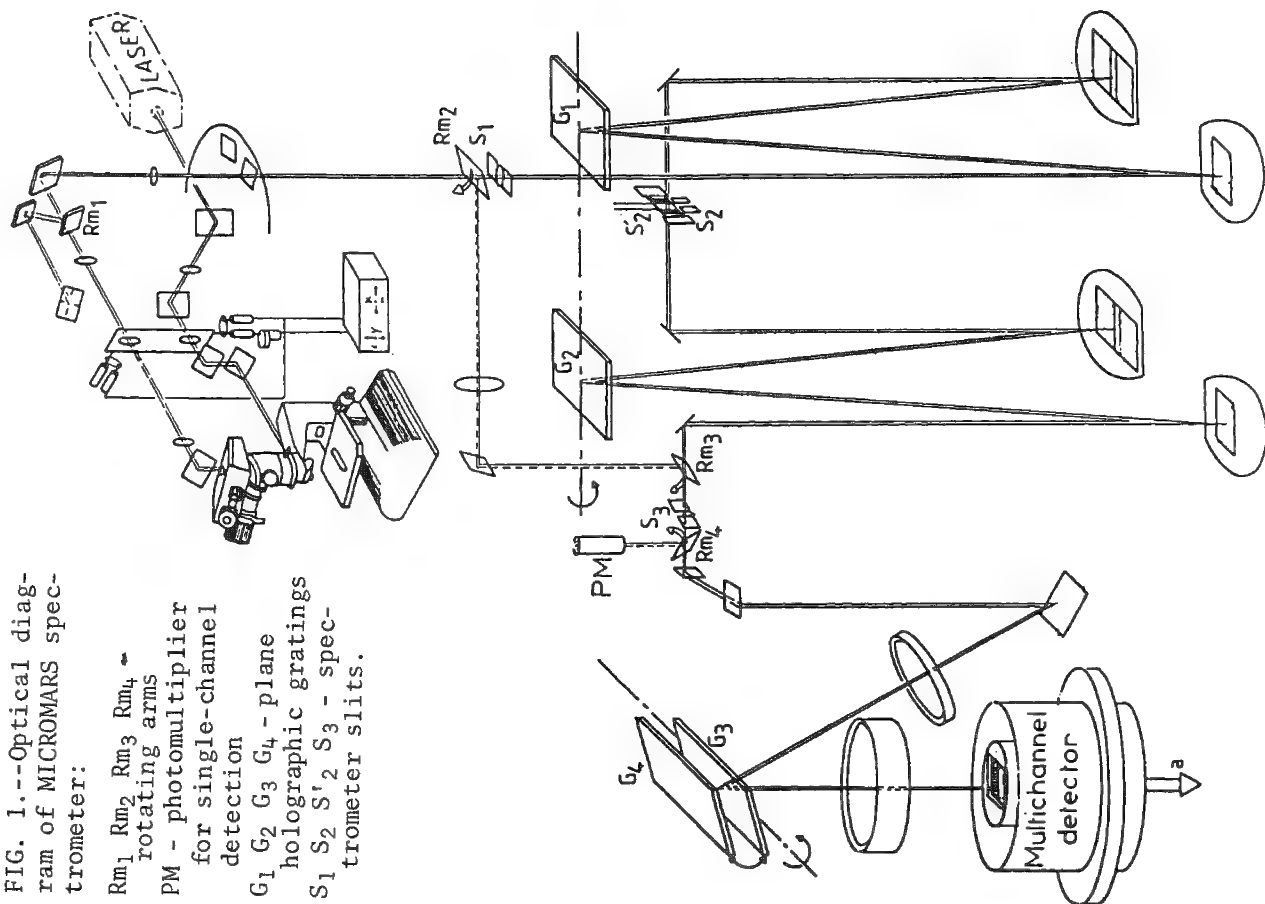ASPIRIN
λ = 488NM, 100MW
F = 200μʳ

FIG. 2.--Comparison of the Raman spectra recorded with same optics by single-channel and multichannel photodetection.

The time of integration varies from 20 to 990 ms by 10ms steps or from 1 to 99 s by 15 steps.

Microscope and Spectrometer Optics (Fig. 1)

The MICROMARS is normally supplied with an Olympus microscope, compatible with a large number of accessories, illuminators, and objectives. Visual observation of the microscopic images is complemented by a built-in color TV system coupled with a special safety filtering device that eliminates any risk when laser illumination of the sample is used. This device is compatible with white-light illumination to insure a precise location of the laser probe with a sharp focus on the observed area of the sample.

A new kind of transfer optics is placed between the microscope and the spectrometer, which enables optimized coupling. The sample is not moved under the microscope objective; instead, it is explored by the motion (actuated by a motor-driven, computer-controlled scanner) of a couple of intermediate lenses, the one deflecting the laser spot over the whole field of the microscope, the other compensating for deviation of the image of the probed area to bring it to the entrance slit of the spectrometer. A fixed sample can thus be analyzed with high accuracy over a wide field, an optical arrangement that has proved to be most convenient for a variety of cumbersome samples (cryostat, variable-temperature or -pressure cells, pieces of art, or industrial materials).

The spectrometer itself comprises a zero-dispersion, double holographic grating foremonochromator, followed by a grating spectrograph. The intermediate slit of the foremonochromator is adjustable to determine the bandpass corresponding to the spectral region covering the multichannel detector. All the mechanical motions of the slits, gratings, and mirrors are driven by stepping motors and are computer controlled.

In addition to multichannel detection, the same dispersing spectrometer can be converted to a low-stray-light monochromator, with a photomultiplier to record Raman spectra by the conventional scanning technique. The capability to analyze the same sample by either single-channel or multichannel photodetectors has permitted a comprehensive comparison of the inherent advantages and limitations of both techniques (Fig. 2).

Applications

As an example of the gain in sensitivity routinely obtained, the spectrum shown in Fig. 3 exhibits the well-known Raman bands of powdered graphite, observed with a 100× microscope objective. It is worth noting that the laser beam power is limited to 8 mW, and the Raman light has been attenuated to 1% by a neutral-density filter of OD = 2. This artificial attenuation serves as a good calibrated test of performance for very weak Raman signals.
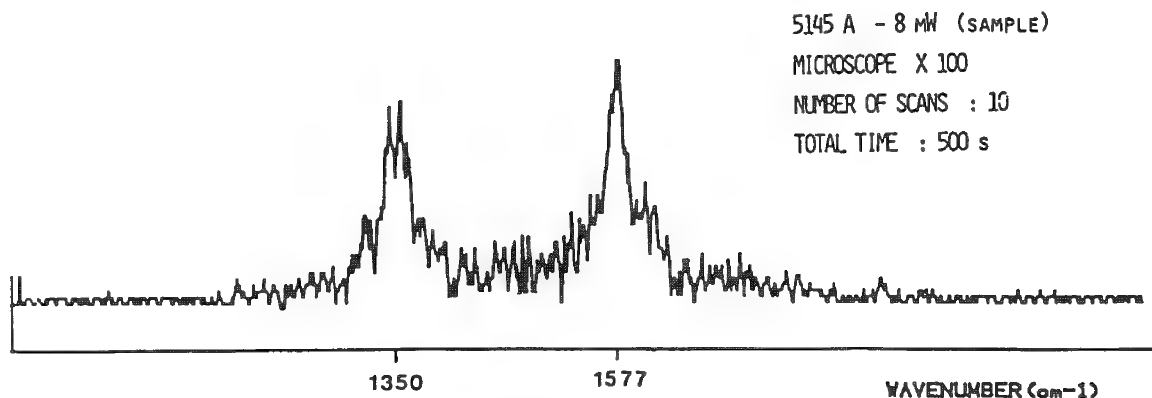

5145 A - 8 mW (SAMPLE)
MICROSCOPE X 100
NUMBER OF SCANS : 10
TOTAL TIME : 500 s

1350   1577   WAVENUMBER (cm-1)

FIG. 3.--Test of sensitivity of MICROMARS spectrometer. Powdered graphite. Intensity of Raman spectrum has been divided by 100.

References

1. M. Delhaye and P. Dhalelincourt, "Raman microprobe and microscope with laser excitation," *J. Raman Spectrosc.* 3: 33, 1975.

2. P. Dhamelincourt, "Etude et réalisation d'une microsonde moleculaire à effet Raman: Quelques domaines d'application," Doctoral Thesis, University of Lille, France, 1979.

3. Proceedings of the "Journées d'étude sur les applications de la microsonde 'MOLE'," *L'Actualité chimique*, April 1980, pp. 11-71.

4. M. Bridoux and M. Delhaye, in R. J. H. Clark and R. E. Hester, Eds., *Advances in Infrared and Raman Spectroscopy*, London: Heyden, 1976, vol. 2, p. 140.

ANALYTICAL APPLICATIONS OF A MULTIPLEX DETECTOR LASER RAMAN MICROPROBE

W. R. Steinbach, C. F. Lohrstorfer, and E. S. Etz

The laser Raman microprobe in use at the McClellan Central Laboratory differs from previously reported instruments[1-5] in that it employs a novel spectrograph mated to a multiplex detector. This instrumental arrangement permits simultaneous recording of broad Raman spectral regions (e.g., Raman shift coverages of 800 to 2400 cm^{-1} are typical) in time periods as short as 30 ms (i.e., detector single scan time). Data acquisition times ranging from a few seconds up to a few minutes are used for weaker Raman signals, such as those from single microscopic particles down to 1 μm in size, or equivalently small sample regions of a macroscopic specimen for which laser power density is a limiting factor. Such relatively short signal integration times are advantageous because they markedly increase sample throughout in the instrument and they significantly optimize the prospects for non-intrusive and nondestructive analysis of the sample which in many cases could be modified due to prolonged exposure to the intense focused laser radiation.

This paper begins with a brief description of the instrument. Emphasis is placed on the performance characteristics of the apparatus that result from the association of the prototype spectrograph and the optical multichannel detection system. Experimental results are then shown which illustrate the micro-Raman measurement of two types of laser irradiation sensitive materials (an organic nitro compound and a polymer) under conditions of broad spectral coverage. The application of the instrument in the identification of microparticles in a "real world" analytical sample will then be discussed. As an example, we present spectra leading to the identification of crystalline silica (α-SiO_2) in a reference sample of volcanic ash from the 18 May 1980 eruption of Mount St. Helens.

The microprobe described here has now been in routine operation for the past year, challenged in its performance by a broad range of difficult microsamples demanding the insights and skills of an experienced analyst. We project from this initial research with this type of advanced micro-Raman instrumentation that much promise lies ahead for the further development of the technique through current advances in both spectrometric and optical detector instrumentation.

Instrument Description

In the development of this new microprobe (Fig. 1) commercially available equipment has been employed. An experimental triple spectrograph of novel design (Model DL-203, Instruments SA, Inc.)[6] and a multichannel detection system (Model 1215 OMA-2, EG&G/Princeton Applied Research Corp.)[6,7] with a cooled silicon intensified target (SIT) vidicon array detector (Model 1254, PARC)[6] are the principal state-of-the-art components incorporated in the design and layout of the instrument. Provisions exist for the use of either an argon ion or krypton ion CW gas laser for Raman excitation. For all work reported here, the 514.5nm line of the argon laser has been used. The Pellin-Broca (P-B) prism is employed in conjunction with a beam expander/spatial filter (not shown) positioned directly ahead of the microscope. The prism and spatial filter combination serves to reject the plasma lines from the laser beam directed at the sample.
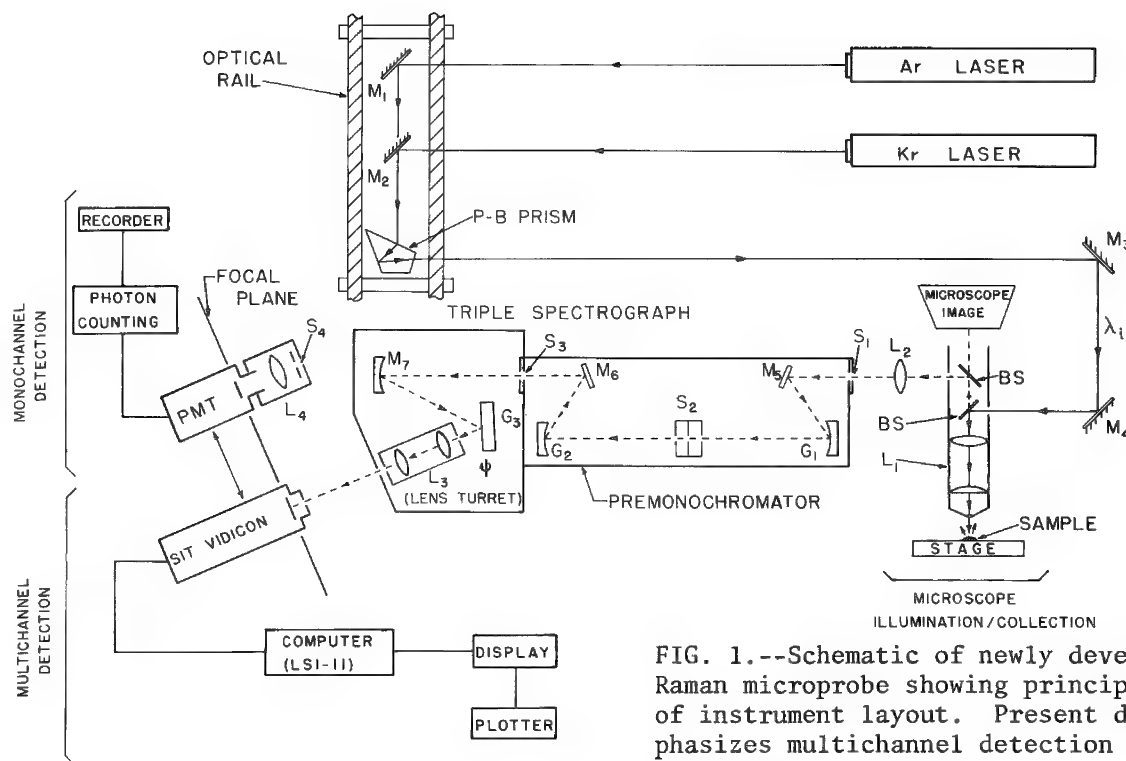

FIG. 1.--Schematic of newly developed laser Raman microprobe showing principal components of instrument layout. Present discussion emphasizes multichannel detection capability in instrument performance.

A modern research-grade microscope retains its original function but has been modified through the addition of two beam splitters (BS, of variable transmission-to-reflection ratio) positioned on sliding mounts in the body-tube of the microscope. The lower beam splitter allows the introduction of the expanded laser beam into the optical path of the microscope. The beam is focused to a microscopic spot on the sample by use of several standard (achromatic) microscope objectives. The focusing objective used most frequently is one with a magnification of 40× and numerical aperture (N.A.) of 0.85. Thus, an incident beam completely filling the back-aperture of the microscope objective has a diffraction-limited spot of 0.7 μm that theoretically defines the optimum lateral resolution of the microprobe measurement. The smallest actual probe spot diameter has not been determined accurately but does appear to be between 1 and 2 μm. Individual particles of interest--in cases where the sample is a heterogeneous collection of microparticulates--are precisely positioned, one at a time, in the focal spot of the laser by translation of the microscope stage. The scattered light (Raman and Rayleigh) is collected by the objective and directed out of the microscope by the upper beam splitter toward the coupling lens L_2. This lens focuses the scattered light onto the entrance slit S_1 of the premonochromator (or prefilter stage) of the spectrograph.

The premonochromator serves as a variable bandpass filter to allow transmission of the Raman light and rejection of the high-intensity exciting line. The center of the bandpass is adjusted by motion of the coupled gratings G_1 and G_2; the width of the bandpass is chosen by variation in the width of the aperture at slit S_2. The gratings used in the prefilter stage (1200 grooves/mm; concave/holographic) result in a dispersion of 4 nm/mm at the focal plane of slit S_2. Typically, fixed slits 12 or 16 mm wide are used as apertures at S_2. These choices result in Raman spectral coverages of 1660 and 2150 cm^{-1}, respectively, when 514.5nm excitation is used. The two gratings (coupled in subtractive dispersion) disperse the light and create an image of S_1 at S_3 without the need for focusing mirrors or lenses. Note that the center and width of the bandpass are chosen together to insure that the laser line is always outside the predetermined bandpass. The final dispersion of the Raman light is accomplished by the third grating in the spectrograph stage (G_3, 2400 grooves/mm; plane/holographic) and one of three output lenses (L_3) mounted on a turret. The final grating can be rotated so that any wavelength is directed down the optic axis of the spectrograph. Photographic lenses with output focal lengths of 55, 105, and 200 mm create a final image

in the plane of the detector (i.e., on the face of the SIT vidicon photocathode) with experimentally determined dispersions of 8.76, 4.59, and 2.41 nm/mm, respectively. Since the active width of the 500-channel detector array extends over 12.5 mm, spectral coverages of 110, 57, and 30 nm (corresponding to Raman shifts from the exciting line of 3400, 1450, and 1070 cm^{-1} with 514.5nm excitation) are in principle achievable. Thus the 105mm lens would be the choice when a 12mm aperture S_2 is employed, and a 16mm slit S_2 would require the use of the 55mm focal-length lens. If optimum spectral resolution is sought, the 200mm lens is required in conjunction with an appropriately narrow slit S_3. (Typically 50µm slits are used at S_3.)

In this work, the PARC OMA-2[6,7] optical multichannel analyzer with nominally 512 channels has been used as a detector   The theory and operation of this detection system used in conjunction with either vidicon or solid-state photodiode array detectors has been described elsewhere.[8,9] At present, we employ the SIT vidicon detector as the actual multichannel light detection device. This tube is cooled at -65°C by means of a methanol bath in the cooled detector housing. The bath is cooled by a freon-based two-stage mechanical refrigeration unit (FTS Systems, Inc.).[6]

The Raman microprobe is also equipped to be operated as a scanning instrument (Fig. 1) for spectrometric rather than spectrographic recording of spectra. In the scanning mode of the instrument, the multichannel detector is replaced by a conventional cooled photomultiplier tube (PMT). With this separate detection system, the monochannel spectrum is obtained by rotation of the third grating (G_3) via a stepping motor drive. Although this mode of operation is employed infrequently, it is useful when selected spectral regions need to be investigated with greater scrutiny. That is the case when data of increased diagnostic value are required and call for results of improved spectral resolution (e.g., typically to acquire spectra with 3-7 cm^{-1} resolution not obtainable under optimum conditions of multichannel operation).

Performance Characteristics

Some performance characteristics of the new microprobe were investigated experimentally and others were assumed on the basis of known figures of merit for each of the individual system components. Of particular interest in this low light level application of the novel polychromator/multichannel detection system were several parameters governing the analytical quality of spectra from individual microparticles. A more comprehensive discussion of these instrumental factors determining system performance will be presented elsewhere.[10] The principal performance characteristics that have been documented include (i) spectral range and light throughput across the spectral bandpass, (ii) stray light behavior and its effect on photometric accuracy, (iii) photometric precision and wavelength accuracy across the face of the detector, (iv) spectral resolution sensitivity, and (v) signal-to-noise and background considerations.

Signal Acquisition. In this work, various signal integration methods for the cooled SIT vidicon detector were examined, such as: real time, in-memory signal integration, variable integration time, and channel grouping. Because the micro-Raman experiment in most cases represents a signal-limited situation, most of the spectra are generally obtained by extended delay target integration techniques.[8] Thus, detector scan and readout parameters must be usually optimized for good signal-to-noise (S/N) measurements from low light level emissions. For most of the spectra it is advantageous to allow the signal to accumulate on the silicon target before electronic readout at the end of the signal integration period. Therefore, instead of reading it out continuously and averaging in computer memory, one allows the signal to integrate on the target for several minutes. For a typical data acquisition time of 3 min, 6000 delay scans (at a frame time of 30 ms) followed by 10 readout scans are employed. The "background" in the multichannel spectra (with use of a cooled SIT tube) can largely be attributed to electronic readout noise, and that background is reproducible and can therefore be subtracted from the spectrum.

Spectral Resolution. The simultaneous spectral coverage provided by the imaging detector is equal to the reciprocal linear dispersion of the spectrograph times the width of the photodiode array. The spectral resolution obtained with the SIT vidicon is determined by the spectral coverage (for each lens in the output optics) and the intrinsic characteristics of the array--principally the channel bandwidth (i.e., 25 µm) and interchannel crosstalk. In

careful measurements, with the 200mm lens, an optimum spectral resolution of about 7 cm^{-1} can be obtained with the microprobe in its present multichannel configuration.

Wavelength Calibration. Wavelength calibration of the instrument (for each output lens) was achieved with the use of spectral calibration lamps, to provide a channel number-to-wavelength (nanometers) conversion. In principle, this conversion is accurate to within a single channel of the detector, about ±1 cm^{-1} for the Raman spectral range considered here. The SIT vidicon, because of its inherent geometric distortion,[9] requires a polynomial-fit calibration which is available in standard software provided with the optical multichannel analyzer (OMA-2).[7] The polynomial least-squares fit based on 8 or 9 spectral lines (spaced across the full width of the detector) and their corresponding exact channel positions provides frequency accuracy of Raman bands estimated to be on the order of 3 to 4 wavenumbers.

Samples Analyzed

For the experimental results presented here, the particle samples in all cases are supported by a sapphire (α-Al$_2$O$_3$) substrate. Sapphire serves as a potentially good heat sink in measurements where the sample (most often a single microscopic particle) undergoes any laser-induced heating arising from optical absorption of the incident radiation. Thus, particles mounted in air and supported by sapphire are less likely to undergo thermally induced chemical modification. Relative to the examples given, no effort has been made to provide additional thermal contact (e.g., by overcoating or embedment in a noninterfering dielectric film) between the particle and the substrate. The particles are simply dispersed on the substrate and subsequently analyzed requiring no further preparation.

The particle samples of trinitrotoluene and polystyrene latex were prepared from well-characterized bulk materials. The sample of volcanic ash examined in this study was one collected in Yakima, Washington (reference sample provided by Battelle Pacific Northwest Laboratories) from the eruption of Mount St. Helens on 18 May 1980.

The Spectra of Microparticles

To illustrate the multiplex advantage of the new microprobe over conventional scanning microprobes, we have acquired the microparticle spectra of several classes of laser radiation sensitive solids. From previous work[11] with the NBS monochannel scanning microprobe, these materials were known to present certain experimental complications arising from time dependent sample modification due to laser-induced heating or photodegradation. Two specific analytical situations are discussed here.

The spectra (Figs. 2-4) are presented as digital plots of scattered intensity (the ordinate represents detector counts; signal levels are not given) versus frequency (or Raman) shift. Figure captions include the relevant experimental parameters. The spectral data have been obtained at variable spectral resolutions and under different conditions of target integration, as mentioned above. The spectra shown here are not background-subtracted, i.e., the contribution to the spectral background by the (thermal) dark current of the SIT detector and that from the readout scans has not been subtracted. In other measurements, the actual dark current ("dark count") stored in computer memory is often subtracted from the spectrum of the sample.

Figure 2 shows the spectrum of a microparticle of TNT with a spectral coverage of just over 1600 cm^{-1}. Note the flat spectral background over the entire spectral region, which gives no indication of sample degradation. Spectra of this nitro compound recorded with a scanning microprobe and 568.2nm excitation exhibit a progressively increasing background toward higher wavenumber shifts.[11] This result has been interpreted as being indicative of slow, time-dependent sample degradation due to photochemical deterioration (photolysis) of the sample. Other scanning microprobe spectra of TNT obtained with 514.5nm excitation exhibit substantially higher spectral backgrounds (with concomitant deterioration of signal-to-background ratio) at much earlier data acquisition times, and lower Raman shifts, very early at the start of the spectral scan. The reason for the flat background associated with the multichannel spectrum is that under the irradiance conditions employed, the entire spectrum is obtained before detectable sample deterioration can set in and affect spectrum quality. The multiplex advantage in terms of data acquisition time, for this example, is about a factor of ten, at the expense of lower spectral resolution. Figure 3 shows the spectrum of another laser-radiation sensitive material--a polystyrene latex microsphere. The polymer
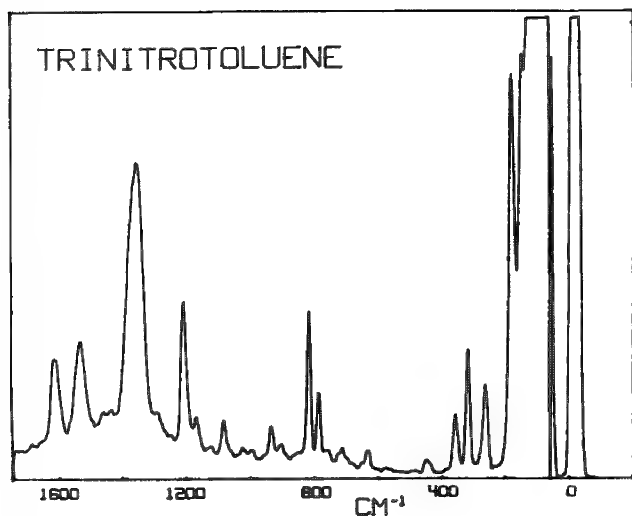
FIG. 2.--Microprobe Raman spectrum of single microcrystal of trinitrotoluene (TNT). Measurement parameters: exciting wavelength, 514.5 nm; laser power (at sample), 25 mW; beam spot, about 15 μm diameter; substrate, sapphire; particle size, 30 × 18 μm; integration time, 3 min; spectral coverage, 48 nm.
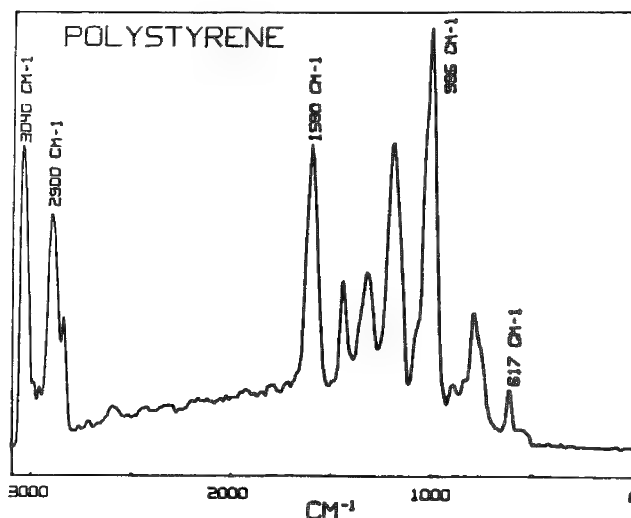

FIG. 3.--Raman spectrum of polystyrene latex microsphere. Measurement parameters: exciting wavelength, 514.5 nm; laser power (at sample), 12 mW; beam spot, about 15 μm diameter; substrate, sapphire; particle size, about 15 μm diameter; integration time, 3 min; spectral coverage, 80 nm.
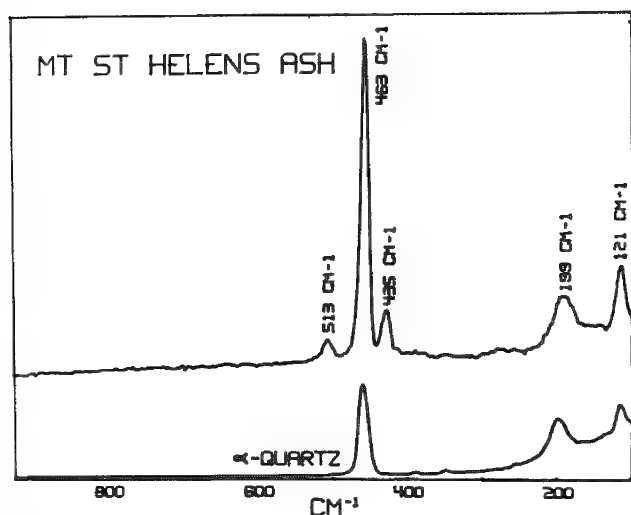

FIG. 4.--Raman spectrum of a crystalline particle isolated from bulk sample of Mount St. Helens volcanic ash. Measurement parameters: exciting wavelength, 514.5 nm; laser power (at sample), 80 mW; beam spot, about 2 μm diameter; substrate, sapphire; particle size, 10 × 14 μm; integration time, 75 s; spectral coverage 24 nm. Lower trace is a reference spectrum of α-SiO₂, obtained from a microscopic particle of single-crystal natural quartz. (Source: Smithsonian Institution.)

is to some degree optically absorbing at 514.5 nm and can tolerate only relatively low laser power densities in the absence of effective provisions for thermal transfer to the supporting substrate.[2,5] With this type of a microsample, the overriding analytical problem is sample stability under potentially destructive conditions of laser-induced heating. With this sample, the largest practical wavenumber coverage available from this instrument is demonstrated. By use of a slit width of 20 mm at S_2, with the bandpass centered at 571 nm, spectral coverage from 610 to 3070 cm^{-1} was achieved. All the principal features of the spectrum in this frequency range are observed. The spectrum was acquired in 3 min of signal integration, a time advantage in the acquisition of the vibrational "finger-print" by a factor of about 18 compared to the corresponding spectrum (of comparable signal-to-noise ratio) obtained in a conventional microprobe with a scanning spectrometer.

Unknown "real-world" samples of microparticulates are routinely analyzed in this instrument, in parallel with measurements involving other microprobes (e.g., electron and ion beam instruments) as part of a materials research program. In recent work, a bulk

sample of Mount St. Helens volcanic ash was examined to characterize the major molecular species in individual particles of the ash. Initially, particles of interest (ranging in size from about 2 μm to 15 μm) were selected by optical microscopy in an ash sample dispersed on sapphire substrate.

The particle whose spectrum is shown in Fig. 4 was of irregular shape and just under 15 μm overall. A focused laser spot of fairly high intensity (about 2.5 MW/cm^2) was used to probe the particle in six different areas. The spectra of the different probed regions of the particle were essentially identical to that shown in Fig. 4, which indicates gross homogeneity of the particle. In these measurements, the best possible spectral resolution (on the order of 6-7 cm^{-1}) was desired together with complete rejection of the laser line in the low-frequency region of the spectrum. These requirements meant the use of the 20mm output lens in conjunction with a 6mm aperture (for a 24nm bandpass) at slit position S$_2$. The choice of these experimental parameters allowed investigating the 100-960cm^{-1} region of the spectrum. Spectra were collected by extended delay target integration to achieve good signal-to-noise ratios.

The strongest line in the spectrum maximizes at 463 cm^{-1} (according to detector calibration) and is consistent with the corresponding band reported[12] for α-quartz at 466 cm^{-1}. Two other references[13,14] report the peak position of this band at a frequency of 465 and 464 cm^{-1}. The two low-frequency lines serve as further confirmation of α-quartz as the major component of this particle, since they correspond very well with the bands for crystalline silica expected at 128 and 206 cm^{-1}.[12] Well over a third of the particles examined in one sample preparation furnished spectra exhibiting a sharp band at 463 cm^{-1}. However, in the spectra of some particles, the gradually increasing spectral background toward the wing of the exciting line made it difficult to detect the suspected presence of the two low frequency bands associated with α-quartz. As further evidence of the presence of α-SiO$_2$ in many of these particles, the reference spectrum of a particle of geological quartz is shown in the lower portion of Fig. 4.

Although α-quartz is definitely a major component in this and other such particles of the volcanic ash, there are additional minor spectral features from other, secondary constituents. The most pronounced spectral features not accounted for by the spectrum of α-quartz appear at frequency shifts 435 and 513 cm^{-1}. The relative intensities of these two bands, with respect to the normally strong 463cm^{-1} line, have been found to vary among the spectra of different particles analyzed. In some cases, the 513cm^{-1} band was twice the intensity of the 463cm^{-1} band. In other cases, the 513cm^{-1} peak was not present at all. Although it is not apparent in the spectrum of Fig. 4, we detected a weak band with peak position at about 420 cm^{-1} in probing other regions of this same particle or in the spectra of other, similar particles. The origins of these bands have not been firmly established, although several possibilities are suggested.

Recent Raman investigations[14,15] of macroscopic bulk samples of Mount St. Helens volcanic ash provide evidence for a band maximizing at 512 cm^{-1}. This peak has been attributed to the presence of plagioclase feldspar in the ash matrix. As part of this same study, these workers also report a sharp spectral feature with peak at 416 cm^{-1}, which they assign to the presence of cristobalite, one of the geologically common polymorphs of crystalline silica. Thus, the occasional presence of a weak band around 420 cm^{-1} may well be attributed to small amounts of cristobalite in particles composed predominantly of α-quartz.

Concluding Comments

The multichannel detection Raman microprobe in use at the McClellan Central Laboratory has a distinct multiplex advantage not possessed by conventional monochannel-detection scanning microprobes. The present configuration of the instrument permits Raman spectral coverages of up to 2600 cm^{-1} in typical data acquisition periods ranging from a few seconds to several minutes. For most analytical samples, a time advantage in data collection approaching a factor of 20 can be realized under typical conditions of the micro-Raman experiment. The demonstrated rapid acquisition of microparticle Raman spectra has significant implications for the analysis of "difficult" microsamples subject to potential chemical/physical modification by prolonged exposure to the high-intensity focused laser radiation. The resultant decrease in spectral resolution from multichannel detection with broad spectral coverage is not a serious limitation in analytical work where qualitative identification of the principal molecular species is the primary goal. Computer control of the detection and

data acquisition system greatly facilitates the recording and housekeeping of spectra from microsamples. Other advantages result from the ease of wavelength calibration, line or Raman band identification, data storage and display, signal measurement, spectral subtractions, and various other kinds of data manipulation. It is clear from this research and parallel work in other laboratories[16-19] that current, significant developments in multichannel micro-Raman systems will profoundly aid in advancing the field.[20]

References

1. M. Delhaye and P. Dhamelincourt, "Raman microprobe and microscope with laser excitation," *J. Raman Spectrosc.* 3: 33-43, 1975.

2. G. J. Rosasco and E. S. Etz, "The Raman microprobe: A new analytical tool," *Res. & Devel.* 28: 20, June 1977.

3. P. Dhamelincourt, F. Wallart, M. Leclercq, A. T. N'Guyen, and D. O. Landon, "Laser Raman molecular microprobe (MOLE)," *Anal. Chem.* 51: 414-421A, 1979.

4. D. O. Landon, "The development of instrumentation for microparticle analysis by Raman spectroscopy," *Microbeam Analysis--1979*, 185-190.

5. G. J. Rosasco, "Raman microprobe spectroscopy," in R. J. H. Clark and R. E. Hester, Eds., *Advances in Infrared and Raman Spectroscopy*, London: Heyden, 1980, vol. 7 (chap. 4), 223-282.

6. Certain commercial equipment, instruments or materials are identified in this paper for adequate specification of the experimental procedure. Such identification does not imply recommendation or endorsement by the U. S. Air Force or by the National Bureau of Standards, nor does it imply that the materials or equipment identified are necessarily the best available for the purpose.

7. OMA is a registered trademark of Princeton Applied Research Corp., an EG&G Company.

8. J. L. Chao, "Applications of the optical multichannel analyzer for low light level signal averaging and two-dimensional mode detection of picosecond laser-generated Raman spectra," *Appl Spectrosc.* 35: 281-289, 1981.

9. Yair Talmi, "Spectrophotometry and spectrofluorometry with the self-scanned photodiode array," *Appl. Spectrosc.* 36: 1-18, 1982.

10. W. R. Steinbach and E. S. Etz, "Analytical advantages of a Raman microprobe with multichannel optical detection," submitted to *Appl. Spectrosc.* 36: 1982.

11. E. S. Etz and J. J. Blaha, "Investigation into the critical measurement aspects of Raman microprobe analysis," *Microbeam Analysis--1979*, 173-184.

12. M. M. Suschinski, *Raman Spectra of Molecules and Crystals*, New York: Israel Program for Scientific Translation, 1972.

13. Fran Adar, M. J. Mitchell, and J. M. Ramsey, "Raman microanalysis of SiO source materials by means of MOLE," *Microbeam Analysis--1979*, 165-168.

14. S. O. Farwell and D. R. Gage, "Crystalline silica in Mount St. Helens ash," *Anal. Chem.* 53: 1529A-1531A, 1981.

15. D. R. Gage and S. O. Farwell, "Laser Raman spectrometry for the determination of crystalline silica polymorphs in volcanic ash," *Anal. Chem.* 53: 2123-2127, 1981.

16. M. Delhaye, M. Bridoux, P. Dhamelincourt, J. Barbillat, E. Da Silva, and B. Roussel, "A new generation of laser Raman microspectrometer: MICROMARS," *Microbeam Analysis--1982*, 273.

17. P. Dhamelincourt, "Instrumentation and recent applications in micro-Raman spectroscopy," *Microbeam Analysis--1982*, 259.

18. F. P. Milanovich, T. Hirschfeld, and D. C. Johnson, "The Lawrence Livermore National Laboratory Raman microprobe," *Microbeam Analysis--1982*, 268.

19. F. J. Purcell and E. S. Etz, "A new spectrograph with a multichannel optical detector for the Raman characterization of microparticles," *Microbeam Analysis--1982*, 299.

20. J. G. Grasselli, M. K. Snavely, and B. J. Bulkin, *Chemical Applications of Raman Spectroscopy*, New York: Wiley-Interscience, 1981.

INFRARED AND RAMAN SPECTROMETRIC STUDIES OF THIN FILMS AND INTERFACES

René Dupeyrat and Michèle Masson

Spectrometric studies of thin films and interfaces are one important aspect of microprobe spectrometry. For many years, workers with interests in physics, chemistry, or biology have published numerous papers concerning the interaction between two media at an interface (powders, vesicles); and more recently, on the structure of thin films, whether crystalline or not. We may ask, what is an interface and what is a thin film? By way of answer, we must consider the limit of a bulk material as the case in which the potential function no longer retains its spherical symmetry. Under that condition, we are in the vicinity of an interface. We can give an order of magnitude of this "vicinity" by saying that it is around ten molecular dimensions in thickness with respect to the geometrical separation of two phases.

We define a thin film as a film limited by two interfaces and for which its thickness is around twenty molecular dimensions. From above we can think of the center of the film as not being different from a bulk material except for a crystalline one.

We can pay special attention to multilayer films and in particular consider mono- and double-layered films. Quite generally, solid thin films are better understood in spectroscopy than are liquid thin films. We can make some statements about (1) solid thin films such as metallic oxide, thickness below 30 Å, and multilayers of phospholipids, thickness below 500 Å; and (2) liquid thin films not yet studied in spectroscopy but well known by workers studying interfacial forces, thickness depending on the nature of liquids (minerals or organic such as polymers).[1]

In the case of an interface we cannot now provide information on a well-defined slice of the sample. In the case of a film we can give an average spectrum of the entire film with its own thickness.

Spectrometric Study of Interfaces

Raman. It is not necessary in this case to have well-characterized thin film (known thickness, etc.) to obtain a good spectrometry; for example, the cases of powders,[3] lamellar phases,[2-4] or vesicles are well known in terms of the Raman effect.

All these spectrometries have as a common goal the increase of the ratio of interface area to sample volume.

Using these methods, we have no problems with the qualitative analysis or determination of interactions (shift of frequencies, degeneracy, intensities); however, they do not allow us to obtain information about relative orientational properties of the molecules (except for oriented lamellar phases); that is the reason for the interest in thin films.

Infrared. One convenient method, well known in infrared technique, is attenuated total reflection (ATR).[5] For a plane interface, we can use a continuous spectrum source and send the beam to a reflecting interface; after a single pass or several passes we obtain the absorption spectrum of the interface, which has to be realized with two media of refractive index n_1 and n_2. If the beam enters medium 2, we have total reflection for $n_1 < n_2$; the evanescent wave in medium 1 has a depth of penetration of around $\lambda/5$ and it is in a layer of this thickness that we have absorption. It is a relatively thick layer (generally more than ten molecular dimensions).

The authors are with the Départment de Recherches Physiques, Laboratoire associé au CNRS No. 71, Université Pierre et Marie Curie, 4 place Jussieu, 75230 Paris Cedex 05, France.

Spectrometric Study of Thin Films

A plane parallel thin film is limited by two interfaces and its spectrometry allows not only a qualitative analysis and the determination of interactions but also the determination of the structure and the orientation of vibrating groups.

This spectrometry is a microprobe spectrometry but it is different from the usual case. The quasi-spherical sample of the usual case is here a flat sample.

Raman Spectrometry. If we assume the resolution of a Raman microprobe to be around 1 cubic micron of sample, in the case of a thin film of thickness t = 200 Å, we need a film of area 1 μm^3/t $\simeq$ 50 μm^2. It is necessary (a) to use a special coupling between microscope and spectrometer; and (b) to use a special device to provide effective illumination of the sample.[6]

IR Spectrometry. A good review appeared recently in a paper by Chollet[7] concerning absorption spectrometry and reflection spectrometry of thin films, as follows: (a) absorption spectrometry of Langmuir-Blodgett films spread on a transparent substrate, and (b) reflection spectrometry of Langmuir-Blodgett films spread on a metallic mirror. It is possible for these two cases to perform dichroism measurements and to give the same information about orientations as in the Raman effect.

Results

The published results are numerous in the case of the Raman effect. We now give a short list of papers published in the field of Raman and IR spectrometries.

In Raman, the thickness limit is generally of the same order of magnitude with resonance[8] or without resonance.[9] It is of the order of one monolayer of an organic molecule.

The papers generally deal with solid-state samples, whether well defined (films specially prepared for the spectrometry) or not. Investigations of films of large thickness were published, for example GaAs[10] and organic polymer films.[11]

Among the studies of films not specially prepared we can give results from numerous experiments on adsorbed films; these experiments are generally realized with the resonance effect. This is the case for adsorbed species on solid surfaces; a recent review has been given by Yamada.[12]

Experiments on interfaces of semi-conductors have been performed by Griffiths.[13] A review is given by Ramsey.[14] With oriented multilamellar phases experiments have been realized by Peticolas.[4-15] A lot of experiments have been described at the liquid crystal congress.[16-17] In IR, the papers on ATR are well known. The best approach is given by Harrick.[5] A good review for the case of specially prepared films is given in the thesis of Chollet.[7]

Conclusion

Raman and IR spectrometries of interfaces and very thin films are now possible. The difficulties are related to the focal depth of the microscope objective and to the heating of the sample. As explained by Dhamelincourt,[17] with the MOLE Raman microprobe we use the focal depth imparts a limitation on the Raman spectrum from the surrounding medium. Recently, Adar[18] gave an estimate of focal depth of 2.5 μm and a beam waist of 0.7 μm. In the case of a thin film 10 to 20 nm thick, the microscope sees generally a larger thickness of the substrate than of the useful film. That is why metallic films (silver,[6] gold, iron) or absorbing films are used as substrates.

At present we have the problem of laser-induced heating.

If the flat sample has a better ratio of area to volume that allows a good dissipation of the heating, the metallic or absorbing substrate is not so good and we are not as optimistic as Etz[20] in a recent paper.

But we agree with the conclusions of all the other that an advantageous approach appears to be the use of a multichannel Raman microprobe, which reduces the time of laser irradiation by a significant factor. As Etz has put it, "Future research efforts in this field will aim at [the investigation of] the effects due to optical absorption [and] the contributions to the scattered intensity by "surface" and "bulk" modes...."[20]

Looking toward the future, we hope the forthcoming progress in Raman spectrometry of thin films and interfaces will be the recording of spectra of slices of 20 Å thickness in a film and the scanning of these slices. As to IR spectrometry, we have an analogous prob-

lem. To reduce the heating, it is easy to direct a monochromatic flux at the sample that can be obtained by the coupling of two monochromators, one for the irradiation and the other for absorption.

To increase the ratio of useful spectrum to substrate spectrum, we can also use a metallic substrate as proposed by Chollet.[7]

We conclude that the molecular spectrometry of very thin films and interfaces will be of central interest for the next few years.

References

1. R. G. Horn and J. N. Israelachvili, "Direct measurement of forces due to solvent structures," *Chem. Physics Letters* 71, 1980.
2. M. Harrand et al., "Polarized Raman spectroscopy of oriented macrodomain of phospholipids containing amphotericin," *Biochem. Biophys. Research Communications*, 1982.
3. R. L. Paul and P. J. Hendra, *Minerals Sci. Eng.* 8: 171, 1976.
4. W. L. Peticolas et al., "Polarized Raman spectra of oriented macrodomain of phospholipids multilayers," to appear in *J. of Raman Spectrosc.* 1982.
5. N. J. Harrick, *N.Y. Acad. Sci.* 101: 928, 1963; *J. Phys. Chem.* 64: 1110, 1960.
6. Y. Levy and R. Dupeyrat, "Méthode d'étude de couches minces et d'interfaces par spectroscopie Raman," *J. de Phys.*, colloque C5, 38 (Supp. 11): 253, 1977.
7. P. A. Chollet, "Etudes par dichroisme infrarouge de la structure des couches monomoléculaires de Langmuir-Blodgett," thèse d'état, Orsay, 1981.
8. T. Takenaka et al., "Raman spectra of benzene, ethyl benzene and dimethylphtalate solubilized in aqueous solutions of surface-active agents," *Bull. Inst. Chem. Research*, Kyoto University, 53 (No. 2), 1975.
9. T. Takenaka and T. Nakanaga, "Resonance Raman spectra of monolayers absorbed at the interface between carbon tetrachloride and an aqueous solution of a surfactant and a dye," *J. Phys. Chem.* 80: 475, 1976.
10. G. Burns et al., "Raman scattering in thin-film waveguides," *Applied Phys. Letters* 22: 3, 1973.
11. J. F. Rabolt et al., "Raman measurements on thin polymer films and organic monolayers," *Appl. Spectrosc.* 34: 517, 1980.
12. H. Yamada, "Resonance Raman spectroscopy of adsorbed species on solid surfaces," *Appl. Spectrosc. Rev.* 17(2): 227-277, 1981.
13. G. P. Schwartz et al., "Raman scattering from anodic oxide-gas interfaces," *Appl. Phys. Lett.* 34: 205, 1979.
14. J. N. Ramsey and H. H. Hausdorff, "Applications of small-area infrared analysis to semiconductor processing problems," *Microbeam Analysis--1981*, 91.
15. W. L. Peticolas et al., "Polarized Raman spectra of oriented monodomains of phospholipid multilayers," to appear in *J. of Raman Spectrosc.*
16. M. Harrand et al., "Polarized Raman spectroscopy of oriented monodomains of phospholipid multilayers," accepted by *Biochem. Biophys. Research Communications*.
17. M. Levy, 7ème Congrès Cristaux Liquides, Bordeaux, 1978.
18. P. Dhamelincourt, "Etude et réalisation d'une microsonde moléculaire à effet Raman," doctoral thesis, Lille University, 1979.
19. F. Adar, "Developments in Raman microanalysis," *Microbeam Analysis--1981*, 67.
20. E. S. Etz, "Empirical quantitation in Raman microprobe analysis," *Microbeam Analysis--1981*, 76.

RAMAN MICROPROBE STUDY OF THE PENETRATION OF AN ANTIBIOTIC IN A THIN FILM OF PHOSPHOLIPIDS WHICH CONTAINS CHOLESTEROL

Michèle Masson and René Dupeyrat

Microprobe Raman studies of thin films require a special association of a microscope and a Raman spectrometer and unique conditions of laser irradiation. Under these conditions, we can calculate, from the depolarization measurements, the orientation of amphotericin in the phospholipidic film. It is clear to everybody that the smallest volume of a sample which allows us to obtain, with a given resolution, the Raman spectrum--using a commercial instrument--is a trivial test of the performance of the spectrometer. In the MOLE Raman microprobe this volume is of the order of a cubic micron. Generally we speak of a cubic "cubic micron," but in films 20 or 40 Å thick we need a larger area than a square micron, as well as a special arrangement between the microscope and the spectrometer and a special device for illumination. This is the situation realized in our instrument. With this system we measure the orientations of molecules in a film; in the present experiments, of amphotericin molecules in a phospholipidic film. We describe briefly the arrangement of the combination microscope/spectrometer, the conditions of illuminating the sample, the measurements of depolarization ratio, and the results from the sample under study.

Conditions of the Spectrometer/Microscope Combination

The rule is to use the Abbe invariant $n_i \overline{A_i B_i} \sin u_i$ each time we have an intermediary image and a diaphragm. In fact this allows us to define the *étendue* (throughput) of the beam (Fig. 1):

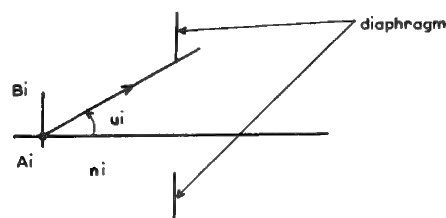$$\varepsilon = n_i^2 S_i \Omega_i \frac{1 + \cos u_i}{2}$$

FIG. 1.--Abbe invariant: $A_i B_i$ = length of object (i^{th} image), u_i = aperture angle of ith diaphragm, n_i = refractive index in vicinity of $A_i B_i$.
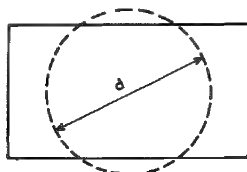

FIG. 2.--Projection of grating in plane of first mirror.

which is an invariant across the microscope or the spectrometer along the beam.

Each instrument has an intrinsic *étendue* but in combination with other components this *étendue* can be reduced owing to the presence of new stops or diaphragms.

We can verify that the intrinsic *étendue* of the microscope is larger than that of the spectrometer. The combination reduces it because the rectangular slits of the spectrometer (or the images of the slits) reduce the circular field of the microscope.

The sample is conjugated with the entrance slit of the spectrometer, and the entrance pupil of the microscope with the grating of the spectrometer (projection of the grating on the first mirror of the spectrometer; Fig. 2). The diameter of the microscope pupil image on the first mirror is about 80 mm.

In the plane of the entrance slit we have the field image (circular) of the microscope, where f is the width of the slit and Kf is the diameter of the field (Fig. 3). The useful area of the slit is approximately Kf^2, and the maximum useful *étendue* of the spectrometer is

The authors are with the Départment de Recherches Physiques, Laboratoire associé au CNRS No. 71, Université Pierre et Marie Curie, 4 place Jussieu, 75230 Paris Cedex 05, France.
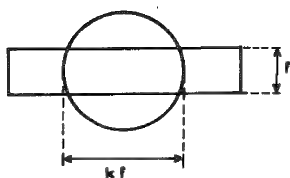
FIG. 3.--Image of objective field of microscope on slit entrance of spectrometer; f = slit width.

$$\varepsilon_s \simeq \frac{\pi}{4}\left(\frac{d}{D}\right)^2 Kf^2$$

where D is the focal distance of the mirror (distance between slit and mirror).

If only a part of the microscope field is illuminated, the *étendue* becomes

$$\varepsilon'_s \simeq \varepsilon_s \frac{w}{AB}$$

where w = radius of the illuminated field of the microscope AB = radius of the total field.

The radius of the illuminated circle in the entrance slit plane is assumed to be larger than f.

If the numerical aperture of the objective is O_n, the *étendue* of the microscope is

$$\varepsilon_M = \pi S O_n^2$$

where S is the area of that part of the sample whose image is inside the entrance slit

$$S = 4\frac{wAB}{K}$$

$$\varepsilon_M = 4\pi O_n^2 \frac{wAB}{K}$$

Instrument Combination

For a good match we need to realize the condition $\varepsilon_M = \varepsilon'_s$. This allows us to determine the length of the slit we have to illuminate;

$$Kf = 4\frac{D}{d} AB\ O_n$$

where Kf represents the useful length of the slit. This length is independent of the waist, but we have to adapt the waist and the beam power to the thermal sensitivity of the sample.

We have now calculated the optical device that couples the microscope and the spectrometer.

Irradiation of the Sample

We use two methods, one direct, the other interferential.

(1) The sample is spread on a metallic surface (Fig. 4). (a) We send the laser beam along a large angle of incidence; the electric field $\vec{E}_0$ of the wave is parallel to the sample. The Raman flux is collected by a microscope objective with its axis normal to the sample plane; i.e., we have a cone of angle u around the normal. (b) We direct the laser beam at an angle of nearly 90°, with $\vec{E}_0$ perpendicular to the plane of the sample. The Raman flux is now collected by a microscope objective with its axis in the plane of the sample.

(2) The thin film is used as a resonant cavity for incident light; e.g., as waveguide,[1,2] or other devices such as a silver-coated prism (Fig. 5), to allow concentration of energy;[3,4] or a film spread on a grating.[5]

In the first method of illunination we have to use an objective with a long working distance, which involves a smaller numerical aperture and consequently a loss of sensitivity of the device. On the other hand, one can also cool the sample, by putting it close to a hollow block of copper cooled with water, which allows heating of the sample as well.

In the second method of illunination we can use a classical objective lens, with a large numerical aperture. Generally we use the 100× objective with numerical aperture $O_n = 0.90$.

It is not always possible to use this second method of illumination, for the following reasons.

a. For an incident TM wave ($\vec{E}_0$ in the incident plane), it is possible to excite the plasmon whatever the film thickness; but the structure of the wave in the film is not simple, which complicates the interpretation of the spectra.

b. For an incident TE wave ($\vec{E}_0$ perpendicular to the incident plane), there is no plasmon excitation, but a cavity resonance can occur only for a film thickness larger than a limit e_0. In our experiments $e_0 \simeq 140$ nm. If the resonance condition is satisfied, the wave in the film is TE, and the analysis of the spectra is the same as for a classical method of illumination.

c. The cooling of the sample is not easy in this method.
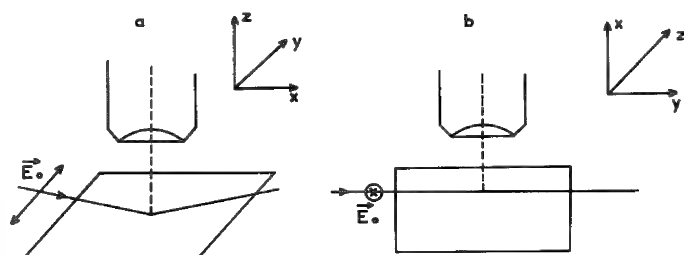
FIG. 4.--Irradiation of sample with $\vec{E}_0$ (a) parallel to plane of sample, (b) perpendicular to plane of sample.
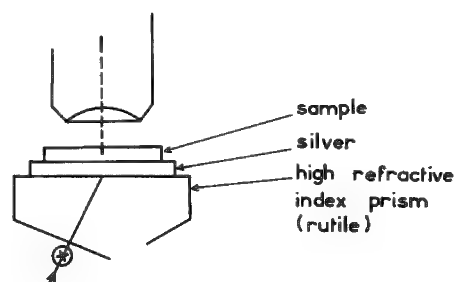
FIG. 5.--Prism coupling device.

Spectrometric Results

The large numerical aperture of the objectives used allows us to obtain information on the molecular orientations from polarization measurements, even in cases of illumination that furnish no results with an objective of smaller aperture.

We calculated the Raman intensities collected for the two polarizations of the incident light and of the Raman light, when the Raman light is collected over an angle u.
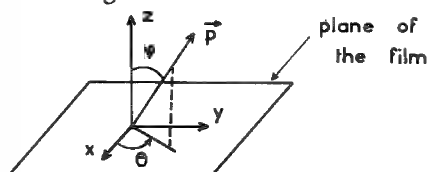
FIG. 6.--Orientation of amphotericin molecule in film.

Assuming that the amphotericin molecules in the film are uniaxially oriented with respect to the Z axis by an angle ϕ, with all values of θ equally possible, we can calculate the depolarization ratios versus ϕ angle (Fig. 6). For the configuration of Fig. 4(a),

$$\frac{I_{YY}}{I_{YX}} = \frac{\frac{1}{16}\left[10(1 - \cos u) + \frac{4}{3}(1 - \cos^3 u) + 2(1 - \cos^5 u)\right]\tan^2\phi + \left[\frac{1}{3}(1 - \cos^3 u) - \frac{1}{5}(1 - \cos^5 u)\right]}{\frac{1}{16}\left[6(1 - \cos u) - \frac{4}{3}(1 - \cos^3 u) + \frac{6}{5}(1 - \cos^5 u)\right]\tan^2\phi + \left[\frac{1}{3}(1 - \cos^3 u) - \frac{1}{5}(1 - \cos^5 u)\right]}$$

This function is plotted for various values of the numerical aperture of the objective lens in Fig. 7.

For the sample illumination and observation shown in Fig. 4(b),

$$\frac{I_{ZZ}}{I_{ZY}} = \frac{\frac{1}{2}\left[(1 - \cos u) + \frac{2}{3}(1 - \cos^3 u) - \frac{3}{5}(1 - \cos^5 u)\right]\tan^2\phi + \left[3(1 - \cos u) + \frac{2}{3}(1 - \cos^3 u) + \frac{3}{5}(1 - \cos^5 u)\right]}{\frac{1}{2}\left[3(1 - \cos u) + 2(1 - \cos^3 u) - \frac{1}{5}(1 - \cos^5 u)\right]\tan^2\phi + \left[(1 - \cos u) - \frac{2}{3}(1 - \cos^3 u) + \frac{1}{5}(1 - \cos^5 u)\right]}$$

This function is plotted in Fig. 8.

From measurement of the same sample (20% cholesterol, 80% phospholipid) we can say that in this film $\phi < 17°$ for the molecule of amphotericin (spectra whown in Figs. 9 and 10).

We studied samples with different concentrations of cholesterol (0 to 50%). For all the samples we find that the amphotericin molecule is nearly perpendicular to the plane

of the film. This result is in agreement with the isotherms of the monolayers drawn by Michèle Hug of the Laboratoire de Chimie Physique, Université Pierre et Marie Curie.
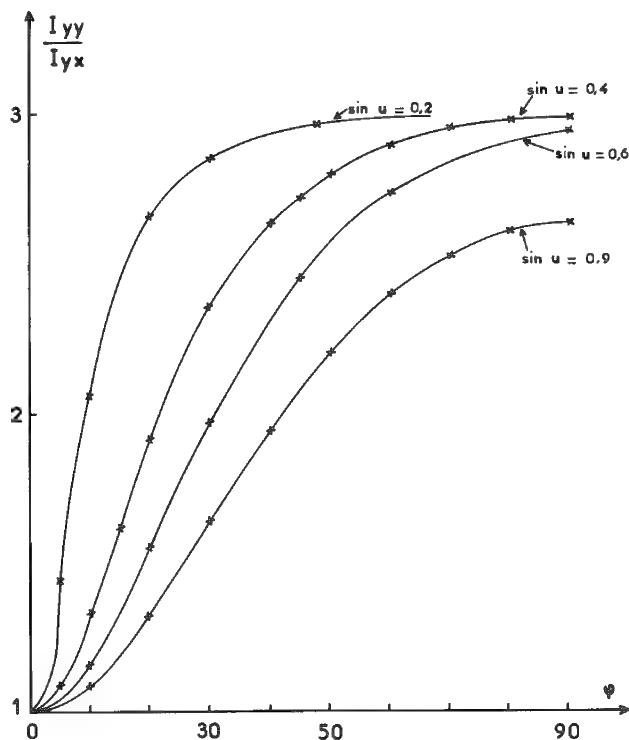

FIG. 7.--Graph of I_{YY}/I_{YX} for the case of Fig. 4(a)
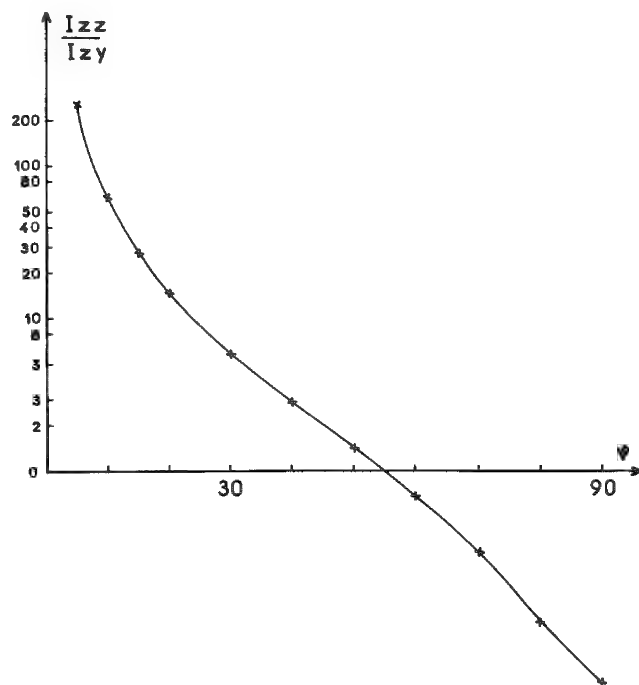

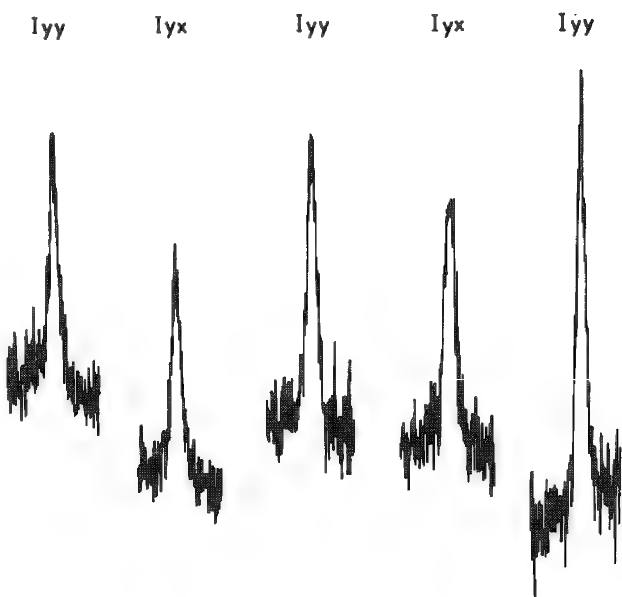FIG. 8.--Graph of I_{ZZ}/I_{ZY} for the case of Fig. 4(b).

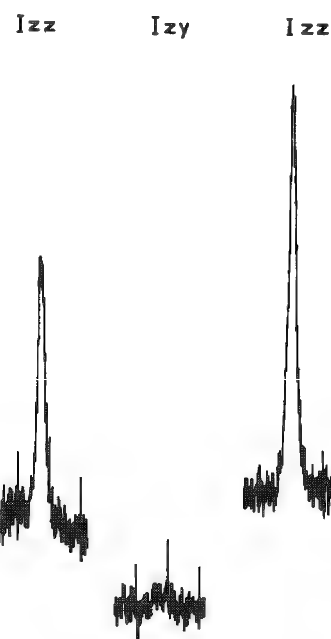FIG. 9.--Recorded spectra for the case of Fig. 4(a).

FIG. 10.--Recorded spectra for the case of Fig. 4(b).

292

Conclusion

We have defined and realized a special combination of a spectrometer and a microscope that has allowed us to study the orientation of amphotericin in a model membrane of phospholipid. When we introduce cholesterol (0 to 50%) in the phospholipidic film, this orientation is defined by an angle with the normal of about 15°. This result is in agreement not only with other works on isotherms but also with the ideas of biologists.[6]

References

1. Y. Levy et al., "Raman scattering of thin films as a waveguide," *Optics Communications* 11: 66, 1974.

2. J. Cipriani et al., "Two methods for Raman spectrum excitation in very thin films," *Japan J. Appl. Phys.* 14 (Suppl. 14-1): 93, 1975.

3. M. Menetrier et al., "Raman spectrum of a layer or thin slide at a solid interface," *Optics Communications* 21: 162, 1977.

4. A. Aurengo et al., "Technical device for obtaining Raman spectra of ultrathin films," *Biochem. Biophys. Res. Comm.* 89: 559-554, 1979.

5. M. Masson et al., "Méthode d'excitation du spectre Raman d'une couche mince utilisant un réseau à grand nombre de traits," *Optics Communications* 20: 162, 1977.

6. Kruigss, Demel, "Polyene antibiotic-sterol interactions in membranes of *Acholeplasma laidlawii* cells and lecitin liposomes: Part III," *B.B.A.* 339: 57-70, 1974.

MICROANALYSIS OF INDUSTRIAL POLYMERS BY RAMAN SPECTROSCOPY

B. W. Cook and G. D. Ogilvie

Chemical and physical properties influence the end uses of industrial polymers. Studies of polymers as solids (the physical state of most industrial polymers) require analytical information describing both the chemical and physical structure.

A polymer is a macromolecule *constituted* from molecular chains and networks composed of sequences of repeat units forming a regular or disordered arrangement. The vibrational spectrum depends on the nature of the chemical repeat unit and its relative position in the molecular chain *(configuration)*. Ideally a full description of the structural model would require a complete vibrational assignment, but that is seldom possible and the model is usually defined through empirical correlations of spectral bands with chemical units *("finger printing")*.

The Raman spectrum provides unique information for describing both the chemical and physical states of order of the polymer. Through the directional properties of Raman scattering the *molecular symmetry* of the polymer can be studied. The relative geometry of the repeat units *(conformation)* can be determined and their degree of regularity in the network *(crystallinity)* estimated; and the alignment of the chain molecules *(orientation)* can be studied.

These features are illustrated in the description of the role of Raman spectroscopy for analysis of microstructures in some industrial polymers.

Historical Perspective: The Fluorescence Problem

For a long time Raman studies of polymers were discouraged by the high fluorescence induced by the exciting radiation, which often completely "swamped" the much weaker Raman emission. To some extent the high fluorescence background levels observed during the spectral measurement can be offset by application of a backing-off potential (zero suppression), but this procedure creates a further problem because the noise level is increased with suppression, even though the S/N ratio is unchanged.

With the advent of the laser as a Raman source the fluorescence problem became less severe. The improvement is achieved by allowing the fluorescence to decay with time through prolonged irradiation of the sample with the laser beam before the spectrum is recorded. The high irradiance of the laser induces excitation of the chromophore to a metastable excited state and its subsequent photodecomposition.

Microscopic examination sometimes reveals that the fluorescence varies from point to point within a bulk sample, since it is often associated with localized chromophoric centres. Imaging techniques can be used to locate the fluorescent and nonfluorescent regions from which Raman spectra can be obtained with the microprobe. Figure 1 compares Raman spectra obtained by probing of such regions in a polyester filament of diameter approximately 20 μm.

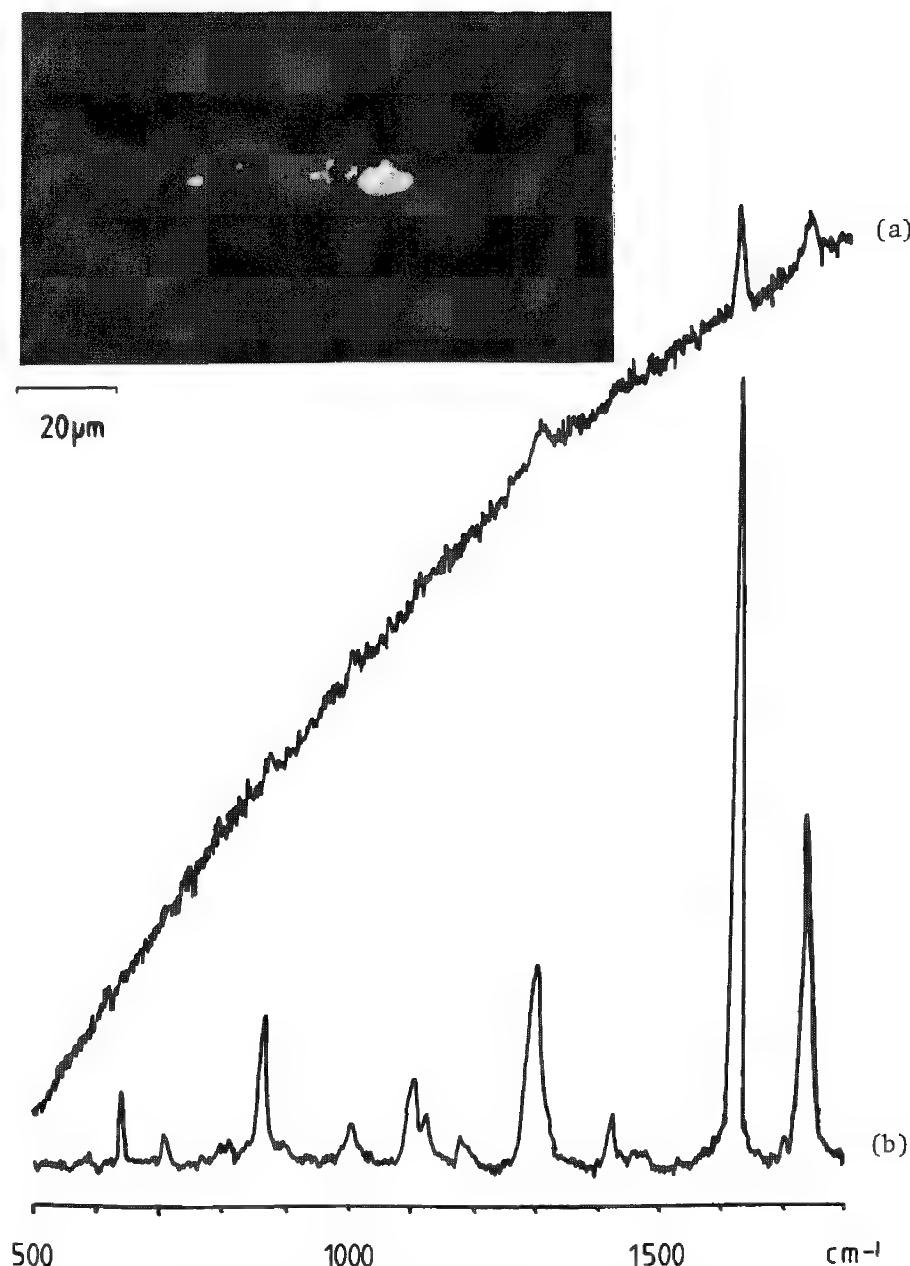Despite fluorescence, for long the bugbear of Raman spectroscopy, the Raman spectra of most industrial polymers can now be obtained without difficulty.

FIG. 1.--Distribution of fluorescene in filament spectra: (a) fluorescent area, (b) nonfluorescent area.

Spectroscopic methods (infrared and Raman) have always been favored for the analysis of synthetic rubbers produced by copolymerizing propylene and ethylene. The micro-Raman technique in proving uniquely valuable for characterization of the microscopic inhomogeneities (1-5 µm) which sometimes separate in these block copolymers or blends.

With conventional reflected or transmitted light microscopy it is difficult to distinguish these inhomogeneities from the surrounding matrix because they have similar refractive indices, so that either phase contrast or differential interference contrast (DIC) microscopy has to be used.[1] When viewed by DIC optical microscopy some commercial propylene-ethylene rubbers have a lunar landscape appearance consisting of a random distribution of smooth and crater-like phases (Fig. 2). Characterization of the separate phases by DIC optical microscopy had been previously confined to their size and shape. The smooth phase was thought to be the homogeneous mix of the propylene and ethylene copolymers and the composition of the separate crater-like phase was not known. We have analyzed some of these materials using the Raman microprobe. Useful Raman spectra have been obtained from samples about 3 µm thick. Differentiation of the phases was improved by evaporation of a very thin (20Å) coating of aluminum on the polymer surface. The matrix (A in Fig. 2) showed the spectral features of the propylene-ethylene copolymer. The spectrum of the separated phase (B in Fig. 2) showed an increase in the bands near to 1450 cm^{-1}. Subtraction of the matrix spectrum from the spectrum of the separated phase gave a difference spectrum characteristic of polyethylene.

Configurational isomers (*cis* and *trans*) arising from a stereoisomeric center such as a C=C band show characteristic bands in their vibrational spectra.[2] Thus, in the Raman spectra of polybutadienes the various configurations are characterized by the C=C stretching vibration at 1664 cm^{-1} in trans-1,4-polybutadiene, 1650 cm^{-1} in cis-1,4-polybutadiene, and 1639 cm^{-1} in syndiotactic-1,2 polybutadiene.
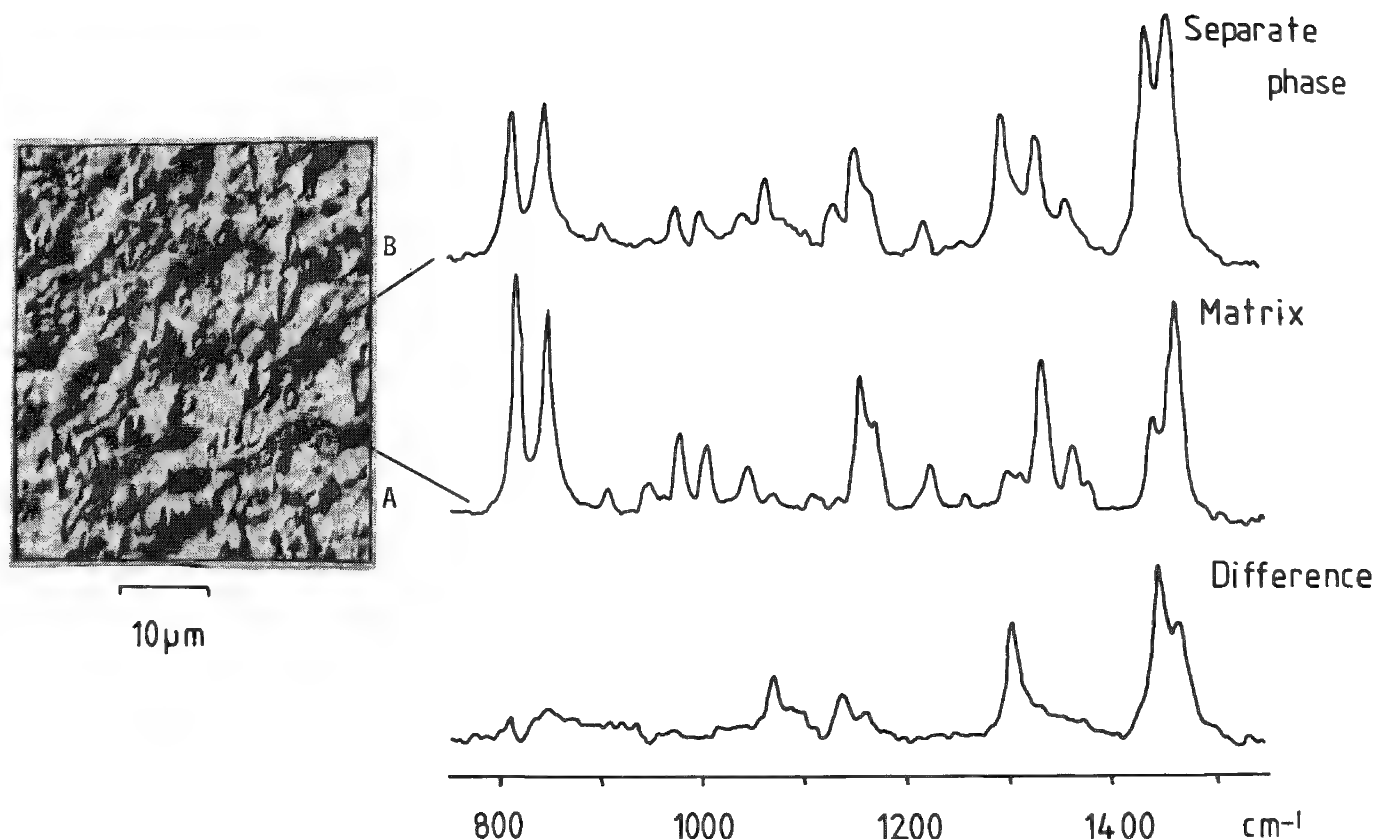
FIG. 2.--Separate phases in copolymers.

These configurations distinguish different *chemical* states, which exist in all phases and are determined by the synthesis route or polymerization catalyst used. The stereochemistry of polypropylene provides a contrasting example. The Raman spectra of the *atactic, isotactic,* and *syndiotactic* forms differ considerably below $\Delta \tilde{\nu} = 1000$ cm^{-1} because they represent conformational isomers. These differences disappear in Raman spectra taken in solution or in the melt. The spectral differences therefore characterize the *conformational* regularity of the polymer chain, although they arise originally from the *stereoregularity* imposed through the stereospecific function of the polymerization catalyst.

A conformational band is associated with a particular intramolecular arrangement in the polymer chain.[2] Figure 3 shows the changes in the Raman spectra of polyethylene terephthalate fibers which occur as the fibers age. The band shown has two peaks at 1118 cm^{-1} and 1097 cm^{-1} and is assigned to an aromatic C--H in-plane bending mode. The 1097cm^{-1} peak is associated with the planarity of the terephthaloyl unit in the crystalline regions. Its Raman intensity increases as a consequence of the gradual and spontaneous relaxation of the intramolecular strains imposed during the spinning process. The molecule attains the thermodynamically more favored planar conformation due to rotation of the carbonyl groups about the carbonyl-phenylene bond. This spontaneous change of conformation has a major influence on the textile performance of the fiber since it means that fibers of different age will contain varying states of order which govern such important end-use properties as dyeing regularity.

Analysis of Morphology

The crystalline state of a polymer is the highest state of order in a regular 3-dimensional network of polymer chains. It requires a regular arrangement of the conformational states within each polymer chain (1-dimensional cyrstallinity). Conformational
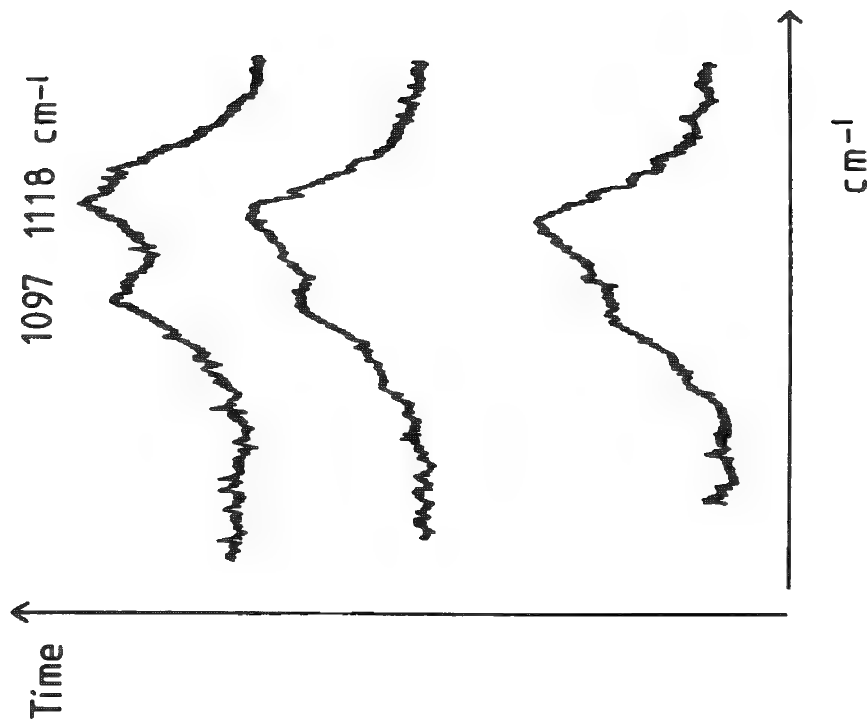
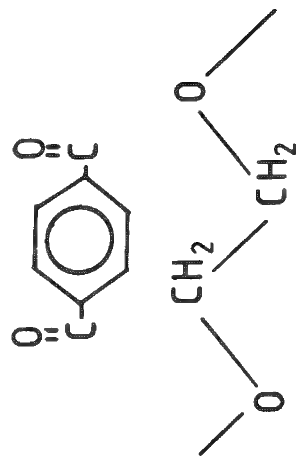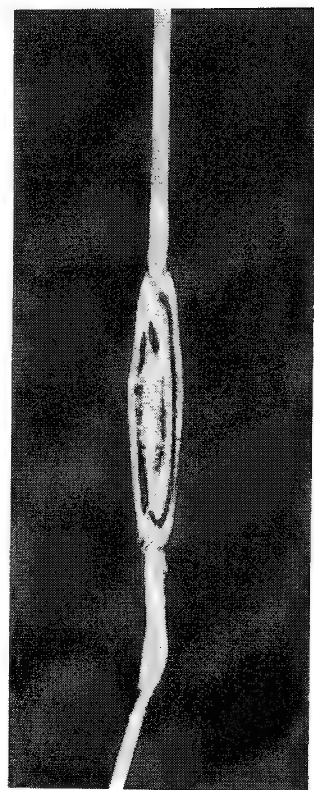P.E.T. Filament Bleb – Cross Polars

50 μm

Crystalline (ρ = 1.3953)

Amorphous (ρ = 1.3330)

1730 cm⁻¹ Carbonyl vibrations

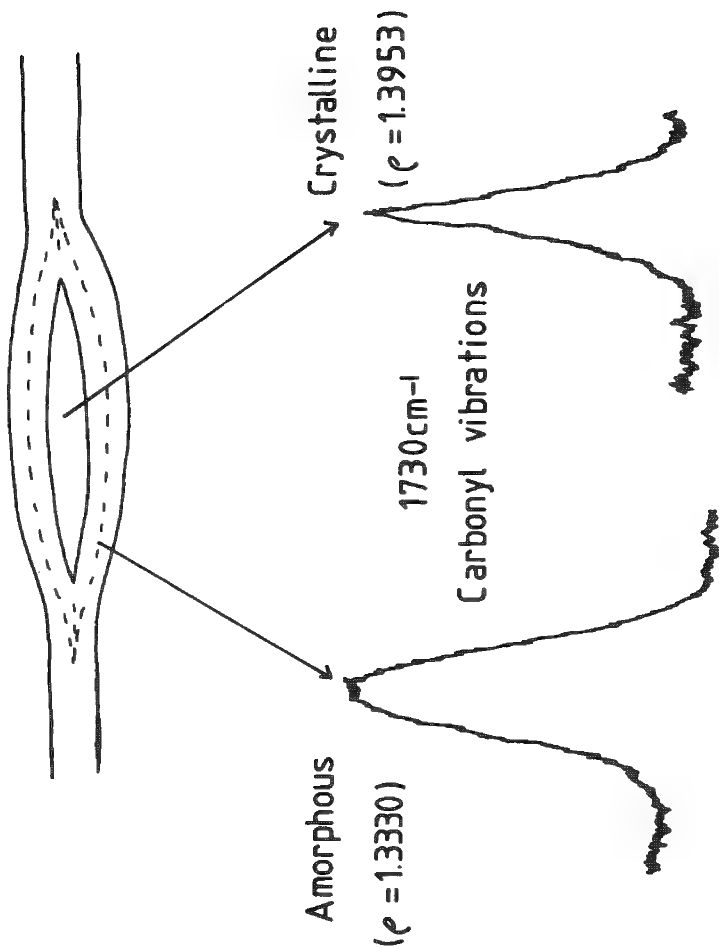FIG. 4.--Bleb in polyethylene terephthalate filament.

1097 1118 cm⁻¹

Time

cm⁻¹

FIG. 3.--Aged polyethylene terephthalate yarns.

bands in vibrational spectra have been used to characterize crystallinity.

The degree of crystallinity in polyethylene terephthalate is obtained by measurement of the bandwidth of the carbonyl stretching vibration at 1730 cm^{-1}.[3] This method has been useful in the analysis of textile defects in polyester fibers. Figure 4 shows a polyester filament containing birefringent discontinuities. The Raman bandwidths of the C=O band recorded with the laser focused in different regions within the filament reveal different degrees of crystallinity. A linear relationship was found for filaments with varying degrees of orientation.[4]

Generally, with increasing crystallinity the associated conformational bands show decreasing bandwidths. The Raman carbonyl bandwidth in polyethylene terephthalate is a measure of the conformational disorder in the molecule due to rotations of the carbonyl groups about the carbonyl-phenylene bond; the C=O groups are rotated out of the plane of the ring by varying amounts. As the polyester crystallizes and its density increases, the structure tends to become more planar and resonance stabilized. The rotational disorder decreases, as demonstrated by the narrowing of the Raman carbonyl bandwidth. Amorphous density may increase with increased orientation without an appreciable increase in the population of the planar *trans* terephthaloyl units which must occur as the polyester crystallizes. Therefore the Raman carbonyl bandwidth may give a better indication of the degree of crystallinity than is provided by the density measurement.

Raman scattering has directional properties governed by the molecular symmetry and the optical geometry used in the experiment. The Raman intensity depends on the electric vector of the exciting radiation, the viewing geometry of the spectrometer, and the symmetry of the vibrational mode concerned. The symmetry associated with the Raman band can be defined by the polarization ratio ρ. Depolarization ratios are defined

$$\rho\ (\theta) = {}^{\shortparallel}I_{\perp}(\theta)/{}^{\shortparallel}I_{\shortparallel}(\theta) \quad \text{and} \quad \rho_{\perp}(\theta) = {}^{\perp}I_{\shortparallel}(\theta)/{}^{\perp}I_{\perp}(\theta)$$

where the superscript preceding I defines the relation of the incident electric vector to the scatter plane and the subscript following I defines the relation of the electric vector of the scattered radiation to the scatter plane.[5] (A scattering plane is the plane containing the direction of propagation of the incident radiation and the direction of observation, which make an angle θ.)

Generally, the fewer the number of optical components in the optical path the closer to the true values are the measurements of ρ. Unfortunately microscopes usually contain several light-transfer optics involving reflection, refraction, absorption, and diffraction phenomena that complicate the measurements. In Raman experiments with optical systems like MOLE (where $\theta = 180°$), the most serious errors are caused by the beam splitter or semitransparent plate, which functions so that the laser radiation entering the sample and the scattered radiation leaving it use the same optical path within the microscope.

Correction factors to account for these optical effects can be derived by calibration of the optical system from white-light measurements and by Raman depolarization measurements of substances with known values of ρ (e.g., CCl_4).[6]

The optical effects can be eliminated by minimization of the selective reflection and transmission characteristics of the beam splitter. Figure 5 shows alternative designs used to measure the depolarization ratios of CCl_4 vibrations that are listed in Table 1. The standard plate reflector (as used in the MOLE) gave the greatest error and the prism reflector gave depolarization ratios close to the reference values. A smaller error is that due to the large collection angles of the high-magnification, high-numerical-aperture objectives. This error was found to be small compared with that of the reflector.

Quantitative measurements of the anisotropy in solid polymers require a more complicated mathematical treatment of the Raman data than is provided by the depolarization ratio. For transversely isotropic polymers such as uniaxially drawn polyethylene terephthalate a quantitative relationship exists between values of $\cos^2\theta$ and $\cos^4\theta$ determined from refractive-index measurements and from Raman measurements, where θ is the angle between the molecular chain axis and the direction of the orienting force
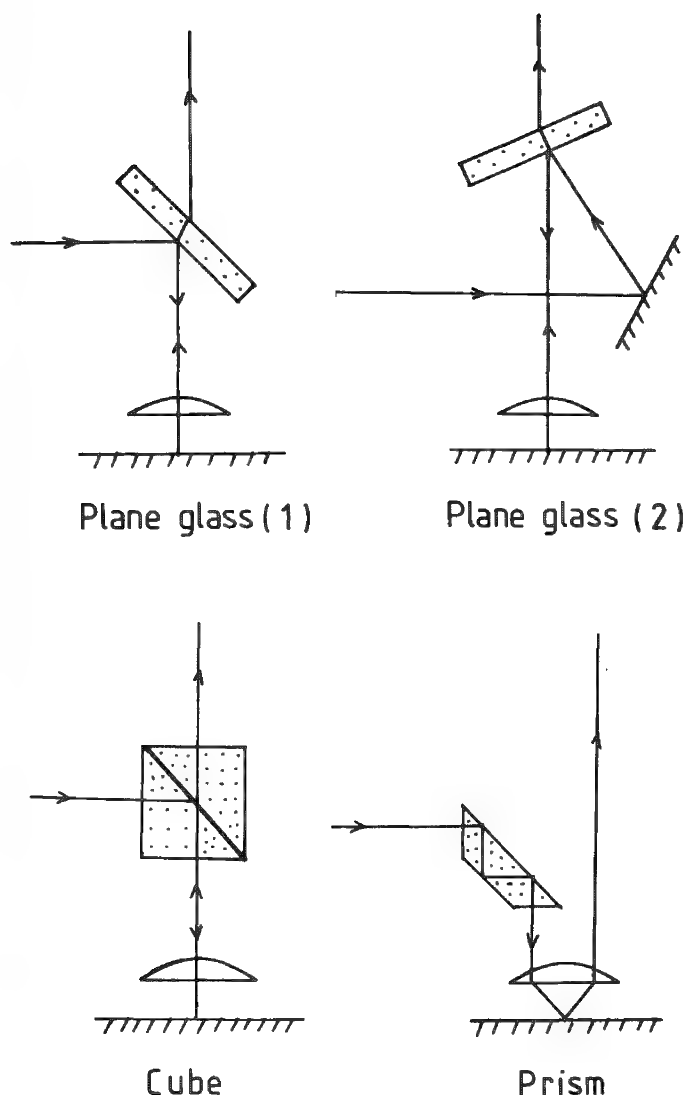
Plane glass (1)   Plane glass (2)

Cube   Prism

FIG. 5.--Beam splitter schematics.

(the draw direction). In practice the degree of orientation in polymers is defined by the orientation functions P_2 and P_4 where $P_2 = \frac{1}{2}(3 \overline{\cos^2\theta} - 1)$ and $P_4 = 35/8 \overline{\cos^4\theta} - 15/4 \overline{\cos^2\theta} + 3/8$, $P_2 = \theta$ and $\overline{\cos^2\theta} = 1/3$ for a completely nonoriented or isotropic polymer, whereas for a perfectly oriented fiber, $P_2 = 1 = \overline{\cos^2\theta}$. (The bars indicate averaging.)

Measurements of orientation in polyester filaments require the filament positioned with its draw axis Ox_3 perpendicular to the plane defined by the incident laser beam Ox_1. In the 180°C Raman experiments in which microscope systems are used the Raman scattering is also observed along Ox_1. The laser radiation is polarized parallel to Ox_1 or Ox_3 and the analyzer is set to transmit scattered radiation polarized parallel to Ox_1 or Ox_3. The corresponding Raman scattering intensities to be measure are I_{33}, I_{23}, and I_{11}, where I_{ij} is the Raman scattering intensity measured when the laser beam is polarized parallel to Oxj and the polarization vector of the analyzer is parallel to Oxi. Using the method of Purvis, Bower, and Ward we obtain the equations which can be solved for P_2 and P_4.[7] (A is a constant.)

$$I_{33} = A(0.169 + 0.512\ P_2 + 0.318\ P_4)$$

$$I_{13} = A(0.093 + 0.066\ P_2 - 0.160\ P_4)$$

$$I_{11} = A(0.169 - 0.256\ P_2 + 0.119\ P_4)$$

The errors from polarization scrambling due to reflection and refraction within the sample can be eliminated by immersion of the filament in a liquid with a similar refractive index. Table 2 compares the values of orientation functions for some polyester fibers obtained from measurements of refractive index (birefringence) and Raman scattering by use of the ring band at $\Delta\tilde{\nu}$ 1616 cm^{-1}. Raman measurements of orientation in polyester filaments by this method have provided a new tool for investigating drawing faults in polyester fibers.

Conclusions

By use of imaging techniques to locate nonfluorescent regions, Raman spectra of synthetic polymers can be measured routinely with Raman microscope systems. Chemical compositions, molecular configurations, and molecular conformations in polymers are identified through their Raman vibrational frequencies.

The Raman microprobe is a useful nondestructive tool for investigations of polymer morphology at the microlevel (1 μm) through measurements of Raman bandwidths. Quantitative measurements of localized molecular symmetry in oriented polymers are possible from Raman polarization experiments if the errors by optical effects in the system and polarization scrambling in the sample are eliminated.

TABLE 1.--Carbon tetrachloride depolarization ratios by Raman microprobe.

Objective			Reflector											
			Plane Glass(1)			Plane Glass(2)			Cube			Prism		
Mag^n	NA	2α	459	314 cm^{-1}	218	459	314 cm^{-1}	218	459	314 cm^{-1}	218	459	314 cm^{-1}	218
5	0.1	11.5°	0.03	0.54	0.54	0.02	0.60	0.61	0.03	0.68	0.72	0.03	0.75	0.75
20	0.4	47.2°	0.02	0.53	0.53	0.02	0.62	0.63	0.03	0.65	0.67	0.03	0.74	0.76
60	0.8	102.3°	0.02	0.54	0.54	0.02	0.63	0.64	0.03	0.67	0.64	0.04	0.78	0.80
100	0.9	128.3°	0.04	0.54	0.53	0.02	0.64	0.65	0.03	0.67	0.68	0.04	0.79	0.82
Reference			0.01	0.75	0.75									

TABLE 2.--Measurement of orientation in polyethylene terephthalate filaments.

Filament Sample	Orientation Coefficients		
	Refractive Index	Micro Raman	
	P2	P2	P4
1	0.58	0.53	0.20
2	0.63	0.60	0.26
3	0.73	0.70	0.54
4	0.84	0.82	0.79

References

1. W. C. McCrone and J. G. Delly, *The Particle Atlas*, Ann Arbor Science, 1973, vol. 1.
2. H. W. Siesler and K. Holland-Mortiz, *Infrared and Raman Spectroscopy of Polymers*, New York: Marcel Dekker, 1980.
3. A. M. Melveger, "Laser Raman Study of crystallinity changes in polyethylene terephthalate," *J. Poly. Sci.* A2: 10, 317-322, 1972.
4. G. D. Ogilvie and L. Addyman, "Raman microscopy of synthetic fibres," *L'actualité chemique*, April 1980, p. 54.
5. D. A. Long, *Raman Spectroscopy*, London: McGraw-Hill.
6. M. E. Andersen and R. Z. Muggli, "Microscopical techniques with the MOLE Raman microprobe," *Anal. Chem.* 53: 1772-1777, 1981.
7. J. Purvis et al., "Molecular orientation in PET studied by polarised Raman scattering," *Polymer* 14: 398-400, 1973.

A NEW SPECTROGRAPH WITH A MULTICHANNEL OPTICAL DETECTOR FOR THE RAMAN CHARACTERIZATION OF MICROPARTICLES

F. J. Purcell and E. S. Etz

Viewed under a microscope, most solid substances are far different from what they seem to the naked eye. Many materials appear as inhomogeneous arrays of particles, crystals, undefined "blobs," and phases with vague boundaries between them. Since the chemical, physical, and biological properties of real-world macrosubstances depend directly on their composition and structure at the microscopic level, there has been an increasing emphasis on microscopic analysis in recent years.

No single technique is sufficient for such analyses. Often merely the identification and quantification of the elements present are all that is needed. Research on alloys is one example; various types of microprobes have proved excellent for such research. What is needed for most other substances are molecular probes that can discern the structural/compound composition of tiny crystals, dust particulates, or biological cells. One technique gaining a rapid foothold is micro-Raman spectroscopy.[1-6] Since a laser beam can be focused down to less than 2 μm in diameter, tiny particles and tiny areas within larger samples may be analyzed. Moreover, because Raman spectroscopy, like its well-known counterpart infrared spectroscopy, yields a molecular "fingerprint" of the substance, its complete identification is often straightforward.

One of the drawbacks of micro-Raman analysis is the potential for irreversible modification (sometimes to the point of destruction) of the sample by the high-intensity laser spot--hardly surprising, since the power density of the focused laser beam at the sample ranges from kilowatts to megawatts per square centimeter. A second major limitation of micro-Raman analysis is common to macro-Raman as well: the Raman effect is exceedingly weak.

Microprobe Design

One way around both of these problems is to employ spectrographic dispersion with multi-channel detection. Instead of acquiring the spectrum point by point, as with a scanning monochromator coupled to a photomultiplier, a multichannel detector views at any given instant a spectral band or in many instances a complete Raman spectrum. The system described is designed to meet the stray-light, spatial, and spectral resolution requirements of micro-Raman spectroscopy, and provides variable dispersion at the focal plane and easy coupling to currently available multichannel detectors. To achieve this goal, a micro-Raman illuminator, the Spex MICRAMATE,[7] was grafted onto the Spex TRIPLEMATE,[7] a triple spectrograph designed specifically to work with optical multichannel analyzers employing diode array detectors.

The MICRAMATE consists of a modified research-grade microscope which focuses laser radiation onto the sample to a spot less than 2 μm in diameter, and the necessary optics to couple the microscope to a spectrometer or a spectrograph, as in the present set-up. The resulting scattered radiation is collected back through the microscope objective and focused onto the entrance slit of the TRIPLEMATE. The minimum spot size is achieved with a 40× microscope objective. There is also a 10× objective for initial viewing of the sample.

The TRIPLEMATE is divided into two sections. A zero-dispersion double spectrometer filters the Rayleigh scatter from the inelastic scatter and transmits a predetermined segment of the spectrum to the second stage, a spectrograph, which disperses the bandpass of the filter stage across the photocathode of a vidicon or diode array detector. A turret in the spectrograph provides mounts for three gratings so that the spectrum reaching the detector may be expanded or contracted by choice of a grating of different groove density. The central wavelength of the spectrum is automatically maintained by an internal microprocessor.

Fellgett[8] was the first to describe what is commonly referred to as the multiplex advantage; that is, the improvement in signal-to-noise achieved by monitoring more than one detection element simultaneously. Thus, for the same sensitivity and spectral resolution, a detector with 700 channels would record a given spectral region 700 times faster than a scanning instrument. Alternatively, if the two corresponding spectra were obtained in the same length of time, the signal-to-noise ratio would be superior by a factor of 26.5 (i.e., the square root of 700) for the spectrum from the multichannel system. Although the multiplex advantage can be realized with state-of-the-art array detector systems, these detectors do not provide the same sensitivity available from cooled photomultiplier tubes serving as detectors in single channel systems. Nevertheless, a considerable advantage in the speed and efficiency of spectral data collection with the multichannel detector is evident. More important, the possibility of sample degradation from the high-intensity laser radiation is minimized significantly if the exposure of the sample to the photon flux is shortened. Fig. 1 gives a diagram of the micro-Raman system described above. In this configuration, the instrument employed a commercially available optical multichannel
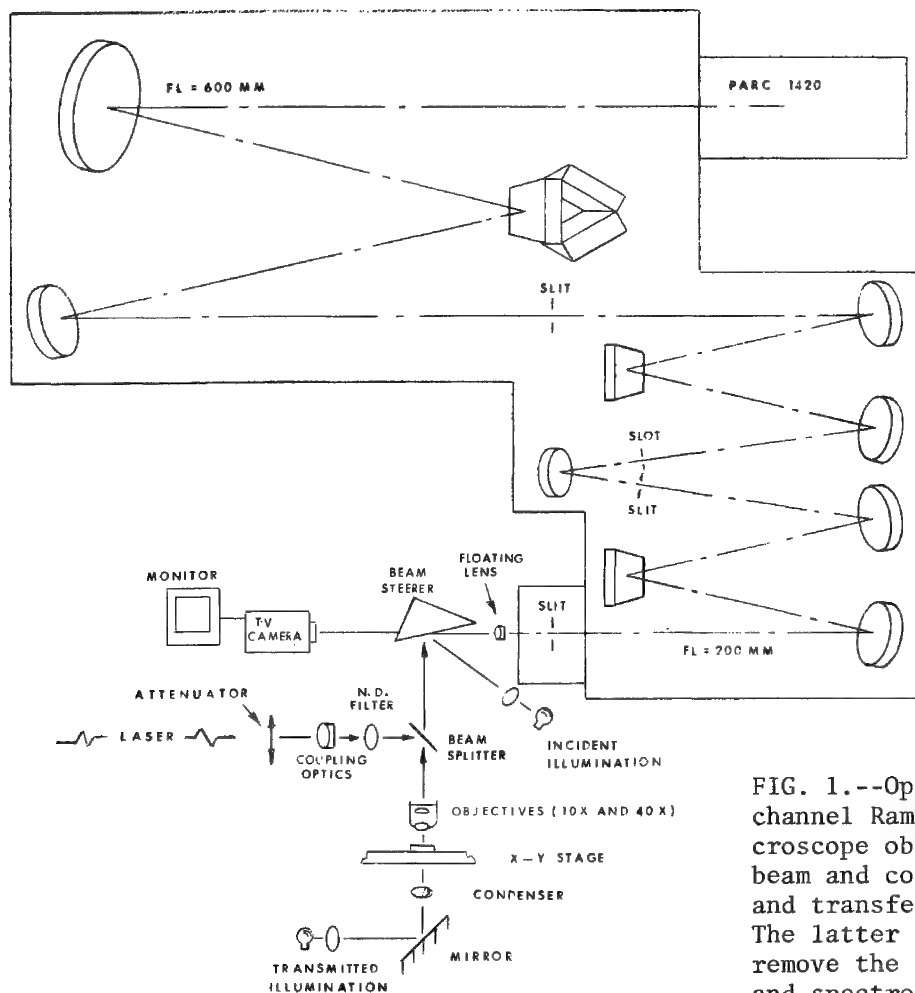

FIG. 1.--Optical schematic of the multichannel Raman microprobe showing how microscope objective both focuses laser beam and collects scattered radiation and transfers it to triple spectrograph. The latter consists of filter stage to remove the unshifted (Rayleigh) radiation and spectrograph with three gratings on a turret to expand or contract spectral coverage displayed on array detector.

302

analyzer (Model 1215 OMA-2, EG&G Princeton Applied Research Corp.)[7] in conjunction with a self-scanned photodiode array detector (Model 1420 intensified silicon photodiode array, EG&G, PARC).[7] Detailed descriptions of this optical multichannel detection system and its various solid state array detectors have been given elsewhere.[9,10]

Analysis of Stack Particles and Boiler Scale from Power Plants

Stack particles and fly ash from oil-fired power plants have been studied by Raman microprobes,[6,11,12] and some of the materials have been characterized as oxygenated sulfur compounds

Stack aerosol samples were provided by the U. S. Environmental Protection Agency (EPA). They were collected with a cascade impactor positioned inside a power plant stack. The particulate sample examined in this study was that collected on the fourth stage of a five-stage impactor from a power plant burning high sulfur content (~2.5 wt%) fuel oil with traces of V, Fe, and Ni. The microcystals found in this sample exhibit variations in size and shape. Some are dendritic (tree-like) cyrstals of various colors (shades of brown to yellow-green); others are large, irregularly shaped colorless crystals with brown and black inclusions. The large size of many of these crystals, relative to the cutoff characteristics of the impactor, indicates that they were formed on the collection surface through the interaction of solids or liquids with the gas phase of the stack aerosol.

Figure 2 shows the spectra of an 18μm particle of V_2O_5, that of a small region of a brown, dendritic crystal from the stack collection, and a third spectrum of a 6 × 10μm brown particle of boiler scale from the same power plant. The spectra clearly demonstrate that the brown material from both the stack effluent of the power plant and the boiler scale is vanadium pentoxide and not any other vanadium compound (e.g., a lower oxide). Vanadium is present in certain crude oils, e.g., those from Venezuela and Mexico,[13] as a result of biological degradation of vanadium containing animal and plant life. Thus, the Raman microprobe data give molecular information about the final combustion products of both the major and minor constituents of the oil. This information is not available from elemental microanalysis alone.

V_2O_5 is a rust-brown solid, laser radiation absorbing material. Raman microprobe measurements are successful only at relatively low irradiance conditions; prolonged exposure to focused laser radiation can induce sample modification. A microparticle spectrum of V_2O_5 can be obtained with a scanning instrument with 514.5 nm excitation, yet the spectra shown here were acquired in a fraction of the time (about one-tenth) of that required for data acquisition on a scanning, monochannel microprobe, all other experimental conditions being equivalent.

Laser Radiation Sensitive Organic Compounds: Picric Acid

Picric acid (2,4,6-trinitrophenol) is one other example of an absorbing, colored (straw yellow) compound that rapidly decomposes in the laser beam. Even at low laser powers (4-5 mW at 514.5 nm), there is noticeable sample decomposition soon after exposure to the focused laser spot. The observed morphological/chemical changes of the sample under these low-irradiance conditions cannot be explained entirely by thermal effects, but rather suggest that photodecomposition is taking place. Under these experimental conditions, it is ordinarily not possible to obtain a satisfactory Raman spectrum from a single microcrystal with a scanning system. However, the spectrum shown in Fig. 3, obtained in a 1min exposure from a 5μm crystal, clearly shows the principal bands of picric acid in the fingerprint region. A 300gr/mm grating in the spectrograph stage of the TRIPLEMATE provided a maximum spectral coverage of approximately 1300 Δcm^{-1}. Only 560 pixels of the diode array were scanned to avoid saturation of the detector in the low-frequency region by the intense laser line. This is a vivid demonstration of the second advantage of a multichannel system, that spectral data can be acquired from microsamples highly unstable under normal, practical measurement conditions.

Investigation of Uranium Compounds

Uranium compounds, such as the oxides, UO_2 and U_3O_8, as well as uranyl nitrate, $UO_2(NO_3)_2 \cdot 6H_2O$, represent another class of optically absorbing compounds that are important from an environmental standpoint. In assessing contamination of the environment
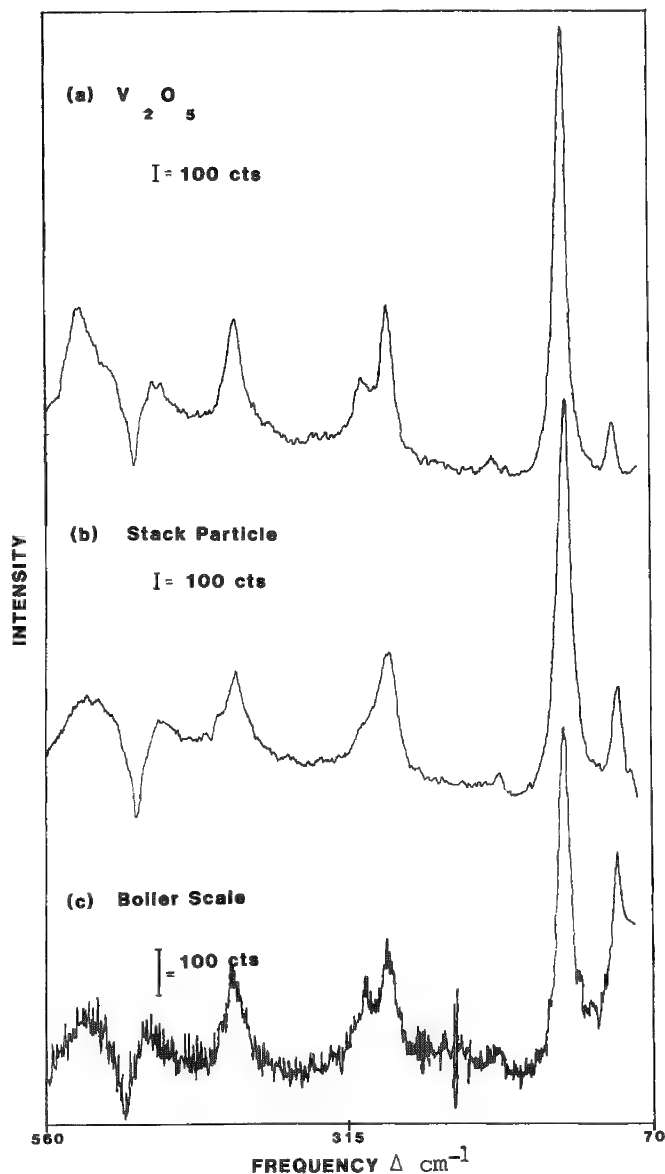
FIG. 2.--Spectra of microparticles of (a) V_2O_5, (b) power plant stack aerosol, (c) oil-fired boiler scale. Measurement parameters: (a) particle size, 18 μm; power, 20 mW (at sample); beam spot, about 2 μm; integration time, 3 min; laser line, 514.5 nm; spectral resolution about 6 cm^{-1}; (b) particle size, 100 μm; power, 15 mW (at sample); beam spot, about 2 μm; integration time, 3 min; laser line, 514.5 nm; spectral resolution, about 6 cm^{-1}; (c) particle size, 6 × 10 μm; power, 7 mW (at sample); beam spot, about 2 μm; integration time, 3 min; laser line 514.5 nm; spectral resolution about 6 cm^{-1}. Particles analyzed were mounted on microscope slides. Negative-going peak in each spectrum with dip at about 500Δ cm^{-1} frequency shift is an artifact in spectral baseline due to a string of damaged photodiodes covering approximately 55 pixels. All spectra presented in this paper represent background-subtracted results.
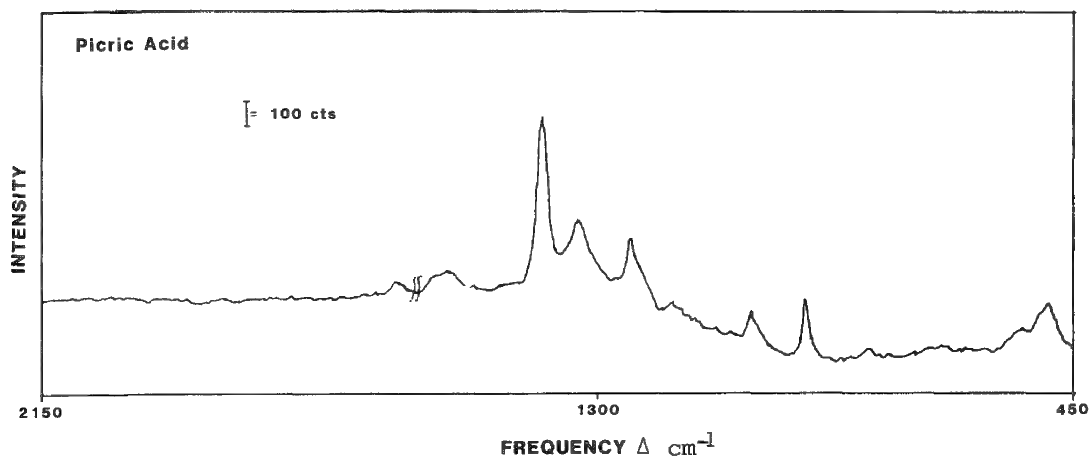

FIG. 3.--Spectrum of a single microcrystal of picric acid. Measurement parameters: particle size, about 5 μm; power, 5 mW (at sample); laser excitation, 514.5 nm; beam spot, about 2 μm; integration time, 1 min; spectral resolution, 20 cm^{-1}; particles suported on sapphire substrate.

around nuclear power plants, for example, uranium compounds are one obvious class of chemical species that requires monitoring. The oxides of uranium are all intensely colored (UO_2 is dark colored, highly opaque) and as micro-Raman samples present a formidable measurement problem owing to laser-induced sample heating. The shorter the irradiation time required, the smaller the chance of sample decomposition and the greater the chance of obtaining a good spectrum. Figure 4 presents spectra of UO_2 and $UO_2(NO_3)_2 \cdot 6H_2O$, each obtained in three minutes of signal integration. The UO_2 spectrum shows a band at 467 Δcm^{-1}, which reveals a significant but undetermined amount of ThO_2 present in the particle. The much weaker band at 445 Δcm^{-1} is due to UO_2. Uranyl nitrate has characteristic Raman bands at 745, 872, and 1040 Δcm^{-1}. Monitoring of individual particles from the atmosphere or the grounds near a nculear power plant gives specific information on the types of species being released into the environment. Thus, any potential environmental hazards may be more accurately assessed, which may permit remedial measures to be focused more effectively.

Biological Applications

Raman spectroscopy has become an invaluable tool to biological research, providing structural and conformational information on a number of problems[14,15]. The micro-Raman technique offers a unique method for obtaining this type of information on a cellular level. One area where work has already begun is the study of the mineralization of hard tissues.[12] This process is not completely understood, and it is difficult to obtain data on intact tissue in a nondestructive manner.

The main emphasis in this area has been on examining the enamel of rat incisors and embryonic chick tibia. The degree of calcification is followed by observation of the 962 Δcm^{-1} Raman band due to the symmetric P-O stretch of the main inorganic component of vertebrate bones, namely calcium hydroxyapatite, $Ca_{10}(PO_4)_6(OH)_2$, which also contains about 2-4% carbonate in the mature tissue.

Dr. Ming S. Tung at the American Dental Association Health Foundation's Research Unit at the National Bureau of Standards has prepared a synthetic carbonate apatite as a model for mature mineralized tissue. The sample studied in this investigation contains about 4.3% carbonate. We have obtained spectra from microparticles of this material with 3 min exposures and 15-20 mW laser power at the sample. A representative spectrum is given in Fig. 5 and shows the strong 962Δcm^{-1} PO_4^{3-} symmetric stretching mode and other weaker bands at the expected frequency shifts.

Conclusions

A Raman microprobe system incorporating a triple spectrograph and a multichannel detector opens up new areas of investigation that had previously presented a considerable challenge to spectroscopic examination by conventional, scanning spectrometer systems. Some of the characteristics of such a microprobe embodying commercially available instrumentation have been presented in this paper. The examples discussed are drawn from preliminary experimentation with the microprobe in the configuration shown in Fig. 1. Above all, the results presented here are intended to illustrate what we consider to be significant, current advances in micro-Raman instrumentation.

References

1. M. Delhaye and P. Dhamelincourt, "Raman microprobe and microscope with laser excitation," *J. Raman Spectrosc.* 3: 33, 1975.

2. G. J. Rosasco et al., "The analysis of discrete fine particles by Raman Spectroscopy," *Appl. Spectrosc.* 29: 396, 1975.

3. G. J. Rosasco and E. S. Etz, "The Raman microprobe: A new analytical tool," *Res. & Devel.* 28: 20, June 1977.

4. G. J. Rosasco, "Microanalysis by Raman spectroscopy," in E. D. Schmid et al., Eds., *Proc. 6th Intern. Conf. Raman Spectroscopy*, London: Heyden, 1978, 389-398.

5. H. S. Bennett and G. J. Rosasco, "Heating microscopic particles with laser beams," *J. Appl. Phys.* 49: 640, 1978.
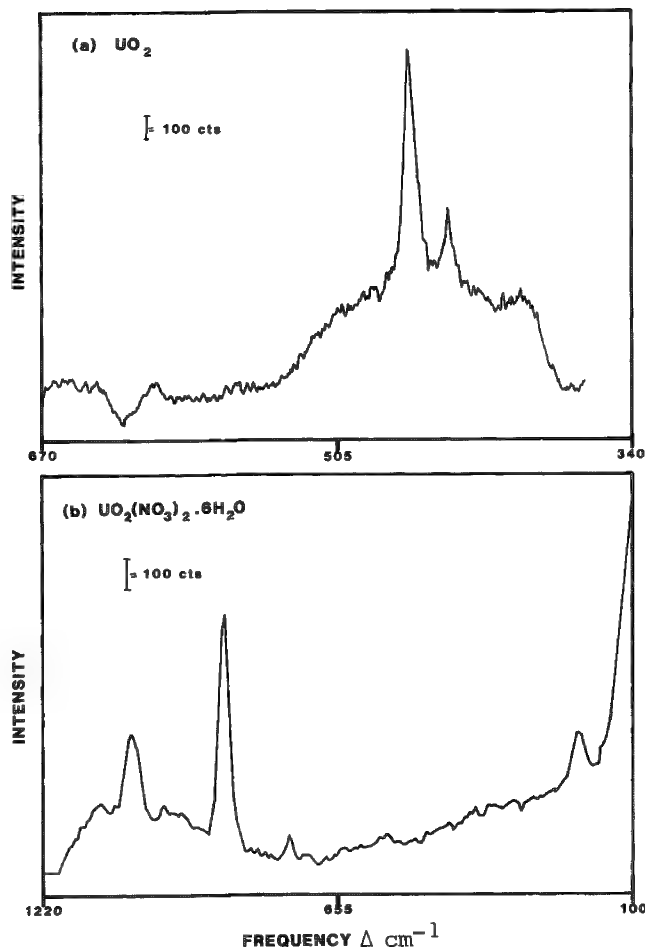
(a) UO$_2$

= 100 cts

INTENSITY

670   505   340

(b) UO$_2$(NO$_3$)$_2$·6H$_2$O

= 100 cts

INTENSITY

1220   655   100

FREQUENCY Δ cm^{-1}

FIG. 4.--Spectra of single microcrystals of
(a) UO$_2$, (b) UO$_2$(NO$_3$)$_2$·6H$_2$O. Measurement
parameters: (a) particle size, 15 μm; power,
6 mW (at sample); laser excitation, 514.5 nm;
beam spot, about 2 μm; integration time,
3 min; spectral resolution, about 6 cm^{-1};
particle supported on sapphire substrate;
(b) particle size, 7 μm; power, 5 mW (at
sample); laser excitation, 514.5 nm; beam
spot, about 2 μm; integration time, 4 min;
spectral resolution about 6 cm^{-1}; particle
supported on sapphire substrate.

Synthetic Apatite

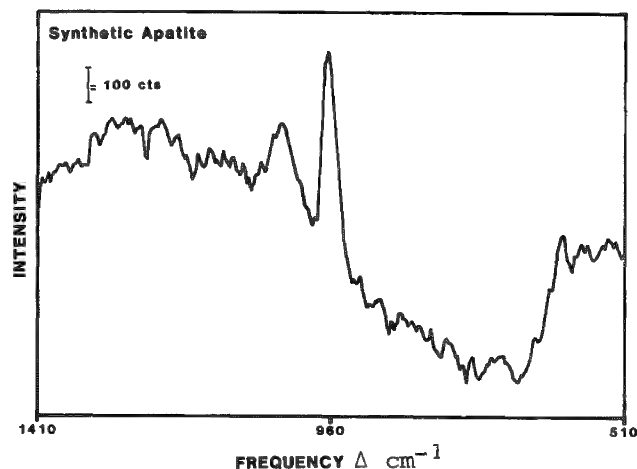= 100 cts

INTENSITY

1410   960   510

FREQUENCY Δ cm^{-1}

FIG. 5.--Spectrum of microcrystals of syn-
thetic carbonate apatite. Measurement
parameters: particle size, 30 μm; power,
20 mW (at sample); laser excitation,
514.5 nm; beam spot, about 2 μm; integra-
tion time, 3 min; spectral resolution,
30 cm^{-1}; particles supported on glass
substrate.

6. E. S. Etz and J. J. Blaha, "In-
vestigation into the critical measurement
aspects of Raman microprobe analysis,"
Microbeam Analysis--1979, 173-184.
7. Certain commercial equipment,
instruments, or materials are identified in
this paper so that the experimental proce-
dure may be adequately specified. Such
identification does not imply recommenda-
tion or endorsement by the National Bureau
of Standards, nor does it imply that the
materials or equipment identified are
necessarily the best available for the pur-
pose.
8. P. Fellgett, Ph.D. thesis, Cambridge
University, Cambridge, 1951.
9. J. L. Chao, "Applications of the
optical multichannel analyzer for low light level signal averaging and two-dimensional mode
detection of picosecond laser-generated Raman spectra," *Appl. Spectrosc.* 35: 281, 1981.
10. Y. Talmi, "Spectrophotometry and spectrofluorometry with the self-scanned photo-
diode array," *Appl. Spectrosc.* 36: 1, 1982.
11. J. J. Blaha et al., "Molecular analysis of microscopic samples with a Raman micro-
probe: Applications to particle characterization," *SEM/1979* I, 93-101.
12. E. S. Etz and J. J. Blaha, "Scope and limitations of single particle analysis by
Raman microprobe spectroscopy," in K. F. J. Heinrich, Ed., *Characterization of particles*,
NBS Special Publication 533, Washington, D.C., 1980, 153-193.
13. "Vanadium," in D. M. Considine, Ed., *Van Nostrand's Scientific Encyclopedia*,
1976, 5th ed., 2272.
14. D. A. Long, *Raman Spectroscopy*, London: McGraw-Hill, 1977.
15. J. G. Grasselli et al., *Chemical Applications of Raman Spectroscopy*, New York:
Wiley, 1981.

RAMAN MICROPROBE SPECTROSCOPY OF CERAMICS

Fran Adar and D. R. Clarke

Although a relatively new microanalysis technique, Raman Microprobe Spectroscopy is already playing a significant role in the characterization of new ceramic materials. Its principal applications to date have utilized the high spatial resolution capability of the technique for phase identification in polyphase ceramics having grain sizes in the range 0.1 to 10 µm. In such microstructural analysis applications, both the theoretical (and attainable) lateral spatial and depth-of-field resolution limitations are of importance. Although the theoretical resolution has been discussed, the attainable resolution in the 180° backscattering configuration, pertinent to the Raman microprobe, has not previously been determined experimentally. A simple experiment for determining these parameters is described, together with preliminary measurements obtained using an Al_2O_3/ZrO_2 ceramic. The utility and advantages of the Raman microprobe are then illustrated with an example drawn from a phase transformation study of boron nitride and the characterization of a CVD silicon nitride.

The majority of applications of Raman microanalysis reported in the literature to date have involved the characterization of fine particles or isolated features, such as bubbles, embedded in weakly scattering matrices; all are strictly microsampling applications. In many applications in materials science, however, where microstructural characterization of phases is required, the individual phases are commensurate in size to the optical beam of the microprobe and strong scattering may also be encountered. Under such circumstances, the ability to distinguish between different phases located in the microstructure is limited by the attainable resolution of the microprobe system. By analogy, the attainable resolution of the electron probe microanalyzer (EPMA) is determined not by the size and energy of the electron probe per se, but rather by the extent of both the beam spreading within the sample and the absorption provided by the sample.

Axial Spatial Resolution

The axial spatial (depth-of-field) resolution of microprobe systems has been discussed in terms of physical optics by a number of investigators.[1-4] Various equations pertaining to the different microprobe configurations have been proposed to include both the depth of focus of the illuminating laser beam by the objective lens and the depth of field of the optics transferring the Raman scattered radiation to the monochromator. The latter, as discussed by Dhamelicourt[3] and Rosasco,[2] can be limited by an aperture placed at an intermediate image plane between the Raman collecting lens and the monochromator entrance slit. Under such optical conditions, fluorescence, scattering, and Raman emission outside the laser focal volume are blocked by the intermediate aperture. According to Dhamelincourt's calculations, when the aperture size is equal to the lateral size of the image of the laser probe, the normalized depth (depth divided by refractive index) from which the Raman signal is collected corresponds to about 2-3 µm above and below the plane of focus.

To test the accuracy of these models, the experimental arrangement shown in Fig. 1 was employed. The sample geometry consisted of a wedge of polycrystalline alumina fused to a lower wedge of polycrystalline Al_2O_3-6 v/o ZrO_2 with the interface inclined at a small
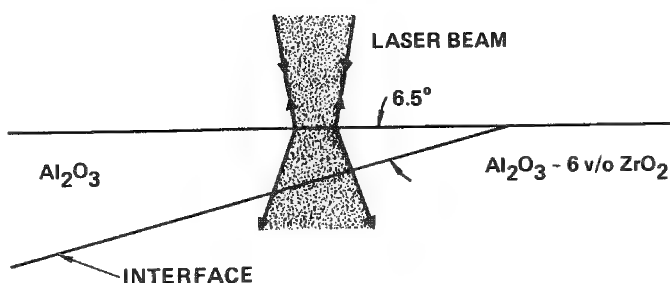
FIG. 1.--Schematic diagram of double-wedge polycrystalline sample used to evaluate axial spatial resolution of Raman microprobe.

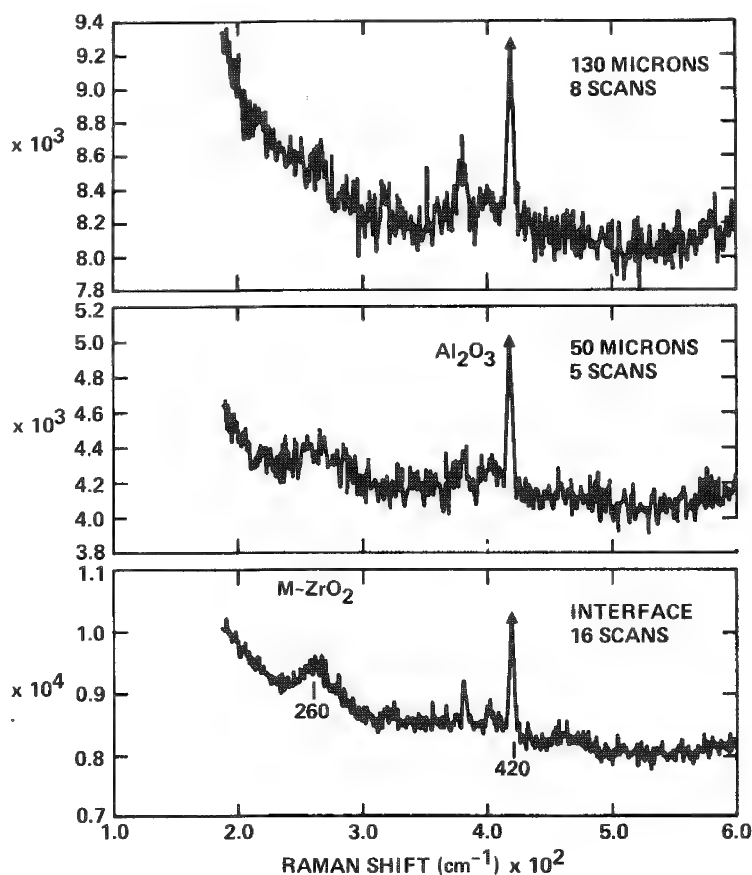FIG. 2.--Raman spectra recorded, with the geometry shown in Fig. 1, at Al_2O_3/Al_2O_3-6 v/o_2 ZrO_2 interface, and at 50 and 130 μm laterally from interface; intensity of the band at 260 cm^{-1}, characteristic of monoclinic ZrO_2, is measure of depth resolution of microprobe. Wedge angle 6.5°.

angle (6.5°) to the top surface of the alumina. The Al_2O_3-ZrO_2 system was chosen in conjunction with our study of the transformation zone size determination in zirconia ceramics.[5] In the experiment, the laser probe was placed at successively greater distances from the wedge interface, and the Raman spectra were recorded at each position. In that the alumina is a weak scatterer and the zirconia is a relatively strong Raman scattering material, the intensity of the zirconia spectra as a function of probe position may be used as a measure of the depth resolution of the microprobe. As an example of the data obtained, the Raman spectra recorded at the indicated distances from the wedge interface are reproduced in Fig. 2. A 10 μm probe was used in the experiment, since the grain size of the Al_2O_3-ZrO_2 material was about 3-4 μm. Also, the intermediate aperture was closed down to about 1 mm to match the size of the image of the probe diameter. When the probe was placed 50 μm or more from the interface (i.e., when the zirconia was about 6 μm below the surface of the sample), the zirconia band at 260 cm^{-1} was no longer discernible, which indicates an upper bound for the depth resolution of the microprobe of about 6 μm. Given that the refractive index of alumina is about 1.76, this experimental values is in reasonable concurrence with that predicted by Dhamelincourt.

Lateral Spatial Resolution

As with the axial spatial resolution, it has been recognized that the lateral resolution is determined by both the illuminating optics and the collector angle subtended by the intermediate aperture of the Raman transfer optics. Consideration of these optics[2-4] suggests that an objective lens having a numerical aperture (n.a.) of 0.9 would focus about 84% of the illuminating laser energy into a diffraction limited spot (1.22 λ/n.a.) of about 0.7 μm diameter and that an intermediate aperture matched to the image size of the illuminating spot should confer a lateral resolution in the focal plane of the objective corresponding to the probe size. Experimentally, the illuminating probe size is relatively simple to measure because the probe can be imaged directly, and observations at conjugate image planes indicate that a 1μm spot size can indeed be formed with objectives of 0.85 and 0.9 n.a. Previous studies of the lateral spatial resolution have emphasized experimental situations where isolated particles are positioned on

a weakly scattering supporting substrate, such as single crystal alumina. In such cases, little stray or multiple scattering from the substrate into the particle and rescattering of the Raman signal back into the collecting optics is to be expected. The experimental situation pertinent to microstructural analysis of phases embedded in polycrystalline samples is significantly different; grain boundaries, intergranular phases, and porosity will introduce additional multiple scattering. For this reason, it is worth while to reevaluate the net attainable lateral resolution. Measurement can be made with the sample geometry shown schematically in F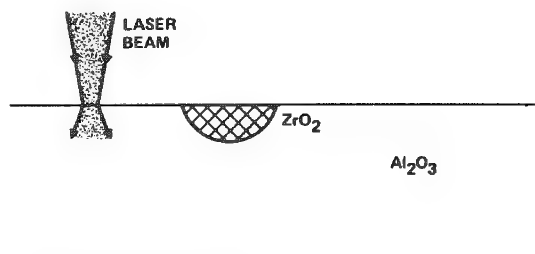ig. 3. By special heat treatment procedures it is possible to make a sample of this geometry and, contained in a polished section, a small ($\simeq$ 1 μm) zirconia grain entrapped in a much larger alumina grain. By recording Raman spectra at successive positions in the alumina grain up to the zirconia particle, a measure of the lateral resolution can be obtained. Preliminary results indicate that no zirconia bands are detectable until the probe is within half the probe diameter of the zirconia particle. The experiment is a quite stringent test, since zirconia is a particularly strong Raman scatterer and the alumina provides a rather weakly absorbing matrix for multiple scattered radiation.

FIG. 3.--Schematic sample geometry for assessing lateral spatial geometry of poly-phase, polycrystalline sample containing embedded phase particle.

Application

Clearly, more refined measurements of both the axial and lateral spatial resolutions are required for a variety of optical conditions, but the preliminary experiments described above indicate the general validity of the estimates derived from transfer optics calculations and confirm their value as guidelines in performing high spatial resolution Raman microprobe analysis. In this section, two applications to the characterization of micron grain size ceramics are briefly presented.

Boron nitride is a commonly used ceramic. In its hexagonal form, for instance, it is used as a high-temperature lubricant and filler, whereas in its cubic form it has applications as an abrasive and cutting material. It is both isomorphous and isoelectric with carbon. One of the problems encountered in the characterization of the microstructure of a polyphase, hot-pressed ceramic containing boron nitride was to determine the polymorphs present after processing. Representative spectra recorded from the micron-sized grains are reproduced in Fig. 4 and are compared with spectra obtained from a cubic boron nitride powder. The spectrum documents the presence of both the cubic and hexagonal polymorphs in the fabricated material. Although an apparently simple application, the problem is intractable when more conventional techniques (e.g., electron probe microanalysis) are used, because of the low atomic weight of B and N and the inability to distinguish polymorphic forms.

Silicon nitride, an important structural and dielectric ceramic, may be prepared by several techniques, including hot-pressing of powders and chemical vapor deposition (CVD). The latter normally leads to a highly pure, fully crystalline material which consists entirely of the alpha polymorph and exhibits the characteristic Raman spectrum shown in Fig. 5. Occasionally, however, the CVD process results in a material containing 1-20 micron sized shiny inclusions that may act as fracture origins on stressing. Sample preparation difficulties have prevented their investigation by analytical electron microscopy in the transmission electron microscope. In the Raman microprobe, however, the inclusions can be readily selected and analyzed. Spectra from three such inclusions are reproduced in Fig. 6. In Fig. 6(a) the sharp bands at 261 and 365 cm^{-1} are the strongest bands of the α-Si$_3$N$_4$ phase. Broad bands centered at about 130 and 390 cm^{-1} appear in the majority of spectra recorded from the inclusions and indicate the presence of a glassy phase. In
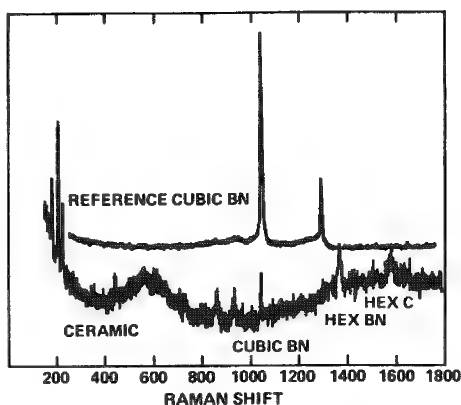
FIG. 4.--Comparison of Raman spectrum obtained from single-crystal particle of cubic boron nitride and a dense ceramic containing both hexagonal and cubic polymorphs of boron nitride.
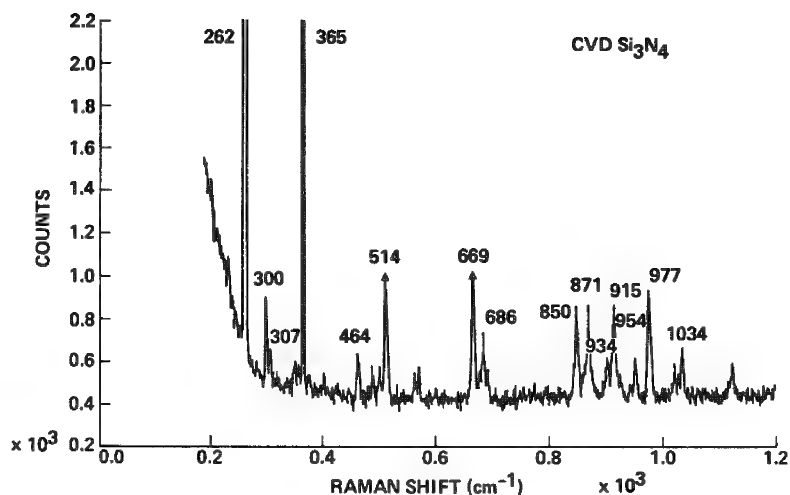

FIG. 5.--Raman spectrum of α-silicon nitride; strongest bands occur at 262 and 365 cm^{-1}

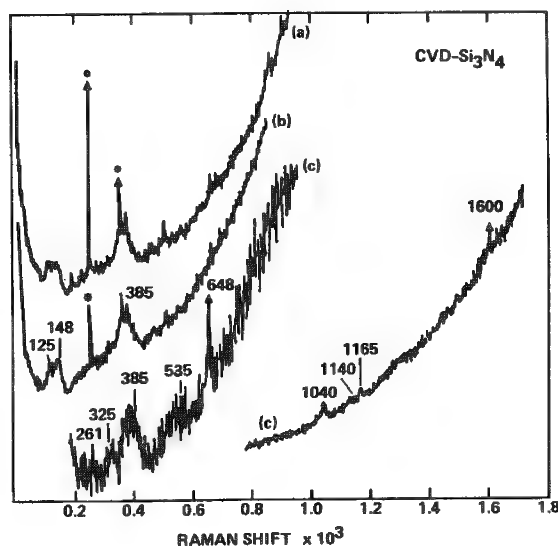FIG. 6.--Spectra recorded from three different shiny inclusions in CVD polycrystalline silicon nitride. Characteristic bands of α-Si_3N_4 are marked by asterisks. Broad bands at about 130 and 390 cm^{-1} indicate presence of glassy phase; band at 1600 cm^{-1} is due to elemental carbon impurity.

the spectrum of Fig. 6(c), the strongest band of the glass phase is centered at 385 cm^{-1}. The spectrum also exhibits a band at 1600 cm^{-1}, indicative of elemental carbon, an impurity introduced during manufacture, which may account for some of the black color. Other bands at 648, 1040, and 1165 cm^{-1} have not been identified.

Other ceramic systems for which the technique of high-resolution Raman microprobe spectroscopy has proved valuable include other silicon-nitride based materials and ceramics developed for the immobilization of nuclear waste.

References

1. T. Hirschfeld, "Raman microprobe: Vibrational spectroscopy in the temtogram range," *J. Opt. Soc. Am.* 63: 476-477, 1973.

2. G. J. Rosasco, "Raman microprobe spectroscopy," in R. J. H. Clark and R. E. Hester, Eds., *Advances in Infrared and Raman Spectroscopy*, London: Heyden, 1980, vol. 7.

3. P. Dhamelincourt, Ph.d. Thesis, University of Lille, 1979.

4. F. Adar, "Developments in Raman microanalysis," in R. H. Geiss, Ed., *Microbeam Analysis--1981*, 67-72.

5. D. R. Clarke and F. Adar, "Measurement of the crystallographically transformed zone produced by fracture in ceramics containing tetragonal zirconia," *J. Am. Ceramic Soc.* 65: 1981.

RAMAN MICROPROBE ANALYSIS OF PRISTINE AND IODINE-DOPED POLYACETYLENE FILMS

L. Lauchlan, T. Woerner, A. G. MacDiarmid, and Fran Adar

The Raman microprobe has been used to study and characterize spectral features of the order of 1 μm in pristine and heavily iodine-doped polyacetylene, $(CH)_x$. The special features of the microprobe have allowed an unambiguous identification of an oriented $(CH)_x$ film polymerized on crystal faces of biphenyl containing disolved Shirakawa catalyst. We also present the first evidence for an inhomogeneous distribution of dopant species (I_3^- and I_5^-) on a scale of this size in free-standing $(CH)_x$ films doped rapidly to saturation with iodine.

Results from transport and optical studies of pure $(CH)_x$ and chemically or electrochemically doped $(CH)_x$ have demonstrated that its electrical, optical, and thermoelectric properties can be varied systematically to span the full range from semiconductor to metal as the dopant concentration is increased.[1-3] The pure polymer is typically prepared as a low-density, flexible film composed of randomly oriented fibrils (ca 200 Å in diameter). Electron microscopy studies have shown that significant alignment of the polymer fibrils can be produced by stretch elongation of the *cis*-film. Such orientation leads to an increase in the electrical conductivity along the direction of stretching of an order of magnitude. Marked optical anisotropy is also introduced. In an effort to produce as-grown oriented $(CH)_x$ film, it has recently been found that acetylene gas may be polymerized directly on crystal faces of biphenyl containing disolved catalyst to give oriented films of $(CH)_x$.[4] $(CH)_x$ films prepared in this manner have been examined under a polarizing optical microscope by reflected light. Regions of the $(CH)_x$ film, many of which are rectangular (ca 0.5 × 0.1mm) can be observed to change from highly reflecting to weakly reflecting when rotated by angles of 45° between crossed polarizers (Fig. 1). Comparison with polarized reflectance micrographs of stretch aligned $(CH)_x$, ($1/1_0 = 2.9$, where 1 and 1_0 are the lengths after and before stretching, respectively) shows the optical effect to be comparable (Fig. 2).

After preparation of material that exhibited orientation, molecular identification was sought. The sample size dictated the Raman microprobe as the technique of choice for this identification.

As mentioned above, one of the more interesting properties of polyacetylene is its ability to be transformed from the semiconducting state to the metallic state by doping of the as-prepared films. Although this system has been extensively studied, controversy remains concerning the homogeneity of chemically doped films.

Variability of dopant species in heavily doped films has been observed with macro-Raman spectroscopy. Differences were observed in materials chemically doped under a variety of conditions and subjected to differing histories (air exposure, isomerization conditions, etc.). In particular, the Raman spectra of polyacetylene doped with iodine exhibit bands that have been assigned to at least two species of iodine.[5-7] I_3^- has a Raman-active fundamental at 106 cm^{-1}; its first and second overtones are also often observed. The Raman-active fundamental band of I_5^- occurs at 160 cm^{-1}.

Independent evidence for heterogeneous doping is derived from visible reflectance measurements. Heavily iodine-doped polyacetylene films indicate some remnant of the interband transition even though such a transition should be absent in the metallic state. This result has been interpreted by the suggestion that the iodine is not dispersed homogeneously.

Using the Raman microprobe we have studied heavily doped free-standing films (ca 80 μm thick) by searching for spatial heterogeneities in the dopant species - I_3^- and I_5^-.
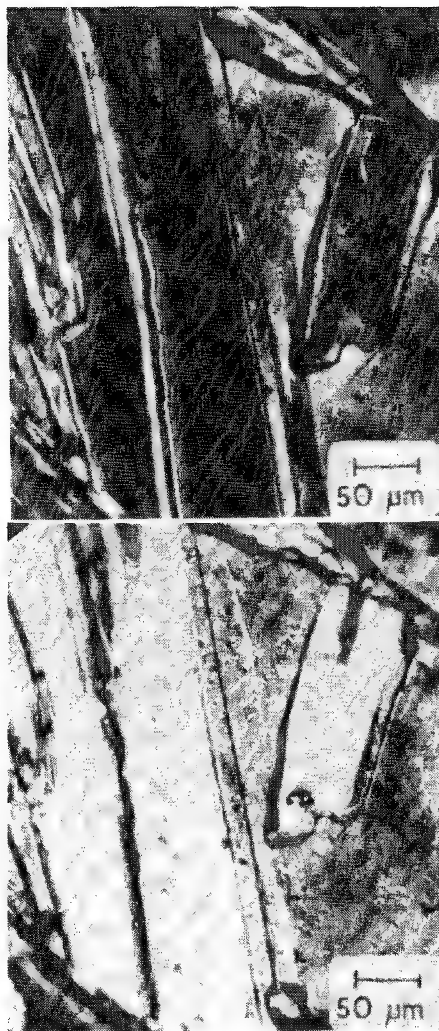
FIG. 1.--Polarized light micrographs of epitaxial $(CH)_x$ film grown on biphenyl taken between crossed polarizers with sample at two orientations 45° apart: maximum relfectivity; minimum reflectivity.
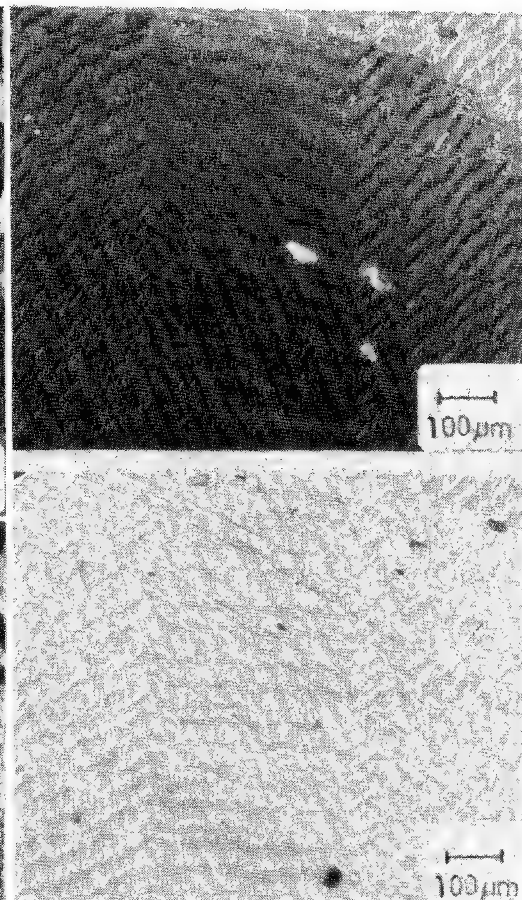
FIG. 2.--Polarized light micrographs of stretch-oriented films, taken under conditions similar to those of Fig. 1.

Experimental

In this study the epitaxially grown film was examined in air. This procedure resulted in some oxidation of the as-prepared material, as monitored by broadening of the bands, while the measurements were being made. However, that did not prevent identification of the film as polyacetylene. Figure 3 shows a spectrum of a free-standing polyacetylene film displayed with a spectrum of an epitaxial film. These bands are characteristic of the conjugated π system of trans-$(CH)_x$. The spectra are nearly identical.

Free-standing films of $(CH)_x$ were doped rapidly to saturation by exposure of cis-$(CH)_x$ to iodine vapor in vacuo for 3-5 hr at room temperature. After pumping for 1 hr the samples were sealed in rectangular quartz tubing in an inert atmosphere. Doping was performed rapidly in order to maximize the possibility for nonuniform doping. Repeated scans of the same spot produced identical spectra from which it can be argued that the laser spot did not drive off appreciable dopant. Figure 4 shows a representative spectrum of doped trans-$(CH)_x$. The intensities of the π system bands are markedly reduced in the doped material.

During polmerization of free-standing films in glass vessels, $(CH)_x$ grows on the glass surfaces wetted by toluene solutions of catalysts. The side of the film that has adhered to the glass is composed of fibrils more densely packed than on the surface facing the acetylene gas. The densely packed side of the film appears shiny whereas the second surface is dull. Raman microprobe spectra were recorded from both surfaces.

Representative spectra from heavily doped free-standing films are shown in Fig. 5. These spectra show differences in relative intensities of I_3^- and I_5^-. Only I_3^- was observed on the shiny surface, even though many spots were examined. On the dull surface I_5^- as well as I_3^- - was observed, and their relative intensities varied as the sampled spot was changed.
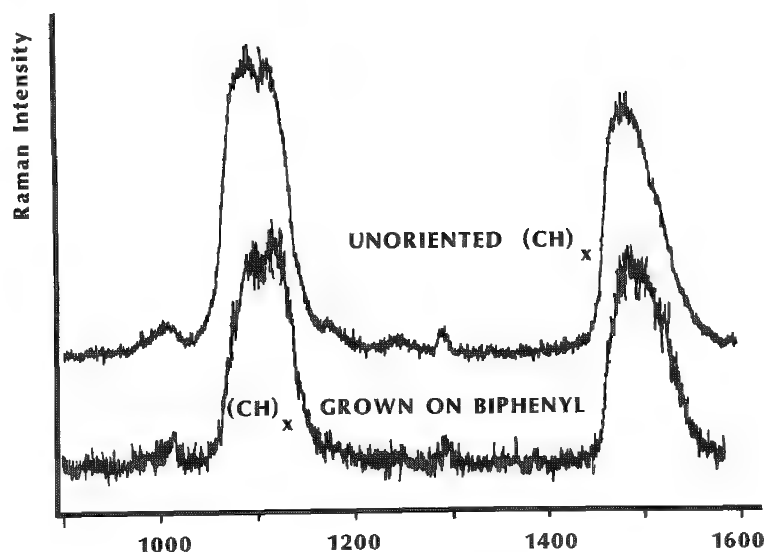
FIG. 3.--Raman microprobe spectra of free-standing polyacetylene and polyacetylene platelet grown on biphenyl. λ_{ex} = 514.5 nm, 400µm slits, 50× objective; conditions for free-standing film: 50 cm^{-1}/min, 2 accumulated scans, 30 mW laser power (ca 3 mW at sample); conditions for platelet: 100 cm^{-1}/min, 1 scan, 10 mW.
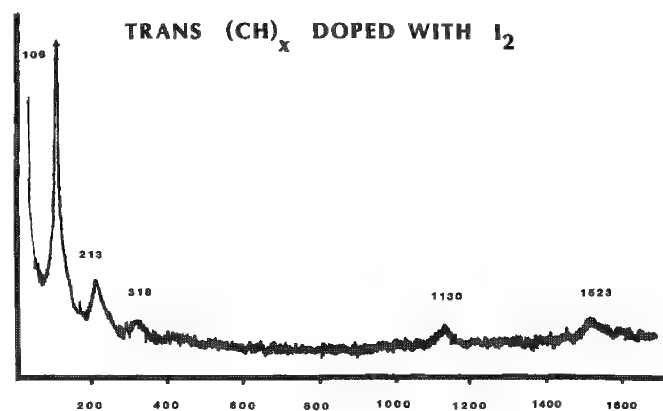

FIG. 4.--Raman spectrum of iodine doped free-standing polyactylene film. Bands between 100 and 350 cm-^{1} are due to I$_3^-$ and I$_5^-$; bands between 1000 and 1600 cm^{-1} are due to the conjugated π system. λ_{ex} = 482.5 nm, 5 mW, 200µm slits, 100 cm^{-1}/min, 50× objective.

FIG. 5.--Raman microprobe spectra of iodine doped free-standing films recorded in low frequency region where bands of I$_3^-$ and I$_5^-$ occur. λ_{ex} = 482.5 nm, 8 mW, 300µm slits, 100 cm^{-1}/min, 4 accumulated scans, 50× objective.

The heterogeneities displayed in Fig. 5 were somewhat surprising. Earlier scanning electron microprobe studies of heavily doped trans-(CH)$_x$ revealed iodine concentrations which were uniform on a scale of 5000 Å (0.5 µm).[8] Examination of shiny and dull sides of the film by x-ray microanalysis exhibited no apparent differences in distribution of iodine atoms. In order to reconcile the electron and Raman microprobe results, one must conclude that iodine is inhomogeneously speciated into I$_3^-$ and I$_5^-$.

Conclusions

The Raman microprobe has allowed the unambiguous molecular identification of epitaxially grown (CH)$_x$. Heavily doped polyacetylene films exhibit heterogeneities of iodine species on the 1µm scale. This result complements SEM results which showed no spatial variation in atomic iodine concentrations in heavily doped films on the 0.5µm scale. The Raman
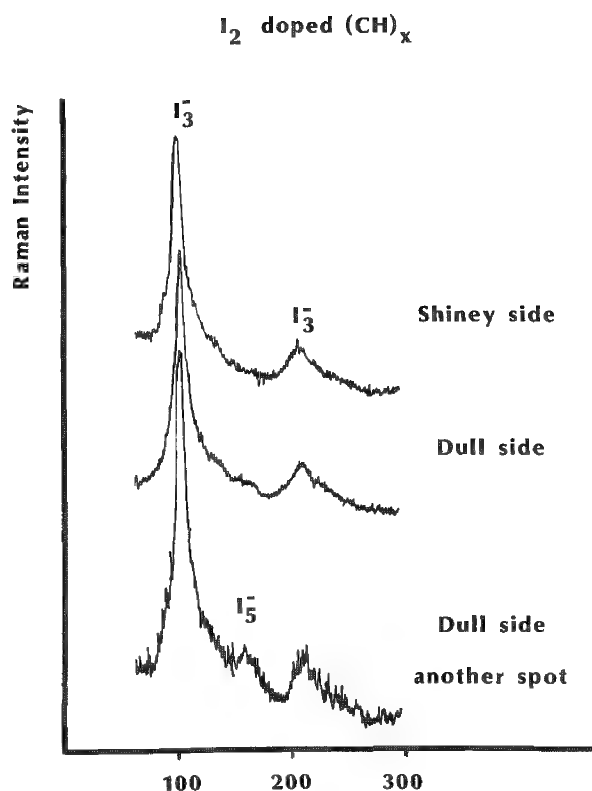
microprobe is unique in providing local information on molecular species in this system.

References

1. T. Ho, H. Shirakawa and S. Ikeda, "Simultaneous polymerization and formation of polyacetylene film on the surface of concentrated soluble Ziegler-type catalyst solution," *J. Polym. Sci.: Polym. Chem. Ed.* 12: 11, 1974.

2. C. K. Chiang, C. R. Fincher Jr., Y. W. Park, A. J. Heeger, H. Shirakawa, E. J. Louis, S. C. Gau. and A. G. MacDiarmid, "Electrical conductivity in doped polyacetylene," *Phys. Rev. Lett.* 39: 1098, 1977.

3. C. R. Fincher Jr., M. Ozaki, A. J. Heeger, and A. G. MacDiarmid, "Donor and acceptor states in lightly doped polyacetylene, $(CH)_x$," *Phys. Rev.* 19: 4140, 1978.

4. T. Woerner, A. G. MacDiarmid, and A. J. Heeger, "Direct synthesis of oriented polyacetylene, $(CH)_x$, from acetylene gas," *J. Polym. Sci: Polym. Lett. Ed.*, in press.

5. S. Lefrant, L. S. Lichtmann, H. Temkin, D. B. Fitchen, D. C. Miller, G. E. Whitwell II, and J. M. Burlitch, "Raman scattering in $(CH)_x$ and $(CH)_x$ treated with bromine and iodine," *Solid State Commun.* 29: 191, 1979.

6. S. L. Hsu, A. J. Signorelli, G. P. Pez, and R. H. Baughman, "Highly conducting iodine derivatives of polyacetylene; Raman, XPS, and X-ray diffraction studies," *J. Chem. Phys.* 69: 106, 1978.

7. I. Harada, M. Tasumi, H. Shirakawa, and S. Ikeda, "Raman spectra of polyacetylene and highly conducting iodine-doped polyacetylene," *Chem. Lett.* p. 1411, 1978.

8. H. Rommelmann, R. Fernquist, H. W. Gibson, A. J. Epstein, M. A. Druy, and T. Woerner, "Morphology and dopant distribution in polyacetylene," *Mol. Cryst. Liq. Cryst.* 77: 177, 1981.

OPTICAL SPECTROSCOPY BY MICROPROBES WITH DIODE ARRAY SYSTEMS

D. O. Landon

Efficient multichannel analysis of optical signals generated in microprobes provides the user with great analytical versatility and allows maximum information to be gathered while sample size and possible damage are minimized. The interesting applications are to Raman, photoluminescence, and cathodoluminescence spectra. This paper is more a presentation of possibilities than of existing realities, yet it is soundly based on thoroughly documented work and techniques.

Definitions

Before we discuss instrumentation further, let us define the three types of spectra we shall be dealing with. The first two are generated in optical microprobe instruments, typically with laser light excitation sources.

Raman spectra are related to vibrational modes of the molecule. One "sees" the molecular structure. The spectra are produced when a laser beam is focused on the sample. Focused laser beams give spot sizes below 1 µm.[1]

Photoluminescence spectra occur through a different mechanism of absorption of one photon and re-emission with a loss of energy. One "sees" electron band gaps and trap and defect energies. These spectra are usually produced with lasers in the same optical cinfiguration as used for Raman spectra.

Cathodoluminescence spectra are produced in electron probe instruments. Cathodoluminescence spectra result from the energy loss that occurs when an electron is transformed into a photon. One "sees" the same physical entities as in photoluminescence. With the typical focused electron beams used, lateral spatial resolution is of the order 2-3 µm.[2]

Discussion

The spectra produced by all of the above phenomena are typically in the range from about 250 nm to 8 µm.

The Raman spectra are almost entirely seen in the wavelength range 300-850 nm. It has been remarked that there is no type of spectral detection in this range that is not better done with a multichannel system as compared to a scanning monochannel one.[3]

At the 1979 MAS meeting small-area Raman measurements were the subject of a symposium. In the few years since, the intensified diode array detector (IDARSS) has taken over as the multichannel detector of choice. The devices have wide spectral range (190-900 nm), offer time-gating capability to a few nanoseconds, and come in several delicious, though expensive, flavors. The pioneers who are working with these detectors are convinced that the expense is well justified by the results.

Large spectral coverages at decent spectral resolution are possible, and the multichannel advantage permits the taking of Raman spectra in a reasonable time with the laser input power held below the damage threshold of sensitive samples.

Photoluminescence (PL) and cathodoluminescence (CL) spectra are quite interesting. Originating in the structure and lattice of the host crystal, they are very sensitive to small changes. Many of the most important transitions for luminescence are not between energy levels in the host material, but involve impurities, point defects, and aggregates of point defects. There is no simple rule that enables the researcher to identify the mechanism responsible for a particular emission by measuring the photon energy, and this lack has certainly inhibited the widespread use of PL and CL, but they are progressing in

The author is with Tracor Northern, Inc., 2551 West Beltline Highway, Middleton, WI 53562.

both theory and instrumentation.[4]

All CL spectra at and above liquid nitrogen temperature consist of fairly broad emission bands, because of coupling to the lattice vibrations. At lower temperatures sharp line spectra begin to be seen.

We referred to the lack of a simple rule for interpreting CL spectra as inhibiting the use of the technique. This lack is in fact being remedied, as the theoreticians are at work to systematize the information and generate a database.[4]

The next inhibition is the lack of really suitable detection equipment. Here, the instrumentation now available will do very well. Once again, the multichannel approach is much superior to conventional wavelength scanning.

In the range from the near UV (280 nm) to the near IR (900 nm), the same detectors as are used in Raman microarea analysis work very well, and since spectral resolution requirements are usually reduced, large spectral coverages in the range 300-900 nm are possible. The PL and CL techniques can produce such rewarding information that there is a growing interest in working in the range 900-3300 nm.

This development brings us squarely up against the need to develop new instrumentation. One requirement is for helium temperature stages. Various mechanical improvements would result, such as lower sample damage and greater intensity of CL spectra. The really important advance associated with lower temperature at the sample would be the resolution of the broad CL bands into line spectra that could be interpreted in fundamental quantum-mechanical terms.[4]

Again, so far, so good. We can hypothesize ease of data gathering using existing diode array spectrographs attached to our microscope via simple lens-fiber optic systems. The low-temperature spectra should permit the generation of a real database in the range to about 900 nm.

Now, back to the near infrared. We wish to examine the CL properties of Group III-V alloy materials.[5] In extensive use in lasers and light-emitting diodes, they are also under intensive development for use in integrated optics. These materials must emit and detect in the range of 1.3-1.6 μm. Ultimately we may see nonsilica fibers, and optical communication even at 4-8 μm. When we get to the range of fundamental electrical and optical properties of dislocations in semiconductors at these wavelengths, we reach the probable end of any interest in developing array detection. The fundamentals of noise theory show that the way to do the job is by multiplex nondispersive infrared detection with some form of Michelson interferometer.

What we have identified is a need for some type of multichannel detection with wavelength dispersive optics for the range 0.9 to about 3 μm. Although lead sulfide is not the only possible choice here, it looks interesting; it has the highest D^* of any near-IR detector and can be fashioned into a multi-array type of detector with discrete sensitive areas in a linear format.

Summary

The program of the 1979 MAS meeting included for the first time a session on Laser Raman Microprobe Analysis. This session served to introduce optical microbeam techniques as effective methodologies for molecular and structural analysis in the microscopic domain, complementary to established methods of elemental analysis. Several manufacturers provide various types of Raman packages for microprobe applications, yet the intensified diode array detector has taken over as the multichannel optical range detector of first choice.

The laser-Raman packages can also be used for photoluminescence (PL) measurements in the same optical range, although less sophisticated optics suffice if the Raman spectra are not sought.

Cathodoluminescence (CL) measurements require only a simple small spectrograph, since the electron beam and scattered electrons produce no stray optical signal. CL spectra cover the UV and visible range between about 260 and 900 nm. The intensified diode array detectors available are perfect for this range, and packages with minispectrographs are commercially available. The experimenter only has to mount an appropriate lens and fiber optics conduit in his microscope to get into business.[6-8]

Efficient PL and CL measurements in the spectral range 0.9-3 μm await the development of sensitive array type infrared detection, but the available technology seems capable of supporting such an effort.

References

1. Fran Adar, "Developments in Raman microanalysis," *Microbeam Analysis--1981*, 67-72.
2. J. N. Ramsey, "Raman, photoluminescence, cathodoluminescence applied to micro-characterization of S/C device materials," *Microbeam Analysis--1980*, 235-238.
3. G. D. Christian, J. B. Callis, and E. R. Davidson, "Array Detectors and Excitation-Emission Matrices in Multicomponent Analysis," in E. L. Wehry, Ed., *Modern Fluorescence Spectroscopy*, New York: Plenum Press, vol. 4.
4. D. B. Holt and S. Datta, "The cathodoluminescent mode as an analytical technique: Its development and prospects," *SEM/1980* I, 259-278.
5. C. B. Norris and C. E. Barnes, "Cathodoluminescence studies of an anomalous ion implantation defect: Introduction in lightly and heavily doped liquid phase epitaxial GaAs:Sn," *Appl.Phys.* 51: 5764-5772, 1980.
6. L. Carlssan and C. G. VanEssen, "An efficient apparatus for studying cathodo-luminescence in the scanning electron microscope," *J. Phys.* E7: 98-100, 1974.
7. W. Brocker and G. Pfefferkorn, "Bibliography on cathodoluminescence, Part II," *SEM/1980* I, 298-302.
8. D. O. Landon, "The development of instrumentation for microparticle analysis by Raman spectroscopy," *Microbeam Analysis--1979*, 185-190.

ANALYSES OF ENZYMES IN SINGLE CELLS BY ARGON LASER FLOW CYTOMETRY

F. A. Dolbeare

Mammalian and bacterial cells and subcellular organelles are chemical packages containing various concentrations of specific chemical substances. These chemical substances can be analyzed on a single cell or particle basis when specific fluorescent probes are used and the particle is passed through a laser beam fluorimeter called a flow cytometer. Individual fluorescent pulses are amplified and converted into a digital form for display on a cathode-ray tube. Depending on the power of the laser and the sensitivity of the detector, particles containing several thousand fluorescent molecules ($<10^{-20}$mole) may be readily quantified. Since a flow cytometer measures the fluorescence from individual particles and not fluorescence of solutions, a spectrofluorometer is used to obtain fluorescence coefficients for each fluorophore. If the substance of interest is an enzyme, it may even be possible to quantify a few dozen molecules per cell, since the catalytic nature of the enzyme permits a large amplification of the fluorescent end product. An enzyme is capable as a catalyst to convert thousands of molecular substrates to product per second. Thus a great sensitivity is achieved.

We have analyzed cells and nuclei for a number of enzymes by using fluorogenic substrates as probes.[1-4] Fluorogenic substrates are generally nonfluorescent compounds that when acted upon by specific enzymes cause the release of a fluorescent product. If we select fluorophores with high quantum efficiencies (e.g., fluorescein and methyl umbelliferone) to make up the fluorogenic substrates, we obtain cells that become highly fluorescent within 15 s of exposure to solutions of the substrates. Viable cells may be added to solutions of specific fluorogenic substrates and rapidly introduced into a stream that passes through the laser beam. Then a large number of cells (2×10^5) is incubated with one of the probes and the fluorescence is measured in a standard spectrofluorometer. The fluorescence may be quantified for a suspension of intact cells or the cells may be disrupted following 1 min of reaction to allow sufficient fluorophore to accumulate to give a meaningful reading. From values obtained by this method, relative activities can be calculated for flow cytometer readings; i.e., one instrument with a capability for measuring particle fluorescence is standardized against an instrument that routinely measures solution fluorescence. Table 1 shows some of the enzymes we have assayed in Chinese hamster (CHO) cells by this method along with the appropriate fluorescent probe, and specific fluorescent data obtained with an argon ion laser flow cytometer. The rate of hydrolysis of the specific probes is given as specific activity, i.e., number of moles of fluorescent substance formed/cell-s.

Discussion

Fluorescein is a much more sensitive probe for the assay of cellular enzymes than is 4-methylumbelliferone. However, the particular enzyme, nonspecific esterase, is either in low abundance or exhibits much lower activity than the other measured enzymes. If fluorescein derivatives were used for the other assays in place of the 4-methylumbelliferone, then much lower levels of these enzymes could be detected by the method.

If instead of whole cells we had analyzed subcellular particles (e.g., lysosomes, which contain the bulk of the enzymes we were studying), we would have found that indeed each particle would have exhibited fluorescence representing the level of enzyme in that particle.

Since as many as a hundred such particles inhabit an intact cell, we would have been quantifying enzyme product levels in the 10^{-20} mole/cell range. Such a technique may be employed to characterize both the number and enzyme content of subcellular particles, even though the particles are only 0.2-0.5 μm in diameter.

TABLE 1

Enzymes	Probe	Δ fluorescence/s	Amole/cell-s
Acid phosphatase	4-Methyl-umbelliferone-phosphate	49.1	0.42
β-galactosidase	" " β-galactoside	7.0	0.6
β-glucuronidase	" " β-glucuronide	17.5	0.15
Nonspecific esterase	Fluorescein diacetate	629.3	0.63

Δfluorescence calculated from channel number divided by gain.
Amole = 10^{-18} mole
Specific activities calculated from fluorescence coefficients for 4-methyl umbelliferone and fluorescein determined by standard spectrofluorometry.

References

1. F. A. Dolbeare and L. S. Cole, "Flow cytometric determinations of DNA, cathepsin B1, and size of rat liver nuclei," *J. Cell Biol*. 75: 406a, 1977.

2. F. Dolbeare, "Flow cytoenzymology: A tool in the search for neoplastic markers," in R. Ruddon, Ed., *Biological Markers of Neoplasia: Basic and Applied Aspects*, New York: Elsevier-North Holland, 1978, 581-586.

3. F. A. Dolbeare and W. Phares, "Naphthol AS-BI phosphatase and naphthol AS-BI βglucuronidase in Chinese hamster ovary cells: Biochemical and flow cytometric studies," *J. Histochem. Cytochem*. 27: 120-124, 1979.

4. F. Dolbeare, "Dynamic assay of enzyme activity in single cells by flow cytometry," *J. Histochem. Cytochem*. 28: 1644-1646, 1979.

APPLICATIONS OF MICROSPECTROFLUOROMETRY TO THE STUDY OF THE LIVING CELL

Elli Kohen, J. G. Hirschberg, Bo Thorell, Cahide Kohen, and Joanne Mansell

It has been said that one cannot understand a process by stopping it.[1] Understanding must move with the flow of the process. Thus metabolic events in the living cell cannot be understood in their "wholeness" neither by recourse to metabolic maps alone, which just represent the "molecular anatomy," nor by mere monitoring of the kinetics of individual enzymes (i.e., their inhibition characteristics and molecular structure). As phrased by Weiss, "It seems ...unsound to expect that it will ever be possible to describe cell behavior solely in reductionist terms of properties of its component elements, that is, without giving a due account of its system character."[2] As expressed by Lotka, what we have before us is a system composed of aggregates of energy transformers adapted by their structure to guide available energy into such channels as to lead to their growth and maintenance.[3] Nearly in similar terms Chance et al. state that living cells contain the ultimate in microelectronics, with complex enzyme systems structured to perform sophisticated electronic and chemical functions, serving as power supplies, gated channels, pumps, receptors, effectors, and transducers.[4]

Methods to study dynamic processes in the intact living cell must be designed to account for the above defined properties. Microspectrofluorometry[5-8] makes it possible to investigate in situ the role of organized multienzyme systems when they operate within the matrix of the intra- and intercellular microenvironment. This method, in conjunction with microinjections of metabolites or modifiers,[9] leads to localization and spectral identification of transient changes[10,11] in the oxido-reduction of intracellular fluorescent coenzymes which bear on new theories for multicomponent metabolic control,[12-14] compartmentation,[8,9] cell-to-cell metabolic cooperation,[6,15-16] and immediate or delayed actions of xenobiotics (e.g., photosensitizers and carcinogens) on mitochondrial, cytosolic, and nuclear pathways. The combined microspectrofluorometry-microinjection approach is therefore well suited to the investigation of intracellular parameters and variables of enzyme activity inaccessible to conventional biochemistry, such as the *sensitivity coefficient*[12,13] (the effect that the change in the concentration of an enzyme has on the overall systemic flux) and the *elasticity coefficient*[12,13] (the effect that the change in substrate concentration has on the rate of one "isolated" enzyme step functioning within the whole system).[17]

Experimental

The microspectrofluorometer (Fig. 1)[5] is designed for a dual purpose: (1) to map fluorescence changes associated with coenzyme oxido-reduction, the distribution and interactions of fluorescent xenobiotics and probes or tracers topographically through the cell or interconnected cells (topographic mode); (2) to analyze spectrally the emission of coenzymes or probes at various intracellular sites (spectral mode).

The aim is to determine a structure and function correlation in the intact living cell(s) in the dynamic context of the changing molecular microarchitecture and reciprocally interacting multienzyme systems within a cell or between cells within a multicellular complex. Thus, the instrumentation is tailored to superimpose a dynamic metabolic map onto the ultrastructure map of the living cell, via:

(1) A maximum aperture, long working distance phase-fluorescence system mounted on an inverted microscope, which allows considerable free distance for cell manipulations and high efficiency in the collection of the emitted fluorescence.

(2) Imaging cell organelles and sites visualized by phase microscopy and followed by phase photography upon detector channels of the optical multichannel analyzer.

(3) Superposition of the metabolic map on an ultrastructural map obtained by electron microscopy from cells premarked and retrieved after microfluorometry.

The planned introduction of a two-dimensional multichannel detector can provide in principle:

(1) Continuous recording of spatio-temporal behavior associated with any point within a cell or interconnected cells.

(2) Multisite recording of fluorescence spectra from selected cell regions.

Thus, for every time interval within the resolution of the system, a matrix can be obtained that reproduces the topographic or spectral behavior of exogenous or endogenous fluorochrome within a cell or cells.

Hypotheses on the regulation of intracellular pathways by controlling "pacemaker" or "rate-limiting" enzymes, versus the possibility that controls are shared among all enzymes,[12,13] are now amenable to exploration by means of sequential injections into the same cell of substrates and modifiers. Thus, a two-manipulator injector system[9] has been built for arbitrary injections of substrates (e.g., of glycolysis, Krebs cycle, pentose shunt) and modifiers (adenine nucleotides including cyclic AMP, ions, and chelators).

Studies of pyridine nucleotide-linked enzyme reactions are made by visualization of cells with red light and detection of blue fluorescence; studies of flavin enzymes are made by visualization with blue light and detection of yellow fluorescence.

The above methods are, in principle, applicable to cells in monolayer culture grown on a glass surface. Specific cell lines are selected for each application:

(1) For the investigation of basic metabolic controls and compartments, the L cell is used, as a line on which a body of knowledge has been built, documented by a decade of microfluorometric studies. X-irradiated L cells[9] provide a giant form easier to manipulate, and extrapolations from the giant are then verified in the nonirradiated L cell. Recently, mitochondria-rich giant L cells, with such enrichment verified by the mitochondrial fluorescent probe DASPMI,[18] have been obtained by serial adaptation to high-sorbitol media (e.g. 0.3-0.4 molar sorbitol).

(2) For the study of carcinogenesis, recourse is made to clones of normal versus spontaneously transformed cells (NCTC clones),[7] clones suitable for chemical carcinogenesis (Heidelberger's C3H/10T1/2 C18),[19] or clones inducible for metabolization of carcinogens (BRL clone).[20]

(3) For the investigation of cell-to-cell metabolic cooperation one studies normal versus transformed cells, hepatoma MH_1C_1,[9] melanomas, and glia versus glioma.[16]

(4) For the study of hormone secretion and regulation, pancreatic islet cells in monolayer culture are used.[21,22]
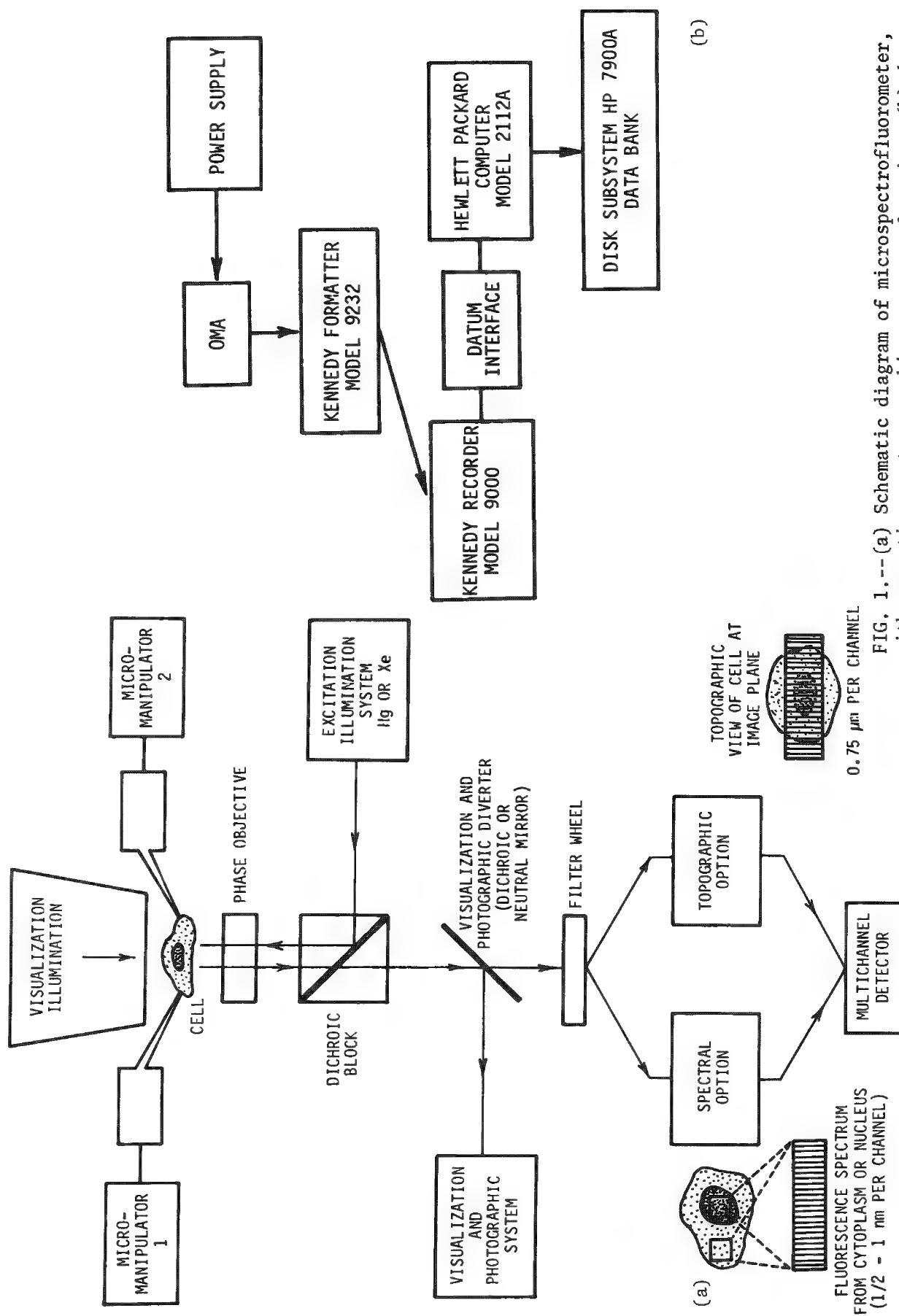
FIG. 1.--(a) Schematic diagram of microspectrofluorometer, with operation on topographic or spectral option; (b) data-processing system.

323

Applications

   A new look at biochemical processes in the living cell: Relationship between metabolic flux and a mosaic of various control parameters. Modifiers are injected (a) alone, to alter the metabolic steady state of a cell; (b) before substrate, to preload a cell; or (c) following substrate, to alter the response to the substrate. Injections of ADP before or after substrate (e.g., glucose-6-P, malate) confirm an inverse relationship between NAD(P)H concentration and ADP concentration, due to the activation of oxidative processes by the latter. Thus, following an injection of ADP it is possible to infer the time course of intracellular ADP concentration from the behavior of intracellular NAD(P)H concentration, since each is the reciprocal of the other.

   Upon injection of ADP in the course of a malate-induced NAD(P)H reduction-reoxidation transient, fluorescence rapidly decreases; a NAD(P)H minimum coincides with the ADP maximum (Fig. 2). Subsequent phosphorylation and ultimate exhaustion of ADP, while malate is still present in sufficient concentration to act as a source of reducing equivalents, leads to a gradual increase of NAD(P)H fluorescence until it returns to the level that existed before injection of ADP[9] or even higher. In this way the relationship between two of the elemental forces of bionergetics, the "force of oxidation" and the "force of phosphorylation," can be investigated.[14] A complex equation,[23] based on the predictions of thermodynamics, links the flux of phosphorylation to the two "forces." This equation includes activity coefficients; stoichiometries of the mitochondrial proton pumps; the permeability of the mitochondrial inner membrane, the relative effects of protonmotive, oxidative, and phosphorylating forces; and the free energies of oxidation and phosphorylation. The equation can be considerably simplified by the assumption of an effectively constant concentration of ATP and an effectively constant oxidation potential (which is the case in Fig. 2) after NAD(P)H returns to maximum. The following differential equation[23] is obtained:

$$\frac{dx}{dt} = \frac{d[ADP]}{dt} = -\alpha - \beta \ln[ADP] \tag{1}$$

$$\text{for} \quad y = \frac{1}{x} = [NADH] \tag{2}$$

with α and β corresponding to known but complicated collections of constants in the equation mentioned above. A near match is obtained between the theoretical and experimental curve of NADH for calculated values of α and β (Fig. 2).

   In such attempts to compare the forces of oxidation and phosphorylation the timing of the ADP injection is critical and has to take place within tenths of a second to a few seconds of the NAD(P)H pulse initiated by malate; otherwise the conditions that validate the above simplified equation are not satisfied, since the pathways will not then be operating at constant oxidation potential.

   Studies to this date do not allow calculations beyond the expressions of contants summarized by α and β. However, in principle once these two values are established, it is also possible to vary the conditions one by one to determine individually the activity coefficients, stoichiometries, permeabilities, and relative values incorporated in α and β.

   Other transients, which illustrate the bistable conditions of intracellular redox states, are the "reverse, oxidation-reduction" transients[9,11] (instead of reduction-reoxidation) obtained for example with Krebs cycle intermediates such as malate, glutamate, and citrate. The same relationships between oxidation and phosphorylation potentials as described above might apply in this case, but the direction of the initial redox change is reversed, probably due to antecedent levels of metabolites and modifiers which alter the balance towards oxidation.

   Another aspect of multienzyme reactions in the intact cell is the compartmentalization of pathways. This effect is studied by observing the responses to sequential injections into the same cell of NAD or NADP-linked substrates from different pathways; for example, malate followed by glucose-6-P (Fig. 3) or isocitrate followed by 6-phosphogluconate.[24] The stepwise NAD(P)H fluorescence changes due to each substrate are clearly observed, but the topographic localization of the responses and their association with specific cell organelles is harder to assess (Fig. 4), due more or less to the diffuse intercellular
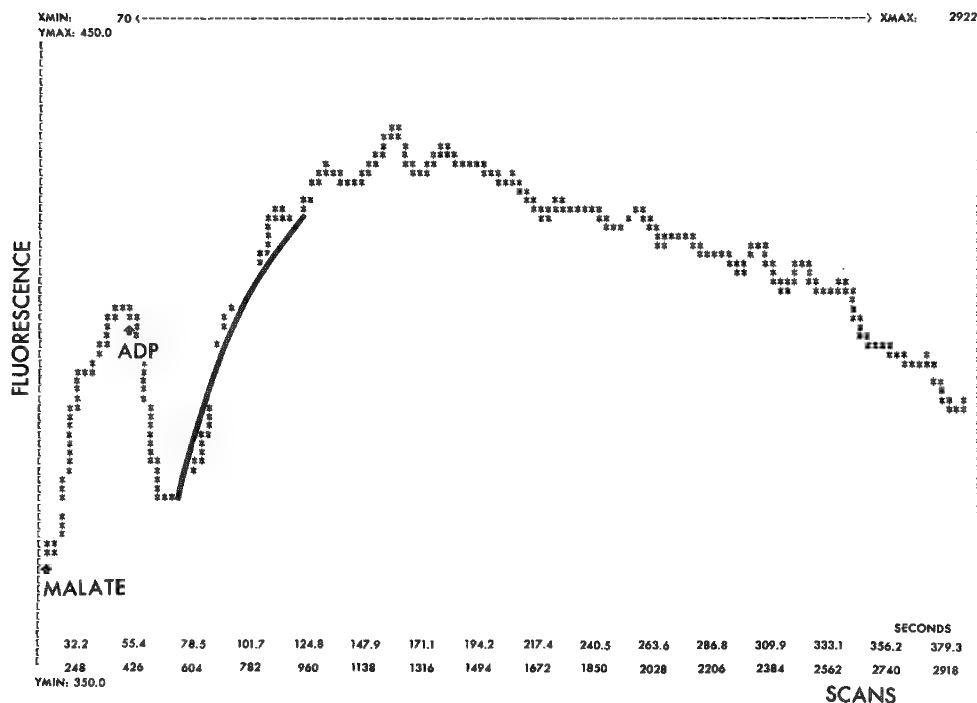
FIG. 2.--"Force of oxidation" vs "force of phosphorylation" relationship (Eq. 1) may be derived from time curve of NAD(P)H response to sequential injections of Malate and ADP into giant L cell produced by x irradiation. Coenzyme fluorescence increases after injection of Malate, drops rapidly after injection of ADP, then spontaneously returns to high level, most likely when phosphorylation of ADP is completed; thus, NAD(P)H maximum corresponds to ADP minimum. Rising branch of V shaped curve (i.e., NAD(P)H concentration, Eq. 2) after ADP injection can be modeled by Eq. (1): instantaneous ADP concentration x corresponds to reciprocal of instantaneous NAD(P)H concentration. Solid line is solution from Eq. (1); asterisk line is experimental result.
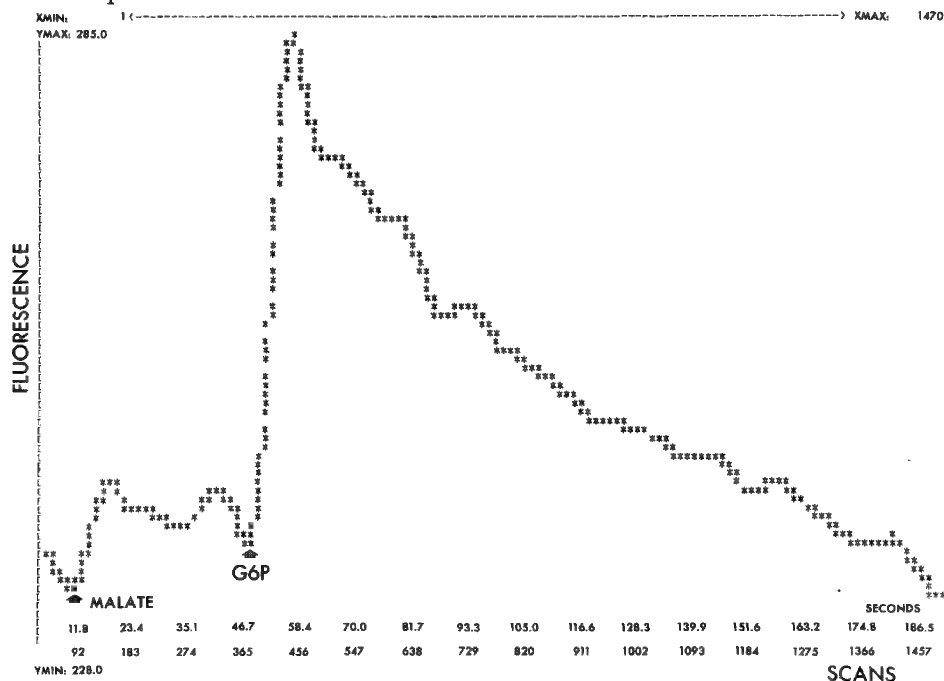
FIG. 3.--Two-step response induced by sequential injections of malate and glucose-6-P into giant L cell produced by gradual adaptation to high molarity culture media. (Observed cell adapted to growth in presence of 0.3 M sorbitol.)

localization of mitochondria, with emergence of compartmentalized responses at sites of more dense mitochondrial aggregation. In this respect the detection of mitochondria-associated NAD(P) redox changes is facilitated in a cell, such as the high molar concentration sorbitol-adapted L cell, which exhibits annulus-like perinuclear zones of high mitochondrial density. Such compartmentalization as may be detected remains associated with relatively weak redox changes; larger redox changes tend to be diffuse due to distribution of mitochondria outside of the zone of aggregation or to involvement of the cytosolic compartment.

Spectral analysis of cell coenzymes. Methods are being developed for the deconvolution of intracellular NAD(P)H spectra in the steady state and in the course of a metabolic transient, into the components free and bound NAD(P)H spectra. Flavin spectra indicate that the metabolically changing components represent a smaller fraction of total intensity in the flavin region of the spectrum, compared to NAD(P)H. Maximal flavin changes are obtained with inhibitors such as azide or cyanide.

FIG. 4.--Topographic analysis of metabolic compartments in L cell sequentially injected with substrates of Krebs cycle (malate) and glycolytic pathway (glucose-6-P = G6P). Abscissa: channels; each channel views a cell strip of about 0.6 wide along topographic scan axis. Ordinate: fluorescence intensity.

Cell-to-cell metabolic cooperation. The spatio-temporal behavior of cells,[17] as determined by coenzyme responses and tracers within the matrix represented by a multicellular assembly, exhibits the following features:

a. Cell-to-cell transfer of chemicals is generally confined to a microdomain consisting of 2-10 cells,[8] which are either contiguous or connected by tentacle-like long extensions. Intercellular passage of material can be rapid, with transit times shorter than 0.1 s, but communication may be also delayed from a few seconds to a few minutes.

b. The metabolic counterparts of "communicating microterritories" defined by fluorescent tracers are "multicellular integrated systems,"[9] with predominance of the "microdomain pattern" suggestive of a finely adjusted microregulation between connected cells.

c. In specialized tissue, such as monolayer cultures of pancreatic islet cells, intercellular communication is evidenced by fluorescence, metabolic response, ultrastructural and immunoanalysis, among insulin, glucagon and somatostatin secreting cells.[25]

d. Discrete graded alterations of cell-to-cell communication in both normal and transformed varieties of cells suggest that even the normal varieties may be functionally altered in terms of communication.

Preliminary evidence suggests that metabolic cooperation may be altered by ions, hormones, ionophores, or substrates. Cells generally deficient in communication, such as the L cell, show some degree of communication, with transit times near the lower limit of the time scale in the presence of dibutyryl cyclic AMP.[9]

The above fragmentary evidence, derived from fluorescence photography and linear scans of cells, awaits further evaluation under conditions designed to investigate the spatio-temporal behavior of multicellular assemblies, such as may be obtained by the two-dimensional scans of fluorescence (see Experimental).
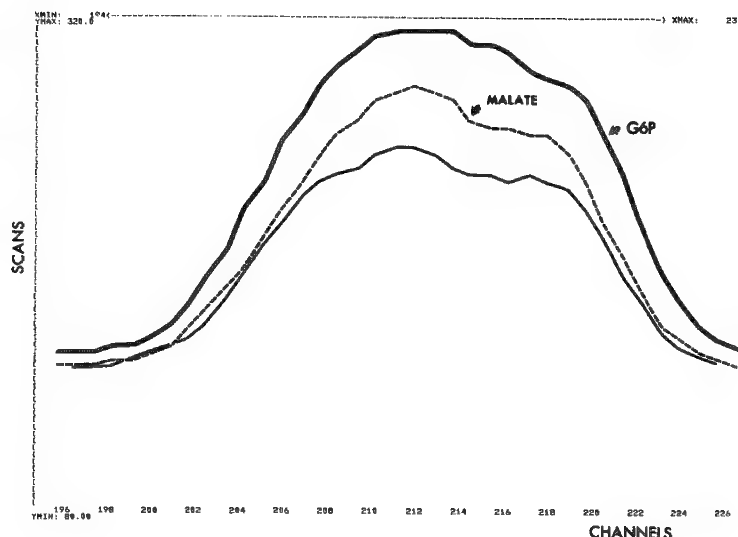
326

Metabolic targets for studies with carcinogens. One such target is the relative response of mitochondrial-extramitochondrial pathways to substrates sequentially injected into the same cell, i.e., malate followed by glucose-6-P, isocitrate followed by 6-phosphogluconate.[24] Following the addition of carcinogens such as dibenzo(a,e)fluoranthene or dimethylnitrosamine, these pathways are affected differentially; thus there is, in the first minutes after such addition, a considerable acceleration of the glucose-6-P or 6-phosphogluconate-linked NAD(P)H pathways, probably due to the high demand placed on NADPH by microsomal metabolization. Subsequently (within 30 min) the response to glycolytic or pentose shunt substrates tends to subside accompanied by the surge of a larger response to Krebs cycle substrate, e.g., isocitrate.

Another target might be the process described by Eq. (1) which involves the relationship between the force of oxidation and the force of phosphorylation.

Spectral studies with photosensitizers, carcinogens; metabolic processes affected by electron tunneling. In both instances the xenobiotic[26] (carcinogen or photosensitizer) is detected at nuclear and extranuclear locations, in either the free or bound form. Independent studies with the photosensitizers on the high quantum yield of extranuclear photodynamic effects suggest that the cellular actions of these compounds may not be limited to their intranuclear interactions.

Blue and red fluorescence emitters are detected in the cytoplasm and nucleus of benzo-(a)pyrene (BP) treated L and BRL cells in culture. In the L cell from 48 hr to several weeks after addition of BP, a blue-enhanced emission (i.e., increase of intensity ratios at 415/440 and 415/460 nm) is predominant in the nucleus and a red-enhanced emission (decrease of the above ratios) in the cytoplasm or extracellular fluid. Treatment with the organosoluble quencher octyl iodide[27] results in narrowing of the nucleo-cytoplasmic differences, largely through removal of the red-enhanced emission.

BRL cells, induced to exert a higher carcinogen-metabolizing activity (by 18h preincubation with benzanthracene) exhibit relative to controls, blue-enhanced emission (Fig. 5) at cytoplasmic and nuclear sites in the first minutes after BP addition.[28] In noninduced BRL cells the same emission increases in the nucleus within 20-40 min.

(a)   (b)
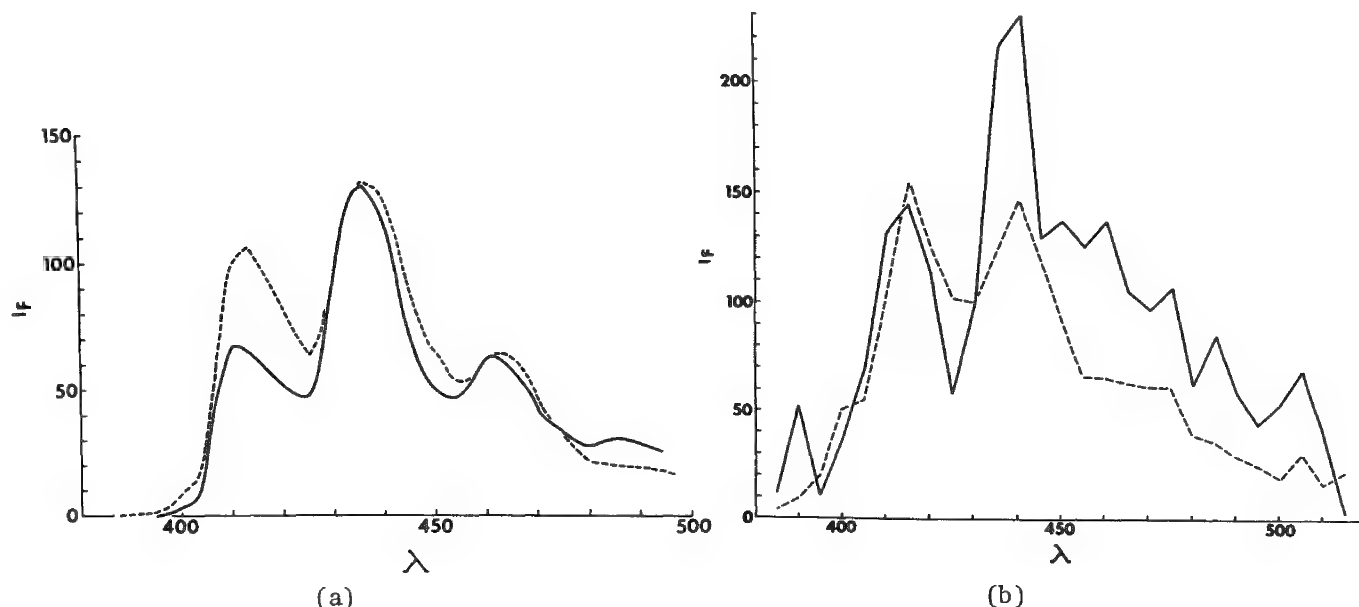
FIG. 5.--(a) Fluorescence spectrum of benzo(a)pyrene in solution (solid line) compared with fluorescence spectrum of cytoplasm of BRL cell incubated for 48 hr in presence of 10^{-6} 1,2-benzanthracene, the last 24 hr also in presence of benzo(a)pyrene (broken line). Fluorescence of induced cell cytoplasm is *blue-enhanced*. Compare 415/440 nm emission ratio in induced BRL cytoplasm and benzo(a)pyrene in solution. (b) Fluorescence spectra recorded from cytoplasm of BRL control cells (solid line) and BRL cells with aryl hydrocarbon hydroxylase system induced by 18h preincubation in the presence of 10^{-6} M benzanthracene (broken line), about 3-5 min after acute addition of 10^{-6} M benzo(a)pyrene. Carcinogen fluorescence in induced cell is blue-enhanced compared to control.

Induced cells progress faster than noninduced cells towards a red-enhanced emission (perhaps a detoxification product), a state that seems to follow the blue-enhanced state.

Some inferences about the nature of blue and red-enhanced emitters can be derived from studies on electron tunneling.[4] It is nonetheless first necessary to ascertain whether the blue and red-enhanced emissions correspond to separate molecular varieties such as metabolites, or whether they could represent the emission of the same molecule in different hydrophobic or aqueous phases or different binding and stacking conditions. From catalogs of BP metabolites with known fluorescence emission spectra it is indeed possible to identify red and blue-enhanced products of BP metabolization.

Many of the most fundamental metabolic processes involve the transfer of electrons between macromolecules in such a way that electrons must tunnel across distances of 5-30 Å through the potential barrier separating the molecules. Shorter-wavelength fluorescence emission corresponds to electrons excited with higher energy, which are therefore more aggressive for intracellular macromolecules or organelle membranes. Thus, from the standpoint of electron tunneling, blue-enhanced emitters would be more active than red-enhanced molecules. It is therefore possible to hypothesize that blue-enhanced emitters could be more toxic (i.e., carcinogenic) than the original molecule, or red-enhanced emitters, so that the latter are good candidates for detoxification products.

Mathematical methods[29] used in the resolution of complex spectra can lead to the identification of such red- and blue-enhanced spectra as components of the sum spectrum recorded from the intact cell. The decomposition of spectra into components is an accepted standard technique. An example of the method is to recognize narrow spectral lines from elements and ions in order to find the number of impurities in an excited gas. However, to apply the method to spectra with broad features (e.g., finding the number of species in fluorescence spectra or dye absorption) is sometimes difficult, because the measurement at a given wavelength may be attributed to many components at once. It is well known that the number of independent spectra (equal to the number of species) in a number of observations is related to the rank of the largest meaningful matrix formed from the observed intensities. Some new computations have shown that there may be more physical meaning in the complete set of the "eigenvalues" and "eigenvectors" of that matrix. A theory is being formulated to utilize that method.[30]

Conclusions

The eventful relevance of this work to the understanding of cellular metabolism is that the in situ distribution of control over the enzymes participating in such metabolism may be evaluated in relation to intracellular compartmentation and structure. The concept of the living cell as a matrix whose spatio-temporal behavior[17] is defined by the distribution of control[12-14] over enzymes participating in a metabolic system sensitive to changes in the concentrations of metabolites and modifiers, can be further broadened to explain and predict the behavior of multicellular integrated systems. The "dynamic biochemistry of the living cell," which is thus developed, leads to new perspectives in cellular physiopathology with multifold applications in areas of biomedical research as varied as bioenergetics, the interregulation of differentiating or specialized hormone-secreting cells and intracellular interactions of xenobiotics among others, photosensitizers, and carcinogens.

References

1. F. Herbert, *Dune*, New York: Berkley Medallion Ed., 1975, cited in G. R. Welch, *Progress Biophys. Molec. Biol.* 32: 103-191, 1977.

2. P. Weiss, "The cell as a unit," *J. Theor. Biol.* 5: 389-397, 1963.

3. A. J. Lotka, "Physical aspects of organic evolution," *Bull. Math. Biophysics* 10: 103-115, 1948.

4. B. Chance et al., "Biological membranes," *Physics Today* October 1980, 33-38.

5. J. G. Hirschberg et al., "A high resolution grating microspectrofluorometer with topographic option for studies in living cells," in Y. Talmi, Ed., *Multichannel Image Detectors*, Washington: ACS Symposium Series, 1979, vol. 102, 263-289.

6. E. Kohen et al., "Structure-correlated microspectrofluorometry of cultured normal and cancer cells," in K. Letnansky, Ed., *Biology of the Cancer Cell*, Amstelveen (The Netherlands): Kupler Medical Publications B.V., 1980, 299-306.

7. E. Kohen et al., "New metabolic parameters for the characterization of cells," *Blood Cells* 6: 753-765, 1980.

8. E. Kohen et al., "Microspectrofluorometric procedures and their applications in biological systems," in E. L. Wehry, Ed., *Modern Fluorescence Spectroscopy*, New York: Plenum, 1981, 3, 295-346.

9. E. Kohen et al., "Examination of single cells my microspectrophotometry and microspectrofluorometry," in P. F. Baker, Ed., *Techniques in Cellular Physiology*, Amsterdam: Elsevier/North Holland, 1980, 103/1-28.

10. B. Chance, "The identification of enzyme-substrate compounds," in E. S. Guzman Barron, Ed., *Modern Trends in Physiology and Biochemistry*, New York: Academic Press, 1952, 25-46.

11. B. Hess, "Organization of glycolysis," in D. B. Davies, Ed., *Rate of Control of Biological Processes*, London: Cambridge University Press, 1973, 105-131.

12. H. Kacser and J. A. Burns, "The control of flux," *ibid.*, pp. 65-104.

13. H. Kacser and J. A. Burns, "Molecular democracy: Who shares the controls?" *Biochem. Soc. Trans.* 7: 1149-1160, 1979.

14. H. V. Westerhoff et al., "Mosaic nonequilibrium thermodynamics describes biological energy transduction," *Proc. Natl. Acad. Sci. USA* 78: 3554-3558, 1981.

15. H. Subak Sharpe et al., "Metabolic cooperation between biochemically marked mammalian cells in culture," *J. Cell Sci.* 4: 353-367, 1969.

16. B. Thorell et al., "Metabolic rates and intercellular transfer of molecules in cultures of human glia and glioma cells," *Med. Biol. Helsinki* 56: 386-392, 1978.

17. G. Rickey Welch, "On the role of organized multienzyme systems in cellular metabolism: a general synthesis," *Progress Biophys. Molec. Biol.* 32: 103-191, 1977.

18. J. Bereiter-Hahn, "Dimethylaminostrylmethylpyridinium iodine(DASPMI) as a fluorescent probe for mitochondria in situ," *Biochim. Biophys. Acta* 423: 1-14, 1976.

19. C. Heidelberger, "Chemical carcinogenesis," *Annu. Rev. Biochem.* 44: 79-121, 1975.

20. J. P. Whitlock and H. V. Gelboin, "Aryl hydrocarbon (benzo[a]pyrene) hydroxylase induction in rat liver cells in culture," *J. Biol. Chem.* 249: 2616-2623, 1974.

21. A. Lambert et al., "Monolayer cell culture of neonatal rat pancreas," *Endocrinology* 90: 239-248, 1972.

22. E. Kohen et al., "Intercellular communication in pancreatic islet monolayer cultures," *Science* 204: 862-865, 1979.

23. E. Kohen et al., "Metabolic control and compartmentation in single living cells," in preparation.

24. E. Kohen et al., "The differential effects of the carcinogen dimethylnitrosamine on isocitrate and 6-phosphogluconate metabolism in single intact cells," *BB Acta* (in press).

25. P. Meda et al., "Direct communication of homologous and heterologous endocrine islet cells in culture," *J. Cell Biol.* 92: 221-226, 1982.

26. H. V. Gelboin, "Benzo(a)pyrene metabolization, activation and carcinogenesis," *Physiol. Rev.* 60: 1107-1166, 1980.

27. C. G. Wade et al., "Selective fluorescence quenching of benzo(a)pyrene and a mutagenic dial epoxyde derivative in mouse cells," *Biochemistry* 17: 4332-4337, 1978.

28. E. Kohen et al., "Microspectrofluorometry of carcinogen-treated cells," *Fifth Annual Cancer Research Seminar*, Tampa, Fla: Am. Cancer Society, 1982, Abstract 2.

29. G. Weber, "Enumeration of components in complex systems by fluorescence spectrophotometry," *Nature* 190: 27-29, 1961.

30. A. W. Wouters et al., "Decomposition of spectra into components: Relation with eigenvalues and eigenvectors of matrices," Florida Section Optical Society of America Winter Meeting in Coral Gables, Jan. 30, 1982 (abstract).

APPLICATION OF FLUORESCENCE MICROSCOPY TO THE STUDY OF THE COMPONENTS OF COAL

R. W. Stanton

Fluorescence microscopy can be used effectively to evaluate coal quality. As a supplement to standard chemical analyses, the petrographic evaluation of coal, including the degree of coalification (maturation), provides useful information for assessing the optimum utilization of a specific bed or block of coal. In recent years, reflected-light microscopy has become a powerful and useful tool for determining the character of coal. For this purpose, white-light, bright-field illumination, and a 50× oil-objective are used to identify petrographic entities in coal. Petrographic (maceral) composition is commonly determined by point counting. In addition, the degree of coalification or rank is precisely indicated by the reflectance of a specific petrographic entity--the vitrinite maceral.

Visible fluorescence techniques are particularly useful for extending the capabilities of the incident light microscope. Various fluorescing macerals (organic petrographic substances) can be readily differentiated and identified. Fluorescence characteristics of these macerals are related to their chemical properties such as the types of carbon bonds and molecular structures.

Fluorescent techniques to study organic-rich sediments and rocks were developed and applied by Jacob,[1] van Gijzel,[2,3] and Ottenjann and others.[4] Initially, these studies concentrated on the measurement of the fluorescence intensities and the spectra. More recently the use of fluorescence in the routine analyses of coal has become an important tool for refining the characterization of coal macerals.

Method

The fluorescence study of coal requires the following equipment: (1) an incident-light microscope; (2) a light source such as a 100W ultrahigh-pressure mercury lamp powered by a stabilized supply; (3) an excitation filter either in the near ultraviolet (360nm) or blue (390nm) range; (4) a dichroic mirror fitted in the vertical illuminator to pass long-wave light (greater than 400 nm) and reflect short-wave light (less than 400 nm) (Fig. 1). For the measurement of spectral fluorescence, additional equipment is required: (1) a continuous interference filter that passes light from 400 to 700 nm; (2) a photomultiplier that is sensitive and can be used to measure the filtered fluorescent intensity; and (3) a microcomputer to store spectral data and construct a corrected summary spectrum from a number of representative measurements.

Analyses are made of polished samples usually consisting of coal particles less than 20 mesh in grain size (less than 850 μm) that have been mixed with an epoxy medium. Each sample is pulverized and subsampled so as to be representative of a much larger amount of coal. Other preparations include small polished blocks of coal that represent a thin layer or layers within the coal bed. The preparations are polished to a relatively scratch-free surface; however, even an unpolished surface can be analyzed because fluorescence does not depend on a perfectly smooth surface.

Coal is composed petrographically of macerals (organic) and minerals (inorganic). The major groups of macerals are: (1) vitrinite, which is derived primarily from wood; (2) exinite, which is hydrocarbon rich substances derived from spores, pollen, algae, cuticles, or resins; and (3) inertinite, which is carbonized remains of other macerals. Qualitatively, fluorescence (commonly blue-light, 390-490 nm) is used to enhance details of the exinite maceral group. In low-rank coal (below medium-volatile bituminous), exinite macerals fluoresce yellow-orange and reveal textural details that facilitate recognition, characterization, and estimation of abundance.[5]

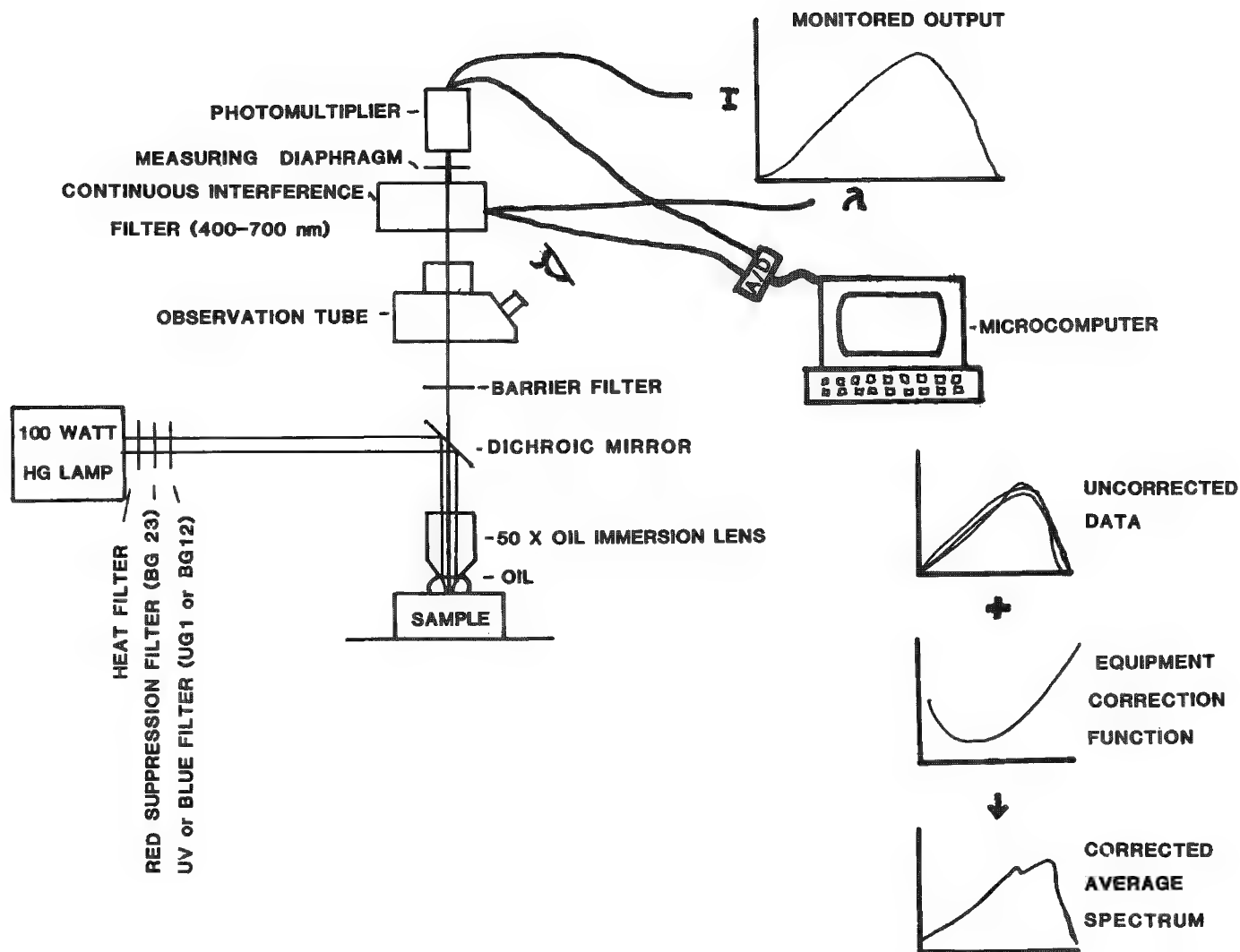The author is at the U.S. Geological Survey in Reston, VA 22092.

FIG. 1.--Microscope and electronic components used in fluorescence measurements on coals.

In addition, certain hydrogen-rich substances may be contained within other macerals such as vitrinite or inertinite. The use of blue-light fluorescence enables recognition of these substances and permits a quantitative evaluation of their abundances.

Spectral fluorescence (ultraviolet light, 370 nm) is useful as a quantitative measure of the degree of coalification or maturation of sedimentary organic materials. The standard technique of measuring vitrinite reflectance is used as a coal-rank indicator for coals within the range of high-volatile bituminous to semianthracite rank (0.70-2.50% reflectance). Within this range the relation between vitrinite reflectance and the rank parameters of fixed carbon is fairly well established.[6] However, below 0.70% reflectance, the relationship does not hold because rank is defined by parameters other than fixed-carbon content, and the difference in reflectance values is not significant to the nearest 0.01%. The use of vitrinite reflectance as an indicator of coal rank is therefore not adequate for low-rank coals. However, the measurement of the spectral fluorescence of sporinite is a useful technique for determining the rank of lignite, subbituminous, and high-volatile bituminous coals.[4] As the degree of coalification increases, the fluorescent intensity of sporinite decreases and the peak of the spectra generally shifts from 500 to 700 nm. This spectral shift in fluorescence takes place in coal whose vitrinite reflectances are generally below 1.22% or whose fixed-carbon contents are less than about 70%.

The maceral sporinite which is composed of the substance sporopollenin was chosen as the best rank indicator because the chemical content of spores probably has been more or less constant throughout geologic time. Although the fluorescence parameters of recent or

uncoalified spores may differ somewhat from spore to spore, these differences become insignificant with a slight increase in rank.[3] Similar changes of fluorescence occur in most spores as coalification increases beyond the peat stage.

Many published results of fluorescent studies are comparable; however, problems still exist in the precise calibration of equipment and standardization of techniques. In order to attain comparable data from different laboratories, workers need to (1) use a standard reference substance such as a uranyl glass to calibrate spectral intensities and (2) use a correction factor for background influence, effects of the microscope optics, the transmission of the interference filter, and the relative sensitivity of the photomultiplier. Some workers have successfully used a standard lamp to correct for equipment sensitivity. Another common problem is the recognition of specific parameters for spectra characterization. Most workers use a red/green quotient Q derived as follows:

$$Q = \frac{\text{relative intensity at 650 nm}}{\text{relative intensity at 500 nm}}$$

Although the Q value has been shown to correlate well with vitrinite reflectance in coal samples of different rank, other parameters are sometimes necessary to explain double-peaked spectra. These parameters include spectral maximum, half-width value, intensity at 546 nm, and percentage alteration after 10 min of excitation.[7]

Conclusions

The application of qualitative and quantitative fluorescence techniques increases the information derived from the microscopic study of coal and dispersed organic matter in sedimentary rocks. The use of blue-light fluorescence enables workers to identify hydrogen-rich substances that may go unnoticed in standard analyses because of their low reflectances. The use of spectral fluorescence measurements provides a microscopic technique to indicate rank in low-rank coals for which the use of vitrinite reflectance is not a sensitive technique.

References

1. H. Jacob, "Neue Erkenntnisse auf dem Gebiet der Lumineszenzmikroskopie fossiler Brennstoffe," *Fortschr. Geol. Rhein. u. Westf.* (Krefeld) 2: 569-588, 1964.

2. P. van Gijzel, "Review of the UV-fluorescence of fresh and fossil exines and exosporia," in Brooks et al., Eds., *Sporopollenin*, New York: Academic Press, 1971, 659-685.

3. P. van Gijzel, "Polychromatic UV-fluorescence microphotometry of fresh and fossil plant substances, with special reference to the location and identification of dispersed organic material in rocks," in Boris Aplern, Ed., *Pétrographie de la matière organique des sediments: Relation avec la paléotempérature et le potentiel pétrolier*, Paris: CNRS, 1975, 69-91.

4. K. Ottenjann, M. Teichmuller, and M. Wolf, "Spectral fluorescence measurements of sporinite in reflected light and their applicability for coalification studies," *Ibid.*, pp. 49-65.

5. W. Spackman, A. Davis, and G. D. Mitchell, "The fluorescence of liptinite macerals," *Brigham Young University Geology Series* 22(3): 59-75, 1976.

6. E. Stach, M. Th. Mackowsky, M. Teichmuller, and others, *Stach's Textbook of Coal Petrology*, Berlin: Gebrüder Borntraeger, 1982, 3d ed.

7. P. van Gijzel, "Recent developments in the application of quantitative fluorescence microscopy in palynology and palaeobotany," *Annales des mines de Belgique*, July-August 1978, 835-851.

STUDIES OF CALCIFIED TISSUES BY RAMAN MICROPROBE ANALYSIS

M. D. Grynpas, E. S. Etz, and W. J. Landis

The large majority of previous studies concerning the physical and chemical nature of bone tissue has utilized bulk material for analysis. Such investigations have been limited in this regard by the fact that whole and even macroscopic samples of bone are very heterogeneous with respect to tissue age and mineral content. This is the result of active remodeling of bone tissue even after longitudinal growth has ceased.[1] Methods have been devised to narrow the heterogeneity of bone samples, including density fractionation, a technique that separates powdered bone into more homogeneous samples of increasing densities and therefore of increasing tissue age.[2] Fractions of lower density contain younger bone mineral, and the distribution of bone material in varying densities is a much more sensitive index of aging and maturation of bone tissue than is the age of the animal. Precisely for the latter reason we have used embryonic chick bone density fractions as well as whole chicken bone powder of various ages in this study. A second approach to reducing the complicating factors from lack of heterogeneity of bone samples under study is to use microscopic methods to examine very small regions or portions of the tissue. In this report, Raman microprobe analysis has been applied for this purpose. The Raman microprobe[3,4] has the dual advantage of being a microscopic method and a spectroscopic method, so that it allows the study of chemical species in a tissue sample. In contrast to x-ray diffraction, Raman spectroscopy does not rely on long-range atomic periodicity in a sample and is sensitive to minor constituents such as CO_3^{2-} and HPO_4^{2-} in bone mineral, molecular entities, or compounds undetectable by x-ray methods. Furthermore, both molecular organic and inorganic constituents of a tissue can be detected and identified equally well, whereas in x-ray diffraction or in x-ray microprobe analysis heavy-constituent elements dominate the pattern. This report investigates by Raman microanalysis the changes in structure and composition of chicken bone of various animal ages (embryonic, 5-week, and 1-year-old) and fractions of chick bone development stages (embryonic density fractions) as well as embryonic chick tibia sections. With advancing age of the bone we found an increase in carbonate CO_3^{2-} content (part of which may be organic), a persistence of organic material not necessarily attributable to collagen, a general increase in mineral content with a concomitant decrease in organic species composition, and a very early disappearance of acid phosphate, HPO_4^{2-}.

Materials and Experimental Technique

Bone Samples. All the bone powders examined consist of mid-diaphyses of chicken tibiae freshly dissected from surrounding soft tissues, frozen in liquid nitrogen, and lyophilized. The bone samples were then reduced in a hammer-percussion mill (cooled by liquid nitrogen) to a powder whose constituent particles range between 1 and 10 μm in size, with an average size of about 5 μm. Powders from the 16-day embryonic chick, 5-week chicken, and 1-year-old chicken were examined without further treatment. The 17-day embryonic chick bone powder was separated into fractions by centrifugation in bromoform-toluene mixtures of increasing densities,[2] ranging from 1.4 to 2.1 g/cm^3 in steps of 0.1 g/cm^3. Each fraction was washed in absolute alcohol, dried to constant weight, and stored in a desiccator. Recovery of start-

ing material was about 90%. Finally, a transverse section of an 18-day embryonic chick tibia, frozen, lyophilized, and embedded in Epon, was cut dry on a microtome to 2 μm thickness, then transferred in ethylene glycol and deposited on a sapphire substrate used for all Raman analyses.[3] Powders were dried on sapphires in absolute ethanol.

Raman Microprobe Measurements. All spectra were recorded on the Raman microprobe of the National Bureau of Standards, which is described elsewhere.[4] The irradiance was between 10 and 20 mW; the beam size, about 15 μm. Each scan was repeated and several particles examined on each sapphire. Spectra of all samples (powders and sections) were obtained with 514.5nm excitation and 5cm^{-1} spectral slits.

Results

The chemical data of the chicken powder samples are shown in Table 1.

TABLE 1.--Chemical data of chicken bone powders.

Sample	Ca%	P%	Ca + PO$_4$%	Ca/P (molar)
16-day chick embryo, unfractionated	19.6	11.0	53.5	1.37
5-week chicken, unfractionated	23.0	10.7	55.8	1.66
1-year chicken, unfractionated	25.5	11.5	60.7	1.71

The Raman microprobe spectra of Fig. 1 show a series of unfractionated chicken bone powder from embryonic chick to 1-year-old chicken with total carbonate content increasing from about 3 wt.% in the embryo to about 6 wt.% in the 1-year matured bone sample. All sample spectra are plotted as scattered intensity (in arbitrary units) versus Raman shift (in wavenumber units, cm^{-1}). The main features of these spectra are phosphate bands from the apatite-like phase of the inorganic mineral component of bone (principal band at about 960 cm^{-1}), three amide bands, and C-H stretching (at about 2940 cm^{-1}) of the organic matrix. Some band assignments are given in Table 2.

TABLE 2.--Band assignment for Raman spectra[5,6,7] (in cm^{-1}).

3325	water	1271 1248	Amide III	960	ν_1 PO$_4$
2934	C-H stretching			854	proline ring
1670 1642	Amide I	1074 1079	ν_1 CO$_3$	594 536	ν_4 PO$_4$
1594	Amide II	1048 1030	ν_3 PO$_4$	464 434	ν_2 PO$_4$
1456 1442	CH$_2$ or CO$_3$	1004	ν_1 organic PO$_4$ or Phenylalanine		
1348 1326	CH$_2$				

Of great interest is the carbonate band at 1074 cm^{-1} and the very sharp band at 1004 cm^{-1} that we shall discuss below. Figure 2 shows the spectra of decalcified mature turkey bone and of a low density fraction (1.5 to 1.6 g/cm^3) and a high density fraction (2.0 to 2.1 g/cm^3) of 17-day chick embryo bone. In the turkey demineralized bone, bands attributable to collagen (amide I, II, and III), noncollagenous proteins, and other organic moieties are shown (C-H and CH$_2$ and CO$_2$ bands). Besides all the organic bands, other very sharp peaks appear at 960 cm^{-1} (PO$_4$$^{3-}$) and 1074 cm^{-1} (CO$_3$$^{2-}$), which may represent remnants of mineral matter or particles which have reprecipitated in the matrix after demineralization. This same sample examined by x-ray diffraction has no apatitic pattern. The 1.5-1.6 density fraction (less than 25% mineral content), representative of very early mineralization (all the mineral constituents are less than a day old), is characterized by a weak, but definitive, phosphate peak at 960 cm^{-1}; no detectable carbonate peak; peaks at 1038 or 1068 cm^{-1}, possibly attributable to HPO$_4$$^{2-}$; all the organic bands detailed above; and the sharp band at 1004 cm^{-1}. In the 2.0-2.1 density fraction, which represents the most mineralized portion of this bone (with a mineral content greater than 60 wt.%), there are present a phosphate band greatly increased in strength at 960 cm^{-1}, a carbonate band at 1074 cm^{-1}, the

organic bands, and the still sharp but decreased band at 1004 cm^{-1}. No presumptive HPO$_4^{2-}$ bands appear.
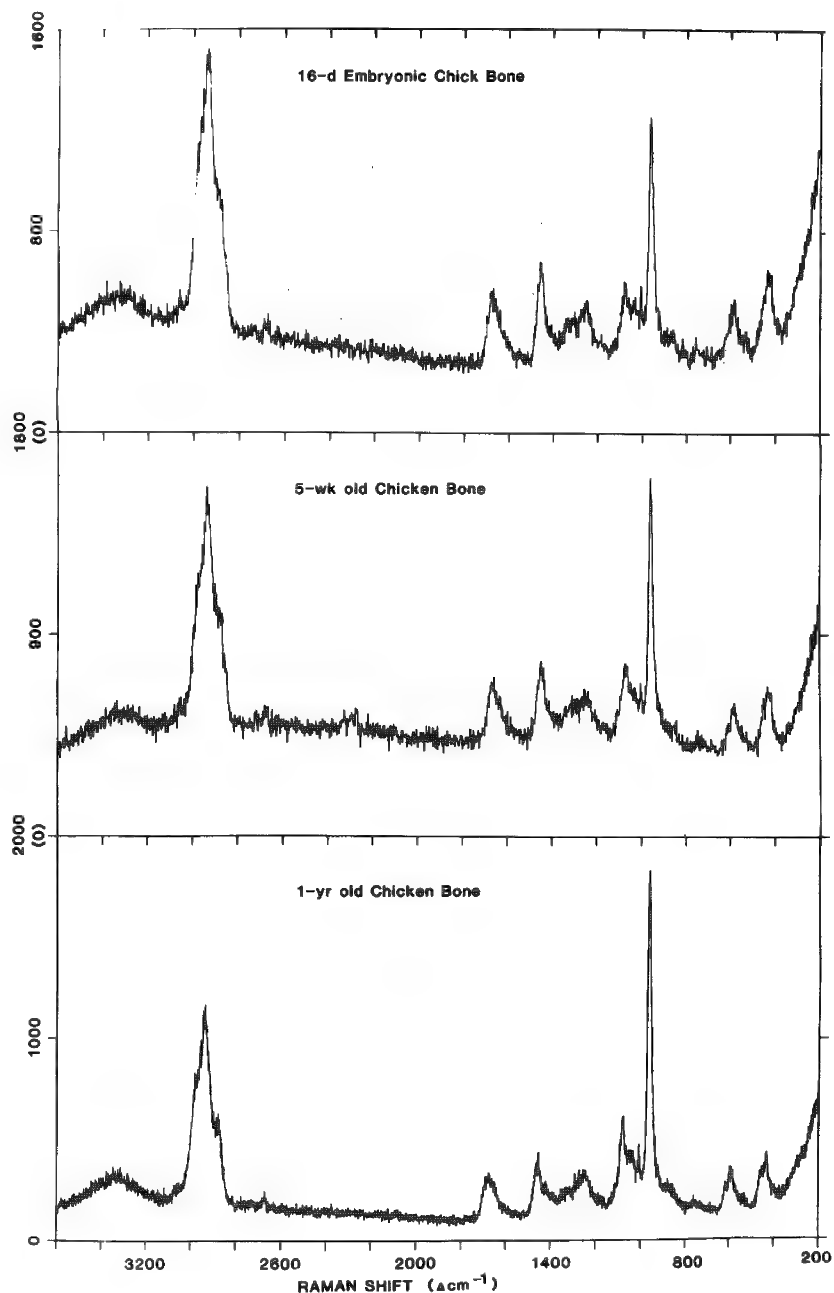
FIG. 1.--Composite of three spectra: particles of unfractionated chick bone powders. Top, 16-day embryonic chick whole bone, 200-3600 cm^{-1}; middle, 5-week chick bone, 200-3600 cm^{-1}; bottom, 1-year whole chick bone, 200-3600 cm^{-1}.

FIG. 2.--Composite of three spectra. Top, decalcified mature turkey bone, 300-1800 cm^{-1}; middle, 17-day embryonic chick bone, density fraction 1.5-1.6, 300-1800 cm^{-1}; bottom, 17-day embryonic chick bone, density fraction 2.0-2.1, 300-1800 cm^{-1}.

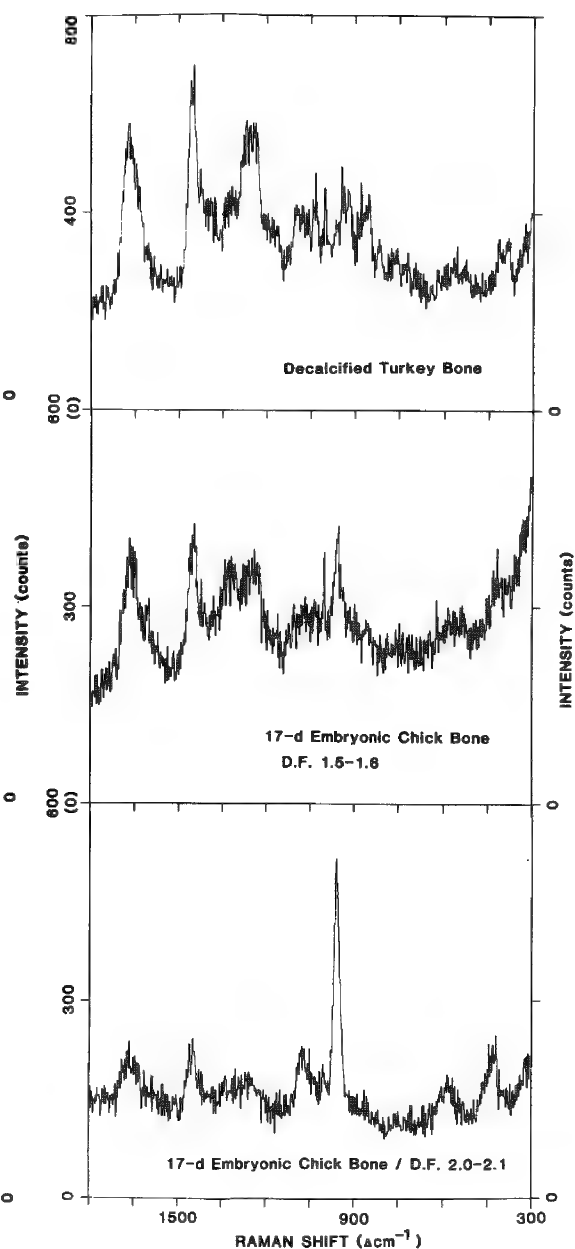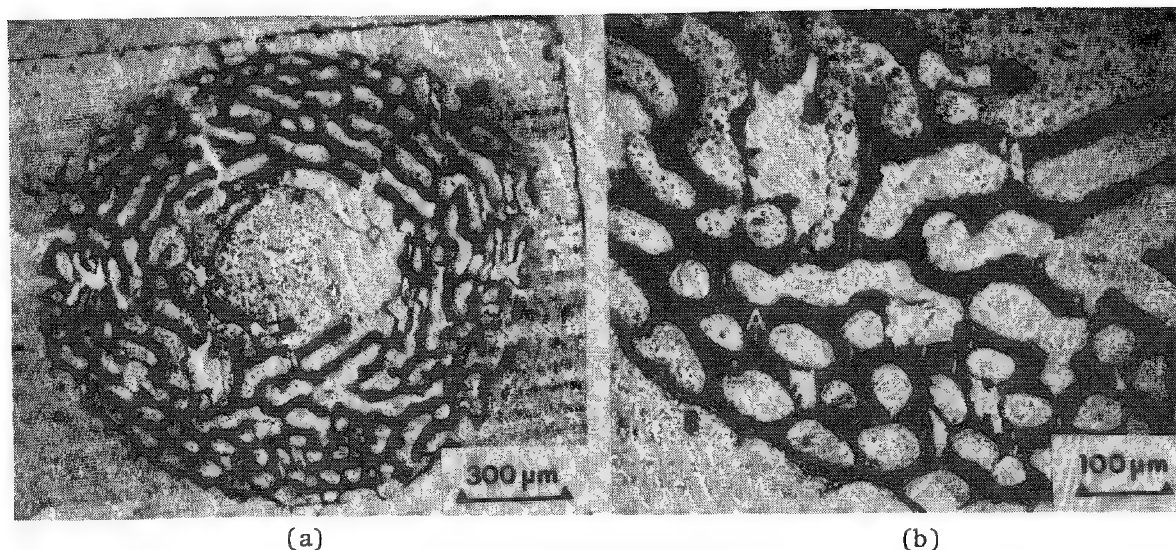FIG. 3.--Optical micrographs: (a) transmitted light, 50×; (b) transmitted light, 125×, of a transverse section (lyophilized) of 18-day embryonic chick tibia, embedded in epoxy (Epon). Thickness of section about 2 μm. Mounted on Sapphire substrate.

Figure 3 shows two optical micrographs of the Epon-embedded chick tibia sectioned transversely (2 μm thick). Two spectra (Fig. 4) were obtained from the section, one from a mineralized zone (A), the other from a nonmineralized area (B) (cf. Fig. 3). In the latter spectrum (Fig. 4b), bands appear, including one at 1452 cm^{-1}, which all seem to originate from the Epon embedding material.[8] Because of the small thickness of the section (2 μm), no obvious bands from the organic matrix of bone are detected. Bands labeled 'S' are due to the scattering from the sapphire substrate. In the spectrum from the mineralized portion of the tissue section (Fig. 4a), the 960 cm^{-1} phosphate, the 1074 cm^{-1} carbonate, the amides, and the sharp band at 1004 cm^{-1} are clearly visible.

Discussion

The sharp band at 1004 cm^{-1}, which can be seen in the spectra of all the bone samples and seems to be decreasing with increasing mineral content, has been attributed by some workers[9] to phenylalanine and by some others to organic phosphate.[5] It remains to be determined which assignment is correct and why this band is so prominent in all the bone patterns. Besides the concurrent increase in phosphate bands and decrease in organic bands, the carbonate seems to be following a smooth increase with animal age.[10] The absence of carbonate is noted only in the very early mineralized phase (low density fraction of embryonic bone) where HPO_4^{2-} seems to be present, a correspondence in agreement with chemical measurements made by Pellegrino and Biltz[11] on developing chick bone.

Although the Raman microprobe is not now fully quantitative because of the complexity of biological specimens,[12] it is nevertheless a very sensitive tool for observing subtle changes in the chemistry and structure of bone mineral. With the direct examination of bone tissue sections by Raman microanalysis, the mineralization process may be followed in situ and correlated with morphology, and the effects of various tissue preparation methods on the chemistry of these biological mineralized tissues may be assessed. The work presented here indicates the extreme utility of the method but many questions remain to be answered--the proper assignment of the sharp band at 1004 cm^{-1}, the changes occurring in the water bands, the effects of tissue preparation on the Raman signal, and others. Answers should come from detailed investigation of these and additional mineralized samples to improve our knowledge of the chemical and structural changes that occur in bone tissue during maturation and aging.

References

1. M. J. Glimcher, "Composition, structure and organization of bone and other mineralized tissues and the mechanism of calcification," in R. O. Greep, E. B. Astwood, Eds., *Handbook of Physiology: Endocrinology*, Washington, D.C.: American Physiological Society, 1976, 7: 25-116.

2. A. H. Roufosse, W. J. Landis, W. K. Sabine, and M. J. Glimcher, "Identification of brushite in newly deposited bone mineral from embryonic chicks," *J. Ultrastruct. Res.* 68: 235, 1979.

3. E. S. Etz, "Raman microprobe analysis: Principles and applications," *SEM/1979* I, 67.

4. E. S. Etz and J. J. Blaha, "Scope and limitations of single particle analysis by Raman microprobe spectroscopy," in J.F.K. Heinrich, Ed., *Characterization of Particles*, NBS Special Publication 533, Washington, D.C., 1980, 253-297.

5. F. S. Casciani, E. S. Etz, D. E. Newbury, and S. B. Doty, "Raman microprobe studies of two mineralizing tissues: Enamel of the rat incisor and the embryonic chick tibia," *SEM/1979* II, 383-391.

6. A. G. Walton, M. J. Deveney, and J. L. Koenig, "Raman spectroscopy of calcified tissue," *Calcified Tissue Res.* 6: 162-167, 1970.

7. B. G. Frushour, and J. L. Koenig, "Raman scattering of collagen, gelatin and elastin," *Biopolymers* 14: 379, 1975.

8. M. K. Antoon, B. E. Zehner, and J. L. Koenig, "Spectroscopic determination of the in situ composition of epoxy matrices in glass reinforced composites," *Polymer Composites* 1: 24, 1980.

9. F. S. Parker, "Biochemical applications of infrared and Raman spectroscopy," *Appl. Spectrosc.* 29: 129, 1975.

10. M. J. Glimcher, L. C. Bonar, M. D. Grynpas, W. J. Landis, and A. H. Roufosse, "Recent studies of bone mineral: Is the amorphous calcium phosphate theory valid?" *J. Cryst. Growth* 53: 100, 1981.

11. E. D. Pellegrino and R. M. Biltz, "Mineralization in the chick embryo: I. Monohydrogen phosphate and carbonate relationships during maturation of the bone crystal complex," *Calcified Tissue Res.* 10: 128, 1972.

12. E. S. Etz, "Empirical quantitation in Raman microprobe analysis," *Microbeam Analysis--1981*, 73-78.
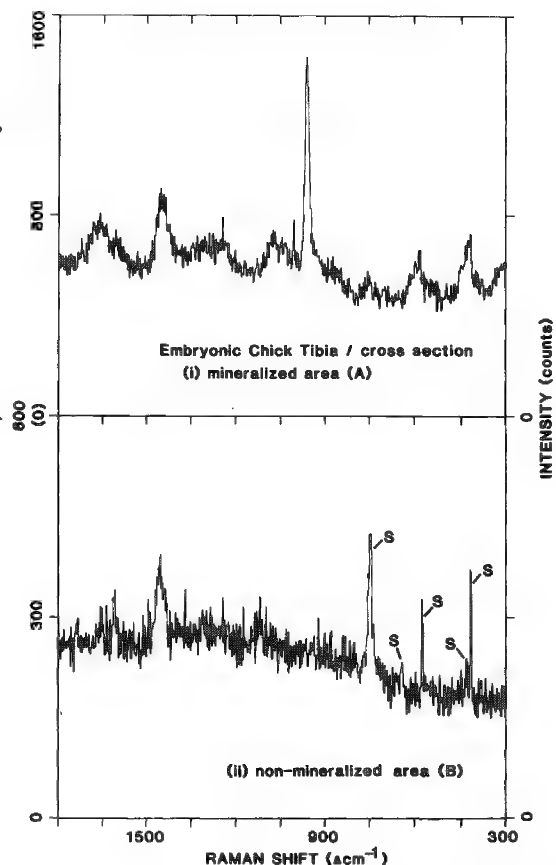
FIG. 4.--Top, spectrum of mineralized zone of 18-day embryonic chick tibia cross section (see point or probe area marked [A] in micrograph of Fig. 3), 300-1800 cm^{-1}; bottom, spectrum of the nonmineralized zone (i.e., organic matrix) of 18-day embryonic chick tibiae cross section (see point or probe area marked [B] in micrograph of Fig. 3), 300-1800 cm^{-1}.

CHARACTERIZATION OF NATIVE OXIDES ON MERCURY CADMIUM TELLURIDE

Fran Adar, R. E. Kvaas, and D. R. Rhiger

The Raman spectrum of an anodically prepared 700Å oxide film on mercury cadmium telluride, $Hg_{0.7}Cd_{0.3}Te$, has been recorded. Raman spectra of microparticles of eight oxides of these metals have also been recorded in order to characterize the native oxide film. The spectrum of the oxide film does not match that of any of the reference compounds--TeO_2 (paratellurite), HgO, Hg_2O, $CdTeO_3$ (two crystal polymorphs), $HgTeO_3$, TeO_3, $CdTeO_4$, H_6TeO_6. The chemical composition of the oxide and its long-range order (crystalline or amorphous) have been considered. In particular, the depletion of mercury, and the ability of Raman spectroscopy to differentiate between $CdTeO3$ and a mixture of CdO and TeO2 is discussed.

Experimental Conditions

The Raman microparticle spectra were recorded either on the MOLE (Molecular Optical Laser Examiner) or on the Ramanor U1000 optically coupled with a microscope for Raman microprobe analysis. The particles were dispersed on a slide and examined without further preparation. Because of the possibility of laser-induced evolution of Hg from Hg_2O, particles of Hg_2O were also examined under water, which served as a heat sink.

The spectrum of the oxide film was recorded on the microscope accesory on the U1000. Because of the fragility of the films to high laser irradiance, the spectrum was recorded by averaging of overnight signals generated by 0.5 to 1.0 mW of laser intensity at the sample. In addition, it was necessary to defocus the laser beam to about 15 μm. Independent scans of different spots on the same sample produced the same spectrum shown here.

Results

Reference Spectra. Spectra of microparticles of the oxides are presented in Figs. 1-7. One sees clearly that the Raman spectra provide a clear fingerprint for composition. Several comments regarding these spectra are useful.

Examination of various particles of TeO_2 indicate some variability in the spectra, which can probably be attributed to excitation of infrared-active extraordinary phonons with wavevectors along axes between z and the x-y plane.[1]

The spectrum of Hg_2O is identical to that of HgO (Fig. 2). Since laser illumination may produce evolution of mercury from Hg_2O, we attempted to minimize this effect (if it were occurring) by examining particles under water. The spectra of Hg_2O under water and in air are essentially identical; the principal difference is the narrower linewidths of the bands of the former. We may thus conclude that either we could not prevent evolution of mercury from the lattice, or that the spectra of the two compounds are identical. In general, the second possibility would not be worthy of consideration. However, in this instance, there is independent evidence that in Hg_2O the second atom of mercury resides in the lattice of HgO without any chemical interaction.[2]

Samples of $CdTeO_3$ from two vendors were examined. The Raman spectra shown in Fig. 4 are quite distinguishable. This result implies the presence of two crystalline polymorphs for this material and was confirmed by x-ray diffraction. In addition, there is considerable variation of lineshape in the spectra of particles in both specimens, which is consistent with the known property of TeO_2 to be a glass former.[3]

Native Oxide. The spectrum recorded from the native oxide is shown in Fig. 8. It consists of a broad band centered at about 715 cm^{-1} and some weaker bands at higher frequency. This spectrum does not match that of any of the reference compounds. Because of the width of the bands one may conclude that the film is amorphous.

Author Adar is at Instruments S.A., Inc., Metuchen, NJ 08840; authors Rhiger and Kvaas, at Santa Barbara Research Center, Goleta, CA 93117.
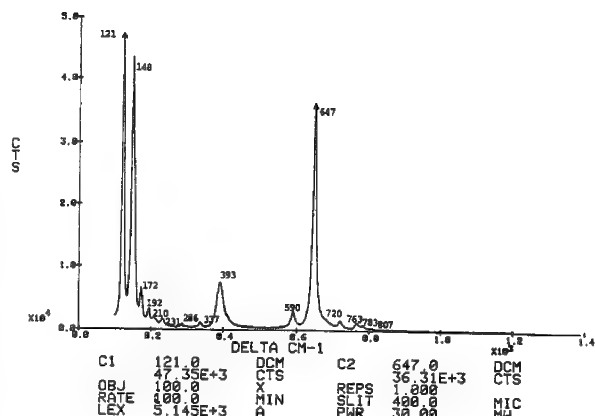
FIG. 1.--Raman spectrum of microparticle of TeO_2, λ_{ex} = 514.5 nm, 400µm slits (4cm^{-1} resolution), 30 mW entering microscope (ca 3 mW at sample), 100×, N.A. = 0.90 objective, 100 cm^{-1}/min.
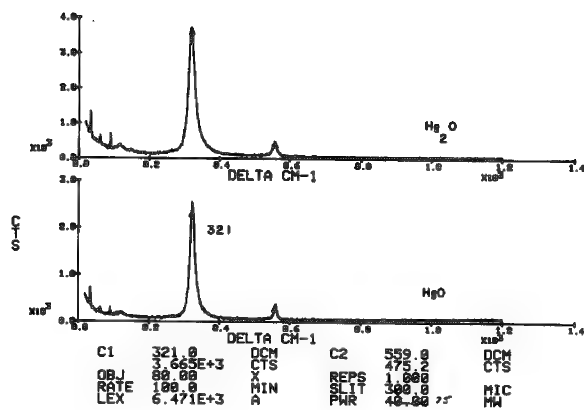
FIG. 2.--Raman spectra of microparticles of Hg_2O and HgO_1, λ_{ex} = 647.1 nm, 300µm slits, 25 mW, 80× N.A. = 0.90 objective, 100 cm^{-1}/min.
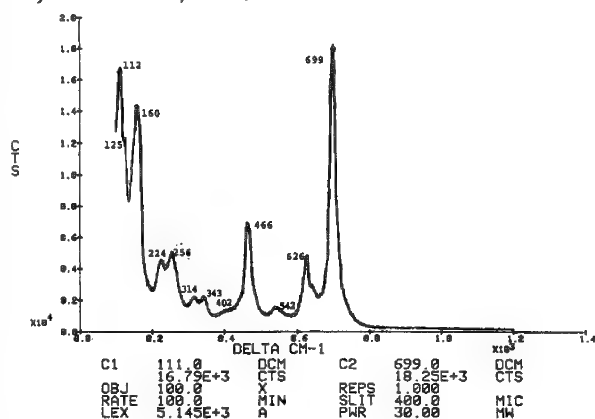
FIG. 3.--Raman spectrum of microparticle of $HgTeO_2$, 514.5 nm, 400µm slits, 30 mW, 100×, 100 cm^{-1}/min.
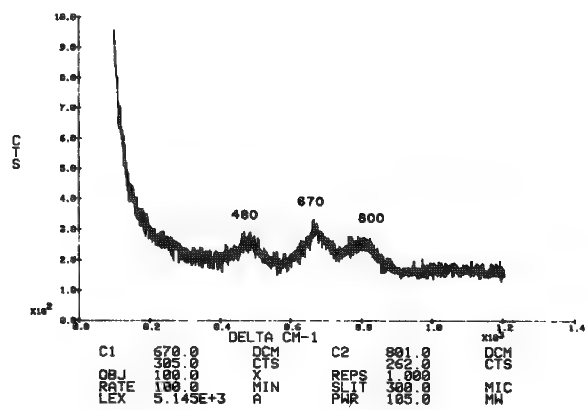
FIG. 5.--Raman spectrum of microparticle of TeO_3, 514.5 nm, 300µm slits, 100 mW, 100×, 100 cm^{-1}/min.
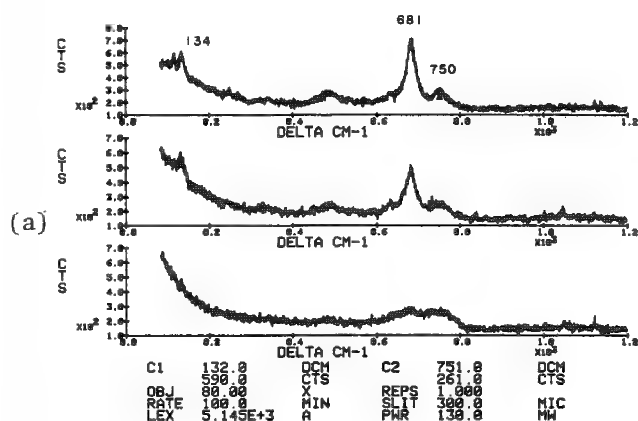
FIG. 4.--Raman spectra of microparticles of $CdTeO_3$; 514.5 nm, 300µm slits, 110 mW, 80×, 100 cm^{-1}/min; (a) a differs from (b) in crystalline phase; individual particles in each sample differed in crystallinity, as judged from linewidths.
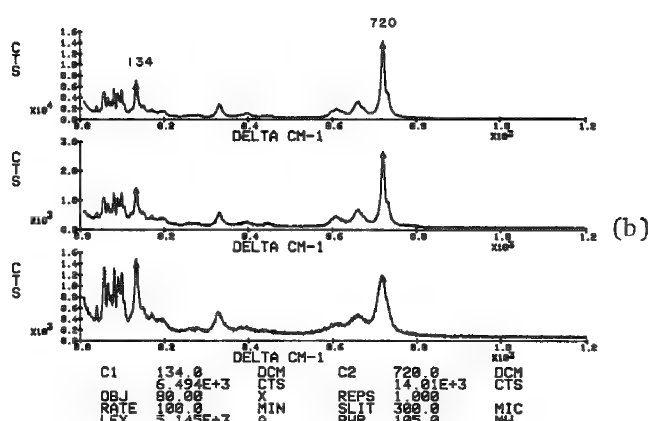
Discussion

The spectrum generated from the native oxide film certainly does not match that of any of the crystalline reference oxides. Based on published data, it might contain substantial glassy TeO_2.[4] XPS and Auger spectroscopy eliminate CdO,[5] the one possibility that is Raman

FIG. 6.--Raman spectrum of microparticle of $CdTeO_4$, 514.5 nm, 300µm slits, 100 mW, 100×, 100 cm^{-1}/min.
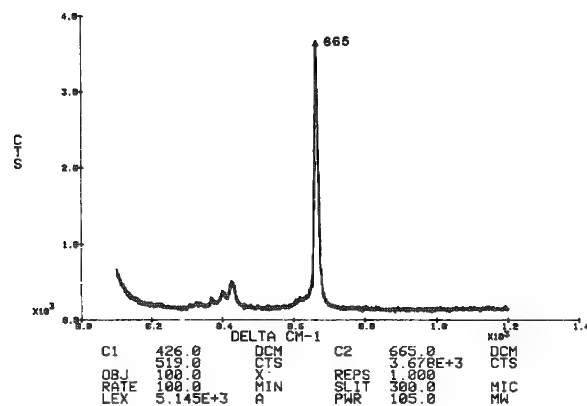
FIG. 7.--Raman spectrum of microparticle of H_6TeO_6, 514.5 nm, 300µm slits, 100 mW, 100×, 100 cm^{-1}/min.
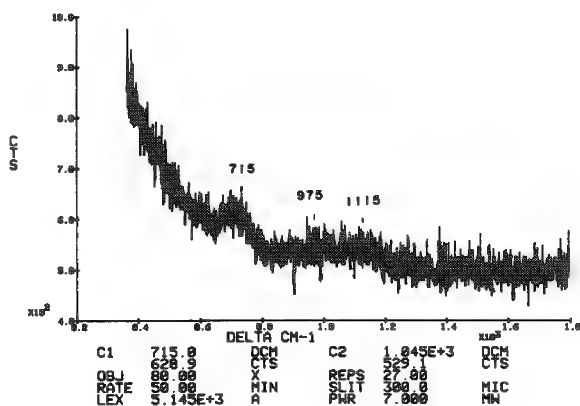
FIG. 8.--Raman spectrum of 700Å native oxide film on $Hg_{0.7}Cd_{0.3}Te$; 514.5 nm, 300µm slits, 7 mW (ca 1 mW at sample), 80×,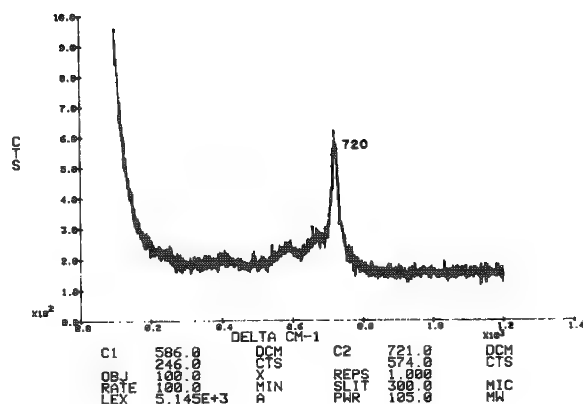 50 cm^{-1}/min, laser beam spot ca 15 µm; this spectrum represents an accumulation of 27 spectra added in succes sive scans.

inactive. However, characterization of more complicated phases of Cd is somewhat ambiguous with the elemental techniques.

The potential of Raman spectroscopy to characterize a crystalline or amorphous phase of the $HgTeO_3$/$CdTeO_3$ solid-solution system is at present being explored for further clarifi- cation of the native oxide film of $Hg_{0.7}Cd_{0.3}Te$. The frequency of the band that was ob- served at 715 cm^{-1} is closest to the strongest bands of $CdTeO_3$ (681 or 720 cm^{-1}, depending on the crystal type), $HgTeO_3$ (699 cm^{-1}), or possibly TeO_3 (three broad bands of equal in- tensity at 500, 670, 800 cm^{-1}). In addition, one sees that examination of the spectra re- corded from several particles of each sample of $CdTeO_3$ indicates substantial variation in linewidths, a result of the tendency of this material to solidify in a glassy phase. Be- cause it is expected that $CdTeO_3$ and $HgTeO_3$ form solid solutions, examination of glasses of known composition will aid in the characterization of the native oxide film. Such experi- ments are being planned for the coming months.

References

1. A. S. Pine and G. Dresselhaus, "Raman scattering in paratellurite, TeO_2," *Phys. Rev.* B5: 4087-4093, 1972.

2. R. E. Kirk and D. F. Othmer, Eds., *Encyclopedia of Chemical Technology*, Easton, Pa.: Mack Printing Co., 1952, vol. 8, 888.

3. S. Neov, I. Gerassimora, K. Krezhov, B. Sydzhimov, and V. Kozkukhavov, *Phys. Status Solidi* A47: 743, 1977.

4. V. P. Cheremisinov and V. P. Zlomanov, "Vibrational spectra and the structure of tellurium dioxide in the crystalline and glassy states," 1961.

5. G. D. Davis, T. S. Sun, S. P. Buchner and N. E. Byer, "Anodic oxide composition and Hg depletion at the oxide-semiconductor interface of $Hg_{1-x}Cd_xTe$," *J. Vac. Sci. Technol.* 19: 472-476, 1981.

LASER MICROPROBE MASS ANALYSIS (LAMMA): CURRENT STATE OF THE ART WITH SPECIAL
EMPHASIS ON BIO-MEDICAL APPLICATIONS

R. Kaufmann

Although the potential benefits and advantages of laser microprobe mass analysis (LAMMA)
have been recognized for a rather long period of time, the advent of this technique in
practical analytical work did not occur before 1978 when the first instrument (LAMMA 500,
Leybold Heraeus) became commercially available that could truly compete with other existing
microprobe techniques. Since that time a rapidly increasing number of successful applica-
tions have been published and the spectrum of applicative fields has been broadened. Orig-
inally developed primarily for biomedical microprobe analysis, the LAMMA principle has now
gained as much acceptance in materials sciences, particle analysis, and--more recently--
organic mass spectrometry, where it is on the way to becoming a unique technique for the
analysis of involatile and/or thermally labile organic compounds.

At present the total number of original reports published amounts to about 150, includ-
ing several reviews and survey papers on the various applicative topics.[1-5] The remainder
of this paper delineates the current state of the art of the LAMMA technique with special
emphasis on biomedical applications; other applicative trends will be treated in additional
contributions by other authors at this conference.

Instrumentation

Instrument design and performance data of the LAMMA 500 instrument have been extensively
published[6-9] with regard to the various fields of applications and hence will not be re-
peated here. Although the LAMMA 500 instrument has only been slightly modified since its
introduction, further improvements and modifications have been achieved, but so far only on
the laboratory level. This applies to the following items:

Laser microscope
Imaging system
Analysis of bulk material (reflecting geometry)
Quantitation
Specimen preparation

Laser Microscope and Imaging System

Coupling of an optical microscope with the output of a laser light source is anything
but a straightforward task, particularly if one aims toward diffraction-limited focusing
of the laser beam. This technique requires consideration of the quality of the laser beam
(divergence, optical modes, beam diameter, intensity distribution across the beam), proper-
ties of alignment and functional components (filter, mirrors, beam splitters, intermediate
optics, precision mounts etc.), and, last but not least, the microscope itself.

Based on the experiences acquired with the current LAMMA 500 instrument the author has
redesigned the whole optical part of the system including the microscope and the illumina-
tion sections. With respect to the industrial version the new concept features:

● reduced transmission losses of laser output energy (only two 90° beam deflections
instead of five)

● considerably improved alignment procedures

● continuously adjustable (polarizing) and separate filters for both pilot and impulse
lasers

The author is with the Institute of Physiology, Department of Clinical Physiology,
University of Düsseldorf, 4000 Düsseldorf, Federal Republic of Germany.

- energy output meter behind optical filter
- independent beam expanders for optimal adaptation of the beam diameter to the entrance pupil of the microscope objective and for correction of the remaining achromatism of the ultrafluar objectives employed
- infinity ray pathway in the optical microscope for better adaptation of additional imaging or analytical components
- UV transmitting transillumination system ($\lambda = 250$ nm)
- incident illumination via fibre optics
- incorporation of a (UV sensitive) TV camera
- adaptation of an OMA detector for monitoring actual laser beam intensity profiles

A schematic drawing of the new concept is shown in Fig. 1.

Figures 2-5 give some impressions of the improvements attained in spatial resolution of both the imaging and the analytical parts of the instrument. With the 100× ultrafluar objective, perforation diameter (in 0.2μm thick sections of an epoxy resin specimen) of 0.3 μm can now routinely be achieved (Fig. 4).

Another considerable improvement (especially for the analysis of unstained tissue sections) came from the incorporation of the UV transillumination. The poor structural information obtained in semithin sections of unstained tissue specimens made it rather difficult and sometimes impossible to correlate analytical data with structural details of the specimen under investigation. In many cases analyses had to be executed blind and the sites of analysis later identified by subsequent staining of the specimen and light microscopic or, if necessary, electron microscopic inspection. Since the absorption edges of nucleic acids start at about 270 nm, and those of the proteins between 250 and 230 nm, UV transillumination was attempted in order to obtain absorption contrast images in otherwise fully transparent semithin sections of epoxy-embedded histological materials. To this end the transillumination system of the LAMMA 500 instrument was redesigned, with UV transparent optics used in combination with a 75W XBO high-pressure xenon lamp. With the aid of reflection band pass filters it was found that light of 250 ± 10 nm gave best results with respect to absorption contrast under the conditions chosen. For image conversion a Philips mini-TV camera (LDM 2600) with a UV-sensitive vidicon (XQ 1453 KV) is employed.

As demonstrated particularly by Figs. 2 and 3 this kind of UV transillumination gives rather satisfactory image contrasts (in comparison with other microscopic imaging techniques such as phase contrast or interference contrast) in the tissue specimens commonly employed for LAMMA analysis.

In addition, since the spatial resolution attained in an optical microscope is correlated to the wavelength of the light, the 250nm illumination will improve the useful magnification of the optical microscope by a factor of 2.5 in comparison to visible light.

Analysis of Bulk Material

In the LAMMA 500 instrument analysis of bulk materials is possible only under the conditions that a specimen is not too extended and that the laser can be focused at grazing incidence on a specimen's edge.

In recognition of these rather limiting conditions and, on the other hand, the large demand for microprobe analysis in bulk materials, a new concept was developed recently, based on an incident (reflection) geometry with respect to laser focusing-, imaging-, and ion extraction elements, as discussed by Hillenkamp in another paper at this conference.

Sensitivity and Reproducibility

As in any microprobe technique, detection limits for LAMMA analysis depend on operational conditions of the instrument as well as a number of properties of the specimen under investigation. The list includes (among many others) parameters such as ionization potential for positive ions and electron affinity for negative ions, binding state of atomic ions in the surrounding matrix, bond strength in organic molecules, stability of ions generated, probability of recombination processes in the laser-induced microplasma and--on the instrument side--the laser wavelength and irradiance in the focus. Detection limits can be therefore specified only for a given analytical problem under well-defined instrumental conditions. The scatter of data published so far for LAMMA analyses is mainly due to the rather different working conditions chosen by the various investigators. For better com-
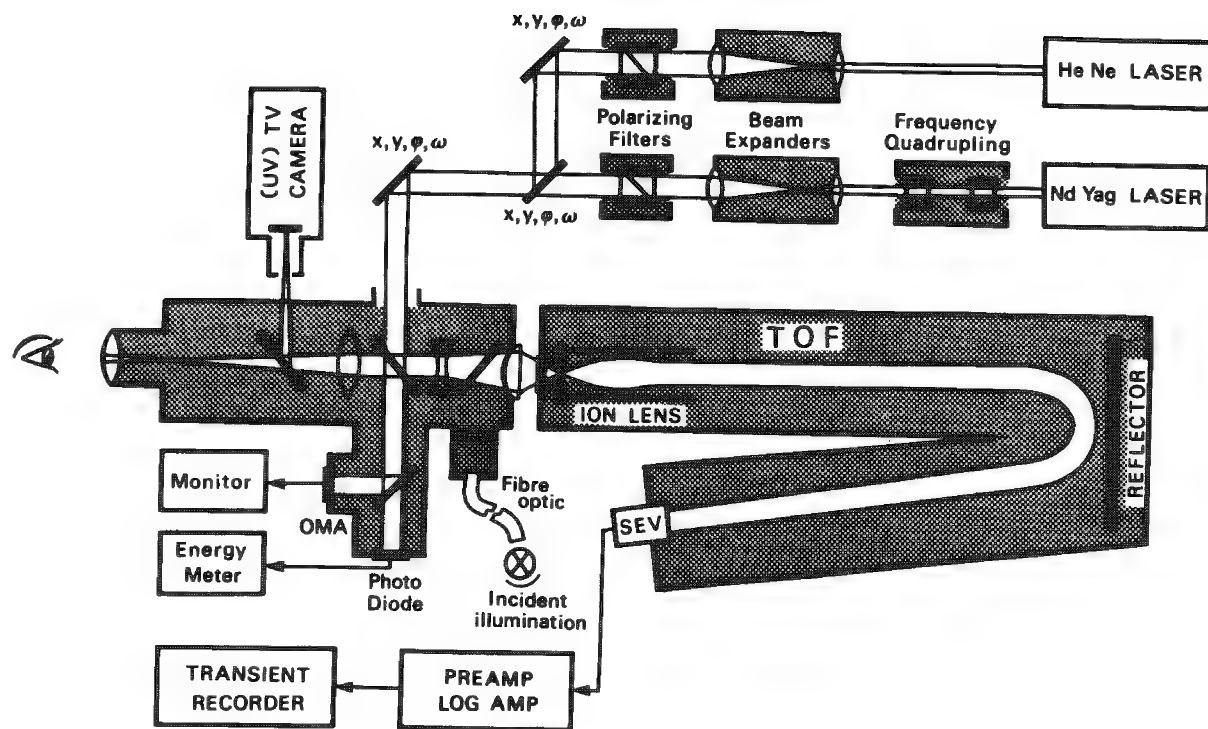
FIG.1.--Schematic modified LAMMA instrument.
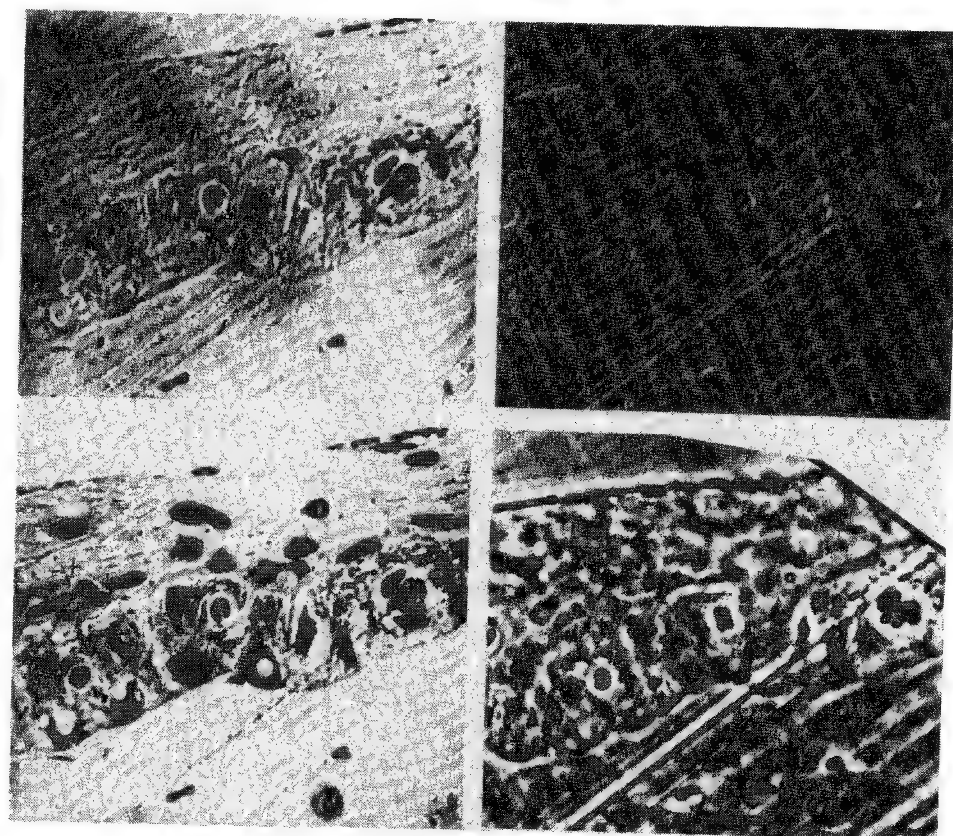
FIG. 2.--Comparison of structural contrasts obtained by various transillumination techniques in unstained 0.3μm section of plastic-embedded tissue specimen: absorption contrast, visible light (upper left), phase contrast (upper right), UV absorption, λ = 350 nm (lower left), UV absorption, λ = 250 nm (lower right). Ultrafluar 32×.
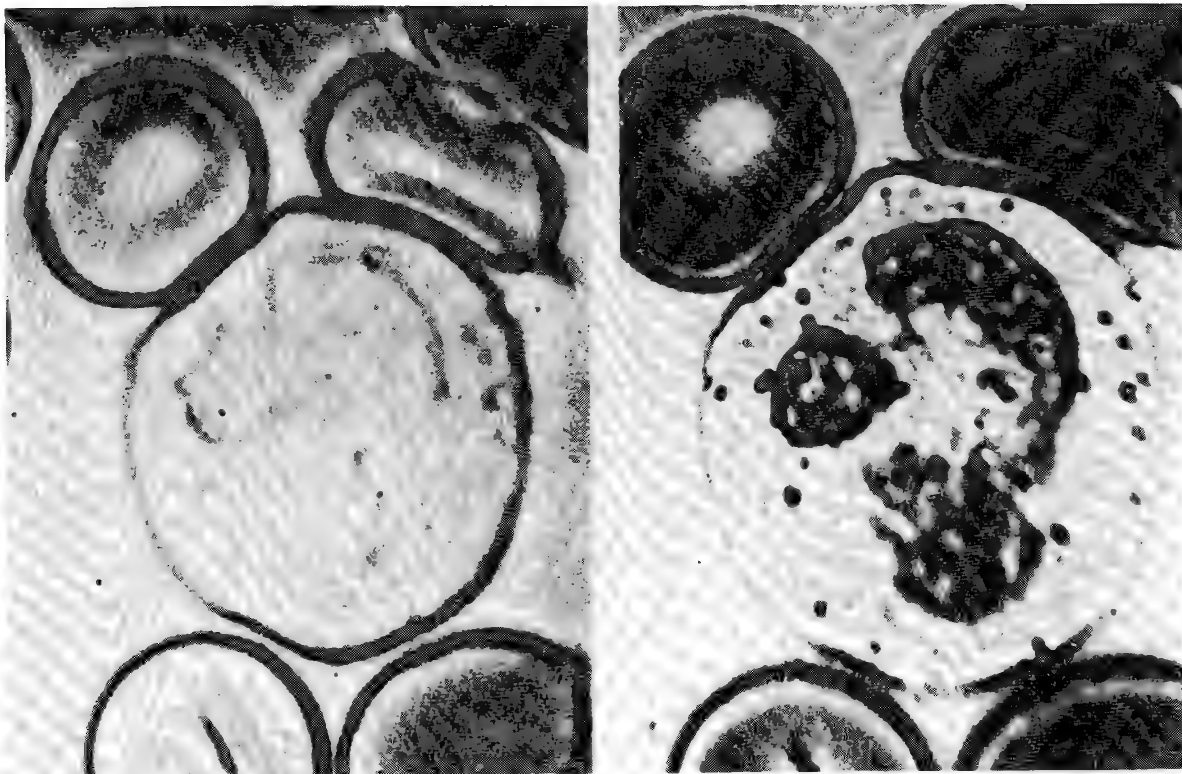
FIG. 3.--Comparison of image contrast obtained in unstained blood smear by transmitting illumination with either visible light (left) or 250nm UV light (right); image diameter, 200 μm.
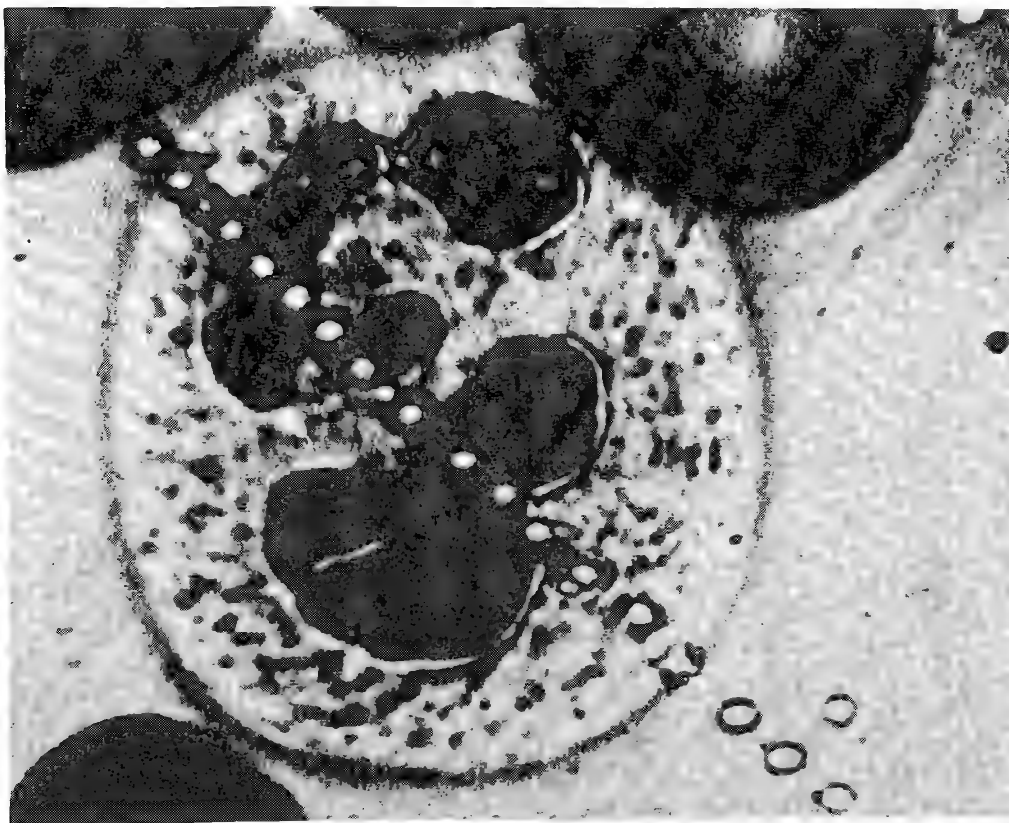
FIG. 4.--Laser perforations obtained in human granulocyte. (100× Ultrafluar). Image contrast by UV transillumination (λ = 250 nm). Mean perforation diameter, 0.4 μm.
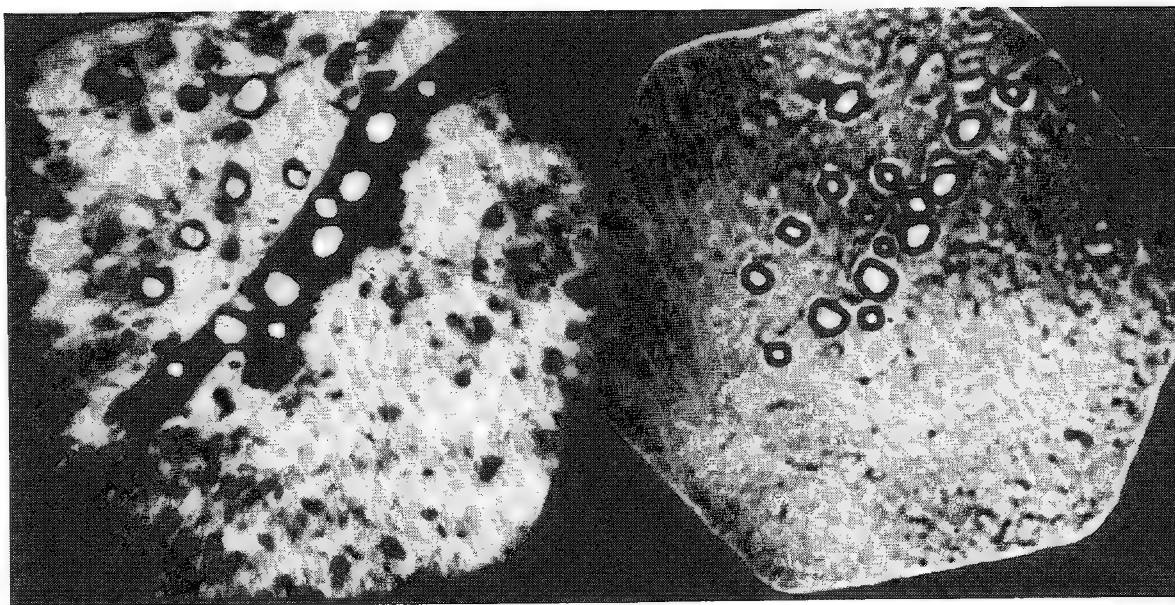
FIG. 5.--Comparison of structural contrast in laser-probed area of foreign body granulation
tissue surrounding piece of metallic copper in vitreous body of rabbit eye. Note dark area
in UV transmission image (left), which has been shown to contain Cu by LAMMA analysis.
(Courtesy of Dr. Paulmann, Department of Ophthalmology, University of Cologne.)

parison of such data in the future it would be best to establish some sort of standard con-
ditions, for instance irradiance set at five times the appearance threshold for ions, laser
wavelength 265 nm, 32 × Ultrafluar.

Table 1 summarizes relative detection limits for element analysis in various matrices.
It should be kept in mind that in LAMMA analysis relative sensitivity depends on the total
amount of material analyzed. The data shown in Table 1 refer to a typical situation, i.e.,
a volume of analyzed material in the range of 2-3 × 10^{-13} cm^3.

The reproducibility of the ion signals from shot to shot depends on the homogeneity of
the sample and--in the analysis of organic molecules originally in solution--strongly on
the choice of a suitable preparation method. For the particularly interesting case of phy-
siological or toxic elements in organic material, reproducibility is typically better than
± 20%. As successive spectra can be recorded at a rate determined by the selection of a
new site for analysis with the microscope stage (i.e., at a rate of several spectra per
minute), averaging over a suitable number of spectra is easy and usually advisable for in-
creased reliability of results.

Comparison with Other Microprobe Techniques

Some investigators have started to execute systematic comparative studies in order to
evaluate performance data of, say, LAMMA, EDAX, or SIMS in the same specimen (see, for ex-
ample, Refs. 5 and 34).

The experience and data available so far indicate that in organic matrices element sen-
sitivity of LAMMA is one to two orders of magnitude better than that of EDAX depending on
the element to be analyzed (Table 2). With respect to SIMS, sensitivity is of the same
order of magnitude for most elements but LAMMA tends to be slightly better for heavy ele-
ments. The potential advantages of LAMMA versus SIMS may be summarized as follows: (1)
matrix effects on ion yield less pronounced, (2) no analog to "differential sputtering,"
(3) no coating required, (4) better imaging capabilities.

Quantitation

In the present state of the LAMMA technique, and with the lack of a theory unifying all
physical effects of ion formation, quantitative analysis with LAMMA is difficult particu-
larly if one looks for *absolute quantitation*. As it is especially difficult or sometimes

impossible to determine the sampled mass volume, the only approach to absolute quantitation would be the use of internal standard reference elements. Under favorable analytical conditions (thin sections of epoxy-resin embedded material coated or doped with known amounts of reference material) such an approach has been successfully applied.[5,10]

TABLE 1.--Relative detection limits (ppmw) for element analysis (positive ions).

	Glass matrices[1]	Organic matrices				Glass matrices[1]	Organic matrices		
		(2)	(3)	(4)			(2)	(3)	(4)
Li	3	1.6	0.4		Nb	7			
Be	25				Ag			1	
B	9				Cd			20	
Na			0.2		Jn	7			
Mg	8		0.4		Cs	6		0.5	
Al			0.3		Ba	6	2.5	0.5	
Si	10				La	4	10.0		
K	0.8		0.1		Ce	5			
Ca		1.6	1	0.4	Pr	3			
Ti	1				Ho	14			
V			0.5		Tm	11			
Co			10		Lu	6			
Cu			15		Ta	6			
Rb			0.5		Pb	10	10.0	0.4	
Sr		2.5	0.5		Th	6			
Y	4				U	6		2.0	

(1) NBS standard reference glasses of the SRM 610-616 series. Limits defined by element signals exceeding 3 times standard deviation of the background noise. No further conditions given.[14]

(2) Data obtained by Schroeder[5] in either natural pigment granula or epoxy resin matrices (0.3μm thick sections, 0.5μm perforations, no threshold related conditions given).

(3) Epoxy-resin (Spurr's low viscosity medium) reference standards containing trace amounts of organo-metallic complexes. Working conditions: 10^{-13} g evaporated material irradiance set at 5 times the damaging threshold, signal intensities, averaged over 5 analyses must exceed 3 times the background noise.[13]

(4) Value measured by Schroeder[5] in a standard specimen of CaF deposited on a 0.3μm epoxy resin section.

TABLE 2.--Comparative detection limits (mmol/1) for some elements in organic matrices (after Schroeder[5]).

Pigment granules	EDX	LAMMA
Ca	1	0.04
Sr	1.5	0.03
Ba	0.8	0.02
La	1.2	0.06
Ca film vacuum deposited	0.8	0.01
Doped spurr		
Li	-	0.5
Sr	1	0.08
Pb	0.5	0.06

TABLE 3.--Relative sensitivity factors (RSF) for trace elements distributed in either NBS 610 reference glass or in an epoxy resin (Spurr's low-viscosity medium): (1) Surkyn and Adams,[14] (2) Wurster et al.,[55] (3) Kaufmann et al.[13]

Isotope	SRM 610 (1)	Epoxy resin		
		(2)	(1)	(3)
7Li	0.19	0.48	0.49	0.64
39K*	1.19*	3.22	4.14*	2.70
41K	4.16		8.95	
86Sr	1.00	2.00	1.73	1.99
88Sr	0.82		1.89	
208Pb	1.00	1.00	1.00	1.00

*39K data unreliable, most probably owing to detector nonlinearity.

For *relative quantitation* the situation is not so restricted provided that linearity between signal intensity and concentration can be assumed. That LAMMA fulfills this prerequisite has been shown for example by Kaufmann et al.[11] This feature in turn opens the possibility of establishing relative sensitivity factors empirically by means of standard reference materials of similar thermal, optical, and chemical properties as the unknown sample. Another approach is to apply the LTE (local thermodynamic equilibrium) model, provided that realistic guesses can be made as to the relevant parameters such as partition functions, electron density, and plasma temperature.

Relative Sensitivity Factors (Empirical Approach). The relative sensitivity factor (RSF) can be defined for an element or isotope x as

$$(RSF)_x = \frac{I_x C_R}{C_x I_R} \tag{1}$$

with I and C denoting the measured peak intensities and concentrations of the element X and of the reference element R, respectively.

Relative sensitivity factors applicable in LAMMA analysis of various materials have been published by Kaufmann et al.[12] for trace metals in epoxy-resin reference material, by Kaufmann et al.[13] for microspheres and fibers made from NBS research material glasses (K 309, K 491), and by Surkyn and Adams[14] for the NBS research and reference glass standards (K 411, K 309, K 961, SRM 610, SRM 612) and for the SRM 1633 fly ash standard. Some RSFs measured by the above authors are summarized in Table 3.

Relative Sensitivity Factors (LTE Approach). With the assumption of a local thermodynamic equilibrium (LTE) in the laser-induced microplasma, the degree of ionization α_x of an element X is given by

$$\alpha_x = \frac{n_x^+}{n_x^+ + n_x^0} \simeq \frac{n_x^+}{n_x^0} \quad (\text{if } n_x^+ \ll n_x^0) \tag{2}$$

(where n_x^0 and n_x^+ are the number densities of neutral atoms and positively charged ions respectively) and can be calculated using the well known Saha-Eggert equation:

$$\frac{n_x^+}{n_x^0} = \frac{2 \, Q_x^+}{Q_x^0 n_e} \frac{2\pi m_e kT^{3/2}}{h^2} \exp \, [-(W - \Delta W)/kT] \tag{3}$$

where n_e is the electron density, T is the plasma temperature, Q_x^0 and Q_x^+ are the partition functions of atoms and ions, respectively, m_e is the electron mass, h is Planck's constant, W is the ionization energy, and ΔW is the Coulomb depression. Ionization energy can be taken from the literature, but partition functions (and their dependence on temperatures above 7000°K) are not easy to obtain. Plasma temperature and electron density under practical analytical conditions have been estimated by Surkyn and Adams[14] to about 13 000°K, whereas Haas et al.[15] obtained best approximation of their data with T = 8000°K. Both groups refer to electron densities of $n_e = 10^{18}$ cm^{-3}.

The model can be used to predict relative sensitivity factors under various experimental conditions (Fig. 6) if, for instance, plasma temperature varies with laser power and provided that reasonable guesses can be made as to partition functions and electron density. For an explicit explanation of how to obtain numerical data applicable to this method the reader is referred to the literature.[16-21]

Such "theoretical" sensitivity factors can be compared with experimentally determined data. Figures 7 and 8 demonstrate that theoretical RSFs as predicted by the LTE model agree rather well with those determined experimentally, at least in selected materials. However, the LTE approach is far from always being an adequate concept for the quantification of LAMMA analyses. Ionization processes occuring in the low-irradiance domain are considered to violate the conditions of a local thermal equilibrium. Furthermore, with reduction of the analyzed volume of material (at spatial resolutions close to diffraction-limited spot sizes) one might be doubtful whether or not there is still enough material and time available to attain a local thermodynamic equilibrium. Matrix effects, the chemical

state of the elements under investigation, and inhomogeneities of energy deposition due to the sample and/or beam geometry may, in addition, limit accuracy.
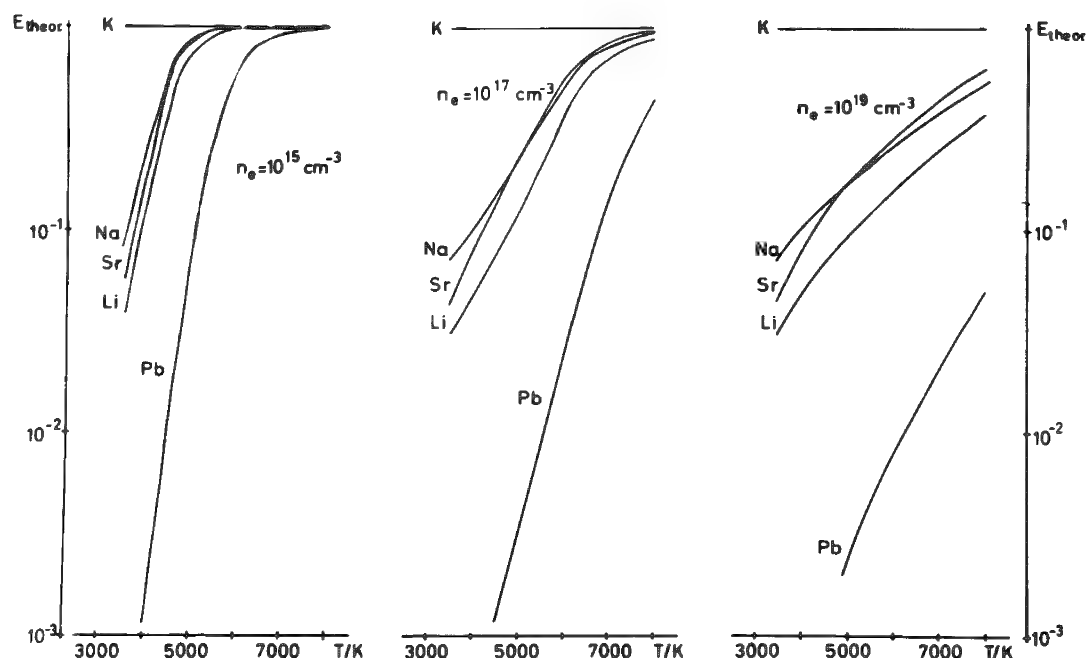
FIG. 6.--Calculated relative sensitivity factors (RSF) for Li, Na, K, Sr, and Pb (normalized to K = 1) as dependent on temperature T and electron density (see Saha-Eggert equation). (After Ref. 1.)
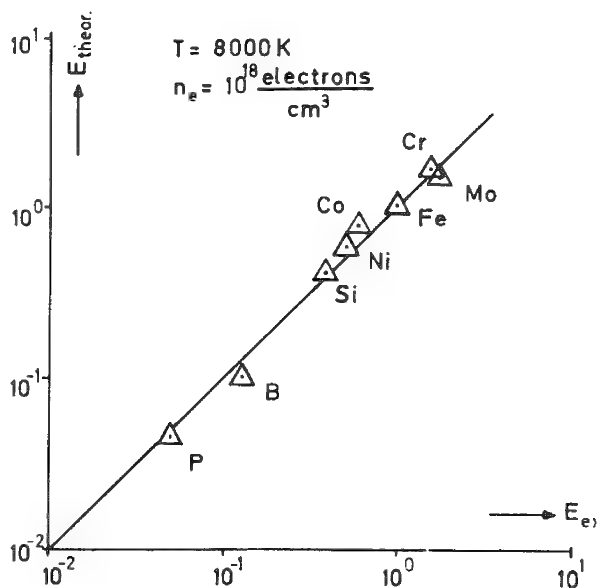
FIG. 7.--RSFs as predicted by LTE model (E_{theor}) vs experimentally determined RSFs in a nickel-iron alloy. (After Ref. 1.)
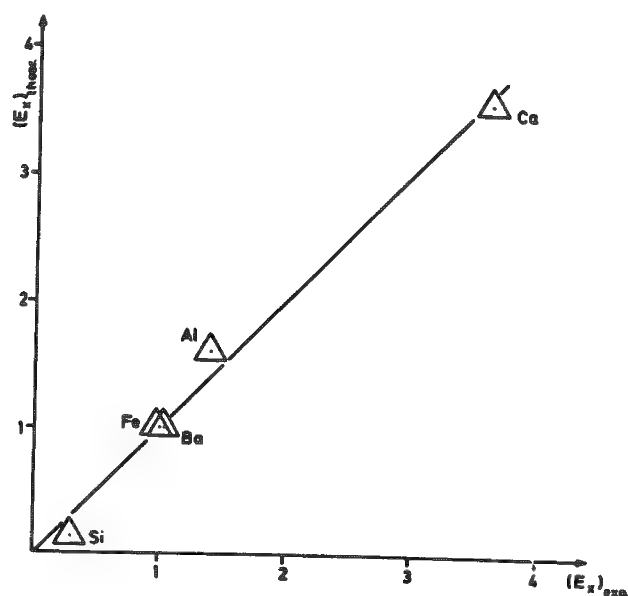
FIG. 8.--RSFs as predicted by LTE model vs RSFs experimentally determined in NBS K 309 standard reference glas assuming T = 8000°K, $n_e = 2 \times 10^{17}$ cm^{-3}, $n_0 = 10^{21}$ cm^{-3}. (After Ref. 1.)

In conclusion, then, quantitation in LAMMA analysis requires careful evaluation of the analytical conditions and, even in the best case, is limited by the "weakness of the methodology" (Surkyn and Adams[14]). Nevertheless, we can say that with further improvements in

the stability of laser emission, precision of focusing, specimen preparation techniques, and signal processing one will end up with a quantitative accuracy comparable to that of the ion microprobe, that is to say 10-20% SD for relative, and 20-50% SD for absolute quantitation.

Specimen Preparation

Unlike in materials sciences where the majority of samples to be microprobed consists of solid-state matter, most biomedical samples are highly hydrated and, with a few exceptions, not directly accessible to any kind of microprobe analysis. (Laser microfluorometry and Raman microprobe are the only techniques principally applicable to living hydrated systems.)

Therefore, specimen preparation for microprobe analysis basically means transforming the specimen into the solid-state phase from which semithin (0.3-1µm) histological sections can be cut.
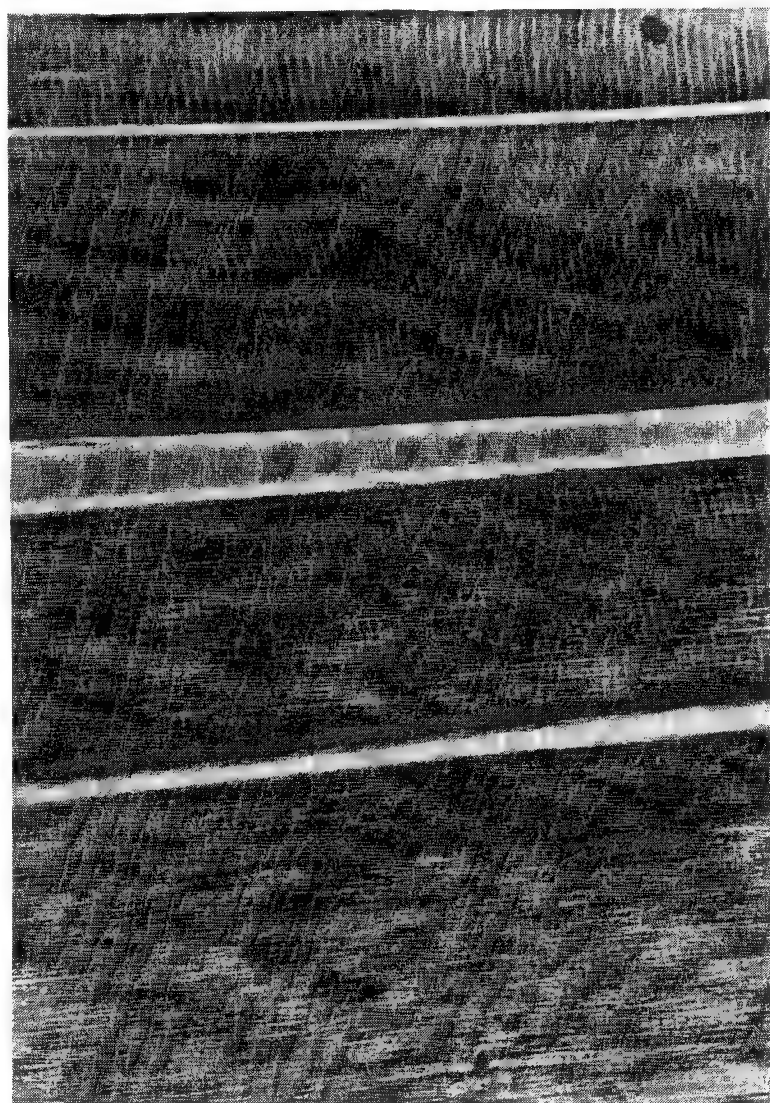
FIG. 9.--0.3µm section of freeze-dried and plastic-embedded muscle specimen (frog's sartorius muscle). Cooling by immersion in super-cooled propane. Surface of specimen is at upper edge of micrograph.

For this purpose conventional fixation and dehydration procedures are not appropriate if one is interested in the analysis of highly diffusible water-soluble compounds such as physiological cations. To prevent intolerable leaching or redistribution of such compounds cryotechniques are most commonly employed. They all start with shock freezing the specimen by either immersion in an appropriate liquid coolant (liquid N_2, freon, propane) or by contact with a polished metal surface cooled down to liquid N_2 or liquid He temperature. This technique gives satisfactory structural preservation over a limited specimen depth where the cooling rate is fast enough to prevent the formation of larger ice crystallites. From the viewpoint of an electron microscopist, a good ultrastructural preservation of shock-frozen specimens is found over a specimen depth of only 10-15 µm, yet the situation is not so restricted for analytical purposes, since ice-crystal damage can be tolerated as long as the extent of damage is below the spatial resolution of the microprobe system. In the case of the LAMMA analysis, 100µm-thick layer of the specimen is acceptable. (Fig. 9).

After shock freezing, the specimen can be further processed in three ways: (1) It can be sectioned in a cryoultramicrotome and the section then analyzed either in the hydrated state (cryostage in the analytical instrument) or after freeze drying at room temperature; (2) the bulk specimen can be freeze-dried in toto in a special freeze-drying device at temperatures below -80°C followed by epoxy-resin embedding under vacuum (Spurr's low-viscosity medium) and cutting dry sections on a conventional ultramicrotome; or (3) instead of freeze drying, freeze substitution by an apolar

medium can be employed before embedding and sectioning. Most of the biological samples used in LAMMA studies were prepared according to the second procedure cited above. In special cases (analysis of Ca) precipitation techniques appear to prevent dislocation of the element to be analyzed even if wet fixation, dehydration, and staining procedures are employed. For a more extensive discussion of preparation techniques for biomedical microprobe analysis the reader is referred to Echlin and Kaufmann.[22]

LAMMA Applications in Biomedical Microprobe Analysis

Since the advent of the LAMMA technique in 1976 many biomedical applications have been performed. They have been related to a rather wide spectrum of scientific problems which are much too broad to be listed in detail (Table 4). Although the following discussion of LAMMA applications attempts to cover the most significant cases where a broader range of interest can be anticipated, the presentation must necessarily be incomplete. A more extensive and complete collection of LAMMA work in general and biomedical applications in particular is contained in the proceedings of the first LAMMA symposium.[23]

TABLE 4.--Biomedical studies performed with the aid of the LAMMA technique.

Electrolytes in tissues
Na, K, Ca, Ba in vertebrate retina[24]
Ca in invertebrate photoreceptor pigments[25]
Na/K ratio in transport-active epithelia of the inner ear[26]
Li, Na, K, Rb, Cs uptake in striated muscle cells[27]
Na/K/Ca ratio in hypoxic mammalian heart[28]
Ca uptake into acini of rat pancreas cells[29]
Na/K ratio in individual mycobacteria[30]

Trace metals in tissues and cells
Fe in glandular cells of a mammalian decidua[31]
Al in skin samples from long-term hemodialysis patients[32]
F in dental materials[33]
Uranium uptake in algae[34]
Pb localization in algae[35]
Cu in heart tissues specimen (Wilson's disease)[36]
Mg/Fe ratios in individual human erythrocytes[37]
Cu distribution in vitreous body around a foreign body[38] (metallic Cu) inclusion
Distribution of inorganic preservatives in wood[39]

Kinetic studies by isotope labelling
Ca^{44} uptake in astacus retina[40]
I^{125} uptake in thyroid gland[37]

Kinetic studies of organics with atomic labels
Intracellular uptake of fluorinated organic compounds in heart muscle cells[31]

Micro(probe) analysis of organic constituents
Detection of phthalates in skin specimen of hemodialized patients[32]
Characterization of organic microcrystals in lichen specimens[41]
Identification of amino citric acid in biological peptides[42]

Material investigations related to biomedicine
Characterization of mineral and asbestos fibers[43]
Chemical histograms of coalmine dust particles[44]
MS characterization of minute purified samples of natural origin[45]
Distribution of cyclic antibiotics in a polymeric matrix

LAMMA Analysis in Particulate Materials

The potential benefits offered by LAMMA in microprobe analysis of particulate materials were recognized soon after the introduction of this technique. A first review on this topic appeared in 1980.[46] A recent survey devoted to this field of application is contained in Ref. 1. Further contributions dealing with specific aspects related to LAMMA analysis of particles or aerosols will be found in Refs. 13, 14, 43, 44.

It appears generally accepted now that the most favorable aspect of LAMMA as applied to chemically nonhomogeneous particulate materials is the speed by which individual particles can be analyzed such that data from a statistically meaningful number of particles can be collected in a reasonable period of time, so that the characterization of mixed particle samples in the form of "chemical histograms" becomes possible for the first time. It is obvious that, for instance, long-distance source tracing of industrial pollutants or the detection of "hot particles" occuring at low abundance is possible only by a technique that allows one to analyze at least several hundred or, preferably, thousands of particles from a mixed sample.

The LAMMA enabled us to study coalmine dust particles that had been characterized for their acute cytotoxicity and chronic histotoxicity by means of classical techniques commonly used for the assessment of lung toxicity of airborne dust samples. The experimental protocol employed is given in Table 5.

TABLE 5.--LAMMA analysis of coalmine dust particles.

QUESTION: Can statistical evaluation of element analysis ("chemical histogram") give firm
indicators of toxicity?

PROTOCOL
Sampling
Number of samples:	11
Collection:	BAT 1 dust sampler
Particle size	1-3 µm

Mineralogical analysis
Determination of the mean content of the following minerals:	Quartz
	Illite
	Kaolinite

LAMMA analysis
Particles analyzed in each sample	500
Evaluation of mass spectra:	Positive ions
	Element abundances
	Correlated abundances (cluster)
	Chemical histogram

Toxicity
Acute cytotoxicity	Inhibition of O_2 consumption in cultures of rabbit lung macrophages (4, 12, and 20 hr after incubation)
Chronic histotoxicity	Fibroblastic area in lymph e-node tissue (QTAPM)

The study, the statistical evaluation of which is still under way, gave a rather clear-cut indication that, by "cluster analysis" of element combinations such as found in the various particle populations by LAMMA, indicators can be deduced which correlate rather strongly with both acute and chronic toxicity (see also Figs. 10 and 11 and Tables 6 and 7). A preliminary report on this study is given in.[44]

Laser Desorption Mass Spectrometry of Organic Compounds

With suitably prepared samples two modes of operation can at least in principle be distinguished. At low laser irradiances ions begin to appear with no visible alteration or damage to the sample. In this mode many successive spectra can be recorded with great reproducibility from the same sample site. These so-called laser desorption (LD) spectra show striking similarities to spectra obtained by field desorption (FD),[47] fission fragment induced desorption (FFID),[48] and, to a lesser extent, secondary ion mass spectrometry (SIMS),[49] the most important other methods that have been successfully applied in the mass spectrometry of nonvolatile, thermally labile bioorganic compounds. The characteristics of these spectra are as follows.

- Substantial yield of parent molecule ions.
- Almost exclusively even-electron ions (no radicals). In the positive spectrum the cationized species $(M + Na)^+$ and $(M + K)^+$ more often than not dominate the protonated $(N + 1)^+$ ones, although no cationized fragment ions have so far been identified. In the spectrum of negative ions the deprotonated $(M - 1)^-$ ion often appears as the base peak. Anionized ions are rare.
- The spectra show specific and reproducible fragmentation patterns that depend on the molecular structure in a complex way that is not yet fully understood. Negative spectra are often simpler; that is, they show fewer lines than the positive ones.
- The more polar the molecules are, the easier it is to obtain desorption spectra.
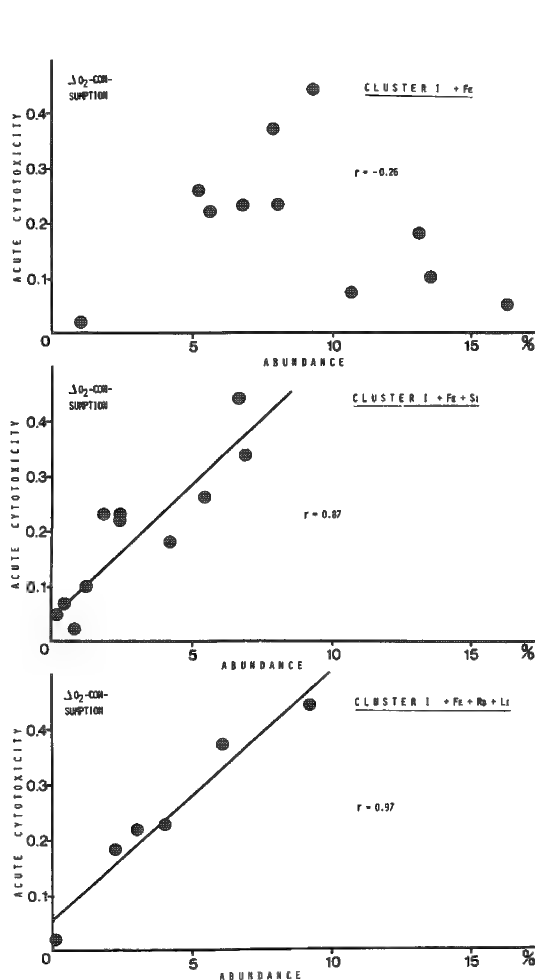
FIG. 10.--Correlation of acute cytotoxicity (Table 5) with abundance of certain element clusters occuring in chemical histogram of 11 samples of coalmine dust particles analyzed by LAMMA according to protocol of Table 5. Although there is no correlation with abundance of cluster I + Fe elements (See Tables 6 and 7 for specification) as shown in upper panel, a fairly good correlation exists when same cluster elements occur in combination with Si (middle panel); and an even better correlation with abundance of element combination consisting of cluster I elements together with Fe, Rb, and Li but with Si absent. (After Ref. 44.)

FIG. 11.--Correlation of chronic histotoxity (see Table 5 for definition of QTAMP) with abundance of certain element clusters occurring in chemical histogram of six samples of coalmine dust particles analyzed by LAMMA according to protocol of Table 5. Combination of cluster I elements with Fe and Si (which is well correlated with acute cytotoxicity as demonstrated by Fig. 10) is only weakly correlated to chronic toxicity (upper panel) but combination of cluster I with Fe, Rb, and Li correlates well with both acute cytotoxicity (Fig. 10) and chronic histotoxicity (lower panel).

Similar spectra have also been obtained by several groups that have used CW and pulsed CO_2-lasers at 10.6 μm wavelength (Posthumus et al.;[50] Kistemaker et al.;[51] Stoll and Röllgen[52]) or free run and Q-switched Nd-lasers at 1.06 μm wavelength (Heresch et al.[53])

TABLE 6.--Example of element cluster analysis in a sample of coalmine dust particles analyzed by LAMMA according to the protocol of Table 5. Highest histo- and cytotoxicity out of 11 samples investigated, despite a rather high incidence of Si-containing element combinations. Note the high abundance of Ca-related clusters. (After Ref. 14.)

Ø 1 - 3 µm N: 500 Code: GR 66		+ Li	+ Si	+ Li + Si	total	Mineral suggested
high abundance element combinations	Al,K	0.2	0.8	–	–	1.0	
	Na,Al,K	–	–	–	–	–	
	Na,Mg,Al,K,Ca (Cluster I)	–	–	–	–	–	
	Cluster I + Fe	1.0	0.8	0.8	2.0	4.6	feldspar
	" + Ti	4.8	–	–	–	4.8	
	" + Ti,Fe	–	1.0	–	1.0	2.0	
	" + Fe,Rb	–	0.2	–	0.2	0.4	
	" + Fe,Rb,Ba	0.4	0.2	0.8	0.6	2.0	
	" + Cu	0.4	–	–	–	0.4	
	Ca (Cluster II)	3.8	–	12.0	–	15.8	
	Cluster II + Mg	4.0	–	–	–	4.0	dolomite
	" + Mg,Fe	0.4	–	–	–	0.4	ankerite
	" + Mg,Al,CaO	48.4	5.4	–	4.8	58.6	
low abundance element combinations	Fe,S	0.8	–	–	–	0.8	pyrite
	Ca,Ti	–	–	–	–	–	
	Be contaminated	–	–	–	–	–	
	Pd contaminated	–	–	–	–	–	
	Zr contaminated	–	–	–	–	–	
	Si (leading element)	–	–	0.6	0.4	1.0	quartz
	others	–	–	–	–	–	
pure organic signals		3.6	0.6	–	–	4.2	
Total		67.8	9.0	14.2	9.0	100%	

TABLE 7.--Example of element cluster analysis in a sample of coalmine dust particles analyzed by LAMMA according to the protocol of Table 5. Highest cyto- and histotoxicity out of 11 camples. Note the high incidence of element clusters containing Si and the absence of Ca-related clusters. (After Ref. 14.)

Ø 1 - 3 µm N: 500 Code: GR 22			+ Li	+ Si	+ Li + Si	total	Mineral suggested
high abundance element combinations	Al, K		0.4	–	–	–	0.4	
	Na, Al, K		2.0	1.2	–	–	3.2	
	Na, Mg, Al, K, Ca (Cluster I)		1.2	0.2	–	0.4	5.4	
	Cluster I	+ Fe	9.2	9.0	6.6	11.0	35.8	feldspar
	"	+ Ti	0.6	0.4	–	–	1.0	
	"	+ Ti, Fe	1.6	2.6	4.8	5.6	14.6	
	"	+ Fe, Rb	0.4	9.2	0.6	3.4	13.6	
	"	+ Fe, Rb, Ba	0.4	8.4	3.2	11.6	23.6	
	"	+ Cu	–	–	–	–	–	
	Ca	(Cluster II)	0.4	–	–	–	0.4	
	Cluster II	+ Mg	–	–	–	–	–	dolomite
	"	+ Mg, Fe	–	–	–	–	–	ankerite
	"	+ Mg, Al, CaO	–	0.6	–	–	0.6	
low abundance element combinations	Fe, S		–	–	–	–	–	pyrite
	Ca, Ti		–	–	–	–	–	
	Be contaminated		–	0.2	–	0.2	0.4	
	Pd contaminated		–	–	–	–	–	
	Zr contaminated		–	–	–	0.2	0.2	
	Si (leading element)		–	–	–	0.2	0.2	quartz
	others							
pure organic signals			0.6	–	–	–	0.6	
Total			16.8	31.8	15.2	36.2	100%	

all with laser-irradiated sample areas 0.1-1 mm in diameter. Apparently all the laser and nonlaser desorption methods induce transition of molecules from the solid state into the gas phase that at least locally have a strong nonequilibrium aspect and thus lead to the formation of large molecules or ions that would not be stable thermally at temperatures at which their vapor pressure is large enough for them to be generated in significant amounts by thermal evaporation in equilibrium. The details of these processes as well as the common and/or different features for the various methods are not yet understood except for FFID (Krueger[54]) and will certainly be subject to intensive investigation in the future.

It is, of course, tempting to think of LAMMA as an "organic microprobe" for relevant organic constituents in complex biomedical samples. Although this ultimate goal appears rather far away with the present state of the art, it may, nevertheless, be considered a realistic possibility at least in special cases (Fig. 12).
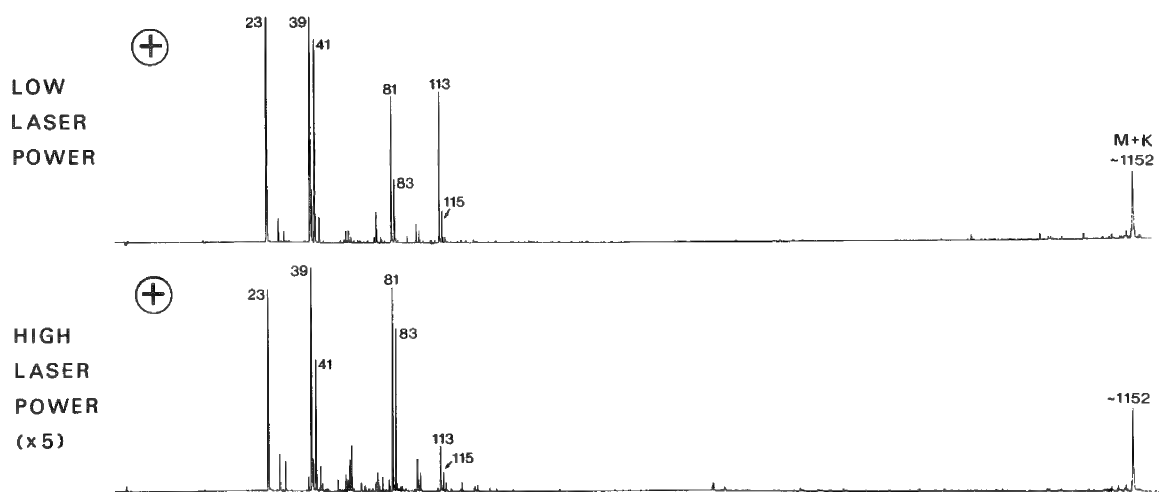

FIG. 12.--LAMMA acting as "organic microprobe." Detection of valinomycin (mol. weight ≃ 1113) dissolved in polymeric resin (PVC-THF matrix). Spectra are remarkably independent of laser power.

Apart from the "futuristic" aspect of an organic microprobe the application of LAMMA in organic mass spectrometry has turned out to be an interesting application field of its own. This is also reflected in some of the other contributions presented at this conference.

The basic problem in the mass spectrometry of all but a few bioorganic molecules is the fact that they are essentially nonvolatile and/or thermally labile, whereas most of the conventional techniques such as electron impact (EI) mass spectrometry require ionization in the gas phase.

The value of several analytical techniques routinely used in biochemistry such as HPLC, HV electrophoresis, etc. could be substantially improved if they could be coupled with a mass spectrometer suited to the analysis small amounts of nonvolatile or thermally labile organic compounds. Though high spatial resolution is not a primary requirement in these applications and may be relaxed to some extent, the extremely small amount of material required for analysis is a distinct advantage that LAMMA can offer for such applications.

The investigation of such important groups of substances as amino acids and small peptides, nucleic acids and their building blocks, glycosides, various hormones and enzymes, and a selection of pharmacological agents have shown that the analytical result depends very strongly on the sample preparation employed. Sample preparation will not only strongly affect the irradiance threshold at which ions begin to appear and the ion yield above threshold, it also has a decisive influence on the fragmentation pattern of the molecular ions. Two techniques have so far proved successful. Both start from highly diluted ($< 10^{-4}$ mol/1^{-1}) solutions of the substances, for example in ethanol or water. Small droplets (< 1 µl) of such solutions, put onto a coated EM grid and transferred into the vacuum chamber for a very fast evaporation of the solvent yield rather homogeneous layers with little or no substructure visible in the microscope. The other, more

substance-consuming method is to use a standard vibrating orifice aerosol generator to form small particles of controllable size in the submicron range and impact them onto a coated EM-grid. For good and reproducible results it seems mandatory to avoid crystal formation of the substances if the crystal size is comparable to or larger than the focal spot of the laser.

Conclusions and Outlook

In the short time since its introduction the technique of laser microprobe mass analysis has acquired the reputation as a serious alternative to other microprobe techniques. In some application areas (particle analysis, organic MS) it has become a uniquely powerful instrument for certain analytical purposes.

Technologically the instrument can certainly still be improved and some of these improvements can be expected in the near future. At the moment, the transient recorder for the fast A/D conversion of the spectra appears to be the most limiting component of the system. An increased time resolution of 5 ns, or possibly 2 or even 1 ns per channel, would not only improve the mass resolution in the range of relative molecular masses above about MU = 200, it should also lead to substantial improvements and simplifications of the ion optics and the mass spectrometer. Even more progress would result from an extension of the dynamic range of the recorder from the present 6 bits to at least 10-bits (1024 points). Many applications that could in principle be performed with LAMMA severely suffer from the rather limited dynamic range available now. There is good reason to believe that the rapid progress in electronic instrumentation during the last decade will continue and eventually provide a recorder better suited for this task. A cryo stage or at least cold stage may be desirable for a number of applications in biomedicine. First steps towards its realization have already been taken.

The number and variety of applications that have already been attempted with the LAMMA technique is surprising considering the short time since realization and availability of the instrument. It can be expected that, with information on the performance of the method becoming more widespread and with more instruments being used by more groups with different backgrounds and interests, many anticipated and unexpected applications will be reported in the years to come. For the developers of a new technique it is one of the most exciting and rewarding experiences to see how the field of application widens, both quantitatively and qualitatively. Rather than speculating about such major lines of future applications they leave it up to the needs and ingenuity of potential applicants to provide new surprises.

References

1. R. Kaufmann and P. Wieser, "Laser microprobe mass analysis in particle analysis," in I. Beddow and A. Vetter, Eds., *Modern Methods of Fine Particle Characterization*, Boca Raton, Fla.: CRC Press, 1982, vol. 3.
2. F. Hillenkamp and R. Kaufmann, "Laser microprobe mass analysis (LAMMA): A new approach in biomedical microanalysis and analytical mass spectrometry," in M. L. Wolbarsht, Ed., *Laser Applications in Medicine and Biology*, New York: Plenum Press, 1982.
3. LAMMA Symposium, Düsseldorf, 8-10 October 1980, *Fresenius Z. anal. Chem.* 308: 3, 1981.
4. J. A. Gardella et al., "Mass spectrometry of molecular solids: Laser microprobe mass analysis (LAMMA) of selected polymers," *Spectroscopy Letters* 13(6): 347-360, 1980.
5. W. H. Schroeder, "Recent progress in LAMMA analysis of biological specimens," *SEM-1982*, in press.
6. R. Hillenkamp et al., "A high sensitivity laser microprobe mass analyzer," *Appl. Phys.* 8: 341-348, 1975.
7. R. Kaufmann et al., "The laser microprobe mass analyzer (LAMMA), a new instrument for biomedical microprobe analysis," *Med. Progr. Technol.* 6: 109-121, 1979.
8. E. Denoyer et al., "Laser microprobe mass spectrometry: 1. Basic principles and performance characteristics," *Anal. Chem.* 54: 26A-41A, 1982.
9. H. Vogt et al., "LAMMA 500 principle and technical description of the instrument," *Fresenius Z. anal. Chem.* 308: 195-200, 1981.
10. W. H. Schroeder et al., "Measuring Ca uptake and release of avertebrate photoreceptor cells by laser microprobe mass spectroscopy," *SEM/1980* II, 647-654.

11. R. Kaufmann, "Laser microprobe mass analysis, achievements and aspects," *SEM/1979 II*, 279-290.

12. R. Kaufmann, "Recent LAMMA studies of physiological cation distributions in retina tissues," *SEM/1980* II, 641-646.

13. R. Kaufmann et al., "Application of the laser microprobe mass analyzer LAMMA in aerosol research," *SEM/1980* II, 607-622.

14. P. Surkyn and F. Adams, "Laser microprobe mass analysis of glass microparticles," *J. Trace and Microprobe Techniques* 1: 1982 (in press).

15. U. Haas et al., "A quantitative interpretation of LAMMA spectra based on a local thermodynamic equilibrium (LTE) model," *Fresenius Z. anal. Chem.* 308: 270-273, 1981.

16. C. A. Andersen and J. R. Hinthorne, "Thermodynamic approach to the quantitative interpretation of sputtered ion mass spectra," *Anal. Chem.* 45: 1421, 1973.

17. L. DeGalan et al., "Electronic partition functions of atoms and ions between 1500K and 7000K," *Spectrochimica acta* 23B: 521, 1968.

18. H. W. Drawin and P. Felenbok, *Data for Plasmas in Local Thermodynamic Equilibrium*, Paris: Gauthier-Villars, 1965.

19. R. Herzberg, *Molecular Spectra and Molecular Structure*, Princeton, N.J.: Van Nostrand, 1966, vols. 1-3.

20. E. A. Moelwyn-Hughes, *Physikalische Chemie*, Stuttgart: Thieme, 1970.

21. A. P. Thorne, *Spectrophysics*, London: Chapmann and Hall, 1974.

22. P. Echlin and R. Kaufmann, Eds., *Microscopica acta* (Suppl. 2), Stuttgart: Hirzel-Verlag, 1978.

23. Ref. 3.

24. R. Kaufmann, "Recent LAMMA studies of physiological cation distributions in retina tissues," *SEM/1980* II, 641-646.

25. W. H. Schroeder, "Quantitative LAMMA analysis of biological specimens: I. Standards, II. Isotope labeling," *Fresenius Z. anal. Chem.* 308: 212-217, 1981.

26. A. Orsulakova et al., "Cation distribution of the cochlea wall (stria vascularis)," *ibid.*, pp. 221-223.

27. L. Edelmann, "Selective accumulation of Li^+, Na^+, K^+, Rb^+, and Cs^+ at protein sites of freeze-dried embedded muscle detected by LAMMA," *ibid.*, pp. 218-220.

28. Hj. Hirche et al., "Preparation and analysis of heart and skeletal muscle specimens with LAMMA," *ibid.*, pp. 224-228.

29. W. Wakasugi et al., "Calcium uptake into acini from rat pancreas: Evidence for intracellular ATP-dependent calcium sequestration," *J. Membrane Biol.* 65: 205-220, 1982.

30. U. Seydel and B. Lindner, "Qualitative and quantitative investigations on mycobacteria with LAMMA," *Fresenius Z. anal. Chem.* 308: 253-257, 1981.

31. R. Kaufmann et al., "Recent advances of laser microprobe mass analysis (LAMMA) as applied to biological and engineering specimens," *Microbeam Analysis--1979*, 63-72.

32. K. D. Kupka et al., "Identification of atoms and molecules in human skin after long-term medical treatment," *Fresenius Z. anal. Chem.* 308: 229-233, 1981.

33. E. Gabriel et al., Preparation methods and LAMMA analysis of dental hard tissue with special respect to fluorine," *Fresenius Z. anal. Chem.* 308: 234-238, 1981.

34. B. Sprey and H. P. Bochem, "Uptake of uranium into the alga dunalielle detected by EDAX and LAMMA," *ibid.*, pp. 239-245.

35. D. W. Lorch and H. Schäfer, "Localization of lead in cells of phymatodocis nordstedtiana (Chlorophyta) with the laser microprobe analyzer (LAMMA 500)," *ibid.*, pp. 246-248.

36. B. Kaduk et al., "Secondary athrocytotic cardiomyopathy: Heart damage due to Wilsons's disease," *Virchows Archiv A. Path. Anat. and Histol.* 387: 67-80, 1980.

37. P. F. Schmidt et al., "LAMMA-investigations of biological and medical specimens," *SEM/1980 II*, 623-634.

38. Paulmann and Kaufmann, personal communication.

39. P. Klein and J. Bauch, "Studies concerning the distribution of inorganic wood preservatives in cell wall layers based on LAMMA," *Fresenius Z. anal. Chem.* 308: 283-286, 1981.

40. Ref. 10.

41. A. Mathey, "LAMMA: New perspectives for lichenology?" *Fresenius Z. anal. Chem.* 308: 249-252, 1981.

42. G. Wilhelm and K.-G. Kupka, "Identification of amino citric acid in biological peptides," Amsterdam: Elsevier/North-Holland, *Biomedical Press*, 123(No. 1): 141-144, 1981.

43. K. R. Spurny and J. Schörmann, "Identification and microanalysis of mineral fibers by LAMMA," *Fresenius Z. anal. Chem.* 308: 274-279, 1981.

44. R. Kaufmann et al., "LAMMA-studies in mineral fibres and coal mine dust particles, *Proc. 12th Ann. Symp. Anal. Chem. of Pollutants*, Amsterdam, 1982.

45. D. M. Hercules et al., "Laser microprobe mass spectrometry: 2. Applications to structural analysis," *Anal. Chemistry* 54: 280A, 1982.

46.   R. Kaufmann and P. Wieser, "Laser microprobe mass analysis (LAMMA) in particle analysis," in K. F. J. Heinrich, Ed., *Characterization of Particles*, NBS Special Publication 533, Washington, D.C., 1980.

47. H. R. Schulten, in D. Glick, Ed., *Methods of Biochemical Analysis*, New York: Wiley, 1980, vol. 24, p. 29.

48. F. R. Krueger and B. Schueler, "Organic mass spectra obtained by fission-frequent and pulsed laser-induced desorption," *Advances in Mass Spectrometry* 8: 918, 1980.

49. A. Eicke et al., "Secondary ion mass spectrometry of nuclic acid components: Tryimidines, purines, nucleosides and nucleotides," *Org. Mass Spectrometry* 15: 289, 1980.

50. M. A. Posthumus et al., "Laser desorption mass spectrometry of polar non-volatile bio-organic molecules," *Anal. Chemistry* 50: 985, 1978.

51. P. G. Kistemaker et al., "Laser-induced desorption mass spectrometry," *Adv. Mass Spectrom.*, London: Institute of Petroleum, 1980, 928.

52. R. Stoll and F. W. Röllgen, "Laser desorption mass spectrometry of thermally labile compounds using a continuous wave CO_2 laser," *Organic Mass Spectrometry* 14: 642, 1979.

53. F. Heresch et al., "Repetitive laser desorption mass spectrometry for nonvolatile organic compounds," *Anal. Chem.* 52: 1803, 1980.

54. F. R. Krueger, "Fast ion induced and collective electronic perturbation at the surface," *Surf. Science* 86: 246, 1981.

55. R. Wurster et al., "Electron microscopical investigations of laser irradiated foils and particles," *Fresenius Z. anal. Chem.* 308: 206, 1981.

LASER MICRO MASS ANALYSIS OF BULK SURFACES

Franz Hillenkamp, Peter Feigl, and Bruno Schueler

Applications of the laser micro mass analyzer in the version that has been commercially available as the LAMMA 500® instrument for some time and that has been used by a number of groups for a variety of different analytical tasks are essentially limited to thin specimens of less than a few micrometers in thickness. The main attractive features of this instrument (spatial resolution below 1 μm, detection sensitivity down to the sub-ppm range, detection of ions of both polarities of molecular as well as atomic constituents, isotope discrimination, and the recording of complete mass spectra for each single analysis) have generated strong interest in the extension of the method to the analysis of bulk specimens and of conductive (particularly metallic) samples. The adaptation of the instrument introduces several new basic aspects of the radiation-specimen interaction and requires major changes in the instrumental approach, because sample observation, laser irradiation, and ion extraction all take place from the same side of the specimen.

It had been demonstrated in a feasibility study[1] that such analyses are in principle possible with only slightly lower performance data as compared to the analysis of thin specimens. In addition, the study revealed that sample observation and proper focusing of the laser beam onto the sample surface as well as the geometry of the ion extraction lens, are very critical. A completely new sample chamber and ion source therefore had to be designed and built. In this paper we describe the concept and performance of the new arrangement and present a few first analytical results.

Principles of Laser-induced Mass Spectrometry

Common to all techniques of laser mass spectrometry is the generation of ions of atomic or molecular constituents of the sample directly out of the solid phase. In general this process requires the transfer of a sizable amount of energy per unit volume of analyzed material from the laser beam to the solid specimen. The absorbed energy may result in a strong perturbation of the solid structure and possibly transition to a liquid or semiliquid phase, leading to the desorption of surface adsorbents or even selective evaporation of more volatile components (desorption mode). In the more common mode of operation, particularly for microprobe analysis, a limited volume in at least the center of the irradiated spot is evaporated and leaves an at least microscopically damaged specimen surface.

Energy transfer to metallic specimens takes place via intraband transitions of the conduction electrons. Absorption is very high, particularly for wavelengths in the UV. The same process is most probably responsible for the major fraction of the transferred energy even in nonabsorbing dielectrics. Population of the conduction band sufficient to initiate this process is believed to occur during the first part of the irradiation pulse, most probably through multiphoton processes.[2] Consequently metals show a rather low (10^6-10^7 W·cm^{-2}) and wavelength-independent damage and ion-generation threshold, whereas dielectrics exhibit much higher thresholds, rising from about 10^8 W·cm^{-2} at 265 nm to about 10^{10} W·cm^{-2} at 532 nm in incident, reflection-corrected irradiance. The role of natural absorption at the wavelength of the laser radiation, originating either from electronic excitation (e.g., of molecular constituents or of shallow electron traps in organic polymers) is still rather unclear. Though threshold irradiances for visible damage or ion generation do not show a systematic relationship to the wavelength-dependent absorption coefficient, such absorption may well help during the initial phase of the conduction band population. Recent experi-

ments[3,4] seem to indicate that desorption of molecules is facilitated for molecules of a given species in the excited state.

Another, still open question is that of the ionization process. For molecular ions ionization most probably takes place in the solid phase during its decomposition and transition into the gas phase, rather than through gas phase reactions. However, one cannot exclude the possibility that in certain cases (depending on the material, laser irradiance, and irradiation geometry) an LTE plasma is formed whose properties would then govern the distribution of observed ions. In that case substantial additional energy could be transferred from the laser beam to this plasma. For the microanalysis of thin specimens with the LAMMA 500® instrument at least, the types and intensity distributions of observed ions do not indicate a strong influence of gas phase or plasma reactions.

In view of these general considerations of laser-induced ion formation, the transition from the analysis of thin specimens in the transmission mode with focusing objective and ion lens on opposite sides of the specimen to the investigation of bulk surfaces with both optics on the same side of the sample introduces several new aspects.

For thin specimen the beam-solid interaction in the evaporation mode is limited by the amount of material in the total volume and may end some time before the end of the laser pulse, followed by a very rapid expansion of the evaporated material. For bulk specimens, interaction is governed instead by the total energy available and transferred to the sample. Geometrical limitations in the possible arrangements of the optics moreover increase the minimum spot size and so increase the total amount of evaporated material by at least a factor of ten under otherwise comparable conditions. All this material furthermore expands toward the incoming laser beam. Higher densities of charged particles must therefore be expected to exist for longer times, which thus increases the likelihood of laser plasma heating of the evaporated material and therefore an undesirably high ion initial energy spread, the chance for unwanted, multiply charged ions, and possibly high degree of fragmentation of molecular ions. It has been demonstrated by Devyatykh et al.[5] That the absorption of laser radiation by the expanding plasma depends not only on material and laser irradiance on the target, but also strongly on the size of the irradiated spot. This effect also shields the sample surface from later parts of the laser pulse, thereby influencing the amount of sampled material. Space- charge effects may in addition cause difficulties for the extraction of ions and their acceleration to a common high energy into the time of flight mass spectrometer. Because of the expected higher ion yield, all these problems should be more severe for metallic samples, which are of considerable interest for bulk analysis--in contrast to thin specimens, which are almost exclusively dielectrics.

Instrument Design

The intended use of the instrument for microprobe analysis requires both a high spatial resolution for specimen sampling and high detection efficiency for a large variety of atomic and if possible also molecular sample constituents. Spatial resolution for sampling is a function of the numerical aperture of the focusing objective; i.e., maximum resolution requires a large cone angle θ of the focused laser beam (Fig. 1). Though such focusing could in principle be achieved with large-diameter optics at con-

FIG. 1.--Schematic arrangement of laser focusing objective and ion lens.

siderable distances from the target surface, optics designed and corrected for near diffraction limited spots usually have short focal lengths and free working distances between front face and specimen surface of the order of a few millimeters at the most. Similar considerations hold for ion optics of high collection efficiency, i.e., acceptance angle. In addition, the distance over which ions are accelerated into the ion lens should be also
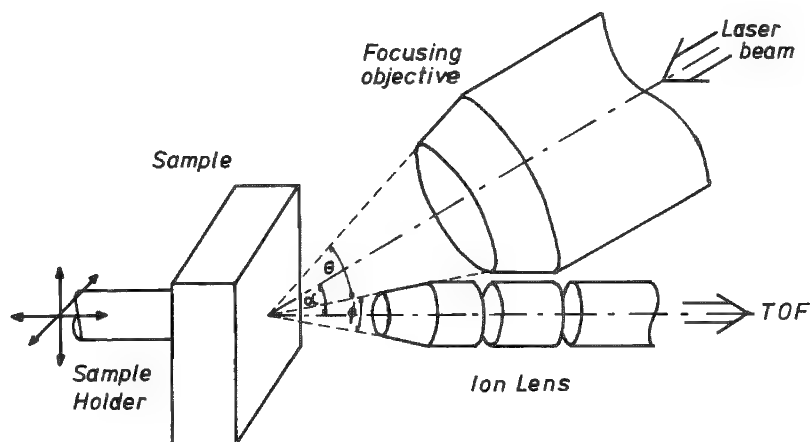
kept to a maximum of only a few millimeters in order to limit the transit-time spread for ions of different initial energy--the limiting factor for mass resolution of the spectrometer. These two requirement impose rather severe geometrical restrictions on the design of the ion source.

At least at irradiances below 10^{10} W·cm^{-2}, and as long a laser-plasma interaction (and therefore selective optical shielding of the target surface) remains limited, the angular emission characteristics are determined by the surface structure and orientation, rather than the direction of incidence of the laser beam. Measurements of the angular distribution have been published for a variety of experimental conditions. It can be deduced from these results that within the range of parameters applicable to microanalysis, the distribution is symmetrical about the surface normal, somewhat peaked in the forward direction, or even close to isotropic. Alignment of the spectrometer axis normal to the target surface was therefore chosen for maximum ion collection efficiency and minimum transit-time spread. The entrance aperture of the ion lens has a diameter of 4.5 mm at a distance of 9 mm from the target surface.

The focusing objective for the laser beam is mounted in a vertical plane above the ion lens with its axis at an angle α to the surface normal (Fig. 1). Two alternatives have been tried with comparable results. A specially designed, slender objective of 13× magnification and numerical aperture of 0.2, corrected for a wavelength of 265 nm, can be mounted at an angle of α = 30°. A commercially available Ultrafluar objective of magnification 10 and numerical aperture 0.2 must be mounted at an angle α = 45° because of its more bulky construction. This objective is corrected throughout the full wavelength range from 220 to 700 nm. The distances between the front surfaces of the two objectives and the focus on the target surface are 15 and 7.4 mm, respectively.

In the course of the preliminary experiments it had turned out that focusing of the laser beam exactly onto the target surface is very critical with respect to reproducibility of the recorded spectra. This effect is thought to be mainly caused by lateral shifts of the focus on the target relative to the spectrometer axis as a result of improper focusing. Observation of the specimen under an angle of 30° or 45° to the surface normal, with the result of only a small stripe of the field of view in focus and with the limited resolution of the focusing objective, turned out to be inadequate for the required focusing accuracy. An additional observation objective of magnification 50 and 0.6 numerical aperture, oriented with its axis normal to the target surface, has therefore been added. It is located sideways of the ion lens-laser objective unit. All these components are mounted on a stage that can be shifted pneumatically such that in one of the two end positions a given location on the target surface is centered in the field of view of the observation objective and centered on the spectrometer axis in the other. The positioning accuracy in the two end positions is better than 3 μm laterally, the spatial resolution of the analysis, and better than 0.5 μm in the depth of the field.

For an actual analysis the observation objective is first shifted into place. The sample surface is properly focused with the aid of the xyz-movable specimen holder and an analytical site of interest is chosen and centered with respect to the eye piece crosshair. Overall magnification of 500 and corresponding resolution, together with the choice of incident dark or light field illumination, greatly facilitate proper location of the specimen. The translation stage is then shifted for analysis. With the help of suitable beam splitters and intermediate microscope optics, the optical paths of the observation and focusing objectives are both fed into a common binocular eye piece. This way the sample can be observed with limited resolution during the analysis as well and emission or fluorescent light be picked up as further analytical information. A dichromatic beam-splitting mirror is used to feed the laser beam colinearly into the optical path of the focusing objective. Intermediate laser focusing optics, field-stop, and a set of attenuating filters in the laser beam path are similar to those of the LAMMA 500® instrument.[6] Specimens several centimeters in extent in all three dimensions can be accommodated.

Also as in the LAMMA 500® instrument, ions of both polarities can be detected. Acceleration potential at the first element of the ion lens is typically ± 3 kV. Flight-time dispersion due to initial energy spread in the field-free drift region of the time-of-flight mass spectrometer (TOF) can be compensated for by an ion reflector at suitable potential. Ion detection by a 17-stage SEV and signal storage and processing is standard, as described for example by Vogt et al.[6]
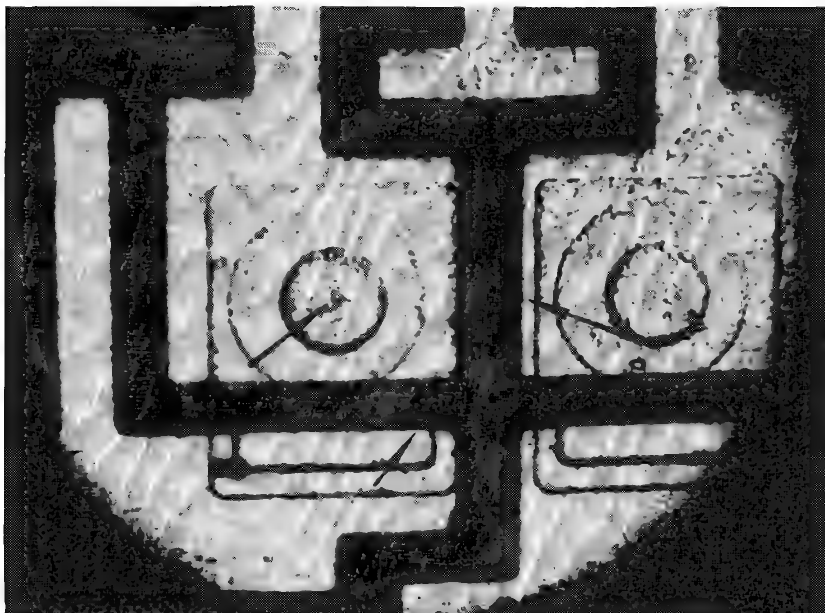
FIG. 2.--Integrated circuit photo-
graphed through observation obser-
vation objective. Spots in center
of left circular structure and on
vertical and horizontal bars are
laser impacts (arrows). Width of
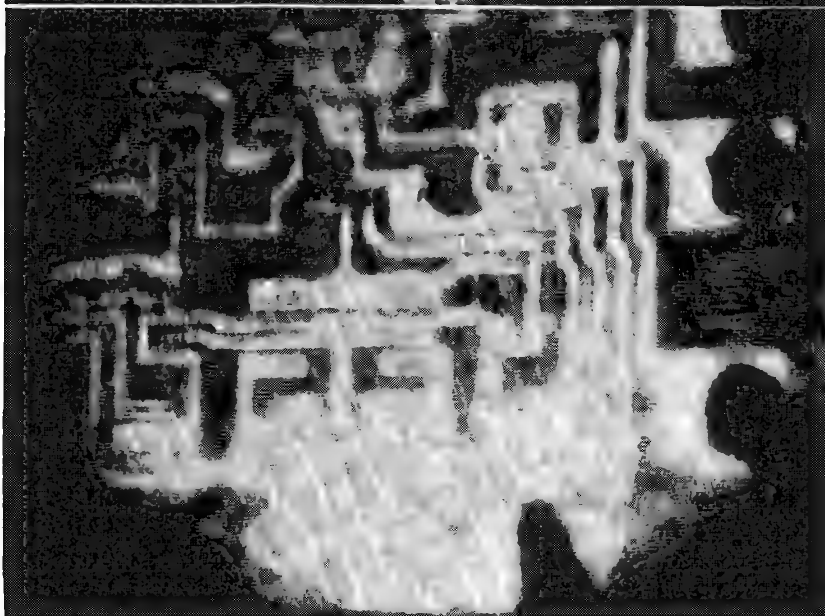bars approximately 15 μm.

FIG. 3.--Integrated circuit photo-
graphed through laser focusing ob-
jective.

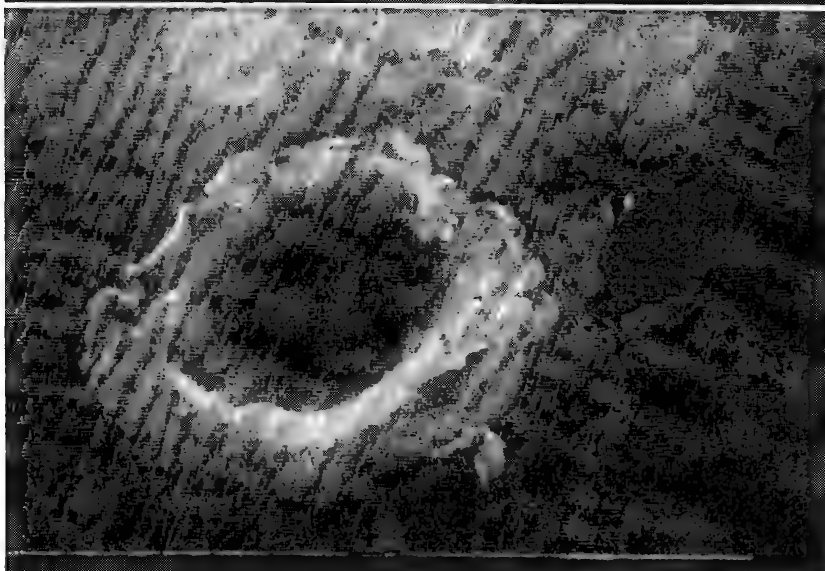FIG. 4.--Scanning electron micro-
graph of laser impact on metal
(brass) surface. Crater diameter
about 4 μm. (Scale at bottom, 0.5
μm.)

Figure 2 shows a photograph of a semiconductor wafer taken through the high-resolution observation objective. Small structural details are clearly visible. A site of analysis can be seen in the center of the left round structure. It was taken at an irradiance of about twice the ion detection threshold and has a diameter of 2 μm, somewhat below the theoretical resolution limit of 3 μm. Two sites on the dark bar structures, taken somewhat above threshold, are 8 and 12 μm in diameter. Figure 3 shows the same wafer, photographed through the laser focusing objective. The loss in resolution and focused field of view is obvious. A spatial resolution of 3 μm is routinely achieved without special precautions. In favorable cases and with careful adjustment of the incident energy, spectra can be recorded from craters as small as 1 μm. Generally high resolution is obtained more easily with dielectric samples as compared to metals, for which crater size increases more rapidly with increasing incident laser energy. Also, elevated crater rims of displaced or splashed, resolidified molten material are more evident for metals, as documented in Fig. 4. Crater depths also depend on the material sampled and on the laser irradiance in the focus. Metals show deeper craters than dielectrics, but further systematic investigations are necessary before general figures can be given.
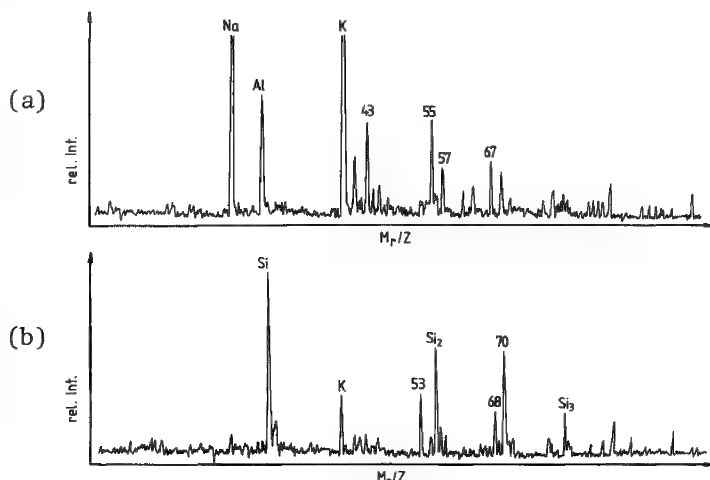

FIG. 5.--Positive ion spectra of two sites of integrated circuit. Top spectrum corresponds to impact in center of left round structure of Fig. 2. Bottom spectrum was recorded from bar structure.
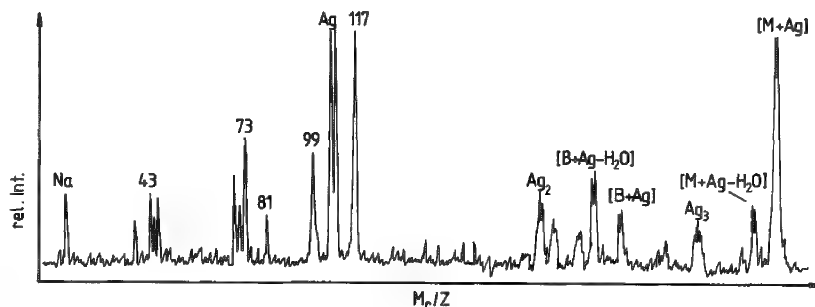

FIG. 6.--Positive ion spectrum of thymidinedihydrate (M, parent molecule; B, nucleobase).

Figure 5 shows two spectra of positive ions recorded from the integrated circuit of Fig. 2. Spectrum 5(a) corresponds to the analysis site in the center of the round, light-appearing structure; 5(b) was taken from the dark-appearing bar. Signals of aluminum, silicon cluster ions, and Na and K, most probably contaminates, are easily identified. No attempt was made in this preliminary test to assign the other signals in the spectra. No ion reflector was used in all the test shots reported here. The peak widths are therefore a direct indication of the surprisingly small initial energy spread of less than 100 eV of the generated ions. For routine analysis, mass resolution can still be improved considerably through the addition of an ion reflector. The same holds for the somewhat poor signal-to-noise ratio.

As an application of the instrument to the mass spectrometry of bioorganic compounds, Fig. 6 shows a positive ion-spectrum of the nucleoside thymidindihydrate. These types of application are very promising, because very homogeneous samples can be prepared by electrospraying a dilute solution of the substance onto a metal substrate. Reproducibility of spectra appears to be much better than with other preparations so far tried with the LAMMA 500® instrument. Very interesting is the high ion yield of the parent molecule and of typical H_2O^--elimination and fragment molecules (base), all cathionized by substrate metal atoms. Such spectra, which show similarities to spectra obtained by secondary ion mass spectrometry, have been obtained for a variety of different molecules.[7]

Within the very limited experience so far gained with the new instrument, a few general trends can be pointed out. For dielectric specimen detection, sensitivity looks very prom-

ising; values down to the ppm range of concentration for sampled areas of 1-3 μm in diameter seem feasible. Reproducibility of spectra is very good, generally better than that obtainable for the analysis of thin specimens. For bulk dielectrics, charging of the sample after a number of successive shots may cause some problems. They can be eliminated for example by a wire mesh placed onto the specimen surface or by a thin coating. Spectra of metallic samples obtained with a preliminary set up have been published previously.[1] With the new instrument, control of the laser irradiance is somewhat less critical because of better focusing, but a strong dependence of the spectra on the incident energy remains. Irradiance on the surface must be kept within about a factor of 2 of the threshold irradiance for ion detection. Beyond this limit mass peaks increase in width and show a complex structure, with a corresponding loss in mass resolution, most probably because of the more pronounced increase of evaporated sample volume with increasing pulse energy and the higher charge density in the cloud, possibly combined with an increasingly strong laser-plasma interaction. Because of this behavior, detection sensitivity for trace-metal constituents in a metal matrix (e.g., for components of alloys) has so far been limited to about 0.1%. The observed phenomena need further investigation, which might also give hints for an optimization of the parameters for metal analysis.

Conclusion

It has been demonstrated that laser micro mass analysis of bulk surfaces is feasible with a spatial resolution of 3 μm or better and a sensitivity in the ppm range at least for dielectric specimens. Further investigations are necessary to assess the detection limit for metallic samples. Some additional instrumental improvements are also desirable. In general, the method promises to become a very valuable tool in various fields of material and microanalysis.

References

1. B. Schueler, R. Nitsche, and F. Hillenkamp, "Possibilities for a laser-induced micro-mass analysis of bulk surfaces," *SEM/1980* II, 597-605.
2. N. Fuerstenau, "Investigation of laser induced damage, evaporation and ionization with homogeneous target foils," *Fresenius Z. anal. Chem.* 308: 201-205, 1981.
3. V. S. Antonov, V. S. Letokhov, and A. N. Shibanov, "Nonthermal desorption of molecular ions of polyatomic molecules induced by UV laser radiation," *Appl. Phys.* 25: 71-76, 1981.
4. V. S. Letokhov, V. G. Movshev, and S. V. Chekalin, *Zh. Eksp. Teor. Fiz.* 28: 480, 1981 (in Russian).
5. G. G. Devyatykh, S. V. Gaponov, I. D. Kovalev, N. V. Larin, V. I. Ludin, G. A. Maksimov, L. I. Pontus, and A. I. Suchkov, "Possible chemical analysis of microscopic regions with a laser mass spectrometer," *Sov. Techn. Phys. Lett.* 2: 356, 1976 (transl. from *Pis'ma Zh. Tekh. Fiz.* 2: 906, 1976).
6. H. Vogt, H. J. Heinen, S. Meier, and R. Wechsung, "LAMMA 500: Principle and technical description of the instrument," *Fresenius Z. anal. Chem.* 308: 195-200, 1981.
7. B. Schueler, P. Feigl, F. R. Krueger, and F. Hillenkamp, "Cationization of organic molecules under pulsed laser induced ion generation," *Org. Mass Spectrom.* 16: 502-506, 1981.

THE PERFORMANCE OF A LASER-INDUCED ION MASS ANALYZER SYSTEM FOR BULK SAMPLES

Trevor Dingle, Barrie W. Griffiths, J. Chris Ruckman, and Charles A. Evans Jr.

A Laser-Induced Ionization Mass Analyzer (LIMA) has been developed that employs a ND-YAG laser and a second-order energy focusing time-of-flight mass spectrometer. The unique features of this instrument are the use of ultra-high vacuum in the sample chamber and the capability to perform analyses in either transmission or reflection. The ability to produce ions from the surfaces of bulk materials allows the analysis of materials previously inaccessible to laser microprobe analysis. These include inclusions in metals, surface particulates, and surface organic contaminants. This paper will describe this instrumentation and some applications unique to the reflection mode of analysis.

Technique

The basic technique used in LIMA is that a short pulse (10ns) of laser radiation (0.53 µm) is focused to a micron-sized spot on the sample. This spot evaporated and ionizes a small volume of the sample. Thus a cloud of ions representative of the sample irradiated is produced at a single instant in time. These ions are mass analyzed by a "time-of-flight" technique, so that a complete mass spectrum is produced from a single laser pulse. By the system we have developed, heavy ions such as lead are detected roughly 80 µs after the laser pulse. Hence LIMA produces analytical data fast; a typical complete mass spectrum can be obtained within 100 µs.

The interaction of pulsed laser energy with a solid target and the subsequent evaporation and ionization of the sampled target volume is complex and no complete theory exists to date. The laser power density, wavelength, and pulse duration all influence the efficiency of ion production, as well as other factors, such as the electrical and structural properties of the sample and its geometry. However, we have observed several interesting effects.

For example, it is apparent from the observation of mass spectra that, as higher power densities are used, thresholds for the ionization of different materials appear to be crossed. At powers sufficient to produce reliable spectra of most of the metallic constituents of stainless steel, we do not observe elements such as carbon, oxygen, or nitrogen with higher ionization potentials. As the power level is increased, we start to observe these trace constituents, but with variable apparent sensitivity. If the power is increased further, these elements begin to appear reliably and reproducibly. However, as the power density is increased toward 10^{10} and 10^{11} W/cm^2, the proportion of multiply charged ions increases, and the initial average energy of ions produced, which can vary from 100 eV to several keV, tends to increase. Another interesting effect we have noticed as the power density is increased is that in some materials (notably pure silicon) long chain molecules from Si$^+$ up to Si$_6^+$ appear. A final surprising observation is that linear organic molecules of high mass number are not disintegrated by the laser beam and, providing the power density is optimized, it is possible to produce spectra from organic molecules with negligible numbers of doubly charged molecule ions and fragments of molecules.

Instrumental

Figure 1 shows an outline drawing of the instrument. The vacuum system is of conventional UHV construction; however, bakeout is limited to 150°C because of Viton sealed optical windows and loading hatch. Pumping is by turbomolecular and ion pumps. A base

---

Authors Dingle and Griffiths are at Cambridge Mass Spectrometry Ltd., Cambridge, England; author Ruckman is at the Atomic Weapons Research Establishment, Aldermaston, England; author Charles A. Evans is at Charles Evans & Associates, San Mateo, CA 94402.

pressure in the region of 5×10^{-10} Torr is readily achieved. The main chamber and the loading chamber are linked by a gate valve and have independent pumping systems. The chamber has been designed so that other analytical techniques complementary to laser induced ion mass analysis can be easily added. Thus, for example, an Auger analyzer and electron gun could be mounted on the system.
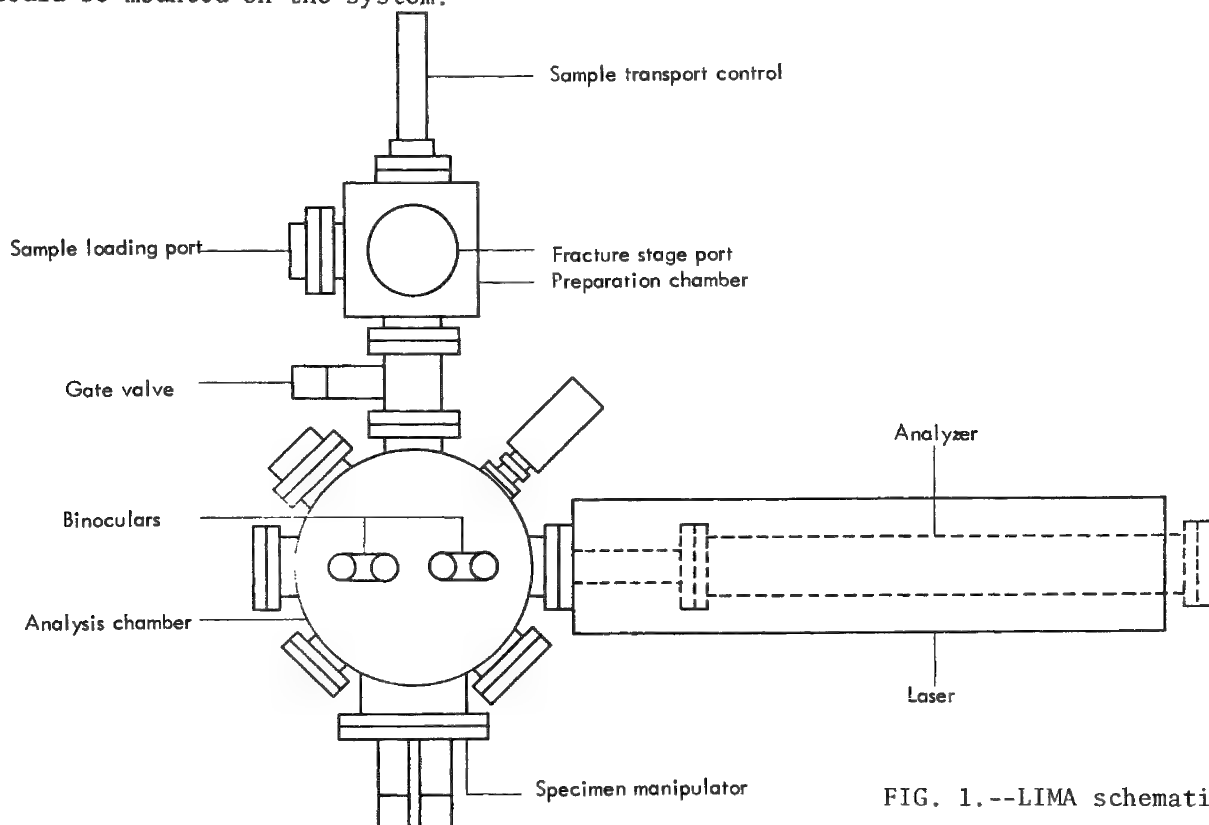

FIG. 1.--LIMA schematic.

A carousel sample carrier for bulk samples or a transmission specimen holder are carried on a precision high-stability UHV manipulator that provides x, y, z motion and rotation. Transfer of samples between the loading chamber and the manipulator is effected by means of a standard magnetically driven UHV transfer mechanism. A sample can be loaded from atmosphere and brought to the analysis position in 5 min.

The ion extraction optics and the objective lens of the laser assembly for the bulk-analysis mode are of a novel design (patent pending) that provides for the laser focusing (and sample viewing) and ion collection to be both normal to the sample surface. This approach insures maximum ion collection efficiency and optimum laser spatial focusing. The laser used (a Nd-YAG) provides 80 mJ of energy at 0.53 μm in a pulse of approximately 10 ns duration in the frequency-doubled mode. The mass analyzer is a "folded-time-of-flight" analyzer. As mentioned before, the energy spread of ions produced from bulk samples is appreciable. Thus it was necessary to provide energy filtering or focusing in a time-of-flight analysis to yield a useful mass resolution. The flight time for the different regions of this spectrometer can be expanded as a Taylor series in terms of the primary energy V_0 and the energy uncertainty ΔV. By careful selection of dimensions and fields it is possible to cancel all first and second order terms in ΔV, and indeed cancel third-order terms over a small range of values. In addition, a choice of reflecting potential only slightly above V_0 defines an upper band to the energy window the spectrometer will accept. If our best estimates of mechanical imperfections and a 40% energy spread are substituted into the equations, we predict a mass resolution for 50% valley of better than 500.

Signal detection is by means of a conventional "Venetian blind" electron multiplier. The main means of recording data is by a transient recorder. The limited dynamic range of this recorder has been increased to around 70 dB by logarithmic signal compression techniques. The stored signal is examined using an oscilloscope or, if hard copy is required, the output is directly to a chart recorder. In addition, a small desktop computer is used to store data and provide manipulation facilities.
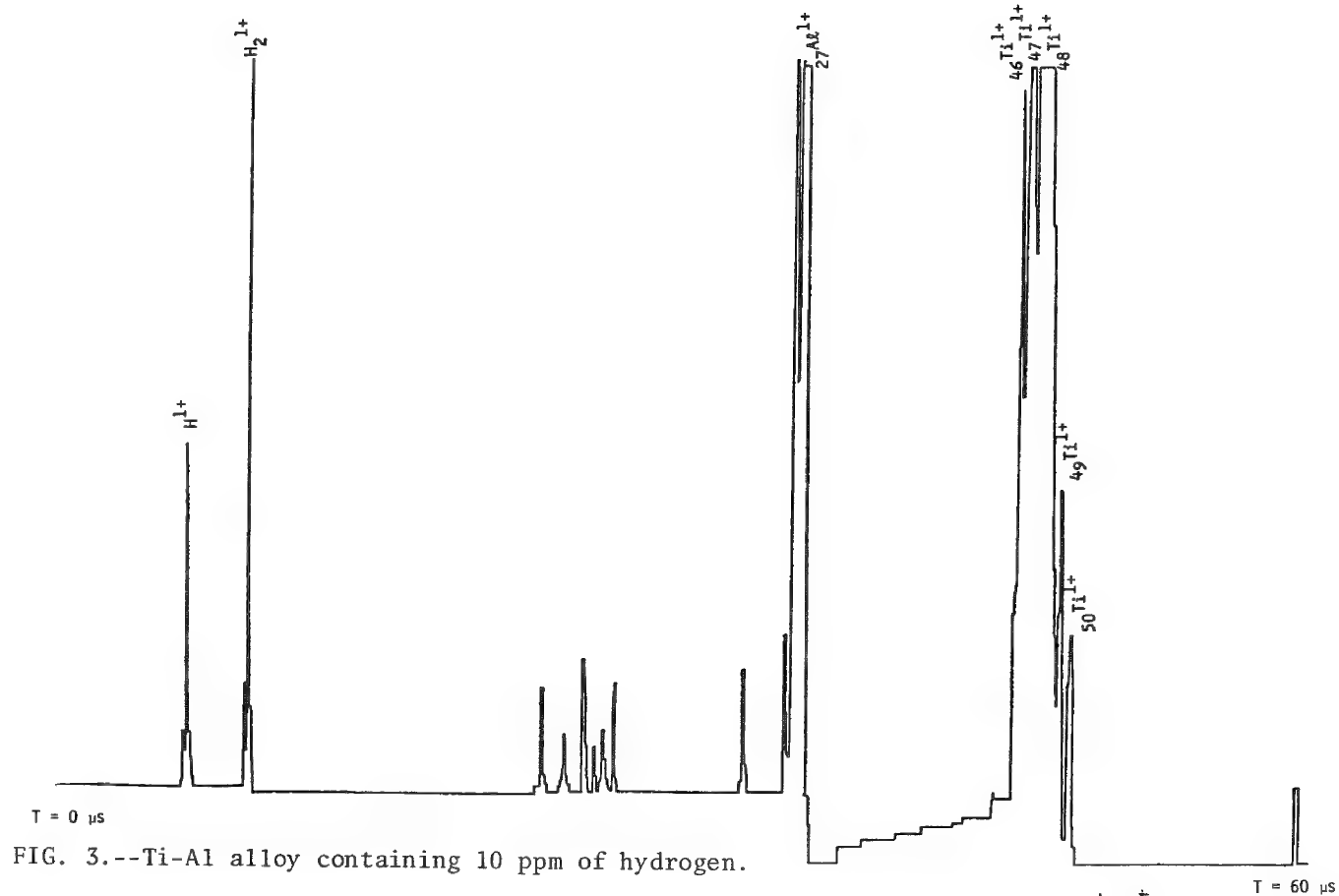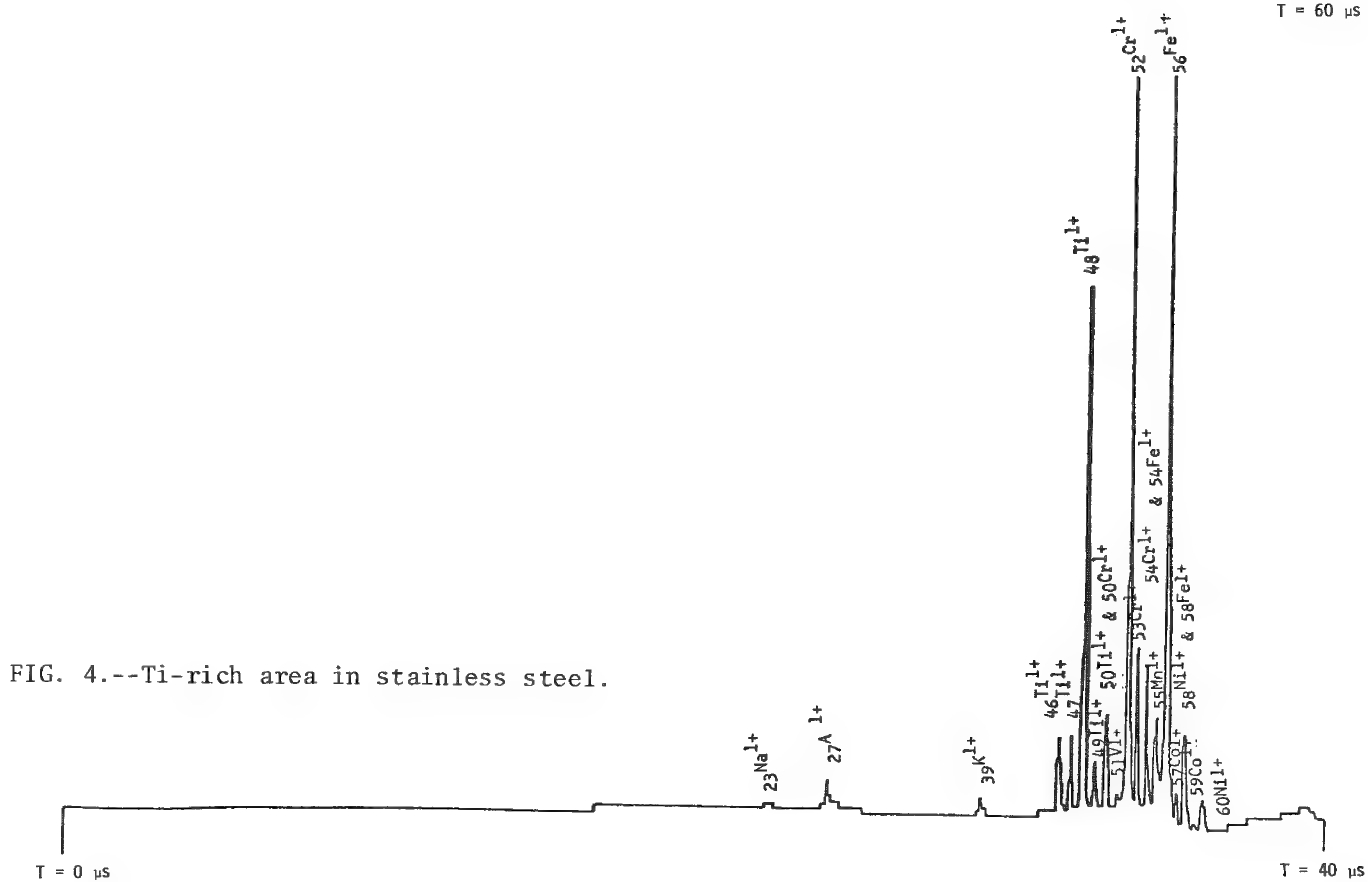
FIG. 3.--Ti-Al alloy containing 10 ppm of hydrogen.

FIG. 4.--Ti-rich area in stainless steel.

Results

The overall performance capabilities of the instrument can be described under the groupings mass resolution, sensitivity, and spatial resolution.

Mass Resolution. If the resolving power is defined as the maximum mass number at which the spectrometer can separate two consecutive mass number signals of similar amplitude to half of their height, the best results we have obtained so far are in excess of 500 (Fig. 2). The resolving power is limited by uncertainty in a particular ion mass flight time, which is caused primarily by energy spread, scattering, and space charge.

T = 60 μs   FIG. 2.--Lead.   T = 80 μs
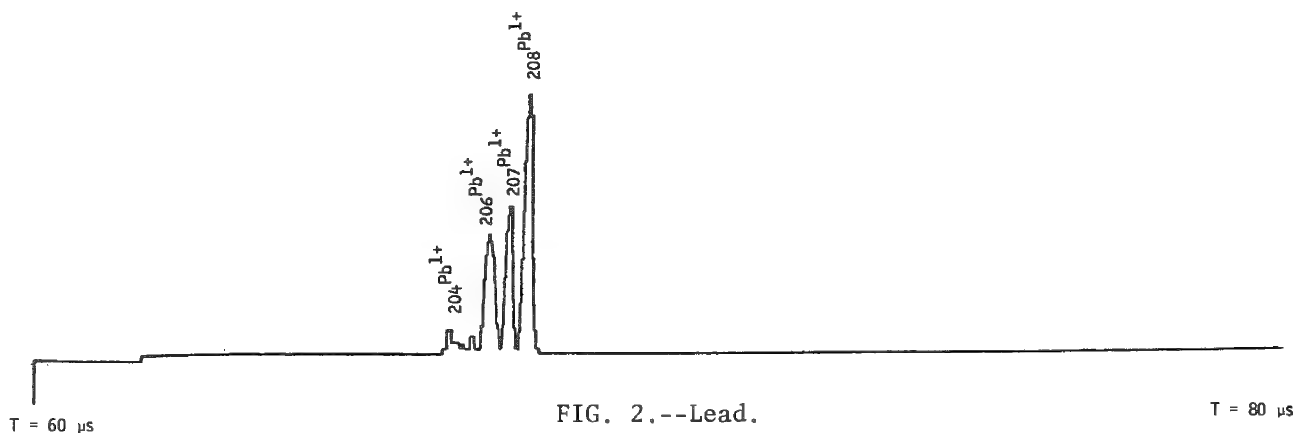
Sensitivity. The sensitivity attainable for most elements in homogeneous bulk samples seems to be better than 10 ppm (Fig. 3). In addition, preliminary results on relative elemental sensitivities have yielded the figures given in Table 1. These data are extremely promising, covering a range of one decade only.

Spatial Resolution. The craters produced by the laser have only been examined optically but it would appear that craters 1-3 μm in diameter can be produced.

TABLE 1.--Relative elemental sensitivities.

Iron (reference)	Fe	1
Chromium	Cr	2.4
Copper	Cu	1.2
Zinc	Zn	2.1
Nickel	Ni	0.6
Manganese	Mn	7.5
Titanium	Ti	1.2
Silicon	Si	1.1
Lead	Pb	1.2

LIMA has been used for a variety of applications. The study of inclusions in bulk metals (Fig. 4) is a typical problem that is suited to this technique. The ability to profile thick surface coatings and oxides rapidly has proved to be particularly useful and we have been able, for example, to detect the concentration with depth to a resolution about 1 μm of hydrogen to less than 10 ppm in 20μm-thick oxide layers on uranium within minutes. The capability to detect surface organics on semiconductor wafers has also proved an asset of the technique. Finally, the study of surface particulares appears from preliminary results to be a particularly promising area, especially if future use is made of the capability of combination with other analytical techniques, such as scanning Auger analysis.

Conclusions

We have built and developed a laser microprobe system of great promise as an analytical tool for bulk sample work. The instrument shows a mass resolution of better than 500 at sensitivity limits in the ppm range.

SCANNING LASER MASS SPECTROMETRY

R. J. Conzemius

Lasers combined with mass spectrometry may in the near future give us the capability for direct quantitative analysis of solids for all elements with no matrix effects, no dissolution required, and no standards necessary, and with a dynamic range from 100% to 10^{-7}% constituents. Our work indicates this statement is true and also indicates that microprocessor control of the instrumentation is relatively straightforward. What is the basis for these optimistic claims? Power density (W cm^{-2}) of the irradiating laser beam in an extremely important parameter. The ion fraction produced per total particles emitted is a general function of laser power density. At lower power densities (10^5-10^8) the ion fraction is very low--generally defined by the Saha-Langmuir equations for ordinary thermal vaporization. The range of ion fraction is thus very large due to elemental specificity caused by differences in volatitlity and ionization potential. As the power density approaches 10^9 W cm^{-2} the ion fraction rises to near unity and the range also narrows dramatically, owing to the transformation from ordinary thermal evaporation to the formation of highly ionized micro plasma just above the specimen.

Our development of the scanning laser mass spectrometer (SLMS) began in 1976 when we purchased a commercial laser and adapted it to a homemade (Mattauch-Herzog) mass spectrometer for the purpose of characterizing solids. The laser is a Nd-doped YAG which is continuously pumped with a water-cooled Kr lamp. It is equipped with an A-O-Q switch which allows a usable pulse repetition rate of 0 to 5000 pps and a pulse width of approximately 150 ns and an instantaneous wattage of 5000 W. The spatial filter is set to use the TEM$_{00}$ mode. Specimen illumination and specimen viewing are co-axial with the laser beam. X and Y mirrors are controlled electrically to give a 2 × 2mm square raster of the focused laser beam on the specimen surface. The objective lens focuses the beam down to a spot diameter of 12 μm with a 3in. working distance and provides a power density of the order of 10^9 W cm^{-2}.

With only a modest manpower commitment to this project it has accomplished a great deal. We have examined relative elemental sensitivities with NBS standards and found the values to be close to unity. Thus, the direct laser excitation provides uniform elemental sensitivity.[1] We have found the system to be highly useful for measuring concentration profiles used in studies of chemical diffusion, electrotransport, and thermotransport.[2] The system has been shown to possess a spatial resolution of 25 μm. We have studied instrument calibration where a series of four standards of Mo in Th gave a 45° straight line passing through zero, which indicates that no concentration effects were present. The ion source has been applied to analysis of films. For example, a sapphire disk containing a 10μm film of Si was analyzed. Both the film and the sapphire could be characterized. The control of the entire system and data acquisition has been accomplished with a small computer.

The combination of the laser ion source with a mass spectrometer provides a powerful analytical technique.[3] Of course there are areas that need further study. What is the dependence of laser beam reflectance on specimen parameters at these power densities? What is the threshold energy for production of the plasma? What is the mechanism of transition to a dense plasma and its subsequent power absorption? What is the role of thermal equilibrium and the dependence of the resulting spectra on recombination during plasma expansion? What are the dependencies of spectra on laser beam parameters? In recent experiments ion production, multiple ion charge intensities, and ion energy

spreads are studied as a function of matrix and of the laser beam power and focal point. These data provide clues to answers for at least some of the questions pertinent to laser mass spectrometry of solids.

References

1. R. J. Conzemius and H. J. Svec, *Anal. Chem.* 50: 1854-1860, 1978.
2. R. J. Conzemius et al., *Anal. Chem.* 53: 1899-1902, 1981.
3. R. J. Conzemius and J. M. Capellen, Int. *J. Mass Spectrom. Ion Phys.* 34: 197-271, 1980.

STUDY OF ASBESTOS BY LASER MICROPROBE MASS ANALYSIS

J. De Waele, P. Van Espen, E. Vansant, and F. Adams

The risks to health, occupational and environmental, arising from the use of asbestos have been widely publicized.[1] The mechanism by which the asbestos fibers exert their biological effects have been the subject of much speculation. The attention, in this respect, has been shifted from geometrical considerations to the possibility that at least part of the biological effects may be associated with some chemical surface characteristics.[2]

A rapidly increasing number of publications illustrate the usefulness of laser microprobe mass spectrometry in single-particle analysis.[3-5] The primary utility of the method in this application appears to lie in the areas of quick routine qualitative and semiquantitative analysis of individual particles of micrometer size for minor and in some conditions trace level inorganic constituents.[6] At the same time there is evidence that my use of the technique as a variable ionization source for mass spectromy, information can be gained regarding the presence of molecular inorganic and organic species present in the microscopical objects.

In this paper we report preliminary results which show that laser microprobe mass analysis can to some extent be used to recognize quicly asbestos fibers in environmental samples and that it can possibly discriminate different asbestos minerals on the basis of a single-fiber analysis. Also, perhaps more important, we show that chemical impurities present at the fiber surface can be detected sensitively.

Methods and Materials

A detailed description of the commercially available laser microprobe mass analyser (LAMMA-500, Leybold-Heraeus, Cologne, FRG) is provided in the literature.[7,8] A frequency quadrupled Q-switched Nd:YAG laser (265 nm, 15 ns pulse width) is focused onto the sample by means of an optical microscope with 32× objective. Samples of asbestos are held onto a Formvar film fixed to a standard copper electron microscope grid. Laser pulse energy on the sample can be varied with a set of transmission filters. It is adjusted either to provide complete vaporization of a micron-sized sample of the fiber, or else to the lowest energy that provides a mass spectrum. Adsorbed impurities into the fiber surface can be detected in this laser desorption (L.D.) operation mode.[9]

UICC standard reference asbestos of South African crocidolite and amosite, Canadian and Rhodesian chrysotile, and Finnish anthophyllite were employed. Neither of these standard samples can be considered homogeneous on the indivᵢdual-fiber level; quantities of the order of 10 mg are necessary as a representative sample. The Canadian chrysotile standard is a mixture of material from eight mines roughly in proportion of their annual production, pooled in one standard material.[10] There are reports in the literature that some of the UICC material is contaminated with adsorbed organic material.[11,12]

Other asbestos samples were used as made available from various sources. Chemicals used were of analytical reagent grade. Organic impurities were adsorbed onto the asbestos surface by a gas phase adsorption process[13] or through equilibration of the fibers with a benzene or water solution.
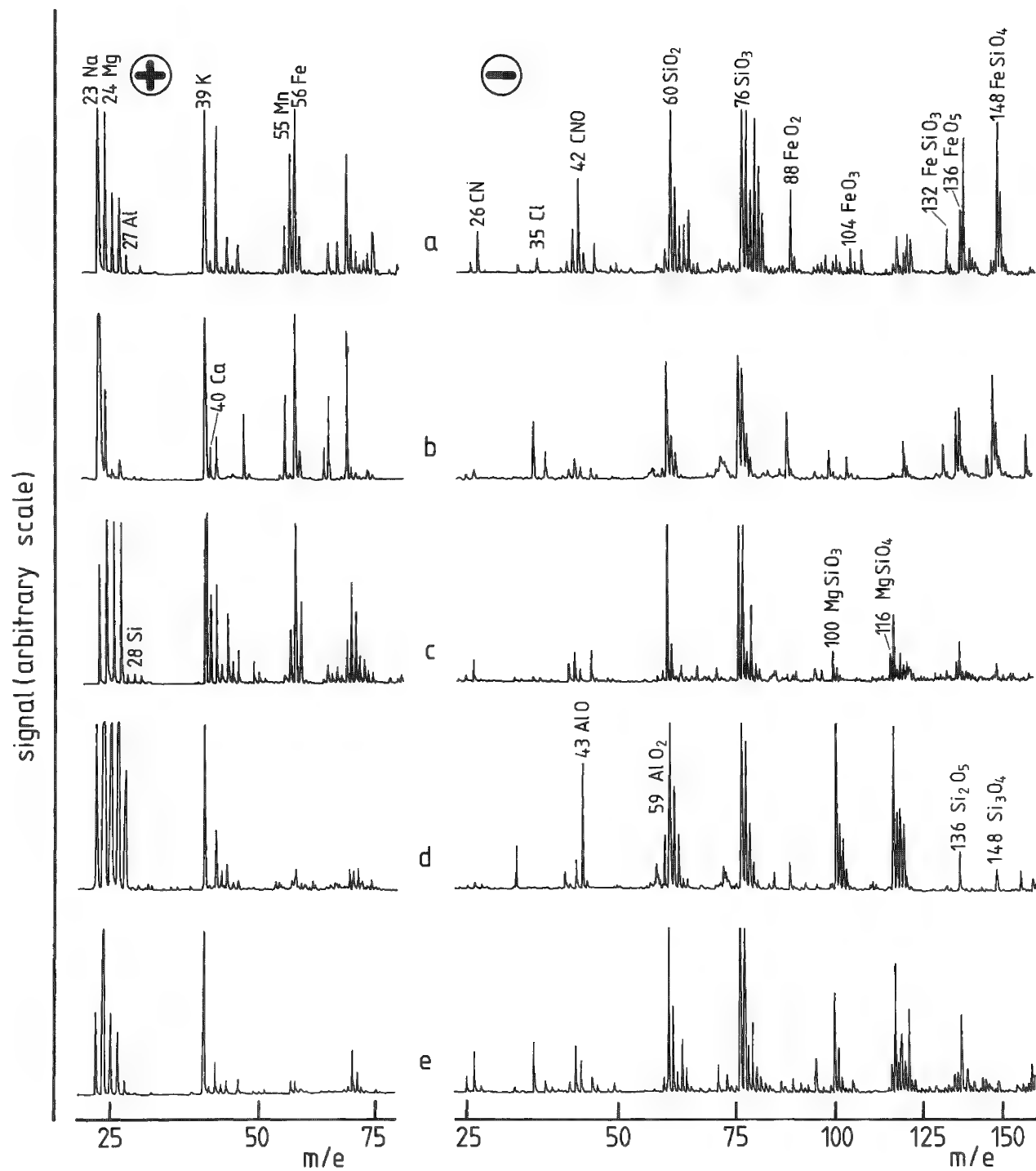

FIG. 1.--Positive and negative LAMMA spectra of UICC asbestos standards: (a) South African amosite, (b) South African crocidolite, (c) Finnish anthophyllite, (d) Rhodesian chysotile, (e) Canadian chysotile.

Figure 1 shows representative positive and negative LAMMA spectra of the UICC standards. They illustrate clearcut differences not only between the amphiboles and the serpentines, but also among various amphiboles and even between the Canadian and the Rhodesian chrysotiles. The reproducibility for subsequent measurements on portions of a single fiber and for fiber-to-fiber analysis is shown in Table 1. The precision is excellent compared with that obtained for LAMMA-analysis of other objects, e.g., fly-ash particles. This is largely the result of the ease with which focusing conditions can be reproduced from one laser shot to the next. The widely differing origin of the fibers in the Canadian chrysotile standard gives rise to large differences in the mass spectra.

TABLE 1.--Relative standard deviations (%) of intensities normalized to magnesium on a single fiber (left) and various fibers (right).

Element	UICC asbestos									
	South African amosite		South African crocidolite		Finnish anthophyllite		Rhodesian chrysotile		Canadian chrysotile B	
Na	40	50	20	70	70	60	100	120	70	150
Al	-	-	-	-	-	-	10	30	50	40
Si	70	100	40	70	70	140	40	50	90	120
K	35	60	30	40	-	-	-	-	80	200
Ca	30	60	-	-	35	50	50	50	70	70
Cr	-	-	-	-	-	-	50	60	-	-
Mn	15	15	50	70	40	50	40	70	60	70
Fe	20	30	25	50	10	25	20	30	36	40

The asbestos mass spectra are characterized by several elemental ion peaks but also by considerable molecular fragment ions in the positive and the negative spectra. For an example, crocidolite (Fig. 2) shows prominent fragment at $m/e = 62(NaK^+)$, $m/e = 72(FeO^+)$, $m/e = 95(MgKO_2^+)$, $m/e = 106$ and 145 (several possibilities) in the positive mass spectrum.

Taking into account that the UICC standards cover about 98% of the commercially used asbestos,[14] one might conclude from these and other measurements[15] that LAMMA is a suitable alternative to existing methods for microchemical characterization of asbestos fibers. The following comments can be made, however:

● A significant chemical instability of chrysotile fibers occurs in environmental samples, in acid solution and in living organisms. Magnesium is quickly leached out but leaching of iron and silicon has been also observed.[15]

● For industrial use asbestos is transferred into a number of products whose composition may significantly differ from that of raw materials.

● Different fibers from a given mineralogy can provide significantly different figerprint mass spectra, as seen in the two UICC chrysotile standards in Fig. 1. Another example is shown in Fig. 3. The elemental composition of tremolite originating from India and from the Philippines (e.g., Na, K, and Cr) differs systematically, and could serve as a basis for identification between material originating from both locations, on condition that the differences are systematical.

● Inhomogeneously distributed trace impurities (cobalt, strontium, rare earths) have

been reported to occur in fibrous zeolites such as erionite.[15] According to our results the concentration of titanium (a minor constituent) is also highly variable in this material (Fig. 4).
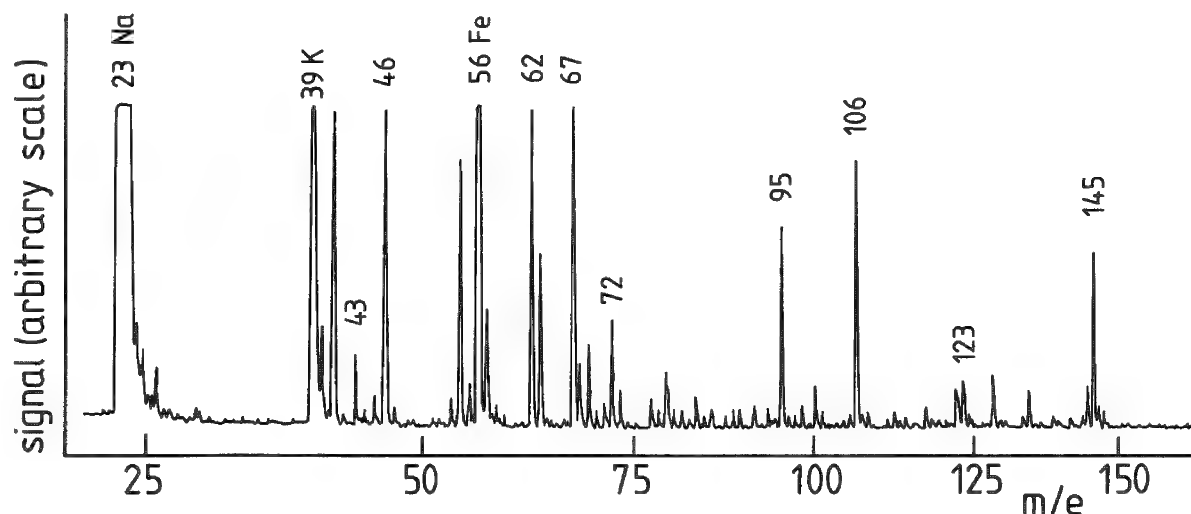

FIG. 2.--Positive LAMMA spectrum of UICC-crocidolite; unassigned peaks are molecular fragments.
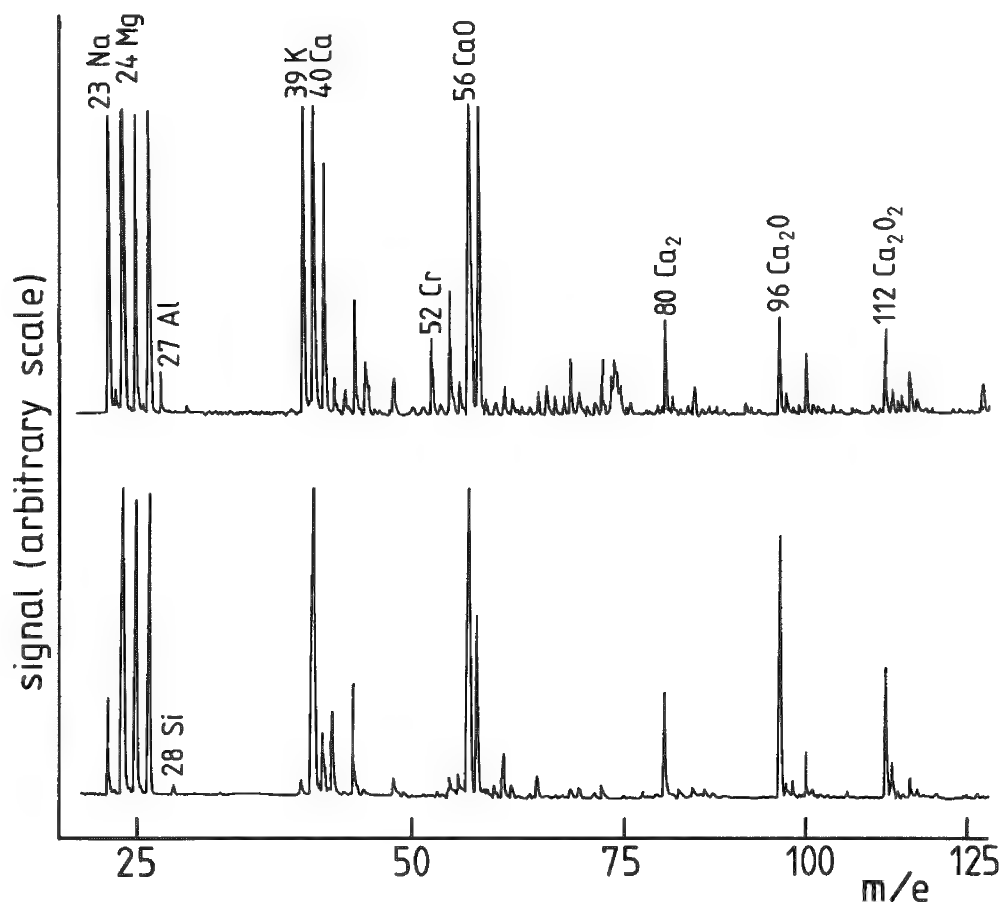

FIG. 3.--Positive LAMMA spectra of tremolite from (a) India, (b) Philippines.
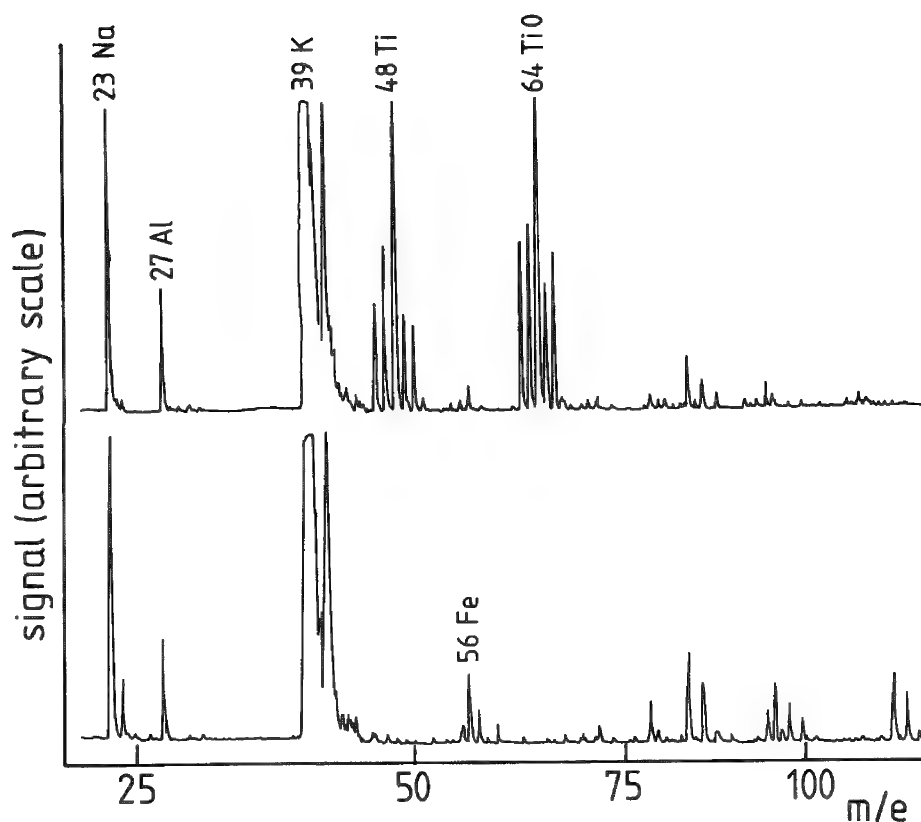
FIG. 4.--Positive spectra of fibrous erionite from Karain, Turkey; titanium-containing
spectrum is exceptionally present.

It is clear from all this that much more systematic research is needed to conclude
whether LAMMA can be considered a safe and quick alternative to other methods (such as
electron microscopy with selected area electron diffraction) for the microscopical
characterization of fibrous particles in the environment.

Surface Analysis of Crocidolite

The UICC crocidolite material was used as an example to determine whether impurities
can be detected at the surface of microscopical asbestos fibers by laser desorption mass
spectrometry. The laser irradiance was decreased considerably below the conditions used
for obtaining the previous spectra. In the LD-mode a rather small number of ions are
formed belonging to a limited number of ion species that are in most cases directly
related to the molecular structure of the material analyzed, often with a high yield of
the parent molecular ions $(M)^+$, protonated $(M+1)^+$, or cationized species $(M+Na)^+$ or
$(M+K)^+$.[9] When laser desorption is applied to asbestos, the fibers remain intact and
the characteristic mass spectrum of the material (see, for example, Fig. 2 for crocido-
lite) vanishes to insignificant intensity.

The following examples from our measurements illustrate some characteristic results
obtained:

1. Benzo[a]pyrene was adsorbed onto crocidolite from teh gas phase leading to a
concentration of 580 μg/g as determined by gas chromatography. Figure 5 shows a positive
LD-mass spectrum measured at different laser irradiances. In these and in other measure-
ments in which the compound was adsorbed onto fly ash particles, a systematic increase
of the molecular ion intensity with decreasing laser irradiance is noted. Also, adsorbed
organic material is not measured on every analysis but the probability of detection
increases sharply for the lowest practical laser irradiances. Under these conditions,
a contribution in the mass spectrum from the crocidolite substrate is absent. As the
laser intensity is increased, the crocidolite mass spectrum becomes gradually more in-
tense, but does not tally with that obtained for untreated crocidolite fibers obtained
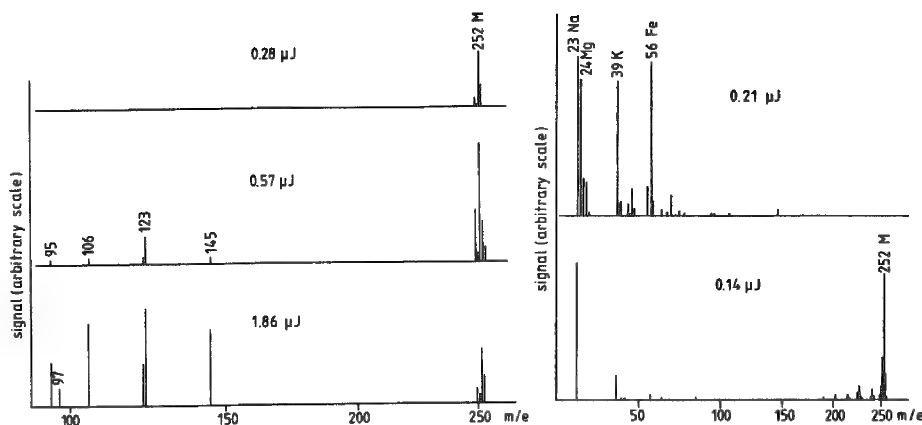
FIG. 5.--Positive laser desorption mass spectrum of benzo[a]pyrene adsorbed on crocidolite from gas phase, measured at various laser irradiances
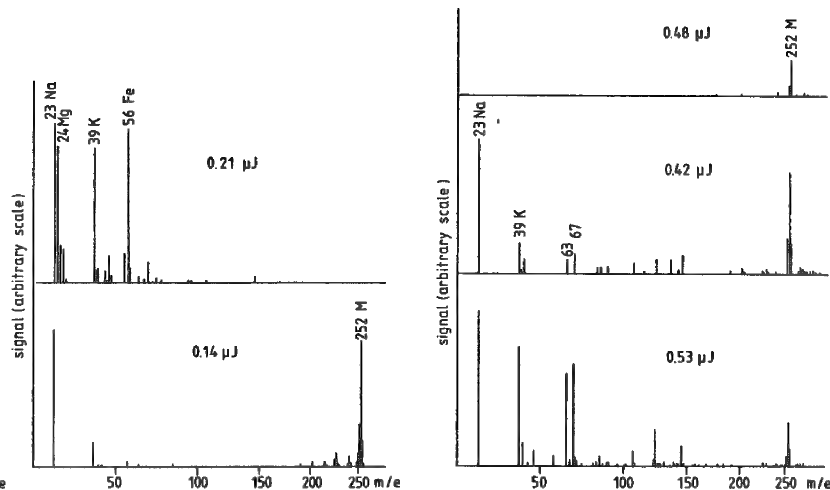
FIG. 6.--(a) Positive spectrum of untreated crocidolite fiber; (b) fiber containing benzo[a]pyrene
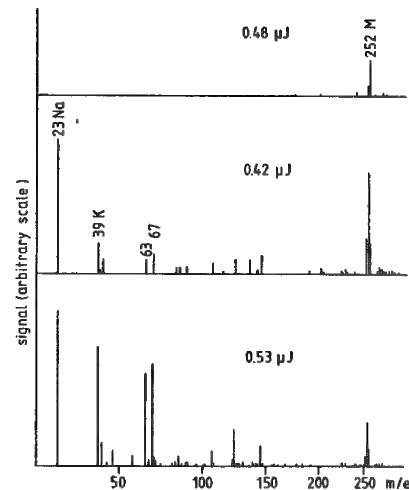
FIG. 7.--Positive mass spectrum of benzo[a]pyrene adsorbed onto crocidolite from (a) to (c); successive laser shots directed at same location
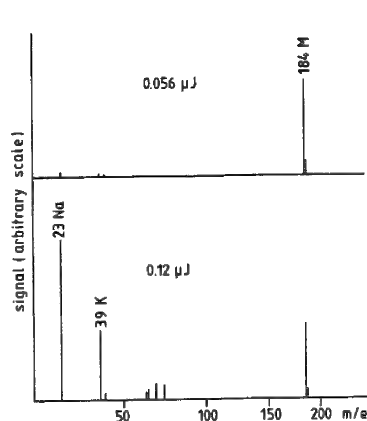
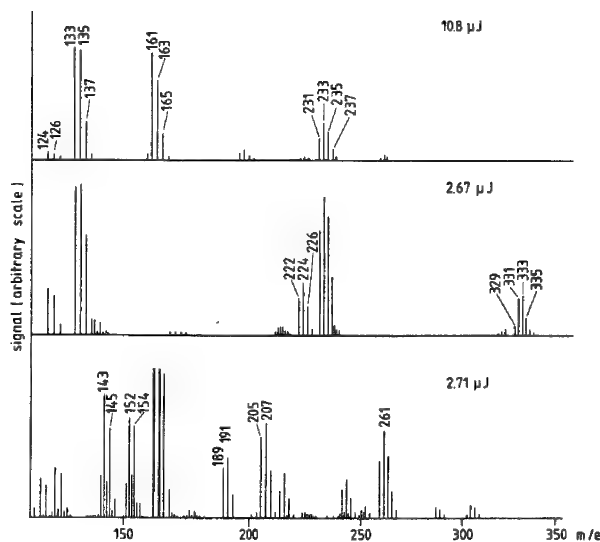FIG. 8.--Positive mass spectrum of benzidine adsorbed onto crocidolite

FIG. 9.--(a) Negative mass spectrum of methyl violet (b) negative and (c) positive spectrum of dimethylaniline adsorbed onto crocidolite. Detection sensitivity is different in (b) and (c).

at a similar irradiance. Mg^+ and Fe^+ are virtually absent from the spectra (Fig. 6). When subsequent laser shorts are directed at the same location, the organic material gradually disappears (Fig. 7), which indicates that LAMMA can be used as a rather crude depth probing device.

Benzidine was adsorbed from aqueous solution (0.0016 M) onto the crocidolite and spectra were obtained at considerably lower laser intensities (Fig. 8) than in the previous example. The same Mg and Fe intensity anomalies can be noted in the spectra.

Dimethylaniline was adsorbed from a benzene solution onto the fibers. This compound has been shown earlier to undergo chemical reactions when adsorbed onto laponite,[16] which leads to the formation of (among other products) methyl violet by catalytic oxidation reactions. Figure 8 shows the negative mass spectrum of methyl violet; Figs. 9(b) and (c) show the negative and the positive spectrum of dimethyl aniline adsorbed onto crocidolite. The characteristic fragmentation pattern of the oxidation product is clearly present in the spectra.

Neither of the laser desorption spectra show any indication of the cationized

376

molecular fragments frequently observed when organic molecules undergo laser desorption in the presence of metals.[17]

It has been shown that the surface of part of the UICC-crocidolite material has been contaminated with 3,3',5,5'-etratertiary butyl diphenoquinone,[12] owing to a catalytic action on polythene in which the material was stored. Laser desorption mass spectra show evidence for heavy molecular fragments that could be related to this or other organic compounds.

The measurements described, though still in progress, amply describe the possibilities of LAMMa as an aid in the surface characterization of individual microscopical fibers.

References

1. P. C. Elmes, "Current information on the health risk of asbestos," *R. Soc. Hlth. J.* 96: 248-252, 1976.

2. J. Dunningan, D. Nadeau, D. Paradis, J.-P. Pele, R. Calvert, J.-M. Lalancette, and M. Cossette, "Cytotoxic and haemolytic effect of native and chemically modified chrysotile," *Proc. Fourth Intern. Conf. Asbestos,* Turin, 26-30 May 1980, 747-772.

3. P. Wieser, R. Wurster, and H. Seiler, "Idenfitication of airborne particles by laser induced mass spectrometry," *Atmos. Environm.* 14: 485-494, 1980.

4. P. Wieser, R. Wurster, and U. Haas, "Application of LAMMA in aerosol research," *Fresenius Z. anal. Chemie* 308: 260-269, 1981.

5. F. Adams, P. Bloch, D. F. S. Natusch, and P. Surkyn, "Microscopical analysis for source identification in air chemistry and air pollution," *Proc. Intern. Conf. Environmental Pollution,* Thessaloniki, Greece, 20-24 September 1981 (in press).

6. E. Denoyer, R. Van Grieken, F. Adams and D. F. S. Natush, "Laser microprobe mass spectrometry: 1. Basic principles and performance characteristics," *Anal. Chem.* 54: 26A-41A, 1982.

7. R. Kaufmann, H. Hillenkamp, and R. Wechsung, "The laser microprobe mass analyser (LAMMA): A new instrument for biomedical microprobe analysis," *Med. Progr. Technol.* 6: 109-120, 1979.

8. H. Vogt, M. J. Heinen, S. Meier, and R. Wechsung, "LAMMA 500, Principle and technical description of the instrument," *Fresenius Z. anal. Chemie* 308: 195-200, 1981.

9. H. J. Heinen, S. Meier, H. Vogt, and R. Wechsung, "Laser desorption mass spectrometry with LAMMA," *ibid.,* pp. 290-296.

10. V. Timbrell and R. E. G. Rendall, "Preparation of the UICC standard reference samples of asbestos," *Powder Technology* 5: 279-287, 1971/1972.

11. V. Timbrell, "Characteristics of the International Union Against Cancer standard reference samples of asbestos," *Pneumoconiosis* (Proc. Int. Conf.), Johannesburg, 1969, 28-36.

12. B. T. Commins and G. W. Gibbs, "Contaminating organic material in asbestos," *Brit. J. Cancer* 23: 358-364, 1969.

13. W. A. Korfmacher, A. M. Miguel, G. Mamantov, E. L. Wehry, and D. F. S. Natusch, "Apparatus for vapor phase adsorption of polycyclic organic matter onto particulate surfaces," *Env. Sci. Technol.*]3: 1229-1232, 1979.

14. V. Timbrell, J. C. Gilson, and I Webster, "UICC standard reference samples of asbestos," *Int. J. Cancer* 3: 406-408, 1968.

15. K. R. Spurny, J. Schormann, and R. Kaufmann, "Identification and microanalysis of mineral fibers by LAMMA," *Fresenius Z. anal. Chemie* 308: 274-279, 1981.

16. E. F. Vansant and S. Yariv, "Adsorption and oxidation of dimethylaniline by Laponite," *J. Chem. Soc., Far. Trans. I* 73: 1815-1824, 1977.

17. K. Balasanmugam, Tuan Anh Dang, R. J. Day and D. M. Hercules, "Some cation and anion attachment reactions in laser desorption mass spectrometry," *Anal. Chem.* 53: 2296-2298, 1981.

ANIONIC SURFACTANT FILMS AS STANDARDS FOR QUANTITATIVE LASER MICROPROBE MASS ANALYSIS

Renaat Gijbels, Paul Verlodt, and Serge Tavernier

The LAMMA-500 instrument which became commercially available a few years ago is suitable for obtaining mass spectra from microvolumes of thin foils (about 1 μm) by single laser shot perforation, since the ions are extracted at an angle of 180° with respect to the incident laser beam. For data quantification, Eppon foils doped with a variety of metallic elements are often used.[1]

Only a few systematic studies are available for quantitative interpretation of at least certain classes of LAMMA results.[2-4] In this paper we describe the preparation of thin surfactant films containing well-known and easily controllable relative concentrations of metal ions. These samples are useful to determine relative sensitivity factors of a number of selected elements (e.g., the alkalis) and to correlate these factors with some convenient physical quantity, such as the first ionization potential of the elements concerned.

Experimental

Laser mass spectra were obtained by using commercially available instrumentation (Leybold-Heraeus LAMMA-500) equipped with a data reduction system, described elsewhere.[5]

The surfactant Na-di-2-ethylhexylsulfosuccinate ("Aerosol-OT" or "Na-AOT") was obtained from Fluka. The corresponding acid was prepared by addition of concentrated sulfuric acid as a dilute solution in ether to an ethanolic solution of Na-AOT, and filtering off of the insoluble sodium sulfate. The Li, K, Rb, and Cs salts were obtained by addition of LiOH, KOH, Rb_2CO_3 or Cs_2CO_3 to the filtrate. Ethanol and ether were distilled at reduced pressure. The residue was dissolved in benzene, water was removed by azeotropic distillation, and benzene by distillation at reduced pressure. The surfactant was finally dissolved in diethylether and filtered. Evaporation of the filtrate yielded M-AOT. For more details see Refs. 6 and 7. The purity of the surfactants was determined by atomic emission spectroscopy, after destruction in nitric and perchloric acids. Results are given in Table 1. We prepared mixtures of the five surfactants by weighing suitable quantities and dissolving them in chloroform. The composition of these mixtures was also determined by atomic emission spectroscopy after evaporation and destruction of the organic material. Results are summarized in Table 2.

In order to prepare samples for laser microprobe mass analysis, 400-mesh copper grids identical with those used in electron microscopy were brought in contact with a beaker wall that had been previously wetted with the surfactant solution in chloroform. After evaporation of the solvent, a single surfactant film was obtained.

The laser beam could easily be focused on such films and a number of single laser firings could be carried out within an opening of the copper grid without complete destruction of the film. The film thickness could be varied up to 1-2 μm by adjustment of the surfactant concentration in the chloroform solution. The above sample preparation obviously does not require to use a supporting film such as Formvar.

The surfactant films were irradiated with 15ns pulses of a frequency-quadrupled Nd-YAG laser (265 nm) at an energy of about 5 to 15 μJ. Both negative and positive ion time-of-flight mass spectra were recorded.

The negative ion mass spectra are characterized by a series of $C_mH_n^-$ clusters ($0 < n < 2$; $1 < m < 15$) that display an even-odd effect in their intensities : clusters

TABLE 1.--Purity determination of the synthesized surfactants by atomic emission spectrometry.

Surfactant	wt.-% Na	wt.-% K	wt.-% purity
Li-AOT	6.15	3.50	90 ± 1
Na-AOT	99.00	0.80	99 ± 1
K -AOT	5.75	94.00	94 ± 1
Rb-AOT	2.75	1.50	95 ± 1
Cs-AOT	5.05	0.50	94 ± 1

TABLE 2.--Composition of surfactant mixtures (in mole %), as determined by atomic emission spectrometry.

	Li-AOT	Na-AOT	K-AOT	Rb-AOT	Cs-AOT
Mixt. 1	17 ± 1	23 ± 1	22 ± 1	19 ± 1	19 ± 1
Mixt. 2	60 ± 2	11.0±0.5	11.0± 0.5	9.0±0.5	9.0 ± 0.5
Mixt. 3	39 ± 1	42 ± 1	11.0± 0.5	4.0±0.5	4.0 ± 0.5
Mixt. 4	8.0 ± 0.5	6.0±0.5	73 ± 2	9.0±0.5	4.0 ± 0.5
Mixt. 5	28 ± 1	32 ± 1	32 ± 1	4.0±0.5	4.0 ± 0.5

with even m are more abundant. The pattern is not unlike that described by Fürstenau[2] for thin carbon foils, at least up to m = 8. The patterns are similar for all the surfactants, and for the surfactant mixtures, although the contribution of heavy cluster ions tends to be more pronounced for surfactants containing the heavy alkalis (Fig. 1).

The intensity of the molecular ion AOT^- (M.W. 422) is rather small in the described experimental conditions. Carbon clusters up to $C_{15}H_n^-$ are observed even though the longest hydrocarbon chain in AOT is C_8 (ethylhexyl), which suggests that these molecular ions could not have been formed by a laser desorption process alone.
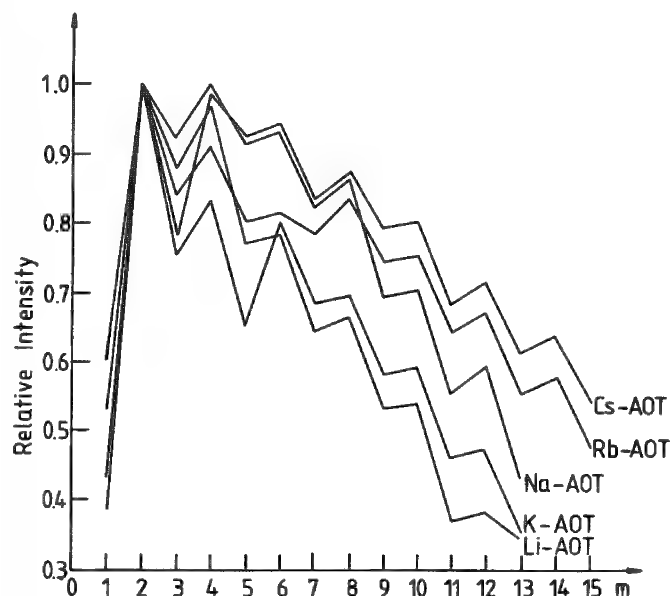
The positive ion spectra are characterized by high alkali metal ion intensities as compared to signals from "organic" origin. Even H^+ and C^+ were not always detected. The organic part of the mass spectra appears to be rather sensitive to small variations in the experimental parameters. This observation has also been made in SIMS experiments on similar surfactants.[8] In Fig. 2 the positive LAMMA spectrum of surfactant mixture No. 1 is represented as an example.

The measured isotope ratios of the polyisotopic elements (i, K, and Rb) do not agree very well with the literature data, mainly owing to the imperfect functioning of the Biomation 8100 transient recorder,[9] and to a lesser extent to the method used for peak area calculation.[10]

In the analysis of surfactant films, prepared as described above, from solutions of different concentrations (from 10^{-6} to 1 mole surfactant per liter of chloroform), a linear relationship was found between the metal ion intensity and the surfactant

FIG. 1.--Relative intensity of negative molecular ions ($\sum_n C_m H_n^-$, 0 < n < 2) as function of number of C atoms (m) in cluster for the various surfactants.

concentration, at least up to about 10^{-3} molar (Fig. 3). This finding suggests that (i) the same volume of surfactant solution is attached to the TEM grid, (ii) after evaporation of the solvent thicker surfactant layers are produced from a solution of higher concentration, and (iii) the measured ion intensity in the positive LAMMA spectra, for given instrumental parameters, is proportional to the film thickness at least over three orders of magnitude.
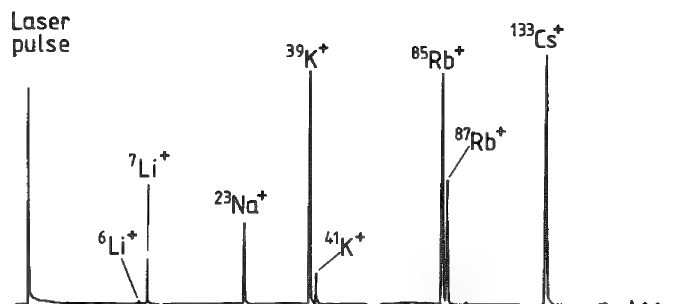
FIG. 2.--Positive ion LAMMA spectrum from sur-
factant mixture No. 1, containing about equi-
molar quantities of Li, Na, K, Rb, and Cs-AOT
(delay 0, input 0.05 V, sampling interval 0.05
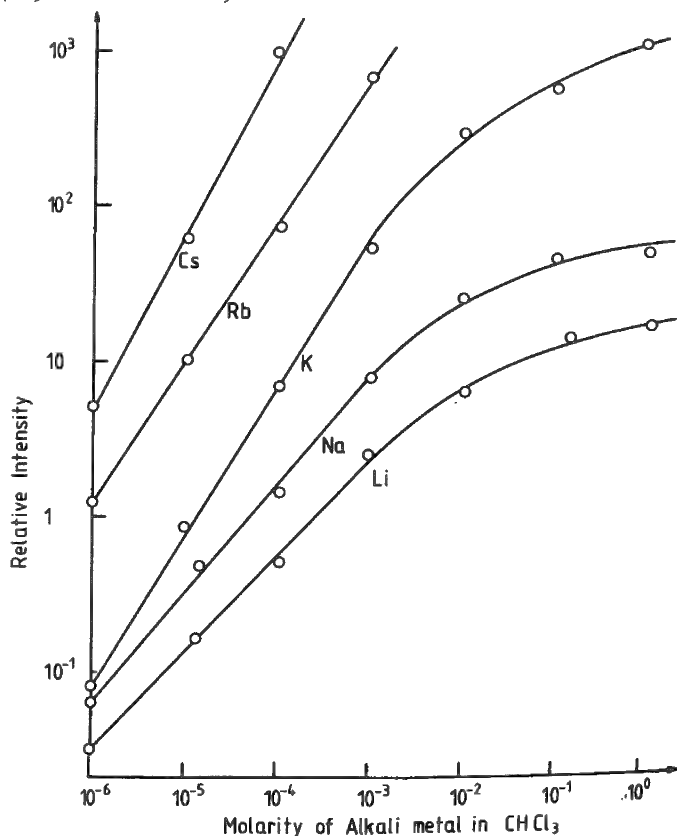μs, filters 1.1).

FIG. 3.--Relative positive metal ion intensity as a function of metal content in chloroform
solution (M/1); surfactant film was prepared as described in text.

FIG. 4.--Normalized positive ion current vs
ionization potential E_M shown corrected
(dashed lines) and uncorrected for electro-
nic partition function ratio $Z_{M^o}(T)/Z_{M^+}(T)$.

Quantitative Analysis: Relative Sensitivity of Alkali Metals

The production of positive alkali metal ions from anionic surfactant films under
laser irradiation is quite reproducible. The intensity of these ions was therefore
studied in more detail in order to assess whether their behavior is similar to that
found for ion bombardment.[8]

According to Morgan and Werner[11] several different equations proposed for the ionization
ratio n_{M^+}/n_{M^o} can be grouped into one general expression

$$n_{M^+}/n_{M^o} = K[Z_{M^+}(T_i)/Z_{M^o}(T_i)] \exp(-E_M/kT_i)$$

where n_{M^+} and n_{M^o} are the number of M+ ions and M^o neutrals, respectively, emitted per
unit time from a sample containing the element M; Z represent an electronic partition
function, E_M is the first ionization potential, and T_i is called the "ionization
temperature." The proportionality constant has a different meaning depending on whether
the Saha-Eggert, the Saha-Langmuir, or the Jurela equation is adopted (see Ref. 11 for details)
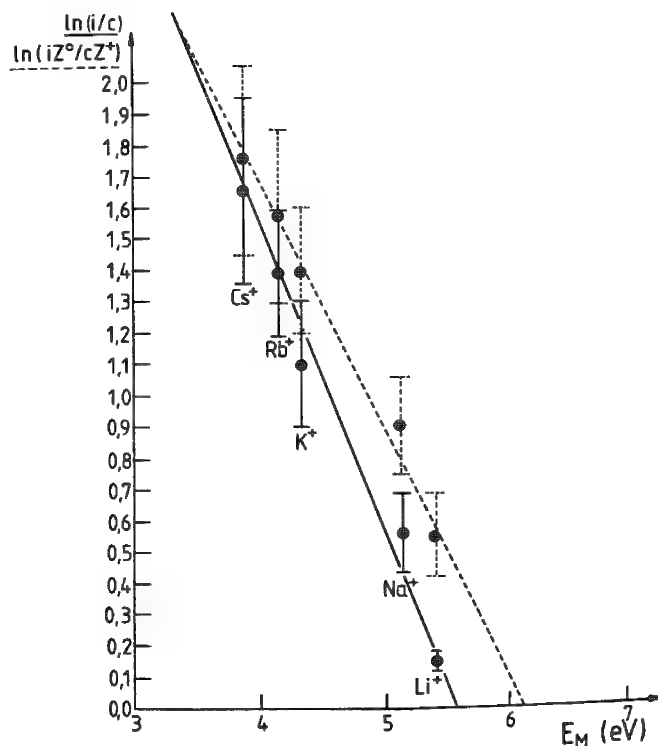
Irrespective of which K (if any) is relevant, it appears that T_i may be derived from a plot of $\log(n_{M+}Z_M\rho/n_M\rho Z_{M+})$ vs E_M. Here n_{M+} is directly related to the total measured current of M^+ ions (corrected for isotopic abundance) whereas for $n_{M}\rho$ one can use the atomic concentration, provided that $n_{M}\rho \sim n_M$, the total number of all M-containing species emitted per unit time. The latter assumption is solely justified by the fact that satisfactory analytical results have been shown to ensue from it in SIMS analysis of metals, silicates, oxides, and surfactants, and apparently also for LAMMA, as is shown below. Blaise[12] has also emphasized that equations of the above type certainly correspond to the best empirical approach to the problem of quantitative analysis by secondary ion emission, but that they should be considered as phenomenological laws; attempts to justify them by thermodynamic considerations are not considered convincing at all. This approach probably also applies to ion emission under pulsed laser irradiation.

Derivation of the "Ionization Temperature T_i."

The calculations are similar to those described by Morgan and Werner[11] for SIMS. The measured peak intensities were normalized to unit analytical concentration in the surfactant mixture, corrected for isotopic abundance θ, multiplied by the electronic partition function ratio $(i_M/C_M\theta)[Z_M\rho(T)/Z_{M+}(T)]$, and plotted on a semilog scale vs. the first ionization potential E_M (Fig. 4). The temperature-dependent partition functions and the E_M values were taken from Drawin and Felenbok.[13] T_i was calculated from the least-squares slope of the straight line in the above semilog plot, and iterations were performed until the T_i values used for Z coincided within 2% with that derived from the slope.

In Fig. 4 (and similar figures for other surfactant mixtures), data from five LAMMA spectra are incorporated together with the standard deviations. Furthermore, it can be seen that a plot of $\log (i/c)$ vs E_M also yields straight lines.

Ionization temperatures calculated from the various surfactant mixtures are summarized in Table 3. The internal consistency is quite satisfactory and the calculated "ionization

TABLE 3.--Calculated "ionization temperatures" (K).

Mixt. 1	10300	Mixt. 4	10500
Mixt. 2	10700	Mixt. 5	10300
Mixt. 3	12200	Average	10800 ± 400

TABLE 4.--Estimated sensitivity of LAMMA (E ≈ 5-15 μJ)

Li	$1 \times 10^{-16}g$	Rb	$1 \times 10^{-17}g$
Na	$1 \times 10^{-16}g$	Cs	$1 \times 10^{-17}g$
K	$1 \times 10^{-16}g$		

temperature" of about $11000°$ K is not even unrealistic, but tends to be higher than that observed in secondary ion emission from similar types of surfactants,[8] i.e., about 6600-$7250°$ K, depending on the selected secondary ion energy window.

Sensitivity

Taking into account the estimated thickness of the surfactant foil (and hence the amount of alkali element per unit area) and the average area of the holes made by laser firing, it is possible to estimate the sensitivity of the various elements in the present experimental conditions (Table 4).

Conclusion

This LAMMA study on anionic surfactant films suggests that some kind of Local Thermal Equilibrium (LTE) model can be used to interpret the relative sensitivity factors of the positive alkali ion emission. It would be desirable to prepare surfactants containing other cations (i.e., nonalkali metal ions) in order to check whether this conclusion for LAMMA has the same validity as in SIMS.[8]

References

1. R. Kaufmann et al., "Laser microprobe mass analysis: Achievements and aspects," *SEM/1979* II, 279-290.

2. N. Fürstenau and F. Hillenkamp, "Laser-induced cluster-ions from thin foils of metals and semiconductors," *Intern. J. Mass Spectrom. Ion Phys.* 37:135-151, 1981.

3. P. Surkyn and F. Adams, "Laser microprobe mass analysis of glass microparticles," *J. Trace & Microprobe Techniques* (in press).

4. U. Haas et al., "A quantitative interpretation of LAMMA spectra based on a Local Thermodynamic Equilibrium (LTE) model," *Fresenius Z. anal. Chem.* 308:270-273, 1981.

5. E. Michiels et al., "Atomic and molecular ion emission from silica in laser mass spectrometry," *Microbeam Analysis--1982*, 383.

6. P. Verlodt, "Study of Laser-induced Mass Spectra of Some Organic Compounds," M.Sc. Thesis, University of Antwerp, 1981.

7. A. Nelen et al., "Substitution of metal ions in anionic surfactans by ion-exchange reactions in non-aqueous solvents," *Bull. Soc. Chim. Belg.* 88:31-36, 1979.

8. A. Nelen et al., "Secondary ion emission by anionic surfactants," *Bull. Soc. Chim. Belg.* 90:325-330, 1981.

9. R. Kaufmann, private communication (1981).

10. H. Nullens, private communication (1981).

11. A.E. Morgan and H.W. Werner, "Semi-quantitative analysis by SIMS using one fitting parameter," *Mikrochim. Acta* 2:31-50, 1978.

12. G. Blaise, in J.P. Thomas and A. Cachard, Eds, *Material Characterization Using Ion Beams*, New York: Plenum, 1978.

13. H.W. Drawin and P. Felenbok, *Data for Plasmas in Local Thermal Equilibrium*, Paris: Gauthier-Villars, 1965.

ATOMIC AND MOLECULAR ION EMISSION FROM SILICA IN LASER MASS SPECTROMETRY

Eric Michiels, Anita Celis, and Renaat Gijbels

A typical feature of "LAMMA" mass spectra is the occurrence of molecular ions. So far the systematic study of molecular ions produced during laser irradiation has been limited to clusters from pure elements, e.g., C, Si, Ge, Ag, Au, Al, Fe,[1] although occasionally alloys[2] and inorganic compounds have been investigated, e.g., ammonium, silver and aluminium perrhenate[3] and iron(III)oxide, sulfate, and chloride.[4] Systematic data on LAMMA spectra of inorganic oxides are being accumulated in the authors' laboratory, e.g., for group IV elements and for the lanthanides.

In this paper we survey the $Si_m^\pm$ and $Si_mO_n^\pm$ ions of mass up to about 560 amu produced when irradiating silica with a frequency quadrupled Q-switched Nd-YAG laser pulse. The experimental molecular ion distributions are similar to those observed in secondary ion mass spectrometry (SIMS). For a given m ($1 < m < 8$) the positive ion yields can conveniently be described by the empirical formulas derived by Plog et al.[5] Maximum intensity is observed at $n = 0$ for $m = 1$, at $n = 2$ for $m = 2$, and at $n = 2m - 1$ or $2m - 2$ for $3 < m < 8$. The average O/Si ratio increases continuously from 0.37 for $m = 1$, to about 2 for $m = 8$. Negative molecular ion yields with $m = 1$ can also be described by Plog's model, but clusters of the form $Si_mO_n^-$ (with $m > 1$) show a different behavior from SIMMS: $Si_mO_{2m+1}^-$ is more intense than $Si_mO_{2m}^-$.

It is clear that the occurrence of molecular ions from a given matrix may interfere with the determination of impurities in the sample. Therefore it is desirable to study systematically the relative abundances of molecular ions using high-purity materials, and to compare them with theoretical and/or empirical models on ion formation.

Unfortunately, no established theoretical model exists at present for calculating ion yields as a function of target and laser parameters. For the quantitative interpretation of LAMMA spectra, the local thermodynamic equilibrium (LTE) model appears to be a useful first approximation.[6-8] Heinen[9] has suggested that molecular ion formation from organic compounds and from inorganic salts by laser irradiation is primarily a thermal process. Furstenau[1,10-11] developed a model for describing the influence of crystal structure on cluster distributions on the assumptions that nonequilibrium effects dominate the laser-induced phase transition and that cluster stability effects are of only minor importance. He concluded that both equilibrium and nonequilibrium properties of the laser-induced evaporation process may determine the occurrence of molecular ions, depending on target as well as on irradiation conditions.

For secondary ion mass spectrometry (SIMS), a more extensive literature is available. Nevertheless, the mechanisms for generating secondary ions, and problems associated with such competing processes as, for instance, release from the solid-state surface, dissociation, and ionization, have to date remained largely uncertain and unresolved and are indicated in only few qualitative or empirical-model studies.[5,12-18]

Experimental

Laser mass spectra were obtained by commercially available instrumentation (Leybold-Heraeus LAMMA-500). The output of a frequency quadrupled Q-switched Nd-YAG laser (265 nm, 15 ns pulse width) was focused onto the sample with the aid of a low power He-Ne pilot laser through an optical microscope fitted with UV-transparent glycerol immersion lenses. A 32× objective was used throughout. The energy delivered to the specimen was about 5 to 15 μJ. For a more detailed description of the equipment, reference is made to the

---

literature.[4,19,20] Data from the transient recorder of the commercial instrument were fed into a Digital MINC-11 microprocessor equipped with dual floppy disks and a video screen. Mass assignments and peak area calculations were performed with the use of a computer program developed by Nullens.[21]

LAMMA spectra were obtained for the following samples:

(a) powdered spectrographically pure SiO_2 from Johnson-Matthey, mounted on a Formvar coated TEM grid;

(b) monodisperse silica spheres, with a diameter of 0.5 μm prepared according to Stöber et al.,[22] also mounted on a Formvar coated TEM grid;

(c) the quartz cover glass (optical window and vacuum seal of the time-of-flight mass spectrometer), by focusing of the laser beam on its inner surface; and

(d) a crystalline mineral quartz sample of the same dimensions as the quartz cover glass (c), and mounted as optical window and vacuum seal instead of the latter.

Samples (a) and (c) were superior because of higher purity; sample geometry (c) and (d) yielded higher ion intensities. Therefore the discussion will be based on the mass spectra obtained from sample (c). All intensities were normalized to Si atomic ions; the resulting values were designated as $I_{rel}^{\pm}$. No corrections have been made for differences in ion-electron conversion efficiencies as a function of ion mass, composition, or charge.

The LAMMA spectra indicated the presence of positive ions of the types $Si_mO_n^+$ ($1 < m < 8$ and $0 < n < 18$). The experimental relative intensities are shown in Table 1. The molecular ions can be classified into groups with the same number of silicon atoms m and a different number of oxygen atoms n. When m increases it is seen that the average O/Si ratio shifts to higher values, until at $m = 8$, $<O/Si> \simeq 2$, i.e., the stoichiometric ratio of SiO_2 is obtained. The maximum intensity within a group is reached at $Si_mO_{2m-2}^+$ for $0 < m < 4$, at $Si_mO_{2m-1}^+$ for $4 \leq m < 7$, and at $Si_mO_{2m}^+$ for $m \geq 7$. It can also be seen that the relative intensity of the various maxima decreases with increasing m, which indicates a smaller formation probability of larger molecular ions. This observation is in good qualitative agreement with the results of Richter and Trapp,[23] obtained with dynamic SIMS of silicon bombarded with O_2^+ and with oxygen gas admitted (up to 300 amu).

Our results for negative ions of type $Si_mO_n^-$ ($1 < m < 9$ and $0 < n < 19$) are shown in Table 2. Maximum intensities are found for ions $Si_mO_{2m+1}^-$, except for $m = 1$, where SiO_2^- and SiO_3^- intensities are similar. These results are also similar to those of Richter and Trapp (o.c.) (up to 256 amu).

Plog et al.[5] have proposed an empirical model for describing secondary ion yields from oxidized metal surfaces and metal oxides. It is based on the hypothesis that for secondary ion species of the type $MeO_n^{\pm}$ a Gaussian curve describes the ion yields as a function of the "fragment valence" K,

$$K = (q + 2n)/m$$

where q is the total charge of the fragment, and m and n are the number of Me and O atoms in the cluster.

A perfect parabola can obviously be fitted through the relative intensities of SiO_n^+ in a semilog plot versus K, since only three experimental points are available (Si^+, SiO^+, and SiO_2^+). The same is true for SiO_n^-, if Si^- is excluded (SiO^-, SiO_2^-, and SiO_3^-) (Fig. 1). The maximum intensities occur at fragment valences $G^+ = 1.56$ and $G^- = 4.08$, respectively. The variances of the parabolas are $\gamma^+ = 1.20$ and $\gamma^- = 1.08$, respectively. In Table 3 our data are compared with those calculated from Richter and Trapp's dynamic SIMS data (Si, bombarded with O_2^+ and flooded with O_2 gas). Richter and Trapp's data for SiO_n^+ and SiO_n^- are shown in Fig. 2.

For positive molecular ions containing more Si atoms ($Si_mO_n^+$, $m > 1$), usually four experimental points are available, so that a more meaningful evaluation of Plog's model is possible. A parabola can easily be fitted through the logarithm of the ion intensities as a function of K (Fig. 3); the average correlation coefficient of these fits is better than 0.99. The parameters I_{max}, G^+, and γ^+ are summarized in Table 3. It can again be seen that the relative maximum I_{max} decreases and shifts to a higher K-value (i.e., a higher O/Si-ratio) when the number of Si atoms increases. The variances γ^+ of the parabolas also decrease with increasing m. The somewhat unexpected increase of γ^+ for the

TABLE 1.--Relative positive ion yields and weighted average O/Si ratios for clusters with a given number of Si atoms.

Cluster	$I_{rel.}^+$	$\langle O/Si\rangle$	Cluster	$I_{rel.}^+$	$\langle O/Si\rangle$
Si^+	1.00		$Si_5O_7^+$	0.0095	
SiO^+	0.54	0.37	$Si_5O_8^+$	0.036	
SiO_2^+	0.018		$Si_5O_9^+$	0.053	1.74
			$Si_5O_{10}^+$	0.017	
Si_2^+	0.062				
Si_2O^+	0.10		$Si_6O_9^+$	0.0029	
$Si_2O_2^+$	0.22	0.83	$Si_6O_{10}^+$	0.014	
$Si_2O_3^+$	0.046		$Si_6O_{11}^+$	0.031	1.82
$Si_2O_4^+$	0.012		$Si_6O_{12}^+$	0.015	
$Si_3O_3^+$	0.062		$Si_7O_{12}^+$	0.0030	
$Si_3O_4^+$	0.19		$Si_7O_{13}^+$	0.0096	
$Si_3O_5^+$	0.13	1.42	$Si_7O_{14}^+$	0.0096	1.91
$Si_3O_6^+$	0.021		$Si_7O_{15}^+$	0.0035	
$Si_4O_5^+$	0.026		$Si_8O_{15}^+$	0.0037	
$Si_4O_6^+$	0.077		$Si_8O_{16}^+$	0.0046	
$Si_4O_7^+$	0.083	1.60	$Si_8O_{17}^+$	0.0048	2.06
$Si_4O_8^+$	0.020		$Si_8O_{18}^+$	0.0032	

TABLE 2.--Relative negative ion yields.

Cluster	$I_{rel.}^-$	Cluster	$I_{rel.}^-$
Si^-	1.00	$Si_5O_{10}^-$	0.067
SiO^-	0.11	$Si_5O_{11}^-$	0.30
SiO_2^-	3.9		
SiO_3^-	4.4	$Si_6O_{13}^-$	0.16
$Si_2O_4^-$	0.62	$Si_7O_{15}^-$	0.067
$Si_2O_5^-$	1.6		
		$Si_8O_{17}^-$	0.056
$Si_3O_6^-$	0.18		
$Si_3O_7^-$	0.67	$Si_9O_{19}^-$	0.047
$Si_4O_8^-$	0.067		
$Si_4O_9^-$	0.56		

FIG. 1.--Relative intensity of ions $SiO_n^\pm$ from pulsed-laser irradiated silica as function of fragment valence K.

FIG. 2.--Relative intensity of ions $SiO_n^\pm$ from oxygen-bombarded silicon (with bleeding of oxygen gas) as function of fragment valence K. (Data taken from Ref. 23.)
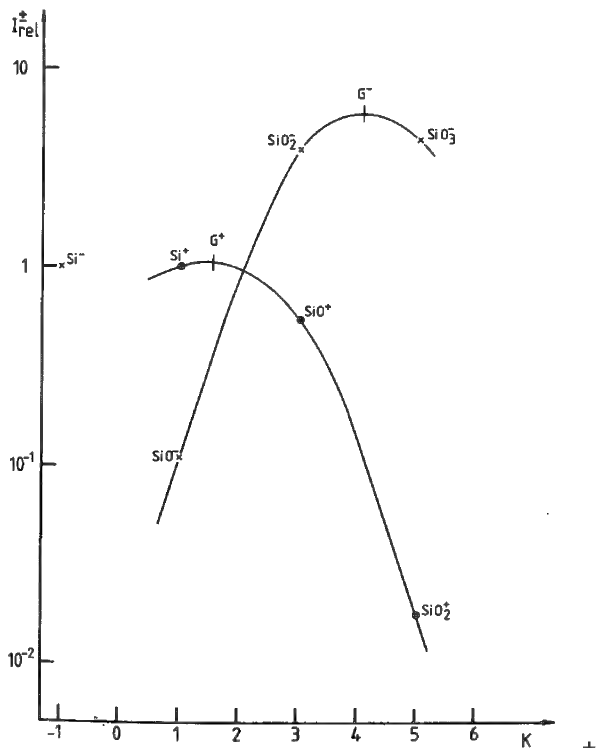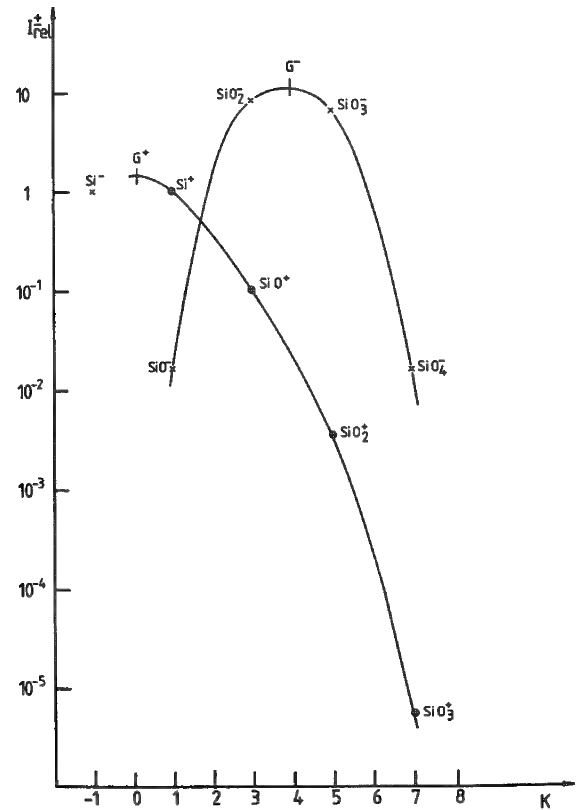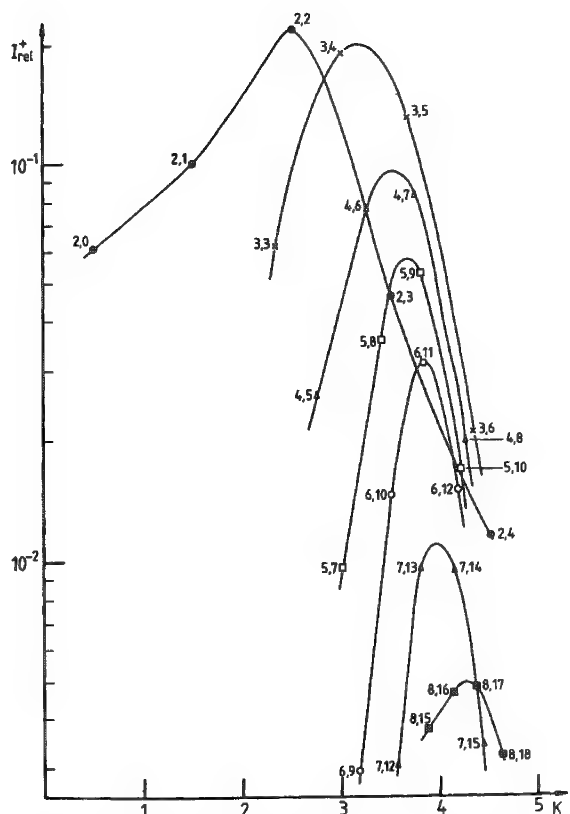
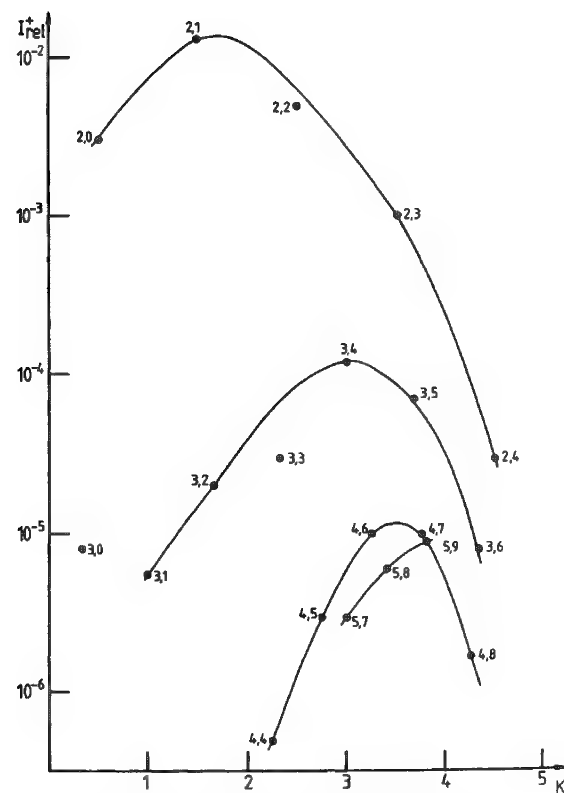FIG. 3.--Relative intensity of ions $Si_mO_n^+$ (m > 1) from pulsed-laser irradiated silica as function of fragment valence K.

FIG. 4.--Relative intensity of the ions $Si_mO_n^+$ (m > 1) from oxygen-bombarded silicon (with bleeding of oxygen gas) as function of fragment valence K. (Data taken from Ref. 23.)

$Si_8O_n^+$ parabola may partly be due to practical difficulties of accurate measurement of the relevant peak areas of signals that are quite close to the detection limit.

Richter and Trapp's[23] dynamic SIMS data on $Si(O_2^+$ bombardment and O_2 gas admission) are presented in Fig. 4, for $Si_mO_n^+$ (2 < m < 5). Comparison of Figs. 3 and 4 shows that Plog's parabolas for dynamic SIMS spectra tend to be broader. Morever, the intensity drop for increasing m is much more pronounced than for LAMMA spectra of SiO_2, even though Richter and Trapp assume that at the accepted energy range of 0-15 eV for the secondary ions, the intensities for the larger clusters are overestimated by a maximum factor of 3 (compared to those for the smaller clusters). The fact that their measurements were performed on silicon at a partial oxygen pressure of "only" 7×10^{-3} Pa is irrevelant, since these data agree rather well with those obtained on thermally oxidized SiO_2 layers on Si.[23] Hence, it will be assumed that the quantitative differences between Figs. 3 and 4 are related to different ion formation probabilities under laser irradiation and ion bombardment. The parameter "energy" is certainly of importance since it is known that the ratio of MO^+/M^+ ion intensities, for instance, decreases with increasing laser power.[24]

TABLE 3.--Parabola parameters of molecular ion yields (see also text).

Type of cluster	I^+_{max} this work (LAMMA)	G^+ this work (LAMMA)	G^+ Ref. 23 (SIMS)	γ^+ this work (LAMMA)	γ^+ Ref. 23 (SIMS)
SiO^+_n	1.11	1.56	0.18	1.20	1.39
$Si_2O^+_n$	0.15	2.02	1.72	1.08	0.81
$Si_3O^+_n$	0.20	3.17	2.85*	0.55	0.77*
$Si_4O^+_n$	0.094	3.47	3.40	0.45	0.46
$Si_5O^+_n$	0.052	3.67	4.16	0.36	(0.75)
$Si_6O^+_n$	0.028	3.83		0.31	
$Si_7O^+_n$	0.011	4.01		0.27	
$Si_8O^+_n$	0.0049	4.22		0.45	

Type of cluster	I^-_{max} this work (LAMMA)	G^- this work (LAMMA)	G^- Ref. 23 (SIMS)	γ^- this work (LAMMA)	γ^- Ref. 23 (SIMS)
SiO^-_n **	6.39	4.08	3.99	1.08	0.81
$Si_mO^-_m$	not applicable				

* Si^+_3 not included in the fitting calculations.

** Si^- not included in the fitting calculations.

For negative molecular ions containing more than one Si atom, we only observe ions of the type $Si_mO^-_{2m+1}$ and, to a lesser extent, $Si_mO^-_{2m}$; hence Plog's model cannot be evaluated for these negative ions. This situation is also encountered in negative SIMS spectra.[23]

Conclusion

In spite of quantitative differences between LAMMA and SIMS spectra of SiO_2, all general features are similar, which suggests that for other materials, too, SIMS literature data can be consulted for estimating the extent of mass spectral interferences that might occur in laser microprobe mass analysis.

References

1. N. Fürstenau and F. Hillenkamp, "Laser-induced cluster ions from thin foils of metals and semiconductors," *Intern. J. Mass Spectrom. Ion Phys.* 37: 135-151, 1981.

2. E. Hamer et al., "LAMMA- and SIMS/AES-measurements on Fe-Ti alloys," *Fresenius Z. Anal. Chem.*, 308: 287-289, 1981.

3. L. Salvati et al., "Laser microprobe mass analysis of NH_4ReO_4, $AgReO_4$ and $Al(ReO_4)_3$," *Spectroscopy Letters*, submitted 1980.

4. E. Denoyer et al., "Laser microprobe mass spectrometry: I. Basic principles and performance characteristics," *Anal. Chem.* 54: 27A-41A, 1982.

5. C. Plog et al., "Empirical formula for the calculation of secondary ion yields from oxidized metal surfaces and metal oxides," *Surface Sci.* 67: 565-580, 1977.

6. U. Haas et al., "A quantitative interpretation of LAMMA spectra based on a local thermodynamic equilibrium (LTE) model," *Fresenius Z. Anal. Chem.* 308: 270-273, 1981.

7. P. Surkyn and F. Adams, "Laser microprobe mass analysis of glass microparticles," *J. Trace and Microprobe Techniques* (in press).

8. R. Gijbels et al., "Anionic surfactant films as standards for quantitative laser microprobe mass analysis," *Microbeam Analysis--1982-378*.

9. H. J. Heinen, "On ion formation in laser desorption mass spectrometry with LAMMA," *Intern. J. Mass Spectrom. Ion Phys.* 38: 309-322, 1981.

10. N. Fürstenau, "Thermodynamic properties of laser induced evaporation processes," *Ion Formation from Organic Solids*, in A. Benninghoven, Ed., Springer Series in Chem. Phys. (in print).

11. N. Fürstenau, "Investigation of laser induced damage, evaporation and ionization with homogeneous inorganic target foils," R. Kaufman and F. Hillenkamp, Eds., *Proc. Symp. Laser-Micro-Mass-Analysis*, Springer (in print).

12. P. Joyes, *J. Phys. Chem. Solids* 32: 1269, 1971.

13. G. Staudemaier, *Radiat. Eff.* 18: 181, 1973.

14. G. P. Können et al., *Radiat. Eff.* 21: 269, 1974; 26: 23, 1975.

15. K. Wittmaack, *Surf. Sci.* 68: 118, 1977.

16. K. Wittmaack, "On the mechanism of cluster emission in sputtering," *Phys. Lett.* A-69: 322, 1979.

17. M. Leleyter and P. Joyes, *J. Phys.* (Paris) 36: 343, 1975.

18. A. E. Morgan and H. W. Werner, "Molecular versus atomic secondary ion emission from solids," *J. Chem. Phys.* 68: 3900-3909, 1978.

19. F. Hillenkamp et al., *Appl. Phys.* 8: 341, 1975.

20. R. Kaufmann et al., Proc. 13th Ann. Conf. Microbeam Analysis, 1978, 16A-16E.

21. H. Nullens, personal communication.

22. W. Stöber et al., "Controlled growth of monodispersive silica spheres in the micron size range," *J. Coll. Interface Sci.* 26: 62-69, 1968.

23. C.-E. Richter and M. Trapp, "Atomic and cluster ion emission from silicon in secondary ion mass spectrometry: I," *Intern. J. Mass Spectrom. Ion Phys.* 38: 21-33, 1981.

24. E. Michiels and R. Gijbels, unpublished data.

LASER MICROPROBE MASS ANALYSIS OF ZWITTERIONIC QUATERNARY AMMONIUM SALTS

K. Balasanmugam and D. M. Hercules

Characterization of involatile and thermolabile compounds by mass spectrometry has been achieved by soft ionization methods such as Field Desorption (FD), Laser Desorption (LD), Chemical Ionization (CI), Fast Atom Bombardment (FAB), and Secondary Ion Mass Spectrometry (SIMS).

The low volatility of quaternary ammonium salts limits the application of Electron Impact (EI) and CI; characterization of these compounds has been reported using SIMS, FD, Chemical Ionization Desorption (CID), and LD. Difficulties in obtaining negative ion spectra in most of the techniques limit their application. Laser Microprobe Mass Analysis (LAMMA) provides a direct ionization method for quaternary ammonium salts; positive and negative ion spectra are of very high intensity.

In this study, the analysis of zwitterionic quaternary ammonium salts of different structural classes will be presented. A dominant intermolecular alkyl transfer reaction leading to "pair production" has been observed for all compounds studied. Such a process was suggested for FD of these compounds, where only the positive component of the pair-production was detected.

$$2 \; R\!-\!\overset{\displaystyle R'}{\underset{\displaystyle R}{N}}(CH_2)_5COO^- \longrightarrow [R\!-\!\overset{\displaystyle R'}{\underset{\displaystyle R'}{N}}(CH_2)_5COOR]^+ \; [\overset{\displaystyle R'}{\underset{\displaystyle R'}{N}}(CH_2)_5COO]^-$$
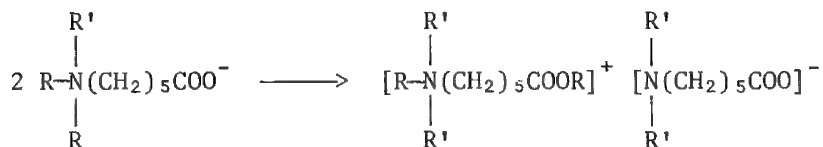
Figure 1 shows the positive and negative ion spectra of one example studied. Methyl group transfer reaction has been confirmed by the detection of both positive and negative components $[(M + CH_3^+)$ and $(M - CH_3^-)]$ of the pair.
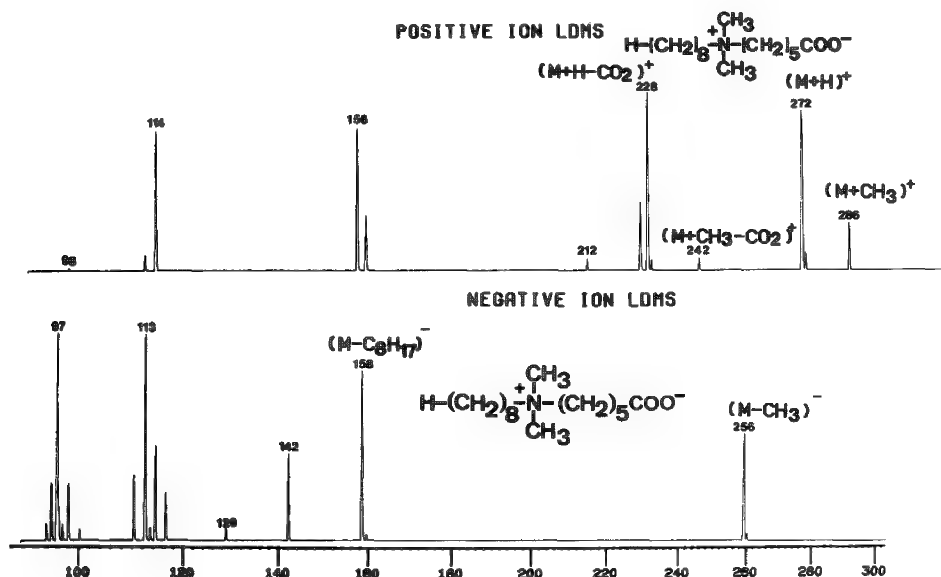

FIG. 1

The authors are at the Department of Chemistry, University of Pittsburgh, Pittsburgh, PA 15260.

ISOTOPIC ANALYSIS WITH THE LASER MICROPROBE MASS ANALYZER

D. S. Simons

The Laser Microprobe Mass Analyzer (LAMMA),[1] which combines a laser ablation ionization source with a time-of-flight mass spectrometer, has proved to be a versatile tool for materials analysis of particles and thin sections.[2] Because a mass spectrometer is used as the detector of the emitted ions, LAMMA is capable of determining isotopic as well as elemental abundance information. However, the author is aware of only one published study to date that has exploited this isotopic capability.[3] It is the purpose of this paper to discuss the performance of LAMMA in the determination of relative isotopic abundances of an element.

The determination of isotopic abundances in LAMMA is inherently more precise than the determination of elemental abundances. In the latter case relative ionization efficiencies among elements can be strongly affected by the details of the laser-solid interaction, in analogy with the well-known matrix effects that arise from the ion-solid interaction in secondary ion mass spectrometry (SIMS). Matrix effects do not occur for the isotopes of a given element since they all have the same electronic properties.

The best relative precision for a single isotopic ratio determination by LAMMA so far is about 5% (one standard deviation), as illustrated by data in Table 1 for the isotopic ratios among the major isotopes of lead, which was present as a constituent of a thin glass

TABLE 1.--Isotopic rations of lead-K1113 glass film: Summary of 10 analyses.

	Peak Height	Peak Area
206/208	0.493	0.507
RSD (1%)	5.1	6.0
207/208	0.447	0.437
RSD (%)	4.5	5.8
206/207	1.104	1.161
RSD (%)	4.8	4.0

film. The relative standard deviations of the ratios for 10 separate spectra of closely spaced regions range from 4% to 6% and are independent of the calculation technique.

One inherent instrumental limitation of precision is the 8-bit resolution of the transient waveform recorder that is used to digitize and store the mass spectrum. The range of uncertainty in the measurement of an intensity that is just below full scale is approximately ±0.5 of the least significant bit for the peak and the same uncertainty will be present in the background determination. The combined relative error is about 0.3% for the peak minus background. Since the ^{206}Pb and ^{207}Pb peaks were about one-half of full scale in this experiment, the digitization error contributes between 0.6% and 0.8% to the uncertainties in the ratios determined by peak height in Table 1. For ratios based on peak area the digitization error has a slightly smaller effect (from 0.5% to 0.7%).

The author is with the Microanalysis Group, Center for Analytical Chemistry, National Bureau of Standards, Washington, D.C. 20234. This work was supported by the Air Force Technical Applications Center under contract T/0411/NP/NBS.

The dynamic accuracy of the transient recorder is a second and more important factor that affects the precision of isotope ratio measurements. Although the accuracy of the analog-to-digital converter may be 8-bits for input signals that vary slowly with time, the bandwidth of the recorder is only 25 MHz. The effective bit resolution is therefore severely degraded if the measured waveform has major frequency components that are comparable to or greater than the bandwidth of the recorder. Figure 1 shows the contents of the transient recorder memory channels for the Pb isotopes taken at a sampling interval of 10 ns. Since the channel contents can change by a factor of 2 in adjacent channels it is clear that frequency components above 25 MHz are present in these pulses. Therefore it is reasonable to conclude that the precision of the transient recorder is reduced by this and other dynamic digitization errors to 4 or 5 bits rather than 8.[4] This conclusion would completely account for the measured ratio precisions shown in Table 1.

An example of the potential application of LAMMA to isotopic analysis problems is the determination of the half-life of ^{187}Re by measurement of the ingrowth with time of ^{187}Os in a sample of rhenium that has been spiked with a known amount of a reference isotope
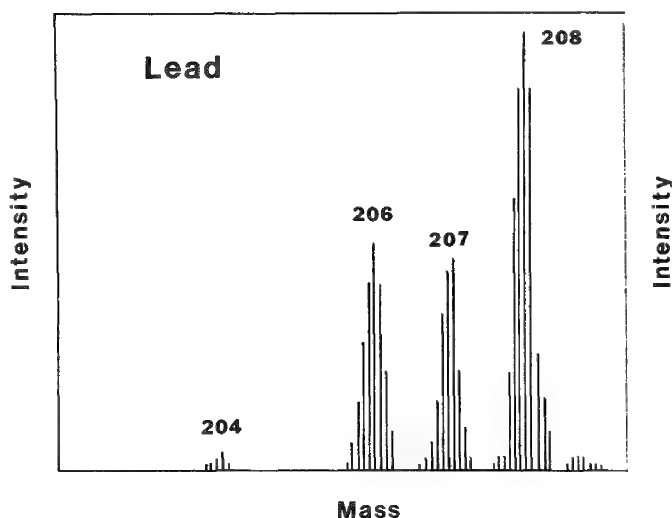

FIG. 1.--LAMMA Spectrum of lead isotopes. Each vertical line represents contents of single memory channel of transient recorder. Sampling time is 10 ns/channel.
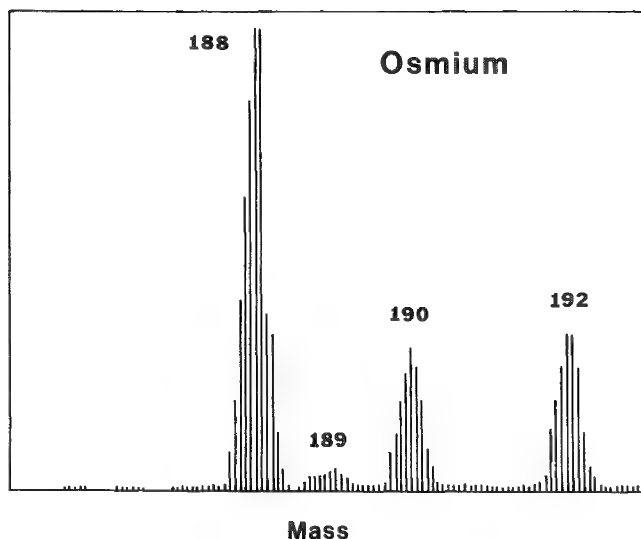

FIG. 2.--LAMMA spectrum of osmium isotopes from non-natural sample of osmium chloride.

such as ^{190}Os. For this experiment the total quantity of ^{187}Os created in one year from 1 kg of rhenium is about 6 ng. With the current state of the art, no other mass spectrometric technique can do a routine isotopic analysis of osmium with this amount of material.

As a test of the capability of LAMMA to perform this type of measurement a blind sample of osmium chloride containing approximately 10 ng of osmium with non-natural isotopic composition was supplied by Dr. Manfred Lindner of Lawrence Livermore National Laboratory. A similar sample of natural osmium was used to calibrate the nonlinear response of the electron multiplier detector. The correction factor for this effect was as large as 30% of the measured ratio for the conditions of this experiment.

A spectrum of the non-natural osmium sample is shown in Fig. 2. It is estimated that less than 1 pg of osmium was comsumed in the acquisition of a single spectrum. Isotopic ratios were calculated from peak areas of 10 such spectra, corrected for detector nonlinearity, and averaged. The resulting values are shown in Table 2 along with the revealed isotopic composition of the sample. It is clear that LAMMA is capable of determining isotopic ratios from less than 1 ng of osmium with an accuracy approaching 1% of the ratio value when the ratio value is greater than 0.2. These preliminary results give confidence that LAMMA can be used to improve greatly the accuracy with which the half-life of ^{187}Re is known at present.

TABLE 2.--Isotopic ratios of osmium (non-natural mixture): Average of 10 analyses.

	186/188	187/188	189/188	190/188	192/188
Ratio determined	<0.005	<0.005	0.037	0.233	0.263
by LAMMA			±0.002[*]	±0.008	±0.007
True ratio	0.0015	0.0019	0.031	0.232	0.256

[*] one standard deviation of the mean

References

1. Certain commercial instruments are identified in this paper in order to specify the experimental procedure adequately. Such identification does not imply NBS recommendation or endorsement, nor does it imply that the equipment identified is necessarily the best available for the purpose. This paper is not subject to copyright.

2. F. Hillenkamp and R. Kaufmann, Eds., Proceedings of LAMMA Symposium, Dusseldorf, 8-10 October 1980, *Z. anal. Chem.* 308: 193-320, 1981.

3. P. Engler and U. Herpers, "Isotopic anomalies of osmium from different deposits determined by the laser microprobe mass analyzer (LAMMA)," *Inorg. Nucl. Chem. Letters* 16: 37-43, 1980.

4. N. A. Robin and R. Ramirez, "Capture fast waveforms accurately with a 2-channel programmable digitizer," *Electronic Design* 28: 50-55, 1980.

AN EXAMPLE OF THE USE OF COMBINED TECHNIQUES OF ANALYTICAL TRANSMISSION ELECTRON MICROSCOPY FOR PHASE IDENTIFICATION

D. G. Konitzer and H. L. Fraser

The general area of analytical transmission electron microscopy has been the subject of considerable development over the past several years.[1,2] Of particular interest for phase identification are the techniques involving energy-dispersive x-ray spectroscopy (EDS), electron energy loss spectroscopy (EELS), and selected area and convergent beam electron diffraction (SAD and CBED, respectively), coupled with either conventional transmission or scanning transmission electron microscopy (TEM and STEM, respectively). The present paper gives an example of phase analysis in a Ti-8Al-4Y alloy, where it is shown that it is often necessary to use a combination of these techniques to permit a unique determination of the identity of a given phase.

The microstructure of arc-melted Ti-8Al-4Y apparently consists of three constituents namely the α-Ti matrix, an interdendritic precipitate, and a finely dispersed phase.[3] The interest in this alloy arises from the possibility of producing a fine dispersion of Y_2O_3, and so the main thrust has been in establishing the nature of the finely dispersed phases. To accomplish this goal, one must first determine the constitution of the starting materials, in particular the nominally pure (99.95%) Y used in these experiments. In fact, it was found that the Y consisted of two phases, one the hexagonal matrix and the second between 5-10 vol% of a precipitate phase.[3] The work described below involves the application of the various analytical techniques for the identification of the second phase present in pure Y and the phases in the as arc-melted Ti-based alloy.

An alloy of Ti-8Al-4Y was arc-melted under Ar from nominally pure components (> 99.95% pure). Thin foils of the elemental components and the alloy were prepared by conventional techniques, and any resultant surface films were removed by Ar ion sputtering in an Auger electron spectrometer. These foils were examined in two Philips EM400T transmission electron microscopes, one equipped with a STEM attachment and an EDS facility, the other with an EELS spectrometer. In addition, a VG HB5 dedicated STEM instrument with both EDS and EELS facilities was used.

Identification of Second-phase Precipitates in Nominally Pure Y.

a. Microchemical Determinations. The microchemistry of the second phase in nominally pure Y was studied by both EDS and EELS in combination with either STEM or TEM. The EDS determination indicated that, regarding elements with $z > 11$, the phase contained only Y (with a small impurity concentration of Ta, present in both matrix and second phase), whereas the EELS studies revealed that a relatively high 0 concentration was also present. From these results, it was thought that the phase was the oxide Y_2O_3, but this stoichiometry could not be established experimentally by these techniques. Electron diffraction was therefore used to determine the crystal structure and lattice parameter of this phase, and in this way uniquely established its nature.

b. Electron Diffraction Studies. At first, SAD patterns were recorded; Fig. 1 shows three such patterns with the incident electron beam parallel to the various zone axes indicated. Although it is clear from this figure that the unit cell is indeed cubic, it was not possible to index the diffraction maxima uniquely on the basis of primitive,
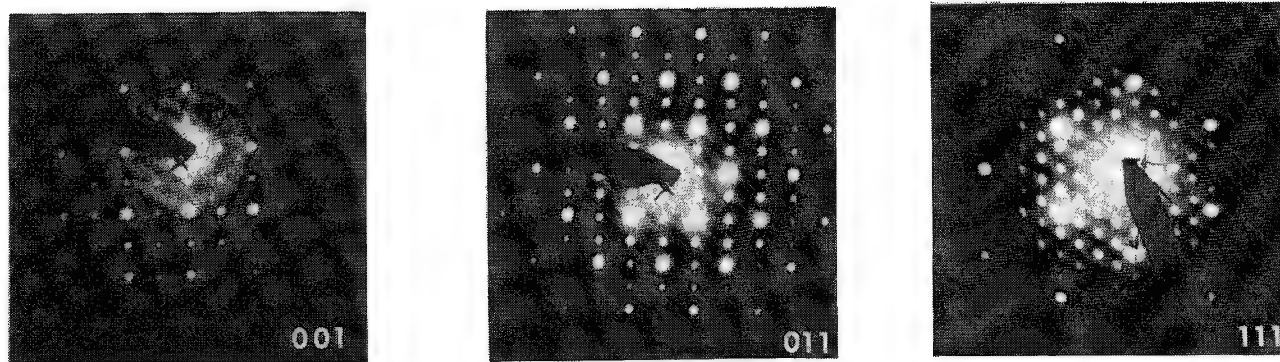
FIG. 1.--Selected area diffraction patterns with electron beam parallel to [001], [011], [111], from region of second phase in pure Y.

face-centered or body-centered cubic cells; some reflections appear to be unexpectedly absent, and relatively intense high-order Bragg reflections are present in the patterns. It was therefore necessary to use CBED to permit structure determination by noting the symmetries exhibited in diffraction patterns.[4] This technique involves positioning a focused probe of electrons with a finite convergence on the feature of interest, and recording the resultant diffraction pattern. The analysis involves three steps: the determination of the point group, of the nature of the unit cell and, finally, of the space group.

    i. Crystal Point Group Determination. The procedure adopted by Buxton et al.[4] is followed, where for a given zone axis the pattern symmetries in the zero-order Laue zone (projection diffraction symmetry), bright field (000 reflection), and whole pattern (including the higher-order Laue zone reflections) are determined. Three different zone axis convergent beam diffraction patterns were recorded in this experiment, corresponding to the incident electron beam being parallel to [001], [011] and [111] (Fig. 2). The resulting symmetries are listed in Table 1, and from Table 2 of Buxton et al. it is possible to deduce the possible diffraction groups of these patterns (listed in the last column of our Table 1). As can be seen, there is an apparent uncertainty in the diffraction group corresponding to the [001] zone axis; however, it is clear from Table 2 that m3 is the only consistent crystal point group which contains one of each of the possible diffraction groups from the three zone axes. It is concluded, then, that the crystal point group of the second phase of interest is m3.

    ii. Determination of the Nature of the Unit Cell. It is possible to construct the reciprocal lattice cell corresponding to the structure of the phase by projecting the positions of reflections in the higher-order Laue zones in the [001] zone axis pattern (Fig. 2a) down onto the zero-order Laue zone. In this particular case, the reciprocal lattice consists of a face-centered cell, and consequently the unit cell in real space must be based on a body-centered cubic cell. Further, the diameters of the rings defined by the higher-order Laue zone reflections may be measured, from which a rather accurate lattice parameter, a, may be deduced.[5] This procedure has been followed in the present work, and a value of a = 1.06 nm has been determined.

    iii. Determination of the Space Group. The space group may be deduced from the information derived above and the absent reflections in the diffraction patterns. Thus, of the seven space groups based on a point group of m3, only two correspond to body-centered cells, namely Im3 and Ia3.[6] We may distinguish between these two space groups by noting that the (011) reflections are absent from the selected area diffraction patterns (Fig. 1); such reflections are indeed forbidden in the case of the Ia3 space group, but are allowed for Im3. It is concluded that the space group of the phase of interest is Ia3. This space group has been shown previously to be consistent with the structure Y_2O_3,[7-9] and it is reasonable to assume that this is indeed the stoichiometry of the second phase present in nominally pure Y. Furthermore, the value of the lattice parameter derived above is essentially identical with that determined by x-ray techniques

TABLE 1.--Experimentally determined pattern symmetries for given zone axes, together with deduced diffraction groups.

Zone Axis	Projection Diffraction Symmetry	Bright Field Symmetry	Whole Pattern Symmetry	Deduced Diffraction Group
[001]	2mm	2mm	2mm	2mm or 2mm1$_R$
[111]	6	3	3	6$_R$
[011]	2mm	-	m	2$_R$mm$_R$

TABLE 2.--All possible crystal point groups containing either 2mm or 2mm1$_R$ diffraction groups. Letter x indicates that given diffraction group is consistent with particular point groups. It is concluded that m3 is the only point group containing one diffraction group from each of the given zone axes.

Zone Axis	Deduced Diffraction Group	Possible Crystal Point Groups						
		m3	$\overline{6}$m2	mm2	mmm	4/mmm	6/mmm	m3m
[001]	2mm		x	x				
	2mm1$_R$	x			x	x	x	x
[111]	6$_R$	x						
[011]	2$_R$mm$_R$	x			x	x	x	x

in bulk Y_2O_3 samples.[9] It is therefore concluded that the second phase in the nominally pure Y used in these experiments is Y_2O_3. Furthermore, it is now possible to associate diffraction patterns with reflections of similar intensities to those in Fig. 1 with the structure Y_2O_3. This fact is used below uniquely to identify both the interdendritic and finely dispersed phases in arc-melted Ti-8Al-4Y alloys.

Identification of the Interdendritic Precipitate

   a. Microchemical Determinations. The microchemistry was studied by STEM coupled with EDS. A bright field transmission electron micrograph of a part of an interdendritic precipitate is shown in Fig. 3(a), and an EDS x-ray spectrum recorded from a point on this feature is shown in Fig. 3(b). It can be seen that the phase is rich in Y, and some Ti is also apparently present. It is not possible to assume that this Ti is alloyed with the Y since it has not been established that the matrix has been totally polished away from the protruding phase. However, the spectrum does indicate that the major constituent of the interdendritic precipitate is Y.

   b. Electron Diffraction Studies. SAD patterns were recorded from the phase of interest, with the electron beam parallel to [001], [111], and [011], and they are essentially identical with those presented in Fig. 1. In view of the microchemical data and the work involving convergent beam electron diffraction, it is concluded that the interdendritic precipitate is also Y_2O_3. It is not possible to comment on the possibility of alloying elements being present in the oxide.
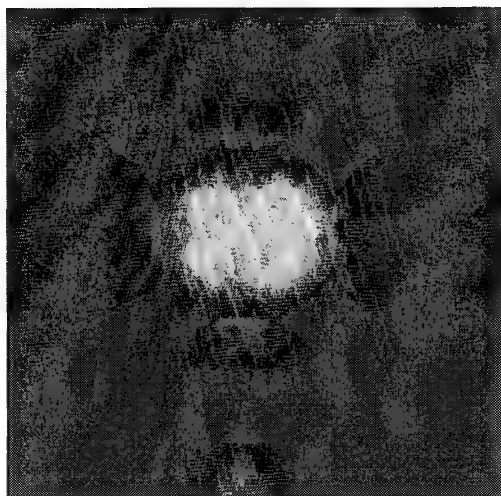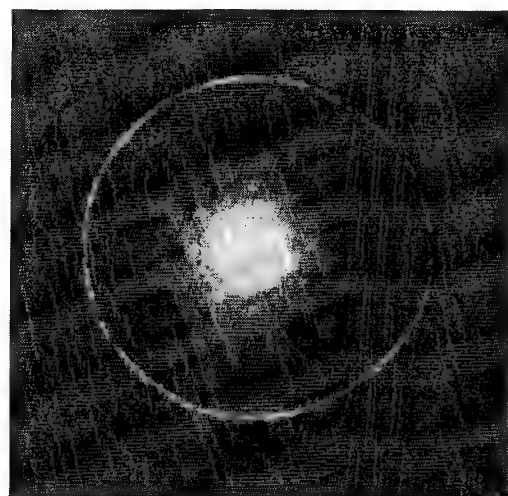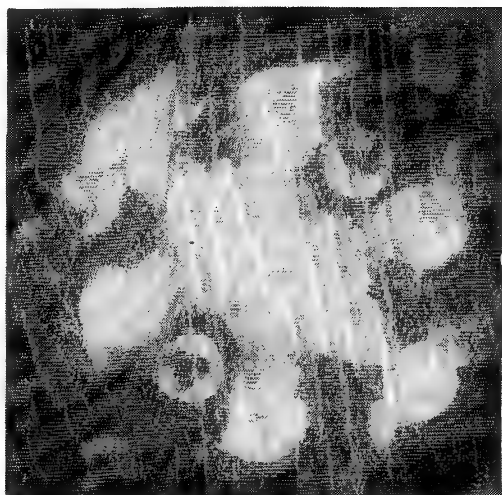
FIG. 2.--(a) [001], (b) [011], (c) [111]: Convergent beam zone axes patterns from second phase in pure Y showing bright field disk, whole pattern, and projection diffraction symmetries.

FIG. 3.--(a) Bright field micrograph of interdendritic region protruding from edge of the foil in arc-melted Ti8A14Y; (b) EDS spectrum from region in (a).

Identification of the Finely Dispersed Phases

   a. Microchemical Determinations. A typical precipitate is shown in Fig. 4(a); the EDS x-ray spectrum that results when the electron probe is focu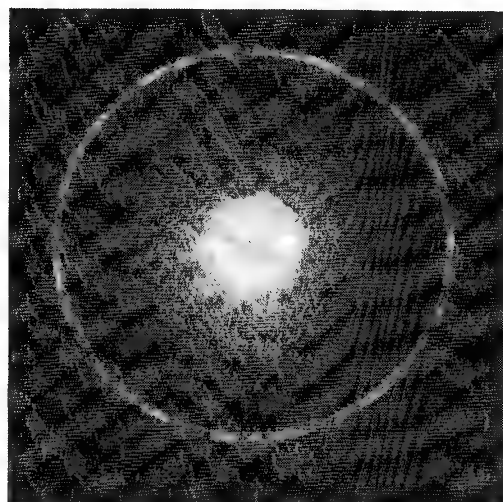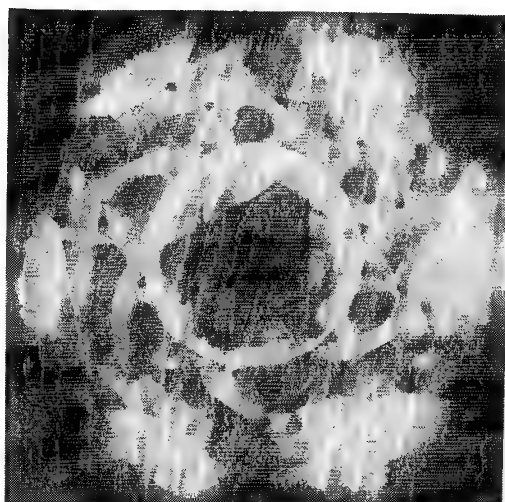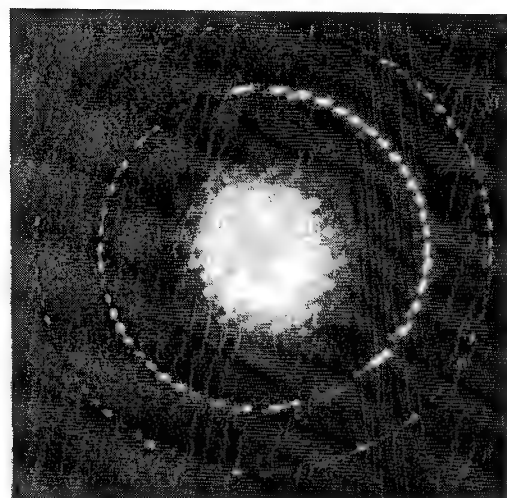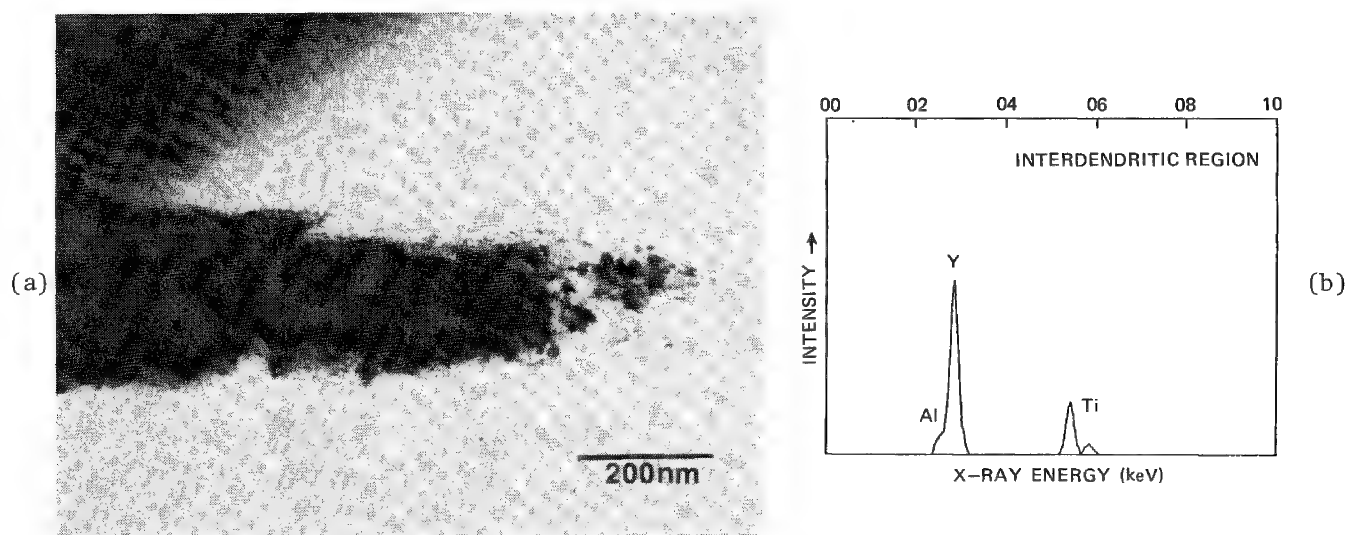sed to a diameter of about 100Å and positioned at the center of the particle image is given in Fig. 4(b). It is expected that the electron beam will be scattered out of the precipitate and so much of the Ti and Al present in this spectrum must be attributed to contributions from the matrix. Thus, it appears that the phase consists mainly of Y. Furthermore, if it were to be assumed that the particle were situated on one side of the thinned matrix, the particle chemistry would be given approximately by the subtraction of the matrix spectrum (Fig. 4c) from the (assumed) combined spectrum (Fig. 4b). Such a manipulation yields a spectrum consisting essentially of the Y peak, which again indicates that, regarding elements with $z \geq 11$, the phase is composed of Y.

   b. Electron Diffraction Studies. Because of the small size of the precipitates, it was not possible to obtain SAD patterns solely from the precipitate. For this reason, the electron probe was focused onto the particle and CBED patterns were recorded with the beam parallel to [111] and [011]. They are shown in Fig. 4(d), and it can be seen that the angle of convergence has been minimized to permit a comparison to be made between these and the selected area patterns shown in Fig. 1. Careful consideration of the positions and intensities of the reflections present in these various patterns leads to the conclusion that they are essentially identical. The structure of the finely dispersed phase is therefore the same as Y_2O_3, and in view of this fact and the microchemical determination described above, it may be concluded that the phase is indeed Y_2O_3.

   The second phase present in nominally pure Y, and the interdendritic precipitates and finely dispersed phases in as arc-melted Ti-8Al-4Y have all been identified as Y_2O_3. The identification was made by a combination of several of the techniques of analytical transmission electron microscopy. The successful structural determination would not have been possible by any one technique alone.

References

   1. *Analytical Electron Microscopy*, Report of a Specialist Workshop, 1976, Cornell University, Ithaca, NY.
   2. *Analytical Electron Microscopy*, Proc. 2nd Workshop, 1978, Cornell University, Ithaca, NY.
   3. B. C. Muddle, D. G. Konitzer, and H. L. Fraser, "Dispersion strengthened titanium alloys by rapid solidification processing," in preparation.

4. B. F. Buxton, J. A. Eades, J. W. Steeds, and G. M. Rackham, "The symmetry of electron diffraction zone axis patterns," *Phil. Trans. Roy. Soc.* A281: 171,

5. J. W. Steeds, "Convergent beam electron diffraction," in J. J. Hren, J. I. Goldstein, and D. C. Joy, Eds., *Introduction to Analytical Electron Microscopy*, New York: Plenum, 1975, 387-422.

6. K. Lonsdale, Ed., *International Tables of X-ray Crystallography*, Birmingham, England: Kynoch Press, 1962.

7. L. Pauling and M. D. Shappell, "The crystal structure of bixbyite and C-modification of the sesquioxides," *L. Kristallogr.* 75: 128, 1932.

8. P. A. Fert, "Structure de quelques oxydes de terres rares," *Bull. Soc. Franc. Miner. Crist.*, 70: 267, 1962.

9. M. G. Paton and E. N. Maslen, "A refinement of the crystal structure of yttria," *Acta Cryst.* 19: 307, 1965.

(a)

(b)

(c)

(d)   (e)
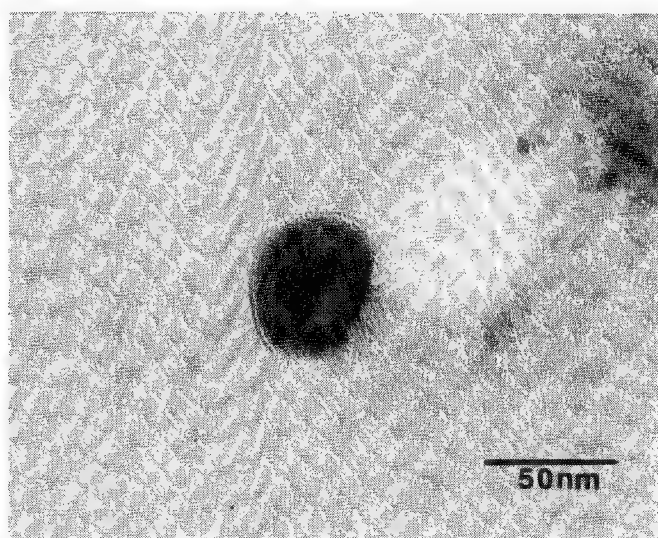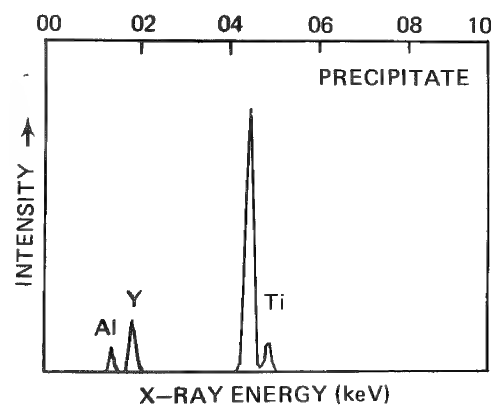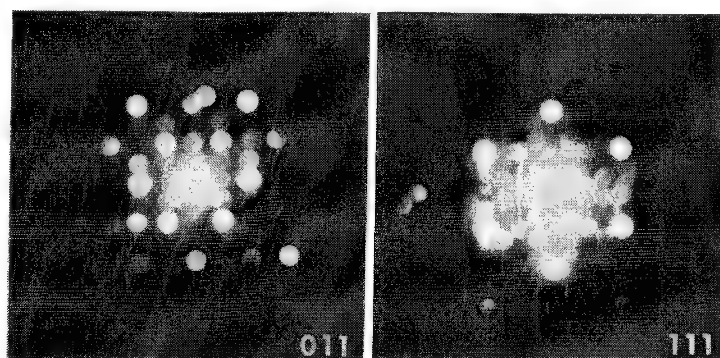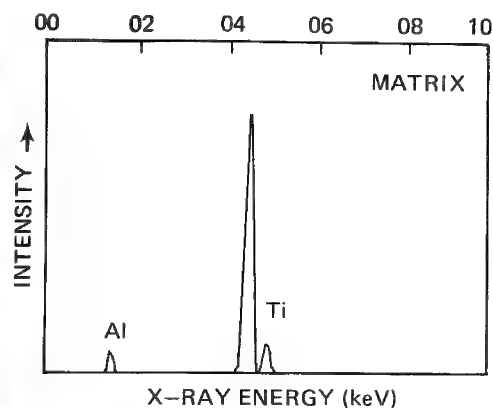
FIG. 4.--(a) Bright field micrograph of a typical dispersoid particle; (b) EDS spectrum obtained when probe is placed on particle; (c) EDS spectrum obtained from adjoining matrix; (d) [011] and (e) [111]: Convergent beam zone axis patterns obtained from particle in (a).

A NEW METHOD OF MEASURING ACTIVATION ENERGY BY ELECTRON PROBE ANALYSIS

G. W. Qiao

It is well known that segregation of elements (such as P, As, Sb, Bi) (especially grain boundary segregation) has very important effects on the mechanical properties (especially on embrittlement and fracture toughness) of steels and alloys. The formation and changes of elements segregation is controled by the diffusion mechanism of the elements. So far, a great many researches into the diffusion and activation energy have been undertaken. But the values calculated from thermodynamics cannot be applied in practical situations because of failure to consider the defects that play a leading role in the diffusion processes; and activation energy is difficult to measure in practice with conventional methods. We have had a try at measuring practical activation energy of phosphorus in steel by EPA.

The principal consideration is as below. The original segregation of the elements (e.g., phosphorus in steel) was formed during solidification of the liquid. When prime austenite grains were formed, segregation of the element should satisfy the formula $C = C_0 \exp(Q/RT)$, where C_0 is the average concentration and C is the concentration at the grain boundaries.[1] At this point, grain boundary segregation of the element is very difficult to measure at so thin grain boundaries even by AES, because the accuracy of AES is poor, and in general the fracture surface is not wholly intergranular and is not plain enough for quantitative analysis. But after solidification the successive processing at a high temperature (e.g., rolling) changes this grain boundary segregation into some kind of body-micro segregation around the grain boundaries, as seen in a considerable number of metallographic microscopic observations. In this case, the sizes of the body-micro segregation regions are still very much smaller than the grain sizes, so the approximate conditions for deducing the above formula still apply. Therefore,

$$Q = RT \ \ln(C/C_0) \tag{1}$$

EPA is accurately qualified for micro-region chemical concentration analysis. By means of measuring the segregation coefficients C/C_0 (statistical mean value) using EPA, we can calculate the activation energy for that situation from Eq. (1).

Although the diffusion activation energy is very structure sensitive, it is mainly controlled by defects formed during plastic deformation. As diffusion of the atoms along dislocation tubes or subgrain boundaries (dislocation network) is virtually the main micro-diffusion mechanism, the higher the density of the defects, the lower the diffusion activation energy. Roughly, the diffusion activation energy Q can be considered inversely proportional to the density of the dislocations ρ, and ρ is proportional to the plastic deformation ratio δ. (In practice, we usually use the area deformation ratio Θ, i.e., $\delta \propto \sqrt{\Theta}$.) Thus we can say that $Q \propto 1/\rho \propto 1/\delta \propto 1/\sqrt{\Theta}$, and

$$\ln(C/C_0) = A/\sqrt{\Theta} \tag{2}$$

where A is a constant.

This linear relationship between logarithm of segregation coefficients and reciprocal of the square root of the area deformation ratio has been proved true by EPA experimental results on 12MnPV steel. The 80kg ingot of 12MnPV steel was subjected to various deformations at 1200°C. We use ($MgCl_2$ + $CuCl_2$) etching reagent for displaying micro-segregation regions of phosphorus in the steel (very clearly). Then the micro-segregation coefficients of phosphorus were determined by EPA. (Every value is the statistical average of several hundred times measured data.) Table 1 summarizes the measured results.

TABLE 1.--Segregation coefficients and deformation ratio

Size (mm)	Average segregation coefficient of P C/C_0	Area deformation ratio Θ	Corresponding activation energy calculated from Eq. (1) $(J\text{-}mol^{-1})$
Ingot	2.52	1:1	11319
78 × 78	1.65	8:1	6133
58 × 58	1.31	15:1	3307
18 diam.	1.07	200:1	829
8 diam.	1.01	1000:1	122

Indeed, there does exist an approximate linear relationship between logarithm of segregation coefficients of phosphorus and the reciprocal of the square root of the area deformation ratio (Fig. 1).
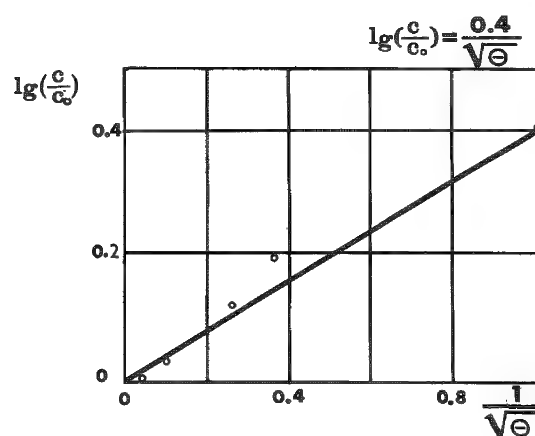
FIG. 1.--Segregation coefficient vs deformation ratio.

Constant A depends on the temperature, materials, and other experimental conditions. From this relationship we can roughly estimate how much the segregation coefficient of the element we can get at a certain deformation ratio. Obviously, both the segregation coefficient and the activation energy are useful references for steeling processing.

References

1. D. McLean, *Grain Boundaries in Metals*, London: Oxford University Press, 1957, 148.

SURFACE CHEMISTRY AND MORPHOLOGY OF 304-SS WELD AND WELD-SCALE MATERIAL

J. M. Burkstrand and D. F. Paul

Chemical reactors, either large scale or small research systems, often use stainless steel (SS) as a primary material for construction. The steel may serve as the reaction vessel itself, as input lines for the reactants, or as internal supports for the materials under study. These vessels and/or components are often modified by welding of the altered steel in place. Occasionally, not enough attention is given to the weld and the effect it can play in the reactor. This paper discusses the surface analysis of a weld in 304-SS in which the back side of the steel was exposed to air during the welding process. Not surprisingly, both the morphology and the surface chemistry of the weld is different from those of the stainless steel. Different components of the steel are seen to be segregated to the surface in different regions. The resultant particle sizes and chemistry are such that some chemical reactions taking place in the vicinity of the weld could be modified.

Although 304 stainless steel is fully austenitic, welding the 304-SS normally produces a structure of a network of retained delta ferrite in an austenite matrix.[1,2] Carbide precipitation on the austenite grain boundaries in the heat-affected zone adjacent to the weld metal is also characteristic of these welds.

Because the welds were made with the inside surface exposed to air, we expect the inside weld surface to be covered by a thick oxide. Various other workers[3-7] have examined these oxides with more bulk sensitive techniques, such as electron dispersive spectroscopy (EDS) (microns depth sensitivity), and have found these oxides to be enriched in different metals, the details of which depended on the location in or near the weld. Little or no work done has been done in examining the surfaces of these 304-SS welds with Auger electron spectroscopy (AES) because of the very small electron beam size needed to examine the highly morphological surfaces. It was the purpose of this work to examine the surfaces ($\lesssim$ 20 Å in depth) with high-resolution Auger.

Experimental

Autogenous (no filler metal added), full-penetration welds were made around the diameter of 304-SS tubes. A tungsten-electrode, inert-gas (Ar) welding technique was used. However, only the outside surface of the weld was shielded by the argon gas; inside the tube the molten weld metal was exposed to air. This technique reproduces the conditions practiced in some cases. After welding, the tubes were sectioned so that the inside weld surfaces could be examined with SEM, Auger electron spectroscopy, and scanning Auger microscopy (SAM).

The surface analysis (SEM, AES, SAM) was carried out with a Physical Electronics high-resolution electron spectrometer (beam voltage to 25 keV, beam diameter $\gtrsim$ 400 Å) located in an ultrahigh-vacuum system (operating pressure < 2.0×10^{-10} Torr). Most of the Auger data were acquired at a beam voltage of 15 keV and a current of 0.05 μA. AES analysis could not be carried out at the more commonly used beam voltages of 5 keV or less because excess charging took place. The higher-energy electron beam penetrated the oxide layer and/or particles in the weld region to the conducting substrate beneath.

The AES data were acquired in three different forms: survey spectra (point or area), multiplexed energy regions (point or area), and maps. The survey spectra were acquired to determine which elements were present in a given point or area. SAM produced maps of the two-dimensional spatial distribution of the elements on the surface. The multiplexed data, when combined with published elemental sensitivity factors,[8] were used to

The authors are at Physical Electronics, 6509 Flying Cloud Drive, Eden Prairie, MN 55344.

obtain quantitative information. When combined with Ar ion etching, three-dimensional quantitative information was obtained.

In acquiring the SAM maps, or when taking elemental line scans, one must correct for any variations in the surface topography. The Auger intensity varies with the angle of emission;[9] unless that is accounted for, an inaccurate knowledge of an element's spatial distribution will result.

Results and Discussion

Both optical and scanning electron microscopy indicated three different kinds of morphology in the weld region: (1) the weld area itself, (2) a scale just adjacent to the weld, and (3) a substrate just beneath the scale. Figures 1-3 show high resolution SEM micrographs of these three areas. Auger survey spectra (after removal of the residual atmospheric surface contamination) and the corresponding elemental concentrations (in atomic %) are shown in Figs. 4-6. The composition of the metallic elements for these three surfaces are listed in Table I, along with the bulk composition of 304-SS (as measured[10] by EDS). It is easy to note which materials have segregated to the surface in the various regions. The SAM maps of the Fe, Mn, and Si (Figs. 7, 8, and 9, respectively) in the weld region (Fig. 1) show the high degree of spatial segretation that exists for these elements. These maps have been corrected for the highly irregular surface. There is a substantial iron concentration on the large particle in the upper right of Fig. 1. The Mn is more evenly distributed, and there are several areas with a high concentration of Si.

Some points in Fig. 1, were selected for both AES survey and quantitative analysis. The quantitative results for the metallic elements are listed in Table 1. As indicated semiquanitatively by the maps, there is a significant variation in the elemental concentration on the surface over the area shown. But in all cases examined on the weld, there is a large segregation of Mn and Si to the surface. The energy positions and line shapes of the AES peaks indicate that the metals are present as oxides, as expected. These same points were examined during Ar ion etching of the surface. At point 2 of Fig. 1, the Si increased slightly 10 Å into the surface, then decreased by a factor of two after only another 50 Å had been removed. At the same time, the Fe and Mn increased proportionally. At point 3 of Fig. 1, the Si decreased by a factor of two after only 25 Å had been removed. In this region, the Mn increased whereas the Fe remained the same. The scale just adjacent to the weld material was also examined with SAM in a similar

TABLE 1.--Metallic composition (atomic %).

	Fe	Cr	Ni	Mn	Si
Bulk 304-SS	69.6	19.0	7.4	2.0	2.0
Weld (Surface)	18.6	<0.1	<0.1	38.8	42.5
Scale (Surface)	87.8	<0.1	<0.1	12.2	<0.1
Base (Surface)	32.6	11.4	17.8	<0.1	38.1
Weld, pt #1	15.8	<0.1	<0.1	53.2	30.9
Weld, pt #2	11.3	<0.1	<0.1	21.9	66.8
Weld, pt #3	8.1	<0.1	<0.1	30.4	61.5
Weld, pt #4	19.8	<0.1	<0.1	55.8	24.3
Weld, pt #5	63.8	<0.1	<0.1	19.9	16.3
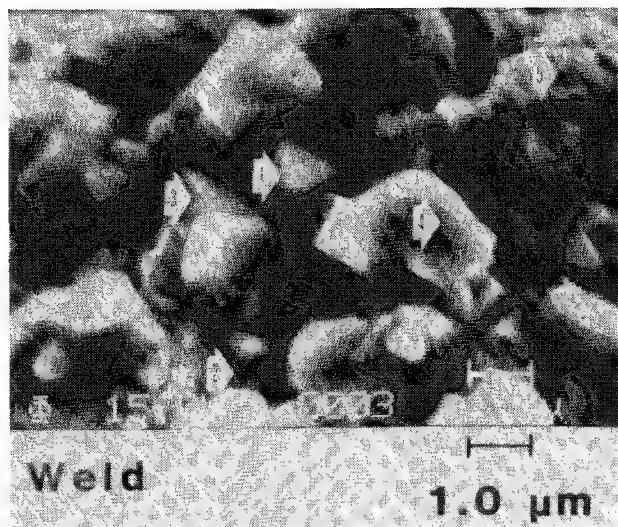
FIG. 1.--SEM micrograph of weld material; labeled points are described in text.

FIG. 4.--AES survey spectrum of weld surface shown in Fig. 1.

FIG. 2.--SEM micrograph of scale, material adjacent to weld.
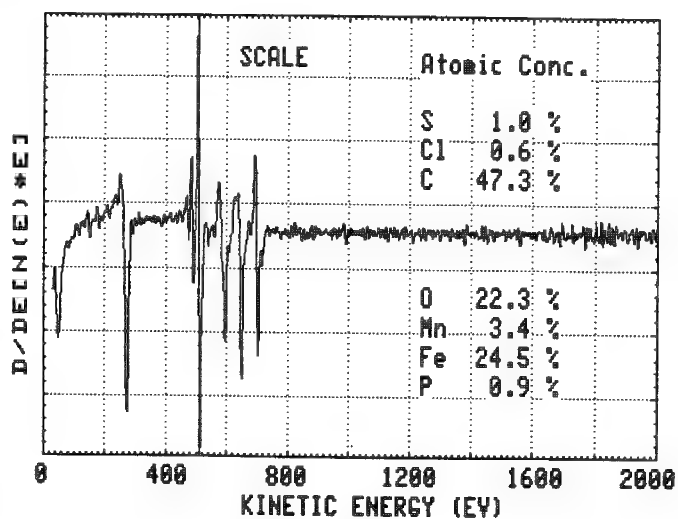
FIG. 5.--AES survey spectrum of scale shown in Fig. 2.
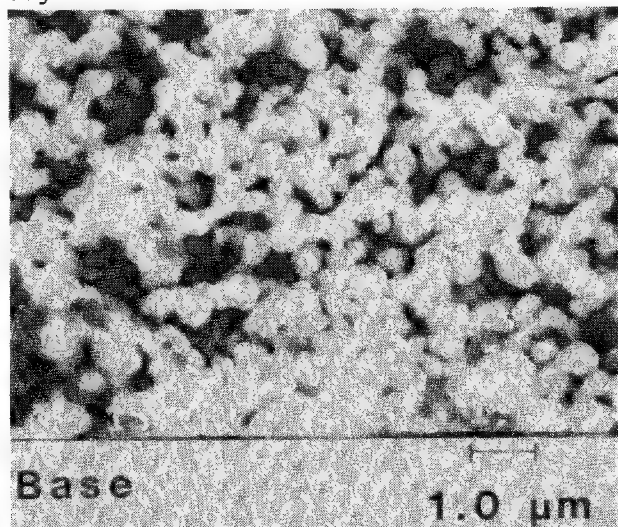

FIG. 3.--SEM micrograph of base, visible when scale is removed.

FIG. 6.--AES survey spectrum of base material shown in Fig. 3.

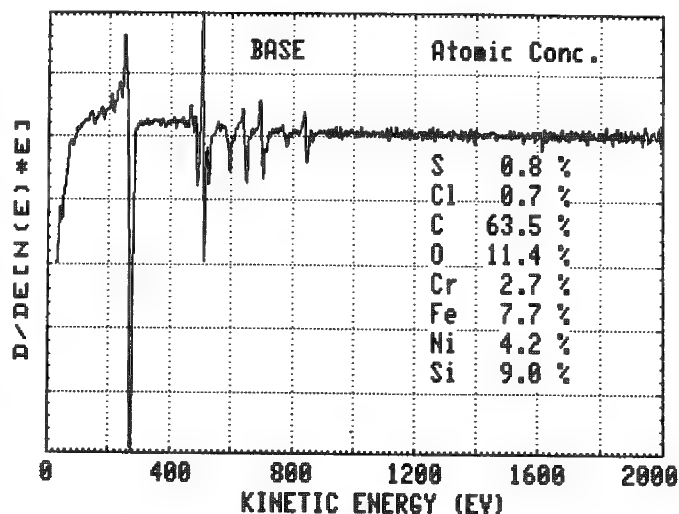fashion. The results, not shown here, indicate that the Mn is rather evenly distributed over the area shown in Fig. 2. The Fe, on the other hand, is more highly concentrated between the "white ribbons" on the surface, and these "white ribbons" show a higher concentration of carbon. Quantitative point analyses confirm that. The same data (i.e., C line shapes) suggest that the majority of the carbon present is in the form of carbide. Thus, we seem to be observing iron carbide formation along the iron oxide grain boundaries.

The AES data from the base (material below the scale, shown in Fig. 3) indicate a larger Si and Ni segregation to the surface. No striking area segregation was seen in the SAM maps; the depth profiles behaved as discussed for the scale subsurface. As the Si decreased, there was an increase in the amount of Cr present, which indicated additional segregation of the Cr in this region.

Conclusion

We have demonstrated that the microstructure and surface chemistry of a 304-SS weld joint exposed to air during welding is vastly different from the original material. The resultant particle size on the weld region is of the order of 1 μm-- a size important in certain catalytic reactions. The Auger surface analyses showed various regions where different elements had segregated to the surface. Because it is the surface chemistry and not the bulk that is important in catalysis, the effects of these kinds of modifications to the 304-SS need to be considered when chemical reactions take place in the vicinity of such a weld.

References

1. W. A. Baeslack III, A. J. Duquette, and W. F. Savage, *Corrosion* 35: 45, 1979.
2. P. E. Manning, C. E. Lyman, and D. J. Duquette, *Corrosion* 36: 246, 1980.
3. G. C. Wood, *Corr. Sci.* 2: 173, 1961.
4. D. Caplan and M. Cohen, *Trans. AIME* 194: 1057, 1952.
5. H. E. Evans, D. A. Hilton, and R. A. Holm, *Oxidation of Metals* 10: 149, 1976.
6. G. C. Allen and R. K. Wild, *J. Electron Spect.* 5: 409, 1974.
7. R. K. Wild, *Corr. Sci.* 17: 87, 1977.
8. L. E. Davis et al., *Handbook of Auger Electron Spectroscopy*, Eden Prairie, Minn.: Physical Electronics, 1976, 13-15.
9. R. L. Gerlach et al. (to be published).
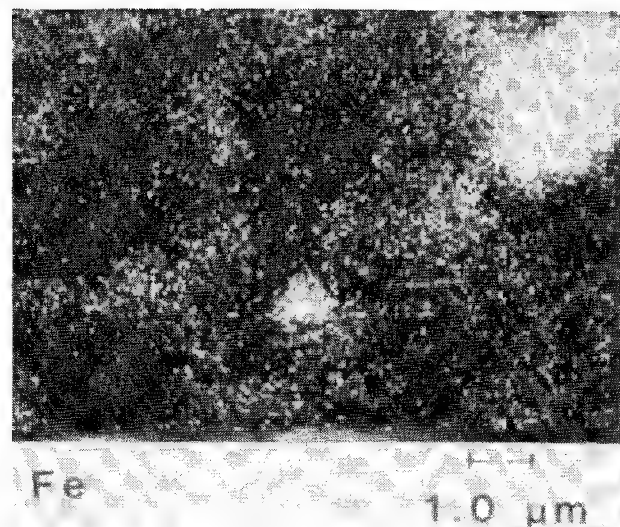10. J. M. Burkstrand (unpublished).

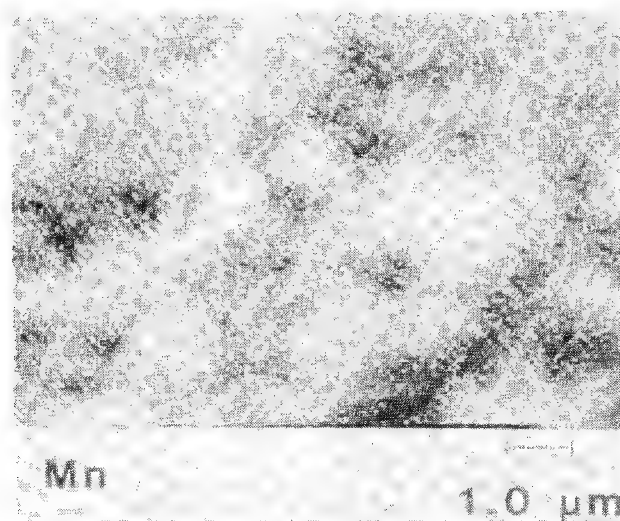FIG. 7.--SAM image for Fe over weld region shown in Fig. 1.

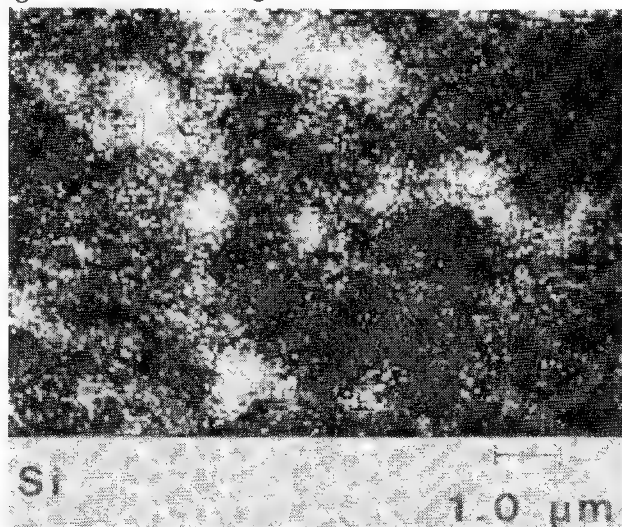FIG. 8.--SAM image for Mn over weld region shown in Fig. 1.

FIG. 9.--SAM image for Si over weld region shown in Fig. 1.

INTERMETALLIC PHASES IN THE Cu/T-6-6-2 ALLOY SYSTEM

J. R. Shappirio, P. C. Calella, and D. W. Eckart

Samples of copper and Ti-6-6-2 alloy, joined by hot isostatic pressing (HIP) techniques, have been found to fail at less than desired shear stress. Microstructural and micro-chemical investigation of such alloy couples revealed that failure occurred within the reaction zone formed between the two metals. The reaction zones were found to have a thickness consistent with the time and temperature of the joining process and to consist of parallel bands of intermetallic phases compositionally dependent on distance from the metal end-members.

Previously reported work involving interactions in copper and titanium systems include diffusion studies[1,2] performed at low solute concentrations, and the phase diagram summary reported in Hansen.[3] Wells[4] has reported on eutectic-based thin film diffusion brazing of Cu and Ti; this work was performed at atmospheric pressure, and at higher temperatures than the present study, so that beta phase decomposition was an important consideration.

Zanner and Fisher[5] have reported on the mechanical properties of diffusion-welded bonds between a commercial bronze rotating band and a Ti-6-6-2 shell body for use in experimental 155mm artillery projectiles; in their studies, the samples were observed to fail in shear in the bronze, and surface preparation of the two metals prior to joining was found to be the key factor affecting the integrity of the weld. Subsequent to their work, experimentation on similar projectiles where copper was substituted for the bronze rotating band resulted in failure on firing with catastropic separation of the rotating band from the shell casing. The present study was initiated to determine the cause of catastropic failure; the results are of interest not only because they lead to a different conclusion relative to the failure mechanism in this specific alloy system, but also because they suggest guidelines of general application in the selection of alloy systems and processing conditions where dissimilar materials must be joined and retain mechanical integrity in a high-stress (shear) environment.

Experimental

Samples of Cu/Ti-6-6-2 alloy joins utilized in this investigation were obtained either from failed fired experimental projectiles or from unfired samples prepared in a manner consistent with size, shape, materials, and fabrication procedures of the actual fired hardware. Joining of the Cu/Ti-6-6-2 alloy was accomplished by HIP diffusion bonding at temperatures ranging from 538 to 593°C at an isostatic pressure of 15 kpsi in a high-temperature cold-wall autoclave; the procedures were essentially identical to those described elsewhere[6] and differed only in cleaning procedures employed and in the manner in which vacuum sealing was accomplished prior to bonding. Prior to bonding, the copper rotating bands were cleaned in a series of baths consisting of acetone, alkaline cleaners, and finally a 5% nitric acid solution. All Ti alloy parts were cleaned sequentially in acetone, alkaline cleaner, a 2% hydrofluoric 40% nitric acid solution, and finally a 50% nitric acid solution. Sealing was accomplished by swaging of the copper band to the Ti alloy projectile body, welding of a pure Ti sleeve to the Ti body over the Cu band, welding of a Ti evacuation tube to the Ti body, evacuation of the area between the Ti sleeve and body, and seal-off of the evacuation tube.

FIG. 1.--Light micrograph showing interface reaction zone developed between Ti-6-6-2 alloy (upper) and copper (lower) reacted at 593°C for 9 hr at 15 kpsi.

FIG. 2.--Scanning electron micrograph of sample as in Fig. 1, showing some microstructural detail in reaction region.

FIG. 3.--Scanning electron micrograph enlarged from Fig. 2 showing increased microstructural detail. Letters refer to energy dispersive X-ray microanalysis points listed in
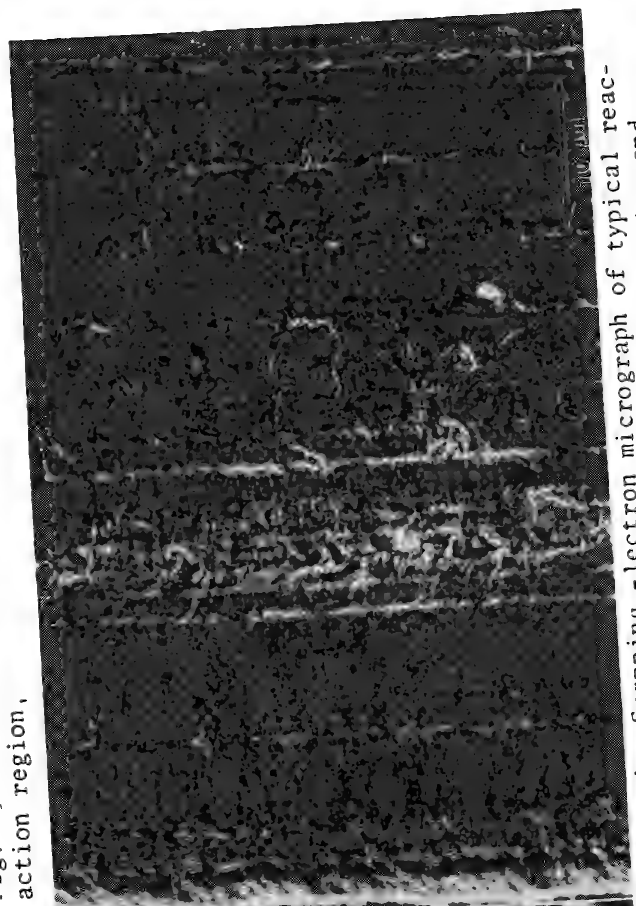
FIG. 4.--Scanning-electron micrograph of typical reaction zone cleaved for x-ray diffractometry and Auger spectrometry investigation.

Samples for light microscope investigation were prepared by standard metallographic techniques and then sequentially etched using Kroll's reagent (2HF:8HNO$_3$:90H$_2$O) swabbed for 20 s for the Ti-6-6-2 alloy and then for 5 s using H$_2$O:NH$_4$OH:H$_2$O for the copper. Typical microstructures thus revealed are illustrated in Fig. 1, a sample treated at 593°C (1100°F) for 9 hr. The reaction zone in this sample is 5 μm wide, the maximum thickness observed in these studies and corresponding to the maximum time-temperature employed. This reaction zone is revealed in greater detail in Fig. 2, a scanning electron micrograph taken on the same etched sample. Details of the reaction zone are now better resolved and at least three distinct layers parallel to the original alloy join may be seen. The region nearest the Ti-6-6-2 alloy, approximately 2.5 μm in width, consists of columnar or prismatic crystallites with long axis perpendicular to the join; morphological characteristics of the other bands were not apparent.

An attempt was made to analyze each of these physically different layers by energy-dispersive x-ray microanalysis. Analysis was performed at the center of each layer, identified as A-F in the micrograph of Fig. 3. The results of these analyses are listed in Table 1; those indicated by an asterisk correspond to the stoichiometric compounds

TABLE 1.--Energy-dispersive x-ray analyses obtained on points in reaction zone identified in Fig. 3. Phases marked (*) are room temperature stable as reported in Ref. 3; those marked (+) identified by x-ray diffractometry (this study).

| Location | Concentration | | Stoichiometry |
	Cu (atomic)	Ti	
A	83.6	16.4	Cu$_5$Ti
B	73.6	26.4	Cu$_3$Ti * +
C	67.6	32.4	Cu$_2$Ti
D	60.7	39.3	Cu$_3$Ti$_2$ *
E	50.2	49.8	CuTi * +
F	33.2	66.8	CuTi$_2$ * +

reported in the phase diagram[3] for this chemical system. However, when similar analyses were performed across the entire reaction zone, with the sample translated in approximately 0.1μm steps between each analysis, a systematically increasing Ti and decreasing Cu concentration was observed, which suggests a complete range of solid solution between the two end members rather than the existence of discrete phases. X-ray line profiles for Al, V, and Sn present in the Ti-alloy were observed to decrease rapidly at the reaction zone interface; thus, these elements do not appear to participate in the diffusion process observed in this alloy system, as also reported by Zanner and Fisher.[5]

Fractures were induced in the Cu-Ti alloy by notching and cleaving of the sample. Samples fractured in this manner were identical in all respects with those which disintegrated during firing, i.e., all fractured samples separated within the reaction zone between the two metals; typical fractured surfaces appear as shown in the scanning electron micrograph of Fig. 4.

X-ray examination of such fractured surfaces confirmed that the rupture always occurred within the reaction zone. Diffractometry performed on opposing sides of the fracture revealed the phase Cu$_3$Ti and Cu metal on the Cu side, and the presence of CuTi, CuTi$_2$ and Ti metal on the Ti side.

Auger electron spectroscopy depth profiling was also performed on the fracture surfaces

just described. Since sputter rates were fairly low, these profiles were not continued for a time sufficient to profile completely through the reaction zone into the unreacted base metal. Nonetheless, they did show that over the distance profiled, estimated at more than 2000 Å (0.2 μm), the composition of the phase was constant. Depth estimates were based on previously determined depth profiling rates measured on SiO_2 films of accurately known thickness combined with estimated sputter yields for Ti metal relative to SiO_2 based on the data due to Wehner.[7]

Conclusions

Reaction zones have been observed between pure copper and Ti-6-6-2 alloy reacted at temperatures up to 593°C at isostatic pressures of 15 kpsi for up to 9 hr. X-ray diffractometry shows the presence of the intermetallic compounds Cu_3Ti, $CuTi$, and $CuTi_2$; optical microscopy indicates that these phases are distributed in bands parallel to the interface and form, by solid-state diffusion, reaction zones up to 5 μm wide with Cu concentration decreasing away from the Cu-rich side. Energy-dispersive x-ray analysis indicates a continuously varying composition across the reaction zone, but Auger spectroscopy/depth profiling reveals a nearly constant Cu/Ti ratio over distances within a single band of up to 2000 Å. Since the volume of x-ray production is larger than the width of any given band, the chemical gradation apparent in the energy dispersive analyses would appear to result from x-ray signal averaging over more than a single-phase region. The weld joints which result from the fabrication process described thus consist of parallel bands of brittle intermetallic compounds in the Cu-Ti system, and are found to fracture and fail within this intermetallic phase region.

The results reported here may have general application to other alloy systems designed for utilization in high-stress environments where there is a tendency for the formation of intermetallic compounds. A possible solution would be to employ an intervening foil of a metal that forms solid solutions rather than intermetallic compounds between both metal end-members to be joined. In the case of a Cu/Ti-6-6-2 alloy system with Nb as the intervening foil, we have observed no intermetallic phases;[8] in preliminary tensile and shear stress strength tests,[9] the strength of the bond exceeded that of the copper, and failure occurred in the copper.

References

1. Y. Iijima, K. Hoshino and K. Hirano, "Diffusion of titanium in copper," *Metallurigcal Trans.* 8A: 997-1001, 1977.

2. O. Caloni, A. Ferrari, and P. Strocchi, "Diffusion of copper in beta titanium," *Electrochim. Metal* 4: 45-48, 1969.

3. M. Hansen, *Constitution of Binary Alloys*, New York: McGraw Hill, 1958.

4. R. R. Wells, "Microstructural control of thin-film diffusion-brazed titanium," *Welding J.* 55(1): 20s-27s, 1976.

5. F. J. Zanner and R. W. Fisher, "Diffusion welding of commercial bronze to a titanium alloy," *ibid.*, 54(4): 105s-112s, 1975.

6. "Welding processes: Resistance and solid-state welding and other joining processes," in W. H. Kearns, Ed., *Welding Handbook*, Miami: American Welding Society, 3(7th), 1980, 321-322.

7. G. K. Wehner, "The aspects of sputtering in surface analysis methods," in A. W. Czanderna, Ed., *Methods of Surface Analysis*, Elsevier Scientific Publishing Co., 1975, 14.

8. P. C. Calella and J. R. Shappirio, to be published.

9. R. Stanton, private communication.

EFFECTS OF SURFACE OXIDES ON THE COMPOSITION OF $(Al_x, Ga_{1-x})As$ FILMS, AS MEASURED BY THE ELECTRON PROBE

N. C. Miller

It is recognized that surface contamination films present problems in microanalysis of thin foils in a STEM.[1] However, surface films can also cause systematic error in a low-voltage bulk electron probe measurement of composition. A low accelerating voltage is chosen to minimize the absorption correction or, in bulk film measurements, to avoid generating x rays from the substrate. Improved high accuracy measurements, by electron probe microanalysis, of the composition of liquid phase epitaxial films of $(Al_x, Ga_{1-x})As$, with $0 < x < 45$ or Al < 23 at.%, have been recently reported.[2] AlCu and GaAs compound standards were used. The measurements were made at 6 keV to minimize the absorption correction for Al Kα x rays. However, at low voltbes (approximately 10 keV or less), the native or polishing oxides on sample and on standards may cause a non-negligible systematic error in the measured composition.

Auger electron spectroscopy has been used to estimate the composition and to measure the thickness of the oxides on the $(Al_x, Ga_{1-x})As$ films and on the standards. In composition measurements, the low-energy Auger peaks of Al, Cu, Ga, and As (30-80 eV) are observed because they have short inelastic mean free paths, 4-8 Å,[3] compared to oxide thicknesses, which are 20-70 Å.

Monte Carlo simulations[4] were carried out to estimate the systematic error that the oxides, on films and on standards, introduce into the electron probe measurements of the composition of $(Al_x, Ga_{1-x})As$ films. Although Auger composition measurements of the oxides on GaAs and on $(Al_x, Ga_{1-x})As$ can only be semiquantitative,[5] the accuracy is sufficient for the calculations of error using Monte Carlo simulations.

Experimental

The Auger measurements have been made with a Perkin-Elmer PH1 model 545A scanning Auger microprobe. Derivative spectra are recorded (dN/dE) with a modulation voltage of 3 V. The incident electron beam is at 3 keV and the current density is kept low at about 5×10^{-3} A/cm^2 to prevent charging. Sputter etching is done at 0.5 keV and 1×10^{-5} A/cm^2, with a static argon pressure of 5×10^{-5} Torr. Sputter etch rates are 5.0 Å/min relative to Ta_2O_5 and 4.4 Å/min relative to Al_2O_3.

Standard oxide and metallic low-energy Auger peaks were obtained by sputter etching through known thin oxides into the underlying metal or alloy on oxidized aluminum, oxidized copper, oxidized InAs, and oxidized GaP. InAs, GaP, and GaAs are wafer from high-purity single crystals, and AlCu is a high purity two-phase alloy (the dominant phase is 50 at.% Al). The $(Al_x, Ga_{1-x})As$ films and all standards are stored in a dry box with flowing dry nitrogen.

Composition vs depth was determined by recording of the low energy Auger peaks vs depth for oxides on nine $(Al_x, Ga_{1-x})As$ films and on GaAs and AlCu. Oxide thicknesses were measured by recording (with multiplexing) oxygen vs sputter etch time.

The AlCu standard was prepared by arc melting from 99.999% pure Al and Cu pieces, in flowing 99.99% purity argon. The alloy lump was then annealed for 2 hr at 600°C in vacuum and slow cooled to room temperature. This anneal resulted in grain growth and stress relief. The alloy was then polished under dry kerosene, to avoid contact with air and water. The kerosene was removed with acetone, followed by a methanol rinse and drying in pure nitrogen. The matrix is 50 at.% Al, the eta_2 phase, and the second

---

The author is a member of the technical staff of GTE Laboratories, Inc., 40 Sylvan Road, Waltham, MA 02254.

phase is the theta phase (66-2/3% Al). The matrix grains are 50-100 µm in size after anneal.

Results and Discussion

From observation of the low-energy Auger peaks, the oxide on AlCu is entirely Al_2O_3 (Fig. 1a).[6] (Some carbon is also present.) As the oxide/alloy interface is approached during sputter etching, the metallic Al (68 eV) and Cu (60 eV) peaks appear at the same depth (Figs. 1b,c). The Al peak has a dramatic change in intensity and in energy (from 54 to 68 eV) in the transition from the oxide to the metal. The Al_2O_3 thickness can be measured either from the oxygen intensity vs time or from the Cu (60 eV) intensity vs time, as in Fig. 2.

Low-energy Auger spectra from a depth profile through a typical native oxide on $(Al_x, Ga_{1-x})As$ are shown in Fig. 3. From the spectra of the standards, the native oxide is made up of Al_2O_3, gallium oxide, and arsenic oxide. A comparison of the depth profiles of GaAs and of oxidized $(Al_x, Ga_{1-x})As$ of various aluminum concentration suggests that the cation ratio is nearly the same in the oxide and in the $(Al_x, Ga_{1-x})As$ film.

The native oxide thickness for $(Al_x, Ga_{1-x})As$ increases linearly from 20 to 60 Å as aluminum concentration increases (Fig. 4). The best fit line is slightly steeper than the boundary lines of the data of Kuphal and Dinges.[7]

Monte Carlo simulations were carried out for oxides on AlCu, GaAs, and $(Al_x, Ga_{1-x})As$, with the oxide compositions discussed in the previous section. The oxide thickness was varied from 20 to 1000 Å, at 6 keV. Graphs of Al $K\alpha$, Ga $L\alpha$, and As $L\alpha$ x-ray intensity vs oxide thickness were plotted from the results of Monte Carlo simulations. The presence of Al_2O_3 on AlCu increases the Al $K\alpha$ intensity by 6.0% per 100 Å of Al_2O_3 (Fig. 5) and decreases the Al x-ray intensity ration (k ratio) measured in electron probe microanalysis . The room-temperature Al_2O_3 on AlCu is at least 40 Å, with a minimum systematic error in Al of 2.4%.

The oxides on GaAs and on $(Al_x, Ga_{1-x})As$ cause a substantially smaller decrease in the three x-ray intensities (Al $K\alpha$, Ga $L\alpha$, and As $L\alpha$). The results are shown in Table 1, in which the measured oxide thickness has been used to obtain the systematic error in x-ray intensity. For Ga and As, the errors from film and from standard are small and partially cancel. For Al, the oxide error of the film is considerably smaller than the oxide error of the AlCu standard. However, for Al, these two errors add in the measured k ratio.

TABLE 1.--Percentage decrease in x-ray intensity for $(Al_x Ga_{1-x})As$ due to surface oxide, from Monte Carlo calculations.

Film Composition (at.%)	Al $K\alpha$ (%)	Ga $L\alpha$ (%)	As $L\alpha$ (%)	Film Thickness (Å)
0% Al		0.2	0.3	20
10% Al	0.5	0.6	0.5	40
15% Al	0.5	1.0	0.9	55
20% Al	0.8	1.2	0.9	67

In general, the more the cation ratio in the oxide differs from that ratio in the substrate, the larger will be the systematic error in the composition measured by low voltage electron probe microanalysis. Of course, the larger the oxide film thickness, the bigger will be the oxide error in the measured composition.

In summary, surface oxides on $(Al_x, Ga_{1-x})As$ cause a negligible error in the measured concentration of Ga and As, but the oxide error in the Al concentration can be estimated and is larger than statistical error in the measurement of Al concentration.

References

1. R. W. Glitz et al., "Considerations of x-ray Absorption for STEM x-ray Analysis of Ni-Al Foils," *Microbeam Analysis*-1981, 309-312.

2. N. C. Miller, S. Zemon, G. P. Werber, and W. Powazinik, submitted to *J. Appl. Phys.*
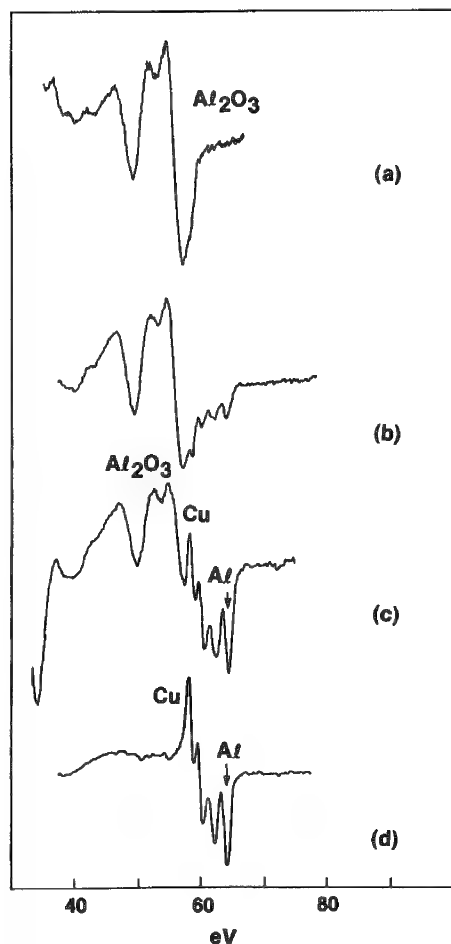
FIG. 1.--Depth profile through
oxide on Al Cu alloy. Low-
energy Al LVV and Cu MVV Auger
peaks. (a) Oxide: Al_2O_3. (b),
(c) Transition from oxide to
alloy. (c) Al-Cu alloy.
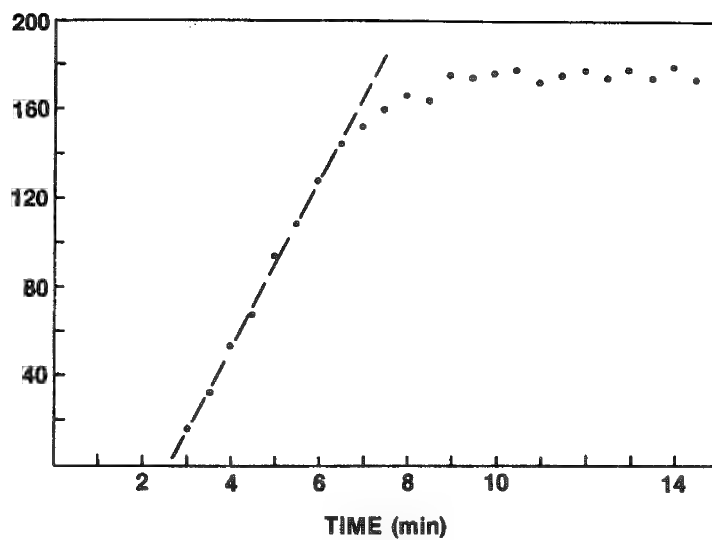
FIG. 2.--Peak-to-peak height of Cu MVV (60 eV)
Auger transition vs sputter etch time. Etch
rate is 4.4 Å/min.
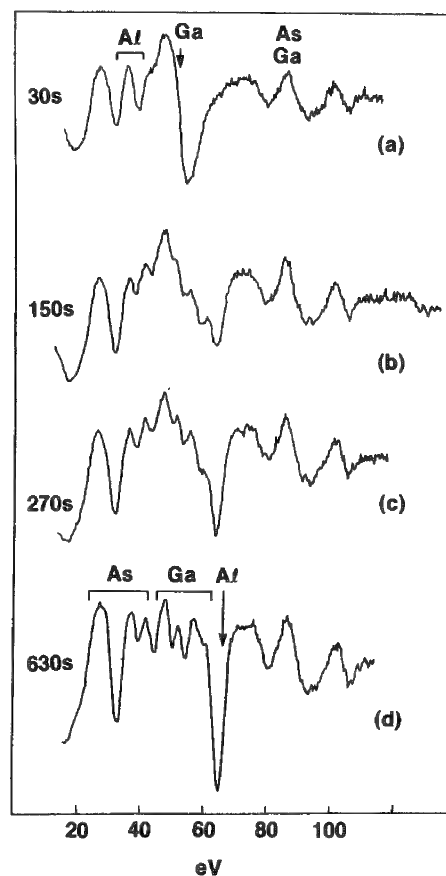
FIG. 3.--Low-energy Al LVV,
Ga MVV, As MVV Auger peaks
in depth profile through
oxide on 22.2% Al film of
$(Al_x, Ga_{1-x})As$. (a) Oxide.
(b), (c) Transition from
oxide to alloy. (d) Alloy.

411

3. C. J. Powell et al., "Attentuation length of low-energy electrons in solids derived from the yield of proton-excited Auger electrons: Beryllium and aluminum," *Phys. Rev.* B16: 1370, 1977.

4. N. C. Miller and D. M. Koffman, "Determination of thin film composition or thickness from electron probe data by Monte Carlo calculations," *Microbeam Analysis-- 1979*, 47-50.

5. R. P. H. Chang, et al., "Physical and electrical properties of plasma-grown oxide on $Ga_{.84}Al_{.36}As$," *J. Appl. Phys.* 48: 5384, 1977.

6. L. E. Davis et al., *Handbook of Auger Electron Spectroscopy*, Physical Electronics Division, Perkin-Elmer Corp., 1976, 2d ed.

7. E. Kuphal and H. W. Dinges, "Composition and refractive index of $Ga_{1-x}Al_xAs$ determined by Ellipsoimetry," *J. Appl. Phys.* 50: 4196, 1979.
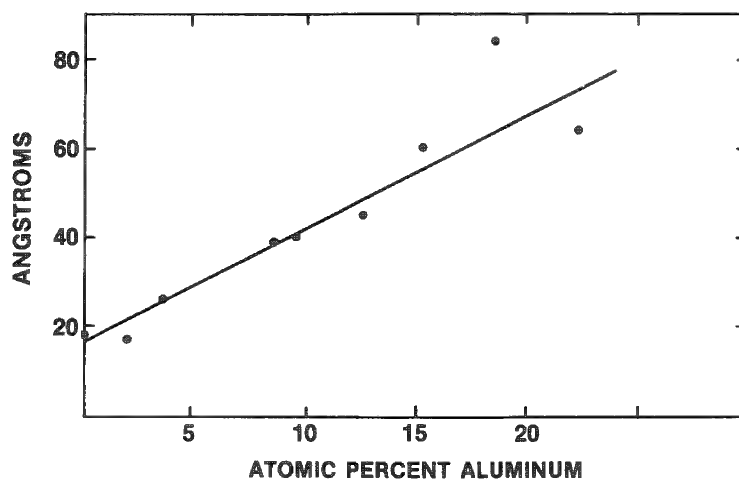
FIG. 4.--Thickness of native oxides on $(Al_x, Ga_{1-x})As$ LPE films vs aluminum concentration (in atomic percent).
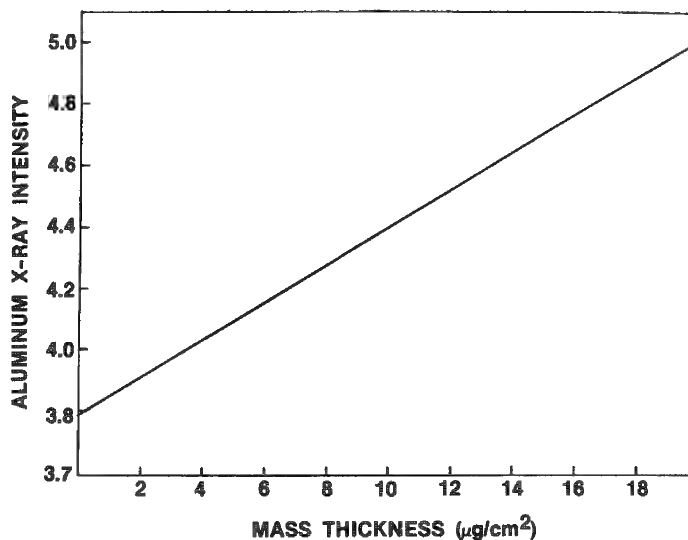
FIG. 5.--Al Kα x-ray intensity (in arbitrary units) vs Al_2O_3 mass thickness on Al-Cu, 6 keV. Density of Al_2O_3 is 4.0 g/cm^3.

USE OF CATHODOLUMINESCENCE AND SIMS IN THE STUDY OF THERMAL CONVERSION OF SEMI-INSULATING GaAs

S. Y. Yin and D. B. Wittry

Because of its high resistivity, chronium-doped GaAs is frequently employed as a substrate for device fabrication. One of the problems encountered in device fabrication with semi-insulating GaAs has been the tendency for thin surface layers of low resistivity to form during heat treatment at temperatures used for epitaxial growth or post ion implantation annealing. In this paper work is described in which cathodoluminescence and SIMS are used to investigate this problem of thermal conversion.

Previous researchers have used a variety of techniques including photoluminescence[1-4] or SIMS[5] because both these techniques provide high sensitivity for detection of impurity effects in GaAs. However, the results of photoluminescence can be misleading because the excitation depth is small compared to thickness of the thermally converted layers (typically 1-2 μm). With cathodoluminescence, for example, the mean carrier generation depth at 40 kV is approximately 2 μm. A comparison of photoemission spectra and cathodoluminescence spectra obtained from the same specimens shows significant differences; some of the strong peaks in the photoluminescence spectra are seen in the cathodoluminescence spectra only when the electron beam voltage is reduced. Thus it seems clear that cathodoluminescence is a preferred method to investigate the mechansims involved in thermal conversion.

In this work fourteen specimens of GaAs were studied, of which six were untreated specimens, four specimens heat-treated in hydrogen in a tube furnace, and four specimens heat-treated by the "melt controlled ambient technique" (MCAT).[6] This technique, developed at Hughes Research Laboratories, involved immersion of a graphite box containing the specimens in a large melt of gallium saturated with GaAs. The box has a sliding lid that may be opened for growing layers by liquid phase epitaxy but is left closed for heat treatment. In the latter case, the vapor pressure of Ga and As are determined by ambient conditions; hence the term MCAT.

Typical cathodoluminescence spectra at 30°K for a specimen that had a very low resistivity surface layer are shown in Fig. 1 (solid line). This specimen was heat-treated in H_2 at 800°C for 30 min. In the same figure, the dotted line represents the 30°K spectra for a specimen from the same ingot but without heat treatment. The 10.088Å (1.23eV) peak has been attributed by Hwang[1] and Williams[7] to recombination involving a Si-donor-Ga-vacancy complex. This peak was observed in all of the specimens examined. The small peak at 8289 Å (1.496 eV) may be due to free electron capture at a shallow neutral acceptor. (The acceptor may be carbon on an arsenic site, as reported by Lum

et al.,[2] since the GaAs was supported by a graphite boat during heat-treatment.) The peak at 8816 Å (1.407 eV) is presumed to be due to a Si-acceptor-As-vacancy complex previously reported in doped samples of bulk GaAs.[8] The peak at 9100 Å (1.363 eV) is presumed to be due to a Si-acceptor-Ga complex (Si_{As}-V_{Ga}),[9] or a shallow donor (Si_{Ga})-Cu acceptor (Cu_{Ga}^-)[1], or recombination at Ga vacancies.[10] The two shoulders at 9320 Å (1.33 eV) and 9570 Å (1.296 eV) are LO phonon replicas of the 9100Å peak.

The 9100Å (1.363eV) peak seems to be a key to the mechanism for thermal conversion because it was found by Hall effect measurements of several specimens that the intensity of this peak increased monotonically with the carrier concentration of the surface layers.

SIMS depth profiles were obtained for twelve of the specimens studied by catho-doluminescence. The secondary ion intensities of Cr, Si, C, Mn, and Cu for the heat-treated specimen of Fig. 1 are shown in Fig. 2. The Cu ion intensity obtained from this specimen is not significantly higher than obtained from other specimens examined. The Si ion intensity is also not unusually high but the heat treatment conditions for this specimen are expected to produce a high As and Ga vacancy concentration. Thus the principal mechanism for thermal conversion of semi-insulating GaAs may be a Si_{As}-V_{Ga} complex formed during heat treatment. Obviously there are other possible interpreta-tions--for example, the depletion in Cr in the converted layer may lower the resistivity--but this explanation cannot account for the increase in the intensity of the 9100Å peak.

A more detailed description of this work and analysis of the results is being submitted for publication elsewhere.

References

1. C. J. Hwang, *J. Appl. Phys.* 39: 5347, 1968.
2. W. Y. Lum et al., *Appl. Phys. Lett.* 30: 1, 1977.
3. P. B. Klein et al., *J. Appl. Phys.* 51: 4861, 1980.
4. H. Birey and J. Sites, *ibid.*, p. 619.
5. H. B. Kim, D. L. Barrett, in *Gallium Arsenide and Related Compounds* (St. Louis) 1976, Conf. Series No. 33b (Institute of Physics, London 1976, 136.
6. C. L. Anderson et al., *J. Electrochem. Soc.* 127: 925, 1980.
7. E. W. Williams, *Phys. Rev.* 168: 922, 1968.
8. E. W. Williams and C. T. Elliott, *Brit. J. Appl. Phys.* (2)2: 1657, 1969.
9. W. Y. Lum and H. H. Wieder, *J. Appl. Phys.* 49: 6187, 1978.
10. K. V. Vaidyanathan et al., *J. Electrochem. Soc.* 124: 1781, 1977.
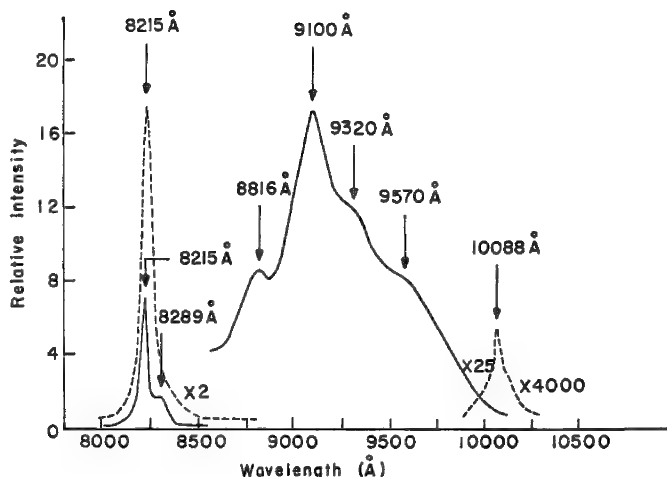
FIG. 1.--Cathodoluminescence spectra of GaAs specimens at 30°K.
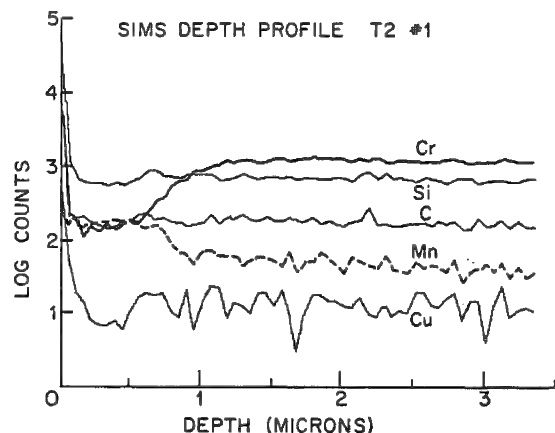
FIG. 2.--Secondary ion intensities for heat-treated specimen of Fig. 1.

FLOW LINES AND MICROSCOPIC ELEMENTAL INHOMOGENEITIES IN AUSTENITIC STAINLESS STEELS

W. C. Mosley Jr.

Flow lines in mechanically formed autenitic stainless steels are known to influence fracture behavior.[1] Enhancement of flow lines by chemical etching is evidence of elemental inhomogeneity. This paper presents the results of electron microprobe analyses to determine the nature of flow lines in three austenitic stainless steels: 21Cr-6Ni-9Mn, 304L, and 19Ni-18Cr.

Experimental

Each stainless-steel specimen was prepared for metallographic examination by grinding, polishing and chemical etching. Areas to be analyzed were marked with hardness indentations and photographed. Specimens were then repolished leaving the indentations to help relocate the analysis areas. An Applied Research Laboratories Scanning Electron Microprobe Quantometer (SEMQ) was used to analyze automatically about fity equally spaced points along lines perpendicular to the flow lines. Each point was analyzed for Cr. Mn, Fe, Ni, P, S, Al, and Si. X-ray intensities of the four major elements were measured with the same spectrometer. Standards were National Bureau of Standards standard reference materials, pure metals, and well-characterized simple compounds. X-ray intensities were converted to elemental concentrations with an online version of Magic IV.[2] Each analysis required about 10 min; therefore, data for each point were normalized to compensate for instrumental drift. Analysis precision was determined by the performance of ten analyses of a single point on a reference specimen of each steel. After analysis, specimens were again etched and photographed to correlate the flow lines with the analysis points which were marked by spots caused by the electron beam. Elemental concentrations for the points along each analysis line were averaged to yield a bulk composition. Standard deviations and ranges in the elemental concentrations are measures of inhomogeneity. Results are also presented as elemental concentration profiles, correlations between concentrations of alloying elements and the concentration of iron, and histograms showing the distributions of elemental concentrations.

Flow lines were observed in specimens of 21Cr-6Ni-9Mn stainless steel from hot rolled bar, a hot cross rolled plate, and high energy rate forgings (seven forging steps) made from the plate. Locations of flow lines correlate with areas depleted in manganese, nickel, and possibly chromium. (Chromium inhomogeneity is only slightly greater than the analysis precision.) Elemental concentration profiles across flow lines on the specimen from the seventh step of high energy rate forging (Fig. 1) are shown in Fig. 2. Concentrations of the major alloying elements decrease with increasing iron concentration (Fig. 3) and are described by:

$$Cr(wt.\ \%) = 20.73 - 0.036 \times Fe(wt.\ \%)$$
$$Mn(wt.\ \%) = 34.52 - 0.386 \times Fe(wt.\ \%)$$
$$Ni(wt.\ \%) = 41.31 - 0.530 \times Fe(wt.\ \%)$$

for $62.5 \leq Fe(wt.\ \%) \leq 66.5$.

FIG. 1.--High energy rate forged 21Cr-6Ni-9Mn
stainless steel.

Fig. 2.--Elemental concentration profiles
across flow lines in high energy rate
forged 21Cr-6Ni-9Mn stainless steel.

FIG. 3.--Cor-
relations be-
tween elemental
concentrations
in high energy
forged 21Cr-
6Ni-9Mn stain-
less steel.

FIG. 4.--Histogram of distributions of
elemental concentrations in high energy
rate forged (solid bars) and hot cross
rolled (dashed bars) 21Cr-6Ni-9Mn
stainless steel.
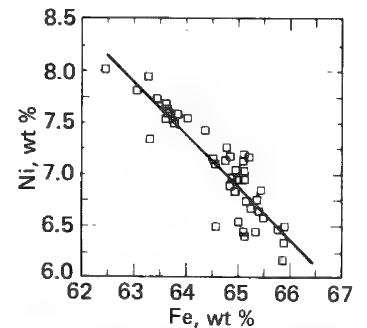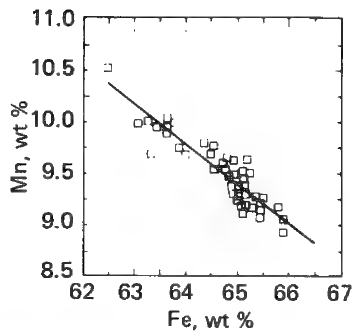
FIG. 5.--High energy rate forged 304L stainless steel.

Results for the bar and plate specimens showed essentially the same correlations between elemental concentrations. Elemental inhomogeneities in the specimens from t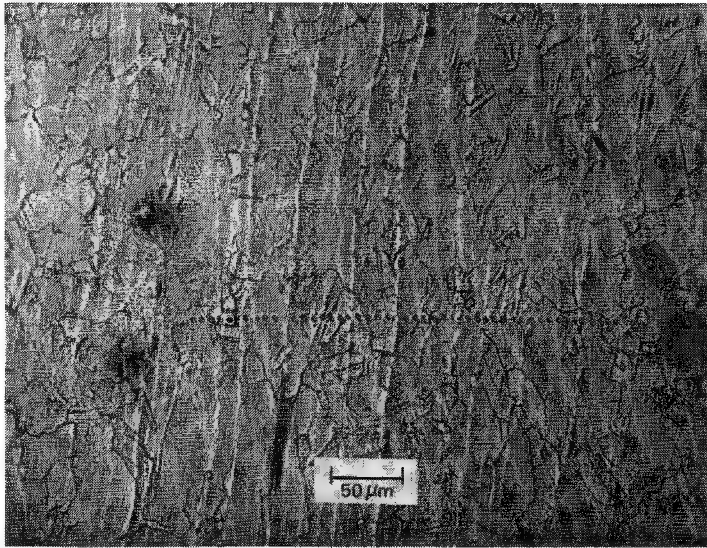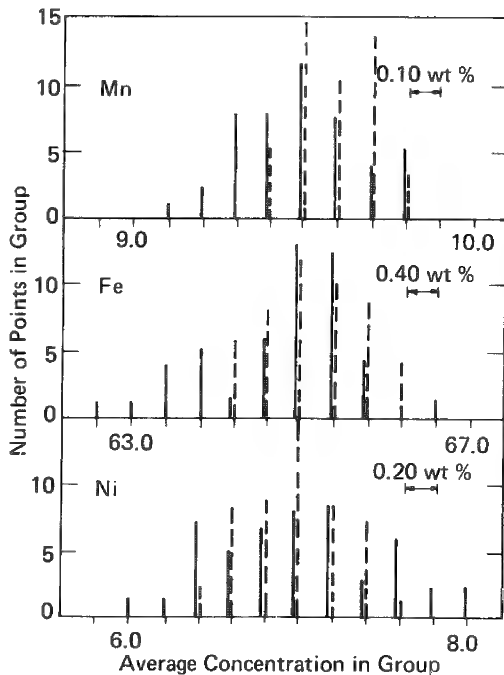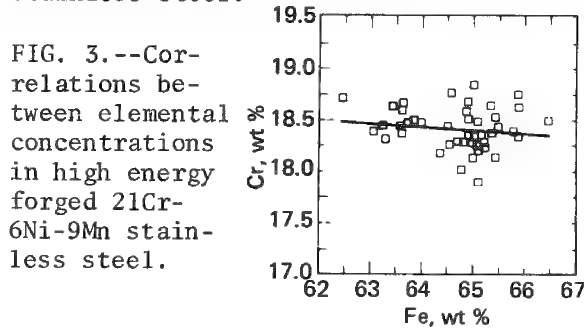he first and seventh steps of high energy rate forging are the same and are greater than those in the bar and plate (Table 1). The histogram of Fig. 4 shows narrow, symmetrical elemental concentration distributions for the plate specimen; those for high energy rate forging are broader, with the iron distribution having a skewness towards lower concentrations.

Flow lines were observed in specimens of 304L stainless steel from hot rolled bar and a high energy rate forging but not in a specimen from hot cross rolled plate. Also, ferrite was present as stringers in the plate and forging. In the forging, the stringers and flow lines were parallel. SEMQ results are presented in Table 2 and Figs. 5-8. Locations of flow lines occur in areas enriched in chromium and iron and depleted in nickel and, possibly, manganese. (Manganese inhomogeneity is only slightly greater than the analysis precision.) Elemental concentration correlations for the austenite in the high energy rate forging are described by:

$$Cr(wt. \%) = -10.17 + 0.394 \times Fe(wt. \%)$$
$$Ni(wt. \%) = 98.65 - 1.257 \times Fe(wt. \%)$$
$$Mn(wt. \%) = 7.64 - 0.086 \times Fe(wt. \%)$$

for $68.8 \leq Fe(wt. \%) \leq 71.2$. Elemental inhomogeneities in the austenite are significantly lower for the plate than for the forging which probably accounts for the absence of flow lines. Chromium and iron concentrations are symmetrically distributed for the plate specimen; the nickel distribution is slightly skewed towards higher concentrations. Elemental concentration distributions for the high energy rate forging are broader with those for iron and chromium being skewed towards lower concentrations.

Analysis of a specimen from a forging of 19Ni-18Cr stainless steel (Figs. 9 and 10) showed that flow lines occur in areas enriched in nickel and chromium. A specimen of the casting from which the forging was made was also analyzed (Figs. 11 and 12). The dendritic cell boundaries of the casting were also enriched in nickel and chromium. Elemental inhomogeneities in the forging were slightly less than those in the casting (Table 3). Elemental concentration correlations are described by:

$$Cr(wt. \%) = 57.33 - 0.635 \times Fe(wt. \%) \text{ and}$$
$$Ni(wt. \%) = 43.13 - 0.375 \times Fe(wt. \%)$$

for the forging (Fig. 13), and

$$Cr(wt. \%) = 55.51 - 0.613 \times Fe(wt. \%) \text{ and}$$
$$Ni(wt. \%) = 46.85 - 0.428 \times Fe(wt. \%)$$

for the casting for $61.4 \leq Fe(wt. \%) \leq 65.6$. The forging and casting had similar elemental concentration distributions which are skewed towards low iron concentrations and high nickel and chromium concentrations (Fig. 14).

Conclusions

Flow lines in mechanically formed austenitic stainless steels correlate with elemental inhomogeneities. Areas in which flow lines occur correspond to austenite compositions that are the last to solidify during cooling from the melts. These inhomogeneities are given directionality by the forming processes. Results for the 304L stainless steel hot cross rolled plate indicate that homogenization can prevent flow line formation. However, high energy rate forging of 304L and 21Cr-6Ni-9Mn stainless steels appears to have increased elemental inhomogeneity and enhanced the flow lines. It is unusual that a mechanical process could cause such a chemical change.

References

1. M. R. Dietrich et al., "J-controlled crack growth as an indicator of hydrogen-stainless steel compatibility," in I. M. Bernstein and A. W. Thompson, Eds., *Hydrogen Effects in Metals*, The Metallurgical Society of AIME, 1981, 637-643.

2. W. J. Hamilton et al., "Automated electron microprobe analysis: a system for the ARL-SEMQ based on mass storage and speed capabilities of the flexible-magnetic disk," *Proc. 12th MAS Conf.*, 1977, 52A.

FIG. 6.--Elemental concentration profiles across flow lines in high energy rate forged 304L stainless steel.
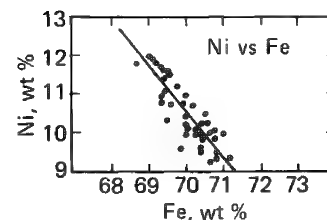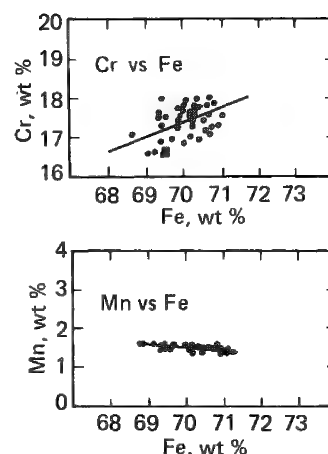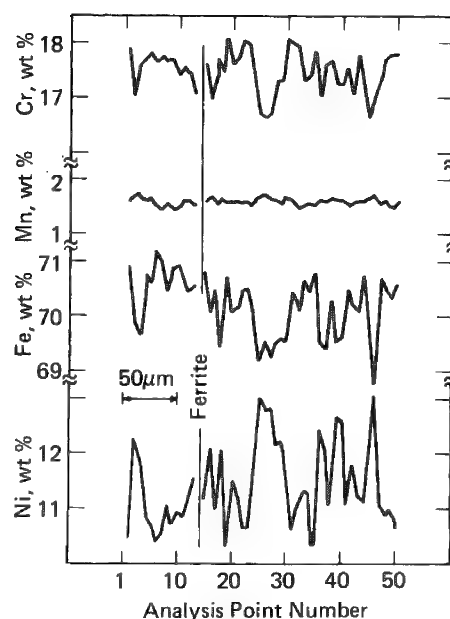
FIG. 7.--Correlation between elemental concentrations in high energy rate forged 304L stainless steel.

TABLE 1.--SEMQ analyses of 21Cr-6Ni-9Mn steel specimens.[1]

Element[2]		Point on annealed specimen	Hot rolled bar	Hot cross rolled plate	High energy rate forging	
					1st step	7th step
Cr	Max.	19.08	19.55	18.45	18.91	18.82
	Avg.	18.82	18.90	18.05	18.36	18.41
	Min.	18.65	18.54	17.73	17.75	17.90
	Std.dev.	0.15	0.20	0.17	0.24	0.20
	Range	0.43	1.01	0.72	1.16	0.92
Mn	Max.	9.37	10.46	10.07	10.25	10.51
	Avg.	9.26	9.74	9.63	9.44	9.49
	Min.	9.22	9.24	9.22	8.81	8.75
	Std.dev.	0.06	0.25	0.21	0.38	0.35
	Range	0.15	1.22	0.86	1.44	1.76
Fe	Max.	64.32	64.29	66.32	66.69	66.48
	Avg.	64.03	63.11	65.18	64.94	64.76
	Min.	63.75	61.08	64.12	62.85	62.48
	Std.dev.	0.16	0.58	0.55	0.93	0.85
	Range	0.57	3.21	2.20	3.84	4.00
Ni	Max.	7.26	8.46	7.52	7.96	8.02
	Avg.	7.09	7.60	6.94	6.98	7.02
	Min.	6.93	6.85	6.39	6.00	5.98
	Std.dev.	0.10	0.38	0.29	0.49	0.49
	Range	0.33	1.61	1.13	1.96	2.04
Si	Max.	0.68	0.40	0.21	0.26	0.24
	Avg.	0.65	0.36	0.18	0.19	0.19
	Min.	0.59	0.31	0.16	0.13	0.16
	Std.dev.	0.03	0.02	0.01	0.03	0.02
	Range	0.09	0.09	0.05	0.13	0.08

[1]Results in wt.%.
[2]Al, S, and P below detection limits of about 0.1 wt.%.

FIG. 8.--Histogram of distributions of elemental contrations in high energy rate forged (solid bars) and hot (dashed bars) 304L stainless steel.
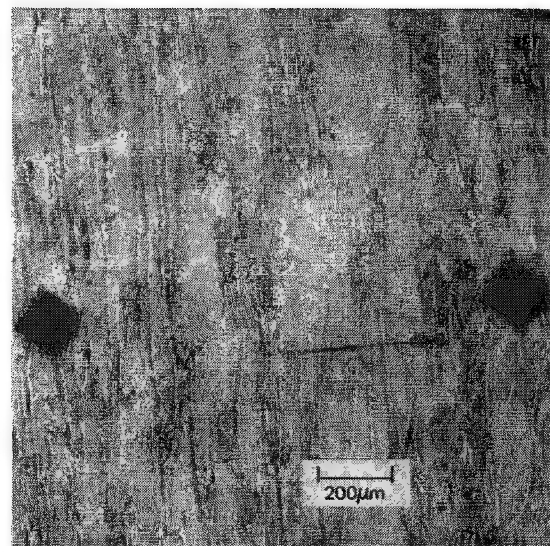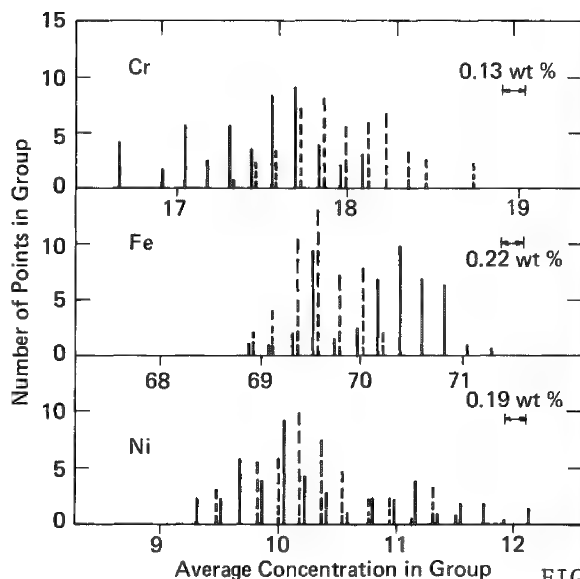
FIG. 9.--Forged 19Ni-18Cr stainless steel.
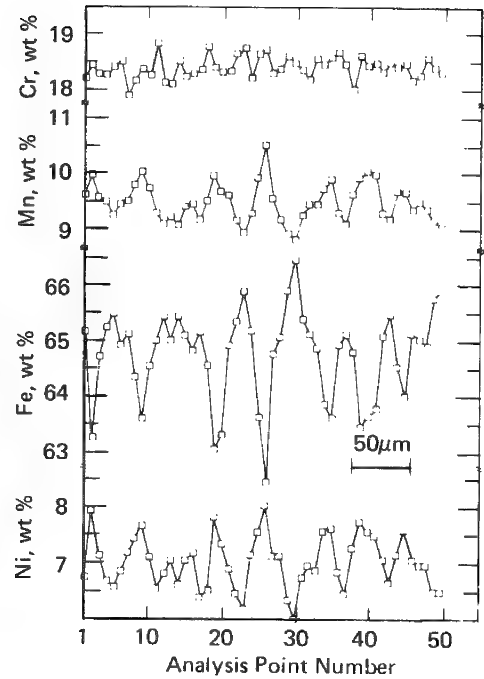
TABLE 2.--SEMQ analyses of 304L steel specimens.[1]

| Element[2] | | Point on high energy rate forging | Hot rolled bar | Hot cross-rolled plate[3] | | High energy rate forging[4] |
				Austenite	Ferrite	Austenite
Cr	Max.	17.56	18.14	18.75	26.08	18.08
	Avg.	17.32	17.37	17.95	25.38	17.46
	Min.	17.14	16.75	17.34	24.69	16.63
	Std.dev.	0.13	0.30	0.30	0.65	0.46
	Range	0.42	1.39	1.41	1.39	1.45
Mn	Max.	1.64	2.07	1.51	1.32	1.71
	Avg.	1.56	1.88	1.44	1.27	1.59
	Min.	1.51	1.72	1.35	1.24	1.45
	Std.dev.	0.03	0.09	0.03	0.03	0.06
	Range	0.13	0.35	0.16	0.08	0.26
Fe	Max.	70.92	68.49	70.30	68.27	71.19
	Avg.	70.73	67.25	69.57	67.92	70.20
	Min.	70.35	65.75	68.85	67.45	68.75
	Std.dev.	0.22	0.75	0.32	0.37	0.56
	Range	0.57	2.74	1.45	0.82	2.44
Ni	Max.	10.42	14.13	11.51	5.12	12.08
	Avg.	10.00	12.82	10.38	4.68	10.43
	Min.	9.73	11.12	9.51	4.37	9.79
	Std.dev.	0.19	0.88	0.48	0.32	0.78
	Range	0.69	3.01	2.00	0.75	2.29
Si	Max.	0.29	0.63	0.51	0.58	0.30
	Avg.	0.25	0.57	0.47	0.54	0.23
	Min.	0.21	0.51	0.43	0.51	0.10
	Std.dev.	0.02	0.03	0.02	0.03	0.06
	Range	0.08	0.12	0.08	0.07	0.20

[1]Results in wt.%.
[2]Al, S, and P below detection limits of about 0.1 wt.%.
[3]No flow lines observed.
[4]Ferrite stingers too thin to analyze.

TABLE 3.--SEMQ analyses of 19Ni-18Cr steel specimens.[1]

Element[2]		Point on forging	Casting	Forging
Cr	Max.	15.90	18.20	18.26
	Avg.	15.76	16.47	16.48
	Min.	15.63	15.42	15.64
	Std.dev.	0.10	0.70	0.63
	Range	0.27	2.78	2.62
Fe	Max.	63.12	65.28	65.58
	Avg.	63.00	63.68	64.37
	Min.	62.80	60.82	61.40
	Std.dev.	0.11	1.12	1.01
	Range	0.32	4.46	4.18
Ni	Max.	21.27	20.65	20.25
	Avg.	21.05	19.63	18.96
	Min.	20.87	18.91	18.35
	Std.dev.	0.10	0.47	0.42
	Range	0.40	1.74	1.90

[1]Results in wt.%.
[2]Mn, Al, Si, P, and S less than detection limits of about 0.1 wt.%.
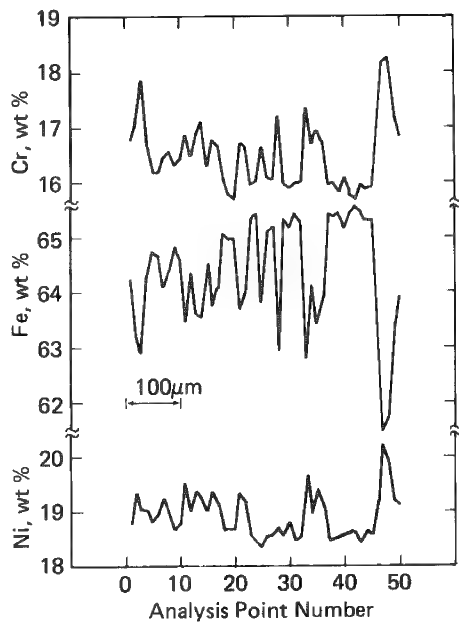
FIG. 10.--Elemental concentration profiles across flow lines in forged 19Ni-18Cr stainless steel.
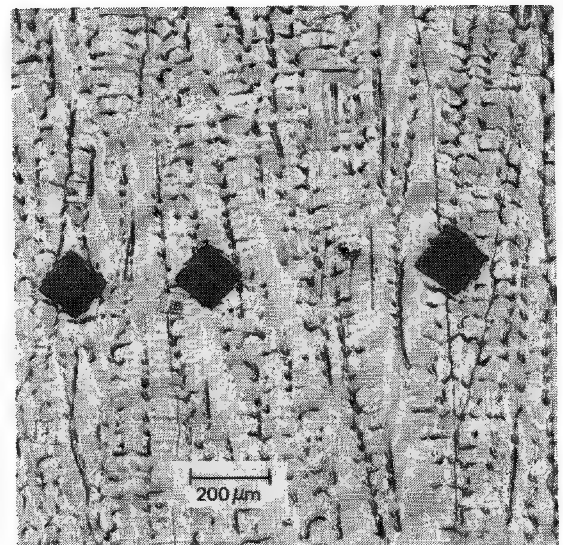
FIG. 11.--Cast 19Ni-18Cr stainless steel.
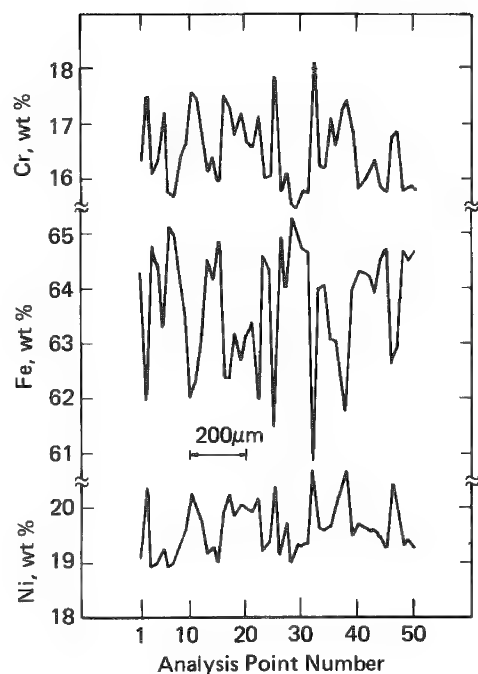
FIG. 12.--Elemental concentration
profiles on cast 19Ni-18Cr stain-
less steel.
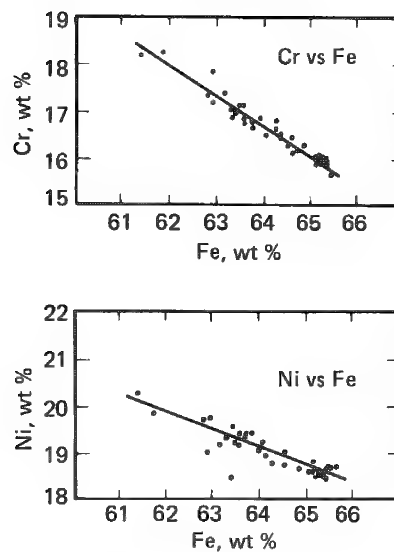
FIG. 13.--Correlation between elemental
concentrations in forged 19Ni-18Cr stain-
less steel.
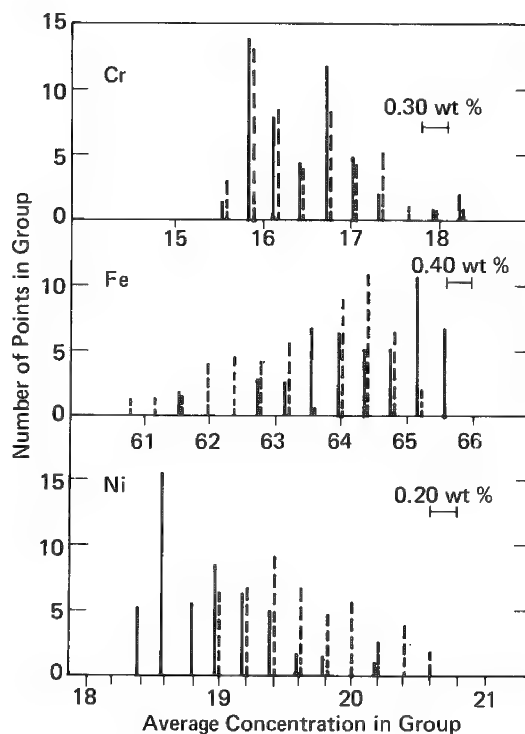
FIG. 14.--Histogram of distributions
of elemental concentrations in
forged (solid bars) and cast (dashed
bars) 19Ni-18Cr stainless
steel.

## QALL, A 16-ELEMENT ANALYTICAL SCHEME FOR EFFICIENT PETROLOGIC WORK ON AN AUTOMATED ARL-SEMQ: APPLICATION TO MICA REFERENCE SAMPLES

T. N. Solberg and J. A. Speer

An analytical scheme, QALL, has been devised to obtain rapid quantitative analyses of minerals in petrographic thin sections on a fully automated, 9-spectrometer ARL-SEMQ. During its five years of use, it has proved to be efficient for a variety of rock-forming minerals. The scheme is presented here with an example of its use on a common and chemically complex mineral, biotite.

Quantitative analysis with the electron microprobe for the petrologic study of igneous, metamorphic, and sedimentary rocks requires satisfaction of several rigorous demands. A useful silicate analysis usually includes at least nine elements (Si, Al, Ti, Fe, Mn, Mg, Ca, K, Na); a complete analysis also lists F and Cl, and, for some minerals, additional minor elements such as Cr, Ba, S, P, or Sr. Further difficulties arise because the sample, a polished thin section, commonly contains between three and twelve rock-forming minerals which vary in average atomic number, concentrations of elements, and coordination of some elements. In addition, the analyses must be accomplished expeditiously, with the same standardization for all minerals, so that a large number can be done in a day.

The instrument at VPI is an ARL SEMQ electron microprobe with six fixed spectrometers and three variable spectrometers. It has ARL automation with a PDP 11/34 computer of 32K memory and two single density floppy disks. Qualitative work for rapid identification is done on a Kevex solid state detector.

Analytical Scheme

The instrument configuration for QALL is given in Table 1. The fixed-channel elements are those most prevalent in silicate, rock-forming minerals. The remaining elements are measured on spectrometers to optimize count rates and resolution while minimizing interferences. The elements are listed in the order in which they are measured with the variable spectrometers. The order was chosen to minimize the driving of the spectrometers and, in the case of F, increase the counting time. Each of the elements, except F, that is measured with a variable spectrometer has 10s counting times. Combined with two 4s background counts for Sr, F has a total counting time of 38 s; elements measured with fixed spectrometers are counted for 48 s. A nearly equal amount of time is involved in driving the spectrometers and with about 20 s required for the calculations, total analysis time is just under 2 min.

The accelerating voltage is 15 kV and beam current is either 10 or 20 nA. The lower beam current is used for smaller particles or for materials that are unstable under the electron beam. Otherwise 20 nA is used to increase precision by increased count rates. A 1μs deadtime constant is assumed for the detectors. Beam current drift is corrected by means of a beam current monitor.

Generally the beam is rastered over a 10×8 μm area (10 000×), to prevent beam damage to the sample while permitting avoidance of surface defects. If a smaller area requires study, such as an exsolved phase, fine-area analysis can be done with use of the scanning secondary-imaging capability. Particles smaller than the analytical volumes can be studied by dispersion on a carbon substrate.[9]

The x-ray intensity data are converted to oxide weight percentages by the ARL computer program based on the alpha factor correction scheme of Ziebold and Oglivie[10] as extended by Bence and Albee[11] using the correction factors of Alee and Ray.[12]

The authors are at the Department of Geological Sciences of the Virginia Polytechnic Institute and State University, Blacksburg, VA 24061-0796.

TABLE 1.--QALL, analytical scheme for quantitative analysis on an automated ARL SEMQ run at an accelerating voltage of 15 keV and beam current of 10 or 20 nA; raster size 10 × 8 μm.

	element	line	time	background	standard (reference)
variable spectrometer	1 (LIF)*				
	Mn	MnKα	10	fixed	[†]syn. tephroite (1)
	Cr	CrKα	10	fixed	chromite, Tiebaghi (2)
	Ti	TiKα	10	fixed	[+]rutile
	Ba	BaLα	10	fixed	[+]syn. Ba-Cl apatite
variable spectrometer	2 (PET)*				
	Cl	ClKα	10	fixed	[+]syn. Ba-Cl apatite
	S	SKα	10	fixed	anhydrite, Stassfurt (3)
	P	PKα	10	fixed	apatite, Durango (4)
	Sr	SrLα	10	measured	syn. SrCO$_3$ (5)
variable spectrometer	3 (RAP)**				
	Na	NaKα	10	fixed	[+]albite, Amelia or Tiburon
	F	FKα	38	fixed	norbergite, Norberg (6)
fixed spectrometers*					
4 (LiF)	Fe	FeKα	48	fixed	fayalite, Rockport (7)
5 (PET)	K	KKα	48	fixed	orthoclase, Benson (8)
6 (PET)	Ca	CaKα	48	fixed	apatite, Durango (4)
7 (ADP)	Si	SiKα	48	fixed	[+]albite, Amelia or Tiburon
8 (ADP)	Al	AlKα	48	fixed	[+]albite, Amelia or Tiburon
9 (TAP)	Mg	MgKα	48	fixed	norbergite, Norberg (6)

[+]intralaboratory standard
[†]contains 0.2 wt% MgO
*sealed proportional detector
**P-10 flow proportional detector

The crystals used in the analysis of particular elements were chosen to optimize the resolution and avoid interferences. Nevertheless, pulse-height discrimination is important in several instances. The Mg fixed channel has a TAP crystal requiring pulse-height discrimination of an interfering third-order CaKα peak. It would be less critical with the better resolution of a RAP crystal. Similarly, there is interference of SiK spectra with SrLα on PET, and interference of FKα by a third-order PKα peak on the RAP crystal, a particular problem in fluorapatites.

Change in the shapes of x-ray spectra peaks as a result of different coordination and valency is a problem for some elements. Difficulties involving fluorine are discussed by Solberg (see p. 148 of this volume). Another peak exhibiting this problem, AlKα, is of particular concern because it is an important element measured on a fixed channel.

All background values except those for Sr are entered as fixed values in counts/ s-nA. The input of backgrounds, required for the fixed spectrometers, decreases the analysis time if done for the variable spectrometers as well. Backgrounds are measured on materials with a range of average atomic numbers and the results are plotted as in Fig. 1. Appropriate backgrounds can be obtained from the plot depending on the average atomic number of the unknown. In practice, rock-forming silicate minerals have only a small range of average atomic numbers and the same background value for an element can be used for all minerals except in the most exacting work with trace elements. Sr
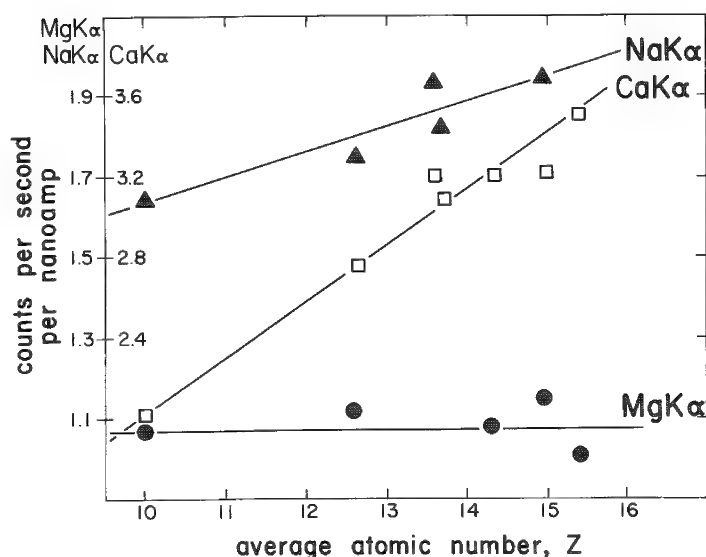
FIG. 1.--Backgrounds measured on materials of differing average atomic number, in counts/s-nA for Na, Ca, and Mg; appropriate backgrounds for unknown are obtained by estimate of its average atomic number.

backgrounds are measured off-peak with PET scanning spectrometer.

During the first few years of QALL use, the beam remained unblanked during the 96 s needed to count and drive the spectrometers, but it was found that this procedure resulted in loss of the volatile elements and extensive decomposition of susceptible minerals. Blanking the beam, except during the 48s analysis time, and rastering the beam in a 8 × 10μm rectangle minimize these problems. There has been a noticeable improvement in the analyses of Na-feldspars, zeolites, and glasses.

Standardization is not required every time different operators begin to collect analyses, on different days, or when a filament is changed. Once the instrument is warmed up, a check of the previous standardization is made with a material of complex chemistry, such as the Kakanui hornblende, or demanding chemistry, such as kyanite. If the analyses are unsatisfactory, any or all of the elements can be restandardized. Depending on the operator, standardization consists of three to ten 10s counting times on the standards. More counts are accumulated for Si, Al, and Na than the other elements because of low counting rates and their mineralogic importance. During standardization, the peak positions of the elements measured on the variable spectrometers are relocated, except for F. The F peak position is entered because the count rate for F is too low to locate accurately the peak position with 2s stepping of the spectrometer during standardization.

The choice of standards is limited by the available material, but generally standards of simple chemistries are preferred. The standards used are listed in Table 1, with references to descriptions and analyses of the materials. Standards should contain a significant concentration of the element being measured in order to minimize counting statistic errors. To save time, some standards can be used for more than one element; e.g., albite is used as a standard for Al and Si as well as Na. All three elements have low count rates and a significant improvement in counting statistics occurs with only a small increase in time.

Application

The analytical scheme QALL has been used successfully in analyzing a variety of compositions in the mineral groups:

amphibole	Al-epidote	ilmenite
biotite	feldspar	white mica
chlorite	garnet	olivine
cordierite	glass	pyroxene
dumortierite	humite	tourmaline

For the carbonate minerals, calcite is the only phase that sums near 100% when a stoichiometric amount of CO_2 is included. The other anydrous carbonates (e.g., dolomite, magnesite, and siderite) yield lower sums that progressively decrease for minerals with lower decomposition temperatures, which suggests that decomposition is the major problem.

Biotite constitutes one of the more important mineral groups commonly studied in petrology and is among the most challenging of minerals to analyze. A good biotite analysis requires determination of at least thirteen contituents, including Fe^{+2}, Fe^{+3},

F, Cl, and H_2O and, in some cases, Li, Rb, and Cs. Solid solutions among dioctahedral, trioctahedral, and hydromicas, and sub-microscopic alterations make a check of the chemistry on the basis of structural formula difficult. Four analyzed biotites were studied: mica-Mg[13], mica-Fe[13], Cl-bio-tite[14] and biotite, R.I. (Wones, personal communication; Fig. 2). The purpose of the study was not to test their suitability as standards but (1) to understand the de-gree of confidence that can be placed on mica analyses using simple, easily charac-terized standards and (2) to choose those biotites which would be effective intra- and interlaboratory monitors of quantitative analysis quality.

The compositions determined for the biotites are presented in Table 2, where they are compared to the reported analysis. Water contents were calculated by means of the computer program, SUPERRECAL.[15] The average of the microprobe analyses generally agrees within the standard deviation with the reported analyses. Systematic differ-ences arise from the inhomogeneities in the bulk samples used for the reported analyses. Most deviation is attributable to the presence of chloritized biotite which results in lower K_2O and higher Al_2O_3 compared to the averaged microprobe analyses. The inclusion of other phases in the bulk samples used for the reported analyses affects the Ti, Ca, P, and C contents. The microprobe analyses show that

FIG. 2.--Projection of microprobe analyses of reference biotites onto phlogopite-annite-eastonite-siderophyllite quadri-lateral. Biotites generally show greater range in tetrahedral aluminum/silicon compositions than in Fe/(Fe + Mg). Ex-treme values are chloritized biotites and are also characterized by lower K_2O values.

the biotites do vary in composition, largely in tetrahedral silicon-aluminum composition. Of the four biotites reported here and three others not reported, the mica-Mg, mica-Fe[13], and Cl-biotite[14] are the most suitable for use as intra- and interlaboratory monitors. There is some compositional variation, but an average of five or more analyses yields compositions comparable with that reported.

References

1. H. Takei, "Czochralski growth of Mn_2SiO_4 (tephroite) single crystal and its properties," *J. Crystal Growth* 34: 125-131, 1976.

2. E. Jarosewich, J. A. Nelen, and J. A. Norberg, "Reference samples for electron microprobe analysis," *Geostandards Newsletter* 4: 43-47, 1980.

3. O. W. Florke, "Kristallographie and röntgenometrische Untersuchungen im System $CaSO_4$-$CaSO_4$ $2H_2O$," *Neues Jb. Mineral. Abh.* 4: 189-240, 1952.

4. E. J. Young, A. T. Myers, E. L. Munson, and N. M. Conklin, "Mineralogy and geochemistry of fluorapatite from Cerro de Mercado, Durango, Mexico," *U. S. Geol. Survey Prof. Paper* 650-D, D84-D93, 1969.

5. J. A. Speer and M. L. Hensley-Dunn, "Strontianite composition and physical properties," *Am. Mineralogist* 61: 1001-1004, 1976.

6. Th. G. Sahama, "Mineralogy of the humite group," *Ann. Acad. Sci. Fennicae III. Geol. Geogr.* 31: 1-50, 1953.

7. N. L. Bowen, J. F. Schairer, and E. Posnjak, "The system Ca_2SiO_4-Fe_2SiO_4," *Am. J. Sci.* (5) 25: 271-297, 1933.

8. D. B. Stewart and T. L. Wright, "Al/Si order and symmetry of natural alkali feldspars, and the relationship of strained cell parameters to bulk compositions," *Bull. Soc. Fr. Mineral. Cristallogr.* 97: 356-377, 1974.

9. T. N. Solberg, J. Abrecht, and D. A. Hewitt, "Graphical procedures for the refinement of electron microprobe analysis of fine-grained particles," *Microbeam Analysis --1981*, 160-162.

10. T. O. Ziebold and R. E. Ogilvie, "An empirical method for electron micro-analysis," *Analytical Chemistry* 36: 322-327, 1964.

11. A. E. Bence and A. L. Albee, "Empirical correction factors for the electron microanalysis of silicates and oxides," *J. Geology* 76: 382-403, 1968.

12. A. L. Albee and L. Ray, "Correction factors for electron-probe microanalysis of silicates, oxides, carbonates, phosphates, and sulfates," *Analytical Chemistry* 42: 1408-1414, 1970.

13. K. Govindaraju, "Report (1968-1978) on two mica reference samples: Biotite mica-Fe and phlogopite Mica-Mg," *Geostandards Newsletter* 3: 3-24, 1979.

14. D. F. Lee, "A chlorine-rich biotite from Lemhi County, Idaho," *Am. Mineralogist* 43: 107-111, 1958.

15. J. C. Rucklidge, "Specifications of Fortran program SUPERRECAL," Department of Geology, University of Toronto, 1971.

TABLE 2.--Reported and determined analyses for the reference biotites.

	biotite - Mg			biotite - Fe			biotite Washington, R.I.			Cl - biotite		
	reported[13]	probe	σ	reported[13]	probe	σ	reported	probe	σ	reported[14]	probe	σ
SiO2	38.30	38.44	(0.39)	34.40	34.50	(0.38)	36.12	36.25	(0.68)	33.09	32.93	(0.45)
Al2O3	15.20	14.87	(0.35)	19.50	18.51	(0.30)	18.60	16.63	(0.59)	17.65	18.15	(0.65)
Fe2O3	1.98			4.64			1.68			2.42		
FeO	6.73 (8.51)*	7.96*	(0.70)	18.91 (23.09)*	22.53*	(0.30)	18.06 (19.57)*	19.33*	(0.51)	29.22 (31.40)*	30.04*	(1.16)
MnO	0.26	0.24	(0.06)	0.35	0.39	(0.06)	0.27	0.27	(0.05)	0.04	0.09	(0.03)
MgO	20.40	20.40	(0.54)	4.55	4.81	(0.17)	9.91	9.88	(0.44)	2.83	2.88	(0.16)
CaO	0.08	0.04	(0.01)	0.43	0.07	(0.04)	0.18	0.05	(0.03)	0.10	0.03	(0.02)
Na2O	0.12	0.26	(0.10)	0.30	0.32	(0.09)	0.28	0.04	(0.04)	0.13	0.10	(0.06)
K2O	10.00	10.48	(0.29)	8.75	9.34	(0.18)	8.79	9.37	(0.36)	9.04	9.13	(0.22)
TiO2	1.63	1.61	(0.31)	2.50	2.49	(0.16)	2.43	2.89	(0.43)	1.30	1.43	(0.13)
P2O5	0.01	0.04		0.45	0.11					0.02		
H2O+	2.09	2.86+	(0.01)	2.91	3.02+	(0.02)	2.81	3.57+	(0.04)	2.92	3.33+	(0.02)
H2O-	0.31			0.43			0.02			0.04		
Cl	0.08	0.13		0.05	0.09	(0.01)	0.23	0.12	(0.03)	1.11	1.13	(0.24)
F	2.85	2.60	(0.18)	1.58	1.55	(0.14)	0.76	0.66	(0.15)	0.23	0.17	(0.04)
BaO	0.45	0.49	(0.09)	0.016	0.06	(0.05)	0.22	0.22	(0.08)	0.09	0.11	(0.04)
SrO	0.003	0.06		0.0006	0.04					0.04		
Cr2O3	0.015			0.013	0.05							
CO2	0.15			0.19								
Rb2O							0.04					
	100.66	100.48		99.96	97.88		100.40	99.30		100.31	99.55	
O≡F+Cl	1.20	1.12		0.67	0.67		0.30	0.31		0.34	0.33	
	99.26	99.36		98.83	97.21		100.10	98.99		99.97	99.22	
number of analyses	23			20			14			22		

*total iron as FeO
+calculated to give 24 (0,OH,F,Cl)

DECIPHERING THE EARLY HISTORY OF THE SOLAR SYSTEM BY MICROANALYSIS OF METEORITES

G. J. Taylor

Many types of meteorites are made of ancient, primitive components that have been only slightly altered since they formed about 4.5 billion years ago. These materials contain the record of the processes that affected planetary materials from the earliest stages of solar system history when a gas-dust cloud (the solar nebula) was colapsing to form the sun and planets. Because many of these components are fine grained, microanalysis is essential in determining their nature and origin. Meteorites also hold information about the thermal evolution of small (few hundred kilometers in radius) bodies in the solar system. This kind of information, which leads to inferences about the structure and fragmentation histories of small planets, can be acquired most effectively by electron microprobe analysis. This paper gives a brief and by no means complete account of meteorite studies involving microanalytical techniques (electron microprobe and scanning and transmission electron microscopy). The emphasis is on what we learn (or hope to learn) from these studies, rather than on the techniques themselves.

Primitive Components in Meteorites: Recorders of Processes in the Solar Nebula

The solar system formed during the gravitational collapse of a vast cloud of interstellar gas and dust. The gas and dust reacted as pressures and temperatures increased during the collapse and during transient high-temperature, high-pressure events. The components in one type of meteorite called Type 3 chondrites (named for their primitive, unmetamorphosed state and for chondrules, millimeter-sized droplets of rapidly crystallized silicate melt which they contain) appear to represent different stages in the history of the solar nebula. Therefore, they contain detailed information about the chemical reactions that took place and the physical-chemical conditions in the nebula, and possibly about conditions in interstellar space before the solar system formed. In many ways the study of the components in chondrites is the most fundamental kind of planetary science-- it tells us what the raw materials of the planets were like.

Chondrite Matrices. Chondrites are composed of chondrules and lumps of metallic Ni, Fe embedded in a dark (usually optically opaque in 30 μm-thick thin sections), fine-grained matrix. The abundance of matrix varies from about 15 to 50 vol.%. It is so fine grained (large grains are 5 μm across), that it was ignored for many years because optical microscopy was unable to discern much about it. During the past several years, however, electron microprobe analyses[1,2] have revealed that matrix is substantially richer in FeO than are chondrules. Somewhat surprisingly, matrix compositions in Type 3 chondrites are very similar to those of CI chondrites, which form the basis of so-called cosmic abundances,[3] excluding H_2O, C, S, and other highly volatile substances. This finding suggests that the FeO-rich matrix may be among the most primitive materials in meteorites and may represent the starting materials for the other components. The mineralogy of chondrite matrices is thus far ill defined. Microprobe and SEM data demonstrate the presence of abundant olivine, with minor amounts of magnetite, sulfides, pyroxene, metallic Ni, Fe, and graphite.[1,2,4-8] Textures are variable; some samples consist of piles of elongated olivine grains resembling match sticks[6] whereas others have a clastic assemblage apparently stuck together with amorphous material (Fig. 1).[2] However, much more work on matrix texture, phase compositions, and mineral abundances is needed. This work will clearly require detailed SEM observations followed by TEM, including analytical TEM.
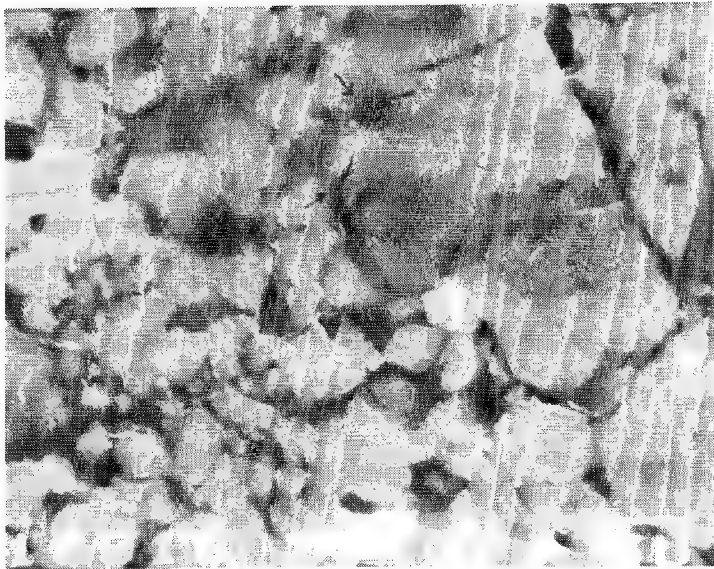
FIG. 1.--SEM backscattered electron image of matrix in Semarkona Type 3 chondrite.[2] Note clastic texture consisting mostly of micron-sized mineral grains. Arrows point to Si-rich, possibly amorphous material.

Graphite-magnetite. Scott et al.[9,10] recently described a previously unrecognized primitive component in chondrites: aggregates that consist largely of submicron graphite and magnetite. Some graphite crystals are large enough ($\sim$ 5 μm) so that the characteristic optical anisotrophy can be observed, but most graphite and all magnetite crystals are too small to be observed unambigiously even with an SEM. X-ray diffraction demonstrates the presence of both phases and preliminary TEM work on one aggregate confirms the x-ray identification (P. Fraundorf, personal communication). Electron microprobe analyses show that the aggregates contain less than about 5 wt.% of elements other than C and Fe. C varies from about 40 to 98 wt.% and covaries with Fe (Fig. 2). (The curvature in Fig. 2 is due to strong absorption of C x rays by Fe; the data were not corrected except for background and drift.) Graphite-magnetite aggregates doubtless formed in the solar nebula, perhaps by reaction of Fe metal with CO, but some grains of graphite and magnetite might have existed prior to the formation of the solar system: there is astronomical evidence for the existence of graphite grains in interstellar space.
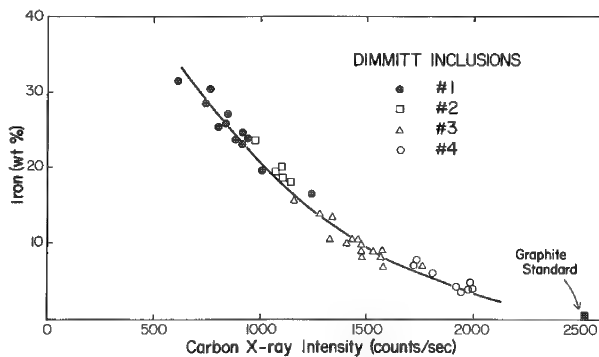
FIG. 2.--Electron microprobe data showing approximate Fe concentration in four graphite-magnetite inclusions (different symbol for each) plotted against the intensity of carbon x rays (K-line, corrected for background). Data define a mixing curve between pure carbon and Fe-rich mineral, which x-ray diffraction and electron diffraction show to be magnetite.

FIG. 3.--Electron microprobe profile across adjacent kamacite (low-Ni) and taenite grains in chondrite. Note characteristic M-shaped profile in taenite.

Metallic Fe, Ni. In Type 3 chondrites, kamacite (metallic Fe, Ni with 5-7 wt.% Ni) contains 0.1 to 1 wt.% Cr, Si, and P, as determined by electron microprobe analysis.[11-14] Kamacite in metamorphosed chondrites contains undetectable amounts of these elements. The high contents of the elements in kamacite of Type 3 chondrites were probably acquired at high temperatures in the solar nebula, in accord with thermodynamic calculations.[15] These high temperatures may have occurred during the formation of chondrules.[16]

Chondrules. These constitute the most abundant component in chondrites. There is uni-

versal agreement that most chondrules were once molten silicate droplets that cooled rapidly. Most are large enough to separate for chemical and isotropic analysis, but microanalytical techniques are also important when one is trying to determine how these objects formed. For example, Gooding[17] examined the surfaces of 141 chondrules using both optical and scanning electron microscopy and found no hypervelocity impact craters, which have characteristic morphologies. This observation seems to rule out most models of chondrule origin involving impact. Furthermore, electron microprobe studies of zoning of olivine crystals within chondrules, when combined with experiments on melts of chondrule composition, suggest that chondrules, though certainly quenched, may have experienced a period of nearly isothermal annealing between the liquidus and solidus.[18] If verified by additional experiments, this finding would place constraints on the physical regime in which chondrules formed.

Ca-Al-rich Inclusions. Many chondrites contain inclusions whose bulk compositions (high content of Ca, Al, Ti, Zr, Os, rare earths, and other refractory elements) indicate formation at very high temperatures ($1500°K$ at 10^{-3} at. pressure) in the solar nebula. These inclusions are usually quite coarse grained (crystals 0.1-1 mm), but are surrounded by fine-grained rims. SEM study of the rims indicates that they represent lower-temperature assemblages than do the coarse-grained cores.[6,19] In many cases, several mineralogically and texturally distinct rims are observed on a single inclusion. The rims clearly represent changing conditions in the region of the solar nebula where the Ca-Al-rich inclusions formed.

Chondrite Thermal Histories. Clues to Asteroid Fragmentation

The cooling rates of chondrites in the temperature range 800-600°K can be determined by plotting the compositions and sizes of compositionally zoned taenite grains (taenite is a high-Ni metallic Fe,Ni mineral).[20,21] The method involves modeling of the growth of taenite grains and development of the characteristic M-shaped profile and comparison with a profile measured in a meteorite (Fig. 3). Taenite grains range in size from a few microns to about 100 μm, and so are ideally suited for electron microprobe analysis. In fact, the measurement of meteorite cooling rates was one of the first applications of electron microprobe analysis to meteorites.[22]

Some chondrites formed from a layer of debris generated by impacts on the surfaces of their parent bodies, which are probably asteroids. These chondrites, called regolith breccias, contain clasts of chondritic rock set in a finer-grained, clastic matrix. Taenite grains in the clastic matrix of an individual regolith breccia have compositions that indicate cooling rates of between 1 and 1000°K/million years. This wide range in cooling rates required that the chondritic rocks that were ground up by repeated impacts to form the clastic matrix came from a wide range of depths within the parent asteroids. Thermal calculations[20] indicate depths ranging from a few kilometers up to about 100 km (on bodies 200 km in radius). How can material from such a wide range of depths be brought to the surface? Impact would appear to be an obvious machanism, but it turns out that impacts are not capable of excavating material from tens of kilometers without disrupting a body a few hundred kilometers in diameter. Consequently, we have been led to the conclusion that the parent asteroids of chondrites must have been broken apart, but then reassembled.[23] This process, which results in a chaotic surface containing materials from throughout the original parent asteroid, was originally proposed by Davis et al. on the basis of theoretical considerations of asteroid mechanical strengths and on relative impact velocities in the asteroid belt.[24]

References

1. H. Y. McSween Jr. and S. M. Richardson, "The composition of carbonaceous chondrite matrix," *Geochim. Cosmochim. Acta* 41: 1145-1161, 1977.
2. G. R. Huss, K. Keil, and G. J. Taylor, "The matrices of unequilibrated ordinary chondrites: Implications for the origin and history of chondrites," *Geochim. Cosmochim. Acta* 45: 33-51, 1981.
3. A. G. W. Cameron, "Abundances of the elements in the solar system," *Space Sci. Rev.* 15: 121-146, 1970.
4. J. S. Allen, S. Nozette, and L. L. Wilkening, "A study of chondrule rims and chondrule irradiation records in unequilibrated ordinary chondrites," *Geochim. Cosmochim. Acta*

44: 1161-1176, 1980.

5.   D. A. Wark, "Birth of the presolar nebula: The sequence of condensation revealed in the Allende meteorite," *Astrophys. and Space Sci.* 65: 275-295, 1979.

6.   J. A. Wood, "Metamorphism in chondrites," *Geochim. Cosmochim. Acta* 26: 739-749, 1962.

7.   M. Christophe-Michel-Levy, "La matrice noire et blanche de la chondrite de Tieschitz(H3)," *Earth Planet. Sci. Lett.* 30: 143-150, 1976.

8.   R. S. Clarke et al., *Smithsonian Contrib. Earth Sci.* 5, 1970.

9.   E. R. D. Scott, G. J. Taylor, A. E. Rubin, A. Okada, and K. Keil, "Graphite-magnetite aggregates in ordinary chondrite meteorites," *Nature* 291: 544-546, 1981.

10.   E. R. D. Scott, A. E. Rubin, G. J. Taylor, and K. Keil, "New kind of Type 3 chondrite with a graphite-magnetite matrix," *Earth Planet Sci. Lett.* 56: 19-31, 1981.

11.   L. H. Fuchs and E. Olsen, "Composition of metal in Type III carbonaceous chondrites and its relevance to the source-assignment of lunar metal," *Earth Planet. Sci. Lett.* 18: 379-384, 1983.

12.   E. R. Rambaldi and J. T. Wasson, "Metal and associated phases in Bishunpur, a highly unequilibrated ordinary chondrite," *Geochim. Cosmochim. Acta* 45: 1001-1016, 1981.

13.   H. Y. McSween, "Carbonaceous chondrites of the Ornans type: A metamorphic sequence." *Geochim. Cosmochim. Acta* 41: 477-491, 1977.

14.   G. J. Taylor, A. Okada, A. E. Rubin, G. R. Huss, and E. R. D. Scott, "The occurrence and implications of carbide-magnetite assemblages in unequilibrated ordinary chondrites," *Lunar and Planetary Science XII* (The Lunar and Planetary Institute, Houston), 1076-1078, 1981.

15.   L. Grossman and E. Olsen, "Origin of the high-temperature fraction of C2 chondrites," *Geochim. Cosmochim. Acta* 38: 173-187, 1974.

16.   E. R. D. Scott, G. J. Taylor, and K. Keil, "Origins of ordinary and carbonaceous Type 3 chondrites and their components," *Lunar and Planetary Science XIII* (The Lunar and Planetary Institute, Houston), 704-705.

17.   J. L. Gooding and K. Keil, "Relative abundances of chondrule primary textural types in ordinary chondrites and their bearing on conditions of chondrule formation," *Meteoritics* 16: 17-44, 1981.

18.   H. Planner and K. Keil, "Evidence for the three-stage cooling history of olivine-porphyritic fluid droplet chondrules," *Geochim. Cosmochim. Acta* 46: 317-330, 1982.

19.   J. M. Allen, L. Grossman, T. Lee, and G. J. Wasserburg, "Mineralogy and petrography of HAL, an isotopically-unusual Allende inclusion," *Geochim. Cosmochim. Acta* 44: 685-699, 1980.

20.   J. A. Wood, "Chondrites: Their metallic minerals, thermal histories and parent planets," *Icarus* 6: 1-49, 1967.

21.   J. Willis and J. I. Goldstein, "A revision of metallographic cooling rate curves for chondrites," *Proc. Lunar Planet. Sci.* (12th), 1135-1143.

22.   J. A. Wood, "The cooling rates and parent planets of several iron meteorites," *Icarus* 3: 429-459, 1964.

23.   G. J. Taylor, E. R. D. Scott, A. E. Rubin, P. Maggiore, and K. Keil, "Structure and fragmentation of the parent asteroids of ordinary chondrites," *Lunar and Planetary Science XIII* (The Lunar and Planetary Institute, Houston), 799-800.

24.   D. R. Davis, C. R. Chapman, R. Greenberg, S. J. Weidenschilling, and A. W. Harris, "Collisional evolution of asteroids: Populations, rotations, and velocities," in T. Gehrels, Ed., *Asteroids*, Tucson: University of Arizona Press, 1979, 528-557.

ELECTRON MICROPROBE ANALYSIS OF TRACE ELEMENTS IN MINERALS AT 10 PPM CONCENTRATIONS

G. A. McKay and R. S. Seymour

One very important approach to deciphering geologic history is through the study of trace element abundances in rocks. Reliable interpretation of such abundance data requires knowledge of the effects of geological processes on trace element abundances. In order to contribute to this knowledge, we are studying the partitioning of various trace elements between silicate melts and several geologically important minerals in controlled laboratory experiments. This investigation requires *in situ* analysis of crystals and glass for trace elements. We have chosen the electron microprobe as our primary analytical tool. In some cases, we are able to "enrich" our experimental materials with amounts of trace elements which are easily measured by conventional microprobe techniques. However, enrichment to these levels is not always possible. Consequently, we have developed an improved technique for analysis at low concentrations.

The major challenge in performing microprobe analyses at low concentrations is to obtain the net x-ray intensity of the characteristic emission line of interest with sufficient precision and accuracy. Because net intensities are not measured directly, but rather are derived by subtraction of background from peak intensities, both background and peak must be measured with very high precision. For example, in our ARL-EMX microprobe at 30 kV, the net intensity of the $L\alpha_1$ emission line from 20 ppm Nd in Fo_{80} olivine is only 1.5% of the intensity of the continuous spectrum background at that wavelength. Hence, in order to measure 20 ppm Nd in our ARL probe with a relative precision of $\pm10\%$, peak and background intensities must each be determined with relative precisions of 0.1%. In principle, it is always possible (though not necessarily practical) to obtain the required counting precision by counting for a sufficiently long interval. For instance, precisions of $\pm0.1\%$ (2σ) may be obtained by accumulation of 3×10^6 counts, which requires counting times for Nd of 2000 s at 1μA sample current on our ARL probe.

Unfortunately, counting statistics are not the only limitation to trace element analyses with the microprobe. In addition to adequate counting precision, peak and background intensities must be measured with sufficient accuracy to limit systematic errors in net intensities to acceptable levels. One major source of systematic error is instrument drift, primarily from instability of the electron beam. For analyses where peak intensity is high relative to background, slight drift in beam current between measurement of peak and background intensities is of little consequence. However, if peak intensity is only slightly higher than background, such drift can result in large systematic errors in net intensity. Over the long counting times required to obtain adequate precision, even the most stable instruments are apt to drift significantly. Provided that drift is not erratic, this problem can be lessened by alternate measurment of peak and background intensities over shorter counting intervals and averaging of the results, rather than measurement of each with only one long counting interval.

A second major source of systematic error arises because background intensity cannot be directly measured at the wavelength of the characteristic line on the sample being analyzed. Conventionally, backgrounds are either interpolated from intensities measured on the unknown sample at wavelengths on either side of the characteristic line, or are measured at the characteristic wavelength on a reference sample very similar in composition to the unknown, but which is known to have a much lower concentration of the element being determined. The first of these approaches is completely unsatisfactory for determination of elements of low concentration because the intensity of the continuous spectrum is

---

Author McKay's address is SN7, NASA, Johnson Space Center, Houston, TX 77058; author Seymour's, Lockheed, 1830 NASA Road 1, Houston, TX 77058.

generally not a linear function of wavelength and interpolation often leads to large systematic errors in the background intensity. The second approach occasionally works very well, provided a reference sample of sufficient compositional similarity to the unknown is available. For example, Goldstein[1] used this method to measure Ge in iron meteorites, with a detection limit of 20 ppm, using Fe-Ni standards to measure backgrounds. However, the intensity of the continuous spectrum is a strong function of composition, especially of average atomic number. Hence, unless the composition of the reference sample is quite close to that of the unknown, this approach can also lead to significant systematic errors. It is often difficult to obtain reference samples of sufficient compositional similarity, particularly for complex silicates.

The analytical technique developed in this study overcomes many of the above difficulties. The approach is to use two separate spectrometers, with one set on-peak, i.e., at the characteristic wavelength, and the other set off-peak, at a nearby wavelength which is free of potential interfering characteristic lines and is therefore suitable for monitoring the intensity of the continuum. Care is taken to insure that no absorption edges for elements likely to be present in significant quantities occur between the on-peak and off-peak wavelengths. On a reference sample similar in composition to the unknown, but which is known to contain a negligible amount of the element being determined, the ratio between on-peak and off-peak intensities is measured with high precision. Then the intensities at both wavelengths are measured with high precision on the unknown. The net intensity for the unknown is given by $I(NET,X) = I(P,X) - I(B,X) \cdot I(P,REF)/I(B,REF)$, where $I(P,X)$ is the intensity measured with the on-peak spectrometer for the unknown, $I(B,X)$ is that measured with the off-peak spectrometer for the unknown, and $I(P,REF)$ and $I(B,REF)$ are these intensities for the reference sample. This net intensity is ratioed to that of a standard in the conventional manner to obtain concentration.

The above technique overcomes problems resulting from instrument drift and minimizes systematic errors in obtaining the background intensity for the unknown at the characteristic wavelength. Because off-peak intensity measurement occurs simultaneously with on-peak measurement, slight drift in electron-beam intensity affects x-ray intensities at both wavelengths proportionately, and hence has negligible effect on the net intensity obtained for the characteristic emission line. Furthermore, to a first approximation, the energy distribution of the continuous spectrum, and hence the ratio of intensities at two different wavelengths, is independent of sample composition. In contrast, the continuum intensity at any single wavelength is approximately proportional to the average atomic number of the sample. Hence, slight differences in composition between the reference sample and the unknown have a much smaller effect on net intensities computed by the ratio method described above than on net intensities obtained by directly subtracting the on-peak intensity for the reference sample from that for the unknown.

Reproducibility of analyses performed by the technique described above is illustrated in Fig. 1. The points represent three separate analyses of the same olivine crystal from an Nd-doped experimental charge. The analyses were performed on three separate days spanning a time of over eight months. The same low-Nd olivine crystal was used as a reference sample for each analysis. The plotted uncertainties represent ±2σ as predicted from Poisson counting statistics. For the analysis on 3/26/81, a statistically significant number (24) of repeated 400 s determinations display a sample standard deviation (3.2 ppm) in excellent agreement with that predicted from counting statistics (3.4 ppm). Analyses on the three different dates are in precise agreement, within analytical uncertainty.

The major factor limiting the precision and sensitivity of trace-element analyses by the techniques described here is the constancy of the intensity ratio between the two spectrometers. We have encountered several sources of variability in this ratio, some of which are understood and some of which are not. On the JSC ARL-EMX probe, this ratio has been found to be quite sensitive to the position of the electron beam on the surface of the sample and to the vertical height (focus) of the sample. However, careful operation can minimize this instrumental source of variability. If care is taken in focusing and if significant beam wander is prevented with the deflection system, the intensity ratios measured on a single sample within an interval of 1-2 hr almost always agree within uncertainties predicted from counting statistics. Commonly, drift in this ratio is noticeable over a period of several hours, possibly due to thermally induced changes in spectro-
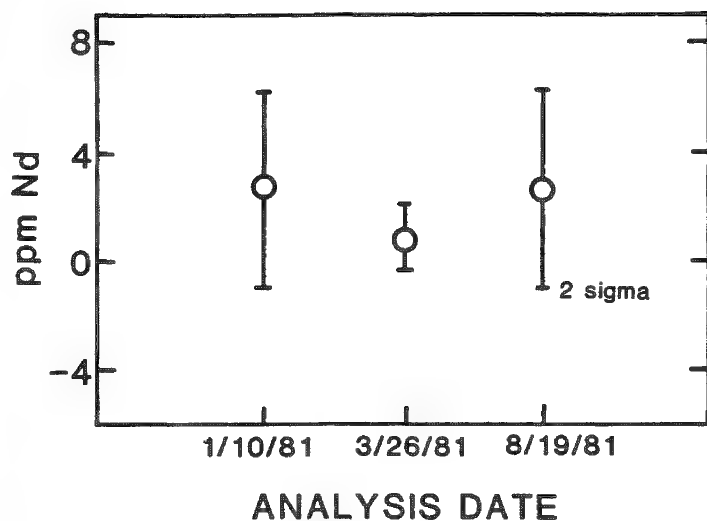
FIG. 1.--Replicate analyses of synthetic olivine grain using Springwater olivine as background reference material. Nd concentrations agree within uncertainty from counting statistics.
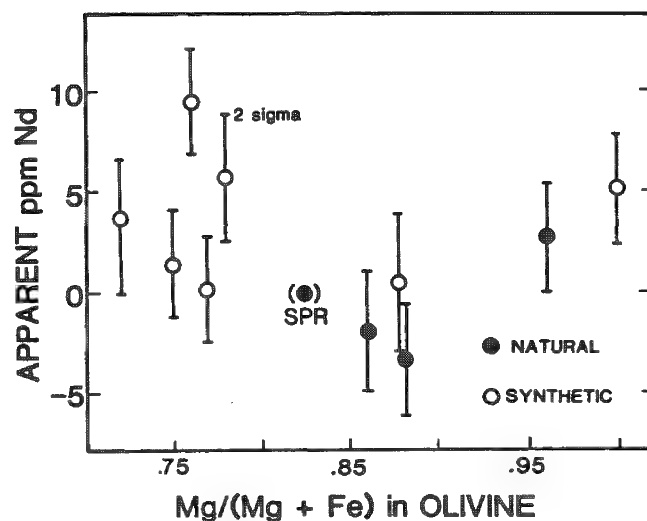
FIG. 2.--Analyses of various synthetic and natural olivine grains assumed to have less than 1 ppm Nd. Springwater (SPR) olivine was used as background reference material. Sample-to-sample variations indicate significance of variability in on-peak/off-peak intensity ratios.

meter geometry. However, such drift is not troublesome if the intensity ratio is measured on the reference sample at least once per hour.

We have also encountered small sample-to-sample variations in on-peak/off-peak intensity ratios. The significance of such variations for Nd analyses of olivine is illustrated in Fig. 2. This figure shows the apparent Nd content of ten olivine samples as measured by the technique described above, plotted against Mg/(Fe + Mg), the major compositional variable of olivine. Analyses were performed at 30 kV and 1 A, with one spectrometer set at the wavelength of the Nd $L\alpha_1$ line and another at an inteference-free position 0.06 Å higher than the peak. Glass REE2 of Drake and Weill[2] was used as the Nd standard, and Springwater Olivine was used as the low-Nd reference sample. For each sample treated as an unknown, 15-22 200s counts were alternated with 200s counts on Springwater. The error bars represent ±2 standard deviations of the mean for each sample.

All the olivines in Fig. 2 are believed to have actual Nd contents of less than 1 ppm. This belief results from the low value for the olivine/melt partition coefficient for Nd (<0.01 according to Refs. 3 and 4; <0.001, Ref. 5), the fact that natural melts with more than 100 ppm Nd are quite rare, and the knowledge that the synthetic olivines produced by us grew from melts with much less than 100 ppm Nd. The apparent Nd contents of at least three of the ten olivine samples differ significantly from zero as arbitrarily defined by Springwater, which indicates sample-to-sample variations in on-peak/off-peak intensity ratios. Until its source is understood, this variability in intensity ratios for low Nd samples provides the major limitation on precision and sensitivity of Nd analyses of olivine in the electron microprobe. To the extent that the 11 olivines shown in Fig. 2 constitute a representative sample of low-Nd olivine, this variability introduces an uncertainty of ±10 ppm (2σ) beyond counting statistics to Nd analyses performed with randomly chosen low-Nd olivines as background reference samples. This 10ppm uncertainty therefore also consitutues the minimum detection limit for Nd currently obtainable by this technique, regardless of counting time.

In summary, we have presented an improved technique for measuring backgrounds during trace-element analysis by electron microprobe which overcomes major difficulties encountered with conventional techniques. The new technique is shown to yield reproducible results to within 4 ppm Nd in olivine, and to have a minimum uncertainty and detection

limit of 10 ppm Nd in olivine. We believe that further refinements of the technique will permit us to apply it to analysis of geologically important trace elements in natural rocks and minerals.

References

1. J. I. Goldstein, "Distribution of Germanium in metallic phases of some iron meteorites," *J. Geophys. Res.* 72: 4689-4696, 1967.
2. M. J. Drake, and D. F. Weill, "New rare earth element standards for electron micro-probe analysis," *Chemical Geology* 10: 179-181, 1972.
3. C. Schnetzler and J. Philipotts, "Partition coefficients of rare earth elements between igneous matrix material and rock-forming mineral phenocrysts, II," *Geochim. Cosmochim. Acta* 34: 331-340, 1970.
4. G. A. McKay and D. F. Weill, "Petrogenesis of KREEP," *Proc. Lunar Sci. Conf.* 7: 2427-2447, 1976.
5. G. A. McKay, "Partitioning of REE between olivine, plagioclass, and synthetic basaltic melts: Implications for the origin of lunar anorthosites" (abstract), *Lunar and Planetary Science* XIII: 493-494, 1981.

MICROSTRUCTURE OF ENTREDICHO MERCURY ORE (CIUDAD REAL, SPAIN)

F. A. Calvo, J. M. Guilemany and J. M. Gómez de Salazar

Scanning Electron Microscopy (SEM) and x-ray Energy Dispersive Spectrometry (EDS) has been applied to the study of the microstructure and composition of mercury ore from Entredicho mine (Almadenejos, Ciudad Real, Spain). Conclusions are in line with those obtained for Almadén ore[1,2] and they support the hypothesis put forward about genesis of that deposit: the impregnation of a porous quarzite rock by magmatic mercury sulfide.

Structure and composition

Entredicho mine is not far from Almadén (Spain), where the world-famous mercury mine is located. Entredicho mine is really a recent *rediscovery* because it was probably exploited in Roman times. Today's works are being carried out in the open.

A previous conventional approach to the ore structure was made by optical microscopy (polished surface, transmited and reflected light) and microradiography. The cinnabar (HgS) is found to fill the spaces between the quartz grains, as well as inside them (microlites). Free mercury is found as drops of various sizes, even as droplets inside the quartz.

Ore samples were broken after cooled in liquid air. Fracture surfaces were metalized with gold and studied by SEM. At low magnification aggregates of small idiomorphic quartz crystals can be seen emerging from cinnabar (Fig. 1). At higher magnification the following interesting details can be observed:
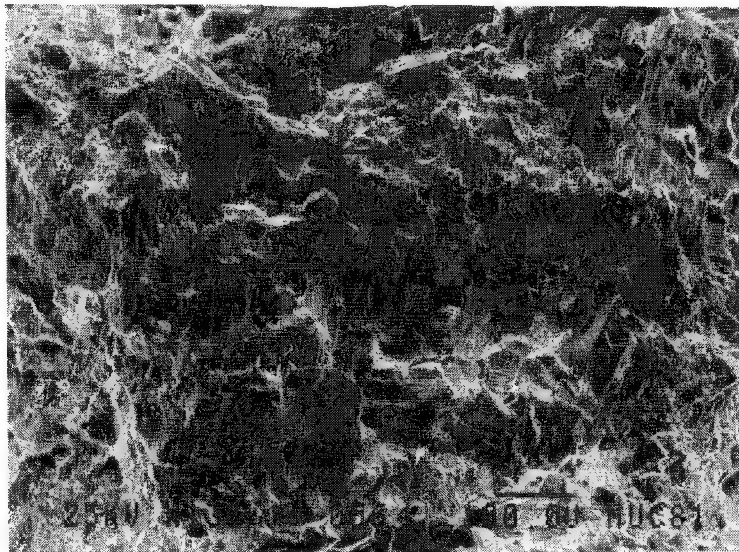
FIG. 1.--Fracture surface. Idiomorphic quartz microcrystals and cinnabar filling spaces.

1. The cinnabar is alotriomorphic around quartz cristals. Every intercrystalline space was filled up with cinnabar (Fig. 2).

2. There is no coherence whatsoever between HgS and SiO_2, although their contact has been very close. It is very easy to detach these constituents (Figs. 3, 9, and 10).

3. Fractured cinnabar exhibits a fibrous-laminar structure (Fig. 2). *Detached* cinnabar shows falt intersecting surfaces forming dihedral angles (Fig. 4).

4. Quartz grains can be seen as (a) well developed idiomorphic crystals (Figs. 2 and 3), (b) not quite developed crystals (unfinished) (Fig. 5), and (c) fracture crystals (Fig. 11).

5. Free mercury has been found (a) within the cinnabar (Fig. 6), (b) within the quartz grains (Fig. 7), and (c) in the contact quartz-cinnabar and at cinnabar grain boundaries (Fig. 8).

6. The contact cinnabar-quartz was so close that the smallest details on the surface of quartz crystals can be seen perfectly reproduced on the detached cinnabar (Figs. 11-14).

The authors are at Departamento de Metalurgia, Facultad de Ciencias Quimicas, Universidad Complutense, Madrid-3, Spain.
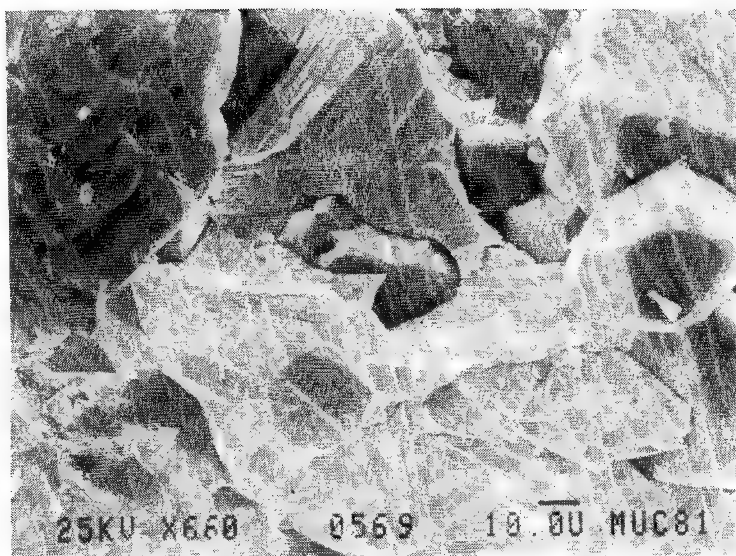
FIG. 2.--Details of Fig. 1. Broken cinnabar filling quartz intercrystalline spaces.

FIG. 3.--Profile correspondence between cinnabar and quartz. Lack of cohesion.

7. Pyrite has been found in low proportion as small idiomorphic crystals associated to the cinnabar (Fig. 15).

8. By microanalysis (EDS), copper has been found in solid solution in cinnabar, and copper and indium in mercury metal.

Discussion

However close their association in the ore, quartz and cinnabar are not singenetic. The quartzitic rock--the host rock--could have been formed from detritus by consolidation under water through dissolution and reprecipitation as suggested by Mackenzie and Grees,[3] with the result of a more or less compact rock with abundant intercrystaline or intergranular spaces; the degree of idiomorphism would depend on the growth conditions.

The facts are:

(a) full impregnation of the rock by HgS,

(b) lack of cohesion and of any kind of interaction between HgS and SiO_2,

(c) printing on HgS of the smallest surfaces details of the quartz grains or crystals that were in contact with it,

(d) existence of free mercury everywhere but in small proportions,

(e) existence of small idiomorphic crystals of pyrite, and

(f) solid solubility of Cu in HgS.

These facts can only be explained if it is accepted that magmatic HgS in a molten state (highly fluid) arrived at the host rock.

Since SiO_2 is chemically inert to HgS even in the molten condition, no interaction other than a sort of casting process on solidification could take place. It is perfectly possible that this magmatic HgS could have more Hg than the stoichiometric; this excess of Hg, being in solution, would possibly have a fluidifying effect on the molten cinnabar. On solidification this Hg was segregated and, as a vapor phase, made its way to the places where it is found. Magmatic conditions also explain the solubility of Cu and the crystalization of pyrite from the molten phase (HgS). There is geological evidence of volcanic phenomena associated with the Almadén deposit.

Conclusions

1. SEM has been a key instrument for the study of the microstructure and composition of mercury ores.

2. The findings in Almadén and Almadénejos ores are coincidents for a common genesic phenomena.

3. The ore is the result of the impregnation of a quartzitic host rock by a magmatic HgS as a molten, highly fluid phase. The geological evidence of volcanism associated with the deposit is very significant.

FIG. 4.--Grain boundaries in cinnabar.
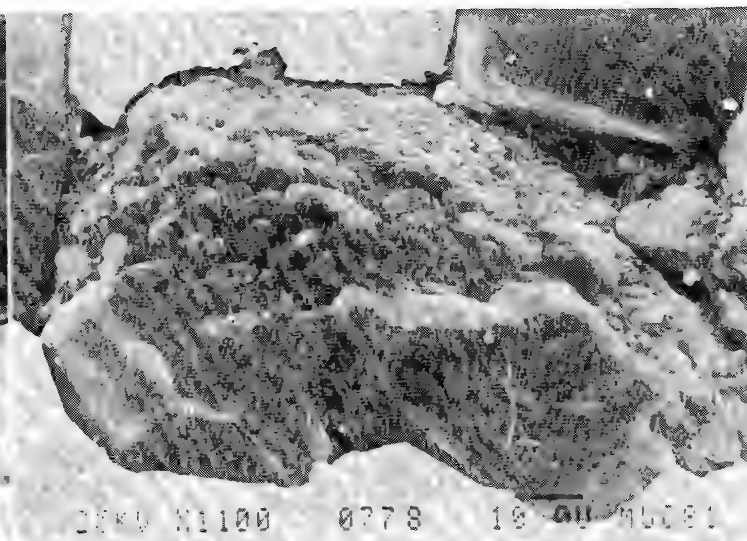
FIG. 5.--Irregular surface in quartz crystal (partially idiomorphic).
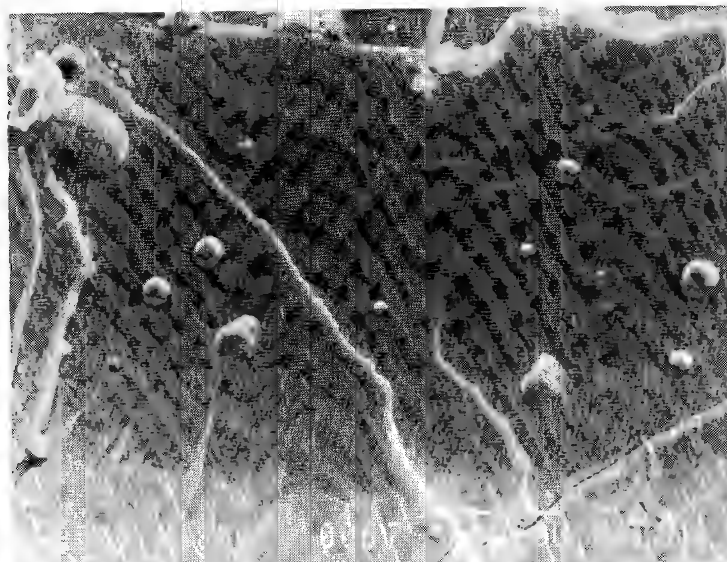
FIG. 6.--Mercury droplets in HgS. Fracture surface.
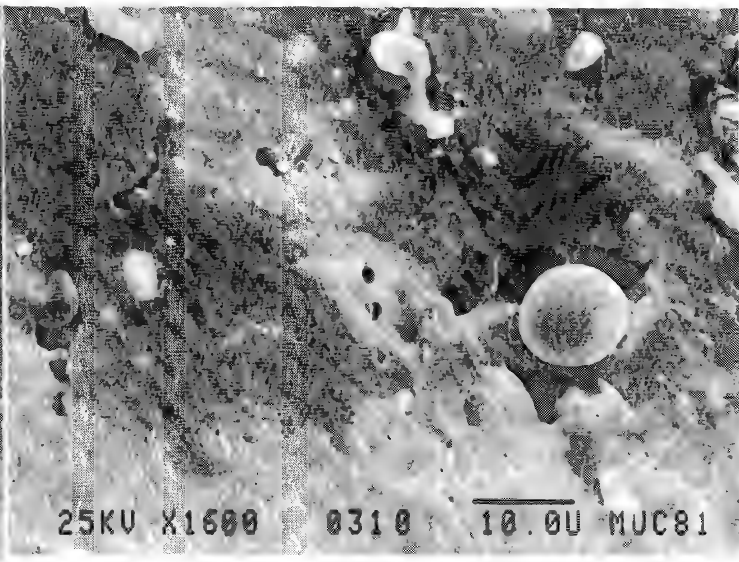
FIG. 7.--Mercury droplets and HgS microlites in quartz crystal. Fracture surface.

4. On solidifying, the excess of Hg in the molten phases (HgS) was segregated. The HgS reached the smallest spaces and cast every detail of the quartz grains surface.

5. No other genesic hypothesis put forward to date could exp ain (a) that every space in the host rock was *completely filled* up with HgS, (b) the existence of metallic mercury, or (c) the high-quality reproduction on HgS of the smallest details on the quartz interphase.

References

1. F. A. Calvo and J. M. Guilemany, "Estructura del mineral de Almadén," *Memorias del 1er Congreso International del Mercurio*, Barcelona (Spain), 1974, 177-188.

2. F. A. Calvo and J. M. Guilemany, "Estudios sobre la estructura y considera ciones sobre la génesis de menas de mercurio: I. Yacimiento de Almadén," Rev. Real Acad. de Ciencias Exactas, Físicas y Naturales. Madrid, 1980, 401-415.

3. F. T. Mackenzie and R. Gees, "Quartz: Synthesis at earth surface conditions," *Science* 173: 533-534, 1977.
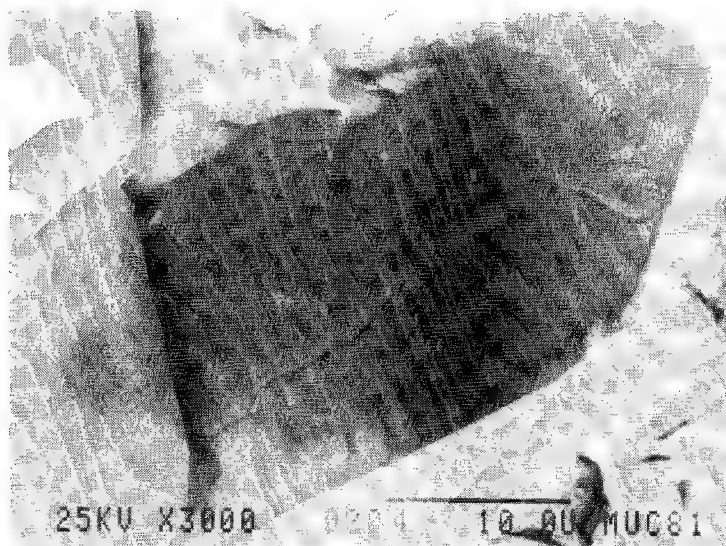
FIG. 8.--Mercury droplets in HgS grain boundaries.
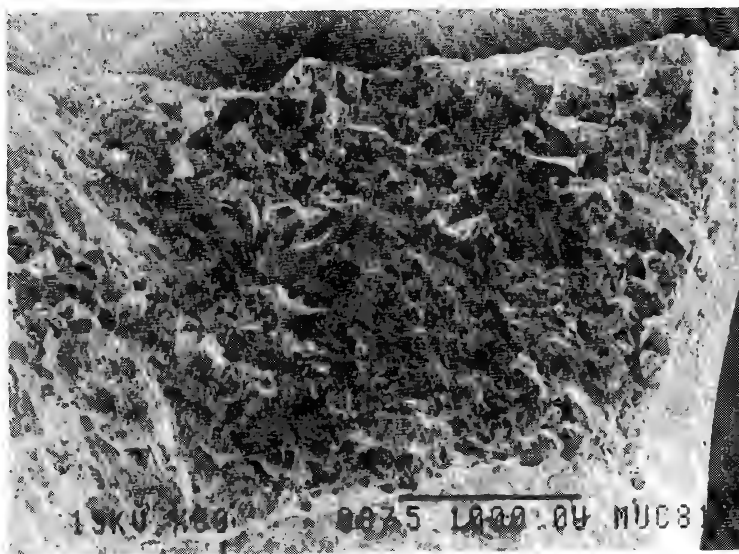
FIG. 9.--Fracture surfaces corresponding to Fig. 10. Impressions of quartz crystals on cinnabar.
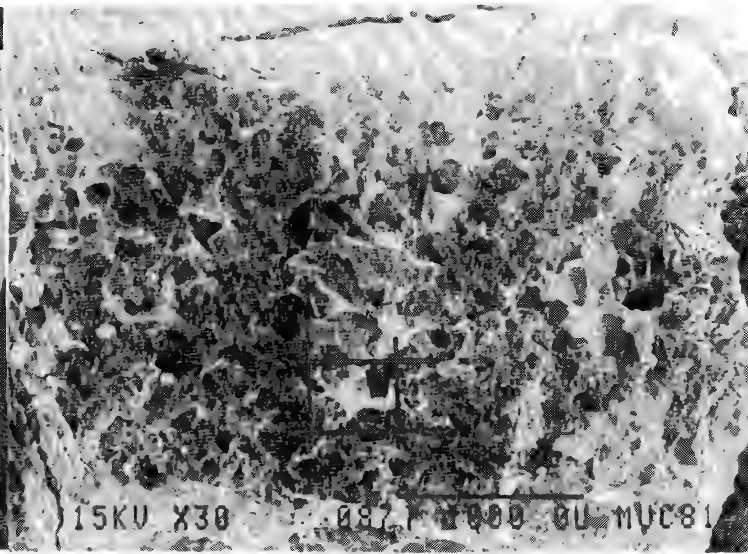
FIG. 10.--Fracture surfaces corresponding to Fig. 9. Impressions of quartz crystals on cinnabar.
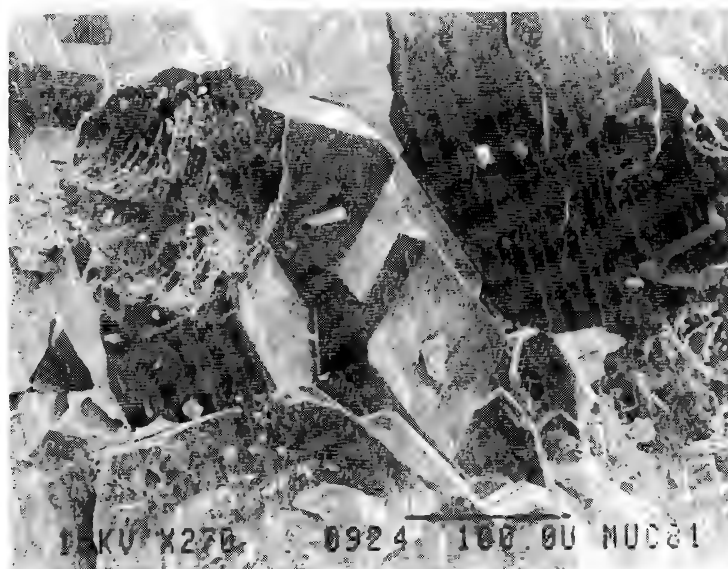
FIG. 11.--Quartz crystal (broken on the top). Detail of Fig. 9.
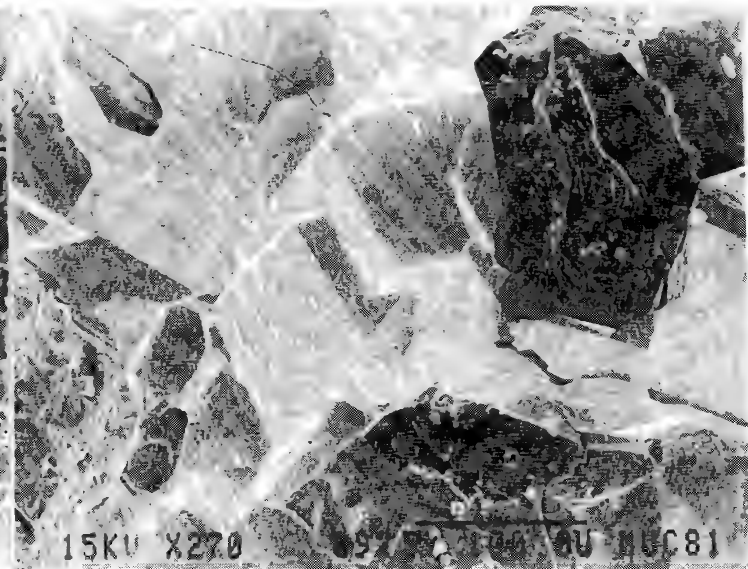
FIG. 12.--Impression left on cinnabar by quartz crystals of Fig. 11. Detail of Fig. 10.

FIG. 13.--Idiomorphic quartz crystal with some irregularities.

FIG. 14.--Impression left by quartz crystal Fig. 13 on cinnabar.
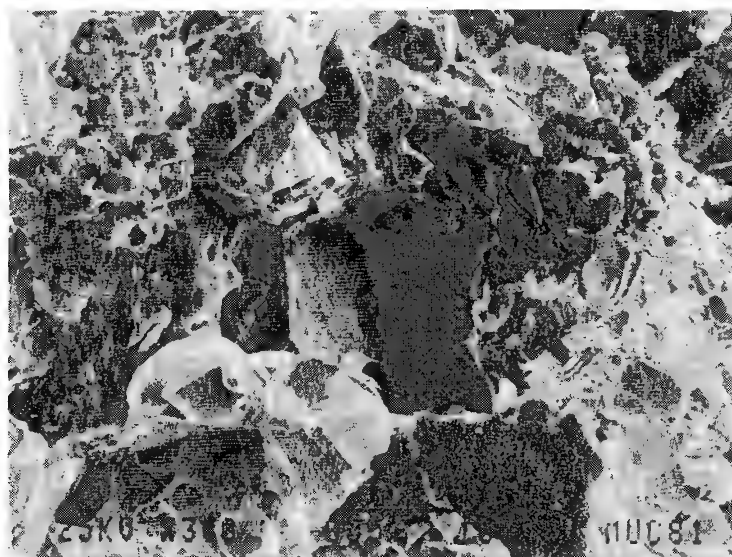
FIG. 15.--Idiomorphic pyrite crystal surrounded by cinnabar.

ENERGY-DISPERSIVE ANALYSIS OF SOME COMMON ROCK FORMING MINERALS

A. B. Merkle and A. O. Sandborg

Energy-dispersive x-ray (EDX) spectra are collected from some common rock-forming minerals by use of a windowless detector. Integrated peak counts for elements present in concentrations greater than 5% yield standard deviations of less than 1%. Quantitative analysis is accomplished by use of mineral standards and a modified version of FRAME C. Average relative error percentage values for oxygen, magnesium, aluminum, and silicon are 1.2, 0.8, 1.3, and 1.9, respectively. Averaged relative error percentage values for calcite, aluminosilicates, and the clay minerals are 0.7, 0.9, and 1.8, respectively.

Silicate and carbonate minerals are comprised of more than 50% by weight of light elements. Therefore, (EDX) analysis using a conventional beryllium window detector yields the direct analysis of less than 50% by weight of the elements present. On the other hand, use of a windowless EDX detector yields the direct analysis of more than 97% by weight of the elements present.

In comparison to conventional EDX analysis, windowless EDX analysis presents no specific problems. The main requirement for windowless analysis is an electron column vacuum of at least 10^{-5} Torr. The sample being analyzed should be subjected to the same rigorous preparation techniques as if the sample were to undergo wavelength-dispersive x-ray (WDX) analysis by use of an electron microprobe. That is to say, the sample should have a flat surface and the electron beam-sample-detector geometry should be well known. Finally, quanitative windowless EDX analysis of minerals should require the use of mineral standards.

Analytical Conditions

EDX spectra for all minerals except muscovite are generated from a Philips 500 SEM. Muscovite spectra are generated from a Philips 505 SEM. Mineral spectra are collected and processed by an EDAX 9100/60 analyzing system with ECON (windowless) detector. Vacuum level for the Philips 500 is 5×10^{-7} Torr. Vacuum level for the Philips 505 is 2×10^{-7} Torr. All samples are gold coated to a thickness of approximately 125 Å. Calcite spectra are accumulated with a 9.0kV accelerating potential. Spectra for all other minerals are accumulated with a 12.0kV accelerating potential. The accelerating potential is verified by observation of the upper limit of the generated x-ray continuum on each spectrum.

Sample tilt for minerals analyzed in the Philips 500 is 20°. Sample tilt for minerals analyzed in the Philips 505 is 10°. These tilt angles yield a take-off angle of 32.1°. Analysis time for calcite and muscovite is 200 live seconds. The analysis time for all other minerals is 180 live seconds. Spot size (auxiliary lens current) is adjusted to yield a count rate of approximately 2500 cps. The analyzer is calibrated so that K_a energy peaks for Al and Cu occur at values of 1.486 keV and 8.040 keV, respectively.

Clay mineral samples montmorillonite, attapulgite, and kaolinite obtained from pressed pellets are mounted so that the surface being analyzed is flat and lies parallel to the sample stub. Mineral fragments calcite, orthoclase, and muscovite are mounted on cleavage faces. Again, as for the clay minerals, the surface being analyzed is flat and lies parallel to the sample stub. Additional information concerning the minerals analyzed is presented in Table 1.

The authors are at Applications Laboratory, EDAX International, Inc., Box 135, Prairie View, IL 60069.

TABLE 1.--Analytical conditions for minerals.

Minerals	Individuals analyzed	Spectra accumulated	Sample surface analyzed	Excitation region
Calcite	3	14	Cleavage	Spot mode at 320x
Orthoclase	2	20	Cleavage	Spot mode at 640x
Muscovite	2	10	Cleavage	Spot mode at 312x
Montmorillonite	2	11	Pressed powder	Area scan 1250x
Attapulgite	2	11	Pressed powder	Area scan 1250x
Kaolinite	2	11	Pressed powder	Area scan 1250x

Corrections and Calculations

As each EDX spectrum is being accumulated, a label is assigned and all significant elemental peaks are identified. After accumulation, the EDX spectrum is stored on disk.

Statistical errors for integrated peak intensities are calculated from the following formula:[3]

$$S = \frac{\sqrt{N + 2B}}{N} \quad (100)$$

where S = statistical error, N = net peak counts, and B = subtracted background counts. On all spectra used in these analyses the integrated peak counts, for elements with concentrations of 5% or more, yield a statistical error between 0.3 and 1.0% of the peak count.

Prior to quantitative analysis each spectrum is subjected to a manual background correction. Quantitative analysis is accomplished by use of mineral standards and a modified version of FRAME C.[2,4]

Standard deviations for analyzed elements are calculated from the following formula:

$$S = \sqrt{\frac{\sum\limits_{i=1}^{N} (x_i - \bar{x})^2}{N - 1}}$$

where S = standard deviation, X_i = concentration of an element, X = average concentration, and N = number of individuals analyzed.

Relative error percentage for an element is calculated from the following formula:

$$R = (T - A) \; (100 \div T)$$

where R = relative error %, T = theoretical (actual) weight %, and A = analyzed weight %.

Average relative error % for a mineral is calculated from the following formula:[1]

$$V = \frac{\left(\sum\limits_{i=1}^{N} |R_i| \right)}{N}$$

where V = average relative error %, R_i = relative error % (elemental), and N = number of elemental determinations for the mineral.

Results

The analytical results for minerals investigated are presented as Tables 2, 3, and 4. Each table contains data for element analyzed, theoretical or actual chemical composition, averaged analyzed weight percentage, standard deviation, relative error percentage,

TABLE 2.--Energy-dispersive analysis.

A. Calcite

Element	Theoretical weight %	Analyzed weight %	Standard deviation	Relative error %
C	12.0	11.8	0.41	-1.7
O	48.0	48.1	0.79	+0.2
Ca	40.0	40.1	1.06	+0.2

Average relative error % 0.7

B. Orthoclase

Element	Theoretical weight %	Analyzed weight %	Standard deviation	Relative error %
O	46.0	45.4	0.42	-1.3
Na		0.4	0.04	
Al	9.7	9.7	0.08	0.0
Si	30.3	30.4	0.43	+0.3
K	14.0	14.0	0.19	0.0

Average relative error % 0.4

TABLE 3.--Energy-dispersive analysis.

A. Muscovite

Element	Theoretical weight %	Analyzed weight %	Standard deviation	Relative error %
O	48.2	48.8	2.11	+1.2
Na		0.24	0.04	
Mg		0.51	0.04	
Al	20.3	20.1	0.51	-1.0
Si	21.1	20.8	0.61	-1.9
K	9.8	6.7	0.57	
Fe		2.8	0.48	
H	0.5			

Average relative error % 1.4

B. Montmorillonite

Element	Chemical composition	Analyzed weight %	Standard deviation	Relative error %
O	53.7	52.9	0.81	-1.5
Mg	3.9	3.9	0.11	0.0
Al	9.3	9.4	0.16	+1.1
Si	28.2	28.8	0.54	+2.1
K	0.2	0.4	0.18	
Ca	2.0	2.2	0.15	
Ti	0.1	0.1	0.10	
Fe	1.1	1.3	0.28	
H	1.1			

Average relative error % 1.2

TABLE 4.--Energy-dispersive analysis.

A. Attapulgite

Element	Chemical composition	Analyzed weight %	Standard deviation	Relative error %
O	53.0	53.4	2.41	+0.8
Mg	6.2	6.3	0.16	+1.6
Al	5.5	5.6	0.18	+1.8
Si	28.5	29.1	1.18	+2.1
K	0.66	0.72	0.17	
Ca	1.4	1.6	0.43	
Ti	0.29	0.19	0.10	
Fe	2.3	1.9	0.79	
H	1.2			

Average relative error % 1.6

B. Kaolinite

Element	Chemical composition	Analyzed weight %	Standard deviation	Relative error %
O	55.7	54.4	2.35	-2.3
Al	21.0	21.6	0.37	+2.8
Si	20.7	21.3	1.30	+2.9
Ti	0.83	1.1	0.74	
H	1.5			

Average relative error % 2.7

and average relative error percentage. Table 5 relates element analyzed, compositional range, and average relative error percentage. The average relative error percentage for the analyzed minerals are listed as follows:

Calcite	0.7	Montmorillonite	1.2
Orthoclase	0.4	Attapulgite	1.6
Muscovite	1.4	Kaolinite	2.7

References

1. R. L. Myklebust and D. E. Newbury, "The use and abuse of a quantitative analysis procedure for energy-dispersive x-ray microanalysis," *Microbeam Analysis--1979*, 231-237.
2. R. L. Myklebust et al., "FRAME C: A compact procedure for quantitative energy-dispersive electron probe x-ray analysis," *Proc. MAS 12th Ann. Conf.*, 1977, 96A-96D.
3. J. C. Russ, "Statistical errors," EDAX EDITor, 1976, Vol. 6, No. 3, 61.
4. J. C. Russ, "Modifications and extensions to NBS FRAME C," *Microbeam Analysis --1979*, 268-272.
5. H. A. Van Oliphant and J. J. Fripiat, *Data Handbook for Clay Materials and Other Non-Metallic Materials*, New York: Pergamon Press, 1979, 13, 25, 34.

TABLE 5.--Average relative error percentage values related to element analyzed and compositional range.

Element	Compositional range (%)	Average relative error %
O	46.0 - 55.7	1.2
Si	20.7 - 30.3	1.9
Al	5.5 - 21.0	1.3
Mg	3.9 - 6.2	0.8
K	6.7 - 14.0	0.0*
Ca	40.0	0.2*
C	12.0	1.7*

*Only one value.

RARE-EARTH PYROSILICATES ($RE_2Si_2O_7$) AS POTENTIAL ELECTRON MICROPROBE STANDARDS

J. A. Speer and T. N. Solberg

Microprobe analyses involving rare earth elements (REE) lag behind those of other elements because of the numerous interfering x-ray spectra and the lack of comparable standards for all the REE. Little can be done about the x-ray spectra (Fig. 1), but the standards are amenable to improvement. Previous standards have included metals, oxides,[1] REE-doped anorthite glass,[2] analyzed minerals, and a limited number of synthetics such as REE-aluminate garnets. Problems with these standards include oxidation of the metals, hygroscopism of some oxides, and (for the minerals and glasses) limited quantities and the necessary testing for homogenization and actual amounts present.

One of the REE silicate compounds[3] appeared to be a promising standard. They contain significant amount of REE are stoichiometric, have high thermal stabilities, and can be manufactured when needed. The simplest compound appeared to be the REE analogs of the minerals thortveitite ($Sc_2Si_2O_7$) and thalenite ($Y_2Si_2O_7$). The $RE_2Si_2O_7$ compounds are known in all the binary REE_2O_3-SiO_2 systems and they show extensive polymorphism.[4]

The members of the REE pyrosilicates have been prepared by direct sintering of the oxides[5,6,7] or by growth from various fluxes.[8,9,10] In this study, the flux method for growing REE pyrosilicates was used and thus allowed relatively large, stoichiometric crystals to form.

The REE pyrosilicates were grown from molten Li_2MoO_4-MoO_3 or Li_2MoO_4-SiO_2 fluxes at approximately 850°C. The starting materials were 99.9% REE oxides and 99.95% SiO_2. All chemicals were from Apache Chemicals, Inc., Seward, Illinois. The charge consisted of between 5 and 10 wt-% of stoichiometric $RE_2O_3 \cdot 2SiO_2$ in the flux, well mixed in a platinum crucible. The charge was held at temperature in a muffle furnace for 4 to 5 days. The charge and crucible were air cooled and the flux was dissolved away in hot water.

The REE pyrosilicates grown thus far are the Pr, Nd, Sm, Tb, Er, Tm, and Y compounds (Fig. 2). The crystals have been as large as 4 mm in the case of Pr and Nd, but most are between 0.5 and 1 mm. X-ray powder and single-crystal work show the crystals to be one of the number of various polymorphs that are possible with these compounds. They are stable under the electron beam and microprobe analyses of the Nd pyrosilicate (Table 1) would suggest near ideal composition.

TABLE 1.--Microprobe analysis of flux-grown Nd-pyrosilicate.

	Flux-grown*	Ideal $Nd_2Si_2O_7$
SiO_2	27.12	26.32
Nd_2O_3	73.49	73.68
	100.61	100.00

*average of 6 analyses. Si-standard, quartz (SiO_2); Nd-standard, Nd-Ga garnet ($Nd_3Ga_5O_{12}$).

The authors are at the Department of Geological Sciences of the Virginia Polytechnic Institute and State University, Blacksburg, VA 24061-0976.
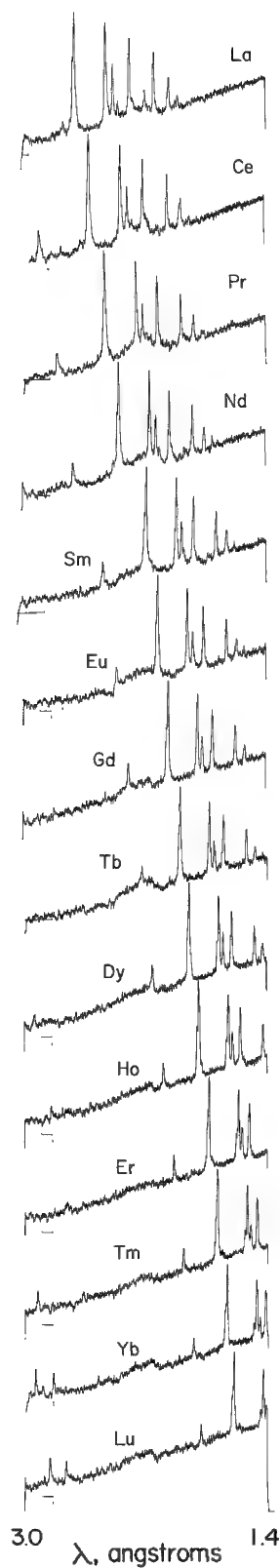
FIG. 1.--X-ray spectra of rare-earth elements with LiF crystal scanning between 3.0 and 1.4A d-spacing.
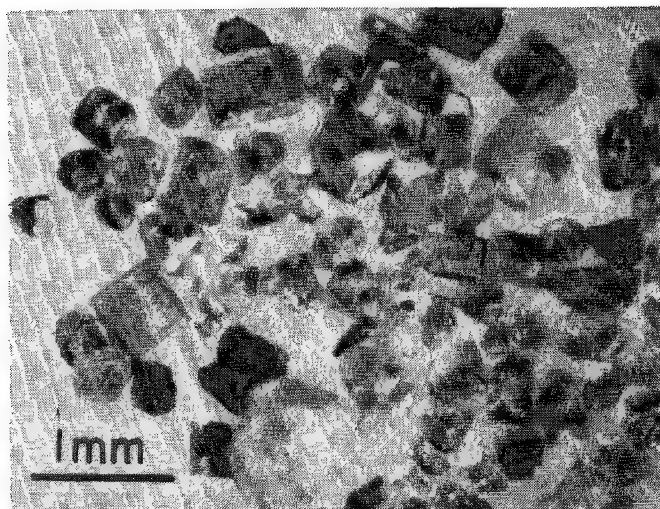
FIG. 2.--Photomicrograph of flux-grown $Pr_2Si_2O_7$ cyrstals.

References

1. R. Amli and W. L. Griffin, "Micro-probe analysis of REE minerals using empirical correction factors," *American Mineralogist* 60: 599-606, 1975.

2. M. J. Drake and D. F. Weill, "New rare earth element standards for electron microprobe analysis," *Chemical Geology* 10: 179-181, 1972.

3. J. Felsche, "The crystal chemistry of the rare-earth silicates," *Structure and Bonding* 13: 100-197, 1973.

4. J. Felsche, "Polymorphism and crystal data of the rare-earth disilicates of type R.E.$_2$Si$_2$O$_7$," *J. of the Less-common Metals* 2]: 1-14, 1970.

5. J. Ito and H. Johnson, "Synthesis and study of yttrialite," *American Mineralogist* 53: 1940-1952, 1968.

6. Yu. I. Smolin and Yu. F. Shepelar, "The crystal structures of the rare earth pyrosilicates," *Acta Cryst.* B26: 484-492, 1970.

7. J. Felsche and W. Hirsiger, "The polymorphs of the rare-earth pyrosilicates R.E.$_2$Si$_2$O$_7$ [R.E.: La, Ce, Pr, Nd, Sm]," *J. of the Less-common Metals* 18: 131-137, 1969.

8. B. M. Wanklyn, F. R. Wondre, G. B. Ansell, and W. Davison, "Flux growth of rare earth silicates and aluminosilicates," *J. Mat. Sci.* 9: 2007-2014, 1974.

9. A. Maqsood, B. M. Wanklyn, and G. Garton, "Flux growth of polymorphic rare-earth disilicates, R$_2$Si$_2$O$_7$(R = Tm, Er, Ho, Dy)," *J. Crystal Growth* 46: 671-680, 1979.

10. B. M. Wanklyn, "Effects of modifying starting compositions for flux growth," *J. Crystal Growth* 43: 336-344, 1979.

METHODS FOR STUDYING MAGNETIC DOMAINS IN THE SCANNING ELECTRON MICROSCOPE (SEM):
A REVIEW

O. C. Wells

Magnetic domains have been studied in the SEM by these four methods:

1. Scanning Lorentz microscopy of the fringing fields in transmission. Following the expressions used by Marton et al.[1] to describe similar methods in the transmission electron microscope, this approach can be divided into the *shadow* method, in which the image of a reference mesh is distorted by the fringing fields,[2] and the *Schlieren* technique, in which the image contrast changes abruptly from bright to dark along a line of constant intercepted flux.[3]

2. Type-1 magnetic contrast, in which the fringing fields above the surface of a solid specimen modulate the collected secondary electron current.[4] An exact mathematical theory has recently been given for the two-dimensional field case.[5]

3. Type-2 magnetic contrast, in which the backscattered electron current is modulated by the internal magnetic fields of the specimen.[6] This approach has been investigated theoretically by the Monte Carlo method.[6,7] The high-voltage version gives information from below the surface.[8] The stroboscopic version gives images from repetitively moving domain walls.[9] The lock-in version reduces (or in some cases eliminates) the topographic and compositional contrasts.[10]

4. Stöhr[11] has reported SEM studies of the magnetic flux in superconductors based on local heating by the electron beam.

Future progress is expected in imaging faster domain motions, lower values of internal flux, and a wider range of applications.

References

1. L. Marton and S. H. Lachenbruch, "Electron optical mapping of electromagnetic fields," *J. Appl. Phys.* 20: 1171-1182, 1949; "Electron optical observation of magnetic fields," *NBS J. Res.* 43: 409-428, 1949.

2. R. F. M. Thornley and J. D. Hutchison, "Magnetic field measurements in the scanning electron microscope," *Appl. Phys. Letters* 13: 249-250, 1968; "Magnetic field measurements in the scanning electron microscope," *IEEE Trans.* MAG-5: 271-275, 1969; "Measure magnetic fields with a scanning electron microscope," *Res./Dev.*, pp. 20-24, August 1969.

3. E. I. Rau and G. V. Spivak, "Scanning electron microscopy of two-dimensional magnetic stray fields," *Scanning* 3: 27-34, 1980.

4. J. R. Banbury and W. C. Nixon, "The direct observation of domain structure and magnetic fields in the scanning electron microscope," *J. Sci. Instrum.* 44: 889-892, 1967; D. C. Joy and J. P. Jakubovics, "Direct observation of magnetic domains by scanning electron microscopy," *Phil. Mag.* 17: 61-69, 1968.

5. O. C. Wells, "Calculation of Type-1 magnetic contrast in the scanning electron microscope (SEM)," *Microbeam Analysis--1981*, 127-130.

6. D. J. Fathers, J. P. Jakubovics, and D. C. Joy, "Magnetic domain contrast from cubic materials in the scanning electron microscope," *Phil. Mag.* 27: 765-768, 1973; D. J. Fathers, J. P. Jakubovics, D. C. Joy, D. E. Newbury, and H. Yakowitz, "A new method of observing magnetic domains by scanning electron microscopy," *Phys. Stat. Sol.* A20: 535-544, 1973 amd 22: 609-619, 1974.

7. D. E. Newbury, H. Yakowitz, and R. L. Myklebust, "Monte Carlo calculations of magnetic contrast from cubic materials in the scanning electron microscope," *Appl. Phys.*

The author is at the IBM Thomas J. Watson Research Center, Box 218, Yorktown Heights, NY 10598.

Letters 23: 488-490, 1973; T. Ikuta and R. Shimizu, "Magnetic domain contrast from ferromagnetic materials in the scanning electron microscope," *Phys. Stat. Sol.* A23: 605-613, 1974; J. P. Jakubovics and O. C. Wells, "Computer simulation of the imaging of magnetic domains in the scanning electron microscope," *J. Magnetism and Mag. Mat.* 15-18: 1523-1525, 1980.

8. R. Shimizu, T. Ikuta, T. Yamamoto, M. Kinoshita, and T. Murayama, "Direct observation of the magnetic domain structure in Mn-Zn ferrite using the 200 kV high voltage scanning electron microscope," *Phys. Stat. Sol.* A26: K87-89 (and 2 plates), 1974; T. Yamamoto, H. Nishizawa, and K. Tsuno, "High voltage scanning electron microscopy for observing magnetic domains," *J. Phys.* D8: L113-114 (and 1 plate), 1975.

9. T. Ikuta and R. Shimizu, "A simple technique for the stroboscopic observation of magnetic domain response using scanning electron microscopy," *J. Phys.* E9: 721-724, 1976.

10. O. C. Wells, "Isolation of Type-2 magnetic contrast in the SEM by a lock-in technique," *J. Appl. Phys.* 35: 644-646, 1979; O. C. Wells and R. J. Savoy, "Magnetic domains in thin-film recording heads as observed in the SEM by a lock-in technique," *IEEE Trans.* MAG-17: 1253-1261, 1981.

11. P. L. Stöhr, "A novel method for high resolution observation of magnetic structures in superconductors," *J. Appl. Phys.* 39: 828-829, 1981.

DEVELOPMENT AND APPLICATION OF FULLY AUTOMATED EBIC TECHNIQUES FOR SOLAR-CELL MEASUREMENTS

P. E. Russell and C. R. Herrington

A fully automated system for EBIC measurements has been developed, based on a Tracor Northern TN-2000 x-ray analysis automation system. The system provides for complete control of both the electron beam and the specimen stage, and automated data gathering. Specific uses include totally automated carrier diffusion length measurements and grain boundary effective surface recombination velocity measurements. The system has been successfully used on both a CAMECA EPMA and a JEOL SEM.

The electron beam induced current (EBIC) technique is a powerful tool for the investigation of semiconductor materials and device properties.[1] The technique utilizes a focused electron beam as a source of electron-hole pair generation in a well-controlled, localized volume. If the sample contains a collecting electrical junction, the short-circuit current response to the electron beam can be measured and/or used as intensity modulation for a short-circuit current, or EBIC, map. The major advantage of EBIC over other techniques is the spatial resolution obtainable. Typically, spatial resolution on the order of 1 μm is easily obtainable and some information on a scale of a tenth or hundreth of a micron can be deduced.

The EBIC technique has two disadvantages: the level of theoretical modeling and the state of the art of the EBIC measurement system. Most modeling to date has utilized a point source carrier generation assumption; in reality, the carrier generation volume is of the order of 1 μm. More exact modeling results in three-dimensional boundary value current flow equations for which analytical solutions cannot be found.

In this work significant improvement in the state of the art in EBIC measurement systems is described. The system developed is totally computer automated and includes such features as beam-current regulation and reproducibility, beam blanking, and automated digital data recording, display, and manipulation. The manual system on which the automation is based is described first, followed by the objectives of automating the system. A complete description of the automated system including hardware, software, and several examples of the use of the system follows. The most commonly desired form of EBIC data is either EBIC or ln EBIC versus beam position. It is this type of output that will be addressed in the following.

Procedure Required for Manual Measurements

The manual technique used to provide an induced current line scan (EBIC versus electron beam position) requires a well-controlled electron beam with a linescan mode, a low-noise and low input impedance picoammeter with analog output, and a strip chart recorder with a DC offset. A slow electron beam scan rate is used (approximately 1 mm/s) and the scan speed must be accurately measured.

Because the instantaneous induced current is typically 10^{-6} to 10^{-12} A, the picoammeter should be as close as possible to the SEM sample chamber (ideally inside the sample chamber) to limit current loss in the cabling and to limit extraneous electrical noise from entering the circuit. The two terminals of the PV device should lead directly into the picoammeter and should remain isolated from the system grounds to avoid electrical noise. The analog output of the picoammeter can then be sent to the video circuitry to obtain an EBIC image or a linescan on the SEM CRT with normal magnification, brightness, and contrast control. This procedure gives a qualitative measure, i.e., a map of the current response of the sample.

The authors are at the Solar Energy Research Institute (Photovoltaic Devices and Measurements Branch), Golden, CO 80401

To make the technique more quantitative, the picoammeter analog output can be fed into a high-resolution strip chart recorder. Appropriate adjustments can then be made on the recorder to obtain a highly detailed and resolvable linescan of I_{EBIC} versus electron beam position. Since the beam scan speed has been accurately measured and the chart speed is known, the beam position axis scale can be determined. This procedure gives accurate quantitative results. The results desired (typically L_{eff} and S_{eff})[2] are derived from the $\ln(I_{EBIC})$ vs position curve. If a logarithmic amplifier or recorder is used, the conversion is greatly simplified; however, the accuracy is questionable.

In practice, it has been found highly desirable to have two searate EBIC measuring arrangements, one for imaging and a separate one for quantitative data gathering. For imaging, one wants to measure the EBIC current continuously, amplify it, and convert it to a 0-10V analog input to the normal SEM display intensity input. Since the output is recorded as an inherently qualitative gray scale on a micrograph, the accurate calibration of this amplifier chain is not crucial. The time response of this imaging circuit must be fast enough for use with normal SEM imaging speeds, although only the slow scan speeds are applicable. The signal can be processed by all normal image processing modes of SEM including DC suppression, gain, nonlinear amplification or gamma, and filtering through a bandpass filter if desired.

The major problem encountered in EBIC imaging is electrical noise pickup, as either random noise (especially at very low current levels) or 60Hz noise from ground-loop problems or improper shielding. To avoid these problems, a current preamplifier is placed in a double-shielded isolated can as close as possible to the microscope, which reduces problems of noise pickup by cable and of cable capacitance.

When quantitative EBIC data are wanted, speed is no longer the major concern for the EBIC measurement circuit, but accurate calibration is crucial. It is desired to measure, as accurately as possible, the EBIC current essentially on a point-by-point basis for correlation with the position of the electron beam on the sample. This mode does not require a signal that is compatible with the SEM image signal processing; the only requirement is that the current values can be read and recorded. For use in a manual mode, a picoammeter with analog output compatible with the strip chart recorder is adequate. The Keithley 480 digital picoammeter chosen for this set-up also provides a digital readout of the current for visual data gathering, if desired. As discussed in the next section, the meter can also be easily read by a computer.

The disadvantages of the manual technique include the tedious nature of the process of picking numbers off the chart, time consumption, and increases in the chance for error. The many advantages of automating this technique are apparent.

Advantages of Automation

With the use of an SEM computer control system the manual linescan technique described above can be completly automated. The computer can then read a digital picoammeter easily, accurately, and quickly. The values are easily stored in computer memory to be manipulated as desired. For instance, the logarithm of the current readings can be derived by one computer program line and then tabulated or plotted on a CRT display or on a digital plotter and stored on a floppy disk. This method saves much time and improves accuracy by eliminating the many chances for human error inherent in the manual method. Measurement repeatability is also improved.

Digital beam control is used to position the beam accurately in known discrete steps, which allows a much more accurate digitized line scan to be plotted. This procedure is much more accurate than the manual analog technique which incorporates error in the scan speed measurement and additional error in the chart speed (depending on the quality of the recorder). With the automated approach, the operator can readily specify the distance between data points and the dwell time for each measurement that is appropriate for the particular device under study. This feature is important for a system designed to be used on all photovoltaic materials. For example, very different scales are used for direct-gap as opposed to indirect-gap materials.

Other advantages of an automated measurement are computer-controlled electron beam-current regulation to within ± 0.1%/hr and computer-controlled beam blanking to minimize beam damage on the specimen. One also has the option of moving a motorized stage in known increments with respect to a fixed beam, to allow very long linescans without introducing

beam divergence problems.

Specifics of the System

The basic EBIC automation system has been designed for a CAMECA MBX electron probe microanalyzer (EPMA), equipped with a Tracor Northern TN-2000 automation package with digital beam control. The normal function of the TN-2000 system is to provide a computer-generated, digital, external input to the scan generator and to control the imaging of an SEM to facilitate x-ray mapping or image analysis. The overall EBIC system has been designed for maximum flexibility and, as discussed below, has been extended to a JEOL 35C. This extension represents the ease with which the system can be modified for use on an SEM or EPMA from another manufacturer. The approach could likewise be extended for use with other automation systems, as long as a digital beam control system is available. (The software would have to be rewritten in the appropriate language.) This extension is currently under investigation for use with an Ortec EDS II system with Image Master option, for which the language ORACL is used.

The TN-2000 system is based on a Digital Equipment Corporation (DEC) PDP 11/23 computer with 64K of core memory. Included are Data Systems DSD 440 dual floppy diskette mass storage system, a DEC LA120 Decwriter III high-speed teletype for hardcopy output, and a Hewlett Packard 7221B four pen digital plotter for graphics output.

The TN-2000 controls the following functions on the EPMA:

1. Beam scanning coils.
2. Faraday cup insertion for beam-current measurement or beam blanking.
3. Fast beam blanking via blanking coils.
4. Stage motion via stepping motor drives in X, Y, and Z directions.
5. Beam current selection (from a user-defined table of 64 currents).
6. Beam current regulation and measurement.
7. All x-ray spectrometers and associated hardware.

By monitoring the current from a beam regulation aperature, the computer continuously adjusts the condenser lens current and keeps the beam current constant.

Using a "CUP" command, the computer places a movable Faraday cup into the beam path. The Keithley picoammeter measures the cup current directly and an ADC reads the analog output of the picoammeter. A scaler is used to count the pulses for visual readout. The beam current is now measured and stored into the software for future reference. The Faraday cup also acts as the beam blanking device most effectively since it is physically located below the beam regulation aperture and therefore does not affect the beam regulation when it is positioned and removed repeatably.

It is sometimes desirable to have very fast (< 1 μs) beam blanking capabilities. This goal is best accomplished by the installation of blanking coils to deflect the electron beam just after the anode. Uses for this type of blanking include lifetime studies based on short-circuit current, or EBIC, decay and the obtaining of very low (i.e., less than one *sun* equivalent) injection levels. A serious problem is encountered when the beam blanking coils are used in conjunction with the beam current regulation. When the beam is blanked, the regulation system responds to the loss of beam current by opening up the condensor lens all the way. When the blanking coils are turned off, the beam is very intense and the regulation system adjusts the condensor lens current until the present current is measured on the regulation aperture. The problem, however, is that the condensor lens is now on the wrong side of crossover, which results in an erratic, unfocused beam. These problems could be overcome by injection of a constant signal to the regulation system during blanking and holding the condensor lens current constant until the beam is restored and allowed to stabilize. This approach would allow operation in a regulated mode for time-resolved EBIC (TREBIC) studies.

The software has been written to allow us to define the beam scan digitally by telling the computer the start point, the end point (within a viewing frame at a given magnification), and the distance to step between each data point depending upon the desired resolution. The computer then steps the beam as defined and counts the current at each data point. A variant is to keep the beam stationary and move the stage in given increments in a given direction. In this case, the resolution is limited to 1 μm whereas the resolution for the digital beam case is only limited to whole increments of CRT picture points

(4095 by 4095 picture points horizontally and vertically across the CRT). It is desirable to use the stage-scan mode in the case of low magnifications to keep the solid angle of the scanning beam to a minimum.

This system has several advantages. The electron beam current is controlled very tightly to prevent induced current fluctuations and there is significant flexibility in controlling the linescan such that an induced current can be measured specifically for a given time for a digitally known location. This arrangement provides much greater accuracy than using a continuous linescan since a continuous linescan case assumes a zero response time of the device specimen which is not always valid. Accuracy, repeatability, and throughput are clearly significantly improved.

Software

THe software is based on the Tracor Northern system and is written in the Flextran[3] computer language. When EBIC is executed, variable space is allocated, utility libraries are loaded, and the program prompts with "EBIC." It then waits for a command entry.

A detailed description of the EBIC command follows. The function, form, and an example are given. In the examples, portions underlined indicate human input and a ↓ indicates a carriage return. Notes are enclosed within parentheses and are written in small characters.

EBIC

Function: Sets up parameters, collects data from linescan, stores data on disk, and plots linescan data on plotter if desired.

There are three choices of how the data are to be manipulated: (1) plot the data after line data are obtained, (2) plot data stored on disk, and (3) store the data on disk and then plot the data. In all cases, the data are displayed on the CRT prior to hard plotting, which allows the operator to observe or scrap and remeasure the data without waiting for a hard plot. Each of the three cases will now be treated individually. Plot scales are $\ln I_{EBIC}$ vs microns.

1. *Plot Data*

For this case, the live data are simply plotted without being stored on disk. The linescan parameters (step size and magnification) as previously set are displayed. The STEP SIZE in microns is the distance between data points, also given in digital beam coordinate units as POINTS with microns between coordinate points specified. The working magnification is given as MAG. One then has the option of changing any of these parameters or simply leaving them as they are. For example, the parameters may be as follows:

```
STEP SIZE = 10.000 UM = 10 POINTS (1 UM/POINT)
MAG = 1.00 KX
OK?
```

If no is the answer to OK, the magnification in KX is requested and a number of coordinate points between data points. The number of coordinate points between data points is used because the beam can only be moved in integer increments of coordinate points. The distance between coordinate points is calculated from the given magnification and displayed so that the micron distance between data points can be easily figured. If a return is the answer to a question, that particular parameter is not changed. Example:

```
MAG (KX) = ? ↓ (Mag stays at 1000X)
SCALE FACTOR = 0.017908 UM/POINT
# POINTS/STEP = 10 ↓
```

The next question is "NEW LINE?" If no is the answer, the previous coordinates of the starting and ending points of the linescan are used. If yes, the starting and ending points of the line scan can be defined by use of the cursor controlled by a joystick. The coordinates of each point are set and displayed when the white button on the joystick is pressed. Once set, the space bar is pressed to begin the linescan. The data appear on the CRT with one data point per channel as the linescan is in progress. Once the linescan has finished, the program asks if the linescan should be hard plotted or not. If no is answered, the "EBIC" prompt is returned. If yes is answered, a plot label is asked for,

which is typed across the top of the plot and can be up to 25 characters. The pen numbers desired for the axes and the plot is then entered. The program then asks if a Least Square Fit is desired. If yes, the X coordinate values of two points, between which the slope or inverse slope is desired, is entered. For "X--VALUE PT #1" enter the micron value of one point and the same for PT #2. The slope of the fitted curve between the two given points is displayed. The effective diffusion length L_{eff}, which is simply the inverse of the slope, is calculated and displayed. One then has the option of printing either the slope or the diffusion length or neither on the plot. The pen is manually positioned to the desired location. The end points of the slope are measured and are also plotted by circles. The operator can repeat this slope measurement as many times as desired by answering Y to "ANOTHER?"

Labels can be printed in any color and in any location on the plot if one gives the answer Y to "PLOT LABELS?" The label (up to 25 characters) and pen number are entered, the pen positioned to the desired location and then ENTER is pressed on the HP plotter to print the label.

There are three options at this point. (1) If a new plot is desired, enter RET. (2) If one wants to return to the EBIC prompt, enter 2. (3) If one wants a plot to be made on the same axis at the same scale enter 1. The previous procedure for "PLOT DATA" is just repeated, only with new data. If the new data are to be plotted on the previous axis and they go off scale, the display states that the data are off scale and returns to the three choices of new plot, EBIC, or plot on same axis. The data can then be retaken with an adjustment made to the hardware to allow the data to fall within scale. An alternative is to plot the data with the largest scale first.

2. *Data from Disk*

The program first asks "DATA FILE # TO BE PLOTTED = ?". The desired file # is entered. The data from that file are brought into memory and displayed on the CRT. The remainder of the procedure is identical to the Plot Data case.

3. *Store Then Plot*

This option begins in the same manner as the Plot Data option. After receiving the answer Y to the "PLOT?" question, the program asks what file number the data should be stored as onto the disk in drive 1. If the file # designated is already used, the program says "FILE # XXX IS USED OK?." If Y is entered, file XXX is replaced. If N, another file # is asked for. A file label can then be entered (up to 20 characters) and the data are transferred to disk with the entered label. The remainder of the procedure is the same as option 1.

```
Form: E(BIC)
Example: EBIC: EBIC ↓
         1 = (PLOT DATA) 2 = (DATA FROM DISK) RET = (STORE THEN PLOT) ETC.
```

A complete listing and discription of the software is available from the authors.

Extension of EBIC on MBX

Some additions have been made to EBIC to extend capabilities and convenience. Hardware and software extensions were needed for the additions.

In come instances it is desirable to maintain a normally incident beam to the sample at all times, which one can do by maintaining the beam in a constant position and scanning the sample stage with respect to the beam. The limitation here is that the stage can only be moved in 1μm units and not less than 1μm.

One can set up a number of linescans on one or several samples by defining all at once the stage and beam coordinates for desired linescan positions. EBIC then consecutively performs the linescans and stores the results on disk without human intervention. EBIC, upon completion, would then turn off the tungsten filament. The data are plotted later at a convenient time.

An EDS acquisition can currently be performed from EBIC by a call for the appropriate Flex module. The '>' symbol preceding a command means the command is a Flex module. Therefore, EDS acquisition can be performed from EBIC. This arrangement can be set up in the multiple line scan mode to take an EDS acquisition during each linescan.

WDS analysis is most easily performed from 'TASK,' an automated WDS analysis program.

From TASK, EBIC can be loaded into the auxiliary program area of TASK, which allows any of the EBIC commands to be performed as well as any of the TASK commands.

With the aid of a computer, it is possible to measure and record the induced current with respect to specific digital beam coordinates over an entire raster scan. With the Tracor Northern Spectra-Chrome 512 color monitor and Tracor Northern Image Processing program up to eight colors can be used to assign to selected current value ranges to produce color induced current maps. That adds a more quantitative feature to the usual gray-scale EBIC image. Using a color mode for display, one can chose either linear or logarithmic scales for color display.

The automated EBIC system has been modified to be used on a JEOL 35C equiped with an identical Tracor Northern TN-2000 system. The modification mainly involved removing commands from EBIC that did not apply. The following features on the Cameca MBX were not available on the 35C:

1. Stepping motor drive X, Y, and Z stage.
2. Computer-controlled beam current regulation.

Because of these deficiencies, a few EBIC commands are not applicable. These commands were simply removed from the program for use on the JEOL system.

Applications

The system described is currently in routine use on both the CAMECA MBX and JEOL 35C systems at the Solar Energy Research Institute. The system has been used extensively for measurement of the electrical properties, especially grain boundary effective surface recombination velocity, of grain boundaries in polycrystalline silicon.[2] Another common use involves fracturing finished devices and taking EBIC data of the cross section. This use has been applied, for example, to the study of the $CuInSe_2$ thin film solar cell.[4] In general, the automated EBIC system is very versatile and aids in the measurement of many localized electrical effects in electronic devices and materials.

References

1. H. J. Leamy, "Charge collection scanning electron microscopy," in O. C. Wells, K. F. J. Heinrich, and D. E. Newbury, Eds., *Physical Electron Microscopy*, New York: Van Nostrand Reinhold, 1981.

2. P. E. Russell, C. R. Herrington, P. H. Holloway, and D. E. Burke, "Effects of heat treatment on grain boundary properties in cast polycrystalline silicon," in E. E. Dike, C. H. Seager, and H. J. Leamy, Eds., *Grain Boundaries in Semiconductors*, New York: North-Holland, 1982.

3. F. H. Shamber; "Flextran," copywrited internal report, Tracor Northern, 2551 West Beltline Highway, Middleton, WI 1975.

4. P. E. Russell, O. Jamjoum, R. K. Ahrenkiel, L. L. Kazmerski, and R. A. Mickelsen, "Properties of the Mo-$CuInSe_2$ interface," accepted for publication, *Appl. Phys. Lett.*, 1982.

CHARACTERIZATION OF NICKEL-BASE SUPERALLOY SINGLE CRYSTALS BY ELECTRON CHANNELING CONTRAST

J. M. Walsh, K. P. Gumz, and D. M. Shah

A major advance in materials technology for advanced gas turbine engines has been the development of superalloy single-crystal high-pressure turbine airfoils.[1-6] Elimination of grain boundaries prohibits component intergranular cracking. The elimination of grain boundaries also permits greater flexibility in alloy design in that it is no longer necessary to add grain boundary strengthening elements such as carbon, boron, zirconium, or hafnium. Elimination of these elements can result in an increase in the melting point of the alloy and can also have a positive impact on strength potential. These crystals are typically grown with [001] parallel to the major stress axis of the part and are normally oriented by the Laue method to assure uniformity of properties from part to part. Electron channeling contrast has been found to be useful for characterizing certain aspects of the growth and processing behavior of these crystals that are not clearly revealed by other techniques. The physics of electron channeling contrast has been discussed at length at previous MAS and EMSA meetings, but the emphasis in this paper is on the practical engineering application of the technique.

One area where channeling contrast has been effectively applied has been in establishing the nature of the subgrain structure that develops in these alloys. The optical micrograph in Fig. 1(a) shows the dendritic structure of Alloy 454 single-crystal superalloy in the heavily etched condition, but the existence or extent of a subgrain structure is not clear. A backscattered electron channeling micrograph of the same area (Fig. 1b) clearly shows a subgrain structure with considerable contrast between adjacent subgrains and, in fact, indicates that the subgrain size coincides exactly with the primary dendrite size. The subgrain boundary established by channeling contrast is shown as a dotted line overlay on Fig. 1(a). Backscattered electron channeling diffraction

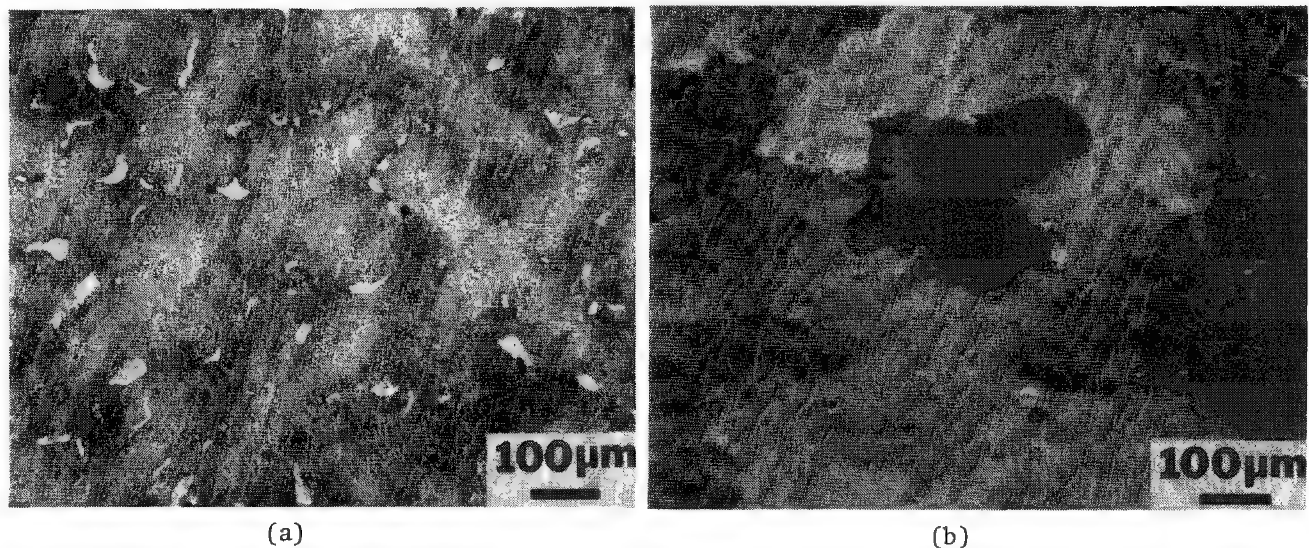(a)   (b)

FIG. 1.--(a) Optical micrograph of Alloy 454; (b) backscattered electron channeling micrograph of Alloy 454.

The authors are with the Materials Engineering and Research Laboratory, Pratt & Whitney Aircraft, Middletown, CT 06457.

patterns (BSE-CDP) taken on both sides of these subgrains indicate misorientations of the order of 1-2°. Misorientations of this order can result in large contrast differences (Fig. 1b) as the channeling micrograph is sensitive to very small changes in orientation.

Since the BSE-CDP imaging is dynamic in nature, it presents some interesting possibilities for the rapid real-time surveying of a large area of specimen for crystallographic orientation and substructure. By observing the BSE-CDP on the CRT while translating the specimen beneath the electron beam, the analyst can establish the location of boundaries by the appearance of a double pattern. Figure 2(a) gives a channeling micrograph for an experimental superalloy crystal; Fig. 2(b) gives the double BSE-CDP observed while this material is scanned.

Because channeling contrast can image the substructure of the alloy so clearly, it has been found to be useful in studying the effect of heat treatment on substructure. Figure 3 shows several examples of subgrain boundary motion in a modified Mar M-200 superalloy crystal as a result of 4 hr exposure at 1232°C. The curved segments of the boundary (e.g., AB, BC) indicate movement of the boundary in the direction of the arrow with pinning occurring at sites A, B, and C (Fig. 3a). The channeling micrograph of
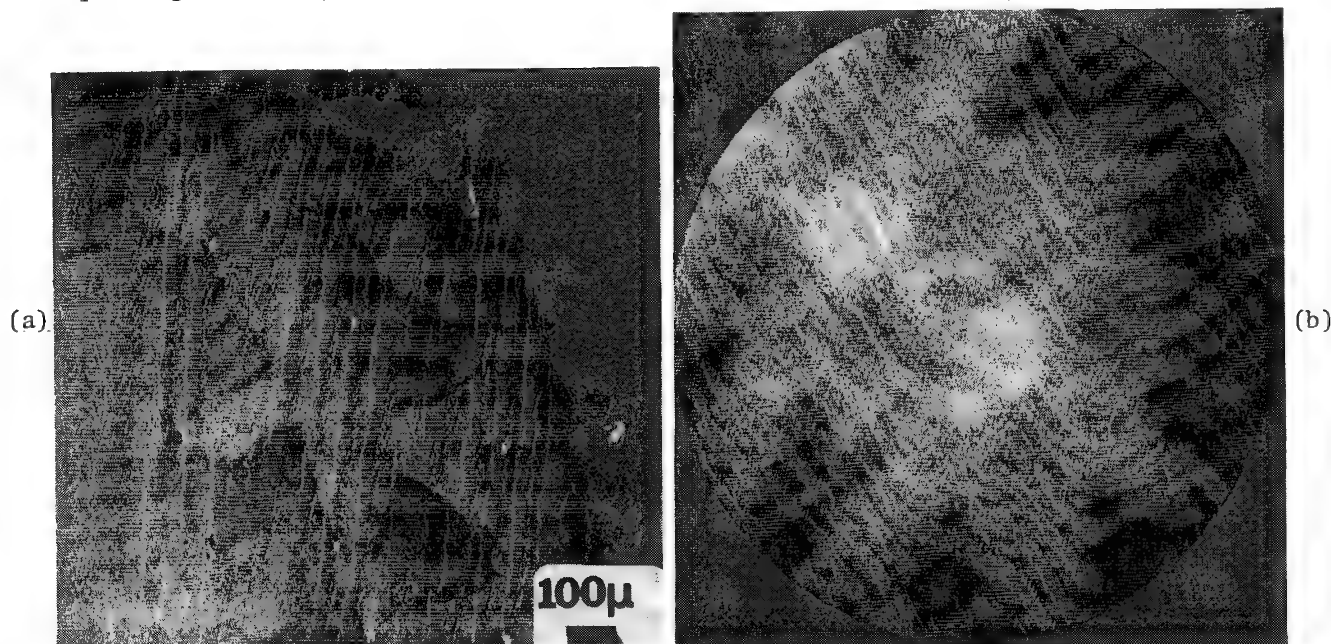

FIG. 2.--(a) Backscattered electron channeling micrograph of experimental superalloy crystal; (b) backscattered electron channeling diffraction pattern observed during scanning crystal shown in (a).

Fig. 3(b) shows a case where a small segment of the boundary is pinned by a micropore while the remainder of the boundary is swept about 10 µm beyond the micropore. This observation has interesting implications, since it provides a way of evaluating the effects of additives on subgrain boundary migration.

Electron channeling contrast is also helpful in studying interface behavior in these alloy systems. Figure 4 shows an example of a single crystal superalloy (right side) bonded to a polycrystalline superalloy (left side) by a transient liquid phase (TLP^{TM}) process. An intermediate zone of about 100 µm develops at the interface that contains multiple grains or subgrains. BSE-CDPs obtained from the individually defined grains or subgrains in this zone all showed the (100) pole and were always within 1-2° of the orientation of the single-crystal substrate, whereas the material to the left of this zone showed a randomly oriented structure. These observations suggest that during the bonding cycle, the existing liquid phase may grow epitaxially from the single-crystal alloy to form the approximately 100 µm-thick single-crystal interaction zone with a detectable grain boundary present only on the left side of this zone. Figure
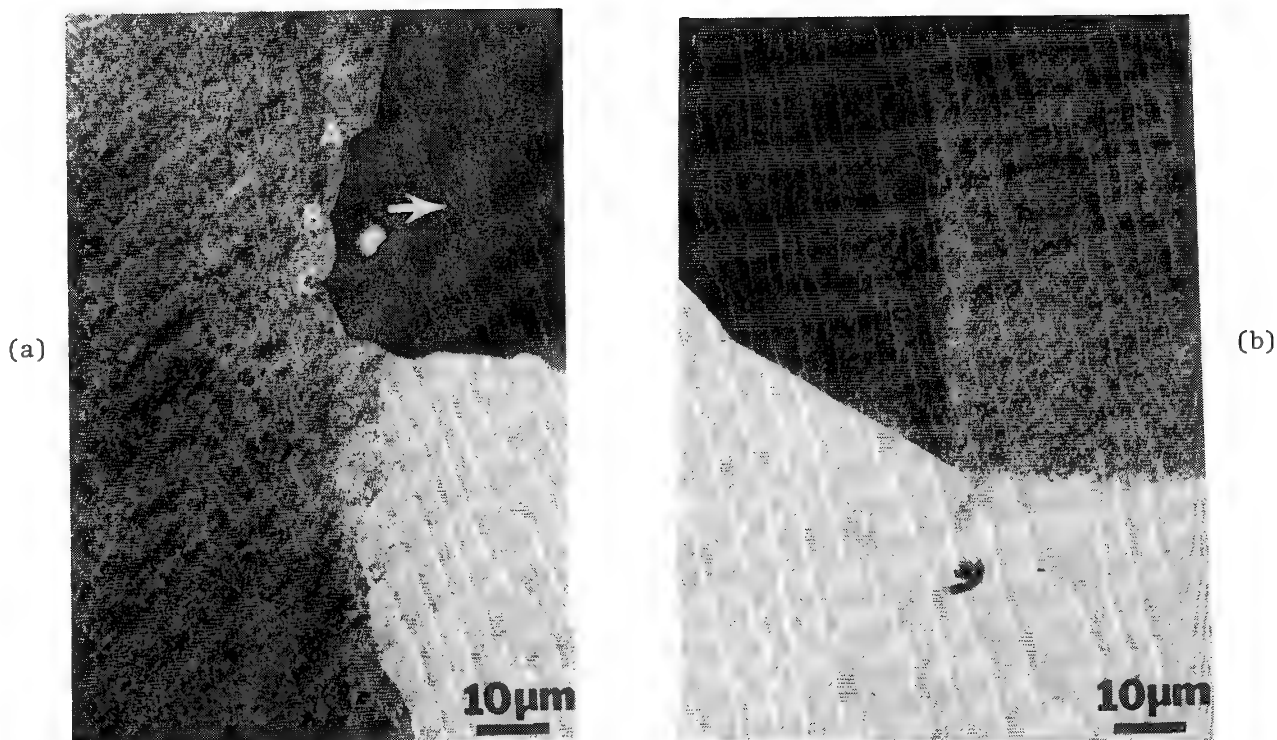
FIG. 3.--Backscattered electron channeling micrographs of modified Mar M-200 crystals showing evidence of subgrain boundaries that have migrated.
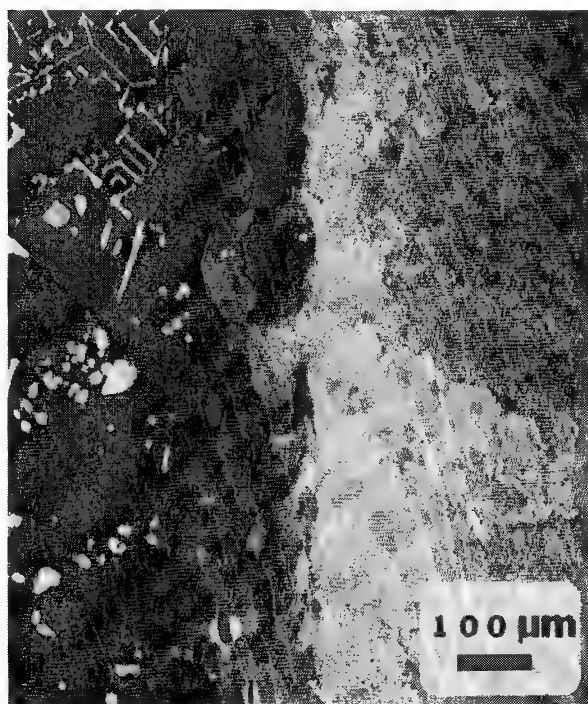
FIG. 4.--Backscattered electron channeling micrograph of single-crystal superalloy (right) bonded to polycrystalline superalloy (left). Note subgrain zone at interface.

5 shows an interfacial condition that developed upon TLP[TM] bonding two Alloy 454 single crystals. BSE-CDPs were taken at the locations indicated and the orientations at the various locations were plotted on the unit stereographic channeling map shown in Fig. 5(b). The orientation of the single crystal material on both sides of the bond was essentially the same and very close to (100), whereas the grains in the interface were randomly oriented and far from (100). It was subsequently established that this apparent recrystallization condition could be reproduced by a deliberate working of the surface of the single-crystal alloy prior to bonding.

In summary, backscattered electron channeling contrast and channeling patterns provide useful information on the nature and extent of subgrain structure in superalloy single crystals. The dynamic nature of this type of imaging, coupled with the ability to get conveniently microstructural and crystal orientation information from the same region at relatively high magnifications, make these techniques especially powerful.

457
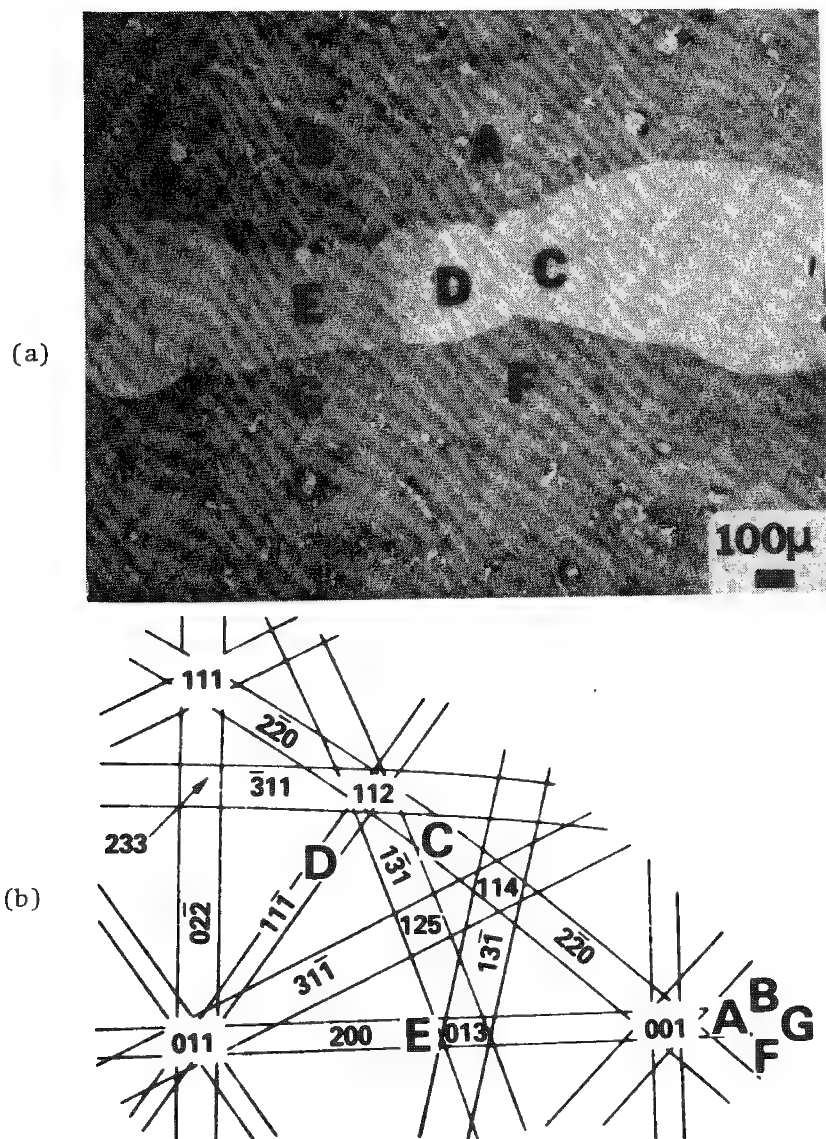
FIG. 5.--(a) Optical micrograph showing interface structure resulting from the bonding of two superalloy crystals; (b) stereographic channeling map showing orientations established at various locations in (a).

References

1. F. L. VerSnyder and B. J. Piearcey, *SAE Journal* 74: 36, 1966.
2. F. L. VerSnyder and M. E. Shank, *Mater. Sci. Eng.* 6: 213-247, 1970.
3. F. L. VerSnyder and M. Gell, in R. I. Jaffee and B. A. Wilcox, Eds., *Fundamental Aspects of Structural Alloy Design*, New York: Plenum Press, 1977, 209.
4. J. Mayfield, *Aviation Week and Space Tech.* 69-73, 1 October 1979.
5. M. Gell, D. N. Duhl, and A. F. Giamei, in J. K. Tien et al., Eds., *Superalloys 1980, Proc. Fourth Intern. Symp. on Superalloys*, Metals Park: ASM, 1980, 205-214.
6. R. R. Irving, *Iron Age* 109-112, 28 September 1981.

INCREASED BEAM BRIGHTNESS IN A JEOL JSM-35 MICROSCOPE

R. C. Piercy

Some of our recent work has been on carbon-carbon composites. These materials are very in-efficient producers of both secondary and backscattered electrons, which makes examination difficult with an electron beam of normal intensity. Some examining is done at relatively high magnifications, so that the degradation of resolution that would accompany decreasing the condenser lens current is not acceptable. Using a different condenser lens polepiece and a different style of tungsten filament, we have achieved a 6-fold increase in specimen current at standard operating conditions, a 4-fold increase at minimum beam conditions and a 150-fold increase at maximum conditions. These increases have been achieved with very little, if any, decrease in resolution. The modifications, the operating conditions, and their advantages and disadvantages will be discussed.

The materials to be examined are carbon-carbon composites composed of graphitic carbon fibers, glassy carbon char, and chemically vapor-deposited microcrystalline carbon. Each sample is one half of the friction couple of a research-scale aircraft brake in the course of testing. Their surfaces must not be changed in any way as they go back to further test-ing after the SEM examination, so that coating the surfaces is not permissible.

The JSM-35 emphasizes resolution over beam brightness, a problem with polished metallur-gical specimens and carbon specimens. With these types of samples visual examination at rapid scan rates is impossible because of the snow. Photographic exposure is recommended as 100 s, again to minimize the snow. Some examinations on these samples are done at 10 000-20 000 times magnification, so that an increase in beam brightness by a simple open-ing of the condenser lens is out of the question. Other means to achieve this increase had to be found.

Early attempts to correct the problem ascertained that this was not a malfunction; modi-fications were necessary. Since the filament load current was normal it appeared that at least part of the problem was in the lenses. The first modification was to replace the nor-mal condenser lens polepiece with the polepiece from a JEOL U-2 microscope. The location of the pole piece is shown in Fig. 1. The two parts are shown side-by-side for comparison in Fig. 2. Several differences are obvious. The bore in the U-2 polepiece is larger, the hole in the aperture is larger, and the U-2 polepiece has no mounting plate and is shorter. Before this polepiece could be used a brass mounting adapter had to be machined to hold the polepiece in the column in the correct position.

Besides the different polepiece, a pointed tungsten filament was substituted for the normal one; Fig. 3 shows the very fine tip welded on to the filament. The result acts like a cross between a normal filament and a thermionically assisted field-emission filament.

The improvement can be seen in Fig. 4. Figure 4(a) is for the standard filament and polepiece at 35 kV, bias 3 (which results in a filament load current of 125 μA), 240 μm fi-nal aperture, condenser lens at 5 o'clock (5:00), with a 25s exposure; Fig. 4(b) is for nearly identical conditions but with a pointed filament and the U-2 polepiece; and likewise for Figs. 4(c) (bias 9, filament load current 45 μA) and Fig. 4(d) (final aperture 100 μm). Even though the conditions in Fig. 4(d) are much more severe than in Fig. 4(a), the former image is clearly superior.

The change in the signal-to-noise ratio is obvious visually but it was also measured photographically (Fig. 5). The upper curve represents a line scan taken under conditions similar to those of Fig. 4(a), the lower curve under conditions similar to Fig. 4(b). The measured signal-to-noise ratios are 2.6:1 and 14.3:1, a 5.5-fold improvement.

Author Robert C. Piercy is at The Bendix Corporation, Aircraft Brake and Strut Division, 3520 West Westmoor St., South Bend, IN 46624.
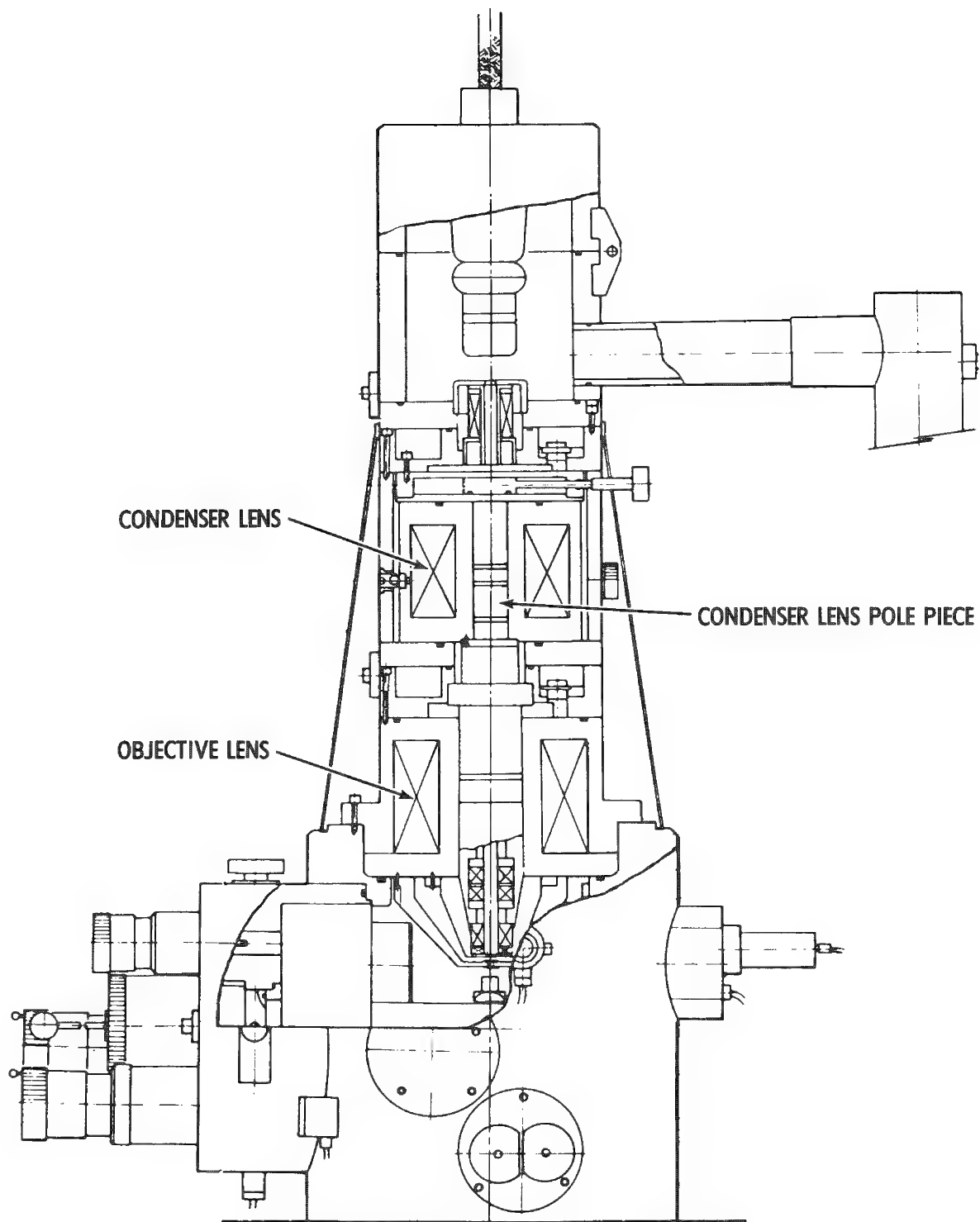
FIG. 1.--Cross section of column of JEOL JSM-35 shows location of polepiece.
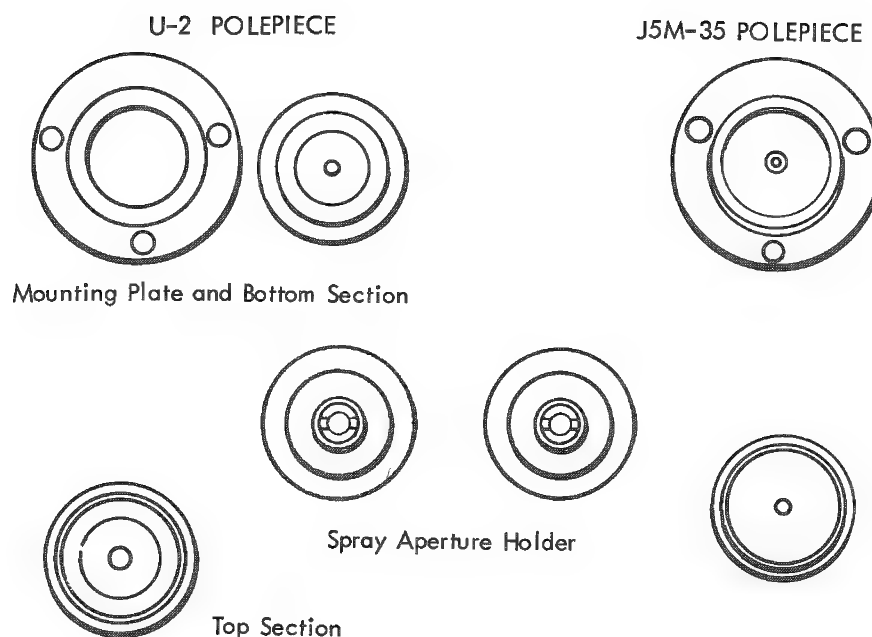
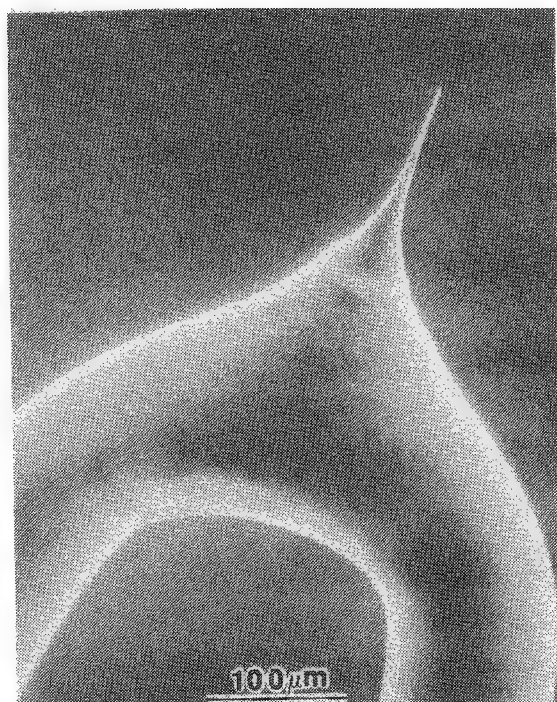FIG. 2.--Disassembled polepieces. U-2 (left) and JSM-35 (right).

FIG. 3.--Photomicrograph of pointed filament showing tip welded onto main filament.

Table 1 shows the results of a series of specimen current measurements taken under a large number of conditions. The specimen was a flat piece of carbon-carbon composite. Carbon was used to keep the back-scattered and secondary electron emissions as low as possible so that the specimen current would be reasonably similar to the beam current since a Faraday cup was not available to allow measurement of the beam current directly. With approximately the same filament emission current there is in most cases 5-to 10-fold increase in the beam current, except for the first and sixth conditions. The maximum beam current is 2 μA, about 150 times greater the original value.

A comparison of columns 2 and 3 shows that each of the changes contributes approximately the same amount of the beam-current increase; and a further comparison with column 4 shows that from line 9 down the specimen current with both modifications is approximately equal to the sum of the currents with each modification. The U-2 polepiece, with its larger bore, can collect and focus more beam electrons, but the focusing action of the condenser lens might be somewhat reduced and resolution might suffer.

The increase in beam current that results from the pointed filaments is due in part to the enhanced emission characteristics of the point, in part to a different electron density distribution in the beam, which would explain the much larger beam currents when the condenser lens current is very low.

Figure 6 is another measure of the contribution of the polepiece. The higher current is indicated by the separation of the curves. The maximum specimen current is about 15 times higher because the specimen current peaks at a higher condenser lens current for the JSM-35 polepiece than for the U-2 polepiece. Moreover, the specimen current drops more slowly with increasing condenser lens current. Most users of this microscope have probably already found that after the 1:00 position of the condenser lens current setting there is almost no further effect on the image. With the U-2 polepiece, however, there is usable control right to the 5:00 position.

461

These advantages are offset by some disadvantages. With the larger-bore polepiece there is a slight loss of resolution. Figure 7 is a photomicrograph of a gold-coated cracked carbon sample; the original photo was at 60 000×. Despite the larger-bore polepiece the resolution is still better than 10 nm; measurements put it at about 6-7 nm. The photographic exposure time again was only 25 s.

Even more significant are two other disadvantages: determination of the saturation point for these filaments is more different than for normal ones, and they are more difficult to align. In the normal filament, there is a gradual rise to a false peak, a drop, and then a rise to a plateau; whereas with the pointed filaments there is a series of successively higher peaks but no plateau (Fig. 8), so that one can easily melt a filament in looking for saturation. The trick is to note the position of the filament current control at which the normal filaments saturate and then operate on the last false peak before that point. (The term "false peak" is used because that is what it resembles, although it may not originate from the same mechanism.) The third curve shows that even with the bias dropped to provide a greater load current, the normal JEOL filament does not provide as bright a beam as does the pointed filament.

(a) (b) (c) (d)
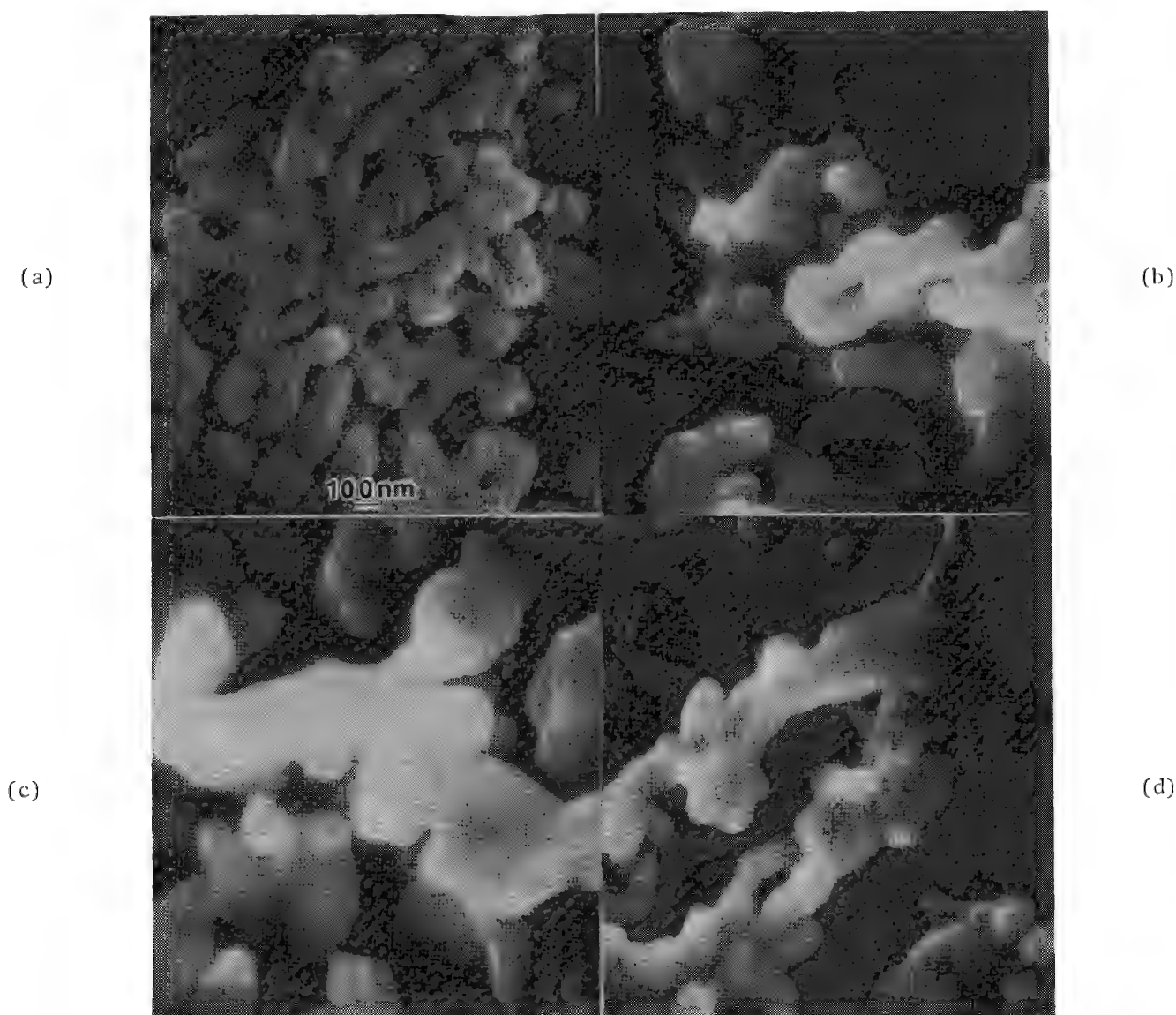
FIG. 4.--Photomicrograph of Al-W alloy: (a) with standard polepiece and standard filament, bias 3, 240 μm final aperture, 25 s exposure, original magnification 30 000×; (b) same with U-2 polepiece and pointed filament substituted; (c) same as (b) but with bias 9; (d) same as (c) but with final aperture 100 μm.

TABLE 1.--Effect of SEM modifications on specimen current (as measured on carbon sample).
Specimen Current

Pole Piece and Filament Used				Operating Conditions		
Filament: JEOL Pole Piece: JSM-35	JEOL U2	Pointed JSM-35	Pointed U2	Bias	Aperture	Condenser Lens Setting
13.5nA	23. nA	140.nA	2000. nA	1	600	Min.
360. pA	680. pA	240.pA	1.7nA	1	600	12:00
2.3nA	3.8nA	6.nA	6. nA	1	240	9:30
50. pA	86. pA	125.pA	280. pA	1	240	12:00
13. pA	16. pA	30.pA	34. pA	1	240	5:00
6.6nA	15. nA	16.nA	340. nA	3	600	9:30
180. pA	440. pA	380.pA	1.2nA	3	600	12:00
1.1nA	4.4nA	14.nA	6. nA	3	240	9:30
28. pA	110. pA	63.pA	180. pA	3	240	12:00
7.3pA	15. pA	20.pA	28. pA	3	240	5:00
3.3nA	17. nA	7.4nA	22. nA	6	600	9:30
88. pA	700. pA	190. pA	800. pA	6	600	12:00
555. pA	3.2nA	1.4nA	4.8nA	6	240	9:30
16. pA	110. pA	29. pA	130. pA	6	240	12:00
4.4pA	15. pA	7.2pA	18. pA	6	240	5:00
3.5nA	8.6nA	4.1nA	14. nA	9	600	9:30
70. pA	320. pA	110. pA	500. pA	9	600	12:00
600. pA	1.9nA	700. pA	2.6nA	9	240	9:30
13. pA	42. pA	17. pA	72. pA	9	240	12:00
3.3pA	7.4pA	4.6pA	12. pA	9	240	5:00
78. pA	280. pA	120. pA	440. pA	9	100	9:30
2.3pA	7.7pA	3.2pA	12. pA	9	100	12:00
0.6pA	1.3pA	1. pA	2.3pA	9	100	5:00

Obviously, these filaments are not suited for microscopes used by large numbers of peo-
ple. The chances are just too great that a good number of filaments would be melted. They
are considerably more expensive than normal filaments but if used carefully in a microscope
with a good vacuum, a normal lifetime can be expected. In our microscope, with the two op-
erators, most last 20-50 hr, and some last 50-100 hr.

The second major disadvantage is the instability of alignment. With normal filaments
it is sufficient to have the filament centered in the hole of the Wehnelt cap. With these
filaments it is necessary to have the fine tip centered. Since it is not visible to the
naked eye and is not always centered on the main tip, some experimenting is sometimes nec-
essary but most of the time centering the visible tip is sufficient. Once centered, the
alignment has a tendency to drift, especially during the first hour or so of operation,
probably owing to wandering of the fine tip. After that first hour, the alignment is fair-
ly stable but should still be checked fairly frequently.

These disadvantages may sound intimidating but are more than offset by the five-fold in-
crease in the S/N ratio. Any JEOL JSM-35 user who is having problems with noisy images and
who is reasonably careful and confident would benefit from this pair of changes. Where
there are many users but the absolute maximum in resolution is not needed, use of the U-2
polepiece is indicated. Anybody who has to do trace analysis with a wavelength-dispersive
spectrometer on a JEOL JSM-35 will certainly benefit from having perhaps as much as 2 µA of
beam current.

Users of other JEOL microscopes may be able to use the U-2 polepiece as well. The only
way to find out whether an improvement results (assuming it fits physically) is to try it
in the microscope. Users of other makes of microscopes would probably benefit from using
the pointed filaments even if only for problem samples such as polished metallurgical spec-
imens. Experiments with bored-out condenser lens polepieces will be left to only the most
adventurous.
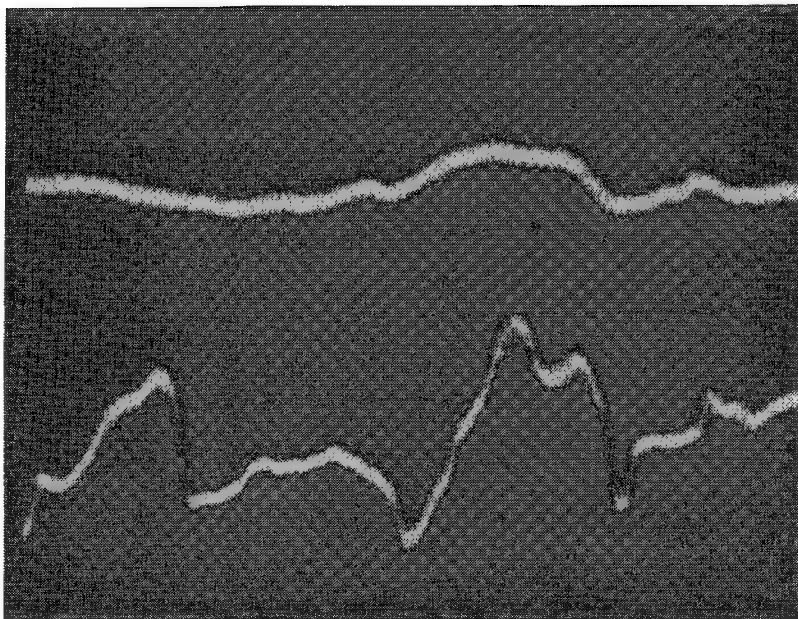
FIG. 5.--Line scan showing signal-to-noise ratios for SEM in original condition (top) and with modifications (below).

FIG. 6.--Specimen current vs condenser lens setting for SEM with pointed filaments and two different polepieces; bias 3, 240 μm final aperture.

FIG. 7.--Photomicrograph of gold-coated cracked-carbon resolution standard, with U-2 polepiece and pointed filaments; bias 3, 240 μm final aperture, 25 s exposure; original magnification 60 000×.

FIG. 8.--Traces of beam brightness vs filament current for normal filament at bias 1 and bias 6 and for pointed filament at bias 6.

THE APPLICATION OF SCANNING ELECTRON MICROSCOPY AND ULTRAVIOLET FLUORESCENCE TO A STUDY OF CHATTANOOGA SHALE SPECIMENS*

L. A. Harris, O. C. Kopp, and R. S. Crouse

Pyrite (FeS_2) is a common mineral in organic-rich sedimentary rocks.[1,2] Numerous studies have been performed to determine the relationship between pyrite and organic matter in these rocks. Most investigators agree on certain aspects of pyri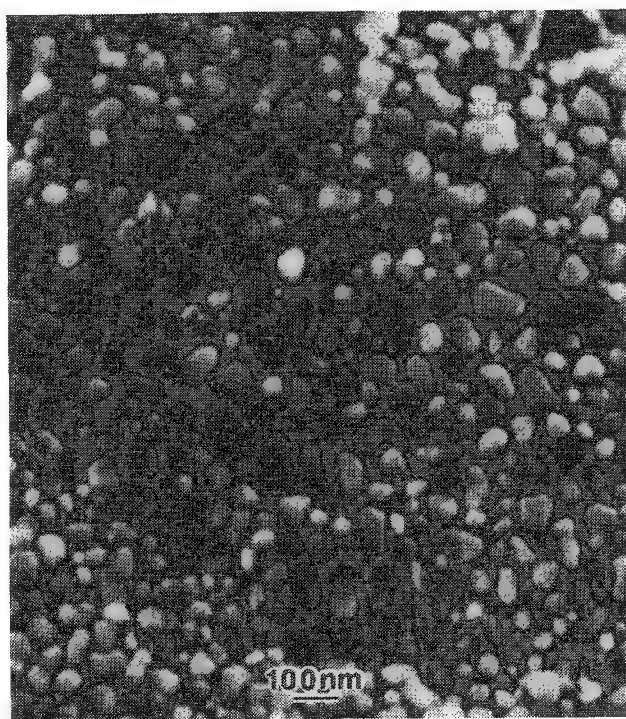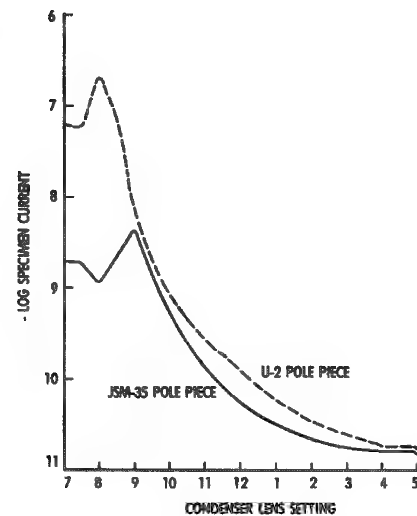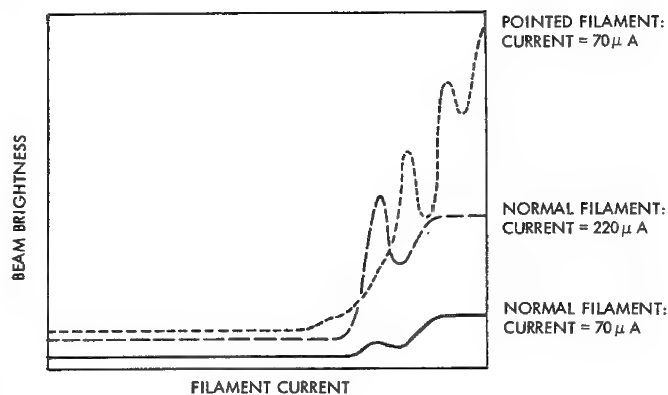te formation. Notably that sulfate-reducing bacteria were necessary to produce the dissolved sulfur for subsequent reactions with iron in minerals or solution.[3] However, the thesis that pyrite framboids were formed as replacements within the micro-organisms either during their lifetime or upon their death has not received the same broad acceptance.

Recently, the authors had opportunity to study a set of samples from the Dowellton and Gassaway members of the Chattanooga shale, one of the better known organic-rich formations of North America. Most of the previous studies relating pyrite to organic matter relied heavily on chemical analyses, x-ray diffraction, and optical microscopy. Of these analytical methods, only microscopy permitted a study of phase relationships; however, the fine-grained nature of shales precludes reliable microstructural analyses by optical microscopy. In the present study, ultraviolet light fluorescence and scanning electron microscopy have been used to investigate the interrelationships of the phases in the shale specimens. Backscattered electron imaging, energy dispersive x-ray analyses, and electron-beam microprobe analyses served as complementary techniques for identifying minerals and enhancing the contrast between phases.

Sample Preparation

Samples were obtained from large blocks of shale by cutting sections both normal and parallel to the bedding. The samples were set in epoxy mounts and polished by standard metallographic techniques. Caution was exercised in not backfilling the samples with epoxy, to eliminate any fluorescence contribution from the epoxy. Samples viewed in the electron microscopy were coated with carbon only.

Presentation and Discussion of Observations

A qualitative optical examination of polished surfaces of several Chattanooga shale specimens clearly showed a positive correlation between the mineral pyrite and organic constitutents. Ultraviolet light fluorescence microscopy of these same specimens revealed intense fluorescent emissions from the irradiated organic constituents (Fig. 1). This technique permitted us to distinguish more clearly between organic and inorganic constituents within the shale microstructure. Pyrite framboids enclosed within organic entities appeared to be a common feature in these specimens.

The fluorescent intensities observed for the above organic constituents appeared to be much stronger than fluorescent emissions obtained from exinite macerals in high volatile bituminous coals which are younger in age than the Chattanooga shale. Differences in the fluorescent character of the organic constituents in shales and coals may be due to at least two factors: first, the source of the organic matter (i.e., whether marine or terrestrial), and second, the packing of the organic constituents in relatively impermeable sediments such as shales might impede the structural and chemical changes

that organic constitutents normally undergo during coalification.

Backscattered electron imaging of identical shale specimens showed pyrite framboids surrounded by organic constituents such as shown in Fig. 2. X-ray microanalyses of slected regions of the above microstructure revealed only iron and sulfur in the framboids (Fig. 3a), whereas the minerals surrounding the organic solid (Fig. 3b) consisted primarily of elements associated with clay minerals. Weak peaks recorded for titanium
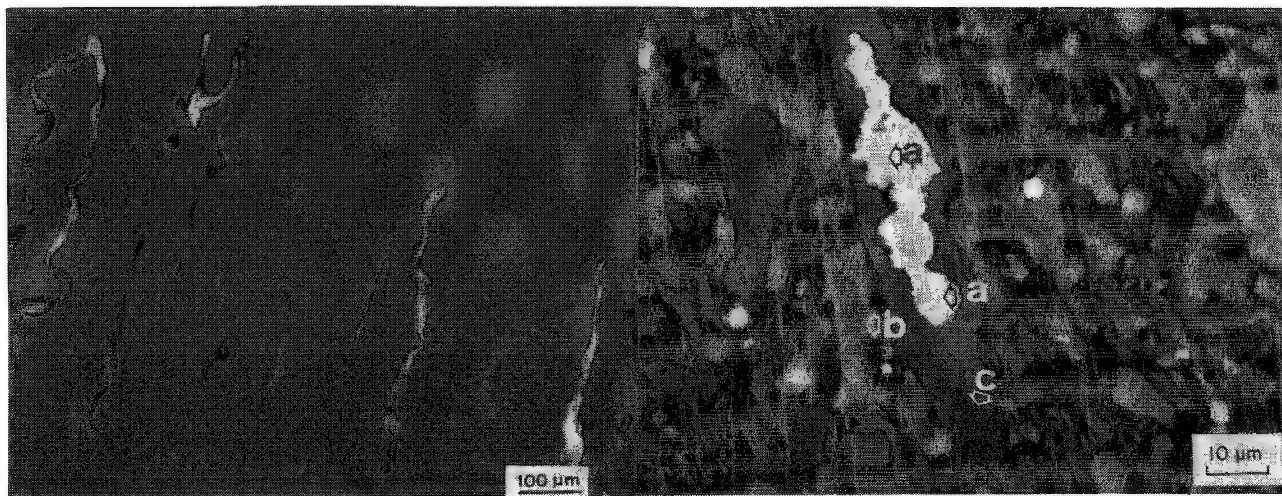
FIG. 1.--Ultraviolet light fluorescence microscopy of Chattanooga Shale shows emission from irradiated organic constituents.

FIG. 2.--Pyrite framboids surrounded by organic material. Backscattered electron image.
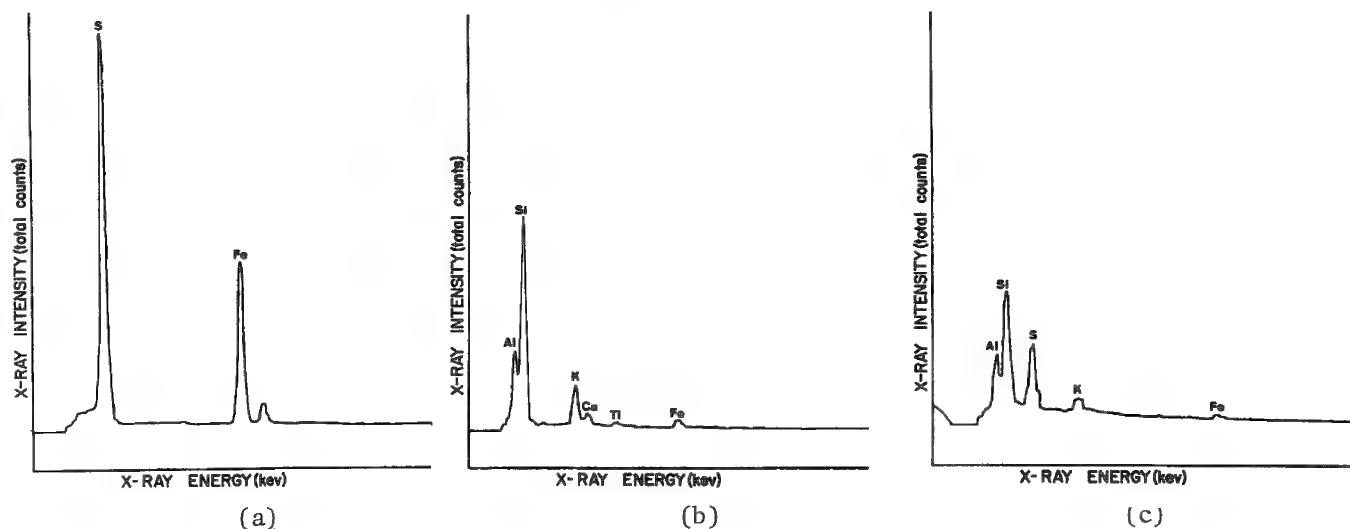
FIG. 3.--Energy-dispersive x-ray spectra of selected areas shown in Fig. 2: (a) taken from framboid shows only S and Fe; (b) from material around organic solid, primarily elements of clay material; and (c) from organic solid shows S peak with mineral elements excited by penetrating electron beam.

and calcium could indicate the presence of rutile (TiO_2) and calcite ($CaCO_3$), respectively, or these elements could be substituting for elements within the clay structure. This may be especially true of titanium, which is known to substitute for aluminum

in clay minerals.[4]

The x-ray spectrum presented in Fig. 3(c) is typical of the energy spectra obtained from several locations within the organic constituent. In addition to the peaks associated with the elements found in clay minerals, a sulfur peak was recorded. The presence of the x-ray spectrum for clay minerals from the organic material is attributed to the penetration of the electron beam through the organic body and its subsequent exciting of the minerals below the surface. However, the strong sulfur peak without any comparable iron peak (from the organic material) suggests the presence of organic sulfur in the maceral. These findings were corroborated by additional analyses of other organic constituents throughout the specimens. In each of the subsequent x-ray analyses, sulfur peaks were associated with the organic entities; iron was not detected.

The observed positive correlation between pyrite and organic constituents is doubtless not fortuitous. However, in this study no direct evidence was obtained that corroborated the thesis that pyrite framboids are due to replacements in microorganisms. Indeed, if that premise were correct we would have expected to observe organic structures within the framboids. Since no organic materials were observed within the framboid structures it must be concluded that the growth mechanism of pyrite framboids was not a replacement process. Suggestions that the internal organic structure of framboids has been removed via wear or dissolution are not consistent with observations of organic constituent in coal, where they are found to be relatively tough and resistant to wear.[5]

In addition to the syngenetic pyrite framboids that were found to be associated with the organic constituents, several occurrences of epigenetic sphalerite (zinc sulfide) were observed. One such example of epigenetic sphalerite growth is shown in Fig. 4. Iron and zinc x-ray maps shown in Figs. 5 and 6, respectively, distinguish between the two minerals. The sphalerite was apparently formed (at a more recent geological time than the pyrite) by the reaction of zinc, carried in percolating ground waters, with the preexisting pyrite.[6] Note that even though the organic constituents surrounding the sulfides contained sulfur, there does not appear to be any sphalerite crystallization other than that observed on the pyrite surface. This observation suggests that organically bound sulfur does not react readily with zinc carried in ground waters. This result may be due to a considerably physico-chemical change from the early stages of diagenesis in which anaerobic conditions prevailed to the more oxidizing conditions that are prevalent in recent times with ground water.

Finally, shales are typically a "potpourri" of minerals. Figure 7 illustrates this observation. For example the pyrite framboid (PY) is adjacent to a titanium-rich mineral (R), probably rutile, and slightly further along the central section of the organic body a quartz (QZ) fragment is located. The location of a variety of minerals within a collapsed exinite in the shale is similar to observations made of sporinite in coal. It is worth noting that the quartz and rutile are considered as detrital minerals washed into the sedimentary basin, whereas pyrite framboids are believed to be due to *in situ* growth during early diagenesis.

Conclusions

Microanalytical techniques such as SEM, EDX, and EMA have been shown to be ideal in determining the "host" phases of the minor and trace elements in the Chattanooga shale. Positive correlations were found between pyrite and organic constituents. However, these observations provided no evidence that micro-organisms acted as hosts for pyrite framboids. It is interesting that appreciable organic sulfur is still present, which suggests that the sulfur used for the formation of pyrite must have been derived mostly from other sources. It may be that the sulfate-reducing bacteria had an affinity for organic matter and that the organic fragments acted as substrates for pyrite growth.

References

1. L. G. Love, "Micro-organisms and the presence of syngenetic pyrite," *Geol. Soc. London Quart. J.* 113: 429-440, 1957.
2. M. H. Scheihing, H. J. Gluskoter, and R. B. Finkelman, "Interstitial networks of kaolinite within pyrite framboids in Meigs Creek coal of Ohio," *J. Sedimentary Petrology*, 48: 723-732, 1978.

3. R. A. Berner, "Sedimentary pyrite formation," *Am. J. Sci.* 268: 1-23, 1970.

4. L. A. Harris, H. E. Barrett, and O. C. Kopp, "Elemental concentrations and their distribution in two bituminous coals of different paleoenvironments," *Intern. J. Coal Geology* 1: 175-193, 1981

5. E. Stach, M-Th. Mackowsky, M. Teichmuller, et. al., Stach's *Textbook of Coal Petrology*, Stuttgart: Gebrüder Borntraeger, 1975.

6. G. D. Nicholls, "The geochemistry of coal bearing starta," in *Coal and Coal-Bearing Strata*, London: Oliver and Boyd, 1968, 269-307.
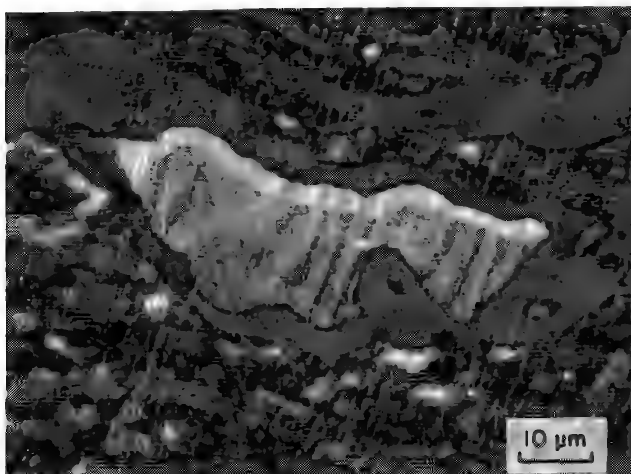
FIG. 4.--Backscattered electron image of pyrite framboid surrounded by sphaelrite.
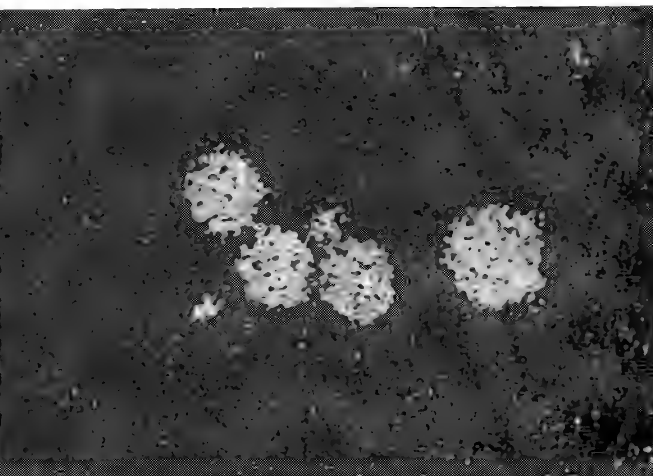

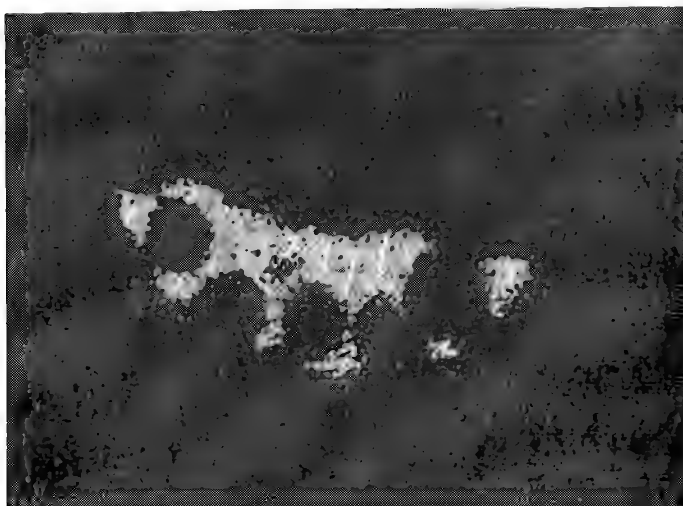FIG. 5.--X-ray dot map of Fe from field in Fig. 4.
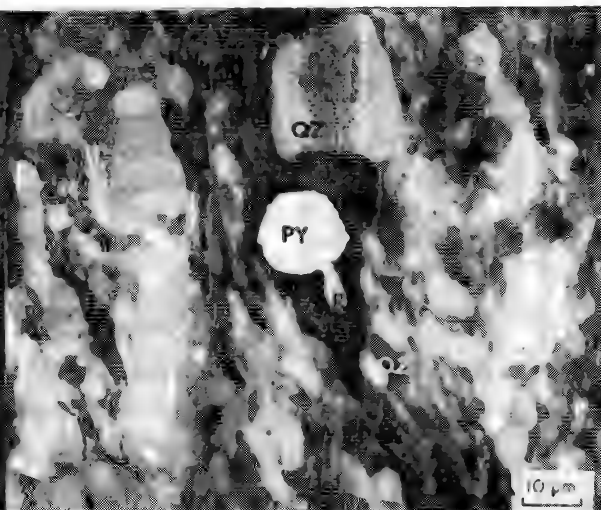

FIG. 6.--X-ray dot map of Zn from field in Fig. 4.

FIG. 7.--Backscattered electron image showing variety of constituents in Chattanooga Shale specimen.

POSSIBILITIES FOR THE USE OF ELECTRON SPIN POLARIZATION IN SCANNING ELECTRON MICROSCOPY

R. J. Celotta and D. T. Pierce

No use has been made to date of the intrinsic magnetic moment of the electron in scanning electron microscopy, with good reason: methods for orienting or detecting the orientation of the free electron's moment have traditionally been cumbersome and inefficient. Since the technology for the production[1] and detection[2,3] of polarized electrons has improved dramatically recently, the time seems appropriate to consider more seriously the possibility of a "polarized electron microscope."

Electron beams are polarized when there is a net orientation of their intrinsic magnetic moments or spins. The degree of polarization of a beam is $P \equiv (n_\uparrow - n_\downarrow)/(n_\downarrow + n_\uparrow)$, where $n_\uparrow$ and $n_\downarrow$ are the numbers of electrons with spins pointing parallel and antiparallel, respectively, to a preferred direction. Spins are randomly oriented in beams formed by conventional means; it is not possible to align the spins by passing the beam through macroscopic electric or magnetic fields. The production or detection of electron polarization is generally accomplished through the use of a spin-dependent emission or scattering process. Electron beams may have their polarization axis parallel to their momentum direction (longitudinal polarization) or at right angles to it (transverse polarization).

The two spin-dependent interactions[4] of greatest importance are the *spin-orbit* interaction and the *exchange* interaction. The first arises in the interaction between the magnetic moment of an incident electron and the magnetic field present in that electron's rest frame due to its motion in the rapidly changing electric field of the ion core. This interaction is strongest for large-angle scattering from high-Z targets and can be very spin selective. For example, for specular scattering from tungsten crystals at an energy of 72 eV and a scattering angle of 150° the cross section for electrons with spins parallel to the scattering plane normal is six times that of electrons with oppositely directed spins![5]

The exchange interaction occurs because electrons must obey the exclusion principle; they cannot occupy exactly the same state. This limitation has the effect of producing a different scattering cross section when a spin-up, rather than spin-down, incident electron scatters from a target with a net spin-up orientation. In electron-atom scattering, this effect would be observed in a polarized-electron, polarized-hydrogen experiment; for solids, scattering polarized electrons from a ferromagnetic material would demonstrate[6] the effect.

A somewhat obvious consequence of these two effects causing spin-dependent cross sections is the production of polarized beams from initially unpolarized beams. Since an unpolarized beam can be thought of as an equal mixture of two 100%, oppositely polarized beams and a spin-dependent scattering process scatters one component preferentially, it follows that the scattered beam is polarized. Hence, one can observe a spin dependence in electron scattering either by monitoring the polarization of a scattered, initially *unpolarized* beam, or by measuring the change in the intensity of the scattered beam when the polarization direction of an initially *polarized* beam is changed.

Although in scanning electron microscopy the spin-orbit effect might be used to emphasize scattering from high-Z materials, we shall concentrate our discussion on the application of electron polarization to imaging magnetic materials. Here use could be made of the fact that the exchange scattering depends on the local net spin density in the target, i.e., the local magnetic ordering. Three methods exist for using polarization to produce magnetic contrast. First, the incident beam could be polarized, which

would give rise to intensity variations in the elastically backscattered electrons as the beam scans through regions of varying magnetic strength or orientation. Second, a conventional primary beam could be used and variations in the polarization of the elastically scattered electrons could be monitored. Third, a conventional primary beam could be used with polarization analysis of the low-energy secondary electrons providing the contrast mechanism.

The first method requires a suitable source of polarized electrons, which could be either the GaAs photoemission source [1,7] or the EuS field emission source. [1,8]

The GaAs photocathode produces 20 μA of current per milliwatt of incident 800nm radiation. If circularly polarized light is used the resulting electron beam is 43% polarized in the direction of the incident light, with the direction of polarization reversible by reversal of the circular polarization of the light. Thus, one obtains a beam of constant current but with a polarization that can be reversed at a convenient frequency such that phase-sensitive detection can be used to isolate sensitively the spin-dependent part of the scattering signal. Little has been done to date toward the design a high-brigthness version of the GaAs source, although use of a finely focused light beam should make such a device possible.

The EuS field-emission source is based on the spin dependence of the internal barrier to emission in a EuS coating on a W field-emission tip. A high polarization (85%) transverse to the emission direction is produced in addition to high brightness. Polarization reversal is less easily accomplished; the tip must be heated and then cooled to below 16.6°K in a transverse orienting magnetic field.

The second and third methods for electron spin polarization contrast in scanning electron microscopy require a spin polarization analyzer. Two types of polarization detector might be considered for use in an electron "polarization" microscope. Both are based on the spin-orbit scattering effect described above. In the Mott detector, [4] electrons are accelerated to an energy of 100-120 keV and scattered from a thin gold foil. A difference in signal between those scattered to the right and left is a measure of the polarization normal to the scattering plane. A fully polarized beam would typically give rise to a right-left asymmetry of ±20%. The scattering is weak, however, so that only 10^{-3} of the incident signal can be collected with large solid angle detection. Alternatively, low-energy scattering, e.g., 150 eV, from a high-Z single cyrstal, can be used[2,3] in exactly the same way. Here the scattered signal is collimated by the diffraction process and smaller detectors can be utilized. The efficiency of this type of detector is equivalent to that of the Mott type and the fact that no high voltages are needed is a significant experimental simplification. On the other hand, this detector, along with the GaAs and field emission sources, needs a clean, 10^{-10} Torr vacuum for operation.

Of these three contrast mechanisms, our current knowledge suggests that the last, polarization analysis of the secondary electrons, has the greatest promise. Both theory and experiment[2] suggest that the exchange interaction would provide vanishingly small contrast for the electron energies typically used in electron microscopy. Application of the first two techniques would probably be limited to incident energies below 1 keV. Recent experimental work[9] has shown that the low-energy secondaries emitted from ferromagnets possess a polarization characteristic of the material. This finding suggests the use of a conventional SEM system augmented by polarization analysis of energy-selected secondary electrons to produce a picture of the magnetization of the outer 20-30 Å of the magnetic domains. The result would be a mapping with a resolution set by the incident beam interaction and giving at each point both the degree and direction of the magnetization. Work is currently under way in our laboratory to test the feasibility and usefulness of such a device.

References

1. R. J. Celotta and D. T. Pierce, "Sources of polarized electrons," *Adv. Atomic & Molecular Phys.* 16: 101-157, 1980.

2. D. T. Pierce and R. J. Celotta, "Spin polarization in electron scattering from surfaces," *Adv. in Elec. & Elec. Phys.* 56: 219, 1981.

3. J. Kirschner and R. Feder, "Spin polarization in double diffraction of low-energy electrons from W(001): Experiment and theory," *Phys. Rev. Lett.* 42: 1008, 1979.

4. J. Kessler, *Polarized Electrons,* New York: Springer, 1976.

5. G.-C. Wang et al., "Symmetry in low-energy-polarized-electron diffraction," *Phys. Rev. Lett.* 42: 1349-1352, 1979; "Polarized low energy electron diffraction (PLEED) from W(100)," *Phys. Rev.* B 23: 1761, 1981.

6. R. J. Celotta et al., "Surface magnetization of ferromagnetic Ni(110): a polarized LEED experiment," *Phys. Rev. Lett.* 43: 728-731, 1979.

7. D. T. Pierce et al., "GaAs spin polarized electron source," *Rev. Sci. Instrum.* 51: 478-499, 1980.

8. E. Kisker et al., "Electron field emission from ferromagnetic europium sulfide on tungsten," *Phys. Rev.* B18: 2256, 1978.

9. J. Unguris et al., to be published.

OPERATION OF A MICROCOMPUTER-BASED MULTICHANNEL ANALYZER WITH ENERGY-DISPERSIVE DETECTORS

D. Hale, John C. Russ, and D. E. Leyden

As the cost of computers and memory has decreased, more and more analytical instruments have either incorporated them alongside more traditional dedicated data-collection devices, or replaced as much as possible of the original instrument designs by the computer. This statement has been strongly true for multichannel analyzers as used for energy-dispersive x-ray analysis by Si(1i) or other detectors. Several standard commercial systems now use the computer, generally a 16-bit LSI-11 or equivalent machine, to store the data. There is still a great diversity in the amount of data collection and the creation of user displays carried out by dedicated hardware or by a general-purpose computer with a specially written program. The former approach has the advantage of speed since it is often possible for several actions to take place simultaneously; the latter has the advantage of low cost and flexibility to add or change functions without alterations in the physical configuration of the instrument.

We have followed the latter path, using a general purpose microcomputer (Apple II+) with 48K bytes of memory. The standard machine incorporates a user keyboard of the familiar typewriter sort, a video display usable for graphics or text displays, the central processor and memory, and an interface bus with multiple card slots. We are using these slots for many different purposes, as reported in several accompanying papers. For our purposes here, only three are important: (1) a disk controller which handles two 5in. floppy-disk drives, each with 143 K bytes of storage, (2) a printer interface which can print either text (letters and numbers) or any graphics image drawn on the video screen, to a dot matrix printer (of either the thermal or impact variety), and (3) a special-purpose pulse-measuring analog to digital converter (ADC) designed to measure amplified pulses from energy dispersive detectors. The modular ADC card has been described previously;[1] it is similar in function to ones used in larger "conventional" MCAs, but built onto a single, modular printed circuit card (Fig. 1).
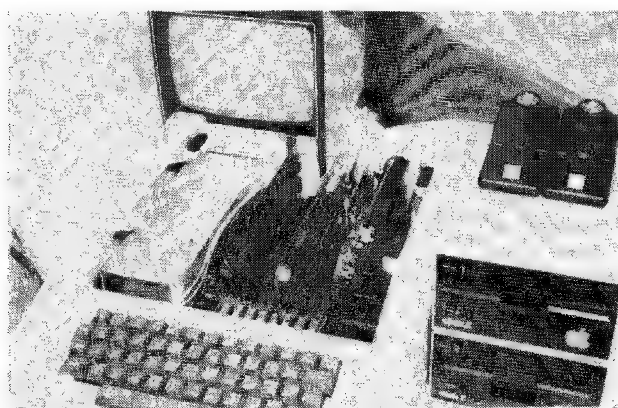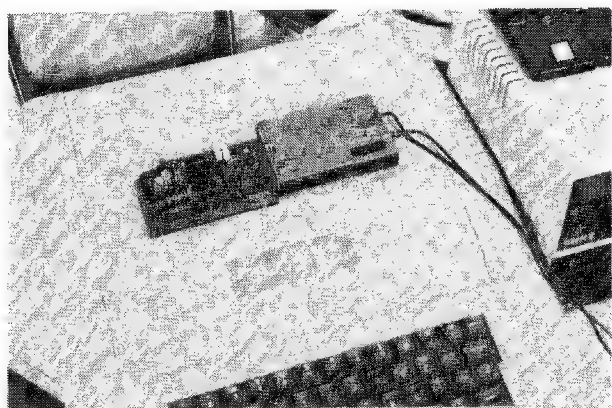

FIG. 1.--Modular ADC card and its position installed in Apple computer.

D. Hale is at the Nucleus, Oak Ridge, Tenn., J. C. Russ, at North Carolina State University, Raleigh, D. E. Leyden, at Colorado State University, Fort Collins.

Data Collection

The ADC card detects an incoming pulse, measures it to obtain a numerical value representing the pulse height, and makes the value (a number, from 0 to 2047 in the 11 bit version of the ADC) available to the processor via the interface bus. It also incorporates a live-time clock which is gated off during the conversion process within the card, and by an externally supplied signal from an amplifier that incorporates pulse pile-up rejection. It is then the responsibility of the microprocessor, working under control of a data-acquisition program, to make use of the numeric information supplied.

For simple spectrum acquisition, the process is the same as it would be in any MCA. The number representing the height of the pulse is used as an address into a block of memory set aside by the program for spectrum stograge, and the contents of the "channel" thus addressed are incremented by one. Processing many such numbers (many x rays) produces a spectrum of the usual sort. Because the memory used is in no way different from the rest of the computer's memory, different data-acquisition program can allocate different memory ranges or different amounts of memory. For electron-excited x-ray micro-analysis on an SEM, where total counts are rarely very large and high-energy elements are difficult to excite, we generally use a 1024-channel memory and 2 bytes per channel. This configuration can store a maximum of 65 535 counts in each channel and provide 20 eV per channel coverage, for instance from 0 to 20 keV. On the other hand, for x-ray photon excitation, particularly at higher energies, or for gamma ray work, a 2048-channel spectrum with 3 bytes per channel (giving over 16 million counts) is more suitable. In some other situations, as we shall see, the spectrum as such is not stored, but counts for particular elements are totalled and stored in memory as a function of time, or for comparison to other stored values for alloy sorting.

Even for conventional spectrum acquisition different options are possible. It is the central processor that must act to carry out the data storage and the creation of the graphics display of the stored spectrum along with various labels and markers, and respong to the user's commands from the keyboard. Which should have the highest priority? Normally we would agree that the storage of data is the most vital function, but we also want to see the spectrum grow before our eyes.

The normal "Analyze" routine is a program that draws and redraws the display, responding to user commands to change the vertical scale up or down, expand or contract the display, or move it horizontally. This process is interrupted whenever the ADC signals that it has data available, and a very short (and fast) "interrupt service routine" reads the value and increments memory. User commands come from the normal computer keyboard, and since no specialiy labelled control buttons are provided, we have chosen mnemonic codes for each function (A = Analyze, C = Clear, and so forth). During the time required to store away the count, the main program (doing the drawing) is halted. At very high count rates (> 10 000 cps) this procedure results in a visible hesitation in the updating of the display, but at most normal count rates it suffers no drawbacks.

For extremely high data-acquisition rates, another strategy can be used. In this mode of operation the main program spends all of its normal time waiting for the ADC card to have data ready, which it then uses to increment memory. This process takes less than half the time of the interrupt service routine described above, and can thus handle higher count rates (provided the amplifier time constant is short enough so that pulse pile-up does not cause all these pulses to be rejected). The display is updated each second of live time, when the ADC card signals the processor to add one to the elapsed live time, and to decrement any preset time counter being used. This once-per-second update produces a discontinuous display that is nonetheless rather comfortable to use, since the data remain without flicker on the screen until updated again. The time needed to redraw the display adds about 5% dead time to the measurement process. Even higher acquisition rates are possible if it is not necessary to store or draw the entire spectrum, and only totals for a few elements need be tallied.

Spectrum Display Modes

The Apple computer has a built-in graphics display that provides 280 horizontal by 192 vertical dots, each represented by a bit in memory (the entire display thus takes about 8K bytes) which can be turned on (white) or off (black) by the program. Various color

combinations are also possible, at somewhat reduced resolution, but the spectrum display modes have been restricted to black and white for greatest sharpness. To draw the spectrum onto the display requires a vertical scale, which normally starts at 192 counts full scale and goes up by factors of 2 to any value needed to exceed the maximum contents of a channel. The horizontal range can be devoted to any 256-channel segment, with every channel showing, or to larger numbers of channels (512, 1024, 2048) with selection of every second, fourth, or eighth channel (the same way that most conventional MCAs using TV displays with a vertical raster scan function). What that means is that users can change the horizontal and vertical scales, and slew, expand, or contract the spectrum, just as they would a "hardware"-based MCA display. The normal spectrum display mode is white on a black background (Fig. 2). Another spectrum can be superimposed, recalled from disk storage. (More than 40 spectra can be stored on one side of one diskette, each with its calibration, live time, and list of identified elements.) The second spectrum is shown as dots either white on black or black on white (Fig. 3). Since each spectrum is stored with its energy calibration, the overlaid spectrum can be recorded at a different calibration from the primary one, and the dot positions will accurately line up peaks at the same energies. It is also possible to vary the relative vertical scales of the two spectra, or to add or subtract one from the other which provides a limited form of stripping to handle peak overlaps.

It is also possible to superimpose various markers onto the spectrum. A "bug" can be moved by the user with a knob attached to a potentiometer or joystick (a standard Apple input device), to read out channel number, energy, and channel counts (Fig. 4). Also, markers can be superimposed for a complete set of 5 K, 11 L, and 5 M lines (all the lines with at least 1% relative intensity from available tables), each with heights appropriate to the selected element (Fig. 5). These markers can be positioned vertically by the user, and can be rapidly advanced through the periodic table by use of the <- and -> keys on the keyboard, until a match is found. Elements whose presence is confirmed by the user (by pressing the + key) are added to a list of up to 16 elements which are saved with the spectrum and available for subsequent quantitative-analysis programs.

Within the data-acquisition programs is also a routine to verify the energy calibration of the spectrum. Unlike most other MCAs, ours permits any calibration (electron volts per channel and zero settings), and obtains it by the user marking the approximate location of two major peaks in the spectrum and entering their energies. Parabolas are then fitted to determine the true centroids, and the gain and zero are calculated and sorted. The system, once calibrated, is generally stable within a few electron volts for long periods of time (weeks) except during system warmup. This method is easier for most users than trying to adjust amplifier controls to achieve exact calibration, and is much less prone to slight miscalibration creeping into the spectra. It is quite compatible with the graphics display format of the Apple, though it would be less so for most conventional raster-scanned MCAs, which is probably why it is not used as much as fixed calibration. All the quanitative software (described elsewhere) uses the calibration data stored with each spectrum.

Elemental Windows or Regions of Interest

Using the aforementioned potentiometer or joystick inputs, the user can position markers to indicate energy windows that correspond to selected elements (or background regions). The counts in such regions can be totalled and the total displayed on the screen during analysis as pulses suitable for x-ray mapping with the SEM are generated at a rear panel connector. This method provides conventional mapping capability, and the updating total indicates the number of dots recorded on the film. Line scans in which the count rate in the energy window is converted to a voltage and used to produce a Y-modulated trace on the SEM are also provided. Unlike systems that use an analog ratemeter to accomplish this result, ours simply counts the pulses within the computer for each period of time and then uses a DAC to produce the corresponding voltage while the pulses are counted for the next time interval. This "digital ratemeter" technique is made especially simple in this sytem since we already employ an interface card with multiple DACs for SEM beam control, and one is available for producing the display signal.

FIG. 3.--Overlay of pure nickel spectrum on one recoreded from stainless steel. It can be vertically scaled to match peak height and subtracted.
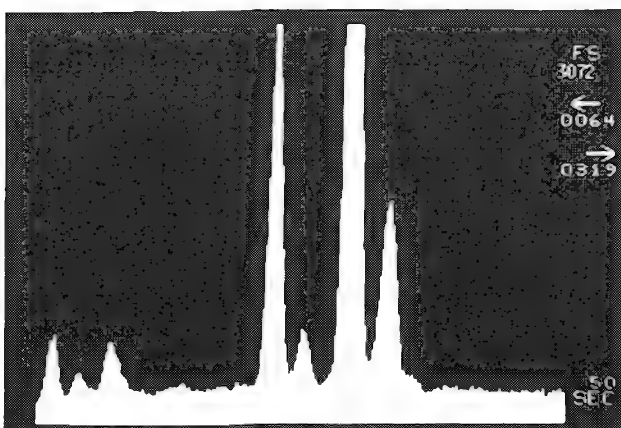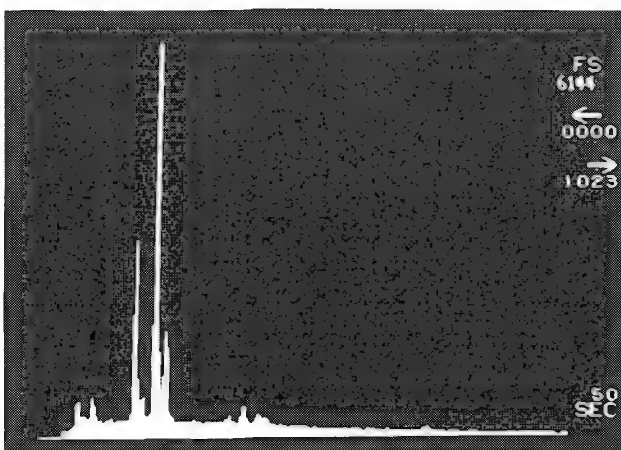
FIG. 2.--Spectrum display during acquisition, showing scale settings, and 256 or 1024 channel display modes. Sample is complex ceramic.
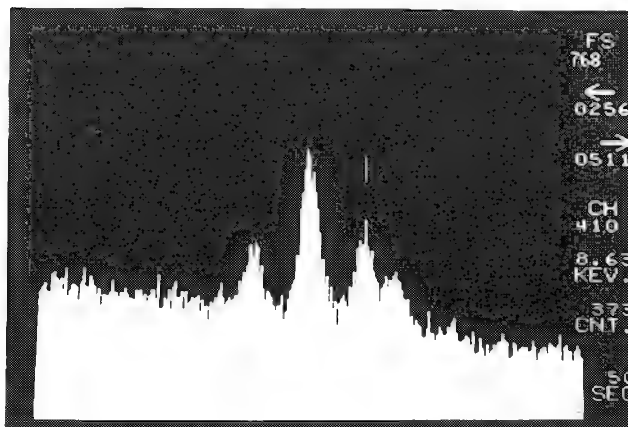
FIG. 4.--"Bug" is positioned by user to read out energy and channel contents.

In addition to live-display line scans, the system can store digital intensity profiles, normally for four energy windows (elements and/or background) at a time, for 256 points across the sample as the beam is scanned either by the SEM's scan generator or by the DAC card. Programming for other numbers of elements or points can be straightforwardly implemented, but we have chosen this method as it allows the data to be stored in the same
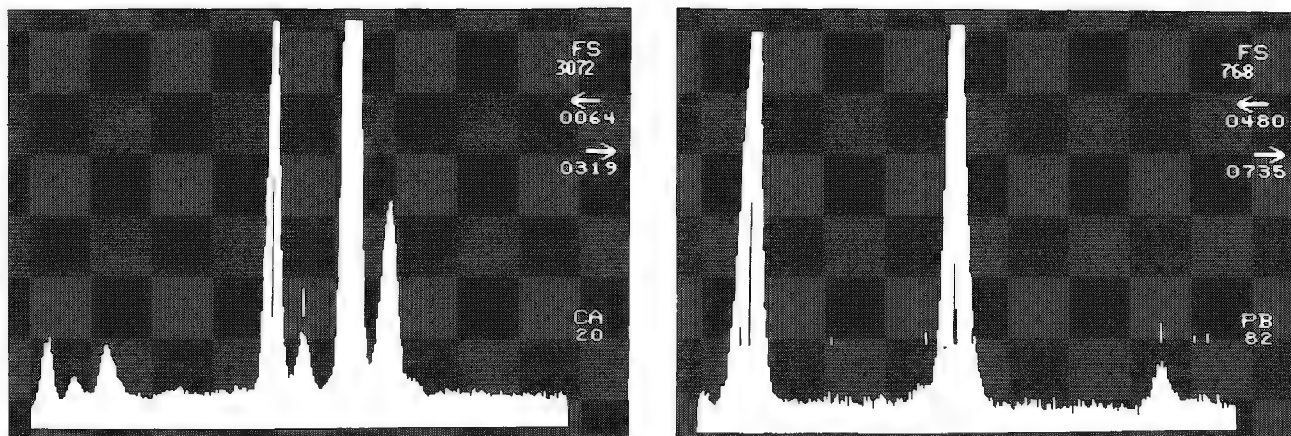
FIG. 5.--Extensive KLM markers, with heights adjusted for each element, are shown on spectrum and used to identify elements present.

memory space as normally used for a spectrum. (Since the ADC card produces digital addresses for each pulse, rather than store all of them, we just total those which fall into the various energy windows set by the user.) During data acquisition the video screen is used to produce a multiple bar-chart ratemeter display. These profiles can also be stored on disk for subsequent examination or analysis.

Memory Configuration

The data-collection programs, graphics display memory, the spectrum itself (and possibly a second one displayed in comparison), and the computer operating system (which allows it to read and write data from the disks, run the printer, and generally to function) all fit easily into the 48K memory of the standard computer. Another 4K is used for memory mapping of the various peripherals, which appear to the processor as memory addresses that can be read from or written to. The final 12K bytes of the processor's available address space is filled by an extended Basic interpreter in read-only memory (ROM), which is available for programs that access the data for various quantitative computations.

The programs described here are in machine language for speed, as this is an important factor for live acquisition and display of spectra. However, they are all written as self-contained subroutines, which facilitates combining them with other programs, or in unusual combinations, to accomplish specific needs. When the spectrum data, graphics display subroutines, and all system support and language interpreter are in memory, about 25K bytes remains for Basic programs to access the data. This amount can be increased to 35K at modest cost in additional memory. Furthermore, many larger programs can be segmented and "chained" to carry out sequential operations, so that quite substantial programs can be realistically executed in the system.

Experience with Various Detectors

Spectra of x-rays and gamma rays from a variety of sources, obtained with a variety of detectors, have confirmed the broad suitability of this computer-based MCA for many different applications. In addition to electron-excited spectra obtained with Si(Li) detectors, we have also used radioisotopes and low-power x-ray tubes to excite larger sample areas. As shown in Fig. 6 the background is lower, as would be expected due to the absence of bremsstrahlung generation in the samples. With Ge(Li) and high-purity germanium detectors, or thallium-activated sodium iodide detectors, spectra of high-energy gamma rays from radioisotopes can be recorded (Fig. 7). They require somewhat different programs for peak identification than do x-ray spectra. However, linear least-squares fitting of spectral components is still a common method for deconvolution.

Finally, current tests are under way with mercuric iodide detectors.[2] They have energy resolution somewhat inferior to Si(Li) detectors in the low-energy (up to
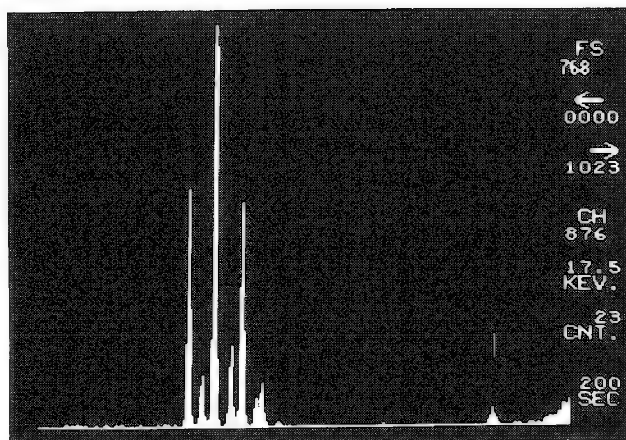
FIG. 6.--Excited by x-rays, this stainless stell spectrum has very low background.
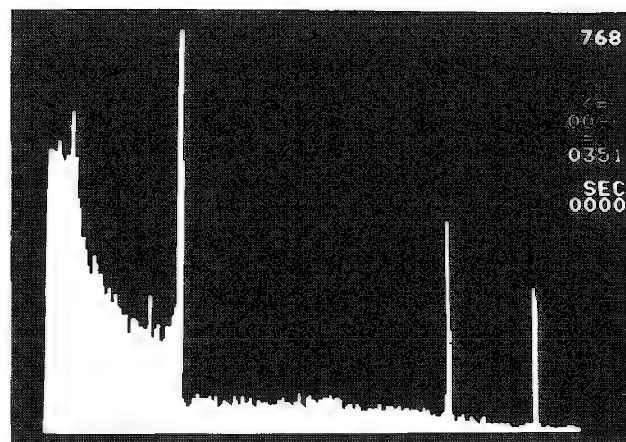
FIG. 7.--Gamma ray spectrum (portion of 2048 channels) from Cs and Co, taken with a Ge detector.

20-40keV) range, but do not require cooling with liquid nitrogen. The advent of room temperature detectors will make it possible to solve many practical problems of detector placement without the limitation of the bulky dewar, and also is expected to open many industrial and remote applications for energy-dispersive analysis. The flexibility of the small computer-based system we have described, unconstrained by specially designed logic circuits for data collection or display, and the access of programs written in high level languages to the data, makes adaptation of this system to these new areas of application as they develop straightforward.

References

1. D. Hale, T. Satterfield, D. Blankenship and J. Russ, "A modular ADC/microcomputer system for energy dispersive x-ray spectroscopy," in P. Predecki et al., Eds., *Advances in X-ray Analysis*, New York: Plenum Press, 1982, vol. 31.
2. A. J. Dabrowski, "Progress in room temperature energy dispersive detectors," *ibid.*

PROCESSING X-RAY SPECTRA, DATA, AND LINE SCANS IN A "PERSONAL" COMPUTER

John C. Russ

Limits of Microcomputers

The use of a microcomputer with a specially designed pulse-measuring analog-to-digital converter (ADC) to collect energy dispersive x-ray spectra is described in an accompanying paper. This combination provides very straightforward, low-cost data acquisition. Because the ADC has interrupt capability, it is possible for the microcomputer to carry on some independent tasks while collecting data, but because the interface card has no DMA (direct memory access), it is still the responsibility of the program and the central processor (a single-chip, model 6502, 8-bit microprocessor) to serve the ADC and store the data. Some computer based multichannel analyzers do give the ADC enough intelligence, in dedicated logic circuits and access to the memory used for spectrum storage, to enable a spectrum to be accumulated without any involvement of the main processor. We have chosen not to use this approach for the ADC, although it is actually used for some other peripherals such as high-speed disk drives for the same computer, because it can limit the flexibility of the system. For instance, we can allocate a spectrum storage region of any size (from 256 to 2048 channels) and any number of counts per channel. Different programs for electron-excited and x-ray fluorescence application use 65536 (2 bytes) and 16 million (3 bytes), respectively. Also, the storage area can be moved anywhere in the main memory of the computer, which with the advent of additional memory boards permitting as much as 320K bytes in the same microcomputer opens more interesting possibilities for multiple spectrum storage without resort to writing the data onto disk.

The program and processor in our system also creates the graphics display, which is facilitated by the built-in 280 × 92 point video graphics screen display, which can be shown at will instead of or in combination with the normal text display. Nevertheless, reading each channel's contents, converting the value to the height of the line which should be drawn (depending on the selections for vertical and horizontal scale settings), and turning on the bits that correspond to white points (and off those which correspond to black), is done entirely by the program and processor. This arrangement contrasts sharply with those of virtually all larger computer-based multichannel analyzers, which employ extensive circuits to generate their displays, some even with a separate processor in addition to the main one. Again the advantage of one approach totally based on software is that it is possible to introduce new display modes with no change in the hardware; the penalty is that of processing time.

In fact, while collecting an energy dispersive x-ray spectrum at moderately high count rates, i.e., over 10 000 cps, which would correspond to a moderately high dead time in most amplifiers used with Si(Li) detectors, the microprocessor in our system is fully occupied with serving the ADC interrupts, refreshing the display screen to give a true live display of the growing spectrum, and placing on the screen some calculated information about scale settings, and other markers. Under those conditions it is not practical to consider having any "real" computing, such as peak or background fitting on previously acquired spectra or quantitative calculations for other sets of intensity data, in concurrent operation.

The hallmark of the "personal" microcomputers is that they are generally limited to one thing at a time. (That is not strictly true, as they do support multiple interrupts and some foreground-background capability, but the only tasks that can really co-exist with extensive mathematical computation are simple ones such as spooling of characters to a printer, monitoring of clocks and external security systems, and so forth, rather than the

---

The author is at the Engineering Research Division of North Carolina State University, Box 5995, Raleigh, NC 27650.

acquisition of data at high rates.) Consequently, we shall limit this discussion of practical forms of data processing to programs that are run after the data have been acquired. Most often they are either loaded from disk to replace the data collection program, with the data remaining in place in memory; or they load the data, usually a spectrum, from disk storage back into memory. Intermediate results may sometimes be passed from one portion of a large program to another, by chaining, or saved on disk for future use by one of several programs.

Languages

The data-acquisition and display programs mentioned above are all written in machine language (or in some cases compiled from high-level languages). Their machine language execution is of course essential because of the speed needed for these operations. In a discussion of the various steps of data processing, it is practical to consider several languages for routine use. The Apple computer is capable of being programmed in Basic, Fortran, Pascal, and several specialized languages such as Forth (a stack oriented language developed originally for instrument control) and Cobol (a well-known business language). Fortran is a popular scientific data-processing language, which is available only as a compiler. What that means is that several steps of porgram entry using the high-level language, its translation to machine level instructions, and the combination of those instructions with other program fragments (including the mathematics libraries) are needed to produce a program that can be "run."

Basic, on the other hand, is most often encountered as an interpreted language. That means that the program, in its high-level language, is stored in memory and each command, variable, and value are translated into machine language instructions as the program is actually execured. This process allows constant access to the program, for ease of changing it or adding extra statements, but the need to translate the instructions each time they are encountered slows down the execution time. Except for this difference, there is actually very little structural difference between Fortran and Basic, in contrast to languages like Pascal and Algol, which have more of a "building-block" structure that emphasizes the creation of small procedures for each program step, and the final assemblage of many such blocks into the final program. These programs are also generally compiled rather than interpreted.

Compiled languages have one advantage for the developer of language (and possible disadvantage for the user) in that the original program (the "source code") need not be supplied with the system. It is practically impossible to decipher the final, compiled machine language program that actually carries out the calculations to see what its intent is, or how it goes about what it does. That is all very well if the program is perfectly "debugged" and the user does not care to know what algorithms it uses, but the history of programs used for electron microanalysis suggests that many users do want access to the source code. Basic, or any interpreted language, automatically provides this access, along with the ability to alter the programs, introduce different models, add additional output, or delete unwanted portions, and so on.

The best of both worlds would seem to be a language that could be run interpretively to develop programs, and to allow access to the source, but which could also be compiled to produce high-speed execution and when necessary to protect against idle tampering with a running program. Fortunately, this solution has become practical. For many personal computers, it is now possible to use a Basic compiler, which takes a Basic program that has been running (and debugged) by use of the normal interpreter, and translates it into machine code instructions that can then be run as a stand-alone program without the interpreter. The typical speed improvement is 3-10 times, depending on the type of program and extent of floating-point arithmetic (which is speeded up least). All the programs described here can be run interpretively, as for instance when they are to be modified for a particular purpose, or may be compiled into machine language for speed.

Spectrum Processing

Linear least-squares fitting of library spectra stored on disk,[1] or of spectra synthesized from modified Gaussian shapes for each of the lines for a given element,[2] is the principal method for deconvoluting spectral overlaps and obtaining net elemental intensities. The least-squares fitting procedure is carried out by matrix inversion to solve the the simultaneous equations for the relative height of each component. The spectral

components can be sections of measured spectra, with or without prior background removal by linear or quadratic interpolation between user-designated points, and with optional "filtering" or differentiation using a convolution function. Alternately, the generated spectra can be previously stored on disk, or generated as needed. The program includes the ability to calculate the energy and relative height to within 2 eV and 1% relative height, as compared to standard tables, for all 5 K-shell, 11 L-shell, and 5 M-shell lines which have more than 1% intensity relative to the principal alpha-1 line for the shell. This procedure ignores variations in peak height ratios due to differential absorption in the sample, and so is not superior to the fitting of stored spectra. Alternately, the height of each emission line for the element can be allowed to vary independently, as a separate component of the fit.

This fitting procedure can handle up to 8 components (either individual lines or complete elemental signatures) covering up to 256 channels (one quarter of the normal 1024-channel spectrum) at a time. A series of such fits covering each group of elemental lines bracketed by designated background points automatically produces a list of total elemental shell intensities for all of the elements in the spectrum that have been previously identified by means of the KLM marker lines (which are generated by the same energy and height algorithm previously mentioned). The fitted spectral components can be displayed for comparison to the original (Fig. 1). This program and method are quite comparable in flexibility, accuracy, and overall performance with those employed in larger systems.

As the answers are identical, it is therefore interesting to compare speed. Computing all the lines for a selected element, for instance to produce the KLM marker lines, takes about 2 s in interpreted Basic, and about 0.2 s when compiled. Generating the complete spectrum for fitting takes up to 12 s (interpreted), and solving the matrix inversion to get net intensities another 20 s if all eight components are present. Consequently, use of stored spectra is faster than use of generated spectra, since loading times from disk are about 6 s per spectrum. To process a spectrum completely in 4 or 5 segments, for 12 elements, takes about 1 min (compiled), which is definitely longer than a comparable program running in, for instance, an LSI-11/23 with hardwared math package (an option available for the Apple, but not incorporated in our system), but not out of proportion to the data-collection time or the needs of our laboratory for data throughout. The final data are stored as elemental intensities in a disk file, for use by the various quantitative correction programs.

ZAF and Other Quantitative Programs

The normal quantitative program used is a version of Frame,[3] which has been extended by the addition of no-standards terms to compute the expected pure element intensity for each element. It also handles oxygen by stoichiometry. For a 12-element oxide system in which many fluorescence terms are present, the program takes 2.5 min. It reads the intensities from the disk file created by spectrum stripping and writes the answers (in weight, atomic, and oxide percent) to disk for subsequent recall. As an alternative, the Frame-C method, which does not require
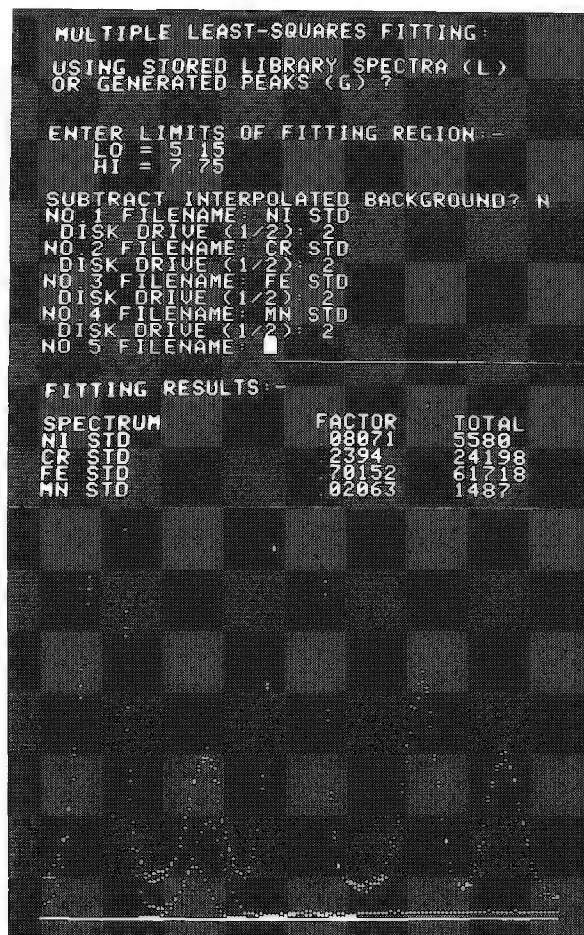

FIG. 1.--Least-squares fit of library Fe, Cr. Ni, and Mn spectra to measured stainless steel spectrum. Display shows, superimposed, original, fitted sum of components, and Cr and Mn peaks which combine to form principal overlap.

previous spectrum processing and iteratively

FIG. 2.--ZAF results from application of modified Frame-C program to a stainless steel.

computes the peak overlaps and spectrum background as functions of composition, along with the ZAF effects, is also available. This is the largest program used, as many additions and enhancements have been added.[4] In interpreted Basic, for a complex 8-element system, this process requires more than 10 min. Compilation reduces the execution time to 3.5 min. Another ZAF method, which requires two sets of intensity data taken at different accelerating voltages, but does not require the user to measure or estimate the x-ray takeoff angle from his sample,[5] takes less than 2 min for a 6-element system. We consider all these times acceptable for routine work. Results are displayed on the video screen (Fig. 2) and can be printed or saved on disk.

In addition to the ZAF programs, there are several other quantitative and semi-quantitative elemental ratios[6] without standards and without correction for absorption and fluorescence (essentially the relative K-ratios for the elements, as they would be passed to a ZAF program). The net intensities are obtained above a background interpolated from three measured points, using a shape based on Kramers' law, with an additional empirical low-energy term. Calculated elemental overlap factors are used to handle peak overlaps. The accuracy is only semiquantitative for bulk samples, but better for thin sections (where the pure-element intensity terms are calculated differently, and absorption and fluorescence are not so important. For particulate or rough samples, the peak-to-local background ratio is used instead of net intensity. The elemental ratios are calculated in about 5 s and then renormalized to total 100% when the list is ended. This method is extremely versatile and fast for comparative analysis of many points.

For thin sections, the Hall or peak-to-background method[7] and the Cliff-Lorimer or ratio method[8] are both provided. These methods accept data from standards, which are stored on disk and used to compute the correction factors as needed. The computations are trivial and the time essentially that needed to read the files (a few seconds). Other more specialized models, including Bence-Albee,[9] are also available. There is also a program to compare the current spectrum in memory to all of the spectra stored on a floppy disk (up to 44 will fit on one side of a 5in. floppy) to find which match most closely. This process uses chi-squared matching and takes about 20 s per spectrum (6 s to read the file back from the disk). The best five spectra are reported, in order of goodness of fit.

All the quantitative programs write their results into disk files and also display them on the screen. These results can then be recalled to construct plots as shown in Fig. 3, either in the form of pie (circle) or bar (histogram) charts. The computer's graphics display capability is well suited to this type of presentation, as well as for
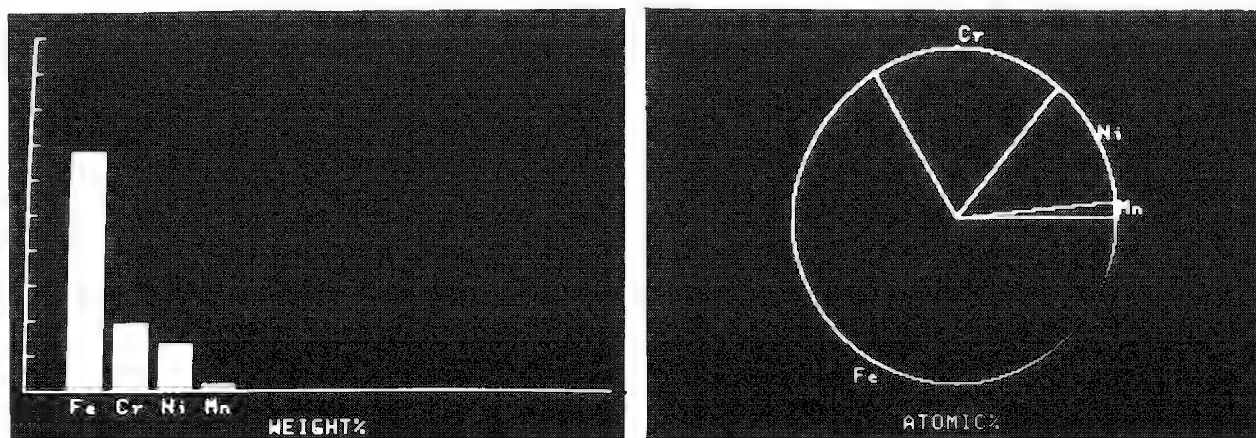

FIG. 3.--Graphic representations of computed concentration results from ZAF and other programs.

calibration curves and other plots. All graphics displays, including spectra, can be printed out on either a thermal or impact dot-matrix printer, for permanent storage.

Utility and Tutorial Programs

As an aid to teaching users about the physics of x-ray production, we have included several programs that operate off line and make extensive use of the graphics capability of the microcomputer. These programs include a simplified multiple scattering Monte Carlo model,[10] which permits any incidence angle and sample thickness to be entered (and could easily be modified for other geometric conditions). Electron trajectories are plotted at the rate of a few hundred per hour, along with the locations of generated x rays. These plots (Fig. 4) give a useful pictorial representation, and in addition the depth distribution of x-ray generation $\phi(\rho z)$ is accumulated for plotting, and
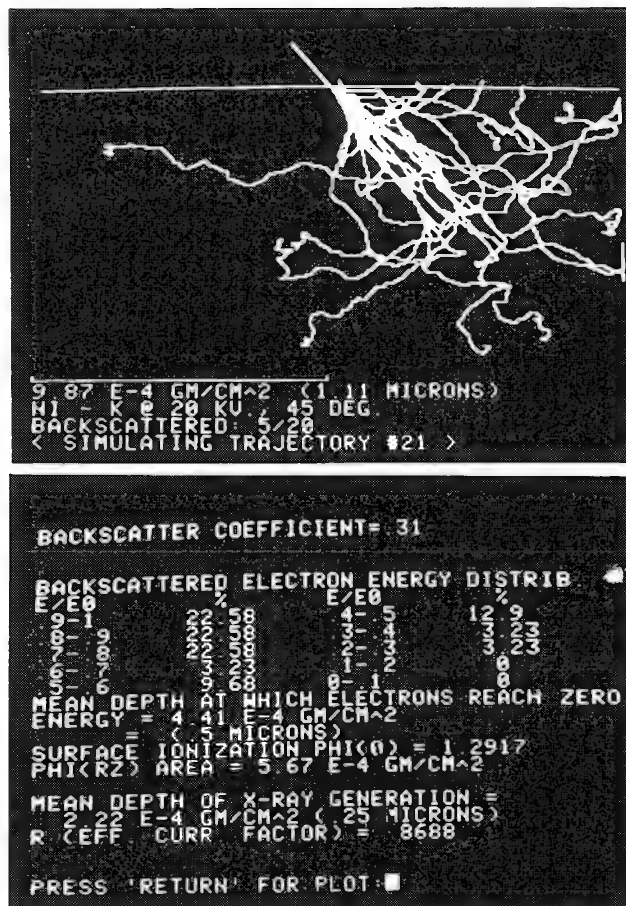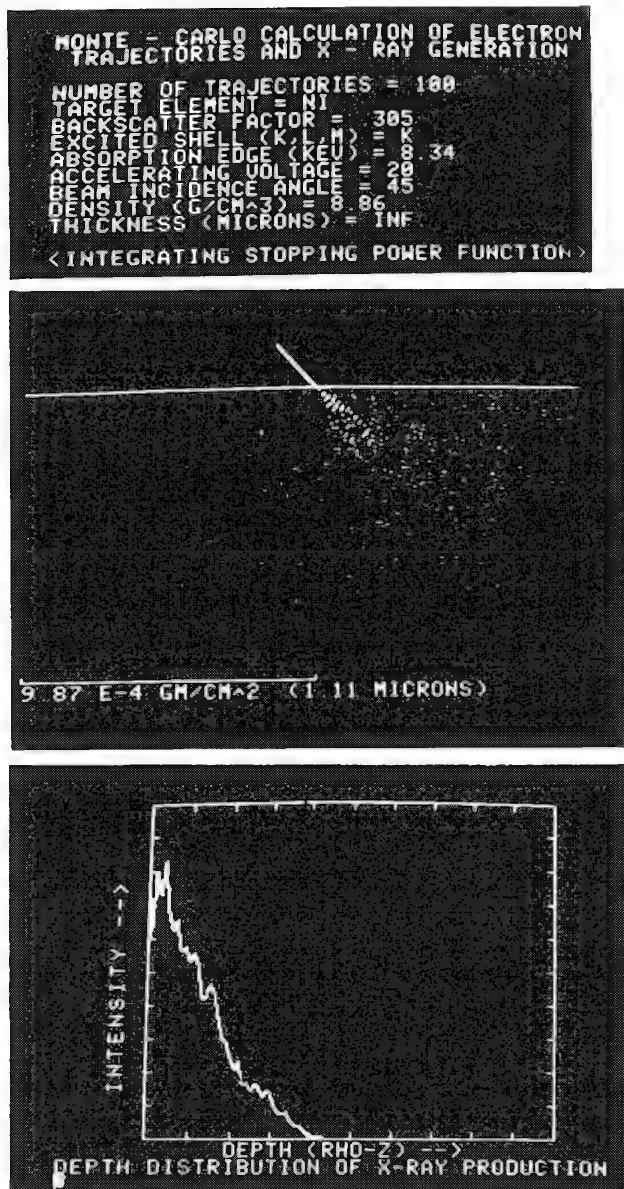
FIG. 4.--Monte-Carlo simulation of electron trajectories and x-ray generation. Sample is nickel, with 20keV electron beam incident at 45°.

the energy distribution of electrons which leave by penetration or backscattering is shown. Another utility program computes $\phi(\rho z)$ curves by use of analytic functions[11] for any composition matrix, draws them on the screen for the generated and emitted x rays (Fig. 5), and reports the depths from which 50 and 90% of the emitted x rays come, for a given takeoff angle. Another program applies ZAF and no-standards calculations to predict and graph the variation in elemental intensities as a function of the surface

tilt angle (Fig. 6). Still other programs display the periodic table and allow access to an extensive database of "handbook" values about the elements; perform conversions between atomic, weight, oxide, and formula representations of concentration; compute x - ray takeoff angles in the SEM; and generally serve to handle the miscellaneous functions we find useful in our laboratory.

FIG. 5.--$\phi(\rho z)$ depth distribution curve for generated (solid line) and emitted (dashed line) x rays of Al (upper curves) and Ti in a ceramic.

FIG. 6.--Computed intensity variations for Al, Ca, and Fe in a complex oxide, as a function of surface tilt angle.
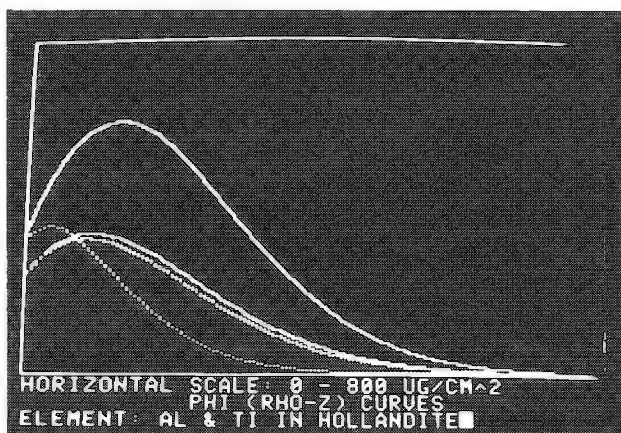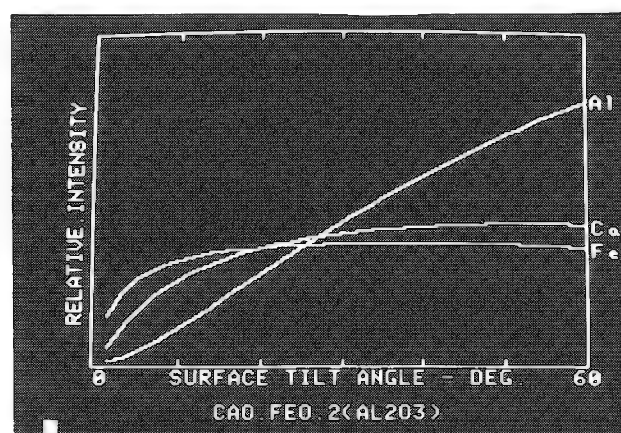
Line Scans

As described in another paper, one of the ways we can use the ADC cards data is to acquire "digital line scans" for multiple elements. These scans are fully digital (unlike systems which define the energy band with analog discriminators), which is one of the advantages of the completely general approach possible with the minimal hardware restraint and total software-based flexibility of this system. Also, since the computer has in it digital-to-analog converters to control the SEM beam scan, one can collect data free from count rate or dead-time effects, by basing the beam advance on the elapsed live time signal from the ADC board.

Normally we accumulate line scans as sequences of 256 points across the sample, for four elements at a time. (Practically any other combination could also be programmed, as needed.) The counts for each element are saved in one quarter of the normal 1024 channel memory used for spectra, and thus easily saved on disk in the same space reserved for a spectrum. To redisplay these data, either after collection or at any later time, it is possible for the user to type in from the keyboard any arithmetic expression in terms of the four elements, ended with the return key, to specify the display. This could range from something as simple as 2,return (which just displays the profile for element number 2) to something as complex as (3-2)/(4-1), return which, provided that windows 2 and 1 are backgrounds for windows set on elements 3 and 4, gives the ratio of net intensities of the two elements. Other possibilities, including 1/(1+2+3+4), the normalized intensity for element 1, or (1-2)/2, the net elemental peak to background ratio to compensate for surface topography or density differences, illustrate the power of the method.[12] Figure 7 shows some examples. Each profile is automatically scaled to fit the display screen, and after plotting can be printed out as well.

If intensities have been measured at a regular array of points, the two-dimensional data set can be plotted in either isometric or contour map display (Fig. 8). A pseudo-color display which codes intensity as color and plots maps of the surface is also provided. Again, arithmetic combinations of the individual elements are permitted. These

FIG. 8.--Isometric and contour map displays of two-dimensional x-ray intensity data.
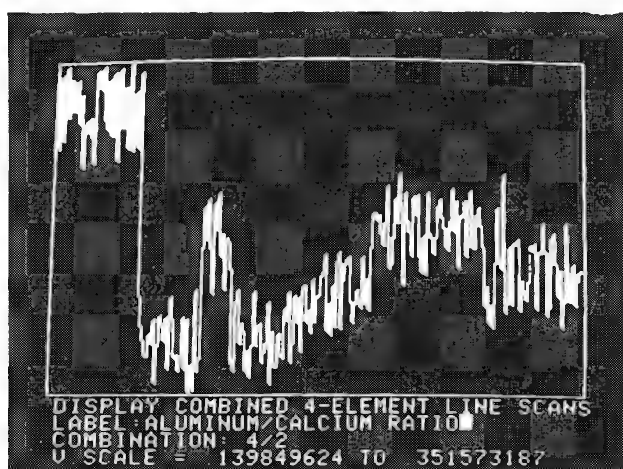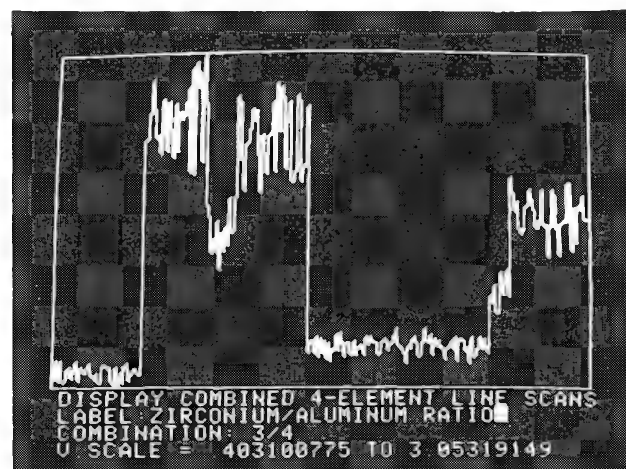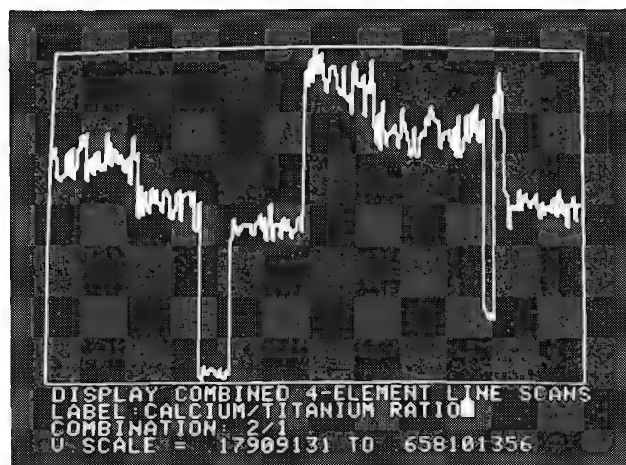
FIG. 7.--Examples of arithmetically combined stored multi-element line scans across complex ceramic.

combinations are often useful as supplements to normal dot-map x-ray scans (which are available with the normal data acquisition program), having lower spatial resolution (the maximum resolution of our beam control DACs is 256×256, although we rarely use more than 40×40 for multipoint measurement) but much greater sensitivity to variations in intensity, and better statistics at each point to permit smaller variations to be seen. And of course, since the data are stored, endless manipulation to find the combination of elements that really characterizes the sample is possible.

Other techniques, including the automatic analysis of many points and subsequent cluster analysis of the data to find phases, are also supported, but reported elsewhere.

Conclusions

It is not the purpose of this paper simply to catalog all the various data-processing

programs that we have adapted to the microcomputer we use to collect energy-dispersive x-ray spectra. Many of these programs are essentially identical to those found in larger machines, and have been well reported in the literature. Instead, we wish to point out the practicality of using them in a microcomputer, the advantages of adding the extensive graphics readouts, and the desirability of allowing user access to the source program. The last is useful whether or not the operator ever indeed modifies or adds to it, as it allows the operator to study it for better understanding of the methods used, and to help uncover any errors that reside, well hidden, in even the most thoroughly tested programs, waiting for the right combination of factors to arise.
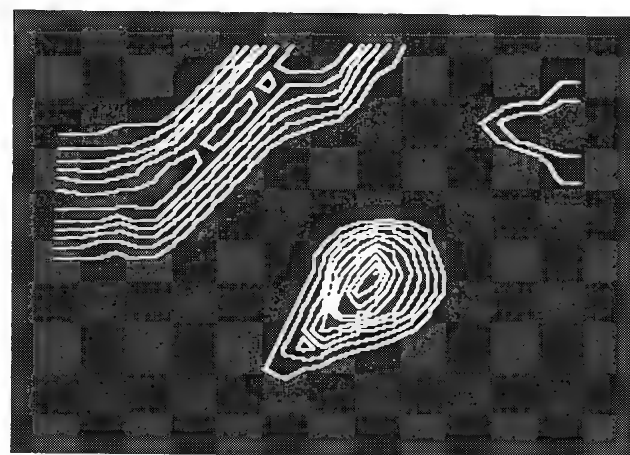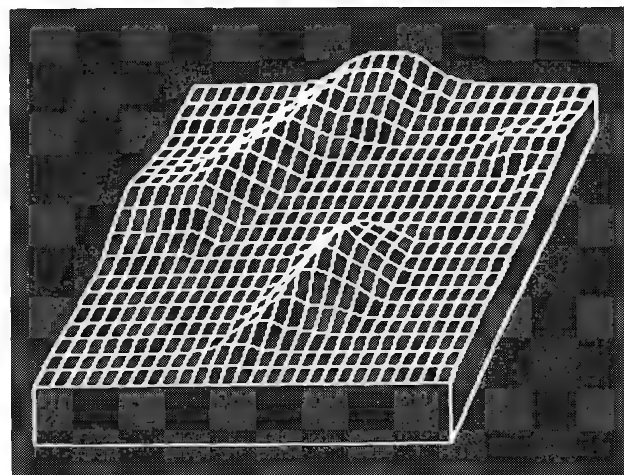
All the programs described run, along with the 1024-channel spectrum and the high-resolution display software, in a 64-Kbyte Apple II+ computer. If the interpreted Basic (rather than compiled) programs are used for quantitative computations, they will run in a 48-Kbyte machine.

The chief penalty of this approach is time. Not so much the execution time of the individual routines, which though slower than larger 16-bit minicomputers is generally adequate for our laboratory needs, but the inability to carry out multiple tasks at once. Our microcomputer is interfaced to collect energy-dispersive x-ray spectra, to control a WD spectrometer, to control the electron beam scan position, and to collect images and measure feature size and shape, either from graphics tablet or video (raster-scan) input. In addition, it maintains records on our SEM users and prepares their monthly bills, and functions as a word processor. But it can only do one of these jobs at a time. It appears that the most economical solution to this problem may not be a larger multitasking minicomputer, but multiple micros.

References

1. J. J. McCarthy and F. H. Schamber, "Least squares fit with digital filter: a status report," in K. F. J. Heinrich, Ed., *Energy Dispersive X-ray Spectrometry*, NBS Special Publication 604, 1981, 273-296.

2. J. C. Russ, "Resolving spectral interferences using non-Gaussian peaks," *Canadian J. Spectroscopy*, February 1976.

3. R. L. Myklebust, C. E. Fiori and K. F. J. Heinrich, *Frame: A Compact Procedure for Quantitative Energy Dispersive Electron Probe X-ray Analysis*, NBS Technical Note 1106, 1979.

4. J. C. Russ, "Modifications and extensions to Frame-C," in *Microbeam Analysis--1979*, 268-272.

5. J. C. Russ and T. M. Hare, "Quantitative x-ray microanalysis on surfaces with unknown orientation," *Canadian J. of Spectroscopy* 1980, 98-105.

6. J. C. Russ, "Interactive displays and simple algorithms as an aid to qualitative analysis of energy dispersive spectra," *Proc. 9th MAS Conf.*, 1978, 46.

7. T. A. Hall, "The microprobe assay of chemical elements," in G. Oster, Ed., *Physical Techniques in Biological Research*, New York: Academic Press, 1971, vol. 1A, 158-275.

8. G. Cliff and G. W. Lorimer, "Quantitative analysis of thin metal foils using EMMA-4: The ratio technique," *Proc. Fifth European Congress on Electron Microscopy*, London: Institute of Physics, 1972, 140.

9. A. E. Bence and A. L. Albee, *Geology* 76: 382, 1968.

10. L. Curgenven and P. Duncumb, *Tube Investments Research Report 303*, 1971; and G. Love, private communcation.

11. J. D. Brown and W. H. Robinson, "Quantitative analysis by $\phi(\rho z)$ curves," *Microbeam Analysis--1979*, 238-240.

RUNNING WAVELENGTH DISPERSIVE X-RAY SPECTROMETERS WITH A MICROCOMPUTER

W. D. Stewart and John C. Russ

Until very recently, most conventional wavelength-dispersive x-ray spectrometry, on either electron microprobes or x-ray fluorescence systems, was carried out by essentially manual methods. Qualitative analysis was performed by scanning at uniform speed (with motor drive) over a range of angles of interest, while a strip-chart recorder plotted the voltage output from a ratemeter connected to the pulse-amplifying nucleonics. Specific counts for an element of interest were obtained by positioning of the goniometer (by hand) at the peak count position, and counting for a preset time. Sometimes (by no means always) additional counts were then taken off the peak to obtain a background count, which might then be deadtime corrected and possibly submitted to a remote computer by punch cards or a time-share terminal for ZAF or other correction procedures.

With the advent of minicomputers and their incorporation within most modern energy-dispersive x-ray systems, which are likely to be mounted on the same microprobe, there has been a steady trend toward more automated control of the WD spectrometer. This trend has encouraged manufacturers of WD spectrometers to design them suitably for stepping-motor-controlled crystal position (two theta angle) as well as including provision for remote selection of crystal, slit, and so forth.

Controlling the WD spectrometer and counting the x-ray pulses requires several different types of programs, for different purposes: rapid scan routines, with automatic peak recognition, to cover large angle ranges quickly for qualitative analysis; programs to slew quickly to a series of predetermined angles corresponding to elements of interest, to count for present times for quantitative analysis; and slow step-scans over smaller angular ranges for valence shift or other similar studies.

Because small vertical displacement of the sample surface shifts the angular position of the crystal and detector for a given peak, in addition to any misalignment of the spectrometer, it is usually wise to incorporate a peak-seeking algorithm into the software for quantitative counting. This process can be carried out on every peak and every sample, or just for the peaks on the standard(s), with the same position values remembered for use with the unknowns. The latter method would be preferred if the elements were present at trace concentration levels in the unknowns, so that the peaks would have no clear maxima. Peak seeking is usually done by step scanning in a coarse pattern (20-30 steps) across the region containing the peak, fitting a parabola to the data to find the maximum, and then counting at that maximum. When counts are taken in this way for quantitative work, separate background counts on either side of the peak are obtained and an interpolation performed to subtract the background from under the peak. Also, dead-time corrections are applied to the intensity data, which are then stored on disk for future use by a correction program (ZAF, calibration curve, regression, or other).

When rapid qualitative scans are being performed, either the count rate is monitored during a very coarse, short counting time-step scan to spot increases which call for a slower and finer set of steps, or a series of short scans are performed over the peak positions corresponding to the principal lines of a large but not unlimited number of possible elements of interest. The latter method will still miss unexpected elements, but is better than the former for detecting the presence of trace peaks which might be missed altogether by the first technique. The scans can be displayed or printed out, to show graphically the presence or absence of measurable amounts of the elements,

---

Author Stewart is at Dapple Systems, Box 2160, Sunnyvale, Calif.; author Russ, at the Engineering Research Division of North Carolina State University, Box 5995, Raleigh, NC 27650.

and the appearance of the spectrum. Other specialized data-collection procedures can be programmed straightforwardly, as the burden of controlling the spectrometer stepping motors and timer, and of counting x-ray pulses, is handled by the interface hardware and a short machine-language subroutine.

Stepping Motor Control

Stepping motors are unlike conventional motors in that they do not move continuously. Each current pulse advances the rotor by a fixed angle increment, usually 200 or 400 steps per revolution. The gearing or drive mechanism to which the motor is connected then defines the number of steps required for a sprescribed motion, for instance in two-theta angle or wavelength.

It is possible to move whatever the motor is driving very slowly, since the pulse rate can be arbitrarily slow. On the other hand, the maximum speed with conventional motors and power supplies is usually about 400-800 steps per second, in order that the motor can reliably start and stop without losing steps. Higher speeds, or applications where the mechanism being driven has substantial inertia (stepping motors are rather low-torque devices) involve the need to accelerate and possibly to decelerate the pulse rate. Sometimes that is done with hardware, but in the system being described here we do it with the software instead. If the distance to be traversed exceeds a certain amount, usually 100 steps, a timing loop is applied to the pulse output, which continuously decrements the delay until the motor has been accelerated to running speed (defined in most cases by the external mechanism and its power requirements).

Stepping motors require substantial current supplies, typically several amperes at a few volts. Separate power supplies with appropriate transformers and filtering are used to produce this power, and the computer simply turns the pulses on and off with logic level (5V) signals from an interface board. The board shown in Fig. 1 comprises both a stepping motor controller capable of driving multiple motors (up to 15, each with a suitable external power supply) and a 24-bit counter (maximum capacity 16 million counts) for incoming x-ray pulses from the system detector and amplifier. The stepping-motor interface is a VIA6522 chip, an intelligent controller that has multiple registers that appear to the host computer as a block of memory addresses, in the range which the Apple reserves for peripheral devices (including the keyboard, disk drives, printer, and other control interfaces). The machine language subroutine which carries out the task of sending out the required pulses and controlling their timing, writes into one of these registers to make the motor turn in one direction and another for the referse direction. Then the register is cleared. The write and clear operations produce a logic pulse which is transmitted to the power supply. Since most of the time spent in this process is in fact dedicated to waiting until it is time for the next pulse to be sent, the possibility exists in principle of carrying out other tasks while that happens.

FIG. 1.--Stepping motor controller and counter interface card.

Actually, there seem to be very few other things which it is then appropriate to be doing, except perhaps controlling another motor, and the program we are using is a dedicated rather than a foreground/background one.

Although the positioning reproducibility of the stepping motor itself is quite good, the mechanism to which it is attached may exhibit backlash. If this is the case, it is usually adequate to correct for it by always approaching each setting from the same direction, with a software loop that goes 100 steps (for instance) past the setting desired when coming down in angle and then moves slowly back up to the intended position. This method is preferable to installing separate position encoders on the spectrometer (or other device), because the encoders are themselves both expensive and of finite accuracy.
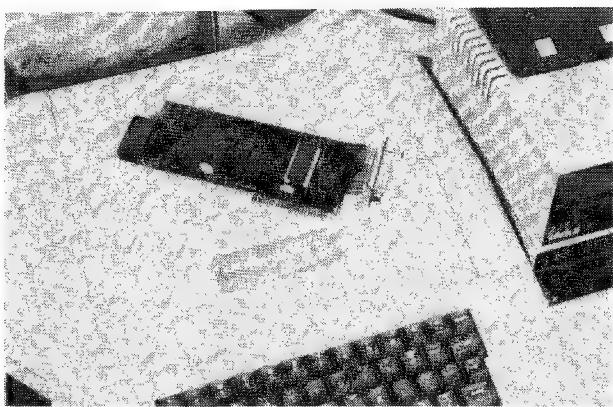
Provided that the motor has enough torque to drive the mechanism, and the speeds used are not excessive, excellent reproducibility of angular position is obtained. The greatest source of error in peak location is due to shifts resulting from sample surface position, and these shifts require peak-seeking as described above.

In the absence of absolute encoding of position, it is necessary to tell the computer where the spectrometer is positioned when the system is first turned on. One could do that in principle by driving to one end until the limit switch is encountered, and then, knowing that position, working from there with the software keeping track of relative movements. In practice, it is generally faster for the user simply to type in the current angle or wavelength setting, which also allows the user to update the position at any time, in case he has manually repositioned the spectrometer. Continuous display of the angle/wavelength setting at which the computer thinks the spectrometer is enables the user to notice any discrepancy and to type in the correction. We find that this feature is rarely used, as the system is very reliable, but that it does make the operators (especially graduate students) feel much more comfortable about what is going on.

Counting Pulses and the Clock Timer

The output from the normal amplifier, which is connected to dedicated scalar-timers and ratemeters in conventional manual systems, is fed to the counter on the interface board. If desired, it can also be connected to any existing nucleonics for a parallel display of the intensity data. The counter register has a capacity of $2^{24}-1$ counts. The operator can clear it by writing to an address on the board; and it is read as three contiguous bytes of memory. These intensity values are then displayed on the screen in real time, plotted (to show a scan in process) on either the video display (Fig. 2) or printer, and saved on disk as desired.
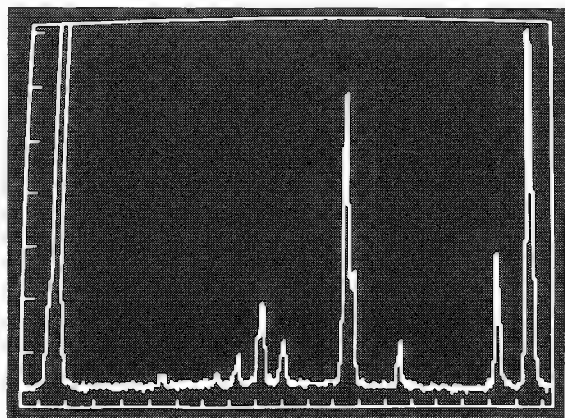
FIG. 2.--Plot on the video display of a wavelength scan.
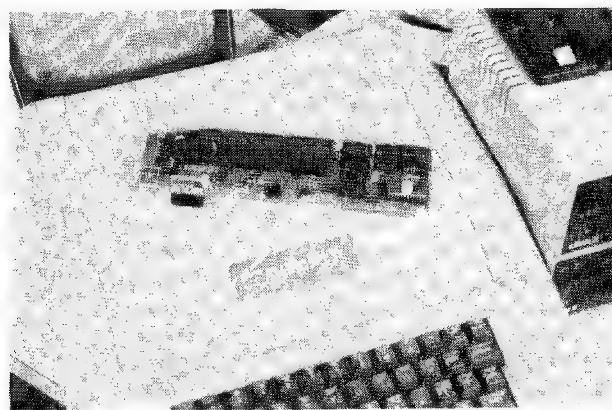
FIG. 3.--Clock card for the Apple microcomputer, with interrupt capability.

Control of the time for data acquisition can be handled in two ways. Since the computer itself incorporateds a highly precise crystal-controlled oscillator that synchronizes all the microprocessor and memory functions, software timing loops can be used to keep track of elapsed time, provided that nothing else can interrupt them. We normally use a timing loop of 20 ms and all counting times are actually carried out as multiples of that basic time. Alternately, if one wants the computer to perform other operations (plotting, disk storage, computations) during the counting operation (particularly if the time is several seconds or more long), a separate clock is required, The one shown in Fig. 3 not only keeps track of time with microsecond accuracy, and can be used to label data with the time and date of acquisition, it can also generate an interrupt on the computer bus at preset time intervals. This capability permits the computer to spend most of its time on other tasks, and just count the interrupts (usually at the same 20ms periods) to determine when the preset analysis time has been completed.

The data collection software has been written so that if the clock is present on the bus it will be used; if not, the software timing loop will be used instead.

The interface card itself can also generate bus interrupts. This capability is used for preset count analysis, where the number of counts to be acquired is first written into the interface registers and then decremented during the counting process. When the value reaches zero the computer reads the system clock, and from the elapsed time since the start of acquisition determines the counting time and hence the count rate. This mode is actually very infrequently used, but was included in the interface design at essentially no cost.

Spectrum Analysis and Other Applications

In addition to the peak-counting procedures described for quantitative analysis, the collection of spectra, either representing a series of short range scans or one long scan, is important as a qualitative analysis tool. To aid the user, these spectra can be displayed on the video screen, with either a linear or logaritmic scale. (The latter is particularly useful when elemental concentrations range from major to trace elements.) They may also be printed, much like a strip-chart recording, on the graphics printer attached to the system. In the latter case, they can include peak labels and other alphanumeric information.

A complete list is available of all major lines (1% relative intensity compared to the alpha-1 line) for elements from atomic number 4 up, which can be searched by element or by wavelength or two-theta angle. Any element with a peak (one of the 5 K, 11 L, and 5 M lines in the table) within 1% of the peak to be identified in the displayed spectrum is listed, and then all of the lines and absorption edges for each of those elements are displayed.

Off-line programs (which operate on previously acquired data which has been stored on disk) are provided for ZAF, Bence-Albee, and calibration curve methods of quantitation. In addition, since the same hardware configuration can be used for x-ray fluorescence spectrometers, multielement regression (based on LaChance-Traill and Rasberry-Heinrich models) and a fundamental parameters (effective wavelength) program are provided. The same hardware control can also be used to automate existing WD x-ray fluorescence spectrometers or x-ray diffractometers, at a fraction of the cost of a new instrument. For the diffraction application, we have written not only data-collection routines, but also a minisearch match that can identify the phases present in complex samples from a set of standard patterns stored on disk.

Finally, stepping motors can be attached to many laboratory instruments, including scanning densitometers to read diffraction pattern films (electron or x ray), and the stage position controls of either electron or light microscopes. Along with interface cards that set or read voltages, the availability of a simple interface to control position via stepping motors is a major key to the flexibility and power that microcomputers bring to the laboratory.

MULTIPOINT X-RAY ANALYSIS BY USE OF THE BACKSCATTERED ELECTRON SIGNAL AS A GUIDE

T. M. Hare, Dale Batchelor, and John C. Russ

The technique to be described here is applicable to the characterization of many multiphase materials. We shall illustrate it with a material of great interest to us, a fine-grained polycrystalline ceramic material (SYNROC) containing at least three major phases, intended for use as a repository for radioactive waste. That means that in addition to the five intended host oxides (of Al, Ca, Ti, Zr, and Ba) another 31 elements can be expected to present in small amounts. We want to find out by x-ray microanalysis (and other techniques) whether the three predicted phases are present and how they change with the introduction of the waste, whether any other phases appear, and where the minor element ions go (which phase acts as a host for which waste element). X-ray diffraction results can answer these questions only partially. There is some uncertainty about the patterns from several of the possible "pure" host phases, occurrence of some additional lines, and shifts with the introduction of dopants making the patterns more complex. In addition, because of the low intensity and probability of overlapping with lines of major phases, X-ray diffraction cannot reliably indicate the presence of minor phases (a few per cent by volume). We also want to know as much as possible about the local neighborhood around each grain, whether it is composed of grains of similar composition (both major and minor elements) or not, and how the radwaste ions distribute themselves during sintering throughout a large sample.

Classic energy-dispersive spectrometry is inadequate to answer these questions for a number of reasons. First, there is no such thing as a "typical" area which can be quantitatively analyzed. No two grains are exactly alike, and to analyze enough grains to draw conclusions about the ways in which one element substitutes for (or is found in conjunction with) another would require an enormous number of analyses, clearly precluding long analysis or computing times. Also, since the material is essentially impervious to etchants, the as-polished surface shows no easy guidelines to the discovery of individual grains, which are in any case so small (1-2 μm) that unequivocal analysis of single grains is undependable.

Cluster Analysis

We have previously reported on a technique that attempts to answer some of these questions by measuring x-ray intensities for the elements of interest, for short times (10-30 s), at a large number of randomly selected points on the sample surface.[1] The normalized intensity values are then plotted in an N-dimensional space (equal to the number of elements measured), and we expect to find (with computer assistance) clusters of points corresponding to individual phases. The number of points in each cluster yields an estimate of the relative volume fraction of the phase, the size and shape of the cluster (above and beyond purely statistical scatter) reflects the extent of substitution or other composition variation and grain size information, and the number of clusters tells us how many phases are present.

This method has given us some valuable information about the major phases. It has become necessary to model the change in the shape of the clusters with grain size, because they grow streamers or bridges toward other clusters if the region excited by the electron beam may cover more than one phase in this fine-grained material. Figure 1 illustrates the presence of clusters in two host materials with different grain sizes, to illustrate the effect of this bridging. This problem is surmountable (with enough

---

The authors are at the North Carolina State University, Box 5995, Raleigh, NC 27650.

points measured), and indeed should in principle tell us something about the probability of two phases being adjacent.

The principal difficulty that remains is that with random point positioning, an inordinately large number of points must be analyzed to find minor phases that may be present. For instance, a phase amounting to 1% by volume would be very significant in terms of the properties (mechanical, thermal, and resistance to leaching out of the rad-waste, if certain ions preferentially collected in the phase), but it would require the analysis of 10 000 locations for confident identification of its presence as a cluster. Even if the phase always occurred next to a particular host phase, or was significantly smaller in grain size, it might still be missed.
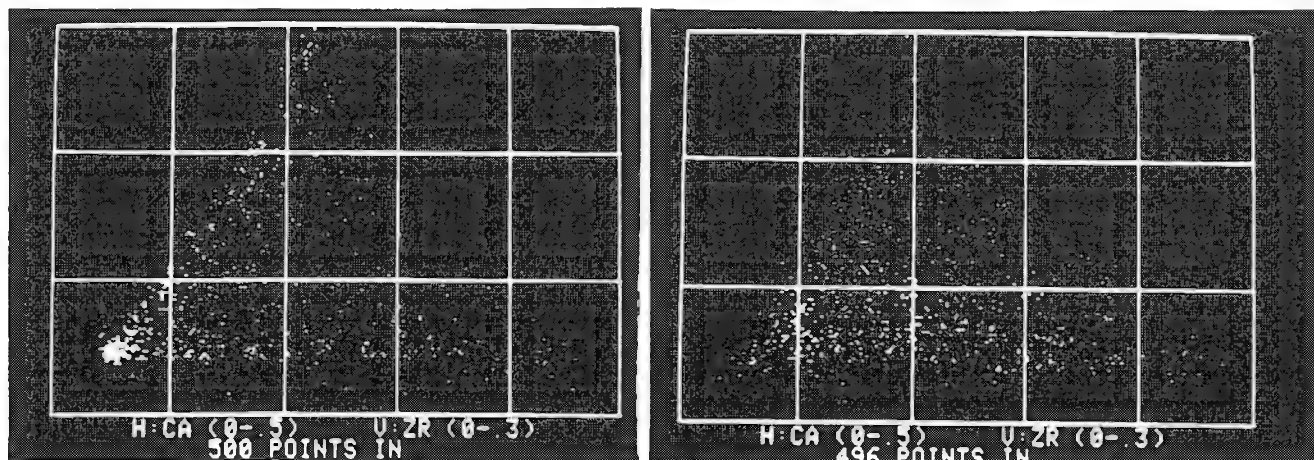

FIG. 1.--Plots of normalized intensities from random multipoint analysis of 10 kV. N-space distribution is projected onto a 2-D (two-element) plane (Ca vs Zr). (a) coarse-grained material (SYNROC, 2-5 µm) with distinct clusters; (b) fine-grained material (SYNROC, 1-2 µm) in which clusters have extensive bridging due to overlapping of analysis region onto several grains.
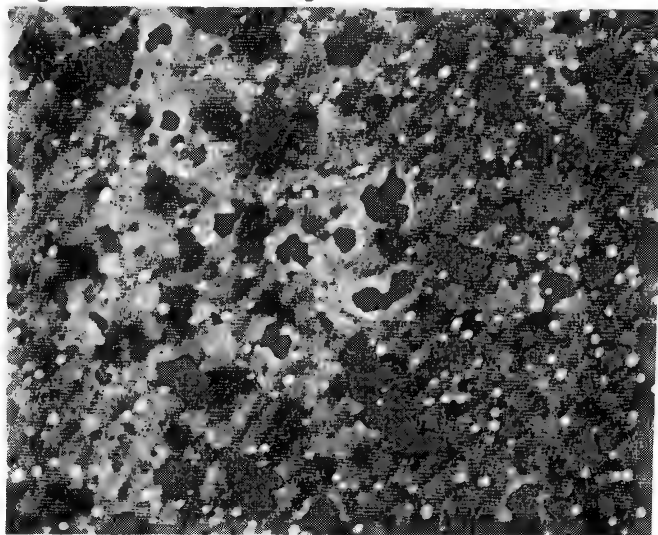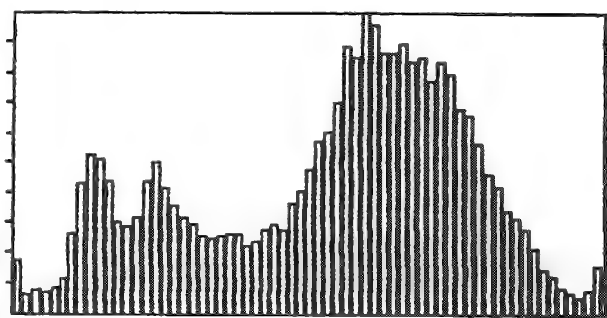
(a)   (b)

FIG. 2.--(a) Backscattered electron image of fine-grained radwaste-doped "SYNROC" multi-phase ceramic. Contrast and black level suppression have been increased to cover gray scale of display with small variation in average atomic number; bright points are actually smaller than shown and have saturated display and film. (b) Histogram of bright-ness readings on backscattered electron image of peaks represent gray levels that corres-pond to points on surface with same average atomic number, and which thus may belong to a single phase.

Backscattered Electron Images

Although there is little or no relief on the polished surfaces placed in the SEM for analysis, so that secondary electron images show no detail except for occasional pores, pits, or scratches, it is possible to obtain contrast in the backscattered electron image. We use a segmented annular backscattered electron detector (G&W Model 30) which in independent tests has shown the ability to resolve average atomic number differences for elements in the $Z = 10-40$ range of about 0.1 to 0.2 Daltons. The fraction of incident electrons which backscatter increases monotonically with atomic number, so differences in average atomic number between the phases makes them distinguishable.

Figure 2(a) shows a representative backscattered electron image of a multiphase ceramic containing 10% simulated radwaste (nonradioactive isotopes of the expected elements, in the expected composition). There is clear visual evidence for several phases. By measuring the image brightness at each point (in a 256×256-point array), we collect the histogram shown in Fig. 2(b). It shows the presence of several phases, which we can identify as at least five phases with subsequent x-ray microanalysis.

From the expected composition of the host phases, we would expect average atomic numbers as follows:

15.0	Zirconolite
13.6-14.6	Hollandite (depending on the barium-titanium ratio)
13.2	Perovskite

We have subsequently identified (by x-ray microanalysis) the small bright phase as heavy metals, chiefly the radwaste elements Mo and Rb, with an average atomic number of more than 40, and the darkest nonpore phase as alumina (resulting from inclusion of shattered grinding media), with a mean atomic number of 12.0. Note that the variation in the Hollandite allows it to cover the entire range between Perovskite and Zirconolite, and with the addition of even small amounts of heavy radwaste elements, to risk confusion with either.

EDX of Selected Grains

Using the backscattered electron image as a guide, we can position the electron beam stationary at the "center" of a region with a selected brightness (presumably a selected average atomic number) and perform an analysis using the energy dispersive spectrometer. This procedure may still cause penetration through to underlying phases of different compsotion, if the grain is thin (see our earlier paper on predicting the depth of analysis in this material),[2] but gives the best chance of getting a set of x-ray intensities characteristic of the selected phase by itself.

From many such points, with each one measured for 20 s at 15 kV, we can again plot the results in N-dimensional space to examine the clusters. The material has a grain size similar to that of Fig. 1(b). We have found that one particular brightness level (the light intermediate gray in Fig. 2) produces intensities that sorted themselves into two evident clusters, representing two different compositions, as shown in Fig. 3, in which it is evident that there are two phases, zirconolite and hollandite.

From the results, three main regions were identified in addition to the dark alumina and bright metal phases. These regions are shown in several two-dimensional projections in Figures 3(c) and (d). It is possible to distinguish the brightness levels of these phases in some cases, as shown in Fig. 4 (where a smaller area of the image was measured, with less variation in detection efficiency). It was also shown that the dark gray (not black) phase (perovskite) is the only phase that contains the radwaste element neodymium.

Conclusions

By combining the use of the backscattered electron image, to indicate phase boundaries, and rudimentary image analysis to find grain centers for beam positioning, one may obtain selected phases for compositional analysis by energy-dispersive x-ray measurement. This procedure is much more efficient than random-point analysis for measurement of minor phases. The variation in composition of phases, and the amounts of various minor elements in each, can be determined. In addition, measurements on the backscattered electron image can reveal the relative abundance (volume fraction) of the phases. This approach is an extremely efficient one for characterizing complex materials.
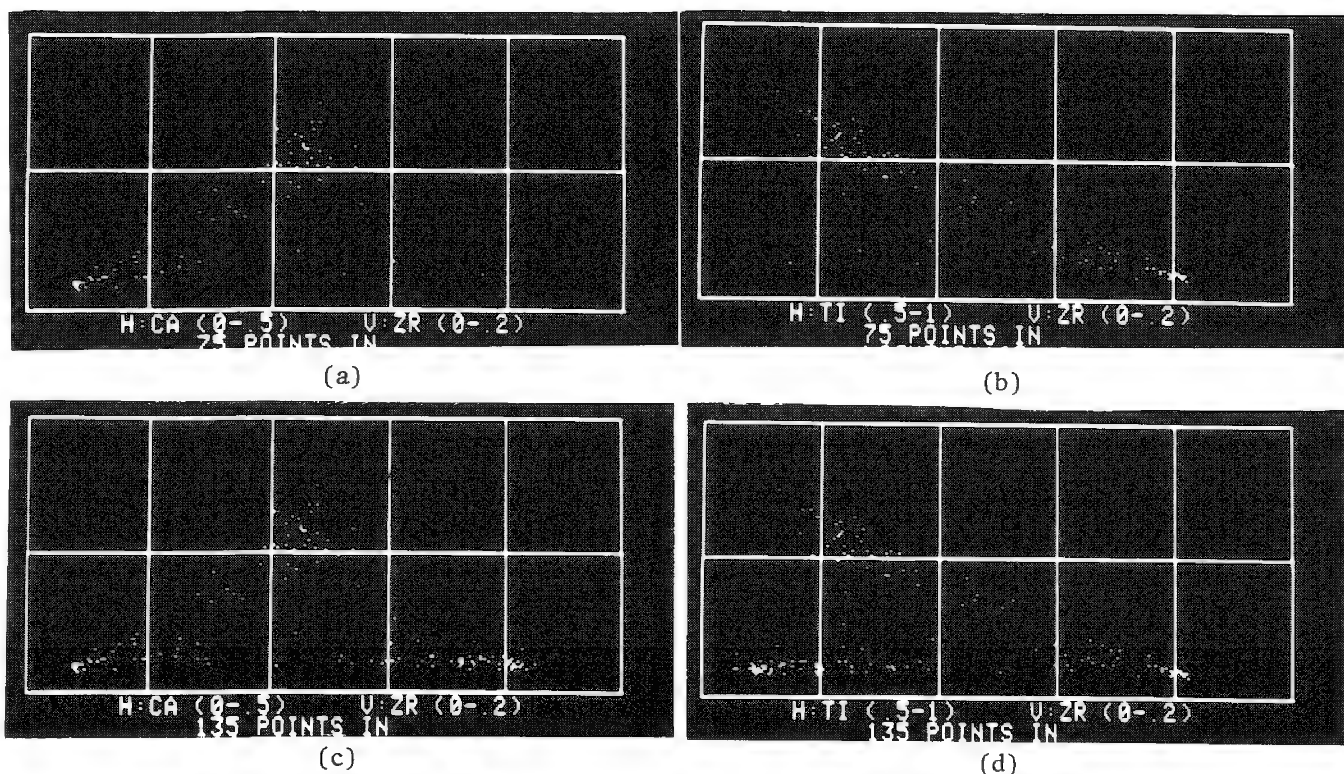
FIG. 3.--Normalized intensity plots from multipoint analysis using backscattered electron signal to select locations corresponding to chosen gray levels in Fig. 2(b). Points from light-gray region fall into two clusters, indicating two compositionally distinct phases with nearly equal average atomic numbers. (a) Ca vs Zr, light-gray area; (b) Zr vs Ti, light-gray area; (c) Ca vs Zr, light- and intermediate-gray areas; (d) Zr vs Ti, light- and intermediate-gray areas.
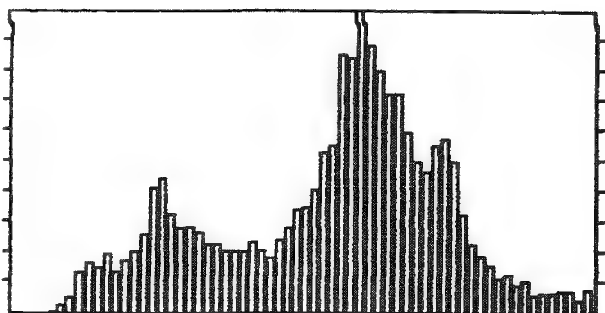
FIG. 4.--Brightness histogram showing two partially resolved peaks in light-gray area on Fig. 2(b), obtained by scanning over reduced area.

References

1. J. C. Russ and T. M. Hare, "Characterization of heterogeneous Polycrystalline materials," *Microbeam Analysis--1981*, 186-189.
2. J. C. Russ, T. M. Hare and A. G. Solomah, "Selective x-ray analysis of individual fine grans for phase identification in SEM," *Canadian J. Spectroscopy* 25: 64-69, 1980.

PROBLEMS ASSOCIATED WITH COMPUTERIZED ANALYSIS OF A LARGE NUMBER OF SMALL PARTICLES

John Gavrilovic and D. A. Brooks

Automated analyses of small particles have been a reality for the past decade. An automated electron microprobe for routine analyses was developed at McCrone Associates as early as 1967.[1] Today, most analytical work is performed by means of the new generation of computer-controlled electron microprobes. Although automated analyses are occasionally performed by scanning electron microscopes and even ion microprobes or ion microscopes, the electron microprobe provides the highest speed with the widest range of elements and best precision.

Our experience with the automated analysis of over 18 000 small particles[2] has revealed three major sources of errors: analytical instrumentation, and x-ray-related and sample-related problems. In this short review we shall summarize and discuss real (experienced) as well as other potential sources of errors.

Analytical Instrumentation Related Problems

In the above mentioned analyses, the instrumentation used was a 1965 ARL EMX electron microprobe equipped with three wavelength-dispersive (WDS) and one ORTEC energy-dispersive spectrometer. The WDS spectrometers were driven by ac motors, which were in turn computer controlled through a set of potentiometers that yielded a resetting precision to within 0.03% of the spectrometer range (Fig. 1).

FIG. 1.--Block diagram of computerized electron microprobe. (Analysis options illustrated.)

Spatial resolution (or size of the electron beam). At a 25nA sample current and a 20kV accelerating potential the average size of the electron beam was 2 μm, which immediately restricted analyses to particles above 2 μm. The high-voltage power supply was probably the least reliable component, which added to spatial resolution degradation.

Stability of sample stage and/or electron beam. In view of the spatial resolution limit of 2 μm, the positioning of the stage and its stability did not present special problems. However, the positioning of the electron beam and its stability were inadequate even for 2μm particles. The main sources of instability were thermal and electrical changes due to contamination build-up within the electron column.

Resetting precision and/or drift of x-ray spectrometers. Fully focusing x-ray spectrometers available on the ARL microprobe were very delicate; thus, our continuous use required realignment once or twice weekly to obtain desired crystal positioning and the respective x-ray intensities required by program parameters.

The authors are at Walter C. McCrone Associates, Inc., 2820 South Michigan Avenue, Chicago, IL 60616.
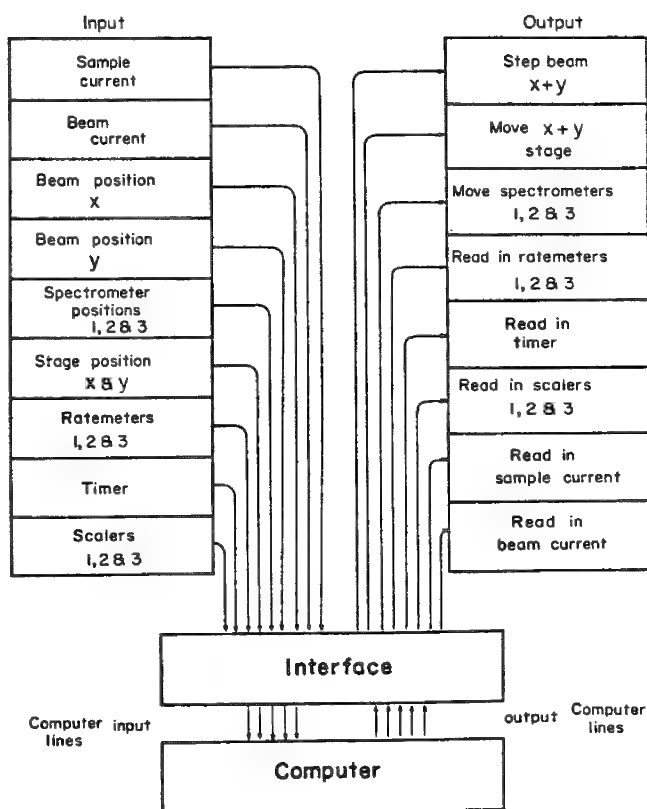
Filament life. Filament life in automated operations was critical. Filament evaporation and the resulting oversaturation caused numerous breakdowns during continuous or long-term runs (24 hr). The possibility of using an undersaturated filament might be more desirable; however, operation under these conditions did not insure adequate stability.

X-ray Related Problems

X-ray related problems were perhaps the largest source of problems in routine automated analysis of small particles.

Optimum excitation voltage. For routine automated analysis an optimum excitation voltage is almost impossible to obtain if elements differing widely in atomic number are to be quantitatively analyzed.

Overlapping of x-ray lines. The presence of higher-order x-ray lines was a major problem when considering the large number of elements (in one case, 27) to be analyzed. This problem was, in fact, compounded as many particles contained several high-atomic-number elements that yield several x-ray lines of short wavelengths.

Counting time. For programming considerations the counting time during our analysis was fixed at 10 s per particle/element. The use of a fixed count collection is statistically preferable but often leads to unacceptably long analysis times.

X-ray absorption vs particle size. The size of the particles being analyzed affects the precision of the analytical results in two ways:

(1) smaller particles have usually low count rates which are inadequate for statistically valid information; and

(2) absorption effects are significantly different for light and heavy elements within small particles in comparison with infinitely large samples.

Sample-related Problems

Dispersion of particles. Sample preparation and sample mounting were initially critical in our automated analyses. The critical part was in achieving a good dispersion of the particles on the sample mount to eliminate overlapping or interference from one particle to the next. During our analyses we encountered some problems as even micrometer-sized particles were found to be frequently agglomerates of submicrometer particles.

Mounting of particles. Groups of particles from the samples to be analyzed were mounted on the electron microprobe mount with diluted collodion solution. An occasional segregation of the small particles toward the periphery of the sample droplets occurred during drying and biased the results. To eliminate the particles drifting in the solution of collodion and amyl acetate extremely small droplets of solution were used.

Data Presentation

A distinct advantage with computerized operations is the extreme flexibility available in data presentation.[3] Once the computer collects sufficient data (complete records of size and chemical composition) for all the small particles analyzed, presentation of such data is left to the imagination of the programmer. In our particular case, once the data collection for each sample had been completed the following output data for each sample were generated.

- a size distribution of particles (Table 1)
- the total number of elements (frequency) (Table 2)
- the concentration vs frequency (Table 3)
- a size composition comparison frequency relationship (Table 4)

Conclusion

Improvements in analytical instrumentation, computer hardware, and the respective software have resulted in more routine automated particle analyses. However, such analyses are not routine and seldom truly automatic. The close cooperation and experience of the electron microprobe operator and the computer analyst in small particle analyses may make the difference between computer-generated data without real value and fully comprehensive characterizations of small-particle samples. Examples of typical computer generated data summaries are given in Tables 1 through 4.

TABLE 1.--Particle size distribution. (Sample A-1; total number of particles analyzed, 1211.)

SIZE RANGE (UM)	NUMBER OF PARTICLES	PERCENT WITHIN RANGE
0.0 - 1.0	195	16.10
>1.0 - 2.0	528	43.60
>2.0 - 3.0	293	24.19
>3.0 - 4.0	99	8.18
>4.0 - 5.0	36	2.97
>5.0 - 6.0	21	1.73
>6.0 - 7.0	20	1.65
>7.0 - 8.0	10	0.83
>8.0	9	0.74

TABLE 2.--Number of particles with major elements. (Sample A-1; total number of particles analyzed, 1211.)

ELEMENTS	NUMBER	ELEMENTS	NUMBER
S	1066	HG	23
PB	659	TL	13
ZN	626	K	12
CU	615	AL	7
O	608	F	4
FE	492	I	3
AS	187	SE	3
MG	168	TE	0
NA	159	TI	0
SI	123	V	0
CA	76	CR	0
CD	48	BR	0
SB	23		

TABLE 4.--Average particle size for particles with major elements. (Sample A-4; total number of particals analyzed, 446.)

ELEMENTS	AVERAGE SIZE	FREQUENCY OF OCCURENCE
AL	3.08	7
CA	2.90	10
AS	2.74	72
FE	2.58	248
PB	2.58	37
ZN	2.50	24
O	2.32	119
CU	2.21	323
S	2.18	316
SI	1.83	121
K	1.62	5
F	1.59	4
I	1.29	3
SB	0.00	0
TE	0.00	0
TI	0.00	0
V	0.00	0
CR	0.00	0
SE	0.00	0
BR	0.00	0
HG	0.00	0
TL	0.00	0
CD	0.00	0
NA	0.00	0
MG	0.00	0

References

1. M. Bayard, "A computer operated microprobe," *Microbeam Analysis--1969*, 25.
2. *Chemical and Physical Characterization of Smelter Dusts*, W. C. McCrone Associates, Inc. NIOSH contract 210-76-0119.
3. C. H. Bowen and D. A. Brooks, "Use of automation in laboratory instrumentation," in W. C. McCrone, Ed., *Particle Atlas*, Ann Arbor Science Publishers, 1980, 6: 1952-1660.

TABLE 3.--Summary of particles with various elements. (Sample A-1; total number of particles analyzed, 1211.)

ELEMENTS	NO.	ELEMENTS	NO.	ELEMENTS	NO.	ELEMENTS	NO.
NO OF PARTICLES CONTAINING ELEMENTS BETWEEN 75% AND 100%							
K	0	V	0	SE	0	S	8
TI	0	AS	14	TL	0	NA	0
ZN	0	HG	0	F	0	I	0
SI	0	O	80	TE	0	CU	14
CD	0	CA	0	FE	19	AL	0
SB	0	CR	0	BR	0	PB	0
MG	0						
NO OF PARTICLES CONTAINING ELEMENTS BETWEEN 50% AND 75%							
K	0	V	0	SE	0	S	39
TI	0	AS	29	TL	0	NA	6
ZN	4	HG	0	F	0	I	0
SI	0	O	27	TE	0	CU	75
CD	0	CA	5	FE	76	AL	2
SB	0	CR	0	BR	0	PB	1
MG	0						
NO OF PARTICLES CONTAINING ELEMENTS BETWEEN 30% AND 50%							
K	2	V	0	SE	0	S	236
TI	0	AS	14	TL	0	NA	19
ZN	10	HG	0	F	0	I	1
SI	3	O	259	TE	0	CU	84
CD	0	CA	14	FE	88	AL	1
SB	0	CR	0	BR	0	PB	24
MG	1						
NO OF PARTICLES CONTAINING ELEMENTS BETWEEN 10% AND 30%							
K	1	V	0	SE	0	S	683
TI	0	AS	48	TL	0	NA	23
ZN	428	HG	1	F	3	I	1
SI	44	O	216	TE	0	CU	152
CD	1	CA	51	FE	148	AL	3
SB	0	CR	0	BR	0	PB	404
MG	108						
NO OF PARTICLES CONTAINING ELEMENTS BETWEEN 5% AND 10%							
K	9	V	0	SE	3	S	100
TI	0	AS	82	TL	13	NA	111
ZN	104	HG	22	F	1	I	1
SI	76	O	26	TE	0	CU	290
CD	47	CA	6	FE	161	AL	1
SB	23	CR	0	BR	0	PB	230
MG	59						

CONTROLLING A SCANNING ELECTRON MICROSCOPE WITH A DEDICATED MICROCOMPUTER

E. M. Gregory, T. M. Hare and John C. Russ

Most scanning electron microscopes, and certainly ours which is a vintage JSM-2, are designed for direct human control of knobs and switches. The specimen stage is mechanical, with back- and side-lash that operators learn to compensate for, but which are not readily motorized or "joystick" controlled. Also, the beam scan (and corresponding scan on the display CRTs) is produced by analog circuitry suitable, in terms of reproducibility and linearity, for the purpose of viewing and photographic recording of images, but inadequate for high-precision image measurement or automated x-ray microanalysis.

However, faced with the need for a more automated microscope with which to conduct some badly needed research but no funds for a new SEM, we have managed to provide all these capabilities and more. The heart of the control system is an Apple II computer, with 65K memory, dual floppy-disk drives, a graphic display screen, and a high-speed dot matrix printer that can dump graphic images as well as letters and numbers. Connecting the computer to the SEM has been accomplished with essentially standard, off-the-self interface cards (Fig. 1) and a small amount of improvisation, plus programming to exercise the needed control, and in some cases circumvent the peculiarities of the microscope (which was never intended for this fate). JEOL has been extremely cooperative in providing the necessary schematic drawings and advice on how to accomplish the desired interfacing.
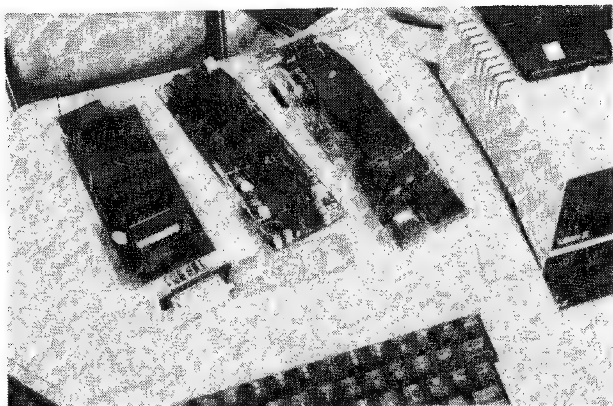

FIG. 1.--Several of the interface cards used with Apple computer: left to right, stepping motor controller and pulse counter, multichannel ADC and DAC, system clock.
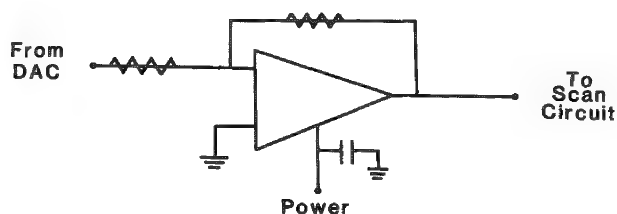

FIG. 2.--Operational amplifier circuit to tailor voltage range of DAC output to scan circuit requirements.

Beam Control

The voltage required for the final-stage amplifier in the scan generator (which

The authors are at the Engineering Research Division of North Carolina State University, Box 5995, Raleigh, NC 27650.

drives both the beam on the sample and in the display CRTs) is ±2 V in the JSM-2. Other microscopes may require other voltages, but generally of the same order of magnitude. By switching in an externally generated voltage in place of the built in generator it is possible to position the beam anywhere in its normal scan area, with an indication of its position with respect to the normal image. The switching is accomplished in our case by a relay mounted inside the SEM cabinet. The 12V relay coil is powered by the computer, so that when the computer is disconnected, normal operation is assured. An operator switch also permits normal scan functions to resume whenever desired.

When the relay is engaged, the scan voltages come from an external connector, which is supplied by a digital-to-analog (DAC) interface card within the computer. This card contains 16 individually addressable DACs, each of which produces a voltage in the range ± 5 V in 256 steps (an 8-bit DAC). A simple circuit (Fig. 2) consisting of an operational amplifier and suitable biasing resistors is mounted on the card to allow us to trim the output voltage to the required range for the SEM. One of the DACs is connected to the X-scan coil and one to the Y-scan coil. One is also available for modulation of the display brightness, to produce photographable displays, and the remainder are spare at this time. (They could in principle be used to control other functions such as lens focus, beam blanking, electron spectrometers and so forth.) Figure 3 shows the complete interconnection diagram.
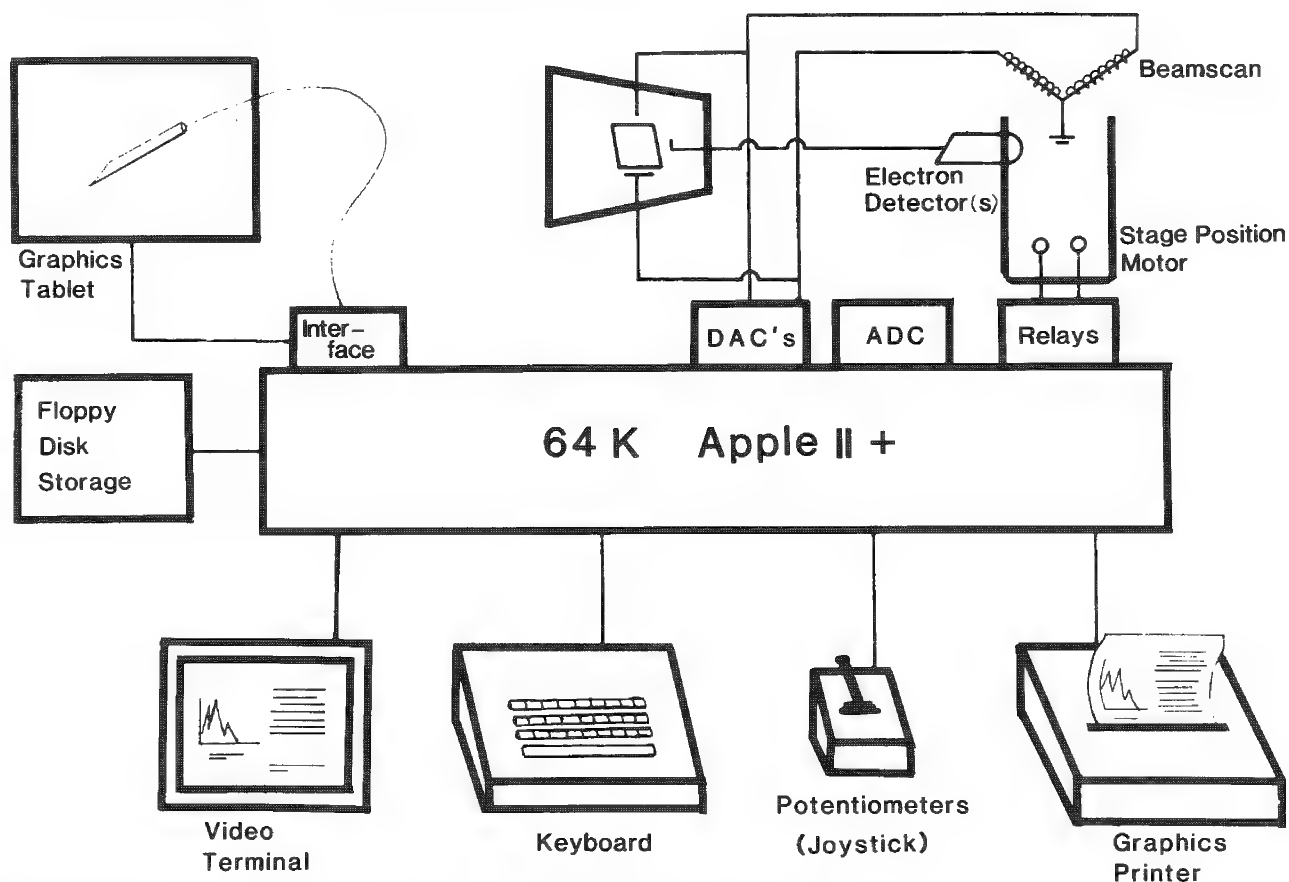
FIG.3.--Block diagram of SEM microcomputer control system.

An array of 256 × 256 points is significantly poorer image resolution than the capability of the display CRT, which approaches 1000 × 1000. Consequently, this external scan generator is not used for routine beam scans or photographic recording of images. As described in an accompanying paper, it does combine well with our image acquisition and measurement capability, and indeed the ADCs (analog-to-digital converters) used for signal measurement are physically located on the same card. Higher-resolution 10,

12, 14, and 16-bit DAC cards are available to offer higher resolution in beam position whenever needed by a specific application. (A 12-bit DAC produces voltages over its output range in 4096 steps, so two would permit positioning the beam anywhere in a 4096 × 4096 array of points.)

To the computer, each of the 16 DAC outputs (and each of the 16 inputs) on the card appears as a memory location within its addressable memory space. To cause the DAC to produce a voltage it is simply necessary to write a number from 0 to 255 at the corresponding address. This value is latched (held) until it is changed or until the computer is switched off. The particular DACs used can provide a total current of 20 mA, and can change their output voltage at the rate of 10 V/ms. Again, higher speed or higher current (up to 150 mA and 3μs settling times) capabilities are commercially available as plug-in cards. In the same way, the ADCs on the card can be read as if they were memory locations, they measure voltages in the same 10V range, and can digitize a value in 70 μs. (Faster times and other voltage ranges are available from several suppliers.)

The card used, and indeed all the various interface cards we have in the computer, are fully compatible with the operating system and with Basic and assembly language programming (as well as other languages). Writing programs to control the beam position has proved to be well within the capabilities of everyone who uses the SEM, ranging from faculty to undergraduates, when special routines are needed for specific applications. A collection of well-tested general purpose routines already exists and can be called from disk for most routine jobs.

Purposes of Beam Control

One purpose of the external beam control capability is to advance the beam slowly stepwise and acquire images for measurement. This process requires, as for several other applications, a time base to control the steps. Normally this time base is provided by a software loop within the program, which uses the system clock and depends on the consistency of time required to execute the same set of instructions over and over. When needed, the time can also be controlled in a number of other ways, including a logic signal trigger from an external source or an interrupt from a crystal-controlled clock, also plugged into the computer. Asynchronous control, based on the acquisition of x-ray data, for instance, is discussed below.

Another technique we have developed and applied to a variety of applications problems dealing with the characterization of heterogeneous materials is automatic collection of x-ray analysis data for a preselected list of elements from a large random number of locations on the sample.[1] Actually, one normally does that by positioning the beam on points in a 16 × 16 matrix covering the entire image area, and counting at each point for a preset time. It is immediately clear that this is hardly a "random" pattern. However, the distance between points is large (controlled by the magnification of the image, which is manually set by the user) compared to the size of the individual grains in the material, which are presumed to define the scale of the inhomogeneities. Hence, it is the microstructure that is assumed to be "random" and the points can indeed be placed in a regular array. Another paper in these proceedings discusses the interpretation of the data collected by this technique.

Another mode of collection of x-ray spectra uses not a random array of points, but a series of preselected ones. This list may come from the computer itself, for instance by finding of the centroids of features (a phase in a solid or a particle on a substrate) by measurement of an image acquired by step scanning a raster. It is also useful sometimes to scan a rather coarse raster over the sample and stop to take data only on points for which the backscattered electron signal, for instance, is within a previously specified range. This method can be used to analyze a larger number of grains of one phase in a multiphase material, for example, if the average atomic number varies between the phases and consequently affects the backscattered electron signal. Similar schemes using transmitted electrons or specimen current can be readily envisaged.

It is also possible to acquire a series of elemental intensities along a line scan across the sample. In this mode of operation, the beam stays at each of the 256 positions

along the line for a present time, typically 1 s, while x-ray pulses are processed by another, specialized interface card that digitizes energy-dispersive x-ray pulses. Counting all the pulses in a range corresponding to particular elements of interst, one can easily build up so-called "digital line scans" showing the distribution of elemental intensity along the line. Since that is done for several elements at once, facilities are then provided to display the data in the form of any entered combination of the various and individual elemental intensities,[2] as shown in Fig. 2.

By controlling the beam scan from the computer, one can dwell on each point for an equal amount of live time in the analysis, so that there is no adverse effect of gross changes in counting rate nor any need to introduce individual dead time corrections for each point, which can be distorted by poor counting statistics. Multi-element line scans acquired in this way are very powerful tools for the qualitative study of elemental distributions in samples. Multiple line scans, forming a raster scan pattern, can be combined when the importance of the sample justifies the long collection times to produce a two-dimensional image. This image for each of the various elements, or for any combination of them as before, can be displayed on the SEM CRT via one of the DAC outputs as mentioned before, to produce a gray-scale image for photographic recording.

Finally, it is possible to position the beam for microanalysis according to points specified by the user, with reference to the normal SEM image, by positioning the beam (and corresponding point on the display CRT) with a joystick (two potentiometers which can be read by the computer, mounted orthogonally on a suitable mechanism). Switching back and forth between the normal scan generator (and image) and the DAC position (and cursor), the user can find the points of interest. Pushing a button instructs the computer to record the coordinates in a list that can later be used for automated quantitative analysis.

A quite different application of electron beam control, with which we have as yet very little experience, and which may require higher precision DACs, is electron beam lithography. Moving the beam along a complex pattern entered either from the keyboard, or using a graphics tablet to trace a line drawing of the pattern to be exposed, is a useful way to produce uniformly exposed, precise lines. This capability is of great interest to researchers dealing with microelectronics and integrated-circuit design, especially in small experimental facilities (such as most universities) where dedicated specialized electron-beam instruments are not available for this purpose.

Other Control Operations

In addition to the electron-beam position, the most useful controls on the SEM for the computer to control are probably the stage position adjustments. These adjustments are mechanical rather than electrical and so call for a different control strategy. We have been using similar computers to control stepping motors that drive x-ray spectrometers (both fluorescence and diffraction), and it seemed logical to adapt this method for the microscope stage as well. Unfortunately, the mechanical reproducibility of the stage is not adequate for this task, as the same position of the various control knobs does not reproduce the same position consistently. The problem is more complex than simple backlash, which could be solved by always approaching the point from the same direction, and involves an interaction of the various movement axes to which we refer as "sidelash." Newer stages may overcome these problems, but this seems not to be a viable solution for our vintage instrument.

Still, even if it is not possible to reproduce the stage position well enough, let us say, to carry out automated x-ray microanalysis over an area of the sample larger than can be reached with the beam scan, or to re-analyze standard samples mounted adjacent to the unknowns from time to time, or even to bring under the beam a Faraday cup to measure beam current and compensate for drift (all things that are quite useful, and routine in many automated microprobes), there are other possible purposes for motorizing the stage. One is simply to be able to step to some new, quasi-random location to continue making measurements of x-ray elemental intensities in the process of sampling many points on a heterogeneous specimen. Another is to process many fields, not necessarily adjacent, in obtaining images to measure particle size distributions. For these purposes, it is necessary to move the stage by some small but not precisely controlled amount.

This control can be achieved far more simply and economically than with a stepping motor. A low-voltage dc motor coupled to the control shafts with O rings (expensive rubber bands) can drive the stage, and the computer can turn them on or off and control direction with simple relays. A single card interface to throw up to 16 solid-state double-pole, double-throw "relays" is available for our microcomputer and is ideally suited to this purpose. The distance of the motion can be controlled simply (and approximately) by the time the motor is powered. We may never know where we have been, but it is a simple matter to assure that we stay within the confines of the sample, and the sampling is certainly "random."

We have not yet tried to interface other SEM control functions with the computer, such as the camera, lens controls, or beam alignment. These have been manual operations for so long that all our operators feel comfortable with them as they are. However, for some other instruments and laboratories that might not be the case. Certainly it seems quite easy and astonishingly inexpensive to interface electrical and mechanical controls, and to read back various image or other signals, into a standard microcomputer. Programs to acquire data or exert control are easy to create in Basic, and where particular control subroutines must be written in machine language for speed, they can be created once and for all as part of a master library of functions, called by name. This procedure makes it easier for each operator to program his/her own experiment. Our experience is that by adding these capabilities to our SEM we have prolonged its useful life many years beyond the expected term, and in some respects have made it easier to use and more flexible than some newer and more costly machines.

References

1. J. C. Russ and T. M. Hare, "Characterization of heterogeneous polycrystalline materials," *Microbeam Analysis--1981*, 186-189.

2. J. C. Russ, "New methods to obtain and present SEM x-ray line scans," *Microbeam Analysis--1979*, 292.

IMAGE ACQUISITION FOR FEATURE DETECTION WITH GRAPHICS TABLET AND VIDEO OUTPUT

John C. Russ and Michael Huns

In many fields of application, the identification of features in images and their measurement has become equal in importance (and more demanding the time required) than simply obtaining them. Our concern for the moment is with images created in the electron microscope, and particularly the scanning electron microscope. This is already a raster-scanned image in most cases, which lends itself readily to the kind of processing to be described. However, the same kinds of measurement algorithms (which are described in detail in an accompanying paper) are applicable to images from other sources, such as light microscopes to which an ordinary TV camera has been attached, and to photographs at any magnification viewed by a video camera. This list naturally includes aerial and space photos as well, so we must always remember that except for changes in the image scale from micrometers to furlongs, the determination of the size of pores or inclusions is no different from that of the acreage devoted to certain crops.

Of fundamental importance in measuring any feature is the ability to distinguish it from the surroundings. In the "normal" SEM image, formed with secondary electrons emitted from the surface and collected by a positive voltage applied to a scintillator, the contrast (change in brightness from place to place) depends largely on surface inclination, and to lesser degrees on surface composition (including very thin layers of contamination), fine-scale roughness, and orientation relative to the detector. The ability of the eye/mind combination to recognize features in such images depends on much more than brightness, and consequently the delineation of boundaries must usually be performed by a human, rather than automatically. This process requires another kind of input device, called a graphics tablet or digitizer pad, which allows the user to mark the perimeter of features with a stylus and transmits the coordinates of the points to the microcomputer. Normally one does that by placing photographs onto the tablet surface, but it is also possible to superimpose the image of the tablet surface and the user's stylus directly onto the video image from the microscope, so that he can "draw" electronically right on the image without photographic recording. The appearance of this mode of entry is shown in Fig. 1.

In the graphics tablet, one locates the tip of a hand-held stylus (some are shaped much like ball point pens, others have crosshairs and magnifiers) above its surface. The body of the tablet has embedded in it a mesh of wires that carry a radio-frequency electromagnetic field. This field is picked up by the sylus, and from the time delay it is possible to locate the tip to within about 0.005 in. (better than the ability of the hand to reproduce in most circumstances). The coordinates of the tip, and whether or not the user is pressing it down (which closes a microswitch contact in the sylus) are presented to the computer by the interface card at a very high rate of speed, about 4000 times per second. Figure 2 shows the interface card.

The processing software reads these values and compares them to the last recorded ones, so that new data are in fact added to the list of points only when the operator moves the stylus. It is practically impossible to move the sylus fast enough to miss any points, and consequently the outline of features is represented by a many-sided polygon with each side about 0.01 in. long. As the line segments are recorded in memory, they are also drawn (at reduced resolution) on the computer's graphics display screen as a record of where the stylus

Author Russ is at the Engineering Research Division of North Carolina State University, Box 5995, Raleigh, NC 27650; and author Huns, at Optomax Inc., 9 Ash Street, Hollis, NH 03049.
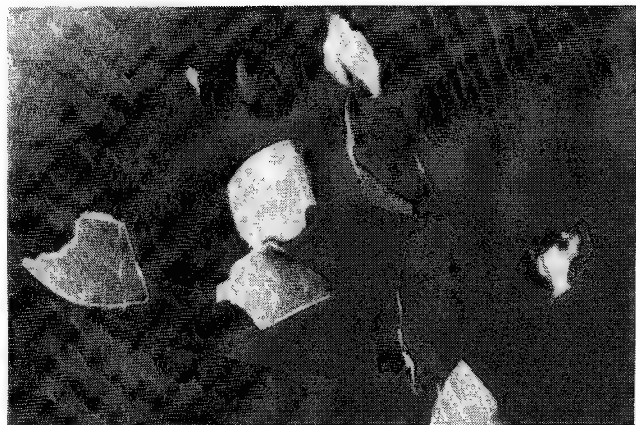
FIG. 1.--Video image of particles in SEM. Contrast is nonuniform on different faces, either brighter or darker than background. Manual outlining with graphics tablet is required.
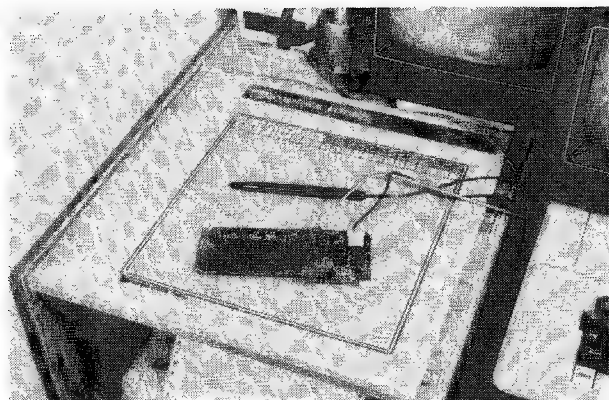

FIG. 2.--Graphics tablet and interface card.

has been. For the 11 × 11in. tablet area we use (even larger pads are available), a "resolution" of 2200 × 2200 points is implied, far higher than the 256 × 256 array of points measured by the video image processor to be described below. However, since the only data that enter the computer are the actual perimeter points, the total amount of data to be handled is much smaller for the graphics tablet than for a video image.

With the graphics tablet, the data as entered into the computer memory are already organized on a feature-by-feature basis so that the various kinds of measurements can be readily performed. However, as each feature must be recognized and outlined by the operator, the time required to build up a database of several thousand particles, for instance, can take many hours of rather tedious hand work from photographs. The danger of subconsciously selecting only certain features, and missing others, or in other ways biasing the data, is always present with this method.

The direct entry of raster-scan images is in principle a much faster and more efficient way to collect large amounts of data. The requirement is that the computer be programmed to recognize features or boundaries, usually based on their brightness compared to the remainder of the image. Backscattered electron images from flat polished surface often show this type of contrast for either grain boundaries (due to polishing or etching relief) or discrete phases (inclusions or voids) in the material. The principal component of this contrast is differences in average atomic number, which changes the fraction of electrons that backscatter and are detected.

Another type of sample often encountered is particles dispersed on a substrate. Using an annular backscattered electron detector with high solid angle, we find that these samples also give useful backscattered electron images. Part of the contrast is still based on atomic number, since the substrate can often be chosen with either a lower or higher atomic number than the particles. In addition, the increase in backscattering around the edges of the particles, where the beam strikes them at grazing incidence, produces a bright outline. It is possible with suitable software to fill in holes in such images to obtain the complete particle projected area.

With raster scan images, it is the brightness at each point that is measured, and some suitable method, usually implemented in software rather than hardware, must be employed to detect the features or boundaries of interest. Usually one simply accomplishes this goal by setting two brightness cutoff levels, using potentiometers whose values can be read by the computer. Any picture point whose brightness lies within the two levels is considered to be in the feature or boundary. It may later be wise to reject isolated pixels from this image, as being due to noise, or to undergo other steps of image post-processing or modification.

The absolute brightness measurement method suffers from problems if there is an overall gradual shading from side to side or center to edge in the original image. That can happen all too easily with a light microscope, due to uneven illumination or uneven

sensitivity in the video camera used. In the SEM, we have not found this to be a problem, but when it does arise one solution is to measure first the brightness from a uniform sample (a gray card in the light microscope, a uniform flat surface in the electron microscope). The observed variation can then be subtracted to find the actual variation in real images. Another method is to use the derivative of brightness as a function of position, either along a single direction (the scan line) or in two directions (by temporarily storing several scan lines for comparison). Either method of compensation slows down the data acquisition rate.

Most raster scan images are acquired at conventional TV rates. Figure 3 shows a simple interface card which digitizes a conventional black-and-white video signal and provides to the host computer a 6 bit (0-63) brightness value for any pixel in a 256 × 256 array on the image. This method functions by triggering on the TV sync pulses to find the start of the image and start of each line, and then using an analog-to-digital converter to read the voltage that corresponds to the desired point. The video signals from SEMs that use a standard TV rate scan are directly compatible with this interface. It is capable of digitizing an entire image in under 4 s, but if the processor is simultaneously making some brightness comparisons to detect features, and measuring lengths of chords through the features, the total acquisition time is over 10 s.

Much slower scans are possible with some systems. Figure 4 shows an interface card for the same microcomputer that has 16 analog-to-digital (ADC) and 16 digital-to-analog (DAC) circuits, each addressable by the computer. The DAC outputs generate voltages in the 0-10 or ±5 volt range, in 256 steps. Two can be connected to the scan amplifiers of the SEM, to position the electron beam directly in X and Y. Then the backscattered electron signal (or any other image signal) can be connected to the ADC input and digitized, which yields an 8 bit (0-255) value. The time required to position the beam and read the signal is about 50 μs with this particular card; other, similar ones can be used with times as short as 10 μs.
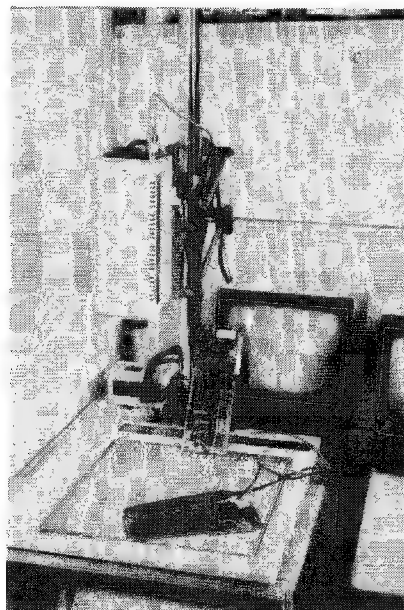

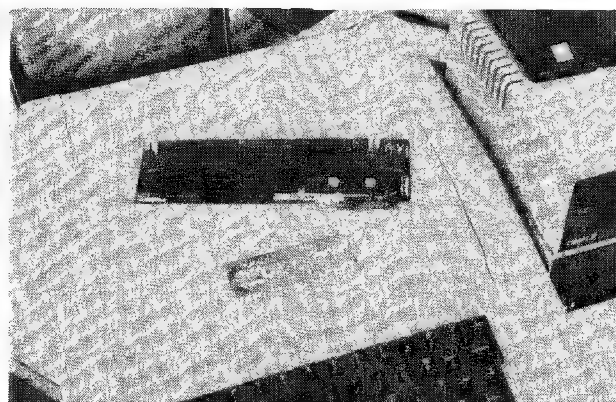FIG. 3.--Video camera input and interface card (also used with video signals from SEM).

FIG. 4.--DAC/ADC card used for slow raster scan of SEM and digitization of backscattered electron and other image signals.

With this interface, the computer can direct the beam to scan a raster, or in principle any other pattern, to input an image. Since the array size is the same 256 × 256 as for the video interface, the same data processing software can be used. There are DACs with 10 (1024 × 1024), 12 (4096 × 4096) and more bits of precision, but they offfter no advantage in this application since the images become too large (too many data points) for the comparatively small computer being used (a 64K Apple II+). Figure 5 shows a typical digitized image and an enlarged section in which the finite pixel size is apparent. Similarly, more resolution in the input ADC is unnecessary for reading image brightness; in fact we often take multiple readings at each location for averaging purposes to reduce image noise.

Figure 3 on p. 500 is diagram of a fully configured system. The host computer is interfaced to a graphics tablet, to a video digitizer, and to a DAC/ADC card as have been described. In addiition, it supports dual floppy-disk drives, a high-speed dot-matrix
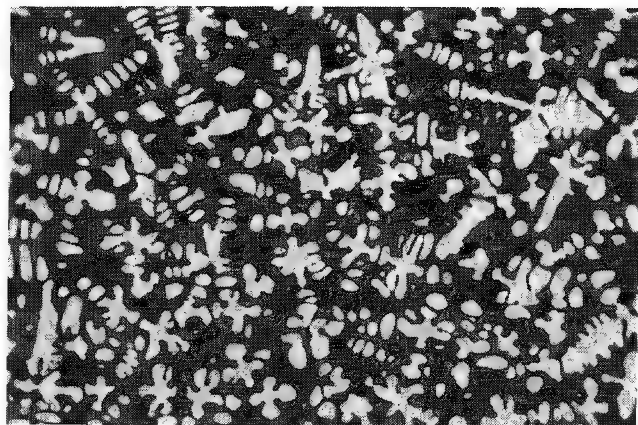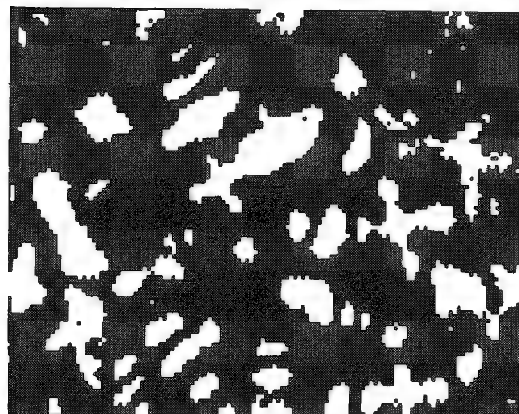
FIG. 5.--Typical gray-scale image and derived 256 × 256-pixel digitized image corresponding to a chosen range of brightness values, with expanded portion showing finite pixel resolution.

printer with graphics capabilities, and an multichannel analyzer card with which it can measure x-ray pulses from a Si(Li) detector. This scheme is used with the beam control capability for automated point analysis. The signal inputs to the ADC card include secondary and backscattered electrons, transmitted electrons, and specimen current. The computer, under program control, can select which of these to use, or even combine them if appropriate.

Although complex software is required to identify and separately measure features in a raster-scanned image, not all stereometric measurements require such feature-specific data. For instance, the grain size of a metal can be determined from the mean intercept length, which is simply the average chort length in a raster scan image where the grains are detected and the boundaries eliminated. Many such image-related rather than feature-related parameters are available.

In addition, instead of using the brightness of each pixel for comparison to present cutoff levels, to discriminate the features of interest, it is also possible to record a brightness histograph of the entire image. The X-Y location of the points is lost, but the histogram shows the variation in brightness (or density, depending on the signal) for the image as a whole. This histogram is sometimes useful in determining where to set the cutoff levels for subsequent discrimination. However, its principal use is in cases where multiple phases are present and each has a different brightness (for instance due to a different average atomic number in each phase producing a variation in electron backscattering). Then the histogram shows discrete peaks for each phase, and from the number of counts in each peak, the relative area of each phase and from the volume fraction can be obtained directly.

Figure 6 illustrates this feature for a multiphase ceramic. The different brightness levels in the backscattered electron image correspond to the peaks in the brightness histogram, and the areas of each peak are read from the display by setting cursors to bracket the peak of interest. The same method would be used with transmission images (light or electron microscope) to measure density. The system then functions as a scanning densitometer.

A related technique, useful for integrated circuits and similar specimens, is to measure the brightness in the SEM image, which could be secondary or backscattered

507

electrons, but in this case is more often electron-beam-induced conductivity, and to plot an isometric view or contour map of brightness (signal strength) as a function of position. These displays (Fig. 7) are extremely useful to convey spatial information on the variation of signal strength, and offer a valuable complement to the normal SEM image capabilities.
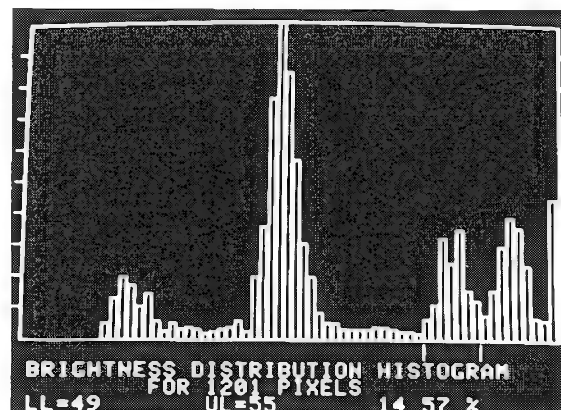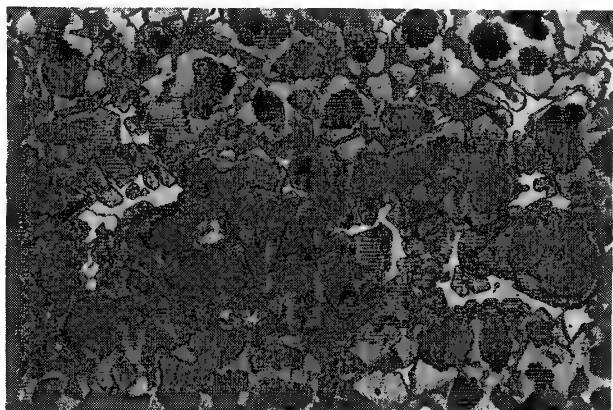

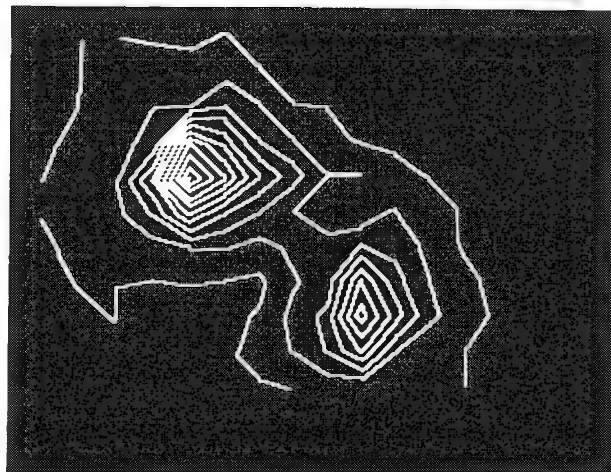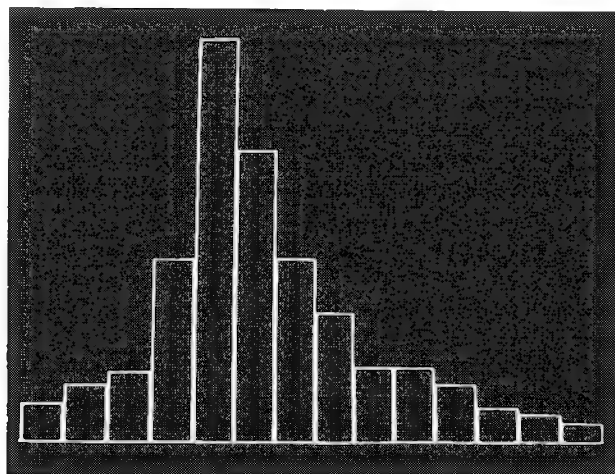FIG. 7.--Brightness histogram of backscattered electron image from multiphase sample. Area in each peak corresponds to volume fraction of phase.
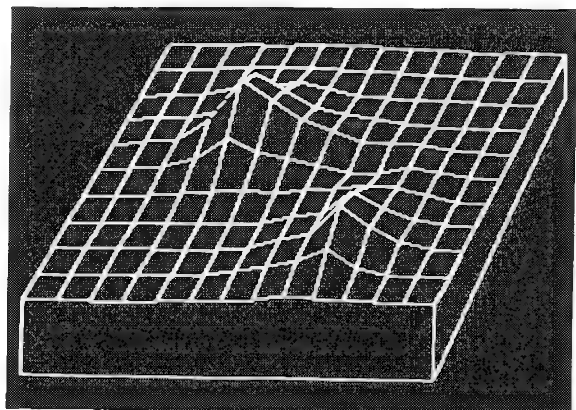

FIG. 7.--Isometric, histogram, and contour map displays of image brightness on small area (11 × 14 points) of image.

IMAGE MEASURING ALGORITHMS FOR A SMALL COMPUTER

T. M. Hare, John C. Russ, and J. Christian Russ

Graphics Tablet Input

Discrimination of features from background, and the measurement of their size, shape and other parameters, is fundamentally different when the image is obtained in a raster-scan or "video" format as compared to human input from a graphics tablet or other similar device. The latter, which in a typical situation would be a surface on which a photograph could be placed, and which reports the X-Y coordinates of a hand-held cursor or stylus to the computer, is in all respects much simpler to use.

In the first instance, the graphics tablet or digitizer pad reports the coordinates, but it is the human, using a very powerful "built-in" image-processing computer, who recognizes the edges of the feature of interest and preserves the connectivity of the perimeter around whatever protrusions or invaginations may be present. This capacity is by no means trivial for pictures such as typical SEM secondary electron images, in which the gray-scale variation may be inconsistent from place to place and can be severely interfered with by statistical noise in the image (especially at fast-scan or TV rates). Furthermore, the data that are stored in the computer for processing are a "string of beads" that outline the perimeter of one feature at a time, without confusion from other nearby features (even those that touch or nearly touch, so long as the human can separate them). Typical graphics tablets such as the one shown in Fig. 1 have spatial resolution of about 0.005 in., so that the several hundred or thousand points along each perimeter are separated by only about 0.01 in., and the fact that the outline is actually a many-sided polygon becomes unimportant in view of the expected smoothness of motion of the operator's hand.

From the stored coordinates of the perimeter points, it is a straightforward operation to obtain the primary measurements of the feature. First of these features is the perimeter, the sum of the lengths of the sides, each calculated as the square root of the sum of the squares of differences of the X and Y values. Next is the area (Fig. 2), obtained as the sum of areas of trapezoids bounded on one side by the line segment adjacent points and on the other by the edge of the tablet (or wherever the nominal zero coordinate lies). The area is taken as positive when the successive points increase in magnitude and negative when they decrease, so that the area outside the figure cancels and leaves the net area of the feature. This measurement is accurate even for very irregular shapes, and simple multiplication and summing is quite fast in even a small computer.

The centroid can be determined in much the same way, where the moment (product of area times center coordinate) of the individual slices are summed and divided by the total area. This determination must be made in two directions to get the X and Y coordinates of the centroid or center of gravity. Feret's diameters (Fig. 3) are projected lengths in any direction. Testing a finite number of directions, to find the maximum and minimum (length and breadth of the feature), requires a simple transformation of coordinates with a table of sine and cosine values. Usually this testing must be performed over at least 16 directions for an accurate estimate of the maximum and minimum. Long and narrow features yield substantial errors in breadth if their axis does not coincide with the direction of the measurement (Fig. 4).

Authors Hare and John C. Russ are at the Engineering Research Division of North Carolina State University, Box 5995, Raleigh, NC 27650; J. Christian Russ is at Scientific MicroPrograms, 213 Merwin Road, Raleigh, NC 27606.
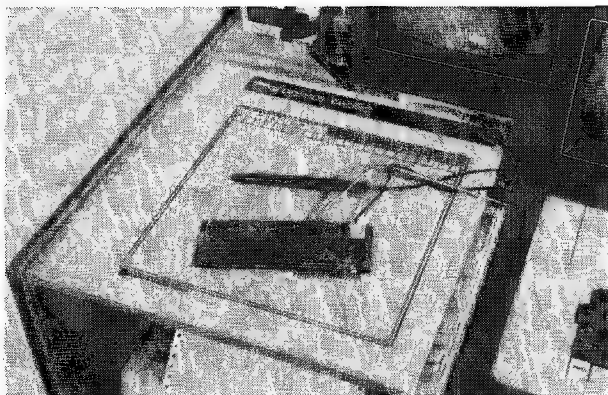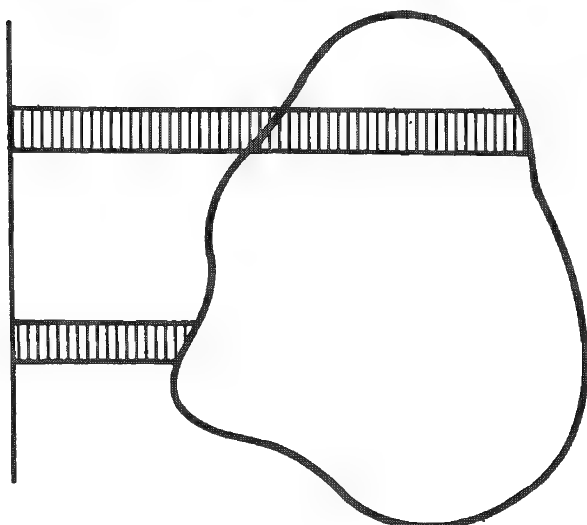
Fig. 1.--Graphics tablet and its interface.

Fig. 2.--Principle of area measurement. Areas of slices add algebraicly depending on direction of motion along perimeter, so that region outside closed feature cancels.
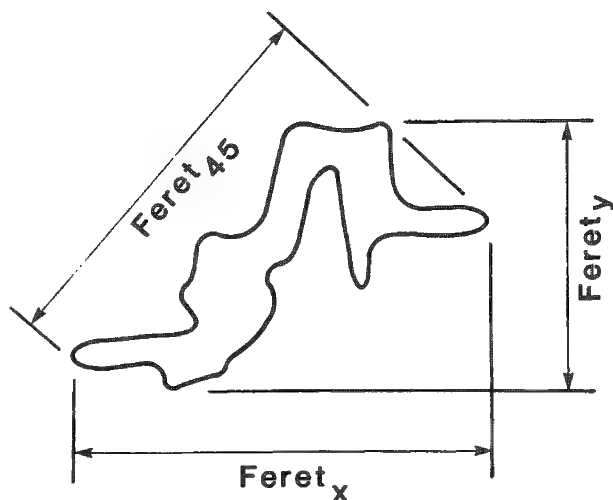

FIG. 3.--Feret's diameters, or projected lengths, are determined in various directions.

FIG. 4.--Breadth of a long narrow feature is mis-estimated by Feret's diameter if it lies at an angle to measurement direction.

Another method for finding the maximum diameter is to carry out an exhaustive search for the greatest distance between any two points. This would take prohibitively long if all combinations of hundreds or thousands of points were involved, but some simple preselection can eliminate most of the points. In Fig. 5 the box formed by two orthogonal Feret's diameters contains the feature. The arcs drawn from the center of each side, with radius equal to the Feret's diameters, defines the segments of the feature that must contain the points that lie farthest apart. Sorting through these points, initially by skipping through them and taking every fifth or tenth point, and then finally each point around an apparent maximum to find the true maximum distance, is fairly fast. Again, only multiplication and adding is necessary, as the square of the distance can be sorted and the square root need not be taken.

From these simple algorithms, the primary measurments can be obtained one feature at a time. These measurements would then be stored, typically in a file on a floppy disk, to accumulate data describing an entire image or series of images. We shall see later on a few possible secondary parameters and statistical analyses which it is useful to obtain from such measurements.

Video Images: Raster Scan Format

Scanning electron microscope images are normally obtained in raster scan format. They may or may not be acquired at actual TV rates, and for purposes of analysis it makes no difference. The physical interface required for a video rate scan is usually different from that for slow scan, and indeed the latter
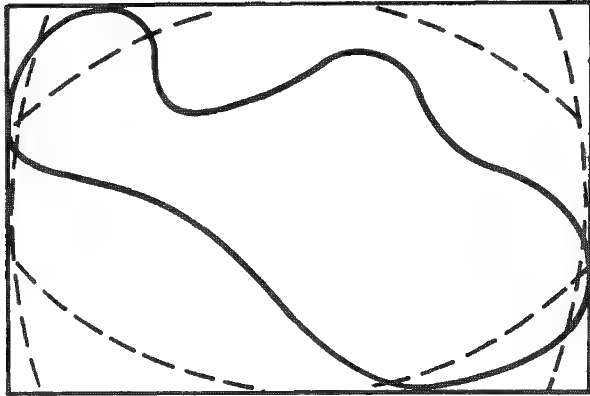
FIG. 5.--To find true maximum diameter, only points lying outside arcs drawn with two orthogonal projected lengths need be considered.
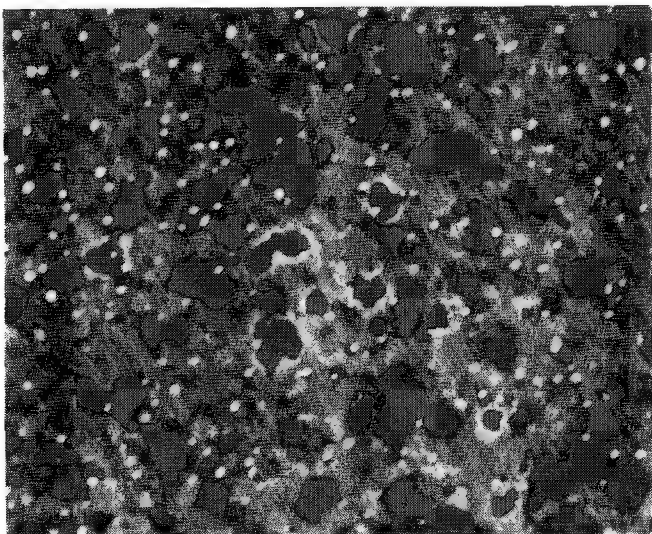

FIG. 6.--Video interface can be used with conventional TV camera to process photographs or light microscope images, or with a conventional TV signal from an SEM.

FIG. 7.--Contrast in this backscattered electron image of complex ceramic is primarily due to atomic number differences among phases.
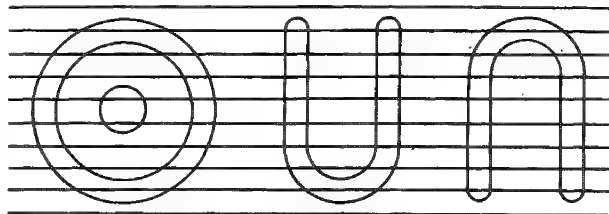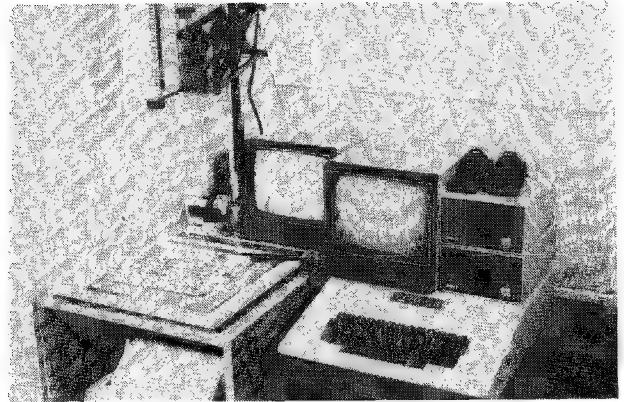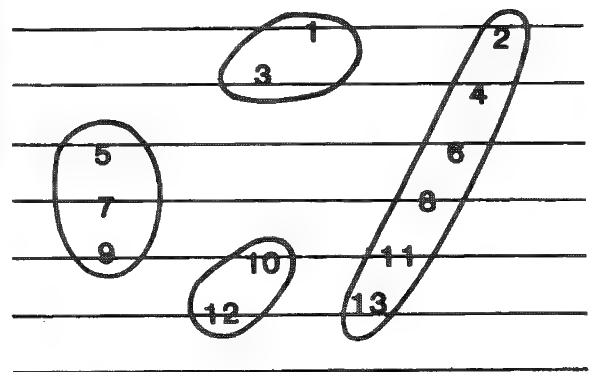

FIG. 8.--Sequence of chords obtained from raster-scanned image must be sorted out to link up ones belonging to each feature.

FIG. 9.--Various situations for joining and branching of features, which must be sorted out by logic.
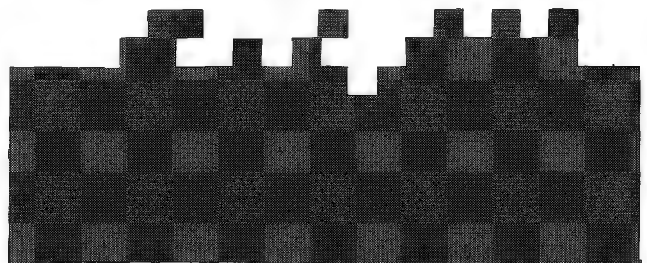

FIG. 10.--Typical rough edge, at pixel resolution level, consists of many irregularities that must be merged and accounted for.

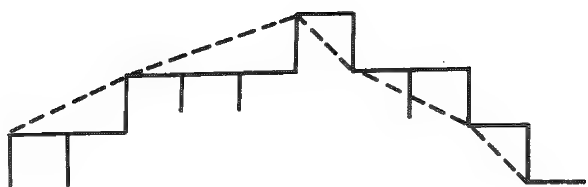FIG. 11.--Perimeter is determined by summing along dashed lines.
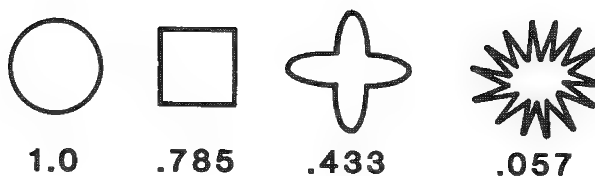

1.0   .785   .433   .057

FIG. 12.--Form factor decreases as feature shape becomes more irregular.

may allow the computer also to control the beam position, stepping it along at a speed determined by the time needed to measure the image signal adequately. With most low-cost analog-to-digital converters, this process takes 10-100 μs per picture point (pixel), so that the entire image, at a resolution of 256 × 256 points, would require a few seconds to digitize (and correspondingly longer for larger numbers of points). Video images can in principle be digitized in a single scan, but it is common to average the relatively noisy signal over several sweeps, and the computer may require some time to store away either the digitized image itself or some measured chord lengths, so that the total image digitization time is still usually a few seconds when a small computer is used. The particular image digitizer we use (Fig. 6) measures the brightness of each image point as a number from 0 to 63 (6 bits of precision) at each of 256 × 256 points on the image.

Since the computer has only 65K words of memory, it cannot store this entire image as a gray scale. Instead, it is processed as it is scanned to produce a very compact list of data in memory that represent the features of interest. This procedure requires first definition of some way of recognizing the edges of features. The most straightforward method is to have the user preselect upper and lower gray-scale or brightness levels that include the features of interest and reject the background (substrate, other features, etc.). We find with most SEM backscattered electron images that this works quite well. We use an annular, large-solid-angle detector that gives excellent atomic number contrast (Fig. 7) and can produce reasonably noise-free images at either slow scan or video rates. Our SEM is capable of scanning at true TV rates, and also of having the beam positioned by external voltages produced by the DAC/ADC interface card in the computer.

The gray-scale preselection is made with two potentiometers read by the computer as continuous repeated sweeps are made through the image and shows on the computer's high-resolution display screen the discriminated image (white pixels where the image brightness is within the selection range, black elsewhere). This display takes only 8K of memory, since only a single bit is needed for each pixel. Each sweep takes from 1/2 to several seconds, depending on the density of sampling the pixels. When a satisfactory setting to distinguish the features of interest has been found, pressing a button instructs the computer to process the image. That is done in one vertical line at a time.

The brightness at each point is measured for the same vertical position as the TV scan reaches each horizontal scan line, and the location of transitions from white to black in the discriminated image noted. These are stored as chord lengths: each chord within a feature requires three numbers, the line number, position of the start, and position of the edge. The result is a compact table easily stored within the computer or on disk, readily displayed on the computer's graphics display, and suitable for processing to obtain measurements, as will be described.

There are other methods that could be chosen to discriminate between features and background besides brightness per se. For secondary electron images, the brightness varies in complex ways with geometry and composition and cannot be easily used with a simple gray-scale test. But edges are frequently enhanced, at least for regular particles sitting on a substrate, and a derivative test, checking the difference between brightness of adjacent pixels, can sometimes be applied. The major difficulty with this approach is that the derivative is directional, following either a vertical line corresponding to the acquisition of the image as described above, or a horizontal line if that format is used to acquire the image. In either case, since the processing must be done as data are obtained and not later, with an entire stored image, features that have edges aligned nearly parallel to the acquisition direction may not be reliably detected. Storing of

a few lines at a time, to permit two-directional derivative testing, is possible in principle but slows down the data acquisition significantly. This method must be regarded as a special case of limited applicability at this time.

The same is true of methods that combine multiple signals, such as bacscattered electrons and x rays. Only practical with slow-scan positioning of the beam by the computer, it is sometimes possible to determine the elemental signature of the feature as a supplement to brightness discrimination. Generally, the extremely low count rate for x rays and the difficulty in determining the proper position for the beam on an irregular surface makes it wiser to process the brightness image first, find the location of all discriminated features, and then direct the beam back to the centers of features later for compositional classification.

Sorting Out Features

In the raster-scan image, stored as the addresses of chords in features in order of address, it is not immediately clear as to which chords belong to which features. Figure 8 shows several features whose chords would be intermixed; the identifying numbers show the order in which they would be actually stored. Logic is required to sort it out. Also, for features that are not convex, there can be protrusions that produce separate chords in the stored table that must be somehow identified as belonging to the same feature. Figure 9 illustrates this situation, with leading-edge protrusions that must be merged later, when the common identity becomes clear in processing a subsequent scan line; trailing-edge protrusions whose identity is known and which need only be summed; and features within features, which must be identified, counted, and measured separately.

The situation is complicated by the fact that feature edges are not smooth, but composed of individual pixels; where edges run nearly parallel to the scan direction, there may be extensive roughness. This crenellation (Fig. 10) produces many small chords that must be merged but whose common identity is not known when they are first encountered.

The logic for accomplishing this merging is carried out in the computer. As each chord is read from the list, it is assigned a feature number. If comparison with the preceding scan line shows that the chord touches or overlaps a chord there, then it is given the same number; otherwise it is assigned a new one. When two previously different number features are joined by a bridging or common chord in a subsequent line, the feature number for all the chords in the second set are set equal to the feature number for the first set. In this way, eventually all the chords are assigned numbers that identify the feature to which they belong. Of course, there is a practical upper limit to the number of features that can be accounted for at any one time. On a single scan line, there can be no more than 128 chords (for 256 points), and so it is never necessary to have more active identification numbers than that. Earlier features that have ended can be written away to a permanent storage region in memory or on disk, to make the identification numbers available for new features.

In addition to simply counting the identified features, we usually wish to measure them. The area is directly obtained as the total number of pixels, converted to real dimensions by a magnification factor previously entered (by the user entering the distance between two identified points in the image). Similarly, the centroid location can be found by simple addition of the chord lengths times their coordinates, to get the average X and Y positions. For nonconvex features this process may give a location that is not within the boundaries of the feature, and may therefore be worthless for re-positioning to measure x ray or other compositional information.

The perimeter of the features can be well approximated by summing of the lengths of hypotenuses of triangles formed by each set of chord ends, as shown schematically in Fig. 11. Additional complexities arise when consecutive chords on one raster line become part of the same particle via a "bridging" chord, and special flags must be set to handle this and other special situations such as the end of a particle. Also, each set of chord end points can be transformed into several rotated coordinate systems to find the extreme points, and find the Feret's diameters to get the particle length and breadth. We have found 16 directions (about every 11°) to be an acceptable compromise between speed of processing and memory storage requirements on the one hand, and the problem of error in the minimum breadth measurement for very long, narrow features on the other, as was mentioned before. The area, perimeter, length, breadth, orientation (angle of the maximum Feret's diameter) and perhaps location of each feature are saved on disk for subsequent processing.

Before these measurements are carried out, it is sometimes useful or necessary to modify the raw image. Rough edges can be smoothed by a process known as "plate and etch." First any black pixel with four or more (out of eight possible) white neighbors is made white. Then any white pixel with more than four black pixels is made black. This process (which can be altered in subtle ways by changes in the number of neighbors required in the two tests) first fills in small irregularities and then erases small protrusions, leaving smoothed edges.

Another image-modification process is to fill all holes. This process is particularly useful with SEM images of particles, which may have holes in the center of the discriminated featrues. The hole-filling process is not trivial, and consists of first inverting the image and finding all features in that image that do not touch the edges. These features must be the insides of bounded regions in the original image, and hence should be added to the original. After that is done, holes are filled in. This modification also wipes out any features within features, of course, and should not be used except when appropriate.

There are also some case in which manual modification of the image is desired, particularly when it is necessary to separate features that ouch each other. (Even if only at a single pixel, this touching would cause the same feature number to be assigned to all the chords, and consequently for the area, perimeter, and so forth to be added together as a single feature.) Manual modification is also useful when a particular feature may have a protrusion or other region that appears in the image to be disconnected, so that one can manually provide the connection that was omitted in the digitized image, possibly because the joining region was different in brightness or too small to be resolved in the fairly low-resolution digitized image. These modifications are carried out by enlargement of any segment of the image on the computer screen, so that individual pixels are apparent, and allowing the operator to position a cursor with a joystick and press a button to turn the pixel either white or black.

Derived Parameters and Statistics

From files of the primary, feature-specific measured data stored on disk, calculation of derived or secondary parameters can be carried out afterward. The nature and possible complexity of derived parameters constitutes the field of stereology: the derivation of three-dimensional parameters from two-dimensional information.[1,2] For instance, a form factor can be defined as the ratio of 4π times area divided by perimeter squared. This value gives, in qualitative terms, the relative amount of inside as compared to outside. It is exactly unity for a perfect circle, and becomes smaller and smaller for more irregular shapes (Fig. 12). This method can be used to estimate the true surface area of irregular shapes (see below). Another form factor that is sometimes used is the aspect ratio, the ratio of the length to breadth of the feature. This is important in choosing a model of proper shape to estimate size distributions.

Two fundamentally different kinds of images are encountered in SEM work. One is of particles on top of a substrate, in which we see the projected area of the particles. It may be reasonable to assume that the height of the particles is comparable to their breadth, although for flat platelets such as some clay minerals that may not be the case. By making a few assumptions about the shape of particles, one can often estimate the volume and surface area, which are generally of greater interest than the measured parameters. The volume can be estimated, for instance, as the volume of an ellipsoid of revolution whose major axis is the length (longest Feret's diameter) of the projected feature, and whose minor axis is either the breadth (minimum Feret's diameter), or another minimum diameter such as the minor diameter of an ellipse with major axis equal to the measured length and area equal to the measured area. From this volume, it is common to take an "equivalent spherical diameter" as the diameter of a sphere of equal volume.

For many purposes, the surface area can be adequately estimated as the surface area of the ellipsoid divided by the form factor (which estimates the additional surface due to local irregularities). This is an imperfect model, which can be off by factors of 50% or more for extreme particle shapes (such as tetrahedra), and furthermore ignores very small scale roughness that is hidden in the projection of overlapping of other protrusions from the particle surface. Nevertheless, it has proved to be useful in many routine applications where surface area is a factor of prime concern.

514

CUMULATIVE LOG NORMAL FOR AREA
AS FCN OF DIAM (UNITS=PIXEL)
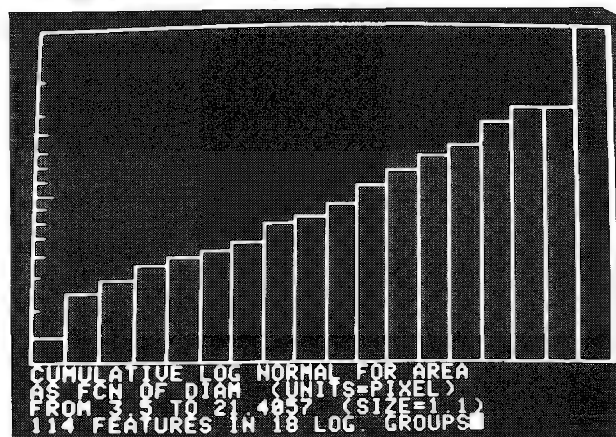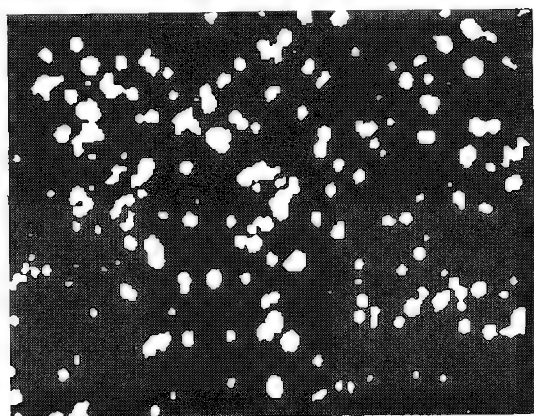FROM 3.5 TO 21.4857 (SIZE=1.1)
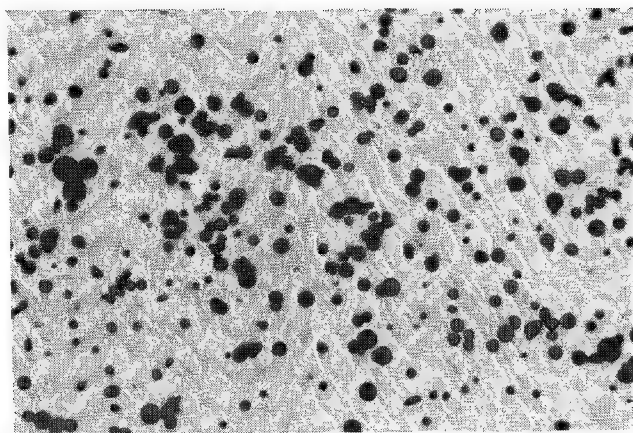114 FEATURES IN 18 LOG. GROUPS

FIG. 13.--Log-normal distribution is commonly observed for particle diameters, volumes, and surface areas.

Distribution plots of number of features versus equivalent spherical diameter (for instance) usually show a log-normal trend. So do plots of the total volume of particles summed for particles in each size class based on diameter, or of total surface area. Programs to plot such distributions are an integral part of the software package we use for this application. The plots appear on the computer's graphics display (Fig. 13 has an example) and may also be printed out on a graphics printer attached to the system.

The examination of flat surfaces that section through a microstructure of dispersed phases in a solid presents a very different set of measurement problems, which are the subject of entire textbooks and symposia. Consider the measurement of either inclusions or porosity in a bulk solid. The area of features presented on the section is not the maximum or projected dimension of the actual inclusion, pore, or phase. Indeed, it is always less. The most common assumption is that all the features that have been measured are sections of spheres, and from this assumption one obtains the size of the three-dimensional particles that would correspond. For various complex shapes it is possible to compute the probability of measuring a section of any particular fractional size, and so tables of coefficients have been determined that convert a size distribution of measured features to one for the presumed shapes. However, to apply the transformation it is necessary to choose the proper shape to model the dispersed phase. The choice between prolate spheroids (used as models for tubular or fibrous shapes) and oblate spheroids (used as models for disks and plateletes) must be based on what can be observed in the section, unless the operator has independent knowledge of the microstructure. However, sections through either kind of spheroids produce ellipses in the section. The distinction can be made because for prolate spheroids, the diameter of the most equiaxed section observed is close in size to the minor diameter of the most unequiaxed section, whereas for oblate spheroids the diameter of the most equiaxed section observed is close to the major diameter of the most unequiaxed. An adequate number of features must be observed for this test to make sense, which is one of the reasons we need to use the computer in the first place.

Many other parameters of stereological interest, such as the spacing of plates, mean distance between features, fiber cross-sectional variations, number of features per unit volume, surface area per unit volume, and so forth, can also be obtained from the database described. Also, extensive statistical analysis programs to report mean and variance, as well as distribution, to find correlations between variables, or functional relationships

(including linear, log, or polynomial fitting), and to carry out multiple regression, analysis of variance, and so on, are included. These parameters are all well within the capabilities of a small computer, limited primarily by the speed with which large disk files can be read.

The programs that digitize the image (either from the interface to the standard TV image or from a slow-scan DAC/ADC card) and which convert it to chord length tables, or which accept the input from the graphics tablet as the user moves the stylus to outline features, are in machine language for speed. So are the routines to determine area, perimeters, and so forth for either the chord length encoded images from raster scan entry, or the perimeter lists from the graphics tablet input. The data analysis programs are all written in standard Basic, for ease of handling disk files, for ease of adapting to particular needs that may arise, and for the built-in documentation provided by variable names and REMark statements.

References

1. E. E. Underwood, *Quantitative Stereology*, Reading, Mass.: Addison-Wesley, 1970.
2. E. R. Weibel, *Stereological Methods*, New York: Academic Press, 1979/80.

COMPUTER GRAPHIC ANALYSIS OF ELECTRON MICROGRAPHS AS A TAXONOMIC TOOL

Caroline Schooley, C. S. Hickman, and W. C. Lane

Shape is frequently important in taxonomic discrimination. In molluscan taxonomy shape traditionally has been described in qualitative terms; however, classical shape description vocabularies are rife with ambiguity.

In order to make quantitative and statistical analyses of both inter- and intra-species variation, it is necessary to develop a vocabulary of quantitative shape descriptors. Quantification of morphology in molluscan systematics has involved primarily morphometric analyses, in which comparisons are made of linear distances between homologous points or landmarks.[1-3] There is a large body of literature dealing with shape description, both for morphology with obvious landmarks and for forms lacking reliable homologous landmarks. It is possible, particularly with the aid of computer, to describe shape without reference to landmarks. This capability is particularly important for describing curvatures and can be done easily from digitized photographic images.

In fact, the capabilities for storing and analyzing complex three-dimensional morphology need not even involve intermediate photographic images. Hardware and software have developed to the point where computers can be programmed to examine objects directly. The use of these more sophisticated forms of technology awaits collaboration between taxonomists and computer software specialists in major academic and industrial settings.

However, the proliferation of low-cost, easy-to-use microcomputers has placed an important taxonomic tool in schools and homes throughout the country. Three-dimensional data from paired stereo micrographs can be analyzed and stored in a variety of ways.[4,5] And special-purpose graphic analysis programming provides a ready-made set of tools for the taxonomist who lacks programming skills.[6]

As a test and simple illustration of the potential of computer-graphic analysis in molluscan research, we selected a stereo pair of the radula of an unusual limpet. The animal is an undescribed species of the genus *Pectinodonta* Dall, 1882, a group of deep-sea limpets that live on water-logged wood and ingest wood using a highly modified form of radula. The curvature of the teeth is of potential importance not only in taxonomic characterization of the new species but also in understanding the mechanical function of the booth as an inferred wood rasp.

A direct lateral view of the curvature of an individual tooth is not possible from the flat-mounted specimen illustrated in Fig. 1. We used the information contained in the stereo pair to plot the curvature on the computer video display and then asked the computer to determine the equation for the curve. This equation provides a description of shape as a set of coefficients of a best-fit power series curve that can be stored numerically. A scanning electron micrograph of a separate preparation (Fig. 2) provides a check on the computer results.

Methods

The computer used is an Apple II equipped with two disk drives, video display, and a graphics tablet (Apple Computer, Inc., Cupertino, Calif.). The Apple Topographic Analysis Program (Scientific Microprograms, Raleigh, N.C.) was modified for our application by Lane Associates (5324 Selma, Fremont, Calif.). Although the same task can be

accomplished with a simpler microprocessor-linked planimeter,[7] we prefer the Apple system because of its great versatility; the same system can perform a wide variety of laboratory tasks.
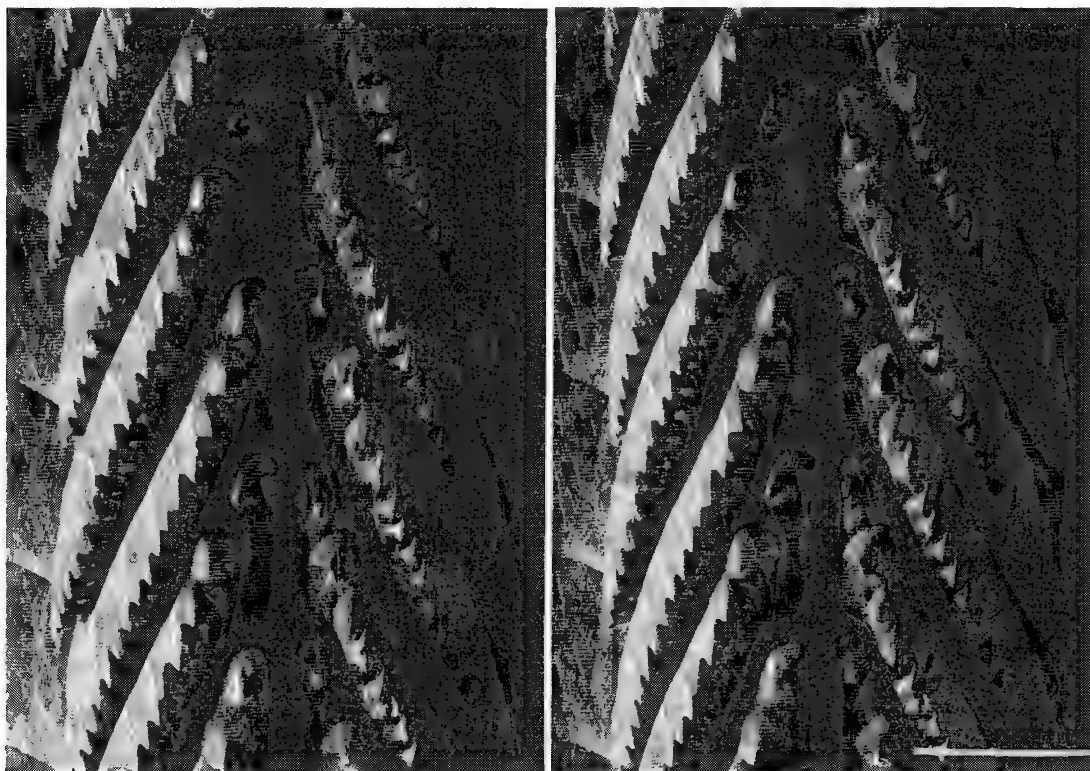

FIG. 1.--Stereo micrographs of flat-mounted radula of undescribed species of the wood-eating limpet *Pectinodonta*. Angular separation of micropgraphs, 7°, bar = 100 μm.

Figures 1 and 2 were placed on the graphics tablet and information on the scale and angular separation of the stereo (7°) were entered into the computer. By use of the graphics tablet stylus, the X-Y coordinates of corresponding points on the top of a selected tooth were then entered. The lateral displacement (parallax) of a point in a stereo pair is determined by its Z-axis height.[5,8] After all points were entered, the computer was asked to: (1) plot their Z-axis location, (2) fit a curve to the points as they lay along the crest of the tooth, and (3) display the coefficients of that curve.

Results

Figure 3 shows the plot of the tooth curvature as it appears on the computer video display for comparison with the curvature of the dissected individual tooth in Fig. 2. The
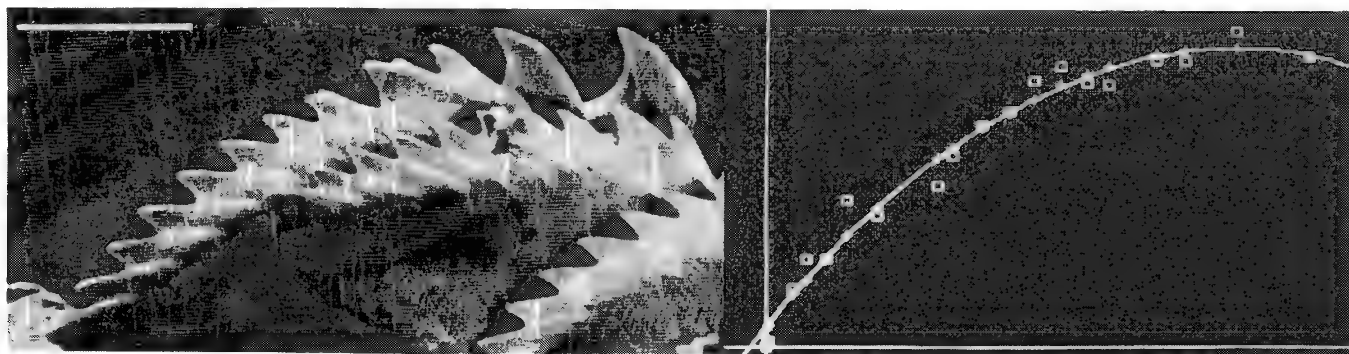

FIG. 2.--Side view of a preparation of a single tooth, illustrated at the same magnification as the video display plot in Fig. 3.

FIG. 3.--Plot of curvature of individual tooth from computer video display for comparison with actual curvature of tooth in Fig. 2.

small size of the paired micrographs (8 × 11 cm) and the limited resolution of the Apple graphics tablet produces a point spread that could be reduced by use of larger prints and a better digitizer, either purchased or user-built.[7,9] However, the computer-generated curve shows an obvious correspondence to the curve of the dissected tooth. The computed coefficients, $A(0) = 5.492$, $A(1) = 0.660$, and $A(2) = -0.001$, allow straight-forward storage of the curve in the computer along with other taxonomic data. The equation into which these are fitted to produce the curve is:

$$y = \sum_{n=0}^{\infty} A_n x^n$$

Implications

The illustration provided here has several important implications for molluscan taxonomists. First, shape description has, in the past, and particularly for curves and complex shapes, been verbal and highly subjective.[10] It can be described in simple mathematical terms and stored for subsequent analyses, such as comparisons of homologous shapes in other individuals or taxa. For the wood-ingesting limpet *Pectinodonta*, which has a radula that differs markedly from the typical radula of other similar limpets, curvature of the unusual, serrate, diagonally arrayed teeth is expected to be helpful in subsequent analysis of tooth function relative to feeding substrates. It will also be very useful to know whether the curvature varies among species of *Pectinodonta*, or (as one might predict if curvature is tightly correlated with function as a wood rasp) if it is constant within the genus.

Second, precise descriptions of shape can be derived from stereo photographs or stereo scanning electron micrographs of complex three-dimensional objects. Scanning electron micrographs provide the standard method of storing a great deal of two-dimensional data about very small objects. But inferences of depth and contour in scanning electron micrographs are subjective, and a single micrograph is not a good source of quantitative information. Stereo micrographs are essential to an understanding of radular morphology,[11,12] but interpretations remain subjective: quantification from stereo pairs is not and easy matter without the aid of computer graphics.

Perhaps the greatest potential of the computer graphics revolution with respect to taxonomic analysis from stereo pairs is the freedom that it allows to view small complex objects from alternative vantage points. In this study, we simply recorded points on a selected line and obtained a curvature, which enables us to see a tooth from the side rather than from a top view. If additional points are plotted, entire objects can be mapped and viewed from a variety of other angles. Dimensions, areas, and volumes can be obtained, stored, and compared.

The software used in this analysis is also capable of the same kind of analysis by use of serial sections in place of stereo photographs. Several other available pre-written programs can provide stereological analysis[7,13] and/or three-dimensional reconstruction for serial sections,[13] but we know of no other that accepts stereo pair data.

Taxonomists traditionally have spent a great deal of time in both the measurement of specimens and in the analysis of measurements. Computer graphic techniques not only offer important shortcuts in the analysis of quantitative data, they can also facilitate the time-consuming process of making measurements in the first place.

References

1. L. Galler and S. J. Gould, "The morphology of a 'hybrid zone' in *Cerion:* Variation in clines, and an ontogenetic relationship between two species in Cuba," *Evol.* 32: 714-727, 1979.

2. S. J. Gould et al., "Genetics and morphometrics of *Cerion* at Pongo Carpet: A new systematic approach to this enigmatic land snail," *Syst. Zool.* 23: 518-535, 1974.

3. A. J. Kohn and A. C. Riggs, "Morphometry of the *Conus* shell," *Syst. Zool.* 24: 346-359, 1975.

4. F. J. Minter and R. C. Piller, "A computerized graphical method for analyzing stereo photo-micrographs," *J. Microscopy* 117: 305-311, 1979.

5. S. G. Roberts and T. F. Page, "A microcomputer-based system for stereogrammatic analysis," *J. Microscopy* 124: 77-88, 1981.

6. L. G. Briarty and P. J. Fischer, "A general-purpose microcomputer program for stereological data collection and processing," *J. Microscopy* 124: 219-223, 1981.

7. L. D. Peachey, "A relatively inexpensive microprocessor-linked digital planimeter for electron microscopic morphometry," *Proc. EMSA* 39: 266-269, 1981.

8. P. G. T. Howell and A. Boyde, "The use of an X-Y digitizer in SEM photogrammetry," *Scanning* 3: 218-219, 1980.

9. N. Atkins and E. Castro-Cid, "A homebrew graphics digitizer," *Byte* 7: 22-84, 1982.

10. C. S. Hickman, "Bathyal gastropods of the family Turridae in the early Oligocene Keasey Formation in Oregon, with a review of some deep-water genera in the Paleocene of the Eastern Pacific," *Bulls. Amer. Paleont.* 70(292): 119, 1976.

11. C. S. Hickman, "Integration of electron scan and light imagery in study of molluscan radulae," *The Veliger* 20(1): 1-8, 1977.

12. C. S. Hickman, "Gastropod radulae and the assessment of form in evolutionary paleontology," *Paleobiology* 6: 276-294, 1980.

13. P. B. Moens and T. Moens, "Computer measurements and graphics of three-dimensional cellular ultrastructure," *J. Ultrastructure Res.* 75: 205-217, 1981.

AN EXPANDABLE OPERATING SYSTEM FOR ON-LINE ANALYSIS OF SINGLE-CRYSTAL ELECTRON DIFFRACTION DATA

P. Fraundorf

Crystal structure determination and analysis based on the techniques of electron diffraction has traditionally been the province of electron microscopists with a background in crystallography. Given the recent widespread juxtaposition of computers and transmission electron microscopes, that need no longer be the case. In fact, with suitable software it is possible to accord to structure analysis, via electron diffraction, the simplicity and on-line convenience already common to compositional analysis via energy-dispersive x-ray (EDX) analysis. However, a fundamental difference exists between applications for compositional and structural analysis. In the former case, the final goal for analysis of a single region is determination of composition. In the latter case, determination of the crystallographic structure of the specimen, and its orientation in the microscope, is often only a first step in the analysis process. One way in which this difference might be reflected in the design of an expandable operating system for single-crystal diffraction analysis is discussed here.

Determination of an Oriented Basis Triplet

As suggested above, applications for crystallographic structure analysis can be conveniently broken into two categories. The first, identification of the basic crystal structure and its orientation in the microscope, is analogous to determination of composition from an EDX spectrum. The output of such an analysis is conveniently expressed as a 3×3 matrix of coordinates for the crystallographic basis vectors in a system referenced to the specimen stage. We refer to this matrix here as an oriented basis triplet (OBT). Two efficient algorithms for determining the OBT of an unknown crystal have recently been described in the literature.[1] A simpler algorithm for determining the OBT for a known crystal has also been published.[2]

In analogy to the "raw" EDX spectrum, the "raw" data file for determination of the OBT for an unknown crystal would contain the observed coordinates for several diffraction spots from the crystal of interest, again in a 3-dimensional system referenced to the specimen stage. Off-line applications of such data have already been published,[3] and hardware to allow on-line input of observed spot coordinates to a microprocessor has also been described in the literature.[4,5]

Postidentification Applications

Although observed spot coordinates constitute the normal "raw" data for determination of the crystal structure and its orientation, the oriented basis triplet itself constitutes the input data for a wide range of postidentification applications. Such applications include the following.

    a. Direct or Miller indexing of arbitrary micrograph directions.

    b. Determination of micrograph coordinates for arbitrary direct and reciprocal lattice vectors.

    c. Determination of goniometer coordinates necessary to access a desired crystallographic direction.

    d. Providing indexed stereographic projections and Kikuchi line maps for the crystal,

as they might appear on the microscope screen for a given set of goniometer and lens settings.

e. Determining the relative crystallographic orientation of two crystal structures, thus for example allowing identification and indexing of twins.

f. Determining the crystallographic orientation of defects and inclusions.

g. Providing indexed convergent beam patterns for the structure, again as they might appear for a given set of goniometer and lens settings.

h. On-line simulations of defect contrast for a given set of goniometer and lens settings, to facilitate on-line identification of observed defect structures.

Conclusions

In summary, a natural division of diffraction analysis techniques into two categories is appropriate: those which operate on observed spot coordinates, and those which operate on an inferred oriented basis triplet. Refined methods for rapid determination of an oriented basis triplet promise to make approximate determination of unknown structures by electron diffraction as convenient and simple as is qualitative determination of unknown compositions by EDX analysis. But beyond that, the development of software to support more advanced on-line applications of crystallographic information has only begun.

References

1. P. Fraundorf, "Stereo analysis of single crystal electron diffraction data," *Ultramicroscopy* 6: 227-236, 1981.

2. P. Fraundorf, "Stereo analysis of electron diffraction from known crystals," *Ultramicroscopy* 7: 203-206, 1981.

3. P. Fraundorf, "Interplanetary dust in the transmission electron microscope: Diverse materials from the early solar system," *Geochim. et Cosmochim. Acta* 45: 915-943, 1981.

4. P. Hagemann, "Interfacing of a TEM/STEM system to a computer," *39th Ann. Proc. EMSA*, 1981, 250-251.

5. M. J. Carr, "Automation of electron diffraction analysis in an analytical electron microscope," *Analytical Electron Microscopy--1981*, 139-146.

IMPROVED SAMPLE CURRENT SIGNAL PROCESSING WITH AN OPTICALLY ISOLATED AMPLIFIER

J. R. Hale

On a multiple-detector microprobe system it was necessary to improve the specimen current amplifier system for imaging with lower specimen currents in the presence of power-line induced system noise. By providing for imaging with lower specimen currents, the usefulness of specimen current signals can be enhanced for working with delicate samples where high probe currents would be destructive. This signal provides the user with unique information free of detector-related orientation effects with no significant dependence on specimen working distance.[1] When the signal is used in conjunction with the secondary image, a more thorough analysis can be made of the studied specimens.[2] The experimental unit provided satisfactory performance down to 100 pA. At this level the induced ground noise was not the main limitation, but rather the noise of the active device chosen for use in the transresistance amplifier.

Preliminary Tests

Following the transresistance amplifier stage, several voltage-amplifying and video-processing stages are usually used to provide the CRT cathode with an adequate drive signal level (typically around 6 V peak-to-peak) for a satisfactory monitor display (Fig. 1). Photographs taken with the existing system below 10 nA showed an excessive amount of noise at the power-line frequency as evidenced by the vertical light and dark hum bands from top to bottom. A photo taken with the video processing amplifier input disconnected from the

$$e_1 = i_{sc} R_f$$
$$e_2 = Av_1 e_1$$
$$e_3 = Av_2(e_2 + e_n)$$
$$e_4 = Av_3 Av_2(e_2 + e_n)$$

i_{sc} : Specimen Current
i_n : Induced Noise Current
e_n : Equivalent Noise Voltage
r_w : Ground Wiring Resistance
R_f : Feedback Resistor

Legend :

$\underline{\nabla}{\scriptstyle S}$: Spectrometer Ground

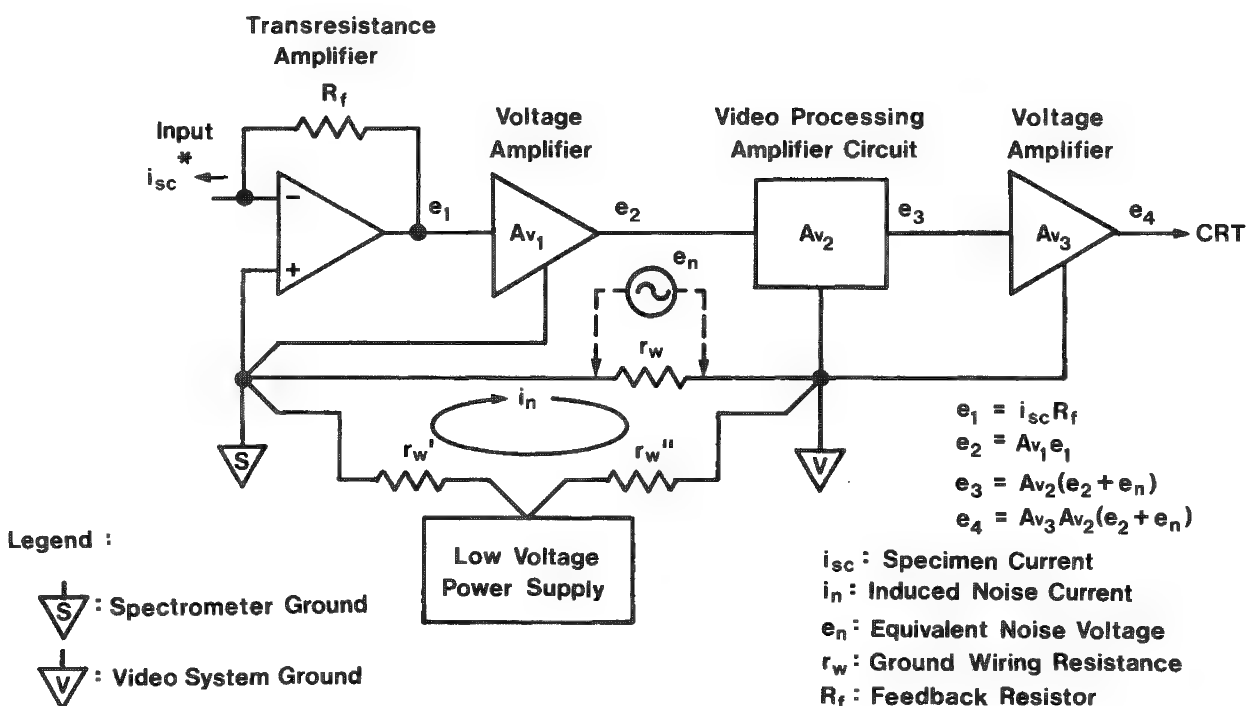$\underline{\nabla}{\scriptstyle V}$: Video System Ground

FIG. 1.--Specimen current signal amplification with direct video system-to-spectrometer ground referencing.

The author is at Bausch & Lomb, Microscopy & Image Analysis Division, 9545 Wentworth Street, Sunland, CA 91040.

preamplifier did not exhibit hum bars for an identical gain setting. To analyze the
problem further a check was made with the electron beam blanked and the preamplifier
reconnected. Again the noise was present, implying two possibilities: (a) either the
noise was capacitively coupled to the preamplifier input, or (b) it was an induced com-
ponent related to the signal grounding referencing for stages following the preamplifier.
Futher experiments with preamplifier input isolation ruled out the first possibility.

An analysis of the system ground revealed that the multiple ground connections be-
tween the spectrometer and video console (safety grounds included) made single-point
ground referencing impractical. The alternative was to break the ground referencing for
the video chain between the spectrometer ground and the video console ground, and thus to
eliminate the ground current noise component.

Design Considerations

The initial signal developed at the output of the transresistance stage with an R_f
value of 5 MΩ is around 50 mV for a specimen current of 10 nA. In the first preampli-
fier design the preamplifier output was the signal output of the transresistance stage,
which would correspond to $AV_1 = 1$ in Fig. 1. As the signal level fell below 50 mV at
the lower operating currents, the noise voltage became a larger fraction of the total
signal as seen by the console video amplifier. To deal with this problem, either the
voltage amplification at the preamplifier could be increased (which would make the induced
noise voltage smaller than the desired signal), or an optical isolation amplifier stage
could be inserted between the preamplifier and the video amplifier input. The main ad-
vantage of the second option was that the noise component was eliminated from the output
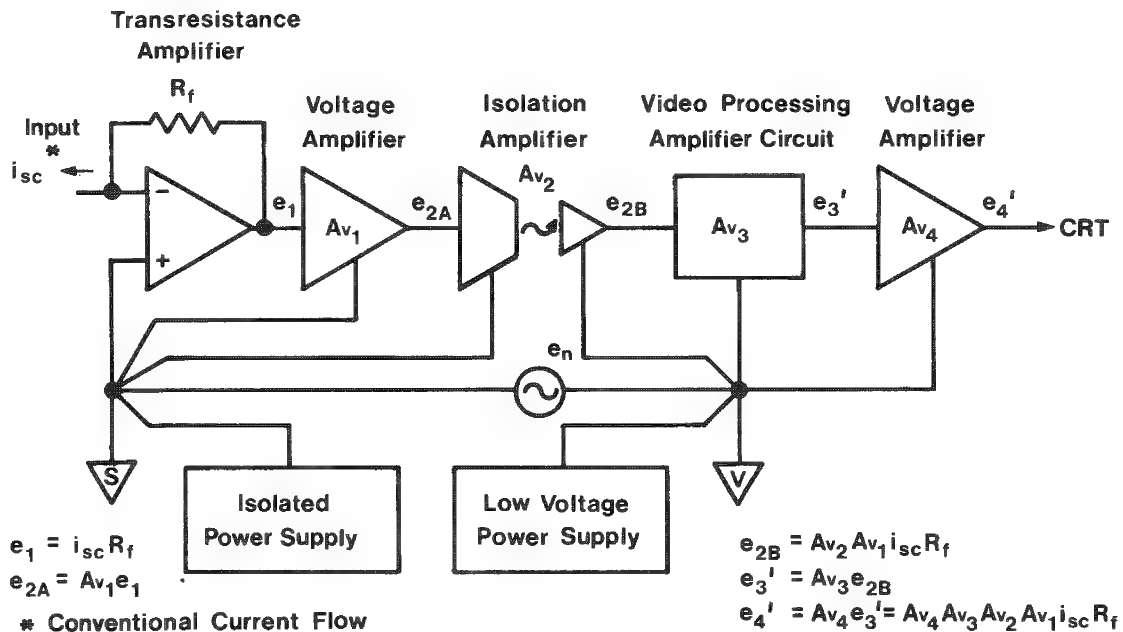signal altogether, as follows (Fig. 2).

FIG. 2.--Specimen current signal amplification with optical isolation.

Both the transresistance stage and the voltage amplifier are referenced to the spec-
trometer ground. The noise component does not enter in at this point as long as the
grounds both converge at spectrometer ground. The other two ground wires that must also
tie in at the spectrometer are the isolated power suppy ground and the isolation amplifier
driver stage ground. A single tiepoint for preamplifier ground allows the initial stages
to operate in a near ideal manner. The isolation stage allows the signal reference point
to be shifted to the video console ground. The video processing amplifier thus does not see
the noise voltage potential that exists between the two system grounds.

Preamplifier Design

The signal output of the transresistance stage is determined by the size of the feedback resistance R_f (Figs. 1 and 2), which should be as large as possible and yet small enough to maintain required bandwidth. Another consideration is amplifier device input current noise, since a high R_f when multiplied by current noise produces an output noise voltage. The gain of the voltage amplification stage following the transresistance stage also affects the choice of R_f: for a given signal output, the higher the gain the smaller R_f can be. The tradeoff is in signal-to-noise ratio. For smaller R_f lower output voltages are obtained for a given current and therefore the device noise becomes critical for both the transresistance stage and for the voltage amplifier. Selectable resistors for R_f provide for extension of the high-current operating limits of the preamplifier. At higher currents, where R_f can be reduced, the bandwidth is increased. The bandwidth of the system then depends on the performance of the amplifier's isolation stage.

Commercially marketed isolation amplifiers are available at present with bandwidths of 15-30 kHz. In the present case, an isolation circuit with optoisolators was preferred, since it offered the greatest potential for improvement of the bandwidth. Such a circuit is described by Nielsen and provides a 50kHz bandwidth with good temperature stability.[3] A similar circuit was used in the present prototype, with an observed bandwidth of about 80 kHz. Although the performance of the isolation circuit was sufficient to overcome the initial noise problem, the limited bandwidth was a shortcoming. Greater bandwidth of the isolation amplifier would provide for faster frame rates in the image display. Further experimentation with high-speed isolators in a test isolator stage recently provided a signal bandwidth of about 900 kHz. The circuit has yet to be incorporated into the main preamplifier for additional testing.

Conclusions

The concept described for use with the specimen current preamplifier provides a means for suppressing the ground-loop system noise that would otherwise make the SEM image unusable for low operating current levels. This technique may be applied to any system in which the desired signal is associated with a ground that is noisy with respect to the ground reference for a remote signal amplifier.

References

1. D. G. Coates, "Pseudo-Kijuchi oreintation analysis in the scanning electron microscope," *SEM/1969*, 27-40.

2. H. Yakowitz et al., "Implications of specimen current and time differentiated imaging in scanning electron microscopy," *SEM/1973*, 174-180.

3. A. Nielsen, "Matched optical couplers stabilize isolation circuit," *Circuits for Electronics Engineers*, 252.

PHOTOTHERMAL DETECTION OF NO_2

Horn-Bond Lin and D. U. Fluckiger

Recently an ultrasensitive photothermal technique, called phase fluctuation optical heterodyne (PFLOH) spectroscopy, has been developed for characterization of weakly absorbing species.[1-6] This technique has been used successfully for studying microwave abosrption characteristic of liquid,[1] for the time dependence of intra-molecular relaxation processes in gases,[2] and for the *in situ* trace detection of atmospheric pollutant gases[3-6] and aerosols.[7] The anticipated absorption sensitivity of a realistic narrow bandwidth (cw) version of this device appears to be less than 10^{-11} cm^{-1} (in terms of absorption coefficient), superior to that of the best previously obtained (10^{-10} to 10^{-9} cm^{-1}) by using photoacoustic spectroscopy. This superior sensitivity and the coherent detection scheme of PFLOH has merited the technique to be accessible for *in situ* characterization of weakly absorbing samples (i.e., ultradiluted sample, single aerosol particle, molecular overtone absorption and micro samples). For example: highly specific, interference-free measurements of molecular gases have been achieved when PFLOH is complemented by a Stark-effect cell[3] or gas chromatograph.[4] In addition, PFLOH has been employed to analyze aerosol absorption,[7] and similar characterization of single particles is also feasible. In this paper, we describe a new version of a PFLOH apparatus which employs visible laser radiation for sample excitation. Hence, these measurements are extended to this spectral region. Preliminary experiments on NO_2 have achieved sensitivity of one part per million and better.

PFLOH spectroscopy uses a Mach-Zehnder interferometer as a photothermal detector to detect coherently the small phase change of a single-frequency laser (a low-power He-Ne laser), which results when it passes through a transparent medium whose density (and consequently refractive index) has been changed by light absorption. In the absence of absorption saturation and thermal diffusion effects, the change in refractive index is related to the absorption coefficient (and consequently the sample concentration), the sample length, and the excitation laser intensity. However, for a given sample, the detected signal is proportional to the energy absorbed by the sample.

For trace-gas monitoring, a laser is operated at a wavelength that is strongly absorbed by the species of interest and is used to excite the sample. The change in local number density can be determined from the concomitant change in the refractive index. It is instructive to estimate this quantity and the magnitude of other quantities involved. If the excitation laser is modulated at frequency ω_m, it can be shown that the corresponding Fourier component of induced index of refraction $\Delta n(t)$ is approximated by

$$\Delta n(t) = (n - 1)I_0\alpha \, \sin(\omega_m t)/2\omega_m C_p T\rho_a \tag{1}$$

where I_0 is the cw intensity of the excitation laser, n is the refractive index of the sample, α is the absorption coefficient of the trace species at the excitation wavelength, ρ_a is the density of the sample, C_p is the specific heat at constant pressure, and T is the ambient temperature in Kelvin. Equation (1) is derived on the assumptions that I_0 is nonsaturating, that the thermal conduction time is greater than ω_m^{-1}, and that the radius of the sample cell (cylindrical symmetry) is much greater than the laser beam diameter. For example, typical values in nitrogen, are $\omega_m = 2\pi \cdot 27$ Hz, $T = 293°K$, $n - 1 = 2.92 \times 10^{-4}$, $\rho_a = 1.165 \times 10^{-3}$ $\tilde{g}$ cm^{-3}, $C_p = 1.006$ $J°K^{-1}g^{-1}$, and $I_0 = 100$ W cm^{-2}.

An amount of 1 part of NO_2 in 10^9 parts (ppb) of N_2 at 1 atmosphere excited by 488nm laser radiation results in an induced index change of $\Delta n = 1.5 \times 10^{-12}$.

A change in index of this magnitude can in fact be measured by use of a laser heterodyne interferometer. In this scheme a stable single-frequency probe beam, usually from a He-Ne laser source, is utilized in a Mach-Zehnder interferometer containing the sample in one of its arms. The He-Ne beam is split into a reference component and a component that passes through the sample which is phase modulated by the time-varying index of refraction. The sample and reference beams are heterodyned in a photodiode and the time-dependent change in the index of refractive is then detected by a lock-in amplifier. The signal from the lock-in amplifier is proportional to the magnitude of Δn as given by Eq. (1).

By the use of a photon-noise-limited single-frequency laser as a probe source, the signal-to-noise ratio (SNR) for coherent detection[8] is

$$\text{SNR} = (\eta P_s)(h\nu\Delta\nu)^{-1} \tag{2}$$

where η is the quantum efficiency of the detector, $h\nu$ is the energy per photon in the laser beam, $\Delta\nu$ is the bandwidth of the signal-processing electronics, and P_s is the signal power associated with the phase fluctuation sidebands of the laser generated by the refractive index fluctuation of the sample. For this SNR = 1, the minimum detectable change in refractive index is found of the order of 10^{-14}, which corresponds to detecting of the order of 1 ppt of NO_2.

Experimental

Our experimental apparatus is shown in Fig. 1. The Mach-Zehnder interferometer is illuminated by a single frequency He-Ne laser (Tropel model 100; λ = 66 nm). This particular laser has been shown to provide better than -35 dB (with respect to 1 µW) noise

FIG. 1.--PFLOH apparatus for visible laser radiations.

power over a 30Hz bandwidth.[9] A beam splitter divides the 633nm radiation between the reference beam and the sample beam. Both excitation beam and He-Ne beam overlap in the sample region. The excitation source is an argon-ion laser operating at 488nm and modulated by a constant-speed mechanical chopper (PAR model 25) at 27 Hz, plane polarized vertically with respect to the He-Ne beam polarization. The 488nm beam enters and leaves the interferometer via two glan polarizer prisms and two dye-laser total-reflector mirrors. The excitation intensity is set so that the nonsaturation and thermal-diffusion-time criteria are met. The small change in phase-front curvature of the sample beam is neglected as it gives rise to only second-order effects in the mixing at the PIN diode photodetector (EC&G, HAD 1000). For proper detection, the interferometer is maintained half way between constructive and destructive interference by a servo system that generates an error voltage from the dc output of the PIN diode. This voltage is used to drive a piezoelectric transducer (PZT) on one of the interferometer mirrors. A lock-in

amplifier (PAR model 128A) is used to extract the signal component at ω_m, the chopping frequency. This PFLOH device is vibrationally and acoustically isolated by means of an air suspension table (NRC model RS-510-8) and an acoustic enclosure.

Result

Our PFLOH system was calibrated by means of a 10 ppm NO_2 in pure N_2 sample. An averaged signal of 250µV was obtained with a 10cm cell and a 0.5W laser. A noise level near 0.2-0.3 µV (30s integration time) was observed. The sensitivity in this case was acoustic noise limited (SNR = 1), equivalent to a sensitivity of 10^{-7} cm^{-1}, corresponding to a detection limit of 10 ppb of NO_2. This preliminary experiment has already shown a sensitivity comparable with that in a recent report of NO_2 measurements by photoacoustic technique with a nonresonant cell.[10] Further work will be on the improvement of the vibrational isolation. An enhancement of two to three orders of magnitude in detection sensitivity can be achieved to approach photon-noise-limited performance.

In addition to the highly sensitive nature of this device, the important features of PFLOH spectroscopy may be summarized as follows:

1. PFLOH yields a signal proportional to the optical path of the sample; i.e., it is scalable.
2. In the absence of thermal blooming, the PFLOH signal depends linearly on various parameters such as sample concentrations, total pressure of the gaseous sample, and the excitation laser intensity.
3. Linear frequency dependence was observed when the excitation laser was modulated in the range $13 < (\omega_m/2\pi) < 4000$ Hz.
4. Very large dynamic range is available; i.e., spanning ppt quantities to a pure sample is possible.
5. *In situ* capabilities.

We have shown a new dimension of PFLOH spectroscopy; that is, the absorption studies of the visible light radiation and, in principle, UV and near-IR radiation absorption as well. However, the technique will not be limited to study the gas phase; it will be possible to study the absorption characteristics of weakly absorbing species of all states of matter so long as they are capable of optical probing.

References

1. C. C. Davis and M. L. Swicord, "Studies of microwave absorption in liquids by optical heterodyne detection of thermally induced refractive index fluctuations," to be published in *Radio Science*.
2. C. C. Davis, "Studies of molecular energy transfer and relaxation process by phase fluctuation optical heterodyne (PFLOH) spectroscopy," *Digest of Conference on Laser Engineering and Applications* (Optical Society of America, Washington, D.C., 1979).
3. A. J. Campillo, H.-B. Lin, C. J. Dodge, and C. C. Davis, "Stark-effect-modulated phase-fluctuation optical heterodyne interferometer for trace gas analysis," *Optics Letters* 5: 424, 1980.
4. H.-B. Lin, J. S. Gaffney, and A. J. Campillo, "Phase fluctuation optical heterodyne spectrometer as a nondestructive detector for gas chromatography," *J. Chromat.* 206: 205, 1981.
5. C. C. Davis, "Trace detection in gases using phase fluctuation optical heterodyne spectroscopy," *Appl. Phys. Lett.* 36: 515, 1980.
6. C. C. Davis and S. J. Petuchowski, "Phase fluctuation optical heterodyne spectroscopy of gases," *Applied Optics* 20: 2539, 1981.
7. A. J. Campillo and H.-B. Lin, "Photothermal spectroscopy of aerosols," *Proc. SPIE* (International Society of Optical Engineering in Laser Spectroscopy for Sensitive Detection) 286: 24-32 1981.
8. Amman Yariv, *Introduction to Optical Electronics*, New York: Holt, Rinehart and Winston, 1976, 2d ed., chap. 11, p. 307.
9. J. H. Cole, "Low frequency laser noise of several commercial lasers," *Applied Optics* 19: 1023, 1980.
10. Alan Fried and Jimmie Hodgeson, "Laser photoacoustic detection of nitrogen dioxide in the gas phase titration of nitric oxide with ozone," *Anal. Chem.* 54: 278, 1982.

Author Index

Notes